

N70-36676

(ACCESSION NUMBER)

795

(PAGES)

✓
(NASA CR OR TMX OR AD NUMBER)

N70-36758

(IMRU)

1

(CODE)

14

(CATEGORY)

FACILITY FORM 60

NASA SP-233

OPTICAL
TELESCOPE
TECHNOLOGY

A workshop held at
Marshall Space Flight Center
Huntsville, Alabama
April 29 - May 1, 1969

Prepared by the Office of Space Science and Applications



Scientific and Technical Information Division
OFFICE OF TECHNOLOGY UTILIZATION
NATIONAL AERONAUTICS AND SPACE ADMINISTRATION
1970
Washington, D.C.

PRECEDING PAGE BLANK NOT FILMED.

FOREWORD

One of the principal NASA goals is the establishment of large spaceborne astronomical observatories. Typical of the telescopes being considered for these observatories is a 3-meter (120-inch), diffraction-limited instrument, which can observe over a wide range of the electromagnetic spectrum, particularly those portions not visible to earthbound telescopes. Such a telescope above the earth's obscuring atmosphere would have 10 times the resolving power of the 200-inch telescope on Mount Palomar operating under the best atmospheric conditions. In addition, the large space telescope would be able to detect stars 100 times fainter than the faintest stars detectable from earth.

An instrument exhibiting such a significant increase in operating performance has a commensurate increase in complexity. Thus, undertaking the design and development of large space observatories requires the consolidated effort of both scientific and engineering skills. A prerequisite to a space observatory is the optical telescope technology that must be accomplished prior to the initiation of the actual design. Many technological developments will be required to improve the instrumentation; for example, improved gratings, lightweight optical mirrors, improved detectors, electronic imaging systems, and ultraviolet transparent materials, to name but a few.

It is to this objective that the Optical Telescope Technology Workshop (OTTW) is addressed. This workshop is a joint undertaking by the Office of Advanced Research and Technology and the Office of Space Science and Applications to assess the present state of the technology, as well as to define specific technological objectives and the research programs required to meet them. We plan to continue this OTTW activity to update the work at intervals of from two to three years.

We would like to express our sincere appreciation to the participants and their organizations for making this first meeting so successful.

John E. Naugle
Associate Administrator,
NASA, Office of Space Science and Applications

Oran W. Nicks
Acting Associate Administrator,
NASA, Office of Advanced Research and Technology

PRECEDING PAGE BLANK NOT FILMED.

CONTENTS

	PAGE
<i>Foreword</i>	iii
<i>WELCOME ADDRESS</i>	1
WERNHER VON BRAUN	
<i>INTRODUCTION</i>	3
JESSE L. MITCHELL	

SESSION I

The Use of Space Telescopes in Observational Astronomy

Chairman: Marcel J. Aucremanne

<i>NASA GOALS AND OBJECTIVES</i>	5	✓
NANCY ROMAN		
<i>THE FUTURE OF PHOTOMETRY AND SPECTROPHOTOMETRY IN SPACE ASTRONOMY</i>	13	✓
ARTHUR D. CODE		
<i>THE ROLE OF SURVEYS IN SPACE ASTRONOMY</i>	17	✓
KARL G. HENZE		
<i>INFRARED OBSERVATIONS IN SPACE ASTRONOMY</i>	25	✓
GERRY NEUGEBAUER		
<i>HIGH-RESOLUTION MEASUREMENTS IN SPACE ASTRONOMY AND THE REQUIREMENTS FOR DIFFRACTION-LIMITED OPTICS</i>	33	✓
LYMAN SPITZER, JR.		

SESSION II

Review of Current Technical Status

Chairman: Henry L. Anderton

<i>TECHNOLOGY OBJECTIVES AND PLANS</i>	39	✓
FRANK J. SULLIVAN		
<i>THE OAO SERIES OF SPACE TELESCOPES</i>	41	✓
JOSEPH PURCELL		

	PAGE	
<i>ONE CONCEPT FOR A 3-METER-CLASS SPACE TELESCOPE</i>	55	✓
DAVID BOGDANOFF		
<i>OPTICAL MATERIALS AND PRIMARY MIRROR DESIGN</i>	65	✓
RODERIC M. SCOTT		
<i>STRUCTURES FOR SPACEBORNE OPTICAL TELESCOPES</i>	69	✓
ERICH F. ENGLER		
<i>A SURVEY OF PRECISION-POINTING SYSTEMS</i>	73	✓
DOUGLAS C. FOSTH		
<i>CONSIDERATIONS RELATING TO USE OF A LARGE ASTRO- NOMICAL TELESCOPE IN SPACE</i>	83	✓
JOHN STRONG		
<i>PHOTOELECTRONIC IMAGING DEVICES</i>	89	✓
SOL NUDELMAN		
<i>SPACE SCIENCES DATA-HANDLING AND MISSION OPER- ATIONS</i>	103	✓
GEORGE H. LUDWIG		
<i>CALIBRATION, SIMULATION, AND TESTING OF LARGE ORBITING STELLAR OBSERVATORIES</i>	113	✓
JAMES L. DIGGINS		

SESSION III

In-Depth Reviews in Key Technical Areas

GROUP A - GENERAL SESSION ON MIRRORS AND OPTICAL MATERIALS

Chairman: Hector C. Ingrao

<i>LENS DESIGN BY LARGE COMPUTERS</i>	133	✓
DAVID S. GREY		
<i>POSSIBILITIES FOR AUTOMATING OPTICAL MANUFACTURE</i>	137	✓
ROBERT R. SHANNON		
<i>MATERIALS CONSIDERATIONS FOR LARGE SPACEBORNE ASTRONOMICAL TELESCOPES</i>	141	✓
JOHN B. SCHROEDER		
<i>PROBLEMS IN ADAPTING SMALL MIRROR FABRICATION TECHNIQUES TO LARGE MIRRORS</i>	149	✓
HOWARD D. HALL		

	PAGE	
<i>SURFACE SMOOTHNESS OF LARGE ASTRONOMICAL MIRRORS: A COLLECTION OF FOUCAULTGRAMS</i>	153	✓
DONALD A. LOOMIS		
<i>ELECTROFORMING OF LARGE MIRRORS</i>	165	✓
F. J. SCHMIDT		
GROUP A - SPECIAL SESSIONS ON MATERIALS, FIGURING, AND OPTICAL DESIGN		
<i>Group A1 - Materials, Mirror Structure, and Fabrication</i>		
<i>Chairman: Francis W. Niedenfuhr</i>		
<i>ISOTROPIC BERYLLIUM FOR MIRROR BLANKS</i>	173	✓
JOHN W. MOBERLY AND HENRY M. BROWN		
<i>THE EFFECTS OF PROCESSING ON THE DIMENSIONAL STABILITY OF BERYLLIUM MIRRORS</i>	181	✓
ROBERT E. MARINGER		
<i>PORE-FREE CERAMICS MADE BY SINTERING</i>	189	✓
J. E. BURKE		
<i>DIMENSIONAL CHANGES IN GLASS AT ROOM TEMPERATURE</i> .	191	✓
J. E. BURKE		
<i>ULE TITANIUM SILICATE FOR MIRRORS</i>	195	✓
CHARLES F. DEVOE		
<i>MIRROR MATERIALS</i>	201	✓
MARVIN C. RIGGERT AND ROBERT F. COPPER		
<i>SHEAR STRAIN PROPERTIES TO 10⁻¹⁰ OF SELECTED MIRROR MATERIALS</i>	207	✓
WILLIAM A. EUL AND W. WILLIAM WOODS		
<i>DEGRADATION OF MIRROR SURFACES IN A PROTON ENVIRONMENT</i>	213	✓
E. L. HOFFMAN		
<i>THE DESIGN OF LIGHTWEIGHT CER-VIT MIRROR BLANKS</i>	219	✓
GEORGE A. SIMMONS		
<i>LIGHTWEIGHT MIRROR STRUCTURES</i>	241	✓
ERIC Y. LOYTTY		

	PAGE	
<i>APPLICATION OF FINITE ELEMENT TECHNIQUES TO THE DESIGN AND MANUFACTURE OF ASTRONOMICAL MIRRORS</i>	249	✓
KETO SOOSAAR		
<i>SELF-WEIGHT LOADED STRUCTURES IN THE CONTEXT OF LIGHTWEIGHT MIRROR APPLICATIONS</i>	257	✓
J. P. DUNCAN		
<i>MAIN MIRROR FOR A 3-METER SPACEBORNE OPTICAL TELESCOPE</i>	281	✓
WILHELM ANGELE		
<i>STRUCTURAL DEFORMATION OF AN ORTHOTROPIC PLATE</i>	283	✓
FRANCIS W. NIEDENFUHR		
<i>TRANSVERSE DEFLECTIONS OF A 45-INCH-DIAMETER, LIGHTWEIGHT MIRROR BLANK: EXPERIMENT AND THEORY</i>	287	✓
W. P. BARNES		
<i>Group A2 - Surface Generation and Figure Sensing</i>		
<i>Chairman: F. Dow Smith</i>		
<i>EVALUATION OF SURFACE FIGURE DURING MANUFACTURING</i>	291	✓
JERROLD ZIMMERMAN		
<i>FIGURE SENSING TECHNIQUES</i>	297	✓
ROBERT CRANE, JR.		
<i>ACTUATORS FOR ACTIVE OPTICS</i>	303	✓
GORDON J. WATT		
<i>SHOP SUPPORTS FOR THE 150-INCH KITT PEAK AND CERRO TOLOLO PRIMARY MIRRORS</i>	307	✓
NORMAN COLE		
<i>HOLOGRAPHIC METHOD OF MONITORING THE PERFORMANCE OF A LARGE TELESCOPE MIRROR</i>	311	✓
KENT E. ERICKSON		
<i>FIGURE CONTROL OF ACTIVE PRIMARY MIRRORS</i>	315	✓
DUNCAN MACKINNON		

Group A3 - Optical Design

PAGE

Chairman: Willem Brouwer

SOME OPTICAL SYSTEMS FOR A SPACEBORNE TELESCOPE . . . 321 ✓
 ABE OFFNER

FIELD CORRECTORS FOR REFLECTING TELESCOPES 327 ✓
 DANIEL H. SCHULTE

*BEHAVIOR OF STRUCTURAL JOINTS AND ASSEMBLIES
 UNDER THERMAL ENVIRONMENT* 335 ✓
 RONDAL G. CRAWFORD

GROUP B - STRUCTURES*Chairman: Josef F. Bluzarich*

STRUCTURAL DESIGN FOR LARGE SPACE TELESCOPES 351 ✓
 BAILEY W. JACKSON

THERMAL DESIGN OF A SATELLITE TELESCOPE 359 ✓
 JERRY ROGOVIN AND N. KOSOWSKI

GENERAL PHILOSOPHY OF MIRROR SUPPORT SYSTEMS 381 ✓
 W. W. BAUSTIAN

*CONSIDERATIONS IN THE DESIGN OF ORBITAL TELESCOPES
 FOR DYNAMIC ENVIRONMENTS* 389 ✓
 C. E. LIFER AND R. E. JEWELL

*THERMAL DEFORMATION PREDICTION IN ORBITING OBSER-
 VATORY STRUCTURES* 401 ✓
 JAMES B. MASON

*CONSIDERATIONS ON PRECISION TEMPERATURE CONTROL
 OF A LARGE ORBITING TELESCOPE* 417 ✓
 SAMUEL KATZOFF

GROUP C - POINT AND STABILIZATION*Chairman: William E. Howell*

*CONTROL SYSTEMS FOR LARGE SPACECRAFT REQUIRING
 PRECISE STABILIZATION* 425 ✓
 WILLARD W. ANDERSON

*STABILIZATION AND CONTROL OF THE APOLLO TELESCOPE
 MOUNT* 437 ✓
 WILLIAM B. CHUBB

x

	PAGE	
<i>STABILIZATION AND CONTROL FOR THE OAO SPACECRAFT SERIES</i>	449	✓
K. W. JENKINS		
<i>STAR TRACKER SYSTEMS</i>	457	✓
LUDWIK I. SEIFERT		
<i>PRECISION POINTING OF LARGE APERTURE, DIFFRACTION-LIMITED SPACE TELESCOPES</i>	465	✓
HERBERT F. WISCHNIA		
<i>CONTROL TECHNOLOGY FOR LARGE ORBITING TELESCOPES</i>	473	✓
GORDON F. BULLOCK, FREDERICK R. MORRELL, AND AARON J. OSTROFF		
GROUP D - INSTRUMENTATION		
Co-Chairmen: James E. Milligan and Kenneth L. Hallam		
<i>THE REQUIREMENTS, DESIGN, AND MANUFACTURE OF OPTICAL GRATINGS FOR SPACE TELESCOPES</i>	485	✓
JOHN STRONG		
<i>THE REQUIREMENTS, DESIGN, AND MANUFACTURE OF OPTICAL FILTERS FOR ASTRONOMICAL SPACE TELESCOPES</i> ..	487	✓
DANIEL J. SCHROEDER		
<i>THE SPACE RADIATION ENVIRONMENT IN LOW ALTITUDE AND LOW INCLINATION ORBITS</i>	495	✓
MARTIN O. BURRELL AND J. W. WATTS, JR.		
<i>IMAGE CONVERTERS AND IMAGE INTENSIFIERS</i>	501	✓
MARTIN ROME		
<i>ELECTRINOGRAPHY</i>	511	✓
JAMES A. HALL		
<i>CAMERA TUBES EMPLOYING ELECTRON-IMAGING CHARGE STORAGE TARGETS</i>	523	✓
GERHARD W. GOETZE		
<i>THE PERFORMANCE AND CAPABILITIES OF RECENTLY DEVELOPED PLUMBICON TV CAMERA PICKUP TUBES</i>	571	✓
RALPH S. LEVITT		
<i>NEW CAMERA TUBE DEVELOPMENTS</i>	583	✓
R. E. SIMON		

	PAGE	xi
<i>THE IMAGE ISOCON AND RELATED DEVELOPMENTS FOR ASTRONOMICAL SPACE TELESCOPES</i>	591	✓
A. D. COPE		
<i>RECENT DEVELOPMENTS IN IMAGE DEVICES</i>	599	✓
KURT SCHLESINGER		
<i>INFRARED IMAGE RECORDING SYSTEMS</i>	605	✓
GEORGE J. ZISSIS		
GROUP E - OPERATIONS AND DATA-HANDLING		
<i>Co-Chairmen: Fred C. Billingsley and George Ludwig</i>		
<i>SURVEYOR SPACECRAFT REAL-TIME PAYLOAD OPERATIONS</i>	615	✓
JACK N. LINDSLEY		
<i>ORBITING ASTRONOMICAL OBSERVATORY MISSION OPERATIONS</i>	635	✓
H. ROBERT LYNN		
<i>APOLLO TELESCOPE MOUNT OPERATIONS AND DATA-HANDLING</i>	645	✓
JAMES M. RIVES		
<i>GROUND-BASED ASTRONOMICAL OPTICAL DATA-HANDLING</i>	657	✓
EDWIN W. DENNISON		
<i>SYSTEM ASPECTS OF THE KITT PEAK AUTOMATIC TELESCOPE</i>	661	✓
PETER R. VOKAC AND FRANK E. STUART		
<i>CONSIDERATIONS FOR DIGITAL IMAGE-PROCESSING</i>	673	✓
F. C. BILLINGSLEY		
<i>ONBOARD COMPUTER FOR ORBITING ASTRONOMICAL OBSERVATORY MISSION</i>	693	✓
RONALD M. MULLER		
GROUP F - CALIBRATION, SIMULATION, AND TEST		
<i>Chairman: James L. Diggins</i>		
<i>VACUUM SYSTEMS FOR SPACE SIMULATION</i>	699	✓
DAVID H. HOLKEBOER		
<i>SPACE THERMAL-SIMULATION SYSTEMS</i>	703	✓
HENRY MAURER		

	PAGE	
<i>VIBRATION ISOLATION OF LARGE MASSES AND VACUUM CHAMBERS</i>	733	✓
ROBERT W. CRAWFORD		
<i>DEGRADATION DUE TO CONTAMINANTS THROUGHOUT THE TEST CYCLE</i>	751	✓
FRED W. PAUL		
<i>HARD RADIATION ENVIRONMENT SIMULATION</i>	759	✓
FRED W. PAUL		
<i>LIGHT SOURCES FOR STELLAR TELESCOPE CALIBRATION FROM 700 TO 7000 ANGSTROMS</i>	767	✓
WILLIAM R. HUNTER		
<i>ABSOLUTE RADIOMETRY IN SPACE ASTRONOMY</i>	775	✓
WILLIAM G. FASTIE		
<i>OPTICAL RESEARCH FACILITIES</i>	781	✓
WILLIAM R. PERSHING		

Welcome Address

Wernher von Braun

NASA George C. Marshall Space Flight Center

I would like to extend a wholehearted welcome to the astronomers, the astrophysicists, and the astronomical engineers who have convened here at the Marshall Space Flight Center for a three-day workshop on the problems of optical telescope technology. Having spent almost three years in the project management of the Apollo Telescope Mount Project, which will deploy and operate several solar telescopes in orbit, we have great appreciation and deep respect for the multitude of technical and operational problems with which space astronomers are confronted. We hope that your symposium will be successful and that the environment of this Center will be stimulating and helpful in at least some of the topic which you plan to discuss.

The Marshall Center has been known for a number of years as a place where large launch vehicles are designed and built. The latest member of the launch vehicle family, Saturn V, has been developed to launch the Apollo capsule on its flight to the moon. We expect that the landing on the lunar surface by two astronauts will be accomplished in July.*

Although the design, fabrication, testing, and launching of vehicles has kept the members of this Center extremely busy during past years, and although the Apollo-carrying Saturn V still requires a very considerable amount of attention and care, we have always held the belief that launch vehicles alone do not make a full space program. They are the means to accomplish an objective, the objective being the exploration of a world that is not fully accessible to us from the surface of the earth. One of the most fascinating, most exciting, and most promising new fields of exploration which the young technology of space flight is opening for us is astronomy from orbit, where we can face the universe without having to look, as Fred Whipple put it, through the "dirty basement window" of the atmosphere. We are very happy about the prospect that our Center will be able to contribute with our technology, and hopefully with our science, to the great progress that space astronomy will undoubtedly make during the next ten or twenty years.

The Apollo Telescope Mount, or ATM-A Project, which is scheduled for launch in 1972, is giving us the opportunity of learning firsthand about the many technical requirements that an astronomical satellite must meet in order to be successful. We feel that we have learned much, and we are confident that ATM-A will be a successful project. We realize, however, how much more we have to learn in order to ensure success for the follow-on program in space astronomy, which includes such ambitious projects as 3-meter, diffraction-limited, optical telescopes. For the space engineer, the multitude of problems includes the production of lightweight, high-precision mirrors; the alignment of complex optical systems; the design of extremely rigid but lightweight structures; achievement of almost perfect thermal balance; attitude control and pointing stability of unprecedented accuracy; and the handling and transmission of huge quantities of data.

* On July 20, 1969 at 4:17 p.m. EST, Neil A. Armstrong and Edwin E. Aldrin, Jr., successfully landed the *Eagle* on the lunar surface. At 10:56 p.m. EST, Armstrong became the first man to set foot on the moon. Liftoff and rendezvous with the orbiting command module was accomplished July 21.

A subject of very particular interest to us is the role of man in space astronomy. Should the astronauts for astronomical satellites include astronomers, or engineers, or both? What functions should they carry out in orbit? Which components of an astronomy payload system should be exchangeable in orbit? We have followed with great satisfaction and sincere admiration the brilliant success of the Orbiting Astronomical Observatory, OAO II. Experience with unmanned satellites of this kind will help us greatly to define the role of man in future space astronomical projects.

The three-day workshop on optical telescope technology, which you are now attending, will cover a huge area of science and engineering. The expanse of this area, reflected in the very rich and fascinating program of presentations, is indicative of the vast number and great diversity of technical problems waiting for the space engineer. We at the George C. Marshall Space Flight Center are most eager to learn of the conclusions and requirements resulting from this workshop, and we will surely put them to good use in the years to come.

To all of our workshop guests who have come to Huntsville for these three days, we wish to extend our heartfelt welcome and our sincerest wishes for a successful meeting.

Introduction

Jesse L. Mitchell

NASA, Office of Space Science and Applications

It was approximately forty years ago that George Ellery Hale proposed to build the world's largest optical telescope. Today, after twenty years of operation, the 200-inch Hale telescope on Mount Palomar still continues to expand the horizons of the universe. Over ten years ago, Lyman Spitzer, Fred Whipple, Art Code, and Jim Kupperian proposed specific observing programs and telescopes that became the basis of the Orbiting Astronomical Observatory (OAO). Today, after four months of operation, the OAO-II continues each day to expand the horizons of our universe as does the Hale telescope.

These two telescopes represent the very best combination of science and technology. The Hale telescope was and is a marvel of technology utilized for science – from the new (in its time) glass pyrex mirror to the intricate yet simple techniques for balancing the multi-ton structure as it swings through its entire range of observing angles. The OAO required the solution of a number of knotty technical problems. Among those recognized at its inception were: (1) the stability and control problem, particularly the development of star trackers, (2) the development of an ultraviolet TV tube, and (3) the development of lightweight mirrors of up to one meter in diameter.

Today you are here to participate with us and to assist us in our long-range planning efforts on spaceborne optical telescopes beyond the OAO and approaching in size the Mount Palomar Hale telescope. We hope this will be a rewarding experience for each of you.

To begin, we plan to give you a preview of the NASA long-range astronomy plans and programs. In turn, we solicit your assistance in detailing the technical steps necessary to accomplish these plans; later we hope to implement them.

The first step in this workshop will be to look at astronomy from the viewpoint of astronomers. We will identify for you the principal goals, objectives, and elements of the NASA Astronomy Program. This will be followed by more detailed discussion of the scientific uses of space telescopes.

The next step will be to look at the Astronomy Program from the viewpoint of the engineers. We will review some of the current technical status of systems and subsystems required for space telescopes.

Having shared together this broad scientific and technical background, we are then asking you to participate in the workshop sessions of your choice. These sessions will be devoted to in-depth reviews of the key technical areas, such as mirrors and optical materials; structures, pointing, and stabilization; instrumentation operations and data handling; and calibration, simulation, and test.

As a result of these sessions, we hope you will be able to define for us the critical technical problems and the general approach to these problems.

Finally, we are seeking your recommendations on the priorities for working these problems and for specific technology programs consistent with our overall astronomy goals and objectives.

On the basis of this workshop and related study work, we plan to prepare a report to be used as a guideline in developing Optical Astronomy Technology Programs for the future.

As we proceed into these programs, both our scientific objectives and the state of the technology will be continually changing as we make new discoveries. Accordingly, we plan to report such activity to update the plans we will make today.

In conclusion, as a barefoot boy in Alabama, I remember reading with fascination everything I could find about the then proposed 200-inch telescope. Several years ago I had the privilege of a detailed tour of this marvel of science and technology. I have also seen the OAO grow from an idea to a reality – a space telescope literally suspended from the heavens on strings of starlight fastened to it by the star trackers. Having seen both of these grow from pictures and descriptions in my mind's eye to working pieces of machinery, I look forward to repeating that experience on an even grander scale as we combine our thoughts on large telescopes and space telescopes – first to imagine and then to build large space telescopes.

You have been invited to this Optical Technology Workshop to take part in that experience, an adventure of exploration at frontiers of our expanding universe. With your assistance in identifying and solving the technological problems, our children and grandchildren will be the beneficiaries of the exciting discoveries that will follow.

On behalf of Dr. John Naugle and NASA, thank you for coming to share this task with us; we look forward to the final results.

NASA Goals and Objectives

Nancy Roman

NASA, Office of Space Science and Applications

N70-36677

My role is to give a general survey of what we are now doing in astronomy and what we plan for the future. The speakers following me will put appreciably more flesh on the reasons why we are doing some of this and what we need in the terms of technology to accomplish it. The more detailed work sessions will be devoted to fine grain aspects of the technological problems.

Let us begin our overview with a definition of our goal and a description of what we are planning to do to reach that goal. In astronomy, our goal is to understand the origin and continuing evolution of the cosmic environment by observing and interpreting the basic physical processes in our solar system, stars, galaxies, and the universe. We have not set a very big task; all we are trying to do is understand everything in the universe!

To do this, we are using a program with a three-pronged thrust. First, we are going to pursue a very broad-based program of astronomical observations in space; and we realize that space observations are not useful unless they are supplemented with observations from the ground. Second, we want to emphasize the research in those wavelengths of the electromagnetic spectrum which do not penetrate the earth's atmosphere as well as research that uses the higher resolution achievable in space. In other words, we are not trying to do in space things that can be done from the ground because, when they can be done from the ground, they can be done more cheaply and also more efficiently. Third, we want to develop specialized telescopes as well as satellites and multiuser observatories to establish versatile, permanent, astronomical observatories in space. On

the ground we may have one big telescope, such as the Hale telescope, but there are many different types of auxiliary instruments that can be placed on that telescope to make it useful to specific problems. We not only have that problem in space but also have a much broader problem in that we are dealing not with a wavelength range from 3000 angstroms to perhaps 10,000 angstroms but with a wavelength range of from hundreds of megaelectron volts (MeV) in the gamma ray region to kilometers or more in the radio region.

What are we trying to do with all of these observations? A very important objective is to look for surprises. It is very difficult to "sell" anyone on the fact that we are looking for surprises, and yet the whole history of science indicates that it is the surprises, the phenomena that cannot be predicted ahead of time, which provide the greatest advances in scientific knowledge. In addition to this, there are other objectives, more specific things we are trying to do.

1. We are trying to study the energy distribution of celestial objects of all kinds, including normal stars and galaxies, quasars, and pulsars, to determine the spatial and temporal distribution of celestial radiation sources of all wavelengths.

2. We wish to determine the fundamental characteristics of interstellar and intergalactic matter and fields, how they affect the more condensed matter, and how they form into and out of the more condensed matter.

3. We want to develop satisfactory models of the structure and physics of both the quiet sun and the processes involved in solar activity in order to understand it and its effects on the earth's environment.

4. We want to study the important processes occurring on planets and other cool members of our own solar system through observations from the vicinity of the earth.

I do not think I need to emphasize the importance of these endeavors and investigations in today's world.

Let us look at some of the programs that we are actually pursuing to reach our goal through these objectives. The first of the successful astronomical satellites (fig. 1) was the Orbiting Solar Observatory (OSO).

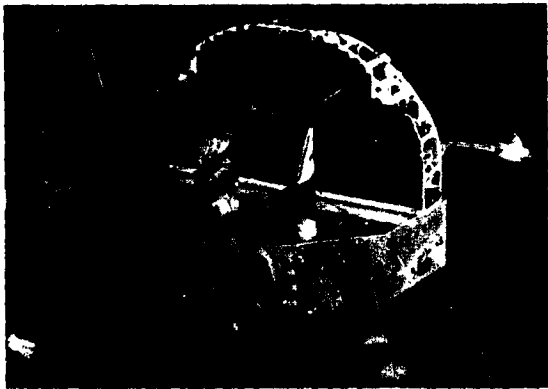


Figure 1. Orbiting Solar Observatory (OSO).

Although it carried experiments outside of the traditional areas of optical astronomy OSO also carried a high resolution spectrometer for the ultraviolet region, from a few hundred angstroms to 3000 angstroms. It also carried parabolic x-ray collimators in which the optical techniques of focusing telescopes have been applied to wavelengths astronomers rarely think of in connection with optical astronomy. OSO carried in its wheel section an objective-grating spectrometer, which has been useful for getting broad energy spectral distributions of a number of objects, including the Andromeda Nebula.

Next in our program is the Orbiting Astronomical Observatory (OAO), figure 2. The first of the OAO's contained 11 telescopes. Four were coupled with ultraviolet vidicons to obtain maps of the sky in different wavelengths in the ultraviolet so that we may have a chance to look for the

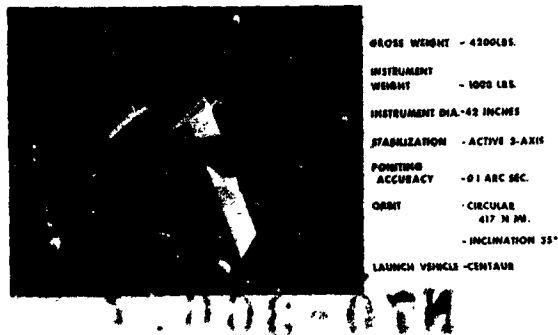


Figure 2. Orbiting Astronomical Observatory (OAO).

surprises and for major features in the ultraviolet that need further investigations and detailed sources. The other seven telescopes, two spectrometers and five photometers, were used to obtain the spectral and energy distributions of a number of discrete objects.

The second satellite in this series, planned for launch in early 1970, is to carry a 38-inch telescope, essentially a standard Cassegrain telescope with a grating spectrometer for moderate resolution spectra of a large number of objects. The third one will carry a 32-inch telescope with a high resolution spectrometer capable of giving resolution up to a tenth of an angstrom in the ultraviolet.

Likely uses of the next OAO would be a repeat of the second instrument but with two very important additions. One would be an increase in the possible resolution from approximately two angstroms, which is the highest resolution available in the second satellite, to a resolution of perhaps one-half an angstrom. Even more important would be the addition of an offset guiding system. There are a number of objects we would like to look at which a 36-inch or 38-inch telescope is capable of observing in the ultraviolet but which are too faint in the normal visible region to provide an adequate signal for guiding the telescope. To solve this problem, we plan to do exactly what astronomers have done on the ground for many years; i.e., we plan to add an offset capability that will guide on a brighter object and still point our major instrument to the faint object or to the nebulous object we wish to study. There are a

number of ideas as to what to do with OAO beyond that, but these ideas will be discussed by other speakers.

Figure 3 is a mockup of the Apollo Telescope Mount (ATM) in the solar program. The ATM is a collection of instruments designed to fly with an early workshop in the Apollo Applications Program (AAP) and carrying five instruments for studying the sun: two parabolic collimators for x-rays, a high-resolution ultraviolet spectrometer, a coronagraph, and a spectroheliograph for the ultraviolet. These are major instruments; all illustrate, as does the OAO, the problems that we are facing in current technology in astronomy, e.g., accurate surfaces because we are dealing with short wavelengths and accurate alignment because we want to point the instruments and hold their pointing precisely. In the case of the ATM, we are going to be recovering film. This leads us to the whole question of the use of the films in space or the use of other imaging detectors to get the same information without having film present.

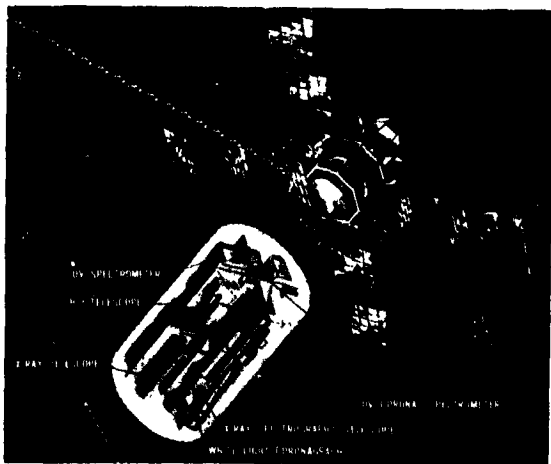


Figure 3. Solar Apollo Telescope Mount (ATM-A).

We have talked about large spacecraft such as the OAO and ATM, but we are also interested in small, specialized spacecraft for tasks that the larger ones cannot do efficiently. Perhaps the best examples of these

specialized spacecraft are the sounding rockets, which, with the attitude capability that currently exists, are very productive in both stellar and solar astronomy. They are used for studying short-lived phenomena, for making specialized experiments, and for testing instrumentation and techniques that will be used later in larger satellites. Their primary advantage is the fast reaction time they can provide.

In the very near future, we are considering a class of Explorer satellites (fig. 4), which we call the Small Astronomy Satellites (SAS). Although they have been developed primarily for high energy astronomy, it looks as if they also have a use in the optical area. In particular, we are planning that the fourth satellite of the series will carry a 16-inch telescope feeding a fairly high resolution spectrometer for studies of planetary atmospheres on a synoptic basis.

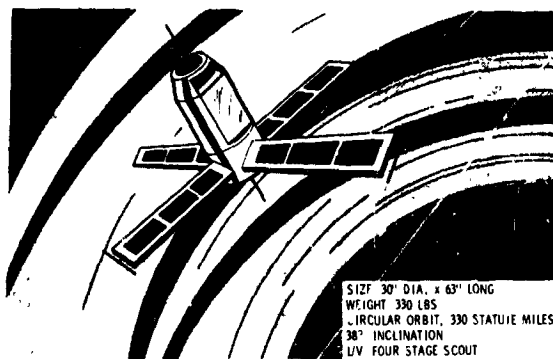


Figure 4. Small Astronomy Satellite (SAS-A); x-ray Explorer.

Also in the very near future is a program that, to some extent, is going on now. At the Ames Research Center, we have a Convair 990 jet aircraft and a small Lear jet, both of which are being used for astronomical observations above the major part of the earth's atmosphere. These aircraft are particularly useful for observations in the infrared, where they are able to gather data above 80 or 90 percent of the absorption of the earth's atmosphere, for dimlight phenomena, such as the study of the solar corona during an eclipse (fig. 5), and for studies of the zodiacal light and airglow.

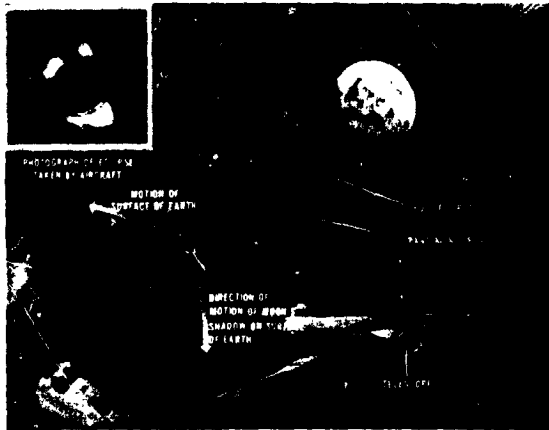


Figure 5. Solar eclipse observation from an airplane.

At the present time, we are flying relatively small instruments (up to 12 inches in aperture) on these planes, but we have recently let a contract for the development and construction of a 36-inch telescope, which will be used for both solar and stellar astronomy in the infrared region of the spectrum. When it is completed, we will actually have the first large manned observatory for nonsolar problems even though the man will not be operating at extremely long distances from the earth.

Figure 6 is an artist's concept of how a number of instruments might be used in connection with the space stations in the mid 1970's. Before we reach that point, however,



Figure 6. Artist's conception of use of instruments in connection with space station.

we are developing a means of flying other specialized instrumentation. Under development at the Marshall Space Flight Center is a small stabilized platform that will carry up to three relatively small telescopes for specialized studies in the ultraviolet. At present, we plan an objective-grating spectrophotometer, wide-field photographic surveys where we can use film to get appreciably higher resolution than we can get with the vidicons on OAO, and a higher resolution spectrometer, very similar to one we are flying on rockets, which we feel can provide substantial information on the spectra of the brighter stars at relatively little effort and expense. This is another instance of how we are using specialized techniques in addition to the major observatories.

Astronomical sources other than the sun are far away. This means (1) they are faint (and astronomers are always intent on collecting every photon they can possibly collect) and (2) they are angularly small; hence, resolution is a problem. In fact, while we do not usually think of the sun as being very faint, the same problems also apply to the sun. To obtain small detail on the sun, which we must have to understand the physics of what is going on, we need high resolution; we still have problems getting an adequate number of photons. Figure 7 illustrates what happens when we look at a source that we know well, the Andromeda Nebula, first with $\frac{1}{2}$ -degree resolution, then with 1 arc minute, and then with 1 arc second. If this is a hundred times farther away, we are looking at a distant galaxy first with a resolution of a quarter of a minute, then with a resolution of a quarter of a second, and finally with a resolution of a hundredth of a second. One hundred times farther than the Andromeda Nebula does not take us very far in the distance scale of the universe. Therefore, we are looking for ways of increasing the resolution and the photon count for future instrumentation. This leads us to our plans for the large space telescopes.

Figure 8 shows how we might get to the large space telescope and indicates that our plans are still somewhat vague and somewhat

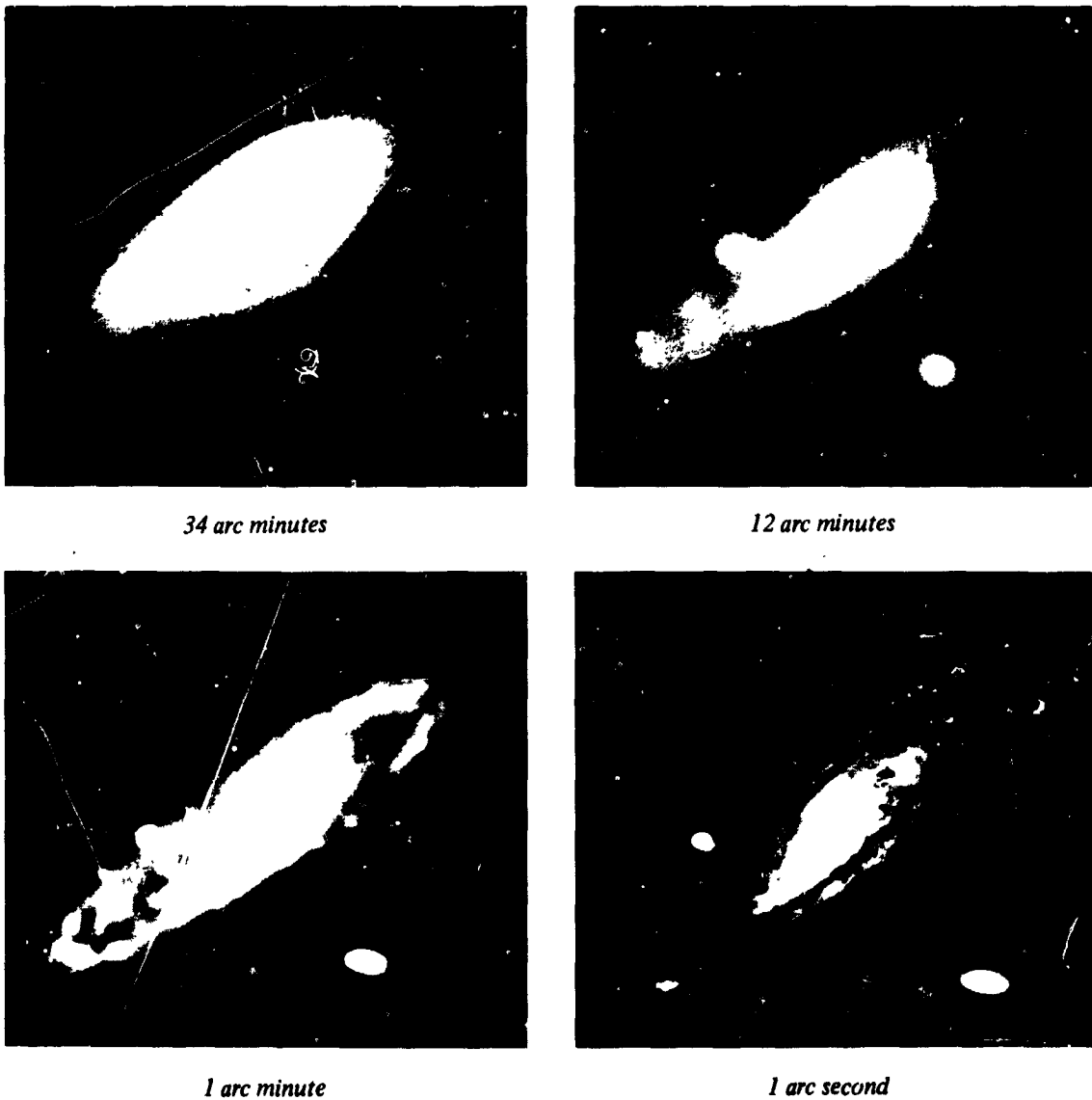


Figure 7. A galaxy as seen at four values of angular resolution.

flexible. Hopefully, one of the results to come out of this workshop will be some hints of the more promising approaches. We are planning the ATM today. We want to go on to the intermediate-sized telescope. We can go by one of two ways, and, in fact, we will probably use aspects of both ways. We can go through the ATM, which is essentially a manned mission making full use of man and the versatility and maintenance that he can

provide, or we can bypass the major experiences of man and rely primarily on the techniques developed to handle the automated spacecraft. In either case, the chances are that the intermediate spacecraft will make some use of the fact that man can work in space and, at the same time, will be planned so that it can operate in an automated mode for long periods of time without requiring the presence of man. The exact way to do this is

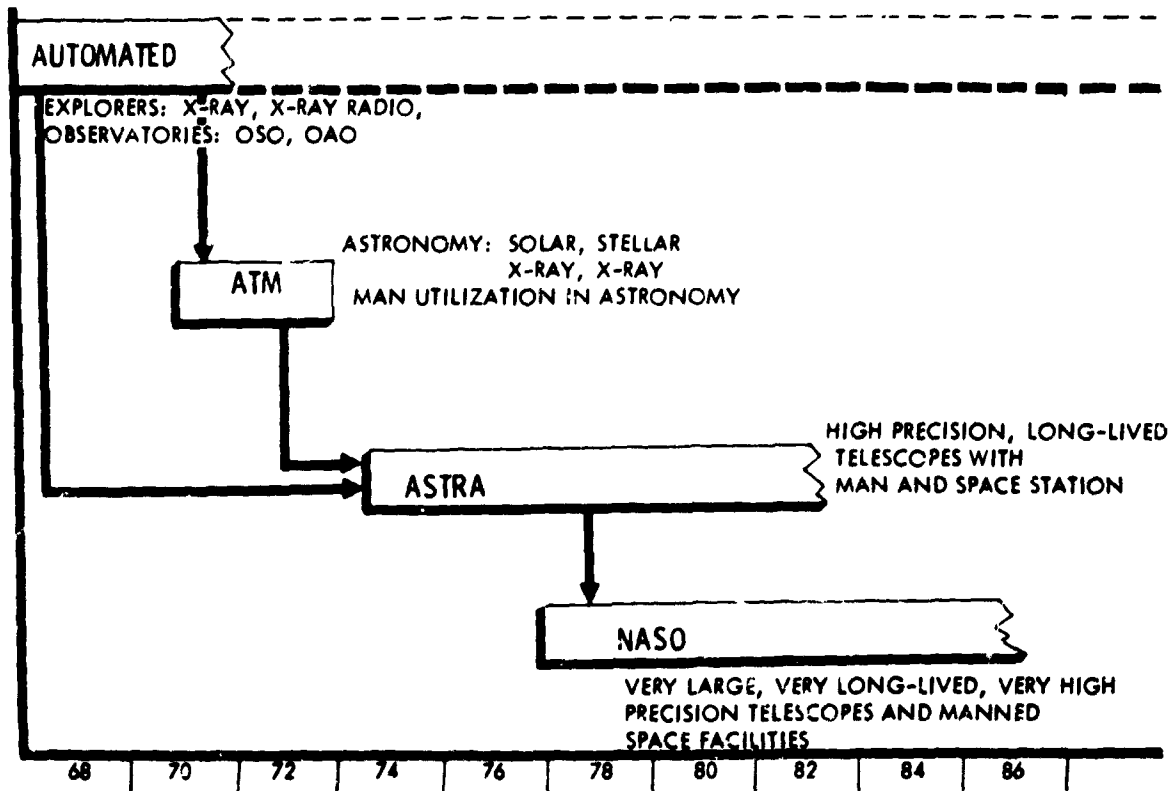


Figure 8. Tentative plan for realizing large space telescope.

still unclear. We want to end up finally with the very large space telescope, the LST, which is going to be part of the National Astronomical Space Observatory (NASO). Do we reach this objective by working through a diffraction-limited telescope of intermediate apertures, such as the 60-inch telescope, or is it better to build a 3-meter telescope and not ask for diffraction-limited performance on the first shot? This is another technological question that is going to have to be answered.

The solar people also are looking for the equivalent of the large space telescopes. In their case, they are looking at focal lengths of up to a hundred feet so that they can get the very high resolutions necessary spectrally and spatially for measuring the sun. They also are looking for intermediate space telescopes. They give their requirements more on the basis of resolution than they do on the basis of aperture. At the present time, they are

talking about the 5-arc-second class; for the intermediate instrument, they are looking for something of the order of 1 arc second; and for the large telescope, they are looking for something of the order of a 0.1-arc-second resolution.

Figure 9 shows a program that we would like to follow in stellar optical astronomy; we could write a similar program for the solar astronomers. (I say "like" because I doubt very much that we will have the resources to follow a program this full, but we can always dream.) We shall continue the rocket program. There is no indication that, as we progress to larger and more sophisticated instrumentation, we are going to rely less on rockets than we are relying today. We want to continue the Explorers, both the Scout class and the Delta class, for the specialized experiments they can do most efficiently. We feel there is a continuing need for OSO's and

PROJECT	1971	1972	1973	1974	1975	1976	1977	1978	1979	1980	1981	1982	1983	1984	1985
ROCKETS	15	17	20	22	24	24	24	24	24	24	24	24	24	24	24
EXPLORERS (SAS)		1	1	1	1	1	1	1	1	1	1	1	1	1	1
OBSERVATORY CLASS		D	E	F	G	H	I	J	-	-	-	-	-	-	-
NEXT STEP BEYOND OBSERVATORIES (Possibly Man Attended)						ASTRA A		ASTRA B		ASTRA C		ASTRA D			
ULTIMATELY DESIRABLE INSTRUMENT (S)	LST START	—————→										LST LAUNCH			
OTHER NEEDS: IR AIRPLANE	1 CONTINUOUSLY, WITH SIZE AND SCOPE DEPENDING ON FUNDS AVAILABLE - —————→ MAXIMUM UP TO 120-INCH TELESCOPE.														

Figure 9. Calendar chart of maximum program for optical space astronomy.

OAO's and instrumentation in that class. We shall get into the intermediate-sized instruments starting in the 1970's. We start now working for the Palomar in space which, ideally, could be launched as early as the early 1980's. Finally, at the same time we are continuing with the airplane observatory, we are also continuing with balloons. All of which leads us to figure 10, an artist's conception of what NASO might look like with the 3-meter optical telescope, a 1-meter aperture parabolic x-ray collimator, perhaps a solar telescope similar to ATM, and various other instruments, all working in conjunction with a space station designed entirely to support astronomical experiments.

I think this brief overview shows that there are technological problems to be solved but also exciting opportunities ahead in space astronomy.



Figure 10. Artist's conception of National Astronomical Space Observatory (NASO).

PRECEDING PAGE BLANK NOT FILMED.

The Future of Photometry and Moderate-Resolution Spectrophotometry in Space Astronomy

Arthur D. Code

University of Wisconsin

N70-36678

Observational astronomy consists solely of systematic measurements of the radiation received from celestial objects and carrying out these measurements in a meaningful way. The astronomer can measure the direction of propagation, the intensity, the spectral distribution, and the state of polarization of this radiation as a function of time. In this paper, I shall confine my remarks to the measurement of the intensity, spectral distribution, and polarization in the optical and vacuum ultraviolet region of the spectrum.

All early missions have been devoted to measurements in the ultraviolet where the terrestrial atmosphere is opaque. The term "moderate-resolution" shall be taken to mean measurements with spectral bandpasses greater than a few angstroms. First, I shall describe briefly the radiation characteristics of celestial objects in this spectral region, then indicate the nature of the photometric measurements currently being carried out on OAO-II. On the basis of this limited practical experience in space astronomy, I shall attempt to indicate the kinds of scientific programs that appear to be indicated for future observations and to highlight some of those problem areas requiring attention.

The sources of radiation include planets, stars, gaseous nebulae, clusters, x-ray stars, galaxies, and quasars as well as the general sky background against which these signals are to be measured. Measurements in the ultraviolet have been carried out for all classes of objects with OAO-II and we now have some reasonable assessment of the general flux levels present. A star of zero magnitude corresponds to

a flux of 3.8×10^{-8} erg cm⁻² sec⁻¹ Å⁻¹ at the effective wavelength of the visual filter bandpass near 5500 angstroms. Table 1 summarizes the approximate stellar fluxes for stars of diverse types.

The actual fluxes vary from these numbers, depending upon bandwidth and upon atmospheric and abundance parameters of the specific stars, but the numbers do provide a basis for estimating sensitivity requirements and can be considerably modified by interstellar absorption. We can anticipate extension of measurements to objects as faint as 25th magnitude, a factor of 10^{10} fainter than the fluxes in table 1. Planets have a spectral distribution similar to the sun and fall between the last two entries in the table.

Table 1. Summary of Approximate Stellar Fluxes* for Stars of Diverse Types

Star Type	$\lambda = 2000\text{\AA}$	$\lambda = 1500\text{\AA}$
B0 V	1×10^7	2×10^7
B5 V	3×10^6	5×10^6
A0 V	1×10^6	2×10^6
A5 V	4×10^5	1×10^6
F0 V	2×10^5	5×10^5
G0 III	2×10^{10}	2×10^{11}

* Flux in erg cm⁻² sec⁻¹ Å⁻¹

For comparison, at $V = 0$ and $\lambda = 5500 \text{\AA}$,
 $F_{\lambda} = 3.8 \times 10^{-8}$ erg cm⁻² Å⁻¹

Gaseous nebulae represent a surface brightness measurement and will have fluxes of the order of 1 percent of the exciting star radiation integrated over their main body.

The brightest x-ray stars, integrated globular cluster measurements, galaxies, and quasars are of the order of 12th magnitude and fall near the lower limit for the OAO-II photometers. Sources such as the brightest x-ray stars, galaxies, and quasars correspond to approximately $2 \times 10^{-13} \text{ erg cm}^{-2} \text{ sec}^{-1} \text{ \AA}^{-1}$ at 2000 angstroms. OAO-II measurements carried out with a focal plane aperture of 10 minutes of arc in diameter yield a signal-to-noise ratio of about 25 for a 1-minute exposure with a contribution from the sky background of the same order as the object. An 80-inch-diameter telescope with a 1-second-of-arc diaphragm could carry out similar measurements on a 25th magnitude object with a 45-minute exposure with instruments of the same efficiency as those on OAO-II.

The sky background consists of residual airglow (Lyman α), zodiacal light, integrated starlight, diffuse galactic light, and extragalactic light components. At 2000 angstroms, the darkest sky regions are measured to be $10^{-19} \text{ erg cm}^{-2} \text{ sec}^{-1} \text{ H}^1 \text{ ster}^{-1}$. Table 2 summarizes the sky brightness.

Table 2. Summary of Sky Brightness *

λ	Galactic Equator	Galactic Pole
5500 Å	8×10^{-8}	2.5×10^{-8}
2500 Å	2×10^{-7}	3.5×10^{-8}
2000 Å	5×10^{-7}	4×10^{-8}
L α (max)	4×10^{-3}	} $\text{erg sec}^{-1} \text{ cm}^{-2} \text{ ster}^{-1}$ $\Delta\lambda \approx 0.02 \text{ \AA}$
L α (min)	6×10^{-4}	

* $\text{erg cm}^{-2} \text{ sec}^{-1} \text{ \AA}^{-1} \text{ ster}^{-1}$

The Lyman α radiation is greater than the energy contained in 1000 angstroms of

sky continuum in near-earth orbit conditions.

An account of the operation of OAO-II and some of the scientific investigations being carried out has been presented by the author in the *Publications of the Astronomical Society of the Pacific* (Vol. 81, p. 475). Experience with the OAO has suggested certain features for consideration for future measurements. In the near future, we would like to obtain measurements of fluxes to an absolute accuracy of the order of 5 percent or better and relative photometry to 2 percent or better on objects down to the 20th magnitude. This suggests offset guidance capabilities to 20th magnitude with 1-second-of-arc fields and 0.1-second-of-arc guidance. Polarization measurement should be considered with an accuracy of the order of a few tenths of a percent. Large dynamic range approximately 10^{6-10} and high time-resolution approximately 10 milliseconds are suggested for some problems; long exposure times of the order of many hours are indicated for other problems.

Some of the problem areas and technological advances indicated by OAO experience are:

1. Studies of effective light baffles for operation in sunlight
2. Considerations for minimizing the effects of the radiation belts, in particular the South Atlantic Anomaly for near-earth operation
3. Absolute calibration techniques for wavelengths shortward of 2000 angstroms
4. Techniques to evaluate scattered light, instrumental profiles, and system calibration and response in flight
5. Improved mirror reflectivities, detector sensitivities, reliable long-life image tubes for photometric purposes, and efficient polarimeters shortward of 2000 angstroms.

Looking somewhat further into the future, astronomers anticipate a large orbiting observatory capable of near diffraction-limited performance of a telescope of the order of a 3-meter aperture. The exciting and unique contributions that such an instrument can make to astronomy are in the area of extragalactic research. Photometry down to 29th magnitude should be possible, primarily

because of the high spatial resolution. (A detailed discussion of the technical requirements and scientific use of such a large orbiting-telescope system has recently been published by the National Academy of Sciences and is entitled *Scientific Uses of the Large Space Telescope*.)

Astronomers want to learn much more about the nature of the physical universe. We need the help of many imaginative and talented engineers and scientists to exploit fully the opportunities available so that we can share the excitement of exploring the universe.

PRECEDING PAGE BLANK NOT FILMED.

The Role of Surveys in Space Astronomy

Karl G. Henize

NASA Manned Spacecraft Center

▲ N70-36679

Perhaps the best reason for my speaking today is simply to assure you that within NASA there are astronomer-astronauts who are anxiously awaiting the space telescopes whose technology you will be discussing during this workshop. As astronomers, we are interested in all types of space telescopes, both manned and unmanned. As astronauts, we are particularly interested in manned telescopes and are firmly convinced that astronauts can and will play an important part in the development and use of large space telescopes in the one- to three-meter aperture range.

During most of my career, I have been a "survey" type of astronomer; consequently, I have been asked to discuss the role of surveys in space astronomy, which I feel is fundamentally the same as in other fields of astronomy. I will start by reviewing the general role of surveys in astronomy.

Let us consider the purposes of astronomical surveys. I would list four: (1) to provide reference data on the physical state and environment of randomly selected stars and nebulae that may from time to time become of special interest to contemporary astronomers, (2) to provide an historical record of the changing cosmos, (3) to provide source data for statistical studies, and (4) to search for unusual stars and unexpected phenomena.

Reference Data on Stars and Nebulae

The first purpose is perhaps the most fundamental. We refer to a definitive set of observations in a well-defined wavelength band gathered in an efficient and uniform

way over the whole sky or a significant fraction of it. The Palomar Sky Atlas best illustrates this purpose. Almost every observational astronomer in the world has at numerous times referred to the Palomar Sky Atlas in order to have a better understanding of the nature of the stars in which he has a special interest. This survey has been especially important in making optical wavelength identifications of objects discovered in other wavelength regions. Prominent examples include the quasars and other radio sources, X-ray sources, and infrared stars. Even when optical identifications are obvious, the environmental data supplied by the Atlas are invaluable. Do certain types of radio sources concentrate in clusters of galaxies? Are pulsars generally involved in gaseous nebulosity? Are there faint blue stars at high galactic latitudes? Do S stars concentrate in obscured regions of the Milky Way? Data concerning such questions are quickly available when an astronomer has a list of objects that may be located and examined on the Palomar Atlas. Without this survey data at hand, months of special observing time might be required to give the required statistical data. In the case of data that must be obtained from space vehicles, the average astronomer may never have the opportunity to gather such data on stars of particular interest to him unless thorough and high quality surveys are made in the wavelength regions that can be reached only from space.

Historical Record of Changing Cosmos

The second purpose of astronomical surveys is similar to the first except that we

expect the data to be of use to future generations as an historical record of changing phenomena. In many ways, astronomy is a science still in its infancy; it is impossible to predict which of the millions of faint stars or galaxies will be of overriding importance to astronomers of future generations. The recent discoveries of quasars and pulsars illustrate the unpredictable turns that astronomical and astrophysical interest may take. Accordingly, it would seem that, when entering the new field of space astronomy, one of our basic concerns should be to provide a fundamental observational record, which will be of value to future astronomers in tracing the history of objects that may become of special interest.

Source Data for Statistical Studies

Surveys are the prime source of data for statistical studies in astronomy. Many of the basic statistical conclusions, upon which our understanding of the composition and structure of the Milky Way Galaxy is based, have been derived from the Henry Draper survey. The fundamental observational verification of current theories of stellar evolution rests largely upon survey-based statistical data that give the galactic distribution of stars, nebulae, and star clusters or that give the frequency distribution of various types of stars, both normal and peculiar, according to spectral type and luminosity.

Statistical applications of data point up the importance of broad coverage, uniformity, and avoidance of selection processes in the conduct of surveys. Unfortunately, very few earth-based surveys have satisfied these three requirements in the degree that might be desired. As a result, the most troublesome problems in stellar statistics are those which arise when we must extrapolate statistics acquired in a small region of the sky over the whole sky, when we must compare and integrate data taken from piecemeal surveys covering small areas of the sky, or when we must make allowances for selection effects in data collected on a star-by-star basis. It is to be hoped that surveys in ultraviolet and X-ray wavelengths will be continued until their

quality and extent will assure little trouble from these problems.

Discovery of Stars and Phenomena

Probably the most exciting part of being a survey astronomer is the possibility, with each new plate, of discovering unique stars or completely unexpected phenomena. Three such examples are the discovery of S stars on Henry Draper survey plates, the discovery of T Tauris stars and symbiotic stars on Mount Wilson H α survey plates, and the discovery of quasars and pulsars as the result of radio survey work. In each instance, the important point is that these objects were not predicted in any way by theoretical considerations but came to light only as the byproduct of systematic survey data collection.

It is frequently said that stellar survey work in ultraviolet wavelengths is pointless because we should be able to predict the ultraviolet character of stars from their known optical characteristics. That such statements are widely accepted is somewhat puzzling inasmuch as they imply that all stars are "normal" or at least "understood" stars and that we know all the physical processes which may take place in stellar atmospheres and in the interstellar medium. The fallacy of these assumptions is demonstrated by the fact that early ultraviolet observations have revealed many unexpected results; for example, the discovery by Morton of P Cygni type of emission lines in ultraviolet spectra of "normal" supergiant stars. Even though we may grant that 99 percent of the stars may be normal and predictable, it is the remaining 1 percent that holds the greatest astrophysical interest and significance. Without survey work and its quick-but-thorough look at tens of thousands of stars in ultraviolet wavelengths, it is possible that large space telescopes may overlook for years the stars that may be of greatest interest in ultraviolet wavelengths.

Observing Techniques for Surveys

In addition to the purposes of astronomical surveys, we should consider the

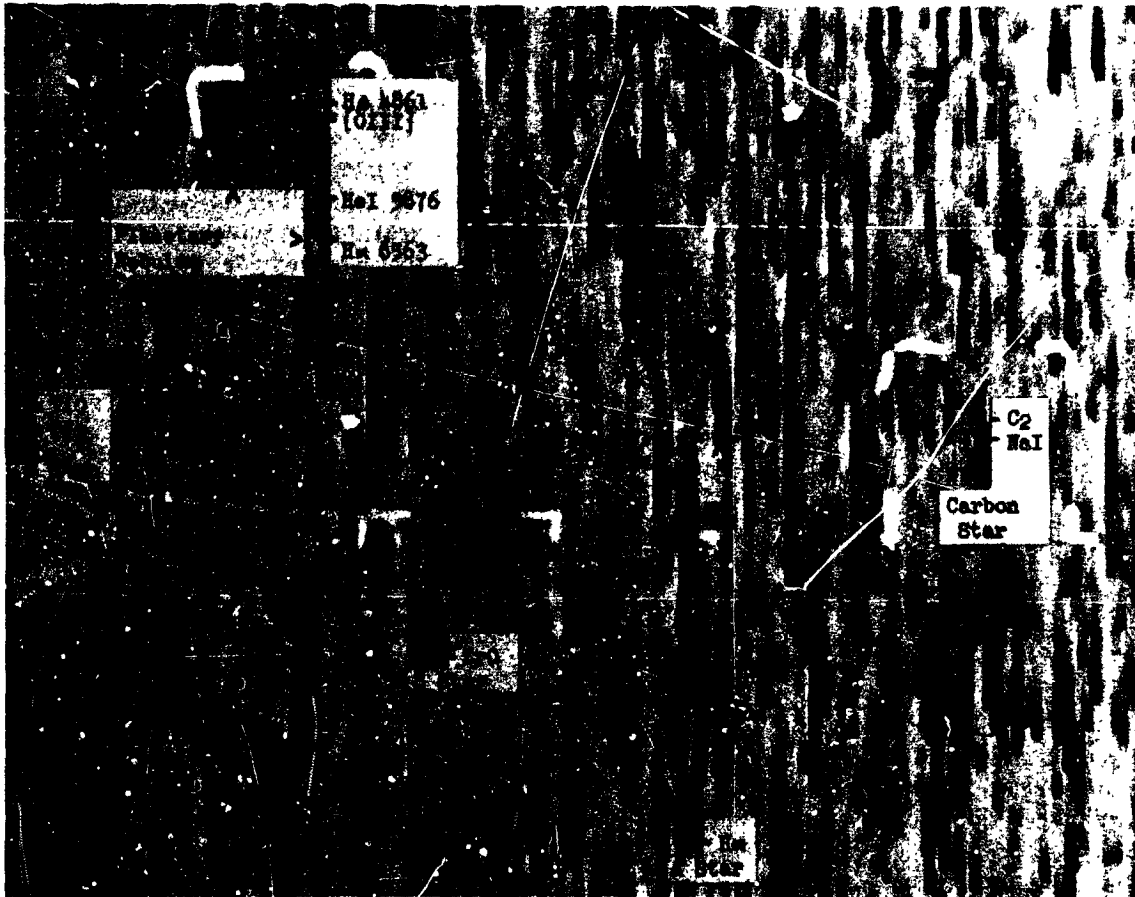


Figure 1. Enlarged portion of objective-prism plate taken in the Michigan - Mount Wilson Southern H α Survey. The spectral region extends from H α at the bottom to H β at the top. Taken on Kodak 103a-E emulsion with yellow plexiglass filter. The field center is RA $13^{\text{h}}50^{\text{m}}$, Dec -67° (1900). Dispersion at H α on the original plate is 450 Å/mm.

observing techniques used. The most familiar type of survey is probably the spectroscopic survey performed either with an objective grating or an objective prism. This technique allows rapid classification of stars according to their grosser physical parameters and structural peculiarities. Low- to moderate-dispersion spectra of hundreds of stars may be obtained in a single exposure with a wide angle camera. The wealth of data on such an exposure is illustrated in figure 1, an enlarged portion of a plate taken in the Michigan Mount Wilson Southern H α Survey. In this instance, red spectra were obtained to search for stars and nebulae showing H-alpha emis-

sion; but it is evident that the plates also contain much useful data on the yellow-red spectra of all types of stars, particularly the red stars, which appear much more conspicuously on these plates than they appear on normal blue photographs. A much better known objective-prism survey is the Henry Draper survey of stellar spectra; this covered the entire sky in the blue-violet wavelength region and resulted in the publication of the spectral classification of approximately 300,000 stars.

Another type of survey is the direct-imaging survey, which is best exemplified by the Palomar Sky Atlas. Figure 2 is a portion

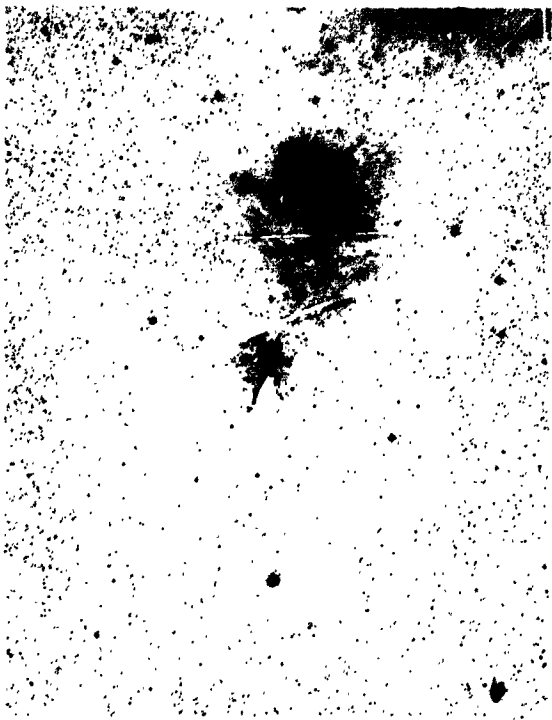


Figure 2. A portion of a Palomar Sky Atlas plate showing NGC 2264. Photographed in red light.

of a Sky Atlas plate, showing a complex relationship between a star cluster and surrounding clouds of interstellar dust and gas. These relationships are graphically portrayed and are immediately obvious by casual visual inspection of these wide-angle survey plates in a way that could not be duplicated by any current system of star-by-star measurement. These plates are "loaded," not only with simple data on stellar magnitudes and positions but also with idea-provoking information on stellar distributions and environments. This is one of the basic values of astronomical surveys.

Up to the present time, astronomical surveys have been conducted mainly by photography. In ultraviolet wavelengths, however, where we must rely on space observations, the difficulty of recovering film has led to the use of electronic detectors whose output may be telemetered to ground stations. Thus, most of the early measurements of the ultraviolet magnitude of stars were made by photometers

using the spin of rockets to scan large areas of the sky. A more recent example of measurement is the Telescope Project of the Smithsonian Astrophysical Observatory, which has made use of a TV type of detector to record ultraviolet color data in four wavelength bands. It must be noted, however, that the large area, high resolution, and moderate photometric accuracy of the photographic emulsion give it an information acquisition rate not yet duplicated by any one electronic detector. Even though electronic detectors have made significant advances in the past few years, I would nevertheless predict that for survey purposes the photographic emulsion will remain the most efficient detector in the foreseeable future. Therefore, in manned telescopes where film may be resupplied and recovered, we should not be surprised to find that photography will continue to be a popular recording technique.

Surveys in Ultraviolet Wavelengths

Let us now consider the status of surveys in ultraviolet wavelengths. The most extensive ultraviolet survey up to now is the Telescope Project now in operation on the Orbiting Astronomical Observatory, OAO-A2. This is a direct-imaging survey employing a TV type of detector that records a 9-degree-square degree field on each exposure. It covers four wavelength regions in the ultraviolet and reaches early B type of stars down to a visual magnitude slightly fainter than 9.0. Other ultraviolet surveys include those by early workers (such as Byrum, Chubb, Friedman, Boggess, Milligan, Stecher, Smith, Bless, and others) in which electronic sensors were scanned over large areas of the sky by spinning rockets. These scans have provided ultraviolet magnitudes in several wavelength regions extending down to early B type of stars with visual magnitudes of fifth magnitude or brighter.

Photographic objective-prism or objective-grating spectroscopic observations have been conducted by Boggess, Morton, Carruthers, Smith, and Henize. Thus far, these have been limited to only a few fields, generally concentrated in the Orion, Scorpius,

Vela, and Cassiopeia regions of the Milky Way; they cover such a small fraction of the sky that they can be considered only as the precursors to true surveys. Only a relatively few of the brighter stars (approximately 15) have been observed so far. Many more ultraviolet spectra have been obtained by the spectrometer of the Wisconsin Experiment Package of the OAO, but, since these are obtained on a star-by-star basis, they may be considered "survey" data only in the broadest sense of the word.

It is clear that ultraviolet survey work is still in its infancy. It seems advisable to press for continuing surveys to insure that all astronomers will have easy access to ultraviolet color data and that the best use will be made of the large space telescopes of the future. It would not be unreasonable to plan a spectrum survey of the Milky Way band to reach BO stars of 9th visual magnitude and a complementary direct-imaging survey of the entire sky in at least two wavelength bands shortward of 3000 angstroms and reaching blue stars and galaxies down to at least 18th visual magnitude.

Technological Problems in Surveys

The following technological problems will be connected with these surveys:

1. Development of large-aperture, wide-angle, ultraviolet optical systems
2. Development of efficient, ultraviolet, long-wave, cutoff filters
3. Development of large objective gratings suitable for ultraviolet spectroscopy
4. Improvement of ultraviolet detectors
5. Achievement of adequate stabilization
6. Development of high-speed-film measurement and data-reduction methods.

The development of wide-angle ultraviolet optical systems has evolved rapidly during the past few years, and it appears that adequate solutions to the problem now exist. Although the classical Schmidt telescope has provided the best wide-angle optical system for visual wavelengths and was used (with CaF

and LiF correcting plates) in some early ultraviolet objective-grating spectroscopy, two defects make it less than ideal for ultraviolet work. First, the use of a transmitting correcting plate restricts the wavelength range that can be reached and limits the aperture that can be attained because of the limited sizes in which ultraviolet transmitting crystals are available. Second, the transmitting materials available have such rapidly varying indices of refraction in the wavelength regions of interest that chromatic aberration restricts the wavelength region in sharp focus to a few hundred angstroms for focal lengths of 50 centimeters or more. It is evident that the ideal ultraviolet optical system must have all-reflecting optics.

The first wide-angle, all-reflecting, ultraviolet, optical system extensively utilized was the "microscope-objective" system developed for astronomers at the Goddard Space Flight Center and Princeton University by Kollsman Instrument Corporation. This system operates at $f/2$ and has a 2-inch aperture, 12-degree field diameter and a 20-arc-second image diameter. For large survey telescopes, however, this instrument has the disadvantage of having too low an angular resolution (1-arc-second image diameters are desired) and a bulky mirror system much larger than the effective aperture.

A second solution that may be considered is the Ritchey-Chretien optical system. A modified Ritchey-Chretien system has been employed by Henize to construct a 6-inch-aperture, objective-prism telescope for use on the Apollo Application Program Orbiting Workshop. Operating at $f/3$, this instrument has a 5-degree field diameter with image diameters of about 15 arc seconds. Although this instrument is extremely compact — a distinct advantage in manned spacecraft in which experiment volumes may be critical — it, too, suffers from insufficient angular resolution to be used as a design for larger survey telescopes.

Two all-reflecting optical designs recently developed appear to give both the angular resolution and the field diameter

required for ultraviolet survey work. The first, developed by Meinel and Tifft at the University of Arizona, uses three mirrors to provide a flat field 5 degrees in diameter with angular aberrations of 5 arc seconds or less. This optical system is illustrated in figure 3. The designers state that large aperture versions of this system can achieve image diameters in the range of 1 arc second or better.

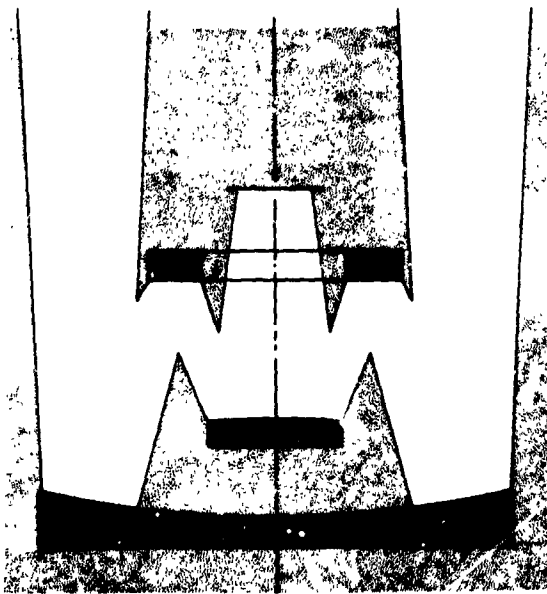


Figure 3. Optical arrangement of the Arizona wide-field, all-reflecting telescope.

The second design is the all-reflecting Schmidt telescope, developed by Lewis C. Epstein of Chrysler Corporation. In this system, the conventional transmitting correcting plate of the classical Schmidt telescope is replaced by a reflecting element. Even though light must pass through the reflecting corrector element in an off-axis manner, the resulting aberrations are small. A 6-inch-aperture prototype has been constructed and yields image diameters less than 4 arc seconds in diameter over a 10-degree field (fig. 4). Ray tracing analysis indicates that the aberration-limited image diameter over this field is less than 1 arc second. Such a

telescope with a 1-meter aperture and an $f/3$ focal ratio should be ideal for a direct-imaging survey of the entire sky. If a suitable grating were to be ruled on the correcting mirror, this system would also serve as an extremely efficient two-mirror, objective-grating spectrograph. Current grating technology makes it unlikely, however, that apertures in excess of 12 inches should be considered for such a system in the near future. Therefore, I would conclude that the problems of wide-angle ultraviolet optical systems are essentially solved.

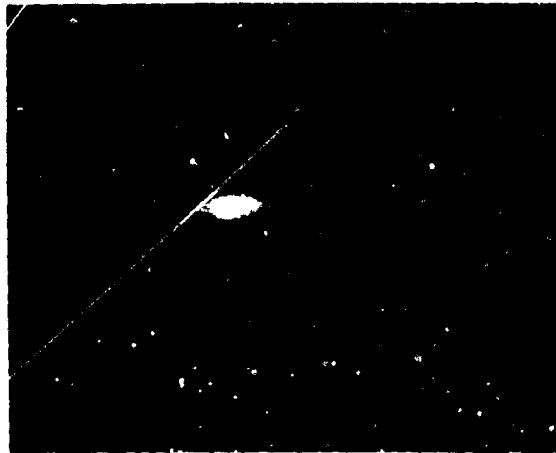


Figure 4. The region of the Andromeda Galaxy photographed with the Epstein all-reflecting Schmidt telescope. Photo by Lewis Epstein, Chrysler Corporation.

In the little time left for discussing other problems, I would stress the development of ultraviolet longwave cutoff filters as one of the most important as well as one of the most difficult problems remaining. If such filters were available, the last obstacle in the way of extending the Palomar Atlas type of survey to ultraviolet wavelengths would be overcome. Perhaps the most practical current solution to this problem is the reflective broad-band interference coatings, which are being incorporated into telescopes proposed by Tifft. This is not yet an ideal solution, however, because the reflection bandwidths are broad and are affected by longer wavelength bands that are

difficult to eliminate when the desired wavelength band is in the 1000- to 1500-angstrom region. Another current solution is the simple aluminum-dielectric interference filter. Unfortunately, these filters are rather inefficient at wavelengths of less than 2000 angstroms, and there is a question of whether they could be produced in the sizes required to cover the photographic fields desirable for survey work. Such fields may be expected to have a diameter of at least 6 inches. Still a third approach is the alkali metal transmission filter. Although such filters appear promising in theory, the problems of producing and preserving them are severe and have not yet been solved. A small program for investigating these problems is being carried out at Northwestern University. The problem of achieving long wavelength cutoff has been efficiently solved for electronic detectors by photocathode technology. The cesium-iodide photocathode provides an excellent method of detecting wavelengths shorter than 1500 angstroms without interference from longer wavelengths.

Summary

In summary, I would like to emphasize two points. First, ultraviolet survey work is an important part of space astronomy and deserves greater attention than it is currently receiving. Not only is it necessary as a means of searching for that small but exciting percentage of stars that may be expected to show anomalies in their ultraviolet radiation, but also it is a means of making moderate-accuracy, spectral, and color data for hundreds of thousands of stars available to all astronomers for statistical studies or for studies of specific sets of stars. Second, if we grant that survey work should be a part of space astronomy, it is to be anticipated that, in the next 10 to 20 years, the most useful and significant of these surveys will probably employ the photographic emulsion as a detector. Figures 5 and 6 show the tremendous information-gathering capacity of the photographic emulsion. In these figures, we see a region of the southern Milky Way in

Carina photographed with the 10-inch aperture, 52-inch focal length, Mount Wilson Cooke triplet camera. The original plate was 37.5 centimeters square. With an average linear resolution of 30 microns over this region, we find that 1.6×10^8 image elements have been recorded in a single exposure; this is more than 100 times the capacity of the



Figure 5. Direct photo in red light of the southern Milky Way in the Carina region. Taken with the Mount Wilson 10-inch Cooke triplet camera on Kodak 103a-E emulsion. The dimension of the field is approximately 9×11 degrees.

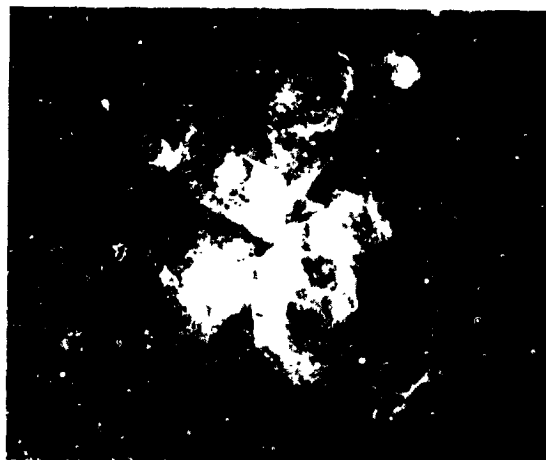


Figure 6. Enlargement of a small section of figure 5 showing the region of the Eta Carinae nebula.

best available electronic detectors. Such a quantum efficiency of the electronic factor more than compensates for the greater detectors.

infrared Observations in Space Astronomy

Gerry Neugebauer
California Institute of Technology

N70-36680

The analogy has been made that talking about the future of infrared astronomy at this time is like having to talk about visual astronomy if all the data that were available were observations which had been made in daylight. I think this comparison is a valid one; hence, most of this discussion today will be about the kinds of measurements that have been made in the past in order to give a frame of reference to what we are working on now and what this can lead to in the future. I will limit my discussion to the stellar type of objects.

For astronomy, the infrared region can be divided into two regions. One region, approximately from 1 to 20 microns, is accessible to ground observations. It is characterized by transmission windows in the earth's atmosphere at about 1, 2, 3, 5, 10, and 20 microns. Detectors used in this region are of the photoconductive type, which will work over this entire range. Examples of these are the lead sulfide and lead selenide detectors. At approximately 5 microns, the germanium bolometer of Frank Low becomes competitive with the photoconductive detectors. At 10 microns and 20 microns, the bolometer is probably a superior detector.

The second wavelength region in the infrared is from approximately 20 microns to 1 millimeter, where optical techniques start becoming radio techniques. Essentially, there are no windows in the earth's atmosphere in this region. Thus, in order to study astronomy at these wavelengths, we have to go outside the earth's atmosphere.

Observations made from the ground have been done with conventional telescopes. The idea is to use a conventional telescope and to

put a photometer at the focal plane. The only novel feature about this type of instrumentation is having a two-beam photometer so that one portion of the sky can be compared against an adjacent portion, thus eliminating the effects of the earth's atmosphere. The technique is fairly straightforward, and, in general, telescopes with diameters that range from 24 inches to 200 inches have been used in this way.

There has been one special telescope (fig. 1) built at the California Institute of Technology. It is a 62-inch-aperture telescope and is made of epoxy that has been spun in the earth's gravitational field to generate the parabolic primary. This fulfills the requirement for a lightweight telescope; it does not fulfill the requirement of a high-resolution surface figure. Its resolution is only about 1 minute of arc, which is good enough to meet the objective of a lightweight, easy to

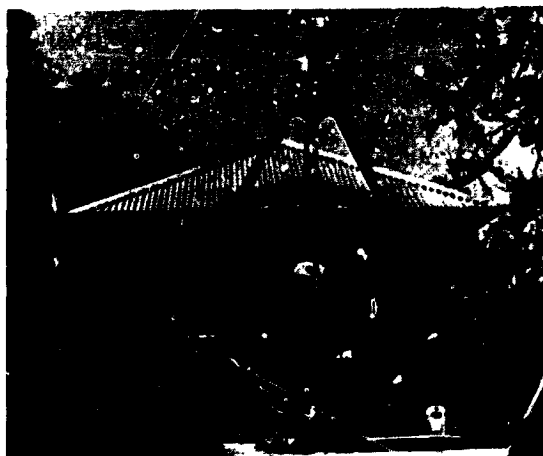


Figure 1. California Institute of Technology 62-inch telescope.

use, inexpensive telescope for conducting a survey in the infrared.

To illustrate how the difficulty of making measurements increases with wavelength, it is interesting to note that on the survey, which was observing at 2.2 microns, we measured between 10,000 to 20,000 objects. At 10 microns, the estimate the number of objects that have been published is only 200; at 20 microns, it is well under 50.

Some measurements have already been made from above the earth's atmosphere. The first were done with balloons. This type of measurement is mainly the work of John Strong, who pioneered this field primarily in planetary work. There has been some stellar spectroscopy with the Stratoscope, and, more recently, there have been observations from balloons at 100 microns to look at the galactic center. It is interesting that this latter telescope had only a 1-inch aperture. Both the Naval Research Laboratory and Cornell have done some rocket work that has been designed mainly to look at the infrared background by using cooled telescopes, these have numbered in the tens of flights. There has also been an airplane program employing a Convair 990 and some work by Frank Low with a 12-inch-aperture telescope in a Lear jet. Most of the work has been done in connection with spectral measurements of the planets. Stellar observations are just beginning.

What types of objects do we plan to measure in the infrared? Ten years ago, if the question had been asked: "What are the infrared characteristics of the stars?", the answer would have been that most stars look just like black bodies with temperatures typically of the order of 3,000° Kelvin or higher. Johnson, at Arizona, measured a large fraction of the bright stars in the infrared and found that this was indeed the case.

Within the last five years, and especially in the last year, this picture has changed radically. This has been the result both of extending the wavelengths beyond 2 microns to the 5-, 10-, and 20-micron windows and of making an unbiased search for infrared objects. The types of infrared stars can be

broken into two groups. The first group are ordinary coolish stars, which, however, show anomalously large infrared radiation at approximately 10 microns. This looks as if there is a circumstellar shell that has been postulated, in some cases, as being made of silicates. The second group are objects that emit essentially all of their radiation in the infrared. Figure 2 shows two plates made with the 48-inch Schmidt telescope; these are the red and the blue plates of an area in Cygnus.



Figure 2. Plates made with 48-inch Schmidt telescope; Cygnus source.

There is an object which is very clearly visible on the red plate but which is missing on the blue plate. At 2 microns, that object is as bright as Vega. At 10 and 20 microns, that object becomes the second brightest star in

the sky. The spectrum of this star is shown in figure 3; its energy is shown as a function of wavelength. When this is compared with the left-hand curve, which is the spectrum of α Her, an ordinary coolish type of star, it is possible to see that the bulk of the energy is in the long wavelength region all the way to 5 and 10 microns.

The other object in figure 3 that also goes to the far infrared is one of the other three brightest objects in the sky at 10 and 20 microns, namely, VY Canis Majoris. It is interesting because every spectrum that has been taken, including the spectra at 2 microns, indicates this is a perfectly ordinary star. It is only at 5 and 10 microns that we begin to see differences. The point is that we do not know as yet how many objects there are which look perfectly normal at 2 microns but at 5 microns show very anomalous behavior. Figure 4 shows the

energy spectrum of the brightest object in the sky at 20 microns, η Carinae, a star in the Carinae nebula. It is plotted in frequency instead of in wavelength; i.e., the long wavelengths are to the left-hand side. The solid curve to the right represents the optical data that should be combined with our infrared data points. The dashed curve is what we think the spectrum should look like once we have taken care of interstellar extinction. The point is fairly obvious; in the visual, the object is something like a fifth or sixth magnitude star, which is pretty inconspicuous. If, on the other hand, we go from 1.6 to 20 microns, we see how the energy really increases. This is a particularly interesting object to me because it blew up in 1860, at which time it was visually as bright as the second brightest star visible at that time. Since then, its visual component has decreased. Unfortunately, there were no

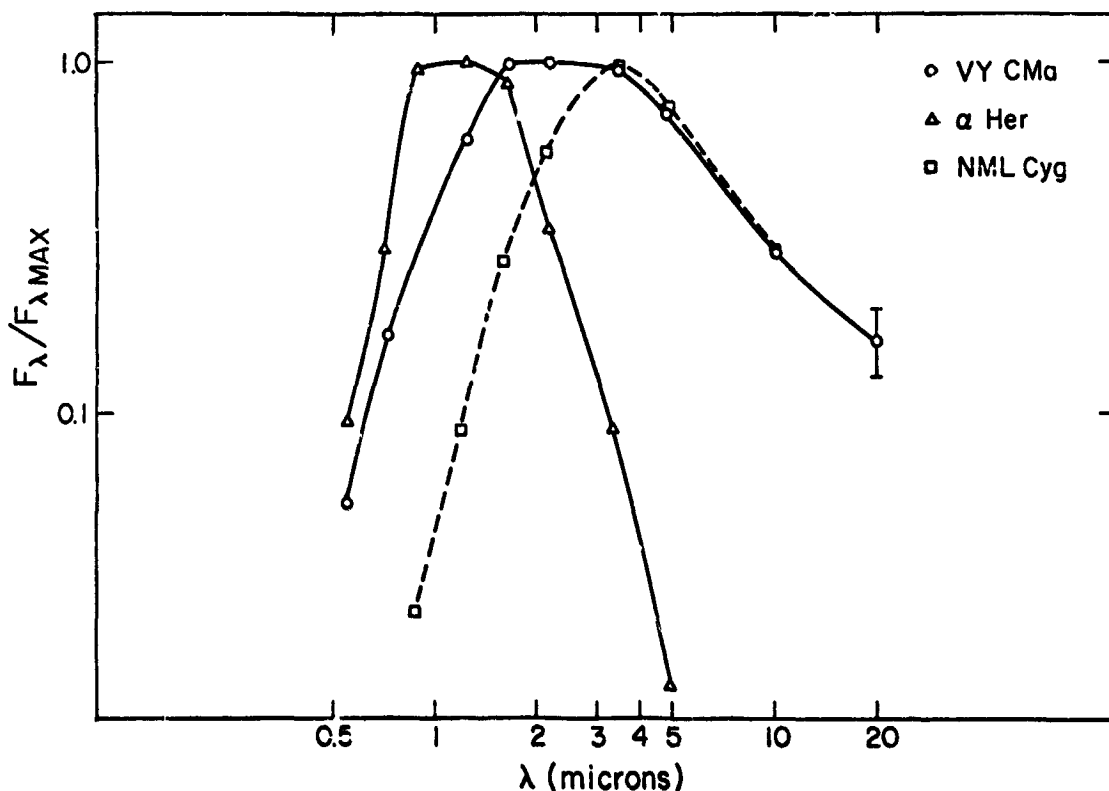


Figure 3. Spectrum of bright star (shown on red plate, fig. 2), Alpha Her, and VY Canis majoris.

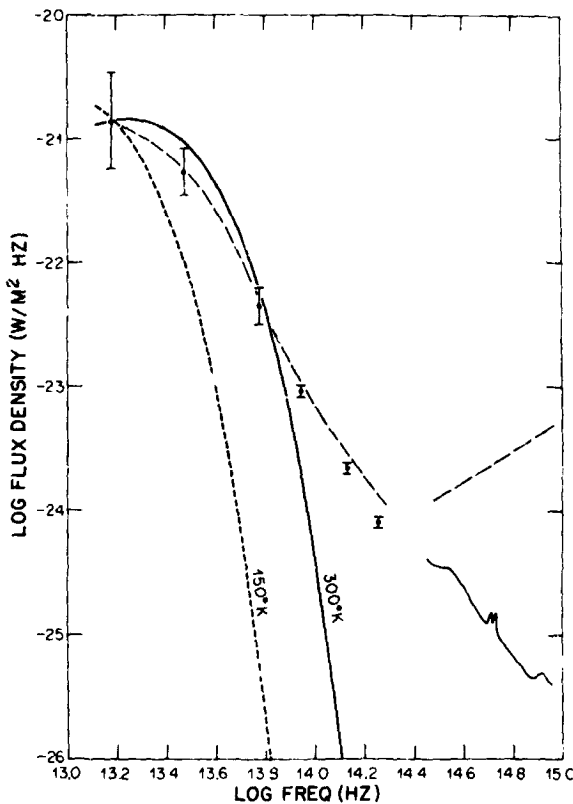


Figure 4. Energy spectrum of Eta Carinae.

infrared measurements made in 1860, but it looks very much as if all of the energy from this visual component has gone into the infrared component, probably by heating a shell of gas.

There is another group of objects found in the infrared that are not associated in any way with visually identified stars. Probably the most important region in this respect is the Orion Nebula. Eric Becklin, at the California Institute of Technology, scanned this area and found a star-like object that cannot be seen in the visual even when looking with the 200-inch telescope. The energy distribution of this corresponds to a temperature typically of the order of 700° Kelvin. Frank Low looked at this general area to try to measure this point-like object at 20 microns. Instead, next to the point-object, he found a nebula that is only a factor of 10 or so dimmer than η Carinae. Its temperature is something of the order of 70° Kelvin. We

think this is an area where the stars are just forming. More recent measurements in the whole Orion region have shown it generally to be a very bright infrared emitter.

The energy distributions can be seen in figure 5, reprinted from a review article in *Science* magazine by Frank Low. The figure shows the energies of a series of different objects. The wavelength is increasing to the right with the sun all the way to the left; this gives us an idea of what a fairly ordinary star looks like. The coolest stars known before 5 or 10 years ago are typified by T Tau. The object in Cygnus shown in figure 5 (NML Cyg) is in the center; the point source in Orion (Becklin's object) and the Orion infrared nebula are peaked at still longer wavelengths. This shows the general range of galactic objects that are apparently present in the infrared.

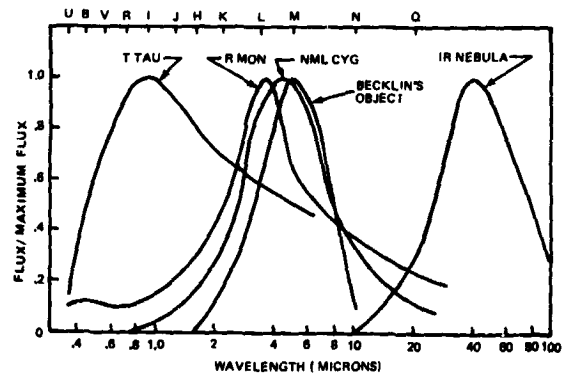


Figure 5. Normalized spectral energy distributions of five objects representing various stages of stellar evolution; all data obtained at University of Arizona on photometric systems designated by letters U, B, V, R, I, J, H, K, L, M, N, Q.

Finally, I would like to go to the grand scale, to what I think is a most interesting aspect of infrared astronomy, namely, the study of infrared from extragalactic objects.

Early infrared measurements of galaxies showed that they look pretty much like a collection of ordinary stars; that is, the energy distributions look like those shown in figure 6 for M31.

A collection of objects, including some other extragalactic objects, is shown in

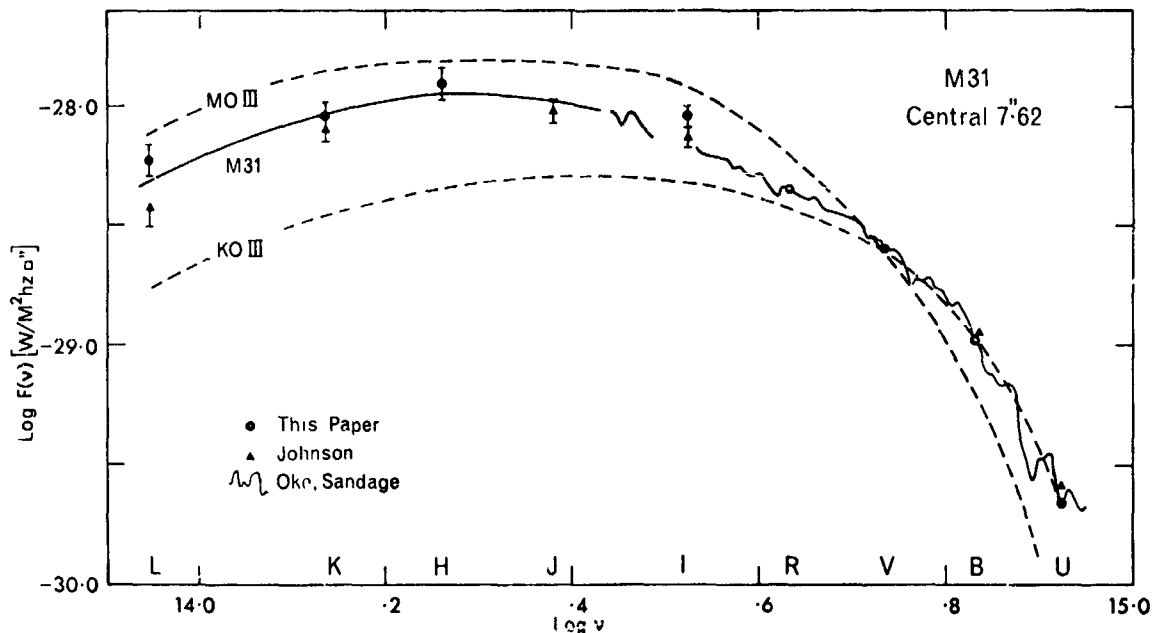


Figure 6. Energy distributions for M31.

figure 7. The striking difference between these objects and the normal galaxies is obvious. In particular, 3C273, which is the brightest of the quasars, rises very sharply in the infrared so that at 20 microns, (frequency $\sim 10^{13}$ Hz), it is essentially as high as it can get. Clearly, this is one object in which the bulk of the energy is in the infrared.

After 3C273 was measured, interest was generated in other types of peculiar galaxies, particularly in the Seyfert galaxies, which are unusual because they have very bright nuclei. When we look at these nuclei in the infrared, we find that they, too, have a very sharp increase to longer wavelengths. NGC 1068, one of the brightest Seyfert galaxies, is included in figure 7. The question is still open as to what these objects are and how they compare with ordinary galaxies. In particular, the question arises if ordinary galaxies, like our own, have a nuclear component which also has the anomalous infrared properties. In the case of our galaxy, we cannot see the nucleus in the visible because of interstellar extinction, which reduces the visual radiation by approximately 10^{11} . In the infrared,

however, at 2 microns, this factor is only down by something like a factor of 10, thus permitting the possible measurement of the galactic center for the first time. Out to 3μ , our galactic nucleus did not look any different from what was expected from a group of ordinary stars. This picture was changed once we started making measurements at 10 and 20 microns. If we look into the center of the galaxy at these wavelengths, we find an energetic core of the order of 16 seconds across. In this case, we find that the spectrum deviates significantly from an ordinary stellar-like spectrum and agrees with the spectrum of the Seyfert type of galaxies. The main difference is that the total energy emitted by the core of the "ordinary" galaxy is less than that emitted by the Seyfert nucleus by a factor of 10^5 .

We are now left with this very fascinating situation: when we looked at our ordinary galaxy in the smallest and finest detail, it is just as extraordinary as the very peculiar Seyfert galaxies. How common this property is is not known. It is going to be very hard to measure other galactic nuclei;

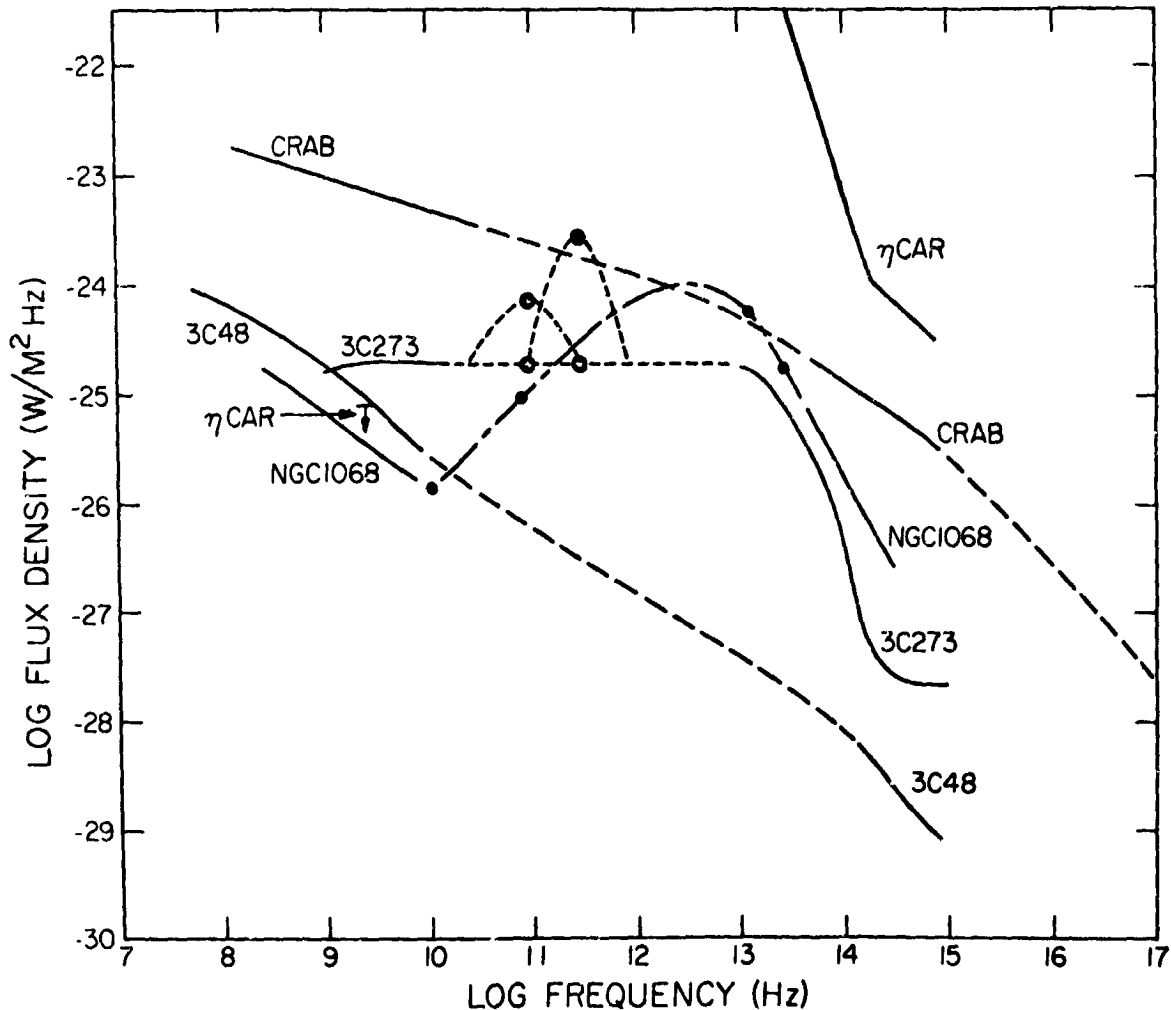


Figure 7. Energy distributions for extragalactic objects.

even the M31 galaxy requires approximately 1/3-arc-second resolution in order to see a comparable core.

What is the future of infrared? I think it is clear that research that can be done from the earth is not appropriate for space; for example, the region from 1 to 20 microns is not appropriate for space research. Clearly, the area to be investigated is from 20 microns to the submillimeter region. Some plans using a Convair 990 with a 36-inch telescope have already been made for such investigation.

The big reason why we cannot give a really accurate description of what we want

to do in infrared astronomy is because there is such a large technological and scientific gap. The scientific gap is obvious. We simply have not been making measurements long enough to be able to predict what we want to do. The technological gap is in the field of detector development. In essentially every single case, the detector sensitivity is a limiting feature of the measurements. The bolometer that Low has developed now has a detectivity, essentially the reciprocal of the noise equivalent power (NEP), of $10^{14} \text{ W}^{-1} \text{ S}^{1/2}$. Theoretically, it can go as high as 10^{17} ; thus, in detector development, there is a factor of

1000 to be gained. It is clear that this is the most important single item that has to be developed in the infrared.

Accompanying this is the whole problem of cryogenics because every infrared detector has to be cooled. The bolometer sensitivity is inversely proportional to the temperature; hence, the investigator has to be working in the general area of 1° or 2° Kelvin. It is essential that detectors and the cyrogenic problem be worked on jointly. Some of the numerology of this problem is shown in figures 8 and 9, which come from the Astronomy Missions Board report. The different curves represent the limits set by telescope mirrors at the temperature shown and with the emissivity noted. The dashed line shows the state of the present bolometers; the

LARGE THROUGHPUT SYSTEMS ($A\Omega = 1 \text{ cm}^2\text{-sr.}$)

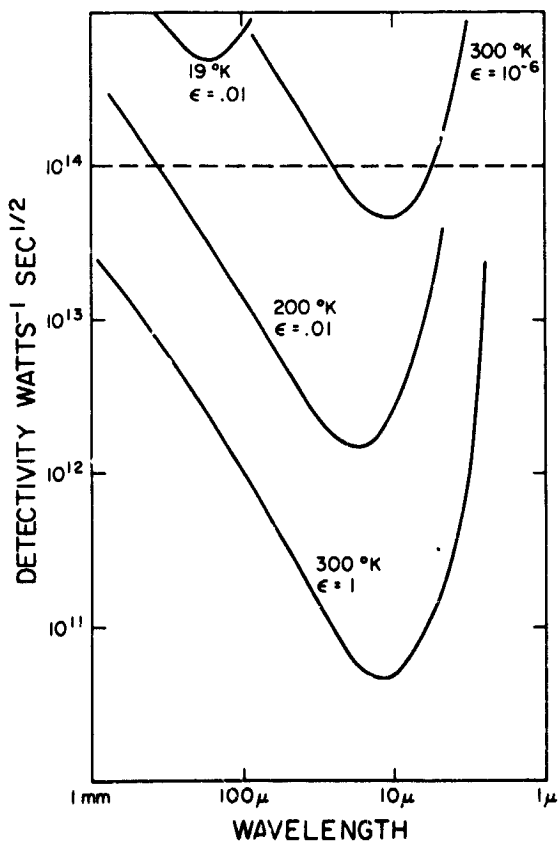


Figure 8. Detector sensitivity, narrow field of view.

POINTED SYSTEMS

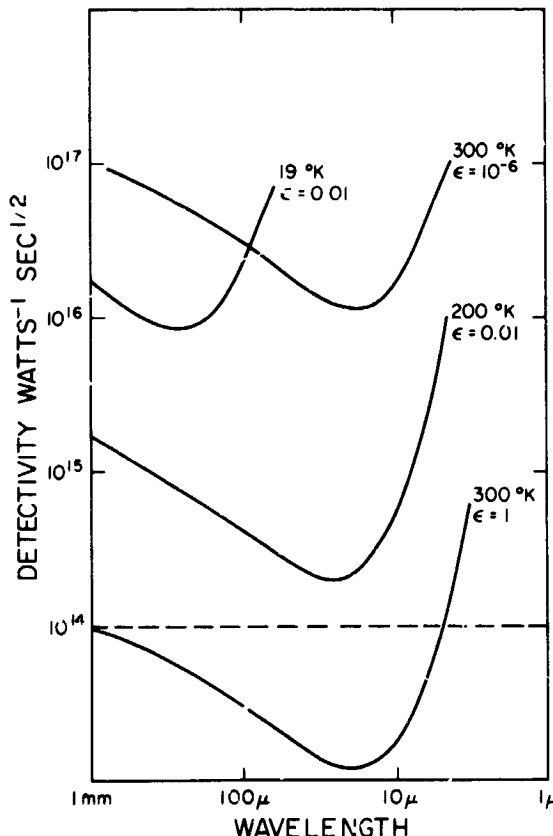


Figure 9. Detector sensitivity, wide field of view.

lowest curve is always the one that limits the system.

The reason there are two figures is that the sensitivity of a detector depends on the background that it sees because, once it reaches a sufficiently high sensitivity, it becomes limited by statistical fluctuations of the photons impinging on it. Therefore, if we want to make very sensitive detectors, we somehow have to remove the background. This can be done either by cooling the telescope or by narrowing the field of view. Figure 8 treats the extreme of making a diffraction-limited telescope; i.e., when we are looking only for a very narrow field of view. Figure 9 is for the kind of a system that we might want if we were looking, for instance, at the infrared background or at large areas like the Orion nebula.

From figure 8, we see that if we have a pointed system but use a room temperature telescope with an emissivity of 1, this would be the limiting case. With a reasonable number like a 1-percent emissivity, this curve is raised by a factor of 10, which would move the solid curve into the middle. This implies that, if we have an emissivity of 1 percent, then, as long as detectors do not improve over what they are now, we could make do with an uncooled telescope. On the other hand, if detectors improve as much as they theoretically can (10^{17}), the telescope would become the limiting feature at very long wavelengths even if it were operating at 20° Kelvin with an emissivity of 1 percent.

It is quite obvious to me that we do not want to restrict ourselves to these narrow field-of-view telescopes. Figure 9 shows that for the wide field case, if we have a telescope of 300° Kelvin, the telescope is already a limiting feature even with an emissivity of 10^{-6} . Therefore, we are required to decrease the temperature of the telescope to some reasonable number like 20° if we want to look with a wide field-of-view system. This means that the cryogenics must be developed not only to be used for the detector itself but also to be able to take advantage of space.

There are some other obvious specialized areas that need to be developed. Materials and, in particular, filters need to be developed for the long wavelengths. At the present time, filters are a "cookbook" kind of a business

out beyond 20 microns. Spectroscopy has to be developed; the problem is special for the infrared because of the detector limitation; hence, we have to take advantage of new techniques. For example, Fourier spectroscopy rather than the more conventional techniques is already being advocated vigorously.

There is also the whole, broad problem of imagery. Dr. Henize pointed out in his paper how important it is to have a picture. When we made the survey at 2 microns, we had to proceed star by star. This is actually a very awkward process. I think it is clear that, if we can develop imagery so that we can make pictures at 2, 10, and 20 microns, this would be an extremely important development. Finally, there is the problem of instrumentation contamination from the spacecraft. By "contamination" I mean that, as the satellite or rocket goes up, there is junk associated with it. Although it is small, it is hot enough to give totally spurious results in the infrared. This problem is one which has to be worked on. It is a technical problem, but it is the kind of problem that is going to be annoying in developing space telescopes.

All of these special problems are unimportant in comparison with the need for an emphasis on detectors and associated cryogenics. I think that this field of investigation, plus keeping open minds so that we are willing to grow with this field, is what is required.

High-Resolution Measurements in Space Astronomy and the Requirements for Diffraction-Limited Optics

Lyman Spitzer, Jr.
Princeton University

N70-36681

There are three topics covered in this paper. First, I will describe some of the astronomical research that might be carried out at high resolution. I interpret high resolution as including not only high spatial resolution but also high spectroscopic resolution, since the two are related technically and an instrument suitable for one is likely to be suitable for the other. Second, I will discuss the critical technological areas where more research and development needs to be done before we can forge ahead and construct the optimum instruments required for this high resolution. Third, I will treat very briefly the instrumental goals; i.e., the large space telescope that we have been talking about for some years and the intermediate steps that might be visualized.

Astronomical Research

The research we wish to conduct is, of course, the subject of primary interest to the astronomical community. Let us begin by posing a number of salient questions. What sort of astronomical observations can be made? Why are astronomers interested in high resolution instruments? At Princeton, we have completed several reports analyzing what could be done with such space instruments. Although the astronomical community does not think with one mind, we have at least begun to plan. Some points are still being debated; a number of others have been agreed to by astronomers with different viewpoints. We are gradually generating a reasoned document that can serve as the basis of a national plan for space astronomy. The enthusiasm of the space astronomers must be

tempered by the experience of those in ground-based astronomy. This experience must be taken into account in any long-range plan.

All of us who have had any contact with the subject are convinced of the enormous importance of scientific data that could be obtained with the telescopes of the future. I shall discuss only two typical problems, chosen from a much more extensive list, that could be explored with high spatial resolution, by which I mean a resolving power of approximately 0.03 arc second.

One is in the field of galactic structure. With increased resolution, much more information should be obtainable. One question that might be studied in detail with such higher resolution is the diameter of the very small galactic nuclei that have been discovered at the center of Seyfert galaxies. The chief astronomical result of the last Stratoscope II flight was to set an upper limit to the diameter of the nucleus in one of the brighter Seyfert galaxies. These results are now being used by one of my collaborators at Princeton to construct a model for these fascinating objects, a model consistent with this upper limit. This model is based upon the general point of view that collisions between stars are responsible for all the activity occurring in these galactic nuclei. Since this picture is by no means definite, the higher resolution offered by the space telescope can begin to provide unambiguous answers concerning the true physical processes of the galactic nuclei.

A brilliant Russian astronomer, Ambartsumian, has suggested that wholly new physical principles must be involved to explain what is going on in these galactic

nuclei. He suggests that a state of matter unfamiliar to physicists, except perhaps with the most powerful atom-smashing machines, may be responsible for phenomena at the center of these nuclei. Whether or not we accept this hypothesis depends in part upon the results that would be achieved with higher resolution studies.

A second field where high resolution imagery is important and where results can be interpreted immediately in terms of physical understanding is in the structure of galactic clouds of gas or nebulae. Such objects include the bright Orion nebula, planetary nebulae, and, perhaps the most spectacular of all, the shells of gas that are emitted in explosions of a supernova, such as the Crab nebula, the Cygnus loop, and other regions where gases ejected initially at a velocity of many thousands of kilometers per second have been slowed down by interaction with the interstellar medium. There is some evidence from the highest resolution picture of these complex filamentary structures that magnetic fields may play a dominant role in the structure of these gas clouds. Photographs of these objects with 10 to 30 times higher resolution will enormously increase our knowledge of the processes taking place within them.

In considering high spectroscopic resolution, I have selected only two applications. By "high spectroscopic resolution" I mean the ability to resolve 0.1 angstrom. With the advanced type of spectroscopic instrument being planned, we can think of getting 0.1-angstrom spectral resolution on a star of 10th magnitude with an exposure of approximately one-half hour with a 120-inch spaceborne telescope. I may point out that, with a telescope providing high spatial resolution, the best way of getting high spectroscopic resolution may be to use a fairly wide entrance slit to admit all or most of the light, thus giving highest efficiency and greatest ease of acquisition, and then to use the sharp image and the guidance precision of the instrument to give the spectroscopic stability and resolution needed.

The first field in which high spectroscopic resolution can be used profitably is the study of the outer atmosphere of the stars. This region, which is generally in a state of violent activity, changing rapidly with time, is a predominant source of ultraviolet radiation and, in the case of the sun, has been extensively explored with space vehicles. With high resolution spectrophotometry from a large spaceborne telescope, we can hope to make similar observations on a wide variety of stars other than the sun and perhaps even for much colder stars and for such faint objects as protostars. These objects, at the extremes of the evolutionary scale, should hold very fascinating and important clues to the origin and fate of stars in general. To obtain high spectral resolution of these objects in the ultraviolet would be a fascinating field of research.

The second field, which is of particular interest to me personally, is high spectroscopic resolution in the ultraviolet for determining the composition and distribution of interstellar gas. With a few trivial exceptions, most of the atoms in interstellar space absorb only in the ultraviolet, an effect that cannot be observed from the ground. By going to the ultraviolet, we get an increase in sensitivity of three orders of magnitude; that is, we can detect interstellar gas with a density of only 1/1000 of that needed for observations in the visible or in the 21-centimeter line of radio astronomy. Thus, high resolution observations can open an essentially new field of research in interstellar studies. With a large space telescope, we could examine the physical nature of the vast halo of gas that is believed to surround the entire galaxy and which may be a dominant physical factor in its origin and evolution.

Critical Areas of Technology

There are critical technological areas that are in particular need of development in order to realize the potentialities of space telescopes. I have excluded most of the items generally needed for space research, such as

reliable components, large amounts of electric power, and data transmission, because these items are not unique to the present discussion. I have considered only the particular technological areas needed for high resolution astronomical purposes.

One such area is the primary mirror, which is of central importance for high resolution. The first problem is one of manufacturing. How do we make a large primary mirror with the desired properties, and, closely related to this problem, how do we test it? Evidently, if we cannot test it, we do not know whether it has been manufactured correctly. This problem has been solved successfully for the 36-inch mirror in Stratoscope II; the solution constitutes a very important result of that program. For the larger instruments, however, there are still a good many uncertainties.

Another problem in connection with the primary mirror is its thermal properties. While fused silica is much better than pyrex, there are new materials being developed, such as ultra-low-expansion quartz and Cervit, that have a thermal coefficient of expansion 10 times lower than fused silica. What are the required properties of materials applicable to large astronomical mirrors? In particular, what is the dimensional stability for thermal cycling and for vibration and aging? One field where development is urgently needed before much emphasis can be put on larger instruments is the testing of material properties in discs with sizes suitable for astronomical use; i.e., 40 to 60 inches. This includes not only manufacturing discs of the proprietary material and size to diffraction limits but also their thermal cycling and vibration testing as well.

Another central problem that must be resolved regarding a larger mirror is whether it should be monolithic, composed of a single disc, or segmented. Segmented mirrors would, I assume, be continually monitored, with all the segments being actively controlled by pulling and pushing them into a perfect figure. This is a very fascinating, challenging field of optical engineering in which more

information is needed for potential application to a larger instrument.

Finally, with high resolution work as in all types of space astronomy, we need improved efficiency of the primary optics. The coatings are presumably subject to degradation produced by air, waste products from the spacecraft, and energetic particles. The extent of this degradation must be known. There are some programs underway to measure the optical degradation of various coatings for short periods in manned missions. Another exceedingly important problem is scattered light, in the vicinity of the spacecraft, that directly affects all astronomical research.

There is also the problem of positioning accuracy. With the success of Stratoscope II in obtaining an rms pointing accuracy comparable with that needed for a large space telescope, an important milestone in this field has been achieved. I am sure, however, that other problems will remain, and both the error sensor and the actuators that move the image around will require further development before a pointing mechanism can be optimized.

Another area that I believe is crucial for the high resolution telescopes of the future concerns the detectors. At Princeton, we have had great enthusiasm for several years for integrating television tubes. I think it is clear that, while film has advantages for an instrument with a wide field of view, for most research programs the wide field is not as important as the high quantum efficiency provided by the photoelectric devices. An extremely important aspect of imaging with electronic readout (as with television) is the opportunity of getting away from all the inherent difficulties associated with photographic plates in space, including fogging by energetic particles, problems of storage and development, etc. It is our opinion that space astronomical research of the future will depend in a very central way upon integrating television camera tubes; thus, the development of effective tubes should play an essential role in space astronomy. An

improvement in the detector efficiency by an order of magnitude has the same astronomical effect, as far as the photon count is concerned, as increasing the aperture of the telescope by a factor of 10.

An extension of these imaging techniques into the far ultraviolet wavelengths less than 1100 angstroms, where image tube faceplates cannot be used, is an important research goal. Similarly, an extension of imaging techniques into the infrared is essential for the large telescope of the future. Although the specific technological developments needed for infrared astronomy have been described in a previous paper, let me reemphasize the importance of increasing the sensitivity against noise of infrared detectors and the importance of developing the cryogenic equipment needed for operation in the satellite environment.

An additional area of technology in connection with detectors is the development of gratings needed for high spectral resolution. Gratings in the ultraviolet have been used for many years in the physics laboratories, where few physicists have been concerned with their efficiency. By "efficiency" we mean how much of the light that hits the gratings actually ends up where we want it. In the physics laboratory, we simply expose the ultraviolet spectroscopic plate as long as necessary to get the proper image density. There is no specific need to take many exposures; hence, the length of one exposure does not matter particularly. On the other hand, with a space telescope, the overall efficiency of the instrument determines the amount of data that can be gathered; hence, the efficiency of the grating is of crucial importance. Very little has been done to improve the efficiency of ultraviolet gratings. Development of efficient gratings in the ultraviolet is probably one of the most important aspects of supporting technology for large telescopes.

One important field not germane to high resolution telescopes but essential to the permanency of very large instruments is manned maintenance. I agree with Dr. Henize

that the primary role of the astronauts is probably not to maintain and operate a space telescope on a moment-to-moment basis, but rather to keep the telescope working on a longer basis; i.e., to maintain it, to update it, to change it, to repair it, and to do all the things that are very difficult to imagine being automated. The greatest uncertainty at the moment in the plans for the large spaceborne telescope is just how man can best be used in connection with such a powerful long-range instrument.

There is a wide range of scale and complexity in the ways that man might be used for the maintenance of a large instrument. At one extreme, we can think of a minimum program where the astronaut floats around the instrument, taking out black boxes and replacing them with others, and then floats back to his capsule, and goes away. This is something we have explored at Princeton in some detail. From the standpoint of the instrument itself, we have convinced ourselves that to take out black boxes and to put others back in, even for a very precise high-resolution instrument, makes very good sense, provided all agree that astronauts can do this on an extravehicular-activity (EVA) basis. On the other hand, it is not clear to us that this is the way that the astronaut developments are going to proceed. It may be that the difficulties with EVA are too great and that this is not an effective way to use astronauts. Perhaps a more efficient method would be to have them go into a pressurized instrument compartment and operate in a shirtsleeve environment to make whatever changes are necessary. Or perhaps we should go to the ultimate in manned maintenance and think of taking the telescope into a large hangar when maintenance is needed. The hangar would then be closed and pressurized, and clean-room facilities would be introduced. After going through suitable air showers, the astronauts would emerge into the hangar and proceed to make whatever repairs are needed.

Somewhere in this range of possibilities lies the optimum way of using man with a

large space telescope. The decision as to how man should be used, depending partly upon man's capability in space and partly upon such matters as economics, will influence the whole design of the telescope.

Astronomical Hardware Goals

What are the specific astronomical hardware goals that we can visualize? The long-range goal is an essentially permanent astronomical facility, which astronomers have designated the Large Space Telescope (LST). We have specified that this LST should have the equivalent resolving power of a 120-inch, diffraction-limited telescope but that the actual aperture might be as great as 150 to 180 inches, depending primarily on the technology and on the diameters of the available launch vehicles. In order to achieve this goal, there might be two such telescopes launched, one as an engineering model and the other as the final instrument.

The intermediate steps between where we are now and this long-range facility are somewhat more controversial. Although I have no specific suggestions to make, I would like to suggest two particular requirements. First, any intermediate facility must be an astronomically significant device. If it is not, it will be very difficult to get astronomers to devote the blood, sweat, and tears that are needed if these astronomers are to contribute any input to this system. If I were asked, as an astronomer, to spend an amount of time comparable to that which I have spent working on the Orbiting Astronomical Observatory (OAO) on an instrument that was an interesting engineering prototype but did not provide key astronomical data, I am sure I would find other areas in which to devote my interests.

The second requirement I suggest is that any intermediate step should advance some of the areas of technology that are crucially important for the large space telescope. I would not suggest that an intermediate step must advance all phases of technology needed for the LST. If a too-ambitious intermediate

step would result in launch only a year or two before the large space telescope, it would mean that such an intermediate program would have very little influence on the LST itself.

My experience with the space field suggests that the group which designs the large space telescope will probably be a different group from that which has designed an intermediate telescope. If any one thing can be predicted, it is that any one group of engineers is likely to want to change any design decisions made by any other group; hence, to make an intermediate instrument a detailed scale model of the large space telescope would make no practical sense at all. To answer basic technological questions in the areas that will be important to the LST is the more useful and important goal. One possible way of looking at an intermediate step is as a smaller instrument that would involve high spatial resolution and high spectroscopic resolution. This would get us involved in the problems of the high resolution mirror, where possibly we could consider segmented optics and some figure control system. It would also give us further experience in acquisition and guidance and would provide an important introduction to the problems of detailed thermal design in a high-resolution instrument. In addition, such a smaller instrument would be used for astronomical research with some of the same detectors that we hope to use in the large space telescope.

The main uncertainty I have in envisioning this intermediate step is whether we would use man or not. This depends entirely upon what the NASA Office of Manned Space Flight recommends that man be used for. If man can be used in a minimum way for EVA maintenance, I hope this technique can be worked into the intermediate step. On the other hand, if man is going to make use of a large enclosed space in orbit, it is very doubtful that it would make sense economically to apply this technique to any instrument smaller than the full-scale large space telescope.

There are many problems in this area, but I remain confident that the large space telescopes of the future will constitute one of

the most important applications of space technology for the enhancement of man's knowledge.

Technology Objectives and Plans

Frank J. Sullivan

NASA, Office of Advanced Research and Technology

70-36682

I represent the group that tries to create and push forward what is often referred to as the "state of the art." For those of you not familiar with the NASA, I am referring to the Office of Advanced Research and Technology, more commonly known as OART. Because Bruce Lundin, Acting Associate Administrator for OART, could not be present at this workshop, he has asked me to convey to you three important points:

1. We are very interested in telescope technology;
2. We intend to continue to work to solve its problems; and
3. We need your inputs to help identify the major problems and how we should approach their solution.

Astronomy has been, and continues to be, one of the NASA's most promising fields of activity. We in the Office of Advanced Research and Technology look forward to having the opportunity to sponsor and to support the technical disciplines that will further observational astronomy — one of the most venerable scientific fields and yet in its infancy from the point of view of new productivity.

Some of the technology problems associated with astronomy seem amenable to solution within our present level of capability and are presently being worked on. Examples of these are active optics and figure sensors, which have been developed and demonstrated in the laboratory but which are, in a sense, crutches or partial engineering solutions to take care of another class of problems. These are the problems that we do not know how to solve or which do not seem likely to be soluble. One example is the construction and figuring of a 2- or 3-meter, monolithic, diffraction-limited, primary mirror suitable for operation in space. Such a mirror would solve many reliability and long-life problems and would probably save a great deal of money. To solve a problem such as this, we normally pursue two avenues — the array of partial solutions and the search for ideal materials — at levels based upon their relative likelihood of success. We intend to follow such a procedure in this particular case.

There is still another aspect of our program that makes life and decision-making interesting, namely, the problem which will be solved by someone else and handed to us on a platter, sometimes right in the middle of a development program. An example is the availability of man for maintenance, for equipment changing, and also, unfortunately, for contaminating the space through which we view astronomical objects. In such cases, we try to plan for all eventualities within the availability of funds, space, and weight and hope that our tradeoffs fit the final facts of life.

The state-of-the-art is, of course, constantly changing; this is demonstrated in the series of talks prepared for this workshop. It is our aim to try to make these changes fit the needs of science, of the nation, and of mankind. In the area of astronomy and technology, no one knows these needs better than you who are taking part in this workshop. We look forward with great interest to the results of your deliberations and assure you they will be used in the most practical and profitable way to forward the state of the technical art related to astronomy.

PRECEDING PAGE BLANK NOT FILMED.

The OAO Series of Space Telescopes

Joseph Purcell

NASA Goddard Space Flight Center

N70-36683

It has been just over a decade since the Orbiting Astronomical Observatory (OAO) has been conceived. OAO-II has almost completed five months of orbital operations. It has been an outstanding engineering success, success in which all involved can take justifiable pride and from which all have derived almost complete personal satisfaction. A brief overview of the OAO program can serve as a baseline against which the ideas discussed in this workshop may be judged.

Pictorial Description

The basic structure is shown in figure 1.

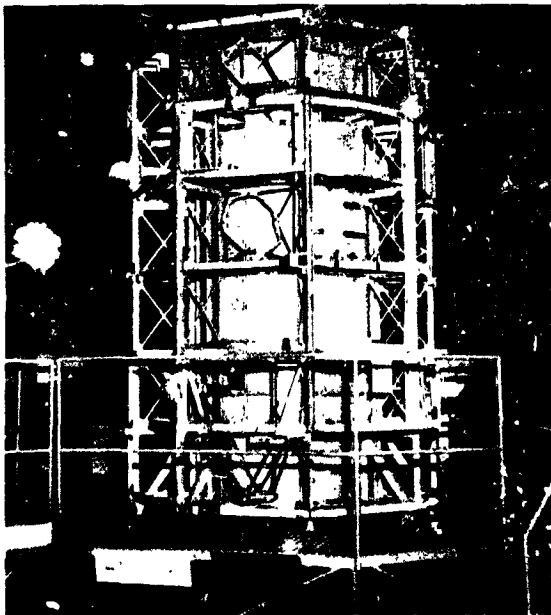


Figure 1. Orbiting Astronomical Observatory (OAO) Structure.

Under all the shiny skins and the super insulation is a fairly complex structure. Figure 2 shows the Wisconsin and Smithsonian Experiment Packages, a cylinder approximately 10 feet long and almost 4 feet in diameter, containing 11 instruments on OAO-II. On future flights, the entire volume will be used for single telescope systems. Figure 3 shows the observatory and the alignment facility. All equipment is integrated, and super insulation



Figure 2. Combined Wisconsin/Smithsonian flight telescope systems for OAO-II.

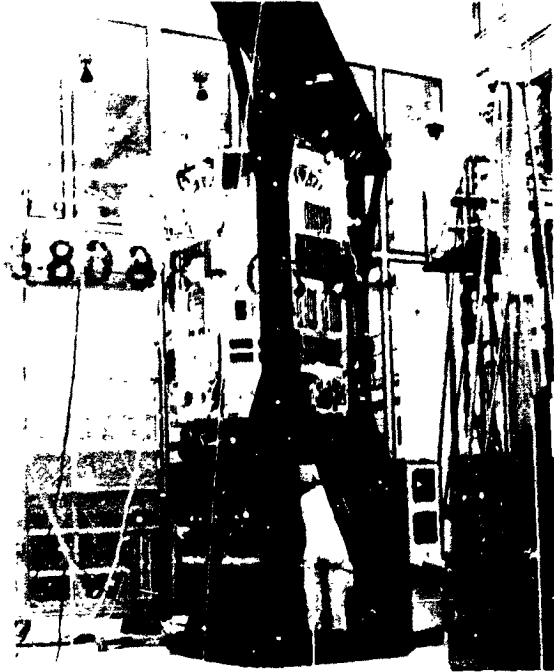


Figure 3. OAO-II in optical alignment facility (August 1968).

blankets are in place. The OAO-II, shown at Cape Kennedy in figure 4, weighs 4400 pounds and is 10 feet high and 21 feet across the solar paddles. We can see the Wisconsin sunshade partially opened at the top of the observatory; two of the six star trackers are also visible at the top. The balance booms are caged in the launched position.

Mission Operations

Although this workshop is devoted largely to space hardware, I would like to discuss mission operations because they are far more complex than the spacecraft. In figure 5 is a projection of the celestial sphere (showing the sun's position) as it was two weeks after we launched. This figure basically defines the observing capability of the OAO system. The shaded area is a 45-degree restricted zone around the sun. Looking closer to the sun would allow it to come over the top of the sunshade and into the telescopes. It takes three months for that area to move aside,

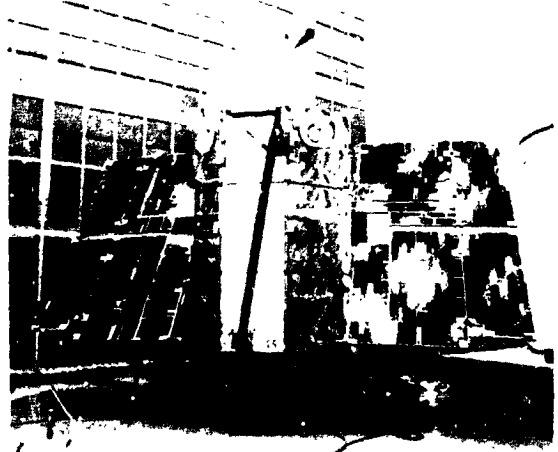


Figure 4. OAO-II at Cape Kennedy (October 1968).

thereby making stars in that region available. We have made observations of Venus slightly inside that boundary by closing the sunshade during the daylight portion of the orbit and opening it immediately upon entry into dark to begin taking the spectral scans. It is possible to look in the 20-degree restricted zone around the anti-sun direction but only for limited times because of a negative power balance at those attitudes. The black line, called the flip circle, defines the hemispheres toward and away from the sun. The spacecraft must be rolled 180 degrees to maximize power after crossing this boundary. Everything except the regions so marked is occulted by the earth at some portion of the orbit, thereby causing some of the operational complexity.

Figure 6 shows the change in occultation pattern. Each block represents the celestial sphere shown in figure 5. The unocculted regions have been removed and replaced by the earth. There are only 10 minutes separation in time, progressing from left to right across this figure, as we go around the 100-minute orbit. In the upper left-hand pattern (top row), we can see that the sun is still above the earth's horizon. In the middle pattern (top row), the sun has set; there is a totally dark earth. A substantial change in pattern is evident in the remainder of the patterns. We can see sun again coming up on

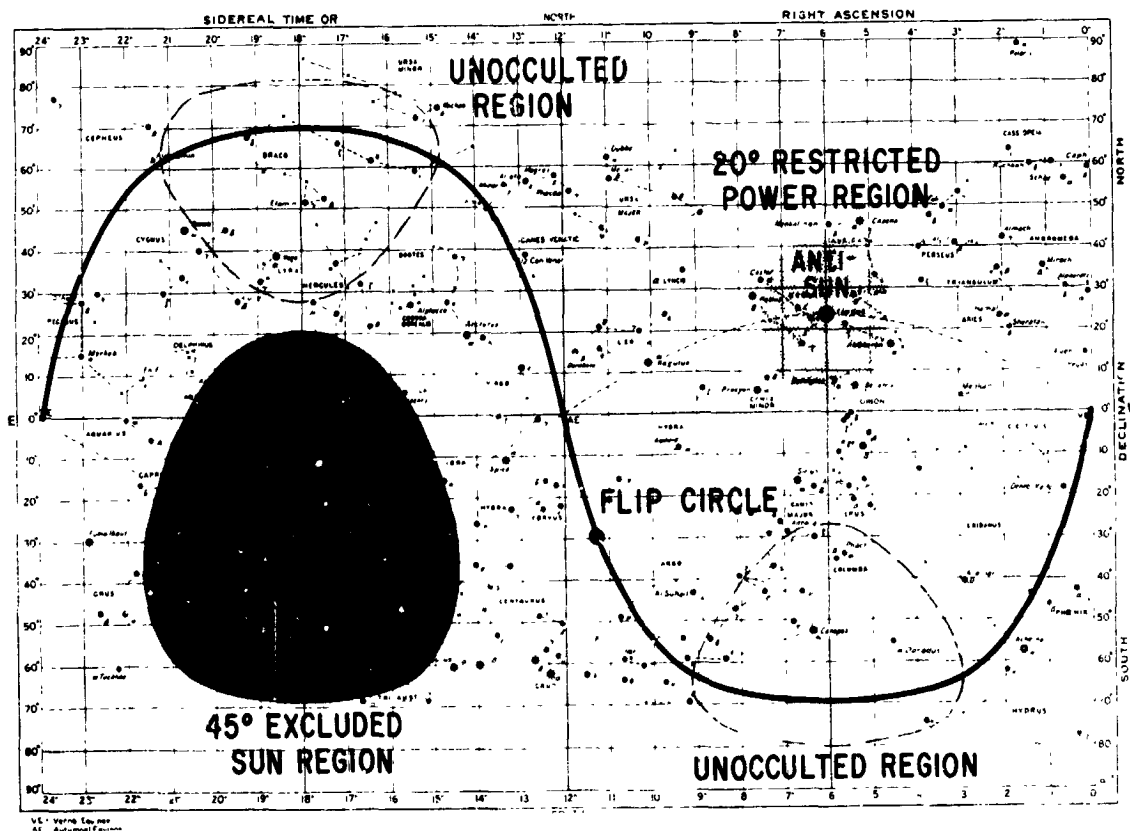


Figure 5. Celestial viewing boundaries for December 21, 1968.

the earth 30 minutes away. Actually, the picture is worse than shown in this illustration because the earth's atmosphere must be accounted for. The star trackers, for example, can only look to within 16 degrees of a bright earth and 5 degrees of a dark earth. The computer, of course, has to know which tracker is assigned to which guide star as these conditions occur and when to include it in the loop or take it out of the loop. This change in patterns happens 14 times a day. It is impossible to speed up a human internal clock by that amount; thus, computer-assisted advanced planning is mandatory to conduct an efficient operation.

The ground system has been simplified in figure 7. On the left is the astronomer who uses the system, which has several computers. Goddard uses the support computer for planning purposes. The output from this computer goes to the control center computer,

which handles the real-time operation processing of telemetry and command data. There are three types of data links that connect the control center to the remote stations: cable, high-frequency radio, and one link through INTELSAT to Santiago. In the control center, we have data in real-time and are also able to command the observatory even though the contact is over a remote station. I would like to emphasize that the astronomer does have direct control; however, the viewing is planned in advance and does not require any real-time "joy sticking." The observatory does precisely what we tell it to do. In fact, OAO is not a cold and impersonal system but rather a unique integration of space and ground systems in which man's intellect has a primary role. The observatory will not function unless we tell it precisely what to do; improper instructions could destroy it.

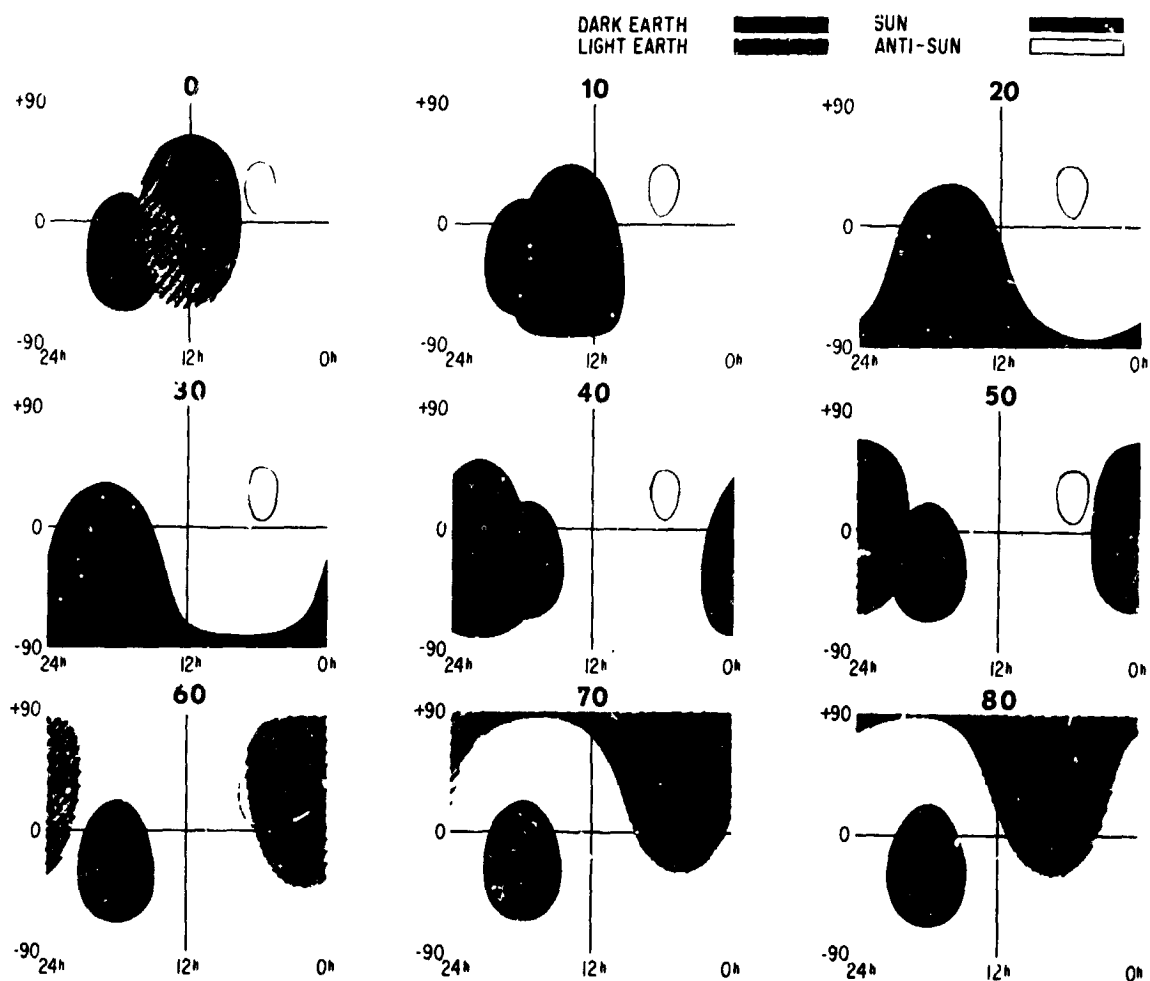


Figure 6. Occultation pattern for December 21, 1968.

Planning Sequence

There are almost 500 man-years of programming in this software system for the planning function. In the planning sequence, the astronomer defines the regions of interest, and the support computer tells him which potential targets are available. From these, he selects the desired targets and feeds that information back to the computer, which prints out the related parameters on the targets chosen. These parameters include when the star is available, where the radiation belt is, where the ground stations are, and all of the other data he needs to know to construct his

observing list. With these parameters, the astronomer can make up specific instructions to his experiment and to the spacecraft. After the third pass through the computer, he has the experiment target list; i.e., a time-ordered sequence of events that the observatory will follow. This list is fed back into the computer for a fourth pass so that the operations staff can add the inputs for operating the ground stations and for functions associated with housekeeping on the observatory. The output of the computer is comprised of a command memory load for the spacecraft and real-time actions that the ground stations will carry out. This output is transferred to the control

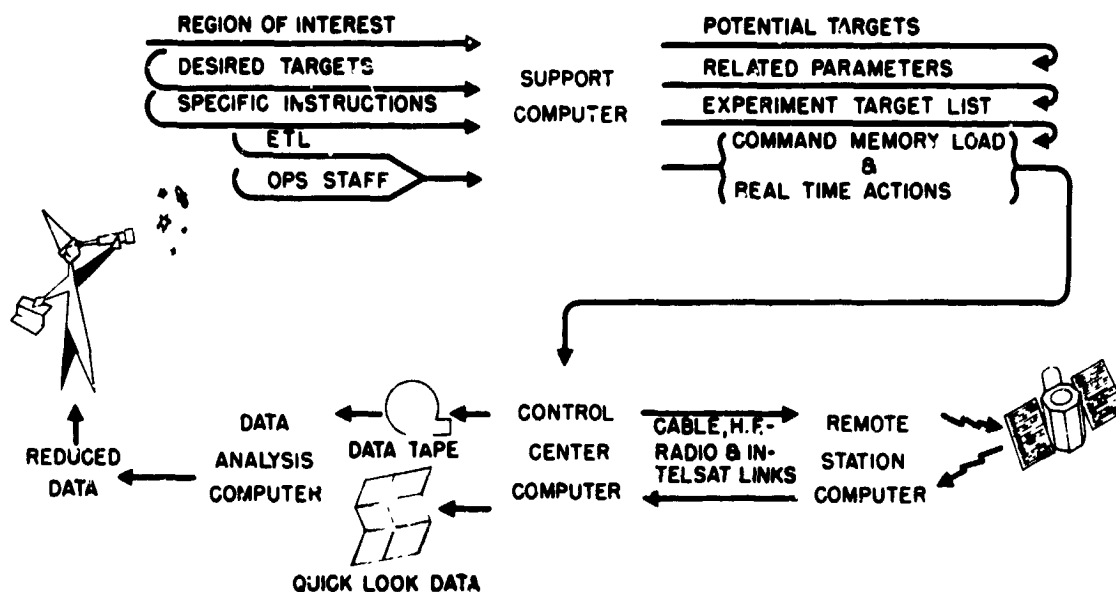


Figure 7. Observatory utilization.

center computer and either sent out in advance to remote stations or, in some cases, commanded directly from the control center. The data comes back into the center when we dump the observatory's data storage at remote stations for quick-look data analysis on magnetic tapes for the data-analysis computer. We have the capability of altering the observing profile if the data should indicate that to be desirable.

The support computer knows all the characteristics of the spacecraft. It is a completely automated system. A few of the constraints that the computer checks are:

- Target-to-sun distance
- Experiment target occulted
- Command memory overflow
- Dynamic and static impingement
- Sun-slew path
- Deviation from optimum roll
- Flip angle detected
- Guide stars unavailable for slew
- Gyros required
- Large slews required
- Time error on experimenter target list (ETL)
- Contact duration less than 5^m

- Delayed mode interval too short
- Real-time slew outside contact

Figure 8 is a world map with a sub-satellite plot for the first five orbits. We have five remote stations that provide from one to three contacts per orbit. The orbit period is 100 minutes. The cross-hatched area is the South Atlantic anomaly, whose location the support computer knows. We do not try to operate the Wisconsin Experiment in that region because the data is not very reliable.

OAO Current Status

The photograph (fig. 9) of the control room shows the display board, which contains complete observatory status. Adjacent to it is the experiment equipment where, when experimenters have quick-look data coming in, they can command their experiment directly. They request permission to do this from the project operations controller, who enables their commands so that they can operate their experiment in real-time.

Extractions of data from the weekly progress report shows us the current status. The OAO has been up 137 days. The

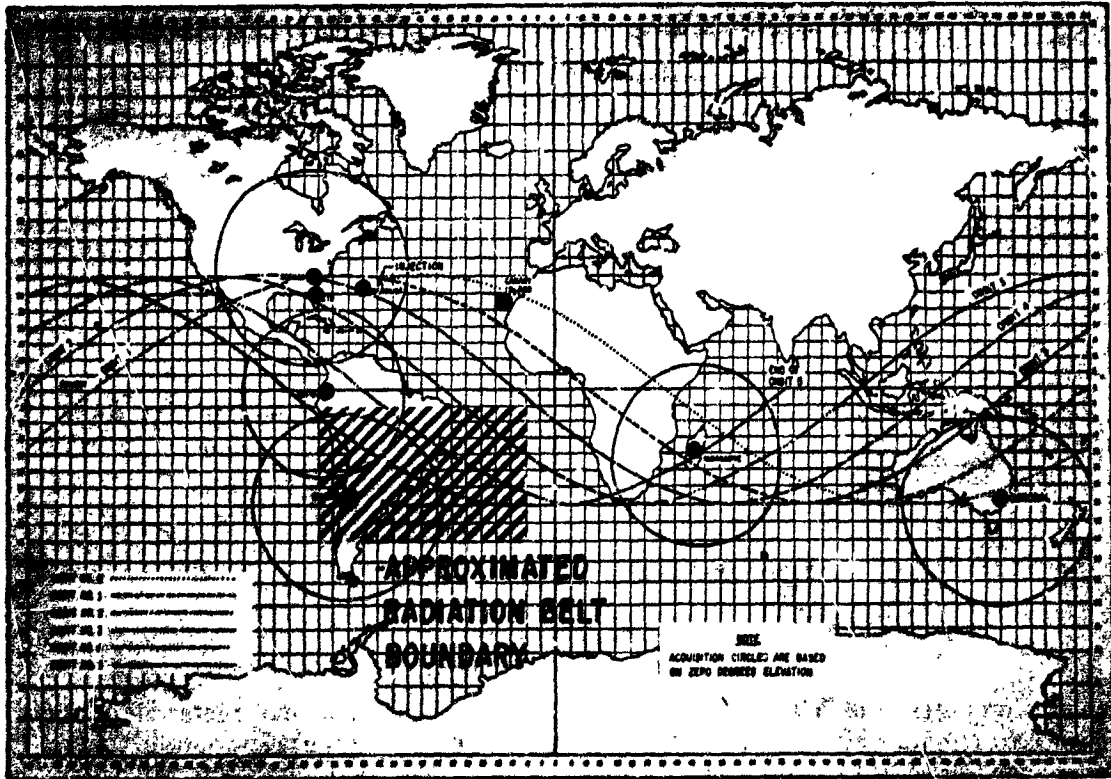


Figure 8. Sub-satellite plot for first five orbits.



Figure 9. OAO operations control center.

Wisconsin Experiment Package (WEP) has looked at 846 separate pointings in which there were 344 unique objects; frequently, they would look at an object and then look at the background. The Smithsonian Astrophysical Observatory (SAO) has looked at 483 different pointings for a total of 1100 pictures. We have flipped the spacecraft 11 times.

OAO Pointing Accuracy

Table 1 presents the present and future performance that we hope to obtain from the spacecraft. We had a pointing accuracy requirement of plus or minus one minute of arc. We aligned within that on the ground. It shifted during launch, as expected; thus, when we were first on station in orbit, we had some 2-arc-minute errors pointing. This has been reduced to plus or minus 30 arc seconds through a calibration program.

We can bias the angles to the star trackers to account for misalignments. With the boresight star tracker (BST), we can point to within plus or minus 5 arc seconds. On the next spacecraft, with the fine guidance of the experiment, we will have a 1-arc-second pointing capability and on the Princeton Experiment Package (PEP), a 0.1-arc-second pointing capability in one axis.

The question of stability always arises. Figure 10 is a reproduction of actual

Table 1. OAO Pointing Accuracy

Star-Tracker Coarse Pointing Before Calibration	± 2 arc min
Star-Tracker Coarse Pointing After Calibration	± 30 arc sec
Boresight Star Tracker (BST) Pointing	$P/Y \approx \pm 5$ arc sec
Spacecraft #3 Goddard Experiment Package (GEP) Pointing	$P/Y = 1$ arc sec (2 mag. star)
Spacecraft #4 Princeton Experiment Package (PEP) Pointing	Pitch = ± 0.1 arc sec Yaw = ± 5 arc sec

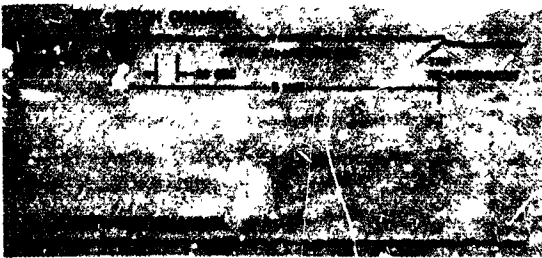


Figure 10. Spacecraft under GST control.

telemetry data. The spacecraft is under control of the gimballed star trackers (GST's), and the curve in the figure is the error signal out of the boresight tracker, an independent measure of the spacecraft performance. Conservatively speaking, we have a plus or minus 3-arc-second stability with a 5-arc-second resolution on the shaft-angle encoders. Dr. Arthur Code has offset point the spacecraft to the slope on the edge of his field-of-view and has come up with a number closer to 1 arc second. In any case, it is the encoder resolution on the star tracker that sets the limitation. On the righthand side of the figure, we can see the effect of a tracker reassignment. We switched in another tracker

because the one that was previously there would have been occulted. This is what limits the pointing accuracy. That transient will not occur, however, when we are under the boresight control or gyro control and will not occur on subsequent missions when we are under control of the inertial reference unit or the experiment fine-error sensor (FES).

The curve in figure 11 was taken from computer runs made on the fourth-flight control-system configuration. We predict 0.02-arc-second jitter while using the Princeton fine-error sensor.

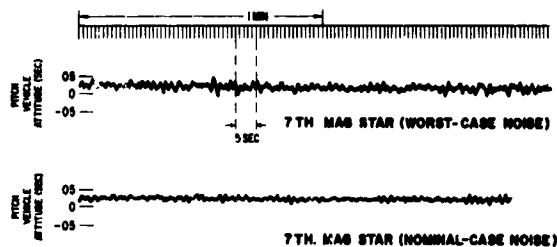


Figure 11. Computer runs showing PEP pointing and jitter.

Another important parameter is settling time after slewing. The slew rate of OAO is 6 degrees per minute. For a 6-degree slew, figure 12 shows that we had predicted on the upper curve almost 1 minute of settling time, equal to the slew time. The dashed curve shows what we actually encountered in orbit; the lower curve shows what we shall get as we

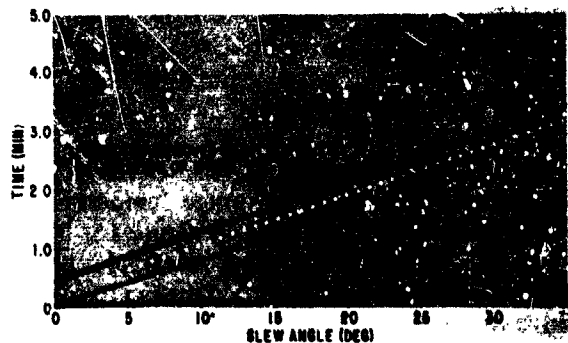


Figure 12. Open-loop settling-time curve; 12 1/2 percent wheel speeds.

calibrate the slew counts for the coarse wheels. We can do this in the support computer. In the next flight, with a closed loop slew under control of an inertial reference unit, settling time becomes negligible. This is represented by the lowest curve in figure 12.

The rate and position sensor (RAPS) is a gyro package used on OAO to hold attitude. The specifications on the gyros were 0.3-degree-per-hour drift rate. For the first thousand orbits (fig. 13), we have achieved between 0.05- and 0.2-degree-per-hour drift rate on these gyros.

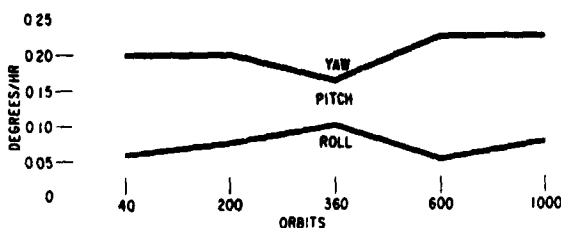


Figure 13. RAPS drift rate.

Figure 14 shows the inertial package for the next flight. In this case, we use precision gyros from MIT; we do a closed loop slew that allows the spacecraft to end up within the field-of-view of the experiment and allows us to predict the drift rate will be 10 arc seconds per hour after compensation in orbit.

On the fourth flight, we will fly an electronically scanned star tracker (ESST) as a controls experiment. We fully expect to go to all electronically scanned trackers on flights beyond OAO-C.

OAO Thermal Subsystem

An important part of the OAO is the thermal subsystem. The average temperature of the structure is plotted in figure 15. The scale along the bottom is the beta angle. Beta zero means the spacecraft is pointing its optical axis in the anti-sun direction and, conversely, beta 180 degrees would be the spacecraft pointing at the sun. We can see the positive power region from beta 20 to 160

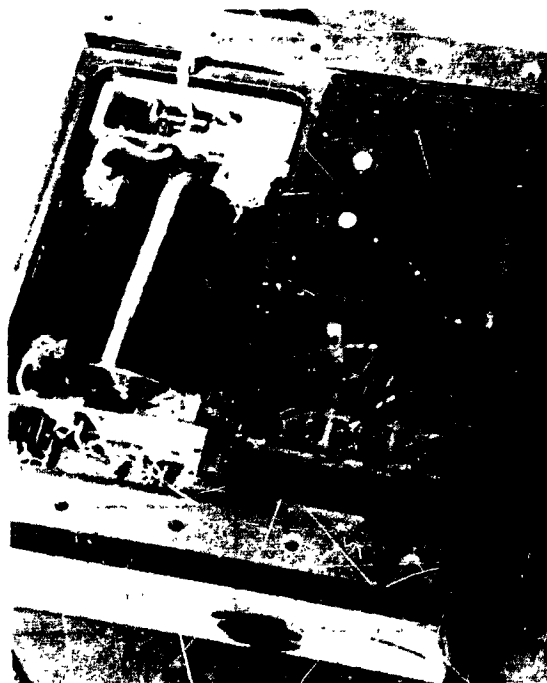


Figure 14. MIT inertial reference unit for OAO.

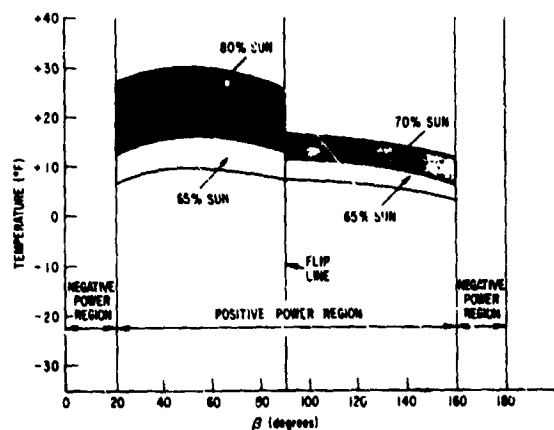


Figure 15. Average structure temperature for OAO-A-2.

degrees. The structure, used to control the temperature of the Wisconsin Experiment, is relatively constant as a function of viewing angle although somewhat sensitive to the percentage of sun time.

Figure 16 shows the effect (shaded areas) of the Wisconsin Experiment detectors

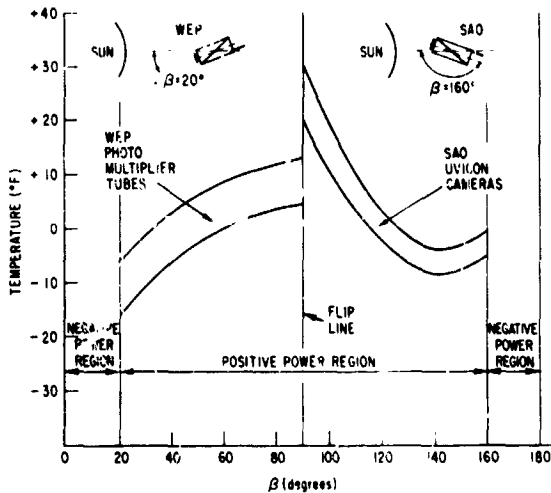


Figure 16. Experiment temperatures for OAO-A-2.

when they are coupled to the structure. They are also sensitive to the aperture. Both detectors have a considerably higher variation than the structure and are totally dependent on its variations as well as the aperture temperature. SAO has a considerably wider range because it is insulated from the structure.

To become oriented to figure 17, let us imagine we are lying down on the floor of the clean room looking up through the central tube of the spacecraft. We can see three heat pipes that have been installed as experiments on the next flight. We are flying them to gain knowledge on how to provide proper thermal environments for large telescope systems. Figure 18 shows a little more detail of the pipe and its mounting saddle, which is bonded to the central tube. The effectiveness on OAO is somewhat limited by the thin gauge of the central tube plus the less-than-100-percent saddle contact. In the future, the pipes will become somewhat more integral to the structure.

In figure 19, the structural temperature and gradients of the OAO-II flight and the next flight are compared. The longitudinal station is at the bottom of the figure, and the broad band represents the OAO-A-2 spacecraft with the sun on the B side or the sun on the A side of the spacecraft imposing a gradient. The circumferential gradients are

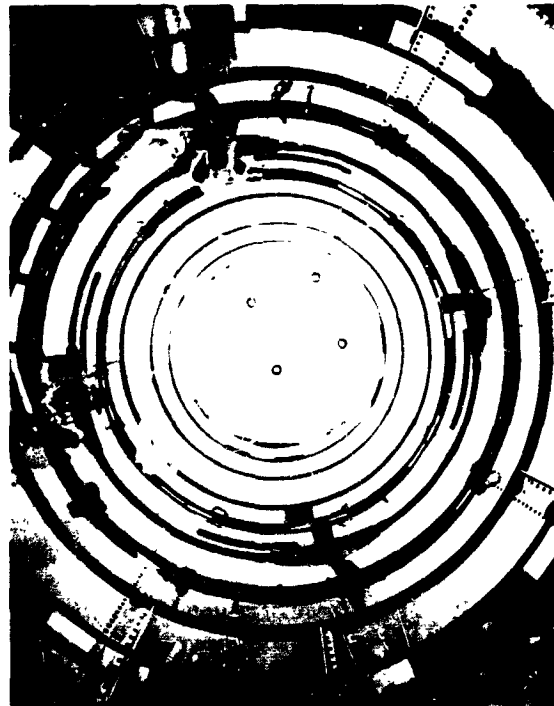


Figure 17. Heat pipe arrangement.

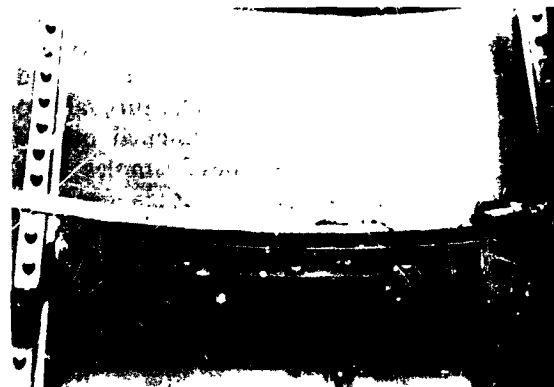


Figure 18. Heat pipe detail.

fairly high on OAO-II because some of the equipments, such as the batteries and the tape recorder, dumped heat into the structure. This was an expediency in the schedule under which we were operating. As we progress to OAO-B, we shall fully insulate the structure. The improvement is a considerably reduced circumferential gradient. The backend of the spacecraft where the heat pipes are has

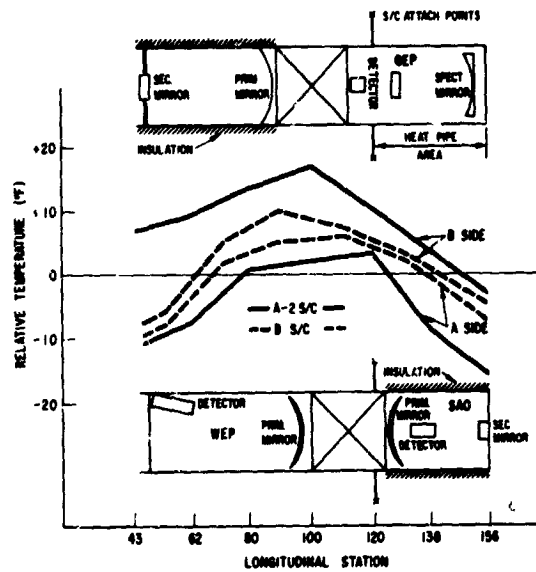


Figure 19. Temperature of central tube relative to average structure temperature.

approximately a 2-degree circumferential gradient.

Another matter of considerable concern to us before launch is the condition of the thermal coatings, which are Alzak skins. We were worried about their degradation and invoked a special quality control program to check them. Samples were punched out of each of the flight skins; these samples were checked; and, if any skin did not meet specifications, it was rejected for flight use. In figure 20, the solar absorption has been plotted on the left against the equivalent sun hours. We flew several samples on an Applied

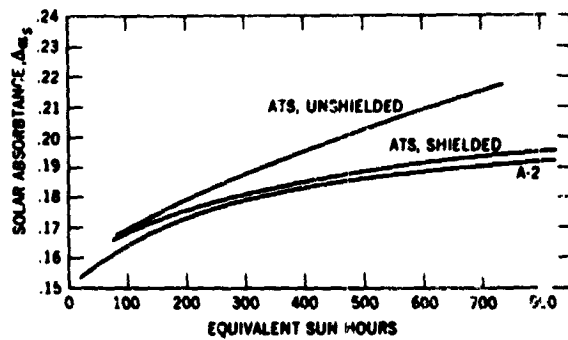


Figure 20. Alzak degradation comparison.

Technology Satellite (ATS). We can readily see the degradation from the unshielded sample and the shielded. The lowest curve represents the data that we have been getting on OAO-II; it presents no problem after well over a year's life.

OAO Power System

Another important subsystem is the power system. In figure 21, looking at beta angles once again, we can see that the array output scribes a butterfly-shaped curve as the spacecraft is pointed at the various angles.

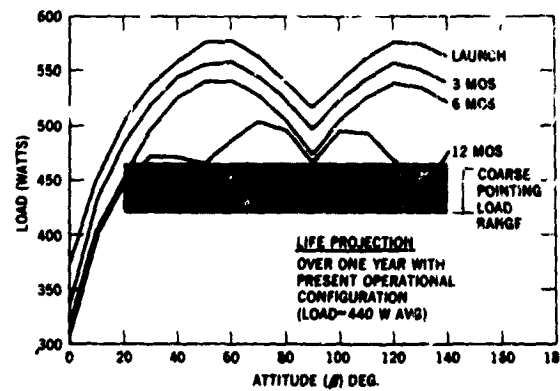


Figure 21. OAO-II: power subsystem load capability (actual) and worst-case predictions.

This occurs because the array is fixed. It is evident that at launch we had a considerable margin. The 3-month, 6-month, and 12-month curves are our worst-case predictions on degradation. The shadowed area is the range in which we normally operate for power. Battery charge control is a very difficult task when the load, the array output, and the battery temperature can all vary; however, the system is working extremely well. We are using the voltage-sensing system to limit the charge. We have ampere-hour integrators and anhydrides as backup. In the OAO-B, we shall continue to have single-sided operation of the spacecraft. Solar cells are on only one side of the arrays. We no longer will have the butterfly curve. The beta angle is somewhat limited at the higher angles (fig. 22).

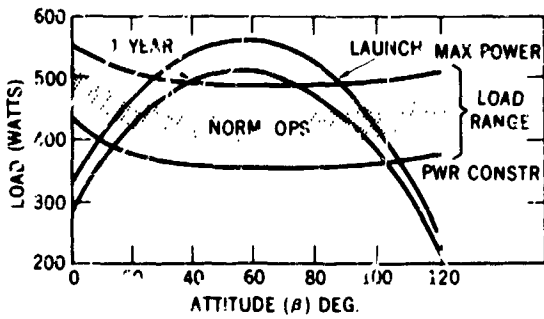


Figure 22. OAO-B: power subsystem load capability (nominal).

Baffle Development

Before launching OAO-II, we recognized that the scattered light would very likely be a problem. It was not feasible to do anything about it for OAO-II because we had a double-ended experiment looking out of both ends of the spacecraft and any change would have delayed the program. We did, however, start baffle development for the next two flights. Figure 23 shows the first light baffle. It is



Figure 23. OAO-B sun baffle.

very difficult to test on the ground; hence, we shall be testing it only in orbit. We expect it to make substantial improvement. If it allows us to operate in daylight, and it should, then we will almost double the observing time. Another advantage is that it provides almost a constant aperture temperature for the experiment.

Reliability Estimates

Figure 24 shows the OAO-B in the clean room at the Goddard Space Flight Center, where it is undergoing equipment and experiment integration. Our first concern for the future is OAO-II. Although I have never attached much importance to reliability estimates, except in a relative sense, I have attempted to quantify the actual experience on a number of Goddard satellites. Figure 25 is a plot of this experience but excludes the experiments and the first launch. It shows the reliability of spacecraft systems after the first launch. On the abscissa we can see the year of launch and the average design life at that time.

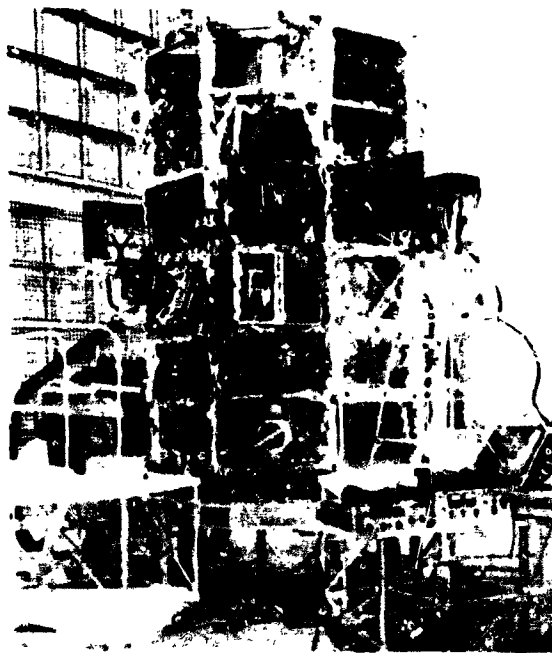


Figure 24. OAO-B buildup (March 1969).

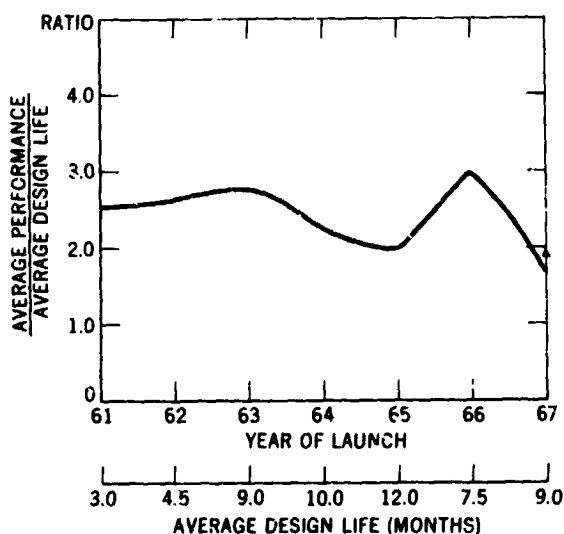


Figure 25. GSFC satellite performance versus design life by year ratio.

We have averaged over twice the design life in orbit. The design life on OAO is one year. Figure 26 presents a reliability projection for OAO based upon a 6-month successful, prelaunch operation. Prior to launch, Grumman used MIL handbook rates and predicted a 0.0001 probability for meeting the 1-year objective. If we factor in failure rates from the Orbiting Geophysical Observatory (OGO) in-orbit experience, the probability increases to 0.2. If we grossly factor in the experience from other Goddard satellites, the probability increases to 0.67. The solid black curve is the demonstrated reliability of OAO-II. We are now almost at the 5-month mark, which can be interpreted two ways:

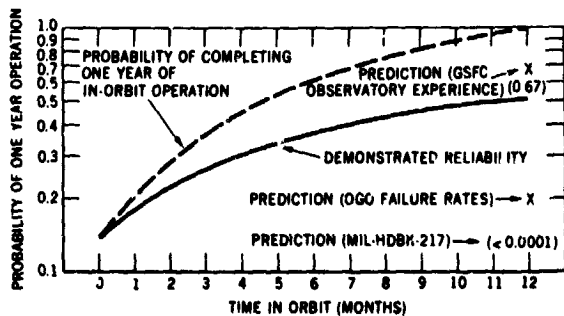


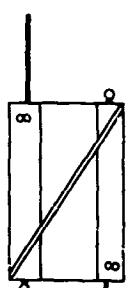
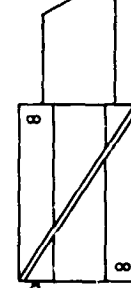
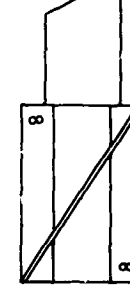
Figure 26. OAO II: reliability based on in-orbit time plus six months prelaunch operation.

(1) we have a 34-percent chance of lasting another year from this point or (2) if we fail now and launch another OAO, it would have a 34-percent chance of lasting a year. The broken curve shows the probability of completing a 1-year operation in orbit. In any case, we now have a 50-percent probability. We do, however, have sufficient confidence in OAO-II to modify the control centers to handle two OAO's in orbit at the same time.

If we ignore random failures, what factors might limit OAO life? Our solar array degradation appears to be no problem; thermal coating degradation is also no problem. We have an abundance of gas supply. The star trackers have shown only a slight decrease in sensitivity. We recently went through an exercise to look through 19 dimmer stars and have added these to the catalog of guide stars that we can use; we see no problem from this very slow degradation of sensitivity of the trackers. There are, of course, such questions as: will the gyro wear out or will the gimbals on the star trackers malfunction? These are hard to answer, but thus far they present no significant problems. Although there has been some rather naive talk about maintainable systems, we certainly should avoid making programmatic decisions of this nature on the basis of reliability predictions.

OAO Evolution

OAO is not a static problem. We have increasingly difficult telescope systems. The pointing accuracy and stability increases an order of magnitude between each flight. Figure 27 summarizes data pertaining to the evolution of OAO. We are progressing through an equipment evolution where we advance from stellar to inertial control, where we phase-in electronically scanned star trackers, where we add the light baffle to the configuration and go to the single-sided operation with an onboard computer and a number of other improvements. In the present program, we are basically test flying components that we shall need in the future. We anticipate an electrical reconfiguration on the spacecraft

CONFIGURATION				
		*OAO-A 2	OAO-B	OAO-C
	TECHNIQUES	STELLAR	STELLAR / INERTIAL	INERTIAL / STELLAR
CONTROLS	GYROS	GE	GE / MIT	MIT
	SUN SENSORS	CSS, FSS, RAPS & ASPECT	CSS, FSS, RAPS & ASPECT	CSS, FSS, RAPS, ASPECT & DSS
	STAR TRACKERS	5 GST'S & BST	5 GS'S & BST	4 GST'S, BST & ESST
THERMAL	EXP. ERROR SENSOR	NONE	FES (1 SEC)	FES (0.1 SEC)
	SIDES IN SUN	DOUBLE	SINGLE	SINGLE
	HEAT PIPES	NO	3	3
POWER	ARRAYS	DOUBLE-SIDED	SINGLE-SIDED	SINGLE-SIDED
	BATTERY CHARGE CONTROL	VOLTAGE SENSE A.H. INTEGRATOR ANHYDRODE	VOLTAGE SENSE A.H. INTEGRATOR ANHYDRODE	VOLTAGE SENSE A.H. INTEGRATOR ANHYDRODE
	BATTERY CAPACITY	60 A.H.	60 A.H.	60 A.H.
DATA-PROCESSING	COMMAND STORAGE	PPDS	PPDS & ACMU	PPDS & COMPUTER
	DATA STORAGE	PPDS	PPDS	PPDS & COMPUTER
COMMUNICATIONS EXPERIMENT	WIDEBAND	8 WATTS (HAC) 18% EFF. WEP & SAO	8 WATTS (GFE) 30% EFF. GEP	8 WATTS (GFE) 30% EFF. PEP & UCL

*Same as OAO-II.

GE - General Electric	BST - Bore-sight Star Tracker	WEP - Wisconsin Experiment Package	ESST - Electronically Scanned Star Tracker
EXP - Experiment	GST - Gimballed Star Tracker	GEP - Goddard Experiment Package	MIT - Massachusetts Institute of Technology
FES - Fine Error Sensor	CSS - Coarse Sun Sensor	PLP - Princeton Experiment Package	PPDS - Primary Processor and Data Storage
FSS - Fine Sun Sensor	RAPS - Rate and Position Sensor	UCL - University College of London	ACMU - Auxiliary Command Memory Unit
DSS - Digital Sun Sensor	HAC - Hughes Aircraft Corporation	GFE - Government Furnished Equipment	

Figure 27. OAO evolution.

for OAO-D and a structural and thermal reconfiguration for OAO-E.

Future OAO Program

We have discussed the reality of today and some of the improvements of the near future. The OAO program, as now structured, will have two more launches, the Goddard Experiment Package (GEP) in 1970 and the Princeton Experiment in 1971. The Apollo Telescope Mount (ATM) is scheduled for 1972; it should answer the question: What can man's intellect in space contribute?

But what lies beyond? We have studied

various advanced configurations for larger systems up to the 120-inch system. We know that it was more difficult to go from nothing to OAO than it will be to evolve into the future. I am confident that the OAO spacecraft systems can be scaled up to meet future needs. We intend to concentrate on the more difficult problems of the telescope and detector systems; however, there does not presently exist a viable program after the scheduled OAO's and ATM's.

How can you contribute? First, recognize that building a reliable space system is a tough job. As scientists, do not hinder these systems with unreasonable requirements. As

engineers, do not blindly accept those requirements; question them. Second, be sure that any new system is optimized for astronomy. We have heard much discussion of future systems. We have a lunar landing system that has been optimized for that purpose. People

may argue about the objectives, but it is an optimized system. Third, recognize that multiple objectives in one mission always conflict and can easily delay and diminish the scientific results.

One Concept for a 3-Meter-Class Space Telescope

David Bogdanoff
The Boeing Company

N70-36684

The present paper summarizes the concept for a 3-meter orbital telescope, which was developed for NASA by The Boeing Company under a contract that spanned the period of 1964 to 1966. Although, during the time that has elapsed since the termination of this contract, considerable work has been done in certain technical areas that suggests solutions different from those posed in this paper, a discussion of the overall concept, the system interfaces, and the solutions to some of the unique problems will provide background for some of the discipline-related papers being presented at this workshop.

The main objective of the investigation was to develop a concept for a large, high performance, orbital observatory that would serve as a goal for the NASA program in the field of Optical Astronomy. In addition, the accompanying engineering studies and analyses would indicate areas where state-of-the-art technology advances were necessary for the development of such a system.

The investigation was constrained by four ground rules:

1. Telescope aperture: 120 inches
2. Boost vehicle for low earth orbit: Saturn 1B
3. Diffraction-limited performance
4. Multipurpose, including imagery, photometry, and spectroscopy.

Many of the design requirements of such a system are relatively independent of the method of orbital operations. In general, these requirements are associated with the basic telescope optics, experiment equipment, the cabin, and the primary structure that ties these elements together. This part of the vehicle can be termed the *baseline telescope*

configuration. The design requirements associated with orbital operations can be handled by the addition of interface structure and subsystems to the baseline configuration.

The approach taken in developing the baseline configuration was to generate the observational requirements very early in the program with the aid of the consultant services of Dr. Z. Kopal. These requirements were then used as guidelines in developing the telescope optics and instrumentation. As the investigation progressed, further iterations were made using the works of Code and Fredrick. As a result, a Cassagrainian type of optical configuration was chosen with two alternate secondary mirrors and the flat-folding mirrors. This system is illustrated schematically in figure 1.

Even in development of the optical schematic, the interface problems between the optical system and the structural design become apparent. These interface problems influenced the selection of the optical system geometry by imposing the following requirements:

1. The size of the secondary mirror and its mounting structure was restricted to a permissible light blockage of the primary mirror. A 39.6-inch diameter was used as the maximum acceptable for the secondary mirror and housing. This corresponds to an obscuration ratio equal to 0.33.

2. The folded light paths at the Cassagrainian focus had to be compatible with a folding mirror and the equipment installation arrangement.

The length of the folded light paths that could be handled within the cabin determined the final location of the secondary mirrors

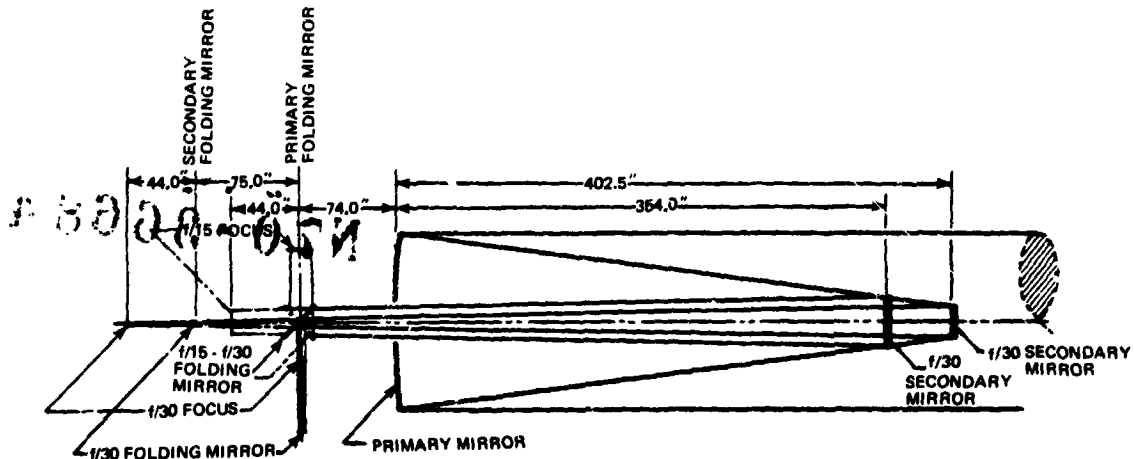


Figure 1. Optical schematic.

relative to the primary mirror. Selection of the experiment equipment arrangement and the folding mirrors were the dominating factors in determining the size and shape of the cabin.

In the development of the baseline configuration, the strong interfaces among the structural, optical, and thermal systems became even more apparent. The baseline configuration shown in figure 2 is, therefore, a compromise to satisfy the requirements imposed by such problems.

The design is based upon the geometry fixed by the $f/4$ primary mirror optical system and upon the requirements for a structural and thermal arrangement that can both satisfy the launch loads and provide acceptable thermal and dynamic characteristics for orbital operation.

A double-shell tubular structure is used for housing the telescope mirrors. The exterior shell, which is separated from the interior shell by layers of super insulation, is attached to the forward end of the cabin and

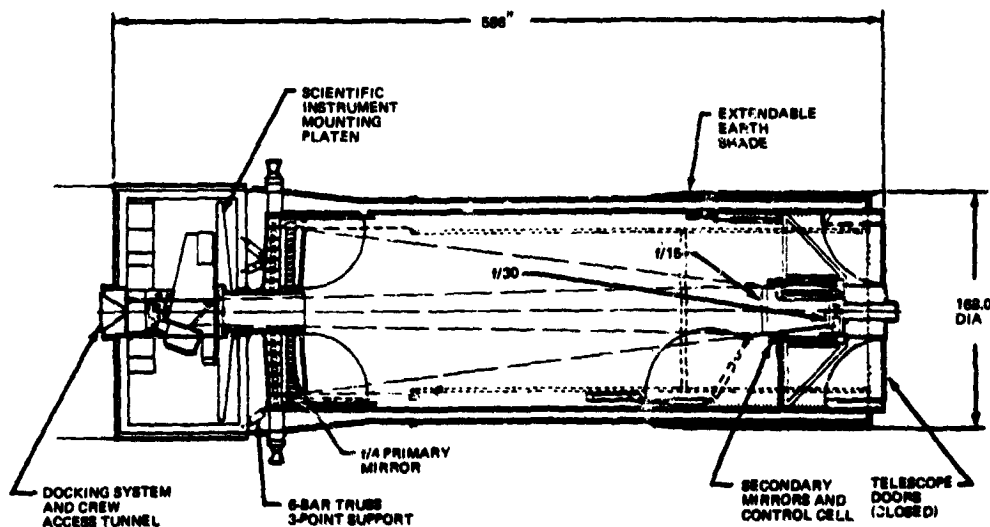


Figure 2. 120-inch manned orbital telescope, baseline configuration.

extends the full length of the telescope. The inner shell of the double wall design is the main structure, which supports or ties together all elements of the optical systems. The complete inner shell, mirrors, mirror support structure, and platen for mounting the scientific instruments are attached to the cabin by a six-bar cantilever truss. The truss is connected to the cabin at three structural attachment points. The overall arrangement of the two shells and three-point mounting is used to decouple the optical system from the outer shell and cabin for thermal isolation and to minimize mechanically induced structural distortions. The three-point mounting permits the plane of the attachment points to tilt without inducing stresses into the optical support structure.

The secondary mirrors, located at the forward end of the telescope, are mounted in a control cell supported by four radial-truss type of spokes attached to the inner shell structure. An examination of the performance requirements revealed the critical nature of the alignment problems of the secondary mirrors with respect to the primary mirror and instruments. Accordingly, the control cell provides a five-axis automated control for aligning the secondary mirrors. Figure 2 also depicts a mechanism for removing and storing the $f/15$ secondary mirror.

To obtain the desired shading from earth radiation while keeping within a reasonable height for the launch configuration, a telescoping section is used at the forward end. This section is extended and fixed into position after the vehicle is in orbit. The earth shade was incorporated into the baseline as a result of the thermal analysis. The purpose of the shade is to place the secondary mirrors and doors inboard of the end of the telescope shell, which is exposed to Earth radiation. The doors in the open position should be in a uniform temperature zone so that, when they are closed, they have little thermal effect on the primary mirror. In the closed position, the doors also require thermal insulation to control their heat transmission when their outer surfaces are exposed directly to the Earth-

emitted-and-reflected radiation in the daylight half of the orbit.

The primary mirror (which, in this concept, was of a beryllium honeycomb construction) is mounted on three-point tangent bars, designed to minimize heat shorts and structural distortions. During boost to orbit, the primary mirror is structurally decoupled from the tangent-bar mounting and is floated on pneumatic bladders to insure that the mirror will retain its figure. There are, however, practical problems involved in the use of pneumatic bladders for boost and also in the engagement of the tangent bars in orbit without damage to the mirror or degradation to its figure. This is an area where further research is recommended.

The platen to which the experiment equipment is mounted is located inside the cabin but is not structurally mounted on it. A flexible bellows is shown (fig. 2) between the platen tubular support and the cabin bulkhead. This permits the cabin bulkhead to be deflected by pressure and temperature variation without producing strains. The cabin is a cylinder with a flat, pressure type of bulkhead on each end. This shape provides volume and space in which a feasible arrangement can be provided for mounting the scientific instruments and for accommodating the crew.

A launch configuration installed on top of the SIV stage of the Saturn 1B is shown in figure 3. The telescope is packaged within a jettisonable boost shroud, similar to the design of the Apollo Lunar Module Adapter. The boost shroud, which includes the nose cone section, is jettisoned after the first-stage burnout of the Saturn 1B. By this technique, the payload to orbit is only penalized by approximately 12 percent of the actual weight of the boost shroud, and the telescope primary structure need only satisfy the boost inertial loads and the actual orbital-operation design requirements. The telescope is supported on top of the SIVB by a truss type of structure that transfers the flight inertial loads to the outer booster structure at six hard-attachment points. Separation of the telescope from the SIVB is also effected at these

attachment points, which are located at the same separation plane as that used for the jettisonable boost shroud.

In flight to orbit, the SIVB places the telescope into a phasing or holding orbit. The SIVB is then separated from the telescope, and two 1000-pound thrust rockets are used to perform the orbit transfer associated with rendezvous maneuvers. This telescope concept was originally conceived to operate in conjunction with a space station, either attached to it or operating in the vicinity of it. Figure 3 shows some of the gimbal support structure for attaching the telescope gimbals to the space station. This gimbal structure would only be present in the designs where the telescope was to be operated when attached to a space station. There would also be a removable boost structure, for example, to protect the instrumentation mountings on the platen and the telescope mirrors during boost. This structure would be removed after boost and before orbital operations. The effective launch mass of this configuration on the Saturn 1B is 27,819 pounds.

The conceptual design, shown in figure 4, is the orbital configuration of the telescope when it is detached for astronomical observation. In this concept, it is presumed that the telescope will be visited periodically for maintenance, for setting up of new experiments, and for the retrieval of film. It is not manned, however, during telescope operation. This detached mode of operation is required to have the following onboard subsystems: reaction jets to supplement the control moment gyro system for target pointing, propulsion for orbit keeping, an electrical power system, and electronic systems for communications, data-handling, and attitude control.

The electrical power supply is a solar cell/battery system. Shown in figure 4 are two foldout solar panels, which are sun-oriented by articulation of the panels about one axis and the rolling of the telescope for the second axis of control. The panels are locked in a fixed position for astronomical observations.

Four clusters of variable-thrust reaction jet subsystems are used for all required propulsion associated with attitude control and

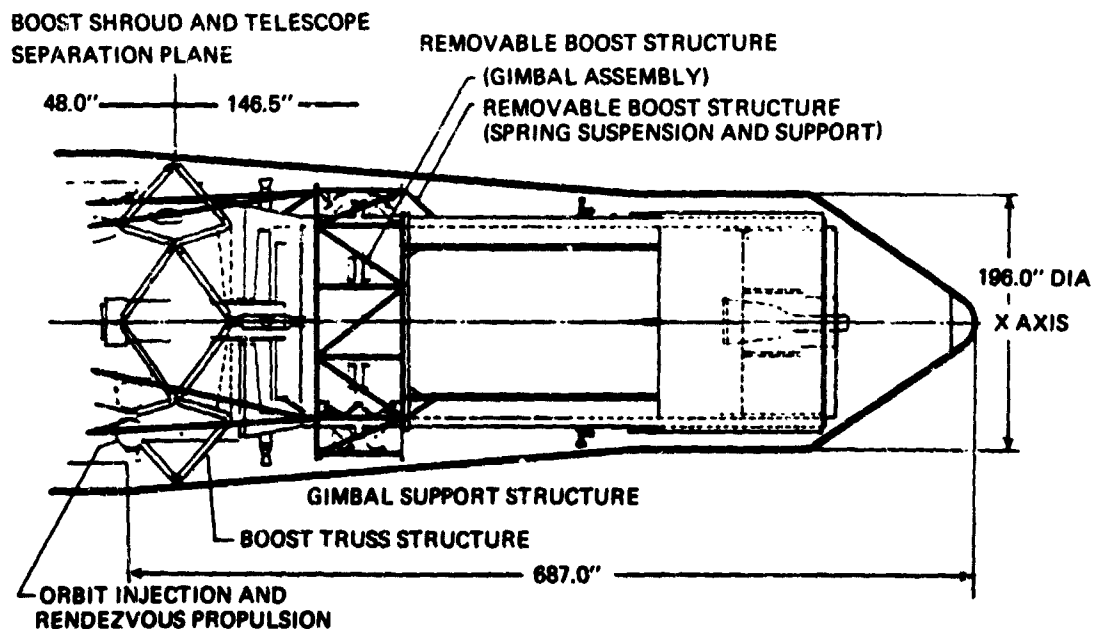


Figure 3. Launch configuration, soft gimbal mode.

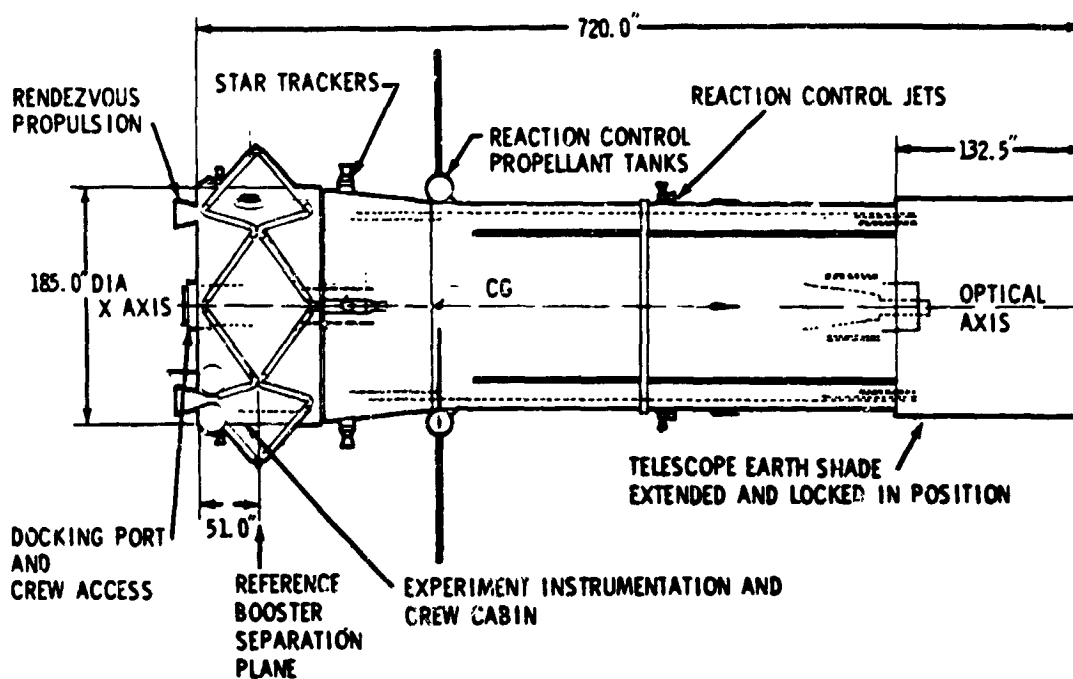


Figure 4. Detached orbital configuration (unmanned during experiment observations).

space maneuvering functions except initial rendezvous. A throttling ratio of approximately 10 to 1 is required to cover the range between low torque thrusters for control-moment gyro desaturation and the thrust levels used for docking. The propellant tanks for the reaction control system are located on the center of gravity of the vehicle pitch and yaw axis. This location minimizes the center-of-gravity shift with propellant usage. Two 1000-pound-thrust rocket engines located at the aft end of the cabin are used for the orbit transfer functions associated with initial rendezvous. Some of the antennas required for communication and guidance are also indicated on figure 4.

The cabin, shown in figure 5, is arranged with all the scientific optical instruments mounted on a rigid base or platen located in the forward section adjacent to the telescope. The supporting subsystems are located around the periphery in the aft section. The platen is a cantilever structure, physically supported from the optical system support base by a tubular section extending thru the cabin bulk-

head. The only physical attachment between the platen structure and the cabin is a bellows located around the platen support tube. This design feature is used to protect the alignment of the scientific instruments with the main telescope optics.

The instruments are positioned radially around folding mirrors on an arc formed by the focal point as the mirrors are rotated. The light beam from the telescope proper is folded once for the $f/15$ experiments and twice for the $f/30$ experiments. The primary folding mirror folds the light 90 degrees, making the light rays parallel with the mounting platen. The mirror can be rotated about the telescope optical axis, thus aligning the focal plane with a selected instrument for $f/15$ observation.

A secondary folding mirror is used in conjunction with the $f/30$ secondary mirror to provide for the $f/30$ instruments positioned radially with respect to the secondary folding mirror.

Clearance from the surface of the platen to the cabin ceiling is approximately 69 inches, which provides an average of

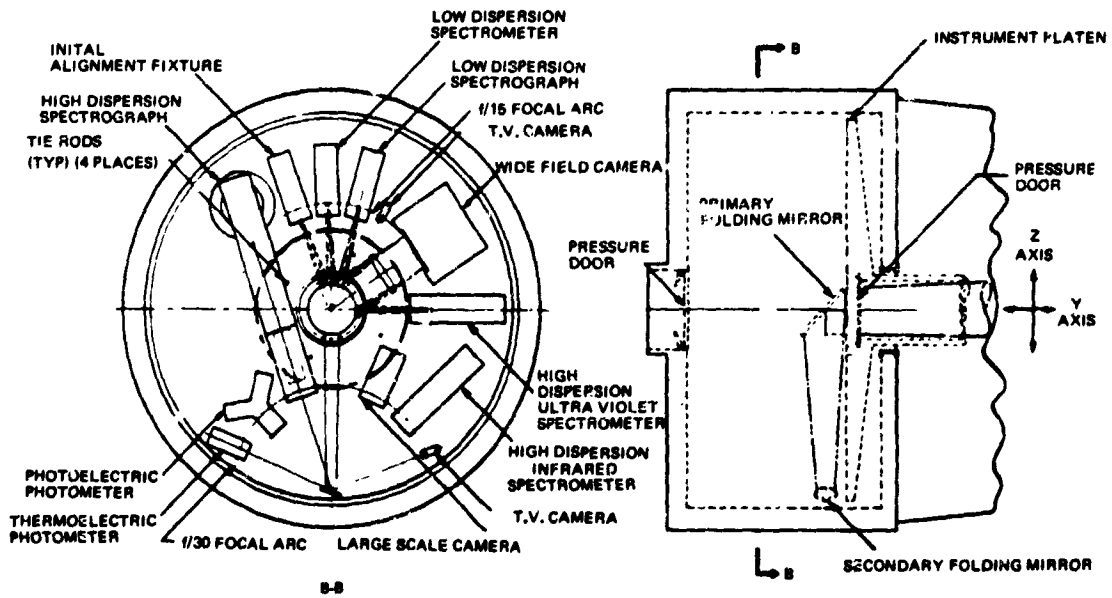


Figure 5. Scientific instrument arrangement.

40 inches clearance above the instruments in which the crewmen can maneuver in a zero gravity environment. All subsystem components are arranged in the upper section around the periphery of the cabin. The subsystems provided in the cabin include communications, data-recording, guidance and control electronics, and emergency pressurization.

A docking cone and mechanism is provided at the cabin end of the telescope. A pressure hatch to seal the cabin at the interface with the telescope is incorporated within the platen. It is remotely actuated and the seal accomplished prior to cabin pressurization. A small, 3-inch-diameter, optically flat window is located in the center of the pressure hatch to allow the passage of a beam of light for gross alignment of the scientific instruments when the cabin is pressurized.

The problem of the alignment of the secondary mirrors with respect to the primary mirror presented some unique problems for such a high performance system. An analysis was made of the permissible tilt and lateral displacement misalignments from the standpoint of coma and astigmatism; the results are shown in figure 6. The thermal distortion

analysis of the supporting structure for the secondaries indicated that these tolerances would be exceeded by any passive design that was investigated. It was therefore decided to incorporate an automated control system for the tilt and lateral displacement.

Position control of the secondary mirrors requires alignment sensors located on the

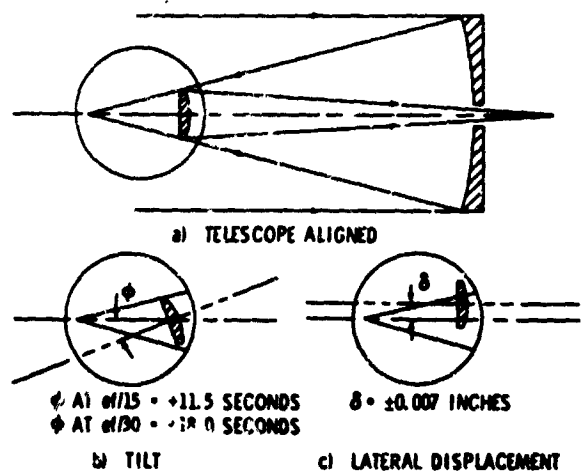


Figure 6. Optical system tolerances; tilt and lateral displacement tolerance of secondary mirror.

primary mirror for each axis of control. Figure 7 shows the conceptual design of a secondary mirror installation developed for the baseline telescope configuration.

The main design features of the support and positioning are:

- A four-legged rigid truss attaching the secondary mirror carriage to the inner telescope wall.
- Both mirrors mounted in a common control cell that has 5 degrees of position control. The position target element required for alignment sensing is mounted on each mirror to eliminate position tolerances between the mirrors and the cell structure.
- Rotational and translational geometry established by three flexure-pivoted struts aligned with the optical axis. Two of these struts can be extended to induce tilt motion,

and the entire three-strut flexure system can be translated by two additional strut actuators grounded on the inner telescope tube.

- Focus adjustment accomplished by positioning a single control actuator that moves the mirror-mounting structure along tubular splined ways.
- A single electric-motor-driven jack screw employed for positioning each of the 5 degrees of mirror freedom provided.

The support of the primary mirror has been dealt with primarily from the structural standpoint. An interrelated problem is the distortion of the mirror in orbit due to thermal gradients. Some idea of the magnitude of this problem can be gained by examining the results of the thermal balance and the resultant structural deflections on such a telescope.

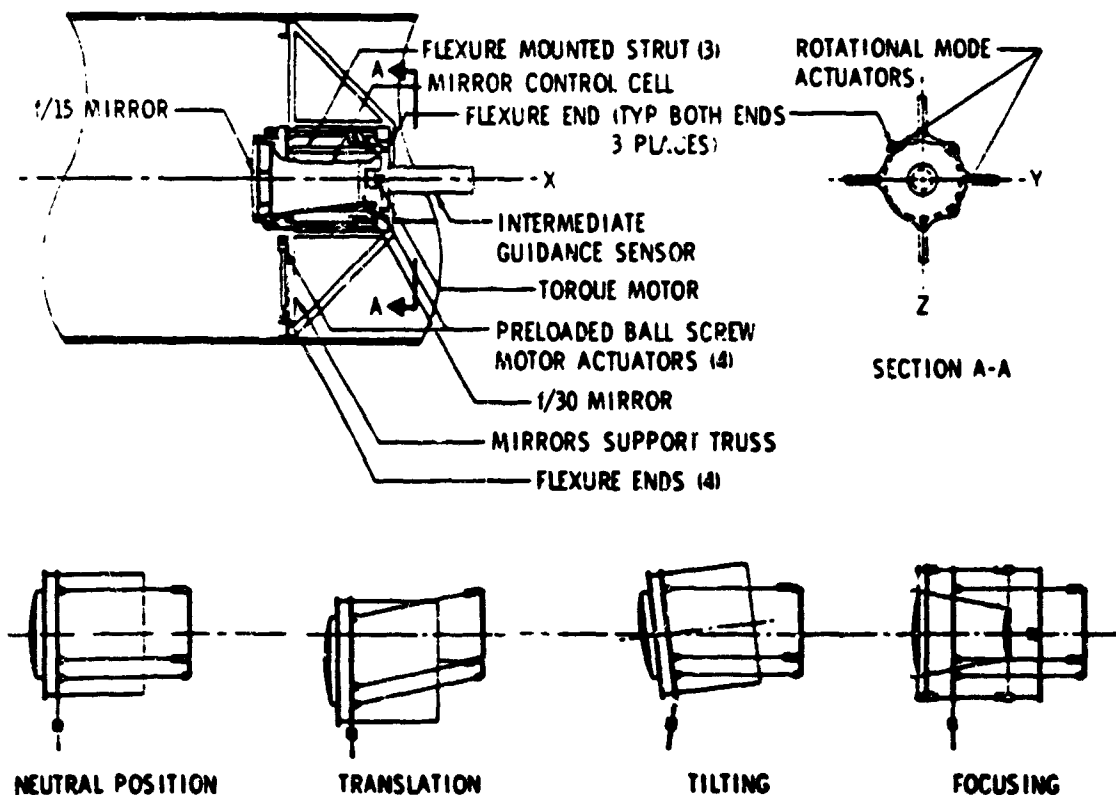


Figure 7. Secondary mirror support and alignment system.

A passive optics approach was taken for the primary mirror; therefore, the thermal distortion was of particular significance. A three-dimensional time-dependent analysis of heat transfer through the telescope structure was conducted. The thermal model of the telescope was relatively complex, and a fairly fine model mesh was considered necessary to simulate accurately incident radiation from the Earth and Sun and radiant exchange between elemental areas of telescope structure with other structures and with space.

The temperature patterns on the primary mirror were computed for two different cases: one in which the mirror continuously viewed space and one in which the primary mirror alternately views space and the sunlit Earth. The three-dimensional carpet plot of figure 8 shows the temperature patterns of the front and back face of the mirror for a 120-degree pie-shaped segment of the mirror in the continuously viewing case. Very similar results were obtained for the intermittent viewing case provided the front doors were closed during the time when the telescope was on the sunlit side of the Earth. The hump in the carpet plot at 60 degrees is due primarily to the transmitted heat flow through the tangent bars. The thermal distortions were computed by analyzing a structural idealization of the mirror; this idealization was based upon a number of simple structural elements joined at the nodes. The temperature pattern supplied inputs at the structural

nodes. The surface deflections are shown in figure 9.

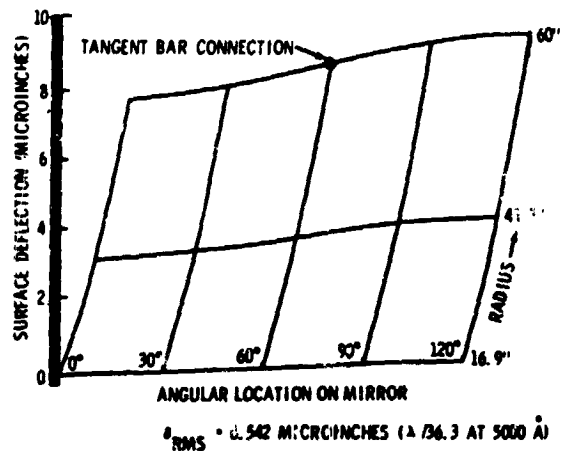


Figure 9. Primary mirror thermal deflections; continuous viewing condition.

To evaluate the consequences of these distortions, a least squares paraboloid was fit to the data and the rms deviation computed. It was found that the resultant focal length change was 0.00946 inch, and the resultant rms deviation from the paraboloid figure was $\lambda/36$ at 5000 angstroms. Although this result was satisfactory, it was achieved by taking detailed precautions in virtually all aspects of telescope design to keep the primary mirror in an isothermal condition. In practice, these design features would be difficult to achieve. The use of a material with a high dimensional

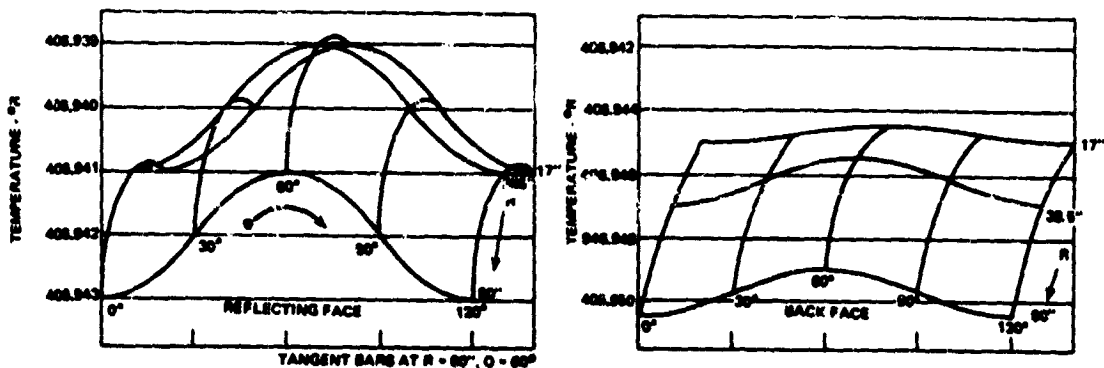


Figure 8. Mirror temperature distribution; continuous space viewing.

The fine pointing and stabilization of the telescope presented one of the most difficult design problems of the whole concept. The nature of the fine pointing requires a very close interface with the telescope and the scientific instrumentation design; hence, each of the observational programs was reviewed to determine the various possible instrument configurations and the advantages and disadvantages of each. Figure 10 summarizes the most stringent of these requirements as well as the requirements for the other functions the attitude control system must perform.

- INITIAL STABILIZATION
ATTITUDE ± 0.25 DEG
RATE ± 0.09 DEG/SEC
- REORIENTATION 5 DEG/2 MIN
- COARSE POINTING ± 3 ARC MIN
- INTERMEDIATE POINTING
PITCH/YAW ± 2 ARC SEC
ROLL ± 4 ARC SEC
- FINE POINTING ± 0.2 SEC OFF-AXIS ACCURACY
PITCH/YAW ± 0.01 SEC ON-AXIS ACCURACY
ROLL ± 0.01 SEC STABILITY
 ± 4 SEC

Figure 10. Control requirements.

The attitude control system proposed for the telescope is shown in block diagram form in figure 11. The system provides automatic stabilization of the residual angular rates of the telescope upon separation from the booster and injection into orbit. During these periods, the gyro reference system and the reaction jets are used. After orbit has been achieved, a stellar reference is acquired through a programmed roll-search procedure to establish a coarse pointing mode in which the attitude reference is obtained from star trackers and control torques are generated by control moment gyros. An intermediate star tracker is required to permit transition from the coarse pointing mode to the fine pointing mode. This sensor would employ its own objective and would be boresighted to the main optics. Attitude hold is maintained by the intermediate-pointing-sensor reference until suitably low pointing errors and error rates are achieved, at which time the control is switched to the fine-pointing sensor.

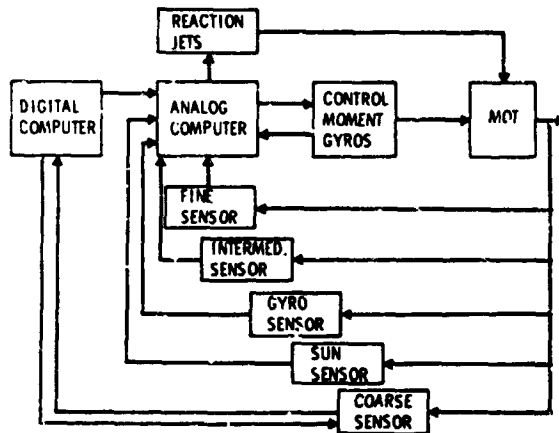


Figure 11. Attitude control system.

During the coarse, intermediate, and fine pointing, the telescope is controlled by torques generated by control moment gyros. These will be desaturated as required by the low-thrust reaction jet system. The fine pointing is illustrated schematically in figure 12. The fine-pointing sensor shares the light from the main optics with the particular instrument being used in the operation for on-axis fine pointing. The errors generated by the sensor are amplified and used to control the control moment.

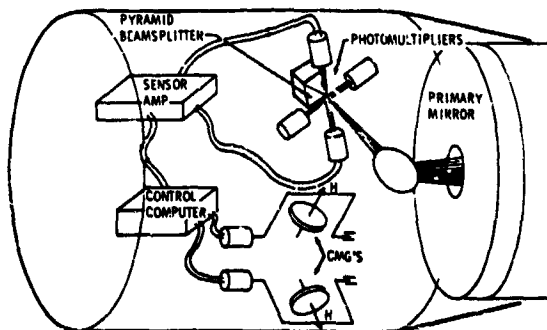


Figure 12. Control system schematic, showing fine pointing only.

The most critical part of the stabilization is obviously the fine pointing and control. Although the analytical work accomplished under this program indicated that the required degree of pointing stabilization could

be achieved with the proposed system, considerably more work involving laboratory tests and possibly tests in orbit is necessary to verify this.

This paper has dealt, in part, with some of the unique design problems for the 3-meter telescope and has indicated what were considered to be feasible solutions at the time. Meanwhile, over three years have elapsed

since the conclusion of this work, and considerable work has been done in the more critical problem areas. It is felt that further design and concept studies should now be carried out on such a telescope in order to provide a focus for the individual technology studies and to assess their impact on overall concepts and telescope design.

Optical Materials and Primary Mirror Design

Roderic M. Scott

The Perkin-Elmer Corporation

N70-36685

At the present time, there appears to be little doubt that the principal element of large space telescopes in the future will be mirrors. These large mirrors will be the aperture-determining components and will provide most of the power for the system. The surface shape of these mirrors may be that of a simple sphere, a paraboloid, or a curve of higher order; they may even lack any semblance to circular symmetry. It will always be of considerable importance, however, that the reflected wave front have the expected shape to very high accuracy.

The standards for a large telescope in space — where no atmosphere will distort the wave front before it reaches the mirror and thus obscure the mirror's own imperfections or absorb the shorter wavelengths that could provide increased resolution for a limited aperture — are far beyond those currently set for large telescopes. Regardless of size, an astronomical telescope in space should be equipped with a primary mirror having a surface accuracy of $1/50\lambda$ rms at the wavelength of interest. It should be our objective to achieve this at 2000 angstroms.

Such a mirror must be made from a material that will be stable enough to receive and to retain an optical surface of the indicated quality. No large pieces of any material have yet been made and tested under conditions that would indicate whether they have the desired stability. A series of investigations to evaluate some current candidates have been underway for some years and are still continuing. The work has utilized small samples measured at a variety of temperatures with very great accuracy so that small time intervals can be extrapolated to the longer ones of interest.

We should not be surprised if it develops that none of the materials now under serious consideration proves adequate for monolithic mirrors of large size and high quality because the quality and stability we are looking for is at least an order of magnitude better than that found in any large astronomical mirrors now in existence.

Some materials, attractive because of their very low expansion coefficients which have the desirable effect of reducing the deformation caused by temperature gradients, may not have sufficiently uniform expansion characteristics to permit their use if there is much change in the overall temperature. Some metals are attractive because of their good thermal conductivity and high stiffness-to-weight ratio. Several have been investigated quite intensively, especially silicon. I feel this metal has a good chance of being very stable from a creep consideration, for it is one of the few metals that is cubic in crystal form and thus isotropic in expansion coefficient as well as attractive in its other mechanical properties.

Once the material has been chosen, the design must be undertaken. Even though large boosters are now available, weight will always be a serious consideration. Whatever weight can be saved in the optics can be used for other useful purposes. The design and fabrication of structures in most otherwise-satisfactory materials has advanced to the point where almost any structure desired can be provided. Not only are the methods of fabrication well developed, but also the software programs are available for computing the deflections of these structures while they are being worked on as well as while they are supported for test and are in use.

There are already well developed and widely used methods for measuring the shape of the optical surface to sufficient accuracy. Large facilities will be required for this purpose, but they do not need to be complex; in some cases, the spacecraft test facilities might be used for this purpose. The principle requirements are a moderate vacuum and freedom from vibration. The interferometers and reduction method are at hand as are the controlled methods of removing or adding material where the tests indicate corrections must be made. The real problem concerns the provision of a structure stable enough and a support reproducible enough to insure that the shape the surface has while being tested resembles the shape it will have while being used.

The question of the effect of size must also be considered. It is the rms variation of the actual surface while in use from the best fitting desired surface that is the important consideration. The best fit is generally determined by a least squares procedure, for that seems to be the way the optics behave with regard to resolution when other adjustments are optimized. For example, a small mirror and a much longer mirror, each with a departure from a sphere of $\lambda/50$, will have the same energy distribution in their scaled diffraction images. The image, however, will be much smaller for the large mirror than for the small one.

If the large mirror is just an array of the small ones, each with $\lambda/50$ as before, it does not follow that the large mirror is also $\lambda/50$. Each of the small mirrors was measured with respect to its best fitting sphere; there has been no assurance that the spheres for each of the small pieces are all the same. For the large mirror, all the "best fitting" spheres must be the same sphere with the same identical radius and center. This, then, is why the difficulty of figuring a large mirror goes up so rapidly with increasing size. It is not a problem of removing the right amount of material from the right place, for that is nearly the same for large or small mirrors; it is a problem of holding the small areas in the right relationship to one another while testing, and in use,

and over long periods of time under a variety of conditions. In addition to the normal effects of various forces, thermal effects and long-term creep are the factors that distort the surface.

It has been proposed that a large mirror be built up of a number of smaller sections. Each small section could then be worked to bring its surface to the required accuracy when compared to the best-fitting ideal surface (or for that part of the surface if it is not spherical). Although this best fit is not as free as the previous case discussed, the positioned variables are still disposable; thus, the problem of each piece is greatly simplified when compared to the problem presented by the surface as a whole. If each piece is positioned with respect to the other so that the location of the "best fitting" surface for each is the common surface for all, the overall array will be diffraction-limited for the large aperture.

To accomplish this, each portion may be made movable, and the whole array may be observed much as it would be if it were a complete monolithic mirror under test. Now, however, each piece may be moved to that position which minimizes its rms and thus the rms of the whole. The function may be performed on the earth in a one g field, in space after launch, and again after some years when the structures may have changed. In fact, it could and should be monitored continuously while in operation to compensate for the many effects of short time variability.

In summary, many materials are being studied and more will be investigated. Many methods of manufacture have been developed, and satisfactory methods of testing are now employed. Yet, while surfaces can be made and tested to almost any accuracy desired under the test conditions, it is not at all clear that surfaces much larger than a meter or two could be delivered into orbit and made to perform to their diffraction limit. It has been suggested that a solution to this dilemma would be to make the mirror of smaller pieces and to adjust them while in use.

It has been my experience that people are much more clever at conversion than at

compromise; thus, in the long run, projects are more successful if a single clear objective is kept in view during design and construction. Compromises for other uses should be inhibited to increase the probability of success for the initial objective. Conversions

to other objectives usually can be made with ease later on. This is important to keep in mind in the continued study and investigation of materials and manufacturing methods for primary mirror design.

PRECEDING PAGE BLANK NOT FILMED.

1A N70-36686

Structures for Spaceborne Optical Telescopes

Erich E. Engler

NASA George C. Marshall Space Flight Center

The design of support structures for spaceborne telescopes is influenced by a number of factors. The choice of structural configuration, the materials utilized, and the analysis methods applied depend to some degree on these criteria. The most important factors are alignment accuracy; dynamic stability and behavior; environmental influences; material selection, weight, and cost; crew considerations, maintainability, and payload integration; and reliability.

All of these factors must be investigated and their relative importance established and included into the analysis and design. Similar factors govern the design of telescopes on earth, but the difference in environment will change or eliminate their importance. In this paper, I will discuss only the telescope support structure because the optical and control aspects will be covered by others. Some of the design approaches selected will satisfy a number of criteria but have no influence on others. Therefore, the relative importance of the various factors is established to have a better understanding of their application to the design.

Obviously, the purpose of sending optical telescopes into space is the observation of heavenly bodies. The better the device can do this, the more useful it is. Therefore, the alignment accuracy, minimum thermal distortion, and dynamic response, which govern the optical quality, are, in my opinion, the most influential factors to be considered.

Another very important factor is the response of the structure to its exposure to the environment. The telescope is exposed to the following different environments: transportation, prelaunch (on the launch vehicle),

launch, docking and attitude control, vacuum, radiation, meteoroids, and temperature.

During the prelaunch, launch, and docking environments, additional supports can be provided to hold the structure. These supports can be removed later. Only the weight and the functional reliability must be considered in the overall assessment.

Environmental protection must also be provided by the telescope structure. Micrometeoroid impingement can degrade the optical properties over an extended time period; therefore, the design approach should consider minimum exposure of optics to meteoroid flux. Thermal aspects, on the other hand, might require an open truss design to minimize thermal gradients and resulting distortions. Thus, lifetime and accuracy requirements have to be traded to find the most optimum overall design. Radiation and vacuum exposure of the structure also have to be investigated. In these instances, the selection of materials to avoid outgassing and subsequent redeposition on optical surfaces are important.

Crew considerations, maintainability, and payload integration must be considered, but they are of lesser importance than those criteria already mentioned. It is felt that ways can be found to satisfy these requirements without sacrifice of the most important aspects.

Reliability in the area of support structures normally does not pose a problem and therefore is not emphasized. Reliable mechanical release devices and uncaging mechanisms can be built without great difficulties.

Weight aspects and material selection are

of lesser importance for telescope structure because only a relatively small weight portion of an experimental satellite is needed for the structure. This is also true for the cost; the structural part is only a fraction of the cost of the overall project.

Thus, the ranking of the design criteria is established in the following order: alignment accuracy; dynamic stability and behavior; environmental influences; reliability; maintainability, crew consideration, and payload integration; and material selection (weight and cost).

In the following discussion, I will show some of the design solutions used in actually-built as well as studied telescope structures and will try to point out the influencing design criteria.

Apollo Telescope Mount

The problem of limiting thermal distortion to stay within permissible alignment values is the most important influence on the design of the Apollo Telescope Mount (ATM). The selected design is a cruciform spar providing the mounting surfaces for all experiments. Two gimbal rings and a roll ring, connected with flexible pivots, provide the pitch, yaw, and roll motions. Caging during powered flight relieves the loads on the flexible pivots. These caging devices are separated by pyrotechnic pin pullers. Operational caging devices provide position-locking of the experiment package when it is not performing experiments. The alignment accuracy needed is 1 arc second; the maximum allowed jitter rate is 1 arc second per second.

The cruciform aluminum spar, one inch thick, 120 inches long, and approximately 80 inches wide, is used for mounting all the experiments. The selected material assures efficient heat distribution. To maintain the accuracy over a span of 120 inches, the forward and aft attachment pads must remain within 0.0005 inch of their aligned position. To reduce weight, 2-inch-diameter holes are machined in all areas of the plates free of experiment attachment surfaces. The material

selected for this purpose is Al 6061-T451, aged to a T6 condition. It has sufficient strength and stiffness to meet all the other load-carrying and dynamic requirements.

The spar and its rings are insulated with high performance insulation and placed in a liquid-cooled cannister, which also has external insulation. The forward and aft cylinder ends are closed, and doors are provided over the viewing ports.

Stringent restrictions are placed upon the use of coatings and organic materials to avoid outgassing and redeposition on optical surfaces. A materials study to investigate a large number of available adhesives, coatings, elastomers, lubricants, films, potting compounds, and metals is prepared to guide the material selection.

Additional meteoroid protection for the experiment package is not required because the surrounding rack with the attached electronic equipment and the cannister provide adequate shielding.

Maintainability and crew considerations posed no problems. The participation of the astronauts is to retrieve the film by extravehicular activity. The integrated payload structure is the rack, which houses the ATM cannister/spar assembly and the necessary electronic equipment. Environmental protection for the crew is provided by the Lunar Module A. nonpropulsive crewquarters similar to the lunar module and mounted atop the rack.

Payload integration presented no special problems. Analysis methods similar to those applied in the Saturn programs are used for thermal, structural, and dynamic compilations.

Orbiting Astronomical Observatory

The Orbiting Astronomical Observatory (OAO) is designed to accommodate many different scientific missions and therefore requires a versatile payload structure. The main assembly is octagon-shaped with a hollow central tube. An active/passive thermal control system, using louvers, insulation, and

both solar and internal heat from the instrument operation, maintains temperature stability to the specified limits.

The primary structure consists of a load-carrying riveted shell, 48 inches in diameter, 113 inches long, surrounded by eight longitudinal trusses and seven radial frames to which the equipment packages and skins are attached; the experiment optics package, with a maximum diameter of 40 inches, is mounted inside the shell. The shell is composed of four chem-milled stiffened skin sections. The frames are of conventional design with beaded webs, except at Station 100, where an aluminum honeycomb web for the equipment support is used. Each truss is made of a one-piece channel, and the aft ends are mounted into a separation fitting.

Star trackers, internal reference unit, and gyro packages are mounted to stainless steel trusses that are connected to the primary aluminum structure. The coarse solar sensors and the gas jets use titanium fittings. In both cases, the steel and titanium fittings give some thermal isolation while the primary aluminum structure keeps thermal gradients to a minimum.

Superinsulation and gold-deposited fiberglass mounts are extensively used. The 48 truncated bays, formed by the frames and trusses, have hinged honeycomb panels for equipment mounts. These panels swing outboard for easy accessibility.

Protection of optical surfaces, similar to the requirements of ATM, is observed. Micrometeoroid shielding of the optical package is provided by surrounding structure and electronic gear.

Focusing X-Ray Telescope

An interesting study investigated the aspects of a Focusing X-Ray Telescope. A number of basic designs were studied, such as telescoping tubes, hinged and scissored trusses, full-length tube and truss, tapered telescoping truss, and tapering telescoping shells. Factors influencing the alignment accuracy (thermal distortions and mechanical joint and geometric rigidity) were rated. The

tapered telescoping truss showed the best overall configuration; further studies in areas of materials and joint design are being performed.

Selection of materials is influenced by: maximum stiffness, minimum weight, maximum damping, minimum cost of material and fabrication, maximum impact resistance, and maximum resistance to thermal distortion. Candidate truss materials studies are: beryllium, Lockalloy, 7075 Al, 6Al 4v Titanium, Invar, nickel.

The members of the telescoping truss are tubular, thin-walled and assumed to be 2 inches in diameter. The base ring consists of 3-inch-diameter tubes. Brazed and bonded joints between the tubes and fittings are being considered. The lower strength of bonded joints is offset by the higher damping coefficient.

The dynamic and thermal analysis shows the following results. The truss has acceptable dynamic distortions for all materials investigated to satisfy jitter requirements of 0.01 arc second per second. The thermal distortions of the truss are far more significant. Aluminum and beryllium yield a displacement of at least one order of magnitude too high to satisfy the alignment accuracy of 2 arc seconds. Since the displacement is a direct result of unsymmetrical distributed length changes in the truss members, the material should have minimum thermal expansion. Of the prime structural materials, titanium has the lowest expansion; however, an active lens-alignment system is necessary even when this material is used. Other materials with even lower expansion coefficients are Invar, low expansion nickel, and tungsten. All are heavy, expensive, and difficult to fabricate; therefore, they are not utilized in the design.

One-Meter, Diffraction-Limited, Optical Telescope

The last design I will discuss is the structure for the 1-meter, diffraction-limited, optical telescope. The experiment is designed to fit into the center hole of the OAO structure. The main innovation is the separation of the

payload structure and the experiment package by a magnetic suspension system.

The main structure is an aluminum tube housing the primary and secondary mirrors. During launch, the experiment package is separated into the instrument package and the primary-mirror-and-secondary-mirror support system (within the tube). Each package is independently mounted to an adapter ring, fixed to the payload structure with four mounting lugs. After orbit insertion, the rigid coupling, provided by the mounting lugs, is severed by a release mechanism. The package is pointed and centered by six magnetic pushers, similar to an electromagnetic speaker.

The primary and secondary mirror are housed in a blackened aluminum tube. The support for the secondary mirror is mounted to the primary mirror support structure and consists of three fiberglass struts, connected at the secondary mirror location by a thin-web spider. This structure resembles a tripod. During launch, the secondary mirror is held in place also by a support attached to the aluminum tube. Once in orbit, the system is released; and the secondary mirror is held only by the tripod. This arrangement yields minimum thermal distortions between the optical surfaces of the telescope and satisfies the alignment accuracy of 0.1 arc second. Micrometeoroid protection is provided by the spacecraft structure.

Summary

In summary, the requirements placed on the structure for the individual payloads are achieved by specific design solutions.

The alignment accuracy of 1 arc second for the ATM required minimum thermal distortion. This is maintained by an aluminum spar, 1 inch thick, surrounded by an actively cooled cannister to minimize thermal gradients. The design also satisfies the dynamic stability and environmental protection criteria.

The versatility demanded of the basic OAO payload structure in connection with minimum attainable thermal and dynamic distortion is met with an aluminum structure and an active/passive thermal control system.

In both cases, ATM and OAO, conventional materials and fabrication technologies are applied; and the specific demands are met by the applied design philosophy.

The two telescope structure studies (the focusing x-ray telescope and the 1-meter, diffraction-limited, optical telescope) also indicate the severeness of the alignment accuracy necessary. Again, the limitation of thermal distortions dictated the design concept. Because of its distance of approximately 480 inches between primary and secondary mirrors, the focusing x-ray telescope experienced thermal distortions of one magnitude larger than permissible. An active alignment system is proposed. The dynamic response and other requirements do not pose any severe design problems.

In all cases, the minimum thermal distortions to meet the pointing accuracy is the outstanding demand for the design engineer to satisfy. In all four cases, available materials, fabrication methods, and basic structural elements were applied to achieve the goal. It can be clearly seen that each experiment must be treated individually and that no structural scheme or layout can be found to satisfy all present and future telescope structures. It depends largely upon the ingenuity and skill of the design engineer to combine known design elements, materials, manufacturing techniques, and proven components to obtain an optimum primary structure that satisfies the telescope requirements.

An important contribution to this process is the availability of sophisticated structural, dynamic, and thermal analysis methods, using electronic computers. These methods give the design engineer an early indication of design shortcomings and also permit investigation of alternate approaches. Structural and thermal tests undertaken early in the program, as in the case of the ATM spar, are also helpful in evaluating the selected configuration.

Future telescopes will certainly put increased demands for accuracy, weight, dynamic stability, and operational requirements on the primary structure housing both the optical and related components.

A N70-36687

A Survey of Precision-Pointing Systems

Douglas C. Fosth
The Boeing Company

Introduction

A survey of precision-pointing systems at this time can refer to only a few vehicles. With the development of orbital vehicle capability, however, consideration can change from the approach of pressing the state-of-the-art in all areas to the orderly technological growth of some subsystems, emphasis being placed upon the few major technology problems. The precision-pointing control system is an area that can now allow technology growth because experience with the existing systems has spanned almost all types of control systems. In addition, industry has conducted research to extend, to develop, and to verify system concepts. Consequently, this paper will discuss existing programs, will consider the types of control systems in more detail, and will present other considerations involved in the system design.

Experience With Existing Programs

Precision pointing of orbiting astronomical telescopes is still in its infancy. The number of flight vehicles to date is very small; i.e., eight for the Orbiting Astronomical Observatory and the Orbiting Solar Observatory. The accuracy requirements have not been as stringent as those desired for high quality observatories. The equipment to date has been operating at or near the diffraction limit, but the size of the equipment has not been large. On the other hand, Stratoscope and Strap, two programs using a balloon and a sounding rocket to the upper atmosphere, have been successfully implemented. The

conclusion is that important, challenging, and interesting work is yet to be done. Consideration must be given to vehicles having stricter requirements, such as the Manned Orbiting Telescope (MOT), the Apollo Telescope Mount (ATM), and the European Scientific Research Organization (ESRO) satellite. The accuracy requirements for these vehicles will be from 0.005 to 0.1 arc second, and the size of the optics will be from 1 to 3 meters. As we approach the upper limits of this size range, the control requirements become most stringent and the task most difficult.

Let us consider the progression of vehicles to date, the specifications for pointing, the type of systems used, and the results obtained.

Stratoscope

The Stratoscope vehicle is a balloon-borne experiment package launched from the National Committee on Atmospheric Research (NCAR) facility at Palestine, Texas. This is the second series of such vehicles, a measure of the success of the program. The current series of vehicles uses a 1-meter telescope for the experiment package and usually has a 5- to 12-hour flight. The vehicles have a pointing requirement of 0.016 arc second with a holding requirement of 1 hour at that accuracy. The operation of the vehicle is virtually accomplished by ground command. The initial acquisition is accomplished by using a coarse television camera with a 10-degree field-of-view to determine where the telescope is aimed and to search for the guide star of the particular experiment. When

the guide star is found, the image is centered in the field-of-view of the coarse telescope by means of balance weights for the horizontal axes and an "inertia wheel" for the vertical axis. At this point, the star should be in the field-of-view of the experiment telescope (a field-of-view of 50 arc minutes). The image is then viewed by a fine television camera and positioned in the proper location on a retro-divider. This divider reflects the signals to the photomultiplier tubes for output signals. When this has been done, the system is locked onto the guide star. A second guide star within the field-of-view is used to provide the necessary position information for complete three-axis control. For the fine-pointing mode, the telescope is maintained by the balance weights and inertia wheel. The image motion is finely controlled by a servoed transfer lens. The system uses a series of devices to control the accurate pointing of the vehicle. As the vehicle drifts away from the ground stations, it is parachuted to earth on command and is recovered.

The Stratoscope II vehicle has been flying since 1964. The performance of the system to date indicates that 0.02-arc-second pointing control can be obtained.

Strap

The Strap experiment package is boosted by using the Aerobee series of sounding rockets; hence, this platform has a much shorter useful life than the balloon vehicle. Because of the size limitations of the booster, the experiment package is much smaller and lighter. The package is fastened to a roll-stabilized platform and boosted with the vehicle spinning to control attitude. Free gyros are used for the position reference on the two horizontal axes. At separation, the vehicle is despun, and the reference gyros are nulled. A preprogrammed series of maneuvers are then carried out to bring the experiment image into the field-of-view; a star tracker is used to provide the null reference at this point. The star tracker has two fields of view: wide-angle scan mode for the search and fine position for the hold mode. In the hold mode,

the tracker nulls on the star. The control system, using derived rates of motion data, actuates gas jets to obtain fine pointing to an accuracy of 10 arc seconds. During this hold phase, the free gyro nulls are updated in preparation for the next maneuver sequence. A maneuver sequence and reacquisition of a new star is repeated several times during the short 6-minute life of the vehicle. When the disturbance torques are too high to be overcome by the reaction control system, experimentation is stopped. The package is recovered following its parachute descent to earth. This series of experiments is essentially independent of the ground station.

The Strap program is currently undergoing fabrication for the third series of vehicles; verification of the concept of using the star tracker will be accomplished on this vehicle. To date, all maneuver sequences have been open loop, and successful operation has been obtained to 1.0 degree for a 6-minute flight.

Orbiting Solar Observatory

The space vehicle that has accumulated the largest number of successful flights and most orbital time for precision observations is the Orbiting Solar Observatory (OSO). This vehicle is basically dual spin where spin stabilization is used for the basic vehicle, but the experiment platform is despun. The OSO has a passive pointing capability of 5 arc minutes about the spin axis. The experiments on the despun platform have a gimbal system to point them in order to provide greater precision than the spin stabilization. These gimbal systems have demonstrated a pointing capability of 30 arc seconds. Six of these vehicles have been flown to date, five of them achieving successful operation.

Orbiting Astronomical Observatory

The Orbiting Astronomical Observatory (OAO) vehicle is the most precise spacecraft that has been flown. This vehicle is tailored for stellar and galactic observation. The vehicle is designed to use inertia wheel stabili-

zation about all three axes for pointing control. The design of the vehicle was accomplished with the specific objective of reducing the inherent disturbance torques due to magnetic field, gravity gradient, thermal expansion, and solar pressure. The vehicle is initially oriented to the sun and is rate-stabilized about the boresight. Six peripheral, two-axis, gimballed star trackers are positioned to recognize a particular orientation of stars. A roll about the boresight is commanded. When four trackers indicate a star acquisition, the maneuver is terminated; and average errors are fed to inertia wheels to hold the attitude. At this point, the vehicle is in the celestial hold mode and as such can control attitude to an accuracy of 1 arc minute. The boresight of the large telescope can therefore be pointed in any direction as a function of positioning the six star trackers on the vehicle. When the fine hold of 0.1 arc second is required, a two-axis star tracker that uses the main telescope optics is activated. This sensor is used to control two fine inertia wheels for the fine-pointing task; the boresight roll data is still taken from the gimballed trackers. Maneuvers are accomplished by moving the gimballed trackers and causing the vehicle to keep the sensor errors nulled. In this way, maneuvers can be made without losing precise position information on the vehicle. Two of these vehicles have been flown, the second being successful to date.

Current and Proposed Programs

The vehicles currently in work or in proposal are logical extensions of the past programs. Four of these programs are the Apollo Telescope Mount, the Manned Orbiting Telescope, the Airborne Optical Telescope, and the European Scientific Research Organization stellar observatory satellite. The Apollo Telescope Mount program is by far the most advanced program at this time; the hardware is in either the construction or the delivered stage. Design and construction has started on the Airborne Optical Telescope. The Manned Orbiting Telescope has recently completed the preliminary design stage to

show the feasibility of such a system. The exact status of the ESRO satellite is indeterminate.

Apollo Telescope Mount

The Apollo Telescope Mount (ATM) is one of the experiments being accomplished with the spare Apollo equipment under the Apollo Applications Program. The mission for the first of these vehicles is solar observation. As would be expected, this is a manned vehicle and will have a SIVB workshop to go with it. The control of the vehicle and the experiment are handled separately by different control systems. The basic vehicle is to be controlled by Control Moment Gyros (CMG's) in the active control mode.

The configuration chosen is the one developed at Langley Research Center and is called the SIXPAC configuration. Three two-degree-of-freedom rotors are used. In the null position, the units are orthogonal. The mechanics of uncoupling the gyros from inter-axis disturbance is handled by an onboard computer that controls all of the gimbal rates. The control laws are designed to minimize inner gimbal motion, to prevent the gyros from orienting their rotors parallel, and to provide the necessary momentum to each axis.

The experiment package is on a servo-driven mount that is anchored to the basic vehicle. The fine pointing and control is accomplished by this unit. The basic orientation of the vehicle during experiments is toward the sun with the star Canopus as the third reference. When the unit is maneuvered away from the sun or the sensors are occulted, rate-integrating gyros are used for position memory. CMG desaturation is accomplished during these periods by using gravity gradient torques. When the vehicle is not performing experiments, it is placed in the "POP" mode; i.e., it is perpendicular to the orbit plane to minimize gravity gradient torques. The accuracies of the two systems during active control periods are 2.5 arc seconds in pitch and yaw and 10 arc minutes in roll. Extensive simulation work is still being

done to assure the performance of the system in orbit.

Manned Orbiting Telescope

The Manned Orbiting Telescope (MOT) is a 3-meter telescope system on a manned vehicle. Because of the accuracies required for the experiments, a different configuration had to be developed. The pointing accuracy required was 0.01 arc second pitch and yaw and 0.2 arc second roll. The techniques used were chosen deliberately to minimize the high-frequency disturbance torques applied to the vehicle. The experiment telescope was placed in a gimbal system about its center of mass. The fastening between the manned vehicle and the gimbal was through very soft springs. The purpose of these springs was to keep both parts of the vehicle in the same orbit and to apply an absolute minimum amount of disturbance torque on the telescope. The onboard control system for the telescope was control moment gyros; however, in the application, it was decided to use six rotors in a scissored pairs configuration. The rotors are each single degree-of-freedom. This type of system was chosen because it allowed the simplest control laws to be developed and the control axes to be virtually uncoupled. Desaturation of the control moment gyros on the telescope can be accomplished by applying a bias torque on the telescope with the manned vehicle. The momentum can then be transferred to the manned vehicle with a minimum amount of effect on the experiment. As with the Orbiting Astronomical Observatory, acquisition is accomplished through a series of sensors. The fine sensor uses the experiment optics to minimize alignment problems. The coarse sensor is a boresighted star tracker located in front of the main telescope secondary optics. Exterior trackers on the telescope provide the preliminary alignments and also provide the signal for the third axis.

Airborne Optical Telescope

The Airborne Optical Telescope is a

general purpose 1-meter telescope that will conduct its experiments on board an airplane. It has unrestricted view through an open port-hole in the fuselage. The telescope is mounted on a spherical air bearing on board the aircraft. It uses two telescopes in addition to the main experiment optics: one for coarse acquisition and a second for fine pointing. The error signal is not derived by operation on the signals from the experiment telescope. The unit is designed to perform offset pointing by changing the orientation of the fine-pointing telescope with respect to the experiment telescope. The telescope is inertially stabilized by using DC torque motors between the vehicle frame and the air bearing. Accuracy requirements are 1 arc second on all three axes, the boresight requirement being needed to accomplish the offset pointing task.

European Scientific Research Organization Satellite

The European Scientific Research Organization (ESRO) satellite is basically the same as the OAO vehicle in the accuracies required and the methods of control chosen.

Types of Systems

There are a large number of ways to provide control of the vehicles. The purpose of this section is to discuss, in greater detail, the following types of systems to be considered for the different applications:

1. Gas Jets
2. Magnetic Control
 - a. Coils
 - b. Magnetic Gap
3. Inertia Wheel
4. Control Moment Gyro
5. Servoed Optics
6. Servoed Platform

It is interesting to note that, except for the magnetic systems, all types of systems have been or will be employed on some type of precision-pointing vehicle.

Gas Jets

Virtually all types of vehicles, including the precision-pointing vehicles, utilize gas jets as a torque source; however, the use of jets as the primary torque source is limited. They are commonly used for despin, spinup, initial acquisition, and maneuvers. Gas jets are ideally suited for small amounts of high torque generation, small amounts of low torque generation, or as users of onboard expendables. If, however, the total impulse required becomes very large, many other types of torque systems are more efficient.

There are several types of jets that can be seriously considered for the precision-pointing task. These include the hydrazine jets and the resisto jets. Through proper system design, these jets can deliver very small torque impulses and, at the same time, maintain a high specific impulse. This is accomplished with hydrazine by burning it into an accumulator and by using small thrusters to eject the small amounts of hot gases. In the case of the resisto jet, the high impulse is obtained by heating the propellant with electric heaters. Because of the inherent simplicity of this torque source, it should be seriously considered for missions with moderate torque-impulse requirements. If there is a requirement for vehicle rates as well as angular pointing, these torque sources may have difficulty because the acceleration is not smooth and the vehicle may experience out-of-tolerance rates. If the impulse size can be kept small, there is still the problem of turn-on and turnoff delays to contend with. With a very narrow deadband, the vehicle will bounce between the two position limits because of the delays in the torque actuation. The predictability or propellant consumption under these circumstances is very difficult.

From a reliability and simplicity standpoint, the gas jet system is difficult to match; however, for a high total impulse or a very narrow deadband, the onboard propellant weight would become excessive.

Magnetic Control

There are two distinct types of control systems that can be built by using magnetic control torques. The systems are classified as magnetic coils and magnetic gap control. These two types of control are considerably different, both in their capability and in their ease of application.

Magnetic Coils. The basic property of the magnetic coil system in its operation is that it uses the earth's magnetic field as a ground to react against. Passing current through a coil generates a torque on the spacecraft. The characteristics of this torque are: (1) it is usually low in magnitude; (2) it cannot exist parallel to the field vector; and (3) it has a very high frequency-response capability. This torque can be generated in a proportional manner or controlled in an on-off manner. From an onboard efficiency standpoint, the on-off type of system is by far the most efficient, the most reliable, and the simplest to implement. Laboratory tests with this type of system have shown an accuracy capability of 1 arc second and a pulse width of a few microseconds using air-bearing simulation techniques. The limitation of torque generation in the plane perpendicular to the field vector imposes a severe handicap upon this type of control. If, however, the vehicle were inserted into a controlled reference field, the control capability could be maintained about the two most important axes. This technique is not satisfactory for complete three-axis control.

Magnetic Gap Control. The magnetic gap system requires a mother vehicle to provide the base for the control system and is, in reality, a very sophisticated way of providing a servoed platform. The principle in this case is that of controlling the location of a magnetic material between two poles by varying the strength of one of the reference poles. The angular control is obtained by linear motion control at each end of the vehicle. This type of system has also been demonstrated in the laboratory to parts of an arc second in pointing accuracy. A very strong

factor in favor of this system is that it can be used to provide control over the 6 degrees of freedom of the experiment vehicle as opposed to the 2 angular degrees of freedom for the coil system previously discussed.

Inertia Wheel

The inertia wheel is the first type of control actuator to be used for the high precision-pointing task. The principle of operation is the generation of torque between the vehicle and a free rotor. The vehicle moves in one direction and the free rotor in the other. Momentum is conserved along that axis. Each axis is controlled, in the same manner, with three orthogonal wheels. These wheels do have an upper speed limit at which momentum must be dumped out of the vehicle by generating an external torque. Gas jets, magnetic coils, or gravity gradient torques are used. As these wheels are accelerated about each axis and operate at speeds away from null, cross-axis torques are generated by the vehicle motion reacting with the momentum vector. The response speed of this system is quite slow because the desired torque must be completely generated by the rotor torque motor. The bandpass of the closed loop system using this type of actuator is low compared to that of the magnetic system. Earth-based tests of this actuator have shown an accuracy approaching 1 arc second.

Control Moment Gyro

The control moment gyro (CMG) is the second type of momentum exchange device to be considered. In the CMG, unlike the inertia wheel, the momentum vector already exists because of the constant-speed rotor. To control the motion of the vehicle, the momentum is moved into or out of the axis being controlled by motion of the rotor gimbals. The level of the torque being developed is related to the gimbal rate and the magnitude of the gimbal angle; hence, the torque motor in this case has only to accelerate a small gimbal to achieve a high control torque. A single-rotor CMG cross-couples

between two vehicle axes. As momentum is removed from one axis, it is added to the other. This cross-coupling is detrimental to performance but is negligible for control with small gimbal angles. If all of the momentum storage capability is needed, analytical uncoupling of the control axes can be achieved by proper control commands to the gimbals.

Another approach is to use the rotors in scissored pairs. In this manner, there is no cross-coupling between the vehicle control axes. The choice still exists between the single- and the 2-degree-of-freedom rotors. If the gimbals of the units can be mechanically synchronized into scissored pairs, there is no difference in the performance of the systems. If, however, these units are not mechanically synchronized, the gimbal servos on the 2-degree-of-freedom units must be designed to transmit the full-load torque being generated by the motion of the other gimbal. The torque motor requirements on the 2-degree-of-freedom units are similar to those required for the inertia wheel. The 2-degree-of-freedom unit does allow a more complete utilization of the momentum stored on the vehicle because of the flexibility in orientation of each momentum vector. The single-degree-of-freedom and the mechanically synchronized rotors have the advantage of torque amplification, passive control capability, and a simpler control law mechanization. The bandpass of these systems is higher than that of the inertia wheel but lower than that of the magnetic systems. Accuracies have been demonstrated in the laboratory for these systems of less than 0.1 arc second.

Servoed Optics

This approach to the problem sounds as if it has all of the answers to all of the problems in precision pointing. Indeed, this approach has worked quite successfully in the Stratoscope program. On the large telescopes, however, this approach is not as satisfactory. There will be servoes on these units to correct the figure of the primary optics and more servoes to keep the secondary optics aligned properly in the flexing vehicle. These systems

operate at the diffraction limits of the equipment, and the field-of-view of the systems moves continually down with increasing size. The use of a transfer lens for motion compensation would introduce distortion into the signal path that would not be there with the nominally nulled system. The impression is that this method would be satisfactory for small systems but would introduce too much image distortion into the larger systems.

Servoed Platform

One application of this type of approach has been discussed in the section on magnetic gap control. This type of system is applicable to vehicles where the experiment package is smaller than the parent vehicle. A gimbal system is provided for the experiment, and torque motors are placed on the gimbals. In the usual configuration, only 2 degrees of freedom are provided by the gimbals. The third axis is controlled by the vehicle. This system has the same torque response limits as the inertia wheel and therefore a slower speed of response than that attainable by other means. The system relies on the parent vehicle providing a well-controlled reference for the unit to move against. The use of bearings or flex pivots in the gimbals implies that threshold torque or spring bias must be accommodated in addition to the inertial torques to the experiment package. This type of approach is similar to that used in the ground-based telescopes, but the reference base for the orbiting vehicle will provide a larger disturbance input. The bandpass of this system will be comparable to that of the inertia wheel.

Best System

At this time, there can be no general conclusions drawn as to which type of system is best because each application depends on the length of operation, the rate and position requirements, and the size of the vehicle. Each of the methods discussed can perform to the requirements under favorable operating conditions, but the amount of flexibility and

the ability to tolerate significantly different operating conditions indicate some systems are better than others.

Other Considerations

In addition to the specific task of providing a control system to hold the vehicle in the desired attitude for the experiment period, the maneuver schemes, target acquisition, and offset pointing requirements must be considered. The choice of the scheme for initial acquisition and maneuvers can have a major impact on the design of the control system.

The first objective of the vehicle is to accomplish the initial acquisition. There is basically one technique in use. For orbiting spacecraft, a sun acquisition followed by a roll to a star lock has become a standard approach. This technique can yield a pointing accuracy of 10 arc seconds for the initial alignment. The change to all stellar references is made after the initial alignment to decrease the pointing error even further. The problems that develop at this time are concerned with the alignment accuracies of the external sensors with respect to the experiment telescope. For this reason, most experiment telescopes obtain the attitude error by using a small amount of the collected light as the input to the control system. Motion about the boresight is still referenced by the external trackers. A sequence of steps is then involved in the usual approach to initial acquisition, moving from the very coarse initial orientation to the fine precision pointing.

Consider the techniques that can be used for maneuvering a spacecraft. The most straightforward is to maneuver about one axis at a time. This approach is amenable to implementation by using a gimballed platform, strapdown gyros, or gimballed star trackers. The two axes not being maneuvered can be commanded to maintain a null position during the sequence; therefore, error propagation should be minimized. The other extreme of maneuver schemes is to perform an Euler angle maneuver, which is a three-axis maneuver by the most direct route to the

desired new heading. This approach can be used in a straightforward manner if quaternions are being used to describe the present position of the vehicle and the new position desired. The maneuvers would be performed at varying rates about all three axes to accomplish the transfer simultaneously about all three axes. The maneuver schemes usually used represent compromises between the one extreme of simplicity and maximum time and the other extreme of complexity and minimum time. Use of the more complex schemes requires that more position and rate information be available on board the spacecraft. The onboard computational requirements of the schemes tend to become more complex with the increasing complexity of the maneuver scheme; however, fixed rate maneuvers about all three axes simultaneously may cause more command resolution problems than the computations of the Euler angle maneuver.

As the size of the telescope and the length of the observation period increase, offset pointing will become a more serious problem. The requirement for offset pointing is determined by the pointing accuracies required and the low light level of the target. The current state-of-the-art for star trackers provides a reasonable operating capability for stars of magnitude +6 to +9 in brightness. The more dim stars are obviously the most difficult to acquire and to track. If the target of interest is of high magnitude in the star-tracker sensitivity band, it cannot be tracked by using the onboard equipment; hence, there is a need to apply offset pointing. Nearby stars in the +6 to +9 magnitude range, or brighter, will be used as the reference system. They are, however, offset from the desired pointing direction and therefore are not tracked by the conventional techniques. The Airborne Optical Telescope uses an auxiliary fine-tracking telescope to obtain this type of tracking. The Stratoscope system also uses off-axis reference stars but within the same telescope field-of-view. For the smaller apertures, use of the same telescope for offset pointing appears feasible because of the "large" field-of-view; however, as the aperture

size increases, the usable field-of-view decreases and pointing accuracies become tighter. This represents a problem area for the large telescopes.

A problem alluded to in the preceding sections is the alignment of the sensors and the experiment telescope. In addition to this alignment problem, the actual focusing of the optics must be considered. For the Manned Orbiting Telescope vehicle, it was concluded that automatic servoed focusing of the system was not only desirable but also necessary. This is to offset the effects of thermal gradients and other structural deformations destroying the focus of the system. If it is necessary to provide an automatic focusing system to align the telescope optics, it is apparent that other sensors on the exterior of the main body will also undergo alignment shifts. Unless there is some way of automatically calibrating the system alignment at each experiment orientation, the alignment of the other sensors outside of the telescope becomes very uncertain and unreliable for fine pointing.

The use of a manned vehicle presents very stringent requirements on the control system design. Studies of both the Apollo Telescope Mount and the Manned Orbiting Telescope have shown that man disturbances to the operation of the system are the most severe from a magnitude and frequency contact. This being the case, steps must be taken to alleviate the effects of this disturbance. The control system designer has several options at his disposal, including:

1. Constrain man during experiment periods.
2. Soft-gimbal the experiment.
3. Servo-isolate the experiment.
4. Use magnetic gap control for the experiment.

To date, the indications are that the first of these options is not being seriously considered. The other three options have been seriously considered, and, depending upon the study, recommendations for adopting each of the methods have been made. The conclusion can be drawn that the most advantageous way

to handle the man disturbances is to keep the experiment system as isolated as possible.

Conclusions

The current state-of-the-art of the pointing and stabilization systems is satisfactory for many applications. A wide variety of techniques are applicable to the missions with the specific operating details providing the additional constraints. From a hardware

standpoint, the torque sources have been or are being developed. The current pacing items as far as system operation is concerned are in the guidance area. The experimenters are looking at more dim objects and desire tighter pointing accuracies. These requirements are incompatible at the present time; new equipment and techniques must be developed. These lead to the area of offset pointing, a technology area requiring development effort.

PRECEDING PAGE BLANK NOT FILMED.

Considerations Relating to Use of a Large Astronomical Telescope in Space

John Strong

The University of Massachusetts

N70-36688

The main purpose of this paper is to collect some of the basic considerations that will govern the full exploitation of astronomical telescopes in space, namely:

1. Freedom from the ultraviolet and infrared atmospheric absorption that limits the spectral frequency bands through which ground-based telescopes can study the heavens

2. Absence in space of the optical turbulence of an atmosphere, such as degrades the spatial resolving power of ground-based telescopes.

These considerations will include some evaluation of the instrumental developments that could be pushed now to expedite this full exploitation — developments that are promised by recent accomplishments. Such developments will include the extension of the existing, conventional, astrophysical art in the ultraviolet toward X-rays and in the infrared toward millimeter radio waves as well as the adaptation of the existing art and new developments to the new environment.

Development of a means of producing large grating with new characteristics will be required for space use. In the far ultraviolet, development of groove-forming procedures for new material will be required. This will include groove formation by holography-resist-etching.

The extension into the far ultraviolet will involve the art of polishing materials for making mirror surfaces and will include studies of pitch-type polishing procedures as well as such new methods as polishing with ice and ion-beam polishing. Studies of the reflectivity and scattering of various new materials will be involved. It may be possible

to remove mirror overcoats from mirrors and gratings in space, by ion-beam etching, and to re-coat them.

In the far infrared, there is promise of a 1000-fold increase in sensitivity of cryo-detectors; and, in another direction, some form of infrared image tube is certainly desirable, considering the burgeoning importance of infrared astronomy.

It will be even more mandatory to avoid wasting information and observing time with a telescope in space than it is with the powerful and expensive land-based telescopes. When a star field or spectrum is studied with instrumentation that provides adequate resolving power at, for example, an $f/1$ aperture, information is wasted if that resolution is not used. When the star field or spectrum is over-resolved, observing time is wasted. We review, below, the criterion for determining a proper match of resolving power and camera aperture to the telescope blur circle. The resolving power that we shall take for the detector — for example, a photographic plate — is 50 line pairs per millimeter (or $\Delta = 20\mu$). We shall take a similar resolving power for a television type of image tube. Such integrating image tubes are currently available and offer a gain in quantum efficiency of a hundred fold or more over that possible with photography.

We review Bowen's analysis, adapting it to the circumstance that practical, limiting, stellar blur circles of a 3-meter, diffraction-limited telescope will be reduced six-fold by being in space:

For a ground-based, mountain telescope the angular seeing blur is

$$\beta_0 = 6 \times 10^{-6} \text{ radians}$$

In space, a 3-meter telescope worked at 6000 Å has an Airy disk of angular diameter

$$1.22 \left[\frac{1.2\mu = 2\lambda}{3 \times 10^6 \mu = D} \right] \cong \frac{1}{2} \times 10^{-6} \text{ radians.}$$

For practical reasons, when we are determining the width of a spectrograph slit that not only will accept all of the collected light that is put in the star image but also will not diffract it outside the rim of the spectrograph collimator optics, we take the blur as twice the Airy disk or

$$\beta_{2\lambda} = 10^{-6} \text{ radians}$$

Figure 1 illustrates Bowen's analysis. D_0 is the diameter of the telescope objective of focal length f_0 ; d_1 and d_2 are diameters of the collimator and camera optics for the spectrograph. A prism is shown to represent the spectrum dispersing means – with angular dispersion, $d\theta/d\lambda$.

The blur circle diameter, b (exaggerated in fig. 1), is

$$b = f_0 \beta$$

where f_0 is the focal length of the telescope.

The matching of the angular apertures of telescope and collimator gives

$$f_1 = \frac{d_1}{D_0} f_0$$

Figure 1 shows three camera focal lengths. The first focal length is too short; it wastes information. The third is too long; it wastes observing time. The intermediate focal length for which Δ , the resolving power of the spectrum recorder, matches the stellar blur circle, $b = f_0 \beta$, is the correct one.

Applying Abbe's Law, with b and Δ representing image sizes and D_0/f_0 and d_2/f_2 representing sines of aperture angles,

$$b \frac{D_0}{f_0} = \Delta \frac{d_2}{f_2}$$

$$\frac{f_2}{d_2} = \frac{\Delta}{\beta_0 D_0}$$

Bowen pointed out that the 200-inch telescope ($D_0 = 5 \times 10^6 \mu$) required $(f/d) = 2/3$ for the camera. The 3-meter telescope

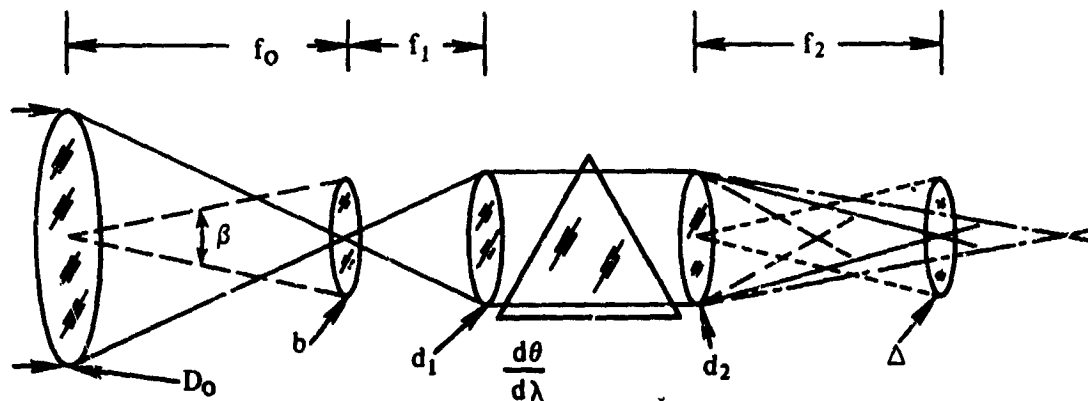


Figure 1. Illustration of Bowen's analysis of proper spectrograph camera to avoid wasting available information or observing time; Hiltner's *Astronomical Techniques*, Chapter 2, "Spectrographs," by I.S. Bowen, The University of Chicago Press (1962).

($D_0 = 3 \times 10^6 \mu$) with $\beta_{2\lambda} = \beta_0/6 = 10^{-6}$ requires, for the camera,

$$\frac{f_2}{d_2} = \frac{\Delta}{\beta_{2\lambda} D_0} = \frac{20}{3} \text{ or } 6.67$$

The important point is this: if the resolving power of the spectrum recorder (television detector) can be improved by a factor of 10, a certain information-packed spectrum can be obtained in a shorter exposure time, shorter by a factor of 100.

For studies involving spatial resolution (such as direct photography rather than spectroscopy), where it is possible to realize Airy disk resolution for the 3-meter telescope, $\beta_d = 1/2 \times 10^{-6}$, the camera focal length required is $f_2/d_2 = 13.3$, rather than 6.67.

The dispersion K, in angstroms per millimeter, required for astronomical studies depends upon the problems that will be undertaken, but one may suppose, as a prudent upper limit, a dispersion that will allow a spectral resolution of $\delta\lambda = 0.08 \text{ \AA}$ the limb to limb Doppler shift for the sun at 6000 \AA . Earlier types of stars will rotate faster, in which case higher instrumental resolving power will be insignificant.

The dispersion of the spectrograph grating and the focal lengths of collimator (f_1) and of the camera (f_2) are all involved in the determination of K. If (for tutorial purposes) we take $f_1 = f_2$, we can compute K and the size of the grating that will be required to yield a resolved spectrum, $\delta\lambda = 0.08 \text{ \AA}$ at 6000 \AA . Taking $\Delta = 50 \text{ mm}$ (50 line pairs resolved) for the detector (spectrum plate or image tube), we get

$$K = 4 \text{ \AA/mm from } K \times \frac{1}{50} = 0.08 \text{ \AA}$$

Now if $\frac{d\lambda}{d\theta}$ is expressed in the units $\frac{\text{micron}}{\text{radian}}$, then

$$K = \frac{d\lambda}{d\theta} \times \frac{10^4 \text{ \AA per micron}}{f_2 \text{ (in millimeters)}}$$

We shall assume a grating that is worked in the Littrow arrangement, with the angle of incidence, ϕ , equal to the angle of diffraction, θ . We further take the grating spacing as: $a = 3.33\mu$. Although this is perhaps not the situation that will be eventually used, it can be modified to taste. From

$$\lambda = \frac{a}{k} (\sin \theta + \sin \phi) = 2 \frac{a}{k} \sin \theta$$

we get

$$\frac{d\lambda}{d\theta} = \frac{a}{k} \cos \theta = \frac{\lambda \cos \theta}{2 \sin \theta} = 1.3\lambda$$

and

$$K = 1.3 \frac{6000}{f_2} = \frac{7800}{f_2} = 4 \frac{\text{\AA}}{\text{mm}}$$

for

$$f_2 = 1950 \text{ mm.}$$

The entrance slit must be narrow enough to subtend less than $0.08 \text{ \AA} = \delta\lambda$ while, at the same time, wide enough to admit all of the starlight within the blur circle:

$$b = f_0 \beta_{2\lambda} = 4.88 \frac{f_0}{D_0} \lambda$$

This consideration determines the collimator focal length, f_1 , the collimator size, and the grating size.

This b, subtending the angle $\delta\theta = b/f_1$ at the grating, together with $\delta\lambda/d\theta = 1.3\lambda$, in the expression

$$\delta\theta \frac{\delta\lambda}{\delta\theta} < 0.08 \text{ \AA}$$

yields

$$\frac{4.88 f_0}{f_1 D_0} \lambda (1.3\lambda) < 0.08 \text{ \AA or } 8 \times 10^{-6} \mu$$

Substituting the value for D_0 gives

$$\frac{f_1}{f_0} > \frac{4.88 (\lambda^2 = 0.36)}{\epsilon \times 10^{-6} \times (3 \times 10^6 = D_0)} > 0.073$$

which, in the expression $d/f_1 = D_0/f_0$, determines collimator rim diameter:

$$d = 0.073 \times 120 = 8.75 \text{ inches}$$

This would be a grating ruled on a disk having a 14-inch diameter.

These are the considerations involved in exploitation of the circumstance that the intrinsic star image illumination of a diffraction-limited telescope in space increases with the fourth power of the diameter of its aperture:

- A power of two from the increase in flux collecting area of the primary
- Another power of two from the decrease in star-blur circle diameter, in the denominator, due to freedom from atmospheric turbulence.

Now let us turn to freedom from atmospheric absorption in the far infrared and far ultraviolet. Considerable study has already been made with balloons and rockets and by the Orbiting Astronomical Observatory (OAO) in the ultraviolet. Confining ourselves to our own specialty, the infrared region, let us consider some of the general principles that point up the infrared limitations.

Interferometric spectroscopy in the hands of the Connes has yielded $\frac{1}{10} \text{ cm}^{-1}$ resolving power in the near infrared Venus spectrum, using a ground-based telescope. It will be very revealing to see this type of application without telluric absorption.

In the hands of Dr. Hanel, interferometric spectroscopy has revealed the infrared emission spectrum of the earth as seen from a space satellite.

Fourier spectroscopy has three advantages:

1. Multiplexing or observing several spectral components concurrently

2. Large *étendue* - to use Steele's term for the spectral throughput of the spectrum analyzer, that is, $A\Omega d\nu$

3. The so-called Fellgett advantage.

The Fellgett advantage is a gain, by a factor of \sqrt{n} , in the signal-to-noise ratio by which each one of n spectral components of a spectrum is known. The advantage arises because, multiplexing, we look with a detector at all spectral components concurrently for a longer time, $n\tau$, than the time to observe each component, τ , if all are observed sequentially. This decrease in noise (effective noise is proportional to the square root of integration time) gives the Fellgett advantage. It is enjoyed when the signal noise is the same for all components when they are observed simultaneously or observed sequentially.

In the case of photon noise, however, the noise is not independent of the flux falling on the detector and increases proportionally to its square root. This noise increase cancels the Fellgett advantage. Even though there is no Fellgett advantage in the photon noise case, there may be information-handling advantages.

Nolt's detector, applied recently on Mauna Kea in Hawaii to the determination of the far infrared spectrum of the sun, operates at 0.4°K. Sinton and Nolt report that it exhibits 10^{-14} watts ENI, with 10^{-15} watts promised. This detector illustrates one of the main characteristics of far infrared spectroscopy; that is, for the infrared, the only "dark room" that can exist is the inside of a helium cryostat because a surround at the temperature T°K has the peak of its intrinsic blackbody emission at

$$\lambda = \frac{2890}{T} \text{ microns}$$

Selective cold filters, which pass only a small spectrum range at the wavelengths under study, are required to prevent overheating and overbiasing of detectors. It does not take much flux to ruin a low temperature of 0.4°K. This characteristic will be of

primary concern when integrating infrared image tubes appear that will require a "dark room."

Another concern will be the degradation of spatial resolving power arising from the increase of the stellar blur circle due to greater infrared diffraction. At $\lambda = 3.6\mu$, the blur circle of the 3-meter telescope will be the same in space as a telescope on a mountain

suffering 6×10^{-6} seeing-blur. At wavelengths longer than 3.6μ , the resolution limit will degrade even further - to minutes at 200μ , etc.

If an intermediate step is intended, before the final large space telescope, it would appear that the telescope involved should be full size but instrumented only for infrared use.

PRECEDING PAGE BLANK NOT FILMED.

Photoelectronic Imaging Devices

Sol Nudelman

University of Rhode Island

N70-36689

Introduction

This paper is tutorial in nature and is intended to provide background material for those interested in elemental photodetectors and photoelectronic imaging devices.

A typical low-light-level television type of system is shown in figure 1. The scene to be viewed is shown on the left side of the figure with a camera lens placed to image the scene on the first photocathode of the camera tube. The camera tube is basically made up of two parts: the front commonly referred to as the intensifier and the rear consisting of an electron-beam scanning type of pickup tube. These two units can be obtained as physically separate devices or can be combined in one envelope (refs. 1 and 2).

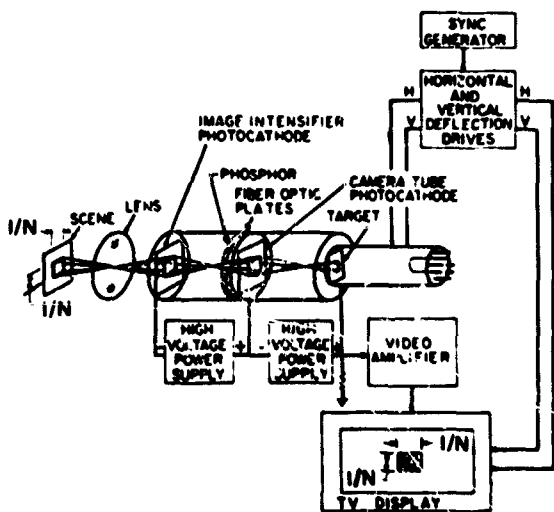


Figure 1. A typical, low-light-level, television, imaging system (by F. Rosell from ref. 9).

The function of the intensifier is to provide photon gain. Intensifier gain is narrow bandwidth gain, which permits amplifying input photon flux to a level where photon noise can dominate the shot noise of the pickup tube. The intensifier photosensor is a photoemitter, which is a film that absorbs photons causing the emission of electrons. These electrons are then accelerated and focused by electron optics and caused to bombard the rear surface of the intensifier, which is coated with a phosphor. The photoelectron pattern emerging from the photocathode is reproduced as a luminescent image, which is viewed by the pickup tube. Intensifiers of this type can provide not only light amplification but also conversion; that is, incident photons might be in the ultra-violet spectral region, and the emitting photon from the phosphor surface might be in the green spectral region. The color of the outgoing photons depends upon the needs of the user being matched to the human, for example, when used as a direct viewing device. When more photons emerge than are incident, the device is functioning as an amplifier or an intensifier. By attaching these units properly in series, it is possible to have gain in each stage and to provide very substantial amplification. Such gain is usually obtained at the expense of degradation in resolution, and, as a result, one is limited in the extent of useful gain achievable by the resolution requirements of the application.

The pickup tube functions with a scanning electron beam, which generates a signal from the scene imaged on its front photosensor surface. The mechanism of scanning permits charge storage, thereby enhancing

signal-to-noise capability but operating with a wide video bandwidth. Thus, the signal obtained by scanning can be transmitted and reexamined remotely as in a television type of display. Often this tube is called a remote device, and the intensifier is called a direct device.

Electron-Beam Scanning Tubes

The vidicon shown in figure 2, is the simplest kind of remote tube. It operates through the use of an electron gun that sends a beam of electrons down the tube to strike a photoconductive layer deposited on a transparent, conducting, glass front surface. A scene to be viewed is focused optically on the photoconductor through a lens. As the scanning electron beam sweeps across the photoconductor surface in a master mode, it deposits electrons on the rear surface of the photoconductive layer. Photons absorbed by the photoconductor from the imaged scene cause electrons to disappear from its rear surface. The result is that the electron beam, on striking a region of the surface that has lost electrons, undertakes to replace the electrons. Because the number of electrons to be replaced depends upon the number of photons that have been absorbed, the process of replacing electrons by the beam generates a signal current that can be capacitively coupled to a preamplifier. The vidicon is characterized by the front-surface photoconductive layer, which is very much like an elemental photoconductive detector in that a resistance change takes place, leading to a corresponding change in current flow, which represents

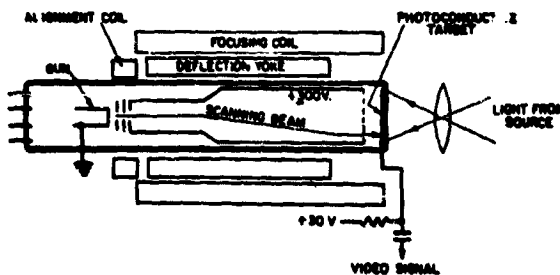


Figure 2. Schematic cross-section of vidicon.

signal. The vidicon customarily uses a photosensitive surface such as antimony trisulfide.

Another device using a similar construction is called the *plumbicon*. It differs from the vidicon in using a different photosensor material called lead oxide. This material appears electronically more complicated than antimony trisulfide in that there is considerable evidence that its photosensitivity depends upon p-n junction effects rather than simply photoconductivity.

The *image orthicon* shown in figure 3, is a more complicated device. There are two areas of difference to be stressed between this tube and the vidicon. First, the photosensitive surface is a photoemitter and not a photoconductor. Electrons are emitted from the rear surface of the photosensors and reimaged on a target surface. The target is constructed from a material called a secondary electron emitter; that is, a material capable of emitting two or more electrons when bombarded by an incident electron. Thus, when photoelectrons strike the target, they cause the target to emit more electrons than are incident; consequently, the target becomes positively charged from a deficiency of electrons. This kind of target provides a means for obtaining gain before scanning with the electron beam. The electron beam from the gun has the same function as it had in the vidicon; that is, to spray charges on the back surface of the target. The image orthicon, however, is set up so that the electrons not retained by the target are reflected back to the region from whence they came. Furthermore, the return beam does not follow the identical path as the incident beam because, as the return beam nears the emitting aperture, it is deflected into an electron multiplier. This kind of amplifier is particularly useful because it permits amplification with little degradation in the signal-to-noise ratio. Since secondary electrons are being removed from one side of the target and being deposited by the beam on the other side, the target must have some electrical conductivity. A resistivity such that the dielectric relaxation time is the same as the frame time insures that these charges can flow through the target and neutralize each

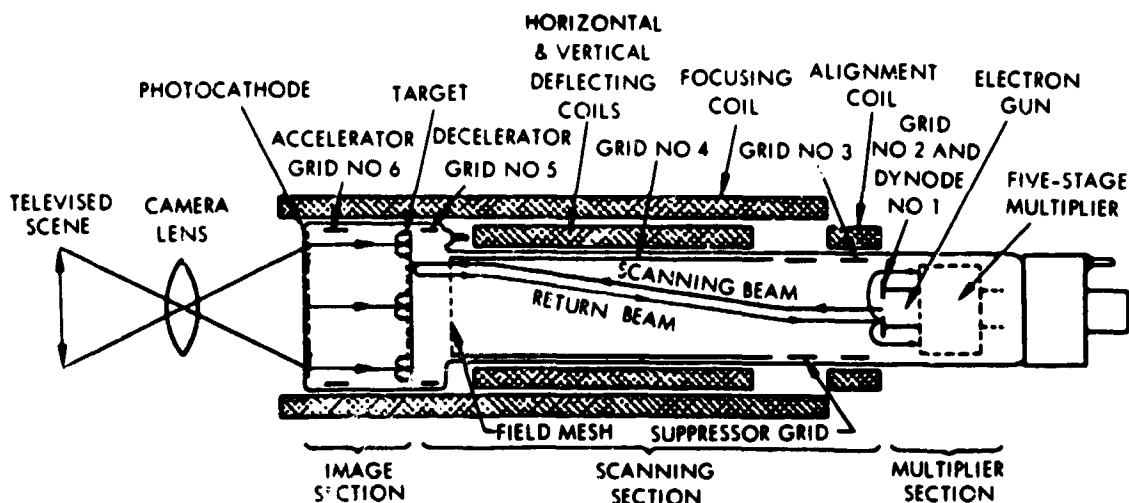


Figure 3. Schematic cross-section of vidicon image orthicon (by K. W. Redington from ref. 10).

other at an appropriate rate. For materials with the usual dielectric constants, a resistivity is required of about 10^{11} ohm centimeters.

A variety of materials have been used for the storage target. Originally, this was a soda lime glass whose conductivity was ionic. Unfortunately, the ions always drifted in the same direction. Eventually, the glass became more resistive, and patterns would "burn in." This image retention became objectionable after only a very few hundred hours of operation. A thin-film magnesium-oxide target (which is electron-conducting) was developed to solve this problem. Not only was magnesium oxide successful in this regard, but it also provided two important bonuses. The secondary emission ratio of magnesium oxide in thin film form is about 15; this gives a gain in the image section about five times as large as a conventional glass target. In addition, the magnesium oxide target is only about one tenth the thickness of the glass target, and its conductivity is anisotropic, being higher through the film than along the surface. Thus, magnesium oxide targets displayed very high resolution and could be operated in a storage or slow scan mode.

A two-stage intensifier image orthicon is shown in figure 4. This device is simply a combination of an image orthicon with two

intensifier stages placed in front of the image orthicon. The two intensifiers are coupled through a thin glass membrane. The front side of this membrane supports a phosphor screen and the back surface a photoemissive coating. Today, the thin glass membrane is often replaced by fiber optics, which permits improvements particularly in the design of the electron optics. The remainder of the tube is the same as the image orthicon.

The *isocon*, shown in figure 5, is similar in structure to the image orthicon or the intensifier image orthicon, with the distinction being in the treatment of the return beam electrons. This device makes use of the scattered electrons rather than those reflected from the rear surface of the target. It contains the same photocathode and target materials as in the image orthicon. The electron optics, however, is set up so that the reflected and scattered electrons in the return beam can be separated from one another, and the scattered electrons alone are permitted to enter the multiplier section of the tube (ref. 3).

The *SEC tube* is shown in figure 6. It differs from the earlier tubes in that the target is made up of a low density material designed to provide enhanced secondary electron conduction (SEC) and considerable gain. The extent of this gain is sufficient to extract the signal from the SEC target directly, as in a

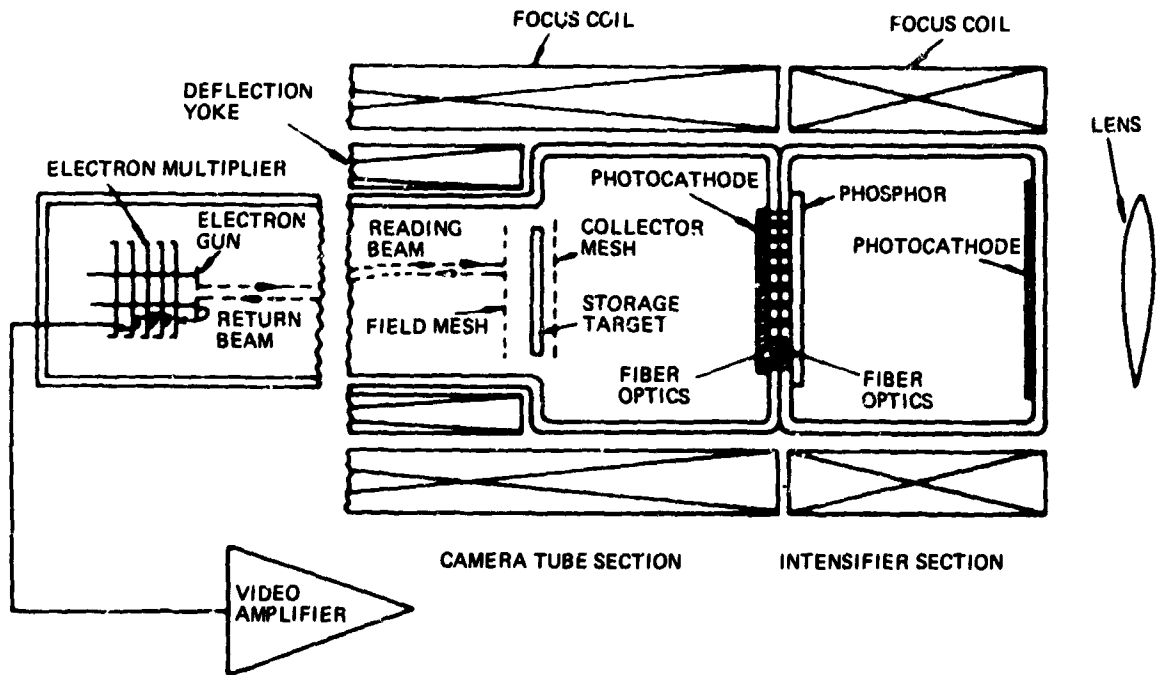


Figure 4. A two-stage intensifier image orthicon: Isocon (by A. D. Cope from ref. 10).

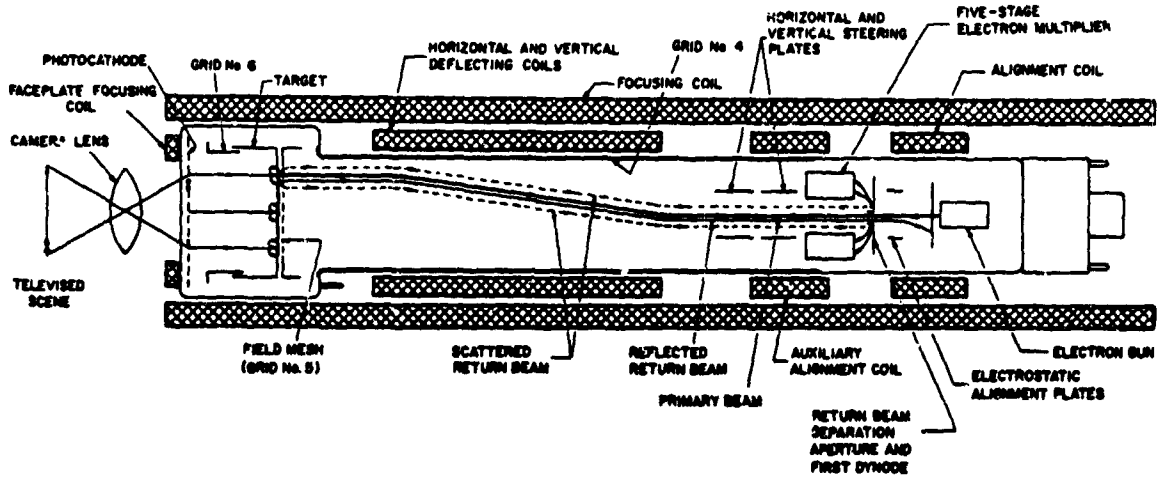


Figure 5. Schematic cross-section of new image isocon (by E. M. Musselman from ref. 10).

vidicon, rather than requiring the use of a return beam and the electron multiplier section (ref. 4).

Electronic Mechanisms in Crystals

In order to understand how these

different kinds of photoelectronic imaging devices operate, it is important to visualize the electronic mechanisms prevailing in photoemissive and photoconductive sensors. A two-dimensional drawing of a crystal characterized by covalent bonding is shown in figure 7. This type of bonding is typical of

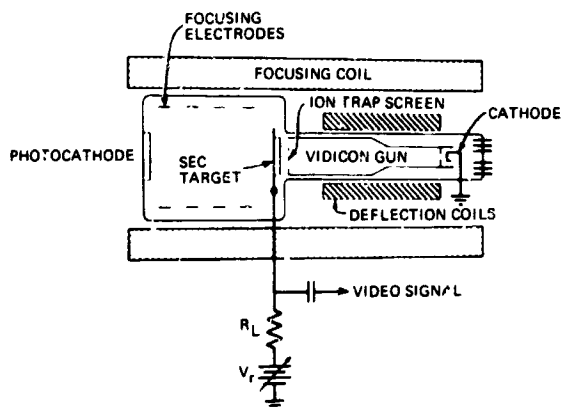


Figure 6. Schematic cross-section of SEC tube (by G. W. Goetze from ref. 10).

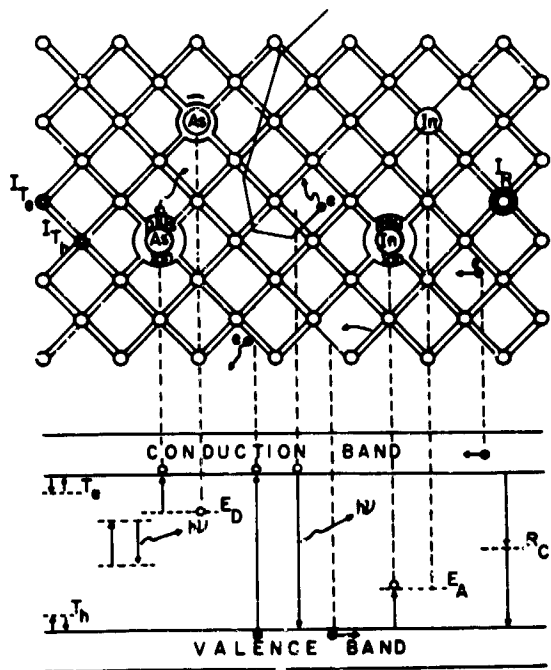


Figure 7. A two-dimensional crystal showing (upper part) lattice for covalent bonding with impurities and (lower part) corresponding energy level diagram.

crystals such as germanium and silicon in the fourth column of the periodic table. Each of the circles represents an atom, and the double pairs of lines represent covalent bonding; that is, two electrons are shared between each two

adjacent atoms. The shared electrons are called valence electrons; these are shown in the energy level diagram as belonging in the valence band. Electrons described by these lines are held and shared between two atoms; they are not free to move about. Electrons that are not shared in this manner and that are free to move about the crystal are said to be in the conduction band. Electrons may be free because they have been shaken loose between atoms due to thermal vibrations or perhaps by absorbing energy from a photon.

Impurities in the lattice are shown in figure 7 as an arsenic impurity and an indium impurity. Indium is in the third column, and arsenic is in the fifth column of the periodic table. Indium, being in the third column, causes a deficiency of one valence electron when it replaces an atom such as germanium or silicon in a crystal. This results in the creation of an energy state in the crystal called an acceptor state. An electron in the valence band that is tied between pairs of atoms may jump from its bound position into the vicinity of the indium atom where it can be captured. When it is captured, the electron sits in this new acceptor energy state and has more energy than it would have had if it were in a normally bound state in the valence band. Accordingly, it is shown as a localized energy state, E_A , slightly above the valence band.

The electron sitting in the acceptor state leaves an electron missing in the valence band, which is referred to as a "hole." The hole can move from one atomic site to another by a jumping mechanism; that is, a valence electron in a nearby atom jumps into the place vacated by the electron in the acceptor state. This jumping process can be repeated, and the hole moved further by an electron from a different nearby atom jumping into the hole. A hole behaves as a positive charge, having a magnitude equal to the charge of an electron. In moving through the crystal, holes behave as an electrical current of positive charges. When a crystal is doped with impurities so that the hole conduction predominates over electron conduction, the crystal is said to be "p" type. The arsenic atom is a fifth column atom and therefore has one extra electron. When

substituted for a germanium or silicon atom in the host crystal lattice, the extra electron is partially shielded from the parent atom. Hence, although the electron is still bound to the parent atom, it is relatively easy for the electron to gain sufficient energy to be freed from its parent. Accordingly, its energy level is only slightly below the conduction band energy and is shown as E_D (fig. 7) and described as a donor energy level. The nearness of the donor level to the conduction band results in more electrons being in the conduction band because they are more easily freed from their parent atom by thermal processes. As a result, electrical conduction by electrons is increased. Material doped so that the electron conduction predominates over hole conduction is said to be "n" type.

Notice that, in the energy level scheme, there is a separation shown between the valence band and the conduction band. This separation is called the energy gap. When an electron is shaken loose from between two atoms (as a result of their thermally induced vibration) and becomes free to roam through the lattice, or when an electron absorbs energy from a photon, the electron is shown on an energy level diagram as a vertical transition from the valence band to the conduction band. Similarly, when an electron that has been free, and is said to be in the conduction band, passes near atoms that have a missing electron between them, the electron will be attracted to that site and may be captured. This process is shown on an energy level diagram as a vertical transition downward. The electron is said to make a transition from the conduction band to the valence band. This transition may occur with the emission of radiation of photon energy, where this energy is equal to the energy gap. The other transitions shown in figure 7 describe absorption and emission processes involving impurities or dislocations and also trapping processes.

The electron trap is indicated in figure 7 by T_E in the energy level diagram. This is associated with an impurity or a crystal dislocation that has the ability to attract and temporarily hold electrons in its vicinity.

Thus, when electrons free to move about the crystal and said to be in the conduction band pass near such an impurity or dislocation site, they can be attracted to that site and then immobilized or trapped in its vicinity for some time. Eventually, through thermal excitation processes, the electron may again become freed and return to the conduction band. This trapping and freeing process may be repeated many times during the lifetime of an electron. It is the main mechanism contributing to longtime decay in photoconductivity and photoluminescence.

Toward the middle of the energy level diagram in figure 7 is shown another localized level, indicated as R_C . This level often acts as a recombination center; that is, where electron recombination processes are maximized. Recombinations downward need not be accompanied by radiation; they may involve an interaction between the electron and the host crystal lattice. In that event, instead of radiation emerging from the crystal, the energy of the electron could be absorbed in the host lattice with a corresponding change in crystalline temperature.

A vidicon photoconductive film is shown in figure 8. The layer is considerably enlarged with light from the scene impinging on one side and the scanning electron beam on the other. Photons absorbed by the material create electron and hole pairs. The holes under the influence of the applied electric field drift toward the surface, which has had electrons deposited by the beam. Electrons drift toward the transparent conducting electrode and leave the photoconductor. The

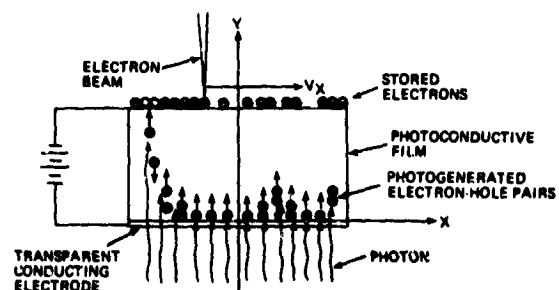


Figure 8. The vidicon photoconductive film.

holes recombine with surface electrons and remove them from the photoconductor. As a result, when the electron beam returns to a place where holes have removed electrons, it puts the electrons back and, through capacitance, couples a signal current into a pre-amplifier (ref. 5).

Imaging devices also use p-n junctions in their photosensitive layer. A rudimentary outline of a p-n junction is shown in figure 9, the upper part depicting crystal type (with n- and p-type regions) and the lower part showing the corresponding energy level diagram. The n- and p-type materials are grown from a common substrate; that is, the substrate may normally be n type or p type, and the remaining type is grown by some treatment of the surface of the substrate. The interface between the n-type and p-type regions constitutes a barrier layer. The barrier is the result of the electrons from the n-type region diffusing into the p-type region and the holes from the p-type region diffusing into the n-type region. This charge displacement creates an internal electric field. The diffusion process is balanced eventually by what is called a drift process. A drift of electrons and

holes results from the internal electric field, thereby causing carriers to move in the opposite direction to that caused by the diffusion process.

The n-type region results from doping the crystal with impurities that contribute extra electrons and donor states; the p-type region contains an excess of impurities that provide acceptor states and an excess of holes. The energy level diagram of figure 9 depicts these levels by D and A for donor and acceptor, respectively. The level referenced as C_F is called the Fermi level. The Fermi level has a special significance in semiconductor physics and is a quantity that appears in the Fermi distribution function. It is that particular energy level which predicts a probability of one-half that an electron in a system following this distribution function would be located at that energy level. Thus, on the n-type side, this probability is high near the conduction band, reflecting the donor's contributing many electrons to the conduction band and shifting the distribution of electrons high up in the energy level scheme. On the p-type side, however, the Fermi level is close to the valence band, reflecting the fact that the acceptor impurities cause the distribution function for electrons to move downward closer to the valence band. Therefore, for the p-type crystal, fewer electrons are in the conduction band than for the n-type material. When an electric field is applied to such a diode type of structure, it causes the energy level on the p-type side to shift higher or lower with respect to the n-type side, depending upon the direction of the applied electric field. For example, if the n-type material is connected to the negative electrode of a battery and the p-type side to the anode of the battery, this is said to be the forward direction for biasing the diode. This results from electrons being more easily drawn from the n-type side to the p-type side and holes being more easily drawn from the p-type to the n-type side. This happens because the applied electric field is opposed to the internal field in the barrier region, resulting in a net reduction of the total field and thereby allowing an easier flow of the

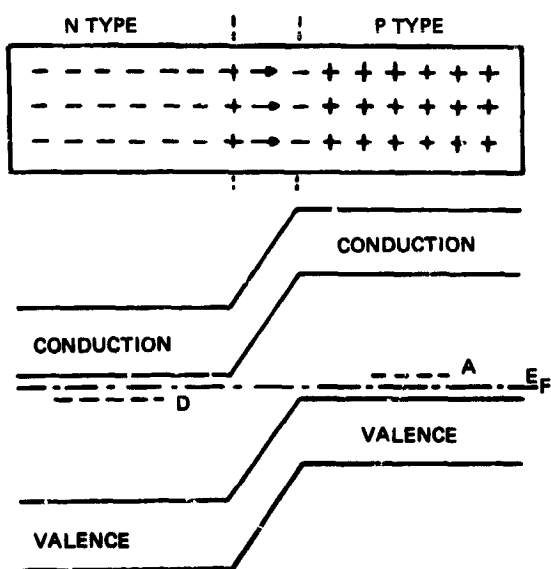


Figure 9. The P-N Junction: showing (upper part) crystal type and (lower part) corresponding energy level diagram.

diffusion type of current. If, however, the electrode polarity is reversed, then the direction of the applied field is the same as the direction of the internal field; and it becomes more difficult for charge carriers to move across the barrier. This corresponds to an increase in the height of the energy band going from the n-type to the p-type side.

A photoelectric effect can be generated when photons are absorbed in the barrier region or within a diffusion length of the minority carrier on either side of the barrier. When this happens, the electrons will be swept into the n-type material; and the holes will be swept into the p-type material. If one were to put electrodes across the crystal diode and to include an appropriate meter, one would find that this process generates a photovoltaic effect. This is the basis of the solar cell and also the photovoltaic detector when it is included in a photoconductive type of circuit.

Silicon Vidicon

The silicon vidicon, which is undergoing intensive research and development, makes use of a photosensor comprising a mosaic of back-biased photodiodes. The electron beam scans the surface of this mosaic of back-biased diodes and deposits electrons as in the vidicon. This is shown in figure 10 (ref. 6). On the opposite side of the surface of the photosensor, photons impinge and are absorbed, thus causing the creation of electrons and holes described for the p-n junction. As a result, holes are swept into the p region, and they remove electrons from the back surface. This type of system has a number of advantages, including far less fragility than the image orthicon type of tube structure. Furthermore, by back-biasing the diodes, it is possible to operate the tubes with storage by using semiconducting materials whose energy gaps would normally be too narrow to use in image tubes. They function with high efficiency and do not suffer unduly from lag. When silicon is used as the target material, the spectral response of the device moves toward

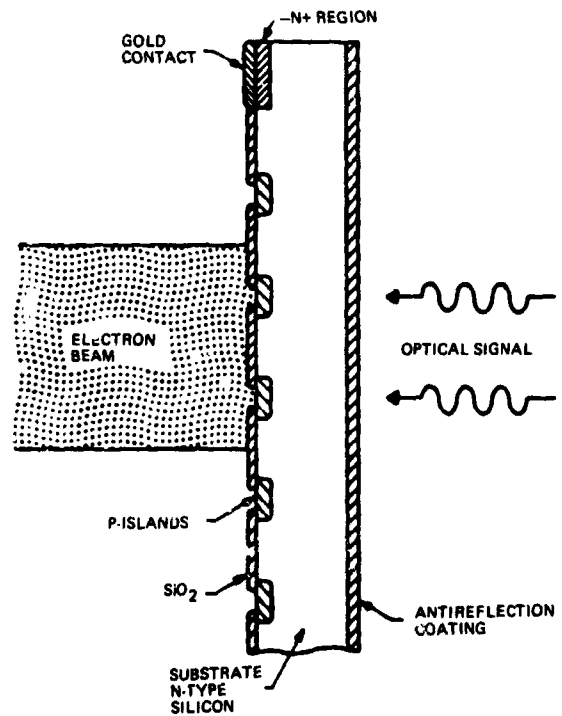


Figure 10. Silicon vidicon mosaic sensor (from refs. 6 and 10).

longer wavelengths, corresponding to the absorption edge of silicon.

A modification of the silicon vidicon is to use the silicon mosaic in an SEC type of image tube. In this approach, a conventional photoemitter front surface is used as the photosensor, and the silicon mosaic is used as a target material from which one can achieve appreciable gain. This is a result of electron-bombardment-induced conductivity. On being accelerated and striking the p-n junction device, electrons from the photoemitter cause many more holes to be created, which results in enhanced depletion of stored charges on the back surface of the target and, correspondingly, an enhanced signal. Gain provided in this manner is considerable and has reached the point where there is a strong likelihood that this type of tube may well become the predominant image tube in many applications in the years ahead.

Photoemission

Photoemitters can now be examined in terms of their band structure. The metallic emitter is depicted in figure 11, where E_W is the energy required for an electron at the Fermi level to escape from the surface and is called the work function. Most electrons that can participate in photoemission are near the Fermi level and thus require the energy, E_W , to escape.

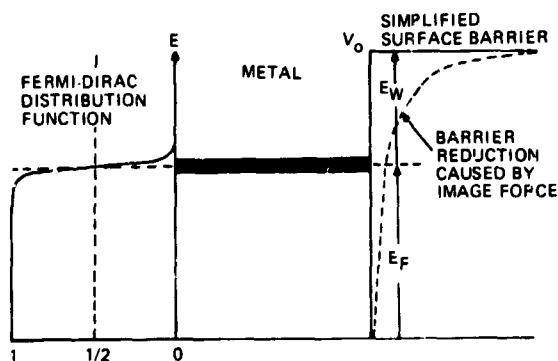


Figure 11. Photoemission from metals.

The semiconducting photoemitter is shown in figure 12 with the usual energy band picture, but the picture ends abruptly where the surface of the crystal meets the vacuum. The valence band and the conduction band are shown. The top of the conduction band corresponds to the vacuum energy level. The dashed, curved line on the right represents a more usual shape for the barrier than the abrupt shape shown at the surface as position zero. The curved shape is the result of electrostatic forces that set up between the atoms comprising the crystal immediately below the surface. Photoelectrons can come from the bottom of the conduction band, or the valence band, or the donor levels. Transitions can be made out of the crystal if energies are given to the electrons from the valence band equal to the energy gap plus the width of the conduction band. This width is called the electron affinity. Electrons can be excited out of the donor levels if they are given enough energy; that is, equal to the depth of the energy level, E_D , plus the electron affinity,

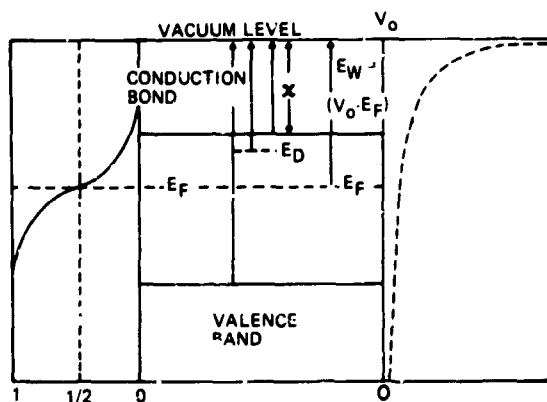


Figure 12. Photoemission from semiconductors.

or, if one is trying to get an electron out of the conduction band essentially, energy is required equal to the electron affinity.

The barrier can be reduced and the electron photoemission improved in two different ways. One way is by placing a monolayer of some metal on the surface whose work function is essentially equal to the energy between the bottom of the semiconductors conduction band and the Fermi level. When two materials are placed in crystallographic contact, their Fermi levels line up; that is, if a metal is placed on the surface of the semiconductor, then its Fermi level (which is the value where the electron probability function is one-half) lines up with the identical level in the crystal. Electrons move back and forth between layers of two different materials until their Fermi levels line up. As a consequence, situations can arise such as those shown in figure 13 (ref. 7).

In figure 13(a) is the general case of a semiconductor, showing the bottom of the conduction band, the top of the valence band, and the Fermi level. If a layer of cesium is placed on top of a semiconductor whose bandgap is not specified, then the Fermi levels line up and the vacuum level of the metal adjusts accordingly. In figure 13(a), the energy gap of a semiconductor is less than 1.4 electron volts. As a result, electrons in the semiconductor conduction band would have to gain enough energy to climb above the barrier or sufficient energy so that it would be

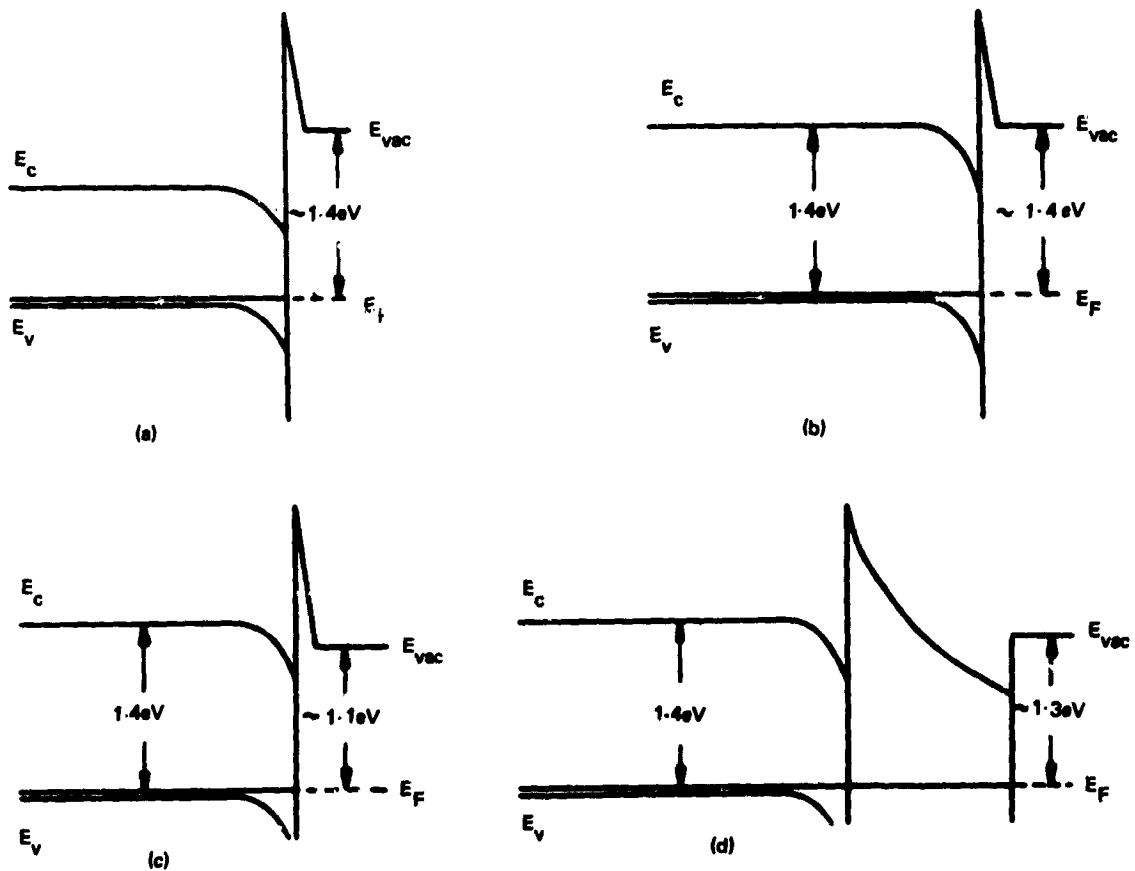


Figure 13. Reduction of surface barriers (from ref. 7).

relatively easy for the electrons to pass through the thin barrier. This latter process is called "tunnelling" and is a phenomenon that arises from quantum mechanical considerations. In the tunnelling process, an electron goes through the thin barrier rather than over it. Figure 13(b) shows a case in which cesium is deposited on gallium arsenide. Since the work function of cesium is essentially equal to the energy from the Fermi level of the p-type gallium arsenide to the bottom of its conduction band, the problem is for the electron to tunnel through the remaining thin barrier. Figures 13(c) and 13(d) show variations on this theme. In figure 13(c), the work function of the cesium and oxygen placed on gallium arsenide turns out to be less than 1.4 electron volts with the result that the

work function is further reduced. In figure 13(d), gallium arsenide is coated with cesium oxide, which has a work function of 1.3 electron volts.

A second way in which electrons can be encouraged to pass out from photoemissive materials is to use a field effect; that is, to deposit a layer on the semiconductor thus creating a barrier layer that can be back-biased. With sufficiently high fields applied across the depletion or barrier region, the work function is effectively reduced, and electrons can be made to pass over the resultant barrier. For any efficient photocathode with a specifically desired spectral limit, it is essential to insure strong absorption of light out to that wavelength by selecting a semiconductor whose bandgap corresponds to

this threshold. Energy required above that value is determined by the effective surface barrier.

The first requirement for high quantum yield is that the escape depth of the excited electrons must be large when compared with the absorption length. Second, a large fraction of the absorbed quanta must excite electrons to energy levels above that of the vacuum. Third, the probability of escape of electrons from the surface must be high. These three requirements for the efficient extraction of excited electrons into vacuum lead to the tunnelling and high field mechanisms already described.

Elemental Photodetectors

The circuitry usually used for an elemental photodetector (ref. 8) is shown in figure 14. It provides a bias current through a load resistor, R_L , and a detector of resistance, R_D . This is coupled through a capacitor to a preamplifier, then to appropriate circuitry, according to the needs of the users. The simple photoconductor detector is nothing more than an elemental material that changes resistance on exposure to photons. The absorbed photons cause a resistance change that causes a variation in voltage across the load resistance, which is then transmitted through the capacitor as a varying signal

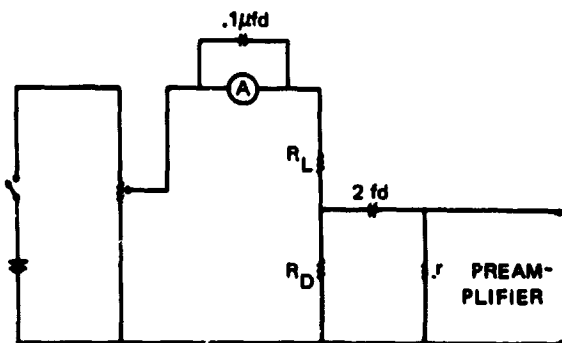


Figure 14. Elemental photoconductive detector circuitry.

voltage. When put into an optical scanning system, this type of detector permits the reproduction of video information.

The kind of information provided the user of infrared elemental detectors is shown in figure 15. The format followed was developed at the Naval Ordnance Laboratory, Corona, in its infrared laboratory. Beginning in the early 1950's, this laboratory had the mission of functioning as a standards laboratory for infrared detectors. Note that, in addition to the operating conditions, absolute information is provided in terms of a quantity called D^* (Detectivity Star). This is a number that rates a detector independent of its surface area and the bandwidth of the measurement. D^* has as its reference the background limiting condition, which is usually depicted as that from a blackbody operating at room temperature. The engineer or applied scientist usually works with the Noise Equivalent Power (NEP), which is that power irradiating a detector when the signal-to-noise ratio is unity. A fundamental unit used on occasion is the Detective Quantum Efficiency (Q_D), which is a measure of the intrinsic ability of the device to convert incident photons into countable charge carriers; that is, its efficiency. Figure 16 shows D^* as a function of wavelength for a variety of detectors and shows in particular how good these detectors are compared to the ideal or background-limited condition. These curves were taken from a brochure of a commercial supplier as an illustration of devices realistically available.

Information provided to the user of image tubes is quite extensive; however, it does lack in one important aspect, in providing absolute information. In my experience, I have only seen a Phillips x-ray tube, for example, described in terms of its Detective Quantum Efficiency. Figure 17 reviews the definitions of NEP, D^* , and Q_D for infrared detectors. Comparable quantities are derivable for image tubes, but as yet they have not been tested for either accuracy or application.

TEST RESULTS		CONDITIONS OF MEASUREMENT	
R (volts/watt) (500, 860)	3.6×10^3	Blackbody temperature (°K)	500
H_N (watts/cps ^{1/2} ·cm ²) (500, 860)	6.1×10^{-10}	Blackbody flux density (μwatts/cm ² , rms)	9.0
P_N (watts/cps ^{1/2}) (500, 860)	7.8×10^{-13}	Chopping frequency (cps)	860
D^* (cm·cps ^{1/2} /watt) (500, 860)	4.5×10^{10}	Noise bandwidth (cps)	6.5
Responsive time constant (μsec)	0.2	Cell temperature (°K)	77
$\frac{R_{\lambda_{max}}}{R_{bb}}$	1.7	Cell current for 860-cps data (μa)	3.9×10^4
Peak wavelength (μ)	8.2	Cell current for D^*_{mm} (μa)	3.9×10^4
Peak detective modu- lation frequency (cps)	$>7.0 \times 10^2$	Load resistance (ohms)	202
D^*_{mm} (cm·cps ^{1/2} /watt)	7.4×10^{10}	CELL DESCRIPTION	
Type	HgCdTe	Transformer	—
Shape of sensitive area (cm)	0.0356 x 0.0356	Relative humidity (%)	36
Area (cm ²)	1.27×10^{-3}	Responsive plane (from window)	—
Dark resistance (ohms)	33	Ambient temperature (°C)	23
Dynamic resistance (ohms)	—	Ambient radiation on detector	296°K only
Field of view	15°		
Window material	IRTRAN 2		

Figure 15. Detector data sheet (by permission of W. L. Eisenman and R. F. Potter, NWC, Corona Laboratories, Corona, California, on Detector 108-HgCdTe. Detector supplied by Texas Instruments Corp.).

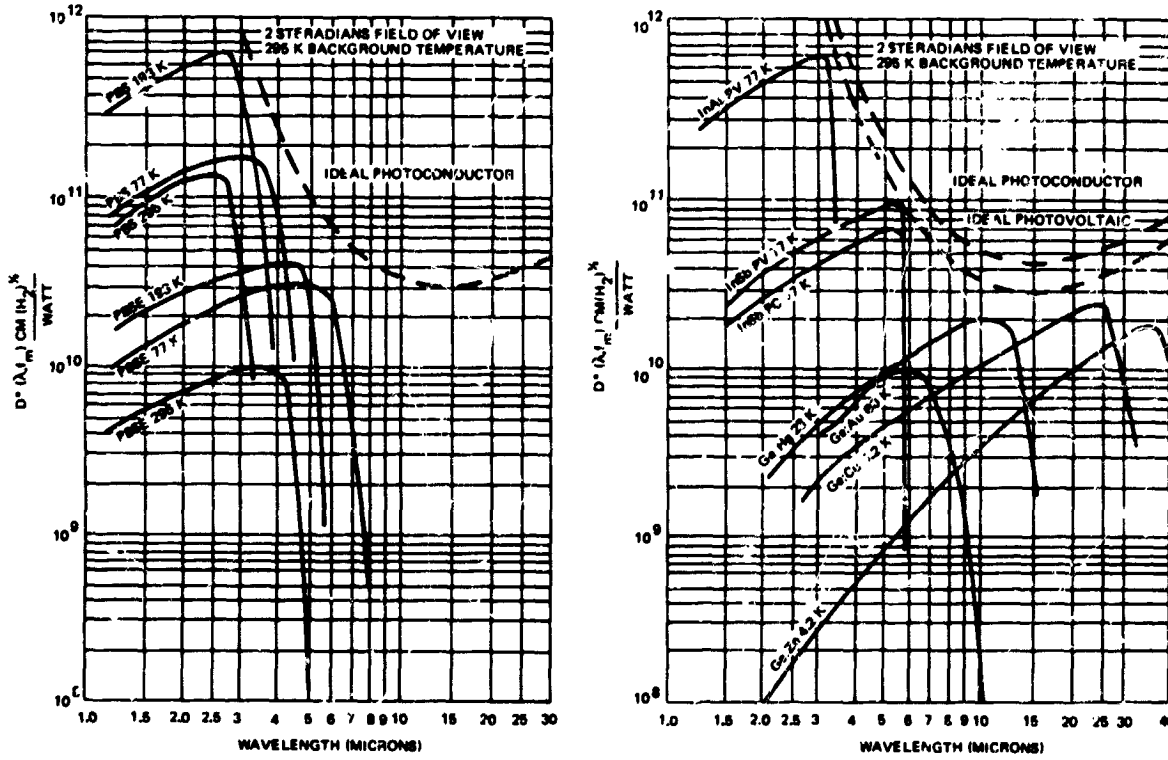


Figure 16. D^* versus wavelength of various photodetectors.

$NEP = \frac{HA}{V_s/V_n} = \frac{2H\sqrt{\eta_B \bar{J}_B}}{\eta_s J_s} \sqrt{A\Delta f}$	ΔF = Bandwidth (Electrical)
$D^* = \frac{\sqrt{A\Delta f}}{NEP}$	η_B = Efficiency of Detector to Background Radiation
$Q_D = \frac{(V_s/V_n)^2}{M_s^2/M_B} = \frac{(V_s/V_n)^2}{J_s^2 T_0 A/J_B}$	η = Efficiency of Detector to Signal Radiation
<p>where</p>	\bar{J}_B = Mean Value of Photon Flux from Background
H = Irradiance	J_s = Photon Flux from Signal
A = Area of Detector	M_B = Mean Square Fluctuation from Background Photons Counted in T_0
V_s = Signal Voltage	M_s = Signal Photons Counted in T_0
V_n = Noise Voltage	T_0 = Integration Time of Detector

Figure 17. Definitions of Noise Equivalent Power (NEP), Detectivity Star (D^*), and Detective Quantum Efficiency (Q_D) as used for infrared detectors.

References

1. Soule, H. V.: *Electro-Optical Photography at Low Illumination Levels*. John Wiley and Sons, New York, 1968.
2. Weimer, P. K.: *Television Camera Tubes - A Research Review*. *Advances in Electronics and Electron Physics*, Vol. 13, Academic Press, New York, 1960, p. 387.
3. Weimer, P. K.: *R.C.A. Review*, vol. 10, no. 366, 1949.
4. Goetze, G. W. and Associates. From a series of five papers in *Advances in Electronics and Electron Physics*, Vol. 22A, Academic Press, New York, 1966.
5. Redington, R. W.: *Journal of Applied Physics*, vol. 29, no. 139, 1958.
6. Crowell, M. H.; and Labuda, E. F.: *B.S.T.J.*, May-June 1969.
7. Schagen, P.; and Turnbull, A. A.: *Proceedings of the 4th Symposium on Photoelectronic Imaging Devices*, *Advances in Electronics and Electron Physics*, Vol. 28A, Academic Press, New York, 1969.
8. Holter, M. H.; Nudelman, S.; Suits, G. H.; Wolfe, W. L.; Zisis, G. J.: *Fundamentals of Infrared Technology*. MacMillan, New York, 1962, Chapters 10, 11 and 12.
9. Biberman, L.; and Nudelman, S.: *Photoelectronic Imaging Devices*, Vol. I, Plenum Press, New York, 1970.
10. Biberman, L.; and Nudelman, S.: *Photoelectronic Imaging Devices*, Vol. II, Plenum Press, New York, 1970.

N70-36690

Space Sciences Data-Handling and Mission Operations

George H. Ludwig

NASA Goddard Space Flight Center

Introduction

If a space mission is to be wholly or partially justified on the basis of the scientific experiments that it may carry, then it is important to realize that the objectives of the mission will be realized not when the spacecraft is activated, nor when the data have been returned, but only after the data have been processed and analyzed and the results published by the experimenters. This paper addresses the problems of processing on the ground the very large volumes of data that are telemetered from modern spacecraft.

To introduce the problem, figure 1 shows the general data flow for a space

mission. It was drawn specifically for the Explorer and Observatory class of spacecraft, but it is also generally applicable. A space experiment system has a number of sensors that feed data in electronic form into various inputs of the data-processing and reduction equipment onboard the spacecraft. The data are collected by a central data-collection subsystem and are telemetered to the ground, where two uses are made of the data. The first is for the real-time and near real-time operations in the control center, with feedback to initiate changes in the performance of the experiments and subsystems onboard the spacecraft. The second is for the processing accomplished for the ultimate analyses by the

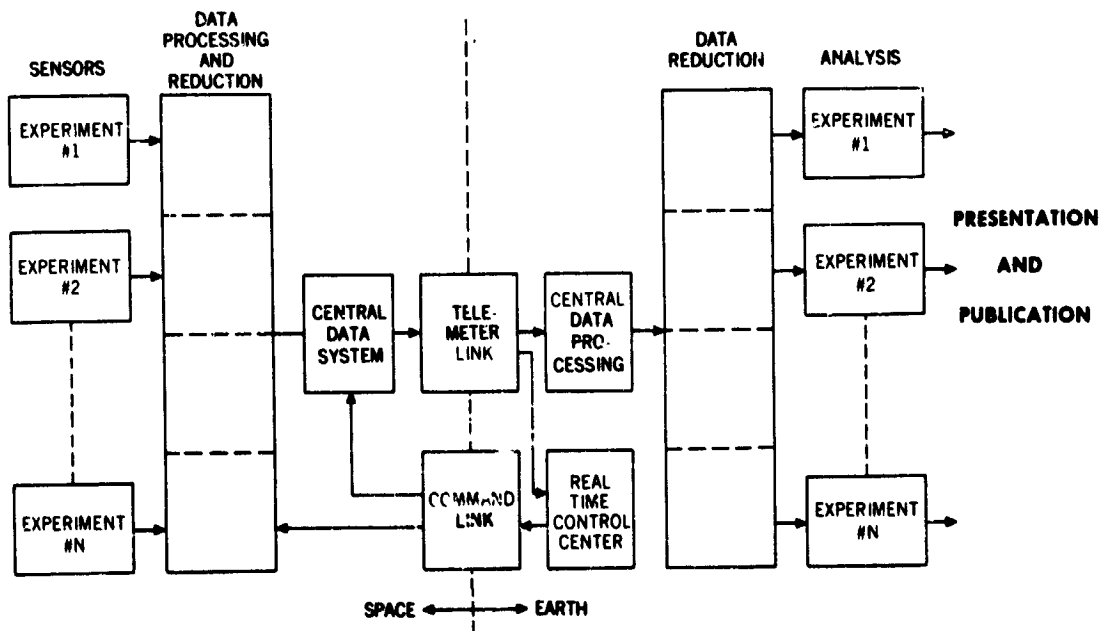


Figure 1. General data flow for a space mission.

investigators. This begins within a central data-processing facility and concludes with the detailed data-reduction and analysis by the individual experimenters.

This paper assumes that the data-acquisition, communication, and data-relay networks will exist at the time the telescopes are launched so that the data transmitted from them can be assembled at a common data-collection point within the necessary time constraints. Data relay in this case may include several forms, from magnetic tapes forwarded by mail (probably only as backup to faster means) to direct data relay, either from the spacecraft to ground stations and then through synchronous relay satellites to a common collection point or directly to the common point through data-collection satellites. The paper deals with two primary questions: (1) what is the present state-of-the-art of the ground processing technology; and (2) what new technology is needed.

Present Technology

To illustrate the present technology, three representative areas are described. The first is the processing performed within the central data-processing facility within the NASA Goddard Space Flight Center for the majority of the space-sciences earth-satellite missions. The second is a brief discussion of a portion of the Nimbus control center dealing with image data. The third is a short discussion of some of the processing that the experimenters must perform before they can reach their conclusions.

Data-processing at the Goddard Space Flight Center is, for most projects, divided into two types. Mission Control Centers for the various projects are responsible for the day-to-day and longer-term operation and evaluation of the spacecraft subsystems. In addition, they optimize the experiment operations to the extent possible without extensive experiment data reduction and analysis. The Central Data-Processing Facility is responsible for assembling the data base for the in-depth reduction and analysis by the experimenters.

This division of functions will continue to be valid for many types of experiments that require limited experimenter interaction on many of the astronomy missions. For this reason, it is likely that a new facility, an Experiment Operations Facility containing provisions for in-depth, near real-time data reduction and analysis, will be needed to provide the information necessary for the effective conduct of the observing program.

Since the operational control will be discussed more completely in other papers, most of this paper will deal with the data-processing necessary for the extensive in-depth analysis of the experiment data.

Figure 2 indicates the data flow within the present Central Data-Processing Facility. Data are received at the central facility from the various data-acquisition stations by (1) analog tapes and (2) real-time data lines of various types. The tapes pass initially through an evaluation procedure to facilitate control of the quality of the processes at the ground stations and to provide quality information to the data users. Following this procedure, all data undergo analog-to-digital conversion. This refers to the conversion of the demodulated receiver output signals into computer-compatible digital signals and includes the removal of noise introduced in the telemetry process. The next major step involves preliminary processing, referred to as "editing," within a digital computer. This editing includes checking the internal consistency of the data and measuring the data error rate. The remaining operations are performed within the large scale computer, which is a Univac 1108 multiprocessor with two central processing units and 196,000 words of core memory.

One of these operations is time tagging. Each data point received from space must be given an accurate standard or Universal Time reference because all linkage of the telemetered data with other correlative data is done through this time linkage. A number of the spacecraft sensors are directional. This requires that the spacecraft attitude be computed at every moment of time. In addition, it is necessary to perform some sorting, elimi-

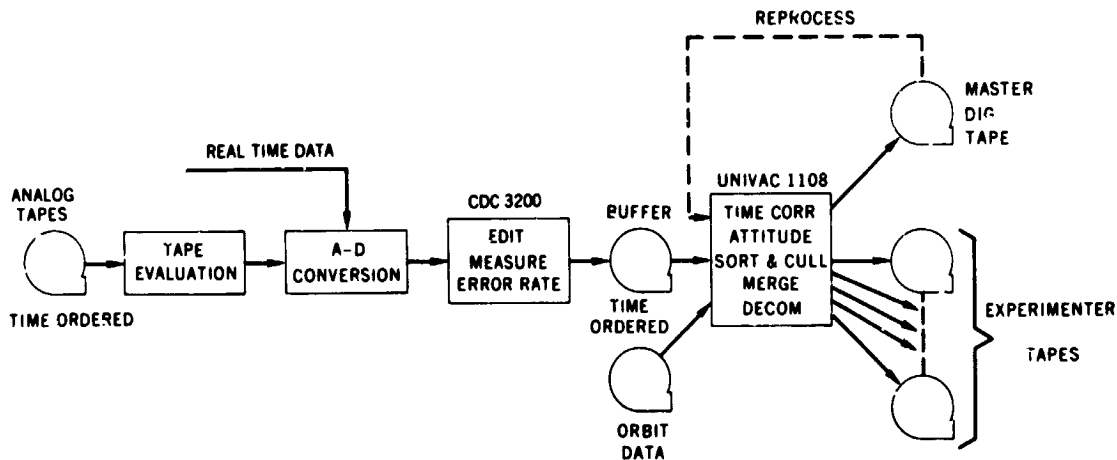


Figure 2. Present central data-processing facility at the Goddard Space Flight Center, functional block diagram.

nating useless data, merging of orbit and other correlative data with the experimental data, and, finally, decommutation (sorting) to form outputs for each of the various experimenters. In addition, a master digital data tape is generated that is retained for a period of time for reprocessing or regeneration of the experimenter's tapes if necessary.

The volume of data being handled at the present time in this central facility is quite large. Figure 3 illustrates the growth in analog tapes arriving at the facility over the past two years and projects this input two years into the future. At the present time, about 2400 tapes per week are arriving for 21 active satellites. This represents about 3.5×10^8

measurements per day, or about 3.5×10^9 bits per day of PCM data. Another way of expressing this data rate is to compute the long-term average bit rate. In these terms, the central facility is receiving data at the rate of 35,000 bits per second for every second of every day. The impact of this data rate on the sizing of the central facility is quite impressive.

Figure 4 is a view of one row of processing lines in the central facility. Three processing lines are included in the figure, two PCM lines and a special-purpose line for digitalizing the signal from rubidium vapor magnetometers in several of the Orbiting

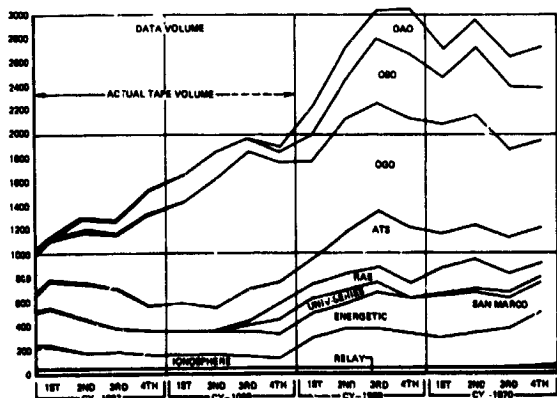


Figure 3. Growth of data volume at GSFC data-processing facility.



Figure 4. Three processing lines in the central facility.

Geophysical Observatory (OGO) spacecraft. The most distant line in figure 4 is shown in figure 5. The various racks include synchronizing and bit-conditioning circuits, a time decoder, and a core buffer memory. (The digital tape recorder is out of the picture on the right.) This line is representative of the class of lines that do not include general purpose computers. The central facility contains 16 major lines of this form and about 16 smaller lines.



Figure 5. Racks including synchronizing and bit-conditioning circuits, a time decoder, and a core buffer memory.

Figures 6 and 7 indicate the size of the complete facility. The row of processors in figure 5 is the third row of racks from the left in figure 6. The second-generation processing systems include CDC 3200 computers on-line with the front end processing equipment for two purposes: setting up the operation and measuring the data quality. Three of these larger systems are shown at the right end of the central equipment bay in figure 6. The Univac 1108 computer is shown in the center of figure 7 and is surrounded by various support equipment. The central facility shown in figures 6 and 7 represents approximately a \$20-million capital investment for handling the data rate presently being

received. It is operated and maintained by a staff of approximately 300 government and contract personnel.

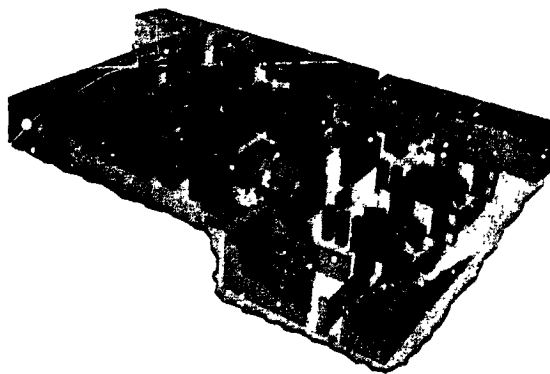


Figure 6. Goddard centralized data-processing facilities, physical plan.

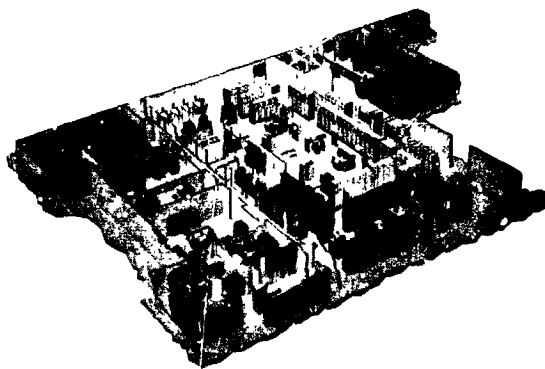


Figure 7. Goddard information-processing computer facilities, physical plan.

The second area of activity to be discussed in this paper involves some of the image data-processing being performed in the Nimbus control center and processing facility. Figure 8 illustrates the handling of the Nimbus Medium Resolution Infrared (MRIR) data obtained from one of the four major experiments being flown on Nimbus II. After analog-to-digital conversion, the image data and orbit are merged to provide gridding directly on the images. Tapes containing the digitalized data are sent to the experimenters for more detailed analysis. Strip charts are

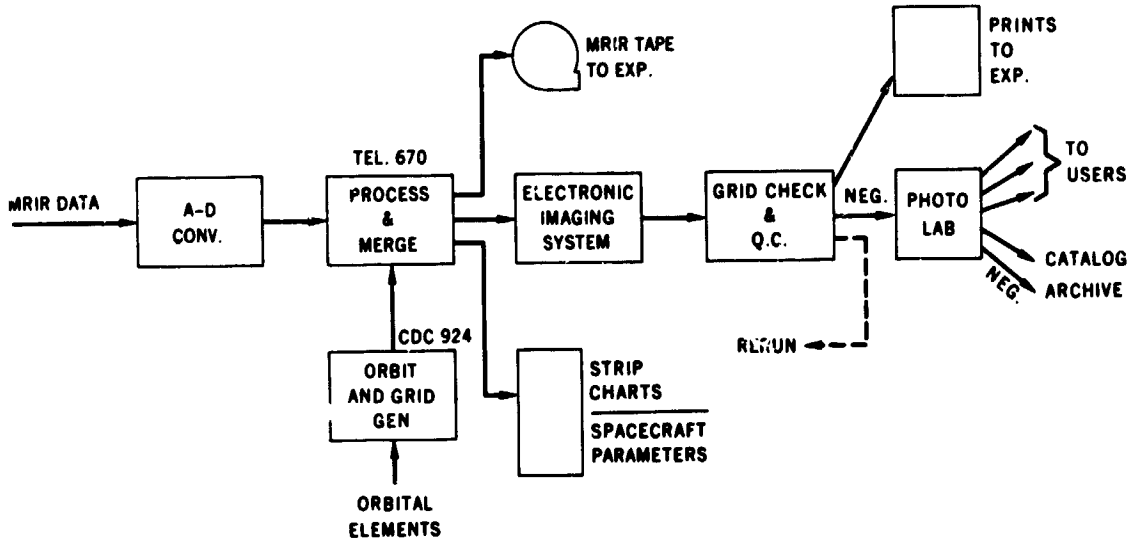


Figure 8. Medium resolution infrared (MRIR) data flow in Nimbus control center.

prepared for spacecraft performance evaluation, and the images are prepared for immediate viewing. Figure 9 indicates one of these image sets. It includes one complete orbit with the two poles being indicated in the gridding on the left. The second strip is the visual presentation, showing that the bottom half of the orbit was in darkness while



Figure 9. Nimbus II multispectral imaging.

the top half was in light. The other spectral regions covered by the instrument are indicated.

After the data leaves the facilities at Goddard, the experimenters must complete a considerable amount of processing for their final analyses after they receive their data. The general data flow is indicated in figure 10. The experimenter passes his data through quality checks, sensor calibrations, and data reduction, which leads to outputs that can be viewed. Tabulations and data plots are the most common output forms;

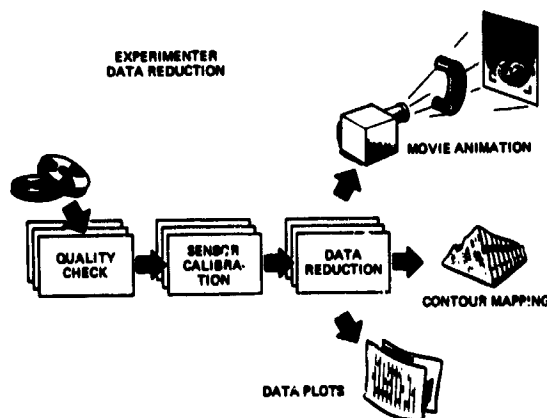


Figure 10. Data reduction by experimenter.

other forms such as motion pictures and color presentations are coming into use. Figure 11 is a sample presentation. It is not by any means one of the most complex. It represents a compilation, by Dr. Norman F. Ness, of six months accumulation of magnetometer data from the IMP-1 spacecraft. This one chart includes a condensation of about 100,000 individual measurements. The magnetic field in the magnetosphere is represented by the vectors; the length of each vector indicates the magnetic field strength at that point; and its direction indicates the field direction.

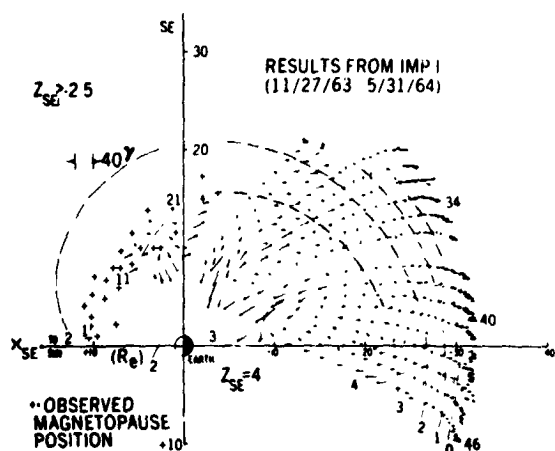


Figure 11. Sample of data plot, a common data-output form.

From this presentation, one can identify the major features of the earth's magnetosphere. It required many weeks of computer processing, manual manipulation, and study in its presentation, and it is only one of many presentations required before the findings of this experiment could be published. It is significant to note that this type of analysis is very unlikely to be performed in any spacecraft by any onboard computer in the foreseeable future. Thus, it will still be necessary to retrieve the data rapidly, with the experimenters in the operational loop, in order to permit this type of analysis.

Emerging Technology

Before moving on to a discussion of future technology, it is of value to address briefly the question of emerging technology. The data flow shown in the present large-scale facility in figure 2 results in a very large amount of materials handling. Two thousand input tapes per week require the handling of 6,000 tapes per week before all the operations have been performed. These lead eventually to about 25,000 bookkeeping transactions per week. Figure 12 indicates a data-processing flow that is receiving considerable study at the present time. It involves the collection of as much of the data as possible in near

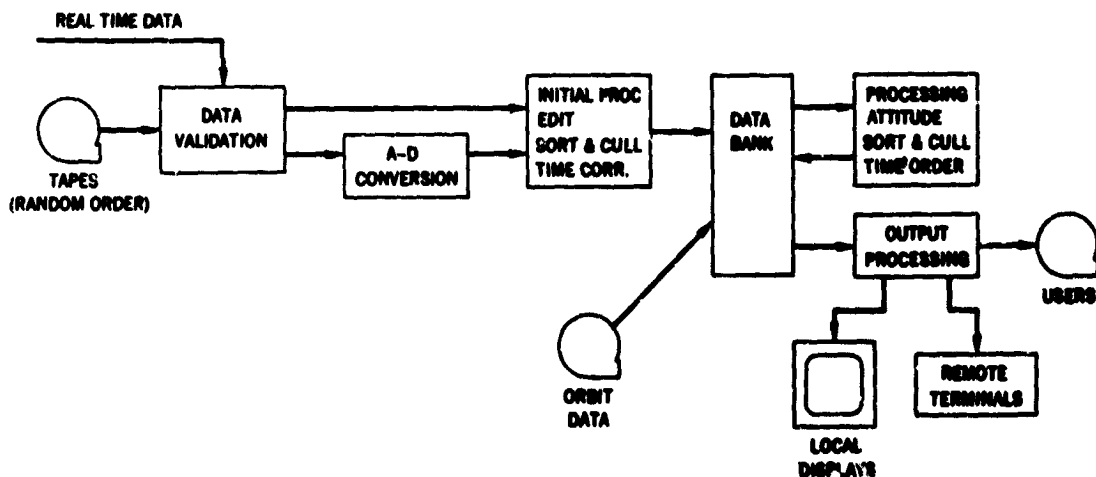


Figure 12. Proposed central data-processing facility, functional block diagram.

real-time by data relay and on-line data validation, analog-to-digital conversion (if required), initial processing and editing, and direct entry into a large data bank. This data bank is envisioned as a hierarchy of different types of storage, including core for fast-access speeds, drums for medium-access speeds, and tapes for slow-access speeds.

The most important new feature, however, will probably be a high-density storage system involving the recording of digital data in optical form on film chips to provide a total on-line data volume of from 10^{10} to 10^{12} bits. With such a data bank, the raw data will be entered into active storage nearly as soon as they are received. More complete processing will then proceed as rapidly as correlative data (such as orbit) are available. The output will be available for delivery from the data bank, immediately in raw form and later in a more highly processed form. This output will be useful both for local display for operational purposes and for remote display to the users for their final analysis. Two factors leading to this data organization are the anti-

icipated increased efficiency through the elimination of much of the manual handling of supplies and the faster data delivery. At the present time, an attempt is made to operate with a six-week backlog or less; that is, considerable effort is expended to provide the bulk of the data six weeks after it has been collected from the spacecraft. The future goal should be to make data available from the data bank within several hours or a day from the time of transmission. This will be especially important for an operationally complex orbiting telescope.

The other major area of emerging technology is that which will be required for the Earth Resources Technology Satellites (ERTS). Of course, ERTS will involve primarily image data, which requires techniques that are considerably different than those for PCM data. The anticipated data flow is indicated in figure 13, with the data entering image processors and with the images becoming available for viewing within a short period. In addition, the PCM data will enter other operations to facilitate the gridding and

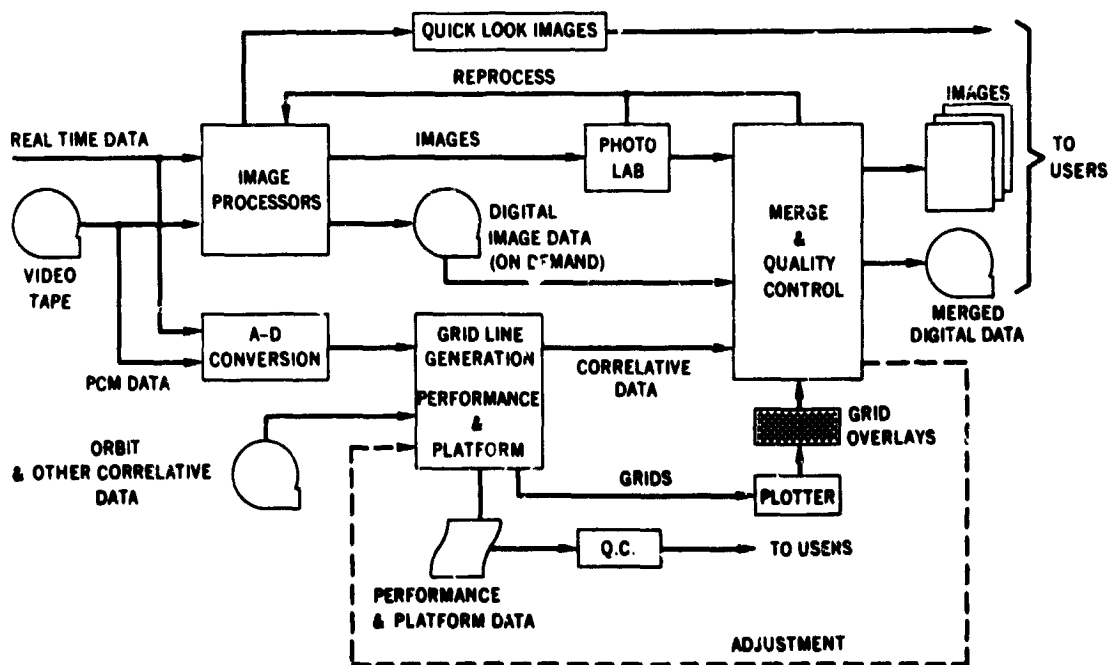


Figure 13. Anticipated data flow in data-processing system for the Earth Resources Technology Satellites (ERTS).

the rectification of the pictures. It is presently expected that gridded overlays will be made available along with the images. This facility is expected to cost from three to four million dollars and will require about two years to build.

Technological Problem Areas

The data volume and rate problems have already been discussed; they are expected to continue to be serious problems. Speed of data delivery has also been mentioned. Now that the experiments are becoming more complex, the experimenters need to receive the information from the experiments much more quickly so that they may be sure they are operating properly and so that they may modify their operation to take advantage of the variability of the experiments and the spacecraft. Therefore, in some cases, it is necessary for the experimenters to receive some portion of their data immediately, especially during critical periods of operation.

Next on the list of major problems is the control of data integrity and quality. The taking of a large number of pictures on a spacecraft without noting the time during which all of the pictures were taken is a threat to the *integrity* of the data. It may result in the absence of correlative information needed to determine the locations and conditions under which the pictures were taken. The question of data *quality* is concerned with the problem of verifying that the entire system, including all the processing operations, is operating properly to ensure that high accuracy and resolution are maintained. This must be done continuously and thoroughly at each processing step.

Control and allocation of processing resources is another major problem. For one reason, this becomes difficult because of the unpredictable nature of the load. Almost any change from expected operation of a spacecraft, other than the complete failure of the spacecraft, results in an increase in the workload in the ground-processing and experimenter's facilities. This increased workload occurs because partial failures onboard the spacecraft

require more processing on the ground either to straighten out the data or to evaluate the spacecraft. The unpredictable lifetimes of scientific missions also introduce large uncertainties in the processing workload.

Selective data acquisition has been proposed as a means for leveling the processing workload, but it has proved to be very difficult. If a certain spacecraft capability exists, in terms of information bandwidth for example, there is a strong tendency for that capability to be used. The reason for this is that many of the experimenters are awaiting unpredictable events because of their value in interpreting nature. Thus, they cannot predict when their experiment must be operating; they simply must operate continuously to ensure readiness.

This rule of full use of capability tends to be slightly less true as the technology evolves. For example, the Orbiting Geophysical Observatory has a telemetry capability of 64,000 bits per second, but it is used only on an average of 7000 to 8000 bits per second by using a controlled data-acquisition sequence. This is achieved by the use of two modes of operation: a monitoring mode at a low data rate that will always intercept the unexpected events and a high-data-rate mode to provide periodic high resolution measurements.

With a manned space station, some additional capability will exist for governing the transmission of data to the ground because a man can monitor the events occurring from the scientific experiments and can eliminate some of the data transmission to the ground. This will be especially true if the space station contains a data buffer to store the data until they have been scanned for significance.

Selective *processing* of data has been found to be a fairly effective way of controlling the use of ground resources. Once the ground processing system becomes saturated, the lowest priority data are placed directly into storage. The data remain available for the exploitation of interesting periods. Selective data-processing implies, however, the need for a scanning or browse file so that the experimenters will know what data exist.

Still another major problem area is the control of the processing facility/experimenter's interfaces. If an experimenter changes his format requirements, this may require several calendar months and quite a few man-months of effort to change the programs in the central processing facility. Therefore, considerable attention must be paid to the question of specifying and understanding the experimenter's data needs.

Finally, there are the problems associated with the data analysis by the various experimenters. These investigators usually have very limited facilities and manpower, especially at universities. Therefore, a very careful study needs to be performed to determine the tradeoffs between the steps performed in a central facility, which may be done in common for many experiments, and all the other steps that the experimenter must perform within his own facilities.

Areas Requiring Additional Technological Development

1. New work is necessary to develop a technological basis for operating onboard scientific-data-processing computers. We know how to build these computers. Several are being built now for a number of future unmanned scientific missions. It is not clear, however, that we know how to control the programming of those computers so that we may be assured of full after-the-fact understanding of the steps performed by these computers.

2. Faster ground processing equipment is needed. The present state-of-the-art permits about one megabit processing rate in terms of special processing equipment, such as signal conditioners, and in terms of computers. If PCM systems will operate at several megabit rates, then faster processing systems will be needed on the ground.

3. The third area involves the utilization of large volumes of image data. Several authors have mentioned image rates of 1000 pictures per day from a future space station. Others have predicted that these will be processed by the use of advanced digital tech-

niques. With present technology, one picture having 4000 by 4000 elements of spatial resolution requires three computer tapes for its storage in digital form. Thus, the 1000 pictures per day will occupy approximately 3000 computer tapes. If these 3000 computer tapes are read by a computer at maximum tape reading speed (5 minutes per tape), ten days will be required simply to read them. Therefore, it should not be expected that that many pictures will be digitized, retaining all of the resolution, by present techniques. In determining what will be done with these pictures, it will probably develop that some new technology will be needed.

4. Needs exist now for on-line, mass data storage in ground computers for systems providing storage of 10^{10} bits, with access times of seconds or less, to provide several weeks or months of data on-line.

5. On-line programming and processing systems and aids are needed. There have been numerous estimates of a programmer's efficiencies in terms of dollars per instruction. These estimates range from \$2 to \$10 per instruction, and many programs contain more than 100,000 instructions. In other words, computer programming is a very slow and expensive process. There is a very great need for improvement in the technology of writing programs and getting them to work properly. In addition, present programming systems are ill-suited for handling telemetry data, especially when it entails manipulating individual bits.

6. Display and presentation technology needs stimulation. This involves the problem of rapid comprehension of very large volumes of data by the experimenters and other users. A number of activities are currently underway in the investigation of color, motion picture displays, three-dimensional displays, etc.; but much more activity is needed in this area.

Conclusion

The data will need to reach the experimenters from orbiting telescopes accurately and rapidly; some of it almost immediately,

some of it within a day, and most of it within a week. It must be in easily usable form, or there will be a tendency not to use it because of its large volume.

It is interesting to note that past experience with unmanned scientific missions has indicated that as many dollars are necessary

for the data-processing and analysis following a launch as are necessary for building the experiments before launch. It appears reasonable to expect that this rule of thumb may also apply to the data-processing for future astronomy missions.

Calibration, Simulation, and Testing of Large Orbiting Stellar Observatories

James L. Diggins

NASA Goddard Space Flight Center

N70-36691

Introduction

In this paper an attempt will be made to present the state-of-the-art in the calibration, simulation, and testing of large orbiting observatories designed to add to our knowledge in the field of *stellar astronomy*. "Large" in this instance means observatories of the Orbiting Astronomical Observatory (OAO) class, namely, 7¼ feet in diameter by 10 feet high and weighing from 4000 to 4600 pounds in the orbital configuration. The largest aperture telescope in the current OAO series is 38 inches in diameter.

In dealing with the environmental *simulation* and the electrical and mechanical functional *testing* aspects, it would be rather pointless to enumerate and to describe the various thermal-vacuum chambers throughout the country that are large enough to handle an OAO for this type of work. There are a minimum of 25 such chambers and at least four of these are equipped with solar simulators of various types. It would be more useful for the purposes of this workshop to discuss the techniques, equipment, and facilities for simulation and testing that have actually been used on the OAO's. In such a discussion, it should become clear how wide a variety of talents and facilities is required to support an observatory of this type.

In the area of *calibration*, all of the optical test facilities used for OAO will be treated in substantial detail. In addition, some concepts for facilities that will be needed for the calibration and evaluation of future space stellar observatories will be presented along with recommendations for developmental projects that will be necessary to support such facilities.

This paper is premised upon a proven, well-established need for full-systems testing. If there is anyone who has any reservations about the validity of this premise, reference 1 should provide sufficient proof of the soundness of applying this test philosophy to any scientific satellite test program. There is also a requirement for components and subsystems tests; however, this paper deals only with full systems or very large subsystems, such as the entire spacecraft or the complete experiment package consisting of a telescope, a spectrometer, and detection devices. After the experiment package is installed into the spacecraft, that configuration will be referred to as an *observatory*.

Calibration, simulation, and testing are the final activities performed just prior to preparations for launch; however, if a meaningful and efficient acceptance test program is to be conducted, calibration, simulation, and test personnel must provide inputs to this program from the concept stage. *The observatory must be designed to be tested.*

Simulation

The types of environmental simulation required for a particular observatory depend in large part upon the nature of the experiments to be performed in orbit, the launch vehicle, and the particular orbit selected. Variations in these parameters, as well as in the configuration and other design aspects of the observatory, can drastically change the relative significance of the various environments and the importance attached to simulating these environments on the ground. Nevertheless, any observatory must withstand the effects of transportation, ground-

handling, launch phase, and orbital vacuum and thermal conditions as well as certain types of hard radiation and magnetic influences.

In general, the determination of the need to simulate a particular environment is made by performing certain analytical studies of the observatory in the light of the anticipated natural and self-generated environments to which the observatory will be subjected from the time of manufacture until the end of its expected useful life in orbit. The validity of such an analysis is dependent upon the exactness of our knowledge of environmental levels and the spacecraft interactions that will be encountered and upon the degree of refinement of the analysis method used. At the present time, the degree of uncertainty in the results of these analyses requires proof of the major assumptions; hence, additional steps are taken to improve our confidence level. These steps become a major consideration in establishing a meaningful test program. For example, in the structural area, a mathematical model is constructed, and response predictions are made for the launch environment. A hardware structural model is built and tested, and the predicted values are verified or refined by measurements. At the same time, actual flight measurements are made on the launch vehicle and are used to refine the driving forces used in the analysis. Later, tests are made on the flight observatory, and a further refinement takes place. Finally, data are collected during the actual launch phase, and the loop is closed. The mathematical modeling and analysis method are "massaged" once more; during this second manipulation, the predictions and the structural test program are easier to handle and are improved.

The same basic analytical approach toward determining simulation and test needs is applied in the thermal area. Experience in working with these analytical tools, refined by test and flight data, has led the "universalists" to the conclusion that near-duplication of the natural solar and planetary thermal radiation environment is *the* way to solve the thermal test problem. On the other

hand, the "specifists" working with a given design or family of designs can often accept simulation of the effects of the natural environment. The gap between these extremes provides the technical and economic arena in which simulation and analysis are debated. In this area of debate, tradeoff decisions are made, and a complimentary system is evolved that will yield proof of the major design assumptions within definable boundaries of risk and dollar expenditure. Such questions as: "Are solar, albedo, and infrared simulators really necessary?" are valid and need to be answered in the light of risk.

Testing

The OAO differs markedly from most other scientific satellites; in orbit, it depends on a closed loop relationship with its ground support system for operation and survival. There is a constant requirement to collect, process, and display data in real-time to enable operations personnel to evaluate performance and to exercise command functions at specified intervals. This high degree of human involvement requires extensive training and intricate knowledge of the abilities of the OAO systems. To ensure the acquiring of this knowledge, the OAO Project personnel have attempted to keep all ground support equipment used throughout the program identical with that used for flight operations. This assimilation of flight-type operational techniques and restraints during systems environmental testing presents a unique set of problems.

The OAO Ground Support System is made up of elements of the NASA Communications (NASCOM) Network, Space Tracking and Data Acquisition Network (STADAN), and the OAO Operation Control Center (OCC). The system provides facilities for transmitting, receiving, and processing the data necessary for operation of the observatory by ground personnel. The commands to control the observatory are provided by the Support Computer Program System (SCPS), figure 1, on an ABM 360/65 computer through the SDS 930 computer central processor.

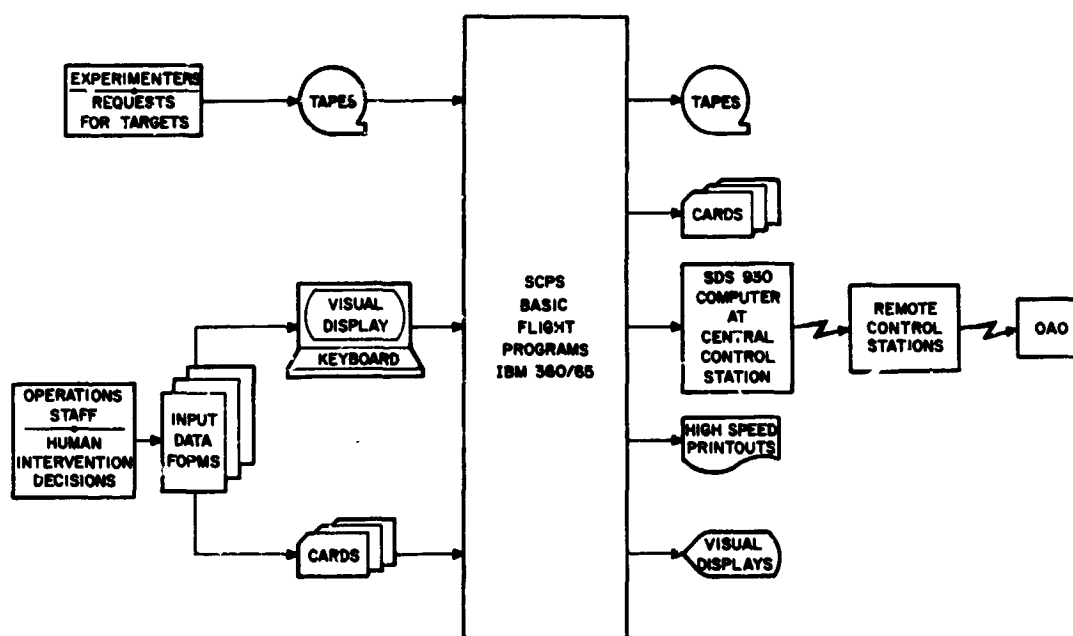


Figure 1. Support computer program system.

The SCPS provides the Orbiting Astronomical Observatory (OAO) with the necessary man-computer linkage between the experimenters and the mission operations staff on the one hand and the orbiting observatory on the other. In the day-to-day operation of the OAO, the SCPS also furnishes command sequences to be sent to the spacecraft to enable it to execute its intended scientific mission while maintaining observatory integrity.

In order to prepare for this type of orbital operation, special data-handling or ground support equipment is used to simulate the electrical and communication interfaces of the spacecraft during the experiment test and calibration program. The same philosophy is applied to the spacecraft and then to the observatory. The tests are conducted under computer program control, and a notably high degree of flexibility and safety is achieved. Safety is stressed because of the often delicate nature of the optical detectors and their corresponding sensitivity to command sequences. Procedural techniques,

which are developed during major subsystem testing and integration buildup, are programmed into the overall test procedure and are used throughout the observatory acceptance and prelaunch test phases.

The Environmental Test Cycle

In the following discussion of the test cycle, no attempt will be made to retain a chronological sequence; instead, the tests will be treated by category. One characteristic of stellar observatories, namely, susceptibility to contamination, has to be mentioned at the outset because it has a major bearing on the adequacy of any test facility and even on the sequence of tests. Contaminants exist in so many forms and can cause such a serious degradation in performance of an optical observatory that this topic will be treated in more detail in other papers. It is mentioned only to provide a basis for understanding some of the comments made in connection with many of the facility descriptions.

Cleanliness

The concern about contamination provides the impetus for performing periodic cleanliness inspections. For this purpose and for numerous electrical and mechanical functional tests in air throughout the test cycle, large clean rooms are needed. Figure 2 shows the OAO A-2 observatory in such a clean room at Cape Kennedy. Details of the methods and equipment used for cleanliness inspections at the Goddard Space Flight Center (GSFC) are given in reference 2. In general, these inspections involve the use of ultraviolet lamps, sun guns, fiberscopes, and examination of samples taken with tapes, wipes, and by vacuuming.

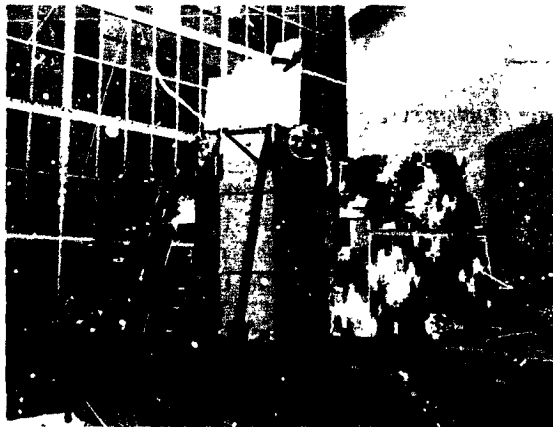


Figure 2. OAO-A2 Observatory in clean room.

We do not have to look very deeply into the matter of clean rooms to find that adequate facilities can be, and have been, designed and built; however, specifications for clean rooms to serve the special needs of stellar observatories are woefully inadequate. This situation stems from a lack of quantitative knowledge of such things as: what concentrations of what size dust particles will confuse a star tracker or cause too much

* The class number of a clean room refers to the number of particles per cubic foot that are 0.3 micron and larger.

scattering in a spectrometer. Similar knowledge regarding corrosive gases and water vapor is equally sparse.

People are the major source of contaminants in a clean room. A good set of guidelines for people to follow are contained in reference 3; however, getting people to think and act in accordance with these procedures is quite another problem.

Integration

The integration of components and subsystems into a spacecraft requires a large clean room area, similar to that shown in figure 3. This is a horizontal laminar flow room using prefilters and HEPA filters. It is class 10,000 or better; without people, class 100 is achieved.* The temperature is controlled between 70° and 74°F with only $\pm 1/2$ ° F variation about the selected control temperature. The humidity control system is currently being upgraded to provide control between 40 and 45 percent relative humidity during any season of the year, instead of the present condition of 45 percent maximum. A positive pressure of 0.2 to 0.4 inch water gage is maintained, and the airflow velocity is 100 feet per minute \pm 20 feet per minute.

Figure 4 shows how the room looks during an actual integration process. Functional testing in this facility is performed

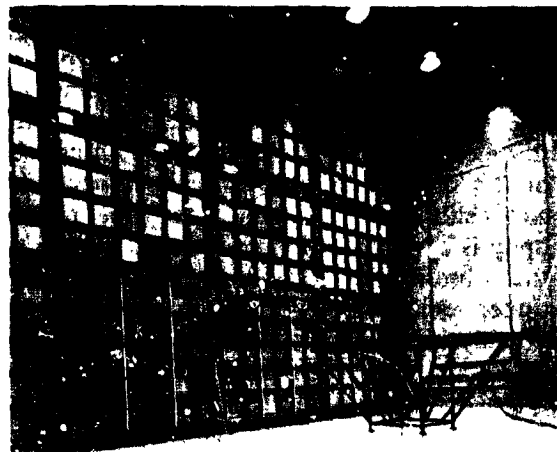


Figure 3. Spacecraft checkout area, empty.

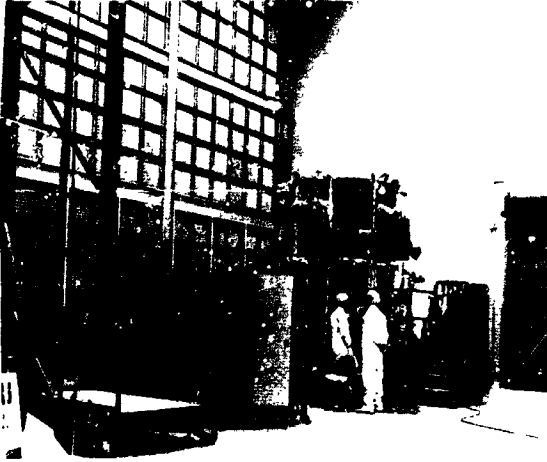


Figure 4. Spacecraft checkout area with OAO spacecraft.

concurrently with the integration activities and between various other environmental tests.

Vibration

Once a meaningful vibration spectrum has been established for an observatory, a facility similar to the one shown in figure 5 is required. This facility consists of a 30,000-pound thrust shaker that can be used vertically or laterally. In figure 5, the OAO is mounted on a slippery table that enables the shaker (on the left) to produce the lateral thrust needed. At the same time, torsion is being introduced by the smaller shaker seen in the background, lower right-hand corner. The shakers and test item are mounted on a spring-isolated, 300,000-pound, reinforced concrete block. The entire room is a laminar downflow, class-10,000 clean room.

Acoustics

During powered flight, particularly at launch and during transonic regime, acoustic energy excites the observatory both through the structural path and by direct acoustic impingement through the shroud. Previous test philosophy has consisted primarily of using random vibration to simulate this flight

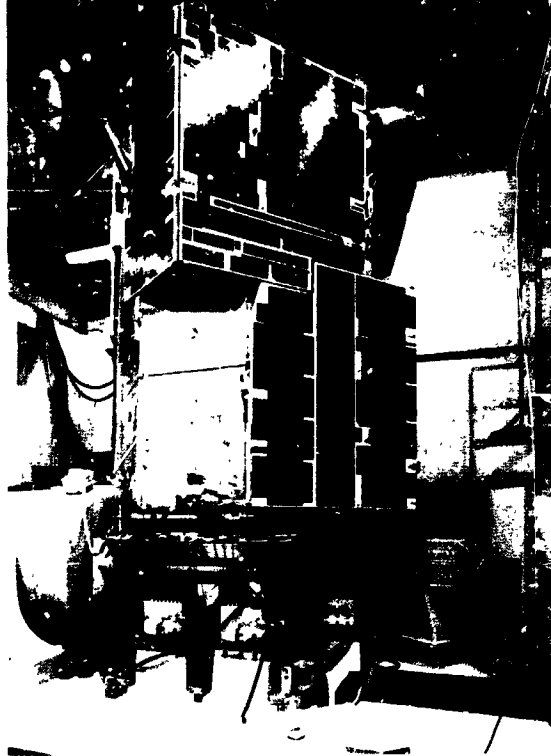


Figure 5. OAO in 30K vibration cell.

environment. Recent studies (ref. 4), however, have indicated that the direct acoustic path may be more severe than previously realized.

As a result, an evolution in test philosophy is occurring; acoustic tests are becoming an increasingly important and necessary segment of the test program of large spacecraft. This is partly due to the practical limitation that random energy induced at the spacecraft interface by a vibration exciter does not distribute itself realistically throughout large structures. In addition, the thermal control systems for large pointed spacecraft employ components such as thin foil skins, thermal louvers, and sun baffles, all of which are particularly sensitive to acoustic excitation because of their panel-like construction. Because of the greater power consumption needs of observatory class spacecraft, the solar paddle surface area is much greater. Also, at least in the case of OAO, an unusually large number of subsystems are

mounted on vibration isolators. These last two considerations necessitate the inclusion of acoustic testing in the environmental test program because the structural and functional integrity of the equipment cannot be demonstrated by vibration exposure.

Launch Phase

In addition to mechanical and acoustical vibrations, the need for real-time pressure profile testing has also shown itself many times in the recent past. Its primary objective is to demonstrate adequate pressure venting of the multilayered, aluminized, mylar insulation used for passive thermal control of large spacecraft. Rupture or "ballooning" of this insulation could easily cause either improper thermal control of the spacecraft or obscuration of the optical elements in the observatory.

To meet the requirements of this combination of launch environments, a Launch Phase Simulator (LPS) has been built at GSFC. Figure 6 is a photograph of this facility; figure 7 is a drawing of its general arrangement. The LPS is described in detail in reference 5. The salient features of this facility are:

1. *Steady acceleration:* 30 g maximum with capability of simulating acceleration rates of the Delta, Agena, and larger classes of liquid-fuel engine boosters.

2. *Acoustic noise:* 150 db rms overall sound pressure level (SPL) exterior to the shroud-enclosed spacecraft. This spectrum is flat from 100 to 700 Hz, with 6 db/octave roll-off from 700 to 12,000 Hz.

3. *Pressure:* programmed to follow the launch pressure profile from 760 torr to 3×10^{-1} torr; i.e., up to an altitude of approximately 190,000 feet.

4. *Mechanical vibration:* three degrees of freedom (longitudinal, lateral, and pitch) from 0.5 to 200 Hz with both sinusoidal and random capability. Multiaxis motion with this system may be either independent or simultaneous. (This system is capable of operation on the centrifuge arm or in an offboard condition mounted on a seismic reaction mass.



Figure 6. Launch-phase simulator.

To date, multiaxis motion has been achieved only in the offboard configuration.)

5. *Time and mode:* Each of these systems can simulate the actual environmental conditions in *real-time* and can be operated in either the automatic or manual mode.

6. *Description:* Physically, the facility is a large centrifuge (60-foot radius to payload center of gravity) weighing approximately 500,000 pounds and having a cylindrical test chamber (12 feet in diameter by 22 feet long) mounted on the end of the centrifuge arm. The chamber houses the acoustic, vacuum, and vibration systems; it can accommodate a payload or spacecraft configuration that weighs up to 5000 pounds and can be contained in an envelope 10 feet in diameter by 15 feet long. The centrifuge is located in an enclosure, or rotunda, 157 feet in diameter by 27 feet high.

This facility has been used for several specific tests on OAO. Perhaps one of the most significant results observed during these tests is shown in figure 8. The rupture of insulation during a real-time pressure pull-down can be seen as it occurred on the prototype Goddard Experiment Package (GEP) for the OAO.

Thermal Vacuum

Once the need for thermal simulation to improve the confidence level of thermal pre-

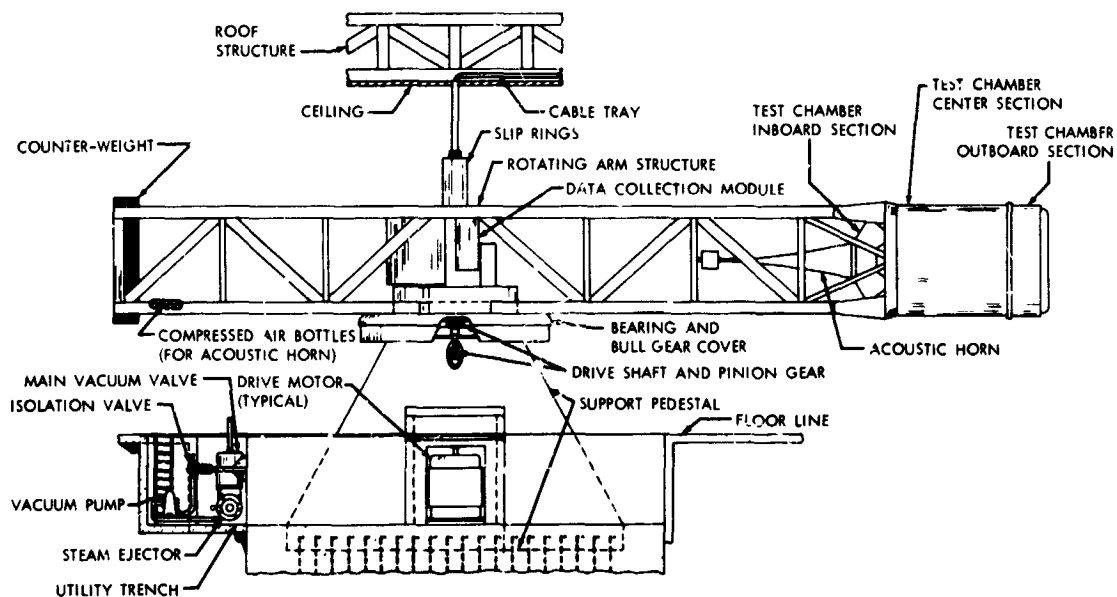


Figure 7. General arrangement of launch-phase simulator.

ditions is established, an observatory of the OAO size requires a test chamber similar to the one shown in the foreground in figure 9. This chamber at GSFC is called the Space Environment Simulator (SES). The chamber in the background in figure 9 is a Dynamic Test Chamber (DTC), in which deployment, separation, and spin tests are performed in vacuum at room temperature. Although the DTC was not used for OAO, a similar

chamber might well be required for future observatories.

The SES chamber has been used extensively for OAO tests. It is described in detail in reference 6. A very detailed description of the test procedure for the OAO A-2 thermal model test is given in reference 7. Some of the salient features of the SES are:

1. Chamber: 33-foot interior diameter by 58 feet high (28 feet by 40 feet, working volume).

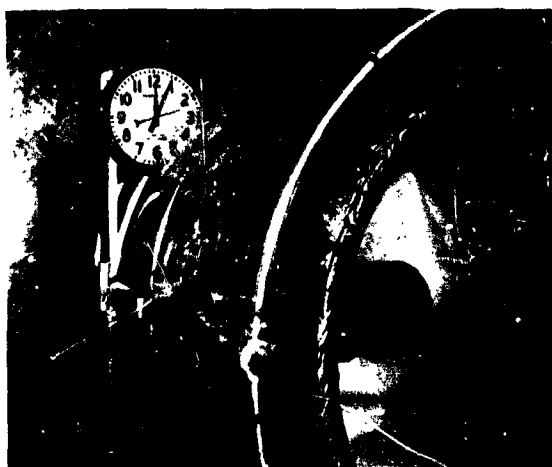


Figure 8. GEP prototype insulation rupture.

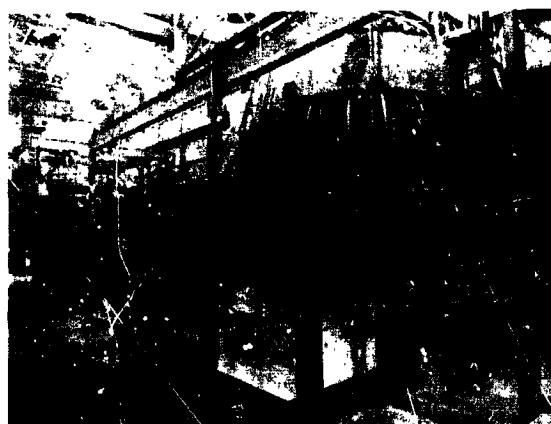


Figure 9. Space environment simulator and dynamic test chamber.

2. Shroud: liquid nitrogen (LN2) at 100°K.
3. Pumps: eight mechanical pumps, eight blowers, 17 oil-diffusion pumps, each having a capacity of 50,000 liters per second and a 32-inch diameter, and a cryopump consisting of 15°K helium-cooled panels covering one-half the height of the chamber.
4. Pump-down time: 13 hours to 1×10^{-9} torr, clean, dry, and empty; 24 hours to 1×10^{-8} torr with full solar simulation.
5. Solar simulator:
 - a. 17½-foot diameter at chamber floor uniform to $\pm 10\%/ft^2$
 - b. Intensity: variable 75 to 150 watts/ ft^2
 - c. Collimation: 2 degrees (half-angle)
 - d. 127 modules using 3.5-kilo-watt, HgXe, short-arc lamp, aluminized ellipsoidal reflector, four quartz lenses, and a Cassegrainian collimating system.

In addition to the above features, the SES is also equipped with a large two-axis positioner so that the aspect angle and spin of a spacecraft can be changed during test.

Figure 10 shows a cross-sectional view of the chamber and depicts the manner in which it was converted to a class-10,000 conventional type of clean room to meet the needs of stellar observatories. It is believed that this is the only thermal-vacuum chamber of its size that has been so modified. This was necessary for OAO to retain its cleanliness status during the test setup phase. Contamination problems associated with operations under thermal-vacuum conditions have received a great deal of attention as have all vacuum chambers utilized for OAO at any configuration level; i.e., component, subsystem, and the like. More definitive work needs to be done in this area.

Magnetics

Depending upon the particular design chosen for an observatory, magnetic testing may be required. For example, on OAO A-1,

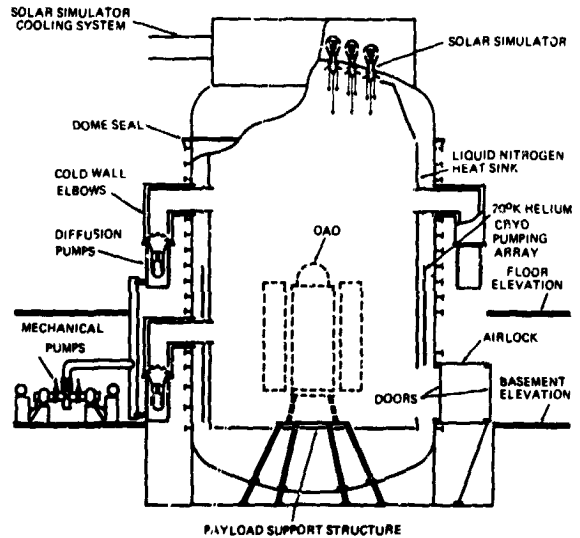


Figure 10. General arrangement of space environment simulator.

the magnetic moment of the flight observatory was measured in an earth-ambient-field facility at Grumman Aircraft Engineering Corporation, and compensating magnets were installed. A zero-field facility suitable for the OAO size of observatory is in operation at the GSFC test complex and is shown in figure 11.

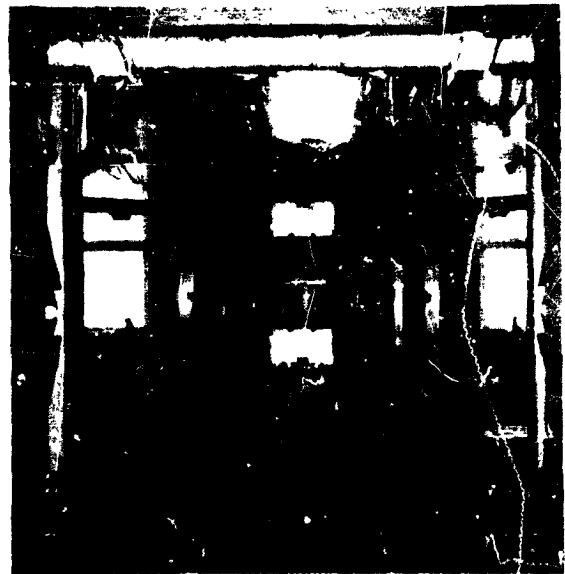


Figure 11. Attitude control test facility.

This photo shows an OAO structural model in the 40-foot coil facility.

A stated restriction on this paper is that it deal only with facilities "large" enough to test major subsystems of the OAO class; however, one of the purposes of this workshop is to exchange information, particularly that which may not be generally known. Therefore, a unique magnetic test facility that could be used for component and small subsystem testing is shown in figure 12. This is a 5-foot cylindrical, nonmagnetic, thermal-vacuum chamber, described in detail in reference 8.

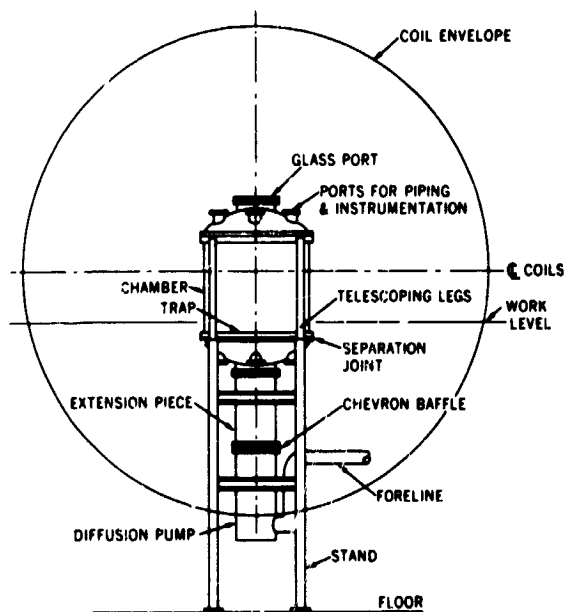


Figure 12. Nonmagnetic thermal-vacuum chamber.

Other Test-Cycle Supporting Facilities

Generally, near the start of the test cycle, mass properties of major subsystems of an observatory must be measured. The precision of measurement needed determines the complexity of weighing, balancing, and moment-of-inertia test facilities. Also, depending on their mode of operation and precision, it may be necessary to house such

facilities in clean rooms; or it may be possible to protect the observatory while it is in a facility.

Throughout the test cycle, substantial data collection, processing, and display capability is needed to handle facility and test data as distinguished from observatory telemetry data. In the GSFC test complex, a centralized data-handling facility is used. It is partially shown in figure 13; a brief description of its capabilities is given in Appendix A.



Figure 13. Centralized data-handling facility.

Optical Calibration and Test Facilities

There are five optical calibration and test facilities used for the OAO program: the vacuum optical bench, the low-temperature optical facility, the Princeton optical bench, the optical alignment facility, and the optical engineering laboratory.

Vacuum Optical Bench

The Vacuum Optical Bench (VOB) was designed and built primarily for performing the radiometric calibration of the stellar experiment packages for the OAO program. A cutaway drawing of the VOB is shown in

figure 14. The facility is located in a three-story, class-10,000 clean room in the test complex of the Test and Evaluation Division at GSFC and has been in use for experiment calibration since late 1964.



Figure 14. Vacuum optical bench (VOB).

The principal elements of the VOB are a vacuum chamber, 7 feet in diameter by 25 feet high, and a removable vertical optical bench. The bench has its own integral star-simulator system, which includes light sources, a vacuum ultraviolet monochromator, a 38-inch aperture Cassegrainian collimator, and a movable beam probe.

The bench is adequately isolated from building vibrations; it stands on a set of kinematic piers mounted on a 9-foot deep concrete block; the chamber rests on the building floor. With the use of an overhead-traveling bridge crane and a special bench up-ender, the entire bench, with an experiment installed, can be positioned vertically

with either end up (for ± 1 g testing) and in or out of the chamber as desired.

The optical experiment to be calibrated is mounted within the optical bench structure and is rigidly held in place on mounting lugs that are geometrically identical to those on the spacecraft. The bench is capable of accepting experiment packages up to 40 inches in diameter by 120 inches long and weighing up to 1000 pounds.

The Star-Simulator System (SSS) is the key system of the VOB with regard to the confidence level that can be established in calibrating a stellar experiment. The SSS can be described by using the optical schematic shown in figure 15. Radiation from a light source, S, is focused by a toroidal mirror, M_1 , onto the entrance slit, A_1 , of the monochromator. Passing through the monochromator, the light is diffracted and focused on a circular exit aperture, A_2 . The exit aperture serves also as the entrance aperture of the main collimator. The collimator optics are an $f/10$ Cassegrainian system with a convex hyperboloid, M_4 , and an $f/2.03$ concave paraboloid, M_5 . The 38-inch diameter output beam of the Cassegrainian collimator is used to irradiate the experiment being calibrated.

The performance requirements of the SSS are unusual. Not only are narrow bandpass, small beam divergence, and both high and low flux levels desired, but also a high degree of uniformity across the collimated beam is necessary. In addition, a high degree of stability with time is needed with regard to the flux level and pointing direction.

In general, the VOB operates over the wavelength range from 1100 to 5000 angstroms. The bandpass can be varied from 2 to 4 angstroms while under vacuum. The total decollimation of the beam at a 2-angstrom bandpass may be as small as 2 arc seconds. A dynamic range of flux of 10^3 can be achieved and reliably measured without resorting to the use of pulse-counting techniques.

Although enclosed light sources are used for some specific purposes, a free-flowing gas discharge source is used for most calibrations.

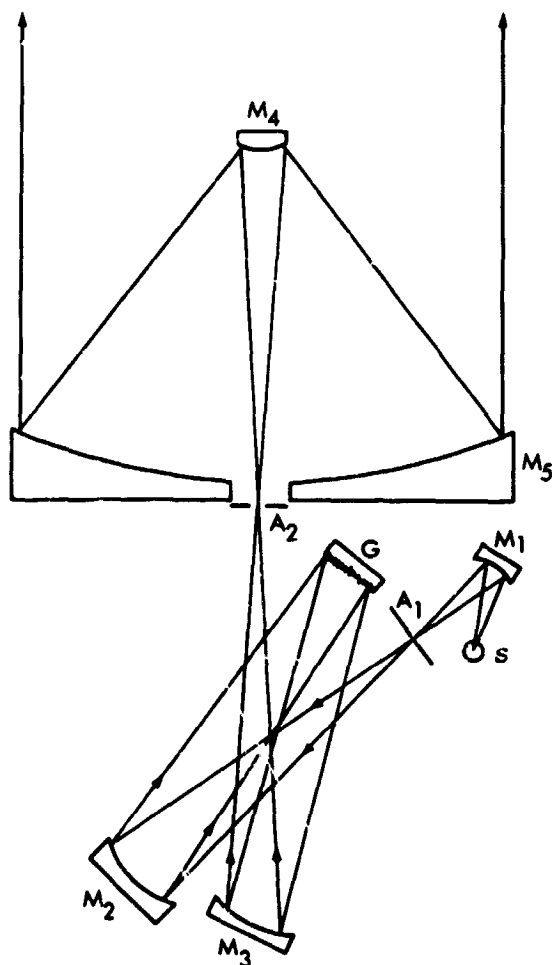


Figure 15. Optical schematic of VOB star simulator system.

A differential pumping system minimizes the pressure rise in the main vacuum chamber. The type of gas, its flow rate, and the light source current can be varied while under vacuum. In addition, a filter changer allows the placement of color and neutral density filters in front of the monochromator entrance slit. Optimization of the source materials and the range of currents has resulted in stable operation for periods in excess of 100 hours.

Specific details of the present monochromator design are given in reference 9. A discussion of the results achieved with this

design and additional details on the VOB are given in reference 10. The original monochromator design consisted of a plane mirror, which rotated about the center of the Rowland circle, and a concave tripartite grating. In 1962, when that first design was selected, no one had ever coated a 38-inch-diameter mirror with aluminum plus a magnesium fluoride overcoating; hence, the reflectance that would be achieved at wavelengths near 1216 angstroms was unknown but was expected to be low. Consequently, the minimum possible number of reflecting surfaces was used throughout the VOB. This was the reason for selecting that particular monochromator design. Due principally to the tripartite grating, large intensity variations existed across the output cone from the monochromator. After the facility was built, it was found that sufficient reflectance was achieved to permit the use of additional reflections. At that point, the monochromator was redesigned. A plane grating was used, and more efficient use of the light source was made by incorporating the toroidal mirror. A dramatic improvement in uniformity in the 38-inch beam occurred, and the flux levels actually increased even though two additional reflecting surfaces were involved.

The Cassegrainian collimator has the focal point inside the hole in the primary mirror. This is a most restricting choice, one to be avoided in any future facility if at all possible. The aluminium-plus-magnesium-fluoride coating techniques have been so refined during the past few years that in December 1968, when the 38-inch diameter primary mirror was last coated, the reflectance obtained at 1216 angstroms was 82.5 percent with only a ± 2 percent variation over the entire surface. Nearly the same degree of uniformity has been achieved using lithium fluoride overcoatings, but a compromise must be made between the reflectance desired at Lyman α and Lyman β . The technique used is described in reference 11.

Each time the mirrors have to be changed, the remounting and realignment of

them is a very time-consuming process. In this f/10 system, the best focus position is very sensitive to intervertex spacing. Adjustments must be made to locate the best focus within the dimensional range available for positioning the monochromator exit aperture. Except for the time required for these initial alignments, the method presently in use is adequate for the non-diffraction-limited optics concurrently on hand. This method involves autocollimating from a large flat, scanning along the optical axis to find the best image position for various intervertex settings, then measuring and photographically recording the return image. This cut-and-try method would not be accurate enough to make effective use of diffraction-limited optics. (Interferometric and other suitable techniques currently available will be discussed in other workshop papers.) Careful consideration must also be given to the adaptability of such techniques for use in a thermal-vacuum environment. This is certainly a "must" for any future calibration facility.

Because it is time-consuming to remove, recoat, and reinstall the VOB collimator optics, degradation of coatings due to any type of contaminant is a matter of continual concern. Regardless of the care exercised, eventually the problem of cleaning the mirrors in place must be faced. This type of cleaning has been successfully done for the magnesium-fluoride overcoated mirrors by flooding the 38-inch-diameter primary mirror with freon TF and immediately drying it with clean, dry, gaseous nitrogen. That statement, however, should be viewed with a great deal of caution because success is largely dependent upon the actual technique used and several other factors, such as the type of tubing, the spray nozzle, the handling, the source of the freon, etc. Cleaning this 38-inch mirror when overcoated with lithium fluoride has not as yet been attempted because to determine the degree of success would require that the chamber be available for three months. Such cleaning, however, has been done on small mirrors by Dr. George Hass at Fort Belvoir.

The intended use of the SSS is to perform an *absolute* radiometric calibration of stellar experiment packages. This requires a detailed knowledge of the absolute flux level in the 38-inch beam and any spatial or temporal variations of the flux level. To obtain such data in the VOB, an $r-\theta$ drive, beam probe is used to transport calibrated multiplier phototubes to scan the 38-inch beam. In a normal scan in the VOB, 3000 data points are obtained. This requires the availability of high-speed data collection, processing, and display equipment.

The calibration of these scanning multiplier phototubes, in order to use them as secondary standards, requires on-site laboratory equipment for performing accurate calibrations in the visible, near ultraviolet, and vacuum ultraviolet. Years of learning time are needed to use such equipment knowledgeably. The on-site requirement stems from two sources. First, there is evidence that such tubes change absolute calibration with time, which makes us want to calibrate them immediately before and after each use period. Second, only a very few organizations are equipped to perform the vacuum ultraviolet portion of the calibrations, and their laboratories are fully utilized in handling their own work. Much more needs to be done in this particular field.

Consideration of the beam-probe drive system and the electronic and electrical equipment involved in the measurement of the flux in the beam opens another door to a whole spectrum of problems. Avoidance of contamination serves as a major constraint on material selection in each case. Some key areas of concern are with motors, lubricants, nonreflecting finishes and coatings, high-voltage cables, connectors and feedthroughs, electrical noise and magnetic field generation. Although it seems that enough is known in these areas to survive today, each time the need arises to stretch the capabilities of the VOB, substantial exploratory work has to be done. The list of usable materials and equipments in these areas must be expanded to meet the needs of future observatories.

Low Temperature Optical Facility

The Low Temperature Optical Facility (LTOF), which is a companion facility to the VOB, was built to determine any misalignments that may occur in the OAO experiment packages when they are subjected to orbital temperatures. Ever since the first test of an experiment was run in late 1964, this facility has been found to be far more useful than was originally envisioned. Consequently, some broad-bandpass calibration capability has been incorporated into the facility. A conceptual drawing of the LTOF is shown in figure 16.



Figure 16. Low temperature optical facility.

The LTOF consists of a controlled-temperature test chamber, 13 feet wide by 43 feet long by 7½ feet high. Inside the chamber, but mounted on a vibration-isolating block via penetrations in the chamber floor, is a 39-inch clear-aperture collimator and a special handling device for experiments. The chamber is provided with a thermal lock for personnel access at low temperatures. The chamber and anteroom meet class-10,000 clean-room requirements.

The temperature in the chamber can be varied from +23° to -60°C at a predetermined rate. Test temperature is held to ±1°C throughout the testing area. The dew point of the air is maintained below -60°C in order to prevent any condensation on components in the chamber.

The collimator is a Newtonian mirror system, which directs the light from several interchangeable light sources in a 39-inch collimated beam to the optical experiment under test. The optical system of the facility is thermally compensated, and means are provided for initial alignment and for checking this alignment at the test temperature.

The special handling device is provided to receive an OAO experiment in the vertical position, to rotate it to the horizontal, to transport it into the chamber, and to serve as a mounting structure during tests. The experiment can be rotated in pitch and yaw ±15 degrees about the geometrical center and 360 degrees about the roll axis for ±1 g testing. The handling device will accept experiment packages up to 40 inches in diameter by 120 inches long and weighing up to 1000 pounds.

An X-Y beam-probe scanning device is provided; it carries a multiplier phototube. The use of a thermoelectric cooler makes it possible to maintain this tube at -20°C at any chamber temperature. The flux level and uniformity in the 39-inch beam are measured by using this scanner. High-speed data collection techniques are employed in much the same fashion as in the VOB. An array of light sources, imaging optics, broad bandpass, and neutral density filters are located in an insulated light-source housing that is maintained at +23°C by a separate air-handling system.

Numerous boresighting and angle-measuring instruments are available, but each presents a unique set of problems because of the low temperatures in the chamber. The proper application of low temperature lubricants and the selection of suitable electrical insulation are most perplexing until one has gained some experience in their use at these low temperatures. An accuracy of 1 arc second in making angle measurements has been achieved and can be improved upon under certain conditions.

It should be pointed out that, since air is used in the LTOF, tests are generally run with all of the elements of an experiment package at a uniform temperature as opposed to a

gradient condition, which would prevail in orbit. Consequently, the information obtained in such tests falls into the category of diagnostic and relative data rather than absolute calibration data. By the same token, since man can enter the chamber, tests such as image quality and resolution tests can be performed easily whereas these would be very difficult, if not impossible, to do in a vacuum.

For the calibration and evaluation of future observatories, a combined thermal-vacuum-optical facility is needed. It has been found to be most difficult to combine the results obtained in the VOB (vacuum only) with those of the LTOF (low temperature only). From an operational standpoint, however, the unique operating modes of each facility should be retained to aid in improving the confidence level one can achieve with regard to the launch readiness of a future observatory.

Princeton Optical Bench

A partial step toward a combined thermal-vacuum-optical facility has been taken with the Princeton Optical Bench (POB), shown diagrammatically in figure 17. The bench and a special optical dome are mounted on a 12-foot-diameter by 15-foot-high thermal-vacuum chamber. Several optical measuring instruments are mounted on an isolated table outside and above the chamber. These instruments consist of a 4-inch-diameter star simulator and several auto-collimators and theodolites. Electronic levels and a pendulous mirror are used to adjust the lines of sight of these instruments parallel to each other. Hanging from the optical table are three servo-driven columns, which penetrate the dome through vacuum-tight bellows. Inside the chamber, the actual bench structure is connected to the columns. At the lower end of the bench is a rigid support ring in which the experiment package and a multi-mode thermal control shroud are mounted.

As the thermal gradients on the experiment package are changed, through the control shroud, to simulate various orbital conditions, the angular relationships among

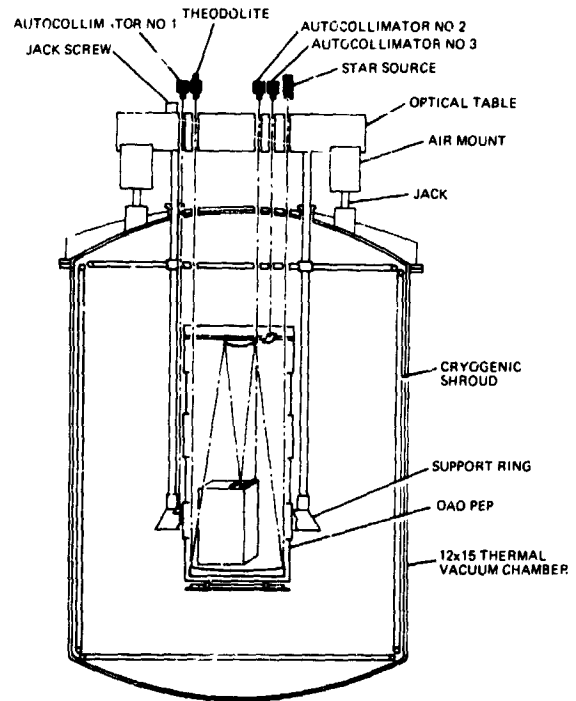


Figure 17. Princeton optical bench, schematic.

the experiment's fine guidance sensor, telescope axis, spectrometer slit location, and several reference mirrors located on critical elements can be measured.

The optical instrument table, from which all other bench components and the experiment are suspended, is isolated from chamber vibrations through air mounts and is also servo-driven to preserve its orientation to gravity. In addition, as thermal gradients change the lengths of the columns, these columns are servo-driven to retain parallelism between the experiment support ring and the optical table.

Acceptance tests using a model of the OAO Princeton Experiment were completed during March 1969. Angle-measuring accuracies of approximately 2 arc seconds were obtained. With this design, isolation from vibrations and other distortions is sufficiently good to keep the jitter in the sub-arc-second region.

Note that all of the optical instruments are mounted external to the thermal-vacuum

chamber. It is likely that in any future facility most of these instruments would have to operate inside the chamber. This would require adaptation, if not modification, of currently available devices.

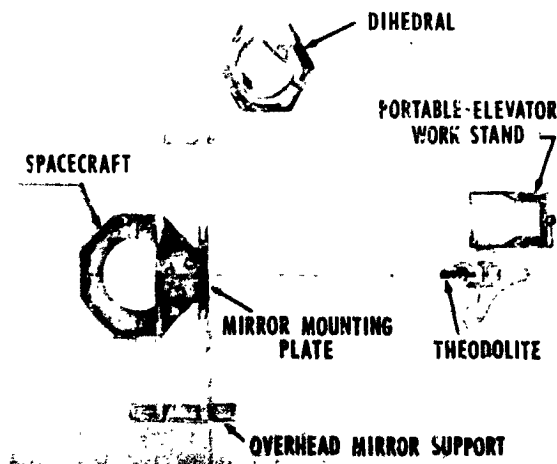
Optical Alignment Facility

To meet the fine alignment and fine photometric requirements of the OAO A-2 complete observatory, the Optical Alignment Facility (OAF) was designed and built at GSFC. This facility incorporates an improved method of optical tooling for the determination of the angular alignment of randomly oriented devices. The OAF is shown schematically in figure 18 and is described in detail in reference 12.

The OAF was designed primarily for determining the roll, pitch, and yaw coordinates of the star trackers, solar sensors, jets, and other components of the OAO. It is located in the spacecraft checkout area, a class-10,000 clean room, in Building 7 near the other environmental facilities of the Test and Evaluation Division.

The OAF consists of a remotely controlled, precision rotary table on which the test object is located, a vertical tooling bar for a first-order theodolite, an overhead structure for locating relay mirrors, and an elevator to enable the operators to position the theodolite at any elevation. The permanent azimuth reference is a dihedral mirror mounted on a heavy sand-filled stand. Electronic levels are used to monitor continuously the gravitational relation of the rotary table and the dihedral reference mirror.

The unique feature of the facility is its inherent capability to measure the pointing direction of any item on the test object, regardless of its location, provided the item can be equipped with a suitable optical test tool. The tool and the relay mirror are viewed in autocollimation, and the azimuth and elevation readings are transformed into coordinates of roll, pitch, and yaw by a computer program using matrix optics methods. The facility uses a single theodolite and only



(General arrangement, plan view)

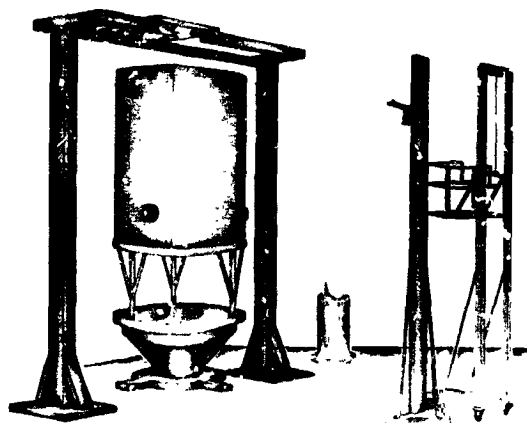


Figure 18. Optical alignment facility.

one azimuth and one gravity reference; hence, the errors are minimum, and an accuracy of 5 to 7 arc seconds is readily obtainable. All of the instrumentation used in the OAF is certified with traceability to the National Bureau of Standards.

The observational procedures are such that six objects, such as star trackers, or 10 to 12 single surfaces, such as jets or solar sensors, can be measured in an 8-hour shift.

Additional instrumentation is on hand to make precision photometric measurements, such as linearity and stellar magnitude, without disturbing the basic facility.

The rotary table and the overhead structure can accommodate objects up to 7 feet in diameter by 10 to 12 feet high and weighing as much as 6000 pounds.

Optical Engineering Laboratory

To support the VOB, LTOF, POB, and OAF, numerous angle-measuring and alignment instruments are required. These instruments must be calibrated frequently to achieve the utmost in angle-measuring accuracy. It soon becomes apparent that an on-site calibration facility is needed because of the quantities of instruments involved, the quick turn-around time needed, and the relatively fragile nature of the instruments. To perform such calibrations, angle generators are now available with an inherent accuracy better than 0.1 arc second; however, the manufacturer can certify this device to only 0.25 arc second. Therefore, one must employ long-path-length laser systems or holographic techniques to calibrate these angle generators more accurately than the certified values.

Perhaps the most accurate angle generator in existence today is one called a single wedge angle generator, which was developed at GSFC. The qualifying term "perhaps" is used because, even though criticism of this device has been openly invited and the accuracies claimed have not been disputed to date, these accuracies are almost unbelievable. A grossly conservative error analysis yields absolute accuracies of 0.001 arc second over a 3-arc-second range of angles generated, 0.01 arc second over a 36-arc-second range, and 0.1 arc second over a 347-arc-second range.

The device consists of a simple wedge that is rotated between a fixed plane mirror used for autoreflexion and a fixed monochromatic autocollimator, which is being calibrated. The angle generated is determined analytically after measuring the rotation angle of the wedge to only 1 arc second and with relatively crude knowledge of the wedge angle and the indices of refraction of the wedge and air. This generator is described more fully in reference 13.

Although it might be useful to convert this device to a two-axis angle generator, the accuracies now obtainable should fulfill the calibration requirements for any auto-collimating instruments that might be needed in any future test facility for the observatories currently being discussed.

An on-site optical engineering laboratory is utilized in support of observatory programs for tasks other than calibration of alignment instruments. Such programs require numerous star simulators, which must be aligned and photometrically calibrated at frequent intervals. In addition, numerous specialized optical gages require calibration and adjustment in support of alignment checks that are performed in a facility like the OAF. Most of this work must be performed in a carefully controlled laboratory environment, and much of it requires clean-room conditions.

Observatory Design Analysis

The importance of designing the observatory so it can be calibrated and tested must be stressed. If such a philosophy is adopted at the concept stage of an observatory program, it will indeed bear fruit. One-of-a-kind calibration facilities require nearly as much time to design, build, and shake down as it does to get an observatory from the concept phase to the ready-to-calibrate stage. With both design and test personnel working together from the beginning, the facility will more nearly meet the needs of the program. This kind of early cooperative effort will yield another benefit. Sufficient time will be available to perform detailed structural, thermal, and optical design analyses to pinpoint the more critical aspects of the observatory design. This makes it possible to improve the observatory during construction and also to generate a meaningful test program that can be run in a minimum amount of time. For observatories even larger and more complex than the current OAO's, even a few days of test time will represent a substantial number of dollars that can be saved.

Some effort in this direction is in progress at GSFC on a project entitled STOP

(Structural Thermal Optical Program). The structural and thermal programs are rather well developed, and a merger of the two is currently taking place. Optical design evaluation programs exist in so many forms that it would be foolhardy to try to mention even the most powerful of these in this paper. Each of these programs is modified by each optical designer to suit his own special types of problems. In the hands of a skilled designer, the programs seem to exist to perform a suitable analysis of the optical designs of any observatory. Some interesting and recent work in telescope design is described in reference 14. The intention at GSFC is to incorporate the "O" (for optical) into the STOP project.

Future Calibration, Simulation, and Test Facilities

Based upon experience gained to date, the current OAO program through flight 4 could well utilize a combined thermal-vacuum-optical calibration facility. The increase in confidence level that could be obtained can be shown to justify the cost, but the required facility cannot be built in the time remaining.

Among the follow-on stellar observatories being considered at this time is one sometimes called ASTRA and sometimes called an Advanced OAO. This observatory would utilize the full shroud volume and payload weight capability of the Centaur. It would be variously a 40-inch, 48-inch, or 60-inch aperture, diffraction-limited telescope with one or more observing instruments carried by a ground-controlled spacecraft. Facilities either exist or with some modifications would be adequate to meet the simulation and testing requirements for full systems testing of this size and type of observatory. A calibration facility would be needed; this might take the form shown in either figure 19 or figure 20. The basic differences between these two concepts are: (1) the figure 19 chamber is soft-mounted while the figure 20 chamber is hard-mounted; (2) the figure 19 chamber is really a two-part chamber with the

upper half, containing the SSS, essentially thermally isolated from the lower half; the figure 20 chamber is a single chamber. In the two-part chamber, a valve between the two can be closed, and the upper section can be returned to ambient quickly when repairs and/or adjustments are required. In the opinion of the author, all of the optical instruments and techniques needed for proving performance of the SSS during calibration of an observatory, and for other monitoring purposes, exist today, but many would require adaptation for use in a thermal-vacuum environment and in clean rooms.

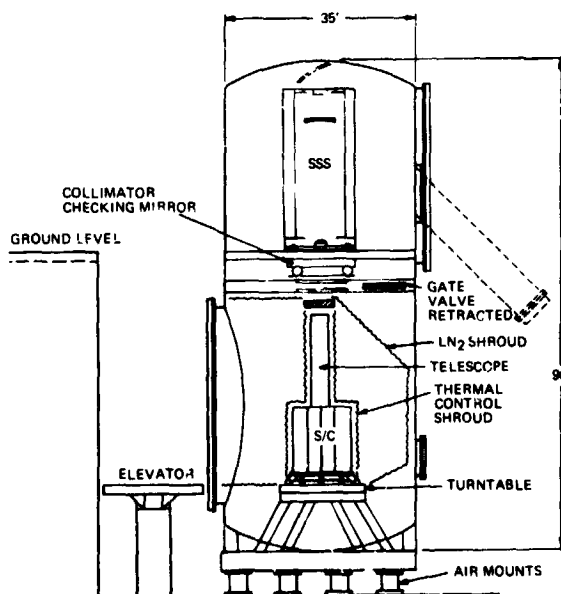


Figure 19. The 35-foot by 90-foot STEF chamber concept.

Similar calibration-chamber concepts have been developed to handle the 120-inch diffraction-limited telescopes of the manned-orbiting-telescope (MOT) type of observatory. Because of the logistics involved in handling such a very large stellar observatory, serious consideration should be given to the feasibility of incorporating all full-systems simulation and testing capabilities as well as the calibration features into a single facility.

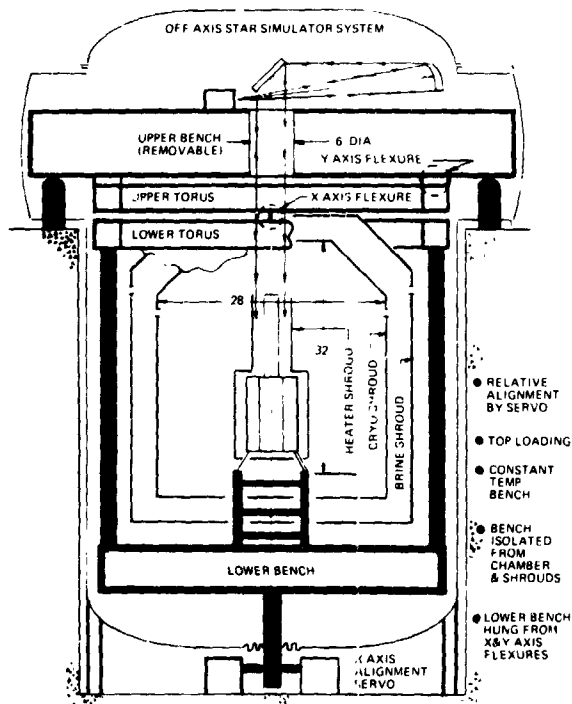


Figure 20. The 50-foot by 90-foot thermal-vacuum-optical bench.

Recommended Research and Development Tasks

In summary, existing simulation and test facilities could be made adequate for the ASTRA or Advanced OAO class of observatories, but a calibration facility does not exist. For the MOT class of observatory, an entire new calibration, simulation, and test facility complex would be required. To prepare for the advent of these second and third generation stellar observatories, the author feels that the following research and development tasks must be pursued to ensure

that adequate calibration, simulation, and test facilities can be made available on a timely and economically sound basis:

1. Perform tradeoff studies of:
 - a. Chamber configurations, pumping systems, and isolation methods
 - b. Star-simulator system configurations, including necessary proof-of-performance and diagnostic instrumentation.
2. Extend and refine present analytical methods for performing structural, thermal, and optical design analyses.
3. Analytically and experimentally establish allowable tolerance levels, and improve detection instrumentation for various contaminants with regard to:
 - a. Mirror coatings
 - b. Scattered light
 - c. Properties of thermal coatings.
4. Develop 0.01-arc-second angle-monitoring device and real-time servo-controlled correction system.
5. Increase number and reliability of noncontaminating materials, motors, lubricants, cements, high-voltage connectors, etc.
6. Devise a method for cleaning contaminated observatories and chambers.
7. Develop primary and secondary radiometric standards, and improve detector calibration accuracy especially in the vacuum ultraviolet region.
8. Develop light sources with improved spatial uniformity, temporal stability, operating life, and dynamic range.
9. Adapt diagnostic instrumentation for star-simulator systems for use in thermal-vacuum chambers.
10. Determine the changes in physical properties of reflecting and transmitting optical materials due to space environments, such as low temperatures, hard radiation, and the like.

References

1. Boeckel, J. H.; Timmins, A.R.; Mercy, K. R.: Goddard Space Flight Center Test Philosophy and the Resultant Record. Paper presented at the Symposium on Long Life Hardware for Space, at MSFC, March 1969.
2. Long, T.: Experiment Inspection Procedure. GSFC-OAO Document.
3. Lekebusch, A. O.: A Contamination Control Manual for the Test and Evaluation Division Facilities. Report X-320-69-2, GSFC, Greenbelt, Maryland, March 1969.
4. Bolt, Beranek & Newman, Inc.: Experimental Study of Sound and Vibration Transmission to a Shroud Enclosed Spacecraft. NASA CR-96144, Contract No. NAS 5-10302, August 1, 1968.
5. Kirchman, E. J.; Arcilesi, C. J.: Advanced Combined Environmental Test Facility. Shock and Vibration Bulletin, bull. 37, p. 3, Washington, D. C., January 1968.
6. Maurer, Henry, Jr.: Space Environment Simulators for Spacecraft Testing at GSFC. Presented at the Symposium on Space Environment Simulators, London, England, November 17, 1964, revised January 13, 1965.
7. Orbiting Astronomical Observatory A-2 Thermal Model Test Procedure. Thermodynamics Branch, GSFC, November 1967.
8. Mosher, E. J.: A Five Foot by Five Foot Non-magnetic Thermal-Vacuum Chamber. Published in the proceedings of the 14th Annual Technical Meeting of the IES, St. Louis, Missouri, April 1968.
9. American Machine & Foundry Company: Alignment Procedure for Vacuum Optical Bench Monochromator. Contract NAS 5-3740, Alexandria, Virginia, December 12, 1965.
10. Diggins, J. L.; Paul, F. W.: A Vacuum Optical Bench for Testing Space Experiment Packages. Published in the proceedings of the AIAA/IES/ASTM Space Simulation Conference, Houston, Texas, September 1966.
11. Bradford, A. P.; Hass, G.; Osantowski, J. F.; Toft, A. R.: Preparation of Mirror Coatings for the Vacuum Ultraviolet in a Two-Meter Evaporator. Applied Optics. November 1968.
12. Appler, R. L.; Howell, B. J.: Optical Alignment of Multiple Components to a Common Coordinate System. Applied Optics, Vol. 7, June 1968, p. 1007.
13. Method for Generating Ultra-Precise Angles. NASA Case No. 4173, patent application.
14. Howell, B. J.: A Design Method for Corrected Ritchey-Chretien Telescopes. Applied Optics, March 1969.

Appendix A

GSFC Test Facilities Data System

The GSFC Test and Evaluation Division has a Test Facilities Data System comprised of a centralized data collection system and four Control Data Corporation (CDC) computers: one 8090, two 160-A's, and one 3100. The primary function of the total system is to collect, to process, and to display on demand selected data from both facilities and spacecraft during environmental testing.

The data collection system has three subsystems for multiplexing and digitizing analog signals at various sampling rates and signal

levels. All three systems can run concurrently. Nominal characteristics of each system are:

1. 2500 channels every 100 seconds; ± 10 millivolts
2. 1500 channels at 5 samples per second; ± 5 volts
3. 150 channels at 100 samples per second; ± 5 volts.

The channels on each system can be supercommutated to obtain higher sampling rates but with a reduction in the number of channels that can be sampled.

The CDC 8090 computer is an integral part of the low-speed data collection system. Input data to the low-speed system (2500 channels sampled every 100 seconds) are converted to engineering units, are checked for high and low limits, and are output to small, 11-column, strip-chart printers located near the test facilities. These data are also recorded on a disk connected to the CDC 3100 computer and are continuously updated so that the latest 8 hours of data are always

available. Remote inquiry stations (CRT/keyboards), connected to the CDC 3100 computer and located throughout the test facility complex, permit the test conductor to retrieve these data, to process them as required, and to display the results on the CRT.

Processing of data from the higher collection rate system is an off-line operation.

The two CDC 160-A's are available on a scheduled basis to satisfy special collection or processing requirements.

Lens Design by Large Computers

David S. Grey
Grey Associates

10N70-36692

This presentation is an attempt to answer questions about the capabilities of computer codes in lens design.

One question usually asked is: Does the computer replace the lens designer? Lens "design" codes are not strictly for lens design but for lens optimization. The lens designer uses the optimization programs to pursue to a local optimum the merits of a lens configuration that the designer specifies by his input data. Any person willing to understand the operating instructions for a lens optimization program can "crib" lens designs from the literature as the starting point for a lens optimization run. This procedure, though often followed, is not lens design on a high level. The lens design game begins in earnest when it becomes necessary to alter the topology of the initial trial system or to invent a new type of lens configuration. Today, the lens designer is just as essential in this role as he ever was. The computer has merely freed the lens designer from the drudgery of pursuing to optimum performance a lens configuration that he thinks has potential merit.

A second question is whether or not an optimization program can properly compare two imperfect images when the lens design goal is not a diffraction-limited system. This question is important in the design of commercial lenses, most of which are not nearly diffraction-limited. A large portion of the art in the design of these lenses is to force as large a fraction of the energy in the image of any particular object point into a small-core image area and to cause the ill-behaved energy to fall as far outside this core as possible. A lens optimization program should in one way or

another cope with this situation. Most of them do, but in all programs some guidance in this matter must be supplied by the program user.

Time is the third question. We are interested in the calendar time that expires from specification of the job until completion as well as the amount of computer time used. A comfortable calendar time is approximately two weeks for a job that in the precomputer era would have taken a year. This amount of time allows the lens designer to operate at a leisurely pace and to satisfy himself that he has explored all the interesting possibilities. During this period, the lens designer might be faced with as many as three jobs simultaneously, depending upon the intricacies of his problems. The amount of computer time varies greatly and depends upon the computer, the optimization code, and how efficiently the user has functioned.

In preparing this paper, I reviewed a series of computer runs I had made in the design of an optical system having 26 surfaces. This system was started completely from scratch; there was absolutely no applicable prior art. The job involved investigating about 45 configuration modifications, and each configuration required 60 to 70 seconds of computer time to optimize. This optimization was done by using a machine language code on the CDC 6600 Computer. (Recent program modifications would halve this computer time.) Under no circumstances would I have undertaken this job with classical lens design methods; it would have been at least a lifetime job.

The fourth pertinent question is: How does the quality of a computer-optimized lens

compare with a lens optimized by classical techniques? (We shall in this and subsequent comparisons grant that the classical techniques will be supported by using a computer to trace rays and to perform other direct slave work.) This question is very difficult to answer completely because the answer depends upon many factors, of which the most vital are:

1. What is the lens problem to be solved?
2. Who is the "classical lens designer" pitted against which optimization program?

At one extreme end of the spectrum is the classical double-gauss lens, six pieces of glass only. There is little or nothing to be gained by computer optimization of such a lens type over what can be accomplished by classical methods. Computer optimization can speed things up, but the quality of the final design is not improved by any noteworthy amount. We must emphasize that the classical double-gauss lens has one outstanding type of residual optical aberration. This residual aberration is inherent to the lens type, and neither man nor computer can remove it. For other more complex lens configurations, we have seen the computer surpass the best efforts produced by classical design by factors ranging from 3 to 10 (measured in terms of a linear function, either wavefront deformation or lateral intercept errors). As we explained before, computer methods can allow design of systems that would be unapproachable by classical methods.

The fifth question, perhaps more of theoretical interest than of practical interest, is: How efficiently do lens optimization programs utilize the computer? To be more specific, what is the ratio of arithmetic operations required by a computer program to those required by classical procedures? My best determination of this ratio is that the computer can be utilized to about 10 percent efficiency; that is, to solve a typical difficult problem in lens design, a properly used computer program will perform about 10 times as many arithmetic operations as required by classical methods.

Large computers can trace rays approximately 10^6 to 10^7 times faster than was possible by desk calculator; they can do this to several more significant decimal digits and without error. Factors of 10^5 to 10^6 are nothing in these days of megatons and national budgets, but they are significant when applied to one's personal time.

A final and most useful application of lens optimization programs is in the interface with the total problem at hand. When a lens designer had solved a problem by classical methods (in a year or so) according to specifications handed him, he would understandably be reluctant to make "minor" modifications to interface the lens with changed requirements. The changes might be well merited, but the lens designer would well merit a vacation, at least from that particular job. If, however, the optical system in question exists as a data deck for a lens optimization program, the lens designer can answer questions posed by mechanical engineers as to what would happen if it were changed a millimeter or so. Reciprocally, the lens designer will have the data to back him up in asking the mechanical engineers to relax at least one of several requirements. Such an interface problem requires almost no computer time, but successful execution of such a procedure requires that both the lens designer and the mechanical engineer understand their jobs.

A very legitimate concern about using a computer to solve a lens optimization problem is whether or not the computer code will produce a design that can be fabricated. There is good reason to expect that, if a computer optimization code proceeds toward obtaining optimal computed performance with no reference to practicality of construction, the end result will, to say the least, be unacceptable to the optical shop. We have found to our amazement that in the majority of cases such concern is ill-founded. Actually, we have often observed that a lens optimization program will virtually make "dummy lenses" of components that we had introduced. Allowed our way as classical

designers, we probably never would have considered removing the lens elements we had introduced for a supposed necessary purpose.

There are well-known methods of dealing with certain difficult aberrations, methods that lead to strict construction tolerances. It is a trivial matter to force a computer code to be as observant of these proprieties as was the classical lens designer. In fact, many computer codes provide such features. It is quite another matter, however, to provide that the computer code compute tolerance sensitivities and carry these as items in optimization. This has also been done and is far more effectual than the rule-of-thumb criteria that were used in classical lens-design procedures.

In conclusion, I shall try to answer the final question: If lens design is done so easily on computers, why is lens design capacity so

short? The computer does not replace the lens designer. The lens designer is asked to treat problems that were hopeless before computer optimization; the lens designer sometimes does tens of revisions in order to interface with other engineers; the lens designer is expected to do a much better job with a computer than by using only classical methods. The computer cannot replace the lens designer's time spent in conference; it can only prove or disprove his decisions. Neither the lens designer nor the computer is responsible for the fact that many completed lens designs are never executed, even as prototypes. There was a time when lens design proposals contained more poetry than fact; today they often contain complete specifications, including seven wavelength, heterochromatic, modulation transfer function (MTF) computations.

PRECEDING PAGE BLANK NOT FILMED.

Possibilities for Automating Optical Manufacture

Robert R. Shannon

University of Arizona

N70-36693

The design and analysis of lenses using large computers has reached a significant stage of development. Indeed the process of optimizing a design has come to be considered "automated." It is now appropriate to determine to what extent the fabrication of optical systems can be automated.

The particular process of automation to be discussed in this paper must be differentiated from the process of mass production. In the mass production type of automation, a repetitive process is developed and refined to attain a quality output through a lengthy procedure or process or work flow control. Development of such a process is not easy, but it requires a somewhat different approach than the automation of manufacture of specialized optical systems of the type needed in a large space telescope.

The production of a finished optical surface is, at the present time, a task for a skilled optical craftsman. Until recently, even the testing or qualification of optical surfaces was not a systematic, quantified process.

The process of producing the surface is almost entirely based upon techniques developed by an empirical method. The method of surface generation by lapping with a pitch lap operated in a quasi-random manner over the surface being polished will probably be the major method of surface generation for a long period of time. This process cannot be described by any simple, linear, physical model, but the process does produce a fine, high-quality surface with few limitations upon the desired aspheric shape of the surface. There are possibilities of automating this technique as well as automating linear ion-removal or vacuum-deposition

methods of surface finishing. The pitch-polishing method, however, appears to be the dominant general method for the manufacture of large optics in the foreseeable future.

What is meant by automation in this context? Once the lens designer has completed his task, a lens-design data sheet exists. One part of this data set may be the analytic description of a surface. This formula needs to be converted into a precise, usually symmetric, surface that not only matches the desired curve shape but also has a very high degree of smoothness or "polish." In concept, one would like to feed the data describing this surface into a computer, to generate a set of machine instructions, and then to feed these to a numerically controlled polishing machine to convert the formula into a surface. Ideally, one pass on the machine would be enough. Actually, the iterative process, in which first coarse steps are followed by finer increments that converge to a solution, will probably continue to be required.

To see how this may be accomplished, it is necessary to review the lens design process. The operation of a modern lens design program depends upon establishing the relationship between a set of variables and the aberrations to be controlled. The relationship is taken to be linear over some range, and a solution is obtained. The solution is evaluated and usually found to be somewhat better but still insufficient because of the nonlinearity of the relationship between variables and aberrations over a wide range. A new solution is found, and another iterative step is taken.

When such a program is used, the lens designer finds that he begins to concentrate

more on the solution and less on the variables. Of course, he must use a sufficient set of variables to be able to attain a solution. These variables must be chosen to have convenient physical properties; otherwise, a solution will be difficult or impossible to obtain. *The designer no longer relates a single property of the aberrations to any single variable.*

A similar process for manufacture can be considered. The variables would be a set of operations on a polishing machine. An empirical input could be obtained in which a data base relating variable to aberration is generated from a series of experiments. The aberrations are the material to be removed from the surface. A lens-design-program approach is converted to a lens-fabricating program in which an optimum set of variable or operations is selected to produce the surface. This set of operations is carried out, and the surface residual errors are evaluated. Iterative steps are taken until the surface comes into solution. *This technique differs from the present art in that at no time is the improvement in the surface ascribed to a single member of the set of operations, or variables, but a total linear combination is taken.*

This system method of manufacture is feasible; all the technology to accomplish the process is available. The task of the optician now changes to parallel that of the lens designer. He must select and develop the best set of input variables, or polishing operations, to be used.

One item of technology that the lens designer uses to complete his design is a merit function, which is a combination of the residual aberrations that describe the state of correction. The proper choice of a merit function is vital to ensure that the design will meet the needs. Thus, several merit functions may be used, differing in detail and depending upon the problem to be solved. An analogous situation exists in manufacturing the surface. After each iterative cycle, detailed test data can be obtained that describe the condition of the surface either in detail or in summary form. By properly weighting the components of this merit function at each stage of the

fabrication process, it is possible to reach the desired solution. The weighting is a task for the optical engineer.

To make this concept clear, let us look at the technology of testing and quantifying a surface. A wavefront or interferometric measurement can be made on a surface. By scanning this test result, a digital representation of the surface can be obtained for input to a computer. The output of the computer can be a contour map. This map shows where material needs to be removed to reduce the mirror surface to the desired shape. In generating this data output, the computer program can also evaluate the surface for alignment, curvature, astigmatism, and residual error. From this residual error, the effect of the surface on the transfer function of the lens can be obtained or a value for the root-mean-square wavefront error. By processing additional data on scattered light from the surface, it is possible to obtain a measure of the quality of surface finish.

All of the test data can be used in constructing a merit function to be corrected by proper application of a combination of variables or operations on the surface. It is my opinion that all of the required technology exists, but the overall system application to the fabrication problem has yet to be carried out.

Finally, the question remains as to whether or not the effort to build this automated system of fabrication is worthwhile. The answer, I suggest, is definitely yes. Much technology has been developed in optical design and testing in which the limitations of the process are not eliminated but avoided through proper application of computer techniques. Designing and testing of lenses have surpassed the ability to manufacture. The lapping process, or pitch polishing, provides the best available surface, but there are problems in its application to a systematic method of operation. No super machine will eliminate these problems, but they must be taken into account.

A consistent program in which the techniques developed in optimization of lens system designs are applied to optimization of

the finished surface is distinctly appropriate at the present time. Such a program provides the only likely method of ensuring that very high quality surfaces of the nature required in a large space telescope can be made on a timely basis.

PRECEDING PAGE BLANK NOT FILMED.

Materials Considerations for Large Spaceborne Astronomical Telescopes

John B. Schroeder
The Perkin-Elmer Corporation

N70-36694

Introduction

Placing astronomical observatories in high earth orbit completely eliminates the degrading effect of the atmosphere. This provides two invaluable advantages over terrestrial astronomy. First, because atmospheric scintillation effects are avoided, the image quality will be determined primarily by two factors: the figure of the optics and the pointing stability. Second, essentially the entire electromagnetic spectrum becomes available for the observation of stellar sources. A large primary mirror will efficiently focus radiation with wavelengths between approximately 40 nanometers and 1 meter—a dynamic range of over 10^7 !

Telescope Specifications and Material Properties

If we apply the Strehl criteria to an astronomical satellite, the optical surface must be within 0.02λ (root-mean-square deviation) of the desired surface and must scatter less than a few percent of the incident energy. Because of the wavelength dependence of both figure and scatter, these specifications are most severe when applied in the vacuum ultraviolet. This means that every point on the mirror surface must be within 1.4 nanometers of the desired geometric surface in order to obtain the desired performance.

It is always desirable to minimize the weight of a space system. Because the launch stresses cannot be allowed to produce permanent deformation of the telescope, micro-yield strength in metals and fracture strength

in brittle materials become a major concern. On the other hand, the forces applied during figuring and testing cannot be allowed to deform the mirror; therefore, the stiffness-to-weight ratio is also important. Table 1 lists the pertinent physical properties of several materials frequently mentioned as candidates for mirror applications. Fused silica and pyrex are included in the table for comparison. Figure 1 shows the mirror weight for several materials as a function of maximum tensile stress during a 30-g launch. The model mirror used in the calculations was a flat, 1-meter in diameter and supported uniformly about its perimeter.

This model is ludicrous in the sense that we could not begin to manufacture and test such a mirror. It does, however, illustrate very clearly the tradeoffs among microyield strength, density, and weight. Another point to recognize is that lightweight structures may be employed to increase the stiffness during manufacture.

Lightweight structures are currently available in fused silica, ULETM, and Cer-Vit[®]. Small, monolithic, lightweight, beryllium mirrors have been prepared at Battelle. It is apparent that lightweight forms can be manufactured in any material.

During operation of the telescope, thermal gradients can be expected to exist in the mirror. The thermal gradients within the mirror will depend upon the target, the material and design employed for both the mirror and its mount, as well as the satellite power dissipation, orbit, thermal shielding, etc. Even though the satellite will be designed to provide as benign an environment as practical, the telescope performance will be determined

Table 1. Physical Properties of Selected Mirror Materials

Material	Melting or Softening Point (°C)	Thermal-Conductivity-to-Thermal-Expansion Ratio (watts/cm x 10 ⁴)	Young's Modulus-to-Density Ratio (cm x 10 ⁸)
Aluminum	660	0.92	2.73
Beryllium	1285	12.	16.6
Cer-Vit	1400	60.	3.7
Fused Silica	1590	3.	3.4
Pyrex	820	0.7	3.0
Silicon	1412	70.	4.9
Titanium	1800	2.1	7.8
TZM	2610	7.8	0.45
ULE	1425	60.	3.2

ultimately by the properties of the mirror material. The transient thermal distortion is proportional to a/D , where a is the linear thermal expansion coefficient and D is the thermal diffusivity. The steady state distortion depends upon a/κ , κ being the thermal conductivity.

An axial thermal gradient would exist in our hypothetical mirrors if 1 percent of the solar flux passed through the mirror and was removed magically from the back surface without introducing radial gradients. These thermal gradients introduce a curvature due to the unequal expansion of the two surfaces. The sagittal departure from a flat is given in table 2. This oversimplified model illustrates that thermally induced deformation of mirror surfaces is minimized by employing materials with a vanishing a/κ ratio or a/D ratio for the dynamic thermal response.

If the telescope is to be applied to infrared astronomy, it will be highly desirable to cool the mirror to cryogenic temperatures to reduce the noise. This has an added advantage because the thermal conductivity of

materials goes through a maximum in the vicinity of 10°K. The magnitude of this thermal conductivity peak depends upon the sample shape and purity; however, a hundred-fold increase can be expected for most materials. The thermal expansion coefficient of many materials changes sign at low temperatures. It will be necessary, therefore, to measure the properties of the candidate materials accurately at the operating temperatures.

The previous comments, in effect, are aimed at maintaining the optical figure of a mirror. Scattered light is also an important factor, particularly at short wavelengths. Microroughness, as opposed to surface figure, is the primary source of scatter. The major sources of microroughness are:

1. Inadequate polishing techniques
2. Inadequate substrates (multiphase, porous, etc.)
3. Inadequate optical coatings.

Care must be taken to differentiate between scatter and absorption. Both reduce the reflectance of a surface. Scatter increases

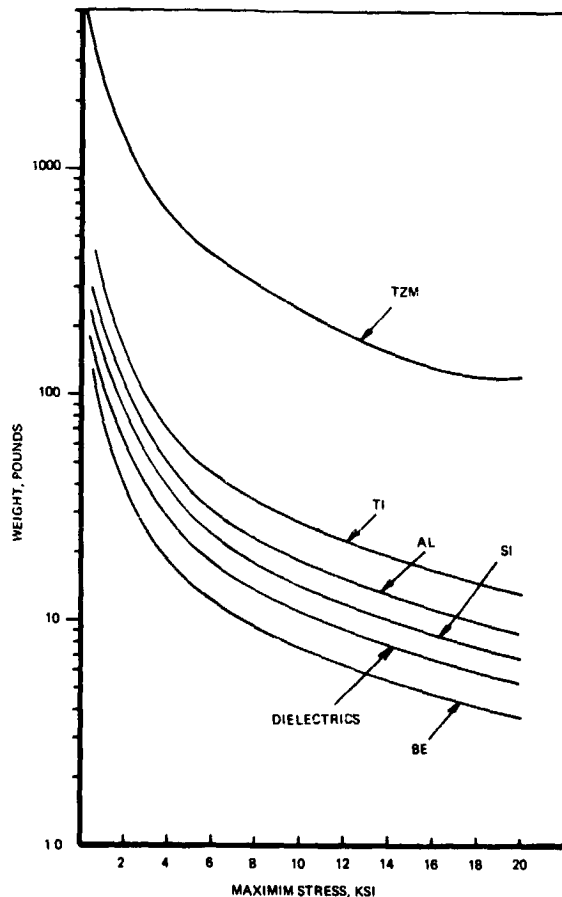


Figure 1. Mirror weight as a function of maximum tensile stress during a 30-g launch.

the noise (i.e., reduces the contrast) in the image plane. On the other hand, absorption increases the thermal load on the mirror. This difference is apparent in the case of aluminum-coated beryllium, where the reflectance at $\lambda = 632.8$ nanometers is reduced by approximately 4 percent from aluminum-coated glass. The scattered energy, however, amounted to only 0.5 percent. This missing energy apparently was absorbed by pores in the surface. Although the reflectivity must be maximized, there is the possibility of selecting the loss mechanism.

Coated glass optics scatter approximately 0.05 percent in the visible. Some representative scatter data are shown in table 3.

Table 2. Sagitta Induced by Conduction of 1.34×10^3 watts/cm² Through a Right Circular Cylinder, 1 Meter in Diameter (Thicknesses Based on Self-Weight Stresses Indicated)

Material	Stress (ksi)	Thickness (mm)	Sagitta (μm)
Aluminum	0.5	38.2	185.0
Beryllium	2.0	11.5	14.0
Cer-Vit	2.0	14.2	2.8
Fused Silica	2.0	14.2	58.0
Pyrex	2.0	14.2	210.0
Silicon	10.0	3.3	2.1
Titanium	10.0	3.3	81.0
TZM	20.0	6.8	22.0
ULE	2.0	14.2	2.8

In the critical hard ultraviolet, there is a complete paucity of data.

In connection with scatter, it should be pointed out that there is a need for good optical coatings in both the ultraviolet and infrared. The problem is primarily due to a lack of materials and data on materials. This is an area that deserves a great deal of developmental effort.

In selecting the mirror material, two ratios are of prime concern: stiffness to weight and thermal conductivity to thermal expansion. Table 4 ranks the leading candidates according to these two criteria and the optical scatter as well. The data presented in table 4 indicate the dilemma is in selecting the material because a different material is superior for each criterion.

Beyond these readily measurable properties, the temporal stability and availability are dominant considerations.

Table 3. Scatter Measurements

Material	Percent Scatter	
	$\lambda = 632.8 \text{ nm}$	$\lambda = 0.19 \text{ nm}$
Cer-Vit	0.11	20.0
Fused Silica/ ULE	0.05	9.0
Silicon		15.0
Beryllium	0.5	30.0

Table 4. Ranking of Materials by Criteria

1. <i>Ratio of Stiffness to Weight</i>
Beryllium
Silicon
Cer-Vit
ULE
2. <i>Ratio of Thermal Conductivity to Thermal Expansion</i>
Silicon
ULE
Cer-Vit
Beryllium
3. <i>Scatter</i>
ULE/Fused Silica
Cer-Vit
Silicon
Beryllium

Temporal Stability

Temporal dimensional stability is probably the least understood requisite property for a space mirror. Sources of dimensional instability are:

1. Relaxation of residual stresses
2. Phase changes
3. Anisotropic properties within polycrystalline bodies
4. Chemical gradients
5. Physical property gradients
6. In-orbit changes in physical properties.

The categories in this list are broad enough to encompass all forms of dimensional change; however, the concern in the first five categories is actually with inhomogeneous behavior. Uniform changes in dimensions are manifested as focal shifts that may be readily corrected.

Because sources of energy to activate dimensional changes, such as applied mechanical stresses, thermal gradients, and ionizing radiation, will be inhomogeneously distributed throughout the mirror volume, the sources of dimensional instability must be minimized rather than homogenized. Therefore, from a dimensional stability point of view, it appears that pure, thermodynamically stable, stress-free, isotropic, and refractory materials are desired. The last item on this list is not commonly considered an important factor, but it can be a useful indicator. The melting temperature is one of the first properties to be determined when a new compound is discovered. Such properties as recrystallization temperature and activation energy for self-diffusion are usually proportional to the melting temperature; hence, refractory materials should be more stable.

At Perkin-Elmer, we have been studying the temporal stability of mirror materials. This program has included very close liaison with the materials manufacturers to insure that the complete sample history is recorded. The purpose of the program is to measure very accurately the changes in dimension and to attempt to identify and to eliminate the sources of instability. Examples of this detective work are described in papers by R. E. Maringer and J. W. Moberly.

The data to be reported are obtained with an interferometer developed as part of this program. Samples 4.2 inches (106 mm) in diameter are placed in a closed-loop, servo-stabilized Fizeau interferometer. Fringe positions are read on 40 or more equally spaced scans. The resulting 300 or more data points are used to compute the best fitting (root-mean-square criterion) plane and the departure at each data point. The data acquisition and reduction is good to at least $\lambda/300$, and the reproducibility is $\lambda/1500$. This means that the results of a 4-week test are accurate to

Table 5. Stability of Selected Materials

Material	Thermal Stability* (nm/°C)	Temporal Stability* (nm/year)
Fused Silica	0.019 to 0.082	23 to 50
Cer-Vit	0.024 to 0.076	17
ULE	0.040 to 0.070	32 to 38
Beryllium	0.64 to 7.4	40 to 600
Beryllium Oxide	0.019	—
Silicon	0.019	—

*Reported as the change of rms figure

better than 40 nanometers per year. Improved precision is available by increasing the observation period.

Twelve samples are stored in the instrument and thermostated to $\pm 0.01^\circ\text{C}$. The samples are positioned under the reference several times a week, and interferograms are taken. Test cycles have been continued for up to 8 weeks.

In order to condense the massive amount of data into a presentable form, table 5 lists the change in rms figure in units of nanometers per year. A variety of sample types are shown. The range of measured values indicates the best and worst samples tested thus far. The spread in the results on beryllium reflects the improvement we have attained in sample preparation.

A great volume of sample history can be found in the ARPA Report (2nd Annual Technical Report, Perkin-Elmer No. 9383; AD No. 842356). The results may be summarized:

1. The instability observed in the dielectric materials is within a factor of two of the instrument limit.
2. Kanigen-coated beryllium is unstable.
3. Properly made beryllium appears to be stable enough for consideration.

4. Preliminary measurements on silicon and beryllium oxide indicate that these materials are also stable.

The reason for testing numerous small samples was to accumulate data on a variety of sample materials and fabrication techniques. The results to date have been very gratifying; however, the question of scaling must be considered unresolved. It is apparent that the maintenance of a precisely controlled environment becomes more difficult as the volume increases. Therefore, we feel strongly that, after incorporating our current findings into the manufacturing process, it will still be necessary to test large samples for temporal stability prior to finalizing the design of a large, orbiting, astronomical telescope.

In orbit, dimensional changes must be considered to insure a long, operational life. An obvious, but not fully studied, source of damage is ionizing radiation. The dose rate is very orbit-dependent. Even with elaborate shielding, the optics will receive a significant gamma dose. In addition, the first surface will be exposed to protons, electrons, and the entire electromagnetic spectrum.

What we know about the effects of ionizing radiation on optical materials can be briefly summarized. Neutron, proton, and heavy ion bombardment are known to produce significant changes in the physical properties of fused silica (including density and index of refraction). A saturation dose of 4×10^{19} neutrons/cm² increases the density of fused silica by 2 percent. In space, a diverse spectra of electron and proton energies is encountered, ranging from a few keV to hundreds of MeV. The protons will be stopped by tens of millimeters of material. Electrons of the same energy penetrate at least an order of magnitude further into matter and produce large quantities of *bremssstrahlung* radiation. Because the high energy *bremssstrahlung* is so penetrating, the entire vehicle will be exposed to a fairly uniform dose of gamma rays. The particle flux is very altitude-dependent. On the other hand, if an orbit is selected to avoid the Van Allen belts, the low-energy solar electron flux is on the order of 10^{12} /m²/sec; hence, the

annual gamma dose will be on the order of 10^{14} rads per year.

Since an axial proton-and-electron-dose gradient will be produced in the primary mirror, a change in the surface curvature can be anticipated. Presumably the same effects will be found in other materials as they are measured.

Although this conference is concerned with the reflecting telescopes, radiation effects in transparent materials (corrector plates, alignment telescopes, etc.) should be mentioned. Figure 2 shows the radiation-induced absorption at a wavelength of 500 nanometers for several optical glasses as a function of x-ray dose. Figure 3 presents the change in index as a function of dose for the same glasses. Some glasses do show a measurable change in properties for very low doses.

Manufacturing Status

Mirrors in excess of 150 inches (3.8 meters) have been manufactured from fused

silica, and comparably sized Cer-Vit mirrors are currently being heat-treated. This can be taken as *prima facie* evidence that the manufacturing technology is available to prepare large, dielectric, mirror blanks. It must be remembered, however, that no homogeneity data of the required sensitivity exist on such massive pieces of material. There are also other areas of concern, particularly the polishing, testing, and dimensional stability of such a large mirror.

The reason for these uncertainties is the lack of experience. No diffraction-limited mirrors of this size have ever been made. In fact, there is no test facility capable of testing such a mirror. The reference mirror for the 100-inch (2.5-meter) test facility at Wright-Patterson Air Force Base has just been tested by several groups and found to be 0.3 λ astigmatic. (The details of this test are presented in the paper by W. Pershing.) Repeated testing of this mirror in vacuum can provide some of the accurate temporal-stability data needed on large samples. Additional data can

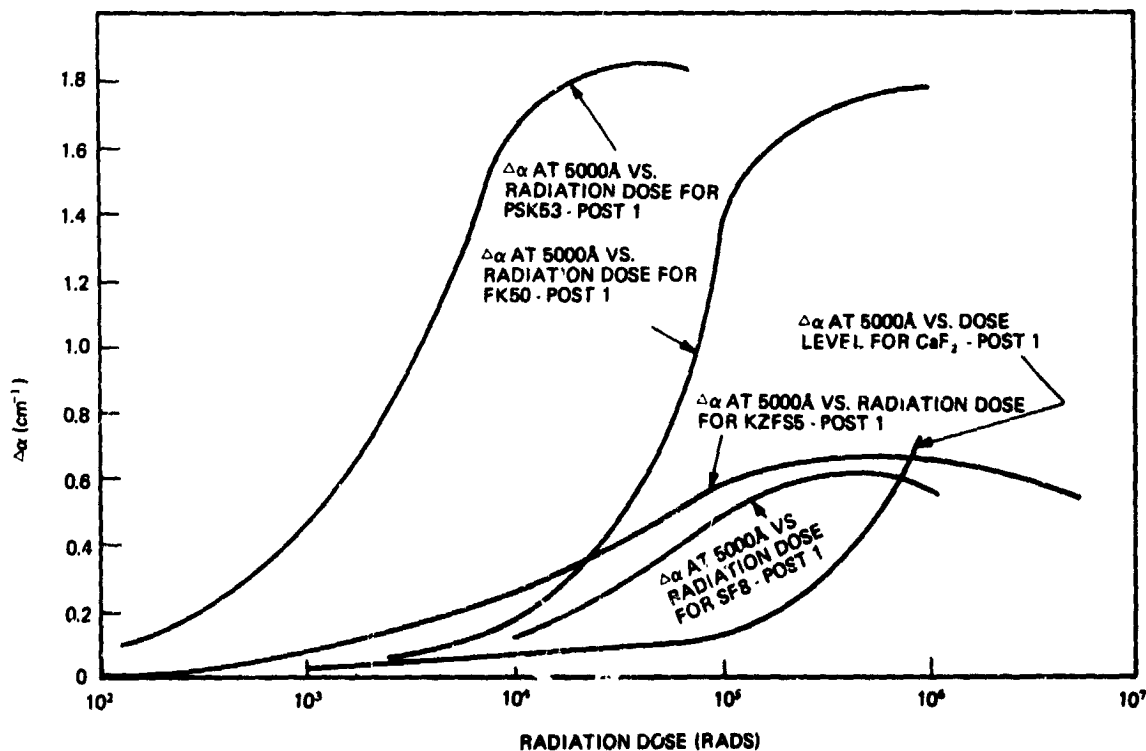


Figure 2. Radiation-induced absorption as a function of radiation dose for various optical glasses.

be obtained by repeated testing of mirrors for the Orbiting Astronomical Observatory (OAO) and Apollo Telescope Mount (ATM) programs.

The situation is even less satisfactory with the other materials. Stable beryllium mirrors can be manufactured in sizes up to approximately 20 inches (0.5 meter), and silicon samples up to 12 inches (0.3 meter) have been prepared. Very extensive development is required before beryllium and/or silicon mirrors 1 to 3 meters in diameter can be manufactured. The earlier remarks about testing would also apply to these mirrors.

Beryllium oxide has a favorable combination of physical properties for mirror applications. Unfortunately, commercial manufacturing practice yields low density (96 percent) and hence poor reflectivity. Translucent beryllium oxide has been produced in the laboratory in small samples. A very considerable amount of binder is added to the translucent material; this may detract from the dimensional stability.

Materials Technology Development Required Prior to Orbiting a Large Astronomical Telescope

At this point in time, it is tempting to assume that there will be several orbiting observatories, each with its own prime mission, such as solar observation, survey of the universe, etc. With this philosophy, we can say with safety that optical figure and dimensional stability will be the primary technical objectives of the designers, with weight and thermal response alternating between second and third in priority.

Because of the massive development required to perfect the manufacturing process and control for any material, the number of candidates should be limited as rapidly as possible. At this time, I feel that we have four candidates: beryllium, silicon, Cer-Vit, and ULE. In some ways, this is a very uneven competition. Although the military and space programs have prompted the rapid development of beryllium technology, new facilities will be required to manufacture large mirrors.

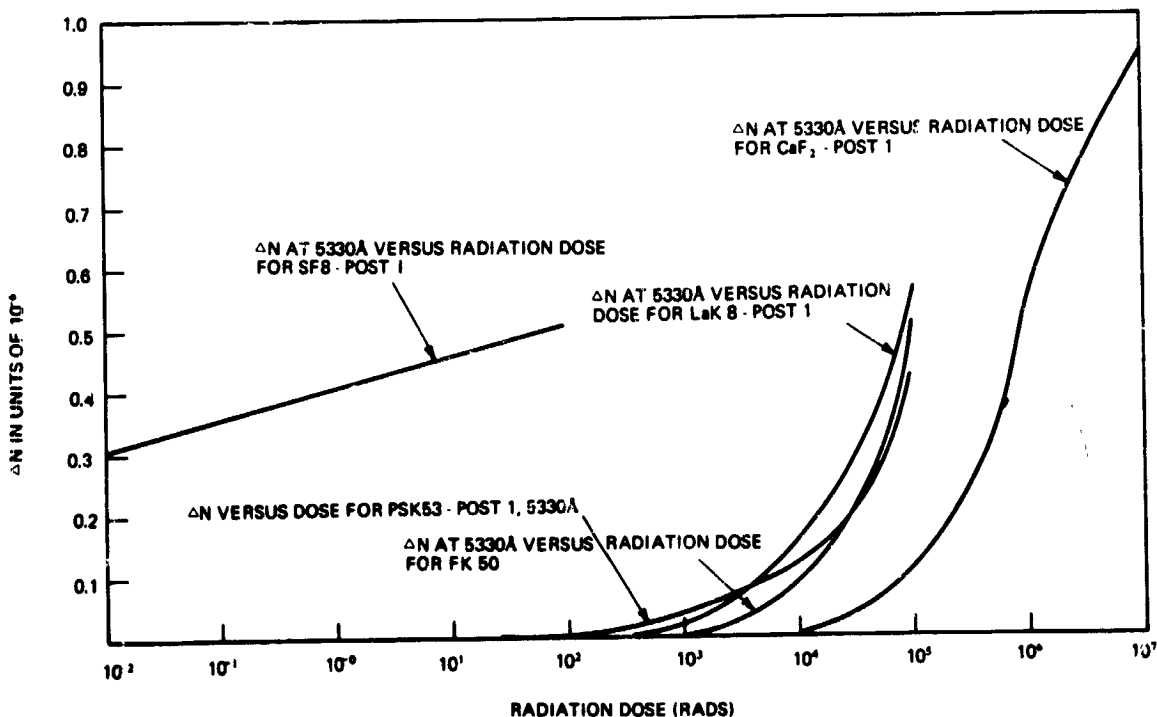


Figure 3. Change in index as a function of radiation dose for various optical glasses.

The semiconductor application of silicon has made it one of the best understood materials known to man. Again, manufacturing techniques must be developed before large mirrors can be prepared. The manufacturing technology of the new dielectric materials is in much better shape. On the other hand, the "unavailable" materials appear to be superior to the new dielectrics. This impasse can be broken by the following steps:

1. Measure the effect of ionization radiation on the dimensional stability of small samples of all four materials.
2. Extend the dimensional stability measurements to cryogenic temperatures.
3. After a period of scale-up, measure the dimensional stability of several fairly large mirrors of each material that passed the radiation test.

Step 3 is time-consuming and expensive, but the penalty for not employing the best material is incalculable. If the mirror is unnecessarily heavy, some instruments will be omitted and some astronomical data will remain uncollected. Conversely, if the figure

of the mirror changes drastically within a short period of time, the telescope will become more or less useless.

Mirrors in the 1-meter-diameter range could be manufactured from each material, mounted on a standard mount, tested, employed by astronomers in the mount, and retested at intervals. This sequence is suggested because the mirrors will be of better quality than terrestrial observatories can utilize and because test facilities are expensive.

A parallel effort during this time period should be the optimization of the design for the mirror and mount. A continuing dialogue between the numerous technical disciplines is essential throughout this development phase. Such a dialogue is justifiable for, if the system planners elect to use a cold mirror without informing the materials people, the radiation and stability measurements will be made incorrectly.

With careful planning and development, I feel that large, dimensionally stable, diffraction-limited optics can be placed in orbit.

N70-36695

Problems in Adapting Small Mirror Fabrication Techniques to Large Mirrors

Howard D. Hall
Owens-Illinois, Inc.

Introduction

More mirrors over 100 inches in diameter are currently being fabricated or planned than have been completed to date. As a result, there is a shortage of experienced personnel available to fabricate these pieces, which must necessarily be worked by people whose experience has been limited to smaller sizes. Difficulties can occur when tools and techniques that have been proven for smaller mirrors, 40 to 60 inches in diameter, are used to fabricate large mirrors. Therefore, I will discuss some of the problems we at Fecker Systems Division have encountered in this area and some of our solutions to these problems. I would be less than honest if I claimed these are the *right* answers, for optical fabrication techniques vary greatly from optical shop to optical shop and between individuals in the same shop. Furthermore, I am limited to the problems that we have actually encountered and to the solutions and rules of thumb that have worked for us.

Microripple

The first problem that occurs in working large mirrors is the decrease in the size of the allowable slope errors. A 4-inch-diameter mirror can resolve 1 arc second, and slope of $1/4$ of an arc second should not detract appreciably from its performance. A 100-inch diameter mirror can resolve $1/25$ of an arc second, and slope error must be limited to $1/100$ of an arc second to utilize it to its fullest. Thus, the larger the mirror (everything else being equal), the more carefully it must

be fabricated and tested. Not only must zonal irregularities be virtually eliminated, but also the "texture" or microripple produced in the mirror's surface by the polisher must be controlled. This microripple may be virtually invisible to both knife-edge and interferometric testing, but it causes light to fall outside the predicted blur circle. The appearance and degree of this microripple depends on polishing pitch hardness, polishing compound, size and configuration of the facets in the polishing surface, polishing pressure, velocity of the polishing tool relative to the workpiece, the speed and asphericity of the mirror, and the size of the polishing tool relative to the mirror. Although very little work has been done concerning the control of microripple, it appears that large polishers, large but unequally sized facets, soft polishing pitch, light polishing pressure, and slow polishing speed tend to minimize or eliminate microripple. The degree to which any measures may be pursued is limited by other considerations. For example, polishing pitch soft enough to completely eliminate microripple may cause an unacceptable "roll-off" at the edge of the mirror; extremely large facets may cause an unacceptable increase in "cold-pressing" periods. If, however, care is taken, techniques can be found that suppress microripple while allowing the mirror to be figured.

Compliance

The compliance or lack of stiffness of large mirrors causes many difficulties unless carefully considered. The compliance of a mirror varies as the square of the diameter for a fixed diameter-to-thickness ratio. A

100-inch-diameter mirror that is 12 inches thick is equivalent to a 40-inch diameter mirror approximately 2 inches thick. Most opticians would consider the larger, thicker mirror less demanding and the thinner, smaller mirror more of a challenge although the two are equivalent. The problem of the compliance of larger mirrors can be solved easily by a well-designed conservative support system. We use a relatively simple relationship for determining the number of supports required. Although the derivation of this relationship is not rigorous, it has proved to be satisfactory for a variety of pieces, ranging from 40 inches in diameter by 4 inches thick, to a mirror 80 inches in diameter by 3 inches thick, to a mirror 103 inches in diameter by 12 inches thick. The number of support points is:

$$N = \frac{1.5r^2}{t} \sqrt{\frac{\rho}{E\Phi}}$$

where N = Number of support points

r = Semi-diameter of the mirror in inches

E = Young's Modulus in pounds per square inch

Φ = Quality of the mirror in allowable surface deformation in inches

ρ = Density in pounds per cubic inch

t = Thickness in inches

(For $\lambda/20$, $\Phi = 1 \times 10^{-6}$ inches)

For $\lambda/20$, $\sqrt{\frac{\rho}{E\Phi}}$ has the following values:

Material	$\sqrt{\frac{\rho}{E\Phi}}$
Cer-Vit®	0.0798
Beryllium	0.040

Aluminium	0.099
Steel	0.099
Fused Silica	0.087
Pyrex, E-3, and	
Duran-50	0.093

It should be noted that these are the number of points necessary to support only the mirror itself, not the mirror and polishing tools. The number of support points must be increased depending upon the weight and stiffness of the polishing tools.

A great variety of systems have been successfully used to support mirrors, including carpeting, foam rubber, and even kinematic devices. Large mirrors deserve supports more sophisticated than foam rubber, but kinematic systems become cumbersome. Figures 1 and 2 show a support system used extensively at Fecker for a variety of work pieces. Each support is a mechanical spring that has been individually calibrated and cut to length to ensure uniformity from point to point. Each spring is permanently attached to the table of the polishing machine.

To prevent the mirror from rocking as the polisher moves over the mirror, some (or



Figure 1. Uncovered view of individual pitch-spring.

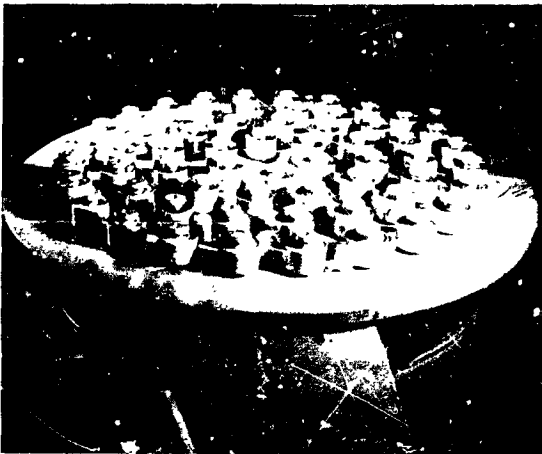


Figure 2. View of pitch-springs permanently attached to table of polishing machine.

all) of the springs are damped by submersion in very soft pitch. A cross-section of such an assembly is shown in figure 3.

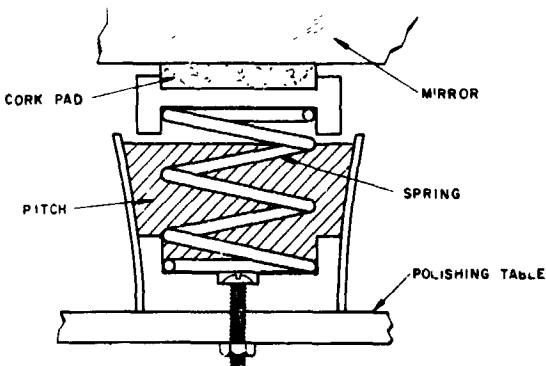


Figure 3. Cross-section of pitch-spring support.

Grinding and Polishing Tools

The compliance of both grinding and polishing tools varies in much the same way as the mirror itself. If a simple ribbed casting is scaled, the compliance varies as the square of the diameter and the unit pressure exerted upon the workpiece by the polisher varies directly with diameter. Thus, a large, compliant, polishing tool will flex and deform when overhanging the mirror in an unex-

pected and somewhat unpredictable manner. The effects produced by such a tool are similarly unexpected and unpredictable. In addition, a compliant tool will tend to conform to the surface of the mirror and will not remove cylinder or astigmatism. If a large tool is designed so as to maintain stiffness, it must necessarily become heavy and thus further increases the pressure between the polishing tool and the mirror. There seems to be little choice in designing, polishing, or grinding tools for a large mirror; if they are to work in a predictable manner and are to produce a regular surface, they must be stiff. The resulting increase in polishing pressure, however, must be compensated. This has been done most frequently by counterbalancing the tool. An alternate approach has been used successfully at Fecker. This is a stiff, lightweight tool fabricated from two plates and a honeycomb core. These three pieces are joined together by epoxy. The resulting tool can be sufficiently stiff to be predictable yet light enough to need no counterbalancing. We have used such tools up to 100 inches in diameter. Such a tool is shown in figures 4 and 5.

Difficulties also occur in the reduction of a high intermediate zone on a large mirror. With small mirrors, the optician may simply alter the shape of the polishing tool, scraping away the pitch from the areas corresponding to low zones and leaving a high area corresponding to the high area to be removed.



Figure 4. Honeycomb tool, used without counterbalancing.

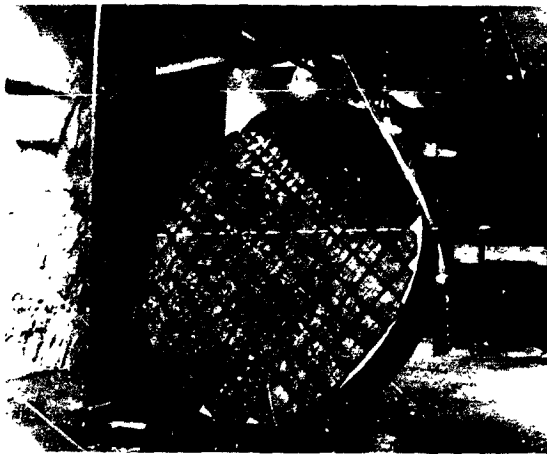


Figure 5. Honeycomb tool showing honeycomb core.

The reduction in area of the polishing tool causes an increase in polishing pressure, but with small mirrors little difficulty is encountered. With large mirrors, the polishing pressure is generally high to begin with, and the reduction in area causes an unacceptable increase in polishing pressure. We have chosen to correct this difficulty by using ring polishers rather than by using a variable counterbalancing system. Figures 6 and 7 show a "family" of such tools and their driving spider. This type of tool has proved extremely useful in working mirrors very fast. A single zone can be vigorously polished while maintaining circular symmetry.

These are some of the problems that occur when tools and techniques that have been used for small mirrors are duplicated to fabricate large mirrors. I hope that this

presentation of some of Fecker's solutions to these problems will be useful both in application and in stimulating the development of other new techniques.

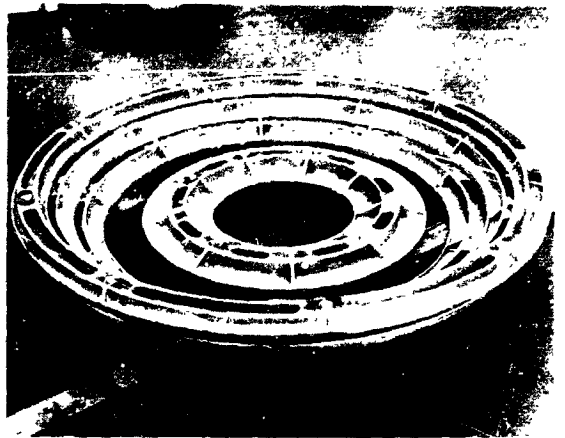


Figure 6. Family of ring tools.

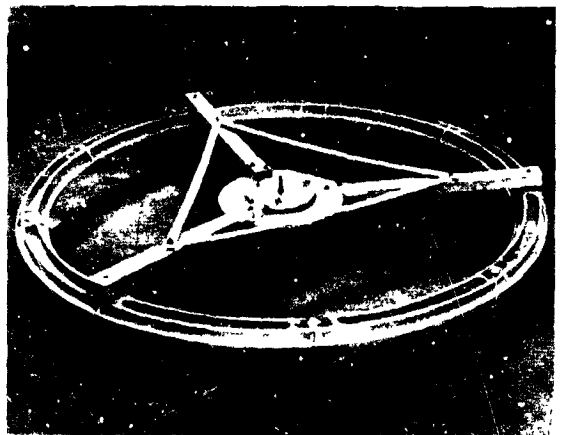


Figure 7. Ring-driving spider.

Surface Smoothness of Large Astronomical Mirrors: A Collection of Foucaultgrams

Donald A. Loomis
University of Arizona

N70-36696

Introduction

The classic $f/5$ primary mirror for large astronomical systems is becoming a thing of the past. Designers are beginning to choose faster f -ratios for their optical telescopes. These optical systems are more efficient; their telescope mounts and housing costs are much lower for equal diameters of primary mirrors. As we gain in this direction, however, we seem to lose in optical performance. As the f -ratio becomes faster, we find that both primary and secondary mirrors take considerably longer to aspherize, thus requiring more skill on the part of the optician to produce a surface that will form images compatible with the computer ray traces.

The main difficulty in making long-focal-length mirrors seems to be in maintaining a symmetrical figure. With the faster mirrors, there is a greater problem in maintaining circular symmetry because the aspherizing requires a greater removal of glass, thereby increasing the "washboard" effect. There is also the problem of removing zones that are produced on the surface with the small tools used for the aspherizing. A typical size for a polishing tool that would be used to smooth a 72-inch, $f/4.2$ mirror would be in the order of 21 inches in diameter. In comparison, the tool to do the same job on a 90-inch $f/2.7$ mirror would be 8 inches in diameter.

It is quite obvious that the burden of producing a good, fast f -ratio mirror is placed upon the optician. Very little communication has taken place between opticians who have produced large optical systems. It is difficult to say whether or not it is because each tries to protect the secrets that have taken him

years to develop. There has been a gradual conveyance of ideas, usually occurring through either department heads or directors who seem to have many of the facts, but this is a poor substitute for the man who is really doing the work and who is faced with this problem from the beginning of the job to its completion. A willingness to exchange ideas and discuss problems could separate good techniques from some of the "old standby" methods, many of which need to be reviewed. This could improve the state-of-the-art considerably.

Analysis of one of the knife-edge photos of one of the major astronomical mirrors in use today reveals that much of the surface roughness (orange peel) can be attributed to the technique used by the opticians. It was very popular to use small cork tools for removing small splotchy zones on some of the large mirrors made in the past. Many of the optical machines today are designed to drive full-sized tools, which are usually very heavy and require a good deal of force to move around on the face of the mirror. This same machinery can also be used to drive the small polisher. The loading, which is approximately 1/5 pound per square inch on the full-sized tool, will often increase to 7 pounds or more per square inch on the sub-sized tool. This removes glass very rapidly, generating quite a bit of heat, with a scrubbing effect that will cause an orange peel surface.

This report includes a number of foucaultgrams with comments on various large astronomical mirrors. Because it is impossible to pinpoint the reasons why many of the mirrors are rough or slightly warped, they are presented to stimulate thinking on

the problems of surface generation and smoothness. Also included in this report are pictures of spherical mirrors that illustrate the surface that we would like to obtain in large aspheric mirrors. The final series of photographs deals with a technique that was developed by the Optical Sciences Center of the University of Arizona for removing

astigmatism and smoothing out the wash-board effect.

200-Inch, $f/3.3$, Pyrex

Final testing on this mirror (fig. 1) was accomplished in the telescope. Photographs A and B have short exposure, thus revealing

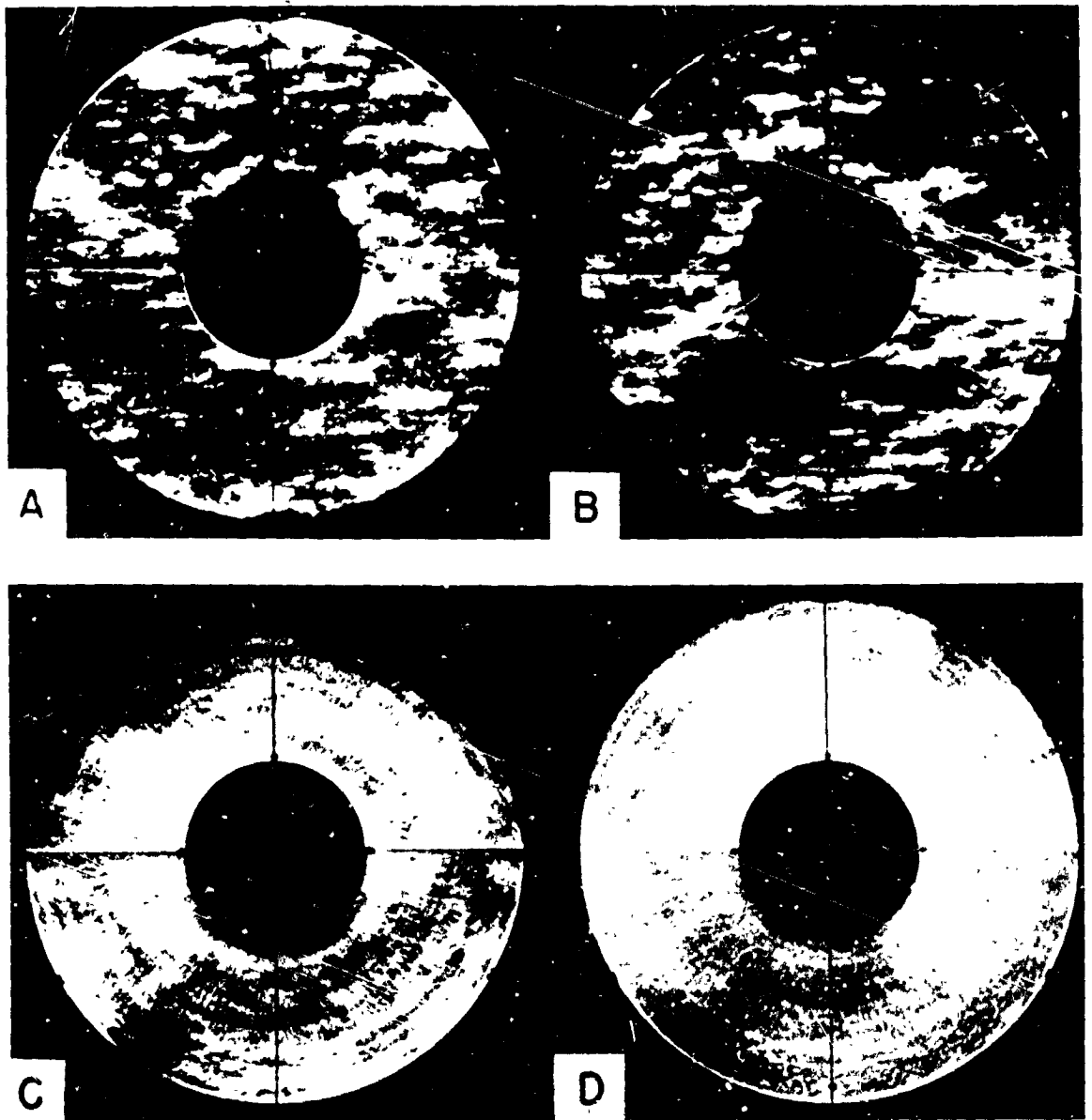


Figure 1. Foucaultgram of Palomar Observatory, 200-inch (508-cm), $f/3.3$, Pyrex mirror, 1948. (Courtesy of I. S. Bowen, Mt. Wilson and Palomar Observatories.)

seeing conditions in the telescope. In photographs C and D, which have a long exposure, seeing conditions are averaged out, thus revealing the true mirror surface.

Because the 200-inch mirror is extremely flexible, astigmatism is reduced to a minimum through the use of the support system in conjunction with the Hartmann tests.

Probably the most obvious problem on the surface of this mirror is the rough appearance (orange peel). A mirror of this f-ratio was quite a bold undertaking in its time, considering its size and f-ratio.

120-Inch, f/5.0, Pyrex

Figure 2 is an unfinished mirror; the photograph illustrates clearly the problems confronting Hendrix. The removal of the lumps and the overcorrection required the use of many Hartmann plates coordinated with knife-edge photos.

This mirror was removed from the optical shop and installed in the telescope for these tests. Means were provided for testing the mirror in the optical shop, but these were found to be inadequate, primarily because of the flexure of the mirror while being tested



Figure 2. Foucaultgram of Lick Observatory, 120-inch (305-cm), f/5.0, Pyrex unfinished mirror, 1959. (Courtesy of H. R. Cowan, Lick Observatory.)

on edge. (A long, horizontal tunnel was provided for this work and later abandoned.)

Figure 3 shows the results of Hendrix' efforts. The main problem encountered in producing this fine surface was maintaining a surface of revolution. Overall, the aspheric is very mild in comparison with some of the new fast mirrors, but the flexibility of this mirror was so great that even the support blocks on the polishing machine were causing small lumps. These would be polished off during smoothing operations; consequently, when the mirror was raised on its support system in the telescope, these areas would show up as depressions. It was impossible to work the mirror with its support system in use without damaging the bearing surfaces and reducing their efficiency.

After a number of years of careful evaluation and hand-figuring, the mirror was completed. It is one of the few examples of hand-correcting an optical surface of this size.

82-Inch, f/5.0, Pyrex

Figure 4 is the 82-inch McDonald; the foucaultgram is of the primary and secondary

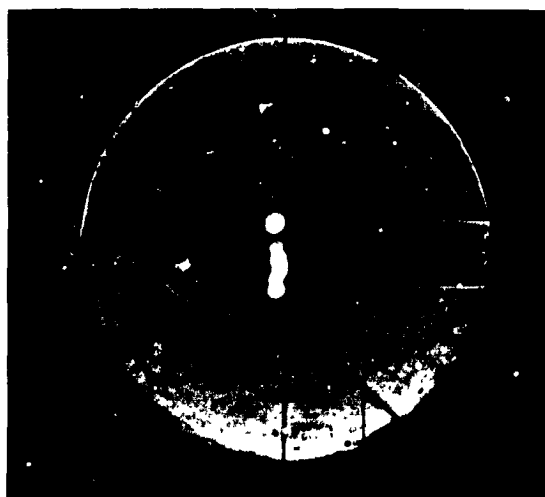


Figure 3. Foucaultgram of Lick Observatory, 120-inch (305-cm), f/5.0, Pyrex mirror, 1959. (Courtesy of H. R. Cowan, Lick Observatory.)

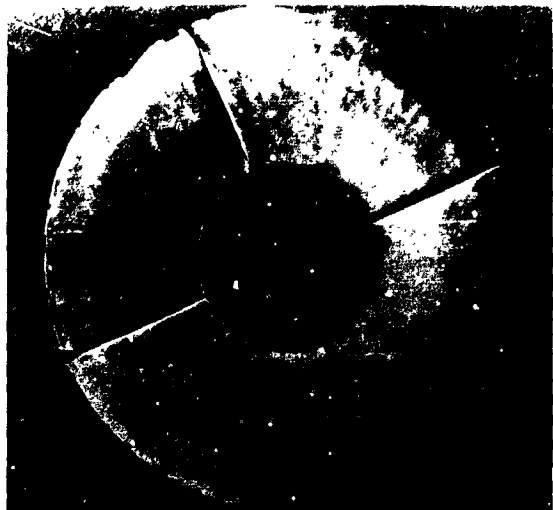


Figure 4. Foucaultgram of McDonald Observatory, 82-inch (208-cm), f/5.0, Pyrex mirror, 1939. (Courtesy of J. Texereau, *Sky & Telescope*, 28, 6, 1964.)

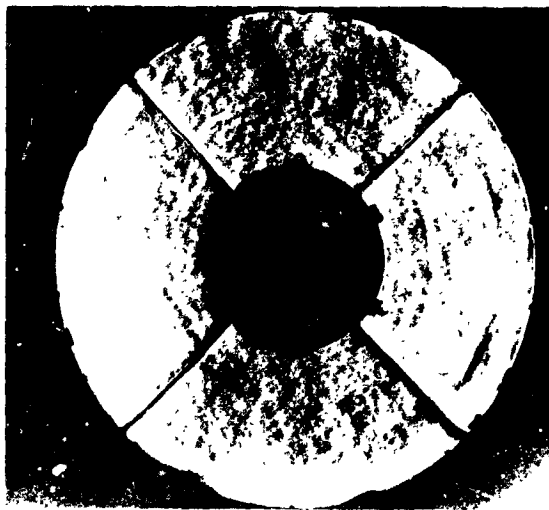


Figure 5. Foucaultgram of McDonald Observatory, 82-inch (208-cm), f/4.0, Pyrex mirror, 1939. (Courtesy of J. Texereau, *Sky & Telescope*, 28, 6, 1964.)

mirrors tested together. One of the problems with which the optician is faced, especially when working with some of the older borosilicate glasses, is determining how much to leave the primary undercorrected to compensate for falling temperature conditions in the telescope. In the higher expansion glasses, the perfectly corrected mirror, especially in the thick, solid type, will usually appear overcorrected throughout most of the best viewing hours. In addition, there is the problem of not knowing exactly what the support system will do to the mirror when it is installed in the telescope, since most of the astronomical mirrors are not made on their support systems in the optical shop.

82-Inch, f/4.0, Pyrex

Figure 5 shows the 82-inch mirror after Texereau accomplished his work on refiguring the secondary to match the primary mirror.

193-Centimeter (77-Inch), f/5.0, Plate Glass

Figure 6 is a 77-inch mirror of plate glass.

84-Inch, Spherical Surface

Before the 84-inch mirror was aspherized, it was considered wise to polish the



Figure 6. Foucaultgram of Observatoire de Haute Provence, 193-cm (77-inch), f/5.0, glass mirror, 1958. (Courtesy of J. Texereau, *Sky & Telescope*, 28, 345, 1964.)

mirror to a sphere to see if there was any detectable astigmatism. We used a full-sized tool, which weighed in the order of 2000 pounds, covered with a very soft polishing pitch about 1/2-inch thick. Since this was just to get the surface polished out, we used an unmilled Barnesite polishing agent. Figure 7 shows the surface it produced, which we found very interesting. As a result of this experience, we decided not to use the same combination of pitch and polishing agent for our final smoothing work.

After the mirror was polished out, we carried on to a spherical surface by using a harder pitch and milled rouge. The very smooth surface that was produced is good evidence to substantiate the need for technique research.

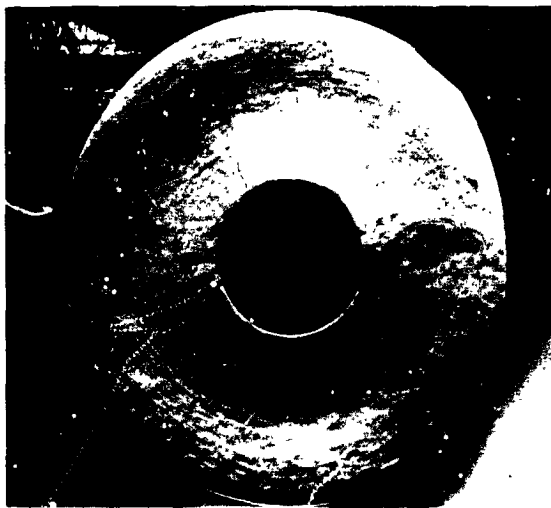


Figure 7. Foucaultgram of 84-inch spherical surface.

84-Inch, f/2.6, Pyrex

Figure 8 shows the 84-inch mirror at various stages of work, as photographed through the null tester. The null tester seemed to be very helpful in achieving surface smoothness. It revealed all the small defects, but it seemed to overlook some of the larger slope problems.

The mirror looked quite symmetrical through the null lens but showed some

astigmatism when tested in the telescope. Since the null lens has to be collimated when in use, it is easy to collimate out astigmatism and to proceed with the work without ever knowing this until the final testing in the telescope.

Figure 9 is a Foucaultgram, taken in the telescope, which shows up surface deformations that were not detectable in the shop. Zonally, the mirror appears about the same.

Hartmann photographs are taken in the telescope and then plotted to give the size of the image and light concentration in the image. These Hartmann profiles, in figure 10, are helpful in determining astigmatism and correction, but they do not tell much about the smoothness of the mirror. Hartmann numbers are raw numbers; they often do not reflect the quality of the optic.

36-Inch, f/3.5, Pyrex

Even at f/3.5, smoothness is not a great problem (fig. 11). There are a few concentric zones, probably in the order of about $\lambda/15$, which are not as noticeable as the 1-1/2 wavelengths of astigmatism.

72-Inch, f/4.2, Duran 50

The 72-inch mirror in figure 12 appears to be quite smooth, both in tests in the optical shop and tests in the telescope. Because of the mild aspheric curve, parabolizing was accomplished in approximately three weeks with a half-sized tool. Upon completion of this work, there were only a few minor ring zones to remove. One is slightly noticeable 8 inches from the edge. It is estimated that this zone is probably in the order of $\lambda/20$.

The appearance of this mirror in the shop resembled that of a good sphere. Probably the biggest problem in making this mirror was astigmatism. Since the mirror was tested on edge, it was hard to be sure whether the sag from the edge support was mirror

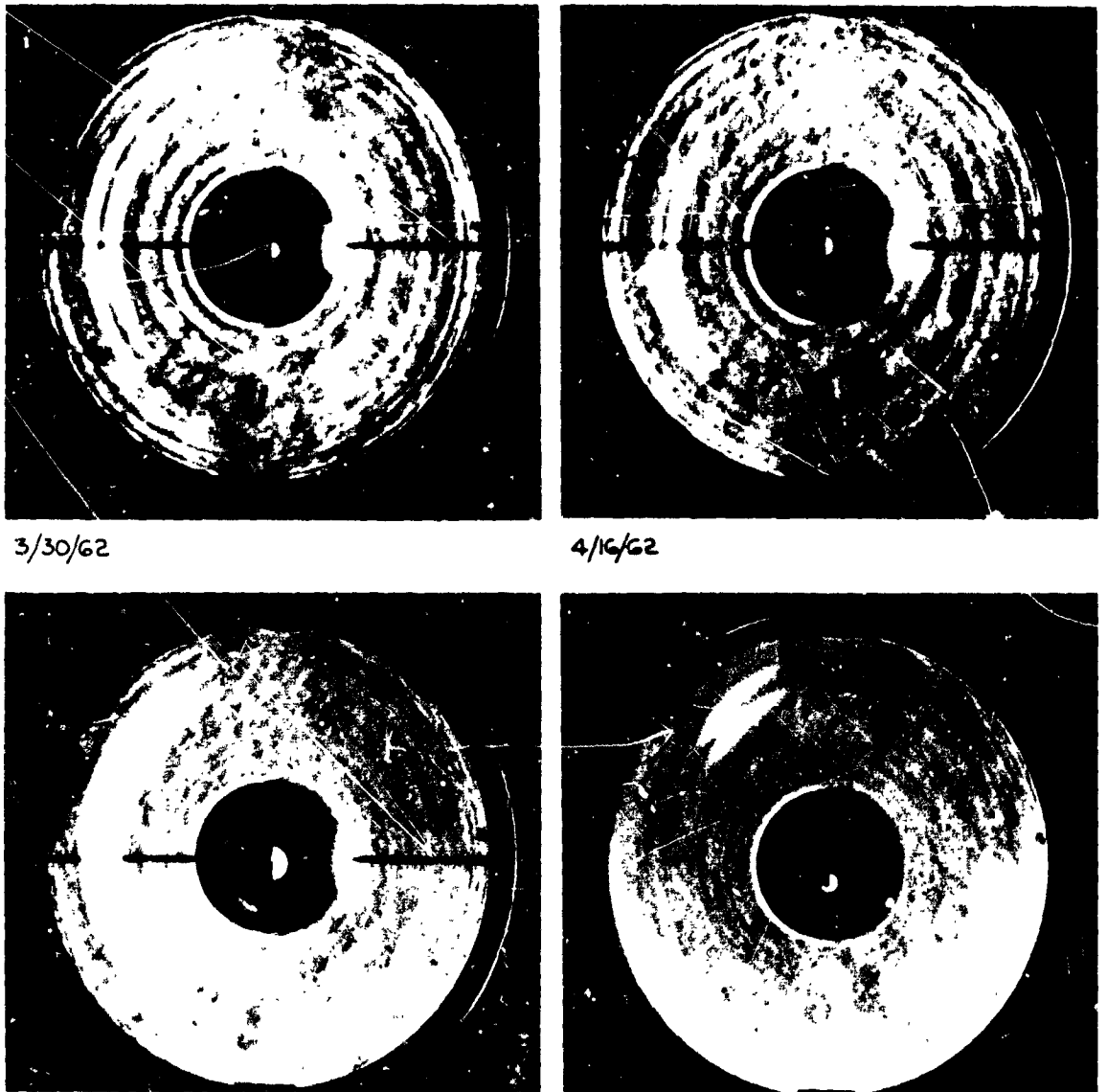


Figure 8. Foucaultgram of Kitt Peak Observatory, 84-inch (213-cm), $f/2.6$, Pyrex mirror, 1961.



Figure 9. Foucaultgram of Kitt Peak Observatory, 84-inch (213-cm), f/2.6, Pyrex mirror, 1961.

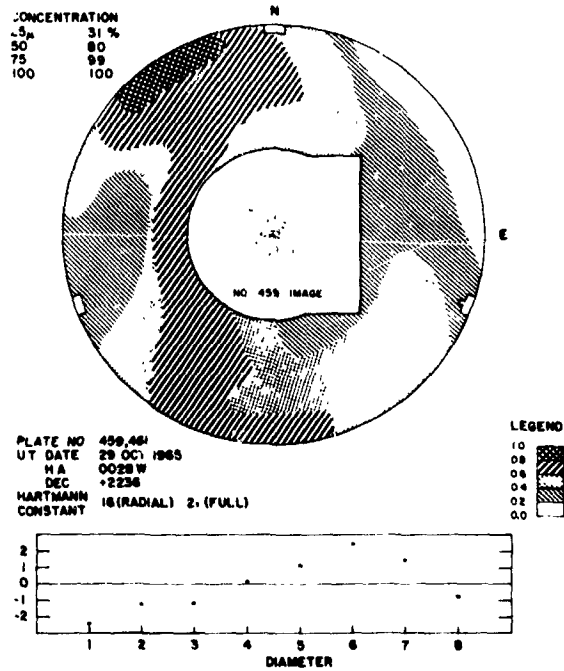


Figure 10. Hartmann profiles: Kitt Peak Observatory, 84-inch (213-cm), f/2.6, Pyrex mirror, 1961. (Courtesy of Kitt Peak National Observatory.)

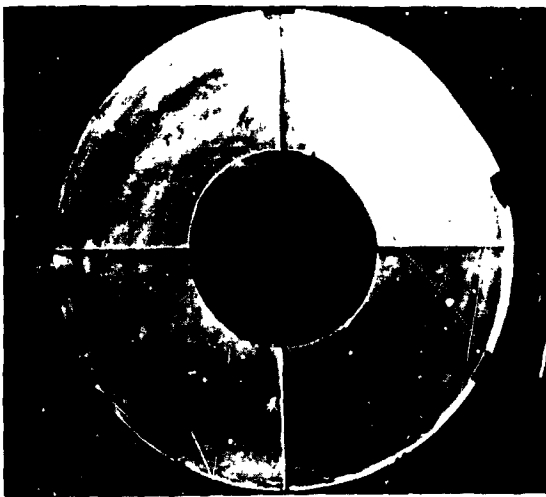


Figure 11. Foucaultgram of 36-inch, f/3.5, Pyrex mirror.



Figure 12. Foucaultgram of Lowell Observatory, 72-inch (183-cm), f/4.2, Duran 50 mirror, 1965.

droop or real astigmatism. Table 1 gives the reduction of the Foucault test, the last column representing height in wavelengths. The mirror was installed in the Perkins telescope and performed as optical shop tests had indicated.

60-Inch, f/3.3, Pyrex

The Foucaultgram in figure 13 was taken through a null tester. When finished, this

Table 1. Foucault Test of 72-inch, f/4.2, Duran 50 Mirror

No.	Reading	Lateral Displacement	Height (λ)
1	.000	.00000	.0000000
2	.013	.00005	.0000000
3	.035	-.00002	.0000000
4	.055	-.00004	-.0000000
5	.083	-.00020	-.0000003
6	.100	-.00009	-.0000005
7	.117	.00007	-.0000003
8	.144	.00004	-.0000003
9	.178	-.00013	-.0000005
10	.204	-.00005	-.0000006
11	.230	.00009	-.0000004
12	.265	.00000	-.0000004
13	.301	-.00005	-.0000005
14	.337	-.00007	-.0000006
15	.371	.00005	-.0000006
16	.406	.00021	-.0000002
17	.455	-.00012	-.0000004
18	.496	-.00006	-.0000005
19	.540	-.00007	-.0000006
20	.583	.00004	-.0000006
21	.635	-.00017	-.0000008
22	.683	-.00013	-.0000011
23	.725	.00030	-.0000006
24	.776	.00038	.0000000
25	.834	.00018	.0000003
26	.894	-.00006	.0000002
27	.949	.00006	.0000003
28	1.005	.00024	.0000007

mirror was quite smooth. By using equipment that was designed for small tools, we were able to keep the pressure on the polishing lap to approximately 1/4 pound per square inch. We found that, by using rouge milled for 100 to 200 hours, we were able to produce a surface that was very smooth and scattered very little light. No results are available at this time on the optical performance in the telescope.



Figure 13. Foucaultgram of Cerro Tololo Observatory, 60-inch (152-cm) Pyrex mirror, 1965.

90-Inch, f/2.7, Fused Quartz

The Foucaultgram in figure 14 was taken through the null tester. Further work and testing was done after this was made. The small artifacts were created by the microscope objective.

A mirror of this f-ratio presented quite a challenge to the optician, for there was little information available on grinding techniques for aspherizing. Therefore, instead of grinding in the hyperbolic curve, which is normally recommended on a mirror of this size and focal length, we decided to polish it in. It took a total of 6 months to polish in the correction and about 3 months to smooth out the small zones.

We found that we were able to smooth out small edge zones during the final figuring



Figure 14. Foucaultgram of Steward Observatory, 90-inch (229-cm), $f/2.7$, fused quartz mirror, 1969.



Figure 15. Three wire tests superimposed; Foucaultgram of Steward Observatory, 90-inch (229-cm), $f/2.7$, fused quartz mirror, 1969.

and to improve a 2-inch rolled edge to almost zero by using a 6-inch diameter tool with a quarter- to half-inch stroke and 140-rpm rotation and by placing the center of the tool over the area that was high. This produced a surface at the edge that seems to be smoother than the central area, which was smoothed by a 12-inch diameter tool with about an 8- to 10-inch stroke. It is believed that, because of the high asphericity of the mirror, the long stroke was producing a misfit between the optical surface and the polishing tool, thus creating a "digging" action at the extremities of the stroke. The no-stroke, rapid rotation technique is very selective. With a 6-inch diameter tool, we were able to pinpoint zones 2 inches wide at the edge. It is noted that this pinpointing action becomes more pronounced as the f -ratio decreases.

Three different wire tests have been superimposed on one print (fig. 15). The small artifacts were created by the microscope objective.

We used the wire method for testing at the radius. This produced a concentric ring on the zone for which it was focused. By plotting in different coordinates, we were able to keep track of the astigmatism, which seemed negligible enough to ignore at this point.

The surface is within $\lambda/8$ of the computed curve. Small circular zones were too small to measure with our wire test. We had set up a scatterplate interferometer to look at these small zones, but they did not show up. These zones are probably about $\lambda/20$.

The mirror is now being coated and will be tested very shortly. This will be the proof of the technique.

60-Inch Sphere, Aluminum

This 60-inch sphere has a 300-foot focal length (fig. 16) and was originally used in the McMath Solar Telescope.

The type of material used for a mirror is very important in terms of smoothness. This particular mirror was polished with Linde A by using a full-sized tool. It produced a 1/3-second image although the small gouges softened the image core considerably.

Probably the main reason for using this type of substrate was its thermal conductive qualities. This substrate is not recommended for high resolution optics.

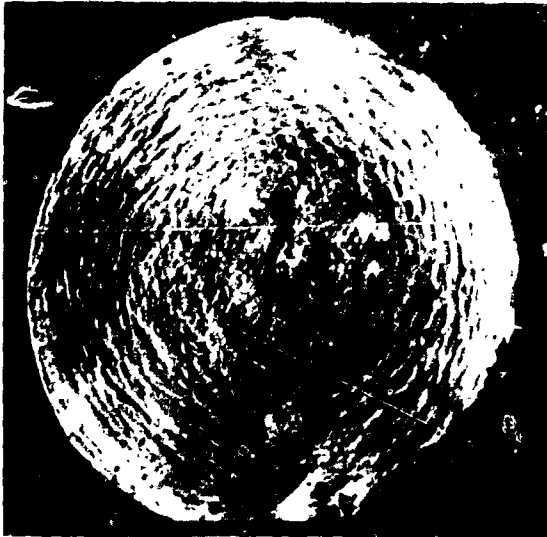


Figure 16. Foucaultgram of 50-inch sphere, aluminum mirror.

60-Inch Sphere, Fused Quartz

Figure 17 shows the quartz replacement mirror for the solar telescope. This mirror was figured by using the same technique used for the 60-inch metal mirror. The main difference was that we used rouge instead of Linde A. This surface produces very low scatter; it



Figure 17. Foucaultgram of 60-inch sphere, fused quartz mirror.

would be ideal if we could make shorter focal length mirrors of this smoothness.

16-Inch Sphere, Early Cer-Vit

The mirror shown in figure 18 is quite smooth even after having a blowtorch applied to the front face. The vertical stripes were caused by hot air.



Figure 18. Foucaultgram of 16-inch sphere, early Cer-Vit mirror, 1966.

36-Inch Sphere, Pyrex

Figure 19 is a phase contrast photo of a 36-inch spherical mirror. This mirror was produced, probably 30 years ago, by using Pyrex as a substrate. It is hard to say what the little gouges are; they are probably on the order of $\lambda/80$.

With the knife-edge test, this mirror appeared to be exceptionally smooth. It is interesting to compare this photo with a phase contrast photo of a 16-inch Cer-Vit sphere (fig. 20), which is representative of our newer zero-expansion glasses.

16-Inch Sphere, Cer-Vit

The phase contrast photo, figure 20, is of a 16-inch Cer-Vit sphere.

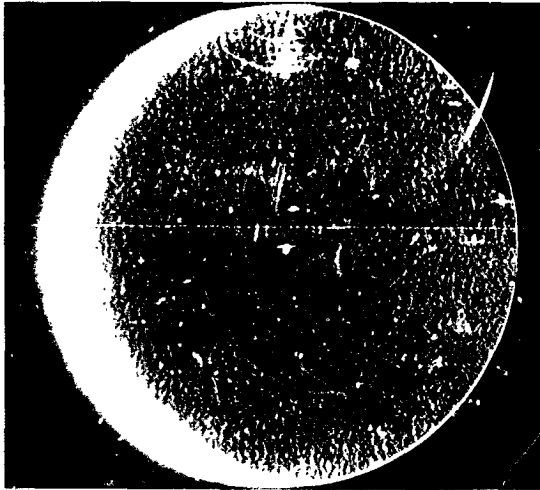


Figure 19. Foucaultgram of 36-inch sphere, Pyrex mirror.

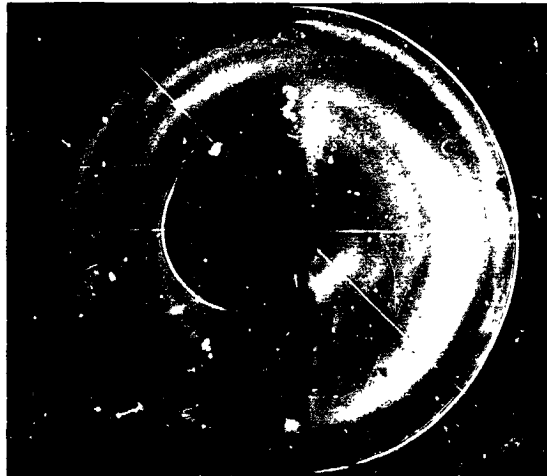


Figure 21. Foucaultgram of 16-inch, $f/1.68$, Cer-Vit mirror.

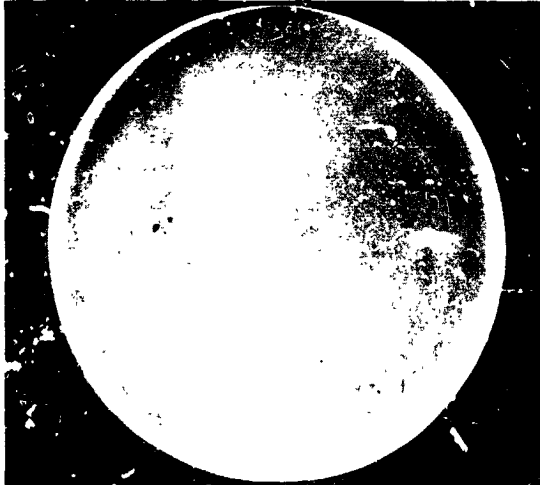


Figure 20. Foucaultgram of 16-inch sphere, Cer-Vit mirror.

16-Inch, $f/1.68$, Cer-Vit

Recently, the optical shop was requested to make a 16-inch, $f/1.68$ parabola (fig. 21). This parabola was to be sliced up into smaller off-axis paraboloids. We found that the total amount of aspheric was too great to polish out (approximately 0.007 inch). Therefore, we decided to grind in the parabolic curve.

Upon completion of this grinding, the mirror was polished out sufficiently with sub-

sized tools to examine the optical surface with a collimator. The mirror was not concentric; it had a number of zones that did not go all the way around. We tried local figuring to take out the astigmatism and found it partially successful, but it did not accomplish the work that we had hoped it would.

Figure 22 shows the mirror after spinning technique was used.

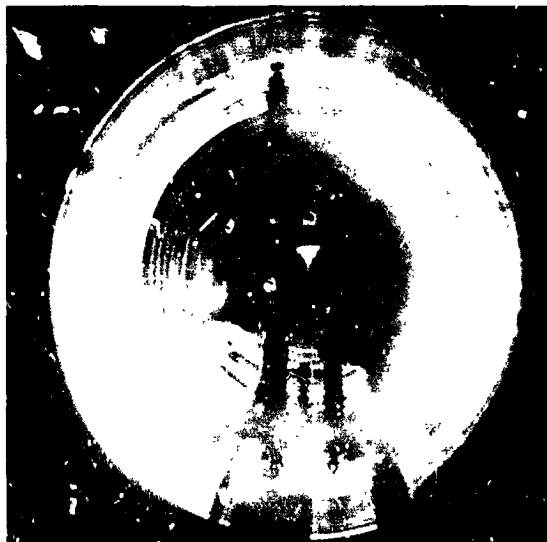


Figure 22. Foucaultgram of 16-inch, $f/1.68$, Cer-Vit mirror, after spinning.

At first we thought we would go back and start over again, but, after studying the problem, which is similar to problems the optician is faced with on larger mirrors, we felt that it was time for some experimentation.

A full-sized tool was made up and pressed on the surface of the mirror to insure a fit between the tool and the mirror; a covering of Barnesite was used between the surfaces to keep them from sticking. After sufficient pressing time was allowed, the mirror was spun at a rapid rate, approximately 100 rpm, with about a 1/2-inch stroke on the polishing tool to prevent any serious grooves from developing, until the general appearances of the glass resembled that of a phonograph record.

The surface was again polished with the sub-sized tools to remove the small circular zones. These zones had a "terrible" appearance but actually measured only fractions of a wavelength deep. They merely had great slopes.

These circular zones were removed in about 30 hours of polishing. We noticed a small amount of astigmatism still present. By repeating the spinning and repolishing the surface with the sub-sized tools, we achieved the surface shown in figure 23.

Even though the focal length of this mirror is very short and therefore is not as sensitive to slope errors as the larger optics, the mirror has a very good appearance for a 16-inch, f/1.68 parabola.

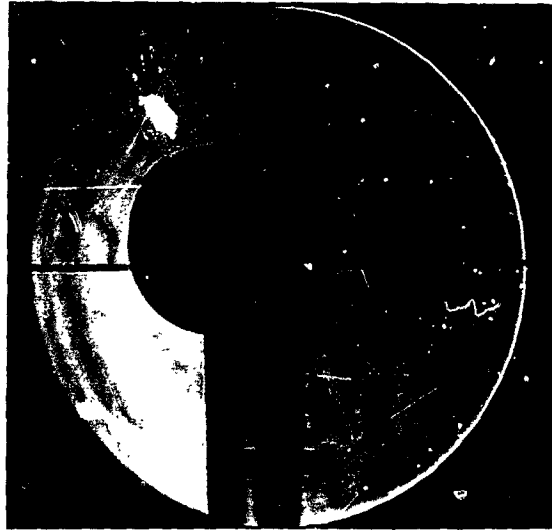


Figure 23. Foucaultgram of 16-inch, f/1.68, Cer-Vit mirror, after repeated spinning and polishing.

Conclusion

This experiment illustrates very dramatically the possibilities that are available for improving the state-of-the-art. Unfortunately, so much of the work accomplished on large mirrors in the past has been on a time-scheduled basis that the optician has been allowed very little time to try any real technique changes. It is apparent that we have not reached the limit of surface smoothness that could be attained on the optical substrate materials available at the present time. There seems to be a direct correlation between optical smoothness and technique.

Electroforming of Large Mirrors

F. J. Schmidt

General Electric Company

N70-36697

Introduction

Weight, durability in launch and space environments, thermal conductivity and isotropy, and projected cost considerations favor metallic mirrors over glass mirrors for large-size reflective optics although, at present, the surface quality and thermal stability of glass mirrors remain superior. Considerable advances have been made during the last few years, however, in the fabrication of metal mirrors.

I would like to identify some of these advances and to indicate a few highly promising research and development areas for application to space telescopes. This paper will discuss five techniques of potential interest for the fabrication of a large space telescope.

Electroforming

Of all the earthbound processes for the fabrication of metal mirrors, electroforming presents the greatest potential. Grinding, milling, and other mechanical processes require considerable wall thickness in the mirror. Typical thickness-versus-diameter ratios are 1:6 or 1:10 for glass and 1:100 for

ground metal mirrors. Such thicknesses result in excessive weight, thermal gradient, and cost. Since only the surface is used, the material utilization efficiency decreases with increasing thickness. In contrast, electroformed mirrors show a ratio of only about 1:1000. Physical forming and deposition processes yield mirrors of inferior surface and metallurgical properties and generally at a high cost.

In electroforming, metal ions are deposited from a room-temperature solution upon an accurate male master. This intimate "atom-to-atom" contact should yield completely faithful replication. The master is reusable; many such mirrors can be electroformed from each master. In practice, electrodeposition stresses have been largely responsible for the degradation observed in a number of past attempts to electroform metal mirrors. Stresses occur, presumably, because of disruption of the orderly atomic lattice by dislocation.

Recently, however, an instrument has been developed that has made it possible to control these stresses to the point where accuracy of reproduction and surface smoothness are assured to about 1λ (green) and 50 angstroms, respectively.*

Although these results were achieved on small mirrors, there is no theoretical or practical limit now known that would preclude any desired precision of replication in any size of electroform. Only by experiment will the actual limits be found.

A number of large mirrors (solar energy concentrators) were made by the Re-Entry Environmental and Systems Division of the General Electric Company between 1962 and

*The average surface roughness was measured by interference microscope photographs of the surface with multiple interference lines, obtained by the Tolansky method. The distance between the Fizeau lines corresponds to one-half the wavelength of the green light used. After an exact measurement of the wavelength, of the fringe displacement, and of the distance between lines, the surface roughness was calculated.

1967 (table 1). These units required accuracies of configuration much less severe than those for astronomical mirrors; typically, slope errors had to be controlled to within a few minutes of arc. Nevertheless, it is interesting to note the accuracy of replication in the case of these large paraboloids. Figure 1 shows the typical accuracy attained during this period by using a double replication

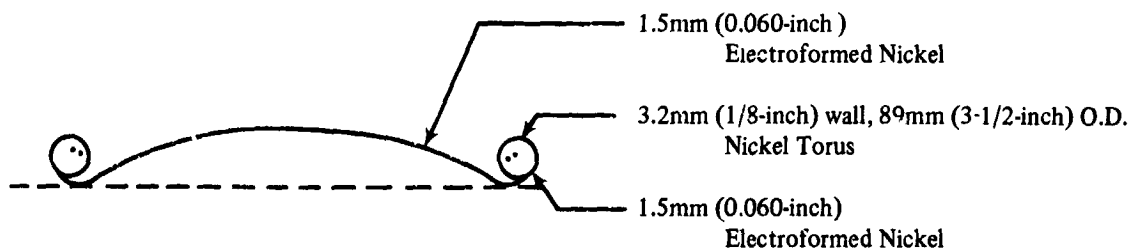
process: spincast epoxy female master, electroformed male nickel intermediate, and electroformed female final replica.

Angular deviation was measured at 824 points on the surface of the mirror with the results shown in figure 1, from which it is evident that departure of the replica from the master was very small in spite of the rather generous requirements.

Table 1. Electroformed Large Mirrors Made by GE

User	Size	Material
GE Missile and Space Division	(22') 6.7m (Segments)	Electroformed Nickel
Jet Propulsion Laboratory	(5') 1.5m	Electroformed Nickel
Jet Propulsion Laboratory	(9-1/2') 2.9m	Electroformed Nickel
NASA Langley Research Center	(9-1/2') 2.9m	Electroformed Nickel
NASA Langley Research Center	(2-1/2') 0.8m (Several)	Electroformed Aluminum
NASA Langley Research Center	(2-1/2') 0.8m (Several)	Electroformed Reinf. Aluminum

GEOMETRIC CONFIGURATION



Typical: Weight, incl. torus

Nickel: 4.35 kg/m² (0.89 lb/sq. ft.)

Aluminum: 2.78 kg/m² (0.57 lb/sq. ft.)

Designed for:

10 g Axial
2 g Tangential Loads
(Launch Environment)

Economics of 100-inch electroformed mirrors,
compared to ground glass mirrors:

Time = < 1/10

Cost = < 1/5

(Drastic decrease in mirror cost
with increasing numbers of units)

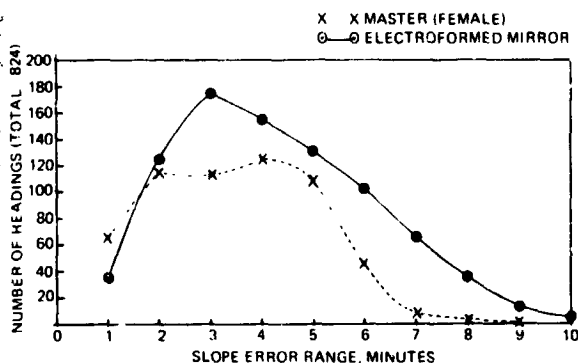


Figure 1. Distribution of slope error in double replication process.

To these considerations should be added the fact that, in direct contrast to thick mirrors of any material, an accurate thin mirror lends itself readily to active figure control.

Figure 2 shows two electroformed aluminum mirrors produced in the General Electric laboratory.

Surface Finishing

Our second technique is the possible improvement of the surfaces of metal mirrors by electrochemical processes. An overriding consideration in the electroforming of mirrors is the fact that these mirrors are fabricated



Figure 2. Two small, electroformed aluminum, thin mirrors: 3 inches and 7 inches in diameter, respectively.

thin (typically 15 to 40 mils). To make them thick would defeat the basic objectives (light weight, minimal front-to-back-face temperature differences, cost, etc.); hence, we may just as well grind in the conventional manner. It should be noted that these electroformed mirrors do not experience distortion due to the removal of gravity because they are produced in what amounts to a zero-gravity environment; i.e., as an adherent skin resting on a substrate. The electroformed mirrors are too thin to be polished and figured; therefore, we must electroform them accurately in the first place. Two potentially applicable processes, electrochemical machining and electropolishing, were investigated, but the accuracies obtainable by these methods are, at best, ± 0.0001 inch, which is two orders of magnitude above diffraction limits in the visible region. It now appears that these processes are unlikely to achieve further improvements in the accuracy of electroformed mirrors.

Reinforced Metal Mirrors

In recent work sponsored by the NASA Langley Research Center, large-scale structural electroforms have been reinforced by electrophoretic codeposition of high strength fibers. Such composites displayed a three-fold increase in ultimate tensile strength and a 50-percent increase in the elastic modulus (the latter much surpasses that of quartz) without affecting the accuracy of replication. Additional dramatic increases in strength and modulus appear quite feasible. This program should be vigorously pursued because it points towards one way of obtaining metal mirrors with high stiffness-to-weight ratio. Besides permitting an aperture increase for a given mirror weight at a given accuracy limit, such reinforcing "fillers" can also decrease the thermal expansion coefficient without a significant effect on thermal conductivity.

Hardened Surfaces

In a somewhat related process, very hard, polishable surfaces have been created on

aluminum electroforms by electrophoretic pigmentation. Polishing of electroforms is undesirable, as indicated previously in this paper; therefore, this process is not of immediate interest although it may be useful in connection with other metal fabrication processes.

Lunar Fabrication

I would like to plant the seed of a radically different approach, namely, lunar fabrication. In the December 1966 issue of *Astronautics and Aeronautics*, Dr. William Tiffet of the Stewart Observatory gave compelling arguments for placing a space telescope on the moon rather than in orbit. I will not repeat his arguments, which were based upon geometrical, environmental, and operational considerations, but I will add this consideration: the cost of fabrication of telescope materials and the operation of a lunar base would be shared by many disciplines.

The generation of oxygen (life support and propellant) is a primary requirement for the growth of self-supporting capability on the moon. There is one proposed oxygen-generation process that not only yields

oxygen as efficiently as any of the other processes but also gives, at no extra cost, highly significant byproducts usable for mirror-and-telescope-structure fabrication. This process employs the GE-proposed lunar fused salt cell, shown in figure 3. While this mobile unit moves slowly along the lunar surface, an auger movement scoops in the soil, which is subsequently melted and electrolyzed as in an earthbound fused-salt metal-producing cell. Oxygen gas and silica are generated at the anode, metal at the cathode, and thermally extracted water is obtained from the heating of the rocks. The process is not sensitive to lunar surface composition, which is shown in table 2. Thus, some metal or alloy could be produced even if we do not know at this time which one it would be.

Because the penalty of lifting thousands of pounds of telescope equipment to the moon is very heavy, I propose fabricating the mirrors and much of the structure on the moon by utilizing the silica or metal obtained from lunar rock. The fabrication tradeoffs will rapidly become more favorable for lunar fabrication when we consider the long-term need for increasing numbers of space telescopes or as the telescopes become too large for launch vehicles.



Figure 3. Artist's conception of lunar mobile metal smelting plant.

Table 2. Probable Elemental Abundance on Lunar Surface*

Element	Percent Weight
Oxygen	33-52
Silicon	17-38
Magnesium	8-18
Iron	1-22
Aluminum	1-10
Sodium	0.2-4
Calcium	0.1-8
Potassium	0.1-5
Nickel	0-2
Carbon	1-11
Hydrogen	0.007-1
<i>Comparative Classification</i>	
Volcanic ashes	
Pumice	
Lava (trachytic and basalt)	
Stone and metallic meteorites	
Tektites	
Quartz porphyries	
Granite	
Tuffs	
Dolerite	
Liparitic pitchstone	
Iron quartzite	
Chondrite rocks	
Achondrite rocks	
Rhyolitic rocks	

*Data obtained from various sources.

The lunar fabrication scheme circumvents the problems of permanent deformation

due to launch environment and fabrication and testing in earth-gravity while operating in the much lower lunar-gravity environment. The fabrication, testing, and operational support systems will also be simplified. The launch support system will be eliminated.

Pertinent technical data on the engineering "energetics" appear in table 3.

If we produce molten metal (or SiO_2) on the moon, the first step in forming a mirror would probably be the spincasting of a low or zero shrinkage composition. Because of lower gravity, a considerably slower rotation than required on earth would be sufficient (about 1 rpm for a paraboloid of a 200-inch focal length). This would simplify the equipment and reduce bearing "noise." The quality of the surface and geometry that could be attained is presently unknown; however, on earth, with rather mediocre equipment located in a high traffic environment, a 2-mil rms finish and 0.5 minute of arc geometry were easily attained in 10-foot spincast paraboloids. Considerably better results can be expected in the lunar environment. Still, such spincast mirrors are sufficiently thick and rigid for polishing and figuring, if needed.

Various novel schemes applicable to the final figuring of silica or rigid metal mirrors in the primitive lunar environment represent an area meriting research and development support. For example, the measurement-and-comparison process may well use certain recent developments in optical metrology that will be favored by the airless lunar environment; long-range interferometry is now possible because of the availability of highly coherent laser illuminators; moreover, long path interferometry is favored by the absence of atmospheric refraction.

In order to establish a standard of comparison, it may be desirable to provide a small mirror having the desired focal length and accuracy of the completed large mirror. This small reference mirror could be set in a recess at the center of the rough blank so that its extended surface would be either above or below the surface of the blank, depending on whether we would add or remove metal for correction.

Table 3. Technical Data on Lunar Metal Production

Reference: Silicate Melt Electrolysis, Feasibility Demonstrations and Basic Studies:

U.S.A.	Bockris (work done in Great Britain)	
Great Britain	Kitchener, Davies	
U.S.S.R.	Esin, Checulin, Boronenkow, Shurygin	
Japan	Adachi, Ogino	

(Note: Significantly little work was done in the U.S.A.)

THE FUSED SALT PROCESS IS QUITE INSENSITIVE TO ORE COMPOSITION.

Cathode Products: Al, Mg, Fe, etc., (As determined by controlled potential.)
98 to 99% Purity (Significant impurity: Si)

Anode Reaction: $\text{SiO}_4^{4-} \rightarrow \text{SiO}_2 + \text{O}_2 + 4e^-$; i.e., quartz and oxygen

Overall: (For Al) 100 g Al for 30 lit. (normal temperature + pressure) O_2
at 1355 amp. hr/lb. Al (with 0.45/lb. Al per lb. O_2)
water of crystallization (if any)

Electrodes (nonconsumable): TiO_2 or Fe_2O_3 or doped Al_2O_3

Voltage: 4 v

Temperature: 1000° if chlorides present;
up to 2000° if no chlorides present

<i>Power:</i> For electrolysis	6 KWH/lb.	(13.2 KWH/kg)
Melting	4 KWH/lb.	(8.8 KWH/kg)
Move, crush, etc.	9 KWH/lb.	(19.8 KWH/kg)

Power Source:

Solar, 1.7m (45 ft.) dish	15 KW
Kilovolt's isotope power system (closed loop, br)	15 KW
SNAP 8	>> 15 KW

Total Estimated Weight, excluding power generation: 2000 lbs.
for 1 lb./hr metal producing plant (0.45 kg/hr) at
15 KW, but considerable increase possible at higher power.

At a distance of two focal lengths, a metrology pylon would be erected on the axis of the reference mirror. On the pylon would be mounted a point source of coherent illumination. The dimensions of the source would be less than the desired resolving power

of the mirror; e.g., a 300-cm, f/10 mirror would resolve $\frac{3000 \times 2 \times \lambda}{300} = 20 \lambda = 10$ microns at 5000 angstroms. If a source somewhat smaller than 10 microns were to illuminate

the reference mirror, an image of the source would be generated nearby in the form of a characteristic Airy disc or diffraction pattern. The image would not be that produced by a source at infinity but would be modified in a predictable way.

Obviously, lunar-based fabrication requires much detailed development in several technologies involved; however, it cannot be lightly discussed in long-range planning for space exploration.

PRECEDING PAGE BLANK NOT FILMED.

N70-36698

Isotropic Beryllium for Mirror Blanks

John W. Moberly and Henry M. Brown

Stanford Research Institute

Introduction

It has been recognized for several years that beryllium should be extremely isotropic for use in optical systems. Aside from its anisotropy, beryllium is ideal for use in such instruments because it possesses low density, high modulus, and reasonably good thermal properties. A critical requirement for such precision parts is uniform expansion of the metal. Beryllium, however, crystallizes at low temperature with a hexagonal close-packed crystal structure that leads to anisotropy in many of its physical parameters. This presents a serious problem that can only be overcome by the use of randomly oriented polycrystalline bodies that are usually produced from beryllium powders.

Nearly all beryllium powder is prepared by some comminution process in which coarse beryllium particles are crushed to finer and finer sizes. Beryllium cleaves primarily on its basal plane, the powder taking on irregular platelet or acicular shapes in which the plane of the particle corresponds to the basal plane of the beryllium crystal. In packing such powders, preferred orientation occurs because the particles tend to align the plane of the platelets (basal plane) normal to the packing direction. During densification of the powders, such as hot-pressing, this tendency is further magnified because the basal plane is also the slip plane and additional particles will plastically deform into this same orientation under the pressing force. Using hydrostatic or isostatic pressing procedures and sintering techniques can greatly reduce the amount of anisotropic texture. Two such processes have been developed: pressureless sintering (ref. 1)

and hot-isostatic pressing (ref. 2). These techniques are capable of producing nontextured samples because the pressing forces are applied equally in all directions, not uniaxially as in conventional hot-pressing.

Anisotropy in polycrystalline materials can be estimated by a relatively simple diffractometer-scanning technique in which the degree of anisotropy is indicated by the relative intensities of selected diffraction peaks. Although such x-ray procedures are not as "foolproof" as pole figure analysis, diffractometer scans yield qualitative data that can be used to measure anisotropy.

Hot-Pressed Beryllium

Unlike most powder metallurgy products that are fabricated by cold-pressing followed by a high temperature sintering, nearly all commercially powdered beryllium is processed by vacuum hot-pressing. During vacuum hot-pressing, beryllium powders contained in a steel or graphite die are uniaxially compressed at pressures of the order of 1000 pounds per square inch for about 1 hour at 1000° to 1100° C. The beryllium billet produced is nearly theoretically dense, having a grain size only slightly larger than the initial powder particle size. Beryllium oxide is present in the same amount as in the initial powder and is usually 2 to 6 weight percent.

Mechanical deformation of polycrystalline beryllium at high temperatures causes the development of a texture (preferred orientation). The grains tend to become aligned with their c-axes parallel to the direction of the applied force. This worked texture is also observed to a lesser

degree in hot-pressed beryllium. For normal structural uses of beryllium, hot-pressed beryllium is considered to be isotropic; however, differences in ultimate tensile strength of 10 percent are often observed between longitudinal and transverse sections of hot-pressed structural-grade beryllium billets (ref. 3). Differences in thermal expansion of nearly 5 percent have been measured for these two directions in hot-pressed billets; for optical application, such differences are intolerable.

The reason for strength and thermal expansion differences is the preferred orientation developed during densification of the powder. Figure 1 shows x-ray diffractometer scans of samples of a hot-pressed beryllium billet; the surfaces x-rayed were perpendicular and parallel to the hot-pressing direction. This figure shows the three most intense beryllium peaks. The (10 $\bar{1}$ 1) peak should be the strongest in a random sample; the intensity of the (10 $\bar{1}$ 0) peak should be 31 percent of the (10 $\bar{1}$ 1) peak; and the (0002) peak should be 28 percent the intensity of the (10 $\bar{1}$ 1) peak (ref. 4). As is evident in figure 1, neither of the scans yield peak intensities in the proper proportion. Because of the applied load during hot-pressing, a number of beryllium grains become aligned with their basal planes, (0002), normal to the pressing direction. X-ray examination in a direction 90 degrees to the pressing direction shows a lower number of basal planes than in a random sample. This behavior is observed in all hot-pressed beryllium.

Isostatically Produced Beryllium

An alternative approach for producing randomly oriented beryllium is to use isostatic or hydrostatic pressing procedures in the densification operations. The pressureless-sintering technique produces dense (over 99 percent of theoretical), fine grain, randomly oriented beryllium (ref. 1). The microstructure of a pressureless-sintered beryllium specimen is seen in the polarized light micrograph of figure 2. A homogeneous, fine grain structure (average grain size of

about 10 to 15 μ) is evident. This sample contains about 2 weight percent beryllium oxide impurity, which appears as a small black precipitate in the micrograph. The oxide is generally present in the grain boundaries.

The degree of randomness of the pressureless-sintered beryllium samples is illustrated in figure 3. This figure shows three x-ray diffractometer scans taken from three orthogonal directions of a small specimen of a pressureless-sintered billet. The relative intensities of the three peaks taken in the three directions are nearly identical, and all are nearly in the proper ratios (ref. 4). X-ray data were also taken of sections cut at a 45-degree angle to the sections used for figure 3, and these data again are in the proper proportion. Finally, pole figures analysis on pressureless-sintered beryllium indicated that the samples examined were essentially random.

Optical Properties of Beryllium Mirrors

Mirrors have been made from the various classes of beryllium mentioned in this report, including several grades of commercially hot-pressed, hot isostatically pressed, and pressureless-sintered beryllium. These mirrors were generally solid blanks, 4.2 inches in diameter by 0.50 inch thick. The samples were polished by Perkin-Elmer to obtain flat, high quality optical surfaces. The mirrors have been evaluated for short-term stability over thermal excursions between 25° and 80° C, called "thermal stability," and long-term flatness dimensional stability measured at constant temperature. The long-term dimensional stability is evaluated by two means (ref. 2). The first uses a precision surface interferometer that records flatness instabilities over a 2-week period at constant temperature; the data are then extrapolated to yield instabilities per year. A second dimensional stability measurement is simply to compare the flatness of the polished mirrors after shelf storage of 12 to 18 months. Longer times are not yet possible because control samples were produced less than 2 years ago.

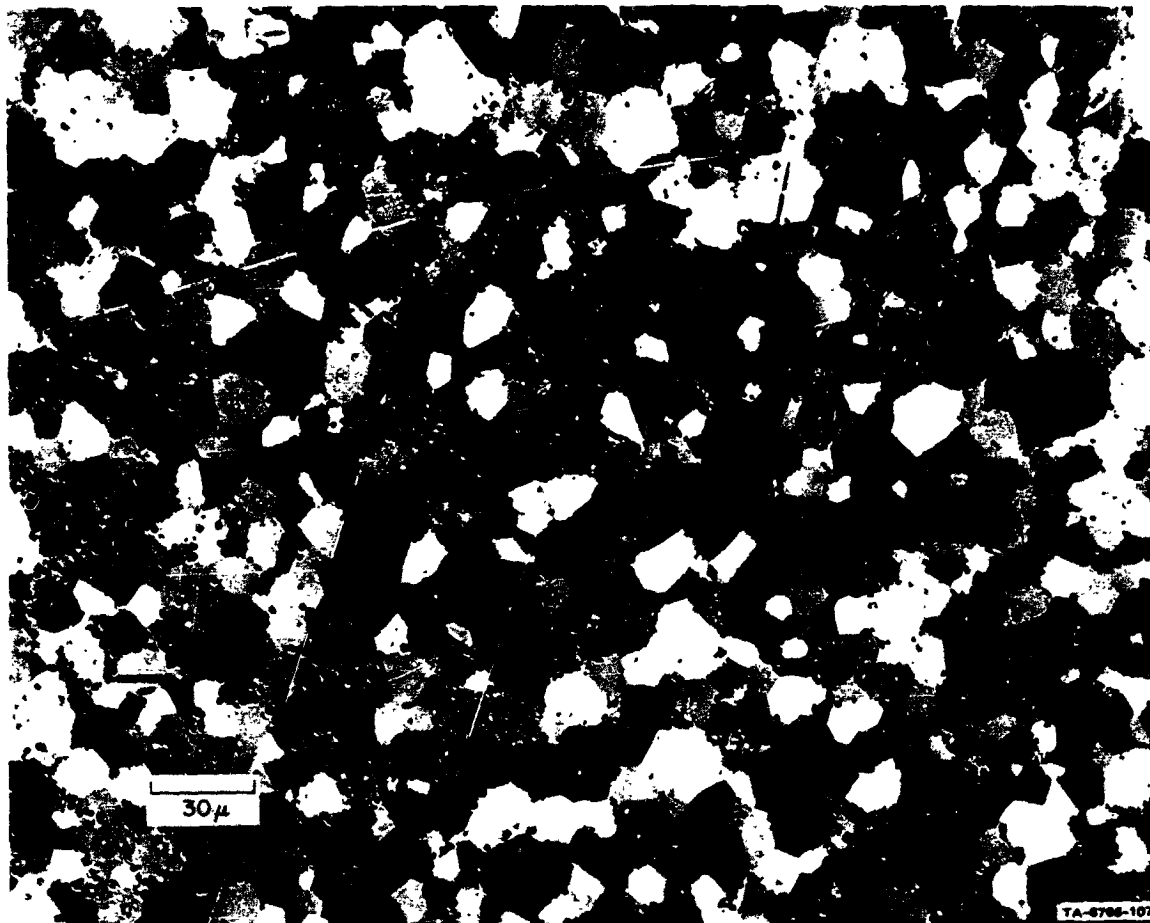


Figure 2. Microstructure of pressureless-sintered beryllium.

Two factors contribute to these thermal instabilities. The first is the overall degree of nonrandomness in the various samples. This is shown in figures 1 and 3 for hot-pressed and pressureless-sintered beryllium. In addition, an important contribution to the instability is the inhomogeneity of the texture across the polished surface. Because the optical measurements have been made on flat surfaces, it is possible that even a significant degree of nonrandomness can exist in the test sample; but, if the texture is uniform over the optical surface, the mirror may not severely distort upon temperature changes. This, however, would not be the case for an optical surface if some curvature was involved; i.e., it would distort even if the texture were uniform across the entire surface. Because of differ-

ences in thermal expansion in the various directions for hot-pressed beryllium, severe distortions occur upon temperature changes.

X-ray diffraction measurements have been made over the optical surfaces for numerous beryllium mirrors. Figure 4 shows the results obtained for a mirror made from a commercially hot-pressed billet. Three scans are shown: one taken at the center of the billet, one at the billet edge, and one at an intermediate position. Several of these traverses were taken; what is shown is representative of all the measurements. It is evident that this mirror is highly textured and that the texture is not uniform across the surface. This sample showed a thermal instability of $1.8 \times 10^{-3} \lambda/^\circ\text{C}$. The x-ray characteristics of the hot-pressed sample are contrasted with

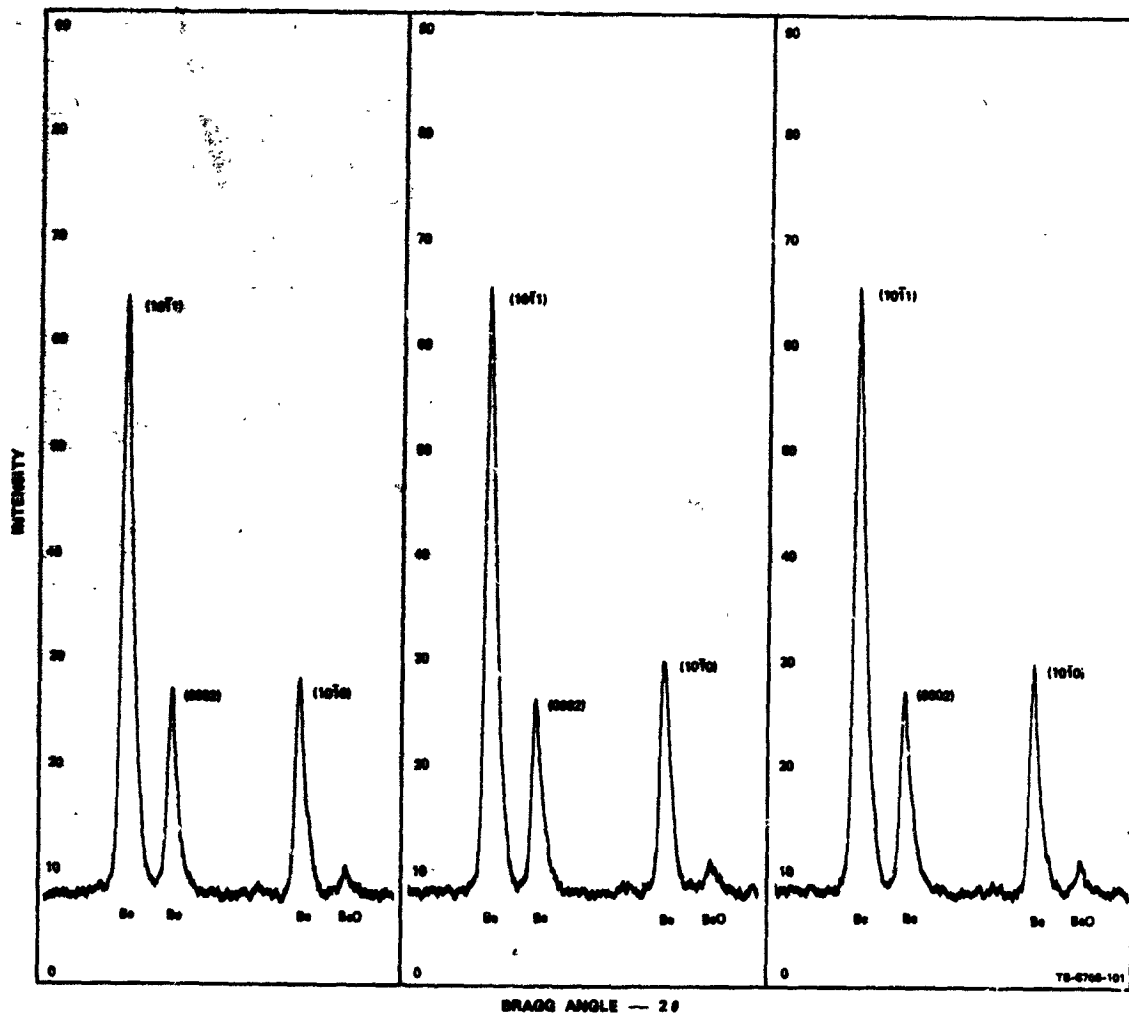


Figure 3. X-ray diffractometer scans taken from three orthogonal sides of a small hydrostatically pressed, pressureless-sintered beryllium cube.

those of a pressureless-sintered mirror, which is shown in figure 5. This sample, although not perfectly random nor homogeneous, is far superior to hot-pressed samples. The actual thermal instability of this pressureless-sintered mirror was $0.41 \times 10^{-3} \lambda/^\circ\text{C}$.

Thermal stability for performance of optical systems would be critical where the mirror would operate at temperatures other than that at which it was polished. In general, all the thermal instabilities in the mirrors tested were elastic in that they returned to their original surface figure when returned to

the original test temperature. Beryllium mirrors that have large thermal instabilities, such as those made from the hot-pressed blanks, would of necessity have to be polished at a temperature near the operating temperature of the mirror.

More critical to many applications is the long-term dimensional instability. Again, the only precise data available are for flat surfaces, but pressureless-sintered mirrors have been shown to be stable to values of $\lambda/20$ per year. These values are approaching the long-term dimensional stability recorded for fused

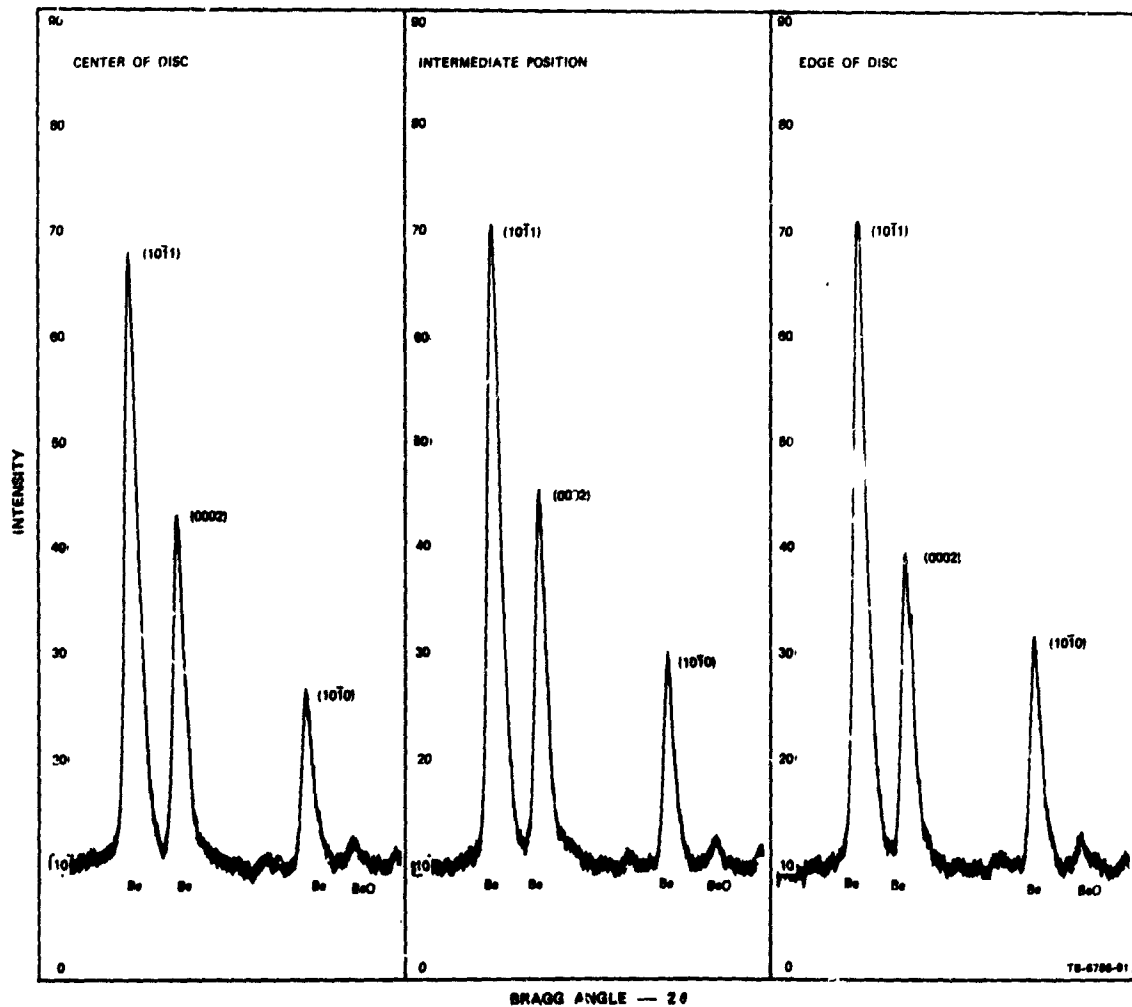


Figure 4. X-ray diffractometer scans of a hot-pressed beryllium mirror.

silica mirrors. Hot-pressed beryllium samples once again are inferior, with instabilities of about $\lambda/4$, or one fifth as good as the pressureless-sintered samples. To date, no direct correlation has been shown between short-term thermal instabilities caused by nonrandom orientation and long-term dimensional instabilities. The long-term instabilities most likely are caused by residual internal strain.

A final comment is appropriate on the manner in which the tested samples were treated after fabrication. Billets having dimen-

sions approaching the final mirror geometry were sintered, thus eliminating excessive machining. After machining, it was necessary that a minimum of 0.010 inch be chemically removed from all machined surfaces, thereby eliminating all machining damage. The blanks were then optically polished. No Kanigan coating was applied. It is felt that surfaces such as Kanigan would only contribute to the various instabilities of the beryllium and, in fact, may far overshadow the satisfactory behavior for the sintered beryllium.

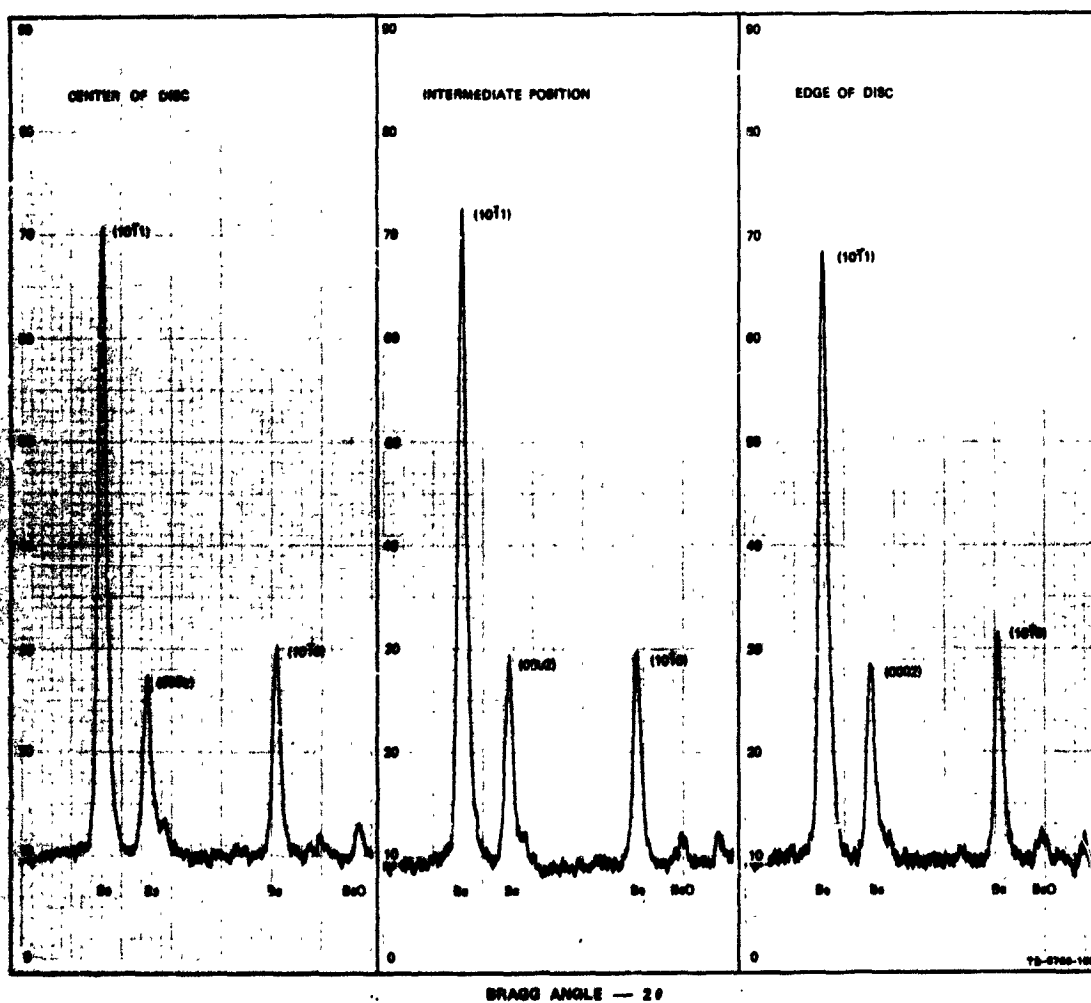


Figure 5. X-ray diffractometer scans of a pressureless-sintered beryllium mirror.

References

1. Moberly, J. W.; Goggin, W. R.; Brown, H. M.: Compacting and Pressureless Sintering of Beryllium Powders. *International Journal of Powder Metallurgy*, vol. 5, no. 2, 1969.
2. Hodge, E. S.; Gripshover, J.; Hanes, H. S.: Properties of Gas-Pressure-Consolidated Beryllium Powder. *Beryllium Technology*, Vol. II, Gordon and Breach, New York, 1966, p. 703.
3. King, B.: New Grades of Beryllium - Their Meaning and Use. Presentation at SAE Meeting, Los Angeles, California, October 1967.
4. Meredith, C. C.; Moberly, J. W.; Barlow, M.: Integrated X-ray Diffraction Measurements of Beryllium. *Journal of Less Common Metals*, 1969, submitted for publication.
5. Perkin-Elmer Corp.: Optical Materials Study Program. Second Annual Technical Report, ARPA Order No. 885, Sept. 1968.
6. Perkin-Elmer Corp.: Unpublished data, Norwalk, Connecticut.

PRECEDING PAGE BLANK NOT FILMED.

N70-36699

The Effects of Processing on the Dimensional Stability of Beryllium Mirrors

Robert E. Maringer

Fattelle Memorial Institute

Introduction

Beryllium has a number of distinctly advantageous properties that make it a promising optical mirror material. It has, above all, a high modulus (3.2×10^4 kg/mm²) and a low density (1.86 g/cc), which combine to give it the highest stiffness-to-density ratio of all the normally considered candidate materials. In addition, beryllium has a relatively high thermal conductivity (1.7 watts/cm °K), which means that it will equilibrate readily after some change in temperature. Recognition of these properties has led to the use of beryllium in telescopic mirrors, gyros, accelerometers, instrument mounts, and other precision devices. The accumulated experience indicates that beryllium is not an ideally stable material. Recent research has resulted in a significant advance in the understanding of the reasons for this instability. It is the purpose of this discussion to point out some of the reasons for this instability and to indicate methods to avoid it.

Mechanisms of Dimensional Instability

At least four distinct mechanisms of dimensional instability (not including over-stressing by the application of an excessive external load) have been identified in beryllium. These are:

1. Relaxation of residual stresses introduced during processing (especially machining)
2. Relaxation of residual stresses existing in an electroless nickel plate or relaxation of thermally-induced stresses between the plate and the beryllium substrate

3. Relaxation of thermally-induced residual stresses resulting from the anisotropy of the thermal expansion coefficients of beryllium

4. A nonuniformity of the preferred orientation of beryllium, which results in nonuniformity of thermally-induced stresses.

Machining Stresses

The most common source of residual stress in beryllium is machining damage. The machining operation itself causes considerable disruption of the surface layers, leaving behind a heavily cold-worked layer. If one examines this worked layer metallographically in cross-section, deformation twins are often observed, extending to a depth of perhaps 0.002 inch below the surface. These have sometimes been taken as evidence of surface damage or residual stress, and the beryllium surface has been etched to a depth of 0.002 inch or so to alleviate the situation. It has been shown (refs. 1 and 2), however, that the damage extends far deeper than this. Using the recommended tools, the recommended rake angle, and the recommended cutting speeds, it has been found that the residual stresses due to lathe machining will occasionally penetrate to depths greater than 0.010 inch, but penetration is more commonly of the order of 0.005 or 0.006 inch. Although the evidence is meager, it appears that the depth of penetration decreases with decreasing grain size and increasing material strength.

These residual stresses introduced by machining have been reported (ref. 3) to be

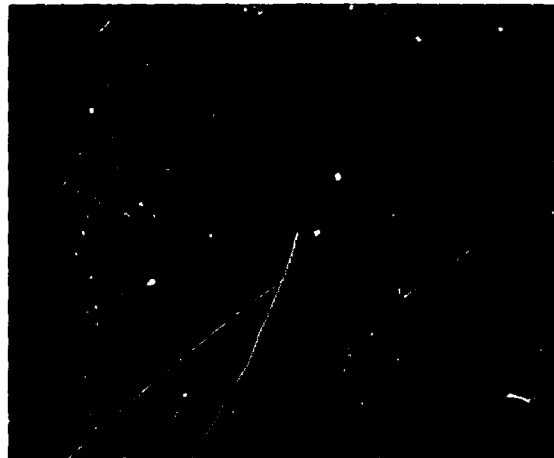
as high as 40,000 pounds per square inch, and, in our own experiments (ref. 1 and 2), we have found stresses as high as 25,000 psi. What this can do to a beryllium mirror is amply demonstrated in figure 1. A 4.2-inch-diameter, 1-inch-thick cylinder of beryllium with machined surfaces was lapped flat on one side. Then the machined back surface was etched off in steps. After removal of 0.0082 inch from the back surface, the interference fringes had changed from straight lines to concentric circles, indicating that the surface was now convex and deviated from flatness by several wavelengths.

It is important to be aware of the fact that this behavior is not limited to beryllium. Figure 2 shows a small mirror of Vega tool steel of a similar aspect ratio. After 0.001 inch of material was removed from the back surface by surface grinding, figure 2(b), the mirror became astigmatic, with the axis of astigmatism being parallel to the direction of the grinding. Etching 0.001 inch from the back surface again changed the mirror figure appreciably, as shown in figure 2(c).

The presence of such residual stresses in beryllium can be catastrophic insofar as mirror behavior is concerned. In the first place,



(a) Interferogram of SRI-I-2, showing surface prior to the chemical removal of beryllium from back surface.



(b) Interferogram of SRI-I-2, showing surface figure after removal of 0.0041-inch-thick layer from back surface.



(c) Interferogram of SRI-I-2, showing surface figure after removal of 0.0082-inch-thick layer from back surface.

Figure 1. Effect of machining stresses on beryllium mirror figure. (Courtesy of Perkin-Elmer Corporation.)



(a) As lapped.



(b) With 0.001-inch surface grind on back face.



(c) With 0.001-inch etch on back face.

Figure 2. Effect of machining and etching on Vega tool steel mirror.

the thermal expansion coefficient differs between the cold-worked layer produced by machining and the annealed base material. This could lead to thermal instability of a mirror. Worse than this, however, is the probability of relaxation of these stresses in service. We have observed (ref. 4) that many materials will creep under stresses even less than their microyield strength (MYS), the stress to cause 10^{-6} plastic strain. For beryllium, the MYS can vary considerably as a function of grade or processing history. This is shown graphically for a number of grades and processing procedures in figure 3. If, for example, S-200 beryllium can be expected to creep (or show stress relaxation) at stresses less than 2000 psi, we have no reason to expect it to sustain residual stresses of 20,000 psi without stress relaxation.

It is interesting to note that most procedures for the stress relief of beryllium call first for rough machining, then for a 1450°F anneal to relieve the stresses, then for finish machining. In effect, one goes through considerable trouble to remove or to minimize the residual stresses due to rough machining; then one proceeds to put them right back in again in finish machining. There is even good evidence (ref. 5) to indicate that the fine cuts used for finish machining put in higher residual stresses than the coarser cuts used in rough machining.

Stress relief by heat treatment is one solution, but it must be done after finish machining as well as after rough machining. The generally accepted stress-relief heat treatment for beryllium removes only little more than half the residual stresses present (ref. 6). Therefore, a far better procedure is to etch chemically all machined surfaces at a depth of at least 0.010 inch. This should be followed by a stress-relief heat treatment to minimize any long-range residual stresses that may be present. If the bare metal surface is to be ground and lapped, enough material should be removed during each step to obliterate the residual stress pattern introduced by the previous step. This will permit the final mirror surface to end up with the thinnest possible layer of disturbed metal and, thus, to have the greatest stability.

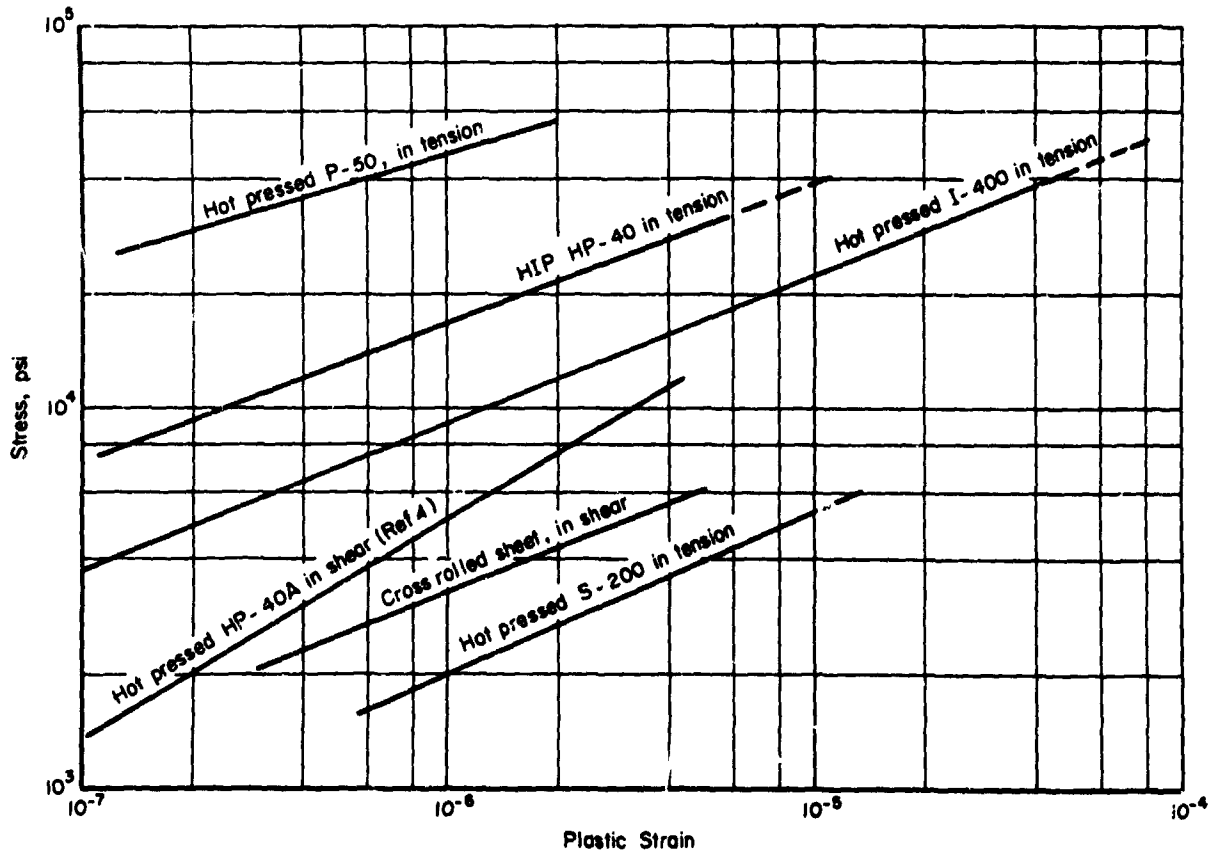


Figure 3. Stress-plastic strain data for various beryllium samples.

This whole area of residual stresses due to machining, lapping, or grinding, and their removal or minimization, represents a grey area of knowledge. We know how bad things are, but optimum machining, lapping, and grinding practice is not known; nor are adequate data available to permit truly optimum heat treatment to relieve stresses introduced by these operations.

Electroless Nickel Plate

Because of its significantly greater ease in polishing, electroless nickel is plated onto most beryllium (and other metal) mirrors. A series of simple experiments (ref. 7) was undertaken to evaluate the residual stress system in this plate. A number of stress-relieved beryllium strips (0.010 inch thick by 0.4 inch wide by 4 inches long) were plated on one side with 0.005 inch of electroless

nickel. Plating was done by various plating companies. The composite thus formed a bimetallic strip. Most of the specimens were given a "stress-relief" heat treatment by the platers after plating and, when delivered to us, were obviously bent. Calculation showed that tensile stresses over 20,000 psi often existed in the plate. Representative strips are shown in figure 4. Significantly, one strip that was delivered in the "as plated" condition was not bent. As shown in figure 5, however, it (Strip No. 1) bent appreciably after exposure to 190°C. In figure 5, the vertical axis represents the extent of bending as measured from the center of a line drawn between the two ends of the specimen to the center of the specimen.

Because the specimen is a bimetallic strip, it will also respond to a change in temperature by a change in its bend radius if the thermal expansion coefficients of the nickel



Figure 4. Curvature (bow-out) caused by plating stresses from Kanigen-nickel deposition on beryllium. (Top to bottom: Companies A, B, C, and D.)

and the beryllium differ. As the data in figure 5 show, this does indeed happen; the temperature dependence of the bending indicates a difference in thermal expansion coefficients of about 2×10^{-6} per degree Celsius.

For precision mirrors, both the residual stresses in the plate and the different thermal-expansion coefficients of the nickel and the beryllium are unacceptable. The easiest and most obvious solution is to eliminate the plate entirely. In less precise applications, or where a polishable surface cannot be otherwise attained, electroless nickel can still be very useful. For best results, however, the mirror should be plated with an even thickness over its entire surface. The structure thus becomes a sandwich, with stresses on the back of the mirror balancing those on the front and with consequent distortion minimized. Care should be taken not to unbalance the situation by excessive thinning of the plate on the reflecting surface of the mirror during polishing.

Potentially, it seems feasible to develop an electroless nickel with a better thermal expansion match, but, to our knowledge, no research in this area is under way.

Thermal Expansion Anisotropy

The crystal structure of beryllium is hexagonal-close-packed, and its thermal-expansion coefficients parallel and perpendicular to the axis of the crystal differ by

about 2×10^{-6} per degree Celsius at room temperature. This means that, in a randomly

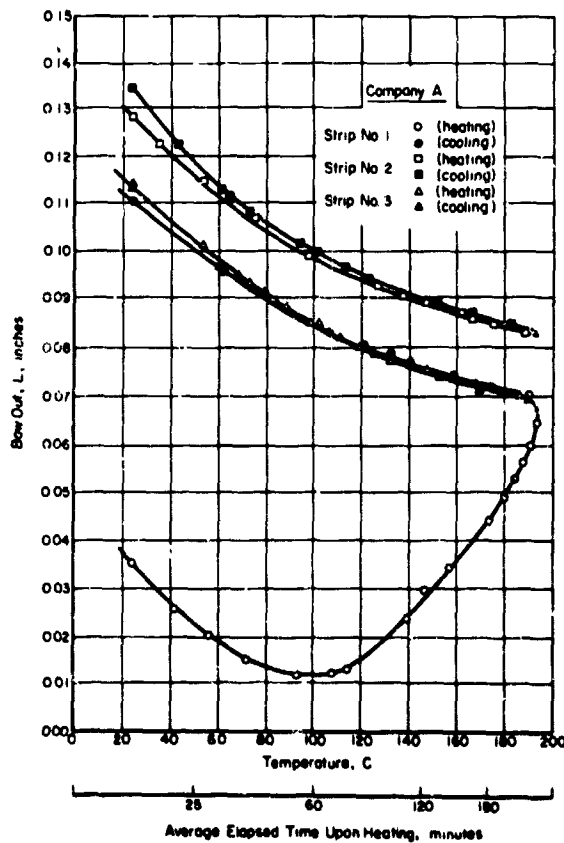


Figure 5. Effect of heating on the curvature of electroless-nickel-plated beryllium strips.

oriented polycrystalline aggregate of beryllium, any change in temperature will result in a buildup of stress between adjacent grains. For adjacent grains whose *C*-axes are oriented at 90 degrees to each other, this stress builds up at about 80 psi per degree Celsius. In some materials, anisotropy of this type leads to rather dramatic dimensional instability, as shown in figure 6 for thermally cycled uranium (ref. 8).



Growth of uranium rod by thermal cycling from 100 to 500°C; original size ½ inch long and ¼ inch in diameter. (a) 2132 cycles (2X); (b) 4882 cycles (2X).



Thermal-cycling growth of highly oriented fine-grained uranium (300°C rolled rod). Growth from 2 to 11.5 inches by 300 cycles from 50 to 550°C.

Figure 6. Dimensional instability of uranium due to thermal cycling (ref. 8).

Fortunately, instability of this magnitude is not observed in beryllium, but it is vital to remember that intergranular stresses exceeding the MYS are built up on cooling. Slow cooling from a stress-relief heat treatment is important in order to permit the partial relaxation of these intergranular stresses. It is also important to cool the sample to below room temperature. This will increase the intergranular stresses still further, permitting them to relax somewhat by continued plastic deformation. Then, when the

beryllium is returned to room temperature, the stresses will be reduced by the now negative ΔT . This appears to be the real rationale behind thermal cycling as a stabilization procedure. Unfortunately, virtually no quantitative data are available to indicate an optimum thermal-cycling stabilization procedure. The current practice of cycling between about -100° to +100°C (done slowly to avoid thermal stress gradients) probably should be considered mandatory but certainly not optimum.

Inhomogeneous Anisotropy

As most people are aware, hot-pressed beryllium has a strongly preferred orientation. Forging or rolling serves to increase this form of anisotropy. One consequence of this anisotropy is a difference in the thermal expansion coefficients of beryllium relative to the direction of pressing or working. This leads to some thermal instability, especially in nonsymmetrical structures or in a structure like a spherical mirror, when different surface elements represent different directions relative to the pressing direction.

There are several ways of decreasing this anisotropy. One of these is the hot isostatic pressing (HIP) method developed by Battelle. This process involves sealing a green powder compact in a mild steel container, then exposing the package to isostatic gas pressure at high temperatures in an autoclave (750°C at 7 kg/mm² for two hours is typical). The resultant product is 100 percent dense, has significantly better MYS values than its hot-pressed equivalent, and has significantly less preferred orientation than its hot-pressed equivalent. A one-piece, hollow mirror blank with an eggcrate internal rib structure made by the HIP process is shown in figure 7.

A second method that appears promising is the pressureless sintering method developed at Stanford Research Laboratory. This method involves exposing a green-pressed compact to high temperatures in vacuum. If the temperature is properly chosen, almost full density can be obtained without excessive grain growth. Preferred orientation, compared

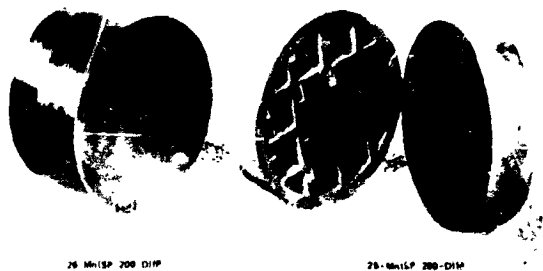


Figure 7. Finished and sectioned SP-200-D mirror blank.

with hot-pressed beryllium, is again significantly reduced.

Mirrors have been fabricated from beryllium prepared by both HIP and pressureless sintering processes. Although these show a marked improvement over mirrors made from hot-pressed beryllium, some thermal instability still exists. An example of this is depicted in figure 8, which shows the interference pattern at 80°C on a HIP beryllium mirror that was flat at 25°C. The deviations from flatness (about 1/4 wavelength) cor-



Figure 8. Surface distortion of ribbed beryllium mirror at 80°C. (Courtesy of the Perkin-Elmer Corporation.)

respond to the underlying rib structure of the mirror. We believe this is due to a slightly different preferred orientation in the polished surface as compared with the rib structures. Moberly (ref. 9) suggests that this anisotropy originates in the preferential stacking of the powder particles, which tend to be flake-like due to the propensity of beryllium to fracture on its basal plane. He has demonstrated that by reattritioning the green-compacted beryllium to produce larger aggregate particles and then recompacting and pressureless sintering, a very isotropic mirror material is produced. It is believed that the reattritioning process will also improve the HIP material; experiments to demonstrate this are under way. Use of spherical powders, for either the HIP or the pressureless sintering process, should also minimize inhomogeneous anisotropy; experiments are under way to demonstrate this.

Conclusion

We believe that the major causes of dimensional instability in beryllium mirrors have been recognized and that corrective measures for all of them are presently or potentially available. Thus, it appears that we are on the threshold of producing beryllium mirrors (and probably mirrors of other metals as well) with stabilities comparable to the best of the ceramic or glass mirrors.

References

1. Maringer, R. E.; Shemanski, R. M., et al.: An Investigation of the Dimensional Stability of Mirror Materials - Summary Report. Battelle Memorial Institute, 15 August 1968.
2. Bloxson, J. T.: Optical Materials Study Program - Second Annual Technical Report. Perkin-Elmer Corporation, September 1968.
3. Bonfield, W.; Sartel, J. A.; Li, C. H.: The Effect of Surface Condition on the Microstrain of Beryllium. *Trans. AIME*, Vol. 227, 1963, pp. 665-673.
4. Maringer, R. E.; Cho, M. M.; Holden, F. C.: Stability of Structural Materials for Spacecraft Application - Final Report. Battelle Memorial Institute, April 16, 1968.

5. Eul, W. A.; Woods, W. W.: Shear Strain Properties to 10^{-10} of Selected Optical Materials. NASA CR-1257, January 1969.
6. Leischer, K. A.: Thermal Treatments for Beryllium Study No. 8-Final Report on Minute-man Producibility. Report No. C5-996/32, Autonetics, Division of North American Aviation, Inc., May 1965.
7. Shemensi, R. M.; Beach, J. G.; Maringer, R. E.: Plating Stresses from Electroless Nickel Deposition of Beryllium. J. Electrochem. Soc., Vol. 116, 1969, pp. 402-408.
8. Holden, A. N.: Physical Metallurgy of Uranium. Addison Wesley, Reading, Mass., 1958.
9. Moberly, J.: Private Communication.

N70-36700

Pore-Free Ceramics Made by Sintering

J. E. Burke

General Electric Research and Development Center

Introduction

Ceramics have been little considered as mirror blank materials because, as conventionally produced, they are multiphase and have several volume percent of pores. The purpose of this brief note is to describe two single-phase pore-free ceramics that might offer advantages as a mirror material under conditions where their special properties would outweigh their disadvantages.

Lucalox[®] aluminum oxide ceramic is made by conventional ceramic-processing techniques from high purity aluminum oxide powder with the addition of about 0.1 weight percent magnesium oxide. The product is a pore-free, polycrystalline material having properties substantially the same as sapphire. The most important of these are set forth in table 1.

Table 1. Properties of Lucalox and Yttralox ceramics

Property	Lucalox [®]	Yttralox [®]
Composition	Al ₂ O ₃ - 99.9% MgO - 0.1%	Y ₂ O ₃ - 91% ThO ₂ - 9%
Crystal structure	Hexagonal	Cubic
Melting point (°C)	2050	2400
Density (gcm ⁻³)	3.98	5.30
Modulus of rupture (psi)	>40,000	~17,000
Young's modulus (psi)	57 x 10 ⁶	25 x 10 ⁶
Coefficient of thermal expansion (°C ⁻¹)	6.3 x 10 ⁻⁶	7.9 x 10 ⁻⁶
Hardness (moh)	9.0	7.2

Yttralox[®] is a material of similar microstructure, also made by cold pressing and sintering from yttrium oxide powder with the addition of several percent of thorium oxide. Its properties are also set forth in table 1.

Potential as Mirror Material

It must be emphasized that these materials are essentially unevaluated as mirror materials; however, they possess certain unique characteristics that recommend them and certain intrinsic disadvantages as well.

Advantages

Yttralox and Lucalox are the only oxide ceramics that can be prepared in reasonable sizes in pore-free, single-phase form. There is no glossy phase present although the specimens are polycrystalline. Because they are prepared by cold pressing and sintering powders, they can be made by present technology in complex shapes and in diameters up to several inches. There is no fundamental limit to size, and, with moderate development, it should be possible to prepare discs from 6 to 10 inches in diameter.

It is characteristic of these oxides that dislocation mobility is exceedingly low at room temperature; hence, the materials will have very great dimensional stability and should not creep at all after polishing. Yttralox is somewhat harder than glass and can be readily polished. Lucalox has the same hardness as sapphire; hence, it is somewhat more difficult to polish.

The outstanding characteristic of Lucalox is its high Young's modulus (nearly

60 million psi). Yttralox has a Young's modulus of 25 million (about 2.5 times glasses). In each case, it should be possible to make thinner blanks for a given diameter than is possible with glass.

Joining techniques are available for these materials. In Lucalox, some joints have been made without the aid of any foreign substances; i.e., by joining the pieces in the green state so that no differences in coefficient of expansion are introduced. It is believed that the same techniques could be applied to Yttralox. More commonly, solder ceramics of lower melting point are used.

Disadvantages

Both materials have relatively high coefficients of expansion; hence, temperature gradients will cause distortions.

Lucalox has a hexagonal crystal structure. Although the polycrystalline body is isotropic as regards coefficient of expansion, the individual grains have slightly different coefficients of expansion in different directions $\alpha = 9.2 \times 10^{-6}$ per degree C parallel to the C-axis, and $\alpha = 8.2 \times 10^{-6}$ per degree C perpendicular to the C-axis). As a result, on a microscopic scale, stresses will develop between grains when the temperature is changed and may cause local distortion. No

direct observation of these distortions has been made to the author's knowledge. This same anisotropy in coefficient of expansion leads to grain boundary shearing stresses that can produce a tendency toward grain boundary cracking in relatively large-grained material. As a consequence, it is difficult to polish surfaces without some chipping ("pull-outs") at unfavorably oriented grain edges.

If Lucalox were to be seriously considered for mirror blanks, it would be most desirable to develop processing techniques to produce a pore-free microstructure at a grain size of 10 microns or less.

Yttralox is cubic, and preliminary observations indicate that it is easier to polish than Lucalox and without pull-outs. Because the coefficient of expansion is the same in all directions, there are no local distortions with change in temperature.

Summary

It is conceivable that Lucalox® and Yttralox® might be useful for astronomical mirrors in which high rigidity would outweigh the disadvantages of a relatively high coefficient of expansion. Joining techniques are available that might permit lightweight structures to be made of these materials.

N70-36701

Dimensional Changes in Glass at Room Temperature

J. E. Burke

General Electric Research and Development Center

It is conventional to characterize commercial glasses by giving the temperatures of the flow point (log viscosity = 7.5 to 8.0), the anneal point (log viscosity = 13.0), and the strain point (log viscosity = 14.5). Experimental observations of viscosity have been made up to viscosities of about 10^{18} , and, very roughly, a linear relationship between log viscosity and the reciprocal of the absolute temperature is found for the range $\log \eta = 9$ to 18. Extrapolations of these viscosity values to room temperature yield computed values of viscosity far in excess of 10^{25} . Such values are clearly immeasurable because, at a viscosity of 10^{25} , the strain rate is 10^{-8} per day at a stress of 100,000 pounds per square inch (ref. 1).

R. W. Douglas (ref. 1) has reported the results of several investigators who have observed analytic effects or other stress relaxations in glasses at temperatures ranging from a few hundred degrees Celsius down to room temperature. It is clear that these distortions must occur by a mechanism different from that which operates to produce viscous flow at elevated temperatures.

A number of observations of analytic effects in glass have been made by using internal friction measurements (ref. 2). At temperatures in the neighborhood of room temperature, it is commonly assumed that these effects are due to the movement of network-modifying ions such as sodium rather than to any rearrangements involving the silicon-oxygen bond.

It is the purpose of this brief report to suggest that such stress-induced ionic movements may produce analytic distortions in the surface of figured mirrors, that the relaxation

times may be long, and that the effects may be surprisingly large. In addition, I should like to call attention to a theoretical analysis of this phenomenon recently made by R. J. Charles (ref. 3).

The simple physical picture of the phenomenon is that, when a stress is applied to a specimen containing a mobile ionic species (such as sodium in glass), the free energy of the system will be reduced if the ions move into the region of tension from the region of compression. Such ionic transport will build up a space charge that will oppose further movement so that, in a suitable time, a steady state composition gradient will be reached. If the external stress is removed, a permanent set will be observed in the piece; gradual relaxation to the original configuration will then occur at a rate controlled by the diffusion coefficient of the mobile species.

If only a single ion is involved, Charles computes that the relaxation times should be relatively short, even at room temperature. Most of the space charge will be concentrated within a few microns of the specimen surfaces, and the relaxation times will be, at most, a few tens of seconds.

If, however, two ion species are present (e.g., sodium and potassium), the first response to the stress application will be the movement of the more mobile sodium ions. A longer term effect will involve the interchange of sodium and the larger potassium ions to produce a further stress relaxation without change in space charge. This latter effect, which involves the movement of many ions over larger distances, will have a much longer time constant, e.g., weeks or months.

There is little direct experimental evidence as yet to support quantitatively the Charles analysis. Some years ago, for a different motivation, Charles performed the experiment shown in figure 1. A filament of soda-lime glass was bent elastically to produce a stress of about 100,000 pounds per square inch and held for about two hours at 250°C. After cooling, it had developed the permanent set shown in the lower part (a) of figure 1. Upon reannealing at 250°C overnight, the fiber recovered the great part of the strain, as shown in the upper part (b) of figure 1.

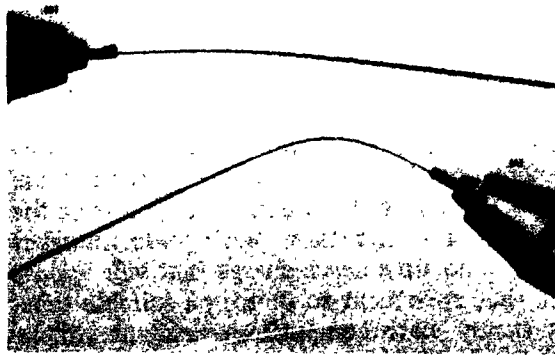


Figure 1. Soda-lime glass fibers: (a) held 4 hours at 250°C at bending stress of 100,000 pounds per square inch and (b) same fiber reheated 4 hours at 250°C.

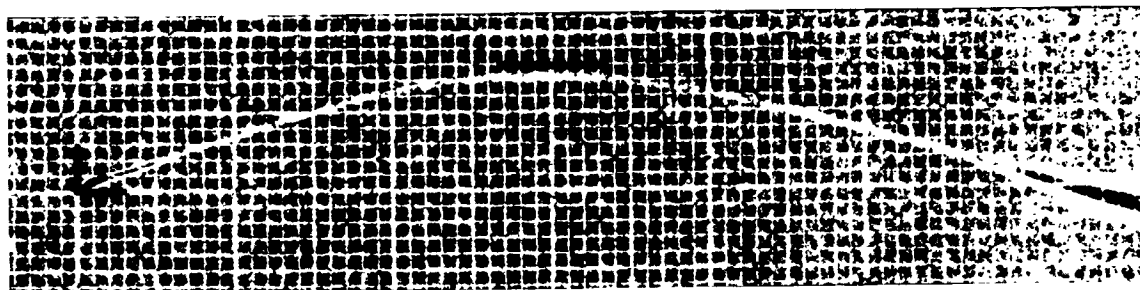
To further check this phenomenon, R. J. Charles, Miss A. M. Turkalo, and I carried out similar experiments on commercial Pyrex-glass cane, drawn into filaments. The 0.010-inch fibers were bent to a small radius to yield a surface stress of about 200,000 pounds per square inch. The bent fibers were then held at 250°C for 68 hours and again cooled to room temperature. Upon removal of the stress, these fibers were found to be bent with an 0.7-inch displacement of the midpoint of the 6-inch fiber, as can be seen in figure 2. Partial recovery to the original shape occurred in 4 hours at 250°C, and, after 20 hours, the offset had been reduced to approximately 0.4 inch.

Fused quartz filaments exposed in a similar fashion showed no discernable set after the same treatment. Similar fused-quartz specimens displayed an exceedingly slight bend (approximately 0.1 inch as measured above) after 20 hours at 650°C.

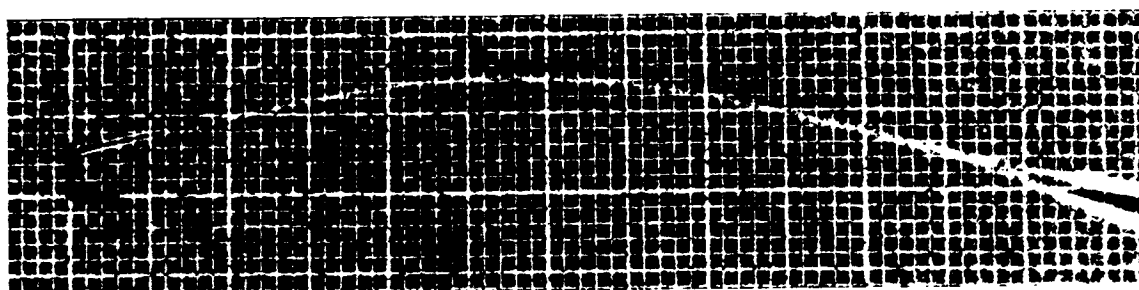
These experiments must be considered as most informal, being performed in a crude fashion to obtain some observations in a short time.

The distortion is assumed to be a consequence of stress-induced ionic motion, as described by Charles (ref. 3). The recovery of the distortion after the load was removed is assumed to occur also by reverse ionic movement and is assumed to parallel the behavior of a mirror surface that intersects a region of residual stress in the underlying blank. The observations show that quite appreciable distortions can occur, over relatively long times, at temperatures at which viscous flow cannot occur by the mechanisms that operate at elevated temperatures. The very much smaller distortions of the fused silica specimen is assumed to be a consequence of purity rather than intrinsically higher softening temperature. Since there are very few mobile alkali ions present, the diffusional distortion mechanism cannot operate.

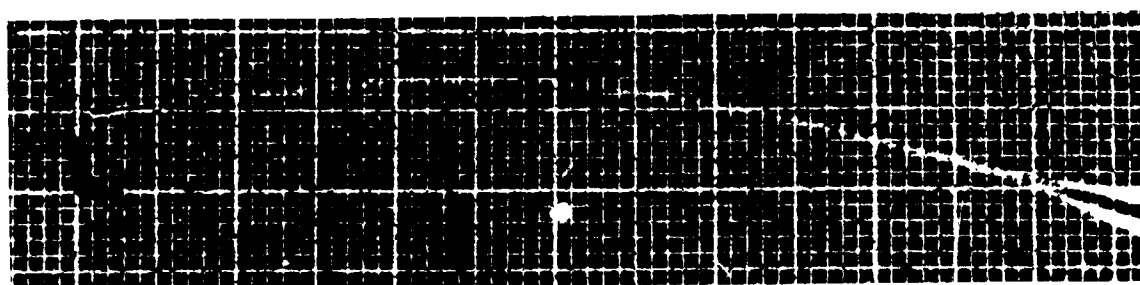
The arguments in this report predict that permissible residual stress level in a mirror blank should be related to the composition of the glass. If it is a relatively pure single-component glass or, more specifically, if it has no highly mobile ions in it, any stressed region revealed in polishing would relax with a very short time constant; hence, relatively large residual stresses would be acceptable. If there were a single mobile ion present, the relaxation should occur in a matter of minutes or perhaps a few hours. With two or more moving ionic species (as probably exist in Pyrex), the relaxation times are many hours even at 250°C and probably months or years at room temperature. In these glasses, residual stresses should be kept to a much lower value.



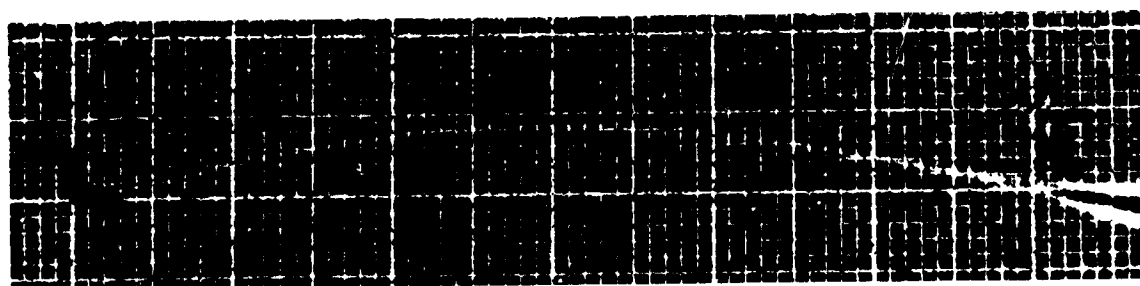
(a) Residual bend in fiber after loading at 200,000 pounds per square inch at 250°C for 68.5 hours.



(b) Partial relaxation in same fiber after heating at 250°C for 4 hours.



(c) Increased relaxation in same fiber after heating at 250°C for 20 hours.



(d) Increased relaxation in same fiber after heating at 250°C for 20 hours.

Figure 2. Recovery of pyrex fiber deformed by bending at 250°C.

The very crude experiments reported are far from quantitative, but the general technique might be made quantitative and might provide a rationale for determining permissible residual stress levels in materials that can be drawn into fibers.

References

1. Frechette, V. D., ed.: Various Papers. Non-Crystalline Solids, John Wiley & Sons, New York, 1960.
2. Kirby, P. L.: "Kinetics of Stress Relaxation in Noncrystalline Solids," Non-Crystalline Solids, John Wiley & Sons, New York, 1960.
3. Charles, R. J.: Stress Induced Binary Diffusion. Journal of the American Electrochemical Society, submitted for publication.

N70-36702

ULE Titanium Silicate for Mirrors

Charles F. DeVoe
Corning Glass Works

Introduction

The properties of ultra-low expansion, ULE titanium silicate (ULETM) are discussed in this paper as a mirror material.

The synthesis of ULE titanium silicate, the fabrication of structures, and the subsequent optical finishing of these structures are all done by the same fundamental processes that have produced several hundred lightweight mirrors over the past 9 years.

This transparent material exhibits the smallest distortion due to temperature changes of any material known ($\alpha = 0 \pm 0.03 \times 10^{-6}$ from 5°C to 35°C).

It is made in boules approximately 6 feet in diameter that can be shaped and fused together without destroying the near-zero thermal expansion properties. This permits the manufacture of fused, monolithic, ultra-lightweight structures.

Glass has been a good mirror-blank material ever since Leibig invented a way to make it highly reflective over a hundred years ago.

The attributes for an ideal mirror material are:

- Dimensional stability
- Polishable
- Low thermal expansion
- High thermal diffusivity
- High elastic-modulus-to-density ratio
- Homogeneous
- Clarity for inspection
- Size capability
- Lightweight capability

Each of these will be discussed in more detail.

Dimensional Stability

In practice, glass appears to have great dimensional stability. Experiments over many years with highly stressed glass objects have failed to show permanent strain or stress release at ordinary temperatures. We, however, were probably looking for gross effects compared to the requirements for a large space telescope. On the other hand, optical objects have retained good figures over many years.

Table 1 is a list of fused-silica mirror blanks supplied by the Corning Glass Works. As far as we know, none of these blanks has demonstrated problems caused by permanent changes of dimensions.

Corning has continually searched for deviations in use from the concept of excellent glass stability. Years ago there was a contention among apparatus glass blowers that long tubing stored horizontally on two brackets would bend in time. Research revealed that glass blowers preferred straight tubing and selected it first, leaving the bent tubing on the rack.

ULE titanium silicate has the same general random, molecular structure as glass and fused silica; thus, dimensional stability as related to structure should be like that of fused silica.

Polishable

Dietz and Bennett (ref. 1) state that "surfaces of fused quartz having a root-mean-square roughness of about 3 angstroms have been obtained by using the bowl feed

20708
 Table 1. Fused Silica Mirror Blanks Supplied by Corning Glass Works

Purchaser	Mirror Blank Size	Weight (lbs.)	Mμ/cm Anneal	Year
Princeton University	37" D x 5 1/4" T	400	30	1959
Princeton University	37" D x 5 1/4" T	400	30	1959
Flagstaff	62" D x 11" T	2,625	22.0	1961
University of Michigan	50" D x 8" T	1,225	8.9	1963
University of Michigan	50" D x 8" T	1,225	7.7	1963
Calif. Inst. of Tech.	61" D x 10" T	2,200	6.5	1964
University of Michigan	62" D x 10" T	2,400	5.3	1964
American Optical (Wright-Patterson AFB)	103" D x 12 1/2" T	7,600	13.5	1965
Kitt Peak	63" D x 9" T	2,250	9.6	1965
University of Texas	108" D x 11 3/4" T	8,500	5.2	1965
Kitt Peak	82" D x 9" T	3,800	9.0	1966
University of Hawaii	88" D x 11 1/2" T	5,525	7.8	1967
Sacramento Peak	64 1/2" D x 10 1/2" T	2,680	5.9	1967
European Southern Obs.	144" D x 21" T	24,500	2.0	1967
Canadian	156 3/4" D x 25" T	33,300	3.0	1967

method." Verbal reports from a number of finishers state that ULE finishes very much like fused silica does.

Thermal Expansion

Figure 1 shows the extremely low thermal expansion of the ULE material (Code 7971) around room temperature. Fused silica also has a region of zero expansion but around the very inconvenient temperature of approximately -150°C . At room temperature, the expansion of fused silica is at least 15 times that of current ULE material. A Pyrex®-brand blank expands by another factor of 4 to 5 more than fused silica does.

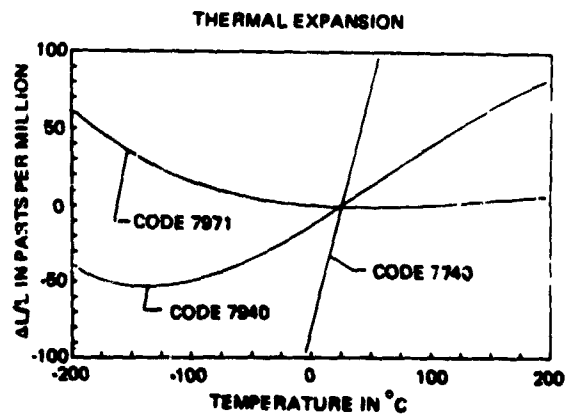


Figure 1. Thermal expansion of the ULE material.

The advent of these very low expansion materials generated the need for more precise measuring techniques. Plummer and Hagy (ref. 2) have described Corning's work with two techniques. One uses a Fizeau interferometer, and the other involves a rod type of dilatometer. The accuracy of the dilatometer has been further improved since that paper was published.

A third method for measuring the overall expansion of a blank will be described by the Itek Corporation in a future issue of "Applied Optics." This involves the use of a holographic interferometer.

A comparison of the current status of these measurements is shown in table 2.

High Thermal Diffusivity

This factor becomes very much less important as the thermal expansion coefficient approaches zero. It is, of course, one of the most important advantages of metals over glass. Selection of a glass for this property would not be significant because of the narrow range of values for most glasses (ref. 3). It is interesting that fused silica is at the top of the range.

High Elastic-Modulus-to- Density Ratio

The spread in this ratio for glasses is not very great; i.e., about 4.43×10^6 psi/gr/cc

for ULE to 5.38 for a low-expansion glass-ceramic. A ratio of the order of 7.5 can be obtained with some glass-ceramics but at great sacrifice of low thermal expansion. On the other hand, beryllium has a ratio of 23.

Homogeneity and Clarity for Inspection

These properties go well together, particularly for a transparent material such as ULE glass. Small differences in composition, such as cords, produce large distortions in transmitted light paths, and birefringence studies can quickly reveal differences in mechanical properties throughout a single piece. The difficult problem, however, is relating these to the actual performance in a mirror blank. Even though some early work demonstrated that satisfactory figures could be obtained on blanks having over 80 millimicrons per centimeter birefringence, much progress has been made in the control of our process to 20 millimicrons per centimeter or less.

Size Capability

Boules, such as the one shown in figure 2, are about 6 feet in diameter as they come from the furnace in which the material

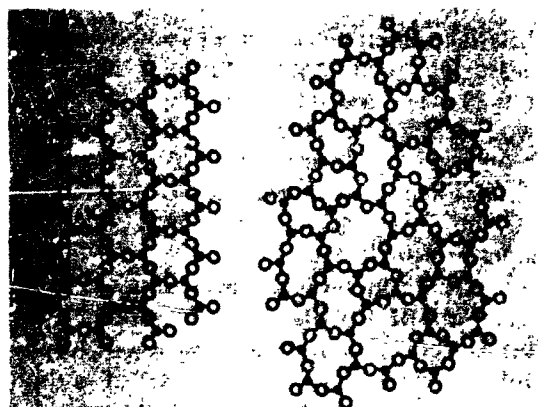
Table 2. Thermal Expansion Measurements; Comparison of Three Methods

1. ITEK		$0.026 \times 10^{-6}/^{\circ}\text{C.}$	21 - 42°C.
	Equivalent	$-0.005 \times 10^{-6}/^{\circ}\text{C.}$	5 - 35°C.
CORNING		$-0.009 \times 10^{-6}/^{\circ}\text{C.}$	5 - 35°C.
2. CORNING	(Private Lab.)	Mechanical and Interferometer	
	9 Samples	$-0.003 \pm 0.012 \times 10^{-6}/^{\circ}\text{C.}$	5 - 35°C.
3. PERKIN-ELMER	(Private Lab.)	Agree within $0.014 \times 10^{-6}/^{\circ}\text{C.}$	

(70% of 60 runs on Corning Glass Works Superdilatometer have spread under 0.006.)



Figure 2. Boule, 6 feet in diameter, as it comes from furnace in which it is produced.



(a) Crystalline silica (b) Fused silica

Figure 3. One-dimensional models developed by Zachariesen and Warren.

is produced from the vapor state. These can be machined and fused together to make larger sizes. As shown in table 1, blanks up to 157 inches in diameter by 25 inches thick have been delivered in fused silica. The same technique and apparatus work for ULE glass.

Lightweight Capability

There is no technical limitation on size capability.

Structure of ULE Glass

Zachariesen (ref. 4) and Warren (ref. 5), using x-ray techniques, developed the one-dimensional model for crystalline silica, shown in figure 3a, and for fused silica, shown in figure 3b. The black dots represent silicon ions, and the circles represent oxygen. Actually, in three dimensions the silicon ions are bonded to four oxygen ions, and each oxygen ion is linked to two silicon ions. When the crystalline silica is heated above the liquidus, the structure opens up and becomes irregular.

Harold Smyth (ref. 6) of Rutgers University has made calculations that account for the zero expansion of fused silica at low temperatures. This property is based on the open structure permitting more lateral vibration of the oxygen ions than when they are

confined in the crystal structure. The temperature around which the expansion changes from positive to negative and the general shape of the expansion-versus-temperature curve can be changed by the addition of titanium. The titanium ions substitute for some of the silicon ions in the random glassy network and permit different vibrational characteristics. This accounts for the zero expansion of ULE titanium silicate around room temperature.

The vibrational concept to explain zero expansion seems to be further confirmed by the large increase in thermal expansion when soda is added to fused silica. According to Warren (ref. 7), the sodium ions occupy holes in the network, as shown in figure 4. These ions limit the lateral vibration of the oxygen so that, when heat is applied, the network expands.

Summary

This great similarity of structure between ULE titanium silicate and fused silica adds all of the advantages of fused silica to the very low thermal expansion of ULE to make it an ideal mirror material.

The fact that this material can be fused with a flame or in a furnace without destroying the near-zero expansion makes possible the construction of any size required.

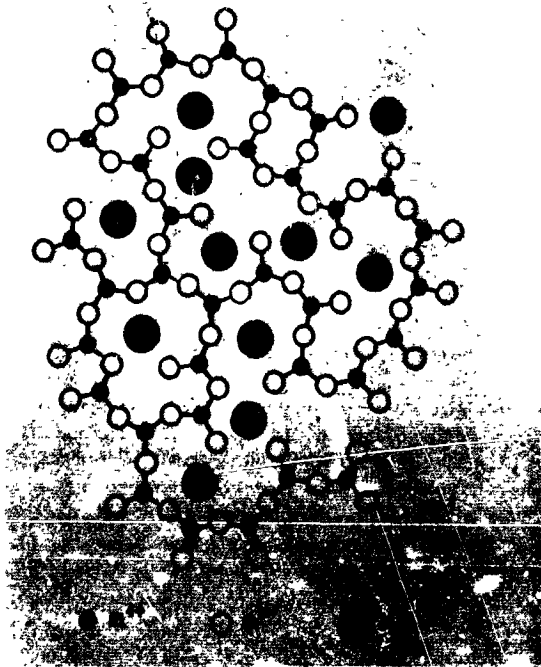


Figure 4. Sodium ions (shaded) occupying holes in network of fused silica.

References

1. Dietz, R. W.; Bennet, J. M.: Bowl Feed Technique for Producing Supersmooth Optical Surfaces. *Applied Optics*, vol. 5, no. 881, 1966.
2. Plummer, W.A.; Fagy, H.E.: Precision Thermal Expansion Measurements on Low Expansion Optical Materials. *Applied Optics*, vol. 7, no. 824, 1968.
3. Shand, E.B.: *Glass Engineering Handbook*. McGraw-Hill Book Company, Inc., New York, 1958, p. 30.
4. Zacharisen, W.H.: Atomic Arrangement in Glass. *Journal of the American Chemical Society*, vol. 54, no. 3841, 1932.
5. Warren, B. E.: X-ray Determination of the Structure of Liquids and Glass. *Journal of Applied Physics*, vol. 8, no. 645, 1937.
6. Smyth, Harold: Booklet published by NSF, Grant No. G24276, February 1966.
7. Warren, B.E.: Summary of Work on Atomic Arrangement in Glass. *Journal of the American Ceramic Society*, vol. 24, no. 256, 1941.

PRECEDING PAGE BLANK NOT FILMED.

N70-36703

Mirror Materials

Marvin C. Riggert and Robert F. Copper

General Electric Company

Four of the important design considerations for high-resolution astronomical mirrors are the thermal stability, thermal expansion, ability to obtain and to retain surface finishes, and the mechanical characteristics of the material used to fabricate these mirrors. These properties are basic to the material and present the limiting factors to distortion-free imaging. In addition, optical surfaces can be deformed by thermal stresses in the mirror material, resulting in a distorted image (ref. 1). The combination of good thermal stability, low thermal expansion, ease of obtaining good optical finishes and the ability of the material to retain these finishes indefinitely, high modulus of both rigidity and elasticity, and a minimum of thermal stresses within the material are of critical importance in the proper selection of the material for optimal performance. Two materials, one the standard in high-resolution mirror blanks and the other a ceramic possessing these characteristics in comparably high quantities, are compared in table 1.

After World War II, the introduction of commercially available fused quartz made possible considerably more effective mirror blanks. A most significant point of progress came with the manufacture and shipment of the 158-inch-diameter mirror blank to the Kitt Peak National Observatory. This 15-ton blank, shown in figure 1, was formed by fusing together several hundred hexagonal quartz ingots and consists of a substrate made from two layers of 6-inch ingots 12 inches high and a cap 5 inches thick made from 21-inch hexagonal ingots. Since the manufacture of this blank, great strides have been made in increasing the ingot sizes for large mirror manufacture. Figure 2 represents the original 6-inch ingots used in the Kitt Peak blank as well as the 21-inch ingots used for the surface. In addition, the newer manufacturing facilities have produced this 72-inch-diameter giant.

This manufacturing accomplishment demonstrates that there now exists no foreseeable theoretical limitation on size for

Table 1. Comparison of Two Mirror Materials

Material	Thermal Expansion	Rigidity Modulus	Modulus of Elasticity	Poisson's Ratio	Stress Level
Fused Quartz	0.55×10^{-6}	4.5×10^6	10.5×10^6	0.16	<10 mm/cm
Lucalox*	8.5×10^{-7}	23×10^6	57×10^6	0.23	None**

*Registered trademark, General Electric Company.

**Lucalox is stress-free. Since it is a polycrystalline material and the crystalline structure is randomly oriented, Lucalox will not hold stresses as amorphous materials do.

single-piece-construction, fused quartz blanks. In addition, the stress levels for these large blanks may be reduced even further. This particular blank showed a stress of approximately 8 millimicrons per centimeter through the 12-inch thickness.

Single-piece-construction, fused-quartz mirror blanks can now be manufactured in sizes in excess of any previously manufactured, and fused ingot construction is now established to a point where almost any size or shape can be produced.

Astronomical mirrors historically are in the form of right circular cylinders. For large, high-performance systems, this form suffers because the self-weight deflection of the mirror, which is proportional to $(D^2/H)^2$ with D being the diameter and H the thickness of the mirror, requires excessively thick and, hence, heavy mirrors to maintain the desired contour (ref. 2). A solution to this has been in the construction of lightweight mirror structures in which material is removed from the mechanically nonusable center portion of the structure and is added to the diameters. The objectives are maximum weight reduction (up to 70 percent), mechanical rigidity approaching that of solid blanks, and economical manufacture.

The simplest approach to taking weight out of a quartz mirror would be by substituting removable cores for quartz ingots in a checkerboard pattern on the bottom half of

a blank. As an alternate, a fused solid blank could be core drilled or otherwise machined on the back side. The limiting factor for weight reduction is the minimum web thickness practical from a manufacturing process; nevertheless, a 50-percent weight reduction is considered attainable. The need for a back-plate is recognized, however, to provide suitable rigidity to the structure. For sometime, it was this need that cast doubt upon the feasibility of producing very large, lightweight, quartz blanks.

Initial efforts centered around making quartz-to-quartz seals of front and back plates to a separating matrix of various configurations. The basic problem involved in doing this is to accomplish a strong, continuous joining of the parts without distorting or sagging of the material. It is also highly desirable from a structural standpoint that the matrix be a continuous network and, if not cast in one piece or machined from a single piece, that the individual elements be sealed together. Because a strong, continuous joint meant that the material had to be heated to a point where the parts would flow together, a degree of sagging and distortion was inevitable. A process for making quartz-to-quartz seals was developed, and, in addition to the inherent distortion, the following limitations were noted:



Figure 1. The 158-inch-diameter mirror blank at Kitt Peak National Observatory.



Figure 2. Original 6-inch and 21-inch ingots used in Kitt Peak mirror blank and a new 72-inch-diameter giant ingot.

1. Inability to expect a continuous, high integrity seal without excessive deformation of the structure

2. Difficulty of sealing to very thin-walled matrices (for maximum weight reduction) without destroying the structure

3. Problems of sealing up to very large sizes

4. Difficulty of sealing the lightweight network together to form a united network of maximum rigidity.

As a result, additional approaches were sought.

Ideally, quartz parts should be sealed together at temperatures well below the softening point, thereby producing highly reliable joints from a structural standpoint and yet not introducing factors that would deteriorate the thermal and mechanical stability of the mirror. The answer was a lower melting glass that seals to quartz, has a thermal expansion coefficient close to quartz, and is mechanically and chemically stable. Such a glass is now available, and a number of lightweight mirrors have been made by using this glass as the bonding medium. This solder glass makes possible the fabrication of lightweight mirrors in an almost limitless variety of substrate designs and makes feasible even the largest lightweight structures under current consideration.

The solder glass has a softening point below the softening point of fused quartz and a thermal expansion coefficient of about 8×10^{-7} as compared to 5.5×10^{-7} for fused quartz. Small, lightweight mirrors made by using the solder glass to seal quartz plates to a substrate of quartz tubing have been tested and found thermally stable over the range between 0° and 80°C . These tests have also established that there is no "print through" due to the use of the solder glasses. In addition, testing has shown that this technique results in highly reliable seals. These results are readily explained by the fact that the seals are diffusion bonded. This not only tends to grade out even minute differences in expansion but also results in acceptably low stresses and highly reliable bonds.

Some of the designs manufactured thus far are:

1. *Cored substrate* figured to accept a machined top plate with a planobackplate. The 25-inch diameter blank shown in figure 3 is an example of this. The weight reduction is 55 percent. This design is quite adaptable to very large sizes, and additional weight reduction may be possible by coring out in the heavier section of the web and removing material in the side of the cored hole; i.e., a "Swiss cheese" effect. The largest blank of this type made thus far is the 25-inch-diameter piece.

2. *Hexagonal tubing sections* as a substrate. In this case, the nest of hexagonal sections were ground to the spherical shape. A solid quartz plate was matched to this curve and sealed to the substrate. The backplate is flat. After the figuring of the top plate, the blank will be of uniform thickness, center to edge. In this particular blank, the hexagonal tubing pieces making up the matrix were not sealed to each other. This can be done, and has been done, on smaller prototypes although some preparatory finishing of the individual hexagonal pieces may be required to assure good contact between pieces. A weight reduction of 63 percent was realized in this design.



Figure 3. Cored substrate design figured to accept a machined top plate with a planobackplate; 25-inch-diameter blank.

3. *Square tubing sections nested and sealed together with solder glass to form a continuous matrix* (figs. 4 and 5). Planomirrors of this design have been made in small prototype sizes, typically 12 inches in diameter, and initial testing of this design is very encouraging. For maximum weight reduction, the squares are assembled in a checkerboard pattern. Typically, wall tubing that is 1 inch by 1 inch by 1/16 inch has been used although capability exists for producing 2-inch square tubing and undoubtedly larger size squares would be used for larger mirrors. This design has great potential for optimizing lightness and rigidity and, as in all other designs, offers "scale up" feasibility. The corners of the individual squares are machined prior to sealing to assure good alignment and contact. Like all potential structures, the



Figure 4. Square tubing sections nested and sealed together with solder glass to form a continuous matrix.

matrix may be figured after sealing and prior to attachment of the top plate so that a uniform top plate thickness is generated. Weight reduction for this design is 63 percent.

4. *Round quartz tubes set apart as separators for the front and back plates.* Very high weight reduction is possible by utilizing this technique, but this design will not give the same rigidity as the other alternates. Twelve-inch-diameter prototypes have been made.

With the increasing requirements for astronomical mirrors, especially for aerospace applications, additional properties of the mirror material become increasingly important. Higher moduli, greater resistance to attack by various atmospheres, lighter weight, and greater thermal diffusivity are parameters that are being sought. As a class, ceramics possess these properties and are becoming more important in mirror applications.

Lucalox[®] ceramic is a polycrystalline material manufactured from a fine-grain, high-purity, aluminum oxide. The microscopically small pores found in conventional materials (shown on the left in fig. 6), which make the materials opaque, have been entirely removed in Lucalox (shown on the right in fig. 6). This material has high chemical and thermal stability, high intergranular bond strengths, high strength-to-weight ratios, and is resistant to oxidation and corrosion. Lucalox has a

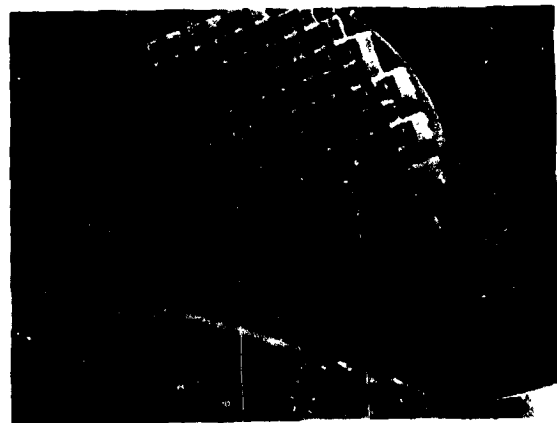


Figure 5. Squares assembled in checkerboard pattern for maximum weight reduction.

density nearly twice that of fused quartz, but its modulus is $5\frac{1}{2}$ times that of fused quartz.

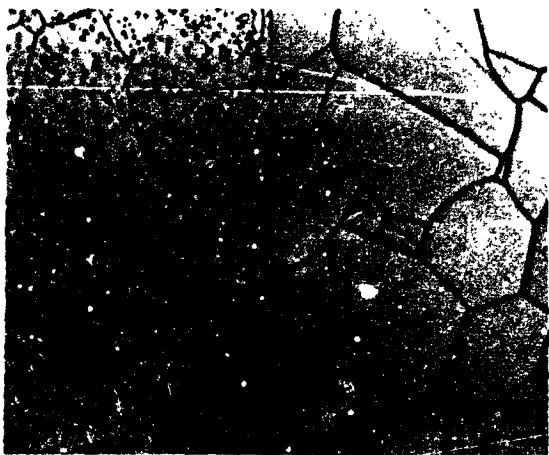


Figure 6. Microscopically small pores found in conventional materials (left) entirely removed in Lucalox (right).

Therefore, mirror structures could be made that have half the thickness of quartz and still maintain greater rigidity. Lucalox can be manufactured in nearly any shape, thus further "lightening" could be instituted by making single-piece mirrors with a ribbing structure on the reverse side. A design has been devised that would allow for a 115-square-inch mirror surface that would weigh less than 4 pounds and would maintain rigidity exceeding that of quartz.

References

1. Hanson, J. N.: Jour. O. S. A., vol. 55, no. 916, 1965.
2. Schroeder, J. B.; Morse, S. E.: An Evaluation of the Thermal Stability of Soldered Lightweight Mirrors. Perkin-Elmer Corporation, to be published.

PRECEDING PAGE BLANK NOT FILMED.

Shear Strain Properties to 10^{-10} of Selected Mirror Materials

William A. Eul and W. William Woods
The Boeing Company

N70-36704

Introduction

The results of a research program, conducted over the period from August 1967 to March 1968, under the microstrain portion of a contract for the investigation of the effects of low energy protons on specular reflectance of surfaces for space mirrors are presented in this paper.

The overall objective of the program was to determine the nonrecoverable deformation of candidate materials for telescope mirrors after application and release of short-term torsional shear stresses. Viscoelastic strain-recovery characteristics were measured. These are presented as well as the nonrecoverable strain-versus-applied-stress data.

Microstrain measurements of heat-treated specimens yielded precise, consistent curves of nonrecoverable strain versus stress. Viscoelastic decay proceeded rapidly, thus allowing testing to be completed in reasonable time intervals. The as-machined specimens, by comparison, were grossly inconsistent in their nonrecoverable strain characteristics, had viscoelastic decay parameters of much larger magnitude, and therefore required long observation time to achieve reasonable measurements. The one exception to this was Cer-Vit® 101, which exhibited identical, consistent behavior both before and after heat treatment.

The viscoelastic recovery characteristic is not readily represented by a first order system, wherein the motion is described by a time exponent of a constant such as the Napierian base (e). The decay is, however, closely represented by a constant negative

exponent of time. The exponent differs with the material and, in some materials, with history and environment.

The relationship between stress and nonrecoverable strain appears to be a power-law characteristic for the materials studied over the range of strain from 10^{-6} to less than 10^{-9} . This implies that there is no observable threshold effect but that a permanent offset, however small, results from any applied stress.

The microstrain testing equipment consists of four major elements: extensometer, loading system, thermal control system, and signal conditioning and recording system. A complete description of this equipment appears in the March 1969 issue of the *IEEE Transactions* under the title "Optical Material Submicrostrain Test Apparatus."

A current study to determine the microyield properties of telescope mirror materials is presently in the testing phase. Identical specimens of fused silica, Cer-Vit, and beryllium are being stressed in torsion, tension, and compression to compare microyield properties. An overlap occurs in the data over the strain range of 10^{-6} to 10^{-8} .

Data Presentation

The computed values of nonrecoverable strain are plotted versus stress on log/log graph paper to produce a smooth curve (fig. 1). A line is fitted by inspection through the points and the slope (N) determined. This slope is the exponent of the stress-strain relationship and determines the correction factor to obtain actual outside fiber plastic

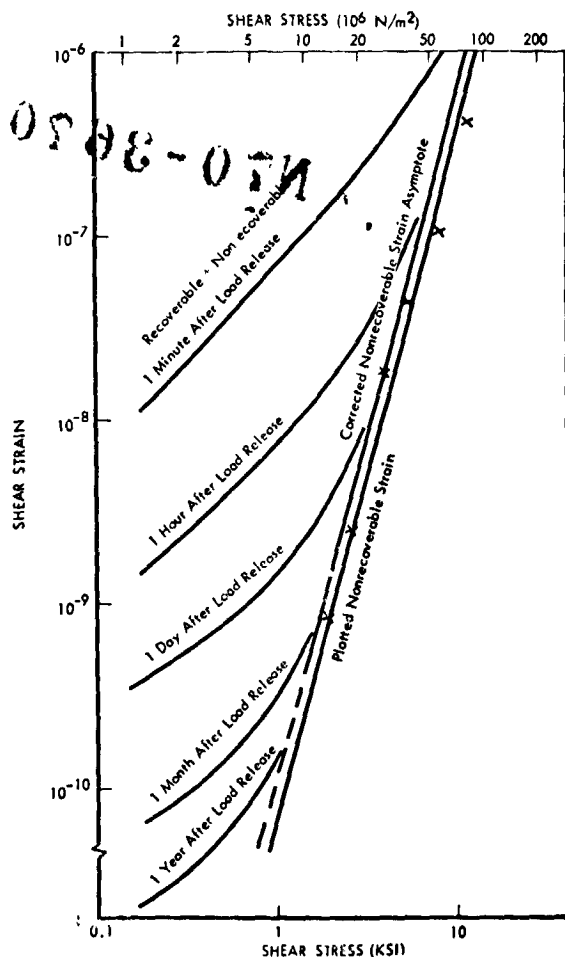


Figure 1. Typical specimen of shear-strain decay characteristics as a function of applied shear stress and time.

strain. The plotted curve is multiplied by this factor $((N + 3)/4)$ to produce a new parallel curve, which is labeled "the nonrecoverable strain asymptote."

The viscoelastic (or recoverable) strain values calculated from the empirical representation are added to this adjusted curve to yield strain values at various time increments (one minute, one hour, etc.).

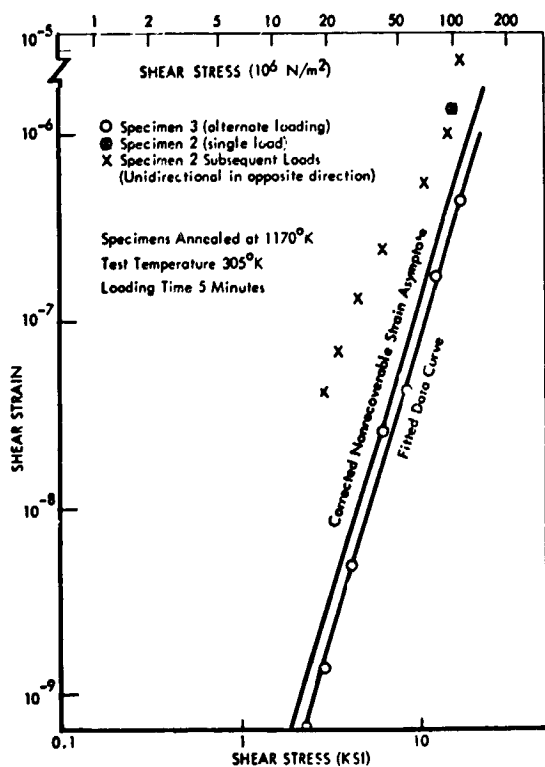
Overall results of the microstrain program are plotted in figures 2, 3, and 4. These curves depict the nonrecoverable (plastic) strain and the viscoelastic offset for various time intervals at a temperature of 305°K.

Nonrecoverable Strain

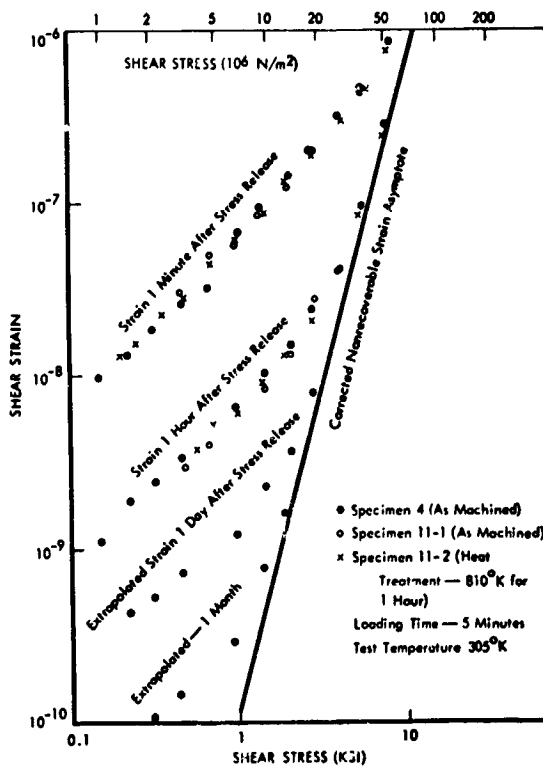
Nonrecoverable strain versus stress data were obtained on both heat-treated (fig. 2) and as-machined (fig. 3) specimens. Data from as-machined, 304L corrosion-resistant steel proved difficult to obtain and are not plotted. Data from heat-treated and as-machined Cer-Vit agree closely, and both are presented in figure 2(b). Two specimens of heat-treated, 304L corrosion-resistant steel were subjected to somewhat different tests, as shown in figure 2(a). Specimen 3 was subjected to progressive alternate loading. Specimen 2-2 was given a single load near the maximum load attempted on specimen 3, for comparison with the alternate loading tests. All subsequent loads on specimen 3 were made in the opposite direction to the single large load, starting at low levels and increasing to levels greater than the initial load. The difference in slope of the two sets of data may be attributed to the Bauschinger effect. The reason for the disparity in magnitude is not obvious, but it may be affected by material inhomogeneities as suggested by surface imperfections.

Of the three Cer-Vit specimens (numbers 4, 5, and 11), the data from number 5 proved essentially unusable because of interference from shoulder cracks induced by the mechanical clamps. Number 4 was fractured in testing. Number 11 was tested before and after heat treatment. As shown in figure 2(b), all three sets of valid data agree closely, indicating good material uniformity and stability of characteristics. A telephone conversation with James Duncan of Owens-Illinois Development Center, Toledo, Ohio, revealed that Cer-Vit is not amenable to annealing because it is completely devitrified and will revitrify before other changes occur. The heat treatment to which the present material was subjected (810°K for 1 hour) is safely below the 1200°K vitrification point.

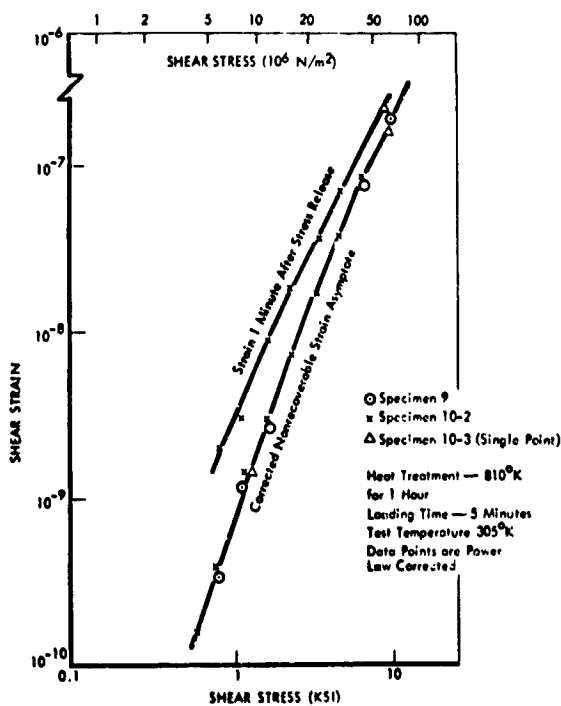
Two specimens of the 7940 fused silica were tested in the heat-treated condition; the results are plotted in figure 2(c). The single-stress performance of specimen 10-3 shows



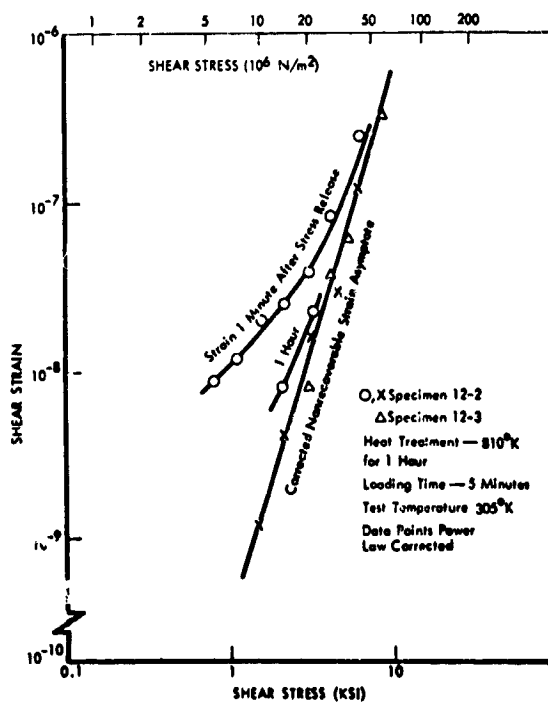
(a) 304L corrosion-resistant steel.



(b) Cer-Vit 101.



(c) 7940 silica.



(d) ULE silica.

Figure 2. Shear strain as a function of applied stress for heat-treated specimens.

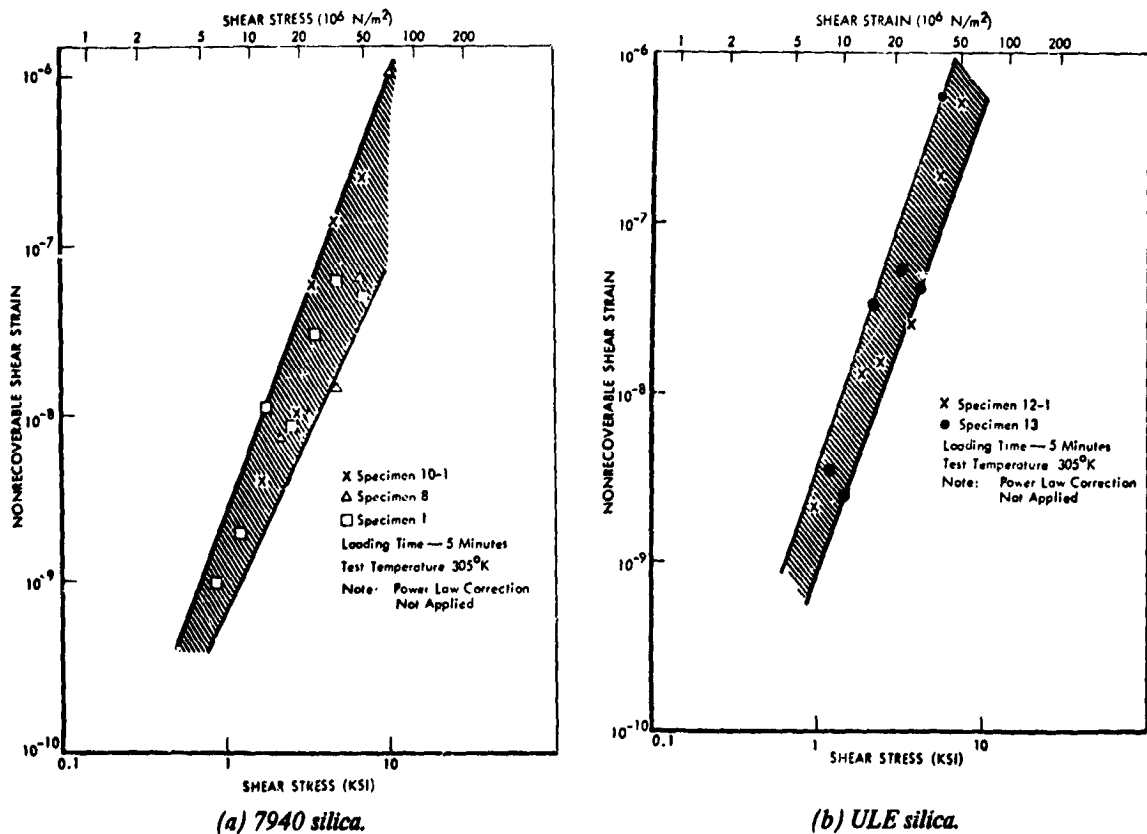


Figure 3. Nonrecoverable shear strain as a function of applied stress for as-machined specimens.

good conformity with that from the alternating loads of specimens 9 and 10-2. This appears to validate the alternating load procedure.

A series of accidents and shortage of time restricted the tests of heat-treated 7971 ULETM silica to two runs of a single specimen. Results are plotted in figure 2(d).

The performance of as-machined specimens of 7940 and 7971 silicas before heat treatment is plotted in figure 3. These data are sufficiently erratic so that a single curve is not representative. Instead, approximate variation limits are indicated, showing roughly one order of magnitude variation in nonrecoverable strain measurements. The mechanism responsible for this erratic behavior is not evident. If a surface condition were responsible, comparison of specimens with different diameters should behave differently. The two tested specimens of ULE 7971

were of differing diameters; thus, one had twice the torsional stiffness of the other. The plotted data do not indicate appreciable differences.

The 810°K heat treatment employed on the silicas has been categorized by the manufacturer as insufficient to cause measurable annealing of body strains. The changes produced are nonetheless quite striking.

A comparison plot of nonrecoverable microstrain characteristics of all stabilized materials tested thus far is shown in figure 4. The curve shown for beryllium is from a previous inhouse program. Other than beryllium, all tested materials have roughly comparable nonrecoverable strain characteristics.

The linear relationship between nonrecoverable stress and strain on a log/log plot implies a power-law relationship. This indicates absence of a strictly defined "proportional limit." In other words, down to the

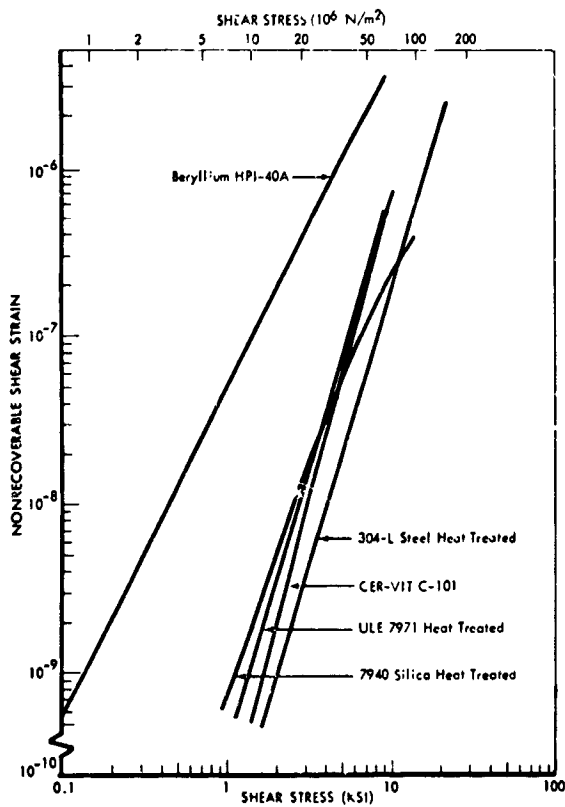


Figure 4. Comparison of nonrecoverable shear strain as a function of applied shear stress for materials tested.

limits of measurement, a nonrecoverable strain is induced by any applied load, however small.

Viscoelastic Decay

The viscoelastic decay characteristics of all materials tested appear to be similar in that they may be represented by a straight-line plot on log/log graph paper. This implies that the decay follows the function:

$$Y = A_0 + A_1 t^{-B}$$

where Y is the strain at any point in time; A_0 is the permanent or nonrecoverable strain; A_1 is the viscoelastic strain at time ($t = 1$); and B is a function of the material and its condition.

Viscoelastic parameters of the various materials were determined as a byproduct of the nonrecoverable strain extrapolation procedure. The elastic strain under load is also listed for comparison. The parameter A_1 is the viscoelastic or recoverable strain at one minute after load release. The parameter B is the time exponent of the decay curve. The parameter A_1 for the heat-treated steel specimens was consistently less than 5×10^{-10} , making a quantitative determination of viscoelastic parameters beyond the capabilities of the instrumentation. Viscoelastic parameters for the heat-treated steel are therefore not listed.

The viscoelastic parameters of Cer-Vit are reasonably consistent between specimens and between the as-machined and heat-treated conditions. The steel, silica, and ULE specimens, however, showed marked changes after heat treatment, with overall reduction and shortening of viscoelastic decay. A comparison of tabulated viscoelastic data of specimens 10 and 12 revealed that the viscoelastic decay rate of the heat-treated silicas was an order of magnitude faster than the as-machined state.

Graphical display of viscoelastic behavior of the materials is shown in figure 2. Wide differences are apparent between the various materials. Of the glassy materials, 7940 silica exhibits the most rapid viscoelastic decay.

Conclusions and Recommendations

The conclusions are categorized in relation to nonrecoverable strain, viscoelastic strain, and viscoelastic theory.

Nonrecoverable Strain Conclusions

1. All materials tested in the micro-strain program exhibited similar nonrecoverable strain characteristics when subjected to appropriate heat treatment.

2. The 7940 and ULE silicas in the as-machined state provided inconsistent nonrecoverable microstrain performance.

3. Causes for the differences in nonrecoverable microstrain performance for 7940

and ULE, between as-machined compared with heat-treated, are not obvious. Postulated reasons include material manufacturing processes, internal strains induced by machining, and surface strains and microstrain cracks induced by grinding.

4. Cer-vit demonstrated no nonrecoverable strain improvement when subjected to a heat-treatment procedure. Influence by variations of the same or similar mechanism cannot be ruled out.

5. Within the measuring capability of the instrumentation (i.e., 10^{-10} nonrecoverable strain), no region of purely elastic stress-strain relationship was found. The elastic limit is implied as being zero stress.

Recommendation for Conclusions 1 thru 5

The optimum procedure to be employed in the fabrication of stable mirrors will depend upon establishing the cause of inconsistent, nonrecoverable, microstrain behavior. Several methods of attack are available for tracking down these sources. Heat-treating the specimens before machining would establish the effect of the machining process. Surface-etching, polishing, or roughening would establish the role of surface-conditioning. A separate program to investigate these aspects is recommended.

Viscoelastic Strain Conclusions

6. The viscoelastic recovery rate of the heat-treated silicas was an order of magnitude faster than in the as-machined state.

7. Heat-treated 7940 silica is superior in viscoelastic recovery rate to either the ULE silica or Cer-Vit.

Recommendation for Conclusions 6 and 7

If viscoelastic recovery rate is important to mirror performance, as in an active mirror system, careful consideration and under-

standing of mirror substrate heat treatment is necessary. Selected variations of heat treatment and ambient test temperature are expected to yield significant differences in both the viscoelastic behavior and the non-recoverable strain. A specimen temperature of 305°K was maintained for all tests in the program. This temperature was chosen as being reasonably close to laboratory ambient, yet high enough above expected excursions of ambient to allow close control of heating. The ambient temperature of mirrors in space will range approximately between ambient and 187°K. A separate program to investigate the effects of heat treatment and test temperatures on mirror substrate viscoelastic strain rates, by using the short-term loading procedure, is recommended.

Viscoelastic Theory Conclusions

8. Past studies on viscoelastic creep behavior of materials have established a linear relationship between strain and the logarithm of time. The present program indicates a more accurate representation to be a linear relationship between the logarithm of strain and the logarithm of time. The significance of this discovery is not immediately obvious. Theoretical analyses formulated to take account of the previous representation do not appear to be readily reconciled with the present one.

Recommendation for Conclusion 8

A review of solid-state viscoelastic theory in the light of Conclusion 8 is in order. It is recommended that creep tests of a number of basic glass types of materials, including those tested in this study, using extended loading periods (1 hour to 1 week) be undertaken. In addition, an outstanding individual in the field of solid-state viscoelastic theory in glasses should be commissioned to participate in the investigation.

Degradation of Mirror Surfaces in a Proton Environment

E. L. Hoffman
NASA Langley Research Center

N70-36705

The Langley Research Center has sponsored a research and development contract to investigate the effects of low energy protons on the specular reflectance of mirror surfaces. Mirror samples were exposed to 10 KeV protons in a 10^{-7} torr vacuum environment. The protons induced contaminant films to be deposited on the mirror surfaces; therefore, studies of the contaminant films were also performed. This paper includes discussions of the test variables investigated, typical specular reflectance results, and the contaminant films.

The variables investigated are summarized in table 1. All reflective surfaces were vacuum-deposited aluminum with overcoatings of magnesium fluoride (MgF_2) or lithium fluoride (LiF). Substrate materials

Table 1. Degradation of Mirror Surfaces in a Proton Environment

REFLECTIVE SURFACES Aluminum with MgF_2 or LiF overcoatings
SUBSTRATE MATERIALS Kanigen-plated HP-40 beryllium 7940 fused silica C-101 Cer-Vit
PROTON IRRADIATION Energy level: 10 KeV Flux: 10^9 to 10^{12} protons \cdot cm^{-2} sec^{-1} Integrated flux: 10^{14} to 10^{16} protons \cdot cm^{-2}
REFLECTANCE MEASUREMENTS 900 to 2500 Å: McPherson monochromator (<i>in situ</i>) 0.2 to 2.5 μ : Cary 14 spectrophotometer 2 to 50 μ : Beckman IR-12 spectrophotometer

included Kanigen-plated HP-40 beryllium, 7940 fused silica, and C-101 Cer-Vit. The proton flux was varied from 10^9 to 10^{12} protons \cdot cm^{-2} sec^{-1} and the integrated flux from 10^{14} to 10^{16} protons \cdot cm^{-2} . The maximum integrated flux approximates about 5 years in space in a synchronous orbit. Specular reflectance was measured from 900 angstroms to 50 microns. In the 900-to-2500-angstrom range, measurements were made *in situ* by using a McPherson 25 monochromator. Measurements in the 0.2-to-2.5-micron range (using a Cary 14 spectrophotometer) and in the 2-to-50-micron range (using a Beckman IR-12 spectrophotometer) were made after samples had been removed from the vacuum chamber. Reflectance measurements made *in situ* after exposure to air revealed that there was some reflectance recovery but that the recovery was generally a small part of the total reflectance change. Major changes in reflectance were obtained within the measurement range of the *in-situ* equipment.

Typical results of the degradation of specular reflectance due to a proton environment can be shown by presenting the data for a magnesium-fluoride-coated Cer-Vit mirror. Data for this mirror are shown in figure 1. The specular reflectance in percent is plotted against wavelength in angstroms for a proton flux of 1.4×10^{11} protons \cdot cm^{-2} sec^{-1} . Data from 900 to 2500 angstroms were obtained *in situ* with the ultraviolet monochromator and from 2500 to 6000 angstroms with the Cary 14 spectrophotometer after the samples were removed from the test chamber. Data are not presented for wavelengths beyond 6000 angstroms because there was essentially

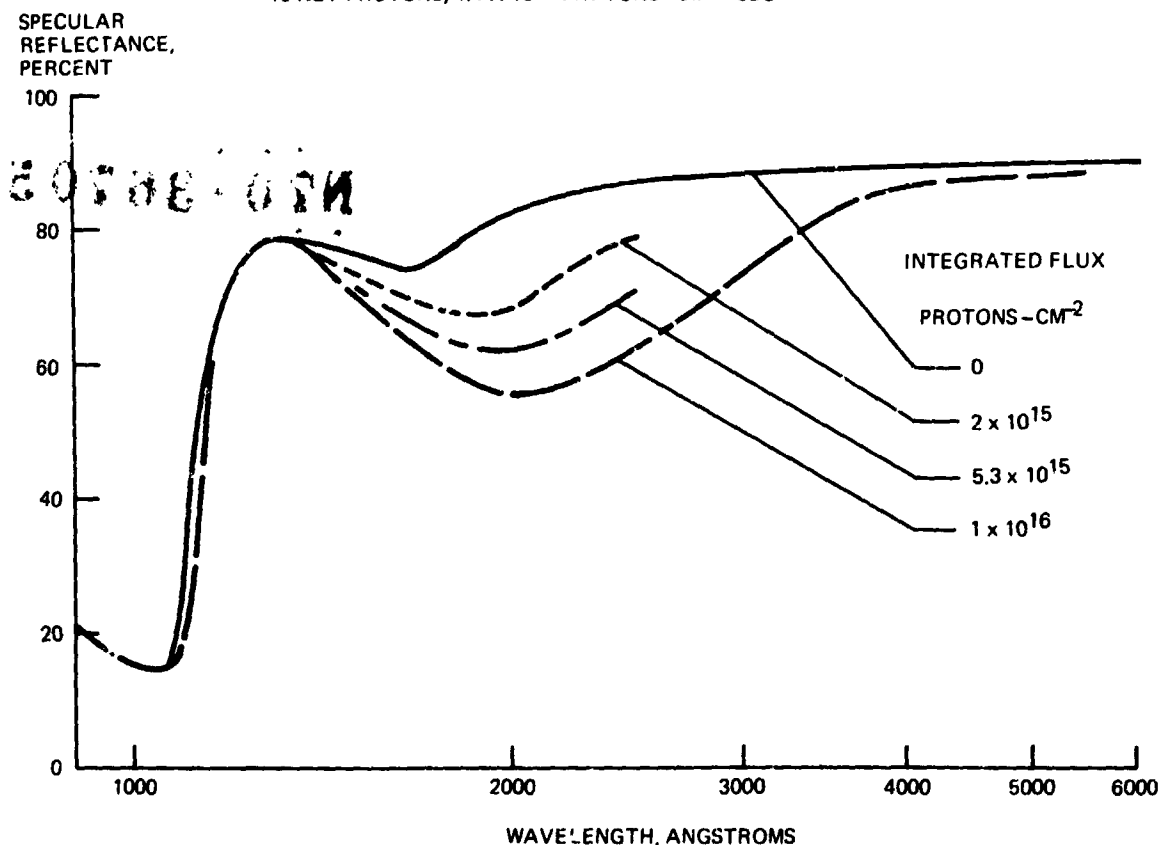
10 KEV PROTONS, 1.4×10^{11} PROTONS-CM⁻² SEC⁻¹

Figure 1. Specular reflectance of MgF₂ coated mirror.

no change in reflectance. The upper curve in figure 1 shows reflectance before irradiation; the lower curve, reflectance after exposure to an integrated flux of 1×10^{16} protons-cm⁻². Some intermediate curves are also shown. Because the protons induced contaminant films to be deposited, the reflectance change is not due only to protons.

Maximum changes in reflectance occur at 2100 angstroms, which is very pronounced in this plot, and also at 1100 angstroms, which is more difficult to see because of the slope of the curves in this wavelength region. Therefore, the changes in reflectance are shown in figure 2. The percent of change in reflectance is plotted against wavelength for the same integrated fluxes as shown in figure 1. The change in reflectance at 1100 angstroms shows as a sharp peak on this plot;

for an integrated flux of 1×10^{16} protons-cm⁻², the change in reflectance is approximately 30 percent at both 1100 and 2100 angstroms. Subsequent experiments with relatively thick magnesium-fluoride coatings showed that contaminant films as thin as 50 angstroms could produce reflectance changes as large as 30 to 40 percent at minimum interference positions while producing essentially no change at maximum interference positions.

The effect of flux and integrated flux on reflectance degradation is shown in the change in reflectance at 2100 angstroms wavelength, figure 3. The percent of change in reflectance is plotted against the integrated proton flux for proton fluxes from 2×10^9 to 1.4×10^{12} protons-cm⁻² sec⁻¹. The increase in reflectance degradation with integrated flux is readily apparent. The main point to be

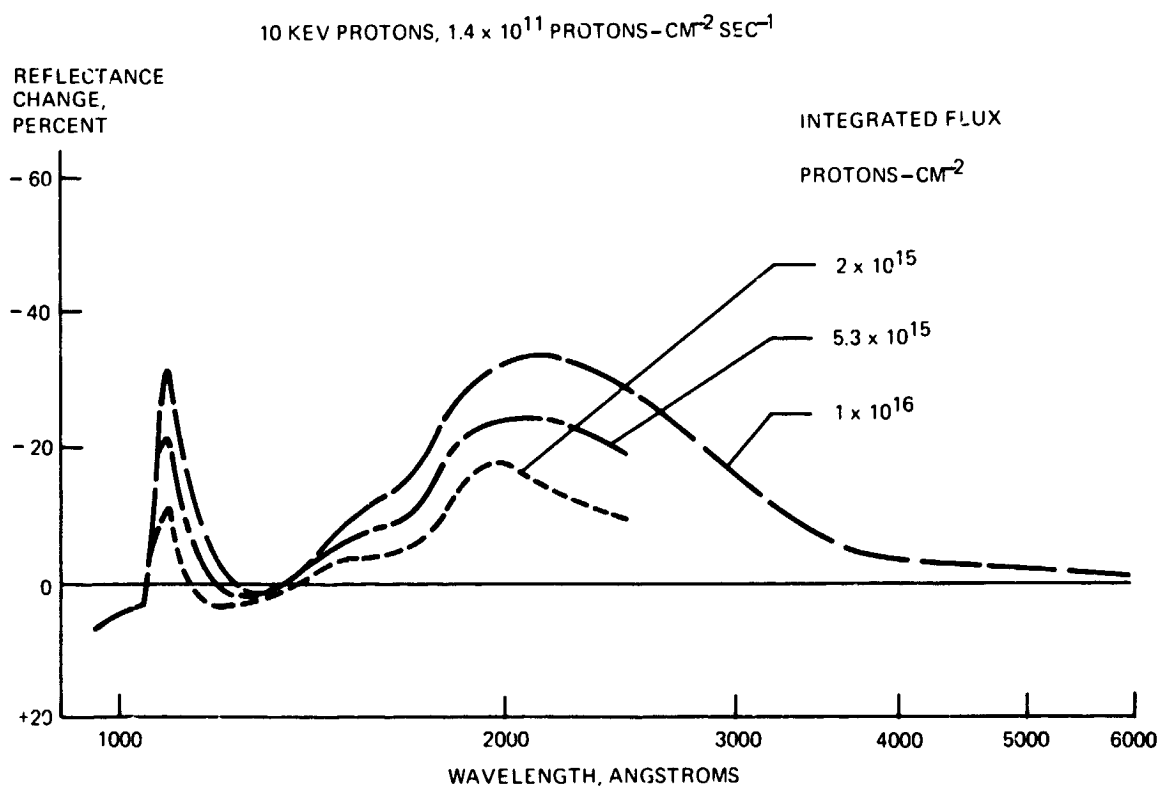


Figure 2. Reflectance degradation of MgF_2 coated mirror.

made, however, is that degradation increases at the lower flux levels, which require the longer exposure times.

Because mirror surfaces are particularly sensitive to contamination, the contamination level in the vacuum chamber was studied extensively. Samples exposed to the vacuum environment for as long as two weeks with the proton beam off showed no appreciable change in reflectance; yet, the increased reflectance degradation with lower flux levels or increased exposure times indicated deposition of a contaminant film. In further studies to determine the presence of contaminant films, it was found that contaminant films were deposited on the mirror samples but only where the surface had been irradiated.

During the course of the contamination studies, methods of removing the films without damaging the reflective surface were

also investigated. A method using atomic oxygen was developed that appears particularly promising.

The change in reflectance due to cleaning with atomic oxygen is shown in figure 4. Specular reflectance in percent is plotted against wavelength in angstroms. The curves for before irradiation and after 1×10^{16} protons-cm⁻² are the same as shown in figure 1. After irradiation, the sample was exposed to atomic oxygen for 5 minutes; the reflectance nearly returned to the before-irradiation curve shown. It should not be concluded that practically all degradation was due to contamination and that practically no degradation would be obtained from protons because the contaminant film, as it was deposited, may have prevented some proton damage or the atomic oxygen cleaning process may have bleached some of the proton damage.

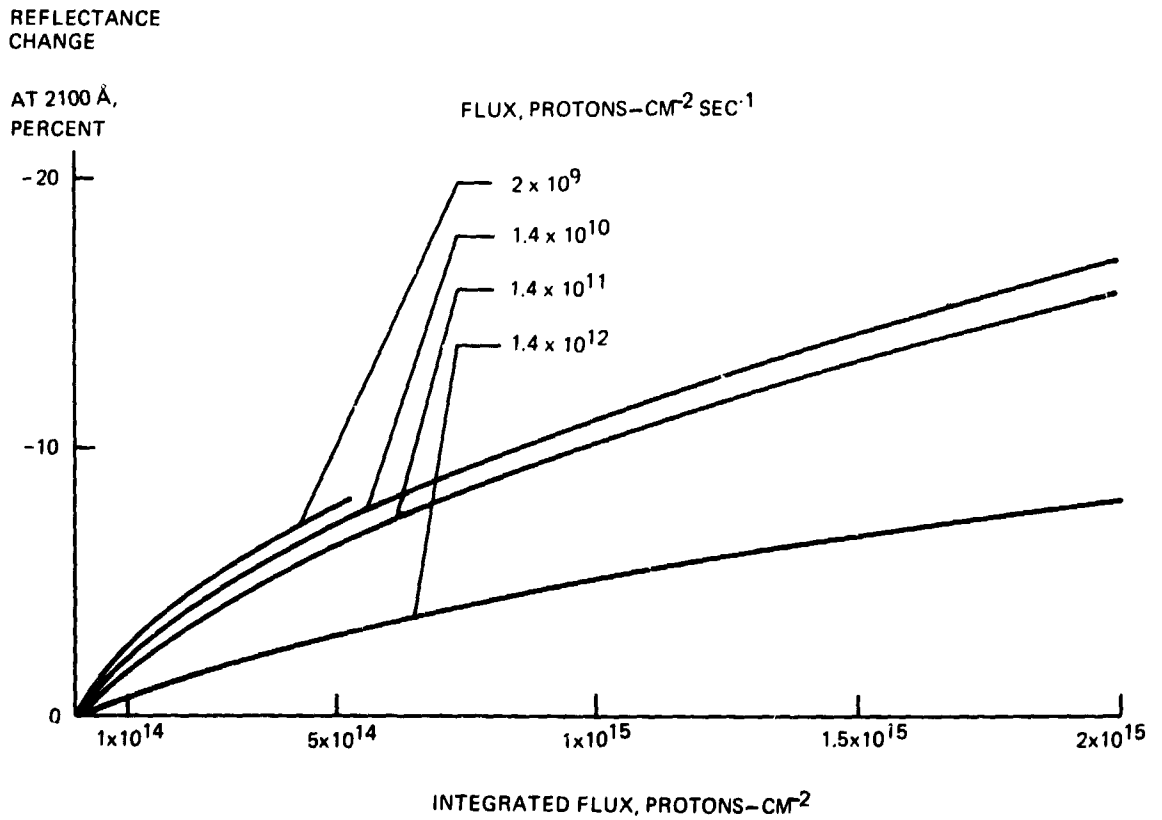


Figure 3. Effect of proton flux on reflectance of MgF_2 coated mirror.

The data presented are for magnesium-fluoride-coated Cer-Vit mirrors. Similar results were also obtained for mirrors with lithium-fluoride coatings. It should also be noted that magnesium-fluoride-coated silver mirrors on space satellite ATS-III in synchronous orbit have experienced degradation. In the 3000-to-4000-angstrom waveband, reflectance has decreased approximately 40 percent on an unshielded mirror and approximately 10 percent on a mirror with a fused silica shield that would stop protons.

Summary

From reports of window contamination on spacecraft and the proton-induced

contamination of the present study, it appears that contamination of mirror surfaces in space may be a more serious problem than proton degradation. Studies of both types of degradation should be continued. Any studies of contamination of mirror surfaces in a vacuum environment should include a radiation source because some types of contaminant films may not be deposited without irradiation. Investigation of proton effects on mirror surfaces requires an ultra-clean vacuum system be used. This should include elimination of all elastomer seals as well as pumping systems using oils. Finally, a mirror-cleaning method has been developed that uses atomic oxygen; this cleaning method may have application to cleaning mirror surfaces in space.

SPECULAR REFLECTANCE, PERCENT

10 KEV PROTONS, 1.4×10^{11} PROTONS- $\text{CM}^2 \text{SEC}^{-1}$

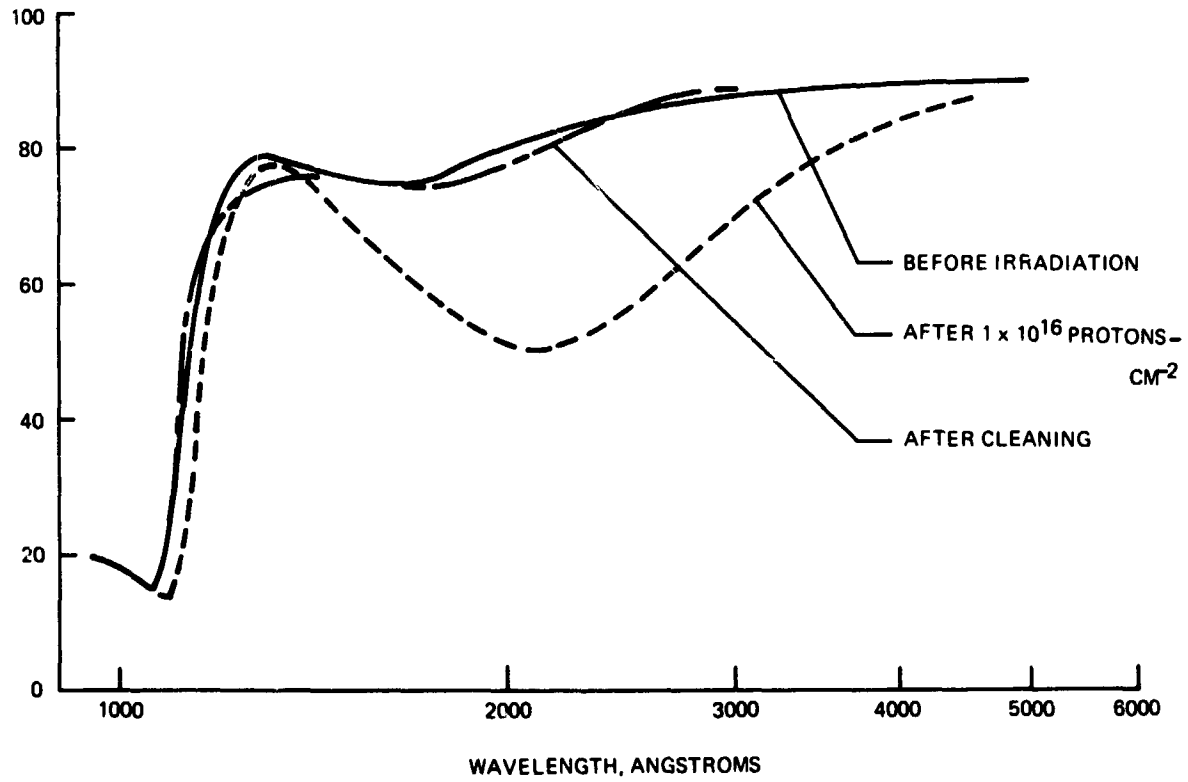


Figure 4. Reflectance of MgF_2 coated mirror after cleaning.

PRECEDING PAGE BLANK NOT FILMED.

The Design of Lightweight Cer-Vit Mirror Blanks

George A. Simmons
Owens-Illinois, Inc.

N70-36706

Introduction

The Orbiting Astronomical Observatory (OAO) program being carried out by NASA has aroused considerable interest in mirrors that will be of suitable design for launching and performance in an earth orbit. A technical review of the requirements for orbiting a large optical telescope will undoubtedly point to the necessity of having a lightweight mirror. Therefore, this paper is concerned with a new technique for producing lightweight mirror blanks from Cer-Vit® C-101 material. After a brief description of the material properties that are important in lightweight mirrors, the technique for producing the mirrors is outlined. Its advantages and limitations are given and some structural designs that can be produced are shown. A complex, but thorough, mathematical analysis of three specific mirror designs was performed, and the results are given in the form of calculated deflection profiles of the lightweight mirrors. A tentative design is presented for a 120-inch-diameter lightweight mirror. Further studies needed to achieve an optimum design for a very large orbiting mirror are listed in this paper.

Material Properties

Cer-Vit C-101 material is a member of a relatively new family of microcrystalline, polycrystalline materials called "glass-ceramics." (Adequate descriptions of glass-ceramics are available in reference 1.) Appendix A briefly outlines pertinent information on the properties of Cer-Vit C-101 that are of importance in lightweight mirror

production and performance; namely, polishability, expansion coefficient, stiffness, microcreep, and stability. It is clear from these data that the C-101 material represents a significant advancement over the materials previously used to make mirror blanks.

Lightweight-Mirror Production Technique

The technique now in use (ref. 2) for producing lightweight mirror blanks of Cer-Vit C-101 material involves the machining of cavities into a solid blank. This approach permits a thorough inspection for quality before adding the expense of the machining operation. Having passed these quality-assurance inspections, the solid blank is processed through the machining area for removal of the as-cast surfaces. Holes are machined into the back of the blank corresponding to the chosen web-structure arrangement. Machine tools operating through these holes are used to undercut the backplate, thus enlarging the holes into accurately positioned cavities and leaving the specified web structure between cavities. This machining technique assures dimensional control of all surfaces, which are then comparable to the surfaces achieved with normal metal-working. After removal of the desired mass of material from the cavities, the mirror is brought to its final external dimensions. The machining completed, the blank is acid-polished to remove any surface imperfections that have been generated, thus returning the blank to its original strength. Studies show that the polishing removes any tiny surface imperfections that might act as stress concentrators. In

addition, a significant strengthening results from the acid-polishing.

This method provides a completely monolithic structure and incorporates a large radius fillet for added strength between webs and between each web and the adjoining back and front plates. Calculations show that the center deflection of an edge-supported plate is reduced to 0.437 times that deflection by this incorporation of a fillet into the structure, thereby significantly increasing the structural stiffness and improving stress distribution.

This process of machining cavities into the blank offers a broad freedom in mirror design. A wide variety of cavity sizes and shapes can be produced, and the web thickness and locations can be freely varied. The process does, however, impose some limitations. At present, the holes in the backplate that open into large cavities must be at least 2-1/4 inches in diameter to permit entry of the working tools. Efforts are being made to develop tooling that will operate through smaller holes. Web thickness down to 1/4 inch is normal, but 1/8-inch-thick webs can be produced. The weight reduction achieved varies with the cavity size and configuration chosen. The ideal size and shape of the cavities will be determined by the shape and size of the mirror, the degree of lightweighting, and the method of mounting. Satisfactory reductions in weight, such as 75 percent removal, can be achieved readily.

Lightweight Designs

The design of an optimum lightweight mirror is a complex matter. First, the stiffness-to-weight ratio that is to be achieved must be defined. Whether the emphasis will be primarily on stiffness or primarily on weight will depend upon the intended application.

Three specific designs were chosen for comparison in order to illustrate more completely the capabilities of the lightweight-mirror production technique. These designs contain triangular, square, and hexagonal cavities, respectively. Each of these mirrors is 64 inches in diameter and 12 inches thick. A

solid Cer-Vit C-101 mirror of these dimensions would weigh 3475 pounds. These dimensions were chosen to obtain a lightweight mirror weighing about 1000 pounds and are *not* intended to indicate what we consider to be an optimized design; rather, they are based upon the present state-of-the-art. The faceplates are 1-inch thick, easily thick enough to avoid any generation of a "waffled" or "quilted" surface during the finishing operation. It has been decided to make the backplate 1-1/2 inches thick, thus obtaining a backplate of the same weight as the front plate. Again, this does not represent an optimum configuration because the weight taken out of the backplate by machining could be used elsewhere more effectively to gain greater stiffness than by increasing the backplate thickness, as was done here.

Figure 1 is a cutaway view of a typical mirror containing triangular cavities, and figure 2 is an engineering drawing of this specific 64-inch mirror blank. Each cavity contains an entrance hole (2 1/2 inches in diameter) in the backplate. The ribs are 0.20-inch thick. All fillets at the intersection of ribs with one another and with the front and back plates have 3/4-inch radii. This leaves a large post of material at the intersection of each set of six triangles. Weight was reduced at little expense to the stiffness by removing material from the centers of these posts by machining a 1 1/2-inch-diameter cylindrical cavity into them. The center-to-center distance of these holes is 7.30 inches.

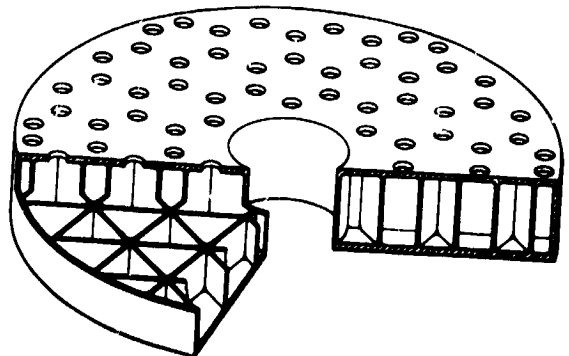


Figure 1. Cutaway view of typical mirror containing triangular cavities.

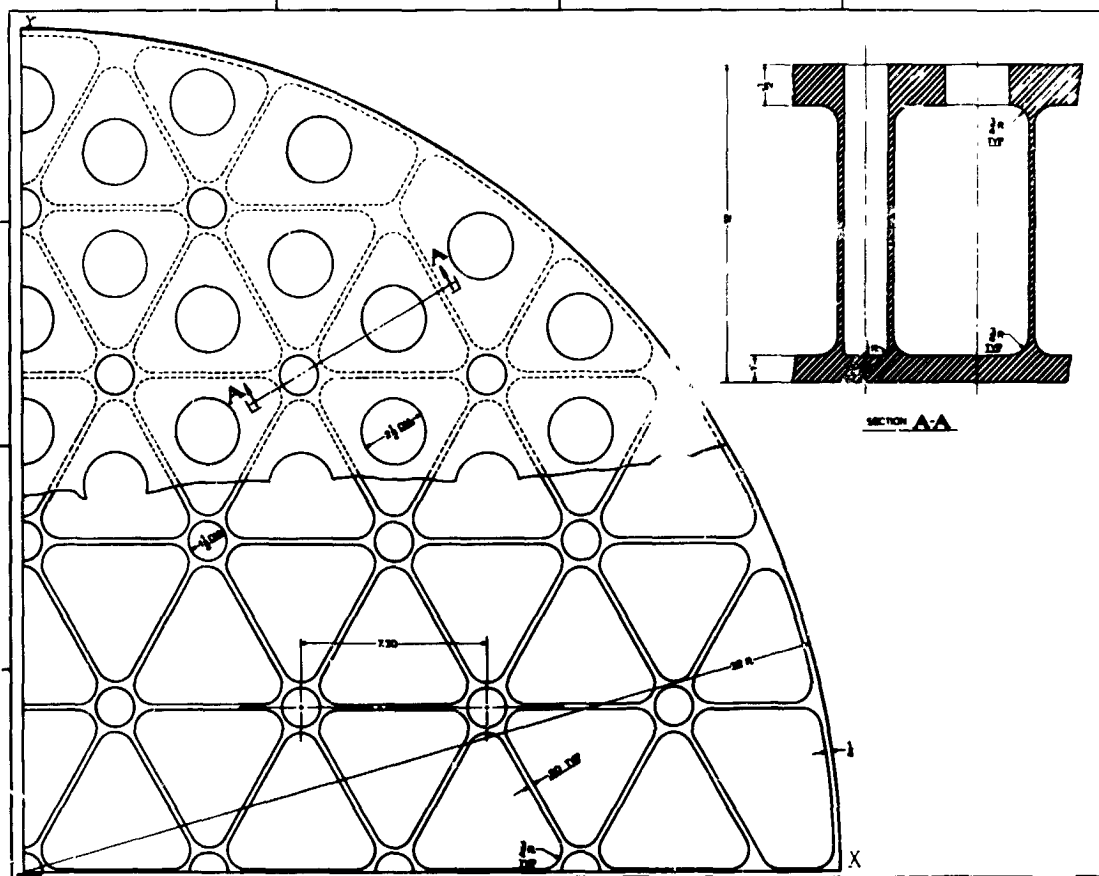


Figure 2. Engineering drawing of 64-inch mirror blank with triangular cavities.

The height of each equilateral triangle is 5-1/4 inches. This blank contains 138 large, shaped cavities and 55 small, cylindrical cavities. Despite the removal of extra weight in the posts, this mirror weighs 1035 pounds.

Figure 3 is a cutaway view of a mirror containing square cavities, and figure 4 is an engineering drawing of this specific mirror. Each of the 145 cavities has an entrance hole 2-1/2 inches in diameter except for a few odd-shaped holes near the edge. The ribs are 0.20-inch thick, and all fillets have 3/4-inch radii. The square cells are 4-1/2 inches wide. This mirror weighs 985 pounds.

Figure 5 is a cutaway view of a mirror containing hexagonal cavities, and figure 6 is an engineering drawing of the 64-inch mirror.

Each of the 145 cavities has an entrance hole 2-1/2 inches in diameter except for a few odd-shaped holes near the edge. The ribs are

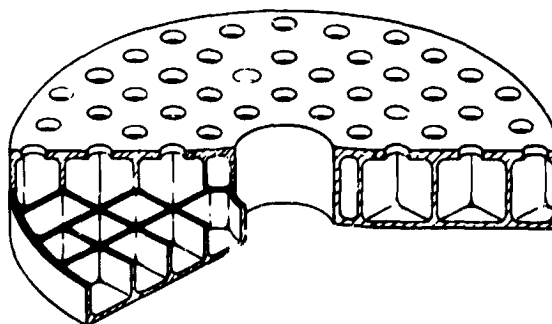


Figure 3. Cutaway view of mirror containing square cavities.

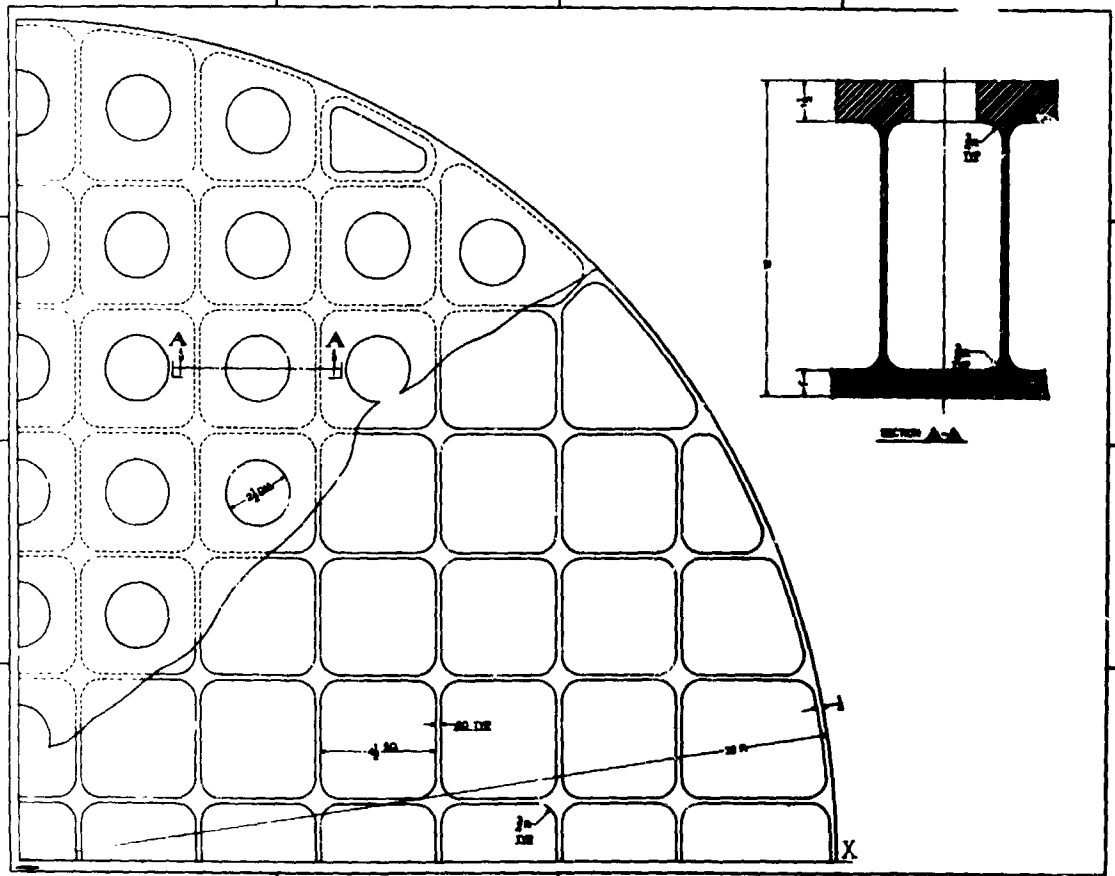


Figure 4. Engineering drawing of mirror with square cavities.

0.20-inch thick, and all fillets have $3/4$ -inch radii. The hexagonal cells are 5.2 inches from wall to wall. This mirror weighs only 880

pounds even though it has the same number of cavities as the mirror shown in figures 3 and 4.

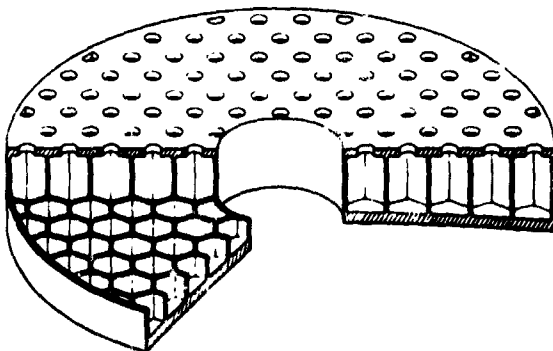


Figure 5. Cutaway view of mirror containing hexagonal cavities.

Calculations of Stiffness

Owens-Illinois scientists have adapted a computer program (ref. 3) for calculating the deflection under load of lightweight mirror blanks. This is a very generalized program and will handle any mirror shape with any module shape and size and any specified mounting system. The general principles of the mathematical treatment are given in Appendix B. Because of its general form, the program requires the use of a very large computer, such as the CDC 6600, to handle mirrors as big as

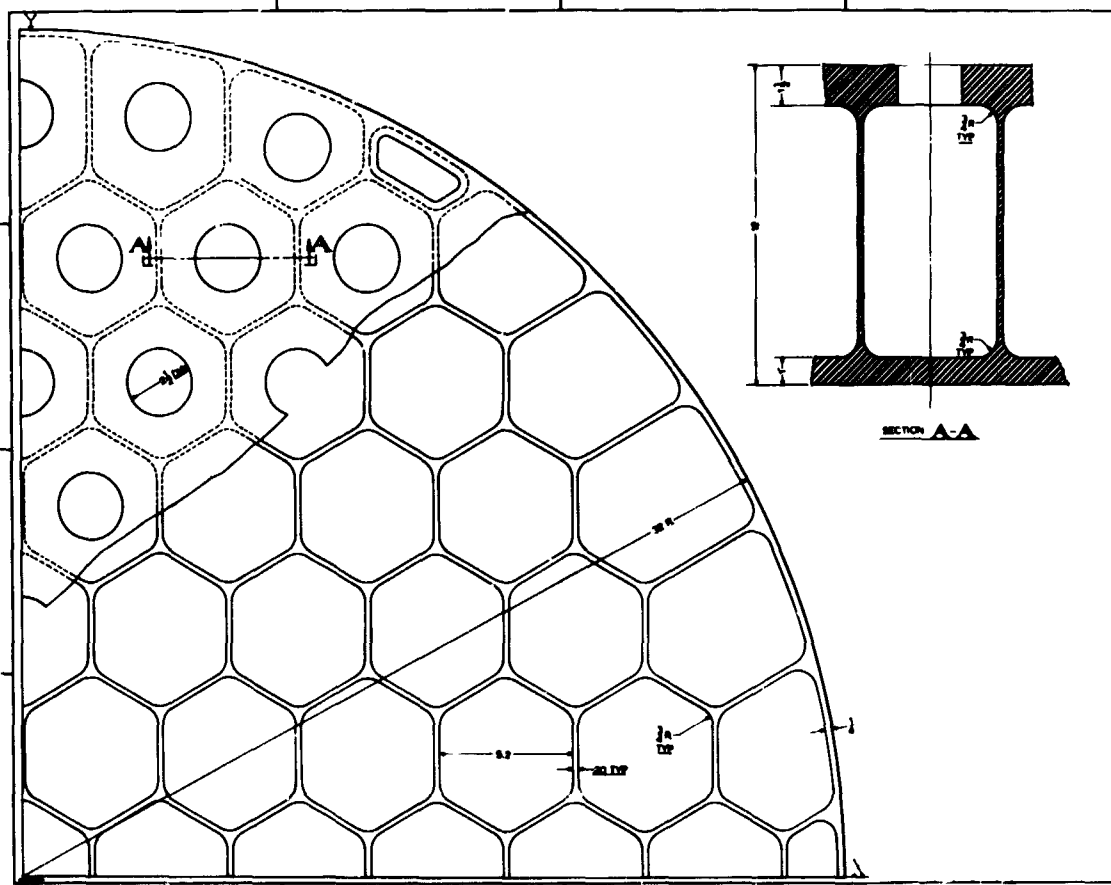


Figure 6. Engineering drawing of 64-inch mirror with hexagonal cavities.

the 64-inch-diameter mirrors described above and larger. Although this program has given results in agreement with known plate-bending experiments, it has not been checked against measured values on a lightweight mirror but should be quite accurate.

The computer program has been used to calculate the deflection of the three specific lightweight mirror blanks, assuming that they are edge-supported and that the deflection is due only to their own weight under normal gravity conditions. A typical result of these calculations is given in figure 7, which shows deflection profiles for the mirror blank containing the square modules. Similar results have been obtained for the mirrors containing the triangular and hexagonal modules. All of

these results are summarized in table 1, which reveals that all the lightweight mirrors are actually stiffer than a corresponding solid mirror. It can readily be seen that the mirror blank containing hexagonal cavities is superior to the other two. Not only is it the lightest weight blank, but also it is the stiffest blank, deflecting less than one-half as much as the solid blank and 90 percent as much as either of the other lightweight blanks. Therefore, the blank with hexagonal cavities decidedly has the best stiffness-to-weight ratio of these three.

Again, it should be emphasized that these mirror designs do *not* represent optimized designs. Owens-Illinois does have, however, a method that probably can be used to

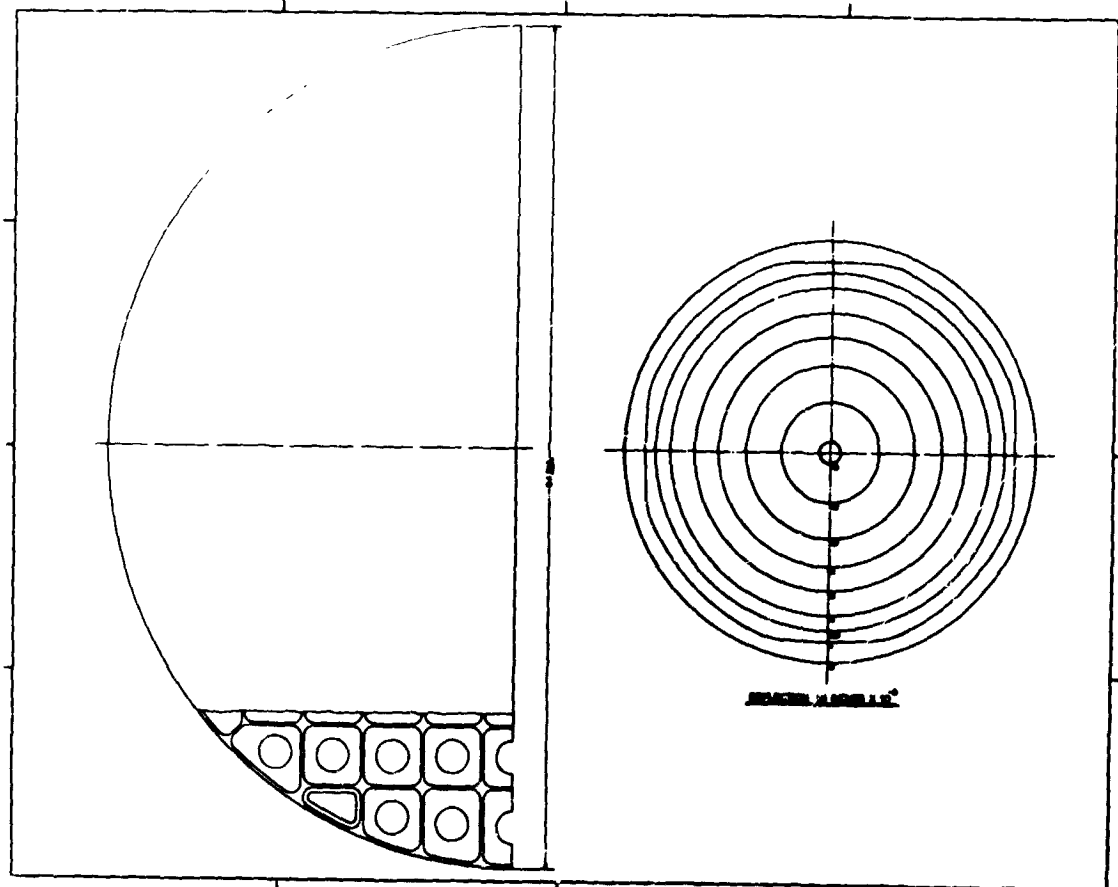


Figure 7. Deflection profiles for mirror blank containing square modules.

optimize these mirror designs after appropriate boundary conditions and objectives have been established. It should therefore be possible to select the minimum faceplate thickness to avoid waffling, the mirror diameter desired, the maximum blank thickness, the mounting technique, etc., and then to determine an optimum design. I am quite positive that a better stiffness-to-weight ratio than that shown here can be achieved through such optimization of the design.

A 120-Inch-Diameter Mirror

Figure 8 shows a tentative design for a 120-inch lightweight mirror blank. This is included because it seems to be a size of

particular interest to those participating in the Optical Telescope Technology Workshop. Again, this represents the present state-of-the-art extended to a larger size rather than an optimum design. Because of the results obtained above, the hexagonal cell structure was chosen for this mirror. The primary objective of this design is to achieve maximum lightweighting rather than stiffness. Despite the much larger mirror size, no attempt has been made to enlarge the modules beyond the size used in the 64-inch-diameter mirror. Figure 8 shows a 120-inch-diameter mirror, 20 inches thick, with 451 cavities, each 5.2 inches wall-to-wall except for odd-shaped cavities at the edge. Again, the webs are 0.20-inch thick, and the fillets have

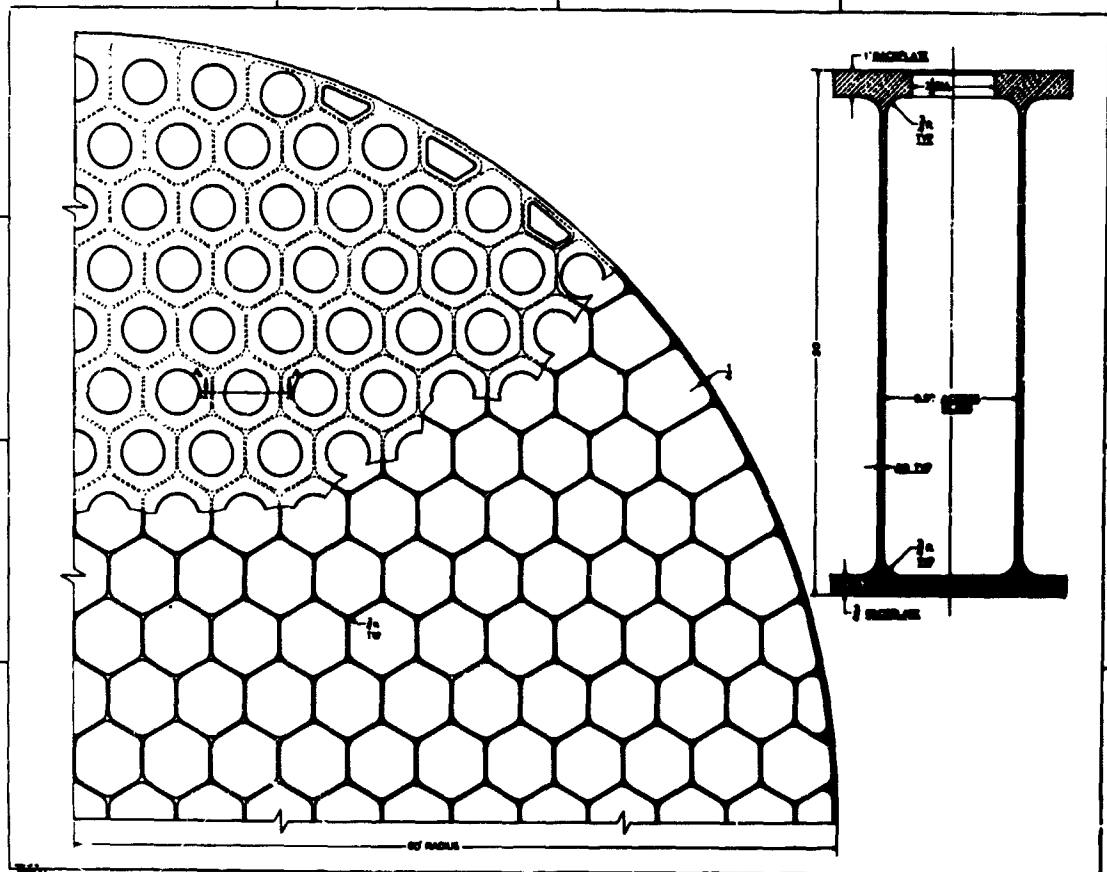


Figure 8. Tentative design for 120-inch lightweight mirror blank.

3/4-inch radius. A solid Cer-Vit mirror blank of this same size would weigh 20,400 pounds. This lightweight mirror is calculated to weigh 3250 pounds, representing an 84-percent reduction in weight.

Insufficient time was available to calculate the stiffness of this mirror blank by using the precise computer program. Instead, its center deflection when edge-supported was estimated by using mathematical approximations, which probably give an answer within 20 percent of the correct value. As seen in table 1, this particular large mirror sags less under its own weight than does a solid mirror blank of the same size. This is true even though 84 percent of the weight of the solid blank has been removed in the lightweighting process. Thus, this mirror has a

distinctly better stiffness-to-weight ratio after lightweighting. Further decreases in the amount of sag can be obtained if a different type of support is used rather than the edge support. It is necessary to design the entire system of mount and mirror, rather than designing the mirror alone, if the optimum is to be achieved. Further improvements could be made if Cer-Vit material were used for structural members (such as spacer rods) in the overall telescope system.

Future Work

Considerable work remains to be done before a truly optimum mirror design has been achieved and refined, but the basic technology for doing this does exist at the present

Table 1. Calculated Stiffness of Lightweight Mirrors

64-Inch Diameter Mirrors, Edge-Supported	Calculated Deflection		Weight (lbs.)	Figure of Merit (stiffness/weight)
	(μ in.)	(λ)		
Solid	36	1.66	3,475	0.8
Square cavities	16.4	0.76	985	6.1
Triangular cavities	15.4	0.71	1,035	6.3
Hexagonal cavities	14.4	0.66	880	7.9
120-Inch-Diameter Mirror	Estimated Deflection			
	(μ in.)	(λ)		
Solid, edge-supported	158	7.3	20,400	0.03
Hexagonal cavities, ring-supported at edge	079	5.3	3,250	0.30

time. An experiment should be run to confirm the results of the computer program for calculating stiffness; i.e., by comparing the calculated and actual measured deflection on a good-sized lightweight mirror. Experiments should be run to determine the minimum faceplate thickness that can be used with various cavity sizes and still avoid a waffling effect from the finishing operations. The Owens-Illinois optimization technique should be further refined and then used to determine the optimum combination of mirror thickness and cell size for a selected mirror diameter to achieve a minimum weight. By this means, a

minimum weight mirror can be designed having an optimum stiffness-to-weight ratio. Further design work should be done to insure that the mounting system also makes the maximum contribution to the mirror stiffness.

Acknowledgment

J. B. Foote assembled Appendix B and was responsible for performing the mirror stiffness calculations. This paper would not have been possible without his much appreciated efforts.

Appendix A

Pertinent Properties of Cer-Vit® Material C-101

Polishability

It has been shown that Cer-Vit C-101 polishes as well as, if not better than, fused silica (ref. 4) using conventional polishing techniques (ref. 5).

Expansion Coefficient

The $\Delta L/L$ curve showing change in length per unit length of Cer-Vit C-101 is shown in figure A-1. The curve for Cer-Vit C-101 is quite flat and lies near the zero-expansion line over a wide temperature range.

Stiffness or Load-Bearing Capability

The Young's modulus (9.42×10^5 Kg/cm²) of Cer-Vit C-101 is about 25 percent higher than that of fused silica, thus indicating that C-101 is a significantly stiffer material. This advantage can be somewhat offset by the density, which is 15 percent higher than that of fused silica. Nevertheless, Dietz and Barnes (ref. 6) have calculated that equivalent deflection is obtained with solid mirrors having a 7-to-1 ratio of diameter to thickness for C-101 and a 6-to-1 ratio for fused silica. Therefore, Cer-Vit C-101 has a significant net advantage.

Microcreep

A 6-inch flat (to $1/4$ wavelength) of Cer-Vit C-101 was deformed 50 wavelengths in a vacuum chuck and held thus for 4 months at room temperature (ref. 6). The calculated maximum stress was over 5,000 pounds per square inch; however, within 7 seconds after the force was removed, the sur-

face was examined interferometrically; and no detectable change from the original flat contour was found.

A precise measurement of microcreep is difficult, but the Boeing Company (ref. 7) has determined the nonrecoverable (plastic) microstrain characteristics of Cer-Vit C-101, 7940 silica, and 7971 ULE silica, by using relaxation curves to measure shear-strain decay as a function of time after load release. The Cer-Vit C-101 samples gave reproducible results, indicating uniformity and stability of characteristics. The original 7940 and ULE silicas gave inconsistent results from sample to sample, indicating a dependence on thermal history. After being subjected to a uniform heat treatment, these specimens gave reproducible results. The final results indicate that all three materials have roughly comparable, nonrecoverable, microcreep characteristics.

The microcreep properties of Cer-Vit C-101 and fused silica were determined at Owens-Illinois, Inc., using loading curves of deflection with time after application of load. Data obtained from three creep determinations with Cer-Vit C-101 were reproducible and exhibited little scatter. Data obtained from three identical creep determinations with fused silica were not reproducible and exhibited considerable scatter. Due to the lack of reproducibility of the fused silica data, it could only be concluded that Cer-Vit C-101 and fused silica have similar microcreep characteristics.

Stability

In 1964, a 16-inch-diameter spherical mirror of Cer-Vit C-101 material was finished, and a photograph was taken of its surface

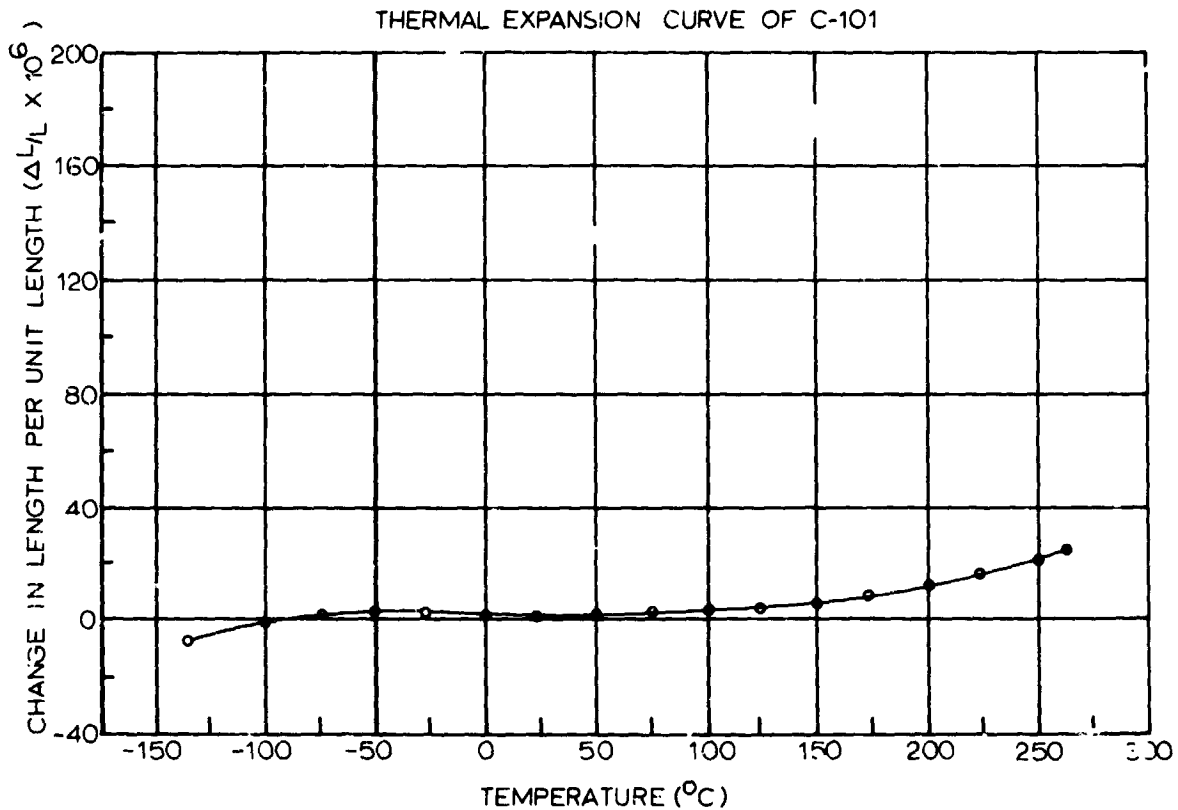


Figure A-1. Expansion coefficient for Cer-Vit[®] material C-101.

contour deviation by using a standard knife-edge technique. This procedure has been repeated each year, and the new photographs have been carefully compared by experienced opticians with the original photograph. No variation in the mirror has been detected, indicating a stability of at least 5 years' duration for a finished, Cer-Vit C-101, mirror-blank surface under ambient conditions.

A single sample of Cer-Vit C-101 material has been periodically subjected to a thermal cycle from liquid nitrogen temperature (minus 200°C) to 300°C. This has been done seven times in the last 3 years. There has been no detectable change in its thermal expansion coefficient during this period despite this thermal cycling.

Samples of C-101 were exposed (ref. 6) to constant elevated temperatures for 8000 hours (essentially 1 year) in an attempt to

accelerate any change that might occur. No measurable change occurred in thermal expansion coefficient, density, or transparency at or below 425°C. These properties are sensitive indicators of changes that can occur in Cer-Vit C-101 at much elevated temperatures after long time periods.

Questar has recently encountered (ref. 8) an instance in which one of its telescopes was exposed to a fire sufficiently hot to melt the aluminum parts and mirror coating (above 1100°F). Even with this exposure to a very high temperature, no change could be detected in the precisely finished figure of the Cer-Vit C-101 mirror in the telescope.

A 16-inch, f/5, Cer-Vit C-101, spherical mirror was finished and tested interferometrically; a computer-drawn plot was made of the surface (ref. 6). The rms deviation from a perfect sphere was 1/40 wavelength. After

27 months, the test was repeated, and no greater deviation from a perfect sphere was found, indicating stability with very precise testing.

Cer-Vit C-101 blanks have been finished to a flat by Aerojet-General, Azusa, California. They were aluminized, overcoated with silicon monoxide, tested interferometrically, and subjected to a cryogenic thermal shock by immersion in liquid hydrogen to 20°K. Upon return to room temperature, they were again tested; comparison with the original interference patterns showed no detectable change. Examination of the aluminum and the overcoat also revealed no change. One of the flats was tested interferometrically while at 20°K, and no detectable change in the flatness was observed.

Ability to be Cut

The Muffoletto Optical Company generated a spherical surface on a round, 1½-inch diameter Cer-Vit blank containing a maximum of 7 millimicrons per centimeter total strain birefringence, then sawed it into a rectangular shape, ground it on its back, and beveled all edges. After this cutting and grinding, the original Foucault test was repeated, and no change in the original radius of curvature of 2305 millimeters was found (within 0.25 millimeters). The figured surface re-

mained spherical within 0.044 of a fringe of 5000 angstroms of light. A similar experiment with a 6½-inch diameter blank finished flat within 1/30 wavelength of 5876-angstrom light revealed no measurable change in flatness.

References

1. McMillan, P.W.: Glass Ceramics. Academic Press, London, 1964.
2. Dietz, R. W.; Bennett, J. M.: Smoothness and Thermal Stability of CER-VIT Optical Material. Applied Optics, vol. 6, no. 1275, 1967.
3. Monnier, R. C.: Fabrication of a 104-cm Mirror From CER-VIT Low Expansion Material. Applied Optics, vol. 6, no. 1437, 1967.
4. Dietz, E. D.; Barnes, W. P., Jr.: Near Zero Thermal Expansion Mirror Material. Presented at Philadelphia Meeting of Am. Astronomical Soc., December 1967, to be published.
5. Eul, W. A.; Woods, W. W.: Shear Strain Properties to 10^{10} of Selected Optical Materials. NASA Report 1-7627, Space Division, The Boeing Company, 1968.
6. Questar Advertisement. Sky and Telescope, vol. 37, no. 4, April 1969, inside front cover.
7. Hudson, W. R., et al.: Discontinuous Orthotropic Plates and Pavement Slabs. Texas University, 1966.
8. Simmons, G. A.: Lightweight CER-VIT Mirrors. Optical Spectra, submitted for publication.

Appendix B

(Assembled by J. B. Foote)

Free-Body Analysis

In order to derive the equations for solution of the bending of a plate or slab, it is helpful to refer to a free-body of the model (ref. 3). In this approach, the plate or slab under consideration is converted into a corresponding array of sectional bars connected so that they represent the bending forces exerted upon these sections. Consider first a section of the assembled slab model centered at any mesh point i, j (fig. B-1). For the present, the x-bar to the left of point i, j is called Bar a and the x-bar to the right of point i, j is called Bar b .

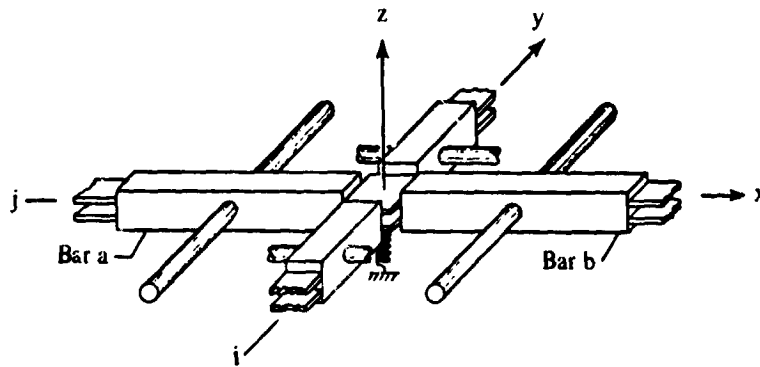


Figure B-1. Typical joint i, j taken from finite-element slab model.

Figure B-2 shows these same bars as a free-body with other members of the model fixed and replaced by a system of equivalent forces. $Q_{i,j}^y$ represents the load carried by the y-beam at this intersection, and the term $\partial^2 w / \partial y^2$ represents the restraint of the y-beam, which provides the Poisson's ratio effect in the x-beam moment. The term $S_f (w_{i,j}^x - w_{i,j}^y)$ represents the load stored in the fictitious spring closure parameter. Figure B-3 shows the

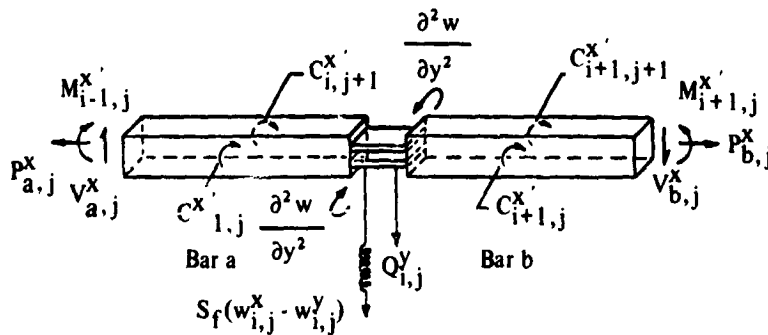


Figure B-2. Free-body of joint i, j with other members of the model replaced by an equivalent force system.

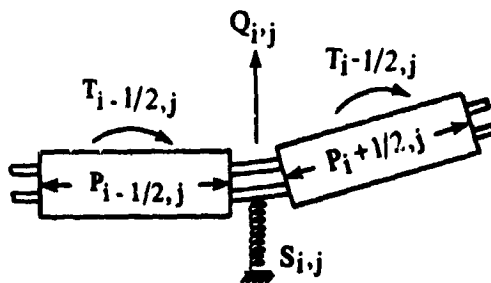


Figure B-3. Typical joint i, j with force and restraint inputs shown.

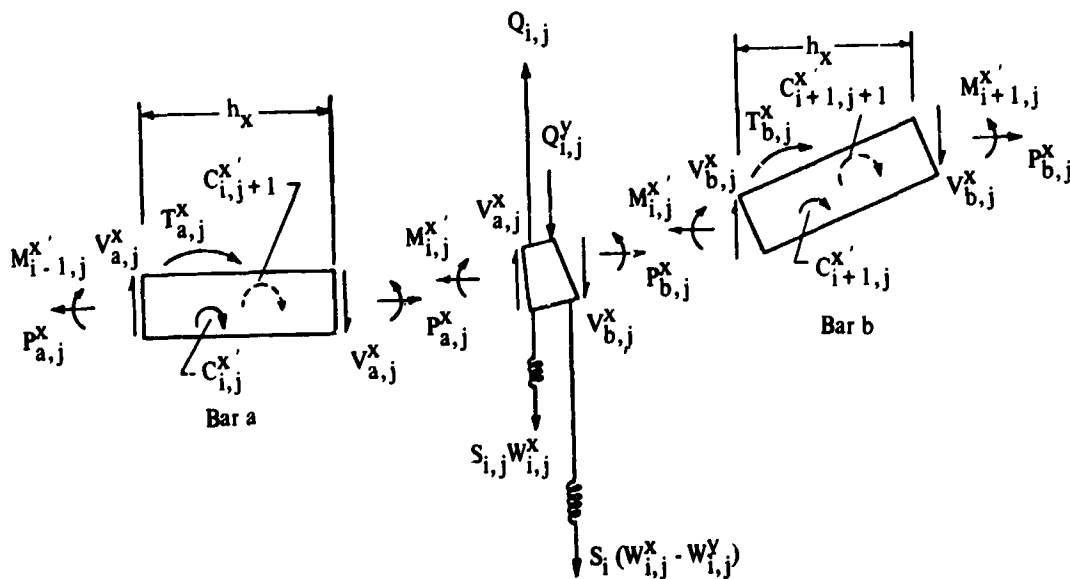


Figure B-4. Generalized free-body of joint i, j with all forces and restraints shown.

external forces that can be applied to these same two bars. Combining the system of equivalent forces and external loads gives the general free-body of the slab model in figure B-4. This free-body is for a section of an x-beam. A similar free-body can be developed for the y-beam by changing all x's for y's, and all y's for x's. For clarity, the symbols on this free-body are redefined as follows:

- a,b - Temporary bar numbering used in derivations to avoid confusion. (none)
- $C_{a,j}^i$ - The torque applied to the a^{th} bar of the j^{th} x-beam by the twist in slab segment a, j. (inch-lb)
- $C_{a,j}$ - Unit torsional stiffness of slab element a, j. ($\frac{\text{inch-lb}}{\text{rad}}$)
- $D_{i,j}^x$ - Average bending stiffness of an orthotropic plate in the x direction at Station i, j. (inch-lb)
- $D_{i,j}^y$ - Average bending stiffness of an orthotropic plate in the y direction at Station i, j. (inch-lb)
- i - An integer used to number mesh points, Stations and Bars along the x-beams in the x direction.
- h_x - The increment length along the x-beams. (inch)

h_y	- The increment length along the y-beams.	(inch)
j	- An integer used to index parts of the model and stationing in the y direction.	
$M_{i,j}^x$	- The bending moment in the x-beam at Station i, j (equals $h_y M_{i,j}^x$).	$\left(\frac{\text{inch-lb}}{\text{inch}}\right)$
$M_{i,j}^x$	- The unit bending moment in the slab in the x direction at Station i, j .	(lb)
$P_{i,j}^x$	- The axial load in the x-beam in Bar i, j (equals $h_y P_{i,j}^x$).	(lb)
$P_{i,j}^x$	- The unit axial load in the x direction at Station i, j .	(lb/inch)
$\Delta P_{i,j}^x$	- Change in axial load in the x-beam occurring at Station i, j .	(lb)
$Q_{i,j}$	- The externally applied load at point i, j .	(lb)
$Q_{i,j}^x$	- The load absorbed internally by the x-beam system at Station i, j .	(lb)
$Q_{i,j}^y$	- The load absorbed internally by the y-beam system at Station i, j .	(lb)
$\overline{QBMX}_{i,j}$	- The load absorbed internally by the x-beam in bending.	(lb)
$\overline{QBMY}_{i,j}$	- The load absorbed internally by the y-beam in bending.	(lb)
$\overline{QTMX}_{i,j}$	- The load absorbed by the x-beam in twisting.	(lb)
$\overline{QTMY}_{i,j}$	- The load absorbed by the y-beam in twisting.	(lb)
$\overline{QPX}_{i,j}$	- The load absorbed by the x-beam system due to axial load.	(lb)
$\overline{QPY}_{i,j}$	- The load absorbed by the y-beam system due to axial load.	(lb)
S_f	- The fictitious spring (closure parameter).	(lb/inch)
$S_{i,j}$	- Support value under the slab at Station i, j .	(lb/inch)
$T_{a,j}^x$	- External torque applied to Bar a on the j^{th} x-beam.	(lb-inch)
$V_{a,j}^x$	- Shear in Bar a of the j^{th} x-beam.	(lb)
$w_{i,j}^x$	- Deflection of the j^{th} x-beam at Station i .	(inch)
$w_{i,j}^y$	- Deflection of the i^{th} y-beam at Station j .	(inch)

$\alpha_{a,j}$	- Angular change across slab element a, j .	(rad)
ν_{xy}	- Poisson's ratio which results in strain in the y direction when a stress is applied in the x direction.	(none)
ν_{yx}	- Poisson's ratio which results in strain in the x direction when a stress is applied in the y direction.	(none)

Summing vertical forces in figure B-4 at joint i, j with "up" taken as positive gives

$$\sum F_{V_{i,j}}^x = Q_{i,j}^y + V_{a,j}^x - V_{b,j}^x - S_{i,j} (w_{i,j}^x) - Q_{i,j} - S_f (w_{i,j}^x - w_{i,j}^y) = 0 \quad (4.1)$$

In order to evaluate the shear $V_{a,j}^x$, sum the moments acting on Bar a about the center of the bar. (Clockwise rotations are positive.) For equilibrium

$$\begin{aligned} \sum M_a = 0 = & M_{i-1,j}^x - M_{i,j}^x + T_{a,j}^x + C_{i,j}^x + C_{i,j+1}^x + V_{a,j}^x h_x \\ & + 2P_{a,j}^x \left(\frac{-w_{i-1,j}^x + w_{i,j}^x}{2} \right) = 0 \end{aligned} \quad (4.2)$$

Multiplying through by h_x and clearing obtains

$$-h_x V_{a,j}^x = M_{i-1,j}^x - M_{i,j}^x + T_{a,j}^x + C_{i,j}^x + C_{i,j+1}^x + P_{a,j}^x (-w_{i-1,j}^x + w_{i,j}^x) \quad (4.3)$$

Likewise summing moments about Bar b and multiplying through by h_x obtains an expression for the shear $V_{b,j}^x$ as follows:

$$-h_x V_{b,j}^x = M_{i,j}^x - M_{i+1,j}^x + T_{b,j}^x + C_{i+1,j}^x + C_{i+1,j+1}^x + P_{b,j}^x (-w_{i,j}^x + w_{i+1,j}^x) \quad (4.4)$$

Multiplying equation 4.1 through by h_x and substituting equations 4.3 and 4.4 for the shears obtains the equation of interest. After convenient grouping of terms and transfer of all known values to the right-hand side of the equation, with a sign change, it becomes

$$\begin{aligned}
& (M_{i-1,j}^{X'} - 2M_{i,j}^{X'} + M_{i+1,j}^{X'}) - (-C_{i,j}^{X'} - C_{i,j+1}^{X'} + C_{i+1,j}^{X'} + C_{i+1,j+1}^{X'}) \\
& + P_{a,j}^X (-w_{i-1,j}^X + w_{i,j}^X) - P_{b,j}^X (-w_{i,i}^X + w_{i+1,j}^X) + S_{i,j} h_x w_{i,j}^X \\
& = h_x [Q_{i,j} - Q_{i,j}^Y - S_f (w_{i,j}^X - w_{i,j}^Y)] - T_{a,j}^X + T_{b,j}^X \tag{4.5}
\end{aligned}$$

This equation relates forces and deflections at point i, j , but all of the prime terms must be evaluated further before the required mathematical manipulations can be performed. It is necessary at this point to substitute the finite-difference formulations of moment. It is convenient to express these in compressed central difference form. Accordingly, they are written at Stations $i-1, j$; i, j ; and $i+1, j$ and are substituted into the equation.

The term $C_{i,j}^{X'}$ represents the force exerted on the x-beam due to the relative rotation between this beam and its neighbors. These expressions must be written for $C^{X'}$ at Stations i, j ; $i, j+1$; $i+1, j$; and $i+1, j+1$.

After making these substitutions, equation 4.5 becomes

$$\begin{aligned}
& h_y D_{i-1,j}^X \left[\left(\frac{w_{i-2,j}^X - 2w_{i-1,j}^X + w_{i,j}^X}{h_x^2} \right) + \nu_{yx} \left(\frac{w_{i-1,j-1}^Y - 2w_{i-1,j}^Y + w_{i-1,j+1}^Y}{h_y^2} \right) \right] \\
& - 2h_x D_{i,j}^X \left[\left(\frac{w_{i-1,j}^X - 2w_{i,j}^X + w_{i+1,j}^X}{h_x^2} \right) + \nu_{yx} \left(\frac{w_{i,j-1}^Y - 2w_{i,j}^Y + w_{i,j+1}^Y}{h_y^2} \right) \right] \\
& + h_y D_{i+1,j}^X \left[\left(\frac{w_{i,j}^X - 2w_{i+1,j}^X + w_{i+2,j}^X}{h_x^2} \right) + \nu_{yx} \left(\frac{w_{i+1,j-1}^Y - 2w_{i+1,j}^Y + w_{i+1,j+1}^Y}{h_y^2} \right) \right] \\
& + \frac{C_{i,j}^X}{h_y} (w_{i-1,j-1}^X - w_{i-1,j}^X - w_{i,j-1}^X + w_{i,j}^X) \\
& + \frac{C_{i,j+1}^X}{h_y} (-w_{i-1,j}^X + w_{i,j}^X + w_{i-1,j+1}^X - w_{i,j+1}^X) \\
& - \frac{C_{i+1,j}^X}{h_y} (-w_{i,j}^X + w_{i+1,j}^X + w_{i,j-1}^X - w_{i+1,j-1}^X)
\end{aligned}$$

$$\begin{aligned}
& - \frac{C_{i+1,j+1}^x}{h_y} (-w_{i,j}^x + w_{i+1,j}^x + w_{i,j+1}^x - w_{i+1,j+1}^x) \\
& + P_{a,j}^x (-w_{i-1,j}^x + w_{i,j}^x) - P_{b,j}^x (-w_{i,j}^x + w_{i+1,j}^x) + h_x (S_{i,j} + S_f) w_{i,j}^x \\
& = h_x (Q_{i,j} - Q_{i,j}^y + S_f w_{i,j}^y) - T_{a,j}^x + T_{b,j}^x \tag{4.6}
\end{aligned}$$

It is convenient in computation to use the same numbering system for bars, torsion bars, and joints. So far in these developments bars have been referred to as a and b . Referring to the numbering system shown above, it will be recognized that in reality a becomes i and b becomes $i+1$. Therefore, for example, $T_{a,j}^x$ becomes $T_{i,j}^x$, $P_{b,j}^x$ becomes $P_{i+1,j}^x$, etc.

This will be an implicit solution for $w_{i,j}^x$, the deflection of the j^{th} x-beam at Station i . It is convenient for solution, however, to utilize the last estimated values for all deflections, w^x , not falling on the j^{th} beam for a particular iteration, and to transfer them to the right-hand side of the equation. Furthermore, all of the y-beam deflections ($w_{i,j}^y$) will be assumed known from a previous iteration and will also appear on the right-hand side of the equation. After making the notation change of a to i and transferring known values to the right-hand side, it is helpful to clear fractions and to rearrange terms. The resulting equation is the equation we seek; it is most conveniently written in terms of five unknown deflections; i.e.,

$$a_x w_{i-2,j}^x + b_x w_{i-1,j}^x + c_x w_{i,j}^x + d_x w_{i+1,j}^x + e_x w_{i+2,j}^x = f_x \tag{4.7}$$

where

$$a_x = \frac{h_y^2}{h_x^2} D_{i-1,j}^x \tag{4.8}$$

$$b_x = -2.0 \frac{h_y^2}{h_x^2} (D_{i-1,j}^x + D_{i,j}^x) - C_{i,j}^x - C_{i,j+1}^x - h_y P_{i,j}^x \tag{4.9}$$

$$\begin{aligned}
c_x &= \frac{h_y^2}{h_x^2} (D_{i-1,j}^x + 4D_{i,j}^x + D_{i+1,j}^x) + C_{i,j}^x + C_{i+1,j}^x + C_{i,j+1}^x \\
& + C_{i+1,j+1}^x + h_x h_y (S_{i,j} + S_f) + h_y (P_{i,j}^x + P_{i+1,j}^x) \tag{4.10}
\end{aligned}$$

$$d_x = -2.0 \frac{h_y^2}{h_x^2} (D_{i,j}^x + D_{i+1,j}^x) - C_{i+1,j}^x - C_{i+1,j+1}^x - h_y P_{i+1,j}^x \quad (4.11)$$

$$e_x = \frac{h_y^2}{h_x^2} D_{i+1,j}^x \quad (4.12)$$

$$\begin{aligned} f_x = & h_x h_y (Q_{i,j}^y - Q_{i,j}^y + S_f w_{i,j}^y) + h_y (T_{i,j}^x + T_{i+1,j}^x) \\ & - \nu_{yx} \left[D_{i-1,j}^x (w_{i-1,j-1}^y - 2w_{i-1,j}^y + w_{i-j,j+1}^y) \right. \\ & - 2D_{i,j}^x (w_{i,j-1}^y - 2w_{i,j}^y + w_{i,j+1}^y) + D_{i+1,j}^x (w_{i+1,j-1}^y - 2w_{i+1,j}^y \\ & \left. + w_{i+1,j+1}^y) \right] - C_{i,j}^x (w_{i-1,j-1}^x - w_{i,j-1}^x) - C_{i,j+1}^x (w_{i-1,j+1}^x - w_{i,j+1}^x) \\ & + C_{i+1,j}^x (w_{i,j-1}^x - w_{i+1,j-1}^x) + C_{i+1,j+1}^x (w_{i,j+1}^x - w_{i+1,j+1}^x) \quad (4.13) \end{aligned}$$

One term remains to be evaluated, $Q_{i,j}^y$, the load absorbed by the y-beams at any time. This load can be evaluated by numerical differentiation of the deflected pattern of the y-beam system, but it can also be done from the free-body analysis by summing vertical forces in terms of load absorbed by both sets of beams, $Q_{i,j}^x$ and $Q_{i,j}^y$. This summation on the free-body in figure B-4 gives

$$Q_{i,j}^y - Q_{i,j}^y - Q_{i,j}^x - S_{i,j} w_{i,j}^x + S_f (w_{i,j}^x - w_{i,j}^y) = 0 \quad (4.14)$$

After necessary algebraic manipulations, the appropriate equation for evaluating $Q_{i,j}^y$ is seen to be as follows:

$$Q_{i,j}^y = \overline{QBMY}_{i,j} + \overline{QIMY}_{i,j} + \overline{QPY}_{i,j} + \frac{T_{i,j}^y - T_{i,j+1}^y}{h_y} \quad (4.15)$$

If this process is repeated for a segment of y-beam, equations comparable to equations 4.7 through 4.13 can be developed for the y-beams.

Summary

Equations 4.7 through 4.13 conveniently describe the model at Station i, j and are statically correct since the summation of forces at any time during the solution will equal zero. There are two such sets of equations, one for the x -system and one for the y -system, at each mesh point, i, j . The number of stations in each direction is equal to the number of increments plus 4. As an example, a problem divided into eight increments in the x direction and eight increments in the y direction would require equations at 12 stations in each direction. Thus, the number of equations required to describe the system would be 288, 144 for the y -beams and 144 for the x -beams. This readily explains the need to resort to digital computers to perform the mathematical manipulations.

Details of Solutions

For solving the large number of simultaneous equations that result in each half-cycle of the alternating-direction iterative method, Matlock and Haliburton used an efficient two-pass method to solve linearly elastic beam-columns. The method involves the elimination of four unknowns, two each in two passes. The first pass from top to bottom eliminates deflections w_{i-2}^x and w_{i-1}^x from each equation. (See equation 4.7.) The second pass, in reverse order, eliminates deflections w_{i+2}^x and w_{i+1}^x from each equation and thus results in the solution for the desired deflection w_i^x .

One of the valuable assets of this method is that boundary conditions as normally discussed are automatically provided with two dummy stations specified at each end of each beam in the system. These dummy stations in reality have no bending stiffness; therefore, a bending stiffness equal to zero is input for them. Equation 4.7 is then formulated for every station in the beam plus two dummy stations on each end.

To solve for $w_{i,j}^x$ then, we consider the plate to be two systems of orthogonal beams interconnected at Station i, j by S_f , the fictitious closure-spring constant. Figure B-5 shows a view of a grid-beam system with closure springs acting during solution. A comparable view of the slab model with torsion bars present is shown in figure B-6.

With the beam-column as a basic tool, we obtain the solution of the system of equations for plates and slabs as follows:

1. Solve each x -beam successively through the system; consider all the y -beams to be held fixed in space. At any particular solution of any x -beam, the fictitious closure spring acts as restraint on the x -beam of interest.
2. After all x -beams have been solved and their new deflection pattern is known, alternate or change directions; and fix the x -beams in this new pattern.

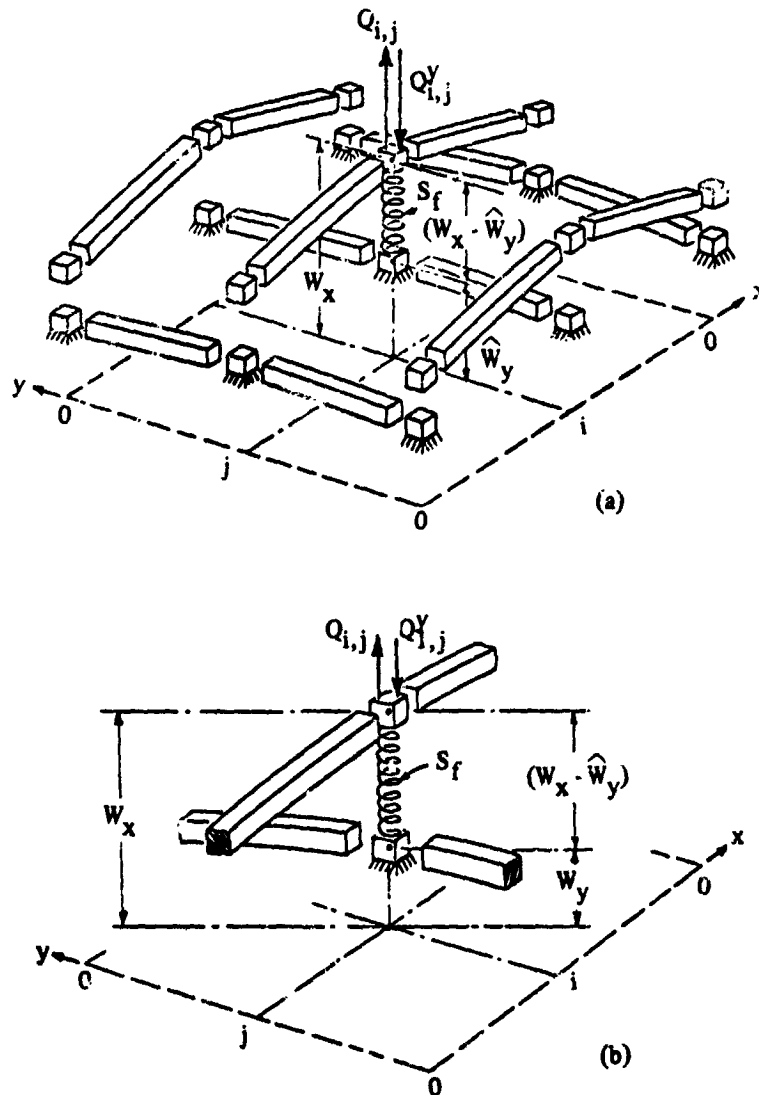


Figure B-5. Grid beam system during closure process with fictitious spring acting between x-beam and y-beam at Station i, j .

3. Solve for the deflected shape of each y-beam in turn. The fictitious springs now act as loads or restraints on the y-beams, serving to transfer the load that has been stored in them from the deflected x-beams.

4. Repeat this procedure alternately until all of the load is properly distributed throughout the system. At this point, the summation of static forces at each joint in the system will equal zero within the specified tolerance, and the deflection of the x-beam system, $w_{i,j}^x$, at any point will equal the deflection of the y-beam system, $w_{i,j}^y$, at the same point within the specified tolerance so that the term $S_f(w_{i,j}^x - w_{i,j}^y)$ vanishes.

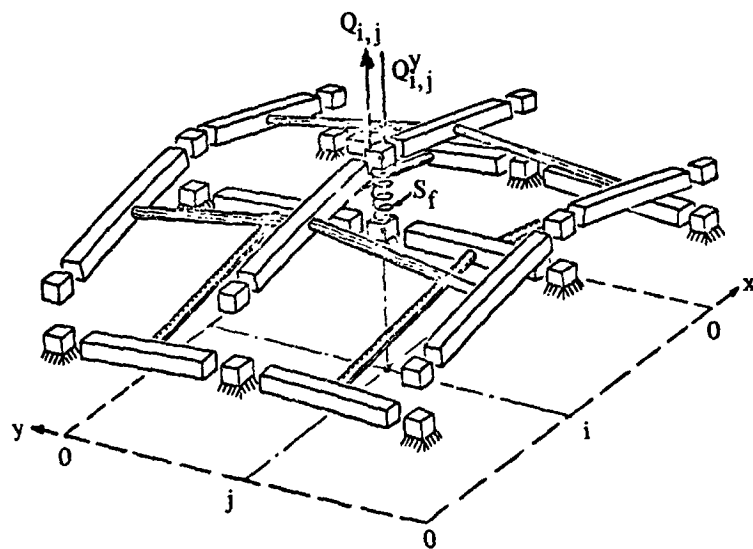


Figure B-6. Plate represented in the closure process as two orthogonal systems with closure spring acting between them at Station i,j .

PRECEDING PAGE BLANK NOT FILMED.

Lightweight Mirror Structures *

Eric Y. Loytty

Corning Glass Works

N70-36707

Introduction

Since 1925, different approaches have been followed in the production of lightweight structures for astronomical mirrors (refs. 1 and 2); however, with the increasing use of optics in sophisticated airborne applications, weight reduction has become a severe problem. Along with the lightweight requirement, thermal stability has become supercritical for the implementation of a successful optical system. The trend in critical airborne or orbiting optical systems is to satisfy the following requirements:

1. A large primary mirror capable of detecting faint sources and increasing the angular precision of the data gathered (ref. 3)
2. Lightweight mirrors capable of withstanding inertial and gravitational forces
3. Dimensional stability in the presence of temperature changes and thermal gradients.

The primary mirror of the 200-inch Hale telescope, located on Palomar Mountain in southern California, is a good example of the design problems involved in making large lightweight mirrors because its design

Hale Telescope Design

The material chosen to manufacture the 200-inch Hale mirror blank was developed in the Corning Glass Works research laboratory (ref. 4). This special borosilicate glass has a

embodies all of the technical reasoning used today in lightweight mirror designs.

linear coefficient of thermal expansion of $2.5 \times 10^{-6} \text{ }^\circ\text{C}^{-1}$. Although the expansivity of this glass was one-third that of a conventional soda-lime composition, a conventional solid design would still have significant thermal distortions. These thermal problems were reduced by designing the mirror with a ribbed back (fig. 1) and the thickest section about 4 inches (ref. 5); therefore, no point in the disk has more than 2 inches for a surface. This reduction in section, along with the increased surface area in contact with the surrounding

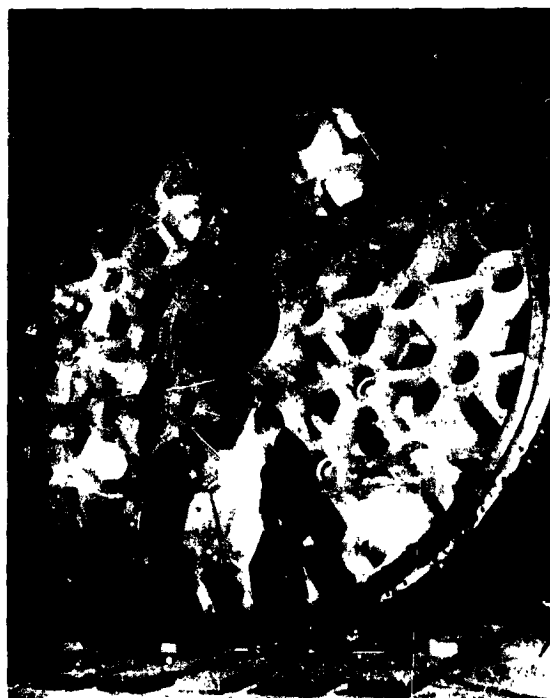


Figure 1. Ribbed-back mirror to reduce thermal problems.

*This paper is an adaptation of the paper "Ultra-lightweight Mirror Blanks," by E.Y. Loytty and C.F. De Voe, which appeared in the *IEEE Transactions on Aerospace and Electronic Systems*, pp. 300-305, Vol. AES-5, No. 2; March 1969.

air, decreased the temperature gradients in the mirror due to ambient temperature changes.

The ribbed design also permitted a weight reduction without a proportionate loss of stiffness. For an equal deflection, under its own weight, a solid disk would have to be between 14 and 15 inches thick (ref. 6) and would weigh about 40 tons. The ribbed blank weighs 20 tons. Thus, a weight saving of 50 percent was achieved.

The lack of a backplate, however, makes this type of structure very inefficient from a weight/rigidity standpoint. A good comparison is an I-beam versus a T-bar. All dimensions (except the bottom section) being equal, the I-beam is much more rigid. In fact, it has been shown (ref. 7) that, when holes over 0.2 times the rib-spacing are placed in a two-plate, ribbed-core structure, substantial weight/rigidity inefficiency develops. For these reasons, Corning Glass Works has concentrated on developing fabrication techniques to allow the manufacture of mirror blanks with integral front plates and backplates.

Fabrication Techniques for Lightweight Mirror Blanks

The following must be included in any discussion of fabrication techniques for lightweight mirror blanks:

- Slotted strut assemblies
- Monolithic core structures
- Monolithic core process
- Core design
- Mounting blocks
- Available configurations
- Machined cores.

Slotted Strut Assemblies

The technique for making a dimensionally stable, lightweight mirror blank from low-expansion materials evolved from the slotted strut or eggcrate assembly developed by Corning in the late 1950's. Figure 2 shows precision-ground struts being fitted together on the faceplate. When the assembly is complete, the top and bottom plates are fused to this assembly. The resultant structure is

much more rigid than a solid mirror of the same weight and weighs up to 70 percent less than a solid mirror with equivalent deflection. Several hundred mirrors have been manufactured using this technique.



Figure 2. Precision-ground struts being fitted together on the faceplate.

Monolithic Core Structures

During the early 1960's, it became apparent to optical system designers that more effective, large, lightweight mirrors would be possible if the efficiency of the eggcrate core could be improved by giving it a continuous shear path; that is, by removing any discontinuities from the ribs.

The possible weight saving by using the monolithic and eggcrate types of blanks is illustrated by the following example. Let us assume mirror blanks with the following dimensions:

1. 80-inch diameter mirror, square-cell core structure
2. 3.5-inch, center-to-center strut spacing
3. 1-inch front plate thickness
4. 1/2-inch backplate thickness
5. 15-percent core density.

If they are simply supported along the edge, the following thicknesses are required for a maximum deformation under 5λ , due to the weight of the blanks:

Core Type	Overall Thickness (in.)	Total Weight (lb.)
Monolithic (sealed)	11.0	1150
Eggcrate (slotted)	15.0	1400
Solid	12.8	5043

Thus, a 72-percent weight saving for the eggcrate core is realized over the equivalent solid, and an additional weight saving of 5 percent (or 250 pounds) is obtained by using a monolithic (one-piece) core, bringing the total weight reduction to 78 percent of the equivalent solid. Figure 3 shows a typical 30-inch-diameter, monolithic, lightweight, mirror blank.



Figure 3. Typical 30-inch-diameter, monolithic, lightweight, mirror blank.

Monolithic Core Process

The Corning Glass Works process for producing a monolithic core consists of building up the desired configuration by fusing pre-machined parts together. Figure 4 shows a typical fusion joint. Because precision parts are used, this fusion technique allows tight dimensional control on both the overall cell size and rib thickness. An added benefit associated with the use of a builtup, fusable structure is reparability. This means that not only can a damaged-in-process core be reworked but also, in certain instances, repairs can be made to mirrors damaged in finishing or end use.

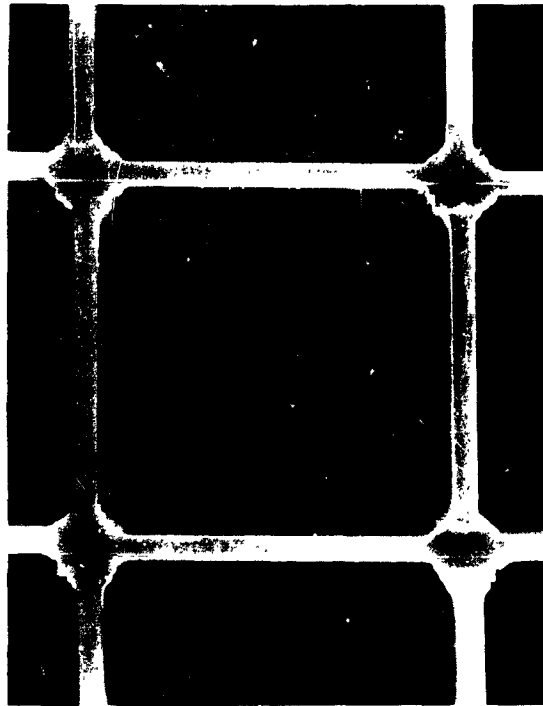


Figure 4. Typical fusion joint of pre-machined joints.

Core Design

Figures 5 and 6 show two types of monolithic cores. The overall size of these cores is technically unlimited. Figure 7 shows the core for an 80-inch-diameter test blank being inspected. There are, however, process limitations in minimum cell size. Present design limitations are shown in table 1.

Mounting Blocks

One of the advantages of a fused core is that mounting blocks can be fused into the core structure. Figure 8 illustrates a solid block fused into a triangular cell. There is only one limitation on this design. For proper fusion to occur, there must be a minimum of a 0.375-inch gap between the core wall and the block. After the front plate and backplate are fused onto this type of core, holes can be drilled into the blocks and mounting arrangements made on the neutral axis of the mirror. Figure 9 shows a blank that was made utilizing this technique.



Figure 5. Monolithic core with triangular cells.



Figure 6. Monolithic core with square cells.



Figure 7. Inspection of core for 80-inch-diameter test blank.



Figure 8. Solid mounting block fused into a triangular cell.

Available Configurations

Grinding a spherical radius on one or both sides of a monolithic core can produce a variety of mirror configurations, such as plano-concave or concave-concave. Sagging or slumping a plano-plano mirror blank will

Table 1. Design Limitations for Fused Monolithic Core Structures: Fused Core, Square Cells*

Core Height (in.)	Minimum Cell Spacing, Center-to-Center (in.)	Rib Thickness	
		Minimum (in.)	Maximum (in.)
under 5	1.5	0.060	0.200
up to 10	2.0	0.100	0.200
up to 25	2.5	0.100	0.200

*Triangular cells can be substituted, in which case the minimum cell spacing should be increased by about 50 percent.

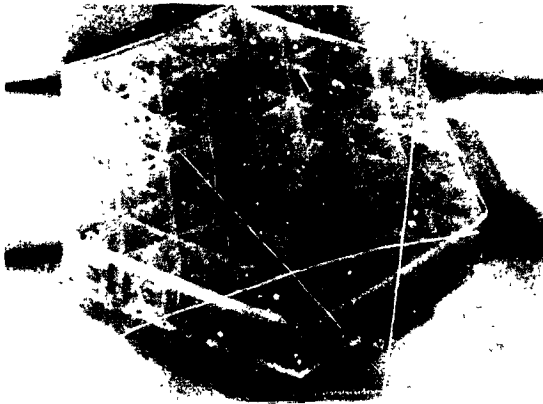


Figure 9. Mirror blank with front plate and backplate fused to core structure into which mounting blocks have been fused.

produce a uniform thickness concave-convex mirror with a spherical radius approximating the required radius.

Machined Cores

A third method for producing lightweight mirrors is used at Corning Glass Works (fig. 10). These mirrors have a core that has been machined out to reduce weight; both top and bottom plates are fused to the core.

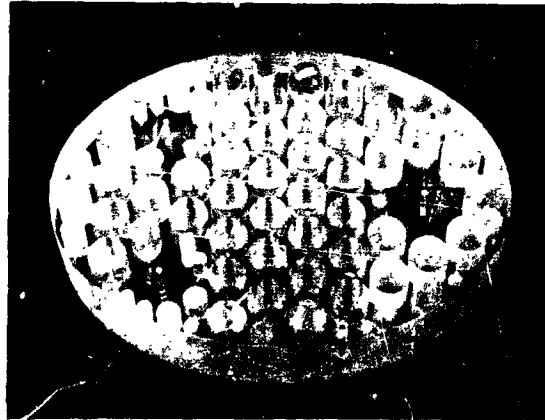


Figure 10. Mirror blank with machined-out core to reduce weight.

Although refined machining techniques are known that would permit large percentages of weight reduction to be obtained, the successful manufacturing of large, defect-free, lightweight, mirror blanks by machining techniques is limited by two conditions:

1. High probability of creating chips, checks, and other related defects in the core during machining
2. Availability of large, homogeneous, defect-free, solid blanks for the core material.

It now appears the monolithic core or buildup technique provides a much higher probability of producing a successful, defect-free blank because of the utilization of small parts that can be disassembled and replaced without significant losses in time or material.

Results

Many of the lightweight mirrors produced by Corning Glass Works have been finished to diffraction-limited tolerances.

One of these mirrors is the Princeton OAO mirror. This 32-inch eggcrate, illustrated in figure 11, has some unique mounting fixtures inserted in the core; it was finished to $\lambda/23.2$ by the Perkin-Elmer Corporation. Figure 12 is a contour plot of this surface.

Figure 13 shows the results of a Ritchey test of a ULE™ monolithic mirror that is similar to the mirror blank illustrated in

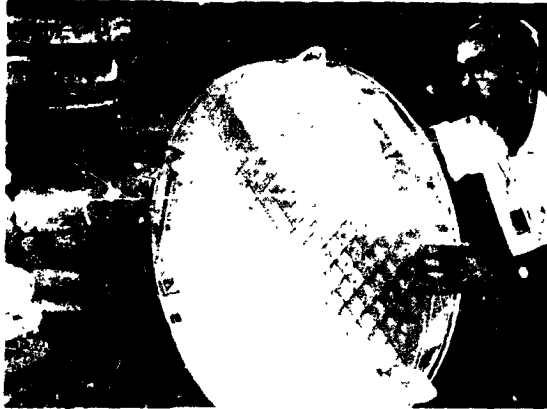


Figure 11. Unique mounting fixtures inserted in 32-inch egg-crate core structure.

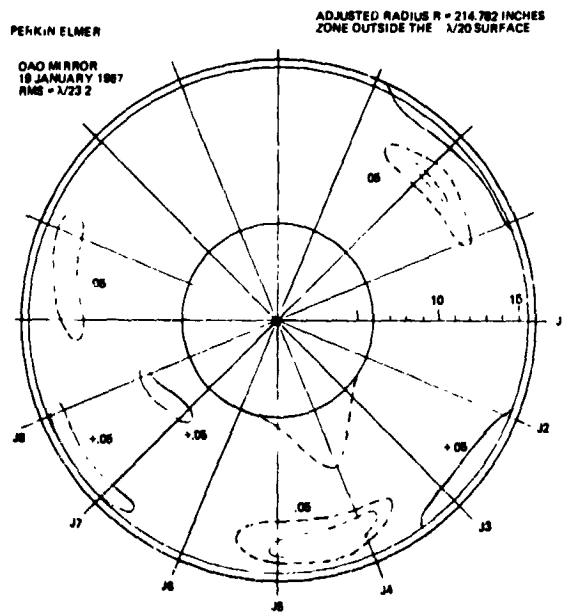


Figure 12. Contour plot of 32-inch Princeton OAO mirror; zones outside the $\pm\lambda/20$ surface after radius optimization.

figure 5. Analysis of this interferogram indicates that the peak-to-peak deviation from curvature is approximately 0.04λ .

Many other mirrors have been finished with similar results; however, due to the proprietary nature of the test procedures, many companies will not release the results.

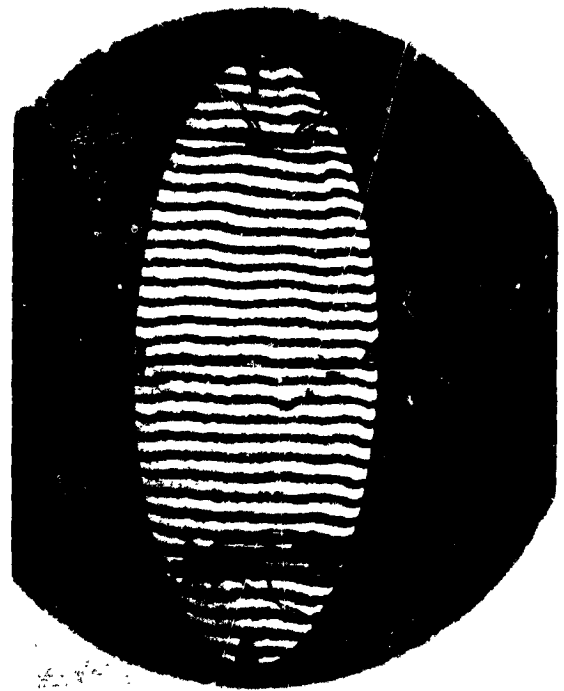


Figure 13. Results of Ritchey test ($0.04\lambda_{rms}$) of 30-inch ULE monolithic mirror.

Conclusion

The combination of a new material with near-zero thermal expansion and the monolithic core technology allows lightweight mirror structures to be manufactured with weight savings approaching 80 percent of the equivalent solid. At the same time, this combination provides exceptional thermal and dimensional stability.

References

1. Ritchey, G. W.: The Modern Photographic Telescope and the New Astronomical Photography. J. Roy, ed., Astron. Soc. Can., vol. 22, no. 5, 1928, pp. 160-161.
2. Ingalls, A. G.: Amateur Telescope Making. Scientific American, New York, 1967, pp. 321-323.
3. Space Research/Directions for the Future. National Acad. Science, Space Science Board, Woods Hole Report 1403, 1966, p. 151.

4. Bowen, I. S.: Statement of the Aims and Limitations of the Program. The Construction of Large Telescopes, Academic Press, New York, 1966, p. 5.
5. McCauley, G. V.: Some Engineering Problems Encountered in Making a 200-Inch Telescope Disc. Bull. Am. Ceram. Soc., Vol. 14, September 1935.
6. Kuiper, G., et al.: Telescopes. University of Chicago Press, Chicago, Ill., 1960.
7. Barnes, W. P.: Private Communication. Itek Corp., Lexington, Mass.

PRECEDING PAGE BLANK NOT FILMED.

Application of Finite Element Techniques to the Design and Manufacture of Astronomical Mirrors

Keto Soosaar

MIT Instrumentation Laboratory

N70-36708

Introduction

A recent development in structural mechanics that has revolutionized problem analysis in civil and aeronautical engineering is the finite element approach (refs. 1, 2, and 3). This computer-oriented method permits the analyst to treat problems of continuum mechanics as well as trusses and frames in a very general way without becoming excessively involved with the detailed behavioral aspects of the problem at hand.

The method operates by dividing a two- or three-dimensional continuum into small segments, triangles or rectangles, over which the analyst will assume that the strain is uniform or distributed according to some known variation. These segments are usually assumed to be connected by pins at the vertices. The individual force-deformation response (that is, the element stiffness matrix) is known from simple elasticity by using the assumed strain function. A number of equations of joint compatibility must be formulated and solved to assure that all common joints between elements deform equally. This leads to matrix operations and to the absolute need for high-speed, large-capacity computers.

The absolute generality of the method and the ease of use makes the finite element method an ideal tool for treating the complex elastomechanics problems that will arise in the design, manufacture, and operation of telescope mirror structures (refs. 4 and 5).

Matrix Structural Analysis

The following steps outline very broadly the procedure followed in finite element (as well as general frame element) formulation.

Assume a relationship between the internal displacements, f , and the node displacements, δ , of an element.

$$\{f\}^e = [N] \cdot \{\delta\}^e \quad (1)$$

Strains are obtained from displacements.

$$\{E\}^e = [B] \cdot \{\delta\}^e \quad (2)$$

Stress-strain relationships are:

$$\{\sigma\}^e = [D]^e \cdot (\{E\} - \{E_0\})^e \quad (3)$$

When virtual nodal displacements are imposed and the principle of stationary potential energy is used, the force-displacement relationships become

$$\begin{aligned} \{F\}^e &= \left(\int [B]^T [D] [B] d(\text{vol}) \right) \{\delta\}^e \\ &\quad - \int [B] [D] \{E_0\} d(\text{vol}) \\ &\quad - \int [N]^T \{P\} d(\text{vol}) \end{aligned} \quad (4)$$

The element stiffness matrix is defined by:

$$[k]^e = \int [B]^T [D] [B] d(\text{vol}) \quad (5)$$

Nodal forces due to distributed loads are:

$$\{F\}_p^e = - \int [N]^T \{p\} d(\text{vol}) \quad (6)$$

Initial strain effects are:

$$\{F\}_{E_0}^e = - \int [B]^T [D] \{E_0\} d(v_0) \quad (7)$$

30708-4011

$$\{F\}^e = [k] \{\delta\}^e + \{F\}_p^e + \{F\}_{E_0}^e \quad (8)$$

For node equilibrium at node i, R equals the external forces:

$$\{R_i\} = \sum_{m=1}^n \{F_i\} \quad (9)$$

Replacing F_i ,

$$\begin{aligned} \{R_i\} &= \sum_{m=1}^n [k_{im}]^e \{\delta\}^e + \sum \{F_i\}_p^e \\ &+ \sum \{F_i\}_{E_0}^e \end{aligned} \quad (10)$$

then the overall equations are summed over element i

$$\{R\} = [K] \{\delta\} + \{F\}_p + \{F\}_{E_0} \quad (11)$$

As a quick example, consider a two-dimensional region divided into triangular elements (fig. 1).

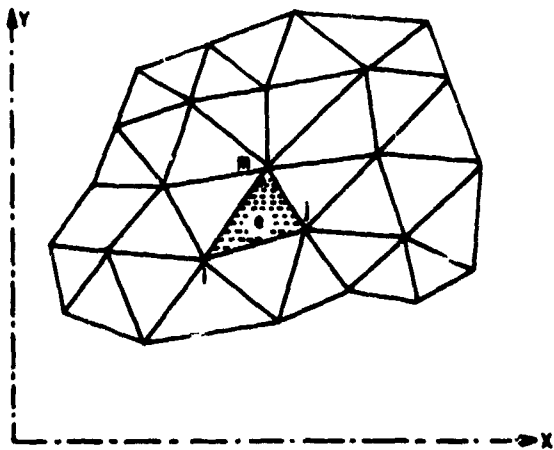


Figure 1. Planar region divided in triangular elements.

Take an individual element of this assembly and formulate its elastic behavior (fig. 2)

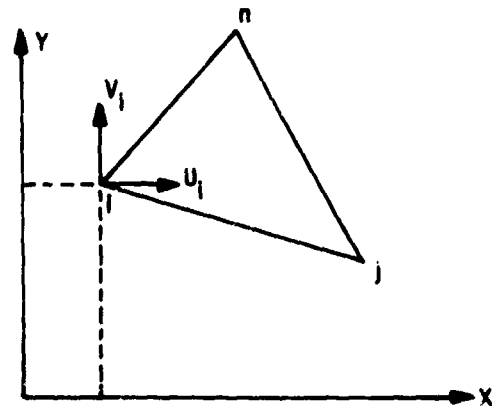


Figure 2. Element formulation.

assuming a constant strain element; then the displacement function used is:

$$\begin{aligned} u &= \alpha_1 + \alpha_2 x + \alpha_3 y \\ v &= \alpha_4 + \alpha_5 x + \alpha_6 y \end{aligned} \quad (12)$$

in terms of joints i, j, m

$$\begin{Bmatrix} U_i \\ U_j \\ U_m \end{Bmatrix} = \begin{bmatrix} 1 & x_i & y_i \\ 1 & x_j & y_j \\ 1 & x_m & y_m \end{bmatrix} \begin{Bmatrix} \alpha_1 \\ \alpha_2 \\ \alpha_3 \end{Bmatrix} \quad (13)$$

When this is inverted to get $\alpha_1, \alpha_2, \alpha_3$ in terms of U_i, U_j, U_m , the joint displacements, a general expression of U is obtained. Similarly, this is possible with the v component, too. Hence,

$$\{f\} = \begin{Bmatrix} u \\ v \end{Bmatrix} = [N] \{\delta\}^e \quad (14)$$

This relationship is expressed in equation 1; thus, the formulation can proceed.

Finite Element Systems

A large number of finite element programs have been developed by industry, but most of them are oriented towards special

purpose applications and, moreover, are not necessarily more efficient than general purpose systems.

A smaller number of general purpose analyzers have also been developed, primarily to collect the elements and to standardize the solution methodology. Even these vary enormously in their scope, capacity, and limitations. Some typical systems are ASKA (ref. 6), SAMIS (ref. 7), ELAS (ref. 8), and STRUDL II (ref. 9). The last of these, which was developed by the Civil Engineering Department at the Massachusetts Institute of Technology, is one of the most comprehensive and powerful of these systems.

STRUDL II was developed to standardize and to collect a large number of existing element types and to organize them in a modular way so that very complex problems involving intermixes of bar and continuous elements can be handled with equal ease. All of this was done within a problem-execution environment having the following general characteristics.

Problem-Oriented Language

The input-output language of STRUDL II is the language an analyst uses in his everyday work. The structure is specified as to geometry, topology, loadings, and types of behavior element. All of these commands are translated into FORTRAN-like statements, and the execution proceeds from them.

Dynamic Memory Allocator

It is difficult to specify the primary/secondary computer storage needed for a complex problem unless one is intimately familiar with the basic operations performed. Then, too, for optimum storage use, the arrays should be shifted from primary to secondary when no longer needed. This, too, tends to make the analyst a computer systems programmer. The STRUDL II dynamic memory allocator (DMA) obviates both needs by allocating the requisite amounts of storage completely automatically at execution time;

it moves the arrays between secondary and primary only when the need arises. A small problem may be solved in its entirety in primary storage while a large one may require a number of memory reorganizations.

Modularity

Although the library of available elements is very extensive, the user may find that the one he needs is still not available. He can add to this by specifying the general stiffness matrix for an element and the array needs for one such element; he can either add it to the general library or include it as part of the input at problem-execution time. A completely free intermix of elements is permitted, constrained only by the requirement that connecting elements have equal degrees of freedom at the joints.

General Capability

At the present time, the capability of the system extends to trussed, framed, folded plate, shell, and rotational elements under the following conditions (fig. 3):

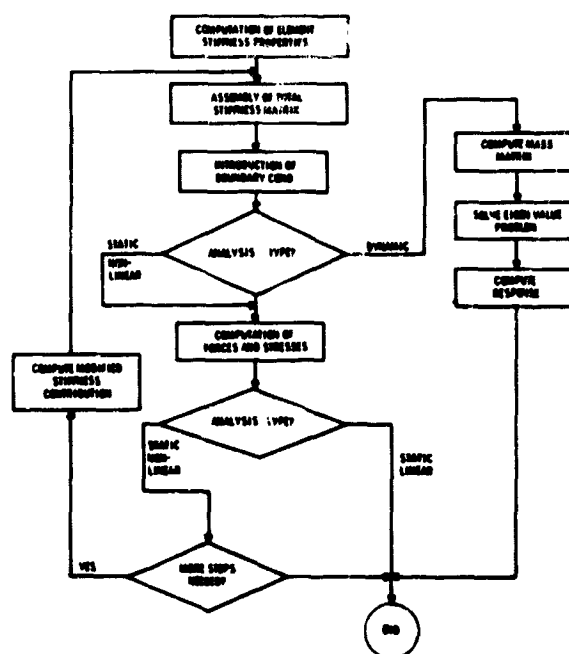


Figure 3. STRUDL II analysis procedure.

Linear static analysis
 Nonlinear and buckling analysis
 Dynamic analysis
 Optimization.

A general formulation has recently been produced that will allow optimization of finite element-composed structures. This is a most significant breakthrough and will greatly expand the general analytical capability.

Mirror Structure Problem

Although the application of finite element methods to optical systems is not necessarily new, the capabilities of the STRUDL II system now make it possible to solve a very large class of structure problems associated with the manufacture and employment of optical mirrors. Two typical problems and a feasible approach to either by finite elements are considered in this paper.

Grinding and Polishing of Ribbed Mirror Structure

The grinding and polishing of ribbed mirrors invariably results in local surface deviations at the ribs. This is a result of non-uniform elastic deformations caused by the grinding tool; that is, more of the stiffer area is ground off than the flexible area. It is difficult to estimate the magnitude of these deviations by ordinary structural analysis methods due to the highly complex, elastic behavior of such structures, but the finite element approach will provide a good estimate. A ribbed mirror structure can be idealized as a series of interconnected folded plates, responding both in bending and stretching (fig. 4). The load from the grinding tool can be considered acting as either an applied force or an applied deformation (fig. 5). The displacements and stresses caused by this tool can be easily obtained.

The specific element used for this analysis is called GSBPE (general stretching and bending plate element). This newly developed element is designed for stress analysis of continuous plate elements and is rectangular in shape. It was based upon stiffness

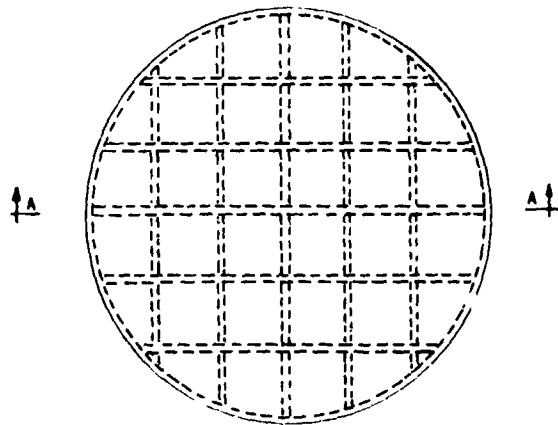


Figure 4. Ribbed mirror idealization.

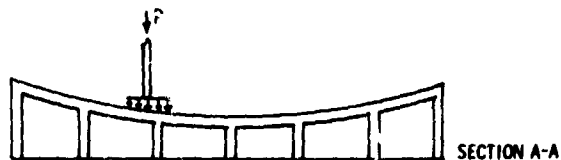


Figure 5. Grinding tool on mirror structure.

matrices developed by Przemieniecki (ref. 3). A typical element layout is shown on figure 6, and segments of the STRUDL II program can be seen in figure 7.

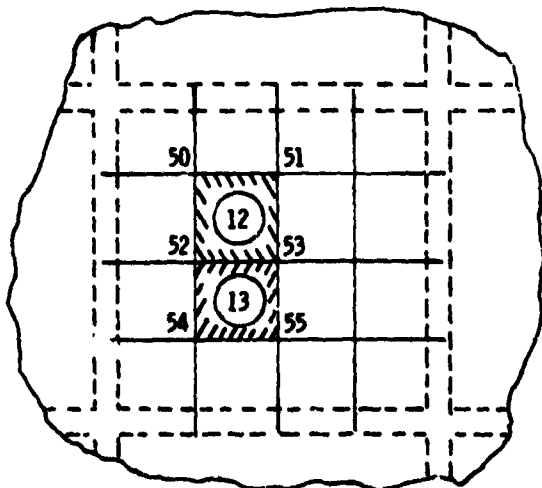


Figure 6. Typical element layout.

```

STRUDN 'MIRROR STRUCTURE'
TYPE FOLDED PLATE
UNITS INCHES LBS
JOINT COORDINATES
.
.
.
51      25.0      36.0
52      20.0      30.0
.
.
.
ELEMENT INCIDENCES
.
.
.
12      50      51      52      53
13      52      53      54      55
.
.
.
ELEMENT PROPERTIES
.
.
.
12, 13 TYPE 'GSBPE' THICKNESS 0.8
.
.
.
CONSTANTS
E 10000000. ALL
POISSON 0.15 ALL
LOADING 'TOOL' ONE
ELEMENT LOADS
.
.
.
12 SURFACE 'GLOBAL' PZ-0.25
LOADING LIST ALL
STIFFNESS ANALYSIS
LIST DISPLACEMENTS, STRESSES ALL
FINISH

```

Figure 7. Typical STRUDL II program for ribbed mirror.

The precision with which the deformation contours may be obtained will depend upon the number of elements chosen for the analysis. The results of such an analysis can then be used to determine the optimum system of mirror thickness, rib number and proportions, and the type of grinding tool and grinding action.

Active Control of Thin Mirrors

The structural behavior of the thin mirror with active control is also fairly readily handled by the finite element analyzer. A number of different element types can be employed. The rather low internal angle of most mirrors discourages the use of a regular shell element because of ill-behavior problems, especially near the crown. A bending and stretching element with zero curvatures tends to give rather conservative results (larger deflections) unless a very large number of elements are employed (ref. 5). That, however, can lead to extremely severe problems of ill-conditioning and round-off error accumulation and would probably result in erroneous information. The desirable element in this case is the shallow shell element. The curvatures of this element can be easily specified; hence, the mathematical response of the structure will more closely represent the physical response.

A very large part of the active-mirror structural complications will come from the actuators. If these electromechanical components have a finite stiffness relative to the mirror shell and if the basic action of the actuator is an applied displacement, then it follows that the amount of displacement that actually occurs will vary with the actuator location on the shell. Certain parts of the shell will be stiffer than others, thus inducing a rather larger load in the actuator to obtain the desired displacement, compressing the actuator elastically, and reducing the actual applied displacement. It is obvious, therefore, that the mirror structure and actuators must be analyzed as a complete, elastic, structural system. It is not enough to analyze the shell under point forces.

Using STRUDL II finite elements, it is possible to solve the system by representing the actuators as truss elements joined to the shell at various shallow-shell elements. The displacements are obtained by applied distortions within the truss elements themselves, which are then analyzed as an entire truss-shell system. From this analysis, the influence surface for the shell distortions is obtained for the control problem.

Optimization

The objective of engineering is always to produce an acceptable solution (ideally, an optimum solution) to a given set of requirements. Most structural problems are sufficiently complex so that even the analysis stage may present some difficulties; hence, the formal optimization problem, which is at least one magnitude more complicated, is often not attempted. What is meant here by optimization is not just the trials of a number of variable combinations but a thorough, systematic, analytical procedure that provides the best possible solution. The definition of "best" will, of course, depend upon the nature of the problem. It may be "weight-related" as in the aircraft structure (refs. 10, 11, and 12), "most reliable" for a spaceborne system that cannot be repaired after deployment (ref. 13), or both "weight and fixed-cost related" as in building construction (ref. 14).

A number of approaches to the optimization problem have been taken over the years. The first attempts looked for closed-form analytical solutions to the problem. These were generally limited to trivially simple structures under a unique loading condition. The bulk of optimization of structures has been performed using formulations and techniques developed in economic analysis.

The approach employing such a mathematical model must contain the following components:

Variables(X). These are the structural properties, such as member areas, that the designer wishes to determine so that the best (optimum) solution is obtained.

Objective function(Z). This is the sum of the structural system costs expressed in terms of the variables.

Constraints. These are the limitations on structural behavior (such as stresses, deformations) expressed in terms of the design variables. These may be equalities or inequalities.

Formally, this can be expressed:

$$\text{minimize } Z = f(X_j)$$

subject to

$$g^1(X_j, Y_j) \leq 0$$

$$g^2(X_j, W_j) = 0$$

$$X_j \geq 0 \quad (15)$$

where Y_j , W_j are limiting values on variable behavior. When the functions f , g_1 , g_2 are linear or convex, then existing mathematical programming methodology can be applied. In general, the structural optimization problem is nonlinear, nonconvex, and integer, and a general solution may be difficult to find.

A number of recent developments, some of which are just beginning to appear in publications, have begun to overcome these analytical difficulties through new methods of formulation. One method that has been developed and is being introduced into the STRUDL II system is the branch-and-bound technique (ref. 15). By using integer values for the design variables and a mix of economic and combinatorial solution technology, it is now possible to achieve optimal solutions for general frame type of structures under multiple loadings with relatively small expenditures of computer time.

A recent and substantial breakthrough is the application of these optimization techniques to continuous structures, such as folded plates and shells, by using finite element methodology. It is now possible to find the best design values (for example, rib sizes and locations for the ribbed mirror structure) so that the desired stress and deformation levels can be maintained. This, too,

can be done with relatively small amounts of computer time. Major work is proceeding in this area at the present time.

Conclusions

There is no doubt but that the finite element method represents the mainstream of advanced structural mechanics analysis today. Sufficient methodology already exists to analyze most problems that will arise in fields such as astronomical mirror structures. Soon the capability will exist to determine the optimum solution to the same problem.

Use of the finite element method is, however, very deceptive. It is extremely easy (even for someone not in the field of structural mechanics) to set up a problem and to solve it using standard algorithms, but extreme caution must be exercised. It is vital to use the correct element for the type of behavior expected, the proper subdivision of the structure, and the proper boundary conditions. In any case, numerical results will be obtained, but they may have little relation to the actual behavior. Ill-conditioning, roundoff accumulation, and errors of improper "discretization" can lead the unwary user far from reality. The present state-of-the-art in structural mechanics permits the analyst to attack an enormous range of problems, but it is most vital that the method limitations, whenever these exist, also be known.

References

1. Argyris, J. H.: *Matrix Methods of Structural Analysis*. Pergamon Press, 1964.
2. Zienkiewicz, O. C.: *The Finite Element Method in Structural and Continuum Mechanics*. McGraw-Hill, 1967.
3. Przemieniecki, J. S.: *Theory of Matrix Structural Analysis*. McGraw-Hill, 1968.
4. Freeman, R. F.; Porter, C. D.; Mu, H. H.: *Photoheliograph - Primary Mirror Development*. Report #750-F, JPL, 1968.
5. Creedon, J. F.; Robertson, H. J.: *Evaluation of Multipoint Interaction in the Design of a Thin Diffraction-Limited Active Mirror*. IEEE Aerospace Journal, March 1969.
6. Argyris, J. H.: *Continua and Discontinua*. Proc. Conf. Matrix Meth. in Struct. Mech., Wright-Patterson AFB, 1965.
7. Lang, T. E.: *Summary of the Functions and Capabilities of SAMIS*. Tech. Report 32-1075, JPL, 1967.
8. Utku, S.; Akyuz, F. A.: *ELAS, Volume I, Users Manual*. JPL, 1968.
9. Logcher, R. D., et al.: *ICES-STRUDL II Engineering User's Manual*. MIT, Civil Engineering Department, 1968.
10. Schmit, L. A.: *Structural Design by Systematic Synthesis*. Proc. 2nd Natl. Conf. on Elec. Comp., ASCE, 1960.
11. Fox, R. L.; Schmit, L. A.: *Advances in the Integrated Approach to Structural Synthesis*. AIAA 6th Annual Structures and Materials Conference, Palm Springs, Calif., 1965.
12. Gellatly, R. A.; Gallagher, R. H.; Lubracki, W. A.: *Development of a Procedure for Automated Synthesis of Minimum Weight Structures*. DDC Report AD-611-310, Oct. 1964.
13. Moses, F.: *Reliability Based Structural Synthesis*. Structural Synthesis Summer Course Notes, Vol. III, Case Institute, 1965.
14. Soosaar, K.; Connell, C. A.: *Optimization of Topology and Geometry of Structural Frames*. Proc. ASCE Spec. Conf., Chicago, 1968.
15. Cella, A.: *Discrete Variable Optimization of Bar Structures*. Ph.D. Thesis, MIT, Civil Engineering Department, Sept. 1968.

PRECEDING PAGE BLANK NOT FILMED.

N70-36709

Self-Weight Loaded Structures in the Context of Lightweight Mirror Applications

J. P. Duncan

The University of British Columbia

Introduction

A mirror is essentially a surface formed by the interface between a substrate and its environment. From practical considerations of polishing and handling, the substrate must have some minimum volume, which, in turn, has weight in the gravitational field. The connected elements of the substrate have centers of mass at which gravitational body forces may be considered as concentrated.

To maintain equilibrium of the substrate, it is necessary that reaction to these distributed body forces be provided at some selected points on a relatively rigid system of reference. To avoid relative displacement of the elements of the substrate, it is desirable to support each element directly so that each body force and its direct reaction equilibrate locally. If local equilibration is not possible, it becomes necessary to connect the input of localized body force to some chosen points of reaction by way of a structure.

An elastic structure is an arrangement of connected elastic members designed to transmit load inputs—forces or torques generalized as tractions and located in space—to points where they are equilibrated by reactions. At all points within the system where transmission between input and output takes place, equilibrium must be maintained locally by forces and moments in the structural members.

These members, kinematically called links, are sometimes connected in pin-jointed forms by joints called "pairs." In many modern structures, the connections are continuous. The structure then becomes a multiple-connected elastic body. Whether

jointed or continuous, the structural members have weight of their own, which in some circumstances may impose on themselves as much distributed input of load as any external traction that the structure is designed to support. Such a case is a structure designed to maintain the desired geometry of a mirror located in a gravitational field.

Some structural analysis treats the weight of members as secondary sources of input. When it is accounted for, such weight is often lumped for analysis at the panel points of the lattice type of structures. Furthermore, much of established analysis is designed to study stresses with margins of safety rather than deformations with extremely high accuracy, as required for astronomical mirrors. Again, the force systems in both terrestrial and space applications are ultimately linked to the earth as the virtually rigid frame of reference, which, at the same time, is the cause of loading through gravitational attraction.

Many structures have an arbitrarily chosen configuration of members linking inputs with outputs (reactions), and many are designed to bridge arbitrarily-specified input and output configurations.

It can be shown that, even for arbitrarily specified configurations of input and output forces, there can be theoretically optima configurations of transmission members. A given optimum configuration, however, changes with each change in the gravitational acceleration vector so that there can be no unique optimum configuration for a structure that changes attitude in a gravitational field and no constant specification for member cross-sectional areas with changing values for the

modulus of a unidirectional acceleration vector.

If the criterion for structural design is to be the maintenance of a surface geometry by an underlying structure grounded at some infinitely rigid frame of support or plane of reference defined by three points, the structural members will tend to be lightly stressed. Small strains and hence small integrated extensions will result. Obviously, it will be desirable to use lightweight material for the transmission members and for the substrate of the surface whose geometrical form is being maintained. These factors suggest a material having a high Young's modulus and a low density. Beryllium has the best combination of these properties, but other materials vie with it on grounds of cost and ease of fabrication.

The above features of rigid structures can be identified in the symbolic diagram, figure 1.

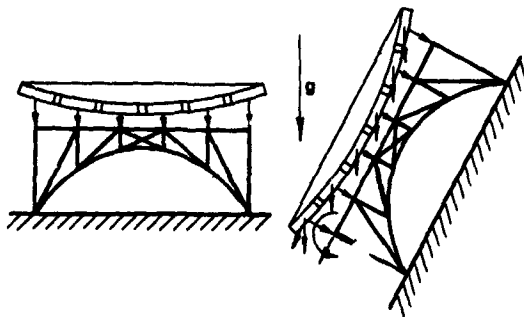


Figure 1. A generalized structure.

Rationale of Mirror Support

In astronomical mirror design, the object is to maintain a geometrical surface form constant as its substrate assumes various attitudes in a gravitational field. One approach, frequently used, is to support each element of substrate mass directly at its center of mass with a force appropriate to the attitude. This is equivalent to limiting the length of path of internal force transmission in a continuous solid to the dimensions of each lump of mass associated with a point of support close to its

center of mass. The transmission of localized body force to a neighboring point of support then induces elastic strains in the continuum, and strain gradients result.

This approach is adopted with large terrestrial telescope mirrors. Appropriate forces of reaction with reference to a rigid ground base (earth) are supplied through mechanical lever systems. The forces are calculated or arranged to equilibrate the weight of each lump of the segmented (or continuous) mirror with a direct reaction of the proper magnitude value for each attitude of the whole mirror.

Ever since Ritchey first proposed desirable proportions for solid cylindrical substrate and subsequently constructed web and flange types of mirrors, the effort to limit the number of supports by accepting a degree of internal transmission of self-weight has continued. It has led to the adoption of "egg box" constructions for lightweight terrestrial and orbiting applications. The approach is to equilibrate the dead weight of the substrate, ultimately on a statically determinate set of three points on a system of reference-determining attitude. The points of secondary reaction with the substrate may be more than three, the number being built up through successions of properly proportioned levers. A simple example of a 12-equalized-point reaction system is illustrated in figure 2. This 12-point mounting jig was designed to provide a close approximation to a uniform shear distribution along the circular boundary of a plate loaded transversely. Even with multi-point support, a degree of internal transmission by flexure and shear will remain. The structure has to be designed to transmit these with very small, acceptable deformations. In addition, these deformations will vary with each attitude; hence, the distortion of the supported mirror must be controlled for the worst case.

The egg-box construction is frequently thought of as a flexural type of structure; however, because of the value of the ratio of the depth of section to the span between supporting reactions often adopted, shear



Figure 2. Photograph of a 12-equalized-point reaction system.

rigidity in its webs may be even more significant in maintaining stiffness than the flexural rigidity provided by the flanges. The two are related of course. It is a question of the significance of transverse shear deflection and the additional curvatures of neutral axes of flexure that might arise from variable shear.

Traditional Circular Mirror

The traditional substrate for an astronomical mirror, large or small, is a homogeneous, right circular cylinder having a ratio of diameter to thickness of 8 to 1 (small aperture) or 6 to 1 (large aperture). These ratios are rules of thumb proposed by Ritchey on the basis of experience. They are felt to be sufficient to limit deflections to acceptable values. The smaller ratio, recommended for very large mirrors, reflects the dependence of self-weight deflection on the ratio of diameter squared to thickness.

The extreme attitudes of a right cylindrical mirror substrate in a gravitational field are as shown in figures 3a and 3b.

If a mirror is sufficiently rigid under self-weight in attitude (fig. 3a), it is likely to be

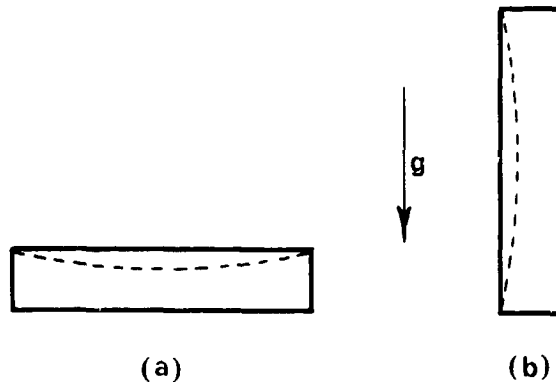


Figure 3. Horizontal and vertical quasi-cylindrical mirrors.

sufficiently rigid in extreme attitude (fig. 3b). The self-weight deformation in attitude (fig. 3b) has been studied by Schwesinger (ref. 1). It is the author's intention to explore deformations in intermediate attitudes by using a combination of analytical and experimental methods. In the sequel, logical systems of supporting the mirror horizontally, as in figure 3a, will be discussed as an introduction to alternative structural concepts for light weight.

Support of Circular Mirrors

An essential element of any structural concept is its reactive system. This may be chosen arbitrarily or determined by the function of the structure.

In view of the foregoing discussion, the following line of argument might be considered in determining a suitable supporting system for a horizontal mirror.

Since the object is to create a surface as the boundary of a substrate and its atmosphere, a thin plate supported on its lower face by hydrostatic pressure, as in figure 4, should serve. The material in the substrate is then supported directly, and internal transmission is confined to direct compression through the thickness of the plate. Theoretically, the thickness of the substrate could be zero, and indeed the consequence, a liquid surface, is often used as a reflective interface.

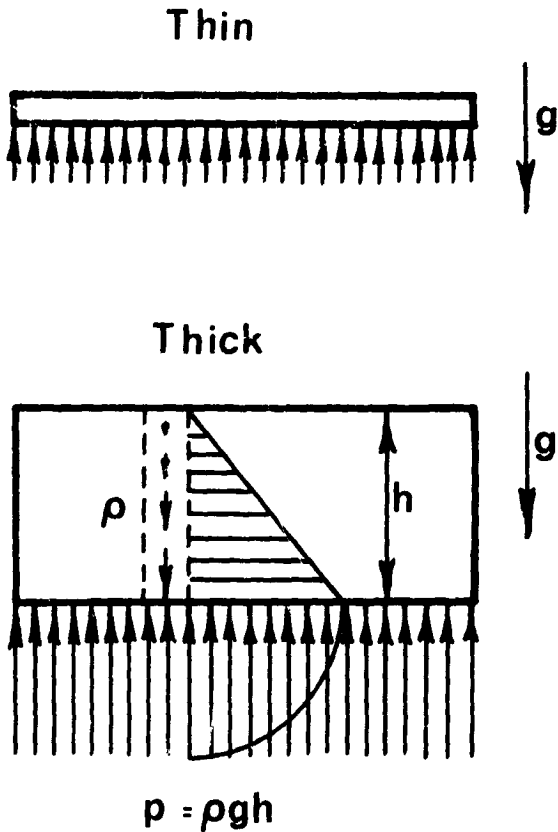


Figure 4. Direct support of a thin plate.

If, for obvious practical reasons, the substrate has any significant thickness and is still supported on its lower face by hydrostatic pressure, it assumes a well-known theoretical form, shown in figure 5, for which the displacements were worked out originally by A. E. H. Love (ref. 2). These deformations are due to the effects of direct internal transmission of vertical body force to vertical reaction on the lower face. Obviously, the deformation will vary with changing values of body accelerations.

Further discussion of the just-floating, high-floating, and fully-immersed elastic solid can be found in reference 3.

If the right circular cylinder is supported by shearing forces along its outer boundary, the body forces are transmitted to these boundary reactions by flexure and shear. Love's elastic displacement solution for the

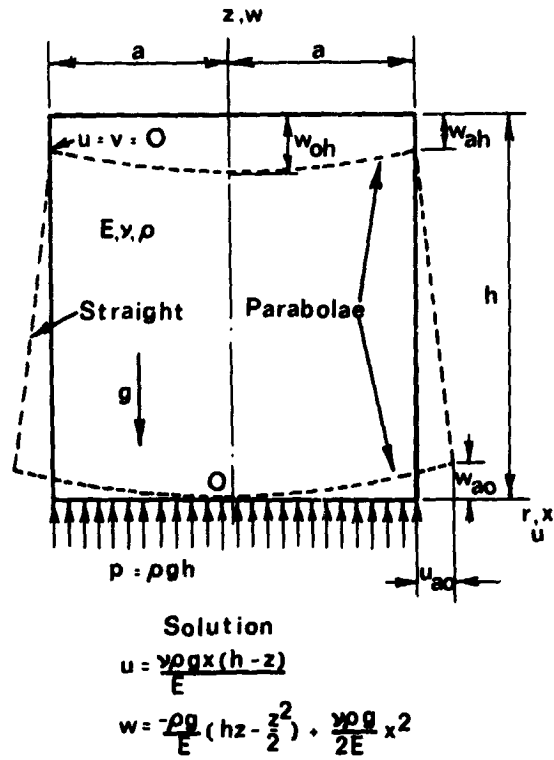


Figure 5. Deformation of a very thick cylinder; Love's solution.

moderately thick plate bent under its own weight and supported by parabolically distributed shear is a superposition of the solution in figure 5 and the well-known Legendre polynomial solution for a uniformly loaded, moderately thick plate. The loading and reaction conditions of these two solutions are shown graphically in figures 6a and 6b, respectively. The deflection resulting from superposition of these solutions, as indicated in figure 6c, is

$$w = -\frac{\rho g \nu}{2E} a^2 - \frac{1}{8} \frac{(2\rho g h)}{D} a^2 \left[\frac{1}{8} \left(\frac{5+\nu}{1+\nu} a^2 \right) + \frac{1}{5} \frac{8+\nu+\nu^2}{1-\nu^2} h^2 \right]$$

where nomenclature is as defined in reference 2.

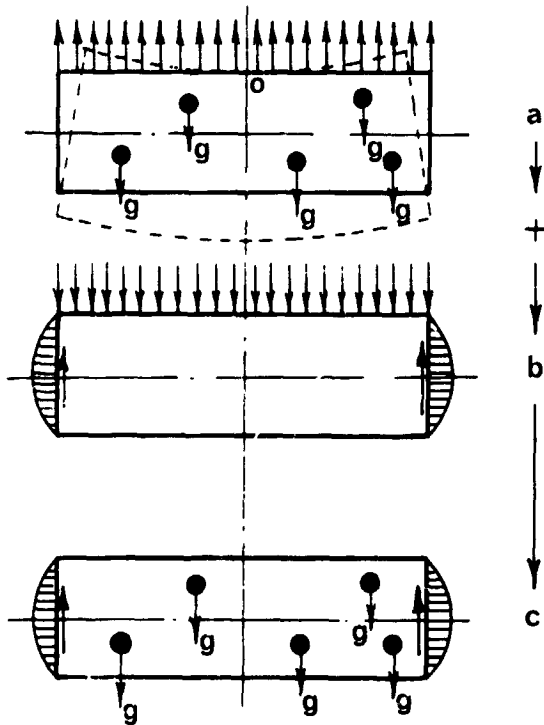


Figure 6. Self-weight deformation of moderately thick plate; Love's solution.

It is well-known that in deep beams and plates much of the resistance to deformation is provided by shear. This has been demonstrated for a few cases in comparative studies by Kenny (ref. 4). Another way of expressing this is to say that analytical stress-field solutions such as the above, which is not dependent on Bernoulli-Euler assumptions, should be used for accurate assessment of plate rigidity. The intermediate approach is to use Bernoulli-Euler thin-plate theory with Rankine-Grashoff approximate shear corrections.

It is not easy to provide continuous support by way of parabolically distributed shear (fig. 6) because of the statical indeterminacy of such arrangements. A logical simplification is to concentrate shear reactions at three equispaced boundary points, as shown in figure 7, or to use a statically determinate distributing arrangement, as illustrated in figure 2. Such systems induce more strain than systems using continuous support

because of additional internal (tangential) transmissions of body forces to reactive points.

It seems likely that the average length of internal transmission by flexure would be reduced by moving the three points of support towards the center of the plate to minimize the greatest lateral deflection. A further logical step would be to increase the number of such points to six or more by using a statically determinate system of linked levers, as symbolized by figure 8.

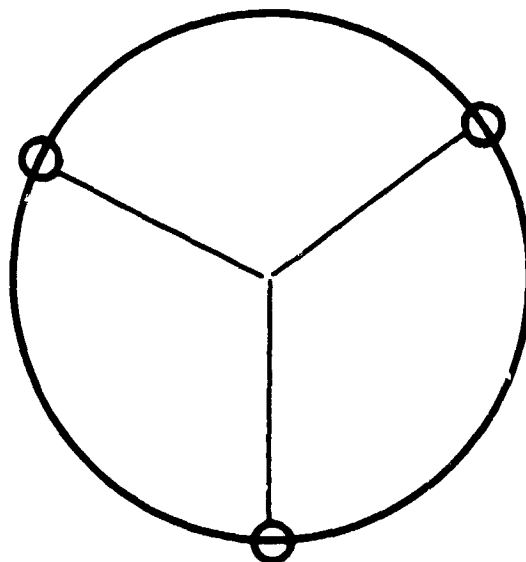


Figure 7. Plate supported at three boundary points.

Several workers have searched for the best locations for points of support, and numerous experimental observations have been made. Emerson's (ref. 5) studies are well-known. Dew's (ref. 6) experimental results of interferometric study of the sagging of thick circular glass plates, figures 9 and 10, illustrate the topography of plates supported on three equispaced points at different radii. Emerson concluded that the three points should be located along a circle whose diameter is 0.7 of the boundary diameter of the plate. Kenny (ref. 4) has studied deflections resulting from three-point support both analytically and experimentally and has made limited assessments of the contributions of shear and bending. Vaughan has compared a

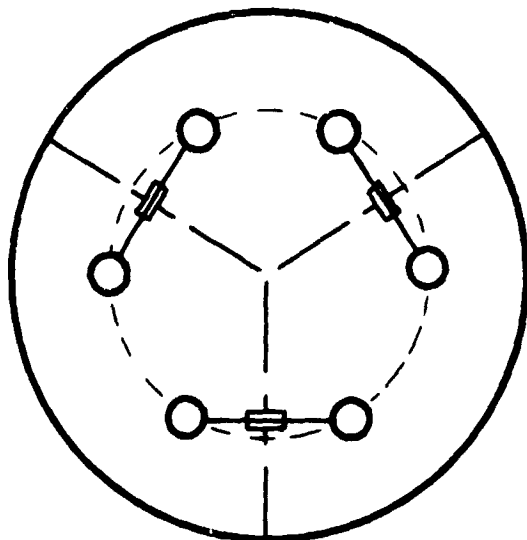


Figure 8. Plate supported at six internal points on balanced levers pivoted at three primary points.

simplified analytical solution with Williams' computed solutions (as reported by Kenny) and with experimental observations on a thin plate, as outlined in Appendix A.

Optimization of Circular Substrate

The fundamental structural theorem of James Clerk Maxwell and its extension by A. G. M. Michell, which have been summarized and discussed by Barnett (ref. 7), provide, from two-dimensional analysis, a clue to the desirable condition of minimum-weight rigid structures in three dimensions. Maxwell's theorem implies that all material employed should be stressed and strained with the same sign to an acceptable maximum limit. Michell's corollary demonstrates that, if material must be used in both tension and compression, it should be disposed in members that are orthogonal at all points—one set being in tension at the maximum acceptable limit and the other in compression at the same numerical limit.

Web and Flange Construction

The material employed in conventional, flexed, homogeneous beams and plates is not

ideally distributed in accordance with the above theorems. One well-known method of redistribution is the adoption of web and flange (I-beam) concepts in one or two dimensions. This relocates the material in a hypothetical rectangular cross-section so that part of the material is in tension or compression and provides a moment of resistance. The rest of the material transmits shear as depicted in figure 11.

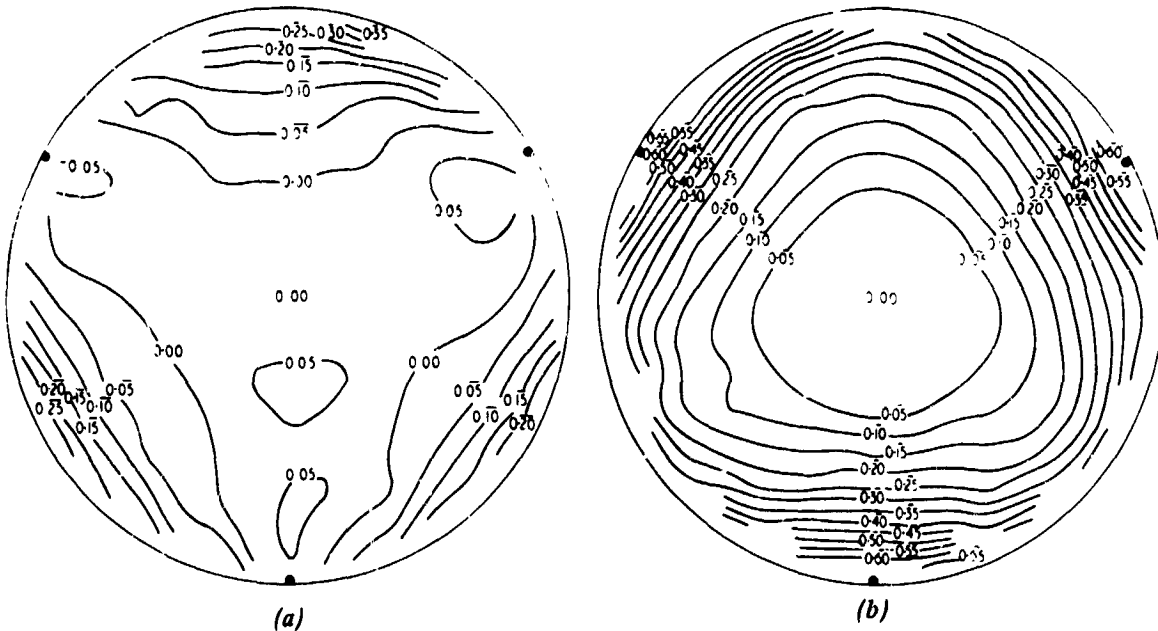
A further improvement of the web is achieved by castellation of an I-beam web. The web is cut along a line resembling an Acme thread. The resulting halves are then relocated and welded as illustrated in figure 12. The logical extension of these ideas into three dimensions leads to the concepts of lattices, geodesic frameworks, and foams.

A greater stiffness-to-weight ratio results, but there is no guarantee that the resulting structure is optimum; nor is it clear whether internal transmission is essentially by shear or bending.

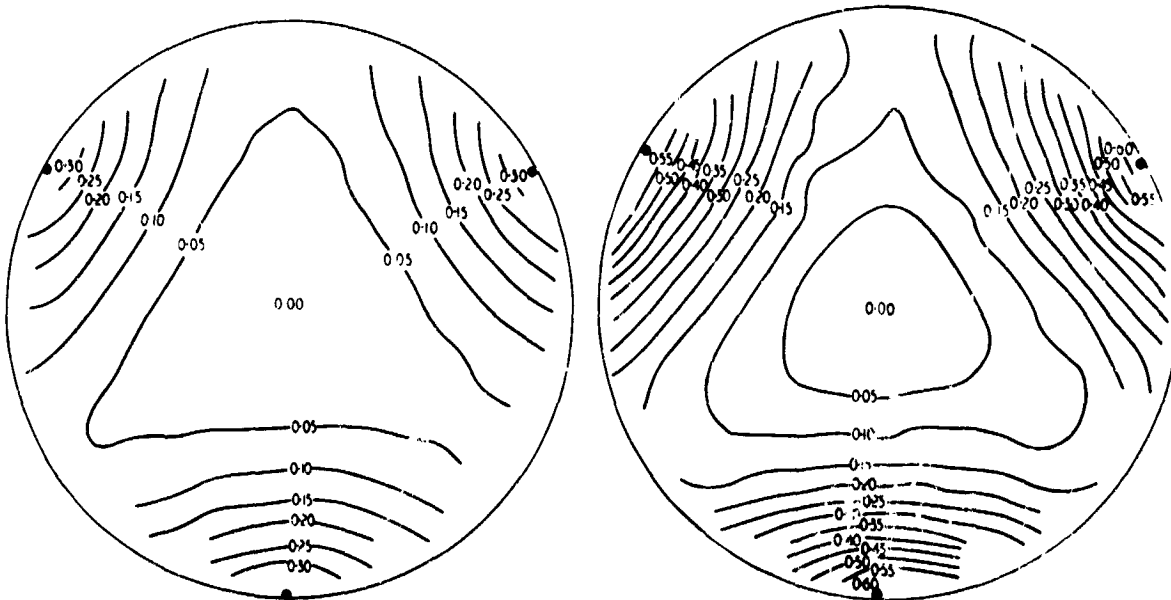
Since a hexagonal or triangular cellular structure has the same theoretical anisotropy as a homogeneous structure, the triangular cell seems to represent a logical pattern of web configuration. Thus, the egg-box construction of mirrors with three sets of webs intersecting at 120 degrees suggests itself in plan as a sandwich construction for mirrors amenable to analysis and experimental study by the general theory and methods outlined by Plantema (ref. 8).

Arch Concepts

A second approach to optimization follows from Maxwell's theorem, which, in space-spanning structures, implies the use of arches, domes, and shells. Figure 13 from reference 4 shows a sequence of plates and arches, some of which have been compared by Kenny (ref. 4). The theory of arching and the relations among arch geometry, load, and stresses have been discussed by Inglis (ref. 9) and others. Some interesting experimental results and facts concerning deformations in arch-like circular plates are to be found in reference 4.



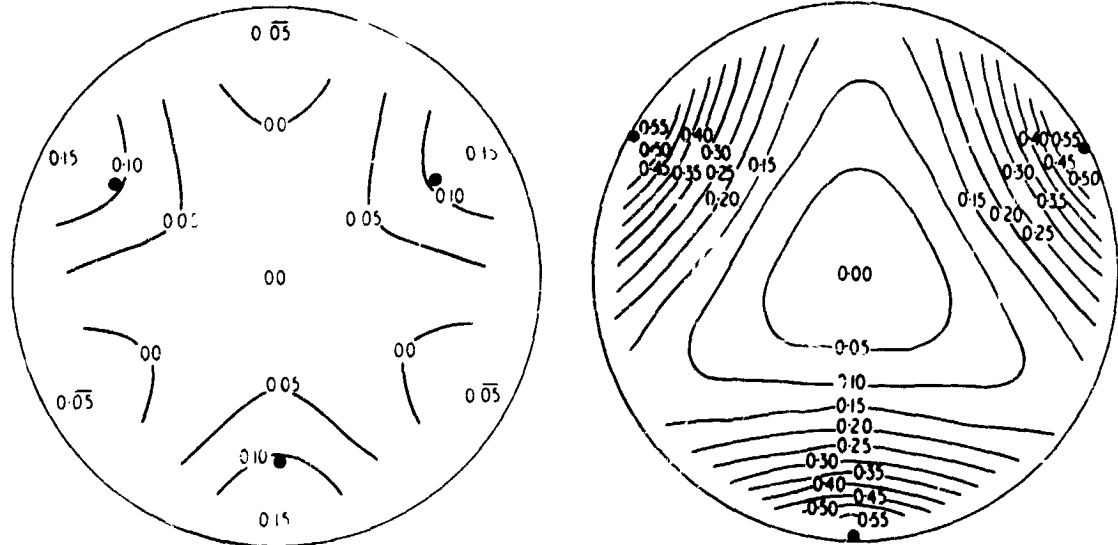
(a) and (b) Contour maps of a 30-centimeter diameter x 5-centimeter circular flat supported at three points on the periphery (1/20 fringe contours): (a) face up; (b) face down.



(c) Sag of the above circular flat.

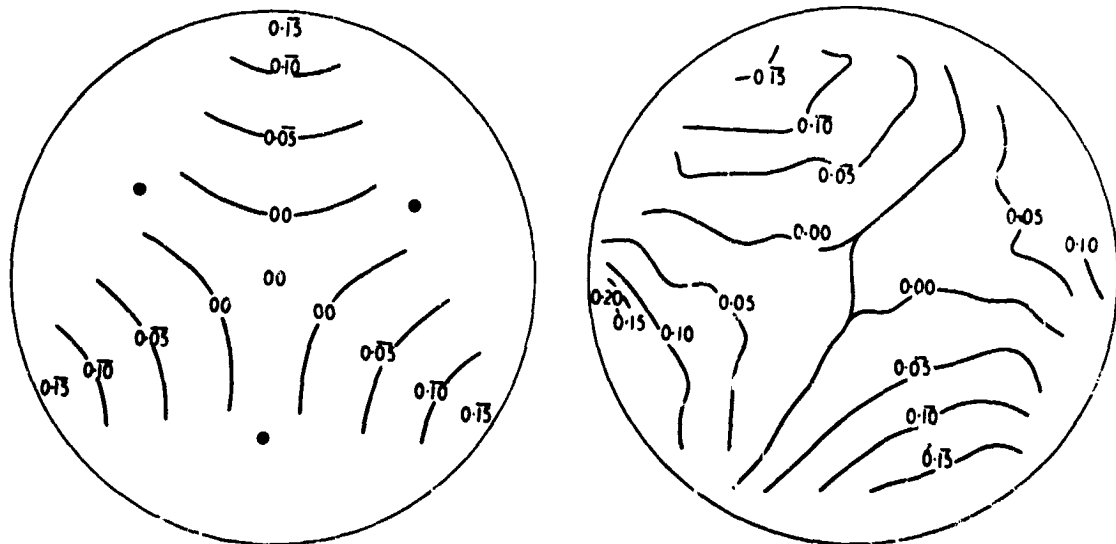
(d) Sag of a 30-centimeter diameter x 3.8-centimeter circular flat supported at three points on the periphery (1/20 fringe contours).

Figure 9. G.D. Dew's interferograms for support at the outer boundary; from his paper "The Measurement of Optical Flatness," Journal of Scientific Instruments, Vol. 43, July 1966, pp. 409-415. (Reprinted with the permission of the author and the publisher, The Institute of Physics and The Physical Society, London, England.)



(a) The sag of a 30-centimeter diameter x 3.8-centimeter flat supported at three points on a circle of 21-centimeters in diameter (1/20 fringe contours).

(b) The sag of a 30-centimeter diameter x 3.8-centimeter flat supported at three points on the periphery (1/20 fringe contours).



(c) The sag of a 30-centimeter diameter x 3.8-centimeter flat supported at three points on a circle of 18-centimeters in diameter (1/20 fringe contours).

(d) The sag of a 30-centimeter diameter x 3.8-centimeter flat supported on a sheet of 100-millimeter p-urethane foam (1/20 fringe contours).

Figure 10. G.D. Dew's interferograms for support within the outer boundary; from his paper "Systems of Minimum Deflection Supports for Optical Flats," *Journal of Scientific Instruments*, Vol. 43, November 1966, pp. 809-811. (Reprinted with the permission of the author and the publisher, The Institute of Physics and The Physical Society, London, England.)

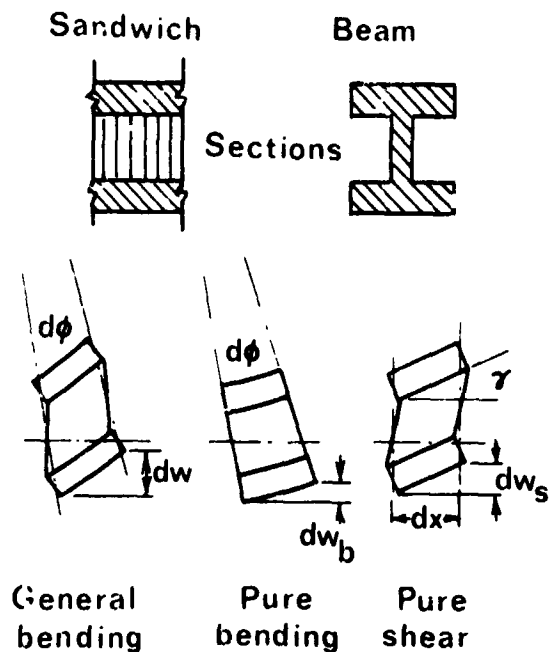


Figure 11. Deformation of I-beam and sandwich-beam sections.

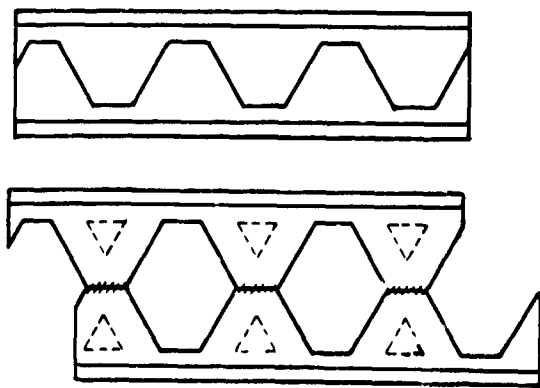


Figure 12. Castellated beam.

Several simple forms similar to that shown in figure 14, nicknamed "the ashtray," have been studied by the following four physical methods:

1. The accentuation of gravitational deformation by immersion in a very dense liquid such as steel in mercury (Duncan, Schroeder) or plastic foams in water (Unwin). The theory of this technique is illustrated in figure 15.

2. The "freezing" of the natural sag of epoxy resin above its transition point when it acquires greatly reduced elastic properties (Kenny). See reference 4.

3. The observation of deflections of silicone rubber models at room temperature (Kenny, Duncan).

4. In prospect, the application of external loading, such as sand, air pressure, lead shot, or tall rods proportional to the weight of structural material, beneath the load (Harvey, Duncan, Vaughan). Information relevant to these studies can be found in references 3 and 4.

Michell Structures

A third approach to optimization is to return to fundamentals by seeking optimum transmission routes from the primary self-weight inputs at the substrate to the chosen points of reaction. Figure 16 indicates this notion in a two-dimensional way. The arbitrary Michell ribbed-plate structures shown include the configurations for a weightless cantilever and a weightless beam of uniform bending. Real transmission members, however, have self-weight; hence, the detail of their ideal geometrical configurations must be calculated to accommodate this continuous input of body force loading. Particulars of real, self-weight-loaded, Michell structures have been computed and tabulated by E. W. Johnson. (See also Appendix B.)

The structures resulting from the concepts illustrated are, essentially, ribbed plates with ribs perforated with lightening holes of special shape and arrangement. It seems likely that the top members of such ribs could be "worked in" to the substrate itself. The resulting structure lacks the backplate that has been so heatedly debated as necessary in egg-box construction. The point is that, if the ribs are essentially a net of orthogonal fibers lying in their own plane, they are stressed similarly to a square plate in shear whose diagonals will be equally stressed with opposite sign. If support is provided essentially in shear, even though some bending is

To obtain verification of experimental techniques and mathematical analysis.

To investigate self-weight deflections of arch type structures and compare their behavior with that of a circular plate of constant thickness with a thickness to diameter ratio of 1/6. (A 3-point support taken as standard).

To obtain estimates of the shear deflections experienced by lightweight structures of the monolithic and eggcrate type.

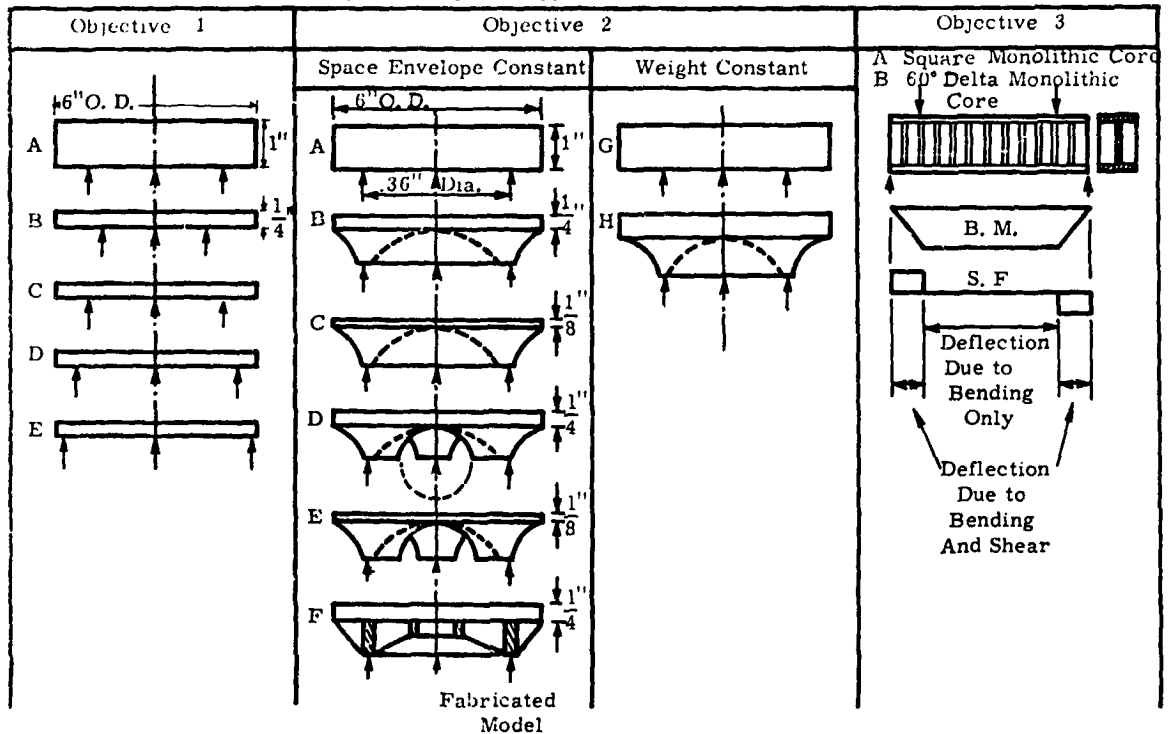


Figure 13. Kenny's table of plates and arches. See reference 4. (Reprinted with the permission of the author and the Perkin-Elmer Corporation.)

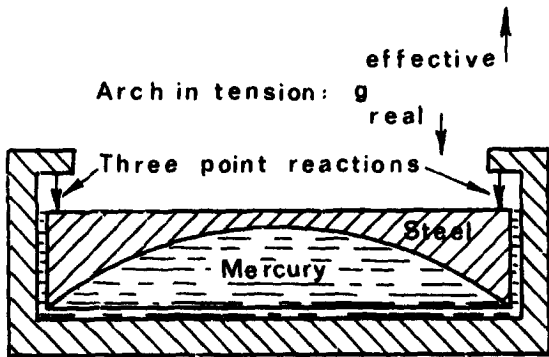


Figure 14. Forcibly submerged, arched substrate.

present, backplates may not be necessary; and ribbed support is in order.

Deformations of ribbed plates under hydrostatic loading (which could be regarded as artificially increasing the effective density of the supported plate) have been studied by Harvey and Duncan (ref. 10). A few observations on overstiffening or understiffening and weight-to-rigidity ratios were made.

A separate outline of some preliminary studies of self-weighted Michell cantilevers by E. W. Johnson is attached as Appendix B. It should be noted that numerically controlled machining makes the fabrication of such structures quite feasible and economical.

FREE BODY DIAGRAM	LOADING CONDITIONS	STRESS SYSTEM
	a. Boundary Conditions b. Body Forces	
<p>A.</p>	<p>a.</p> $\sigma_n = -k\gamma y$ $\tau_n = 0$ <p>R = reactions</p> <p>b.</p> $Y = \gamma$	σ_e τ_e
<p>B.</p>	<p>a.</p> $\sigma_n = -k\gamma y$ $\tau_n = 0$ <p>b.</p> $Y = k\gamma$	$\sigma_{(k\gamma)} = -k\gamma y$ $\text{all } \tau_{(k\gamma)} = 0$
<p>C.</p>	<p>a.</p> $\sigma_n = 0$ $\tau_n = 0$ <p>R = reactions</p> <p>b.</p> $Y = -(k-1)\gamma$	$\sigma_{(k\gamma)} = (\sigma_e + k\gamma y)$ $\tau_{(k\gamma)} = \tau_e$
<p>D.</p>	<p>a.</p> $\sigma_n = 0$ $\tau_n = 0$ <p>$\frac{1}{k-1} R = \text{reactions}$</p> <p>b.</p> $Y = -\gamma$	$\sigma_\gamma = \frac{1}{k-1} (\sigma_e + k\gamma y)$ $\tau_\gamma = \frac{1}{k-1} (\tau_e)$

- A. Body of density γ submerged in a liquid of greater density $k\gamma$.
- B. Body of density $k\gamma$ submerged in a liquid of its own density.
- C. Difference of above two, multiple gravity.
- D. Gravity

Figure 15. Graphic presentation of the immersion analogy of gravity; from "Gravitational Stresses Determined Using Immersion Techniques," V. J. Parks, A. J. Durelli, and L. Ferrer, Journal of Applied Mechanics, No. 67-APM-11; contributed to the Applied Mechanics Conference, Pasadena, California, June 1967, under the auspices of the Society of Mechanical Engineers. (Copyrighted by publisher; permission granted to reprint.)

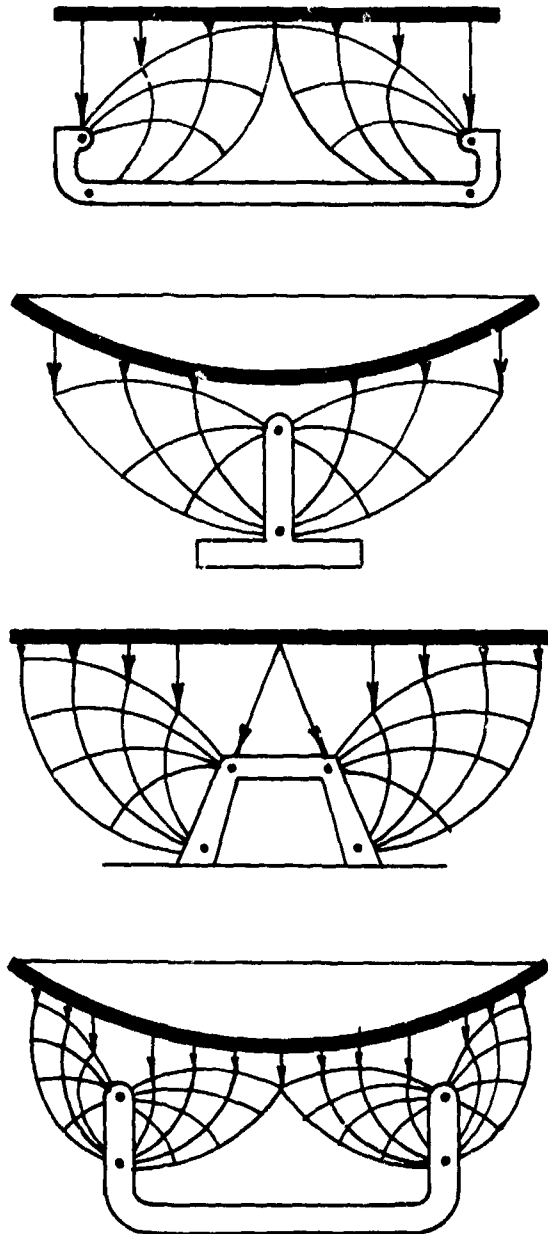


Figure 16. Michell structures.

Shear Deflection in Substrate

It is clear from general theory as well as recent experiments and studies by Kenny (ref. 4) that shear deflection in substrate is as important as flexural deflection. Thus,

wherever substrates are called upon to resist deformation through a degree of flexure, a knowledge of the shear modulus of either continuous plates and slabs or of the webs of sandwich plates is needed to predict deformations in a body-force field.

In his recent text, *Sandwich Construction*, Plantema (ref. 8) develops a general theory in which the moment of resistance is regarded as residing in the flanges and shear resistance in the webs of two-dimensional, I-beam constructions. He gives two techniques for determining shear rigidity of the webs or cores of sandwich constructions. One is a three-point loading test on a beam of typical core, and the other is a direct shearing of the core by compression loading.

Because the core configurations used in fabricated space mirrors have many complicated geometrics that defy simple theoretical treatment, each configuration needs experimental testing for shear rigidity.

Kenny (ref. 4) has recently used a four-point loading technique on a plexiglass strip-model of mirror core to assess the relative magnitude of flexural and shear deflections. A report of completed studies of the shear rigidity of triangularly pitched perforated plate is in preparation by Duncan and Santosham at the University of British Columbia.

Logical Development of a Mirror Substrate

Assume first that, from polishing considerations, the mirror requires an immediate substrate in the form of a relatively thin plate. As shown in figure 17, the elements of this plate need uniformly distributed upthrust in the vertical direction to equilibrate gravitational forces directly, thus avoiding flexural distortion.

The object is to maintain the thin plate in an unflexed state. If this is achieved, the plate will be unstrained in a flexural sense; hence, it can be regarded as a quasi-rigid body. If the upthrust is provided by a set of many discrete compression members, the above ideal conditions will be closely approximated.

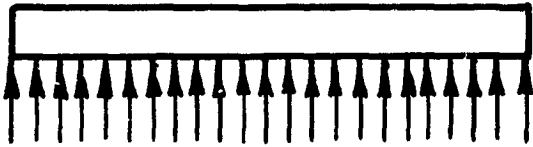


Figure 17. Hydrostatically supported thin plate.

Assume next that, in conformity with the principles of Michell's structural theorem, these compression members are extended in design away from the plate to arbitrarily selected points of reaction.

This may be done in various ways. If the locations of the point or points of reaction are chosen arbitrarily and the direction of the reaction is selected, there will be solutions to the structural net required (the Hencky-Prandtl slip-line nets of plasticity), and the requisite cross-sectional areas of the members to ensure a uniform maximum-acceptable stress level can be computed.

To minimize the coordinate space occupied by the Michell structures given below as examples, it was necessary to keep the point or points of reaction close to the plate itself, as shown in figures 18a and 18b, rather than in the remote location shown in figure 18c.

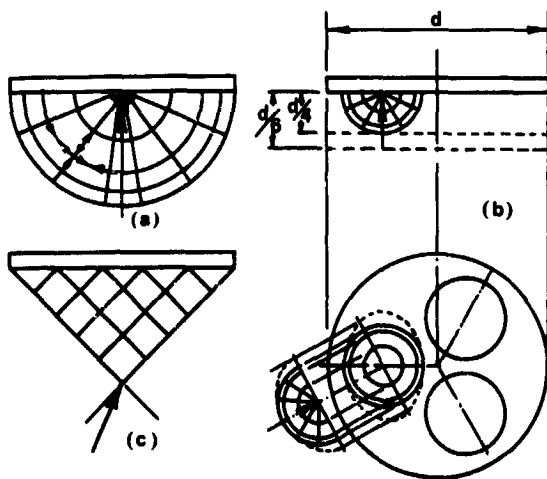


Figure 18. Michell distributive support systems.

If a single reaction with torque stabilization is chosen as a basis for the support and attitude-control of a mirror, the cross-section of the structure will have an area $d \times \frac{d}{2}$. If three-point reaction is chosen, it should be possible to design the structure within an area of $d \times \frac{d}{5}$, as shown in figure 18b. Ritchey's recommended cross-section for large, solid, right cylindrical mirrors was $d \times \frac{d}{6}$.

The members of the particular Michell structure shown constitute an orthogonal system of compressive arcs and tensile radials, all stressed to the same numerical value. This value would be fixed by proportioning the cross-sectional areas of the struts and ties and by stepping the area of the ties at each arc. All arcs would have the same cross-sectional area if the ends of each arc were intended to support the same weight of substrate.

It is assumed that the distributed weight of the Michell structures would be much less than that of the plate, but any distributed weight of a real structure can easily be allowed for by adjustment of member cross-sectional areas.

Ideal, theoretical, Michell structures are statically determinate. Real and practicable structures approximate to the ideal.

The result of straining the Michell structure due to the effect of gravitational forces is to raise the point of application of load *relatively* to the plate, which should remain virtually undistorted. In relation to the reaction point, the plate is like a rigid foundation, remaining unstrained (except locally) due to the application of the concentrated compressive forces exerted by the arc members. Actually, if the reactive points are regarded as the points of reference, the plate will drop bodily without distortion of its surface.

The three points of figure 18b may be located at a radius of about 0.66 diameter, and thus the plate alone would have minimum deformation, as shown in Appendix A. The addition of the Michell distributing structure should significantly remove remaining deviations from a plane surface with a minimum of additional weight.

The possibility of including an ellipse to define the end locations of the outer members is indicated. This would constitute an approximation designed for better distributing the number of points of direct support of the plate with less than optimum geometry. In addition, the plate thickness can be reduced to a practical minimum, as determined by polishing and handling considerations.

The two-dimensional structural forms can be located in several radial directions

through each point of reaction to form a rib-like stiffening "spider." If these rib structures are densely packed angularly, a system of spherical shells and interpenetrating cones results. A considerable stiffening should ensue and some further weight saving would be made possible by the induction of plane strain rather than plane stress conditions in the now contiguous rib-structures.

References

1. Schwesinger, G.: *Journal of the Optical Society of America*, Vol. 44, 1954, pp. 417-424.
2. Love, A.E.H.: *A Treatise on the Mathematical Theory of Elasticity*. Dover Publications, Inc., New York, N.Y., 1944.
3. Duncan, J.P.: *The Elimination of Gravity-Induced Displacements in an Elastic Solid by Immersion in an Ideal Fluid*. Unpublished typescript with bibliography, 1967.
4. Kenny, B.: *The Deflection of Optical Structures*. Perkin-Elmer Private Report ER 9538, 1968.
5. Emerson, W.B.: *Journal of Research of the National Bureau of Standards*, Vol. 49, 1952, pp. 241-247.
6. Dew, G.D.: *Journal Sci. Inst.*, Vol. 43, 1966, pp. 409-415 and pp. 809-811.
7. Barnett, R.L.: *Survey of Optimum Structural Design*. *Experimental Mechanics*, December 1966, pp. 19A-26A.
8. Plantema, F.J.: *Sandwich Construction*. John Wiley & Sons, 1966.
9. Inglis, Sir Charles: *Applied Mechanics for Engineers*. Dover Publications, Inc., New York, N.Y., 1963.
10. Harvey, J.; and Duncan, J.P.: *Rigidity of Rib-Reinforced Cover Plates*. *Proc. Inst. Mech. Eng., Applied Mechanics Group*, vol. 177, no. 5, 1963, pp. 115-123.

Appendix A

The Deflection of a Multi-point-Supported Plate

(Henry Vaughan)

Mirrors are frequently supported at three or more points by statically determinate supporting systems. It is desirable to have a simple method of calculating the self-weight deflections resulting from the uniformly distributed gravitational body forces. For thin plates, these body forces may be replaced by a uniformly distributed surface load.

Various Methods

Williams has worked out an exact series solution requiring computer evaluation. This is contained in a report by Kenny (ref. 1). Williams' method, however, is not easily adaptable to design purposes, particularly if shear distortion is to be included.

Duncan suggested the following method, which leads to a very simple expression for the deflection surface. The method is not mathematically exact, but the result ensuing from the simplifying assumptions can be compared with the exact result; and errors can easily be estimated.

If one starts with Micheli's solution for a clamped plate (ref. 2) under a single-point load, a simple extension yields the solution for any number of point loads regularly spaced around a concentric circle. Expressions for the moment and shear at the edge of the plate for N loads are easily evaluated and summed. If the loads are not too close to the edge of the plate, then the distributions of the edge forces are almost exactly sinusoidal. In particular, figure A-1 shows the comparison of the edge bending moment with a sinusoidal

wave, the amplitude of which has been evaluated analytically. Similarly, figure A-2 shows the edge shearing force. Both of these curves are for $N = 3$ and $b/a = 1/2$, where $b =$ radius

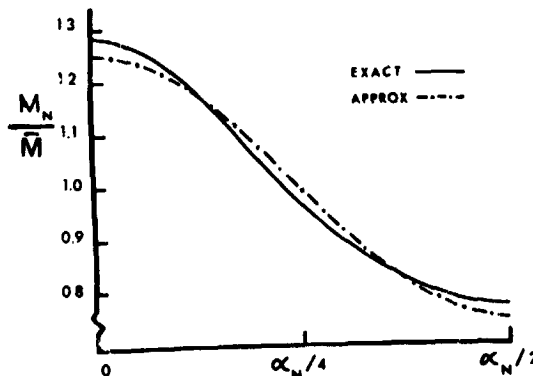


Figure A-1. Edge bending moment M_N/M , $N = 3$, $\gamma = 1/2$.

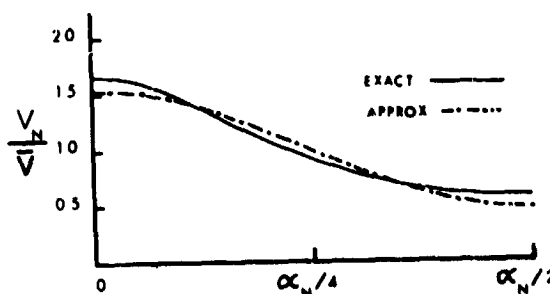


Figure A-2. Edge shearing force V_N/V , $N = 3$, $\gamma = 1/2$.

of support circle and a = radius of plate. Note that $b/a = \gamma$ in the figure.

Agreement is better for larger N but worse for larger values of b/a . Clearly a suitable increase in N and an increase in b/a will yield a similar degree of agreement, as shown in figures A-1 and A-2.

It is a simple matter to free the edge of the plate of the approximate sinusoidal edge forces and to equilibrate the point reactions by superimposing a uniformly distributed surface load. The deflection of a free, uniformly loaded, point-supported plate can be obtained immediately.

The most fundamental case is when there are only three point supports. Contours of equal deflection are given in figures A-3 and A-4 for $\gamma = 0.5$ and $\gamma = 2/3$, respectively. Figure A-4 shows that the central area of the plate is remarkably flat for $\gamma = 2/3$. This particular arrangement is very close to the best support circle for three supports, based on optimizing the maximum deviation from the flat.

The contours show values of $\omega(x, \theta)$, where ω is a nondimensional displacement given by

$$w(x, \theta) = qa^4 \omega(x, \theta) / 100D$$

where q = normal force per unit area of plate surface and D = thin-plate bending rigidity.

Experimental Procedure

Because of its simplicity, the method developed by Ligtenberg was used with the refinements introduced by de Haas and Loof (ref. 3). The moiré fringes obtained by Ligtenberg's method represent lines of equal partial slope. Deflections through sections parallel to the original setting of the plate are found by

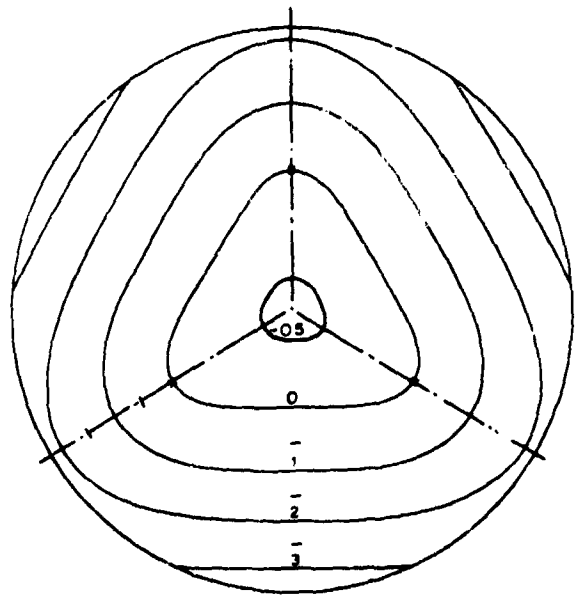


Figure A-3. Contours of equal deflection, $N = 3$, $\gamma = 1/2$.

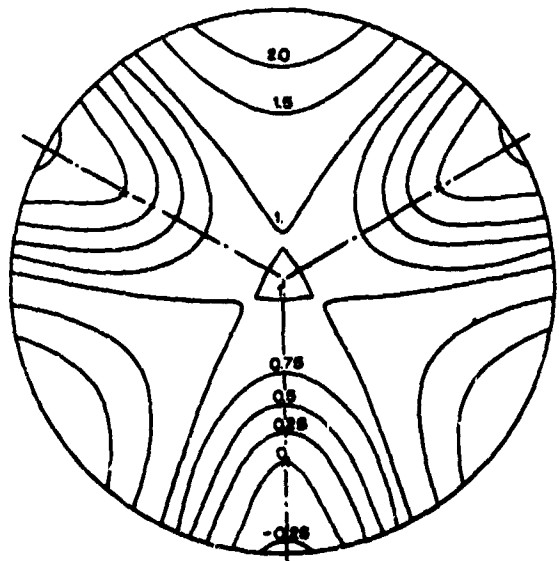


Figure A-4. Contours of equal deflection, $N = 3$, $\gamma = 2/3$.

graphical integration; then, orientation of the plate is required for sections at different angular settings.

The plates used in the experiments were 7 inches in diameter, 1/8 inch thick and made of plexiglass, for which $E \approx 4.5 \times 10^5$ pounds per square inch and $\nu \approx 0.35$. The uniform load was provided by several inches of lead shot, kept in place by a loosely fitting cylinder. The point reactions were provided by three, small, spherical bearings that were allowed to travel along three knife edges forming part of the external structure. This enabled different values of γ to be examined at will.

Figure A-5 shows the moiré patterns for equal slopes through sections given by $\theta = 0^\circ$, $\theta = 15^\circ$, and $\theta = 30^\circ$ for $\gamma = 0.66$ and $N = 3$. Clearly, the three patterns are sufficient to give the deflections for the whole field at 15-degree intervals.

Figure A-5 has been used to calculate the deflections, and the results may be compared with the theoretical results in figure A-6.

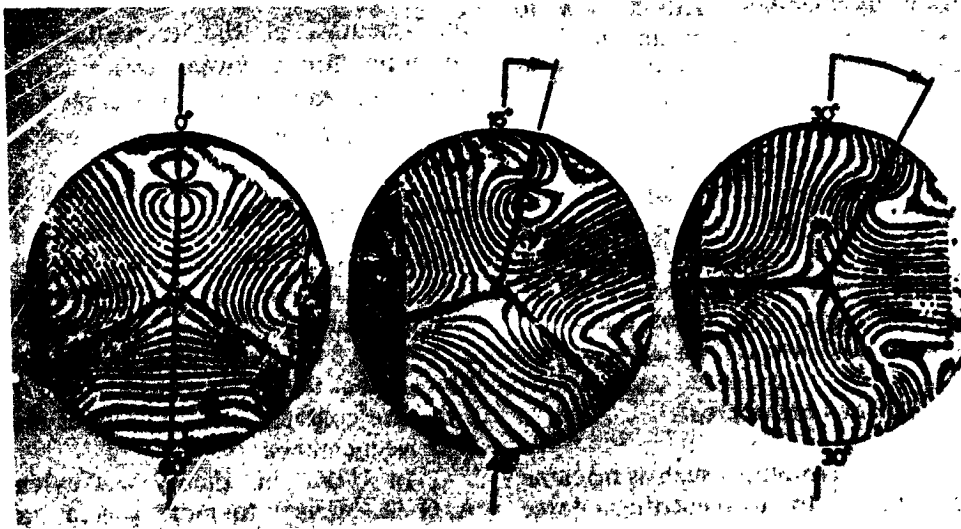


Figure A-5. Moiré contours of equal partial slope (after filtering).

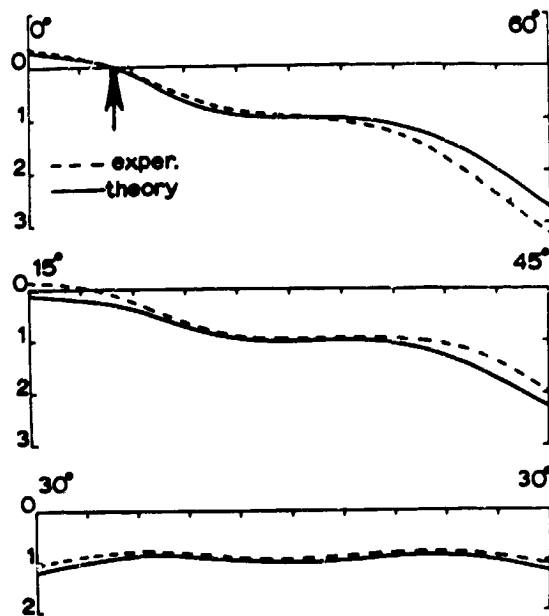


Figure A-6. Deflection $\omega(x, \theta)$ through center of plate at 15-degree intervals, $N = 3$, $\gamma = 2/3$.

References

1. Kenny, B.: The Deflection of Optical Structures. Perkin-Elmer Private Report ER 9538, 1968.
2. Michell, J.H.: The Flexure of a Circular Plate. London Mathematical Society, Vol. XXXIV, 1901, pp. 223-238.
3. de Haas, H.M.; and Loof, H.W.: An Optical Method to Facilitate the Interpretation of Moiré Pictures. VDI-Berichte, No. 102, 1966, pp. 65-70.

Appendix B

Optimum Self-Weight Loaded Structures

(E. W. Johnson)

Introduction

Although very large structures were erected in antiquity, modern structures of ever-increasing complexity and size have followed the development of new engineering knowledge and techniques of analysis.

In designing structures such as latticed bridges, on which the greatest load is their own weight, external loads are commonly lumped with self-weight loading at the nodes. Only in the largest structures have designers of necessity considered seriously the optimum configuration of members with a view to using material to the best advantage. This implies that, ideally, all material employed should be stressed to the same acceptable limit.

Some examples of this approach are the uses of arches in place of flexed structures and the development of I-beams and similar sectioned beams to distribute the cross-sectional area of the member better. Other fields of application are astronomical mirrors, radio telescopes, and aircraft fuselages.

Dynamically Loaded Structures

In small-scale structures such as machine components, inertia forces (centrifugal force and the force of gravity) are important elements of loading and are sometimes dominant. Little attempt has been made to optimize the distribution of material in these small members, particularly in cases where the function of the member is to remain very rigid rather than to sustain loads.

The ever-increasing demand for reduced payloads in space vehicles and higher speeds

in land-based machinery calls for the elimination in design of all useless mass. This, in turn, implies that the configuration of the member should be such that all elements of material are stressed and strained to acceptable maximum limits.

With the advent of numerically controlled machining, the difficulty and cost of removing inefficiently used material from the raw mass has been reduced. It is thus feasible to pursue a lattice type of construction on a small scale. Whether the structure be large or small, there is room to look again in terms of fundamentals at the theoretical optimum structure for a given service rather than merely to search by variational techniques for the best proportions within a preconceived structural type.

Fundamental Theory

In 1869, James Clerk Maxwell established a theorem specifying the optimum stressed state of material required to support a system of forces acting in a given space. He showed that the volume was a minimum if the structure contained only tensile or only compressive members.

In 1904, this theory was extended by A. G. M. Michell to more general structures containing both tensile and compressive members. He showed that an optimum or minimum volume structure must consist entirely of members that carry either tensile or compressive forces—their cross-sections being such that the stress is constant at all points. The sets of tensile and compressive members of fibers must be orthogonal, with the network containing an infinite number of them. This

theory has been extended by A. S. L. Chan and others to consider simple beams and cantilevers carrying a concentrated load.

Approximations to Optimum Structures

The theoretical optimum structure is difficult or impossible to manufacture, but it offers a standard against which more practical frameworks can be compared. As a two-dimensional example, a cantilever could be made, having a few (five or ten) widely spaced fibers, whose cross-sectional area may be adjusted to maintain a constant stress level at all points. Such a structure is shown in figure B-1, which represents a cantilever carrying a unit load perpendicular to its axis at the end remote from its pinned supports. The member widths are adjusted to maintain uniform stress at all points. For analysis, the joints could be considered as pinned; then the links would be straight and would form chords to the theoretical curved fibers.

Analysis can also be extended to cantilevers (and beams) carrying several concentrated loads at the pin joints. In particular, these loads could represent the self-weight of the structure plus any external loading imposed. Examples of such structures are ribbed plates or individual members of larger structures. Theoretical analysis of ideal structures of this kind has been undertaken together with preliminary investigation of the effects of the simplifying assumptions made to facilitate solution.

A family of cantilevers similar to that shown in figure B-1 has been analyzed. All cantilevers have the same span (10 inches) and differ only in the support spacing and the number of fibers. These vary from one to ten, radiating from each support point, one set being in tension and the other in compression. Of necessity, each member is straight between intersections.

Figure B-2 compares the volumes of the range of structures examined. The Michell conditions determine the optimum structure for any span and specific set of loading conditions. Such an optimum structure has less volume than any other other structure which

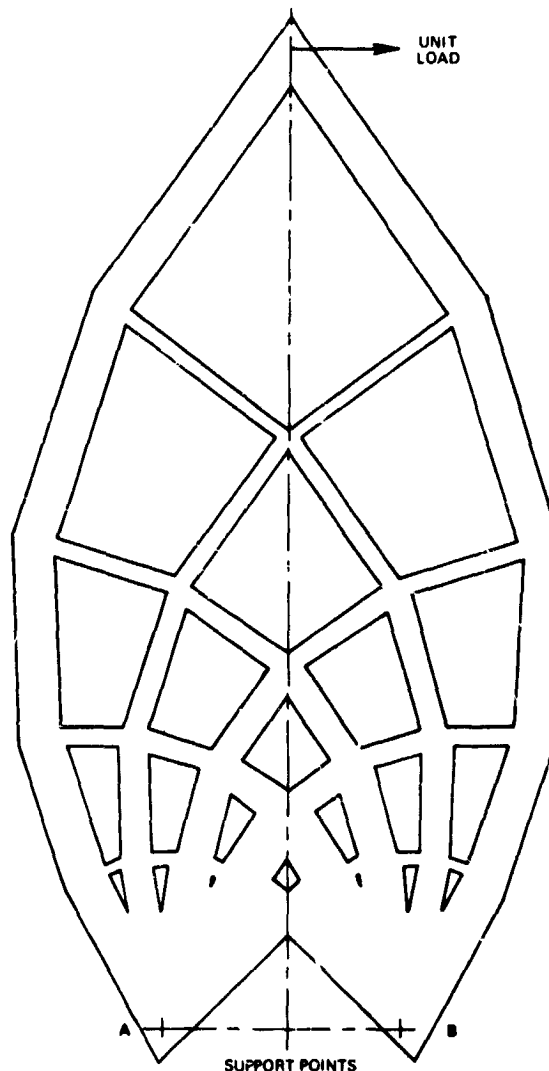


Figure B-1. Geometry of a five-fiber Michell cantilever.

may be designed to replace it. This is illustrated in the graph (fig. B-2), which compares the actual volumes of a series of cantilevers of varying fiber count with the corresponding theoretical structures having the same fan angle, the angle being subtended at A or B by the extreme fibers.

The curve shows that, even with such a crude approximation to the infinite case as represented by a structure of five fibers, the volume is only 4 percent greater than the minimum to which the curve asymptotes.

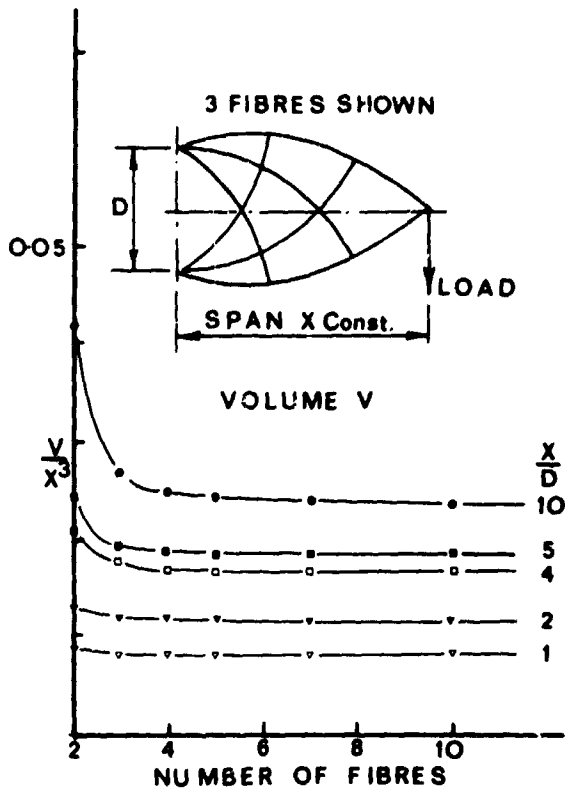


Figure B-2. Dependence of pin-jointed cantilever volume on number of fibers for various ratio of X/D ; $t = \text{thickness} = 1/4 \text{ inch}$; $E = \text{Young's Modulus} = 300,000 \text{ psi}$; $\sigma = \text{constant normal stress} = 300 \text{ psi}$; $\text{Load} = 100 \text{ lb. in all cases}$; $X = 10 \text{ inches in all cases}$.

Such structures would be relatively easy to manufacture and would be of considerable value in design.

Figure B-3 shows several models approximating the Michell criteria and which have already been made for testing. These include a small five-fiber cantilever and two ten-fiber cantilevers. In the latter case, one model is made with quadrilateral cutouts; in the former case, these are approximated by circular holes. The resulting configuration is a somewhat cruder approximation to the optimum structure but is considerably easier to manufacture.

The largest model is of a Michell beam designed to transmit pure bending. It may be



Figure B-3. Plastic Michell cantilevers and beam made by numerically controlled machining.

considered as four cantilevers arranged symmetrically.

Figure B-4 shows the South Bend milling machine on which the models were cut. The table drives are powered by "Slo-Syn" synchronous motors, which are controlled by commands printed on a paper tape. These commands position the tool in Cartesian or Polar coordinates and thus enable these complex shapes to be made rapidly yet accurately.

The control system of this machine enables straight lines to be cut most simply if they are parallel to the major axes of the milling machine table. Lines at an angle to these axes require cutting in a series of small steps, thereby necessitating perhaps a hundred commands per inch of cut to maintain a smooth surface.

Avoiding the latter complication was accomplished by mounting the plastic sheet on a rotary table whose angular position could be changed by machine command. For minimum overhang, the center of the plate

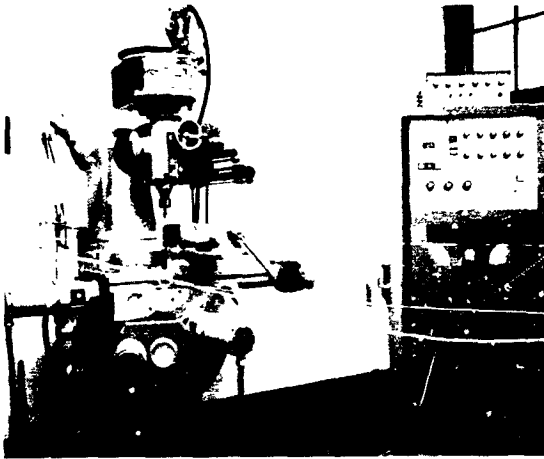


Figure B-4. South Bend numerically controlled milling machine.

was placed at the center of the rotation of the table. The centerline, as shown in figure B-1, was placed parallel with the long or X-axis of the milling table.

Study of figure B-1 reveals that each pair of members meeting at a joint are perpendicular. Thus, if the table is rotated so that any one member is parallel with the long axis of the milling table, several other members will also be parallel, or perpendicular, to this direction. It is a simple matter to mill the sides of this family of members because their lengths and widths are known from the geometry of the structure and the requirement for uniform stress at all points. The coordinate of each point may thus be calculated. An offset also has to be allowed for the radius of the milling cutter since the machine commands relate to the coordinates of its axis of rotation.

A sequence of point-to-point steps, listed in figure B-5, may thus be compiled to specify

traverses of the milling cutter in a series of straight-line cuts along the parallel faces of this family of members. "Miscellaneous function" commands are added to instruct the cutting head to rise and to fall wherever necessary in order to move between the cut-outs. Another "miscellaneous function" signal controls the movement of the rotary table to align the next sequence of members. This procedure is repeated until the program fully details the manufacture of one-half of the structure; for example, all cuts to the right of the centerline, shown in figure B-1.

This program, figure B-5, is transferred to punched tape, which is placed in the tape reader for the milling machine. When run, the tape passes through a sensing head that, via suitable circuitry, instructs the Slo-Syn motor to maneuver the cutter and to produce a finished part. When half the cantilever has been milled, the tape is rewound; and the controls adjusted so that all positive "y" coordinates (perpendicular to the centerline) are automatically read as negative, and vice versa. This is known as mirror-imaging; it enables the second half of the model to be cut from the same tape.

When this work has been completed, it is hoped that the results will indicate ways in which plate-fabricated structures can be most logically lightened by the technique of the lightening hole. The ideal Michell structures with limited numbers of fibers have webs containing quadrilateral holes of various sizes and relative location. Lightening holes are frequently designed into web-like plate-structures and machine frames on an intuitive basis; however, it appears that there is a logical basis of lightening that leaves residual material in an optimum configuration.

NUMERICAL TAPE CONTROL PROGRAM

DEPARTMENT OF MECHANICAL ENGINEERING, UNIVERSITY OF BRITISH COLUMBIA

DATE April 15, 1969	PART NAME 5 fibre	WORK ORDER NO.
CHECKED BY DATE	MICHELL CANTILEVER	
SHEET 1 OF 3	REMARKS USE: $\frac{1}{8}$ " DIA MILLING CUTTER	
TAPE NO. Milling	Origin is 8.000" left of Axis of Rotation.	

SEQ NO.	TAB OR EOB	- OR +	X MOVEMENT	TAB OR EOB	- OR +	Y MOVEMENT	TAB OR EOB	M FUNCTION	EOB	INSTRUCTIONS
	E									Turntable + 35.8° before starting tape.
1	T		8000	T			T	55	E	
2	T		4350	T	-	3137	T	55	E	
3	T	-	3502	T			T	52	E	
4	T	-	112	T		483	T	535	E	
5	T			T		1910	T	52	E	
6	T	-	1724	E						
7	T	-	219	T		340	T	535	E	
8	T			T		1001	T	52	E	
9	T	-	945	E						
10	T	-	295	T		453	T	535	E	First Sequence
11	T			T		333	T	52	E	
12	T	-	533	E						
13	T		103	T		692	T	535	E	
14	T			T	-	207	T	52	E	
15	T		287	E						
16	T		528	T	-	381	T	535	E	
17	T			T	-	547	T	52	E	
18	T		759	E						
19	T		379	T	-	273	T	535	E	
20	T			T	-	1147	T	52	E	
21	T		1583	E						
22	T		296	T	-	213	T	535	E	
23	T			T	-	2019	T	52	E	
24	T		2799	E	-					
25	T	-	1959	T	-	10	T	06535	E	Rotate table - 18.4°

Figure B-5. Numerical tape control program; five-fiber Michell cantilever (Sheet 1 of 3)

NUMERICAL TAPE CONTROL PROGRAM

DEPARTMENT OF MECHANICAL ENGINEERING, UNIVERSITY OF BRITISH COLUMBIA

PREPARED BY DATE April 15, 1969	PART NAME 5 fibre MICHELL CANTILEVER	WORK ORDER NO.
CHECKED BY DATE	REMARKS	
SHEET 2 OF 3		
TAPE NO		

SEQ NO	TAB OR EOB	+ OR -	X INCREMENT	TAB OR EOB	+ OR -	Y INCREMENT	TAB OR EOB	M FUNCT	EOB	INSTRUCTIONS
26	T	-	2619	T			T	52	E	
27	T	-	116	T		501	T	535	E	
28	T			T		1157	T	52	E	
29	T	-	1374	E						
30	T	-	225	T		390	T	535	E	
31	T			T		490	T	52	E	
32	T	-	817	E						
33	T		86	T		561	T	535	E	Second Sequence
34	T			T	-	147	T	52	E	
35	T		611	E						
36	T		422	T	-	337	T	535	E	
37	T			T	-	651	T	52	E	
38	T		1213	E						
39	T		315	T	-	254	T	535	E	
40	T			T	-	1268	T	52	E	
41	T		2239	E						
42	T	-	1445	T	-	580	T	06535	E	Rotate table - 18.4°
43	T	-	2062	T			T	52	E	
44	T	-	118	T		520	T	535	E	
45	T			T		548	T	52	E	
46	T	-	1103	E						
47	T		73	T		593	T	535	E	Third Sequence
48	T			T	-	240	T	52	E	
49	T		930	E						
50	T		336	T	-	229	T	535	E	
51	T			T	-	663	T	52	E	
52	T		1670	E						
53	T	-	776	T	-	954	T	06535	E	Rotate table - 18.4°

MECH ENG 3-53
FORM 128

Figure B-5. Numerical tape control program; five-fiber Michell cantilever (Sheet 2 of 3).

N70-36710

Main Mirror for a 3-Meter Spaceborne Optical Telescope

Wilhelm Angele

NASA George C. Marshall Space Flight Center

Introduction

The problems for orbiting telescope reflectors are many. High optical quality and light weight are the subject of this paper. The material selection for the reflector is of great importance. The weight-to-stiffness ratio should be a minimum. Form stability over a large temperature range is one of the basic requirements; the temperature expansion should be near zero. The material must be very uniform (homogeneous) and non-corrosive.

Design Proposal

A symmetrical mirror is proposed, shown in figure 1, with an identical curvature on front and back. The design uses a thin-walled shell, consisting of two parabolic surfaces and two cylindrical parts, one for the outside diameter and one for the Cassegrainian bore. Inside of this shell is a core of foam made of microballons. Shell and foam core are fused at the entire boundary surface. The materials for the structure must be identical in thermal behavior and near zero in thermal expansion. The symmetrical shape, front and back to be equally concave, is proposed to minimize distortion caused by temperature changes or delayed residual stress relaxation.

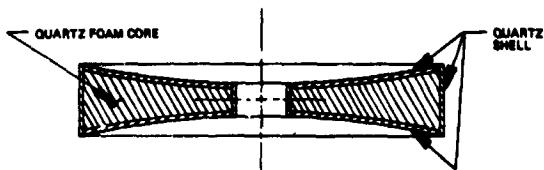


Figure 1. Symmetrical reflector.

Discussion

It is realized that a sphere is the geometrical form of highest stiffness and therefore of lowest deformation due to internal forces that may cause bending or twisting. The second best form for stiffness is considered to be a biconvex lens. Because at least one side of the reflector body has to be concave, it is assumed that complete symmetry (concave-concave) would offer high stability against stress changes. To prove this assumption is a part of the proposed feasibility study.

The thickness of the mirror could be very small to suffice for the quiet orbital flight at near-zero gravity. The requirement for stiffness of the mirror is given by the manufacturing, finishing, handling, shipping, and launching, rather than by the flight condition in orbit. To save weight, the mirror thickness should be a minimum, or the mirror should be made of lightweight material, or both. To compensate for gravitational forces, which make final figuring very difficult, the mirror should be floating 50 percent submerged in a liquid during grinding, finishing, storage, and even during launch. (Details on floating are discussed in the paragraph on finishing.)

Foam Core Versus Honeycomb Structures

The proposal of using a cellular microstructure (foam) as core of the mirror blank has several advantages over other types of lightweight structures. Core drilling is expensive, especially if the holes are very numerous and small. Casted cavities, like the

pattern of the 200-inch Hale mirror, are too large and have the inherent danger of showing the quilting effect because of elastic deformation during polishing. Eggcrate design has similar problems. Large cavities eccentrically or centrally located to the mirror thickness may also impair the mirror quality at temperature changes (the quilting effect again). Therefore, it can be safely assumed that a very fine cellular structure may be the best way to save weight without endangering the figure. Depending upon the type of foam, up to 80 percent of the weight may be saved in the mirror blank as compared to a solid blank.

Manufacturing

There are several problems to be solved. One is forming the 3-meter parabolic reflector to the right curvature to require a minimum amount of stock removal in final finishing. This operation, starting with a flat disk, may be accomplished in an over by using vacuum or gas pressure and a form die of proper dimensions. The cylindrical parts of the shell must be formed to fit over the 3-meter outside diameter of the parabolic reflector and inside of the center-bore (Cassegrainian opening). The fit should allow the parabolic reflector to slide as the core material (foam) shrinks during the sintering process. Proper tooling must prevent the form change of the parabolic parts while at fusing temperature. The fusing process needs to be developed for this particular application, e.g., temperature profile over time, form tooling, pressure, etc. The assembly-fusing process must accomplish a stiff foam well-bonded to the shell over the entire surface. Ultrasonic testing may be practical to inspect the bond. Complete stress-relieving of the whole assembly is most important.

Finishing

During finishing, the reflector should be floating in a liquid of twice its density to

eliminate the sagging of the center portion due to gravity. The reflector would submerge to half of its thickness so that the buoyancy force at every surface element would be equal to the weight of the particular area. See figure 2. This balance of forces is very desirable but hard to accomplish considering the shifting weight of the polishing tool. At least the flotation gives a fairly uniform support. The need for holding the mirror against rotating and lateral motions in the flotation vat during finishing causes additional problems. Arresting the mirror in plaster of Paris or in a dissolvable soft material of the right density may be a solution. The reflector should be finished at both sides to enhance form stability.

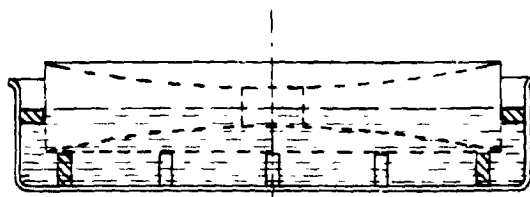


Figure 2. Floating reflector, 50 percent submerged.

Testing

To avoid distortion of the figure by gravity, the testing of the mirror should be done in the flotation vat, properly limited against lateral shifting.

Concluding Remarks

It is realized that the above proposal is very unusual and a radically new approach to the problem, but it has enough merits to invite a feasibility study. The proposals of symmetry and quartz foam core are independent ideas and can be employed together or separately.

Structural Deformation of an Orthotropic Plate

Francis W. Niedenfuhr
 Department of Defense
 Advanced Research Projects Agency

N70-36711

In the design of mirrors and support cells, we have frequently to deal with the effects of point loads inducing the deformation of elastic plates. Such problems are relatively well studied for isotropic plates, but the effects of structurally induced orthotropy are not often discussed. Carefully chosen patterns of orthotropy can be usefully employed, however, to control local deformations in a manner that would be advantageous to an optical system designer. A case in point is the design of a connecting structure that carries the weight of a large mirror into a three-point kinematic support. Viewed from the mirror-support end, it is highly desirable that the connecting structure deflect in a radially symmetrical pattern so that the mirror is supported uniformly around its edge or mounting ring. A three-point kinematic support, on the other hand, induces a deformation pattern of plate bending of the type

$$W = \sum_{0,3,6,\dots}^{\infty} F_n(r) \cos n\theta \quad (1)$$

In this note, it is shown that, with the proper use of constructional orthotropy, the functions F_n of equation (1) can be made to decrease very rapidly with increasing radius, r , so that it is possible to design a plate which at $r = a$ carries three-point loads, yet at $r = b$ has a deformation pattern of the type $W = \text{constant}$; i.e., the deflection does not depend on the polar angle θ at $r = b$. A mirror attached to this plate at $r = b$ would then be perfectly uniformly supported. The general scheme of support envisioned is as shown in figure 1.

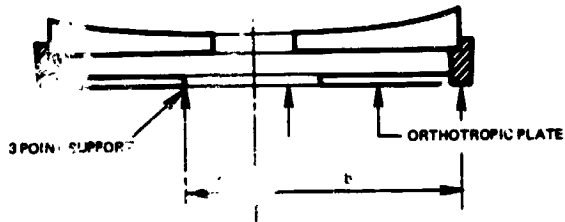


Figure 1. General scheme of mirror support.

Since we do not have a specific cell design in mind, but wish only to demonstrate the qualitative effect, it will suffice to deal with the analysis of an infinite circular plate, bounded by a hole of radius a , where it is subjected to three concentrated forces, P , separated from each other by 120 degrees, as shown in figure 2.

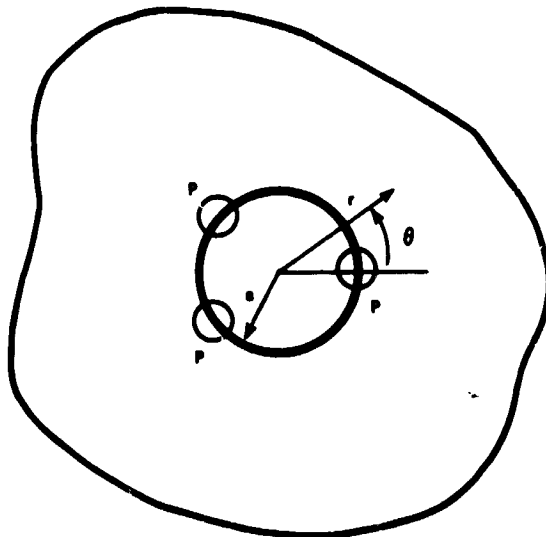


Figure 2. Coordinates used in analysis.

Lekhnitsky, in his book *Anisotropic Plates*, GITTL, Moscow 1957 (in Russian), gives the basic equation governing polar orthotropic plates:

$$\begin{aligned} D_r \frac{\partial^4 W}{\partial r^4} + \frac{2}{r^2} D_{r\theta} \frac{\partial^4 W}{\partial r^2 \partial \theta^2} + \frac{D_\theta}{r^4} \frac{\partial^4 W}{\partial \theta^4} \\ + \frac{2}{r} D_r \frac{\partial^3 W}{\partial r^3} - \frac{2}{r^3} D_{r\theta} \frac{\partial^3 W}{\partial r \partial \theta^2} \\ - \frac{D_\theta}{r^2} \frac{\partial^2 W}{\partial r^2} + \frac{2}{r^4} (D_\theta + D_{r\theta}) \frac{\partial^2 W}{\partial \theta^2} \\ + \frac{D_\theta}{r^3} \frac{\partial W}{\partial r} = q(r, \theta) \end{aligned} \quad (2)$$

Where D_r , D_θ , and $D_{r\theta}$ are the bending stiffnesses, w is the deflection; and q is the transverse load. In the case of isotropy, $D_r = D_{r\theta} = D_\theta = D$ and equation (2) reduces to the usual Lagrange plate equation

$$D \nabla^4 W = q \quad (3)$$

We shall consider a solution of equation (2) in the form of equation (1) for the case shown in figure 2 and shall study the rate of decay of the functions F_n in the orthotropic case as compared to an isotropic plate of the same weight. The end result of the analysis is that, in the orthotropic case, these functions can be made to decay very rapidly with increasing radius.

For the problem under consideration, the boundary conditions are

$$M_r = 0 \quad \text{at } r = a, \quad (4)$$

and

$$\begin{aligned} V_r &= Q_r + \frac{1}{r} \frac{\partial M_{r\theta}}{\partial \theta} \\ &= \frac{P}{a\pi} \left[\frac{3}{2} + 2 \sum_{3,6,9,\dots}^{\infty} \cos n\theta \right] \end{aligned} \quad (5)$$

while

$$\frac{\partial W}{\partial r} \rightarrow 0 \quad \text{as } r \rightarrow \infty \quad (6)$$

We shall consider the orthotropy induced by milling circumferential rings on the plate. This leaves the radial stiffness, D_r , and twisting stiffness, $D_{r\theta}$, unchanged from those of an isotropic plate so that they can be set equal to D , where

$$D = \frac{Eh^3}{12(1-\nu^2)} \quad (7)$$

These rings will, however, increase the circumferential bending stiffness D_θ relative to D so that we can write

$$D_\theta = kD \quad (8)$$

where k is a parameter determined from the geometry of the stiffening rings.

To obtain the solutions of interest, we substitute equations (1) and (8) in equation (2). Then, seeking solutions of the type

$$F_n(r) = r^p \quad (9)$$

we obtain the characteristic quartic equation

$$\begin{aligned} p^4 - 4p^3 + [5 - 2n^2 - k] p^2 + [4n^2 + 2k - 2] p \\ + [kn^4 - 2n^2(1+k)] = 0 \end{aligned} \quad (10)$$

Observing that the sum of the roots is 4, we tentatively try factors of the type

$$(p - 1 \pm \beta_1)(p - 1 \pm \beta_2) = 0 \quad (11)$$

Multiplying together four factors of this type and identifying the resulting coefficients with

those of equation (10), we ultimately find auxiliary equations for β_1 and β_2 :

$$\beta_1^4 - (1 + 2n^2 + k) \beta_1^2 + k(n^2 - 1)^2 = 0 \tag{12}$$

$$\beta_1^2 - \beta_2^2 = k(n^2 - 1)^2 \tag{13}$$

These are easily solved. A useful formula for β_1^2 is

$$2\beta_1^2 = (1 + 2n^2 + k) \pm [k^2 - 2k(2n^4 - 6n^2 + 1) + (4n^4 + 4n^2 + 1)]^{1/2} \tag{14}$$

From equation (14) we note that each of the four roots of equation (10) increases in absolute magnitude with increasing n . Since we are interested in those roots, p , which give us the *lowest* rate of decay of F_n (i.e., the worst case, structurally), we confine our further considerations to the cases $n = 0$ and $n = 3$.

Furthermore, it is appropriate at this point to introduce some definite configuration for the circumferential stiffening rings. Figure 3 shows a radial cross-section of a typical case.

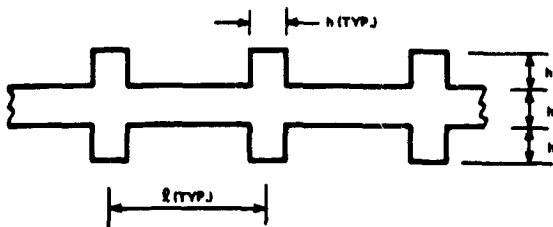


Figure 3. Radial cross-section of typical stiffened plate.

For this case,

$$k = \frac{D\theta}{D} = \frac{1}{h^3} \left[h^3 + (3h)^3 \frac{h}{l} \right] = 1 + 27 \frac{h}{l} \tag{15}$$

$l = 5h$ yields $k = 6.4$ and gives a reasonable looking arrangement. Then, using equations (13) and (14), we find for $n = 0, 3$

$$F_0 = A_0 + B_0 r^2 + C_0 r^{1 - \sqrt{6.4}} + D_0 r^{1 + \sqrt{6.4}}$$

and

$$F_3 = r^{-4.06} [A_3 \cos(1.94 \ln r) + B_3 \sin(1.94 \ln r)] + r^{+4.06} [C_3 \cos(1.94 \ln r) + D_3 \sin(1.94 \ln r)] \tag{16}$$

The corresponding solutions for the isotropic case, denoted by $I F_n$ are

$$I F_0 = A_0 + B_0 r^2 + C_0 \ln r + D_0 r^2 \ln r$$

$$I F_3 = A_3 r^{-3} + B_3 r^{-1} + C_3 r^3 + D_3 r^5 \tag{17}$$

Direct comparison of equations (16) and (17) indicates that the bending effects damp out much more rapidly in the orthotropic case. Figure 4 shows the results of some numerical calculations using the boundary conditions expressed in equations (4), (5), and (6) and neglecting Poisson's ratio.

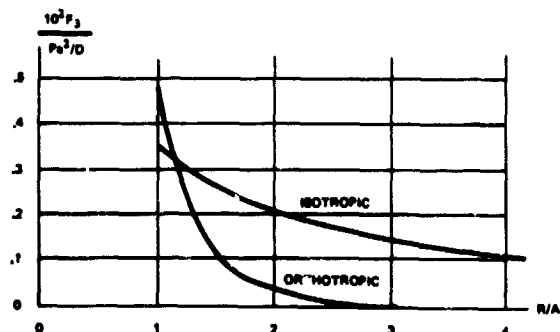


Figure 4. Variation of bending effects with radius.

The data in figure 4 were calculated for two plates of *equal weight*, which makes the ring reinforced plate a bit thinner overall, thus accounting for its larger deflection at the edge of the hole.

The example given rather clearly points out that *ring* reinforcements are very effective for damping out *circumferential* bending. It is at the same time intuitively obvious that *radial* reinforcements will inhibit *radial* bending but not circumferential bending. It is,

of course, those elastic modes containing a high degree of circumferential bending which induce optically damaging mirror deformations and which are impossible to compensate for by refocusing.

It is hoped that the results described in this note may prove useful in the design of fixtures for handling and testing large mirrors on the earth and also, perhaps, in some phase of mounting for orbital use.

Transverse Deflections of a 45-Inch-Diameter, Lightweight Mirror Blank: Experiment and Theory

W. P. Barnes
Itek Corporation

N70-36712

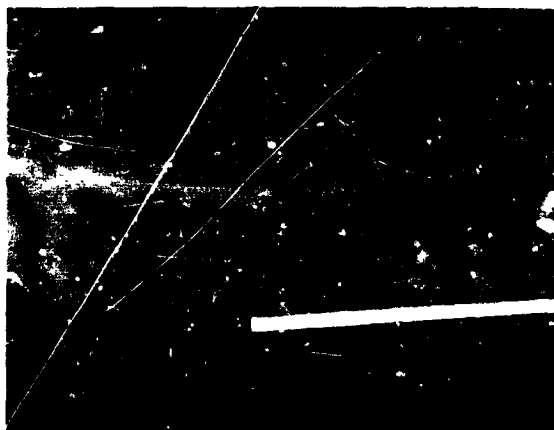
Introduction

In the design of lightweight mirror structures consisting of two thin plates connected by a core structure whose mean density is substantially less than that of a solid core, the influence of shear forces on the total deflection may equal or exceed that of the pure bending behavior of the mirror blank. Some considerations of the overall bending and shear behavior of such structures, for circularly symmetric support, will appear shortly in *Applied Optics* (ref. 1). In this discussion, we consider the case of a centrally loaded mirror supported at three points equally spaced around the edge of the blank. The theoretical calculation for this case is developed and compared with deflections measured, by using holographic interferometry, on a 45-inch-diameter mirror blank loaned to us by Heraeus-Schott Quarzschmelze GMBH. An exposition of the holographic technique we have used will also appear in *Applied Optics* (ref. 2).

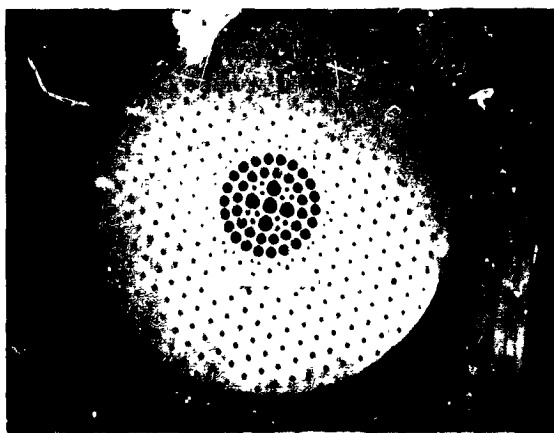
Experimental Results

The mirror blank fabricated by Heraeus-Schott consists of a monolithic core and a backplate of their opaque fused silica. Weight has been removed from the core by drilling and milling 2-inch-diameter blind holes to within 1 inch of the rear surface with 7/16-inch-diameter venting holes carried through the rear plate. To this core and backplate structure is fused a solid disk of clear fused silica. Photographs of the rear and a portion of the edge of the structure are shown in figure 1. (Some dimensional details are con-

sidered further in the "Theoretical Treatment.") The central area of this blank has been prepared for a Cassegrain perforation.



(a) Portion of edge



(b) Rear view

Figure 1. Heraeus-Schott lightweight mirror blank.

With appropriate fixturing and force measurement, the holographic interferogram of figure 2 was obtained with a central load



Figure 2. Holographic interferogram obtained with central load (c. 250 pounds, and three-point edge support.

and three-point edge support. The deflection data obtained from this interferogram, along a diametral line through one support point, are shown in figure 3. A moderate interpolation, at $r = 0$, was made to establish the reference $w = 0$ at $r = 0$, while requiring $dw/dr = 0$ at $r = 0$. The data shown are for a central load of 250 pounds. The total weight of this blank was 430 pounds.

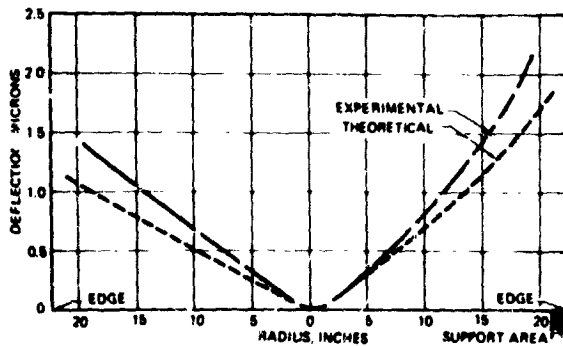


Figure 3. Deflection versus radius along one diameter through a support

Theoretical Treatment

In my paper (ref. 1), I have developed expressions for the flexural rigidity, D , and a shear coefficient, K , from both elementary considerations and the work of Timoshenko and Woinowsky-Kreiger (ref. 3) and Cowper (ref. 4). A representative cross-section of a lightweight structure with uniformly thick ribs is shown in figure 4, and the expressions are

$$D = \left[\frac{Eh^3}{12(1-\nu^2)} \right] [1 - (1-\alpha)(1-2\alpha)^3]$$

$$\frac{1}{K} = \frac{2t}{\alpha(1-t)} + 1$$

where

- E = Young's modulus
- ν = Poisson's ratio for the blank material
- h = total blank thickness
- α = ratio of rib thickness to "rib spacing" (assuming uniform rib)
- t = ratio of plate thickness to total blank thickness (assuming symmetrical construction)

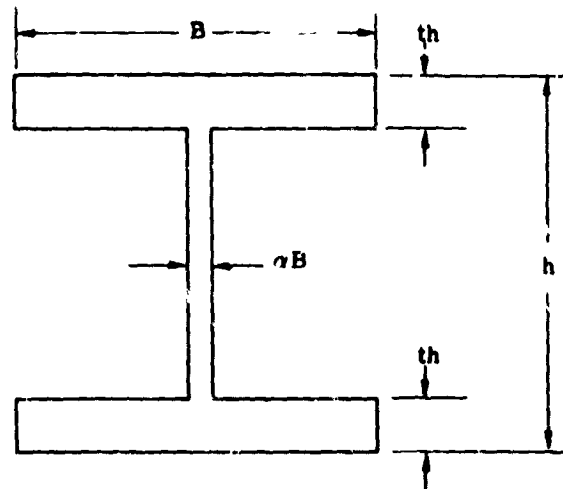


Figure 4. Typical cross-sectional element (B = cell spacing; t = ratio of plate thickness to total thickness; h = total thickness; α = ratio of rib thickness to cell spacing).

For this blank, the ribs are not of uniform thickness, nor is the front plate, because of local sag during fusing and the subsequent grinding of the front surface to a smooth curve. Measurements of the blank yielded the following:

- Front plate thickness = 3/4 ± 1/8 inch
- Backplate thickness = 1 ± 1/16 inch
- Total thickness = 6-1/4 inches
- Outside diameter = 44-5/8 inches

An average value of $t = 0.14$ was used in the calculations, and the value of α used was calculated by equating the mean core density to that of a core with ribs of uniform thickness, first subtracting the plate weight for the above value of t from the total measured weight of the blank, yielding $\alpha = 0.21$.

For our case, following Timoshenko (ref. 3), we may obtain the bending deflection, w_b , in radial coordinates ρ (normalized) and θ by

$$w_b = \frac{Pa^2}{2\pi D} \left\{ \left[\frac{3 + \nu}{8(1 + \nu)} \right] \rho^2 - \frac{\rho^2 \ln \rho}{4} + \frac{1}{3 + \nu} \sum_{m=3,6,9,\dots}^{\infty} \left[\frac{1}{m(m-1)} + \frac{2(1 + \nu) / (1 - \nu)}{m^2(m-1)} - \frac{\rho^2}{m(m+1)} \right] \rho^m \cos m\theta \right\}$$

where

- P = central load
- a = outer radius of blank

Combining Timoshenko and Cowper (ref. 4), we find the r derivative of the shear deflection, w_s , to be

$$\frac{\partial w_s}{\partial r} = \frac{\partial w_s}{\partial a \rho} = \frac{V_r}{GKh}$$

where

- V = effective vertical reaction, per unit length, on an r face
- G = shear modulus of blank material

Timoshenko also gives V as

$$V = Q_r - \left(\frac{1}{r \partial \theta} \right) (M_{r\theta})$$

where

$$Q_r = -D \frac{\partial}{\partial r} (\nabla^2 w_b)$$

$$\nabla^2 = \frac{\partial^2}{\partial r^2} + \frac{1}{r} \frac{\partial}{\partial r} + \frac{1}{r^2} \frac{\partial^2}{\partial \theta^2}$$

$$M_{r\theta} = (1 - \nu) D \left[\frac{1}{r} \frac{\partial^2}{\partial r \partial \theta} - \frac{1}{r^2} \frac{\partial^2}{\partial \theta^2} \right] w_b$$

Applying these operations to the expression for w_b , taking the central load to be uniformly distributed over a small circle of normalized radius b , we obtain at $\rho = b, \theta = 0$:

$$w_s = \frac{1}{2} \left(\frac{P}{2\pi GKh} \right)$$

and for $\rho > b; \theta = 0$:

$$w_s = \frac{P}{2\pi GKh} \left(\ln \frac{\rho}{b} + \frac{1}{2} + \sum_{m=3,6,9,\dots}^{\infty} \left\{ \left[\frac{4 - (1 - \nu)m}{(3 + \nu)m} \right] (\rho^m - b^m) + \left[\frac{(1 - \nu)m + 2(1 + \nu)}{(3 + \nu)(m - 2)} \right] (\rho^{m-2} - b^{m-2}) \right\} \cos m\theta \right)$$

The calculated variation of the total deflection, $w_b + w_s$ is also plotted on figure 3.

Conclusions

It is somewhat premature to draw firm conclusions from the above calculations, but

it appears that we may be able to establish a well founded and fairly elementary theoretical basis for the calculation of the transverse deflections of lightweight mirror structures. At this point in time, our principal need is a more extensive comparison with experiments including a reasonable range of the parameters of α and t .

References

1. Barnes, W. P., Jr.: Optimal Design of Cored Mirror Structures. Applied Optics, to be published.
2. Van Deelen, W.; Nisenson, P.: Real-Time Holographic Interferometry. Applied Optics, to be published.
3. Timoshenko, S.; Woinowsky-Kreiger, S.: Theory of Plates and Shells. Second ed., McGraw-Hill Book Co., Inc., New York, 1959.
4. Cowper, G. R.: The Shear Coefficient in Timoshenko's Beam Theory. Journal of Applied Mechanics, vol. 33, no. 2, June 1966.

Evaluation of Surface Figure During Manufacturing

Jerrold Zimmerman

Itek Corporation

N70-36718

Introduction

The system analyst, or the user, of a telescope system requires information concerning the surface figure of the optical components in order to infer the characteristics of the wavefront produced by the system and, hence, the resolution or other performance measure. In space astronomy, where the aberrations produced by surface figure errors may be considered to be more important to ultimate system performance than in earth-based astronomy, this information should be a highly accurate, absolute measure.

On the other hand, the optician, while also requiring information concerning the surface figure of the optical components, has a substantially different reason. The optician must remove portions of the surface of the optical components in order to correct the figure to some predetermined tolerance. The nature and precision of the measurement technique used will vary with the nature and precision of the surface removal technique used.

This paper discusses these differences and makes recommendations of appropriate techniques to be used, especially during the final stages of figuring.

Stages of Large Mirror Manufacturing

The process of manufacturing large mirrors (as opposed to refractive components of photographic lenses) will be considered as proceeding in stages:

Generating. The mirror blank is machined to its general mechanical configuration. Up to several centimeters may be

removed during this process while the figure accuracy may be held to within 5 to 10 microns. (Surface roughness is approximately 10 times that amount.) The most significant figure error to be eliminated, or at least to be kept to a minimum, is rotational asymmetry. If an asymmetric surface error is introduced at this stage and discovered later on, the only correction usually possible is to regenerate or, at best, to regrind.

Grinding. The surface roughness is reduced to 3 to 5 microns, generally by loose, abrasive, grinding techniques. The figure is refined to within 1 to 3 microns of the required figure.

Polishing. The surface is brought to a smooth, highly reflecting finish with fine abrasive on a resilient lap. The figure is kept to within the tolerances produced in grinding.

Figuring. The same surface removal techniques as in polishing are used, but the surface is corrected to the required figure (generally less than 0.1 micron).

Qualification or Acceptance Testing. The surface is evaluated to determine whether or not it is within the specified tolerances.

Surface-Figure Measurement Technique

The method used to evaluate surface figure may be categorized as being either mechanical or optical, and the optical methods as either slope or contour measurements. The best use of the mechanical methods is during generating and the early stages of grinding.

Optical measurements of surface figure become more useful during final grinding and when the surface is polished.

Application of Tests During Manufacturing

Surface measurements during the generating and grinding stages of the manufacturing process are, in general, limited to mechanical measurements. Even so, by using several of the readily available precision indicator probes (air gauges and electromechanical probes, for example), it is possible to read the relative position of points on the surface to within 1 to 2 microns.

We have experimented recently at Itek with various techniques for treating ground surfaces with wax in order to allow the use of interferometric techniques for figure evaluation even at this early stage of manufacture.

Once the reflectance of the surface has been increased, either by wax application or by polishing, it is possible to use optical techniques for surface figure measurements. The optical tests generally used during polishing and the early stages of figuring are geometrical slope measurements, such as the Foucault knife-edge test (ref. 1) or the Ronchi grating test (ref. 2) using low frequency gratings. Both of these techniques are very sensitive tests for zonal aberrations; however, they are qualitative, indicating to the optician the location of the zonal aberration but being somewhat ambiguous in giving a quantitative evaluation of their magnitude. More quantitative measurements, which are also limited to slope, may be used at this point in the manufacturing process by applying interferometric techniques. The most common of the slope-measuring interferometers are Wavefront Shearing Interferometers (WSI), either of the beam division type described by Saunders (ref. 3) and Brown (ref. 4) or the high frequency Ronchi grating (ref. 5), which produces a wavefront shear by diffraction. These measurements of slope are more quantitative than the slope measurements produced by the knife-edge test, but they have several weaknesses.

The interferogram produced by the wavefront shearing interferometers is a contour of the slope of the wavefront or, in essence, the partial derivative of the wavefront with respect to the direction of shear.

Saunders (ref. 3) has pointed out that the WSI data may be integrated to obtain the profile of the wavefront only in the direction of shear and only at points that are spaced equal to the amount of shear.

Therefore, in order to obtain the contour of the entire wavefront, several interferograms, with the shear direction relative to the surface under test different in each, are reduced to a wavefront profile and then fitted to the same surface. The reduction of the WSI interferogram to a wavefront profile consists of applying a numerical integration process. The effects of any smoothing or any error in any individual datum point are cumulative and affect more than just that one point, thereby leading to an overall error in the wavefront profile.

Furthermore, because the surface figure profile may be obtained in only one direction (the shear direction) per interferogram, these techniques are quite susceptible to errors in the measurement of surface asymmetry, which is one of the more difficult surface aberrations to correct during final figuring.

In order to obviate the disadvantages inherent in the admittedly convenient-to-use measurements of wavefront slope, it is necessary to use an interferometric technique that provides a direct measure of surface contour and one which is equally sensitive to errors in two dimensions. The two most common instruments used for this purpose are the Twyman-Green and the Burch Scatterplate (sometimes called Diffusion) Interferometers (ref. 6).

Until recently, the principle advantage possessed by the Burch interferometer over the Twyman-Green, was that the Burch interferometer did not require an external reference surface in order to produce interference. The Twyman-Green required a reference of the same size as the mirror to be tested because of the limited coherence length of light sources available. With the advent of Twyman-Green interferometers using helium-neon gas lasers as sources, this advantage of the scatterplate has been eliminated. In fact, the inherently low visibility fringes produced by the scatterplate place it at a disadvantage

when compared to the high visibility fringes produced with the Laser-illuminated Unequal Path Interferometer (LUPI) of the type described by Houston (ref. 7). One of the considerable advantages of the LUPI pointed out by Houston is its easy adaptability to null lenses, which permit the fabrication of aspheric surfaces in a very direct manner.

The tests that must be accomplished for final acceptance contain problems similar to those faced during the final stages of figuring. The final acceptance test usually requires the data describing the surface contour to be stated in terms more closely related to image quality than a simple peak-to-peak number. For example, a first-class manufacturer of optical components produced for Itek a spherical mirror of 0.85-meter diameter with a radius of curvature of 8.3 meters. The specification for the mirror required that the rms wavefront deviation error produced by the mirror at the center of curvature was to be less than $\lambda/20$ (where λ is equal to 632.8nm). Tests made with a WSI by the manufacturer indicated that the wavefront produced by the mirror was within this tolerance (0.045λ). Itek performed an acceptance test on this mirror using an Itek LUPI and found that the rms wavefront produced by the mirror was 0.053λ . An examination of the data indicated that, due to the particular asymmetric nature of the surface, the WSI data was inaccurate because of (1) the one dimensional nature of the interferometer, (2) errors introduced by the integration technique of data reduction which produced some smoothing, and (3), of most significance, errors introduced by the sampling pattern on the surface.

The LUPI is used at the center of curvature of the spherical mirror with a diverging lens to produce a spherical wavefront. The returning wavefront interferes with an internally produced reference wave, producing an interferogram (fig. 1) in which each fringe is a contour line of equal optical path difference between the test and reference wavefront. The optical path difference from one fringe to the next is equal to one wavelength of the light from the helium-neon gas laser, 632.8 nanometers.

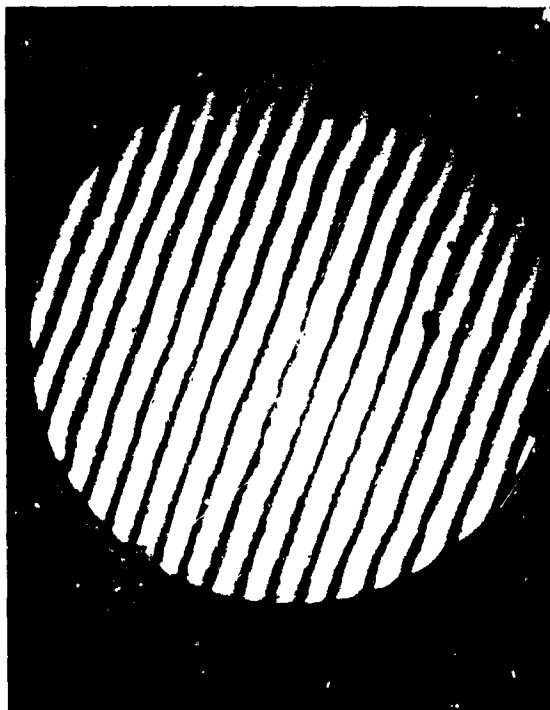


Figure 1. LUPI interferogram of 0.85-meter-diameter mirror.

The interferogram is converted to a digital map of X and Y coordinates of the fringes with points nearly equally spaced over the surface, usually in a matrix of 17 x 17 sample points (fig. 2.) A digital computer analyzes the digital map, fitting the data in a least square deviation manner to a sphere. From these results, the computer produces a contour map (fig. 3) of the wavefront and computes an rms value of the wavefront defined by:

$$\text{rms} = \left[\sum_{i,j=(1,1)}^{nm} \frac{(D(i,j))^2}{nm} \right]^{1/2}$$

where $D(i,j)$ is the deviation from the best fitting sphere at the coordinates (i,j) , and $1 \leq i \leq n$, $1 \leq j \leq m$, nm being the total number of points sampled.

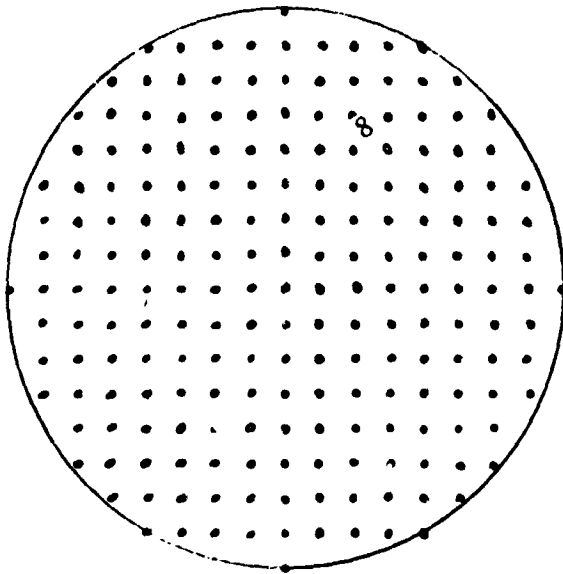


Figure 2. Sampling patterns for computing rms wavefront from LUPI interferogram.

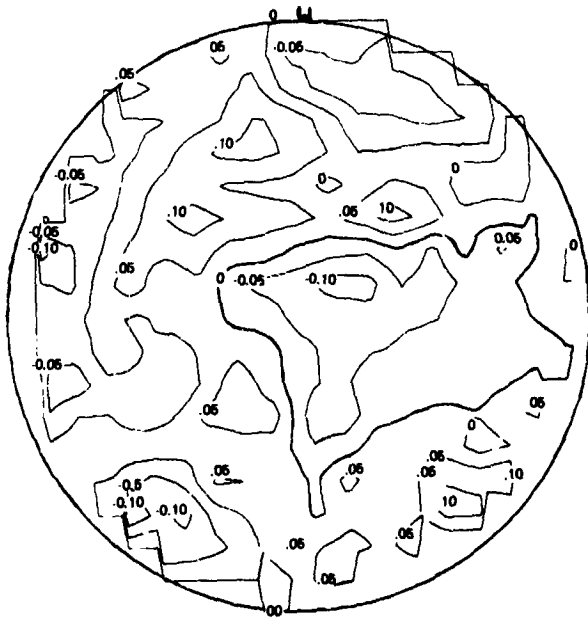


Figure 3. Contour map obtained from interferogram shown in figure 1.

In this evaluation, every point, each containing an equal amount of information about the wavefront, carries an equal weight in the computation.

In the WSI tests performed by the mirror manufacturer, eight interferograms (a representative example shown in fig. 4), oriented at 45 degrees relative to each other, were obtained with 16 data points along each diameter (sphere = $D/16$). These data, when reduced, give wavefront deviation across 4 diameters (since the $0^\circ = 180^\circ$ raw data are for the same diameter as the $180^\circ - 0^\circ$ data) as shown in fig. 5.

The rms value of the wavefront is given by:

$$\text{rms} = \left[\frac{\sum_{i,j=1,1}^{n,m} W_{(i,j)} (D_{(i,j)})^2}{\sum_{i,j=1,1}^{n,m} W_{(i,j)}} \right]^{1/2}$$

where $D_{(i,j)}$ is the deviation of the wavefront coordinates (i,j) ,

$W_{(i,j)}$ is the weighing factor applied to each point,

n,m are the number of points on each radius and the number of radii sampled, respectively.



Figure 4. WSI interferogram of 0.8-meter-diameter mirror.

We may obtain the weighing factor $W_{(i,j)}$ by considering the area that each data point is supposed to represent. In polar coordinates (ρ, θ) , the area for each data point can be represented by:

$$A_{(i,j)} = \frac{2\pi \rho d\rho}{m}$$

The weight ($W_{(i,j)}$) is given by:

$$W_{(i,j)} = \frac{A_{(i,j)}}{A_T} = \frac{2\pi \rho d\rho}{m(\pi \rho_{\max}^2)}$$

where A_T = the total area of the wavefront being examined,

ρ_{\max} = the radius of the wavefront, and

m = number of radii along which samples are taken.

Since all points are equally spaced in the radial direction, the term $\frac{2d\rho}{m\rho_{\max}}$ is constant for all points, so that the weighing factor, is

$$W_{(i,j)} \propto \rho$$

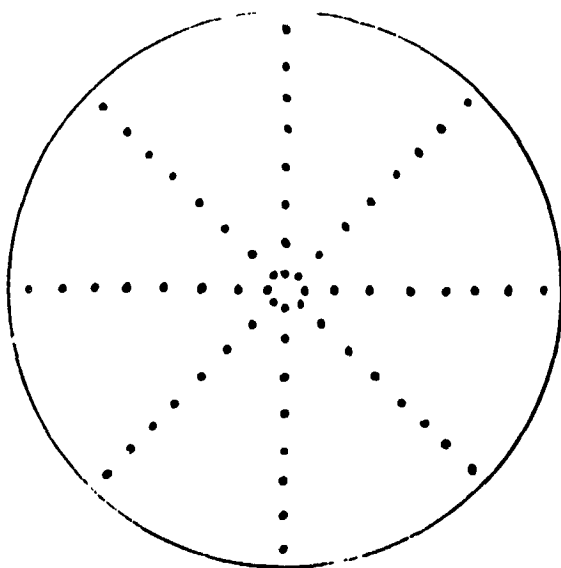


Figure 5. Sampling patterns for computing rms wavefront from WSI interferogram.

In the sampling pattern used by the manufacturer, the radius of the outer ring of data points is 15 times the radius of the inner ring; i.e., a point on the outer ring is weighted 15 times as much as a point on the inner ring even though it contains the same amount of information about the wavefront.

In order to resolve the differences in test results, the contour map produced at Itek was reevaluated, the rms wavefront being computed with the unequally weighted points of the WSI data reduction technique. The remaining discrepancy was found to be less than 0.002λ !

The wavefront contour measured with the LUPI can be Fourier-transformed in two dimensions to obtain a system Modulation Transfer Function (MTF), which leads to a minor variation in the usual method of specifying optical surfaces. The surface requirement is given in terms of the rms wavefront produced; however, when the required figure is approached to within approximately 50 percent, the interferograms are reduced to MTF in addition to wavefront contour. The optical components are accepted directly on the basis of MTF, regardless of whether the wavefront meets the goal specification. Details of this technique were reported by Lerman (ref. 8) and Minnick and Rancourt (ref. 9).

Conclusion

Testing of the surface figure of optical components should give results that are useful to the optician and sufficiently accurate for the system analyst. Experience has shown that the most reliable and convenient technique for accomplishing this objective is dual-beam interferometry, which produces direct, two-dimensional, wavefront contours.

References

1. Porter, R. W.: *Amateur Telescope Making*. Third ed., Scientific American Publishing Company, New York, 1933, p. 55.
2. Adachi, I.: *Atti della Fond. G. Ronchi*, ed., vol. 15, no. 461, 1960.

3. Saunders, J. B.: J. Research Natl. Bur. Standards, vol. 68C, no. 155, 1964.
4. Brown, D. S.: Proc. Phys. Soc., vol. B-67, no. 232, 1954.
5. Ronchi, V : Atti della Fond, G. Ronchi, ed., vol. 17, no. 93, 1962.
6. Burch, J. M.: Nature, vol. 171, no. 889, 1953.
7. Houston, J. B., Jr.; Buccini, C. J.; O'Neill, P. K.: Applied Optics, vol. 6, no. 1237, 1967.
8. Lerman, S. H.: SPIE Seminar Proceedings. SPIE, vol. 13, no. 51, 1969.
9. Minnick, W. A.; Rancourt, J. D.: SPIE Seminar Proceedings. SPIE, vol. 13, no. 87, 1969.

Figure-Sensing Techniques

Robert Crane, Jr.

The Perkin-Elmer Corporation

N70-36714

This paper describes briefly the application of two different figure-sensing interferometers currently used by Perkin-Elmer for testing large optics. The first is the scatterplate interferometer that was used in the final testing of the Stratoscope II primary mirror. The second is a phase-measuring interferometer, which was used as a figure sensor in an active optics demonstration.

The Stratoscope II primary mirror consists of a solid, 36-inch, fused silica paraboloid. During manufacture, this paraboloid was supported in a vertical position and was measured with an equal path interferometer. For the final figuring, the mirror was supported on its counterweight support assembly, as it was to be used in the telescope, and was tested in a vertical vacuum tank with the scatterplate interferometer. Final hand-figuring was done on the basis of the data extracted from the scatterplate interferograms.

Figure 1 shows the optical arrangement for a scatterplate interferometer. The source of illumination is located at the left in the figure; the optical element being tested, located at the right, is not seen in the illustration. The scatterplate is a flat glass plate having a large number of scattering centers on one surface. The only special characteristic of the plate is that the scatterers appear in pairs, with each pair located symmetrically about the center of the plate. This means that, for each scatter point above the center line shown in figure 1, there will be a corresponding second scatter point located an equal distance below the center line. The scatterplate is located with its center on the optical axis and slightly in front of the center of curvature of

the mirror being tested. Interference takes place in this interferometer between two spherical bundles of rays whose centers of divergence are separated by a small distance, shown as "2S" in figure 1.

As the source of illumination passes through this scatterplate, it is divided into two portions. The first portion is scattered by the first set of small scattering points. Each point generates a divergent bundle of rays that fully illuminates the mirror being tested. These bundles are reimaged at a point close to the scatterplate but on the opposite side of the center of curvature of the mirror. Each bundle then diverges and continues to the film plane.

The second portion of the incident light is unaffected by the scatterplate and is imaged on the surface of the mirror being tested. This portion is reflected back through the scatterplate again. A portion of this return beam is then scattered by the point in the scatterplate to form a second set of diverging bundles of rays. In this case, the centers of divergence are located on the surface of the scatterplate. Thus, two spherical bundles of rays are formed, and interference takes place between the two. For the geometry shown and for a perfect spherical mirror under test, the fringe pattern will consist of a series of circular fringes identical to a zone plate. Figure 2 shows an example of a fringe pattern obtained when measuring a parabolic mirror without a null corrector.

An important advantage of the scatterplate interferometer is that there are no extra optical elements within the interference path other than the mirror being tested and the scatterplate itself. In addition, the data are

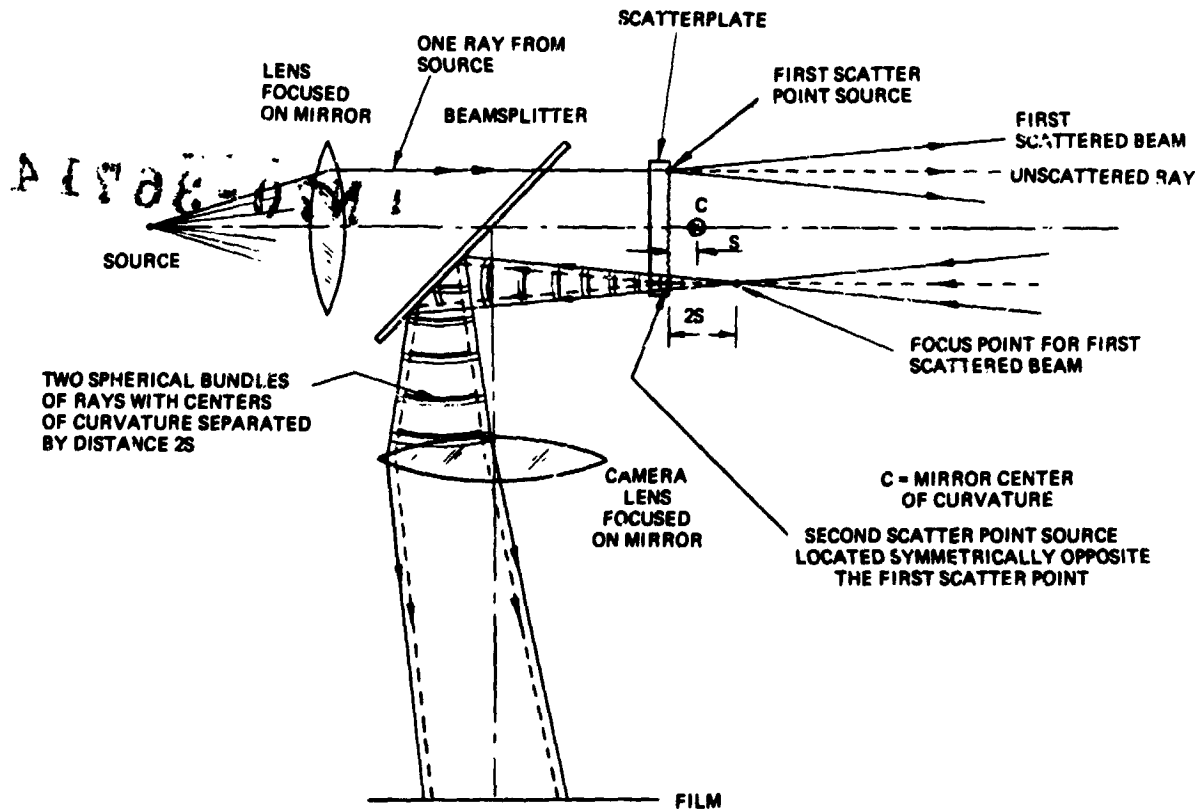


Figure 1. Scatterplate interferometer optical arrangement; the element to be tested is located (off figure) to the right.

collected in one short exposure of the film; hence, drift factors are not significant. In the application at Perkin-Elmer, the fringe pattern is fed to an automatic scanning device, which converts the fringe data into a digital format. These data are processed by computer to find the exact radius and position of the best-fit reference surface for comparison with the mirror under test. By using this technique, it was possible to test and figure the Stratoscope mirror to an accuracy of $\lambda/54$ rms. It might be of interest to note that the same mirror was again measured by the scatterplate technique after a 2-year period, during which it underwent several balloon flights, and was found to have essentially the same figure as when it was first manufactured.

The active optics experiment was conducted with a three-segment, 20-inch-diameter, spherical mirror. The mirror was

made by first manufacturing a solid 20-inch-diameter mirror and then cutting it into three pieces. Before being cut into segments, the mirror had a figure error of $\lambda/34$ rms.

After the mirror was cut, the segments were mounted on a flexible support assembly, shown in figure 3. Each segment was held at its center of gravity by a flexure-bearing universal joint. The universal joint was mounted at the end of a cantilever rod that, in turn, was held by two flexure blades. Each segment has three degrees of motion, two in tilt and one axial. The figure sensor was located at the center of curvature of the mirror. Segment alignment errors were measured and converted into control signals for actuators that were used to position the mirror. Three actuators were used for each segment. In this fashion, closed loop control was obtained with an overall figure accuracy

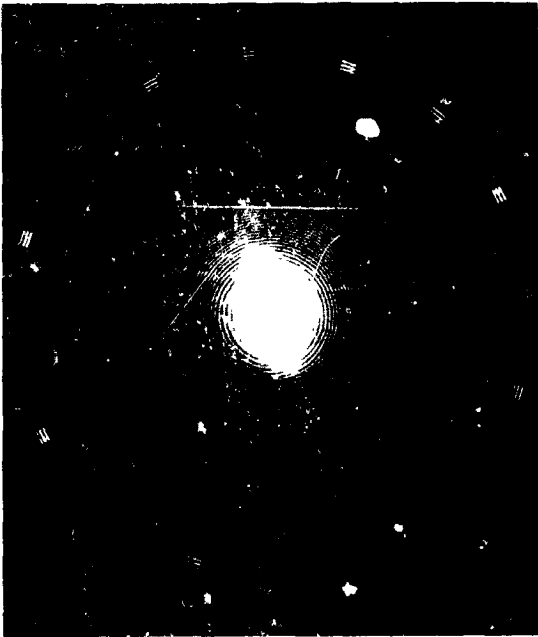


Figure 2 Typical fringe pattern from scatterplate interferometer; this pattern was obtained when measuring parabola without a null correction; outer zone of the parabola was formed on the surface and at the center of the scatterplate.

actually better than that of the 20-inch-diameter mirror before it was cut into segments.

The figure sensor arrangement is shown in figure 4. This consists of a modified Twyman-Green interferometer illuminated by a laser source. The input beam is collimated as

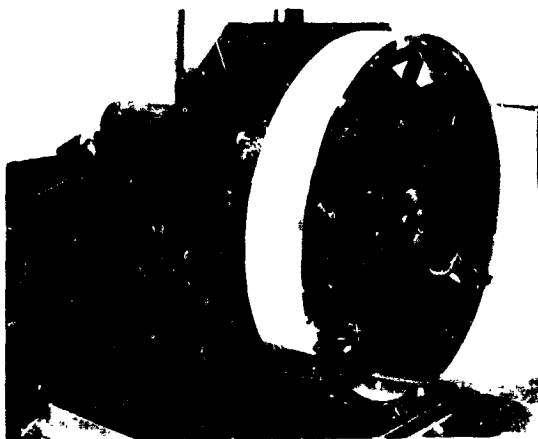


Figure 3. The 20-inch segmented mirror assembly.

it passes through the beamsplitter. The reference beam is reflected from a flat reflector. The test beam passes through a lens and diverges to fill completely the mirror under test. For a spherical test element, the center of divergence is set to coincide with the center of curvature of the mirror. Four typical fringe patterns are shown at the top of figure 4. For a perfect spherical mirror under test and with the center of curvature of the mirror coinciding with the center of divergence, the fringe pattern will have equal intensity over the whole fringe plane. Tilt errors will produce line fringes. Axial alignment errors will produce circular fringes. Localized figure errors will produce a localized difference in the fringe intensity. For the active control, it was desired to extract figure and alignment errors on a real-time basis and to make measurements to small fractions of a fringe. To meet this need, the concept of the phase-measuring interferometer was developed.

The phase-measuring interferometer is a two-beam interferometer in which the fringe pattern is analyzed electronically to permit real-time error sensing. Figure 5 is a schematic of a simplified version with coherent illumination and with plane reflecting surfaces in each interference beam path. If both reflectors are perfectly plane and parallel to the wavefront, interference will occur between

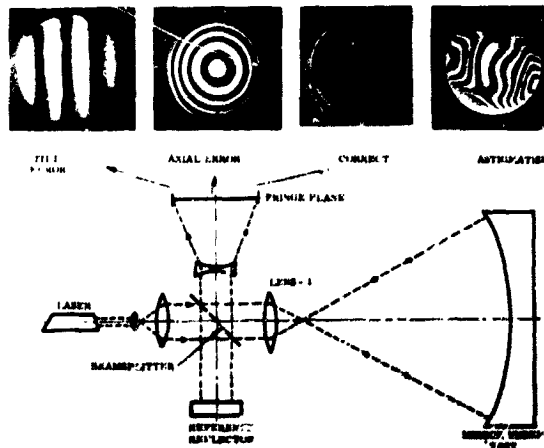


Figure 4. Figure sensor optical arrangement; the interferograms (at top) show typical fringe patterns for a misaligned mirror under test.

two plane parallel wavefronts, thus producing a fringe pattern with uniform intensity over its entirety. If the reference reflector is translated at constant velocity along the optical axis normal to the wavefront, then the fringe pattern intensity will vary through maximum and minimum levels in a sinusoidal fashion with identical phase over the entire pattern. Two detectors are placed in the fringe plane: one at a position arbitrarily selected as a reference and one at a position corresponding to a spot to be tested on the test surface. These detectors convert the cycling fringe pattern into two cycling electronic voltages, or carriers. If a small portion of the test surface is high in relation to the rest of the surface, there will be a relative phase shift of the electronic signal generated from the corresponding point in the fringe pattern. Phase shifts between the two signals are then measured by an electronic phase detector to generate a DC voltage proportional to phase and, hence, proportional to figure error. Figure 6 shows the components of a phase-measuring interferometer set up in a Perkin-Elmer test laboratory.

The principal advantage of the phase-measuring interferometer is that data may be extracted in real-time for use in a control

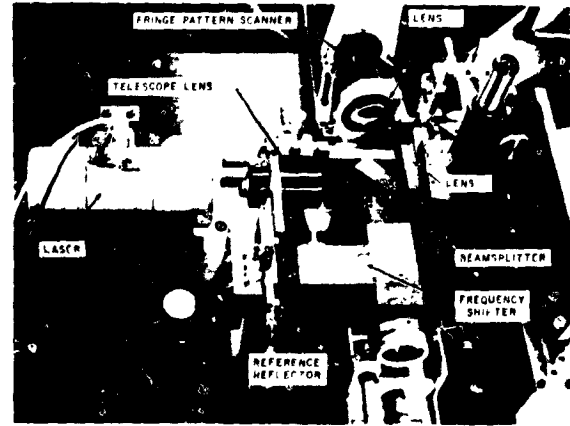


Figure 6. Phase-measuring interferometer components.

system. In addition, figure errors on the order of $\lambda/100$ may be measured with reliability. Figure 7 shows an example of the output data from a phase-measuring interferometer. This is actually a raster scan and shows the horizontal profile of a test flat. Figure 8 shows the result of a raster scan of the segmented active mirror while it was being controlled. These data show an average figure error of $\lambda/40$. Subsequent improvements were made in the active control system that resulted in an overall average figure error of $\lambda/60$.

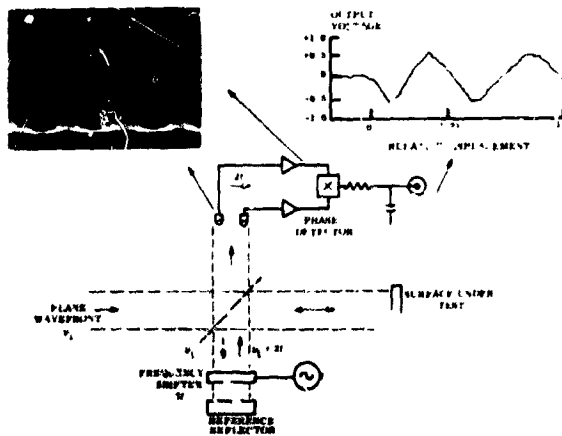


Figure 5. Phase-measuring interferometer concept; small photograph (upper left) shows typical electronic forms; graph (upper right) shows typical calibration of output voltage versus figure error in wavelengths.

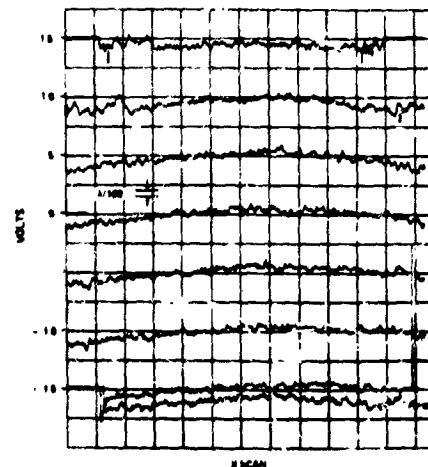


Figure 7. Output data from phase-measuring interferometer; a set of horizontal profiles showing the figure error measured with a small test element; raster scan of phase-measuring interferometer using reference flat in measuring arm.

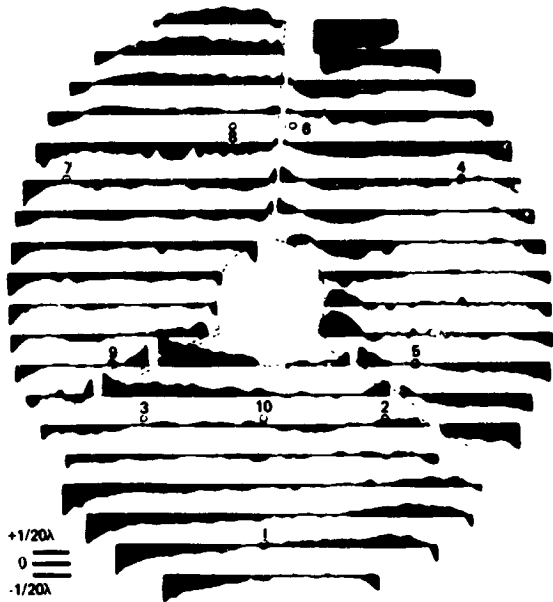


Figure 8. Measured figure error profiles for active optics demonstration; prepared from an average of three raster scans of composite mirror while control system was in operation; data obtained from scanning spot of phase-measuring interferometer; figure error determined by integration of profiles is $1/40$ wavelength average.

Recent work on advanced figure-sensing techniques has devised a method for measuring aspheric surfaces. A concept for the application of the phase-measuring figure sensor in a large, actively controlled, telescope system is shown in figure 9.

In conclusion, laboratory work has demonstrated that figure-sensing techniques have been developed to the point where they can now be applied to large, actively controlled, telescope systems.

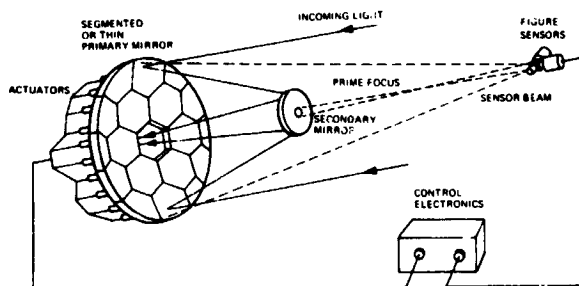


Figure 9. Active optics concept utilizing a phase-measuring figure sensor.

PRECEDING PAGE BLANK NOT FILMED.

Actuators for Active Optics

Gordon J. Watt

The Perkin-Elmer Corporation

N70-36715

The growing field of active optics has stimulated the need to produce minute deflections in various portions of optical systems. Actuators must operate in conjunction with precise measuring devices that continuously monitor the optical surfaces. Because the mounting is also associated with deformations, it becomes an integral part of the overall control system. Such systems feature multiple loop servomechanisms operating with microinch precision. These actuators may be an integral part of the base isolation system or may operate in tandem with it.

At the Perkin-Elmer Corporation, we have concentrated on two basic actuator systems: one produces minute deflections and the other, minute forces. Depending on the mechanical characteristics of the optical surface and its mounting, the overall forward actuating system may behave as:

1. *A displacement system* where inertial forces are predominant
2. *A forcing system* where compliance (or stiffness) of the optical structure produces the resistance to displacement
3. *An intermediate system* where stress and strain in the optical structure produce important dynamic effects to be handled by the actuators.

The intermediate system is more difficult to handle analytically but much easier to realize in a practical structure. In a practical actuator, one must also consider the total stress-strain and inertial force relationship. Even though we are now concentrating at opposite extremes of the mechanical parametric scale for synthetic analytical

reasons, we shall eventually choose a hybrid actuator for functional simplicity, just as electronic engineers have compromised between pure voltage and current sources to achieve simplicity and economy. We have already been forced to recognize the stiffness of the forcing actuators and the compliance of the displacement actuators as important factors in system design.

Figure 1 shows a typical actuator system mounted on a mirror assembly. The three-element segmented mirror is displaced by actuators that convert large displacements of an integrating lead screw into small displacements at the mirror surface, by utilizing a combination of soft and stiff springs in the actuator assembly. The mirrors are supported at three points; thus, they are not bent by actuator displacements or forces.

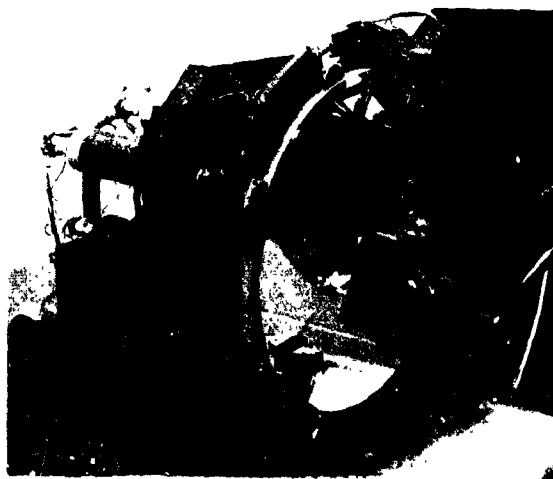


Figure 1. Typical actuator system mounted on a mirror assembly.

Figure 2 is an exploded view of the actuator. The servomotor gear box at the left drives the lead screw, which displaces the soft spring against the stiff springs, producing a minute output displacement at the right end of the actuator.

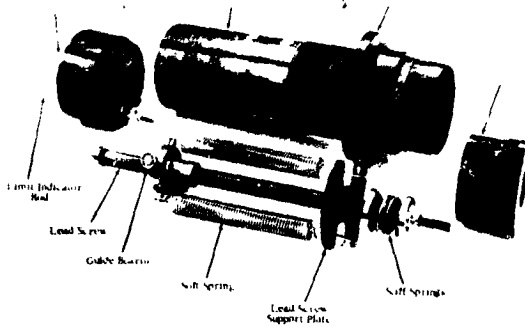


Figure 2. Exploded view of a typical actuator.

A similar forcing type of actuator is shown in figure 3. In this case, an integrating drive produces a force proportional to the displacement of a spring. The exploded view in figure 4 depicts the operations of the actuator. Force produced by the spring at the right is transmitted to an optical structure through the tiny rod at the end of the actuator. This actuator configuration is used in flexible optical systems where resistance to displacement is provided by the optical structure itself.

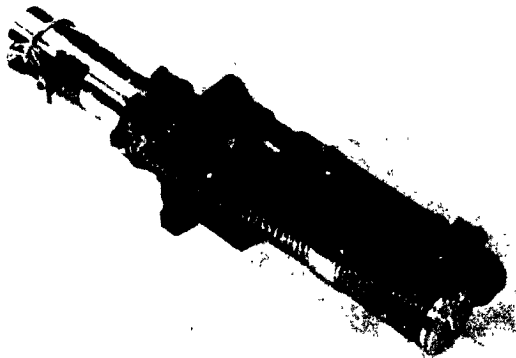


Figure 3. Forcing type of actuator.

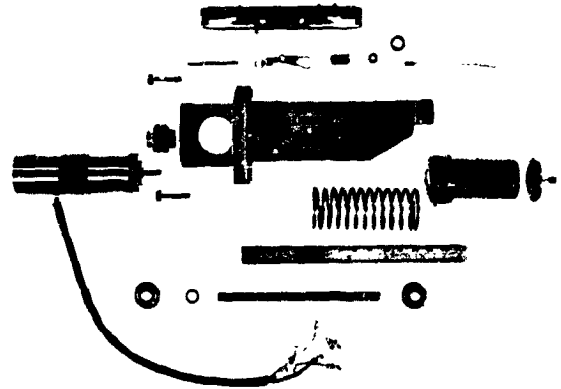


Figure 4. Exploded view of a forcing type of actuator.

An actuator better qualified as a displacement device is shown in figure 5. In this case, stiffness is built into the basic structure. An Invar shaft is passed through a piezo-electric cylinder with an interference fit. Relative displacement between the two is controlled by electric fields between conducting surfaces on the outside of the cylinder and the grounded Invar shaft. Interference may be controlled by a bias voltage between the two. Selective voltage pulses between rings distort the piezo-electric material and cause either the cylinder to creep along the shaft or the shaft to be pushed through the cylinder by peristalsis.

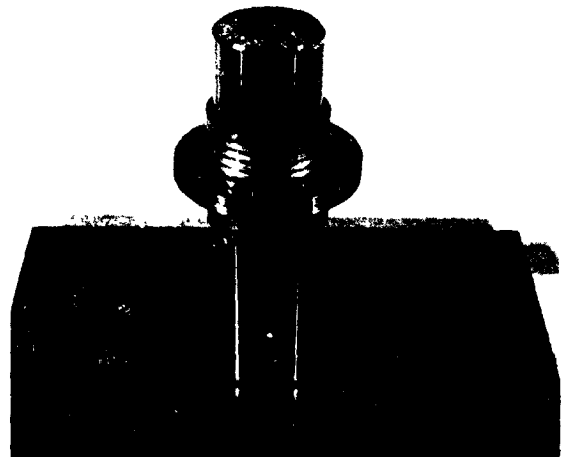


Figure 5. Actuator suitable for use as a displacement device.

The present version, shown in figure 5, has a supporting ring to locate the cylinder. A small relief is situated between the cylinder and ring. Because of the relief, it behaves somewhat like a conventional inchworm actuator. On the other hand, the integral relation between the cylinder and shaft provides high stiffness and wide bandwidth. It has worked successfully up to 10 kilocycles and down to 1 cycle per second. With further development, either of these ranges might be extended.

Actuator motion is obtained by passing a train of voltage pulses from left to right along the cylinder, resulting in a net incremental advance of the shaft in the same direction. Motion of the center support ring on the piezo-electric cylinder is shown in figure 6 by the path of the short arrow relative to the shaft. Vertical hatching represents an axial compression in the cylinder elements; horizontal hatching indicates tension.

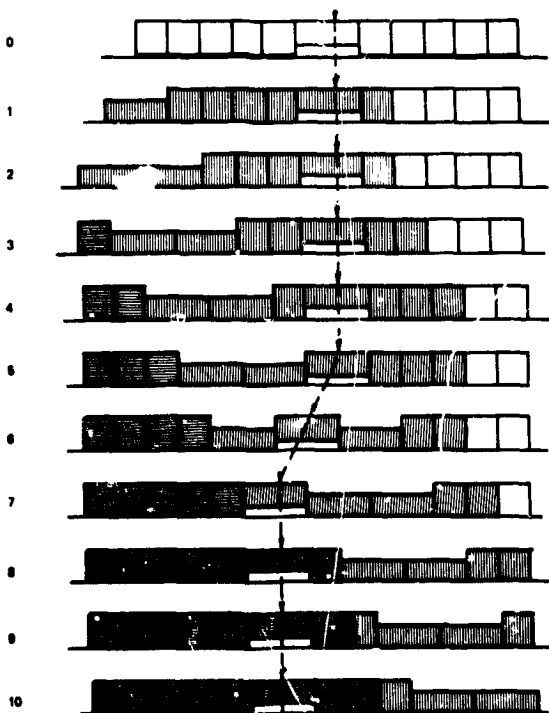


Figure 6. Schematic of actuator motion.

Compression to the left of center and tension to the right of center results in a reverse motion. The following steps are schematically depicted in figure 6.

1. In step 1, the first pulse reflects a compression wave to the center. The shaft backs up slightly relative to the central support ring.

2. The second step results in a greater backward motion because the friction of the first and second rings is involved.

3. An even greater motion backward occurs in the third, fourth, and fifth steps because the first rings provide backup to the expanding sections. Notice that a tension wave has started from the left and a compressive wave has progressed beyond the center.

4. The first real effect of a compressive wave to the right of the center happens in the sixth step when the first and largest forward advance of the shaft occurs.

5. A second smaller forward advance occurs when the second ring to the right of the center expands and compresses.

6. In the eighth, ninth, and tenth steps, the tension wave crosses the center and causes further backward motions.

7. The net effect of a sequence is to leave the cylinder slightly in tension on the shaft. The net motion is forward.

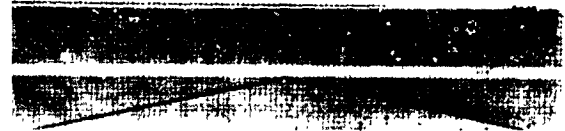
Evaluation of the experimental actuator requires careful measurement of displacements at each cycle of the voltage pulse train. To measure displacement of a small mirror on the end of the actuator shaft, an interferometer was arranged as shown in figure 7. An electromagnetic probe was used to record displacements for a series of pulse trains. Results of actuator displacement at three different pulse voltage amplitudes are shown in figure 8. The linearity of the displacement curves demonstrates the consistency of the steps. The pulse train direction was reversed at the middle of each curve.

Certain conclusions have been derived from the work accomplished thus far. The first and most important conclusion is that the experimental actuator design is sound.

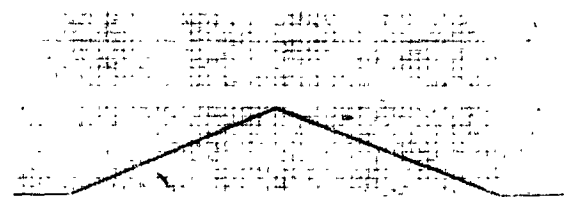


Figure 7. Interferometer arrangement to monitor displacement.

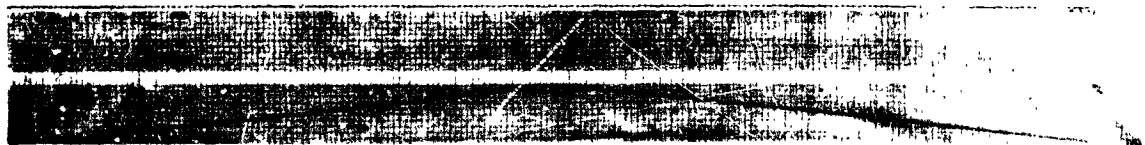
Speculations regarding friction and load effects, surface finish, compatibility of materials, and thermal effects have been resolved by testing. The actuator design is simple and manufacturable. The structure is rigid and rugged. The assembly can be handled and used without contamination or breakage.



(a) 1 millionth inch/step.



(b) 2 millionth inch/step.



(c) 0.5 millionth inch/step.

Figure 8. Results of actuator displacement at three different pulse voltage amplitudes.

Shop Supports for the 150-Inch Kitt Peak and Cerro Tololo Primary Mirrors

Norman Cole

Kitt Peak National Observatory

N70-36716

We traditionally have reserved final evaluation of optical components until they have been installed in their cells and the entire instrument has been tested as a unit. This is reasonably practical in the case of small optics because removal and refiguring, should they prove advisable, are easy and quick. As the optical elements increase in size, however, the difficulties and risks of handling also increase. In the case of large mirrors to be installed in remote areas or in space, the expense and time lost in returning the mirrors to the optical shop for retouching are prohibitive. These factors are now widely recognized, and various plans have been devised to insure that the mirror figure seen in the telescope will be the same as that seen in the optical shop.

It is rather obviously desirable to carry out the shop tests on the same supports that carry the mirror in the telescope, but, surprisingly, this has seldom been carried out. This is partly due to physical limitations, such as the lack of vertical test towers, in the optical shop; but, more important, most support systems for telescope mirrors are not robust enough to withstand the additional load introduced by the polishing action of the large tools necessary to generate a figure of revolution.

Because the supports adopted for the primary mirrors of the 150-inch telescopes for Kitt Peak and Cerro Tololo (ref. 1) do lend themselves to use in the optical shop, we have been able to pay proper attention to the careful support of the blanks during figuring and testing.

Figure 1 shows the upper surface of the grinding table fitted with the arrays of air pads, cushion blocks, and air bearings upon

which the first of the two big mirrors is now being worked. In figure 2, one of the pad pistons has been removed to show the roll diaphragm, which is the heart of this type of support.

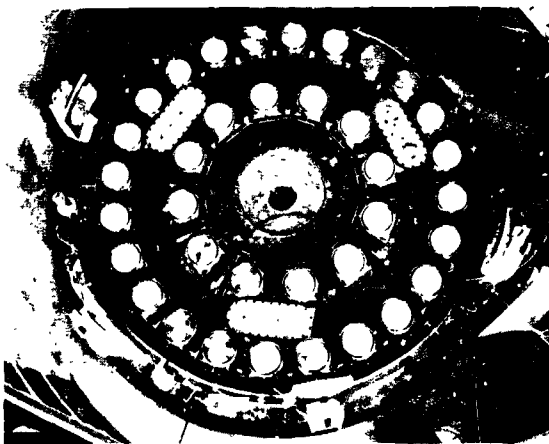


Figure 1. Upper surface of grinding table.



Figure 2. Pad piston removed to show roll diaphragm.

The two rings of circular air pressure pads are identical to those which will be used in the telescope assembly. It is upon these pads that the mirror rests while being optically tested from the top of the vertical tower (fig. 3). Three of the 24 pads in the outer ring are deflated, and a thin spacer is inserted between the pad piston and the back of the mirror. These three pads become hard defining points, but they carry an equal share

of the load with the remaining inflated air pads, just as will be the case in the telescope. The two rings of supports carry slightly different pressures, and appropriate floating weights maintain the proper pressure on each. Both arrays operate at less than 8 pounds per square inch.

The mirror cannot be polished with the support configuration as it will be in the telescope because, the moment a polishing tool is applied, its weight is transmitted onto the three defining points, thus warping the mirror. Accordingly, before the polishing, the spacers on the defining pads are removed; the pads are reconnected to the manifold of the outer ring; and the mirror becomes fully floating. Polishing-tool weight presses the mirror downward slightly until its back contacts 36 cushion blocks. These rectangular rubber blocks (fig. 2) serve to carry only the additional load imposed by the polishing tool. Mirror weight is still carried by the air supports.

Great care is exercised to see that the rubber blocks exert equal force on the back of the mirror under tool loading. The rear face of the mirror and the upper face of the grinding table are lapped to match, and the rubber blocks are ground to equal height. In addition, the rear face of the mirror is polished and tested optically to assure symmetry. Even so, as added insurance, the mirror is shifted on its supports at regular intervals to distribute any discrepancies in support symmetrically around the blank. For this purpose, the mirror is raised slightly above the support pads on three oval air bearings (fig. 1). Air at 100 pounds per square inch is fed through small holes in the flat surfaces of the air bearings, and the mirror can be easily rotated by hand while thus supported on a thin film of moving air. During the polishing and testing, the air bearings are in a retracted position and do not touch the glass.

The whole system operates quickly and conveniently. The mirror can be rotated and recentered in 10 minutes; it can be readied for test in less time than it takes to reach the top of the test tower.

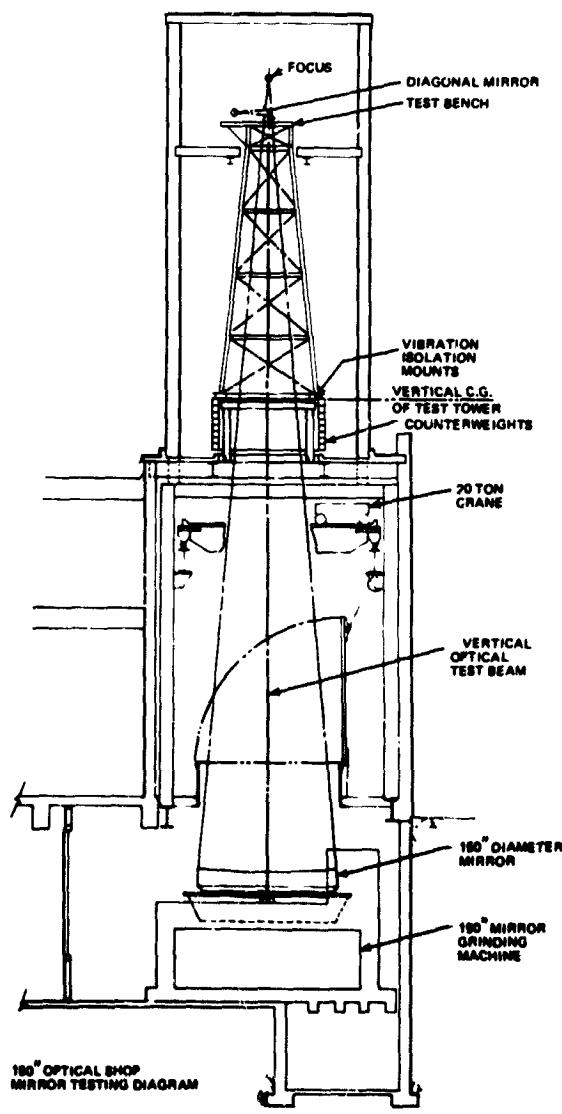


Figure 3. 150-inch optical-shop mirror-testing diagram.

The mirror figure will be thoroughly tested in the spherical stage before any aspherizing is started. Mainstays of the optical tests will be a longitudinal wire test, an unequal-path laser interferometer, and a null lens. We feel that it is essential to assure ourselves that we have a true figure of revolution before beginning the long process of aspherizing with small tools. Tools having less than a 36-inch diameter will have little, if any, success in removing astigmatism if any exists at the outset.

The mirror is still approaching the spherical stage. It is too early to predict

complete success for the support system; however, preliminary tests justify optimism.

Summary

The air-pad-support system, devised for the Kitt Peak and Cerro Tololo 150-inch mirrors, lends itself to use in the optical shop. The system permits polishing with a 9000-pound tool, and yet, without removal from the polishing machine, the mirror can be tested on the same support system that it will have in the telescope. Testing is carried out at the top of a 70-foot tower where a turret mirror can select any of several test devices.

Reference

1. Pearson, E. T.: Design Philosophy of Primary Mirror Supports for the KPNO 150-Inch Tele-

scope. Engineering Dept. Tech. Report No. 5, Kitt Peak National Observatory, 1969.

PRECEDING PAGE BLANK NOT FILMED.

Holographic Method of Monitoring the Performance of a Large Telescope Mirror

Kent E. Erickson
Keuffel & Esser Co.

1 N70-36717

Introduction

No method of monitoring the performance of a large, two-element orbiting telescope that does not use starlight is completely direct. The aim of the approach presented in this paper is to be direct to the extent that the monitor should exhibit the net effect, at the focal plane, of errors in figure, tilt, and focus of the primary mirror.

Principle

To be as direct as possible, the monitoring light should traverse the optical system as nearly as possible in the same way as starlight does. (See fig. 1.) There is no objection to the monitoring light traversing the system in the reverse direction except the practical one, that the light then proceeds toward the stars and is lost.

To avert complete loss of light, one may imprint on the primary mirror a very faint hologram produced by an "object wave" coming from infinity and a "reference wave" diverging from the focal plane. When illuminated by the "reference wave" coming from the focal plane, the hologram regenerates the "object wave." The telescope then returns this wave to the focal plane. After this round trip through the telescope, the wave may be monitored interferometrically.

Fortunately, the accuracy of this method does not depend upon the accuracy with which the hologram can be generated. If the hologram is not perfect, the wave shape that corresponds to perfect performance of the primary mirror can be calibrated. The desired interference pattern may then be synthesized and used as a reference.

Calibration of the System

Calibration is done by making simultaneous interferograms of the shape of the primary mirror and the shape of the wave diffracted by the hologram. The figure of the primary mirror need not be perfect during calibration; the effect of deformation can be removed analytically in synthesizing the desired pattern.

The calibration setup is shown in figure 2. The tilt of the primary mirror must be controlled during calibration so that its axis is perpendicular to the surface of the secondary mirror. This condition may be monitored interferometrically by placing a laser source at a point, P, (fig. 2) on the axis of the hologram near its focal plane. When proper alignment is achieved, the wave will return upon itself with radial symmetry. This test presupposes that the axis of the hologram is effectively coincident with the axis of the primary mirror. If the primary mirror is nearly spherical, its axis is not sharply defined; and the degree of coincidence is not critical.

It does not appear practical to adjust the focus precisely during calibration. The final adjustment must be done in orbit by shifting the focal plane to optimize the sharpness of stellar images.

The figure and tilt of the secondary mirror are *not* monitored by this system. They could be monitored by means of a hologram on the secondary mirror similar to that on the primary mirror, but the greater rigidity of the surface and the looser tolerance to tilt scarcely warrant it.

During calibration (as well as in orbit), the tilt of the secondary mirror must be controlled so that its axis intersects the primary

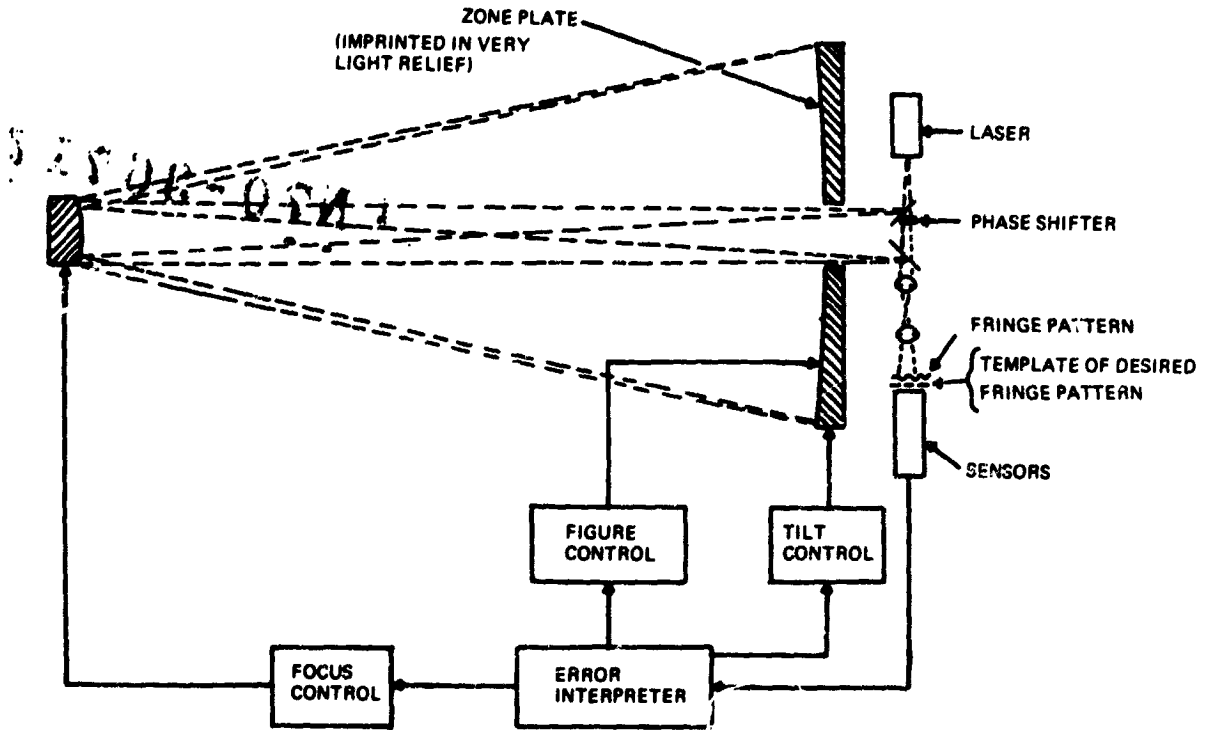


Figure 1. Schematic of telescope monitoring and control.

mirror at its axial point. This is not a particularly severe requirement. For diffraction-limited performance, the tolerance is of the order of several arc seconds (ref. 1).

Radial distortion of the hologram will affect the calibration. Gravitational distortion is minor and can be allowed for analytically. If the mirror blank is made of low expansion material ($\alpha \approx 10^{-7}/^{\circ}\text{C}$), thermal distortion is scarcely significant until thermal gradients exceed $10^{\circ}\text{C}/\text{meter}$. Adjustment of the focus is not required until temperature changes approach 10°C . If the mirror is segmented, however, radial constraint of the segments is required to tolerances of the order of 1 micron.

Structure of the Hologram and Its Effect on Stellar Images

The hologram consists of circular zones. Phase zones are easier to make and are optically more efficient than absorbing zones. The

pattern will thus be in low relief with a uniformly reflective overcoat over the entire surface.

The minimum spatial period of the zones is given by $a = 4\lambda f$. For an $f = 4$ mirror, $a = 10\mu$ if $\lambda = 0.6328\mu$.

Any practical method of generating the zones will probably give them a square rather than a sinusoidal profile. The step height of the raised zones must be large enough to diffract sufficient light into the first order for monitoring purposes but not so large as to diffract away an unacceptably large amount of starlight. For a small step height, t , the diffraction efficiency, ϵ , is given by:

$$\epsilon_1 = 16 \left(\frac{t}{\lambda} \right)^2 \quad (\text{first order only})$$

$$\epsilon = 4\pi^2 \left(\frac{t}{\lambda} \right)^2 \quad (\text{all orders combined})$$

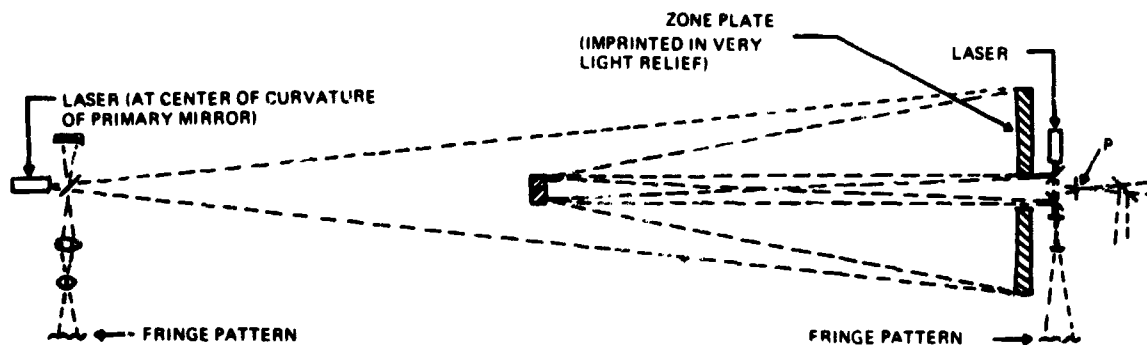


Figure 2. Calibration setup.

For helium-neon (He-Ne) light ($\lambda = 0.6328\mu$), a diffraction efficiency of $\epsilon_1 = 0.1\%$ should suffice. This requires a step height of $t = 50\text{\AA}$. For starlight at $\lambda = 0.2\mu$, the diffraction efficiency would then be $\epsilon = 2.5\%$; and at $\lambda = 0.1\mu$, it would be $\epsilon = 10\%$. For still shorter wavelengths, slightly absorbing zones would be more efficient than phase zones.

Nearly all the starlight diffracted by the hologram will miss the secondary mirror, and that which reaches the focal plane will be out of focus. Scattered light from the monitoring beam is likely to be the more serious problem.

Generation of the Hologram

There are two radically different approaches to generating the zones of the hologram: by a rotary process and by holography.

Rotary Process

In theory the zones could be cut one by one with a focused laser beam. (See fig. 3) The beam might expose a photoresist, or it might remove (by evaporation) some overcoat of absorbing material. The radial tolerance could be met with a fringe counter whose reference beam was reflected from a polished sphere mounted directly to the mirror so as to remove errors from instability in the axis of rotation.

In practice, however, the process would be exceedingly long and tedious because of the following factors:

1. The immense total length of the zones (of the order of 1000 kilometers)
2. The gradual variation required in the width of the zones
3. The awkwardness of measuring along a curved surface
4. The high precision required in the focus as well as in the radial control.

Factors 1 and 2 could be alleviated by using a long template, positioned radially and illuminated either by a laser beam or by an arc lamp. The surface could be coated with a photoresist, and several zones could be generated for each rotation of the mirror. If the reduction ratio were large, the zones in the template would be fairly coarse.

Holographic Process

Ideally, the hologram should have a zone pattern identical to the interference pattern between two coherent waves: a plane wave approaching along the axis of the mirror and a spherical wave diverging from the focus of the mirror. Both waves should have the same wavelength, λ_0 , as the light used for monitoring. Figure 4 is a schematic of a zone plate generator.

To avoid having to generate a truly plane wave over so large an aperture, it is necessary to modify the geometry. Fortunately, the pattern alters very little if both waves diverge from two points, P and Q, a finite distance away, provided the wavelength of the light is reduced accordingly. In practice, one must use an available wavelength, λ , and select

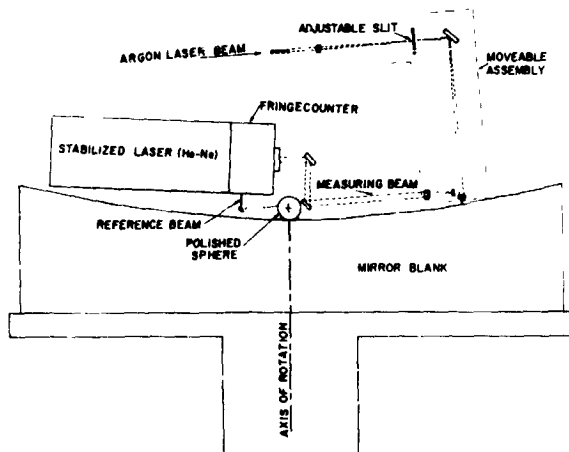


Figure 3. Precision zone plate cutter.

points P and Q accordingly. If one chooses $\lambda_0 = 0.6328\mu$ and $\lambda = 0.4480\mu$, then points P and Q lie at distances of 5.1 and 1.03 focal lengths from the mirror.

Photographic materials and laser sources are approaching the point where an area of 10 square meters can be exposed in one second with a resolution of 1000 lines per millimeter. The author does not know what prospects there are of such materials being coated with adequate uniformity on a large curved surface or being used in a washoff process that would permit etching (or vacuum coating) through the exposed zones.

powerful lasers and more sensitive processes (photographic, xerographic, or photoetching) will greatly reduce the exposure times required; otherwise, the entire holographic setup must be mounted inside a vacuum chamber on a seismic block.

Variant Systems

Certain "far out" variants of this holographic approach to monitoring could be considered. One, for example, is to station an image tube at approximately 300 meters from the telescope and to use a weak hologram on the primary mirror to focus the monitoring wave (originating at the focal plane) to a point approximately 15 meters beyond the image tube. A second wave, coherent with the first, could be sent directly (e.g., via a hole in the secondary) so as to interfere with the first wave across the aperture of the image tube. A circular pattern (containing some 300 fringes) would be formed. This pattern, when compared with the ideal pattern, would reveal the general features of the aberrations in the telescope. The finer details would be lost by diffraction.

Such an arrangement would have the virtue of checking out the performance of the entire telescope. Furthermore, the zones of the hologram would be coarse enough to be easily generated.

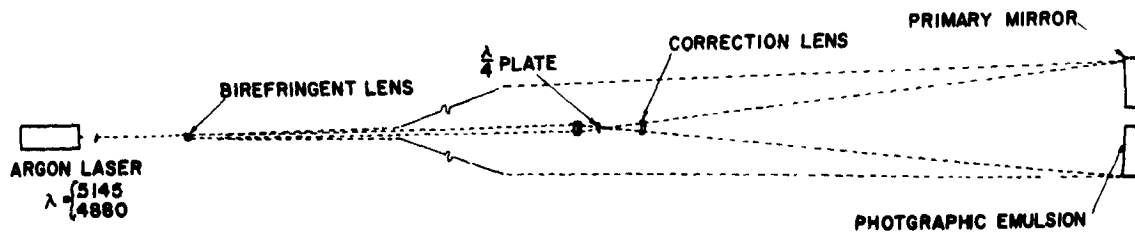


Figure 4. Schematic of zone plate generator.

In any case, the obstacles are severe. The scale of the holographic setup is enormous; i.e., from 100 to 300 meters, unless folded. It is to be hoped that, within a few years, more

Reference

1. Tschunko, Hubert F. A.; Hurwitz, Martin G.: Geometrical Optical Image Aberrations of Single and Double Mirrors. Applied Optics, vol. 8, no. 2, February 8, 1969.

N70-36718

Figure Control of Active Primary Mirrors

Duncan MacKinnon
MIT Instrumentation Laboratory

Introduction

The resolving power of an earthbound telescope is primarily limited by fluctuations in the earth's atmosphere. An orbiting telescope, on the other hand, is not subject to limitations imposed by an unsteady atmospheric environment; therefore, it is possible to envision a large instrument that is diffraction-limited over a major part of its useful spectrum of observation. The full realization of the maximum resolving power requires the accurate maintenance of the shape or figure of the primary mirror. Although it would be possible to polish a large mirror to the required accuracy, stresses introduced by thermal variations in the mirror and fluctuations in support structure loads can create surface perturbations that exceed the surface accuracy limits required for diffraction-limited performance.

Thermoelastic deformation magnitude is conventionally controlled by careful mirror and mirror-support-structure design and thermal environment control. An alternative approach utilizes an active system to maintain the correct mirror figure. An active surface control system is illustrated in figure 1. The mirror surface figure is compared to a desired reference surface by the figure sensor. Error data is then fed to a figure-control-system computer that generates a set of surface actuator commands, which are

transmitted to the actuator array. A correct choice of control algorithm ensures that the surface error is reduced by the actuator commands.

Control of Distributed Parameter Systems

The most general view of the mirror figure-regulation problem is afforded by studying the behavior of the partial differential equation that describes the mirror subject to distributed and point boundary conditions. The mirror support structure may impose distributed or point boundary conditions depending upon the design configuration of the structure. The effects of stresses created by the temperature distribution in the mirror and its support structure may be treated as distributed disturbances* acting on the system. The reflecting surface actuators

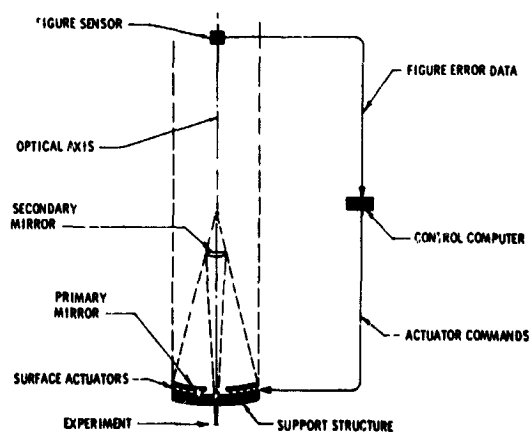


Figure 1. Primary-mirror figure control system.

*A rigorous study of thermal effects necessitates the derivation of the partial differential "heat" equations for the mirror and mirror support structure.

apply loads or deflections at an array of points on the rear surface of the primary mirror; these may be treated as boundary conditions.

The actual shape of the mirror surface is conveniently described in a three-dimensional set of polar coordinates. The x-axis corresponds to the optical axis of the system. Positions in planes orthogonal to the x-axis are described by specifying radius from the optical axis, r , and an angle, θ , relative to a reference plane that contains the optical axis. In this coordinate system, the surface of the mirror is described by a function of the form

$$x = X(r, \theta) \quad (1)$$

The surface coordinates, x , are a complex function of time, actuator forces, thermal disturbances, and support boundary conditions.

The desired mirror figure may also be defined by a function of the polar coordinates r, θ

$$s = S(r, \theta) \quad (2)$$

The error, e , between the desired surface and the actual surface at any coordinate (r, θ) may then be determined by measuring the difference between equations 1 and 2.

$$e = E(r, \theta) = S(r, \theta) - X(r, \theta) \quad (3)$$

The object of the control system is to minimize some function of e , such as the integral square error.

$$e_{is} = \int_0^{2\pi} \int_0^{r_m} E^2(r, \theta) \, r \, dr \, d\theta \quad (4)$$

where r_m is the radius of the mirror.

Control of systems described by partial differential equations has only recently received serious attention from control theorists. The earliest theoretical work to appear in control journals was carried out in

the U.S.S.R. by Butkovskii (refs. 1-5). More recent work has been carried out by a number of Russian and American investigators. An excellent review of the control literature and the theory of optimal control of distributed parameter systems may be found in Erzberger's thesis (ref. 6).

The control of a distributed parameter system is complicated by the infinite dimensionality of the controlled variable; i.e., all the points in a surface. As a result, practical control of distributed systems has always necessitated replacing the distributed system by a lumped model. The model is normally linearized about some nominal set of surface figure, support, and actuator load conditions and is characterized by a set of ordinary differential equations

$$M_1 \delta \dot{x} = M_2 \delta x + M_3 \delta m \quad (5)$$

where M_1 , M_2 , and M_3 are $n \times n$ matrices. $\delta \dot{x}$ and δx are n -vectors that represent the derivative and the value of the surface perturbations in x at n discrete locations. The n -vector, δm , is an array of perturbations in the surface actuator outputs. If the required changes in the controlled variable, x , are slowly varying, compared with the dynamics of the system of differential equations, it may be possible to neglect $\delta \dot{x}$ and to investigate the control of the algebraic set of equations

$$0 = M_2 \delta x + M_3 \delta m \quad (6)$$

This appears to be a reasonable assumption in the case of the mirror figure-control system because the disturbances introduced by thermal effects propagate comparatively slowly through the mirror and its support structure. Control of a dynamic system subject to constraints of equations 5 or 6 may be handled by conventional control theory.

Mirror Figure Control Algorithms

The design of a mirror figure control system for a large telescope presents the control engineer with a number of unique and challenging problems. Among them are:

1. An accuracy criterion that demands a root-mean-square surface error measured in microns

2. A large dimension, multivariable, control problem imposed by the size of the actuator array. (This is particularly true in the case of a continuous mirror where figure modification must be achieved by elastic deformation.)

Additional problems, of a more conventional nature, are introduced as a result of nonlinearities, noise, and scale factor errors in the surface actuators and figure sensor.

Let us assume that the mirror surface deflection parallel to the optical axis is monitored at the n locations of the actuators. The n deflection measurements may be represented by an n dimension vector, δx . The corresponding actuator force or deflection increments are elements of a vector δm . If we assume that the mirror material is isotropic and that equation 6 is valid, the relationship between δx and δm may be written:

$$\delta x = A\delta m \quad (7)$$

where A is an $x \times n$ matrix and the elements of A are defined

$$a_{ij} = \lim_{\delta m_j \rightarrow 0} \frac{\delta x_i}{\delta m_j} \quad (8)$$

Suppose that the measured error between the desired and actual surface figures is a vector e . The error is reduced to zero if δx is $-e$

$$\delta x = -e = A\delta m \quad (9)$$

or

$$\delta m = -A^{-1}e \quad (10)$$

Thus a control δm may be found, providing the inverse A^{-1} of the matrix A exists.

If the actuators are of the deflection type (ref. 7), operation of an actuator

produces measured deflections that are confined to the actuator location. As a result, the matrix A is diagonal, and the elements of A have the form

$$a_{ij} = \begin{cases} 0 & i \neq j \\ k_{ii} & i = j \end{cases} \quad (11)$$

where k_{ii} is a scale factor associated with the i th actuator. The elements of A^{-1} have the form

$$b_{ij} = \begin{cases} 0 & i \neq j \\ k_{ii}^{-1} & i = j \end{cases} \quad (12)$$

Equation 4 may then be written

$$\delta m_i = -b_{ii}e_i \quad i = 1, n \quad (13)$$

Thus, surface control may be achieved by using a trivial feedback control law. Unfortunately, it is very difficult to achieve the support rigidity required for pure deflection actuation. Additional problems arise as a result of the precision manufacturing tolerances required for constructing such actuators.

Surface modification may also be achieved by applying loads to an array of discrete points distributed over the rear surface of the primary mirror. Load actuators produce deflections at adjoining measurement points, as shown in reference 8.* As a result, the matrix A is no longer diagonal, and the control in equation 10 must be constructed in the form

$$\delta m_i = -\sum_{j=1}^n b_{ij}e_j \quad i = 1, n \quad (14)$$

where b_{ij} is an element of the inverse A^{-1} . Because the dimension of A is large,* it is no small task to obtain the inverse, A^{-1} , of A in terms of computation time and memory requirements. Additional problems arise as a result of errors in the definition of A , which can propagate to large values in A^{-1} . Subsequent variations in A (due to actuator failure, for example) require laborious recomputation.

*The thin mirror described in reference 8 utilizes 61 actuators; hence, it is necessary to invert a 61 x 61 matrix in order to solve the control problem.

Thus, while the load type of actuators offer advantages in simplicity and cost, a significant increase in control algorithm complexity is incurred if a straightforward approach to the solution is followed.

An alternative approach to the control problem utilizes the theory of *optimal control*. Optimal control requires the definition of a performance index that reflects the goal of the control process. Mathematical optimization techniques may then be applied to generate a control or sequence of controls that optimize the performance index. An optimal control problem may be formulated in the following way.

Find a control vector δm_{opt} that minimizes the performance index*

$$J = \sum_{i=1}^n e_i^2 = e' e \quad (15)$$

subject to the constraints

$$\delta x = A \delta m \quad (16)$$

This problem appears commonly in the field of econometrics, where a number of solution techniques have been developed. Among the most important techniques are *quadratic programming* (ref. 9) and Bellman's *dynamic programming* (ref. 10). Because these methods generally require a large computational ability, they are not usually suitable for on-line control.

Another class of optimization techniques that have been successfully applied to a wide range of control problems is based upon the Calculus of Variations. A large number of systematic iterative optimizations by parameter variation methods have been developed. Perhaps the simplest is the *gradient method* or the *method of steepest descent* (ref. 11). The gradient method bases control strategy on the first variation of the performance index, J .

* e' is the transpose of the vector e . The performance index is a discrete representation of the integral squared error functional in equation 4.

The variation in the performance index (eq. 15) may be written

$$\begin{aligned} \delta J &= (e + \delta e)' (e + \delta e) - e' e \\ &= \frac{\partial J'}{\partial m} \delta m + \frac{1}{2} \delta m' \frac{\partial^2 J}{\partial m^2} \delta m \quad (17) \end{aligned}$$

where

$$\frac{\partial J}{\partial m} = 2A' e \quad (18)$$

$$\frac{\partial^2 J}{\partial m^2} = A' A \quad (19)$$

The first variation is identified as $\frac{\partial J}{\partial m} \delta m$. If δm is sufficiently small, the first variation will dominate and δJ may be written

$$\delta J \approx \frac{\partial J}{\partial m} \delta m \quad (20)$$

Suppose that the control increment, δm , is selected so that

$$\delta m = -\epsilon \frac{\partial J}{\partial m} \quad (21)$$

where ϵ is a positive number. If ϵ is sufficiently small, equation 20 is valid and the variation, δJ , may be written

$$\delta m = -\epsilon \frac{\partial J^2}{\partial m} \quad (22)$$

Since the right-hand side of equation 22 is negative definite, it is apparent that the control increment (eq. 21) results in a reduction in the figure error index.

The properties of the first variation form the basis for an algorithm (shown in fig. 2) that systematically evaluates the optimal control. The iterative loop is initiated by the evaluation of $\frac{\partial J}{\partial m}$ using a mathematic model of the system or the actual system (in an analog computer fashion). The control m is then incremented by δm in equation 21. The performance index with the new control, $m + \delta m$, is

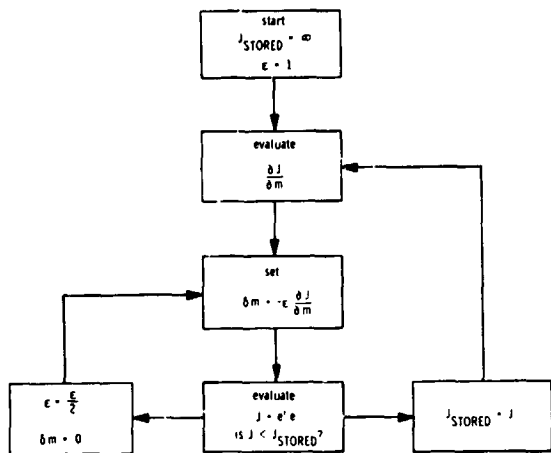


Figure 2. First variation algorithm.

evaluated and compared to its stored value. If δJ is negative, the value of J has improved; the new control is retained; and the value of J stored. A positive δJ , on the other hand, indicates that too large a control step has been taken, and equation 20 has not been satisfied. The value of ϵ must be decreased, and the control restored to its original value. This process may be repeated in a continuous fashion or terminated when the value of J has been reduced below a suitable threshold. If the minimum is unique, the sequence of controls always converges to the optimum solution.

Although first variation algorithms are simple in structure and place modest demands on computer size, they are characterized by slow convergence rates. Convergence rates may be improved by using more sophisticated methods to evaluate ϵ .

A common procedure for increasing the convergence rate is the consideration of higher order variations in the performance index in algorithm synthesis. Suppose that the second variation, $\delta m' \frac{\delta^2 J}{\delta m^2} \delta m$, in equation 17 is considered and the variation, δJ , is required to vanish (thus satisfying the first necessary condition of the Calculus of Variations; ref. 12). Then

$$2A'(e + A\delta m) = 0 \quad (23)$$

or

$$\delta m = -A^{-1}e \quad (24)$$

Since equation 24 is identical to equation 10, it is apparent that convergence to the optimal solution is achieved in one step. This property is characteristic of the linear optimal control problem (ref. 13). Unfortunately, the direct utilization of the second variation requires the inversion of the matrix A , which results in the computational problems associated with the direct algebraic solution described above.

Conclusions

The most significant control problems are associated with the development of a pure surface deflection actuator or, alternatively, with the construction of a practical control algorithm for use with surface load actuators. The development of surface deflection actuators is clouded by problems associated with support and mirror structural elasticity. Load-actuator control algorithm construction, on the other hand, is hampered by the large dimensionality of the multivariable controller. The application of the *optimal control theory* may offer a feasible load-actuator algorithm if satisfactory convergence rates can be achieved. Additional careful analysis is required to evaluate the effect of sensor and actuator errors on system performance.

References

1. Butkovskii, A. G.; Lerner, A. Ya.: Optimum Control of Systems with Distributed Parameters. *Avtomatika i Telemekhanika*, vol. 21, no. 6, 1960, pp. 682-691.
2. Butkovskii, A. G.; Lerner, A. Ya.: Optimum Control Systems with Distributed Parameters. *Doklady Akademii Nauk SSSR*, vol. 134, no. 4, October 1960, pp. 778-781.
3. Butkovskii, A. G.: Optimum Processes in Systems with Distributed Parameters. *Avtomatika i Telemekhanika*, vol. 22, no. 1, January 1961, pp. 17-26.
4. Butkovskii, A. G.: Some Approximate Methods for Solving Problems of Control of Distributed

- Parameter Systems. *Avtomatika i Telemekhanika*, vol. 22, no. 12, December 1961, pp. 1565-1575.
5. Butkovskii, A. G.: The Maximum Principle for Optimum Systems with Distributed Parameters. *Avtomatika i Telemekhanika*, vol. 22, no. 10, October 1961, pp. 1288-1301.
 6. Erzberger, H.: An Approach to the Control of Distributed Parameter Systems. Ph.D. Thesis, Cornell University, 1955.
 7. Crane, R., Jr.: An Experimental Twenty-Inch Segmented Active Mirror. *IEEE Transactions on Aerospace and Electronic Systems*, March 1967.
 8. Creedon, J.; Robertson, H.: Evaluation of Multi-point Interaction in the Design of a Thin Diffraction Limited Active Mirror. *IEEE Transactions on Aerospace and Electronic Systems*, March 1967.
 9. Koopmans, T. C., ed.: *Activity Analysis of Production and Allocation*. Cowles Commission, University of Chicago, 1951.
 10. Bellman, R.: *Dynamic Programming*. Princeton University Press, 1957.
 11. Ladd, H.: A Unified Theory for Constrained Minimization in the Hilbert Space. Ph.D. Thesis, MIT, 1968.
 12. Gelfand and Fomin: *Calculus of Variations*. Prentice Hall, 1963.
 13. Merriam, C. W., III: A Computational Method for Feedback Control Optimization. *Information and Control*, No. 8, 1965.

Some Optical Systems for a Spaceborne Telescope

Abe Offner
The Perkin-Elmer Corporation

N70-36719

In choosing a form for a space telescope, we can make use of the knowledge and experience gained from the long history of astronomical telescopes. Since, however, each successful design is a compromise in which the limitations imposed by its environment and mode of operation are taken into account, it is useful to reexamine the candidate optical systems for attaining the goals of the National Aeronautics and Space Administration. Following Münch (ref. 1), we assume that a diffraction-limited guidance field of 3 arc minutes will satisfy all the guidance requirements and will also be sufficient for most high-resolution astronomical programs with a 3-meter aperture telescope.

Before comparing optical systems, it is necessary to define the term "diffraction-limited" more precisely. In absence of aberration, a system with an unobscured, unapodized, circular aperture forms an image of a star that consists of a central disc surrounded by the well-known ring pattern in which 84 percent of the energy is within the first dark ring. Small amounts of aberration reduce the proportion of the energy within the first dark ring of the diffraction pattern without affecting its diameter. Because central obscuration has a similar influence on the diffraction pattern, it may be treated as an aberration.

Historically, a system has been called "diffraction-limited" if the wavefront produced by it, when forming the image of a star, departs by no more than one-fourth the wavelength, λ , of the image-forming light from a reference sphere that approximates it most closely. In the case of spherical aberration, this results in a decrease of 20 percent in the

normalized intensity at the diffraction focus. For other aberrations, the $\lambda/4$ criterion results in values of the normalized intensity (or Strehl ratio), which may differ appreciably from 0.8. For this reason, a criterion based upon the value of the Strehl ratio has been proposed by Maréchal (ref. 2). For diffraction patterns formed by unobscured apertures in which the radius of the first dark ring is constant, the relative energy within the first dark ring is closely approximated by 84 percent of the Strehl ratio so that an equivalent to Maréchal's criteria for unobscured apertures is obtained by substituting for the Strehl ratio the normalized relative energy within the first dark ring (i.e., $1/0.84$ times the relative energy).

The advantage of this criterion is that the effects of obscuration as well as aberration, figure, and the like can be taken into account. A diffraction-limited system can now be defined as one in which the normalized relative energy within the first dark ring of the diffraction pattern of the image of a star formed by the system is greater than some number, say 0.8. This value, which we may call NRE, corresponds quite closely to the so-called Rayleigh criterion of $\lambda/4$ in the case of spherical aberration and coma. Since the reduction in the relative energy within the first dark ring is proportional to the mean square of the wave aberration, a reasonable tolerance for the residual amounts of these aberrations in a design is $\lambda/8$, which uses up one-fourth of the system tolerance.

A system with obvious advantages from the point of view of manufacture, testing, and alignment consists of a single spherical mirror with a detector at its focus. If we choose a

sufficiently large focal length for the mirror, it forms diffraction-limited images on a spherical surface. The f-number, N , and diameter, D , corresponding to $\lambda/8$ spherical aberration (or a loss of 5 percent of the relative energy inside the first dark ring) is given by the expression

$$N = \frac{D^{1/3}}{(256\lambda)^{1/3}} \quad (1)$$

At $\lambda = 5 \times 10^{-7}$ meter, $N = 20 D^{1/3}$ so that for $D = 3$ meters, $N = 29$. (Allowing a loss of 20 percent of the relative energy in the central disc would reduce N to 23.) An $f/29$ system has a resolving power of about 60 cycles per millimeter in the visual region of the spectrum and is thus suited to the capabilities of likely detectors; however, the distance from the mirror to the focal plane of the system is 87 meters. Although such a length is prohibitive for an earth-based telescope, this is not necessarily true in space. The addition of a small Newtonian diagonal to this system would cause negligible obscuration (less than 10 percent for a 3-minute field). The diagonal could be tilted for fine guidance. The advantages of the availability of a wider-than-minimal field for unusual experiments, minimal alignment problems, low obscuration ratio, and ease of baffling make this a very strong candidate for a diffraction-limited, 3-meter space telescope. The costs and probability of success of all other candidate systems should be compared with those of this simple system.

A shorter optical system can be achieved by substituting a paraboloidal mirror for the spherical one. In this case, the only aberration of importance for the small required field is coma. The simifield angle, θ , at which the coma of a paraboloid results in a wavefront error of $\lambda/8$, is given by the expression

$$\theta = 8N^2 (\lambda/D) \quad (2)$$

To achieve $2\theta = 3$ minutes at $\lambda = 5 \times 10^{-7}$ meter and $D = 3$ meters requires $N = 18.4$. If the requirements are relaxed to allow at the edge of the guidance field an NRE of 0.8 due to the inherent coma of the

primary mirror, then $N = 13$. The single mirror system in which the mirror is paraboloidal retains many of the advantages of the single spherical mirror. The field can be made shorter, but this results in the requirement of a detector with greater resolving power. While the diffraction-limited field of the spherical mirror can be extended appreciably above 3 minutes, this cannot be done in the case of the paraboloid mirror without adding optical elements.

In a two-mirror optical system, the advantages of a short physical length and a long equivalent focal length can be simultaneously achieved in the well-known Cassegrain and Gregorian arrangements. Such systems can be sufficiently well corrected so that over a 3-minute field the loss in the NRE due to aberrations is negligible. This imagery is achieved if two mirrors of proper figure are maintained at the proper separation and are aligned so that their axes are coincident. Tolerances for departures from the nominal situation can be obtained in terms of the amount by which they reduce the proportion of the energy in the central disc. These tolerances are functions primarily of the f-number of the primary mirror. We have computed them (see Appendix A) for a Cassegrain system in which the final image is at the primary mirror so that the separation, d , between the two mirrors is also the back focus. No plausible systems of this type have tolerances that differ significantly from those calculated.

Since a hyperboloidal mirror forms an aberration-free image of a (virtual) point object at its geometrical near focus, a misalignment of the axes of the primary and secondary mirrors has no effect on the axial imagery at the Cassegrain focus, provided that the focus of the primary mirror is at the (geometric) focus of the secondary hyperboloid (fig. 1). In the case of off-axis aberrations, a difference in the compensation between primary and secondary mirror contributions is introduced by the angle between the two image surfaces at the virtual image. For an $f/1$ primary mirror and a 2-degree angle between the primary and secondary mirror axes, the change in coma at the edge of a 3-minute total field is $\lambda/16$ at $\lambda = 5 \times 10^{-7}$

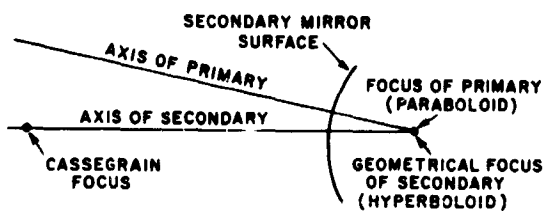


Figure 1. Permissible misalignment of mirror axes in Cassegrain telescope.

meter and $D = 3$ meters. Thus, the tolerances on decentration, tilt, and separation of the two mirrors can be reduced to tolerances on the departure from coincidence of their foci if the angle between the axes of the two mirrors is reasonably small (fig. 2). (For systems, such as the Ritchie-Chrétien, in which the two foci do not coincide, these tolerances can be expressed in terms of the departure from nominal separations of the two foci.)

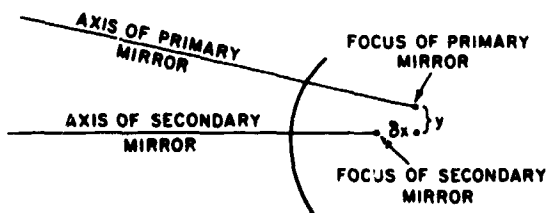


Figure 2. Parameters for mirror-positioning tolerances.

A longitudinal separation, δx_t , of the foci of the primary and secondary mirrors results in spherical aberration at a displaced image position. The longitudinal tolerance, δx_t , corresponding to a maximum departure, W_t , from the closest sphere is derived in Appendix A. In terms of the secondary magnification, m , and Cassegrain f-number, N , it is given by the expression

$$\delta x_t = \frac{512 N^4}{m^2(m^2-1)} W_t \quad (3)$$

For values of m for which $m^2 \gg 1$,

$$\delta x_t = 512 N_p^4 W_t \quad (4)$$

where N_p is the f-number of the primary mirror.

A lateral displacement, y , of the focus of the primary mirror from that of the secondary mirror results in coma on an image plane that is tilted by m times the angle between the axes of the two mirrors. The lateral tolerance, y , corresponding to a maximum departure, W_t , from the closest reference sphere is given by the expression

$$y_t = \frac{64 N^3}{m(m^2-1)} W_t \quad (5)$$

When $m^2 \gg 1$, this can be approximated by the expression

$$y_t = (64 N_p^3) W_t \quad (6)$$

For an $f/2$ primary mirror and $W_t = \lambda/8$ at $\lambda = 5 \times 10^{-7}$ meter, $\delta x_t = 0.512$ millimeter for $m^2 \gg 1$. The same system has a lateral tolerance $y_t = 0.032$ millimeter. The value of the lateral tolerance is proportional to the cube of the primary mirror f-number. The lateral tolerance on a system with an $f/1$ primary mirror is thus 0.004 millimeter. Increasing the value of W_t to a value that reduces the NRE to 0.8 as a result of this misalignment alone merely doubles this tolerance. Since the reduction in length achieved by a two-mirror system is approximately N_p/N , large reductions in length are accompanied by very tight tolerances in the permissible lateral separations of the foci of the two mirrors.

A further restriction in the design of a two-mirror system is the need to keep the obscuration ratio low. Examination of figure 3 shows that for an obscuring aperture whose diameter is r in units of the system diameter, the NRE is closely approximated by the expression for the relative intensity at the center of the diffraction pattern

$$\text{NRE} = 1 - r^2 (2 - r^2) \approx 1 - 1.8r^2 \quad (7)$$

It can be seen that, in terms of NRE, the effect of an obscuration ratio of 1 to 6 is the same as that of one-eighth wave of third-order spherical aberration. Although it is not difficult to keep the obscuration by the secondary mirror below this figure, the requirements for baffling in the presence of the

earth, sun, and moon may either increase the obscuration ratio or restrict the use of the system.

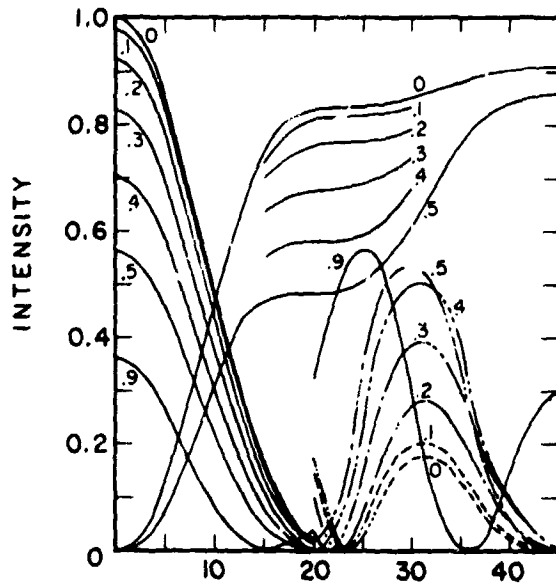


Figure 3. Energy distribution in diffraction pattern corresponding to apertures with central obscuration.

Appendix A

The following are the computations of positioning tolerances for a Cassegrain system whose back focus is at the primary mirror.

Longitudinal Tolerance

The hyperbola, *S*, of figure A-1 is the intersection of the hyperboloidal secondary mirror with a plane containing the axes of the hyperbola. Its foci are at *F* and *F'*, and its center is at *C*. In terms of rectangular coordinates with origin, *O*, at the pole of the hyperbola and the *x*-axis along the optical axis, the equation of the hyperbola is

$$\frac{(x+a)^2}{a^2} - \frac{y^2}{ar} = 1 \quad (\text{A1})$$

where *a* is the distance *CO* and *r* is the radius of curvature of the hyperbola at its pole. Solving equation (A1) for *x*, we have

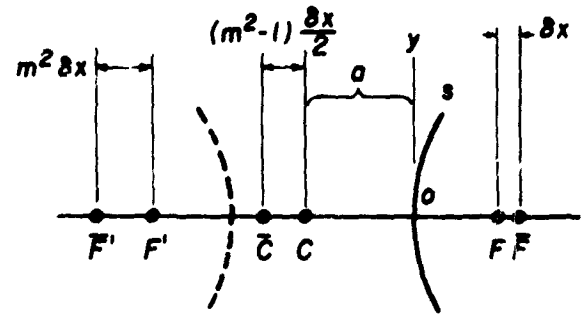


Figure A1. Geometry for computing the effect of longitudinal separation of foci.

$$x = \frac{y^2}{2r} - \frac{y^4}{8ar^2} + 0 \left(\frac{y^6}{a^2 r^3} \right) \quad (\text{A2})$$

When the primary focus is at *F*, the secondary mirror forms an image at *F'* at the magnification *m*. If the primary focus is displaced a distance, δx , to \bar{F} , the secondary image is formed at \bar{F}' , which is at the distance $m^2 \delta x$ from *F*. A hyperboloidal mirror with pole at *O* and foci at \bar{F} and \bar{F}' would form an aberration-free image at \bar{F}' . Using barred variables to refer to the correct hyperbola, we can describe it by an expression similar to equation (A3)

$$\bar{x} = \frac{\bar{y}^2}{2r} - \frac{\bar{y}^4}{8a\bar{r}^2} \quad (\text{A3})$$

where the *r* is not barred because it must have the same value for the two hyperbolae. Since \bar{a} is the distance $\bar{C}O$, we have

$$\bar{a} = a + (m^2 - 1) \delta x / 2 \quad (\text{A4})$$

For $\bar{y} = y$, we have from equations (A2), (A3), and (A4)

$$x - \bar{x} = \frac{y^4}{8r^2} \left(\frac{1}{a} - \frac{1}{\bar{a}} \right) \simeq \frac{y^4 (m^2 - 1) \delta x}{16 a^2 r^2} \quad (\text{A5})$$

where we have made the approximation $a\bar{a} = a^2$. For the Cassegrain image at the primary mirror, the separation, *d*, between the two mirrors is equal to the back focal length $\bar{F}O$. From the properties of the hyperbola,

$$d = \sqrt{a^2 + ar} + a = m \left[\sqrt{a^2 + ar} - a \right] \quad (\text{A6})$$

Hence

$$d^2/m = ar \quad (\text{A7})$$

For the value of y at the edge of the mirror, the f -number, N , of the Cassegrain system is given by

$$N = d/2y \quad (\text{A8})$$

Making the substitutions from equations (A7) and (A8) in equation (A5), we obtain the relation

$$x - \bar{x} = \frac{m^2(m^2-1)}{256 N^4} \delta x \quad (\text{A9})$$

This is the departure of the edge of the actual hyperboloid from the surface that would give aberration-free imagery. Since the image defect is third-order spherical aberration, the departure of the aberrated wave from the nearest sphere is given by the expression

$$W = \frac{2(x-\bar{x})^2}{4} = \frac{m^2(m^2-1)}{512 N^4} \delta x^2 \quad (\text{A10})$$

The tolerance on longitudinal separation of the foci of the two mirrors, δx_t , can then be related to the tolerance on the resultant wave aberration, W_t , by the expression

$$\delta x_t = \frac{512 N^4}{m^2(m^2-1)} W_t \quad (\text{A11})$$

For $m^2 \gg 1$, this reduces to the expression

$$\delta x_t = 512 N_p^4 W_t \quad (\text{A12})$$

where N_p is the f -number of the primary mirror.

Lateral Tolerance

For moderate angles between the axes of the two mirrors, the image deterioration caused by either lateral shift or tilt is proportional to the resultant lateral displacement, y , of the primary focus from the secondary focus (fig. 2). The only significant aberration introduced by a small displacement is the coma of the hyperboloid for an object point at this height. For Cassegrain f -number, N , the maximum departure, W , of the comatic wavefront from the best-fitting reference sphere is given by the expression

$$W = \frac{m(m^2-1)y}{64 N^3} \quad (\text{A13})$$

The tolerance on the lateral separation of the foci of the two mirrors, y_t , is related to the tolerance on the resultant wave aberration, W_t , by the expression

$$y_t = \frac{64 N^3 W_t}{m(m^2-1)} \quad (\text{A14})$$

For $m^2 \gg 1$, this can be approximated by the expression

$$y_t = (64 N_p^3) W_t \quad (\text{A15})$$

If we set equal tolerances on W_t due to longitudinal and lateral separations of the foci of the two mirrors,

$$y_t = \delta x_t / 8 N_p \quad (\text{A16})$$

References

1. Münch, G.: Space Research, No. 172, National Academy of Sciences - National Research Council, Washington, D. C., 1961.
2. Maréchal, A.: Rev. d'Optique, vol. 26, no. 257, 1947.

PRECEDING PAGE BLANK NOT FILMED.

N70-36720

Field Correctors for Reflecting Telescopes

Daniel H. Schulte
Itek Corporation

Introduction

In spaceborne astronomy programs, the use of reflecting or catadioptric telescopes will be almost universal because of their intrinsic achromatism and resolving-power capabilities. Since many of the earlier programs will be of a survey nature, the use of instruments having a sufficiently large field-of-view is also particularly desirable to make the best use of the sometimes limited time in orbit. In this paper, we will discuss various alternatives to achieve a large field for the cases of one-, two-, and three-mirror systems.

One-Mirror Systems

The single parabolic mirror is seriously afflicted with coma; its magnitude as a function of off-axis distance and f-ratio can be computed by the rule of thumb:

$$\text{length of coma blur per minute off-axis} \\ = \frac{10 \text{ seconds of arc}}{(\text{f-ratio})^2}$$

Thus, we see that the 200-inch, f/3.3 telescope shows 1 second of arc of coma at 1 minute of arc off-axis. Because this is a large amount even for an instrument limited by atmospheric seeing, a series of correcting lenses was designed by F. E. Ross (ref. 1) to cancel the third-order coma contribution of the primary and the partly balanced astigmatism and higher-order aberrations. The Ross corrector generally used a close-spaced positive-negative pair. Since, to the on axis bundle, the lenses resemble a thick plane-parallel plate, some means are needed to

remove the spherical aberration thus introduced. Ross used a thin meniscus farther up the beam while Rosin (ref. 2) proposed slight additional aspherization of the primary mirror, which has no effect on its coma contribution. Recently, Baranne, Kohler, and Wynne (refs. 3, 4, 5) have published more complex designs for spherical-element correctors that increase the seeing-limited field to more than 1/2-degree diameter for f/2.5 - f/3.0 primaries. Figure 1 is a Wynne corrector for the f/2.8 prime focus of the Kitt Peak 150-inch telescope. Figure 2 is a design by R. Wientzen of a corrector for an f/2.5 parabola being built at Itek Corporation. Gascoigne, Köhler, Meinel, Schulte, and Wynne (refs. 6, 4, 7, 8, 9) have also investigated the use of aspheric-surfaced lenses in the converging beam. No information is available at present on the difficulties of fabrication and testing these systems although several of them are to be incorporated in the various over-100-inch telescopes now under construction. The large overall length of a prime focus system places it at a disadvantage for space astronomy, but it could be of value for programs requiring fast f-ratios and small central obstructions.

Two-Mirror Systems

Spherical aberration and coma can be simultaneously corrected with the use of two aspheric mirrors. This is the family of aplanatic telescopes of which the Ritchey-Chretien is the most well-known member. The other members of the family are shown in figure 3, which is adapted from a paper by J. Landi-Dessy (ref. 10). His notation is the same as Linfoot, who also investigated the

problem in a general way (ref. 11). The ξ -coordinate is the ratio of secondary radius to primary radius, while η is the ratio of the height of an axial ray at the two respective mirrors. By using these dimensionless parameters, it is possible to locate the whole domain of two-mirror systems on this diagram. The "virtual" regions are those where either the radius of the secondary or its location (or both, as in the upper left quadrant) is such that the final beam is divergent. Since the

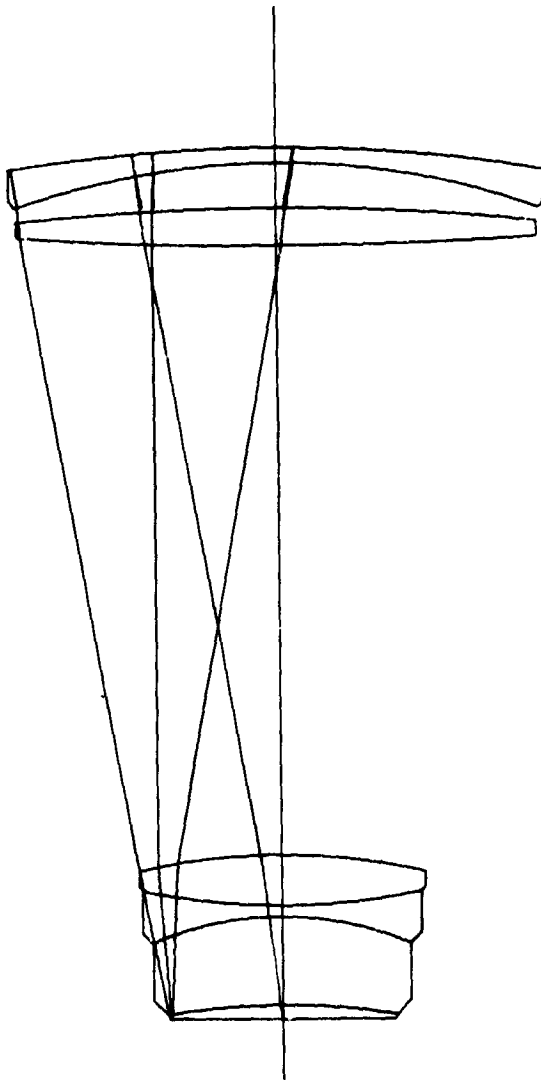


Figure 1. Corrector for $f/2.8$ Ritchey-Chrétien primary.

Schwartzchild systems have concave secondaries located inside the focal point of the primary mirror, real images are always formed; and this quadrant is fully populated. All of the systems are correctable for spherical aberration and coma by aspherizing, as previously mentioned. In addition, there exist loci in all three quadrants on which one of the other third-order aberrations is also corrected. There are distortion-free cases in all three quadrants, but there are no Cassegrain or Gregorian configurations for which either astigmatism or field curvature is corrected. Schwartzschild systems exist which are corrected for distortion, field curvature (the "Classical Schwartzschild") or astigmatism ("Couder anastigmat"). Because the mirror separation is greater than the equivalent focal length, Schwartzschild telescopes have been little used except in small versions (as for the Telescope program).

One other application has been published by Epstein (ref. 12). This is described as an off-axis reflecting Schmidt camera, but it can also be thought of as a degenerate case of a Schwartzschild system with $\xi = 0$; i.e., a flat but aspheric primary. This primary, or more familiarly the reflecting Schmidt plate, is located at the center of curvature of the spherical "secondary." This follows the rule for the more general Couder anastigmat (mirror separation equals 2 times equivalent focal length). To avoid complete self-obstruction, this system must be used far enough off-axis for the incoming bundle to clear the spherical mirror completely on its way to the aspheric flat. The astigmatism introduced by the obliquity of the aspheric is small enough to permit use of this arrangement to about $f/4$. For faster systems, it may be necessary to use nonrotationally-symmetric aspherics to remedy the obliquity effect.

Two-Mirror Field-Corrected Systems

If the instrument-package configuration does not permit use of one of the "self-correcting" two-mirror systems, refracting field-correcting systems can be used with

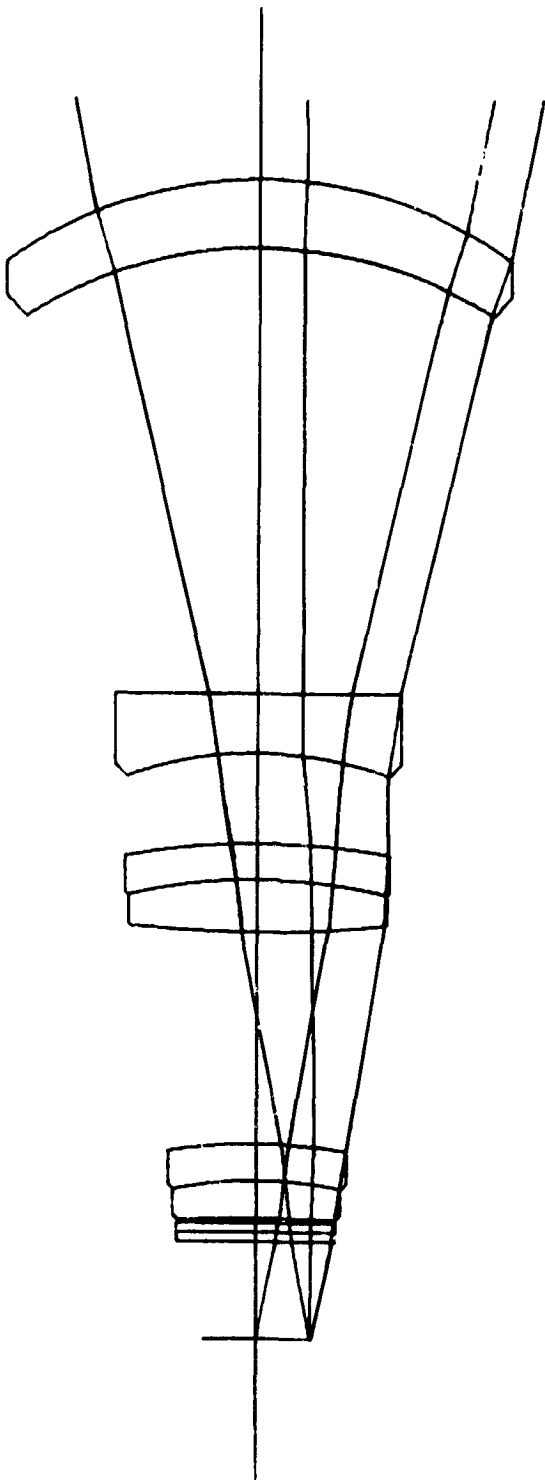


Figure 2. Corrector for $f/2.5$ parabola.

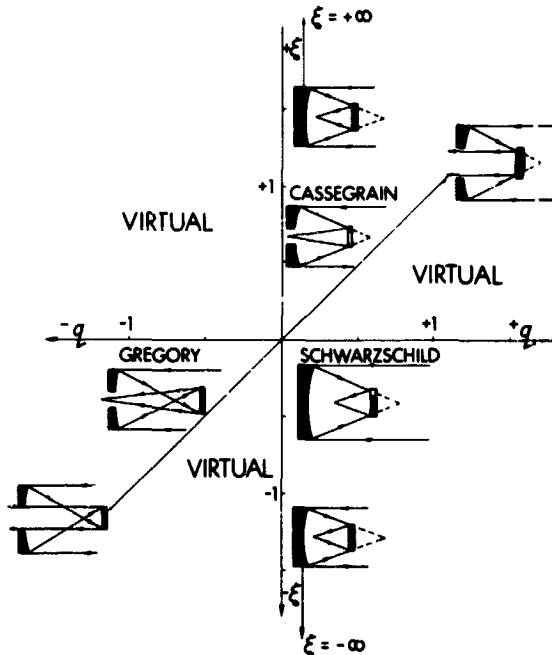


Figure 3. ξ - q diagram of two-mirror systems.

more arbitrarily selected two-mirror inputs, the favorite being Cassegrains. In general, Gregorians compare poorly with Cassegrains because the former have greater total length for the same focal configuration. Their field curvature tends to be greater than for equivalent Cassegrains; it is also opposite in sign, which could be an advantage in special circumstances involving relay lenses.

The remainder of this section will be concerned with the Ritchey-Chretien variation of Cassegrain systems. Landi-Dessy, Puch, and Simon (ref. 13) have recently published a paper on the third-order aberrations of corrected Cassegrains (assuming aspheric corrector plates), which can be helpful in finding suitable starting points for a design. One-, two-, and three-lens correctors have been designed by Köhler, Rosin, Wilson, and Wynne (refs. 4, 14, 15, 5). Wilson points out that better performance can be obtained by designing the system as a whole; i.e., by allowing the mirror surfaces to depart slightly from the exact Ritchey-Chretien solution to facilitate higher order aberration balancing. This was also discussed by

Gascoigne and Schulte (refs. 6 and 16) in the case of aspheric field correctors. For diffraction-limited performance over fields 1 degree and more in diameter, this procedure becomes a necessity. Figures 4 and 5 show the total layout and the correcting lenses for such a system for a $1\frac{1}{2}$ -degree-diameter, distortion-free, flat field. Four elements are generally sufficient for telescopes of this type if there is complete freedom in selecting the type of glass. This may lead to objectionable ultraviolet absorption if special glasses are used. One way to avoid this difficulty (or, if more important, to reduce the number of lens elements needed) is to allow the presence of some field curvature and/or distortion, neither of which degrades the resolution. The corrector can be nearly zero power, thereby allowing the use of normal glasses without introducing chromatic aberration such as lateral color and secondary longitudinal color.

Figures 6 and 7 show a telescope designed for a somewhat unusual space-astronomy application. The holes drilled through the corrector group allow the formation of an on-axis image with the ultraviolet unabsorbed by glass; this feeds an ultraviolet spectrophotometer. For offset guiding, two reference stars must also be observed within a 15-minute radius of the object of interest. Although the spectral range can be more limited, the image size of the reference stars must be comparable to that of the on-axis image. In addition, it is desirable to have telecentricity; i.e., the central ray of each off-axis bundle should be nearly parallel to the axis. This is because the reference stars are individually reimaged by high magnification, periscope-like systems; thus, varying inclination of the off-axis bundles would give rise to heavy vignetting as they traveled through the long periscopes. In addition, a flat field is required for the outer region so that the longitudinal positions of the final images of the guide stars do not change with distance off-axis. It should be apparent from the lens drawing that the telecentric requirement places great demands on the field group; four elements are none too many, even for only a $1/2$ -degree field diameter. This $f/8.5$

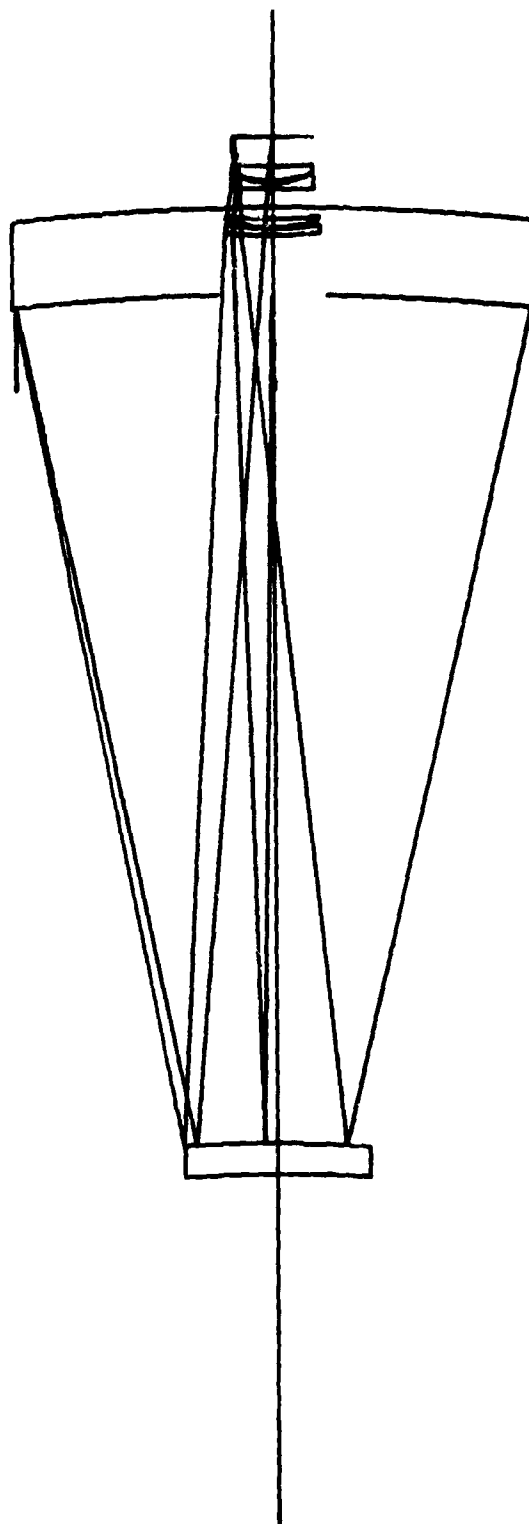


Figure 4. $F/2.5-f/6.0$ corrected Cassegrain.

system has an $f/3$ primary; the design difficulties multiply if an $f/2$ primary is used. Correction of the larger intrinsic field

curvature is at cross-purposes with making the chief rays parallel to the axis.

Three-Mirror Systems

The family of three-mirror systems cannot be plotted in two dimensions; hence, attention must be confined to one or two special cases of interest while realizing that many possible solutions probably exist for any given set of requirements.

Recently, Baker (ref. 17) proposed what he called a "two-mirror corrector" to use with existing parabolic mirrors. The converging beam from the parabola is recollimated by a parabolic convex mirror. A spherical concave mirror with its center of curvature at the vertex of the convex mirror then reimages the parallel bundle. If the convex mirror is made slightly nonparabolic to cancel the spherical aberration of the concave mirror, the final image is, to a high degree, free from spherical aberration, coma, and astigmatism. In addition, the curvature of the three mirrors can be distributed in a way to yield a flat field. Figure 8 shows a representative Baker three-mirror system. Slight additional aspheric touchup on all three mirrors, plus small departures from the exact spacing relationships implied above, brings about the balancing of the higher-order aberrations so that fields of 2 degrees or more in diameter can be realized with exceedingly fine resolution. For the design shown in figure 8, the image size is less than 1/100-second-of-arc diameter at 33 minutes off-axis.

Again, as in the case of corrected Cassegrains, three-mirror telescopes that fit a desired configuration but that are not "naturally" corrected for field aberrations (as the Baker reflectors are) can nevertheless benefit from field correctors. The latter tend to be less complex because of the help provided by the third available aspheric mirror. In fact, often the only significant aberration to be corrected by lenses is the field curvature contributed by the mirrors. Figure 9 is such a design; this $f/6$ system was made quite short by the use of a fast primary. The third mirror near the vertex of the primary is a basically

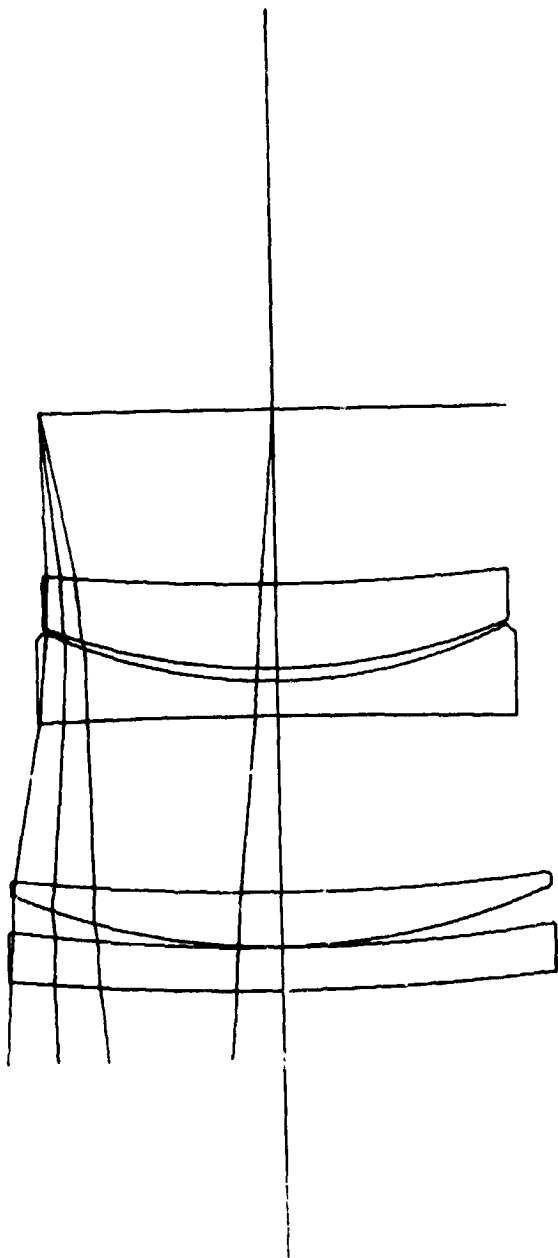


Figure 5. Field-correcting lenses for $f/2.5 - f/6.0$ Cassegrain.

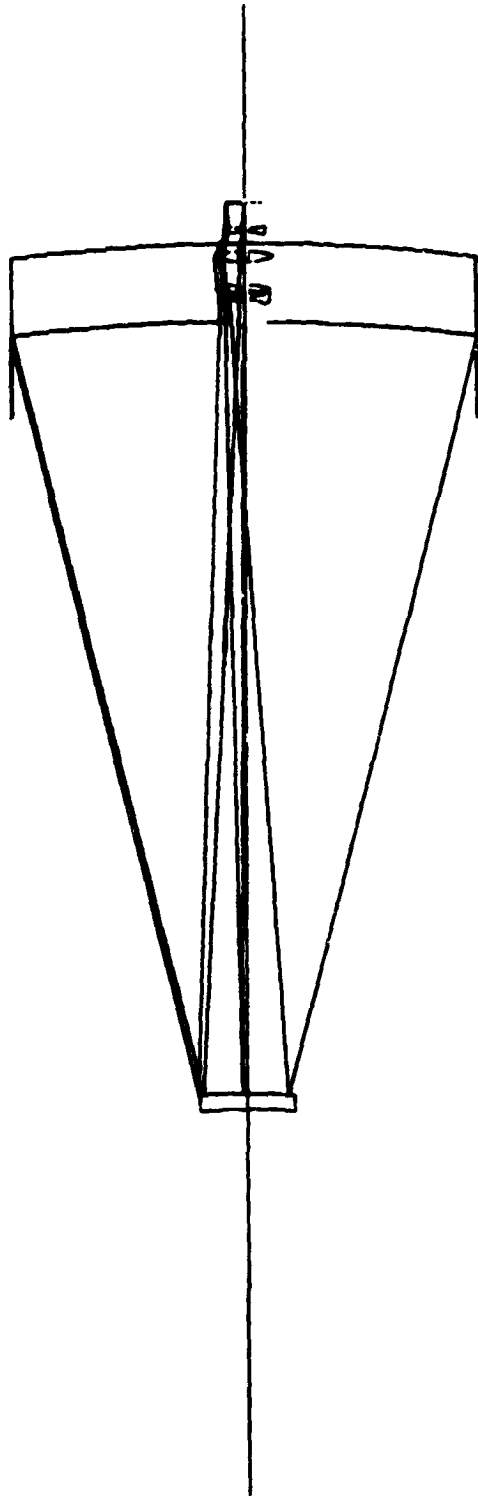


Figure 6. $F/3.0 - f/8.5$ telecentric Cassegrain.

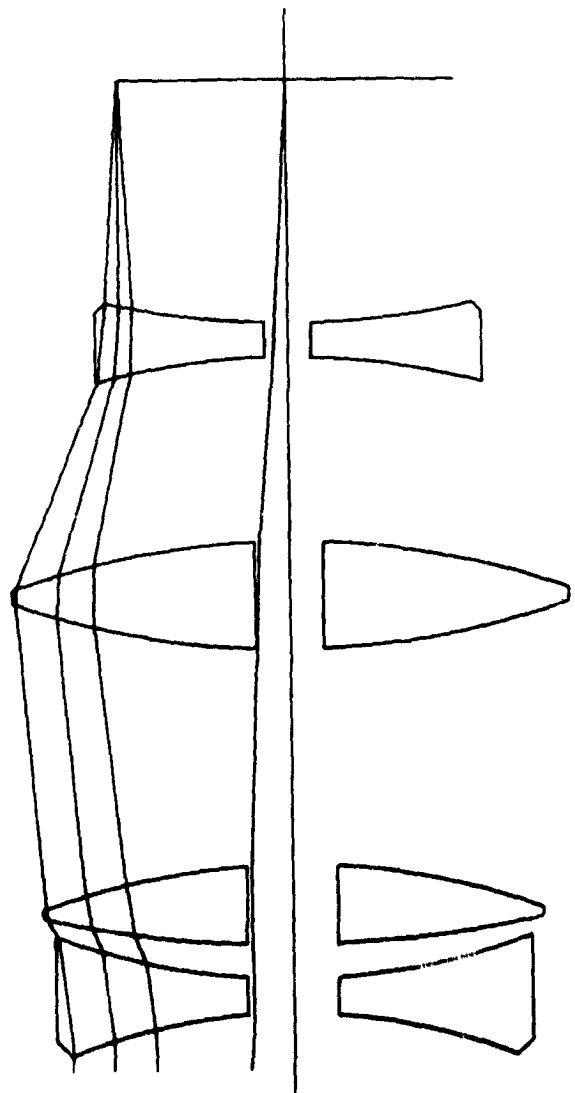


Figure 7. Field corrector for telecentric Cassegrain.
There is no glass in the path of the on-axis bundle.

flat aspheric. Only two lenses were needed (mostly to flatten the field) for a 1-degree-diameter field.

In this discussion, it was possible to mention only briefly a few of the configurations that may be useful in space astronomy. Any detailed study must be made with the astronomical requirements in mind, as well as the vehicle to be used, and also the relative difficulties of fabrication and alignment.

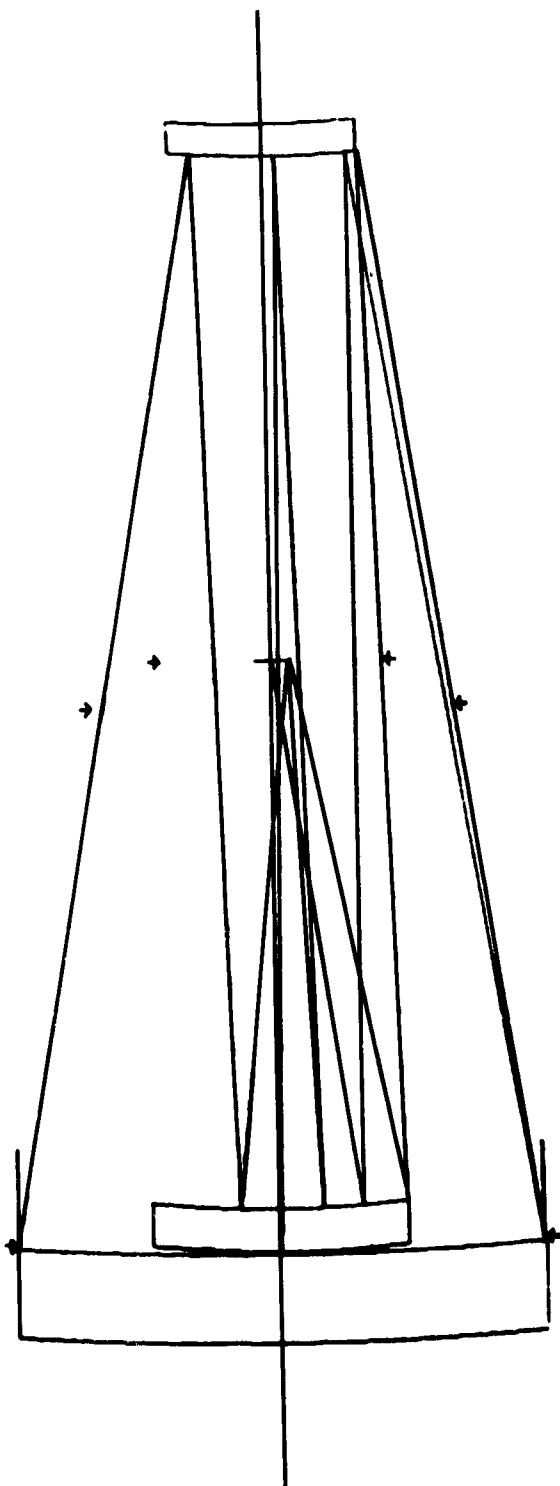


Figure 8. $F/9 - f/10$ Baker three-mirror telescope.

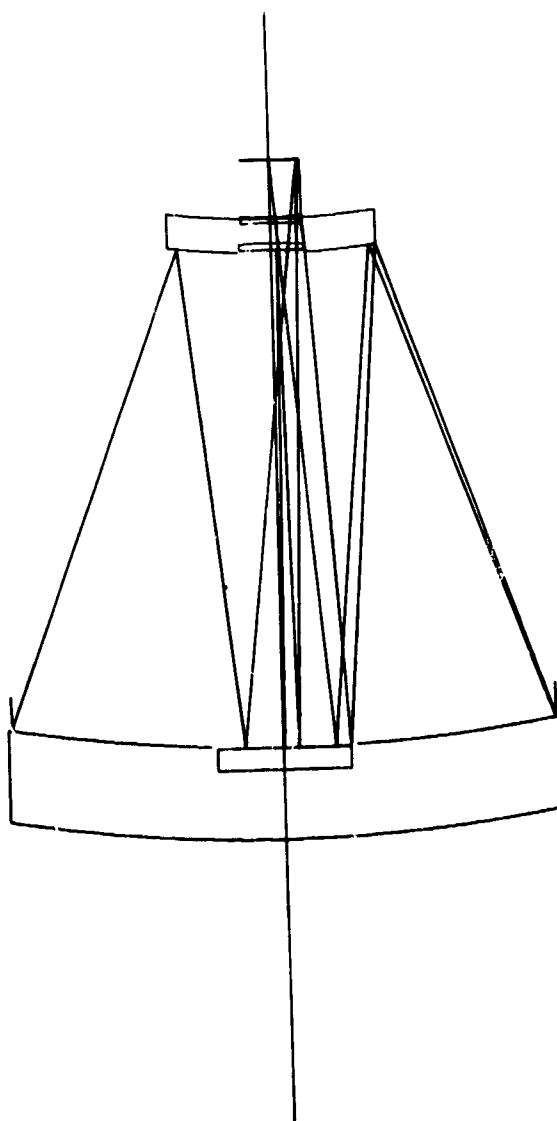


Figure 9. $F/1.4 - f/6.0$ corrected three-mirror system.

References

1. Ross, F. E.: *Astrophysics Journal*, vol. 81, no. 156, 1935.
2. Rosin, S.: *Journal of the Optical Society of America*, vol. 51, no. 331, 1961.
3. Baranne, A.: *Reports to the European Southern Observatory Committee, 1964 & 1965*, unpublished.
4. Köhler, H.: *Applied Optics*, vol. 7, no. 241, 1968.
5. Wynne, C. G.: *Applied Optics*, vol. 4, no. 1185, 1965.
6. Gascoigne, S. C. B.: *The Observatory*, vol. 85, no. 79, 1965.
7. Meinel, A. B.: *Astrophysics Journal*, vol. 118, no. 335, 1953.
8. Schulte, D.: *Applied Optics*, vol. 5, no. 313, 1966.
9. Wynne, C. G.: *Proc. Phys. Soc.*, vol. B62, no. 772, London, 1949.
10. Landi-Dessy, J.; Puch, A.: *Mem. Soc. Astr. Ital.*, vol. 37, no. 657, 1966.
11. Linfoot, E. H.: *Recent Advances in Optics*. Clarendon Press, Oxford, 1956.
12. Epstein, L. C.: *Sky & Telescope*, vol. 33, no. 204, 1967.
13. Landi-Dessy, J.; Puch, A.; Simon, J. M.: *Mem. Soc. Astr. Ital.*, vol. 38, no. 1, 1967.
14. Rosin, S.: *Applied Optics*, vol. 5, no. 675, 1966.
15. Wilson, R. N.: *Applied Optics*, vol. 7, no. 253, 1968.
16. Schulte, D.: *Applied Optics*, vol. 5, no. 309, 1966.
17. Baker, J.: *On Improving the Effectiveness of Large Telescopes*. Presentation at meeting of the National Academy of Science, Seattle, 1966.

Behavior of Structural Joints and Assemblies Under Thermal Environment

Rondal G. Crawford

NASA George C. Marshall Space Flight Center

N70-36721

Introduction

The basis of this paper is the work performed by the General Electric Company for NASA in their studies of design guidelines for sterilization of spacecraft structures, design criteria for typical planetary spacecraft to be sterilized by heating, and design criteria for typical Mars landing capsules requiring sterilization. The purpose of this work was to establish guidelines for the design of planetary spacecraft subject to heat sterilization.

Analytical and test phases on typical spacecraft structures were conducted with the primary emphasis placed on the response of structural and mechanical components to elevated temperatures. The range of environments investigated extended from 25° to 150°C, and the heat-soak duration extended up to 64 hours.

The portions of this work covered in this paper are: (1) thermostructural test of a typical planetary spacecraft, (2) an alignment test to determine the magnitude of permanent distortions during testing of the typical planetary spacecraft, and (3) a study of structural joints.

Thermostructural Vehicle Tests

The thermostructural vehicle tests were divided into two groups: the Vehicle-A series and the Vehicle-B series.

Test Objectives

The primary objective of these tests was to determine the effect of a thermal sterilizing environment on a typical 200-pound planetary lander.

It is important to know the time required to reach sterilizing temperatures (approximately 125°C) and the time to cool to room temperature. These times will vary with vehicle configurations. Determination of heating and cooling times for the test vehicle was therefore a major objective of the test. In addition, the test determined the relationship between analytically predicted and experimentally measured stresses and temperatures at critical locations. The parameters that were measured and compared included thermal gradients, thermal rise times, and stresses. The comparison with analytically predicted values was an integral part of this test, and no test data were considered before analytical predictions were completed.

Test Vehicle

Selection of a test vehicle was based upon the specific requirements (1) to determine the length of the heating and cooling transient times and (2) to compare predicted thermal and structural analyses with test results.

Two test vehicles were assembled from major elements of a General Electric reentry vehicle. The differences between the two vehicles were mainly in the degree of complexity and assembly control. Vehicle A was a complex vehicle used to study the effects of different heating methods and cycles on the thermal transients and gradients in a realistic entry package. Vehicle B was a less complex vehicle that could be controlled and readily analyzed, both thermally and structurally.

Both vehicles used the same thermal shield, thrust cone, aft cover, and base plate.

The heat shield was made from General Electric ESM material with a fiberglass liner.

The major structural components of the thermostructural test vehicles are shown in figure 1, which is valid for both Vehicles A and B.

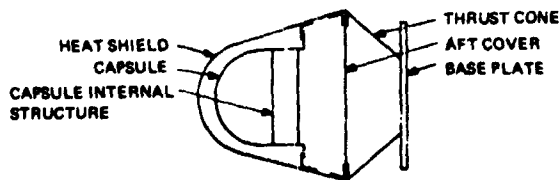


Figure 1. Thermostructural test vehicle.

Test Oven

The oven used for the tests was a GECO Model FT72. This oven is shown in figures 2 and 3.

The oven has a thermostatic control, which senses air temperature and is used to regulate the oven temperature. There are three heaters in the system that can be energized at will. If all heaters are turned off, the oven fan will operate and will recirculate air as long as the power is on at the main control. The choice of the number of heaters to be on is usually at the discretion of the operator, but these heaters can also be operated automatically.



Figure 2. Thermostructural test oven, doors closed.

Vehicle A Test

1. *Purpose.* The purposes of the Vehicle-A series of tests on the complex, densely packed vehicle were (1) to evaluate the effects of various heating methods on the transient thermal times, (2) to determine the amount of permanent distortion caused by heating, (3) to attempt to obtain meaningful data on the effect on bolt torques, and (4) to determine visually any detrimental effects on equipment and paints within the vehicle. No analysis was performed on this vehicle prior to testing.

2. *Vehicle Description.* The capsule in Vehicle A contains structure and components that were originally designed for flight in this capsule. Because these components were not designed to withstand heat sterilization, certain of them were removed to eliminate possible safety hazards. Replacements were added to maintain the thermostructural characteristics of the vehicle. Vehicle A closely resembles the actual packing density, air-flow restrictions, heat-flow paths, and thermal mass of a flight vehicle. Major elements of Vehicle A are shown in figures 4, 5, 6, and 7.

3. *Instrumentation.* Prior to assembly, Vehicle A was instrumented with 104 thermocouples, located in the oven and on the vehicle. Heat paths were monitored from the mounting plate through the mounting

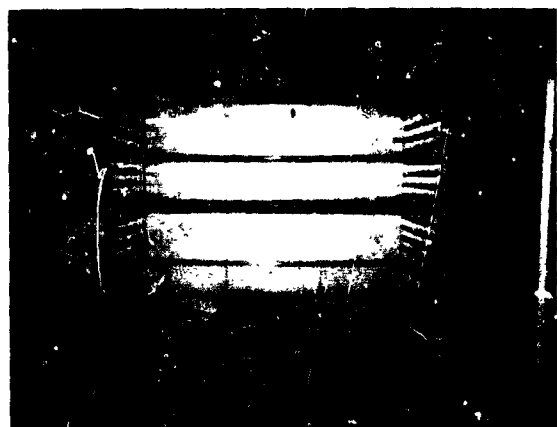


Figure 3. Thermostructural test oven, doors open.

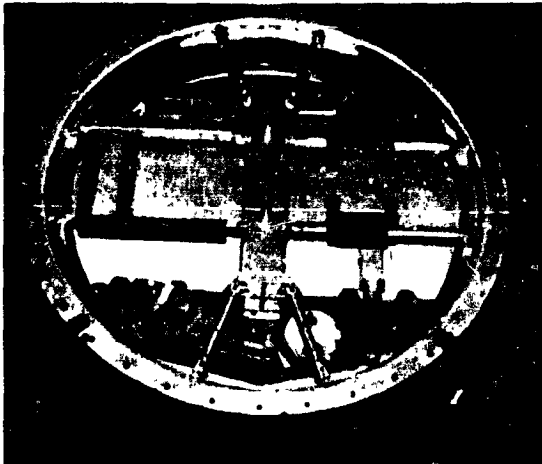


Figure 4. Capsule assembly with cover removed.

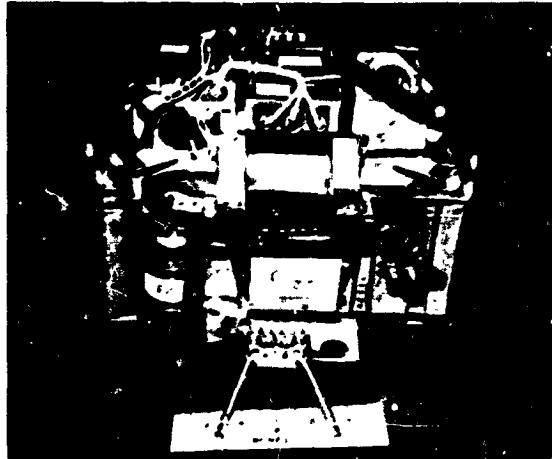


Figure 5. Capsule internal components and support structure.

brackets to the wall of the components and into the interior of the components. A complete temperature history of the components was obtained in this manner. Figure 7 shows the test vehicle installed in the oven.

4. *Test Conditions.* Four separate tests were performed on Vehicle A in order to evaluate the effects of forced heat convection. The test conditions are summarized in table 1.

For all four tests, the oven air temperature was increased from room temperature at

the rate of 2°F per minute. The upper temperature limit for Tests A-1 through A-3 was 302°F (150°C). For Test A-4, the oven air was deliberately overheated to 342°F, and the canister was permitted to heat to 325°F. The oven temperature was then gradually lowered at a variable rate such that the vehicle did not exceed 300°F.

A 9-hour temperature soak was included in the A-2 test and a 64-hour soak in the A-3 test. The soak period was defined as beginning when the coldest thermocouple reached approximately 300°F.

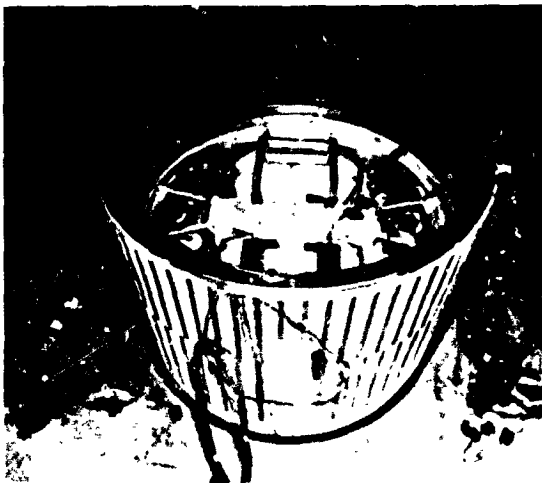


Figure 6. Capsule installed.

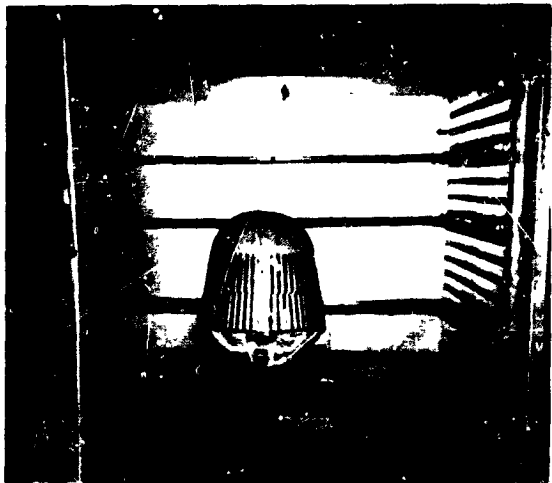


Figure 7. Vehicle A installed in oven.

Table 1. Vehicle-A Test Condition Summary

Test No.	Canister	Oven Fans	Fan Inside Canister	Fan Inside Vehicle
A-1	No	Yes	—	Yes
A-2	No	Yes	—	No
A-3	Yes	Yes	No	No
A-4	Yes	Yes	No	No

5. *Test Results.* Table 2 (ref. 1) shows a summary of the important test results for the Vehicle-A test series. It is of interest to note that the time to reach maximum temperature difference is, in the majority of cases, approximately equal to the heat-up time but increases as the forced convection devices (fans) are eliminated. This is to be expected because the presence of gas circulators improves the uniformity of heating throughout the vehicle, thus reducing large potential gradients and eliminating smaller ones.

Of the four conditions tested, the A-2 condition imposed the most severe thermal gradients on the capsule. They were caused by having the heat shield and the capsule structure at the capsule/shield interface heated quickly by the oven fans. With no air circulation (and thus no forced convection) within

the capsule, the inside portions of the structure heated up more slowly.

Vehicle B Test

1. *Purpose.* The purpose of the Vehicle-B series of tests was (1) to determine if presently accepted analysis methods are adequate for predicting temperatures and stresses due to heat sterilization, (2) to isolate the problem areas where high stresses exist and to investigate methods of reducing them, (3) to perform an optical alignment check before and after a heat-sterilization cycle to determine relative distortions between structural elements, and (4) to determine visually observable effects on the structure and components.

Prior to testing, thermostructural analyses were performed for all three test conditions to predict the temperatures and stresses produced in the vehicle during the transient and steady-state phase. No analysis was performed for the optical alignment test.

2. *Vehicle Description.* Vehicle B is shown in figure 8. The difference between Vehicles A and B is in the structure and component arrangement within the payload capsule. The internal capsule structure and

Table 2. Vehicle-A Summary of Test Results

Test Conditions	Test	Elements	Maximum Temperature Difference, ΔT ($^{\circ}F$)	Time to Reach Maximum ΔT (hr)	Time to Reach 290 $^{\circ}F$ (hr)	Time to Reach 300 $^{\circ}F$ (hr)
Oven Fans, Vehicle Fan	A1	Heat Shield and Thrust Cone	18	2	2-3/4	
		Capsule Structure	48	2	4-1/2	
		Components			4-1/2	7
Oven Fans Only, No Vehicle Fan	A2	Heat Shield and Thrust Cone	50	2	5-1/2	
		Capsule Structure	86	2-1/2	8	
		Components			8	12
Oven Fans Only Vehicle in Canister	A3	Heat Shield and Thrust Cone	58	2	8-1/2	
		Capsule Structure	61	3	14	
		Components			14	23
Oven Fans Only, Vehicle in Canister, 25 $^{\circ}F$ Canister Overheat	A4	Heat Shield and Thrust Cone	64	2-3/4	7-1/2	
		Capsule Structure	61	3	10	
		Components			10-1/2	18

component arrangement was simplified for the Vehicle B tests so that it could be more readily analyzed.

3. *Pretest Thermal Analysis.* An analysis of the transient thermal behavior of Test Vehicle B was performed, using a digital-computer heat-transfer program, to predict the temperature-time behavior of the vehicle during the heating cycle from the 20°C (70°F) initial temperature to the 150°C (302°F) temperature. Similarly, the same program was used to determine the cool-down thermal response when going from 150°C (302°F) to 21°C (70°F). Both cases were assumed to occur at a predetermined rate, which was two hours for the heating cycle and an instantaneous drop to 70°F for the cooling cycle.

4. *Thermostructural Analysis.* A complete thermostructural analysis of Test Vehicle B was performed as a part of the overall test program. The purposes of the Vehicle-B test series were: (1) a comparison of analytically and experimentally determined temperatures and stresses and (2) an experimental evaluation of the stresses likely to be encountered during thermal testing of a planetary spacecraft. The analysis was needed to pinpoint areas of high stress for proper location of strain gauges as well as to provide a comparison with test results.

Figure 9 (ref. 2) shows the vehicle breakdown for thermostructural analysis. It was subdivided into three shell portions (members 1 through 5, 6 through 12, and 13 through 15 of fig. 9) and the internal capsule structure portion (member 16). Each complete shell portion was directly analyzed by computer. The three shell portions were then joined by making rings 3 and 12, and 5 and 13, respectively, compatible with respect to radial loads and deflections at four equally spaced, circumferential points (bolt locations).

The vehicle utilized an entry shield made from GE ESM-1000 material. This is an advanced elastomeric ablation material suitable for low heat flux. It has a very low modulus of elasticity; thus, small stresses are induced in the material by temperature gradi-

ents. The shield material was bonded to a fiberglass liner. The stiffness of the elastomeric heat shield was negligible compared with that of the liner. Therefore, its effect was not included in the structural analysis although its effect on the thermal analysis was considerable.

As shown in figure 9, the shell structure was broken into separate pieces where it was joined to a ring or where a change in curvature occurred. The internal structure (member 16) was joined to the capsule ring (member 10) by using compatibility of lateral and longitudinal loads and displacements of the cross beams and the ring at the four juncture locations.

Joining two rings of dissimilar materials with a four-point attachment results in high stresses. Two such joints existed: one between the liner and the capsule (members 3 and 12) and the other between the liner and the thrust cone (members 5 and 13). Typical stress-time relations are presented in figure 10.

5. *Instrumentation.* Vehicle B was instrumented with 125 thermocouples and 42 active strain gauges. The instrumented Vehicle B is shown in figure 11.

6. *Test Conditions.* Three separate tests were performed on Vehicle B in order to evaluate the induced thermal stresses for natural and forced convective heating methods. The test conditions are summarized in table 3.

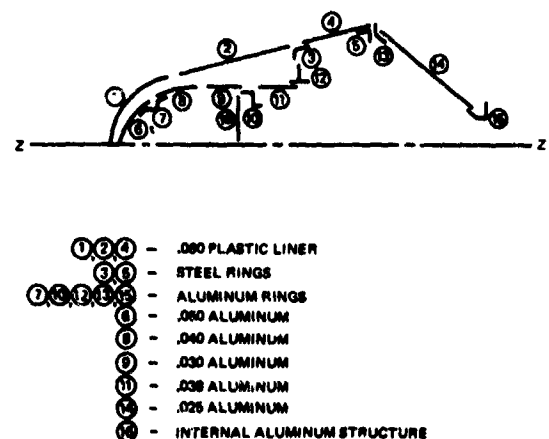


Figure 9. Vehicle B, structural model.

Table 3. Vehicle-B Test Condition Summary

Test No	Canister	Oven Fans	Fan Inside Canister	Fan Inside Vehicle
B-1	Yes	Yes	Yes	Yes
B-2	Yes	Yes	Yes	No
B-3	Yes	Yes	No	No

The vehicle was enclosed within the canister that had been fabricated for tests A-3 and A-4 of Vehicle A. As in the Vehicle-A series of tests, the oven temperature was increased from 70° to 300°F at a constant rate of 2°F per minute. Steady-state was defined as starting when the coldest component reached 300°F. The oven air temperature was lowered at the rate of 2°F per minute for the cool-down portion of test B-3. No cool-down data were taken from the B-1 and B-2 tests.

The Vehicle-B series of tests did not include a 300°F extended soak period as did the Vehicle-A series because the optical alignment test was run on Vehicle B prior to the other tests. This test did include a 60-hour soak at 300°F.

7. Test Results. Table 4 (ref. 3) shows a summary of the test results. Similar to Vehicle A, the maximum temperature difference during heat-up occurred for each test at the time the oven air reached its maximum of 300°F. Overall heat-up times of 6-1/4 hours for tests B-1 and B-2 were somewhat less than those for the equivalent A-1 (9

hours) and A-2 (12 hours) tests. This was due to the smaller thermal mass of Vehicle B and to the addition of the canister. For the A-1 and A-2 tests, the vehicle had been exposed directly to the oven air without enclosure in a canister. This fact also accounts for the change in maximum temperature differences for Vehicle B. The maximum temperature difference in a given area for the Vehicle-B heat-up was 47°F for the heat shield and thrust cone (test B-2); whereas it was 86°F for the capsule structure of Vehicle A (test A-2).

Prior to testing, thermal and structural analyses were performed on Vehicle B. Typical temperature-time predictions for the transient periods are shown in figures 12 and 13 (ref. 4).

It may be noted from the heating curves that, in general, the heat-up times were predicted to be longer than the test data showed. Reasons for this conservatism may be attributed to the following:

a. Mass distribution: The limited model breakdown used for these predictions required the allocation of more than one item to a single thermal mass even though the internal heat-flow paths were not uniform. This was particularly true for component 26, where temperatures were predicted on the inside but heat paths from the outside to the inside were estimated.

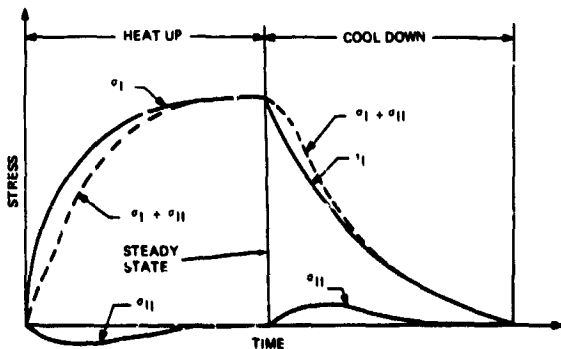


Figure 10. Stress-time relations.



Figure 11. Instrumented Vehicle B, aft view.

Table 4. Summary of Transient Temperatures for Vehicle B

Test Conditions	Test	Elements	Maximum Temperature Difference, ΔT ($^{\circ}F$)	Time to Reach Maximum ΔT (hr)	Time to Reach 290 $^{\circ}F$ (hr)	Time to Reach 300 $^{\circ}F$ (hr)
Oven Fan, Canister Fan, Vehicle Fan	B-1	Heat Shield and Thrust Cone	42	1-3/4	4-1/2	—
		Capsule Structure	18	2	4-1/4	—
		Components	—	—	5-1/4	6-1/4
Oven Fan, Canister Fan, No Vehicle Fan	B-2	Heat Shield and Thrust Cone	47	2	3-3/4	—
		Capsule Structure	20	2	3-3/4	—
		Components	—	—	5-1/4	6-1/4
Oven Fan, No Canister Fan, No Vehicle Fan	B-3	Heat Shield and Thrust Cone	46	2-1/4	9	—
		Capsule Structure	20	2-1/2	9-1/4	—
		Components	—	—	10-1/4	12
Oven Fan, No Canister Fan, No Vehicle Fan	B-3 Cool-Down	Heat Shield and Thrust Cone	57	3-1/2	—	—
		Capsule Structure	26	2-1/2	—	—
		Components	—	—	—	—

b. Convection coefficients: Because of the component density within the vehicle, areas where the fan could be located were limited; forced convection coefficients were estimated. Velocities within the vehicle varied locally due to blockage flow distribution. This could not be accounted for in the analysis without running preliminary tests.

Since the free convection mode is dependent on orientation, dimensions, and temperature differences, it is difficult to predict. For computation purposes, one value, an assumed average for the capsule or canister, was used in spite of local variations.

Alignment Test

Permanent distortions of the structure due to thermal environment may cause major problems in a spacecraft. They may lead to load redistribution within structural elements and at joints, interferences between components and/or adjacent structural members, and other similar occurrences. Current analytical techniques are generally adequate to predict such large effects. These effects may be alleviated substantially by proper control of design materials and manufacturing processes. Aside from the gross clearance

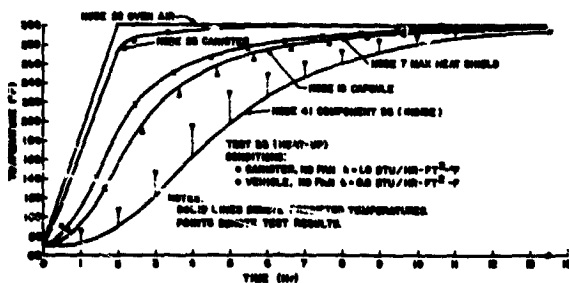


Figure 12. Test B-3, heat-up, comparison of predicted and measured temperatures.

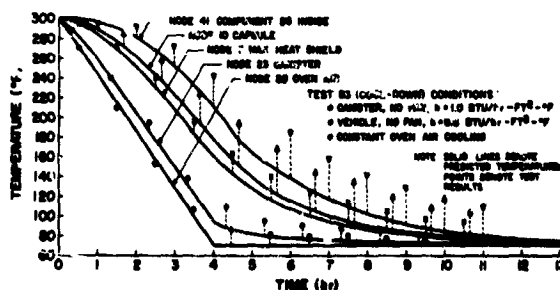


Figure 13. Test B-3, cool-down, comparison of predicted and measured temperatures.

problems, there are specific areas in the vehicle where relatively small distortions may be detrimental to the mission. Depending upon the particular design, it may be possible to correct for minor distortion by mechanical adjustments, but distortion due to thermal environment may be difficult to identify and to correct.

Depending upon the type of guidance and communications systems used on the spacecraft, it may be necessary to install components, such as antennas, nozzles, and gyros, which require alignment accuracies within minutes or seconds of arc. Because the vehicle is inaccessible, it is important to determine to what degree permanent thermal distortions affect the individual component mountings and, as a result, the overall vehicle system design.

Although some of the permanent distortions due to thermal sterilization are amenable to analysis, no analytical methods exist to predict distortions that result from such factors as:

1. Raw material manufacture
2. Residual stresses resulting from forming of detail parts
3. Heat treatment history of detail parts
4. Stresses caused by assembly restraints, such as welding fixtures and riveting jigs

5. Joint slippage caused by differential thermal expansion of mating parts.

After careful consideration of the thermocouple and strain gauge instrumentation planned for the Vehicle-B series of tests, it was concluded that the accuracy of the measurements would not be sufficient to detect permanent distortions to the degree that could be critical for alignment. It was therefore decided to add an alignment test to the Vehicle-B test series, which included optical inspections before and after a 60-hour soak at 300°F.

Test Procedure

The thrust cone and aft cover were eliminated from Vehicle B for this test to permit line-of-sight access before and after the heating cycle. The payload capsule and components of this vehicle had not been previously heated. This assured that residual stresses had not been previously relieved.

Eleven surface mirrors with an optical flatness tolerance of ± 1 arc second were installed on the vehicle, as shown in figure 14 (ref. 5). Mirrors A and L were magnetically attached; the remaining mirrors were bonded with GE RTV-102 silicone adhesive. The thickness of the silicone film was approximately 0.005 inch. A photograph of the alignment test setup is shown in figure 15 (ref. 5).

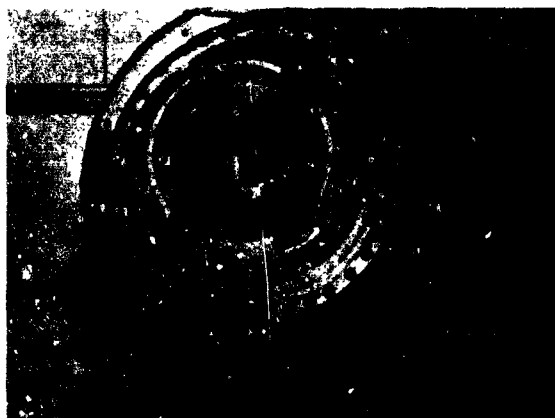


Figure 14. Mirror installation for alignment test.



Figure 15. Alignment test setup.

Prior to the heating cycle, an alignment check was made on the mirrors by using a Brunson theodolite. Mirror A was used as the reference mirror, and the angular variations (with respect to mirror A) of the other ten mirrors about the X- and Y-axes were recorded by using standard techniques of autocollimation. The Z-axis is the longitudinal axis of the vehicle while X and Y are lateral axes; X is positive to the right; Y is positive upward in figure 14.

After the initial alignment readings were taken, the oven air was increased at the rate of 2°F per minute to 300°F. The vehicle was soaked at that temperature for 60 hours following attainment of thermal equilibrium of the coldest component. The oven was then cooled to room temperature at the rate of 2°F per minute. After cooling, the angular variations of all the mirrors with respect to mirror A were again measured.

Results

The changes in angle between mirror A and the other mirrors, before and after heating, taken about the X- and Y-axes, are shown in table 5 (ref. 5). The relative distortion between any two mirrors can be obtained by subtracting their corresponding angular changes about a given axis. For example: The largest relative rotation between two mirrors about the Y-axis occurred between mirror C (+17'49") and mirror F (-7'47"). The relative angular distortion between these two mirrors was thus equal to 25'36".

The maximum rotation about the X-axis occurred between mirrors E and F; it was equal to 10'10". The maximum rotation about the Y-axis occurred between mirrors C and F; it was equal to 25'36". The maximum total rotation occurred between mirrors C and F; it was equal to 25'40". Table 6 (ref. 5) shows the total relative rotation between any two mirrors.

This test brought the structural distortion problem into its proper perspective; however, it did not prove that permanent distortions can be disregarded. Prior to this

Table 5. Alignment Test Results

Mirror	Rotation		Location
	X-Axis	Y-Axis	
A	0	0	Aft Shield Ring
B	+ 22"	- 1'17"	Aft Shield Ring
C	-4'21"	+17'49"	Interim Shield Ring (Capsule Attached)
D	+1'11"	+ 3'29"	Aft Capsule Ring
E	+4'12"	- 2'17"	Interim Capsule Ring
F	-5'58"	- 7'47"	Component 30 (Cover)
G	+1'9"	+ 1'27"	Component 26 (Base Plate)
*H	+1'27"	-30'24"	Internal Beam Structure
J	-1'53"	- 1'34"	Internal Beam Structure
K	+1'28"	+ 2'3"	Forward Capsule Ring
**I	-38"	-	Aft Shield Ring

*This mirror was disturbed during alignment.

**This mirror was installed at an angle such that the Y-axis reading was outside the range of the theodolite.

test, the degree to which distortion could affect the structure was not known. Estimates ranged from gross visual failures to the other extreme of no effect at all. The test indicated that, for a vehicle of the size and construction tested, angular distortions due to the temperature cycle are in the order of arc minutes. The significance of this conclusion is of importance in the area of alignment-sensitive components.

Structural-Joint Study

One of the goals of this study was the evaluation of structural joints that occur in a typical spacecraft.

Some joints are easily recognized as "structure" while others are less easily categorized. For the former types, there is extensive literature for thermostructural behavior. For the latter, which are by far the most

Table 6. Total Relative Rotation Between Mirrors

Mirror	B	C	D	E	F	G	J	K
A	1'19"	18'20"	3'40"	4'53"	9'48"	1'51"	2'27"	2'31"
B		19'37"	4'50"	3'58"	9'4"	2'50"	2'16"	3'30"
C			15'42"	21'48"	25'40"	20'0"	20'24"	16'48"
D				6'0"	13'18"	2'2"	5'54"	1'27"
E					11'35"	4'46"	6'5"	5'7"
F						11'37"	7'26"	12'18"
G							3'2"	0'41"
J								4'57"

troublesome from an analytical standpoint, the literature is much less extensive. Because the intent of this study was to determine the behavior of structural elements, no attempt has been made to identify all of the problems that will occur in the "grey areas." During the course of the study, however, it became apparent that many of the most serious problems connected with spacecraft sterilization will be in these grey areas. Accordingly, an awareness of the total problem has been indicated by grouping several joints in a miscellaneous category.

Figure 16 (ref. 6) presents a matrix of typical structural joints that were used in the evaluation.

Discussion

Because joints of all types were of interest, involving a range of manufacturing processes and procedures, it was necessary to group joints into loose categories. The most reasonable classification seems to be grouping by type, as shown in figure 16. To obtain this summary, a study was made of the proposed configurations for Mariner and Voyager planetary landers. The study was restricted to the

lander portion. To evaluate current joining techniques for space vehicles, it was necessary to evaluate drawings from other programs.

A joint rating, shown in table 7 (ref. 6), was prepared to compare various joining techniques in order of preference in the following areas:

1. Design
2. Stress analysis
3. Thermal analysis
4. Manufacturing
5. Reliability
6. Biophysics
7. Weight

Thermal Analysis and Design of Joints

1. *Atmosphere.* Design of joints for maximum thermal conductivity is generally not required for sterilization compatibility. These analyses indicate that steady-state sterilization temperatures can be reached more rapidly by improving convective heating than by increasing conduction across joints. The following conclusions are the result of testing a wide range of typical spacecraft structural joints.

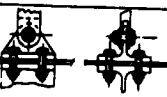
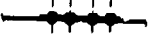
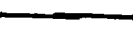
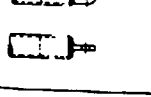
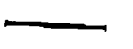
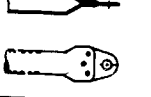
	A	B	C	D	E
1 BOLTED					
2 RIVETED					
3 FUSION WELDED					
4 SPOT & BEAM WELDED					
5 BRAZED					
6 BONDED					
7 MISC					

Figure 16. Typical spacecraft structural joints.

a. Interface conductance may vary considerably for seemingly identical specimens manufactured at the same plant. A similar range of variation is found in identical specimens fabricated under extremely careful laboratory conditions.

b. Skin thickness has some effect on interface conductance, but this may be obscured by manufacturing variations.

c. No significant effect of cleanliness of the joint or interface conductance could be found.

d. The rate of heat flow into the specimen has a pronounced effect on the interface conductance. In most cases, the

interface conductance increases with increasing rate of heat flow, but this trend may be obscured unless the interface pressure between skin and stringer is carefully controlled by such means as screw torque.

e. The interface conductance usually increases with an increase in torque on the screws attaching the skin to the stringer, but there can be exceptions.

f. In specimens with a sandwich material at the interface, the good conductors give high interface-conductance values, but factors other than the thickness and conductivity of the sandwich material appear to be significant.

Table 7. Ratings of Joining Techniques, Structural Joint Study

Category Rating	Design	Stress Analysis	Thermal Analysis	Manu- facturing	Reliability	Biophysics	Weight
1	Riveted	Bolted	Fusion-Welded	Riveted	Bolted	Fusion-Welded	Fusion-Welded
2	Bolted	Riveted	Brazed	Bolted	Riveted	Seam-Welded	Seam-Welded
3	Bonded	Fusion-Welded	Bonded	Bonded	Bonded	Spotwelded	Spotwelded
4	Fusion-Welded	Bonded	Bolted	Fusion-Welded	Fusion-Welded	Riveted	Riveted
5	Spotwelded	Brazed	Seam-Welded	Resistance-Welded	Spotwelded	Bolted	Bolted
6	Brazed	Spotwelded	Spotwelded	Brazed	Brazed	Brazed	Brazed
7	-	-	Riveted	-	-	Bonded	Bonded

g. In specimens of various material combinations, the lowest interface-conductance values were found for Inconel X and the 6AL-4V titanium alloy. The interface conductance for these specimens was found to be comparable with that of a specimen of aluminum alloy with an asbestos sandwich material at the interface.

h. The type of connection used between skin and stringers may have an appreciable effect on the interface conductance. Interface-conductance values varying by as much as 10 to 1 may be expected at the same mean interface temperature. The ratio between the highest and lowest value may be as great as 25 to 1.

i. In comparisons of the effect of types of connections on the interface conductance, alloy steel screws, high shear pins, and lock-bolts give the highest values, and blind and exploding types of rivets give the lowest; there may, however, be an occasional exception.

j. Interface conductance does not vary with the length of time between tests.

2. *Vacuum.* The results of joint studies in high vacuum revealed the following major conclusions:

a. If two thin sheets of metal are bolted together, heat transfer from one sheet to the other is closely concentrated around the bolt.

b. At a given heat-energy load, the temperature drop across a bolted joint decreases rapidly as the bolt is tightened to a minimum torque level. Increasing the bolt load above this level does not increase the temperature drop significantly.

c. The insertion, between a flange and a mounting base, of a soft shim material possessing low thermal resistance is of little practical value in increasing heat transfer efficiency of structural joints in a conducting gaseous atmosphere.

d. The temperature distribution around a bolt holding a flange to a heat sink is symmetrical. The temperature drop from a thin flange to a heat sink increases abruptly at a short distance from the perimeter of the bolthead and the nut.

Summary and Conclusions

The conclusions drawn on the behavior of structural joints and assemblies under thermal environment are summarized in two groups: (1) the thermostructural tests and alignment test and (2) the structural joint study.

The tests performed on a 200-pound earth reentry vehicle and the structural joint study yielded considerable information that may be used in the design of spacecraft.

Thermostructural Vehicle Tests and Alignment Test

The test vehicle was subjected to a total of eight thermal cycles from room temperature to 300°F. Three of these tests included 300°F temperature soaks of 9-hour, 60-hour, and 64-hour duration, respectively. The variable of these tests was the degree of forced convection.

For the first four tests (Vehicle-A series), a dimensional inspection before and after testing did not indicate significant structural distortion. The transient heating and cooling times were determined by measuring the times required for the coldest portion of the vehicle to reach temperature. An optical alignment test was performed on the fifth test to determine the magnitude of permanent distortions that might affect alignment-sensitive components on the vehicle. Prior to the final three tests (Vehicle-B series), temperatures and stresses at critical locations on the test vehicle were calculated, and these were compared with the measured values at the conclusion of the tests.

Thermal analysis predictions for a condition B-4 indicated that temperature gradients are considerably reduced if fans are installed within the vehicle but not within the canister. This condition was not tested during this program, but it should be tested on subsequent programs as an aid in determining optimum heating methods.

These tests led to the following general conclusions:

1. The heating and cooling times vary considerably with the degree of forced convection. During the Vehicle-A test series, these transient periods varied from 7 to 23 hours, depending on the amount of air circulation.

2. The transient periods should be shortened as much as possible to approach instantaneous heating and cooling. This permits the vehicle and components to be exposed to high temperature for the shortest period of time. From the Vehicle-B test series, it was concluded that, for most locations, the stresses caused by temperature differences during the transient period were considerably lower than those caused by boost or flight loads for which the vehicle would be designed. The largest thermally-induced stresses occurred at steady-state between stiffening structural elements of different thermal expansivities. These stresses and the stress level changes in preloaded joints must be considered in any design.

3. In general, electrical components and equipment located in the vehicle will take longer to heat and to cool than the structure. This was borne out during these tests. To increase the heating and cooling rates, fans should be installed in the vehicle at critical locations; heat paths to and within components should be optimized; and, in some cases, it may be necessary to install heaters within the components.

4. Structural distortions due to heat sterilization are minimal. This was shown in both the dimensional and optical alignment tests. Heat sterilization does not unduly complicate the mounting of alignment-sensitive components, such as gyros, antennas, and attitude control nozzles, on the vehicle. The alignment test showed that, for a vehicle of the type tested, the distortion caused by heat sterilization is in the order of arc minutes.

Structural Joint Study

Concern with thermal cycling effects on structural and mechanical joints leads to a general study of the problems that are attributable to the heat-sterilization environment.

The general conclusion that can be drawn is that the selection, design, and fabrication of joints to withstand the thermal cycling environment do not present any unique or limiting problems that could interfere with a successful spacecraft program. The major points supporting this conclusion may be briefly summarized:

1. It is not practical to make all joints of a typical spacecraft under biologically controlled (clean-room) conditions.

2. No types of joints or joining processes can be eliminated solely on the basis of incompatibility with thermal sterilization requirements.

3. Structural design of joints that require thermal sterilization does not require new techniques or methods.

4. With very few exceptions, design of joints for maximum thermal conductivity is not required for thermal sterilization compatibility.

5. A number of specific types of fasteners must be eliminated because they are not compatible with the thermal sterilization cycle.

6. Joining processes for use within a clean room require special development and special monitoring.

7. Reliability may be improved by application of clean-room techniques and procedures.

References

1. Crawford, Rondal; Tenny, Brooks; Fried, Erwin: Thermal Sterilization of Spacecraft Structures. *Journal of Spacecraft and Rockets*, vol. 3, no. 8, August 1966.
2. Crawford, Rondal; Tenny, Brooks: Design Requirements for the Sterilization Containers of Planetary Landers. AIAA Second Annual Meeting, Paper No. 65-387, July 1965
3. Crawford, Rondal; Kepple, Richard: Design Criteria for Typical Planetary Spacecraft to be Sterilized by Heating. First Annual Conference of Spacecraft Sterilization Technology, November 1965.
4. Lorech, Harold: Design Criteria for Typical Mars Landing Capsules Requiring Sterilization. Document No. 675D4223, Contract NAS8-11372, Phase III, January 1967.
5. Lorech, Harold: Design Criteria for Typical Planetary Spacecraft to be Sterilized by Heating. Document No. 655D4518, Contract NAS8-11372, Phase I, December 1965.
6. Lorech, Harold: A Study of Design Guidelines for Sterilization of Spacecraft Structures. Spacecraft Department, General Electric Company, NASA CR-61005, August 1964.

PRECEDING PAGE BLANK NOT FILMED.

N70-36722

Structural Design for Large Space Telescopes

Bailey W. Jackson
Kollsman Instrument Corporation

Introduction

The structural problems encountered in designing and building large ground-based telescopes have been well-defined in the building of over 47 such telescopes having apertures of 36 inches or more. The structural engineering required in designing apertures of this size has a great impact on whether the telescope performance will approach the theoretical resolution limits at all pointing angles. The experience and approaches taken by earlier designers of large telescopes can be valuable in defining the requirements for larger and more accurate instruments.

The experience factors for large space-qualified telescopes are not so readily available nor so numerous. The problem factor has increased because problems common to ground-based telescopes are assuming a greater magnitude in the space application. A few such problems are: thermal stabilization and temperature gradients, structural integrity through launch environment, maintenance of reflective surfaces, focusing and alignment, and the like.

The Goddard Experiment Package (GEP) is an instrument that is scheduled for flight on the next Orbital Astronomical Observatory (OAO-B). Figure 1 shows the GEP in its final stages of assembly at Kollsman. It has been space-qualified and, at the present time, is being calibrated and integrated with the spacecraft at Goddard Space Flight Center (GSFC). The GEP has an $f/5$, 38-inch diameter, Ritchey Chrétien form of Cassegrain telescope; it is used as a collector for an Ebert-Fastie type of spectrometer (fig. 2). The GEP has the capability of collecting

energy from point or extended objects in the 1000-to-4000-angstrom range with a spectral resolution of 2 angstroms. The GEP guidance system provides fine-pointing error signals to the spacecraft with an accuracy of 0.1 arc second from a first magnitude star. Figure 3 shows the optical layout of the GEP.

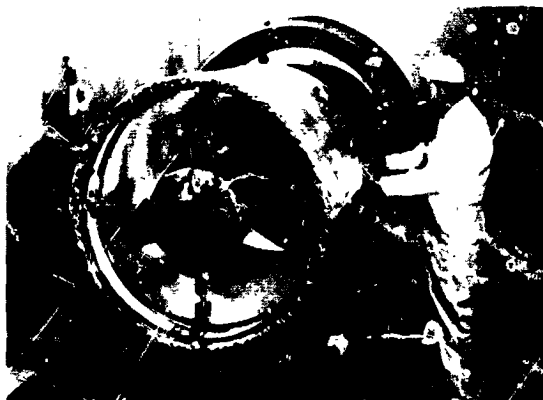


Figure 2. GEP optical assembly.

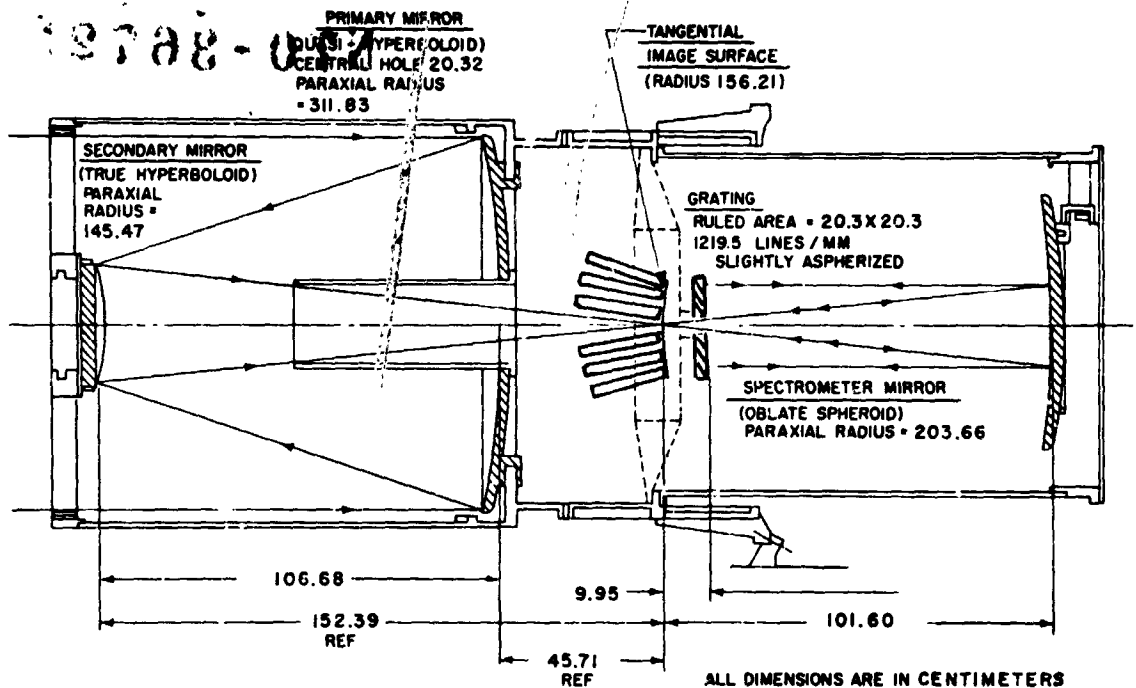


Figure 3. Optical layout of GEP.

The optical structure assembly provides the container and support for all parts of the GEP and maintains correct alignment and spacing of these components throughout launch and orbital environments. Most critical is the support for the optical elements because of the sensitivity of those elements to dimensional changes or strains. Figure 4 is a cutaway view of the optical structure. The structure can be considered as a composite of three sections: the forward portion is the telescope section; the middle is the main casting; the aft portion is the spectrometer section. The main casting provides attachment points to the spacecraft.

Design Philosophy

The structural design criteria, used to obtain the required optical performance, dictated that all allowable stress must be below the precision elastic limit when the anticipated launch loads are applied. (There has been considerable work performed to date in establishing the precision elastic limit of most structural materials.) Load factors were

calculated for each hung mass, which took into account the beam mode shape (assuming the telescope tube as a beam), transmissibility, damping spring constants (EI), etc. For these load factors, a safety factor of 1.5 was applied, and, in the case of joints, a safety factor of 2.0 was used. Many iterations of paper designs were made to shift some local resonances by changing wall thicknesses or configurations.

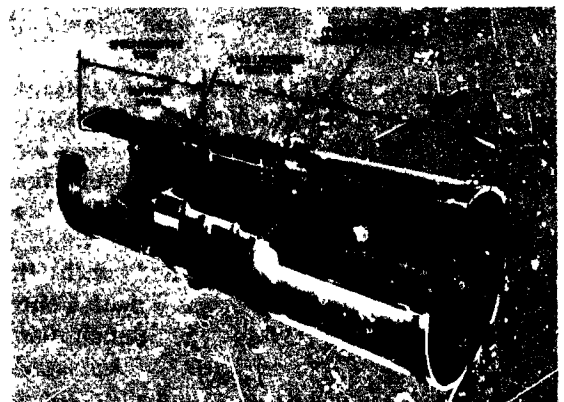


Figure 4. GEP structure.

Mirror Support Structures

The allowable weight of the GEP was to be 900 pounds, which included interconnecting cables to the spacecraft and any counterbalancing weights that would have to be added to the spacecraft. A further requirement was that the GEP was to be completely ground-tested, thus the optical system also had to perform satisfactorily in a one-g field. If the primary mirror were glass and constructed by the classical seat-of-the-pants diameter to a thickness ratio of 6:1, the mirror alone would weigh some 600 pounds.

Many materials and configurations were evaluated; a thin beryllium mirror seemed best for this application. The thickness was to be evaluated so that its figure would not change significantly when going from a one-g field to a zero-g field, thereby degrading the telescope performance.

Equations were written to determine the change in the elastic curve of a mirror under its own weight and mounted on three points at a selected radius in the horizontal orientation (fig. 5). The results were then applied to the mirrored surface and ray-traced with the telescope to predict and to compare the performances in one-g and zero-g fields. The following method was used to determine these equations.

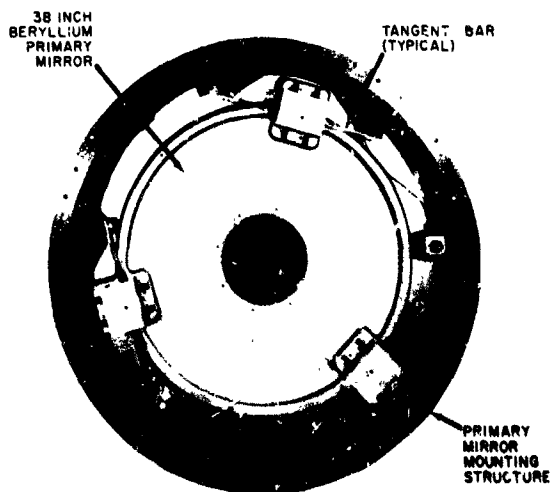


Figure 5. GEP primary mirror mount.

Determine the equation for the radial elastic curve of a circular flat plate, with a central hole, simply supported, in a one-g field. Refer to figure 6, and^d

1. Solve for the elastic curve on an edge-supported plate with a central hole under a uniform load (q).
2. Solve for the elastic curve on an edge-supported plate with a central hole under an annular shear load.
3. Choose the load in Step 2 so that it is equal and opposite to the load in Step 1 in order that supports will be free-ended when 1 and 2 are summed.
4. Relate deflections, W , to new support, C , by setting $W = 0$ when $r = C$.

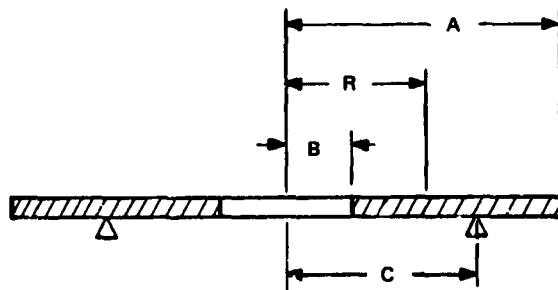


Figure 6. Mirror design; flat plate theory.

Primary Mirror Mount

The primary mirror is mounted on three bars (identified as tangent bars) which, in turn, are attached to the primary mirror mounting cell (shown in fig. 5). The tangent bars are 1/4 inch by 2-1/4 inches by 15-1/4 inches. The 1/4-inch dimension is in the radial direction and practically eliminates any radial loads being transmitted to the mirror as a result of differential expansion between the mirror and its aluminum cell. There are no adjustments provided for mounting or aligning the primary mirror. Close control of tolerances for the tangent bars and their mountings insure proper alignment of the optical axis to the mechanical axis.

Secondary Mirror Mount

The secondary mirror (figs. 7 and 8) is mounted on the focus drive mechanism. It is supported on the mechanism by means of three hermetically sealed ball splines. These splines are driven longitudinally by the focus mechanism in response to focus-adjust commands from the ground station. This, in turn, varies the longitudinal position of the secondary mirror and, consequently, adjusts the telescope focus.

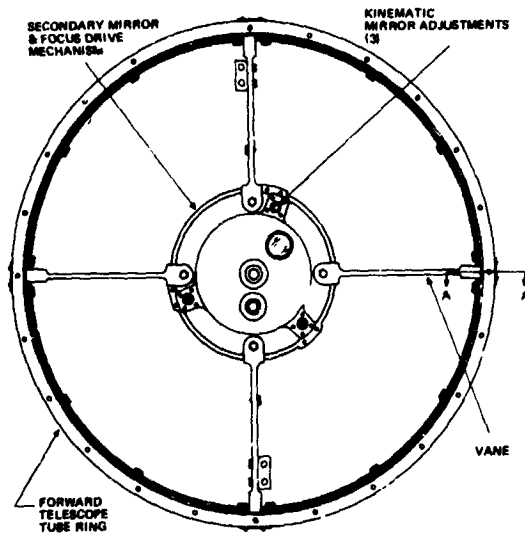


Figure 7. GEP secondary mirror mount.

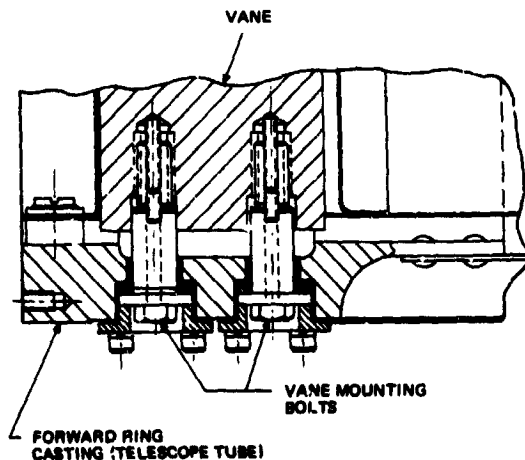


Figure 8. Vane-mounting detail.

The housing of the focus mechanism is supported by four thin aluminum vanes, which are bolted through insulated bushings to the forward ring casting of the telescope tube (fig. 8). The vane-mounting bolts provide the adjustment for centering the secondary mirror on the GEP optical axis. This is accomplished by relaxing the bolts retaining one vane and tightening the bolts retaining the opposite vane. After the centering adjustment, the vane-mounting bolts are torqued in order to prestress the vanes and telescope tube, thereby insuring accurate mirror alignment throughout and after the launch environment.

Three kinematic adjustments are also provided on the focus mechanism. These adjustments are used during assembly to remove mirror tilt and to establish the initial longitudinal position.

Spectrometer Mirror Mount

The spectrometer mirror (fig. 9) is mounted to the rear casting of the spectrometer tube by means of three tangent-bar assemblies. The tangent bars minimize strains in the radial direction caused by differential expansion between the mirror and its support.

The spectrometer mirror adjustments provide two degrees of freedom: translation and tilt. Translation along the optical axis is

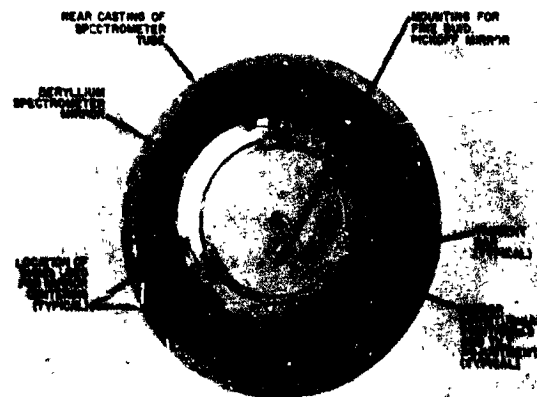


Figure 9. GEP spectrometer mirror mount.

provided by screws on each tangent-bar assembly. The screws have ball and socket attachments to the mirror to eliminate moments being introduced to the mirror from tilt adjustments. The centering of the mirror was established by careful tolerance control in the design of the structure.

Telescope Tube Construction

The structural tube that supports the secondary mirror assembly can be best discussed after examining the parameters that influenced its design. The GEP optical unit is mounted in a 48-inch-diameter well in the spacecraft. The spacecraft thermal profile at the time of the GEP design had a longitudinal gradient of 10° to 25°F and a circumferential gradient of 5° to 10°F. The gradients varied with the pointing angle relative to the earth's sunline. The maximum permissible heat loss to space by the GEP was to be 28 BTU's per hour. If the telescope tube were thermally

coupled to the well of the spacecraft, there would be disastrous effects on the telescope performance; therefore, thermal insulation was provided. The NRC-2 insulation, shown schematically in figure 10, isolates the tube from both space and the spacecraft.

In order to compensate for a variation of average temperature, it was postulated that, if a theoretical telescope could be built with everything having the same coefficient of expansion, the performance would be just as good at any average equilibrium temperature. The materials, however, were not all the same since a beryllium primary mirror and a quartz secondary mirror are used. Thus, in order to obtain an athermalized design, aluminum and titanium were selected for the structural tube materials. Their lengths were computed so that the coefficients of expansion of the materials maintained the focal plane in position by changing the tube length appropriately with the change in curvature of the optical elements as a function of temperature.

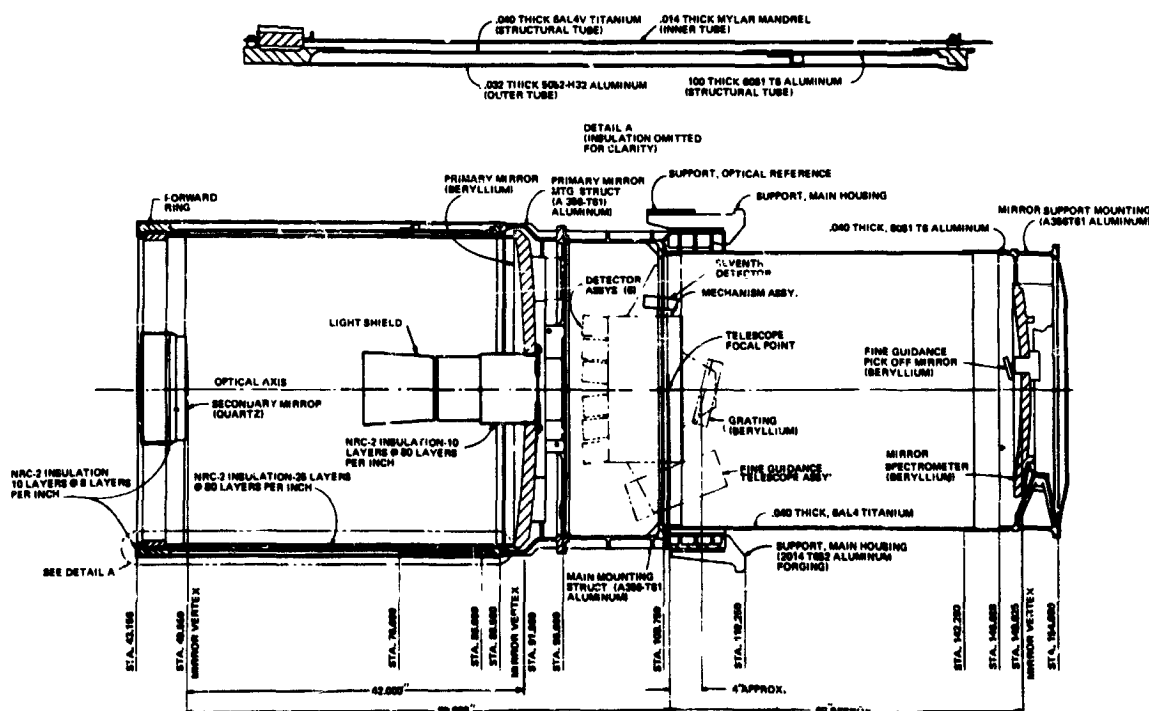


Figure 10. Construction details of GEP optical structure.

This is shown in figure 10, a detailed view of telescope tube construction. The aluminum sheath shown has the effect of a thermal shunt providing some heat to the forward ring assembly and has a tendency to smooth out residual circumferential gradients.

Testing

Kollsman Instrument Corporation performed qualification-level sine and acceptance-level random vibration testing in-house as part of the engineering evaluation of the GEP. Accelerometers were placed at strategic points for evaluation of all critical points. Figure 11 shows the X-axis excitation. Figure 12 shows the Y-axis and Z-axis excitation. Figure 13 shows the GEP on a 20-foot boom, used to simulate 11.5-g steady-state acceleration. After completion of testing, the optical performance was evaluated, and the GEP disassembled for part inspection, cleaning, and recoating of the optical surfaces. The results of the evaluation showed some defocusing and an image shift in the focal plane of about 40 arc seconds. Some of the bushings that were used as thermal insulators for the inner mandrel of the telescope were cracked. The image shift was traced to scoring of the three kinematic adjustment screws that

are used to support the secondary focusing drive mechanism. The adjustment screws and the bushings were redesigned as a result of these tests.

The prototype GEP was rebuilt and sent to Goddard Space Flight Center, where it was married with a prototype spacecraft for acceptance-level sine and qualification-level random vibration tests. A performance evaluation after these tests revealed that everything was satisfactory.

Additional problems arose from the thermal-vacuum test. Heat exchange between the GEP and the spacecraft was estimated to be over 100 BTU's per hour instead of 28 BTU's per hour. A few of the action items

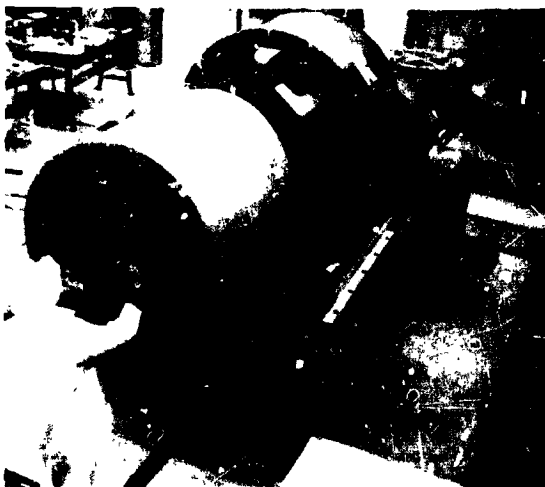


Figure 11. Vibration testing of GEP; X-axis.



Figure 12. Vibration testing of GEP; Y-axis and Z-axis.



Figure 13. Acceleration testing of GEP.

resulting from the first thermal test on the prototype were:

1. Heat losses through the support screws on the inner mandrel accounted for a large percentage of the loss. The mandrel itself was acting as a fin for the screws; hence, the mandrel material was changed from titanium to mylar to reduce conduction. The color was changed from black to the natural white of the dull side of mylar. (The changing from black to white in the mandrel required considerable testing for scattered light.)

2. The secondary mirror and vane were originally insulated from the forward ring in order not to reduce the ring temperature excessively. It was learned from the test that the vane assembly was insulated too well and the secondary and drive assembly tried to reach the cold plate temperature. The correction was to increase the secondary mirror insulation from 10 layers to 25 layers of NRC and to install a 4-watt heater in the secondary mechanism assembly.

3. The 205-node mathematical model of the GEP did not predict some of the results that were found in the test. As a result, a comparison of inputs and assumptions had to be correlated between the two. It should be noted, however, that approximately 95 percent of the test results were in close agreement with predicted temperatures.

4. Further analysis showed 28 BTU's per hour to be unrealistic. The GEP heat loss allowance was revised to a more realistic limit of 55 BTU's per hour.

Conclusions

The preceding information outlined only the highlights of the structural concepts learned from our experience with earth-bound telescopes and with space telescopes. Application of the lessons from these experiences and continuing innovation will enable future space telescopes of larger diameter and increased performance requirements to be designed with confidence.

PRECEDING PAGE BLANK NOT FILMED.

N70-36723

Thermal Design of a Satellite Telescope

J. Rogovin and N. Kosowski

Grumman Aircraft Engineering Corporation

Introduction

Thermal design requirements have always had a considerable impact on the design of astronomy vehicles; however, with the advent of large telescopes with precise pointing requirements, the influence of thermal design is even more pronounced. The present state-of-the-art in thermal control, the advanced techniques to be used on large astronomy vehicles, and the design considerations generic to advanced spacecraft are reviewed in this paper. The thermal-control techniques presently used are reviewed through a discussion of the Grumman Orbiting Astronomical Observatory (OAO). The general thermal design and performance of the OAO passive/active control system are presented along with analytical, test, and flight data. Candidate thermal-control techniques for advanced spacecraft are reviewed with particular emphasis given to heat pipes, louvers, insulations, and coatings. Design concepts for the advanced OAO #3 and #4 satellites are included.

There are several design problems, which by their general nature, will be generic to almost all advanced astronomy vehicles. These areas include possible integration of man and operation in proximity to a large space station or space base. Each of these topics is discussed as to its impact on vehicle design and the type of thermal control system needed.

Present State-of-the-Art

Successfully launched December 7, 1968, the OAO A-2 spacecraft is the forerunner of large astronomy vehicles designed

to help astronomers learn more about the evolution and structure of the universe. Passive and active temperature control are the two principal methods of thermal control used in the A-2 spacecraft. Passive temperature control is achieved with thermal coatings, NRC-2 superinsulation, and conductive-path control. In the active system, louvers and thermostat-controlled electrical heaters are used.

The primary objectives of the OAO thermal control system are to provide precise temperature control for the Smithsonian Astrophysical Observatory (SAO), Wisconsin University experiment package (WEP), the structure, and the spacecraft electronic equipment. How these objectives and the operation of the thermal-control system are achieved in the A-2 spacecraft and a presentation of analytical, test, and flight data are included in this discussion.

External Thermal Environment

The OAO is designed to be launched into a circular 500-mile orbit with a period of 101 minutes. It is capable of being oriented to any star for a matter of minutes or days during an estimated lifetime of one year. During this time, the spacecraft will be in sunlight from 65 to 83 percent of the time, corresponding to orbital planes of 0° and 58.45° to the ecliptic.

The solar constant is assumed to be 440 BTU/hr ft² with a yearly average earth-albedo rate of 35 percent of the sun's energy. Earth radiation is taken as that from a -10°F black-body source. Transient flat-plate calculations

have been made according to the orientation while spacecraft orbits the earth. From these are derived average orbital heat fluxes owing to solar, albedo, and earth radiation. Since the OAO structure and equipment masses are large, transient heat fluxes are required only in determining temperatures of the skin, solar paddles, sunshade, and external fittings.

The sun spectrum is assumed to be a $10,200^{\circ}\text{F}$ blackbody when integrating spectral reflectance measurements of materials to determine their absorptance of solar radiation. These same values of absorptance are used when calculating heat fluxes due to albedo radiation. Because the telescopes operate in the deep ultraviolet region of the spectrum (1100 and 3000 angstroms), low outgassing materials must be used throughout the satellite to prevent contamination of the mirror surfaces.

Description of Spacecraft

As shown in figure 1, the satellite is an octahedron, 80 inches across the flats and 118 inches long. Solar paddles extend perpendicularly from sides C and G at an angle of 33 degrees to the central axis. A cylindrical hole the full length of the spacecraft and 48 inches in diameter accommodates the primary telescope system. Sunshades are provided at the optical openings to prevent sun impingement inside the telescope cavity when it is oriented to a star.

Internally, aluminum trusses and shelves are integrally connected to the 48-inch-diameter structural tube and form 48 truncated bays, as seen in figure 2. These bays house the electronic equipment, which is mounted to hinged honeycomb panels. The



Figure 2. OAO A-2 spacecraft.

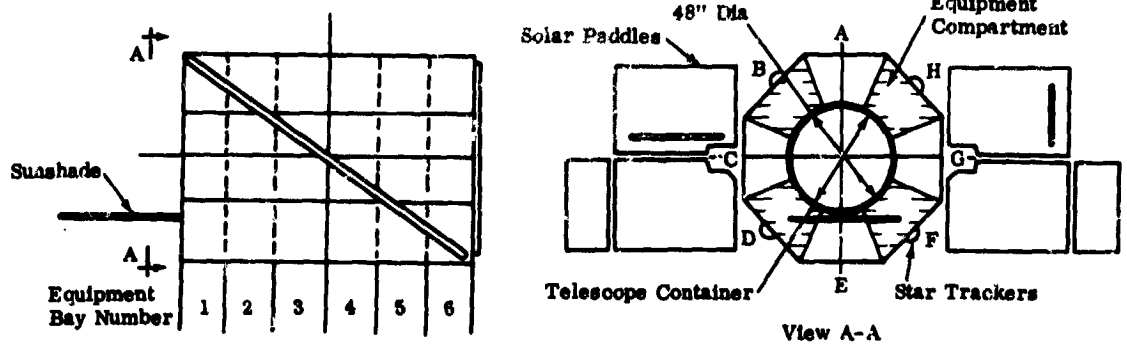


Figure 1. Diagrammatic representation of orbiting astronomical observatory.

panels swing outboard to permit access to the equipment and wiring installed in the spacecraft. Ten-mil, polished, aluminum skins (Alcoa Alzak) protect the equipment and are used as both a thermal damper to incident radiation and a heat radiator. The skins are thermally isolated from the structure by nylon insulators.

During slewing maneuvers, the satellite can revolve about any of its three axes. When positioned to a star, it is roll-oriented so that the earth-sun line is always parallel to the C and G skins (fig. 1). This position allows maximum solar-paddle output and provides the OAO with a set of stable temperature skins that are used as symmetrical radiators to cool the spacecraft structure.

Electronic Equipment Thermal Control

Each bay in the spacecraft except Bays 1, 2, and 6 of the C side and Bays 1, 2, 5, and 6 of the G side are available for electronic equipment. These C and G sides are used as a valve to control spacecraft temperature. Electronic equipment is located in 31

bays; seven bays are used to house external trackers. The packages are sized for the bay dimensions and, if small, are tied with other boxes to insure a high thermal inertia. In general, the boxes are bolted to honeycomb panels that are positioned parallel to the external skins and approximately two inches away. A silicone rubber compound, RTV-40 and 25-percent alumina, is used to provide good thermal contact between box and honeycomb panel. The honeycomb panel is hinged from the structure on fiberglass mounts so that the honeycomb with the equipment can be swung outward for easy access after installation.

Figure 3 is a schematic diagram of a typical equipment bay. The structure tube and shelves are insulated with 25 layers of NRC-2 insulation, aluminized on one side. The external skins are ten mils thick with an Alzak finish on the outside and black epoxy-paint finish on the inside. Alzak has a nominal solar absorptance (α_s) equal to 0.15 and a nominal infrared emittance (ϵ) equal to 0.75. The black paint has a nominal infrared emittance equal to 0.87.

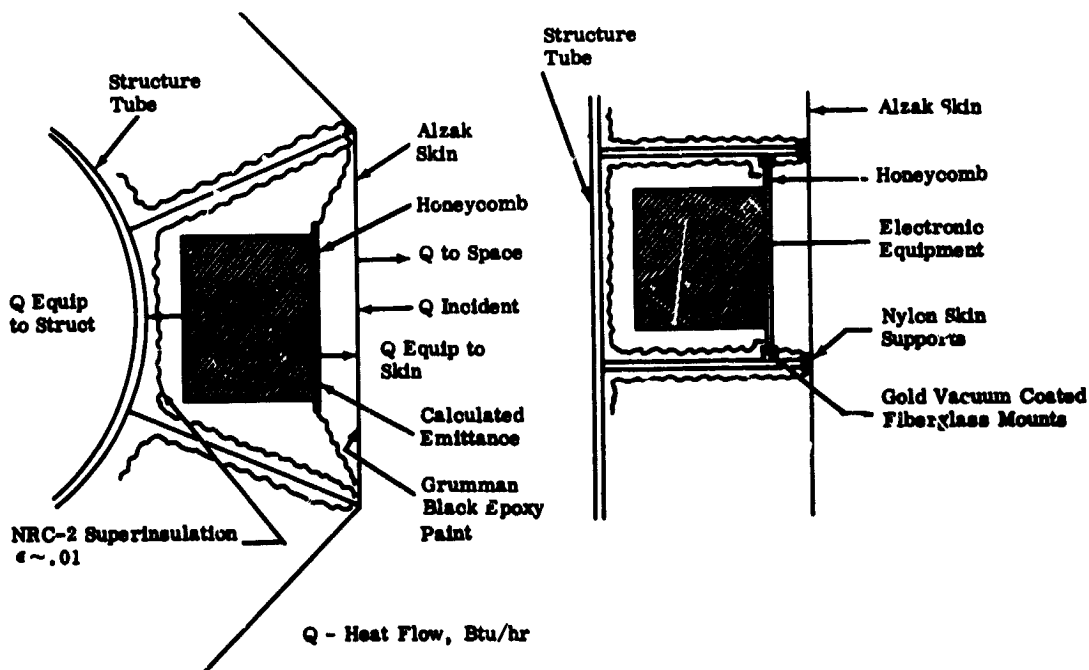


Figure 3. Typical equipment bay on OAO.

The thermal control of the electronic equipment is achieved primarily by a passive design approach. Each box is designed to conduct and to radiate all its heat to the heat-sink surface, which is mounted to the honeycomb panel. The heat is then conducted through the honeycomb panel, which radiates the heat to the external skin. The external skin subsequently radiates this heat to space. The radiation coupling between the honeycomb panel and the skin acts like a valve and is used to control equipment to desired temperatures.

Active control in the form of thermostat-controlled heaters mounted on the honeycomb panels is used when minimum design temperatures cannot be maintained in a passive manner. To minimize the impact of heater power on the power supply subsystem, additional active control in the form of louvers mounted to the honeycomb panel is employed when significant power savings can be achieved. A typical louver installation is shown in figure 4. The louvers are closed during cold conditions, thus reducing the radiative coupling from heat sink to skin. Open louvers raise the coupling during high temperature conditions.

Results of a parametric study on Bay B-5 are presented in figure 5, which can be used to illustrate the heater power saved when a louver is installed. The radiation (AF) coupling between honeycomb and skin is plotted on the abscissa and heat sink temper-



Figure 4. Typical louver installation, used for additional, active thermal control.

ature on the ordinate. The Bay B-5 equipment dissipation varies between 1.1 and 28.3 watts. The acceptance temperature limits for the heat sink are 0° to 130° F. For an AF value of 1.24 ft^2 , figure 5 indicates that total equipment and heater power dissipation of 14.0 watts is required to maintain a 0° F heat sink for the cold case. A louver will lower the AF to 0.44, thus reducing power dissipation requirements to seven watts. A louver installed on this heat sink panel will save seven watts of heater power during cold conditions.

Structure Temperature Control

The thermal design of the OAO structure must meet two principal criteria. First, the temperature gradient of the internal structure is determined by the maximum allowable distortion of the structure. Second, the experimental package and the internal structure must be maintained at the equilibrium temperature levels acceptable to the experimenters. The telescopes of the A-2 spacecraft are thermally coupled to the structure and insulated from space. Therefore, the telescopes, if properly insulated, will run within a few degrees of the mean structure temperature.

Structure temperature control, as illustrated in figure 6, is achieved with thermal coatings, NRC-2 superinsulation, and conductive path control. The spacecraft structure is fabricated out of chem-milled aluminum alloy, which has a high coefficient of thermal conductivity. To isolate the structure thermally from heat sinks and sources, stainless steel, nylon, and fiberglass are used as connecting members, thereby minimizing heat conduction to and from the structure.

NRC-2 insulation is wrapped around various members to control radiant heat transfer. Decreasing insulation between the electronic equipment and the structure increases the structural equilibrium temperature. Thus, the various insulators control the influx of heat from various sources to the structure.

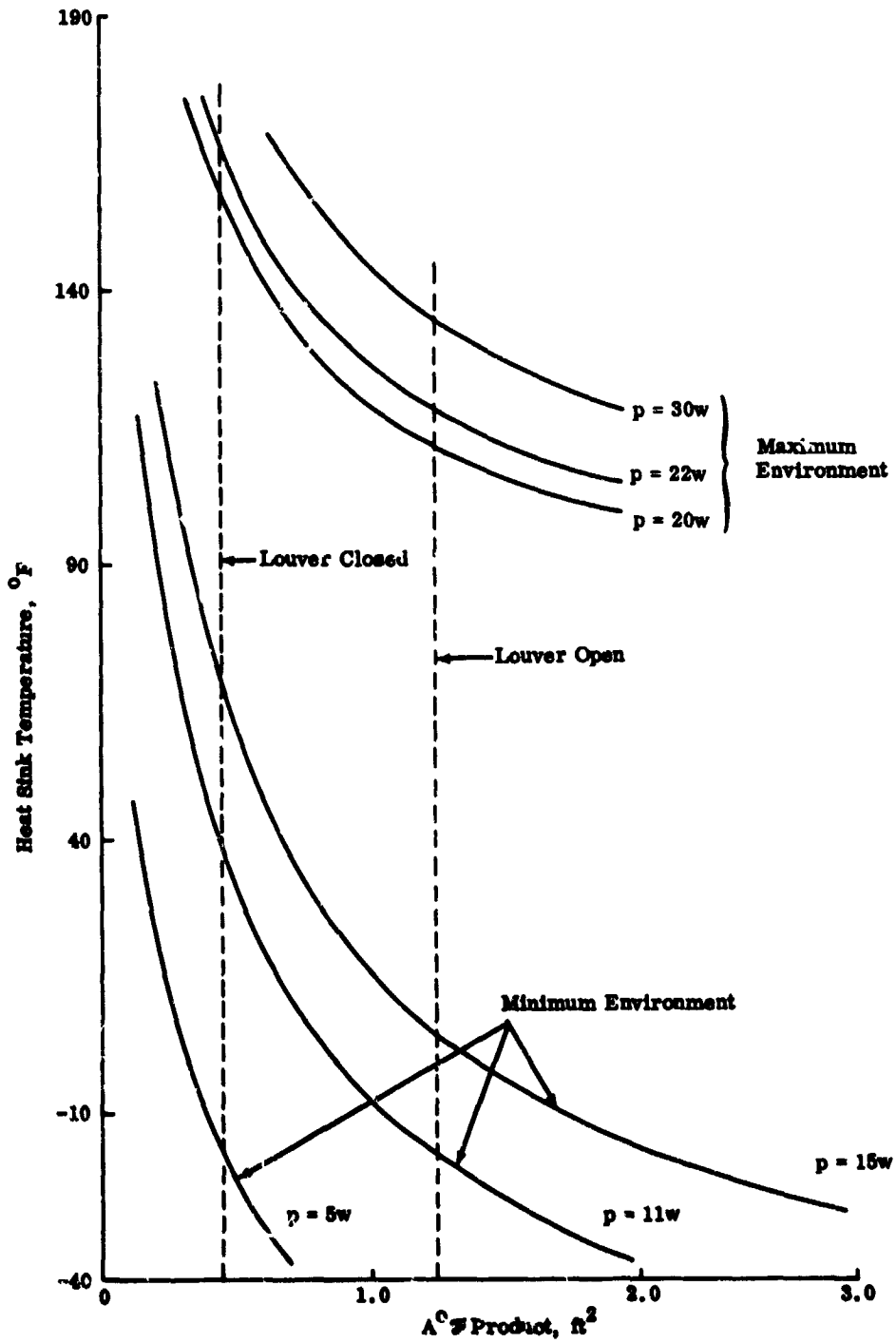


Figure 5. Bay B-5 thermal characteristics.

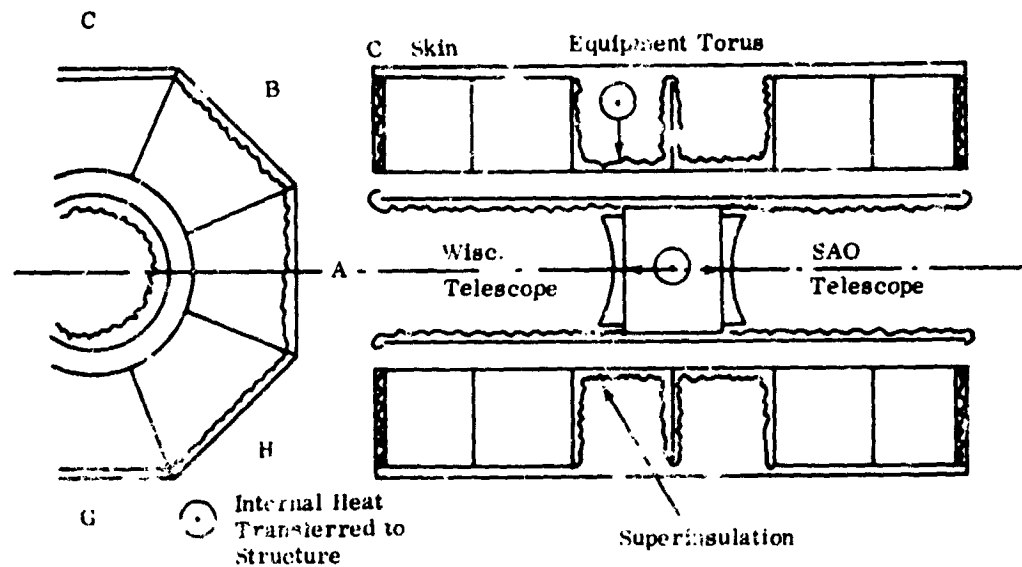


Figure 6. Structure temperature control of OAO.

The primary source of heat to the structure is from the equipment. Ten to 20 percent of the heat dissipated by the equipment is radiated and conducted to the structure. The structure rejects heat to two primary sinks:

1. Thermally stable skins C-1, C-2, C-6, G-1, G-2, G-5, and G-6
2. The experiment container.

Secondary paths of heat rejection by the structure are to the nonequipment bay skins of sides A, B, D, E, F, and H and to the forward and aft end skins, all of which are insulated with NRC-2 insulation. These secondary sinks account for approximately 10 percent or less of the total heat rejected by the structure. The heat rejection of the structure to the C and G skins is controllable and is the "valve" in the thermal design of the OAO. Variation of coatings and insulation in these bays is used to obtain the operational structure temperature.

Experiment Temperature Control

The experiment package comprises the primary telescope system plus associated electronic equipment. All electronic equipment that is not required to be within the telescope

envelope is stored in Bays E-4 and E-5 and is handled in the same manner as other spacecraft electronic equipment. Any type of optical telescope may be housed within the 40-inch-diameter container. Interior surfaces of the telescope and the sunshade are painted black in order to prevent incident earth-albedo reflections from washing out the star image on the detector.

In order to achieve thermal stability, the telescope is insulated from open-end radiation to space and is thermally linked to the spacecraft via conduction through four aluminum lugs and via radiation between the 40-inch container and the OAO 48-inch tube. The spacecraft structure is designed to provide the desired mean operating temperature for the telescope. This eliminates temperature differences between spacecraft and telescope that would cause misalignment of the star trackers and telescope axis. By insulating the telescope from space and by having the telescope and spacecraft thermally linked, the telescope gains the stability inherent in the OAO and becomes insensitive to the radical environment changes at the open end. For this design, the telescope operates within a few degrees of the structure; however, it also

assumes thermal gradients similar to those of the OAO structure tube.

Spacecraft Thermal Performance

The OAO A-2 was launched on December 7, 1968, at 0840 GMT, from the Eastern Test Range in Florida. Its Atlas-Centaur booster placed the observatory into an orbit inclined 34.9 degrees to the equator with a period of 100.3 minutes, an apogee of 488 statute miles, and a perigee of 479 statute miles. All subsequent data has shown that all component temperatures are within operating limits and that, as of April 1969, the performance of the thermal subsystem is excellent.

The performance of the electronic-equipment thermal control system is illustrated in figure 7, which shows the range in operating temperatures for all equipment bays as of the first 650 orbits (exclusive of launch and post-launch temperatures). Superimposed are the upper and lower acceptance limits as well as the predicted maximum and minimum operating levels independent of spacecraft orientation. Inspection of this figure reveals that all flight equipment temperatures are within their acceptable limits. Agreement between flight and computed temperatures is excellent, as shown in table 1, with 95 percent of the calculated equipment temperatures being within 10°F of the flight data.

Figure 8 compares predicted structural gradients with flight temperatures. The comparison reveals:

1. Flight circumferential gradients are larger than calculated or observed in ground testing.

2. Flight structure temperatures are always higher on the sunlit side of the spacecraft.

The thermal performance of the Wisconsin Experiment is shown in figure 9. Since this experiment package is strongly coupled to the spacecraft structure by design, the control of the experiment temperature by the spacecraft thermal design is exemplified in this figure.

Figure 10 is a comparison of Alzak degradation rates observed on the OAO, on

Table 1. Comparison of Equipment Flight Telemetry With Predictions

Bay	Component	Flight (°F)	Calculated (°F)
A-2	DC/DC Conv HS	61	66
A-3	Inverter HS	74	68
A-4	WBT HS	76	75
A-5	Tape Recorder HS	48	44
B-2	Diode Box	61	66
B-3	DLU	79	70
B-4	ST-1 Electronics	79	78
B-5	RAPS	79	78
C-3	Reg Converter	74	75
C-4	Batteries	53	53
D-2	EDHE	50	50
D-3	FWJC (P)	61	58
D-4	ST-3 Electronics	38	35
D-5	RAPS Signal Proc	40	45
E-1	PRU	48	52
E-2	FCU	23	28
E-3	SCU	53	50
E-4	SAO Electronics	36	30
E-5	WEP Electronics	52	57
F-2	SDHE	42	42
F-3	Coarse Wheel (Y)	40	44
F-4	ST-5 Electronics	42	37
F-5	RAPS Gyro	141	142
G-3	IBM-140	65	74
G-4	IBM-230	88	92
H-2	BST Electronics	43	54
H-3	Coarse Wheel (R)	53	61
H-4	Phasolver	86	86
H-5	CCJB	60	62

the Applied Technology Satellite (ATS-3), and in Grumman laboratory tests. Preliminary results indicate that the OAO degradation rate in solar absorptance will approach a change no greater than 0.07. Projection of the

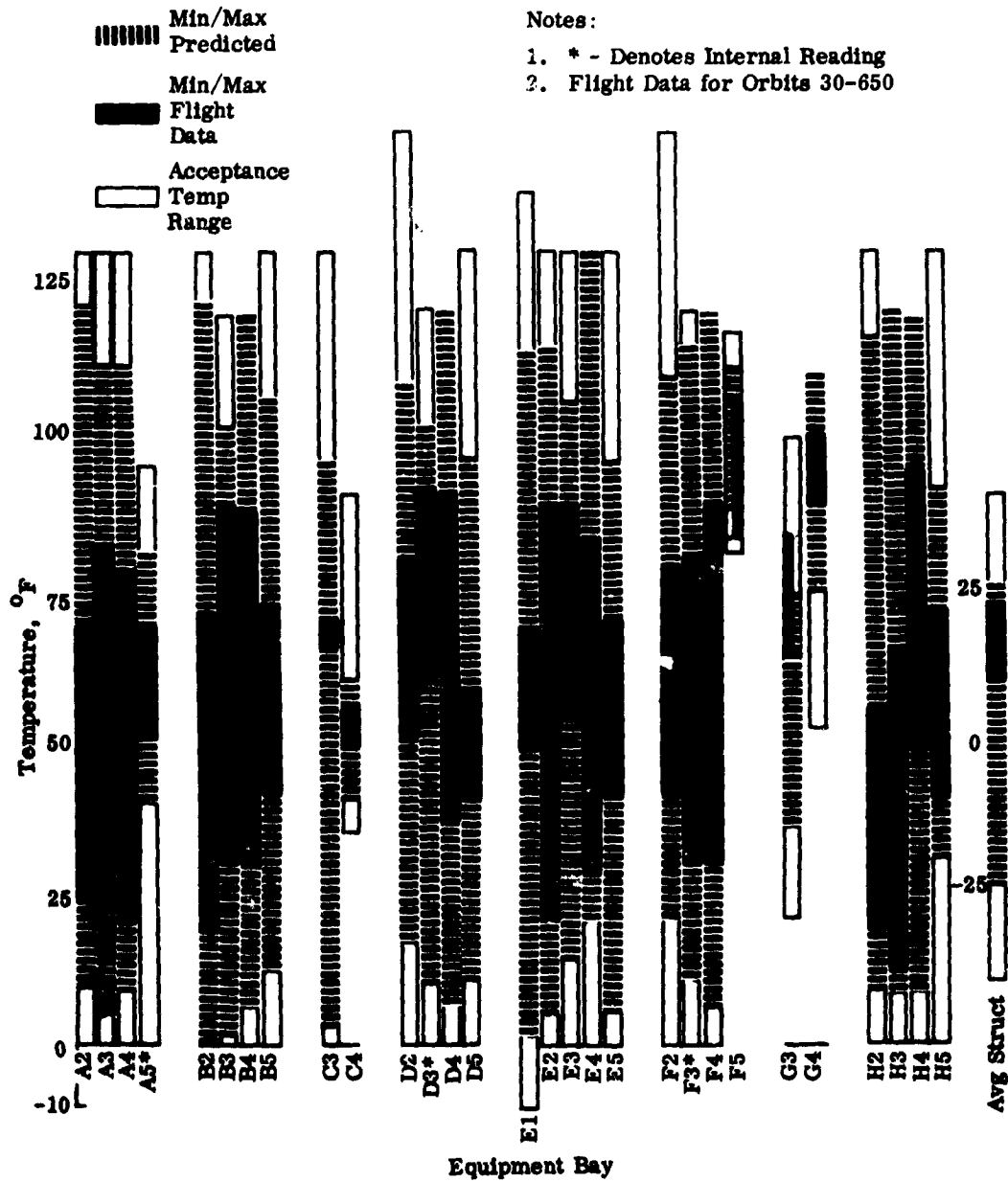


Figure 7. Equipment operating temperatures in OAO.

thermal-control system with future degradation of Alzak predicts no equipment temperatures exceeding their expected operating limits for a mission time of more than one year.

Advanced Thermal-Control Techniques

The next generation of astronomy vehicles will have stringent requirements for fine-pointing accuracy, reliability, long-life

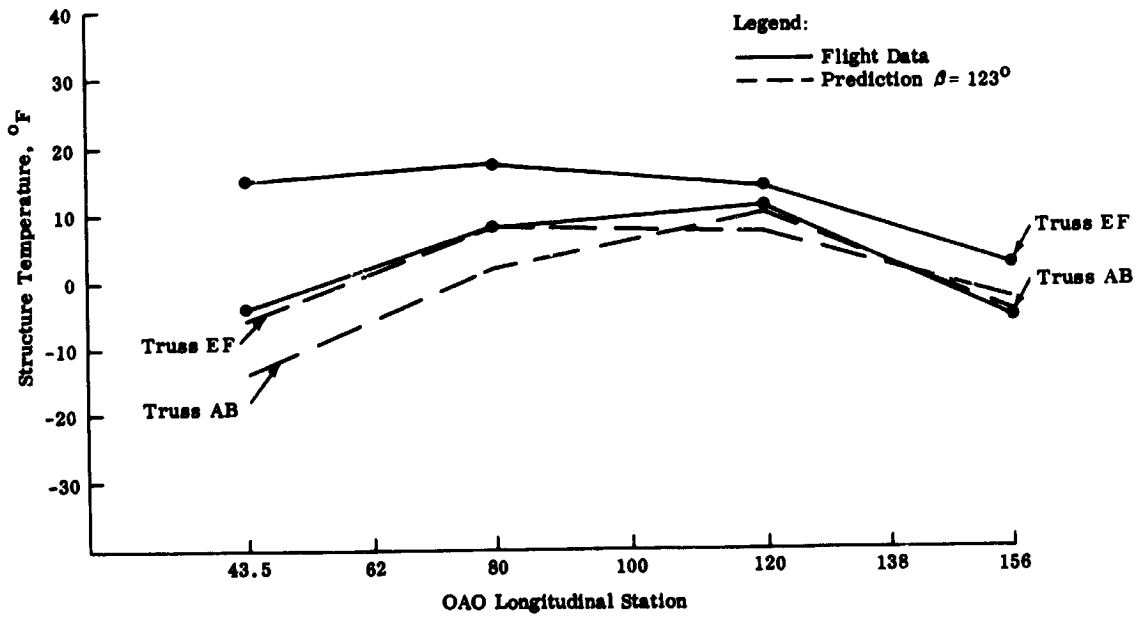


Figure 8. Flight-telemetry structural gradients.

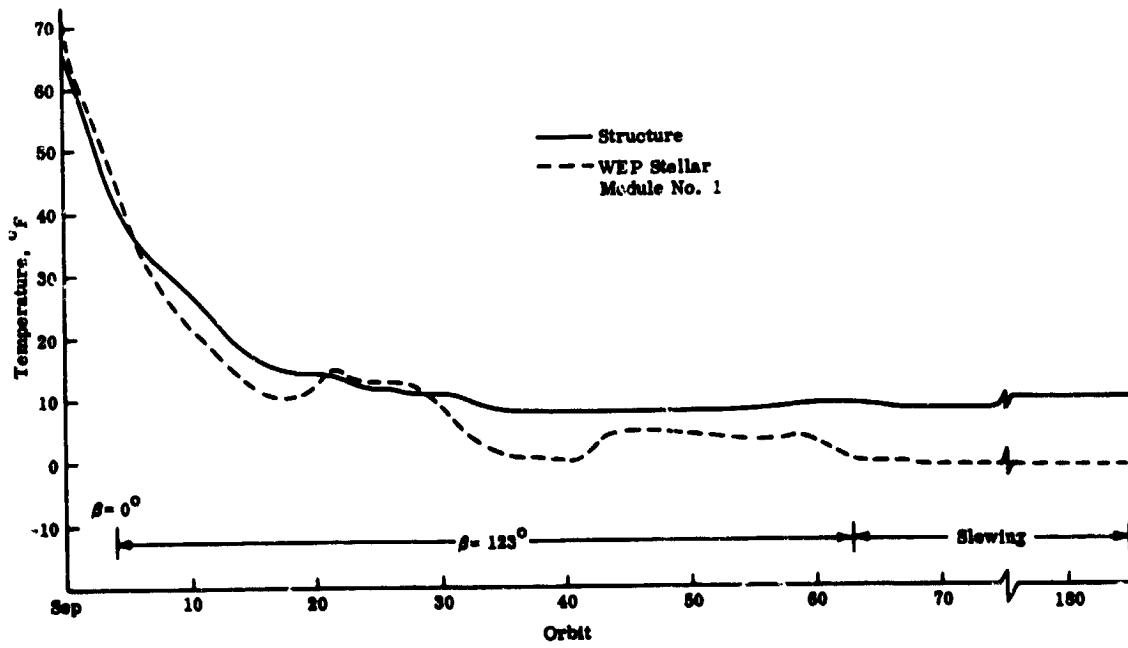


Figure 9. Temperature history of experiment and structure.

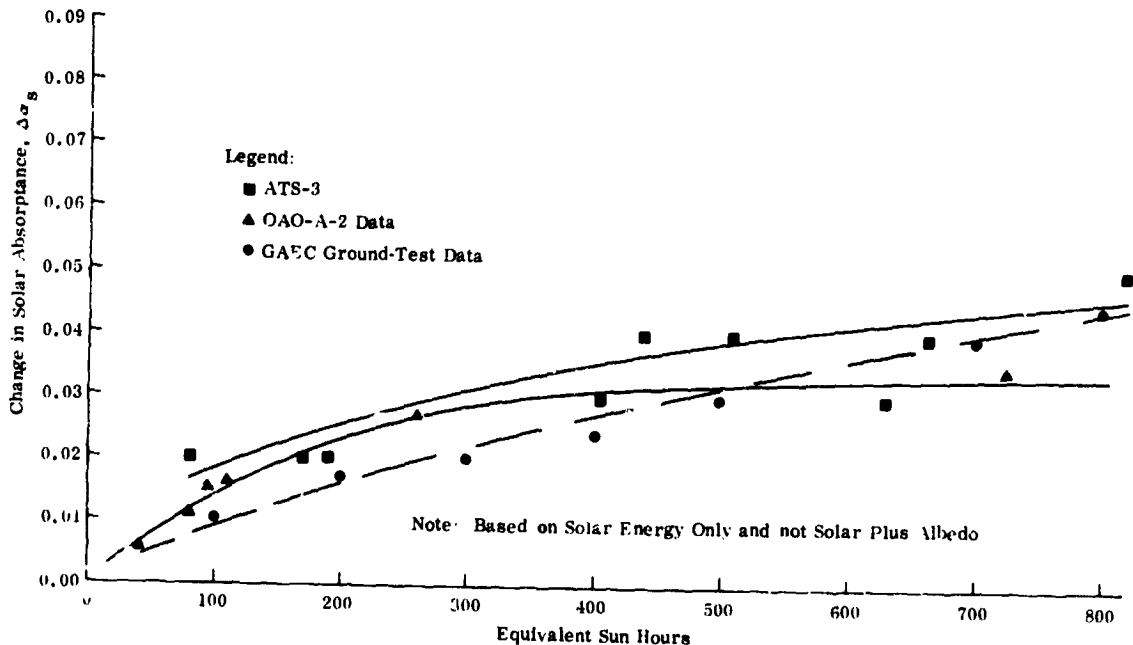


Figure 10. Alzak degradation comparison.

assurance, and operational flexibility. There are several major thermal-design considerations that will be prerequisites for achieving these objectives. Such considerations include: tighter temperature control for the telescope, minimum consumption of heater power, and narrower equipment-operating temperature range for wider variations in the duty cycle and environment of the equipment. New and improved thermal control techniques are being developed to meet the aforementioned objectives. Candidate schemes for controlling the temperature of advanced vehicles are reviewed in this paper through a discussion of active and passive control devices.

Heat Pipes

The heat pipe is a device for transferring heat by a closed-cycle evaporation/condensation process. Two highly desirable characteristics are inherent in its performance: extremely high effective thermal conductance and near isothermal operation.

Used in connection with the thermal control of a space vehicle, heat pipes are ideal for tasks such as isothermalization and temperature control of equipment with varying duty cycles in a varying environment.

For proper operation, astronomy satellite experiments may require a limit on potential structural distortions. To eliminate detrimental structural distortions, it is necessary to reduce thermal gradients in the structure to a tolerable minimum. Attaching heat pipes to the spacecraft structure is one method of reducing structural thermal gradients with a relatively low weight penalty. In such heat pipes, sections opposite hot structure elements will function as evaporators, and sections opposite colder structure elements will function as condensers. Condenser and evaporator sections may switch functions in response to a shift in the temperature distribution of the structure.

Figure 11 illustrates a specially designed network of heat pipes for an OAO spacecraft. The network consists of a grid of longitudinal and hoop pipes attached to the surface of the cylindrical cavity that houses the telescope

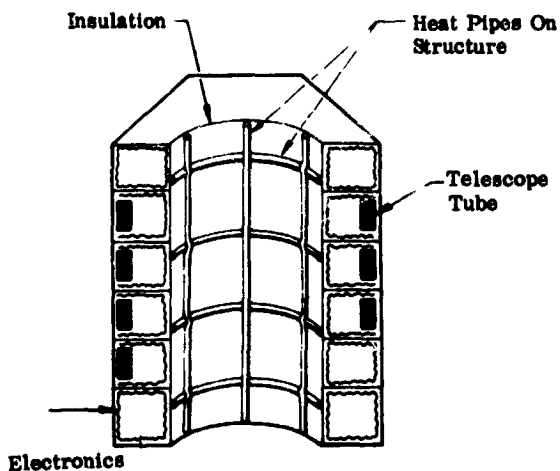


Figure 11. OAO isothermalizer application.

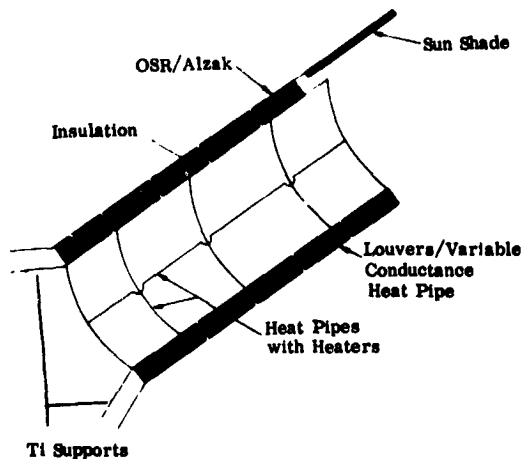


Figure 12. Thermal control of telescope.

tube. Figure 12 shows a section of an advanced spacecraft with an externally mounted telescope; heat-pipe grid is attached to the inner side of the telescope tube. The outside surface of the tube is covered with insulation, which, in turn, may be shielded from the environment in several ways, depending upon the severity of the environment and the design requirements:

1. Alzak surfaces
2. Optical solar reflector (OSR) coatings
3. Louvers or variable conductance heat pipes.

The design in figure 12 is capable of providing a stable, nearly isothermal environment for telescope operation. The inner heat-pipe grid makes a major contribution by drastically reducing temperature gradients in the telescope tube.

The effectiveness of a heat pipe in removing temperature gradients is shown in figure 13. The hoop type of isothermalizer heat pipes were installed on the #3 and #4 OAO spacecraft. Figure 13 compares the temperature distributions for the #3 OAO spacecraft with and without heat pipes. The data shown are based on computations, with conservative assumptions.

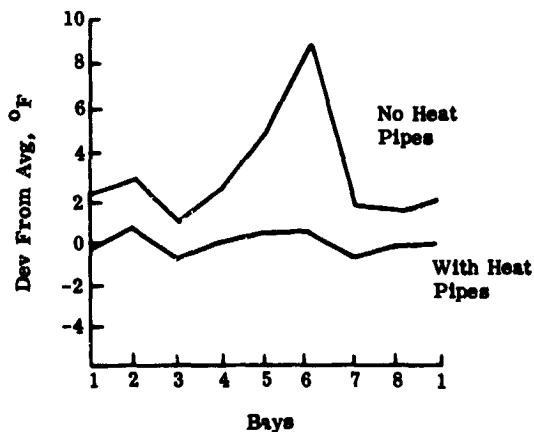


Figure 13. Effect of heat pipes on OAO spacecraft #3.

Another more advanced concept is that of structure-integral heat pipes. With early specification of thermal requirements, structure elements may be designed with hollow plenums of desired shape and size, which, upon assembly, are filled with a heat-pipe working fluid. This results in weight savings and more efficient heat-pipe operation. Such a plenum heat pipe would lend itself, for example, to temperature gradient reduction in solar paddles, thus increasing solar-energy conversion efficiency. Current programs include the development of such heat pipes.

One area of particularly effective heat-pipe application is the thermal coupling of equipment facing the sun with equipment located in the shade, thus reducing their temperature difference. If the spacecraft rotates, the heat-pipe evaporator and condenser rapidly switch functions, thereby reducing equipment temperature excursions. Equipment units often, however, require vibration isolation; in such cases, rigid heat pipes cannot be used. The development of flexible heat pipes is being currently considered for just such applications. In addition to providing thermal coupling with vibration isolation, such heat pipes offer greater design and routing flexibility.

Under certain conditions, the low thermal resistance of the heat pipe becomes a liability; for example, periods of vehicle operation with electrical and electronic equipments powered down, periods of low or zero thermal environment input to the vehicle, and periods of extravehicular activity by the crew, when the metabolic load is removed from the environmental control system of the vehicle. At these times, the presence of ordinary heat pipes for thermal coupling between the heat sources and the outside environment may create excessive heat flow from the vehicle. As a result, the low temperature limits for electrical and electronic equipment may be exceeded; liquid consumables may freeze or, in the case of propellants, become unusable; and the crew may experience discomfort from the cold.

If the effective conductance of a heat pipe could be modulated when the heat load varied, the scope of application of the heat pipe could be greatly expanded. To accomplish this modulation, a heat pipe having a valve in the vapor passage and operated by a sensing element in the condenser has been proposed. Another proposed approach is the use of a bellows sensitive to the vapor pressure in the vapor path. The bellows would act as a variable flow restrictor, limiting the evaporation/condensation processes when a reduction in input heat flux caused the vapor pressure to drop.

Another promising approach to varying the conductance of a heat pipe appears to be the introduction of a noncondensing gas into the vapor chamber of the pipe. The molecules of the noncondensable gas, impelled by the movement of the vapor, migrate toward the cooler end of the pipe. Their presence in the vicinity of the condenser inhibits the condensation process by reducing the molecular concentration of the vapor at the liquid/gas interface and by raising the effective temperature gradient between the vapor and the liquid.

A Grumman-funded program was established to study, both analytically and experimentally, the feasibility of such a heat pipe and to define its performance spectra. This program, in progress for some time, shows tangible progress in both the theoretical and test phases.

An example of the application of the variable-conductance heat pipe to satellite equipment is a proposed design for the OAO batteries (fig. 14). The battery problem on the OAO affords an excellent opportunity for using a variable-conductance heat pipe. The battery-power output spectrum and the allowable operating temperature range are such that some means of modulating the thermal

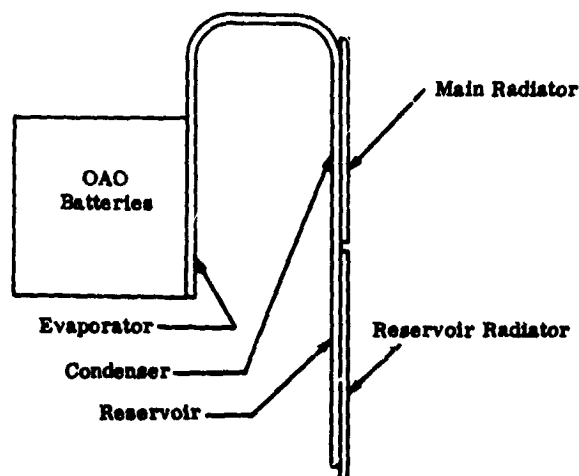


Figure 14. Spacecraft application of variable-conductance heat pipe.

coupling between the battery and the outside thermal environment must be used. The existing design employs a space louver between the battery mounting surface and the vehicle thermal radiator. Bimetallic elements sensitive to local skin temperature adjust the louver position to moderate the battery temperature fluctuations caused by changes in external thermal conditions. Despite the use of louvers, it is still necessary, under certain operating conditions, to use electric heaters in the batteries to prevent freezing. Advanced development study at Grumman has shown the feasibility of using variable-conductance heat pipes to couple the batteries to the thermal radiators, such as Alzak skins. The resultant design would reduce heater power from 20 watts to 4 watts, would reduce weight from 40 pounds to approximately 7 pounds, and would cut the required radiator area from two bays to one. A breadboard model of such a variable-conductance heat pipe has been built and is undergoing tests at the present time.

Thermal Switches

Thermal switches control temperature by regulating the conductance between the controlled body and its heat sink or source. This is achieved by temperature-induced contact or by separation of the surfaces of two thermal conductors in the switch. One of these conductors is thermally connected to the controlled body; the other conductor is tied to a heat sink or a source. In another variant of the thermal switch, control is achieved by regulation of the length of a fluid element in the heat path. Temperature-induced motion is usually provided by either bimetallic elements or fluid expansion and contraction.

A bimetallic element consists of two strips of dissimilar metal welded together. The two metals have different coefficients of expansion. Any change in temperature induces different rates of expansion or contraction in each of the strips, forcing the element to bend. This movement is utilized in making or breaking contact between two

conductor surfaces. Such a switch provides a very high maximum to minimum conductance ratio. In practice, however, this ratio is difficult to achieve and to maintain because of the difficulty of achieving and maintaining a perfect thermal contact between the two surfaces.

Fluid expansion and contraction can be used in several ways to obtain heat conduction regulation. In the simplest type of switch, fluid expansion can make or break contact between two surfaces. This is similar to the bimetallic switch with all its advantages and disadvantages. In another type of switch, a sensor fluid moves a solid piston by expanding or contracting. The piston changes the thickness of a film of secondary fluid between conductor surfaces, thus changing, in effect, the overall switch conductance. In this case, the ratio of maximum to minimum conductance is relatively small, and the temperature range over which it is attainable is relatively large when compared to other thermal switches.

Despite some difficulties, there is a continued interest in thermal switches because some switches are very sensitive and respond to very small changes in temperature of the controlled body.

Thermal Louvers

Thermal louvers control temperature by regulating radiation between a controlled body and its heat sink or source. This is achieved by temperature-induced adjustment of louver blade angles—ranging from fully closed to fully open louvers. Motive power for the louvers can be provided by:

1. Bimetallic elements
2. Fluid expansion and contraction
3. An electric motor triggered by temperature sensors.

A typical louver installation is shown in figures 4 and 15(a). In this case, louvers are inserted between the controlled equipment and a radiator. Changing angles of the louver slats regulates heat transfer rates between the equipment and radiator. The slat angle can be set by individual bimetallic springs or by

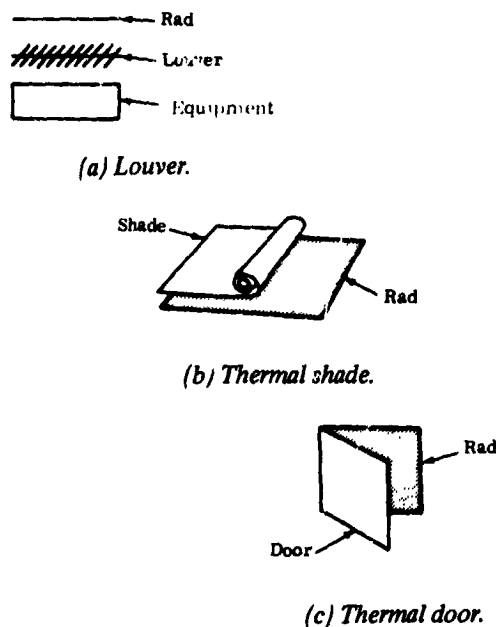


Figure 15. Active systems for thermal control.

single mechanisms activated by fluid expansion or other temperature sensors. In all cases, the louver-activating mechanism must respond to the temperature of the controlled body.

Another method of louver installation involves removing the radiator plate that shields the louvers from environmental extremes. The regulation range of the louvers in this installation is increased, but special problems are incurred. For example, the louver operating in direct sunshine would tend to heat up and would open slats at the very moment when it may be the least desirable. One possible way of solving this problem is to regulate the slat angles of the louvers with a small electric motor triggered from temperature sensors attached to the equipment and insulated from the environment.

Thermal Shades and Thermal Doors

A thermal shade, shown in figure 15(b), is essentially a surface cover made of a flexible material that is rolled off or on the surface in response to a temperature signal.

Motive power can be provided by bimetallic elements, fluid volume changes, or an electric motor. Thermal shades partially cover or shade the controlled surface at some temperatures, thus creating and aggravating existing thermal gradients. To solve the problem of gradients, it is necessary to lengthen the shade and its travel distance and to provide a perforation pattern along the length of the shade material. These perforations decrease in size as the shade moves to cover the equipment. As a result, the contrast between the shaded and unshaded section of the controlled equipment is sharply reduced, and temperature regulation is more gradual over the entire equipment surface.

Thermal doors, shown in figure 15(c), automatically open or close as a function of temperature, thus exposing or covering a high-emittance radiating surface. The outer surface of the door is covered with a low-emittance coating. Here, too, movement is provided by bimetallic elements, fluid volume changes, or electric motor.

One of the major advantages of shades or doors compared to louvers is that, in the open condition, the hot-case insertion loss for shades or doors can be very small. In the case of the louvers, the support frame and the suspended blades, even when fully opened, reduce the hot-case heat-rejection capability of the surface by more than 20 percent. The use of a single control mechanism to move the shade or door does, however, decrease its reliability. Most louvers are built with individually controlled blades. The probability of all louver-blade control mechanisms failing at once is very remote compared to the failure probability of a single control mechanism. In addition, individual controls on blades respond to local temperatures and help smooth gradients; the thermal shade or door cannot do this.

Insulation

The most common method of thermal control to minimize heat leaks from a large surface is multilayer insulation. The efforts in this area include the proper venting design to

insure interstitial pressure levels no greater than 10^{-4} torr and detailed attention to the proper handling of penetrations, layer spacing with spacers, and number of thermal shields for a particular configuration. Current work on optimum insulation performance suggests an advantage for broadside-venting over edge-venting when the number of layers is greater than ten or when it is a large insulation blanket. The broadside-venting specification for hole area fraction must take into account the gas load and the total number of thermal shields involved in a particular design. For a given hole area fraction, the hole diameter and corresponding hole spacing should be as small as possible and preferably of the same order as the gap height. Currently the smallest hole size available on the open market is larger than desired (1/16-inch diameter). Experiments performed on a 16-inch-diameter

spherical tank calorimeter at Grumman with perforated, double-sided, aluminized mylar with nylon spacers gave values of heat flux versus number of layers, as shown in figure 16. For this particular insulation and hole area fraction, further improvement may be possible by increasing the number of layers beyond 30. The values shown are superior to the crinkled, single-sided, aluminized mylar used at the present time in most vehicle insulation design (fig. 16).

For general design purposes, the hole area fraction used should increase with the number of layers in the blanket. For a given gas load per layer there will be an optimum number of layers with a corresponding hole fraction for minimum heat flux. Further increase of layers with the same hole area fraction and gas load per layer will increase

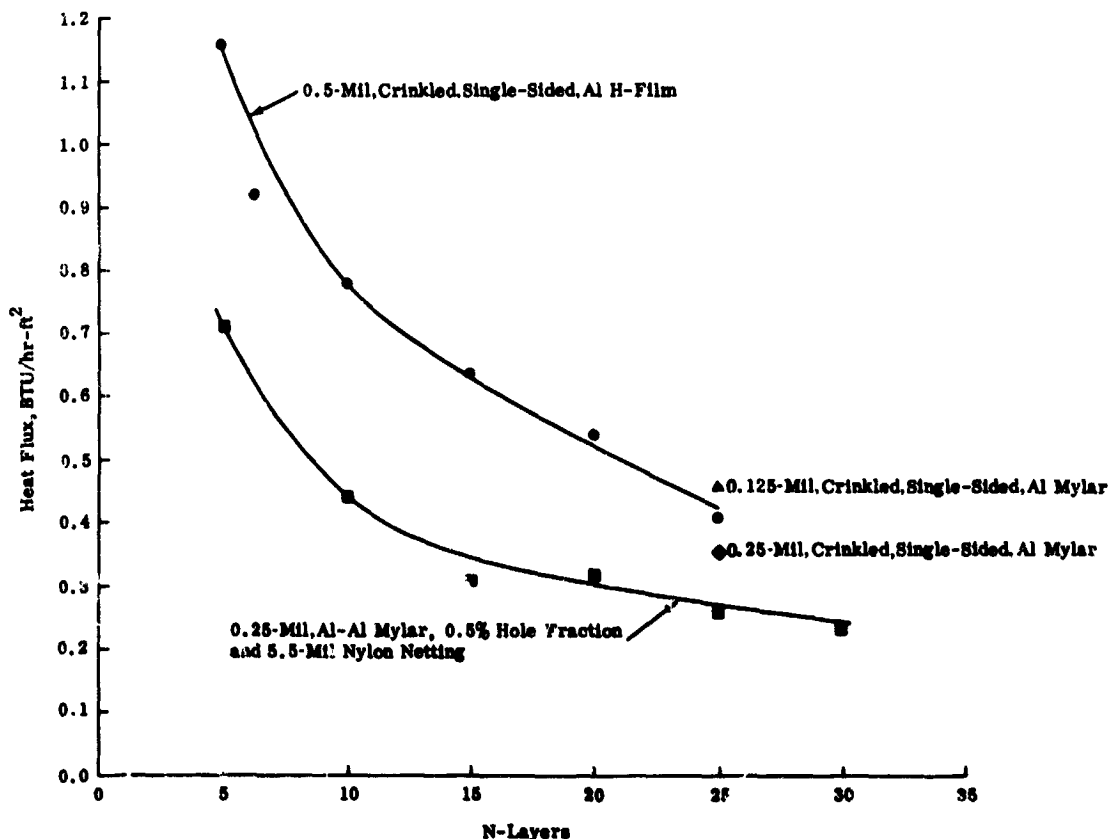


Figure 16. Effect of layers on heat flux through multilayer insulation.

the total blanket heat flux due to an increase in interstitial gas pressure.

Thermal-Control Coatings

Thermal control can be achieved in some cases, and aided in all cases, by using so-called "selective radiator" surfaces. The selective radiators used in most spacecraft absorb low fractions of impinging solar radiation and couple this property with a high emittance in the low-temperature region. Because of the characteristics described, only a small fraction of impinging solar energy is absorbed without lowering significantly the heat-rejection capability of the radiator at equipment temperatures. This reduces the excursion extremes of equipment temperatures between periods when the equipment is exposed to direct sunlight and periods when the equipment is in the shade.

Table 2 lists solar-radiation-absorption coefficients and emittances for various coatings. A comparison reveals that the OSR coating offers significant advantages in performance over the other coatings. It consists essentially of small 1-inch by 1-inch mirrors

covering the entire outside surface of the radiator. Attachment to the radiator is made with an LTV type of cement or double-backed H-film tape.

The absorptance ($\alpha=0.05$ to 0.1) and emittance ($\epsilon = 0.70$ to 0.80) for the OSR is combined into a parameter α/ϵ ($\alpha/\epsilon = 0.06$ to 0.15), which is a figure of merit for comparing coatings. This figure of merit is an indirect measure of temperature stability obtainable with a given coating. (The ranges of α , ϵ , and α/ϵ shown for OSR reflect the techniques of installing the individual mirrors, especially the spacing of the mirrors.)

Comparison of the various coatings listed in table 2 reveals that use of the OSR coating would result in a significant narrowing of equipment temperature excursions. In addition, OSR shows excellent durability; its performance is not degraded after exposure to the space environment. Figure 17 shows the effect of exposure to solar radiation on the absorptance of several coatings. OSR remains unaffected, whereas TiO_2 (titanium dioxide) and Alzak deteriorate.

The OSR coating is clearly superior to the other coatings used, and further study of its feasibility for use in space is warranted.

Table 2. Typical Thermal-Control Coatings

Coating	α	ϵ	α/ϵ	UV Degradation Resistance	Handling Ease
Z-93	0.18	0.87	0.20	Fair	Poor
Alzak	0.15	0.75	0.20	Good	Good
S-13G	0.19	0.91	0.21	Poor	Good
LTV 602	0.19	0.91	0.21	Poor	Good
OSR	0.05 to 0.1	0.70 to 0.80	0.06 to 0.15	Excellent	Poor
GSFC 101	0.19	0.91	0.21	Poor	Good
TiO_2	0.22	0.91	0.24	Poor	Good

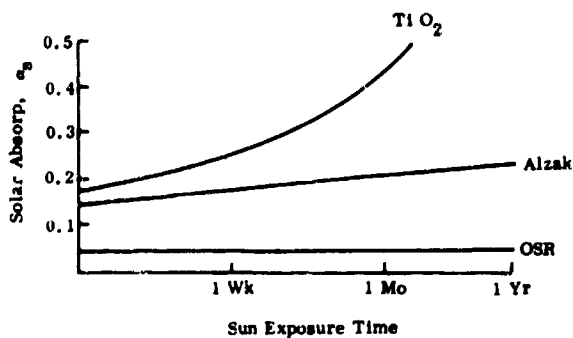


Figure 17. Ultraviolet degradation of thermal-control surfaces.

Generic Considerations

There are several design problems related to advanced astronomy vehicles that fall into a general category, namely, the areas related to possible integration of man and operation of a vehicle in proximity to a space station or space base.

Integration of Man

Advanced astronomy spacecraft may be either man-attended for short periods of time or actually man-operated for days or weeks. In each of these concepts, vehicle design is strongly influenced by the presence of man. At first thought, one would expect the need for life support capabilities to be the single greatest area of design impact; however, many of the major vehicle problem areas are actually the result of man-induced environments, such as plume impingement, gas leakage, etc., rather than the result of man himself. These design considerations are more easily understood in the context of man-attended and manned spacecraft concepts.

Man-Attended Telescope

A man-attended spacecraft is influenced in its external configuration, equipment design, internal arrangement, telescope design, and experiment operation by the transient

presence of man. In the same manner, the transient nature of man's visit influences his life support system choice and perhaps even his type of dress.

The first portion of the spacecraft that is "aware" of man is the external configuration. As the astronaut approaches in his logistic vehicle, external surfaces of the astronomy vehicle will be impinged upon by plumes from the reaction control engines. These plumes can degrade and/or damage thermal-control surfaces, solar arrays, sun shades, and experiment optics. A typical plume is shown in figure 18. The extent of the potential damage can be seen in the extent of the shaded areas, shown in figure 19, which depict the exotic thermal-protection schemes needed to protect the lunar module from service module plumes. This plume impingement problem is equally severe after docking, during attitude-control firings, and during retrofiring when the logistic vehicle leaves. Extreme care must be exercised in basic vehicle design and mission planning to overcome this problem. For example, it appears absolutely necessary that the following be considered:

1. Experiment protection by closing of sun shade
2. Solar array design capable of being folded during manned attendance
3. Low degradation thermal coating, such as optical solar reflectors
4. Constraintment of both approach angle and rate of approach of logistic vehicle,

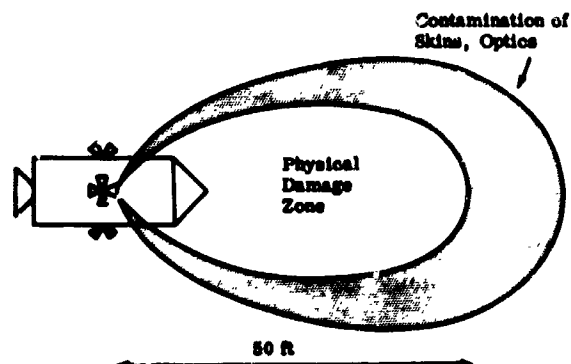


Figure 18. Plume impingement.

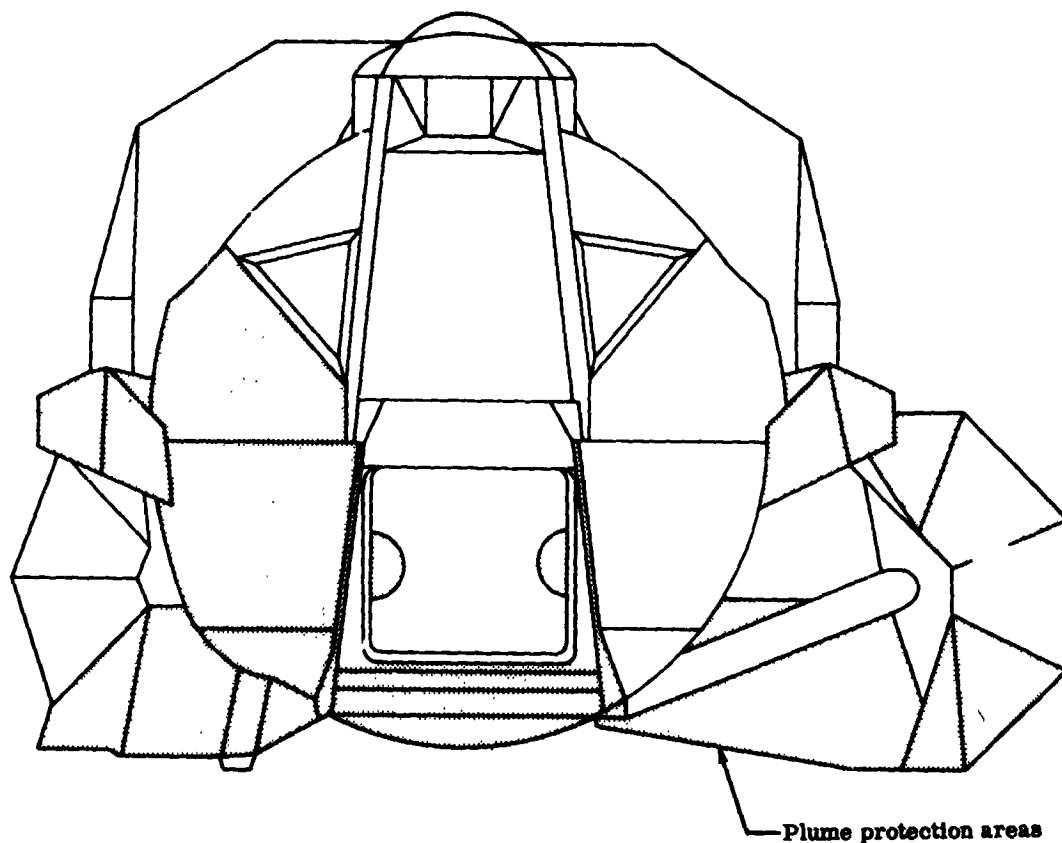


Figure 19. LM-4 thermal protection for front of ascent stage.

as well as type of attitude-control duty cycle and vehicle-separation technique

5. Investigation of the possibility, although remote, of a cold-gas logistic reaction-control system (RCS) for use at close range.

Basic telescope design is another area influenced by man's presence. The RCS plumes previously mentioned are a problem. In addition, the leakage of water vapor out of the pressurized compartment could degrade optics and must be prevented. Telescope structural attachment is also an area of concern. Many advanced thermal-isolation techniques make use of a strong structural support for launch and boost loads that, once in space, is automatically released to provide thermal isolation. Reactivation of such a device would be necessary to withstand

physical loads during docking, attitude control, and orbit-keeping by the main propulsion engine of the logistic vehicle. Orbit-keeping would be the worst condition. It is mentioned because it is possible that a man-attended vehicle could imply the presence nearby of a large manned spacecraft or space station. The drag characteristics of an astronomy vehicle ($M/C_D A$) are such that the vehicle could not provide long life in the low orbits, 250 to 350 nautical miles, indigenous to most large space stations. Telescope operation is also constrained after man leaves the vehicle because his presence had previously disturbed the overall thermal balance of the spacecraft. At the present time, it is anticipated that a cold telescope (below 273°K) will not thermally stabilize for at least two days after man leaves the satellite.

The last area of consideration in a man-attended satellite is the life-support system for the man. This support system must furnish oxygen and cooling and must remove the metabolic byproducts, carbon dioxide and water. For short visits, such as encountered in this type of vehicle, the basic life-support equipment would most likely be in the logistic vehicle. Transfer of the needed gases and coolants into and out of the astronomy vehicle would be a function of astronaut dress. If the astronaut is suited with only mask and gloves off, cooling is provided by the liquid-cooled suit. The oxygen supply and the removal of carbon dioxide and water are controlled by ducting. This life-support technique is the least complex for the astronomy vehicle. It is, however, the least desirable for the astronaut's movement and maintenance capabilities. If he is unsuited in a true shirt-sleeve environment, he is best able to perform his assigned tasks. Control of his environment is, however, fairly complex. Fans, heat exchangers, and the like are needed and will complicate the logistic vehicle interfaces.

Either of these life-support techniques are feasible. The thermally-preferred method is a suited astronaut. A shirt-sleeve environment will present some major problems, but it can be supplied if overall tradeoffs indicate its desirability.

Manned Telescopes

A manned-operation astronomy vehicle can be thought of as a manned spacecraft with a telescope attached; however, this type of vehicle is, by definition, a much larger, heavier, more complex spacecraft. Life support for man and the cooling of guidance and communication equipment require an active thermal-control system using liquid-cooling loops, space radiators, and stored oxygen and water. (It is not the purpose of this paper to discuss manned spacecraft design; therefore, the remarks on this topic will be limited to those areas germane to astronomy applications.)

Many of the problem areas and design considerations outlined for man-attended

vehicles are also generic to manned operation vehicles. Plume impingement is still a problem although a less severe one because some liberties can be taken in canting engines, changing docking-latch locations, or using plume deflectors. Design of spacecraft equipment is easier because the active liquid-cooling loop allows more flexibility in packaging.

Unfortunately, telescope operation is extremely complex. Plume problems exist constantly. Gas leakages from the cabin bear water vapor into experiment compartments and introduce a constant danger of electrostatic discharge in high-voltage systems. Life-support functions are carried out by the manned section of the spacecraft and have only minor impact on astronomy design. This apparent separation of the spacecraft into two sections gives rise to the concept of actually making two spacecraft sections: (1) a man-rated vehicle capable of life support and data-handling and (2) a section for experiments. In this way, a highly cost-effective, multi-experiment program is possible by using the one-man-rated vehicle and attaching astronomy, solar, earth resources, and x-ray types of experiment packages. This concept appears particularly worthy of further study by both NASA and industry.

Operation in Proximity to a Space Station

Advanced astronomy spacecraft may be required to operate in the vicinity of a large space station or space base. In this operating mode, thermal control of equipment, operating temperatures of the telescope, and contamination of coatings and optics are strongly influenced by the presence of the space station. (The problem of contamination by exhaust products from the reaction control system has been defined in the previous discussion of the man-attended telescope.)

The electronic equipment in an astronomy vehicle will usually be thermally controlled by an active system using louvers. In order for this type of thermal control to properly operate, the skins of the vehicle

must have an unobstructed view to space. Some of the thermal control skins for an observatory very close to the space station will have their view to space blocked by the station. This blockage is directly related to the distance from the space station, as illustrated in figure 20. A standard semipassive system would require that the observatory have a view to space of between 0.85 and 0.95, depending upon exposure to sunlight. This would require a minimum deployment distance of 12 feet. The deployment distance can be reduced by adding heat pipes to the observatory. These pipes transfer heat from the obstructed equipment compartments around the vehicle to those compartments having a full view to space. For the case shown in figure 20, this technique reduces the minimum deployment distance from 12 feet to 6 feet.

The temperature required for the observatory telescope varies according to the type of experiment being performed. Solar experiments tend to operate at room temperature; astronomy experiments require reference temperatures below 0°F and as low as -80°F. The unsymmetrical view to space of this telescope will induce gradients in the telescope just as it does in the electronics. Heat pipes should be used to minimize these gradients. Experiment temperature variations are shown

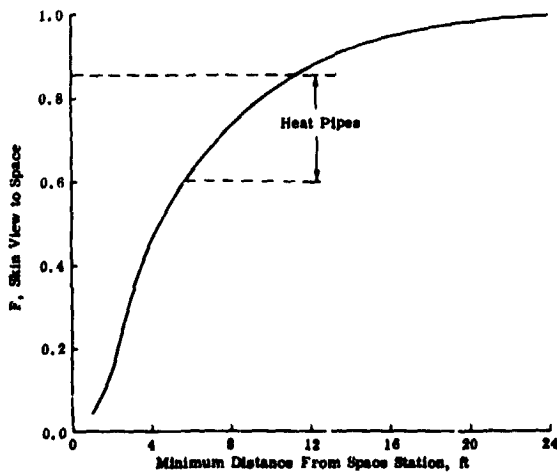


Figure 20. Space-station effect on OAO type of equipment.

in figure 21 as influenced by experiment/space-station proximity and vehicle shadowing effects. This range of 10°F to -50°F is similar to that of the OAO. It would be favorable to the experiments if this range were narrower. One method of lowering the magnitude of this excursion is to use the space station to shade the instrument from the sun. One possible shading arrangement is shown in figure 22.

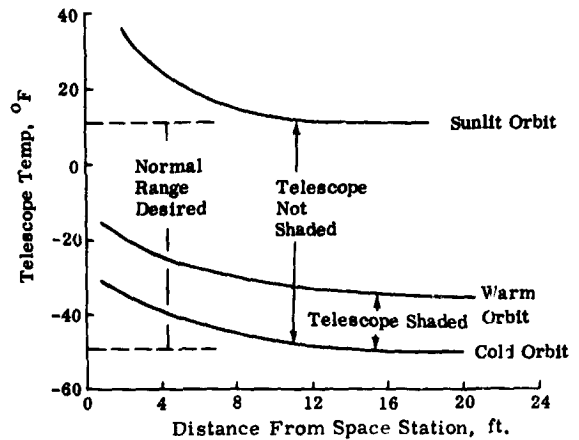


Figure 21. Telescope temperature variations.

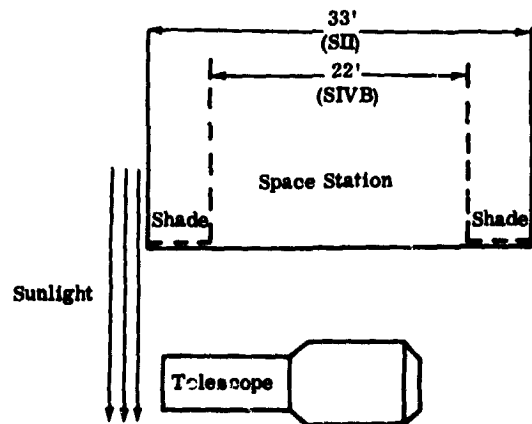


Figure 22. Possible shading arrangement of observatory.

Summary

The various passive and active thermal-control techniques described represent a set of devices and methods that the thermal

designer can use for achieving his design objectives. Any single application may best be served by a particular method or device or by some combination of these. Tradeoff studies between the techniques reviewed are generally effective only when considered for a specific application. Furthermore, as new techniques develop, with improvements introduced into one or another of the control devices, such tradeoff conclusions may be altered. At the present time, each of the devices described is eligible as the best application for some set of design circumstances. For example, on a single vehicle, one equipment bay may have a variable-conductance heat pipe with an OSR-covered radiator. The next bay may be equipped with externally mounted louvers or a thermal shade. It is this mixing and combining of the various devices that offers great flexibility for effective thermal control.

Advanced astronomy vehicles will have their designs greatly influenced by the presence of man and his induced environments. Solutions to all of the anticipated problems appear within the state-of-the-art for 1973 although some operational constraints may be needed. There is no clear thermal preference between man-attended and manned spacecraft concepts. Plume impingement appears to be the major area of concern for a man-attended telescope. Telescope contamination by gas leakage and plumes are the areas of concern when the telescope is manned. Should the vehicle use a manned concept, the development of a common manned module with multiexperiment capabilities (attached prior to launch) seems worthy of consideration.

PRECEDING PAGE BLANK NOT FILMED.

N70-36724

General Philosophy of Mirror Support Systems

W. W. Baustian

Kitt Peak National Observatory

Mirror support systems for terrestrial telescopes include four basic elements: (1) the axial and radial supports, (2) the defining units, (3) a set of jacks for supporting the mirror when the axial supports are inoperative, and (4) the cell on or in which the foregoing elements are mounted. In addition, suitable safety stops should be installed above, but free of the mirror, to provide seismic safeties and to prevent the mirror from tipping forward in case the telescope is accidentally pointed below the horizon. The installation and removal of the mirror from the telescope and cell for re-aluminizing should be considered in the overall design of the system. Provision for washing the mirror in the telescope is also important and should be kept in mind in developing the system.

Mirror Supports

The mirror supports must fulfill the basic requirement that the mirror be supported in such a fashion that its performance is as though it were weightless. To do this, the design of the supports must provide that each support assembly, axial and radial, sustain only its component of the mirror load, with an absolute minimum restraint in any direction normal to this component. The overall friction in the supports, particularly the axial, must be kept down to 0.1 percent for ribbed or lightweight mirrors. For solid mirrors, the allowable friction may be increased to two or three times this value. Provision must be made for accommodation of the differential thermal expansion between the mirror and the steel support structure. The normal or cross loads due to differential thermal expansion

are included in the frictional limitations mentioned above.

In the past, two basic systems have been used for the supports. One involves the use of counterbalancing levers and the other uses air bags, either in the form of a number of individual circular bags or several annular bags. For large mirrors, variation in pressure in the several annular zones must be provided because of the varying thickness of the mirror where the back of the mirror is kept flat. These air bags apply only to axial supports. The design of all supports must provide for load-carrying capacity proportional to the function of the slope angle of the mirror.

Axial Supports

For the lever type of axial or back supports, a leverage ratio of 5:1 to 7:1 is generally used. The ball bearings for the pivots should be conservatively rated for static service, but they should also be kept as small as possible to keep the friction radius to a minimum. Experience with the 120-inch Lick telescope indicated that a 5 or 10 minute run-in, at approximately 500 rpm, of all the bearings used in the supports noticeably decreased the friction. The explanation for this is probably the smoothing out of the as-ground finish of the races. On both the 120-inch Lick telescope and the 84-inch telescope at Kitt Peak, we have used groups of three levers acting against one support ring. To provide for differential expansion, pushrods transmit the load from the levers to the support rings. The ends of the pushrods may be gimbal attached or may be provided with hardened coned points that are seated in

coned sockets. The radius of the cone points should be designed to produce a pressure of around 150,000 pounds per square inch. The length of the pushrods should be such that the effect of angular displacement, due to differential expansion, is insignificant.

In the more recent telescopes, the use of air bags has gained in popularity because of the simplicity of design of the support units themselves. The overall cost savings of this system, including the pressure regulators and compressors, is probably not as great as would appear at first glance. The overall response of the two systems is about the same. A proposed modification of the "piston" type of support would require that suitable internal cavities be machined in the blank to compensate for the variable thickness of the mirror. Thus, a uniform pressure would be used below the entire area of the mirror. Another solution would be to make the back surface parallel to the front surface. An objection to this is the difficulty of support during the figuring of the mirror.

The 150-inch Kitt Peak design uses 33 air-bag-supported pads arranged in two circular arrays. Three defining supports are substituted for pads in the outer array. The general design of these supports is shown in figure 1. The roll diaphragm is a thin neoprene bellows, made by Bellofram and containing no fabric. The maximum air pressure is 8 pounds per square inch. The bellows are uniformly responsive in all directions to differential expansion. The use of annular bags poses a problem in this respect and requires some additional provision to accommodate the expansion differential. In addition, annular bags must be fabricated as special items, whereas the Bellofram diaphragms are a manufactured stock item. An additional feature of the individual pad system is that it permits some adjustment of the radii of the two (or more) arrays.

A single air bag has been used for one or two smaller telescopes of about a 60-inch aperture and of larger focal ratio. Use has also been made of the mirror as a "piston" with mercury band edge supports as "piston rings." It is not felt that these systems are satis-

factory for the larger mirrors of small focal ratio presently being used in modern telescopes.

At this time, the only pressure regulator with sufficiently sensitive response uses an air-bearing-supported piston in a cylinder assembly, which is mounted on the telescope tube with its axis parallel to the axis of the telescope tube. One regulator is used for each circular array of pads because of the requirement for a different pressure in each array. A proposal to use individual regulators for each pad to correct errors in mirror figures does not appear valid because this correction effect would vary with the pointing of the telescope.

A slope-responsive diaphragm type of regulator has been used on a 60-inch telescope primary mirror and for some secondary mirrors where the pressures are negative. From the experience to date, it appears that this form of regulator is not sensitive enough to meet the more rigid requirements for large mirrors; however, plans call for its use for the secondaries on the 150-inch telescope.

For large mirrors with fairly high slewing rates, the required air compressor capacity becomes considerable when using the air-bearing piston regulator. In addition, the size of the connecting piping must be large enough to keep the pressure lag to a minimum.

(The distribution of supports and pressures has not been discussed because this is an entire field of its own and is the subject of other engineering reports.)

Radial Supports

The radial support of mirrors is usually accomplished with lever systems, particularly in the larger sized mirrors. Mercury flotation bands have been used in some telescopes,

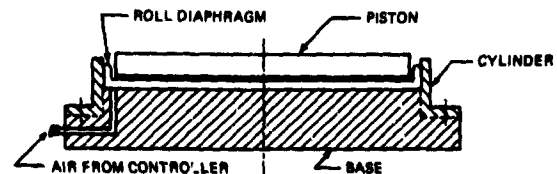


Figure 1. Air-bag-supported pad.

especially those of smaller sizes. They are also worthy of serious consideration for the support of secondaries for large telescopes because of their simplicity and light weight. The amount of mercury in the tube, or tubes, should be the exact amount required to "float" the mirror so that its optical center coincides with the optical center of the telescope tube. Consequently, there will be no lateral shift of the mirror for various telescope pointings and therefore no need for additional center-defining points. In fact, the latter should definitely not be used with this system, thereby eliminating the possibility of conflict of restraints. With the "piston" type of axial air support, the mercury bands are pressurized to provide a suitable piston seal.

The lever type of radial supports for ribbed mirrors is usually incorporated in assemblies with the axial supports. The load point for each lever is adjusted to coincide with the calculated center of gravity of the element being supported by that lever. Therefore, these support units extend up into pockets or recesses in the back of the mirror. The levers are gimbal-mounted, as are the load rings at the ends of the levers. To accommodate differential expansion, a linear ball bearing is placed between the load ring and the mirror. The leverage ratio is usually 5:1 to 7:1. For large mirrors, seasonal adjustments may be necessary; hence, provision should be made to shift the radial support subassembly both for this and for original alignment.

For large solid mirrors, I believe only the push type of lever systems has been used thus far. The levers have generally been distributed around the outer edge of the mirror. A better figure can be maintained if they can be divided between the outer rim and the central hole in the mirror. In the 150-inch telescope, we are using this system with the weight being equally divided between the two sets of supports. Because only half the supports are active and their loads are proportional to the square of the cosine, the leverage ratio is usually on the order of 30:1. In general, a compound leverage system is used. The load point on the mirror should be in the plane of the average center of gravity of the mirror.

For large mirrors, particularly those with a short focal ratio, this causes problems; some improvement is achieved by the use of both external and internal edge systems. The relatively heavy pressure pads in contact with the mirror should be counterweight-supported to cancel edge-droop effect. Accommodation of differential expansion in the axial direction may be incorporated with pad counterbalance by pivoting the pad pushrod in the main counterweight lever. Radial expansion differences may be handled by providing for seasonal adjustments or by using a concentrically stacked, bimetallic, temperature-compensated pushrod. We have been using alternate tubes of Invar and 7075-T6 or 2024-T6 aluminum.

Defining

In general, four center-defining points have been used so that alignment in the two coordinates is more easily accomplished. For solid mirrors, the defining points may act directly on the edge of the center hole, or, if central radial supports are used, four of the lever arms of these units can be micrometer-controlled for the purpose. For the separate center points, radial expansion may be balanced by means of the bimetal compensators already mentioned. Axial freedom is provided for by means of a hardened ball between two hardened flats. Dial indicators are installed to aid in centering and to provide for repeatability during reinstallation of the mirror after aluminizing.

With ribbed mirrors, the radial support levers may also be used for center-defining. Since these levers are gimbal-mounted, expansion compensation is easily provided for by restraining the levers by means of radial slotted stops, as shown in figure 2.

Collimation of mirrors with the lever type of axial supports is done conveniently by micrometer control of three equally spaced levers in the outer array of supports. If the support units contain more than one lever, only one lever in each of the three need be controlled.

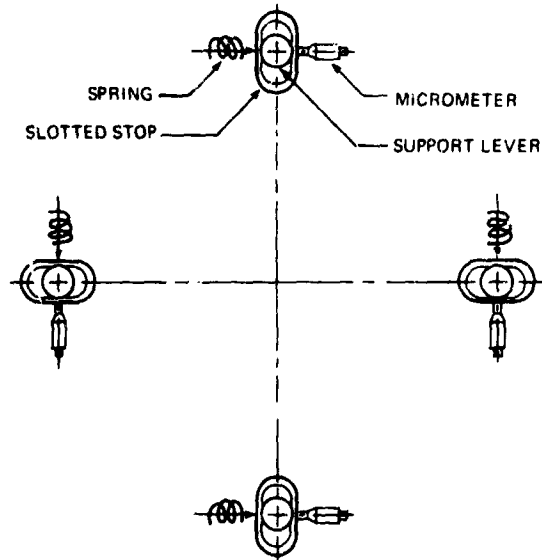


Figure 2. Center-defining, by using radial support levers.

With air-bag supports, separate collimation units may be located between supports in the outer array or substituted for three of the supports themselves. In the more recently built telescopes and those being built, load-sensing elements are being installed in the collimating units for monitoring the air-bag pressure. Dial indicators should be installed to monitor mirror position, too.

To aid collimation during both original setup and routine adjustments, it would be well to develop an auxiliary optical system to facilitate this operation. In a sophisticated design, it could be used to perform the collimating operation automatically on command.

Mirror Cell

The mirror supports, defining units, Coudé No. 3 secondary mirror, and the Cassegrain instrument mounting plate are all mounted on a cell. This cell, in turn, is bolted either to the lower ring girder of the telescope tube or directly to the ends of the lower Serrurier truss members. Usually, only four attachment points are used in either case.

From both fabrication and operational standpoints, it is best to use a flat cell; that is, a cell that is not cup-like in cross-section.

Welded fabrication is the most economical, with top and bottom plates reinforced by internal webs or ribs. Provision should be made for good venting of all cavities. If it is planned to leave the mirror on the cell while aluminizing, this should be taken into consideration both in the welding procedure and in the painting of all surfaces. The weldment should be stress-relieved. It is usually best to machine all the upper surface of the cell and the outer edge. The machining of the lower surface may be limited to the mounting surfaces for the Coudé No. 3 secondary mirror, the Cassegrain mounting plate, and miscellaneous spot facing, as required. A symmetrical layout of radial and chordal webs will also effect a reasonable economy in fabrication. The maximum cell deflection is usually limited to about 0.005 inch. It is emphasized that the complete cell and support assembly should be designed for optimum ease of removal and disassembly of the mirror for aluminizing.

The Cassegrain mounting plate consists of an instrument mounting plate, ball-bearing-mounted on a base assembly, which is bolted to the underside of the mirror cell. The present trend of instrumentation is such that the capacity of this unit should be a minimum of several thousand pounds at a moment arm of 3 or more feet. Provision should be included for manual rotational positioning and clamping and for position readout. Although the bearing for the Cassegrain mounting plate should be of good quality, it is unreasonable to use it also for driving during an observation. For this purpose, it is best to use a precise bearing designed into the instrument having this special requirement.

Jack Pads

Three jack pads are added to the cell to support the mirror when the mirror supports are not in operation or when any or all of the mirror supports have been removed. With air-pad supports, it is possible to combine the jacking and collimating functions in one unit. Operation of the jacks is from the back of the cell.

Resume of Existing Support Systems

The 200-inch Hale Telescope at Mt. Palomar, built early in the 1930's, was the first ribbed pyrex mirror ever made. It was a pioneering effort, and the first mirror supports (36 in number) had excessive friction problems. Based on tests and a better knowledge of the requirements, a redesigned support system was built and installed. In Dr. I. S. Bowen's article on the 200-inch telescope, he describes these supports:

"The mirror is mounted on thirty-six support mechanisms of the type shown in figure 3, one being inserted in each of the thirty-six holes shown in the mirror blank. The support band, B, which makes contact with the mirror, is placed in a plane normal to the optic axis through the center of gravity of the mirror. As the telescope is turned away from the zenith, the lower end of the support system, including the weights, W, attempts to swing about the gimbals, G_1 , and thereby exerts a force on the band B through the gimbals G_2 in the direction normal to the optic axis. The weights and lever arms are so adjusted that the force exerted just balances the component in the opposite direction of the pull of gravity on the section of the mirror assigned to this support. Likewise, the weights, W, pivot about bearings, P, in such a way as to exert a force along the rod, R, which is transmitted to the ring, S, by the gimbals G_2 . These weights and lever arms are likewise adjusted so that the force exerted balances the component parallel to the optic axis of the pull of gravity on this same section of the mirror. The mirror is therefore floating on these support systems, and no forces are transmitted across the mirror."^{*}

*I. S. Bowen, "The 200-Inch Hale Telescope," *Telescopes, Stars and Stellar Systems*, ed. by Gerald P. Kuiper and Barbara M. Middlehurst, Vol. I.

The mirror cell is cast steel, reflecting the practice and costs of that period. It is a flat disc with four attachment brackets bolted to the outer rim. Fans have been installed in the lower plate openings to aid in air-conditioning the mirror and cell during ambient temperature changes.

The 120-inch telescope at Lick Observatory, designed and built after World War II, profited from the experience obtained with the 200-inch. The mirror cell is of welded construction and contains 18 mirror supports for the ribbed pyrex mirror. These support units are removable from the back of the mirror cell without having to remove the mirror. Such is not the case with the 200-inch supports. This requirement was a direct result of experience with the 200-inch telescope.

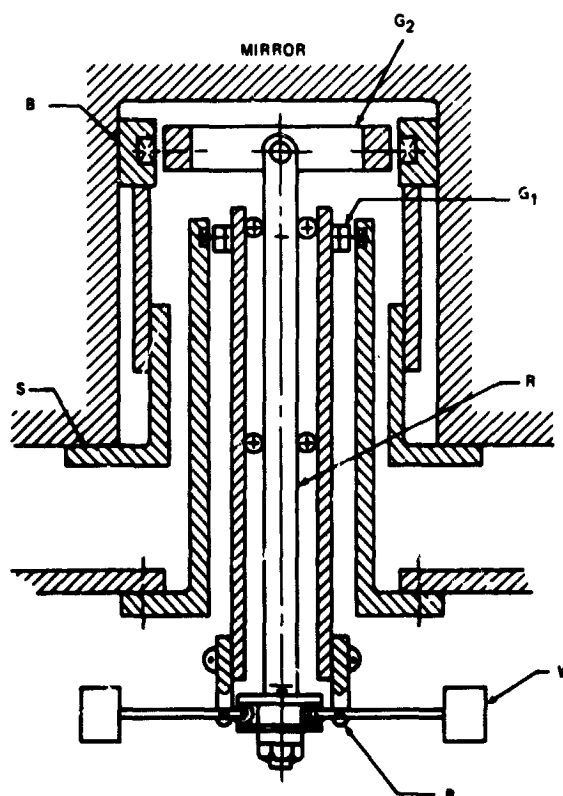


Figure 3. The 200-inch-mirror support mechanism.

Figure 4 shows the 120-inch mirror support system. It will be noted that the axial and radial components are separate components. In general, this would seem to be preferred for optimum adjustment. The radial load is carried by pad ring, P, which is balanced by weight W_1 through an axial bearing, B, and gimbal G_2 . The lever is gimbal-mounted on G_1 . The support, S, for G_1 is laterally adjustable with respect to the assembly mounting plate, MP, which, in turn, is laterally adjustable with respect to the mirror cell.

The axial load is carried on ring R, which is supported on three gimbal-attached pushrods, PR, that are adjustable in length. The radial loading of ring R itself is balanced by counterweight W_3 . The axial mirror load is balanced by weight W_2 .

Three of the axial support levers are micrometer-controlled for collimation. Two center-defining units are located in diametrically opposed, triangular pockets adjacent to the center hole in the mirror. Both coordinate adjustments are provided in the two units.

The cell and supports for the 84-inch telescope at Kitt Peak National Observatory are essentially a copy of the 120-inch design with the following exceptions:

1. The axial support pushrods are of the cone point and socket type.
2. Center defining is accomplished by the radial slotted stops referred to previously in figure 2.

The two 150-inch telescopes for the Kitt Peak National Observatory and the Cerro Tololo Inter-American Observatory in Chile have solid mirrors of fused silica and Cer-Vit, respectively. These mirrors, 158-inch outer diameter by 24 inches thick, have relatively large center holes with 50-inch inner diameter. The cell is a welded fabrication with four attachment brackets bolted to the outside rim. The axial supports are air bags, as shown in figure 1.

The radial supports consist of an outer and inner array with 24 units in each. The outer support, shown in figure 5, has a counterbalanced pad supported at A on the main counterweight lever. This lever is

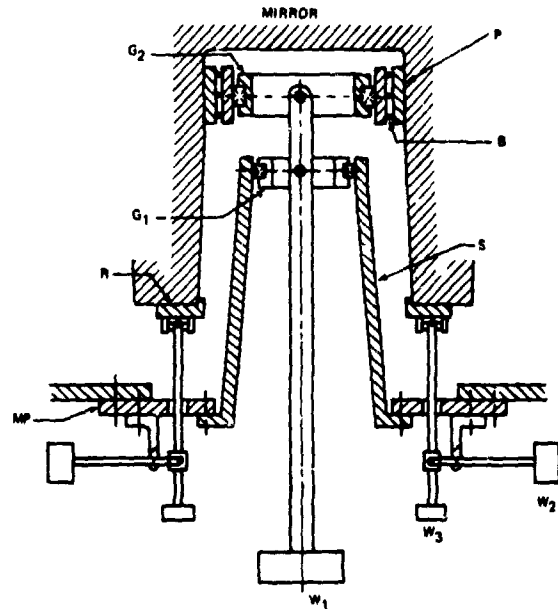


Figure 4. The 120-inch-mirror support unit.

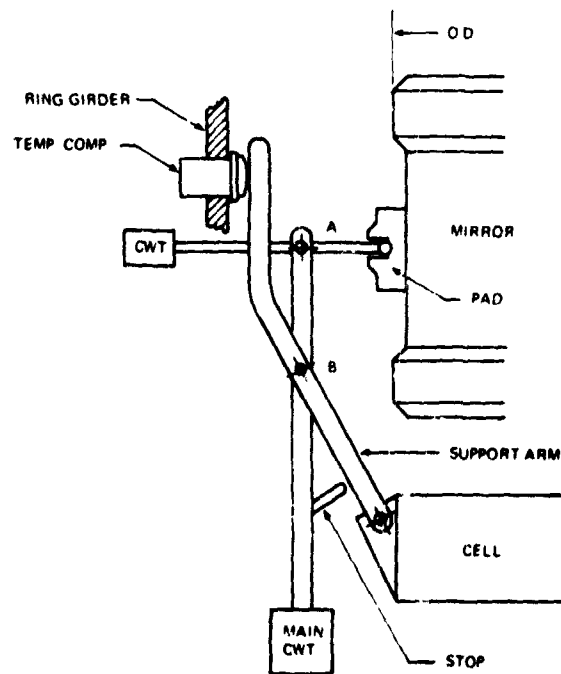


Figure 5. The 150-inch outer radial support.

pivoted about point B on a support arm, which is pivoted on the end of the cell and bears, at the upper end, against a temperature-compensated support mounted in the ring girder of the tube. The leverage ratio is 20:1.

The inner radial support, shown in figure 6, is a compound lever system supported in pivots A and B. Four of the units are used for center-defining. The pushrod is temperature-compensated, and pad weight is balanced by the counterweight, CWT. The ends of the push link between the primary and secondary levers are cone points. The overall leverage ratio is 73:1.

The combination jack pad and collimating unit, shown in figure 7, is provided with a dual-range load cell: 0 to 1,000 pounds for collimating service and 0 to 10,000 pounds when used as a jack pad. The rollers accommodate differential expansion. Lead springs support the load-cell assembly at its center of gravity so that no moment of force is added to the mirror or to the load cell when the telescope is pointed away from the zenith.

Space Telescope Design

Since the function of the mirror supports of terrestrial telescopes is to simulate mirror weightlessness, support units are not needed for space telescopes. Support is needed for the mirror only during the launch period, and then only to protect the mirror against excessive loading or damage.

Space telescopes do require defining units, which must be equipped with remote monitoring and controls. These units should be retracted during launch (to prevent damage) and then used to lift the mirror off the launch supports into operation position after the telescope is in orbit. Temperature compensation becomes a more rigorous requirement for space telescopes than it is for terrestrial telescopes.

To summarize, it would appear that the only elements common to space and terrestrial mirror support assemblies are the defining units and the provisions for the accommodation of differential expansion between the mirror and the support assembly.

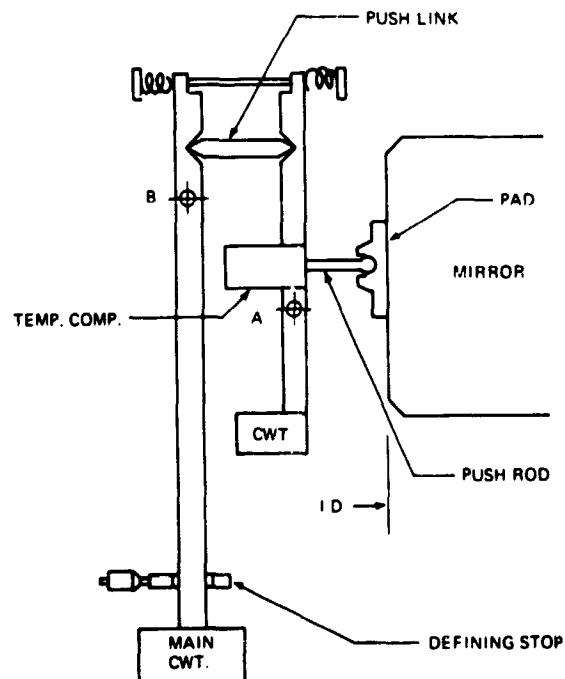


Figure 6. The 150-inch inner radial support.

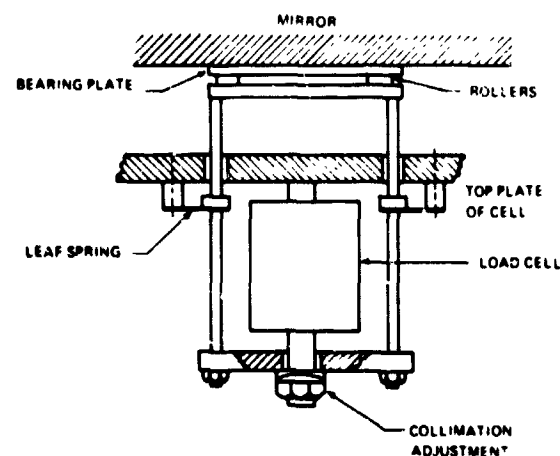


Figure 7. The 150-inch combination jack pad and collimating unit.

Considerations in the Design of Orbital Telescopes for Dynamic Environments

C. E. Lier and R. E. Jewell

NASA George C. Marshall Space Flight Center

Introduction

Since its discovery in 1608, man has been fascinated by the discoveries that the telescope enabled him to make regarding those heavenly bodies which so greatly influenced his existence, the sun and the moon. Through the development of larger and more powerful telescopes, astronomers have acquired increasingly detailed knowledge of these bodies and have delved into the mysteries of distant stars and other galactic systems. The trend in these telescopes has been toward larger physical sizes and greater weights (up to one million pounds), with locations selected and mounts designed to exclude, as much as possible, disturbances caused by base motions in order to achieve measurement accuracy. The most severe "dynamic" design conditions for these telescope structures and components were probably the transportation and handling conditions prior to or during assembly.

The advantages of orbital telescope operations, for both terrestrial and celestial observation, have led man to place telescopes atop fire-breathing generators of acoustic and vibratory energy (rockets) in order to accelerate them into earth orbit. The dynamic conditions during this launch operation and, subsequently, in the near-void of earth orbit are quite contrary to the past history of telescopes (except perhaps when subjected to violent earthquakes or when being dropped from the top of the "Leaning Tower of Pisa." A further complication arose with the decision to couple men and telescopes in orbital operations in order to gain operational flexibility and other advantages. There is an obvious incompatibility between man's nature

and the requirement for quiescence. Man must breathe; he is usually moving about in some inefficient way and often coughs, sneezes, scratches, etc. In an earth observatory, these actions might affect only his associates, but in an orbital observatory, where measurements of radiation from a small precise area of the sun are being made, they could be sufficient to ruin an experiment unless precautions were taken in the system design. As a result of these significant changes in design requirements, it was quite probable that "new" problems would be encountered by the scientists and engineers who had been working in the area of telescope system design and development. Similarly, those scientists and engineers who had previously been concerned with the problems of launching men and their life-support systems into orbit would meet "new" challenges in the development of payload systems involving large but delicate telescopes.

It is the intent of this paper to describe the dynamic environments (acoustic, vibration, shock) that a telescope assembly might see for a variety of launch vehicles, to discuss current state-of-the-art approaches to designing for these environments, and to discuss some of the "unusual" aspects of telescope design for dynamics. The paper is not comprehensive of all the work that has been done; it will reference only a few cases of which the authors are aware through personal activity and through a review of the literature. It is hoped that as a result of this paper the reader will be convinced (1) that the dynamics environments are quite important and should be considered throughout the design of a telescope system and (2) that the dynamic behavior of a large telescope and of the

structure tying it to the launch vehicle and/or orbital assembly cannot be treated separately but must be considered as a dynamic system in most cases.

Dynamic Environments During Launch

The dynamic environment of a rocket launch vehicle in the "payload" area is a constantly changing combination of acoustic and mechanical excitation and response. The principal sources of energy are the engine exhaust, engine vibration, sudden release of stored energy from engine thrust (holddown release and engine cutoff) or from vehicle bending moments resulting from ground winds, aerodynamic turbulence, buffeting, boundary layer shocks, and staging operations, including pyrotechnic devices, engine startup, and shroud deployment. A comparison of typical time histories of vibration and acoustic levels through the launch phase and the frequency variation for several points in time along these curves is shown in figure 1.

Note that the composite (all frequencies combined) vibration level tends to generally follow the acoustic level since the acoustics source provides energy over the entire frequency spectrum of concern and is a major contribution to payload vibration. The relative amplitudes of the peak acoustic and vibration levels represented in the figure vary, depending on launch vehicle characteristics such as engine acoustic power, vehicle height, nose cone and shroud profiles, and vibro-acoustic transfer characteristics of the payload shroud and support structure.

Note also that the frequency characteristics of the acoustic environments change significantly through the launch phase. As the vehicle velocity increases to near Mach I, the spectrum shifts gradually downward. Above Mach I, at maximum aerodynamic pressure (Max Q), the spectrum shifts drastically upward in frequency. The primary acoustic energy source at lift-off is engine noise, and at Mach I and Max Q the primary source is aerodynamic. The shift between Mach I and Max Q is a result of changes in flow and

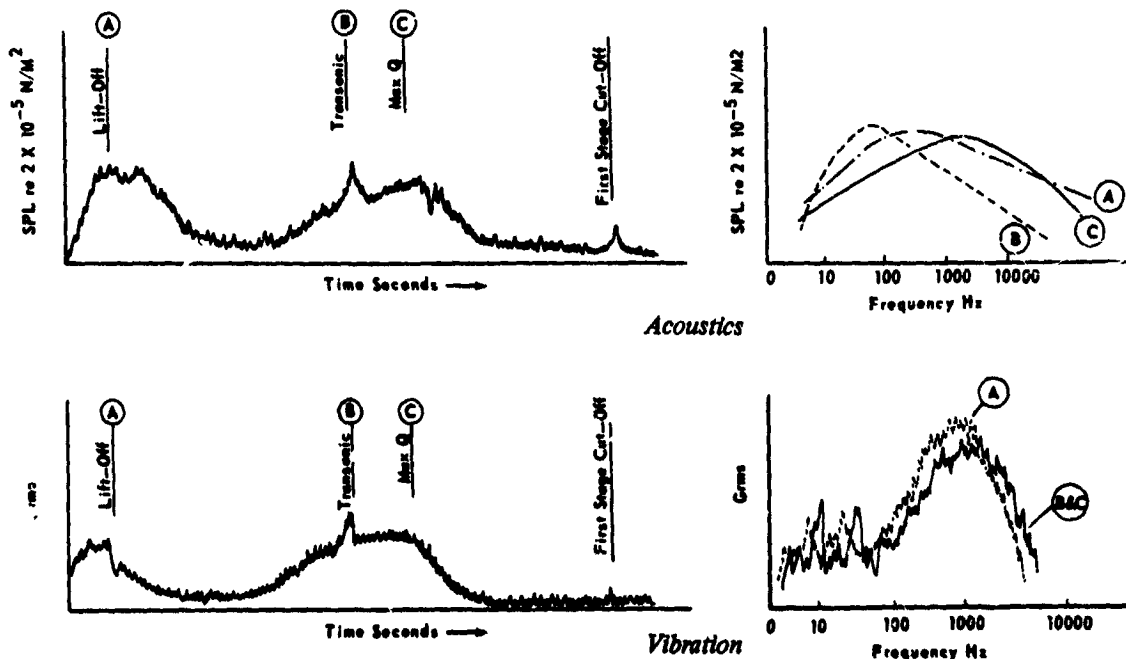


Figure 1. Comparison of typical acoustic and vibration responses for payload regions of launch vehicles.

boundary layer characteristics, which vary greatly between launch vehicles.

The shifts in vibration response frequencies are also significant. The sharp "spikes" in the low-frequency region represent the overall vehicle modal responses, which are excited by release transients and, later in flight, by wind gusts and vehicle maneuvers. During flight, these spikes shift upward in frequency. This shift is a steady change caused by expulsion of propellant mass during flight. For the response region above 200 hertz, note that the peak in the response spectrum is at a slightly higher frequency. This is the result of decreased vibroacoustic efficiency on the part of the aerodynamics rather than any change in dynamic system.

Generalized acoustic data for several launch vehicles are provided in figures 2 through 5. These data are presented to provide a "feel" for the magnitude of environments that can be expected and to indicate the degree to which engine acoustic and aerodynamic data from an extensive collection of vehicles can be correlated by judicious selection of nondimensionalizing parameters. It is reiterated that the configuration of the payload shroud will influence both the external and internal acoustics and vibrations and will be of considerable importance in the design of the telescope dynamic system. Figure 6 is an example of the differences in vibration for three different payloads launched on the first stage booster.

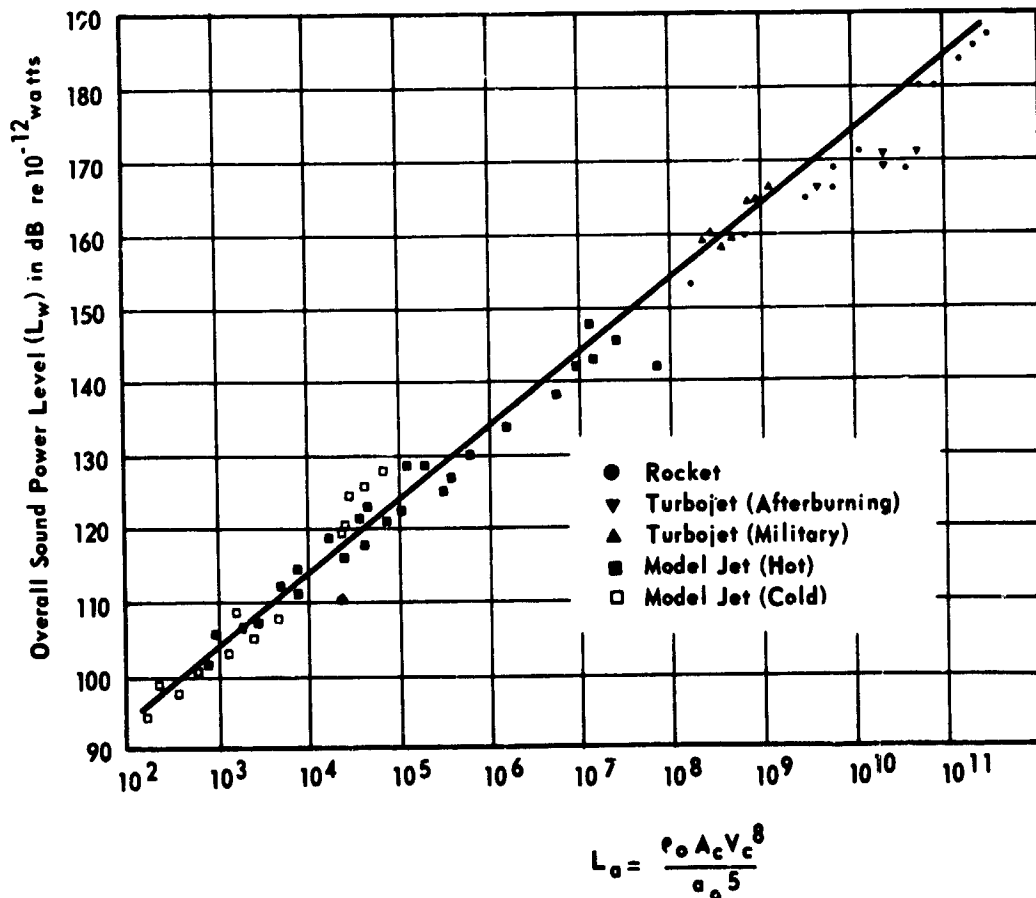


Figure 2. Total acoustic power for jet flows compared to a revised Lighthill parameter based on characteristic velocity and diameter.

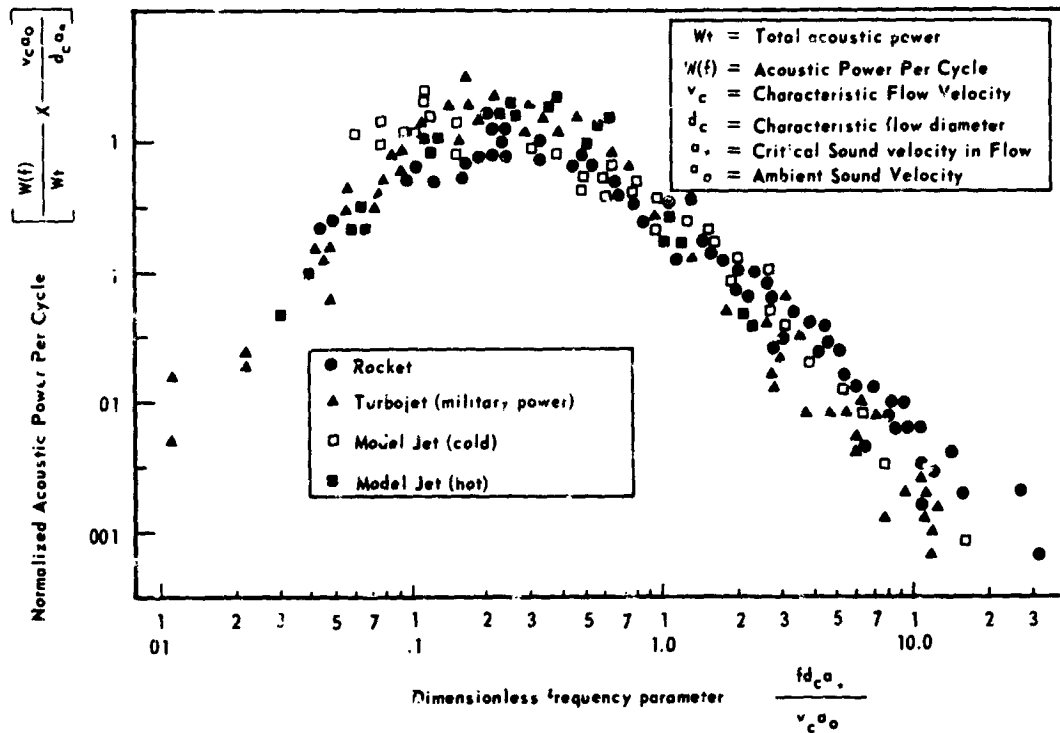


Figure 3. Normalized acoustic power per cycle for jet flows as a function of a nondimensional frequency parameter.

Dynamic Environments During Orbital Operations

Fortunately, the tremendous vibro-acoustic environments previously discussed can exist only in the atmosphere. After sufficient burn time to insert the payload into orbit, the unwary dynamic analyst might think that all will be calm and serene; however, it is this portion of a mission in which the most insidious problems in structural dynamics can occur. If the system is not required to reenter the earth's atmosphere, the orbiting configuration is often one from which antennae, solar panels, and various structural appendages are allowed to unfold and protrude. The result may be a dynamic system without symmetry and one which has the appearance of being extremely fragile. It is true that for its own coordinate system it is generally at rest and would remain so unless some perturbation of the forces acting on the

system occurs; however, the sources for such perturbations are many and varied. For example, thrust required for orbital change or course correction will tend to "shock" the system into response of its many modes. Attitude control system, whether for the whole orbiting assembly or for some part of it, will "ring" the resonances of the dynamic system. Operating equipment such as pumps, fans, valves or any reciprocating or rotating mechanisms will provide steady-state input forcing function. In addition, man himself represents a significant dynamic forcing function. His movements in and about the spacecraft, his involuntary actions such as heartbeat, coughing, sneezing, and even his planned actions for the accomplishment of an experiment—all impart energy to the dynamic system, which will respond in some manner. None of the forcing functions mentioned would normally present any significant problems with regard to the integrity of the structure, but, on the

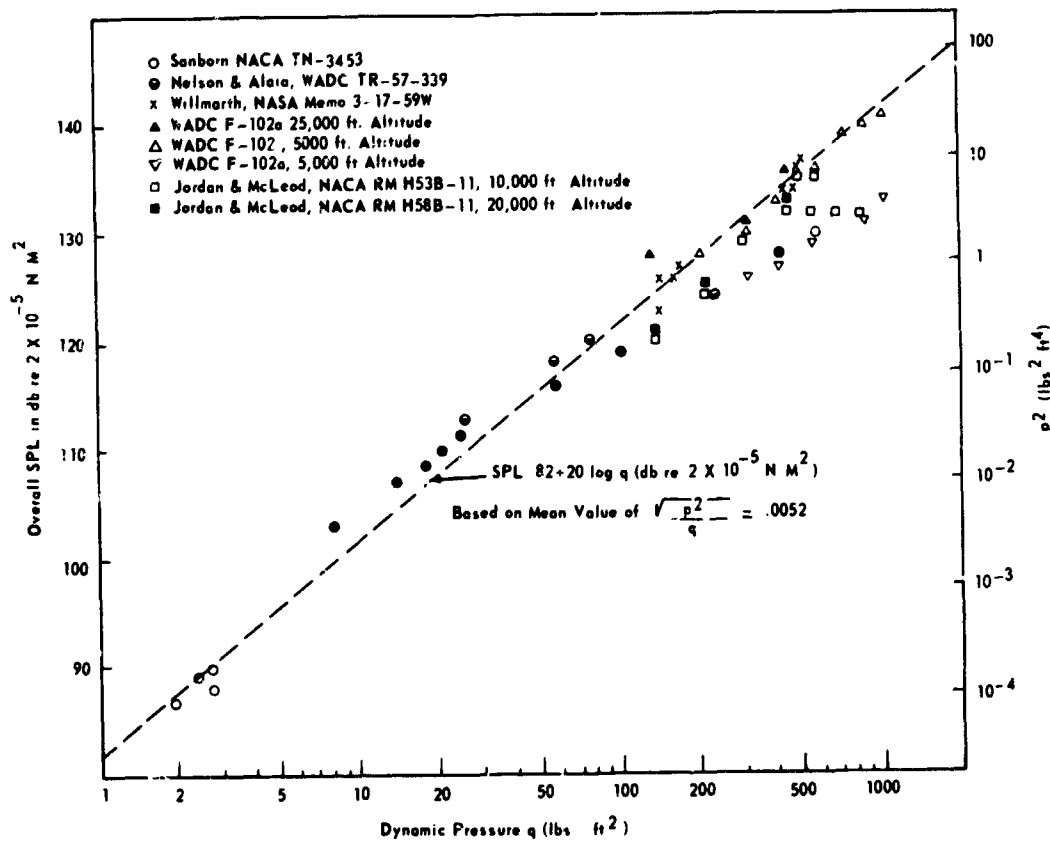


Figure 4. Overall sound pressure level and mean square fluctuating pressure (p^2) in turbulent boundary layer as a function of free-stream dynamic pressure.

other hand, the dynamic responses that result may prohibit accomplishing certain precise and delicate experiments, especially those experiments where a high degree of long-term stability is required.

An example of subsystem dynamic response that can result from the operation of onboard equipment is shown in figure 7. The analysis was carried out for the Apollo Telescope Mount (ATM) spar and ring assembly with the input forcing function occurring at the gimbal ring. The amplitude of the forcing function was estimated to be 1.4 pounds and was treated as one period of a sinusoid. Note from the figure that the response indicates a significant number of resonances below 35 hertz and that a singular input from the yaw actuator causes displacement response in all three axes as well as a rotation about the Y

axis. The displacements are quite small and are of no detriment to the structure; however, continuous displacements of this type for a precise optical system are quite significant.

Recently, the authors encountered an example of the effect of man on the orbiting mechanical system. An experiment was planned to study the reactions of liquid under long-term low-level acceleration. The magnitude of acceleration was to vary as a parameter from 10^{-4} to 10^{-6} g's referenced to one earth g. For the dynamic system that was considered, it was very quickly determined that the normal voluntary motions of the astronaut could not be tolerated because the dynamic acceleration imported to the experiment package by the motion of a limb was prohibitive to maintaining the constant low acceleration required. An indication of the

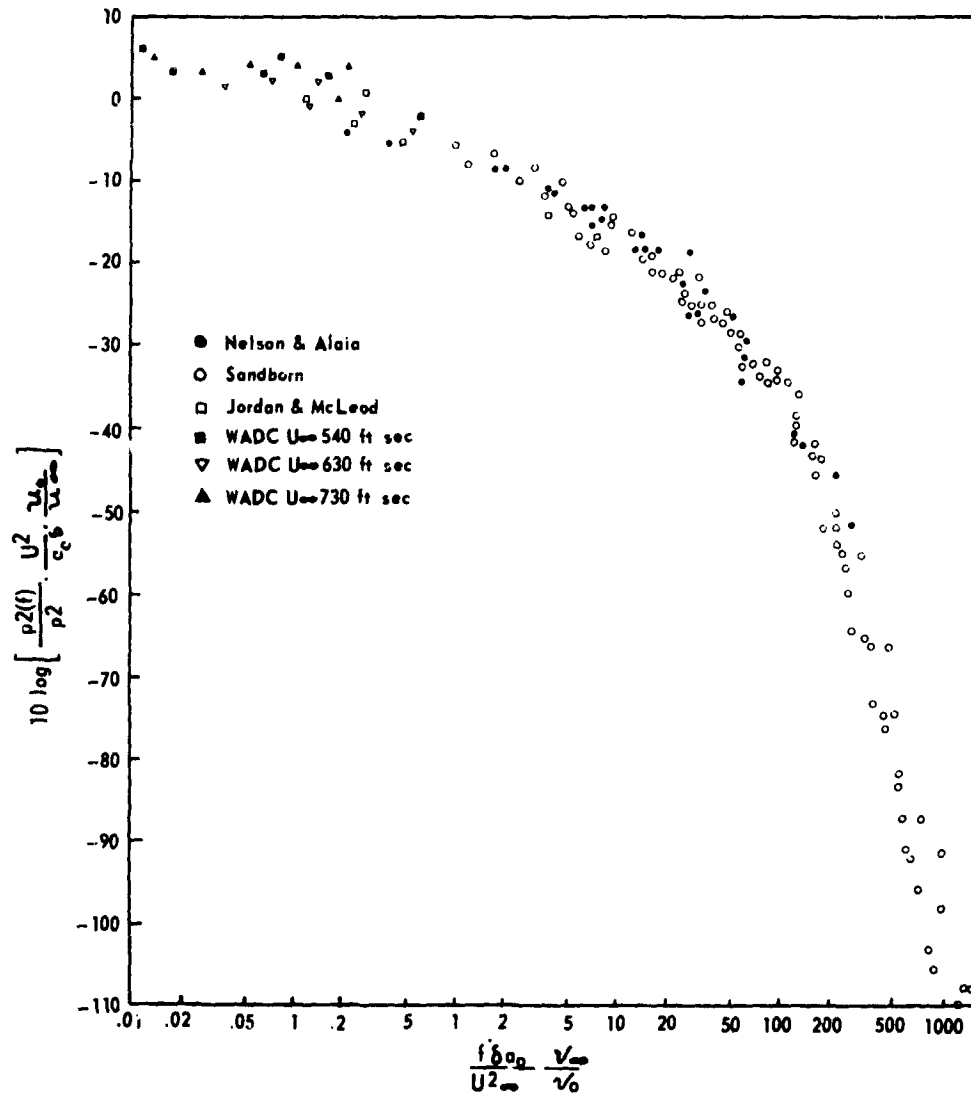


Figure 5. Normalized fractional mean square pressure per cycle in the turbulent boundary layer.

detail to which the problem was studied is shown in figure 8. Plotted on this figure is the acceleration response of the orbital system to normal heartbeat and to a cough. The obvious conclusion is that such inputs would cause a relatively large-scale perturbation of the acceleration parameter. With careful, dynamic design analyses, however, such difficulties can be resolved. Consultation with the structural dynamicist early in the design and development phase of an experiment system can cope with these types of problems.

Effects of Dynamic Environments on Structures and Equipment

The telescope structural designer should be concerned with two aspects of dynamic environment effects: (1) the capability of the structure to perform its design functions after exposure to severe conditions and (2) detrimental effects of structural response on attached equipment and systems. The first consideration is generally one of structural

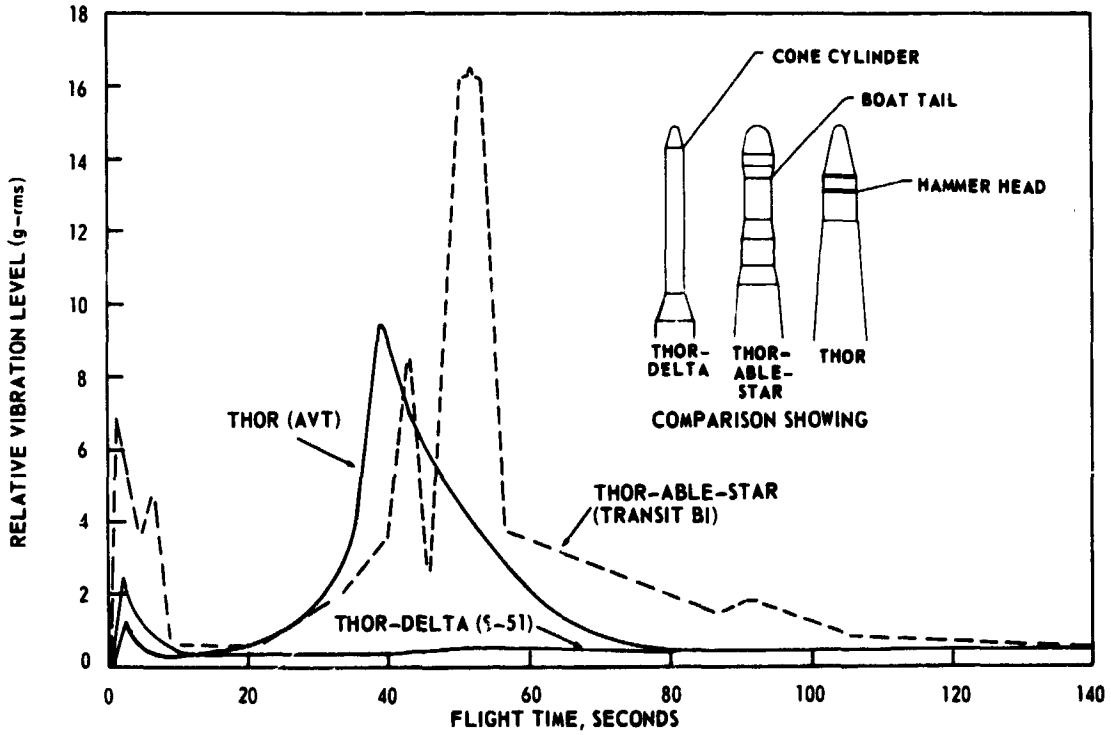


Figure 6. Effect of payload shroud configuration on vibration response amplitudes.

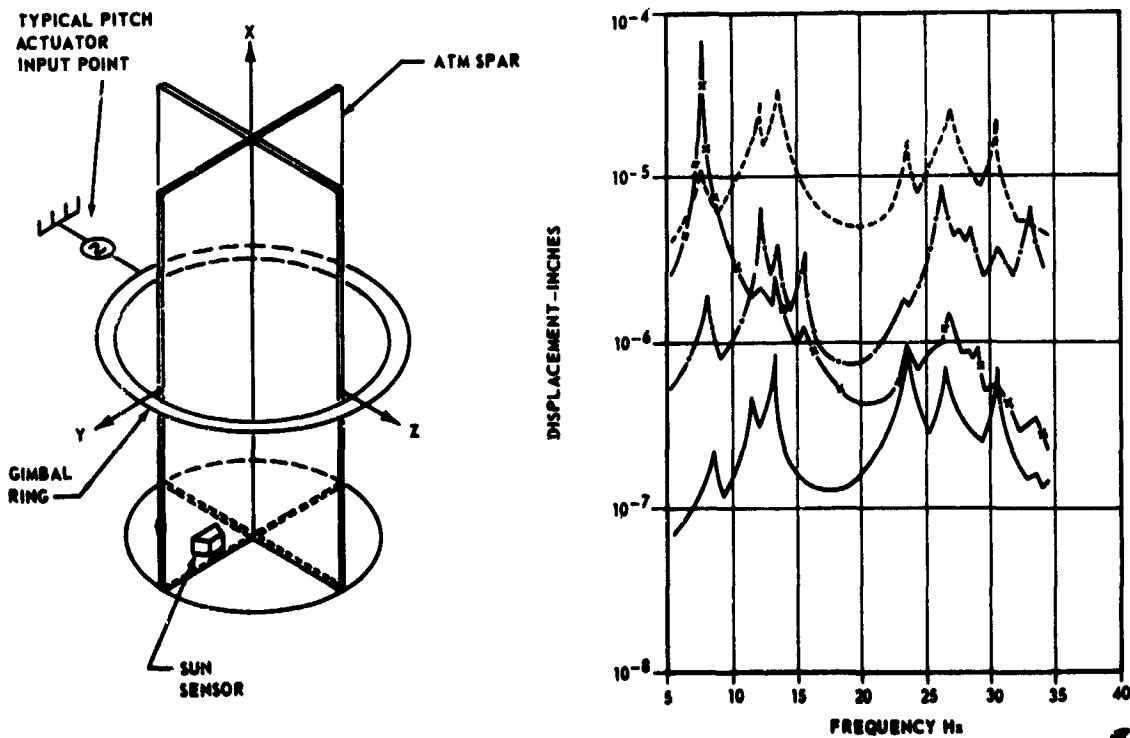
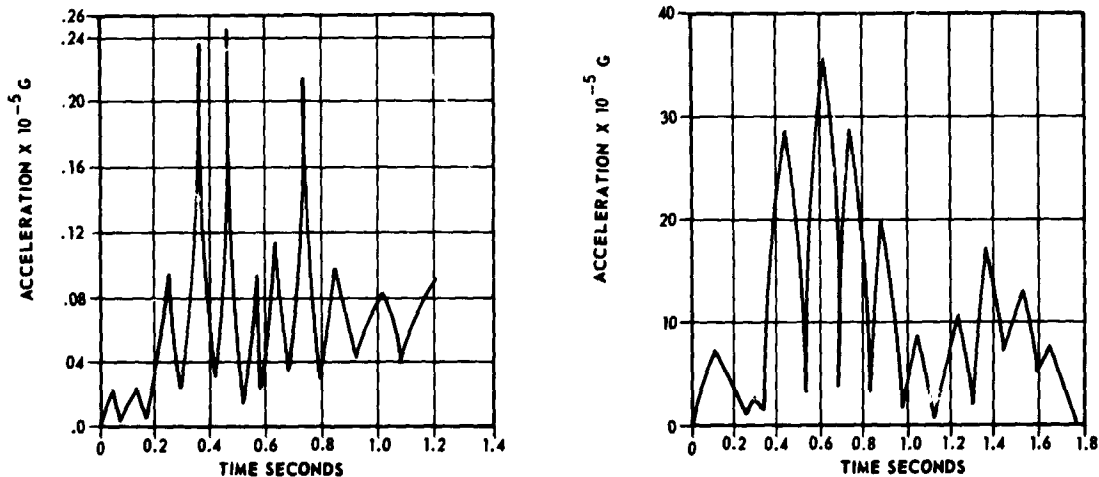


Figure 7. ATM subsystem dynamic response resulting from operation of onboard equipment.



(a) Heartbeat: resultant acceleration output, station 6. (b) Cough: resultant acceleration output, station 6.

Figure 8. Orbiting system: dynamic accelerations resulting from crew motion.

strength; the second is one of structural refinement.

The severe acoustic, vibration, and shock environments of launch, boost, and docking can result in stresses that cause failure or permanent deformations in structural members. Joints tend to loosen, mating parts wear, and flaws in welds and solder joints tend to propagate under exposure to these conditions. As a result, critical alignments may change; bearing performance may deteriorate; and electronics can malfunction.

The quasi-sinusoid, discrete-frequency, and transient environments have their most significant effects when their characteristic frequency coincides closely with structural and equipment resonant frequencies and when the responses are amplified.

The random environments have their most significant effects when structural and equipment resonances occur in frequency bands where high vibration or acoustic energy is concentrated; however, problems can be encountered over a wide frequency range because the energy is usually broadly distributed. Random environments have the capability of exciting several resonances simultaneously, with random phase relationships, thereby increasing the relative displacements of adjacent parts.

Designing for Dynamic Environments

The design of a new payload for a launch vehicle for the dynamic environments of launch and orbital operations involves two major technologies: (1) environmental prediction or definition and (2) design analyses.

Environmental prediction or definition methods fall generally into two categories: (1) methods based strictly upon analytical treatment of the launch vehicle and payload parameters (e.g., thrust, aerodynamic pressures, skin thicknesses, velocity, etc.) and (2) methods involving interpolation or extrapolation of previously acquired data from the same or similar launch vehicles.

Several techniques for predicting acoustic levels due to the turbulent mixing in rocket exhaust are well documented in the literature. The most widely used is a semi-empirical method developed by Dyer in which he describes the general features of the sound field as a function of the functional and geometric features of the rocket engine. His method accounts for the effects of the acoustic near-field, the longitudinal and circumferential correlation of the pressures on a cylinder in the field, and the effects of vehicle motion. Estimates of the engine-generated

acoustic environment obtained by using the basics of Dyer's method have given excellent engineering results.

Methods for estimating the aerodynamic noise environment are more varied. This is true mainly because the flow over the structure and the associated boundary layer conditions are rapidly changing. The root-mean-square fluctuating pressure can range from one percent to as much as 15 percent of the free-stream dynamic pressure around the vehicle. The actual value at a particular point on the structure is a function of the vehicle trajectory and the overall and localized geometry. No one technique can be singled out; however, a summarization is given in a state-of-the-art monograph on random noise and vibration sponsored by the Shock and Vibration Information Center.

The random vibration levels during launch and boost in the payload areas are directly related to these acoustic environments. Most of the techniques for predicting these random levels are described in reference 1. The most widely used methods are generally wholly empirical and represent extrapolation techniques similar to those proposed initially by Macaffey and Smith. As many as a dozen or so variations have evolved from their basic approach, each one attempting to improve the prediction scheme through the use of new data or better structural definition. At the other end of the "analysis spectrum" are the totally classical analytical approaches, which are excellent for predicting response of the first few natural modes of vibration but fail miserably to define adequately the higher frequency part of the response spectrum.

A rather new approach has been suggested by Lyon, Ungar, *et al.* This technique is known as "statistical energy analysis," in which the system is known to possess a large number of modes in a given frequency bandwidth and a concept of structural modal density is used. The detail of the individual modes are, for this analysis, deemed to be unimportant. The energy of each mode (and therefore of each bandwidth) can be estimated solely as a function of system damping.

Individual bandwidth responses are calculated, and the entire response spectrum can be established in an incremental fashion. A unique feature of this approach is for complicated structures, amazingly simple formulae can be developed that provide generally excellent results in the upper part of the frequency spectrum. The method has proved to be useful for estimating the vibration environment in launch vehicles where no applicable empirical approach is available.

The low-frequency "vehicle dynamics" quasi-sinusoid environments must be derived from vibration analyses of the entire launch vehicle system with applied forcing functions such as holddown release, ground winds, flight wind gusts, engine gimbals, engine cut-offs, staging, engine startings, etc. These analyses are normally done as separate lateral and longitudinal analyses, assuming negligible coupling. Previous flight data may also be used to refine the accuracy of these analyses, particularly from the standpoint of assumed damping values.

Because almost no orbital, environmental, dynamic data is available, prediction of the levels encountered in orbital operations is almost purely analytical. Various forcing functions and perturbations can be (and have been) defined, as in references 2 and 3, but these must be analytically applied through dynamic response programs to derive accelerations for structure and equipment.

In all of these steps to define the environments for a new payload, it must be remembered that the statistical characteristics must be identified and maintained. For example, the dynamic levels calculated from response analyses for wind gusts or engine shutdown must be in terms of the probability of occurrence of those wind gusts or shutdown conditions (thrust tail-offs). If the design goal of confidence is established early in the program, the values may be expressed consistently in terms of this confidence level; however, the statistical definition should not be lost nor forgotten.

Once the environment has been predicted or defined and expressed in terms of design criteria, it is the task of the structural

designer and analyst to provide assurance that the structure can withstand those criteria and still perform its functions and that the response conditions imposed on attached equipment and systems will not exceed specified limits. The tools in this work are (1) the mathematical and analog models of the structural/mechanical system and (2) the high-speed digital and analog computers, which extract modal frequencies, mode shapes, and responses to the specified forcing functions.

The methods of mathematical formulation of dynamic analysis models for solution of free (natural) vibration mode shapes and frequencies of structures can be categorized by the governing equations into (1) energy methods, (2) differential equation methods, and (3) integral equation methods. There are numerous examples of each category; references 4 and 5 provide excellent descriptions of many of them. The energy methods are based upon application of one or more of the principles of mechanical energy and make use of assumed displacement functions without strict adherence to boundary conditions. The differential equation methods require the application of boundary conditions, and solutions must explicitly satisfy those conditions. The integral equation methods involve use of influence functions, which implicitly satisfy the boundary conditions but are not applied in order to solve the equations.

The response amplitude to a dynamic forcing function (displacement, force, acceleration, pressure, etc.) may be calculated throughout a structural or mechanical system by several methods. These methods include frequency response methods and normal mode methods. In these methods of response calculation, the role of damping is critical to the accuracy of the results, and, wherever possible, empirical data from laboratory tests and previous flights of similar structure should be used in the estimation of damping. References 4 and 5 give detailed treatment of these methods and the use of computers in their application to all types of forced response problems.

The dynamics analysis work on any large telescope (or other payload) system should be

an integral part of the design program. As soon as sufficient information on weight, dimensions, and structural arrangement is available, a simple analysis model should be formulated and preliminary frequency and mode shapes derived. Such models may be effectively used in selecting optimum configurations from several candidates and will aid in the environmental vibration-level predictions. As individual subsystems and components are designed, the model should be improved to include mass and stiffness distribution; and forced response programs should be accomplished. These analyses will provide the design with interface and internal design loads as well as response vibration acceleration and displacements. Figure 9 shows the possible integration of dynamics analysis into a design program.

Some additional derivatives from the dynamics analyses are:

1. Indication of need for development tests to define unknown characteristics
2. Indication of design weaknesses and areas where changes are desirable (dynamically)
3. Indication of effects of proposed design changes on system dynamics
4. Dynamic transfer functions for use in specification of equipment design and test levels.

Special Considerations for Telescope Assemblies and Equipment

Large orbital telescopes have certain characteristics which impose unusual dynamic constraints on the designers. Some of the most important "different" characteristics are: (1) the large physical dimensions (focal length, mirror and barrel diameters), (2) close tolerances on alignment of surfaces, axes, apertures, etc., which are quite distant from each other, (3) heavy weights of components and telescope structure relative to support structure weight, (4) high stiffnesses of telescopes relative to support structure stiffness, (5) low rigid-body frequencies of telescopes on their mounts, and (6) limitations on allowable distortions due to thermal

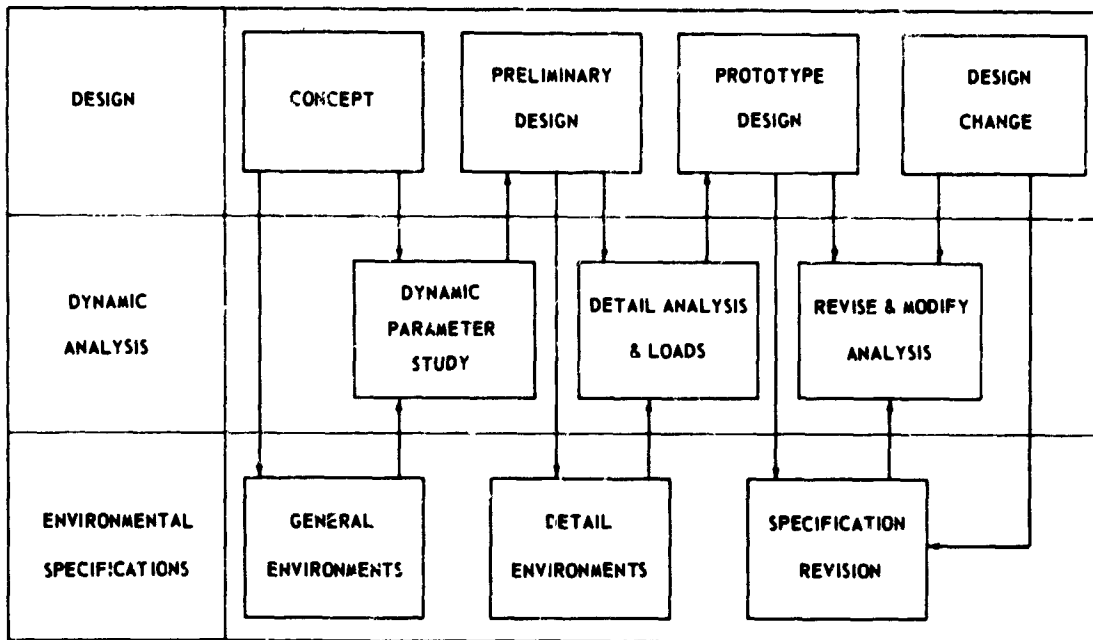


Figure 9. Dynamic support of design.

and other orbital conditions, such as astronaut motions.

In the normal dynamic analysis of spacecraft, it is often assumed that the equipment and experiments are "lumped masses" located at discrete points on the structure and that, because of the usually small dimensions and weights of these items, analysis results are sufficiently accurate. For a system involving one or more large telescopes, however, this assumption cannot be made because of the six characteristics mentioned above. The telescope and the structure that supports it during launch and in orbital operation must be analyzed as a dynamic system, with the mass and stiffness distribution of the telescope modeled as carefully as that of the structure. Early analyses of the ATM canister assumed the telescopes to be lumped masses located at the points where they attached to the "spar" structure; these analyses were later found to be significantly in error, both in loads and frequencies.

Because of the requirement for close tolerances, both internal to the telescope and with respect to structural bench marks and

axes, the use of vibration and shock isolators of conventional design is practically impossible. This problem is further complicated by the limitations on thermal transfer and on material properties (outgassing, etc.). This limits the variety of approaches a designer or dynamicist can take to solve dynamic response problems.

Another result of the above characteristics of large telescopes is that the critical system resonances are quite low in frequency, well below 50 hertz. This means that the highest response loads may be caused by "vehicle dynamics" vibration levels, which are difficult to predict in amplitude for new vehicle systems. Therefore, the dynamicist must carefully analyze for response to "vehicle dynamics."

A special consideration in telescope design for dynamic environments is the susceptibility of certain types of components to acoustics. These types are characterized by large surface areas and relatively light weight, such as thin printed-circuit boards, heater panels, and electronics. A method of calculating response stresses for simple panels is

given in reference 6; however, development or qualification tests should be performed whenever there is doubt about acoustic susceptibility. References 7 through 11 provide further detailed considerations of acoustic environments and their effect on equipment.

References

1. Summary of Random Vibration Prediction Procedures. NASA CR-1302, April 1969
2. Crew Motion and the Dynamic Environment of Spaceborne Experiments. DAC 60963, January 1958, revised March 1968.
3. Chubb, W. B.; Shultz, D. C.; Seltzer, S. N.: Attitude Control and Precision Pointing of the Apollo Telescope Mount. Paper 67-534, AIAA Conference on Guidance, Control and Flight Dynamics, Huntsville, Alabama, August 14-16, 1967.
4. Munty, Walter C.; Rubinstein, Moshe F.: Dynamics of Structures. Prentice-Hall, Inc., 1964.
5. Pestel, E. C.; Leckie, F. A.: Matrix Methods in Elastomechanics. McGraw-Hill Book Co., Inc., 1963.
6. Clarkson, B. L.: The Effect of Jet Noise on Aircraft Structures. The Aeronautical Quarterly, Vol. X, May 1959.
7. Lyon, R. H.: Random Noise and Vibration in Space Vehicles - SVIC Monograph. Bolt Beranek and Newman, eds., 1967.
8. Crandall, Stephen H., ed.: Random Vibration. Technology Press, 1958.
9. Eldred, K., et al.: Structural Vibrations in Space Vehicles. Wadd Technical Report 61-62, December 1961.
10. Noise and Acoustic Fatigue in Aeronautics. Lecture Series, University of Southampton, England, Staff, Dayton, Ohio, September 1961.
11. Development of Vibration Design Procedures for the Orbiting Astronomical Observatory. Shock and Vibration Bull. 31, Pt. II, March 1963.

N70-36726

Thermal Deformation Prediction in Orbiting Observatory Structures

James B. Mason

NASA Goddard Space Flight Center

Introduction

In recent years, the finite element method of matrix structural analysis has gained wide acceptance in the engineering community for the solution of structural problems. Along with this trend, NASA began the development of a general-purpose computer program based upon this technology for use in the analysis of large and/or complex structures. The NASTRAN* computer program (ref. 1) is the result of these efforts, and with this and other finite element programs comes the opportunity for the solution of both static and dynamic structural problems heretofore untreatable.

One area of application in which the finite element method holds much promise is that of prediction of thermal deformations in orbiting spacecraft. Study in this area is taking place at the Goddard Space Flight Center as part of the Structural-Thermal-Optical Program (STOP), which has as its objective the development of analytical techniques and procedures for use in predicting the thermal deformations and optical degradations in a structural system from a knowledge of thermal heating rates and/or temperature gradients. Another area of application of these methods at Goddard is that of detailed dynamic analysis of spacecraft structures.

This paper presents a review of this work as it pertains to space telescopes and attempts to identify problem areas associated with the analysis of this type of structure. A background discussion of the finite element method as it is applied to static thermal deformation problems and to thermally induced

vibration problems is included. Work being done under the STOP Project is summarized, and examples of the two general classes of thermal deformation problems considered in this program are given. In addition, an example of the treatment of thermally induced vibrations of a flat plate is included to demonstrate the applicability of the finite element method to this class of problem.

The free vibration analysis of the OAO spacecraft, as performed at Goddard, and its correlation with OAO modal-survey tests is described. A discussion of the reduction scheme, utilized to reduce the size of the frequency model for use in an independent forced-response analysis of the entire launch vehicle and spacecraft, is also presented.

The paper concludes with a summary of problem areas, plans for future work, and a discussion of the potential of the finite element method in the analysis and design of optical space telescopes.

Thermal Deformation Predictions by Finite Elements

Background

The matrix-displacement formulation of the static and dynamic thermal deformation problem is used in the following development (refs. 2, 3, and 4). All of the usual assumptions of linear elasticity are employed, and the conversion of mechanical energy into heat is neglected. With this latter assumption, the determination of the temperature distribution in the structure is uncoupled from the elasticity problem and may be obtained by independent analysis or test.

In the finite element approach to structural analysis problems, the body to be

*NASA Structural Analysis Program.

analyzed is idealized to a new structure composed of an assemblage of finite structural elements joined at grid points. The individual discrete elements have known elastic properties defined by a number of grid point degrees-of-freedom, which are sufficient to represent the stress and displacement behavior of the element adequately. Because thermoelasticity problems may be considered as initial strain problems and because the initial strains may be treated as additional mechanical loads acting on the elements, one may write the force-displacement relations for the thermally strained i^{th} element by the stiffness equation

$$\{x\}_i = [k]_i \{u\}_i + \{x_T\}_i \quad (1)$$

where

$\{x\}_i \sim$ forces acting at the grid points of element i

$[k]_i \sim$ stiffness matrix of element i

$\{u\}_i \sim$ grid point displacements of element i

$\{x_T\}_i \sim$ thermally equivalent mechanical loads acting at the grid points of element i

The equivalent mechanical loads $\{x_T\}_i$ are obtained as those required to remove the initial thermal strains in the discrete element.

Assembly of the element matrices, equation 1, to form the idealized structure results in the following set of equations describing the static behavior of the structure.

$$\{X\} = [K] \{U\} + \{X_T\} \quad (2)$$

where

$\{X\} \sim$ external applied loads acting at the grid points of the assembled structure

$[K] \sim$ stiffness matrix of the assembled structure

$\{U\} \sim$ grid point displacements of the assembled structure

$\{X_T\} \sim$ thermally equivalent mechanical loads acting at the grid points of assembled structure

In equation 2, the equivalent mechanical loads acting at a grid point of the assembled structure are obtained as the vectorial sum, at the grid point, of the loads $\{x_T\}_i$ of all elements joined at that grid point.

In many practical problems, the temperature variations in the structure change rapidly with time, and the effects of inertia cannot be neglected. In these cases, the study of thermally induced vibrations by finite element techniques can be accomplished by modification of equation 2 to include inertia effects. Using the well-known principle of d'Alembert, the negatives of the inertia forces

$$- [M] \{\ddot{U}\} \quad (3)$$

where

$[M] \sim$ mass matrix of the assembled structure

$\{\ddot{U}\} \sim$ grid point accelerations of the assembled structure

are treated as additional applied loads acting on the structure. In addition, the equivalent mechanical loads become time-dependent forcing functions. Thus, from equations 2 and 3 for the case of no externally applied loading, we can write

$$[M] \{\ddot{U}\} + [K] \{U\} = -\{X(t)\} \quad (4)$$

Examination of equation 4 shows that the problem of thermally induced vibrations in finite element structures is reduced to that of obtaining the dynamic response to a forced vibration in which the external forcing functions become the negatives of the equivalent mechanical loads. Upon the determination of $\{X_T\}$ as a function of time, t , and imposition

of boundary conditions, equation 4 is solved for the unknown grid-point displacements $\{U(t)\}$ of the idealized structure.

Equations 2 and 4 describe the mathematical problem to be solved by the NASTRAN computer program in the solution of static or dynamic thermal deformation problems from known temperature distributions. In general, input to the NASTRAN program consists of:

1. Program control definition
2. Coordinate system definition
3. Grid point definition
4. Finite element type definition
5. Material property definition (temperature dependent, orthotropic)
6. Geometric constraints (including boundary conditions)
7. Grid-point temperature information and/or thermally equivalent mechanical loads
8. Output solution.

With this data, the program automatically assembles the stiffness and mass matrices of the assembled structure, calculates and/or assembles the equivalent mechanical loads*, applies geometric constraints, and solves for the required grid-point deflections.

Structural-Thermal-Optical Program

The overall objective of the Structural-Thermal-Optical Program (STOP) at Goddard is the development of methods for determining structural deformations and optical degradations in a system from knowledge of the temperature gradients and thermal inputs. As both the title of the project and its objective imply, the program is an interdisciplinary

*For static analysis, the program automatically calculates and assembles the equivalent mechanical loads from input grid-point temperatures for inclusion of the effects of axial (beams) and planar (plates) thermal expansion and contraction. For analysis of transverse temperature gradients across the thickness of elements and for time-dependent analyses, equivalent mechanical loads must be obtained external to the NASTRAN program and entered by the user at structural grid points.

study. The following discussion focuses on the structural aspects of this program.

Two general classifications of thermal deformation problems as they relate to orbiting optical telescopes have been identified for investigation by the STOP program. The first of these deals with the prediction of thermally produced misalignments of the spacecraft that result in pointing, guidance, tracking, and similar alignment problems. The second class of problems concerns loss of optical performance due to thermal deformations of major optical surfaces of the experiment. The division into two classes is not intended to be considered rigid since alignment problems, for example, cannot be ignored when evaluating the optical performance of the telescope. For analysis purposes, however, this division is desirable because analytical techniques and discipline interfaces do tend to differ according to these two classifications.

In this paper are descriptions of three examples of static thermal deformation studies performed to exercise and to evaluate the thermal and structural analytical procedures and computer programs available at Goddard and also to identify associated problem areas. The first two are examples of the alignment type of problem; the third is an example of a thermal deformation study of a structural component typical of a major optical surface.

Example 1: OAO Star-Tracker Alignment Analysis. The star-tracker study (refs. 5 and 6) was undertaken to investigate the feasibility of both thermal and structural analytical procedures and to test techniques to obtain the thermal deformations of a critical guidance component of the Orbiting Astronomical Observatory (OAO) spacecraft. A longitudinal OAO star-tracker mount installed in a thermally controllable bay was utilized for this investigation.

As indicated in the star-tracker mount test configuration shown in figure 1, two Goddard-developed microtilt sensors* were

*The microtilt sensor was developed by the Test and Evaluation Division at Goddard. It is a device for

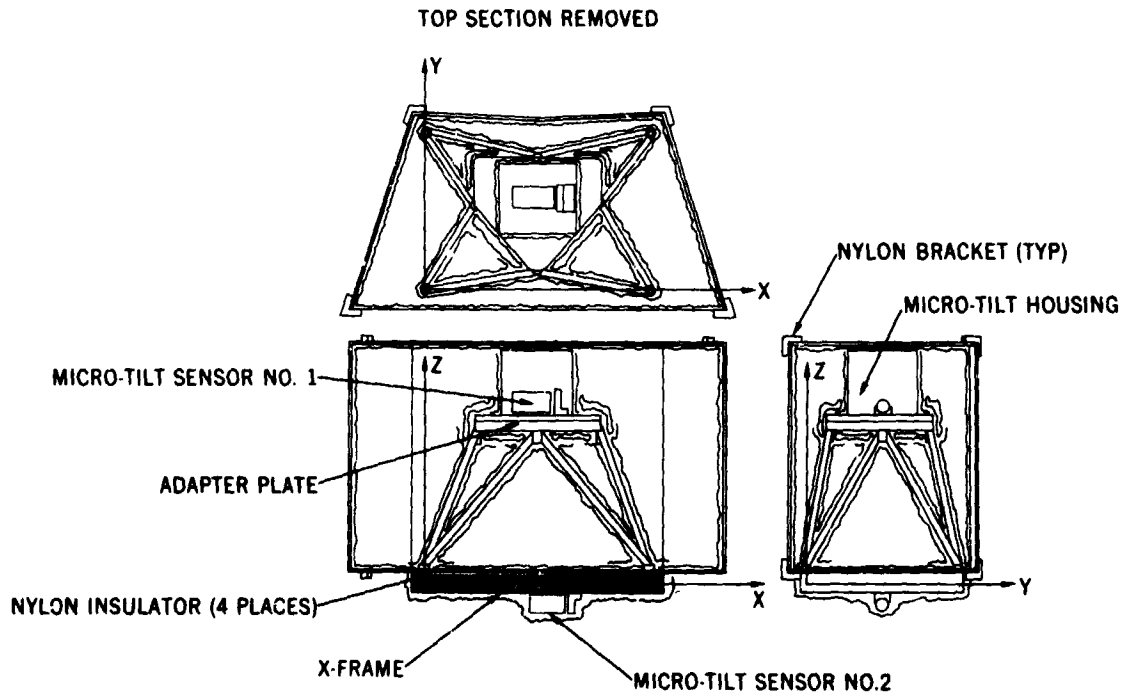


Figure 1. Schematic of star-tracker mount in its STOP test configuration.

attached to the structure. Tilt sensor #1 was placed at the top of the mount on the adapter plate near the point at which the actual star tracker would be mounted, and tilt sensor #2 was attached to the test support X-frame (a welded stainless steel frame of 1.0-inch by 1.0-inch steel stock) to which the four feet of the star-tracker mount and the heater plate were both bolted. This complete assembly was suspended in an evacuated and cooled vacuum chamber, after which the thermal deformation test was run over a period of approximately 2 weeks. (The primary reason for such a long test period was that approximately 40 hours was required by the star-

measuring minute angular displacements. Basically, the sensor is a simple pendulum whose shaft is fitted with two pairs of semiconductor strain gages mounted on mutually perpendicular axes. Any angular movement with respect to gravity will produce a distortion in the corresponding gage pairs, thereby providing a measure of the angle of rotation. The design goal was a usable sensitivity of 0.1 arc seconds.

tracker mount to reach steady-state from level to level for thermal analysis correlation.) Relative rotation measurements of the Y-axis for correlation with analysis were obtained as the difference indicated between the two microtilt sensors at four steady-state temperature conditions.

The finite element model of the star-tracker mount is shown in figure 2. The model includes representation of the star-tracker mount-leg assembly attached at its upper ends to the adapter plate and at its lower ends to the test-support X-frame and heater plate. The model required 35 grid points, 52 finite elements, and 209 unconstrained degrees-of-freedom; i.e., rotations and displacements.

Beam elements were used for the representation of the adapter plate, leg assembly, and the test-support X-frame. The heater plate was represented using four triangular plate elements. With the use of the above elements, both extensional and bending behavior is accounted for in the model. In addition, the beam elements representing the

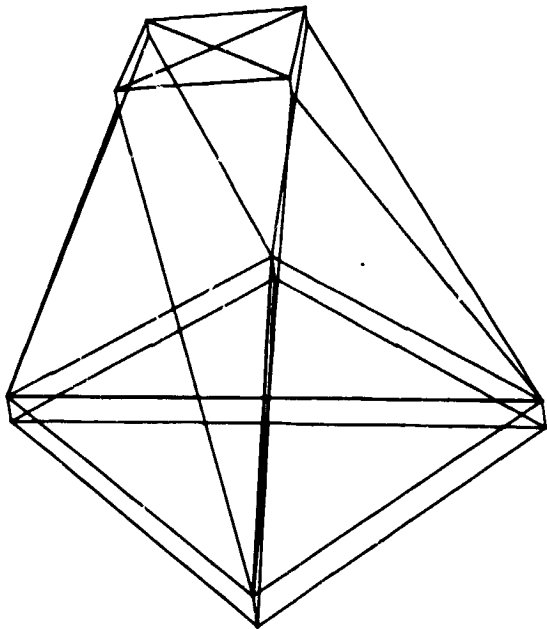


Figure 2. Finite element model of star tracker in its STOP test configuration, undeformed shape.

adapter plate were constrained against bending. These constraints conform to the assumptions that no temperature gradients exist through the thickness of the adapter plate (this being confirmed by test), which would cause bending out of the plane of the adapter, and that the bending stiffness of the adapter is such that bending of the adapter from mechanical loads may be neglected.

With input grid-point temperatures obtained experimentally, the NASTRAN program automatically calculated the required equivalent mechanical loads for inclusion of the effects of axial thermal expansion and contraction of the beam elements and the planar expansions and contractions of the flat, triangular, plate elements. The effects of transverse temperature gradients existing through the thickness of the X-frame, however, were included by directly inputting equivalent mechanical loads at the grid points corresponding to the X-frame. For a temperature distribution varying linearly across the thickness and with a sectional distribution remaining invariant along the length of a uni-

form rectangular section beam, the required equivalent mechanical moments, M_i^T , to be applied at the ends of the i^{th} beam element can be shown to be given by

$$M_i^T = E_i I_i a_i \left[\frac{T_i^u - T_i^l}{h} \right]_i \quad (5)$$

where E_i = modulus of elasticity of beam element i

I_i = moment of inertia of beam element i

a_i = coefficient of thermal expansion of beam element i

$T_i^u - T_i^l$ = temperature difference between the upper and lower surfaces of beam element i

h_i = thickness of beam element i

For the structural analyses, the grid point corresponding to the attachment point on the X-frame of the #2 microtilt sensor was rigidly constrained from all motion so that all analytical deflection predictions for the model were made relative to this point.

Table 1 gives both experimental and analytical results of the Y-axis relative rotations measured from the liquid-nitrogen (LN_2) case (i.e., both theory and experiment are zeroed at the LN_2 condition). The liquid-nitrogen condition corresponds to the test chamber evacuated to 1×10^{-6} torr by mechanical and diffusion pumps and liquid nitrogen circulated to the walls of the chamber. Figure 3 shows the deformed star tracker corresponding to the *hot temperature case*. The deformations shown in this figure are greatly exaggerated for viewing.

From table 1, it is seen that agreement between analysis and experiment should be the cause of much optimism when consideration is given to the magnitude of the thermal rotations under investigation. One must also

Table 1. Star-Tracker Y-Axis Thermal Rotations: A Comparison of Analytical and Experimental Results

Test Case	Analytical Predictions		Test Measurements	
	Y-Rotation (arc sec)	Total Change (arc sec)	Y-Rotation (arc sec)	Total Change (arc sec)
LN ₂	0	+55	0	+32
Cold	+55		+32	
Hot	+17(49)*	-38	+3	-29
Grad. 1	+20	+3	+18	+15
Grad. 2	-3	-23	+6	-12

* Neglecting transverse gradient effects existing across the X-frame.

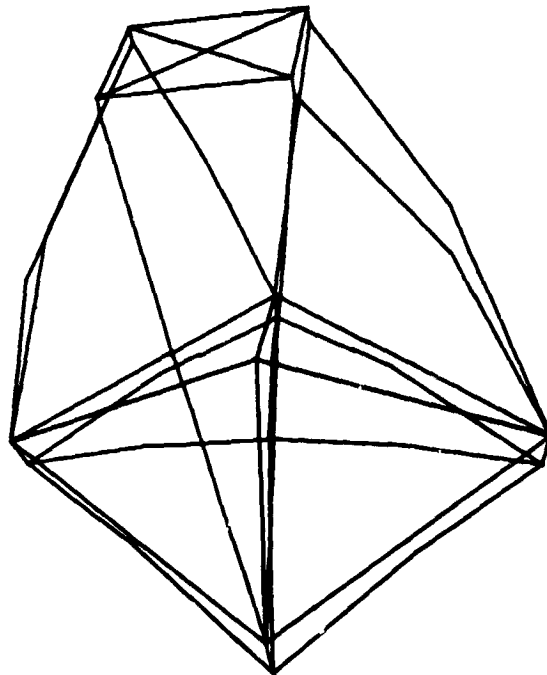


Figure 3. Finite element model of star tracker in its STOP test configuration, deformed shape (hot case).

remember the long time span covered by these tests and the fact that this was one of the first actual applications of the microtilt sensors.

One indication of the critical nature of the above predictions can be shown by observing the effects of neglecting the influence of the transverse temperature gradients existing across the thickness of the X-frame. While these gradients are of the order of only 0.5°C for the hot case considered (see bracketed quantity in table 1), their neglect may result in much error. In this instance, it becomes obvious that transverse temperature effects should be included because of the relatively high stiffness of the X-frame compared to that of the legs and the fact that microtilt sensor #2 is mounted directly to this frame; however, the requirement for accurate temperature prediction and/or temperature instrumentation during test is demonstrated.

Example 2: Alignment Analysis of OAO-GEP Secondary Mirror Support Structure. This analysis was conducted with the intent of studying both thermal and structural analysis techniques for their feasibility in predicting thermal deformations of a relatively large and complex structure (refs. 7 and 8). For this purpose a structural analysis for thermal displacements of the Goddard Experiment Package (GEP) between Station 43.156 and Station 86.000 of the Optical Structure Assembly was performed (fig. 4) using a theoretically obtained temperature distribution.

Figure 5 shows the finite element model used in the analysis. The complete model consisted of 511 grid points (with approximately 2200 degrees-of-freedom after imposition of boundary conditions, etc.), 336 quadrilateral plate elements, 8 triangular plate elements, and 12 beam elements. For the thermal deformation analysis, the grid point degrees-of-freedom at the base of the telescope tube, Station 86.000, were constrained to boundary conditions corresponding to the telescope tube clamped to a rigid ring that expands in the radial direction due to a uniform temperature change.

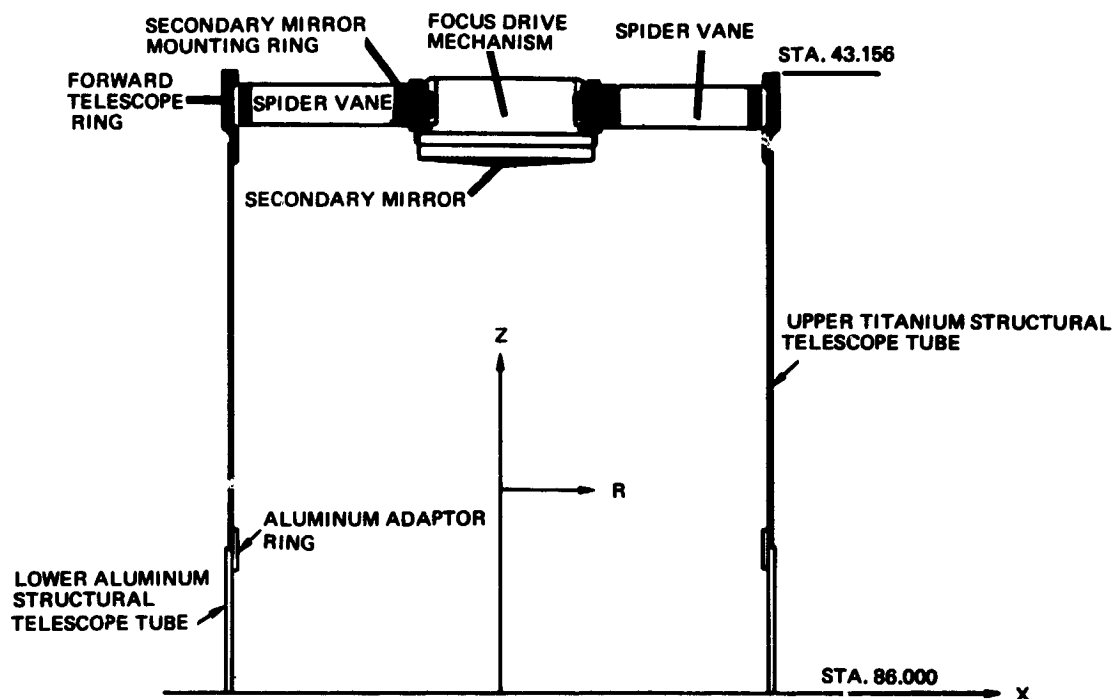


Figure 4. Schematic of GEP/STOP secondary mirror analysis optical assembly.

This approximates the actual conditions at this location because the base of the telescope tube is attached to a heavy aluminum ring which, according to predicted temperatures, assumes an approximately uniform temperature distribution. With these assumed boundary conditions, the displacements and rotations predicted from the finite element analysis can be viewed as indicative of the motion relative to the primary-mirror optical axis because the assumed constraints should correspond approximately to the actual behavior of this section of the GEP.

Figure 6 shows a greatly magnified view of the thermally deformed GEP structure. Table 2 gives the predicted motion of the secondary mirror; i.e., considering the mirror and its mount as a structure "lumped" at a central grid point.

Example 3: Thermal Deformation Analysis of Optical Surfaces. Example 3 illustrates the type of structural analysis planned for this phase of STOP. Figure 7 shows the spherical shell segment with center cutout

being considered; figure 8 presents the finite element model. This thin elastic shell is dimensionally similar to the primary mirror of the OAO-GEP.

Table 2. Secondary-Mirror Thermal Displacement Predictions for Theoretically Obtained Temperature Distributions

X DISPLACEMENT	= -2×10^{-4} IN.
Y DISPLACEMENT	= -3×10^{-4} IN.
Z DISPLACEMENT	= -100×10^{-6} IN.
ROTATION ABOUT THE X-AXIS	= -2 ARC SEC
ROTATION ABOUT THE Y-AXIS	= -1 ARC SEC

For demonstration purposes, the finite element model has been subjected to a localized hot spot on its surface. A perspective view of the deformed mirror, to a greatly magnified scale, is given in figure 9. Output from the NASTRAN program for this analysis is in the form of grid-point displacements and rotations. It should be noted that the grid-point rotations can be viewed as the rotations that a line (the line being originally normal to

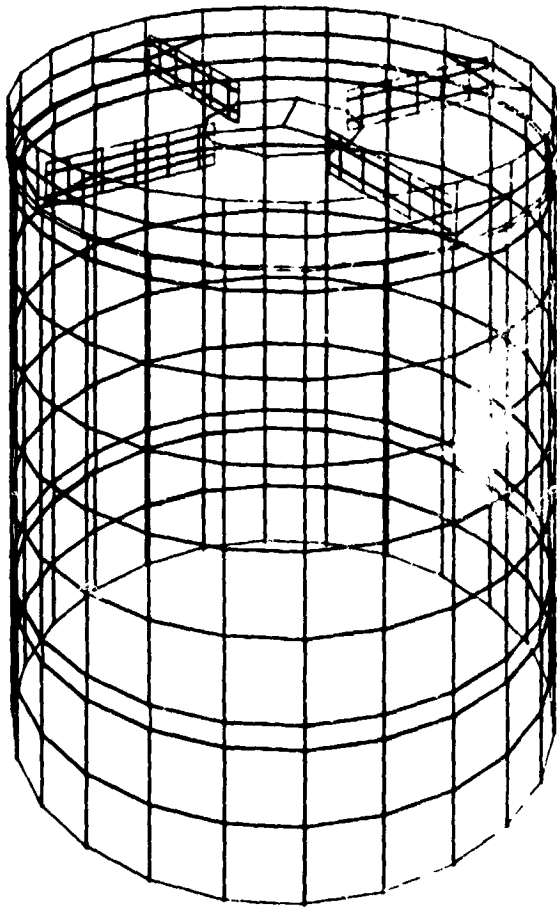


Figure 5. Finite element model of GEP, undeformed shape.

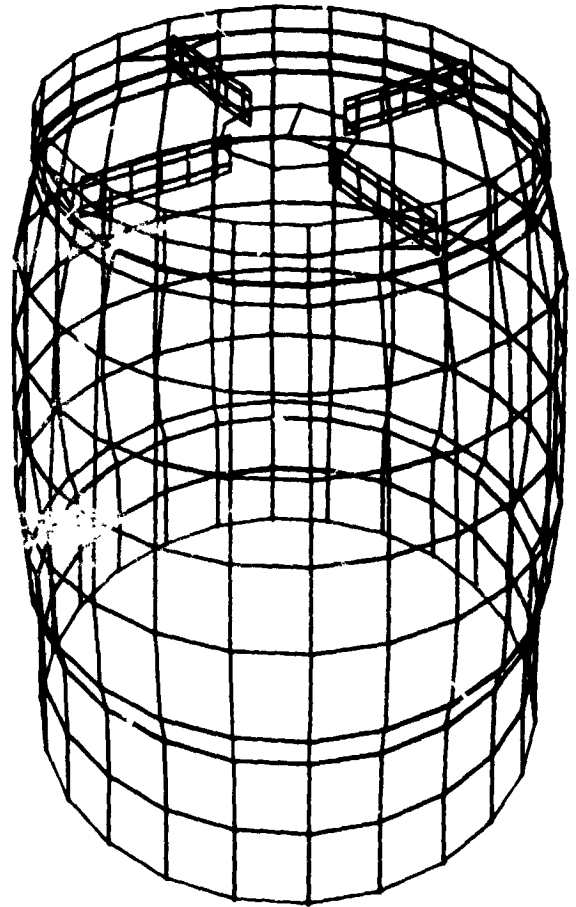


Figure 6. Finite element model of GEP, deformed shape.

the middle surface of the shell at a grid point) would experience as the mirror deformed. This information, together with ray-tracing procedures, should be very useful in the study of the degradation in the optical performance of the mirror.

Thermally Induced Vibrations

Consideration of thermally induced vibrations (ref. 4) may become necessary in future space-telescope structures. When consideration is given to the demanding accuracy requirements envisioned for some of these vehicles (on the order of 1/100 arc

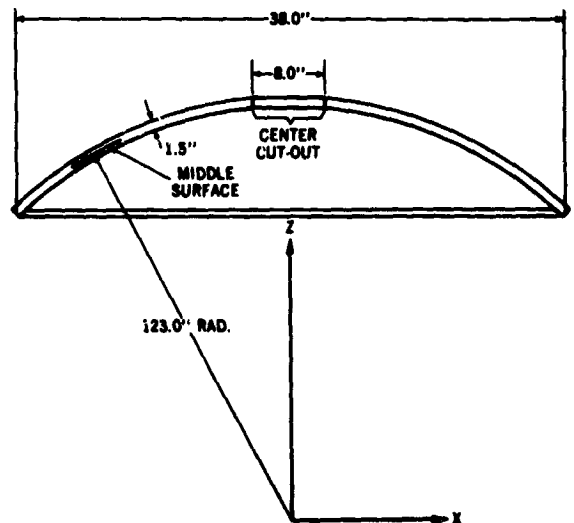


Figure 7. Schematic of spherical cap with cutout.

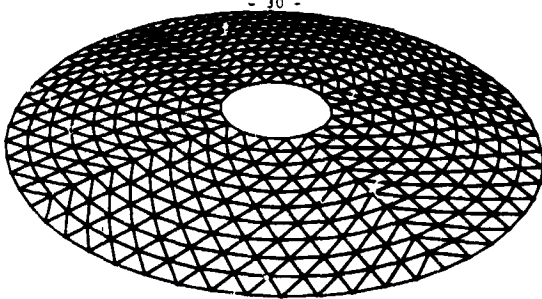


Figure 8. Finite element model of spherical cap with cutout, undeformed shape.

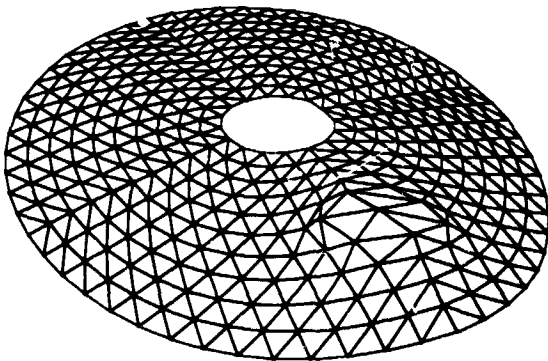


Figure 9. Finite element model of spherical cap with cutout, deformed shape (hot-spot).

second), the necessity for the inclusion of these effects in any analysis of the craft seems probable.

The results of a finite element study of a simply supported square plate (8.0 feet by 8.0 feet by 0.1 foot) subjected to a step heat input, Q , on face $Z = +\frac{h}{2}$ and insulated on face $Z = -\frac{h}{2}$ are given to demonstrate the applicability of the finite element method for treating thermally induced vibration problems (fig. 10). As shown in figure 10, a quarter symmetry model consisting of a four-by-four network of square-plates (1.0 foot by 1.0 foot by 0.1 foot) bending elements was used.

For the problem under consideration, the time-dependent temperature distribution, $T(z,t)$, through the thickness of the plate is given by the expression

$$T(z,\tau) = \frac{hQ}{\tilde{k}} \left\{ \tau + \frac{1}{2} \left(\frac{z}{h} + \frac{1}{2} \right)^2 - \frac{1}{6} - \frac{2}{\pi^2} \sum_{j=1}^{\infty} \frac{(-1)^j e^{-j^2 \pi^2 \tau}}{j^2} \cos j\pi \left(\frac{z}{h} + \frac{1}{2} \right) \right\} \quad (6)$$

where

$$\tau = \left(\frac{kt}{h^2} \right) \sim \text{nondimensional time parameter}$$

$$\tilde{k} \sim \text{thermal conductivity}$$

$$\frac{\tilde{k}}{k} \sim \text{thermal diffusivity}$$

$$h \sim \text{plate thickness}$$

$$t \sim \text{time}$$

$$Q \sim \text{heat input}$$

$$z \sim \text{transverse coordinate}$$

If the bending behavior of only the plate is considered, the equivalent mechanical grid point loads, M_{pt} (in this case moments) required for constraint of the finite plate element with temperature distribution given by equation 6 can be found to be

$$M_{pT}(t) = \frac{2a Q E h^3}{(1-\nu) \pi^4 \tilde{k}} \left[\frac{\pi^4}{96} - \sum_{j=1,3,5} \frac{e^{-j^2 \pi^2 \tau}}{j^4} \right] \quad (7)$$

where

$$E \sim \text{modulus of elasticity}$$

$$a \sim \text{coefficient of thermal expansion}$$

$$\nu \sim \text{Poisson's ratio}$$

Since the temperature distribution does not vary over the planform of the plate in this example, the vectorial sum of the equivalent

mechanical thermal moments at the internal grid points of the assembled plate model are zero. Thus, the problem reduces to a forced response analysis of the quarter symmetry model loaded as shown in figure 11.

Solution of this finite element model was obtained by using lumped mass and modal acceleration techniques, and the results for midpoint displacement (w) versus time (t) for a hypothetical problem are given and are compared to theory in figure 12.

The results of this study demonstrate that the structural vibrations induced by uncoupled, transient, temperature distributions may be treated by a forced response

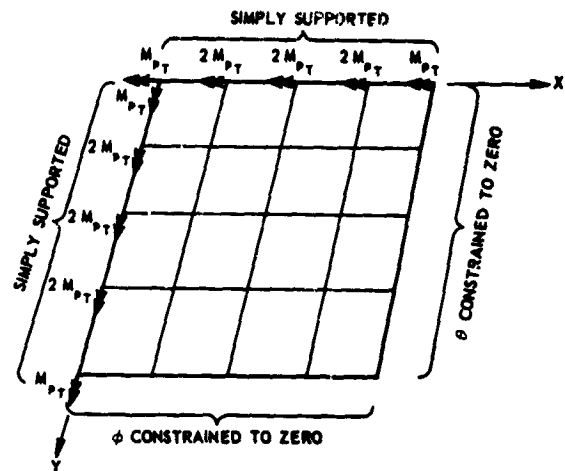
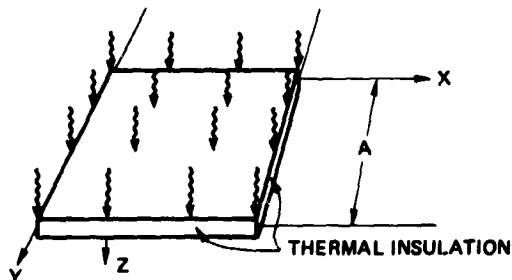
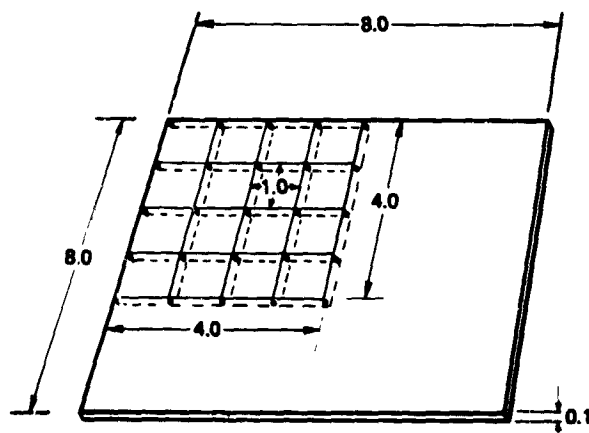


Figure 11. Quarter symmetry model with applied equivalent mechanical loads.



(a) Simply supported square plate exposed to step heat input.



(b) Quarter symmetry model of simply supported square plate.

Figure 10. Sample thermal vibration problem.

analysis of the finite element model excited by time-dependent mechanical loads applied at the grid points of the model. The requirement for implementation of these methods for the analysis of practical spacecraft structures, however, demands much study.

Dynamic Analysis of OAO-A2 Spacecraft

This paper describes some of the dynamic analyses performed at Goddard in support of the OAO project. The finite element analyses described were performed on the Martin-Company-developed SB-038 computer program before the availability of NASTRAN. In brief, a finite element model of the OAO-A2 was obtained in its modal-survey test configuration. The model was then refined by using modal test data, which was obtained from vibration shaker tests of the basic craft structure and attached interstage. Mass properties of the test configuration model were then adjusted to those of the actual spacecraft in its flight configuration, and this revised model was analyzed for frequencies and mode shapes. From this rather detailed finite element model, a reduced model was obtained for use in a forced response analysis of the entire launch vehicle and spacecraft.

The model utilized in the normal mode analysis of the OAO is described; the result of this analysis is compared to test, and the reduction procedure used to obtain the simplified model is discussed.

OAO Model for Analysis

The initial finite element model of the OAO-A2 was representative of the craft in its modal-survey test configuration (ref. 9). This configuration is comprised of the basic spacecraft structure, with simulated experiment and electronic packages, and an interstage attaching the craft to the shaker table.

Detailed modeling of the interstage was not feasible because of the limited capacity of the SB-038 program and the unknowns associated with the mechanical connections in this area. For these reasons, the decision was

made to produce a rather detailed model of the spacecraft and to represent the interstage by a coarse series of elastic elements that would be "tuned," using modal-survey test data, to account for this structure accurately. In addition, the Smithsonian Astrophysical Observatory (SAO) and Wisconsin Experiment Package (WEP) experiments were represented by fully rigid elements arranged symmetrically about the axis of the craft. The complete model is shown in figure 13. It includes 128 grid points and 588 structural elements.

Analysis Compared to Test

As indicated previously, the finite element model was "tuned" to account for the interstage section of the test structure. Test results showed that the first bending, first

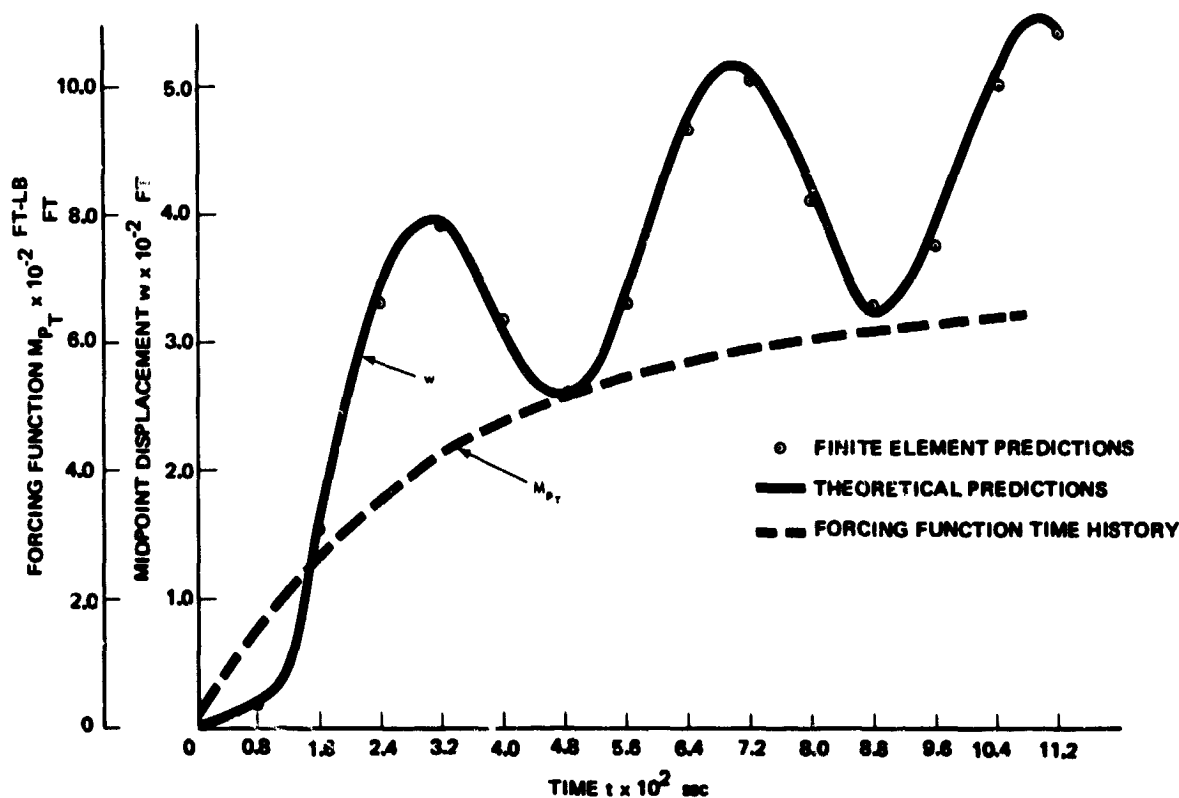


Figure 12. Thermally-induced plate vibrations (theoretical and finite element midpoint displacement predictions for plate forcing function M_{p_T}).

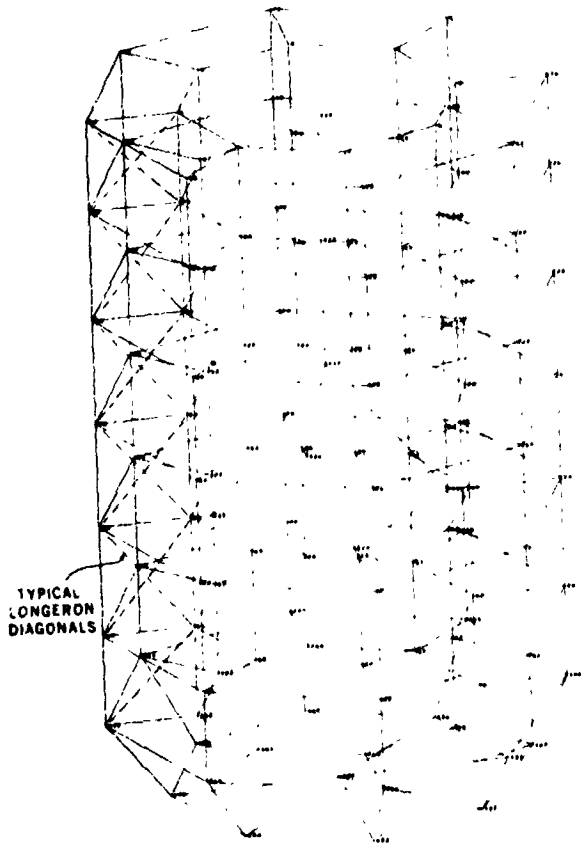


Figure 13. Finite element model of OAO basic craft with idealized experiment packages on interstage.

torsion, and first longitudinal modes were principally functions of the interstage region. An example of this is shown quite clearly in figure 14 where we observe that all motion appears to originate in the interstage structure for the first bending mode. By "tuning" the effective elastic properties of the interstage model to the measured response of the first bending and first torsion modes, the influence of the interstage region was accurately included in the finite element model. The success of this procedure can be seen in table 3. Good agreement is shown between both the two tuned modes and the first longitudinal mode, which is basically a function of the interstage.

An interesting example of the value of analysis in the interpretation of test results

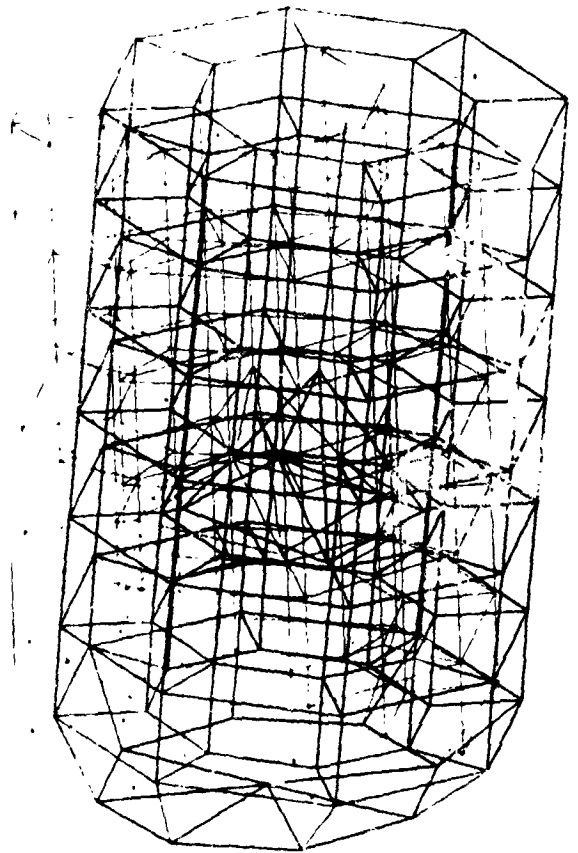


Figure 14. First bending mode of OAO basic craft on interstage.

and vice versa can be gained by referring to table 3. The analysis found a second bending mode at 25 cycles per second—consisting principally of rigid-body motion of the rigid experiment model. This was not found in the test data because recovery of test instrumentation data on the experiment was not accomplished in this frequency region. In addition, the analysis yielded a pair of symmetric third bending modes at 51 cycles per second; these were not found in the test, but test data yielded one lateral mode, at 42 cycles per second, which did not appear in the analysis.

A reevaluation of both finite element analysis and test procedures was performed to explain these discrepancies. A further evaluation of the modal-survey test data did reveal

Table 3. Modal-Survey Analysis and Test Correlation

Finite Element Results (cps)	Mode Type	Modal Survey Test Results (cps)
11	1st. Bending	11
11		11
16	1st. Torsion	16
25	2nd. Bending (Rigid-Body Experiment)	42
25		51
40	1st. Longitudinal	40
51	3rd. Bending	42
51		51
56	2nd. Torsion	
71	2nd. Longitudinal	

a significant lateral response in the 51-cps region, but with a different motion in the simulated experiment than that at 42 cycles per second. An examination of the dummy experiment hardware to determine the reasons for missing the lateral mode at 42 cycles per second revealed that the dummy experiment hardware could not behave as a rigid symmetric body, as intended, for the lower modes. (The actual experiments, however, would behave in this manner in the frequency range of interest.)

As mentioned above, these assumptions result in the analytical prediction of a repeated pair of modes at 51 cycles per second. It was concluded that the lack of symmetry in the actual dummy experiment resulted in the lowering of one of these lateral modes to 42 cycles per second.

With the development of the finite element model corresponding to the craft in its test configuration completed, the mass distribution of the model was adjusted to conform to the actual flight configuration of the

OAO-A2. This revised flight model was analyzed to provide normal modes and corresponding frequencies.

Reduction Procedure

It was then necessary to use the above flight model to produce a nine-mass-point model that would have the same elastic and dynamic characteristics as the large model for frequencies up to 60 cycles per second. The reduction was accomplished by subjecting the detailed model to a series of self-equilibrating load sets, which defined average elastic behavior of the structure with respect to its centerline at specific segments and degrees-of-freedom. Mass properties calculated for the reduction were those translational and rotary inertias defining each mass set that was condensed.

Static and dynamic checks of the simplified model were compared with the detailed analysis. All values within the region of interest were within 3 percent except the pair of third lateral bending modes, which matched the detailed model within 14 percent. Much of this difference can be attributed to the absence of mass coupling (first moments and cross products) in the reduced model. This was necessary because the program to be used for the actual forced-response analysis could not make use of such information.

Conclusions and Problem Areas

It has been demonstrated that the finite element method, coupled with the current generation of computers and modern computer programs, provides the structural analyst with the capability of treating complex problems in more detail than possible in the past. The ability of these methods to predict the static and dynamic behavior of space telescope structures, including behavior induced by thermal loading, has been shown.

The potentials of this type of analysis are indeed great. For example, the possibility of almost real-time thermal deformation

predictions using telemetered temperature data from space, and subsequent spacecraft corrections based on this analysis, is certainly possible in the not too distant future.

Problem areas, however, do remain, and much work is required for their solution. Four areas that seem particularly pertinent to the field of orbiting telescope structure, but not unique to this area, are discussed in this paper. These areas are: accuracy of solution, modeling structures, problem-size reduction, and interface programs.

Accuracy of Solution

Before discussing this problem in some detail, a brief example is required to demonstrate some subtleties concerning accuracy in structural analysis predictions in optical systems. The comment is often made that a structural analyst cannot predict deformations on the order of a few arc seconds because of numerical inaccuracy in his computer program, unknowns in the physical properties, poor mechanical joint definition, etc. What is sometimes forgotten is the fact that these structural deformations are usually the result of very small loads; that is, we are not attempting to predict perturbations on the order of an arc second but rather total deformations of this order. In other words if our loads are well defined, we should generally expect no more percentage of error in our final solution than in any other type of structural analysis.

The question does remain, however, as to the effects on thermal deformations of small initial nonlinearities caused by slack in joints, initial imperfections, etc. This is a poorly defined problem area that warrants the attention of the designer and fabricator in addition to that of the structural analyst. Looking at the question of accuracy as it pertains to finite element analysis of optical space telescopes, one may consider three major groups of contributing factors:

1. Those due to the computer and the computer program (solution order, precision used, algorithm efficiency, matrix conditioning, etc.)

2. Those due to structural idealization

3. Those due to errors in the calculation and application of applied loads (including applied temperatures).

The first group is the object of much current study (ref. 10). Its particular effects have no special meaning to the field of optical space telescope analysis, but they apply equally to the entire field of matrix structural analysis. These effects are probably the smallest of the three groups and will not be discussed.

The second group will be commented on in the problem area dealing with *Modeling Studies*. It is sufficient to say that this area depends mainly on the experience of the analyst and the characteristics of the available finite elements.

The third problem area is the cause of our greatest concern in dealing with optical structures. In particular, this area is most critical in the analysis of thermally induced deformations. The present thermal analyzer programs, available at Goddard, do not appear to be of sufficient size to predict structural temperatures adequately in the detail required for an accurate deformation analysis of a spacecraft the size of the OAO. One possible way to correct this situation is to add thermal analyzer capabilities to the NASTRAN program, which could be based on the finite element method of thermal analysis, and to utilize the large and advanced mathematical routines contained in the present program.

Modeling Studies

Modeling studies are required to evaluate structural idealization procedures in order to minimize inaccuracies in the finite-element model representation of the actual structure. In general, finite element methods provide reliable data only when the structure is properly idealized and when the results of the analysis are properly evaluated by an experienced analyst.

Much work remains in this general area and, in particular, within the area of modeling of major optical surfaces. Accuracy requirements and the apparent need to include three-

dimensional elasticity and temperature effects demand that well planned modeling studies be conducted. These studies will aim at both the evaluation of various elements and the determination of network patterns for best results.

Problem-Size Reduction.

The accuracy required in the static and normal mode analysis of orbiting structures will often lead to large models requiring sizeable amounts of computer time for solution. When another dimension, such as time, is added in the forced-response analysis of the structure, it will often be required that the number of unknowns be reduced so that satisfactory results can be obtained in a reasonable amount of machine time. Because of this, work is required in both the development of new methods and the evaluation of existing methods to reduce the number of unknowns in a given problem.

Interface Programs

In the most general case of thermal deformation analysis, the temperature distribution is required as a function of both space and time. The magnitude of data represented by this for practical problems requires (1) the automated communication and interpolation, in both space and time, of temperature data to the structural program and (2) the automatic calculation of thermally equivalent mechanical loads and solution of the deformation problem by the structural program.

In addition, the coupling of the structural program with a ray-tracing program for the communication of data would complete the analysis flow and would allow for optical degradation predictions as a function of time. Programs of this type are not now available but must be present before large-scale application of these methods to practical problems can begin.

References

1. Technical Evaluation Report for the Definition of the NASA General Purpose Digital Program for Structural Analysis. Computer Science Corp., 1966.
2. Przemieniecki, J. S.: Theory of Matrix Structural Analysis. McGraw-Hill, 1968.
3. Zienkiewicz, O. C.: The Finite Element Method in Structural and Continuum Mechanics. McGraw-Hill, 1967.
4. Mason, J. B.: Analysis of Thermally Induced Structural Vibrations by Finite Element Techniques. NASA X-321-68-333, 1968.
5. Rosette, K. L.; Jarrell, T. W.: Structural Thermal Optical Program (STOP), Phase I, Revised Verification Test Procedure. GSFC, Greenbelt, Maryland, 1968.
6. Rosette, K. L.; Mason, J. B.; Jarrell, T. W.: Structural Thermal Optical Program (STOP), Phase I, Results of Feasibility Study to Investigate the Use of Analytical Techniques to Evaluate Thermal Elastic Response of Space Structures. DIRS # 01487, GSFC, Greenbelt, Maryland, 1968.
7. Rosenbaum, W. S.: Structural Thermal Optical Program (STOP), Phase I, Theoretical Thermal Analysis of the Orbiting Astronomical Observatory Goddard Experiment Package Secondary Mirror Mount. DIRS # 01610, GSFC, Greenbelt, Maryland, 1969.
8. Mason, J. B.: Structural Thermal Optical Program (STOP), Phase I, Analytical Thermal Deformation Analysis of the Orbiting Astronomical Observatory Goddard Experiment Package Secondary Mirror Mount. DIRS # 01704, GSFC, Greenbelt, Maryland, 1969.
9. Butler, T. G.; McConnell, R. D.; Cook, W. L.: Dynamic Analysis of the OAO - Interim Report. GSFC, Greenbelt, Maryland, 1967.
10. Phillips-Ford Corp.: Determination of Guidelines for Finite Element Structural Analysis. NASA CR (to be assigned), 1969.

PRECEDING PAGE BLANK NOT FILMED.

N70-36727

Considerations on Precision Temperature Control of a Large Orbiting Telescope

S. Katzoff

NASA Langley Research Center

Introduction

Quantitative specification of the temperature uniformity and temperature constancy of a large orbiting telescope will not be possible until one can also specify telescope operating temperature, materials, environment, and types of construction and operation. It would be desirable, however, to establish a background of information on what might be feasible and what might be required to establish a high degree of perfection with regard to both uniformity and constancy of temperature. Among other advantages, a reasonably practical, precise, temperature control could alleviate the requirements for continual testing and adjustment of the optics while in orbit.

This paper presents the results of calculations relative to this problem. The basic idealized configuration that has been studied is a large telescope tube made of 1-millimeter-thick aluminum and wrapped in superinsulation. The types of radiation environment considered correspond roughly to synchronous orbits and to near-earth orbits, mainly the former. The discussion will indicate the nature of the problem and how it might be alleviated by means of heated collars near the tube opening, heat pipes and vapor chambers, and enclosing balloons. Mathematical methods have not been detailed in this paper because they are assumed to be of immediate interest to only a small part of the audience.

Infinite Cylinder

Calculations were made for the infinite cylinder in synchronous orbit, in low orbit, and with ring heat pipes.

Synchronous Orbit

Figure 1 shows results for an infinitely long cylinder oriented at right angles to solar radiation and with no appreciable radiation input to the shaded half, as in synchronous orbit. The inside is assumed to be perfectly black, and the external surface is assumed to have a solar-absorptance/thermal-emittance ratio of 1/3. For one case, figure 1(a), the insulation is assumed to provide a heat-transfer rate of 0.0025 [(external temperature)⁴ - (internal temperature)⁴]. In figure 1(b), the factor is taken as 0.025.

With either type of insulation, the mean internal temperature is about 225°K. For the heavier insulation, the subsolar elements of the cylinder will be about 0.3° warmer than the shaded elements. For the lighter insulation, the difference will be about 10 times as much or about 3°. These difference values are approximately proportional to the temperatures themselves. For example, if the external surface has an absorptance/emittance ratio of 1 instead of 1/3, all temperatures will be increased by 3^{1/4} (or about 4/3); and the temperature differences will also be increased. For these calculations, it was assumed that the diameter of the cylinder was so large (say, 3 meters) that circumferential conduction heat transfer in the cylinder wall, which is of 1-millimeter-thick aluminum, is small compared with radiation heat transfer.

Possible nonuniformity of the insulation must be considered in all discussions of the thermal problem. If the nonuniformity is 30 percent, the internal temperature may be 233°K instead of 225°K, as indicated in figure 1(c). This degree of nonuniformity

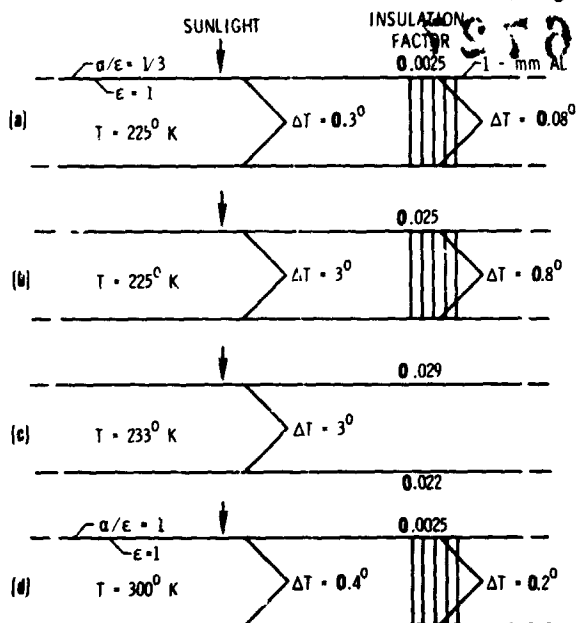


Figure 1. Infinite cylinder in sunlight.

seems not unlikely; however, a maldistribution in which all the higher-conductance insulation is on the sunlit side and all the lower-conductance insulation is on the shaded side is probably unrealistically extreme. In any case, it is worth remembering that possible nonuniformities in insulation, environment, coatings, contact resistances, and the like must be considered in any analysis that is concerned with temperature uniformity.

Low Orbit

The preceding results for the infinitely long cylinder will be modified in at least two respects when the cylinder is brought in from a synchronous orbit to a fairly close orbit about the earth. First, both the thermal radiation and the reflected solar radiation from the earth will provide heat inputs to the shaded half of the cylinder that may total about half of that provided by the direct sunlight on the sunlit half. The indicated temperature nonuniformities will be reduced to half. Second, the thermal input to the cylinder will no longer be constant because the cylinder will periodically be in the earth's shadow. This alternate heating and cooling, however,

will be heavily damped by the thermal inertia of the insulation and the cylinder wall. With the cylinder assumed to be of 1-millimeter-thick aluminum and the insulation assumed to be made of 30 to 50 layers of aluminized polymer film with some spacer material between adjacent layers, the total amplitude of the temperature oscillation within the cylinder should be about 0.03° .

Ring Heat Pipes

Calculations were made of the improvement in temperature uniformity that might be achieved by welding heat pipes around the cylinder. For the calculations, the heat pipes were assumed to be isothermal rings.

If the heat pipes are spaced 40 centimeters apart, the maximum temperature nonuniformity (the temperature midway between the heat pipes on the subsolar elements minus the temperature midway between the heat pipes on the shaded elements) is reduced by a factor of about 4. Putting the heat pipes still closer together reduces the nonuniformity further. The temperature difference varies nearly as the square of the spacing.

These calculations were for the case in which the mean temperature within the cylinder was about 225°K . The effectiveness of the heat pipes in reducing temperature nonuniformity decreases with increasing temperature because radiation heat transfer is proportional to differences in T^4 , whereas conduction heat transfer is proportional to differences in T . The net effect is that the improvement in uniformity achieved by adding heat pipes (with a given spacing) varies, roughly, inversely as T^3 . Thus, for a cylinder temperature of 300°K (as for an outer-surface absorptance/emittance ratio of 1), the heat pipes spaced at 40 centimeters reduce the nonuniformity by a factor of only about 2.

Finite Open-Ended Tube

A cylindrical tube of finite length, with one end open and the other end closed with a

perfect flat mirror, was used in the calculations as a representation of a telescope tube.

General Characteristics

The results for the finite open-ended tube typically differ from those for the infinite cylinder in three respects:

1. If the tube is covered with insulation comparable with the insulation previously assumed for the infinite cylinder, the escape of radiation from the open end will result in a mean internal temperature far below that for the infinite cylinder (which was about 225°K).
2. Because the tube wall near the opening loses much of its radiation directly to space, the wall temperatures decrease rapidly toward the opening.
3. Although the wall temperature decreases toward the opening, the temperature difference between the subsolar elements and the shaded elements increases.

These effects are shown in figure 2 for a tube that is 6 diameters long.

Putting circumferential heat pipes around the tube would reduce the circumferential temperature nonuniformity but not the large longitudinal variation (unless the heat pipes were heated by some external means).

Heated Collar

A heated collar in the end of the tube will greatly reduce the longitudinal temperature variation. Figure 3 shows calculated temperatures for a tube having a uniform-temperature heated collar 3 radii long. The length of the collar is not critical. For example, a much shorter collar at a higher temperature would have the same effect.

The upper curve is for the tube normal to the sunlight, for which case the infinite cylinder had a mean internal temperature of 225°. If the collar is maintained at a temperature only 3° higher, the remainder of the tube will now be at the same uniform temperature as the infinite cylinder. The lower curve is for the case in which there is no external radi-

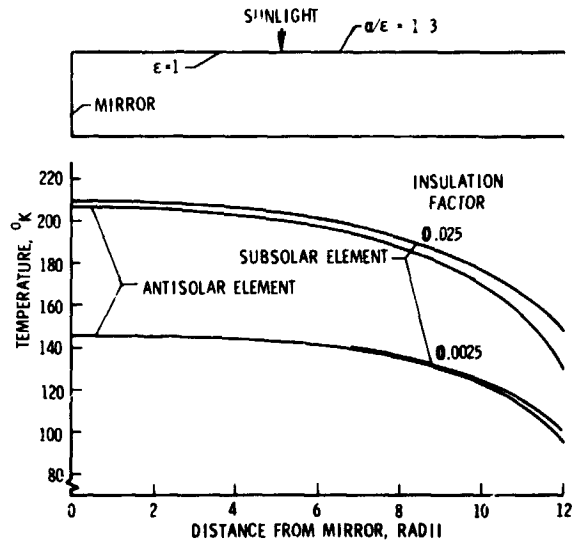


Figure 2. Temperatures in insulated tube.

ation input at all, as if the tube axis were aligned with the sunlight. The tube loses energy by radiation to space over its entire cylindrical surface. The wall temperature in this case is about 5° lower near the mirror than near the heated collar, and its average value is about 5° less than that for the tube oriented normal to the sunlight. The average temperature for this case can be raised by raising the collar temperature, but the longitudinal variation will remain.

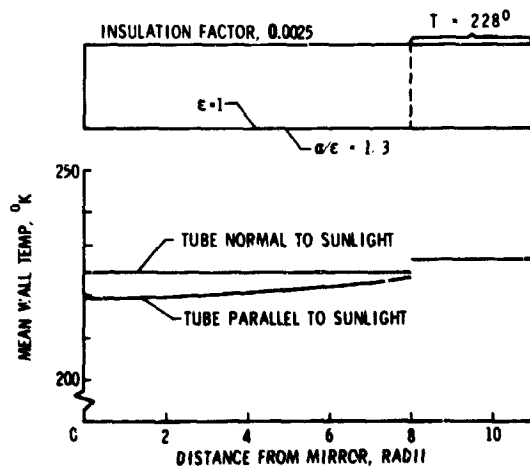


Figure 3. Insulated tube with fixed-temperature section.

Extending the insulated tube beyond the heated collar will reduce the radiation loss out of the opening and thus will reduce the heat-input requirement to the collar without affecting the general nature of these results. For example, extending the tube 3 radii beyond the end of the collar would reduce the radiation heat loss out of the opening by a factor of about 5.

Longitudinal Heat Pipes

Welding longitudinal heat pipes along the tube (fig. 4) would greatly reduce the longitudinal temperature variation, shown in figure 2, and would also nearly eliminate any longitudinal temperature nonuniformity due to variability of the insulation, shown in figure 1. The tube temperature, however, would now be quite low because of the increased radiation losses out of the open end. For this case, the tube temperature would be about 176°K for the lightly insulated tube and about 110°K for the heavily insulated tube. If the heat pipes were 40 centimeters apart, the wall temperature, midway between the heat pipes right at the opening, would be about 2.5° less than the heat-pipe temperature for the lightly insulated tube and would be about 0.5° less for the heavily insulated tube. Extending the tube beyond the ends of the heat pipes would conserve heat and thus would provide a higher temperature, and also a more uniform temperature, in the section containing the heat pipes.

To summarize, it has been shown that: (1) a heated collar in a well-insulated tube can provide a relatively constant mean temperature but cannot assure longitudinal temperature uniformity to better than a few degrees; (2) longitudinal uniformity can be improved by longitudinal heat pipes; and (3) extending the tube beyond the uniform-temperature section will minimize the escape of radiation. Combinations of longitudinal heat pipes with circumferential heat pipes (fig. 4) and collars are reasonably apparent but were not studied.

Mirror Temperature Uniformity

The mirror requires an especially uniform and, presumably, constant temperature.

Its front face, because of the specular coating, has a relatively low but not negligible radiation interchange with the inside of the tube. The back surface is, or can be made, highly absorptive to radiation. The approach to very precise thermal control of the mirror would appear to be mainly through radiation interchange with an accurately isothermal, constant-temperature disk behind it. Keeping at least the lower part of the telescope tube at the same constant and uniform temperature would appear to be a desirable auxiliary goal.

Vapor Chamber

The disk could be the surface of a thin, flat, vapor chamber, heavily insulated on the side away from the mirror (lower sketch in fig. 4). Bringing the lower ends of the longitudinal heat pipes into the chamber will assure that the tube itself has nearly the same temperature as the vapor chamber, thus providing the desired nearly-isothermal radiation environment for the mirror. This approach eliminates or reduces the need for the heated collar although it transfers the problem of supplying carefully controlled heat from the collar to the vapor chamber.

Heat-Pipe Temperatures

The surface of the vapor chamber may be assumed to have an extremely uniform temperature. The temperatures of the long

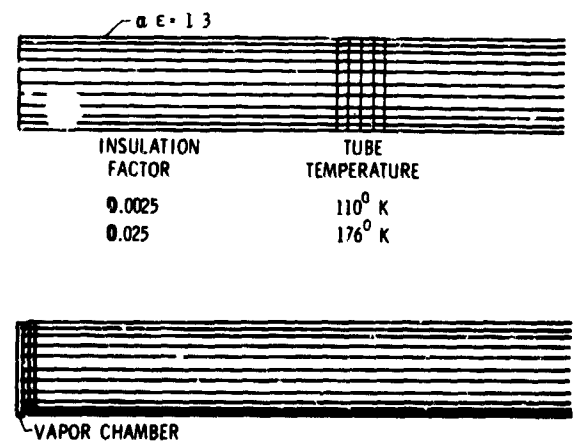


Figure 4. Tube with longitudinal heat pipes.

heat pipes, however, will be less uniform, mainly because of the temperature drops through the wick (here assumed to be 0.25 millimeters thick). For the configuration shown in figure 4 (with no external radiation heat input, light insulation, a temperature of 225°K, and heat pipes 40 centimeters apart), the temperature drop through the wick in the main part of the heat pipe might be about 0.1°. The portion of the heat pipe that lies within the vapor chamber is perhaps only one-tenth as long as the portion that extends along the telescope tube; furthermore, it has wicking on both its inner and outer surfaces. Hence, the temperature drop between the vapor chamber and the inside of the heat pipe might be about 2° and is thus the major part of the temperature difference between the telescope tube and the vapor chamber.

The preceding calculation neglects the heat lost by radiation out of the tube opening (and which must be abstracted from the adjacent ends of the heat pipes) and thus underestimates the problem. If the heat pipes extend all the way to the opening, this heat loss will require an additional 2° temperature drop across the heat-pipe wicks in the vapor chamber. (This result assumes a 3-meter-diameter tube with heat pipes 40 centimeters apart.) Extending the tube 3 radii beyond the isothermal part (the part served by the heat pipes) will reduce this heat loss by a factor of 5, as previously mentioned, and correspondingly will reduce the additional temperature drop across the heat-pipe wicks to about 0.5°. These additional temperature drops vary with the fourth power of the tube temperature. For example, they would be three times as large if the tube temperature were 300°K instead of 225°K.

A separately heated collar near the tube opening could minimize the heat-transfer requirements of the heat pipes and could nearly eliminate any temperature difference between the vapor chamber and the telescope tube.

Balloon Enclosures

In his 1962 paper in the *American Scientist*, Professor Spitzer suggested that the

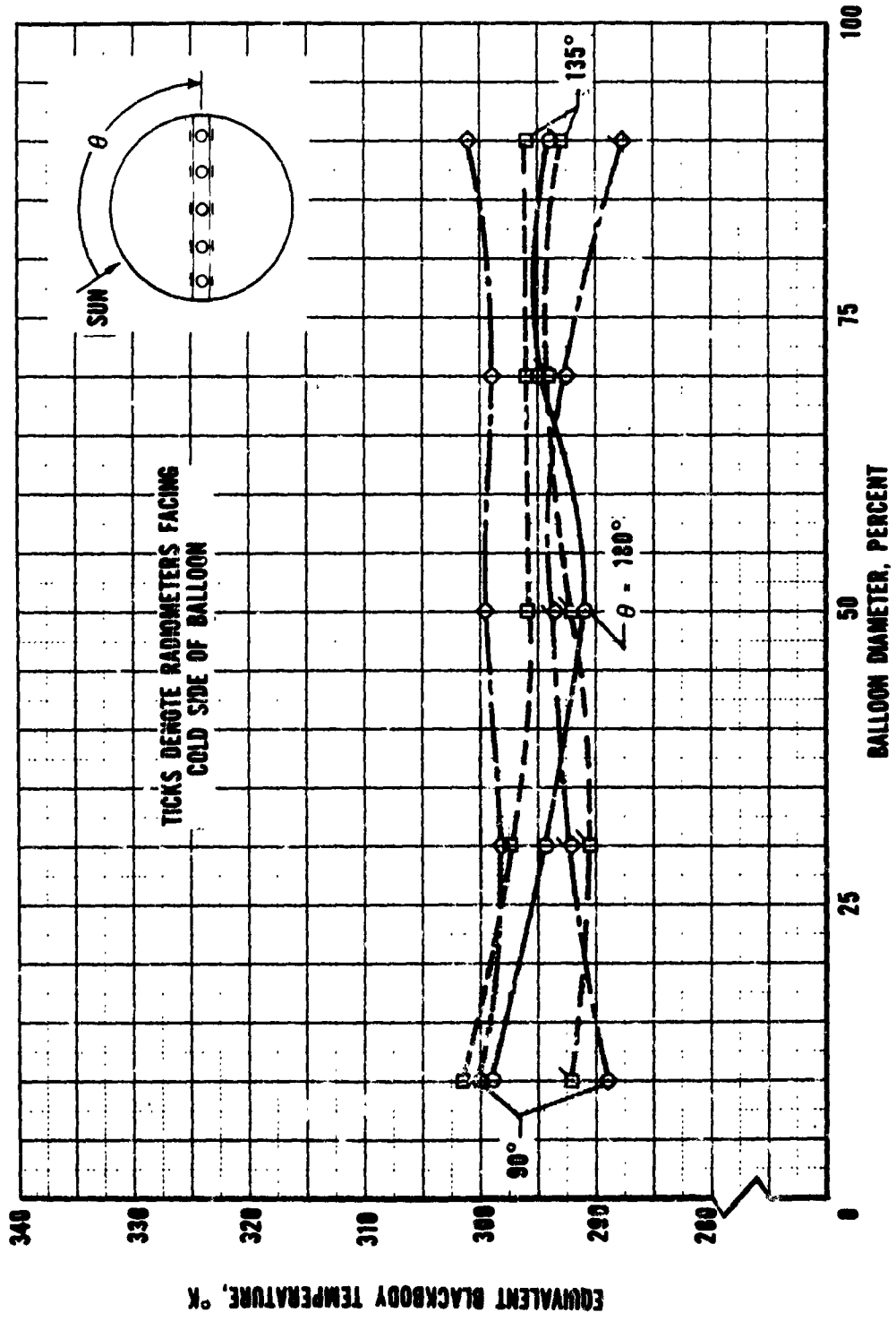
thermal problem could be lightened by enclosing the entire telescope in a balloon. A model of such an arrangement has been studied in a space simulation chamber at the Langley Research Center. Some results are shown in figure 5 (from a paper by George E. Sweet; to be published). The external surface had an average solar-absorptance/thermal-emittance ratio of 1.1, which provided a mean internal radiation temperature of about 290°K when the balloon was irradiated with simulated sunlight. The inside surface of the balloon was lightly anodized; the outside surface of the "telescope" tube was specular. The temperature of the radiation striking the outside surface of the tube was uniform to within about $\pm 5^\circ$ for a range of orientations. This uniformity, considered in terms of variations in (radiation temperature)⁴, is over 20 times better than that for an unenclosed tube irradiated from one side by sunlight. Furthermore, as figure 5 shows, the mean radiation temperature over the tube is almost independent of the orientation of the tube relative to the sun.

The balloon could thus be very helpful although, without some additional thermal control, it cannot provide extreme temperature uniformity and constancy. When one considers what types of additional means would be required to achieve such very precise thermal control, one returns again to the previously discussed vapor chamber, collar, insulation, and heat pipes. Use of the balloon should, however, greatly simplify the design requirements for all of these components.

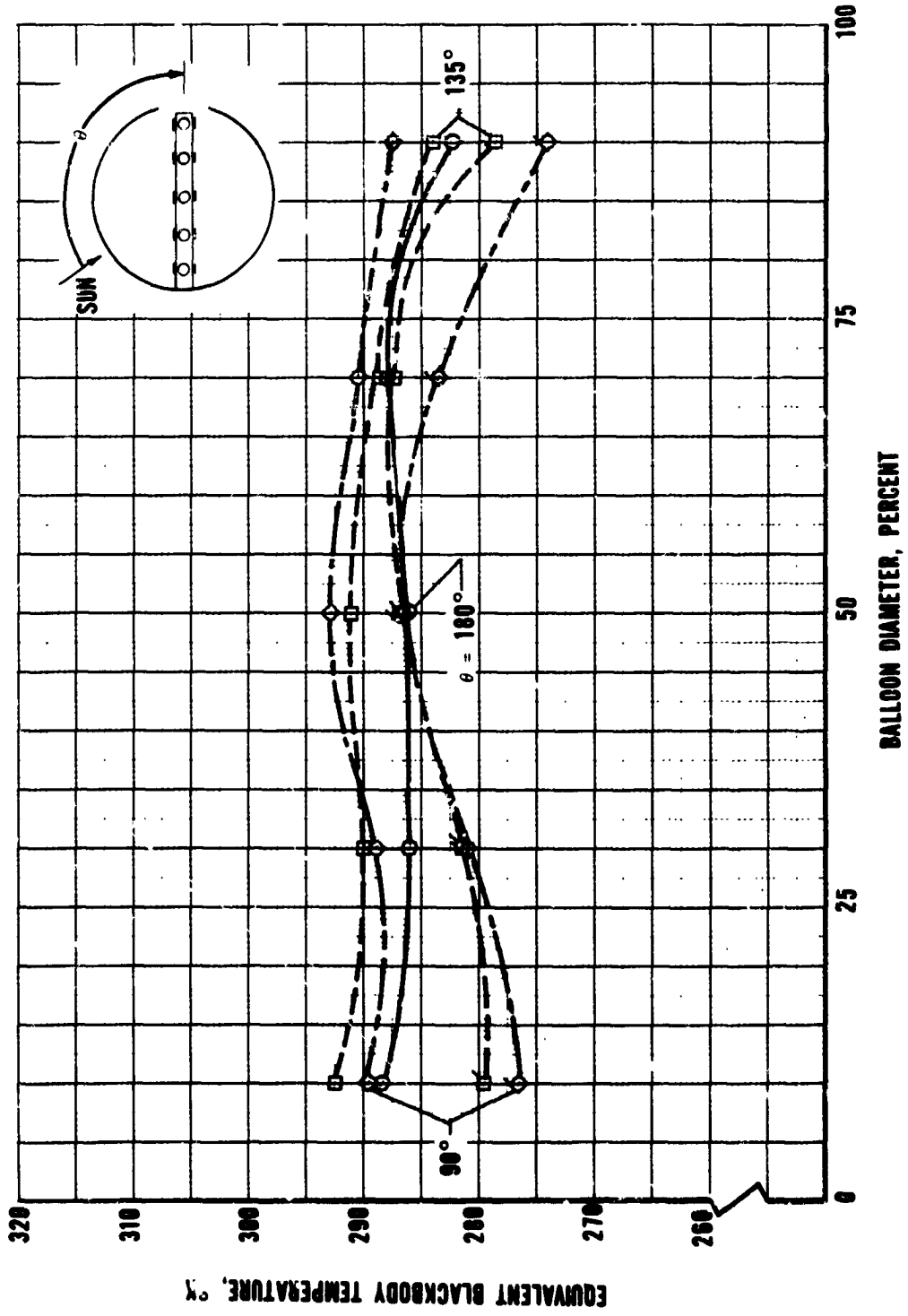
Concluding Remarks

This paper has discussed some approaches to achieving very precise thermal control of a large orbiting telescope. All of these approaches involve considerable effort, cost, weight, and complexity and, accordingly, would not be used without first carefully judging the need. They represent a reserve from which to draw as the occasion warrants.

The technology required for these approaches is not yet completely in hand. For



(a) Porthole closed; internal heaters off.



(b) Porthole open; internal heaters off.
 Figure 5. Radiation temperature inside balloon; porthole located at the 100 percent diameter.

example, heat pipes as long as those discussed in this paper have not yet been built, nor have the large vapor chambers been built, especially vapor chambers containing many inserted heat pipes. Study of the means of supplying carefully controlled heat to the vapor chamber or to the heated collar is also

required. Methods of supplying the heat electrically are reasonably apparent; however, solar heat would seem to be a preferable source. Therefore, methods of transferring solar heat in a carefully controlled manner (perhaps with electrical heating as a fine control) require development.

N70-36728

Control Systems for Large Spacecraft Requiring Precise Stabilization

Willard W. Anderson
NASA Langley Research Center

Introduction

Langley Research Center personnel are engaged in research efforts directed toward the development of integrated vehicle stabilization and experiment pointing systems for large spacecraft. This work was initially focused on the Apollo Telescope Mount (ATM) cluster (fig. 1) and is currently focused on the mid-70's space station. Work on the ATM included control moment gyro (CMG) configuration (fig. 2, ref. 1) and control logic definition (fig. 3), CMG-system test-plan development (ref. 2), CMG full-scale prototype unit evaluation (fig. 4), 3-CMG digital-hardware ATM static simulation (fig. 5, ref. 3), and 3-CMG digital-hardware ATM dynamic simulation (fig. 6). Current effort on space station systems development is twofold: establishing what the systems are and determining how they should be simulated.

Typical Space Station Configuration

A candidate station is shown in figure 7. Configuration definition is an obvious and necessary step in the development of a dynamic model of a space station. The rationale for this configuration definition includes the following:

1. Space operations hangar and logistics docking facilities are located on the opposite end of the station from the experiment areas for minimum interference with experiment activities.

2. Hangar and logistics systems are isolated from the station by an airlock and are used for emergency shelter.

3. Manned centrifuge is located near the center of gravity of the station to minimize disturbance inputs from the centrifuge.

4. CMG system and noisy equipment are isolated from living and experiment areas by the centrifuge to localize noise environment.

5. Single-gimbal solar array (with station roll axis as second gimbal) is used to provide experiment pointing flexibility and to simplify operation. This gimbal is located near the machinery area and center of gravity of the station.

6. Earth-resources module is located along the minimum axis of inertia of the station to eliminate gravity gradients in earth-pointing mode.

7. Station has near-spherical inertia distribution to minimize gravity-gradient disturbances.

8. Space hangar is used as a counterweight for artificial gravity mode.

9. Station design provides for expansion capability.

These general design criteria have resulted in a configuration that should be typical of a long-term orbiting space station. Mass, inertia, and dimensional data for this configuration are being developed (refs. 4, 5).

Research effort is organized into four areas: vehicle stabilization, vehicle dynamics, experiment pointing, and disturbances. These four areas comprise the integrated physical system being studied.

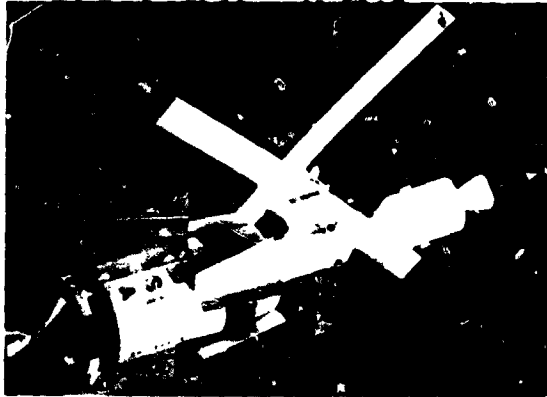


Figure 1. ATM cluster.



Figure 4. CMG torque measurement system.

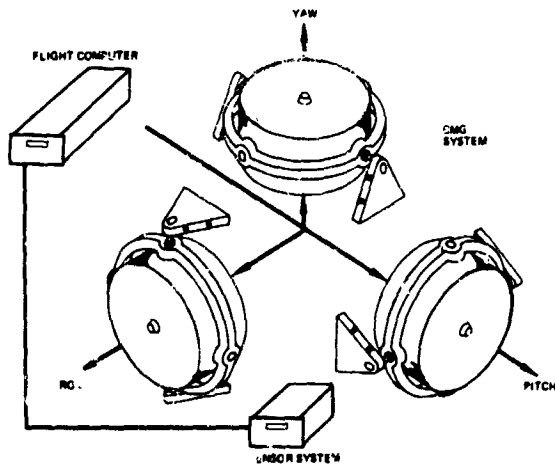


Figure 2. Schematic of SIXPAC configuration.



Figure 5. CMG system test setup.

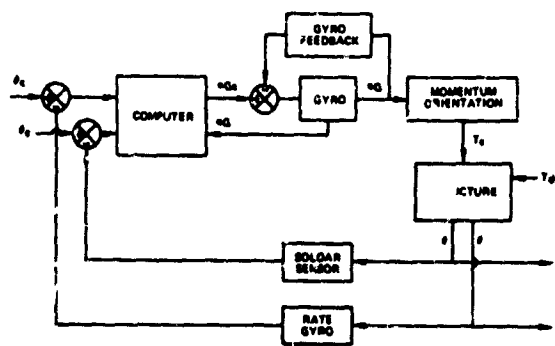


Figure 3. Simplified block diagram for single-axis control.



Figure 6. CMG control-flight test bed.

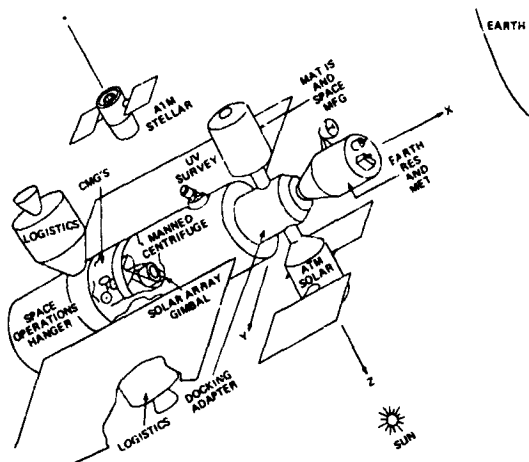


Figure 7. Typical space-station configuration.

Vehicle Stabilization

Precise, long-term stabilization of a large manned spacecraft requires an advanced or second-generation CMG system, relative to the ATM CMG system. Large angle maneuver, possible long-term earth pointing, and artificial g (spinning) operational modes require continuous, spherical, CMG, momentum vector freedom and therefore make the SIXPAC configuration (ATM) attractive. Inner and outer CMG axis slip rings are required as are improved actuator-gimbal bandwidths, minimum smooth rates, and critical-component-replacement capability. On the assumption that solar panels will provide power, DC brushless spin motors appear to offer power savings.

The state-of-the-art of the logic for the vehicle stabilization system is proportional and rate-limited with CMG torque produced by gimbal rate commands from analog steering laws. These steering laws (ref. 6) are either open loop, torque feedback, or momentum feedback as exists on ATM (ref. 7). Current research is directed toward optimal, state-space vector systems using a digital control computer.

Reference-sensor system concepts for vehicle attitude include solar reference (analog or digital solar sensors) with star

tracker update, earth reference (horizon scanner) with solar or stellar update, stellar reference with solar update, and inertial unit during large angle, maneuver-reference transition.

Vehicle Dynamics

Large multimodule spacecraft with solar arrays characteristically have several low-frequency (less than 1.0 hertz) flexible-body modes superimposed on large-inertia rigid-body modes. High docking-connection compliance, necessitated by docking requirements themselves, and solar array size, necessitated by large spacecraft system power demands, are the main contributors to vehicle flexibility. Variable rigid-body and flexible-body dynamics is a second important spacecraft characteristic. The variation is a result of continuous solar array reorientation and basic configuration changes when modules or logistic vehicles are docked or undocked. State-of-the-art vehicle stabilization systems (for example, ATM) include separate vehicle-bending-mode filters that are designed to gain stabilize one configuration only. A single, adaptive, phase-stabilized, digital system is an obvious solution to variable low-frequency vehicle bending; however, considerable research effort is required before prototype hardware can be built.

Experiment Pointing Systems

Broad categories of experiments requiring low ambient acceleration, pointing control, or free-flying modules include space biology, space manufacturing, earth resources, solar astronomy, astronomy survey, high energy astronomy, and both stellar and galactic astronomy.

Low ambient acceleration can be obtained by passive systems that isolate flexible-body vibration, provided that rigid-body slewing rates are below controlled upper bounds. Pointing control can be provided by passive isolation of the experiment package or canister from vehicle vibration and by active

control, using sensors on board the experiment package and torquing against the vehicle inertia or against onboard stored momentum.

An artist's concept of the ATM vernier-pointing control system (VPCS) is shown in figure 8. This two-degree-of-freedom system has passive (low torsional stiffness springs) and active (DC torquers and onboard sensors) pitch and yaw pointing control, with an accuracy of 2.5 arc seconds. Roll positioning capability is also provided. Initial analyses of the ATM VPCS with ideal sensors indicate an order of magnitude improvement in pointing accuracy is possible with this system (ref. 8).

Six-degree-of-freedom systems attached to the main vehicle may possibly provide the 0.01-arc-second accuracy required for galactic astronomy; however, complete six-degree-of-freedom isolation or free-flying experiment modules may be required.

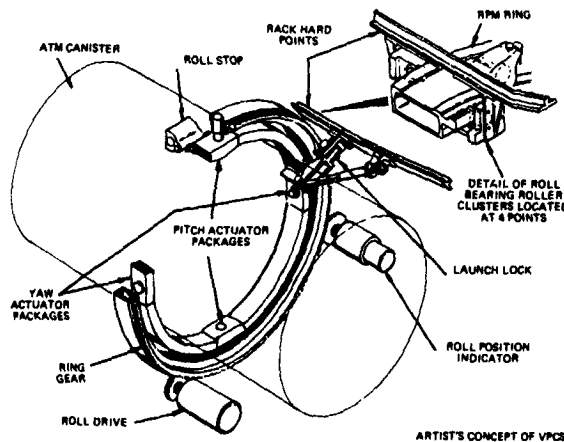


Figure 8. ATM vernier-pointing control system.

Disturbances

Vehicle and experiment package disturbances are appropriately grouped as long or short term. Long-term disturbances are primarily gravity-gradient and aerodynamic torques. Gravity-gradient torques act on a spacecraft in a plane perpendicular to local vertical and are a function of vehicle inertia differences and attitude orientation, being zero at any orientation for a vehicle with a

spherical inertia ellipsoid. Aerodynamic torques result when the center of pressure and center of mass of the vehicle are not coincident. Long-term disturbances act on rigid-body modes and affect vehicle stabilization primarily. Short-term disturbances include crew-motion and onboard-machinery (for example, a centrifuge) local force and moment profiles. These disturbances are internal to the spacecraft and act primarily on vehicle and experiment-package flexible-body modes affecting vehicle and experiment-package pointing.

Long-term (external) disturbance torques will saturate a CMG system when the time integral of the disturbance torque exceeds the initial stored momentum of the system. Gravity-gradient desaturation logic can prevent this condition by orienting the vehicle so that the time integral of the disturbance torques is bounded at a value that is below the stored momentum of the CMG system. If pointing requirements conflict with gravity-gradient desaturation orientations, desaturation must be accomplished by using reaction-jet torques; however, long-term fuel requirements and limitations on contamination of the external environment of the spacecraft may prohibit reaction-jet use. A technique is being developed at the Langley Research Center called "quiescent dump," whereby the spacecraft performs desaturation maneuvers during periods of experiment-pointing inactivity and, for given experiments, chooses vehicle orientations that minimize accumulated momentum.

Short-term disturbances excite flexible-body modes. The energy associated with these modes passes from the vehicle, through the passive isolation system of the experiment package, to the experimental apparatus itself and may ruin a given experiment. Control-system active damping (phase stabilization) of the lower bending modes reduces vehicle energy level. Phase stabilization requires CMG bandwidths well above the frequencies of any modes to be actively damped. CMG optimization work at the Langley Research Center and the Marshall Space Flight Center includes effort to improve CMG gimbal drive

response by using low backlash and antibacklash mechanical transmissions. Direct-drive hydraulic torquers are also being considered for future spacecraft having hydraulic systems on board.

Integrated System Control Functions

Spacecraft performance can be evaluated by simulating the control functions associated with spacecraft operational modes. A performance index that considers the performance of each simulated control function can provide a quantitative system rating. This performance index is an initial requirement prior to any system development. The following is a list of spacecraft pointing and stabilization control functions:

- Long-term vehicle stability
- Long-term experiment pointing
- Large angle spacecraft maneuvers
- Simultaneous target tracking
- Solar array pointing
- Short-term vehicle damping
- Short-term experiment pointing
- Centrifuge operation
- Crew operations
- Module or logistic vehicle docking
- Free-fly module control
- Spacecraft transition to spin
- Spinning spacecraft control

These control functions will be examined at the Langley Research Center by using a space-station, digital-computer-hardware simulation, including man-in-the-loop.

Simulation Description

The following is a description of the proposed Langley Research Center space station simulation. The simulation is intended as a general-purpose engineering tool to aid and to help direct effort on space-station-vehicle and experiment-pointing systems research. It is a logical extension of initial theoretical analyses and nonreal-time computer simulation and will serve as a focal point for integrated research on total system

capability. The proposed simulation is illustrated in figures 9 and 10.

Central control is provided by a program control station (fig. 11). This station allows control over the Langley Research Center CDC 6600 computer and input/output hardware. The station includes a simulation console for data entry and control, a display console for post-operation data display, a typewriter for data exit and operator comment, recorders, X-Y plotters, and site communications. The computer system allows memory up to 130,000 60-bit words, 192 digital-to-analog converters (to sites), 80 analog-to-digital converters (from sites), and 960 discretes each from sites and to sites. The application time per iteration for simulation calculation is shown in figure 12. The refined Langley Research Center ATM simulation presently uses 6.5 milliseconds operating with a frame time of 1/32 of a second, while dedicated machine availability is 27 milliseconds at this frame time. This allows an increase in simulation complexity of over 400 percent. Computer main routines will include vehicle rigid-body and flexible-body dynamics, CMG steering laws, CMG gravity-gradient desaturation logic, vehicle-pointing-control logic, external and internal disturbance profiles, vehicle and experiment attitude and update logic, monitor and diagnostic logic, and the pointing-control logic and hardware simulation for earth, solar, and stellar experiments.

A second-generation CMG system (modified SIXPAC, fig. 5) mounted in torque measurement fixtures (similar to the fixture shown in fig. 4), which, in turn, is mounted on the inner axis of a three-axis-control flight test bed (fig. 6), is housed at the second simulation site. CMG electronics and simulation interface electronics are housed in an adjacent control room (fig. 13). Two, 14-channel, FM tape recorders in this control room allow continuous, prerecorded, astronaut-force and moment-disturbance profiles to be fed to the computer.

The third simulation site is the Free-Body Dynamics Facility (fig. 14). This 60-foot sphere will serve as a sensor location

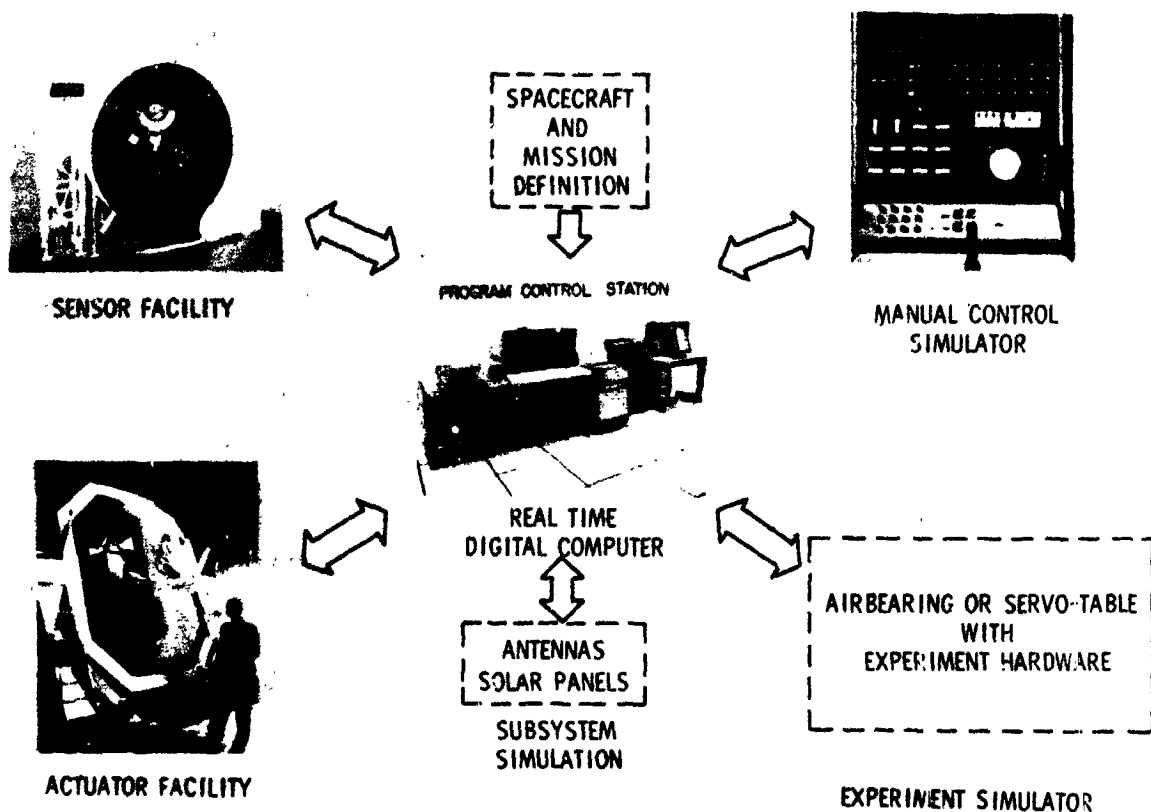


Figure 9. Simulation configuration; full-scale, control-system test concept.

and will allow actual sensor characteristics and their limitations to be included in the real-time simulation. The sensors will be mounted on a small, high-accuracy, computer-driven, servo table (fig. 15) positioned at the center of the sphere. Planet, solar, and stellar radiation simulators (figs. 16, 17, and 18) housed in the sphere will be rotated or positioned to simulate the position and attitude of the space station in orbit.

An integrated vehicle-and-experiment-pointing-systems control console (shown as a cardboard model in fig. 19 and in initial layout form in fig. 20) will be housed at the fourth simulation site. This console will allow

an evaluation of man's computer-aided capability both to control the vehicle-and-experiment pointing systems and to monitor and diagnose system status, failure, and redundant component switching.

The earth, solar, and stellar pointing subsystems comprise the final simulation sites. Specific simulation software and hardware at these sites is not defined at the present time. The concept of experiment-pointing-system evaluation, coupled with control-system hardware and computer software, has been defined. Figure 21 shows an example, the ATM solar-experiment test setup at the Marshall Space Flight Center.

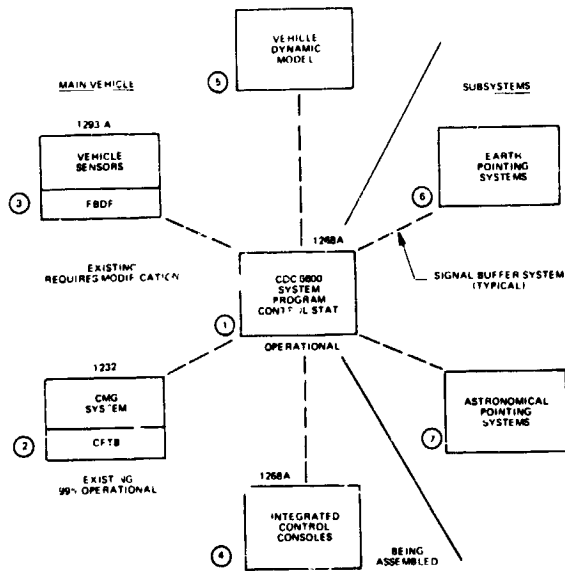


Figure 10. Space-station simulation.

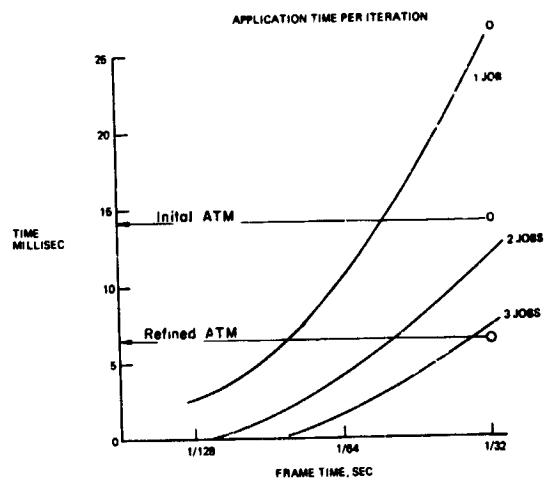


Figure 12. Computer computational capability.

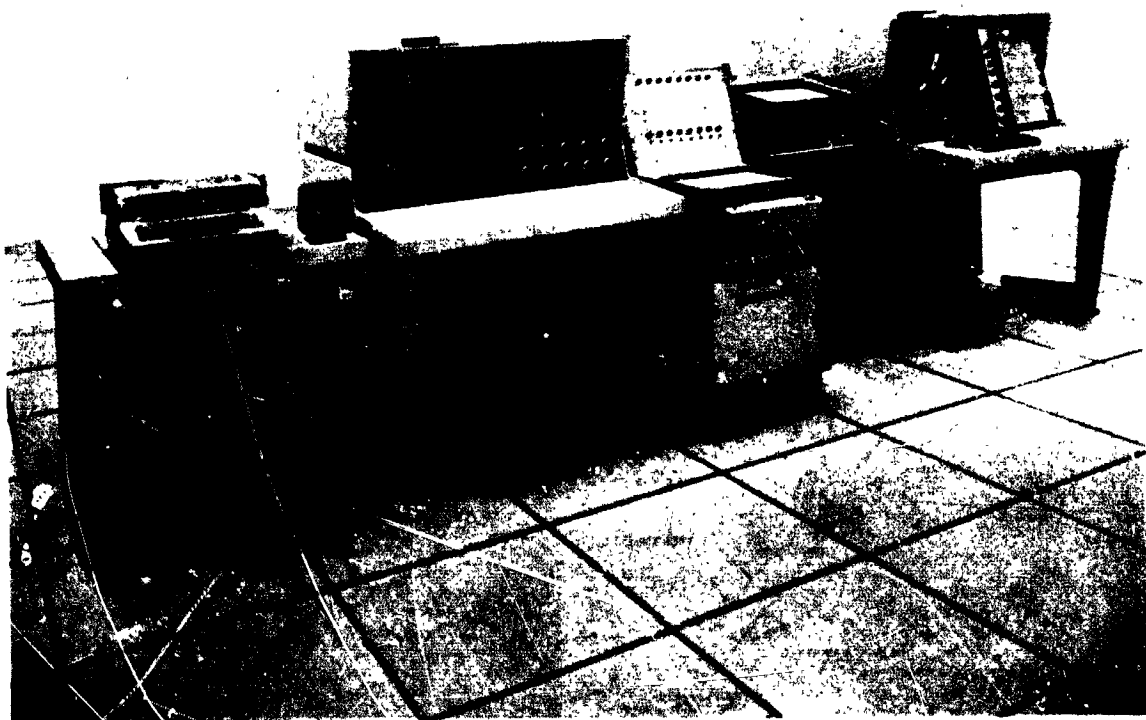


Figure 11. Program control station.

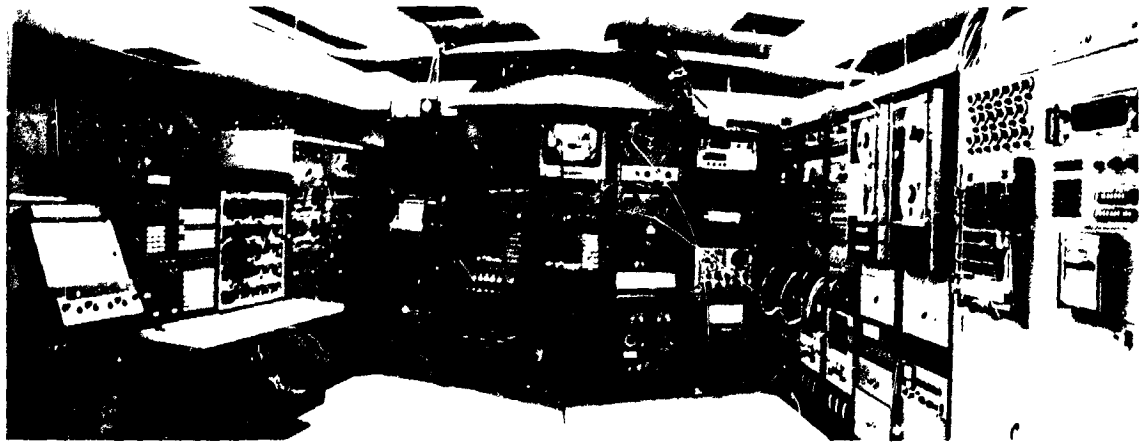


Figure 13. CMG control room.

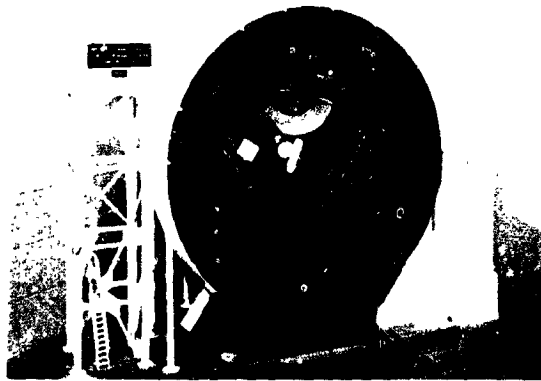


Figure 14. Free-body dynamics facility model.



Figure 16. Free-body dynamics facility, planet radiation source.

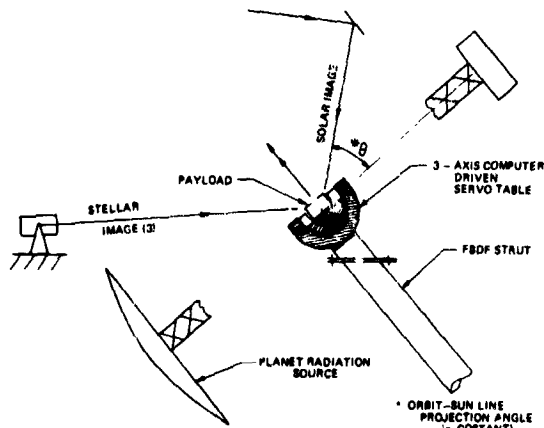


Figure 15. Free-body dynamics facility, site 3.



Figure 17. Free-body dynamics facility, solar radiation source.



Figure 18. Free-body dynamics facility, stellar radiation source.



Figure 19. Control console model.

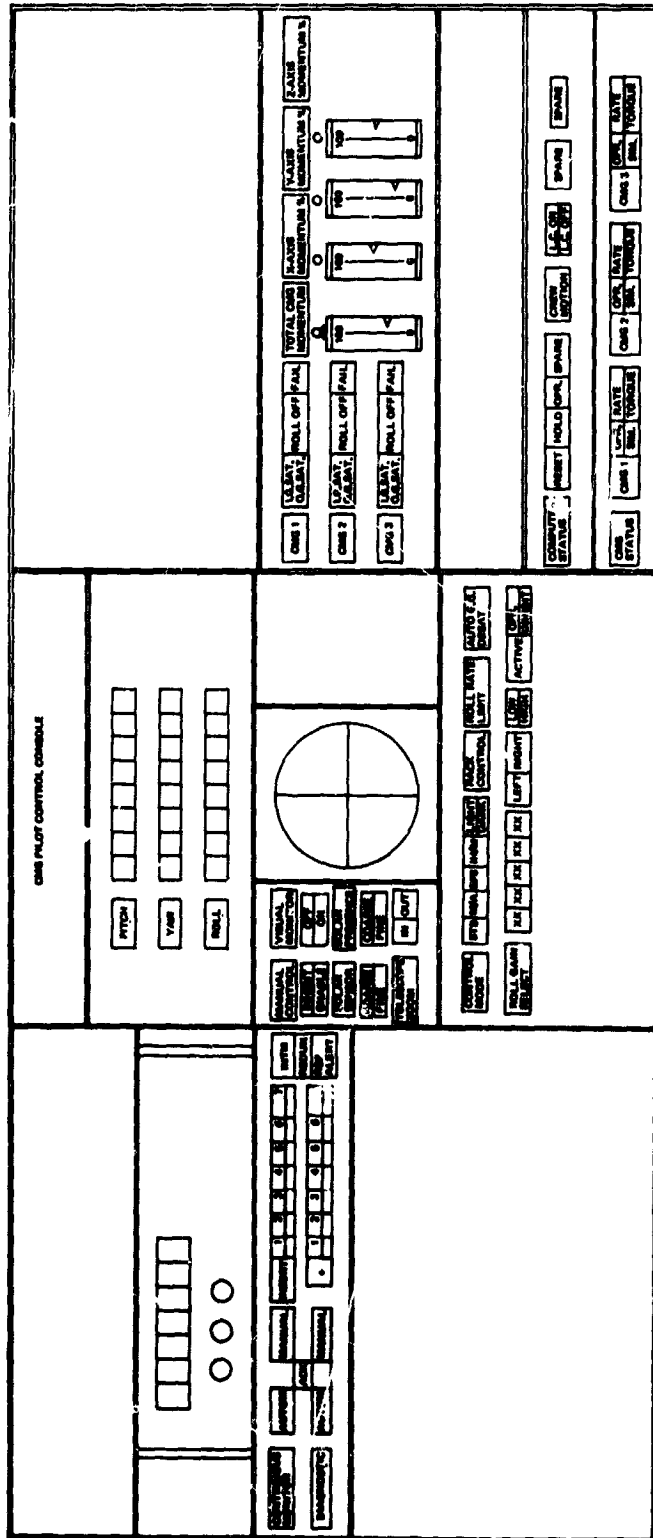


Figure 20. Control console layout.

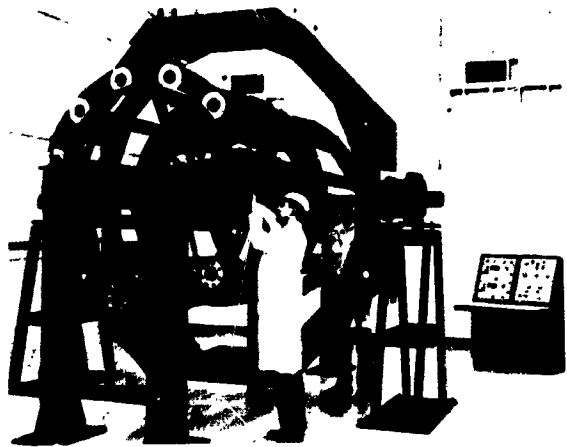


Figure 21. Experiment-pointing control simulator.

Conclusions

Basic definitions of vehicle-stabilization and experiment-package pointing systems exist for a space station typical of the one illustrated in figure 7. Detailed research on these systems is being accomplished. The ATM cluster will provide data on flight-hardware versions of initial systems. The Langley Research Center space-station simulation will provide a capability to evaluate proposed future systems, to establish control-computer requirements as well as monitoring and diagnostic requirements, to evaluate simulation techniques to determine capability, and to define pointing-control-system impact on total station design.

References

1. Kurzhals, P. R.; Grantham, C.: A System for Inertial Experiment Pointing and Attitude Control. NASA TR R-247, August 1966.
2. Control Flight Test Simulator - Study Phase Report. NASA Contract No. NASA-4155, Sperry Gyroscope Company, September 1964.
3. Keckler, C. R., et al.: Real Time Digital Computer-Hardware Simulation of an ATM Mission with CMG System Stabilization. Proposed NASA TN, Oct. 1968.
4. Experiment Program for Manned Orbital Workshops. Payloads Directorate, Advanced Manned Missions Program, Office of Manned Space Flight, August 14, 1968.
5. Experiment Program for Advanced Technology. Advanced Technology Experiments Working Group, Langley Research Center, March 15, 1969.
6. Johnston, W.: Preliminary Comparison of Three CMG Control Laws and Their Impact on Performance and Hardware. Bendix Report No. MT 13,434, March 3, 1967.
7. Chubb, W. B.; Epstein, M.: Application of Control Moment Gyros in the Attitude Control of the Apollo Telescope Mount. AIAA Paper No. 68-866, August 1968.
8. Smith, P. G.: The Pointing Accuracy of an Orbiting Gimbal Mounted Telescope. TM-69-1022-2, Bellcomm Technical Memorandum, February 1969.

Stabilization and Control of the Apollo Telescope Mount

W. B. Chubb

NASA George C. Marshall Space Flight Center

Introduction

The Apollo Telescope Mount (ATM) is a manned solar observatory. The broad objective of ATM experiments is to increase our knowledge of the solar environment by observing it from a station above the major portion of the earth's atmosphere. It is being developed for launch during 1972.

The ATM with its associated cluster (fig. 1) will be placed in 334-kilometer (180-nautical-mile) circular orbit at an orbital inclination relative to the earth's equatorial plane of 35 degrees. A manned flight duration of 56 days is planned. This is to be followed by an unmanned storage mode in which a limited amount of experimental data will continue to be gathered.

The major objectives of the ATM are:

1. To obtain specific data on the characteristics of the sun through observation of various portions of its electromagnetic spectrum

2. To obtain engineering data for aid in the design and establishment of future manned solar and stellar observatories.

To meet the scientific objectives of the ATM mission, it was necessary to develop a pointing and control subsystem (PCS) that would meet the high-accuracy pointing requirements of the ATM experiments under both external and internal disturbances such as gravity gradient, aerodynamic, and onboard astronaut motion. It was also necessary to minimize the expulsion of mass from the vehicle when taking scientific data to avoid contamination of the sensitive elements of the various ATM experiments. A third consideration was to keep the weight of the system to a minimum.

The developed PCS was divided into two major pointing and control subsystems: one to provide pointing and control of the cluster and the other to provide fine pointing and control of the experiment spar. In compliance with mission objectives, a momentum-exchange device was chosen as the control torque source for cluster control. The momentum-exchange device selected was the control moment gyro (CMG), and the subsystem using CMG's as actuators was the "CMG control subsystem." The fine pointing and control requirements of the spar resulted in the development of a control system using flex-pivot gimbal bearings* for control about two axes and an open-loop, roll, crank-around device to meet positioning requirements about the third axis. Dynamic control about

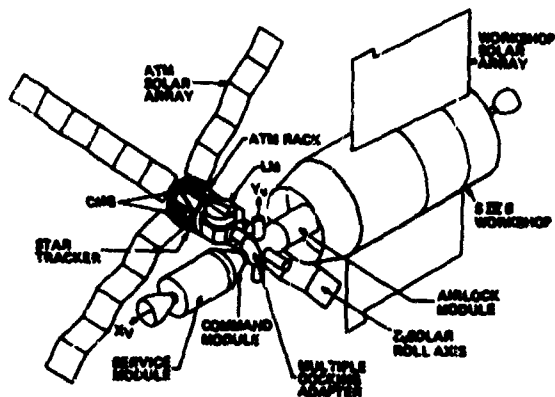


Figure 1. Apollo applications program, flights 3 & 4.

* A flex-pivot gimbal bearing is made of a pair of flat cross-leaf springs, is welded to and supported by rotating sleeves, has no backlash, and provides limited angular travel.

the third axis is supplied by the CMG control subsystem. The control system associated with fine pointing and control of the spar is known as the experiment pointing and control (EPC) subsystem.

System Requirements

The ATM PCS is required to point an experiment spar to any spot on or near the solar disc and, in the face of disturbance torques (table 1) encountered by the manned

Table 1. Major Disturbance Torques

Disturbance Torque	Peak Torque (NM)	Frequency
Gravity gradient	8	Twice orbital period
Aerodynamic	2	Orbital period
Magnetic	0.16*	Orbital period
Man motion	720	Predominantly 0.1 to 1 Hz
Venting and gas leakage	Not specified	Variable

* Maximum average torque per orbit

space station in its 334-kilometer, circular orbit, to maintain its required pointing accuracy and stability as illustrated in table 2.*

These pointing requirements are illustrated in figure 2, which portrays the experiment-package reference axis offset from the line-of-sight to the center of the sun by the maximum offset angle, ϕ_0 , of 20 arc minutes (solar radius is 16 arc minutes). At this

* For the PCS design requirements, roll is defined as the angular rotation about the line-of-sight from the experiment package to the center of the sun, and pitch and yaw are the small angular deviations of the experiment package with respect to this line-of-sight.

Table 2. Pointing Accuracy and Stability

System	Pointing	Stability (For 15 min)
CMG roll	± 10 arc min	± 7.5 arc min
CMG pitch and yaw	± 4 arc min	± 9 arc min
EPC roll	± 10 arc min	—
EPC pitch and yaw	± 2.5 arc sec	± 2.5 arc sec

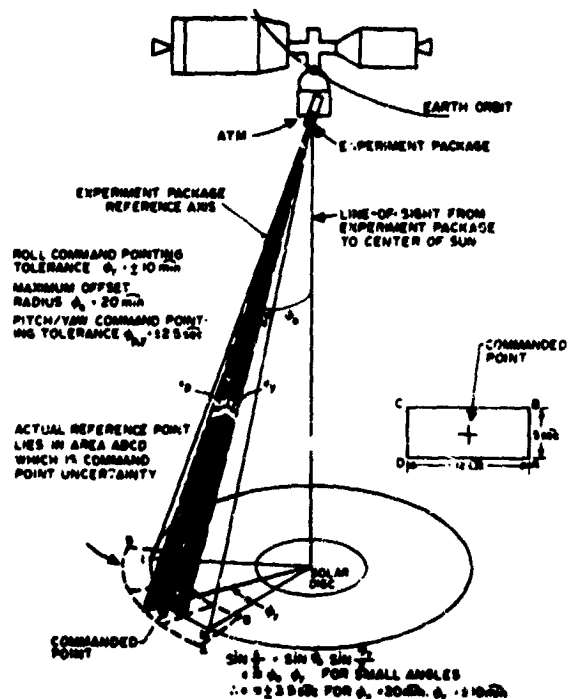


Figure 2. Command pointing requirements.

offset angle and because of the ± 10 -arc-minute uncertainty of the roll angle, ϕ_r , the commanded point in the plane of the solar disc will lie anywhere along arc length LM, which, for small angles, may be approximated by $e = \pm 3.5$ arc seconds. If, in addition, the ± 2.5 -arc-second uncertainty of pitch and yaw is included, the actual commanded reference point will lie anywhere within region

ABCD, which is the command point uncertainty (fig. 2). Since all angles are small, area ABCD may be considered to be a rectangle with a width of 5 arc seconds (illustrated by ϵ_p) and a length of 12 arc seconds (illustrated by ϵ_y) at an offset angle, $\phi_o = 20$ arc minutes.

The control system stability requirements around any actual reference point are illustrated in figure 3, where point A is considered as the actual commanded reference point. Arc length, PQ, in the plane of the solar disc is generated by the ± 7.5 -arc-minute roll excursion during a 15-minute time interval with a 20-arc-minute offset from the center of the sun. It may be approximated by an angle, ϕ_y , of ± 2.5 arc seconds. The inclusion of pitch and yaw uncertainty of ± 2.5 arc seconds generates the area EFGH, which is the locus of points for the control of the experiment package reference axis around the commanded reference point A. Since all

angles are small, area EFGH may be approximated as a rectangle with a width of 5 arc seconds (ϕ_p) and a length of 10 arc seconds (ϕ_y), again assuming a 20-arc-minute offset angle. Since the center of area EFGH can be any point within area ABCD, the command pointing uncertainty may be combined with that for the control around an actual reference point. This results in an overall experiment-package pointing uncertainty that may be approximated by a rectangle with a width of 10 arc seconds and a length of 22 arc seconds, as illustrated in figure 3.

CMG Control Subsystem

The CMG control subsystem is a momentum-exchange control system. The momentum-exchange devices are three orthogonally mounted, double-gimbaled CMG's (fig. 4); each has a stored momentum capability of 2700 Newton seconds. The moments of inertia and mass data of the ATM cluster are presented in table 3.

The use of CMG's in the pointing and control of a large manned space station is new, and the problems associated with that type of system are unique and were unsolved. Some of the problems encountered in the development of the CMG control subsystem were:

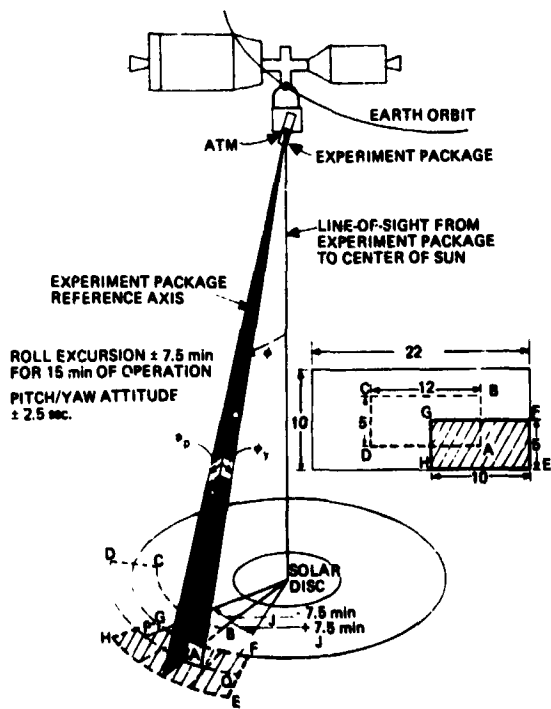


Figure 3. Control requirements around actual reference point (15-minute period).

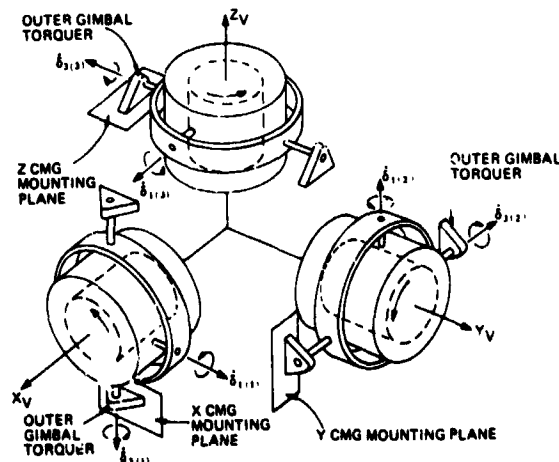


Figure 4. CMG cluster.

Table 3. Moments of Inertia and Mass of ATM Cluster

I_1	=	$0.8711 \times 10^6 \text{ kg}\cdot\text{m}^2$
I_2	=	$0.5497 \times 10^7 \text{ kg}\cdot\text{m}^2$
I_3	=	$0.5254 \times 10^7 \text{ kg}\cdot\text{m}^2$
Mass	=	$0.5409 \times 10^5 \text{ kg}$

1. An acceptable control law for use of the CMG's in control of the ATM cluster.

2. A means for preventing the CMG's from "falling into" an undesirable orientation such as that which would not allow the use of the CMG's to control the spacecraft even though the CMG cluster was not in its saturated momentum state.

3. A means of desaturating the CMG cluster periodically without the use of a mass-expulsion reaction control system (RCS). A method was needed to permit torques produced by an external force field, such as gravity gradient, to be used to effect CMG momentum desaturation.

4. The optimal orientation of the vehicle to minimize external bias torques that would tend to saturate the CMG cluster; i.e., the placement of the minimum principal axis of inertia into the orbital plane.

Acceptable control laws for use of the CMG's in control of the ATM cluster were developed. A detailed derivation of these laws is given in references 1, 2, and 3; only the basic concepts considered in the development of these control laws will be discussed in this paper. Figure 5 shows a single CMG.

The CMG is a two-degree-of-freedom gyroscopic device used to generate controlled moments on its mounting base. It consists of a constant-speed wheel held in a housing; this is called the inner gimbal. The inner gimbal is coupled to the outer gimbal through a pivot that is perpendicular to the wheel spin vector. The outer gimbal is coupled to the base by the outer pivot. The two pivots are driven by geared torquers.

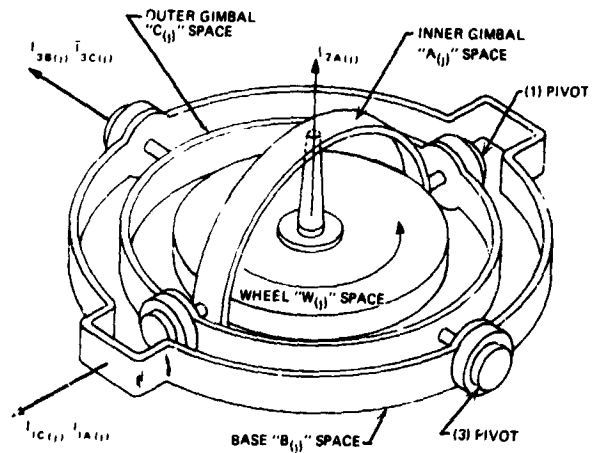


Figure 5. The "j" control moment gyro (CMG).

The reaction moment of an ideal cluster of CMG's on the vehicle can be expressed by equation 1.

$$\bar{M}_{RV} = - \left. \frac{d\bar{H}_{TV}}{dt} \right|_{I\text{-space}} = - \left[\left. \frac{d\bar{H}_{TV}}{dt} \right|_V + \bar{\omega}_{IV} \times \bar{H}_{TV} \right] \quad (1)$$

where \bar{H}_{TV} is the total angular momentum of the CMG cluster as expressed in vehicle space and $\bar{\omega}_{IV}$ is the inertial angular velocity of the vehicle. Equation 1 can be simplified by expressing the individual momentum of each CMG in inner gimbal space, as shown in equation 2.

$$\bar{M}_{RV} = - \left(\sum_{j=1}^3 \left. \frac{d\bar{H}_{A(j)}}{dt} \right|_{A\text{-space}} + \bar{\omega}_{VA(j)} \times \bar{H}_{A(j)} + \bar{\omega}_{IV} \times \bar{H}_{TV} \right) \quad (2)$$

With the assumption that $\bar{\omega}_{IV} \ll \bar{\omega}_{VA(j)}$ and a constant wheel speed; i.e.

$$\left. \frac{d\bar{H}_{A(j)}}{dt} \right|_{A\text{-space}} = 0$$

equation 2 reduces to equation 3

$$\bar{M}_{RV} = - \sum_{j=1}^3 \bar{\omega}_{VA(j)} \times \bar{H}_{A(j)} \quad (3)$$

Equation 3 may be expressed in matrix form [1] relating the reaction moment about the various vehicle axes to the torquer rate commands on the individual CMG inner and outer gimbals, equation 4.

$$\begin{bmatrix} M_{RXV} \\ M_{RYV} \\ M_{RZV} \end{bmatrix} = [A] \begin{bmatrix} \dot{\delta}_{1(1)} \\ \dot{\delta}_{1(2)} \\ \dot{\delta}_{1(3)} \\ \dot{\delta}_{3(1)} \\ \dot{\delta}_{3(2)} \\ \dot{\delta}_{3(3)} \end{bmatrix} \quad (4)$$

The six CMG relative gimbal rates must be commanded, based upon information derived from body-mounted attitude and rate sensors. Because these sensors are aligned to the geometric body axes, they provide information relative only to these three axes. This three-dimensional information must now be routed or "steered" to provide six commanded CMG gimbal rates that will produce a reaction moment to cancel optimally any disturbance moment. The law that governs this generation of a six-dimensional vector based upon three-axis information is called *the steering law*, which is given in generalized form by equation 5, where M_{CXV} is the commanded moment about the \bar{I}_{XV} vector based on body-mounted sensor information $[T_s]$ is the steering law; $\dot{\delta}_{i(j)C'}$ is the commanded gimbal rate of the i^{th} pivot of the j^{th} CMG.

Assuming that $\dot{\delta}_{i(j)C} = \dot{\delta}_{i(j)}$ and combining equations 4 and 5, we arrive at an expression that relates the commanded torques to the actual vehicle torques, as shown in equation 6.

$$\begin{bmatrix} \dot{\delta}_{1(1)C'} \\ \dot{\delta}_{1(2)C'} \\ \dot{\delta}_{1(3)C'} \\ \dot{\delta}_{3(1)C'} \\ \dot{\delta}_{3(2)C'} \\ \dot{\delta}_{3(3)C'} \end{bmatrix} = [T_s] \begin{bmatrix} M_{CXV} \\ M_{CYV} \\ M_{CZV} \end{bmatrix} \quad (5)$$

$$\begin{bmatrix} M_{RXV} \\ M_{RYV} \\ M_{RZV} \end{bmatrix} = [A] [T_s] \begin{bmatrix} M_{CXV} \\ M_{CYV} \\ M_{CZV} \end{bmatrix} \quad (6)$$

To control the CMG cluster optimally, we require the matrix $[A][T_s]$ to be an identity $[A][T_s] = [I]$; this requires the steering law matrix to be the inverse of the CMG cluster matrix $[A]$. Since, however, $[A]$ is not a square matrix, no inverse exists; and any attempt to get an inverse results in a steering law that exhibits no control for many CMG gimbal-angle combinations. Thus, this approach at formulating a steering law fails, and another approach must be sought.

A close inspection of equation 3 reveals that, to nullify a disturbance torque, the H-vector of each CMG must be made to swing into the direction of the disturbance torque. Based upon this consideration, a steering law (the cross-product steering law) can be postulated by equation 7.

$$\bar{\omega}_{VA(j)C'} = K_{SL} \bar{I}_{2A(j)} \times \bar{\alpha}_{TV} \quad (7)$$

where $\bar{\omega}_{VA(j)C'}$ is the commanded j^{th} CMG momentum vector rate relative to vehicle

Essentially, the bias rates can be considered as the sum of the two rates: one from the distribution law, $\delta \dot{D}i(j)$ and the other from the rotation law, $\delta \dot{R}i(j)$,

$$\delta \dot{i}(j) \text{ BC} = \delta \dot{D}i(j) + \delta \dot{R}i(j) \quad (9)$$

In addition to eliminating the possibility of "falling into" the antiparallel case, the isogonal distribution and rotation law has also improved the performance of the CMG cluster by extending the bandwidth of the direct gain and by reducing the cross-coupling torques. This improvement is evident in figures 7 and 8, which show the direct and cross-coupling frequency response of the CMG cluster with and without the distribution and rotation laws (for the same total momentum).

Figure 9 shows an antiparallel configuration and a possible orientation with the aid of the distribution and rotation laws.

The developed CMG control system, including its numerous nonlinearities, was simulated on a large hybrid computer. The

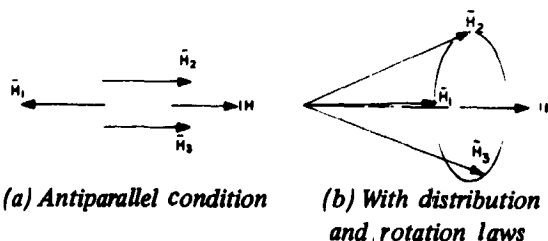


Figure 9. H-vector configuration.

system operated in a satisfactory manner for small initial conditions (0.1 to 0.5 degree) and slowly varying external torques (gravity gradient, etc.). If, however, the initial CMG orientation was highly nonisogonal or if two-CMG operation was considered, it was found that oscillatory and, in some cases, unstable operation resulted.

This was remedied by adding a variable-gain-feedback term from the "H" error signal to the input of the H integrator. A simplified diagram of the system, as now designed, is shown in figure 10.

To desaturate the CMG cluster periodically and without the use of a mass-expulsion reaction control system, a method was developed utilizing the earth's gravity-gradient force field to effect CMG momentum desaturation. This method is described in detail in reference 4. The basic concept is best described with the aid of figure 11, which depicts the per orbit momentum build-up of the CMG cluster caused by gravity gradient and aerodynamic torques. A careful inspection of this figure reveals that, if periodic CMG desaturation were not provided, the CMG cluster would be saturated for progressively larger portions of an orbit after the first orbit. The axis of saturation would be roughly the X-axis of the vehicle. This means that, after complete saturation, the CMG cluster could not compensate for a disturbance torque about the axis of saturation.

An investigation of the causes of the predominant noncyclic torques (i.e., gravity gradient and aerodynamic) reveals that, with the given vehicle configuration and mission requirements (i.e., point vehicle Z-axis at radiometric center of sun every daylight

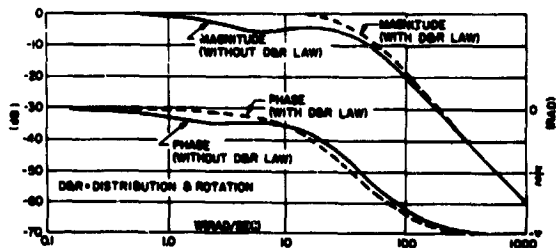


Figure 7. H-vector control law response, M_{rx}/M_{cx} .

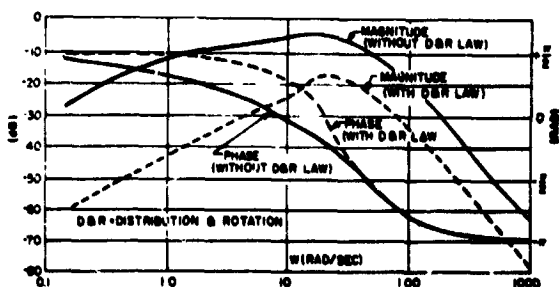


Figure 8. H-vector control law response, M_{rx}/M_{cx} .

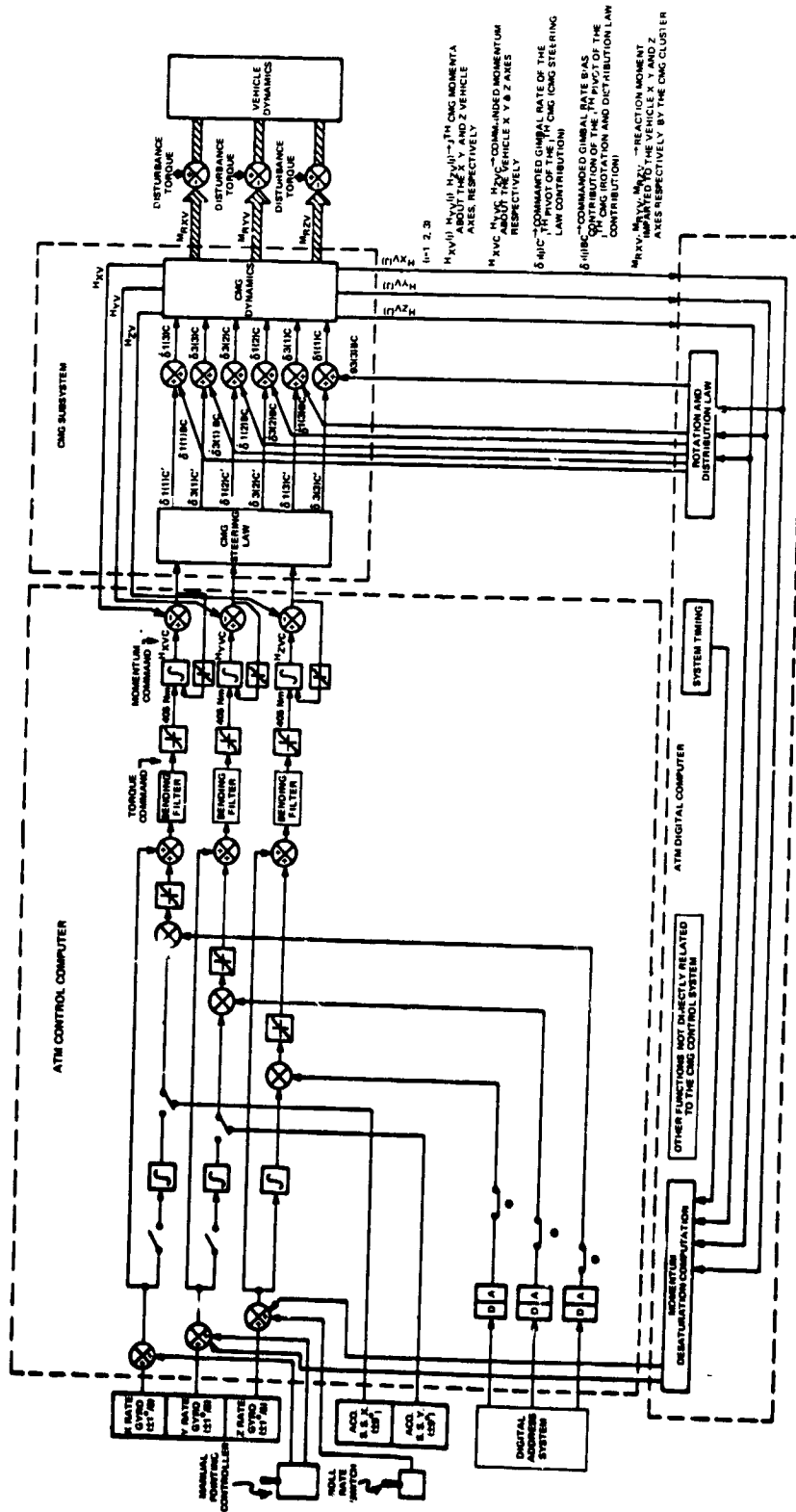


Figure 10. Functional block diagram of ATM pointing control subsystem (CMG control).

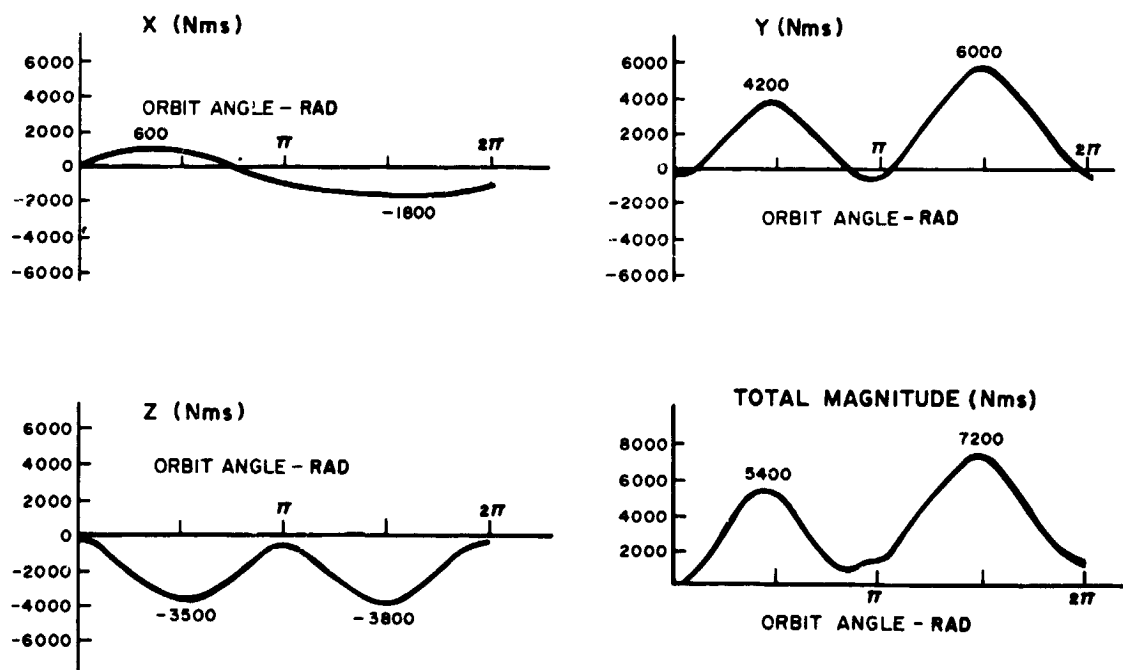


Figure 11. Combined disturbance impulse (solar inclination = -30 degrees).

period), it is not possible to eliminate the noncyclic torques but it is possible to minimize them.

This problem of CMG momentum management was attacked in two separate ways:

1. The noncyclic disturbance torques were minimized by finding an optimal vehicle orientation while still meeting the requirement that the vehicle Z-axis point to the center of the solar disk. This was accomplished by sampling the vehicle momentum at a specified time during the daylight orbital period and comparing it with the sample from the previous day. The compared sample indicated whether the bias momentum components about the various vehicle axes were increasing or decreasing. This information was then translated into appropriate angle position commands about the vehicle Z-axis to ensure minimization of bias momentum accumulation.

2. The saturation effects of the remaining noncyclic disturbance torques were nullified by periodically producing controlled bias torques that would tend to desaturate the

CMG cluster. These controlled bias torques are produced by employing rectified components of the gravity-gradient torques encountered during the night portion of the orbit to desaturate the CMG cluster. The rectification of the gravity-gradient torques is made possible by maneuvering the vehicle about two axes during the night side of the orbit. The magnitude of the maneuver angles is a function of the momentum accumulation during the daylight portion of the orbit.

Experiment Pointing and Control Subsystem

The experiment pointing and control (EPC) subsystem utilizes flex-pivot gimbal bearings for control about two axes and an open-loop positioning device to meet positioning requirements about the third axis. The flex pivots allow approximately ± 2 degrees of rotation of the X and Y axes while the roll positioning device allows for a rotation of ± 120 degrees about the experiment-package Z-axis. A block diagram of this system is shown in figure 12.

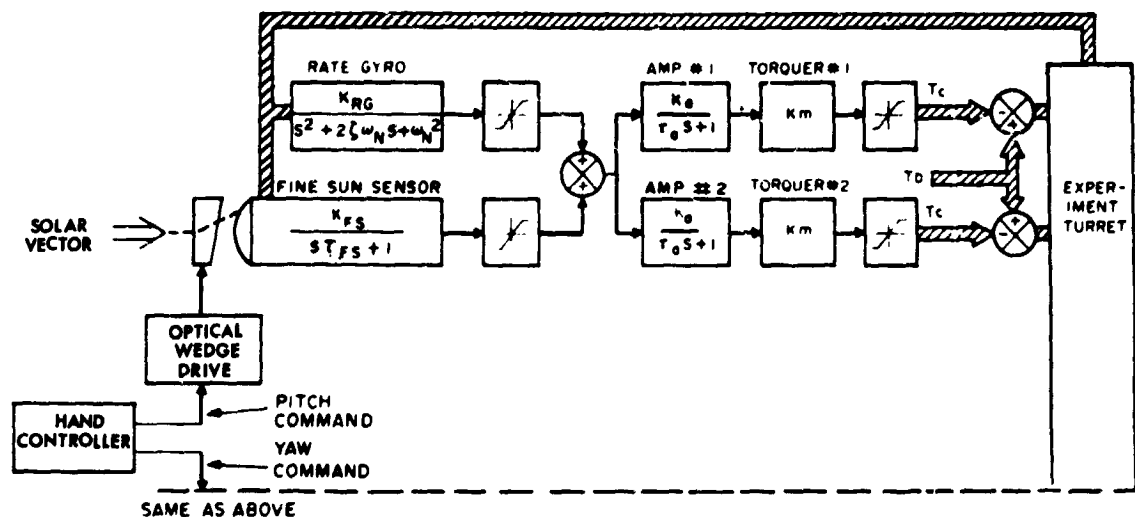


Figure 12. Experiment pointing and control (EPC) subsystem.

While the EPC subsystem provides automatic control of the experiment-package X and Y axes, manual positioning of these two axes is provided for the purpose of offset pointing. Fine sun sensors (FSS) are used for sensing spar attitude errors, with rate gyros sensing rates. The ATM control computer (ATMCC) conditions the signals of the sensors to provide rate-plus-displacement command signals to the flex-pivot actuators (DC torque motors).

The experiment package can be offset-pointed in the X and Y axes over a range of ± 20 arc minutes, with the center of the solar disk being the zero position. The solar disk measures approximately 32 arc minutes from limb to limb. Offset-pointing is accomplished by positioning an optical wedge located in each of the fine sun sensors. The wedge is mounted in the path of the sunlight passing through the FSS optics and can be rotated to refract the sunlight at a fixed angle in a controlled direction. The wedges are positioned by a drive mechanism controlled by the astronaut via the manual pointing controller. The wedge drive varies from ± 135 arc seconds per second near zero offset positions to 76 arc seconds per second for wedge positions near the 20-arc-second sun offset position. A wedge offset produces an FSS output error

voltage that causes the spar to rotate about the appropriate axis (X or Y) and to point the FSS, and thereby the experiment package, in a direction that will drive the FSS output voltage to null. Stability is then automatically maintained by the EPC subsystem. The experiments are aligned to the FSS. The position of each FSS wedge is displayed on the PCS control and display panel and corresponds to the experiment-package offset position from the center of the sun in the X- or Y-axis. The panel also contains television displays of the sun, as viewed through experiment telescopes, and experiment readout displays to assist the astronaut in pointing the experiment package.

The roll-positioning mechanism (RPM) is used to rotate the spar about the Z-axis. The mechanism is commanded by the astronaut via the manual pointing controller (rate switches) located on the control and display panel. Spar roll rates of ± 7 , ± 3.5 , ± 0.7 , and ± 0.35 degrees per second can be commanded. Once the spar is positioned, the roll-positioning mechanism will hold the location until a repositioning command is received. The astronaut repositions the spar in accordance with experiment demand requirements. The spar roll position is displayed on the control and display panel.

ATM Pointing Capability

The ATM pointing and stability requirements listed in table 2 were developed as a result of the pointing and stability requirements of the various individual ATM experiments. The ability of the ATM pointing and control system to meet these requirements was established analytically by performing a detailed error analysis of the system. This analysis is being continually updated as additional input data become available. A Monte Carlo procedure was employed for the determination of system position-and-rate output errors for various model configurations of both the CMG control system and the EPC subsystem (ref. 5). System dynamics were evaluated on hybrid computer simulations of the system (ref. 6). The results of these studies are summarized in tables 4 and 5. The numbers not in parentheses are system requirements; those within the parentheses represent the presently estimated 2σ system capability.

The main errors associated with the pitch and yaw control of the EPC subsystem were those caused by FSS null accuracy (± 1.4 arc seconds) and FSS wedge readout resolution (± 1.25 arc seconds). The effect of man-motion disturbances was nearly negligible, the most significant being the ± 0.2 -arc-second position displacement as a result of astronaut's wall-pushoff disturbance (fig. 13). The main error source in experiment roll reference determination is due to the roll-positioning-

Table 4. Pointing Capability 2σ of EPC Subsystem

System Axis	Pointing Uncertainty	Stability (For 15 min)
EPC X	± 2.5 arc sec (1.77 arc sec)	± 2.5 arc sec (0.63 arc sec)
EPC Y	± 2.5 arc sec (1.77 arc sec)	± 2.5 arc sec (0.63 arc sec)
EPC Z	± 10 arc min	CMG control system
Roll reference	± 7.0 arc min	

Table 5. Pointing Capability 2σ of CMG Control System

System Axis	Pointing Uncertainty	Stability (For 15 min)
CMG X	± 4 arc min (± 2.75 arc min)	± 9 arc min (± 3.6 arc min)
CMG Y	± 4 arc min (± 2.75 arc min)	± 9 arc min (± 5.7 arc min)
CMG Z	± 10 arc min (± 0.624 arc min)	± 7.5 arc min (± 5.0 arc min)

mechanism readout and positioning errors, which are on the order of $\pm 5 M (2\sigma)$.

The error sources associated with the pointing uncertainty of the CMG control system are due mainly to an accumulation of various electronic gain-null offset and drift terms. The stability error source is the result of the astronaut's wall-pushoff disturbances.

Conclusions

Based upon high-accuracy pointing requirements, an ATM pointing and control

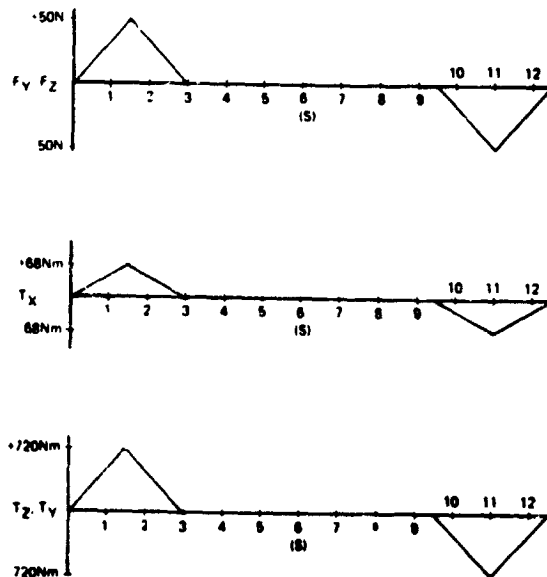


Figure 13. Wall-pushoff disturbance by astronaut.

system (PCS) has been developed to meet experiment objectives. A significant portion of the PCS is capable of manual operation. Astronaut operation is thus available to perform various functions, such as those which require judgment to select scientific targets and to point experiments to these targets. Many functions, such as attitude pointing stability, are performed by closed-loop automatic control in order to keep the number of tasks required of the astronaut within reason; however, the manual control capability and television-optics display system make it possible for the astronaut to improve some of these functions, such as offset pointing and experiment line-of-sight calibration.

The system is unique in that it utilizes the energy source of its operating environment to effect the desired pointing and control requirements of the space station. The electrical energy required to power both the experiments and the pointing-and-control system is supplied through onboard storage devices via large solar panels. The principal disturbance torques are cyclic, and the momentum storage-and-dissipation characteristics of the CMG's are ideally suited to operation in this type of environment. The accumulation of momentum by noncyclic torques is compensated for by maneuvering the space station, during the night portion of the orbit, against the gravity-gradient field in such a manner as to nullify the noncyclic bias-torque effect.

The pointing and control systems developed meet the experiment pointing requirements. The same type of system with improved electronics, improved sensors, and

some minor limitations on astronaut motion during observation periods might achieve pointing accuracies on the order of 0.1 to 0.01 arc second (ref. 7).

References

1. Chubb, W. B.; Epstein, M.: Application of Control Moment Gyros in the Attitude Control of the Apollo Telescope Mount. AIAA Paper No. 68-866, August 1968.
2. Morine, L. A.; O'Connor, B. J.: A Description of the CMG and Its Application to Space Vehicle Control. AIAA Paper No. 67-589, August 1967.
3. Kennel, H. F.: Individual Angular Momentum Vector Distribution and Rotation Laws for Three Double-Gimbaled Control Moment Gyros. Marshall Space Flight Center, NASA TMX-53696, January 1968.
4. Kennel, H. F.: Angular Momentum Desaturation for ATM Cluster Configuration Using Gravity Gradient Torques. Marshall Space Flight Center, NASA TMX-53748, May 27, 1968.
5. Blue, J. C.; Margosian, Z.: PCS Static Error Budget Analysis—APP Payload Integration Technical Report, ED 20002-551, Martin Marietta Corporation, Denver Division, June 28, 1968.
6. Kimery, R.: Stability Analysis of Experiment Pointing Control System. S.P. 213-0160, Space Support Division, Sperry Rand Corporation, Huntsville, Alabama, December 17, 1968.
7. Smith, P. G.: Astronomy Manned Space Flight Attitude Control Telescope Systems. Technical Memorandum TM 69-1022-2, Bellcomm Inc., Washington, D. C., February 17, 1969.

Stabilization and Control for the OAO Spacecraft Series

K. W. Jenkins

General Electric Company

N70-36730

Requirements

The Orbiting Astronomical Observatory (OAO) Spacecraft is designed to provide a stable platform for optical telescopes up to 40 inches in diameter and 10 feet long and capable of pointing accuracies down to 0.1 arc second. General Electric developed the stabilization and control (S&C) subsystem for the observatory.

The OAO S&C subsystem has some of the most stringent performance requirements of any satellite. The telescope is rigidly mounted to the vehicle inside a central well; therefore, pointing of the telescope requires that the entire vehicle be pointed. Because the astronomer may desire to look anywhere in the sky, the spacecraft is required to orient to any point in the celestial sphere. Fine guidance is derived from the main telescope itself. Fine-pointing accuracies down to 0.1 arc second are required.

Because of these high accuracies, the main telescope field-of-view is restricted; hence, the S&C subsystem must point the vehicle anywhere in the sky to 1.0 arc minute. The subsystem must also be capable of holding this orientation to within ± 15 arc seconds for 50 minutes of time. When pointing at a defined star, the OAO must be capable of holding that star to 0.1 arc second for up to $1\frac{1}{2}$ orbits. Finally, OAO is required to be capable of reorienting from one star to another. It must be capable of a 2-degree slew in 30 seconds and/or a 30-degree slew in 3 minutes. Total angles slewed on all axes shall be up to 3000 per day.

This performance was to be achieved for a vehicle that ultimately weighed 4400

pounds and had an inertia of 1500 slug feet squared. Useful lifetime in orbit was to be one year.

Design

The primary position reference chosen for OAO was a system of gimballed star trackers. Six of these trackers are placed around the vehicle. Each tracker has a field-of-view of ± 45 degrees about two axes so that the set of six provides complete spherical coverage.

The high accuracy pointing is achieved by using sensors with narrow fields-of-view; therefore, acquisition modes are required. At separation, the vehicle orientation is random. A set of coarse sun sensors is used to orient the vehicle so that the negative roll axis points to the sun. This maneuver is accomplished by using cold gas jets. After stabilizing on the sun, control is switched to a set of fine sun sensors, and the fine reaction wheels are activated to provide pointing to the sun to 0.25 degree. Selected star trackers are turned on and commanded to preset positions. The vehicle is then rolled about the sunline until stars simultaneously appear in the trackers. When this occurs, the trackers are put into track mode; the search is stopped; and the tracker gimbal errors are used to control the fine wheels.

The star-tracker mode, illustrated in figure 1, is the basic *coarse-pointing* mode. In order to minimize the disturbance torques during pointing, the vehicle is made inertially spherical through the addition of balance booms. These can be seen in the general spacecraft view shown in figure 2. The same

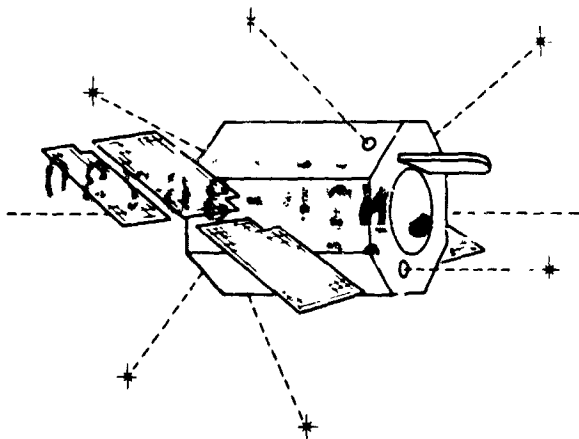


Figure 1. OAO star acquisition; star-tracker or basic coarse-pointing mode.

basic fine wheel loop is used for *fine pointing* except that the pitch and yaw error signals are derived from the main telescope to provide control to arc-second accuracies.



Figure 2. OAO spacecraft with balance booms shown.

Buildup of reaction wheel speed due to solar pressure is counteracted in two ways. First, low-thrust gas jets are fired to reduce system momentum if the wheels reach 70 percent no-load speed. These jets are sized so that they do not exceed the wheel torque. As a result, wheel unloading does not disturb the vehicle. Second, a magnetic unloading system (MUS) consisting of magnetometers and torquing bars is provided. The MUS torques against the earth's magnetic field in such a manner as to hold the wheel speed low.

For reorientation of the spacecraft, a second set of reaction wheels is provided. These wheels can be programmed to rotate a fixed number of revolutions, thereby moving the vehicle a known amount.

Figure 3 is a block diagram of the S&C subsystem. The logic to control mode switches, etc., is contained in the programmer and star-tracker signal controller (PSSC). Stored commands are issued by the vehicle programmer, the PPDS (primary processor and data storage).

Development

In addition to the usual development process for electronic components, the OAO subsystem had two unique development areas, the star tracker and the air-bearing table (ABT) test facility.

The original star-tracker design was a pressurized dome design, shown in figure 4. One of the requirements placed upon the tracker is that it be capable of seeing a +2M star within 32 degrees of the sunline. To meet this requirement, it was necessary to remove the dome and to provide a light baffle consisting of a "minaret"; figure 5 shows how this was done. Figure 6 shows the redesigned tracker. The tracker opto-mechanical package is supplied by Kollsman Instrument Corp.

It was also necessary to test the ability of the tracker to see the star 32 degrees from the sun. A special solar impingement facility was developed to perform this test. The test is conducted inside a 30-foot-diameter thermal-vacuum chamber. The equipment arrangement in the chamber is shown in figure 7. The

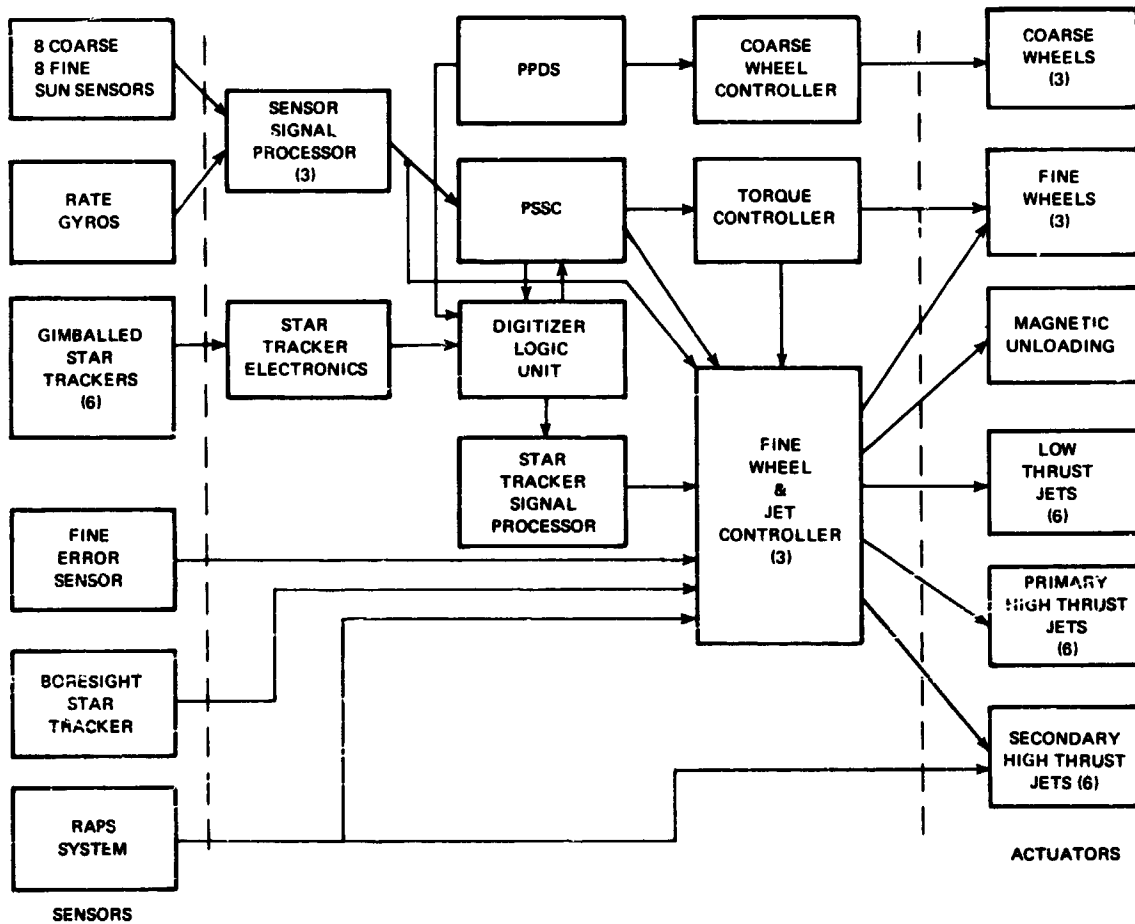


Figure 3. Functional block diagram of stabilization and control (S&C) subsystem.

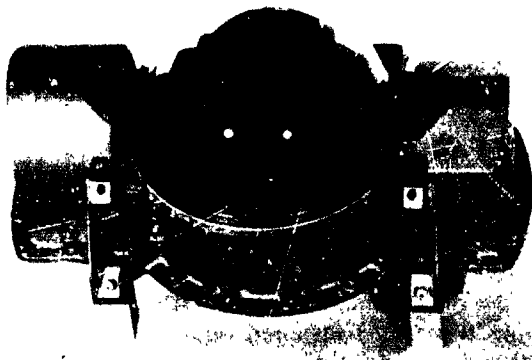


Figure 4. First delivered star tracker, pressurized dome design.

carbon arc and optics barrel provide illumination of approximately one solar constant over a 9-inch-diameter circle. The traveling mirror is translated and rotated to vary the angle between the optical axis and the sun over a range of 60 degrees to 25 degrees. The tracker stand provides 360-degree rotation about the optical axis. A 4-inch-diameter star simulator is used for alignment and tracking. The star magnitude can be adjusted over the range of -1.0M to +3.0M. The star simulator is located behind an opening in a glass wall set at an angle to the optical axis so that light reflected from the tracker is both absorbed and reflected into a light trap lined with flocking material. All chamber walls are covered with

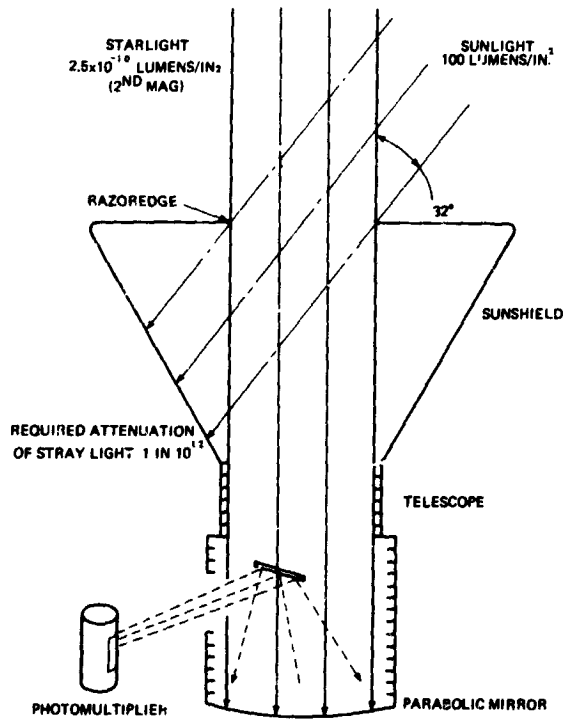


Figure 5. Star tracker - solar impingement.

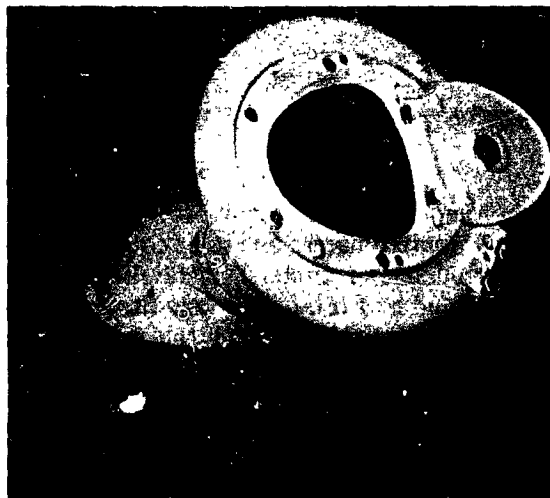


Figure 6. Redesigned star tracker.

flocking material. A movable shield, also covered with flocking material, can be rotated in front of the star to provide a black target for the tracker.

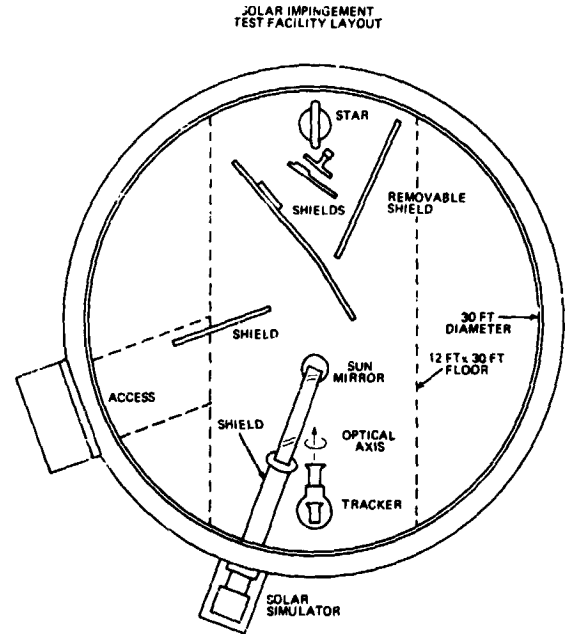


Figure 7. Test facility layout for solar impingement.

The air-bearing-table facility was used to demonstrate the quantitative performance of the complete subsystem. This facility simulates the dynamic characteristics of the OAO spacecraft on a one-to-one basis. For the purpose of structural rigidity, the platform is ruggedly constructed, weighing 8500 pounds, with inertias of 1450 slug feet squared. This compares with 3600 pounds for the spacecraft with the same inertias. The roll axis (the optical axis of the main experiment) of the air-bearing table is vertical, and pitch and yaw axes are horizontal. The design allows ± 30 degrees of freedom of movement about the pitch and yaw axes and unlimited freedom about the roll axis. The platform uses a 10-inch, stainless-steel bearing with a multi-orifice, floating seat design.

A solar simulator (carbon arc source and optical system) installed outside the test cell projects a 4-foot-diameter beam horizontally through a port in the wall of the cell onto the air-bearing platform. The beam has an intensity of 20 percent of a zero air mass sun at the platform surface.

The angular position and rate of the air-bearing table are determined from a system that is mounted external to the table itself. In order to cover an angular range equivalent to the freedom of travel of the air-bearing table and to meet the OAO accuracy requirements, coarse and fine measuring systems are used. The coarse position and rate system operates over the complete angular freedom of travel of the air-bearing platform (± 30 degrees in pitch and yaw and 360 degrees in roll). This electromechanical servosystem uses an optical sensing head to track illuminated targets. Transducers are coupled to the mechanical drive to measure the equivalent angular position of the platform to an accuracy of 3 arc minutes. Rate information is obtained from a tachometer linked to the mechanical drive and summed with the derivative of the error signal from the optical sensing head. Its accuracy is 0.01 degree per second. The fine-position measuring system consists of three single-axis, automatic recording autocollimators; each has a linear field-of-view of ± 7.5 arc minutes, thereby allowing sufficient overlap with the coarse system. This system produces records to better than ± 1 arc second.

With this facility, operation of all modes was verified. Fine pointing was demonstrated down to 1 arc second. Table unbalance torques were controlled to less than 0.1 inch-ounce.

OAO Design Evolution

As the development effort progressed, it became apparent that an inertial reference system could provide an attitude hold mode in the event of temporary loss of stars. The inertial reference is unaffected by stray light and earth occultation. An additional requirement was identified: to provide a backup mode for optimum solar power collection. To implement these requirements, a RAPS (rate and position sensor) gyro package was added. The RAPS system is a set of three integrating rate gyros, which can be operated in either position or rate mode. In position mode, they hold spacecraft drift to less than ± 0.3 degree in one hour. In rate mode, RAPS is used in conjunction with sun sensors to perform the

sunbathing function. The RAPS system was flown on the second spacecraft.

For the third OAO vehicle, the RAPS package was replaced by a more sophisticated inertial reference unit (IRU) built by the Massachusetts Institute of Technology. The IRU is a pulse rebalanced system with in-orbit drift calibration. Using the in-orbit calibration, the drift is projected to be better than 0.001 degree in one hour. The IRU will allow OAO to operate for several orbits without using any gimballed star trackers. In fact, once the IRU drift has been calibrated out, it is possible to operate with only roll tracker fixes because the main telescope itself provides the pitch-yaw fix. In addition, the IRU has a slew capability that allows the vehicle to be reoriented accurately from one star to another without the use of trackers.

Thus, the evolution of OAO is toward an inertial primary reference with star-tracker updating used occasionally.

Operations

OAO is limited to about ten minutes under line-of-sight control of any one ground station. Total contact time per orbit is about 15 percent. As a result, OAO has two modes of operation: real-time mode and delay mode. During the station contact, the spacecraft and experiment data is dumped to the station, and the commands necessary for operation of the spacecraft until the next contact are loaded into the spacecraft memory.

The complexity of the OAO requires a large number of commands. Commands are needed to position the various star trackers as different guide stars are occulted by the earth. Commands are used to enable reorientation of the spacecraft and to control the mode sequences from slew to coarse pointing to fine pointing. The determination of command sequences is performed in the Mission Control Center at the Goddard Space Flight Center (GSFC). For example, the tracker occultation schedule is calculated at GSFC by using the computers located at the Center, and the final sequence of commands and execution times is then transmitted to one of the ground stations for transmission to OAO.

Similarly, all telemetry is sent back to GSFC, where the data are examined and any necessary corrective action is taken.

The ground station is a necessary part of OAO. The observatory cannot operate for any length of time without the computational facilities of the ground station. OAO is literally "flown from the ground."

Design Evolution

The development of the OAO S&C subsystem provides several guidelines for the future design of orbiting telescopes.

1. *The primary position reference will be inertial with a star tracker used for re-zeroing and drift correction.* The inertial (gyro) system is unaffected by occultation effects and the stray light problems that affect trackers. Use of a high-accuracy inertial reference allows use of a fixed star tracker with a small field-of-view (say 10 degrees by 10 degrees). Furthermore, the telescope itself provides two axes of information. Several trackers of suitable quality are now available. Because of the need for arc-second accuracy, the gyro system will be a strapped-down type rather than a platform.

2. *An onboard digital computer will be used to control the logical operation of the spacecraft and as part of the attitude control loops.* The present OAO has the equivalent in hard-wired logic of a small digital computer. The computer will be used to reduce the dependency of the vehicle on the ground station, to process the inertial-unit and star-tracker outputs into a position reference, to perform the initial stabilization, and to control the mode sequence. In addition, the computer can provide telemetry formatting and preliminary experimenter data reduction. Figure 8 shows a block diagram of such a system. (Compare this diagram to figure 3.) The computer characteristics will be approximately:

Weight	40 pounds
Size	0.5 cubic foot
Power	30 watts
MTBF*	5 years

*Mean Time Between Failures.

The computer will be memory-oriented and modular with interrupt capability. The high reliability will be achieved by using high reliability parts, 100-percent screening and burn in, LSI, and modular redundancy at the processor and memory level.

3. *As the size increases, the actuators will change from AC to DC wheels and then to control moment gyros (CMG's).* An isolation system will be needed with CMG's. As telescope size increases, the telescope inertias increasingly dominate the vehicle; therefore, the vehicle will have a much smaller roll than pitch or yaw inertia. Provision of balance booms to achieve spherical inertias will become prohibitive. For an 80-inch-diameter telescope, tip weights of 300 pounds on the end of 20-foot booms are estimated. These would correct the 8000-slug-foot-squared inertia unbalance providing a spherical inertia of approximately 20,000 slug feet squared. For an 80-inch telescope, DC wheels are the probable choice. Figure 9 shows some torque-power curves illustrating the advantage of DC wheels at the higher torque levels. Figure 10 shows the relationship of weight versus momentum for reaction wheel systems.

For a 120-inch-diameter telescope, control moment gyros are mandatory because the inertias are on the order of 130,000 slug feet squared in pitch yaw and 22,000 slug feet squared in roll. The vehicle will require a momentum storage of 150 to 200 foot-pounds per second, clearly outside the capability of wheels. Figures 11 and 12 give corresponding curves for CMG weight and power, respectively. Use of CMG's will also require some type of suspension system because the CMG gimbal striction prevents it from pointing to 0.01 arc second.

4. *Less systems testing will be done on the ground.* As the telescope size increases, so do the pointing requirements. Air-bearing tables are effectively limited to about 1.6 arc second. Further OAO experience has validated the basic capability of the reaction wheel system. Present OAO system testing is limited to electrical testing of the S&C subsystem with suitable stimulus applied artificially to the trackers and gyros. This testing is

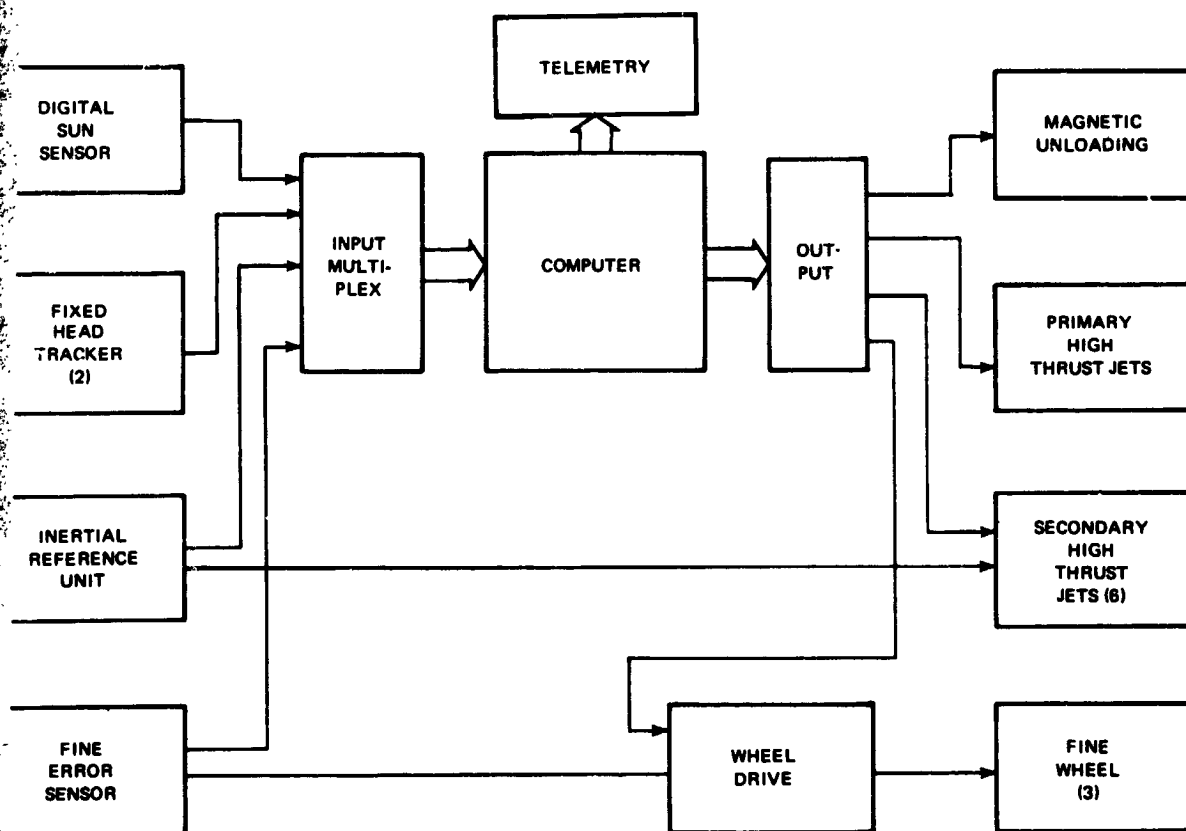


Figure 8. Functional block diagram of proposed onboard digital computer for future orbiting telescopes.

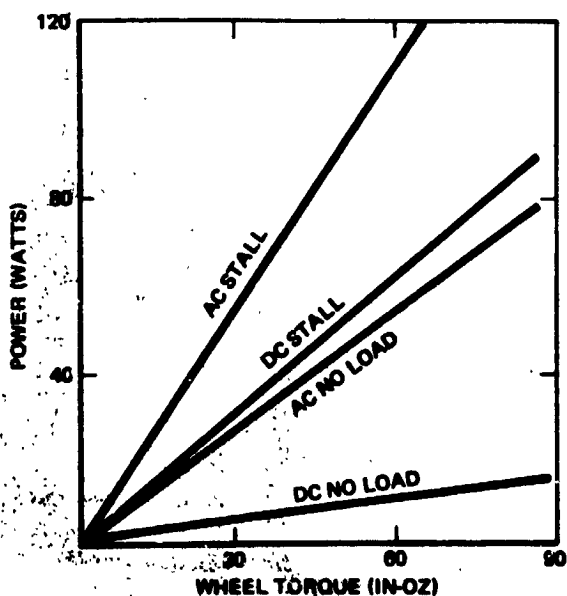


Figure 9. Relationship of power to wheel torque for DC wheels.

meant to verify the compatibility of the system.

An exception to this trend will be the need to test suspension systems for very large telescopes. For example, the magnetic suspension system appears attractive; however, its isolation capability is dependent upon the uniformity of the field within the pusher. Detailed tests of this phenomenon are required prior to adoption of this design.

Summary

The present OAO design has been validated by extensive ground testing and the successful flight of A-2. The design is evolving from a stellar primary reference to an inertial primary reference. In addition, the use of onboard computers in spacecraft control will

grow. The key technology for future vehicles will be the isolation systems needed to operate very large telescopes because the required CMG actuators are incapable of the fine pointing required. These systems will be needed at 120-inch-diameter telescopes. For an 80-inch-diameter telescope, it will still be possible to use reaction wheels powered by DC motors.

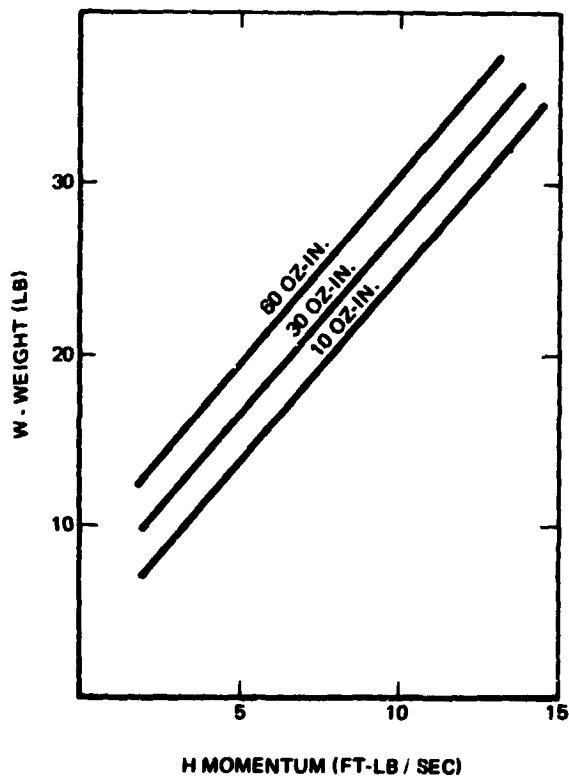


Figure 10. Relationship of weight to momentum for reaction wheel systems.

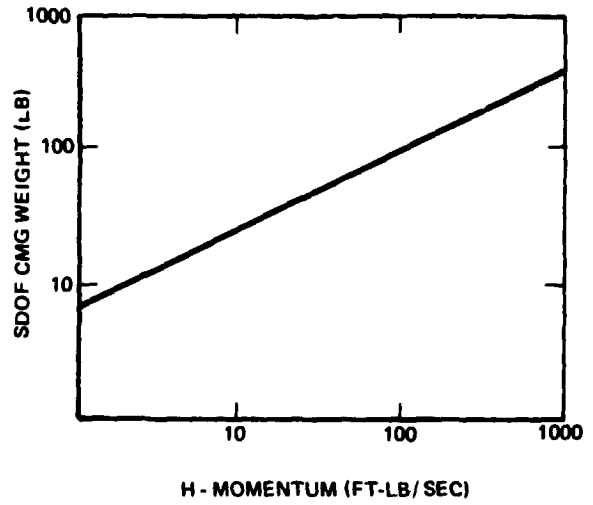


Figure 11. Relationship of weight to momentum for CMG.

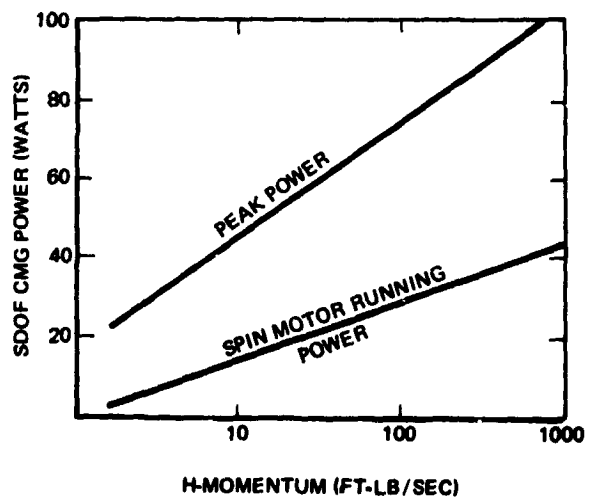


Figure 12. Relationship of CMG power to momentum.

Star-Tracker Systems

N70-36731

Ludwik I. Seifert

Kollsman Instrument Corporation

Guide Targets

Some preliminary thoughts were given to celestial references available for aiming and for long-term pointing of the 3-meter telescope during observation of an experimental target. For most cases, the target itself will not be useful as a guide source. In many instances, the photon flux will be insufficient (quasars: +16 to +20 magnitude); other targets will not be suitable for guidance because of their extended shape; and some targets may have a spectral response outside of the guidance detector.

For a brief review of actual conditions, a number of experimental targets was selected at random (table 1), and, using their celestial coordinates, brighter suitable guide stars (+7.5 magnitude and up) were picked, one for each target. Figure 1 shows these guide stars by magnitude and offset angle from their respective targets. As shown in this graph, for the listed radio and x-ray sources and Seyfert galaxies, the majority of suitable guide stars are of the +6.5 to +7.5 magnitude and have an offset angle between 5 and 60 arc minutes. Only one guide star required an offset angle of 90 arc minutes. Some targets offered more than one guide star, and, in some instances, a tradeoff between magnitude and offset angle was possible. The dashed lines in the graph connect such alternate guide stars.

As the preliminary review of the fine-pointing techniques for the 3-meter telescope progressed, it became obvious that:

1. The hole in the primary mirror (if any) will not permit an offset of more than 30 arc minutes in the f/30 telescope, and

placement of the fine-pointing sensor in front of the primary mirror may be objectionable.

2. By using the full 3-meter aperture for guidance, outside of the active experimental field-of-view, guide stars down to 9 or 10 magnitude will offer the required pointing stability.

In addition, at least two guide stars for each target shall be used in order to compensate for errors due to roll instability. These errors increase linearly with the offset angle for low offsets ($\tan 1^\circ \cong \text{arc } 1^\circ$).

For the above reasons, a smaller offset angle shall be considered. It is proposed that a study of guide stars as a function of experimenter targets be instituted prior to an actual instrumentation study.

A poll of prospective experimenters for the purpose of listing targets, their characteristics, duration of the experiment, and suggested guide stars may prove very useful.

Suggested Instrumentation for Aiming

A brief review of experimental flight experiences, specifically those of the Orbiting Astronomical Observatory (OAO) A-2, is important to this discussion.

The OAO spacecraft uses a General Electric attitude control system, which provides the inertial wheel actuators, one each for pointing correction in pitch, yaw, and roll axes. Six Kollsman star trackers, appropriately located on the spacecraft, sense spacecraft pointing by means of simultaneous tracking of three or more preselected stars. Figure 2 shows one of these star trackers. Its telescope is mounted on two gimbals, afford-

Table 1. Representative Targets for the 3-Meter Orbiting Telescope and Their Nearest Guide Stars

#	Type	Name	1970			Guide Star 1		Guide Star 2		Guide Star 3		
			Right Ascension h	m	DEC		MAG.	Offset arc-min	MAG.	Offset arc-min	MAG.	Offset arc-min
					degree	min						
1	R	Kepler S'nova	24.0		+63	57	+7.0	40				
2	R	Andromeda Gal.	41.0		+41	06	+7.5	30				
3	S	NGC 1068	02	40.0	-00	14	+3.5	45				
4	R	Fornax A	03	21	-37	17	+7.0	25				
5	RX	Crab Neb. M1 (Tau XR-1)	05	32.6	+22	00	+6.5	30				
6	R	Orion Neb. M42	05	33.8	-05	25	+6.5	<5 (bgd)				
7	R	IC 443	06	15.5	+22	36	+3.0	50				
8	R	Rosette Neb.	06	30.4	+04	53	+7.0	6				
9	X	Leo XR-1	09	33.0	+08	36	+7.5	30	+5.5	90		
10	S	NGC 3516	11	03.4	+72	50	+7.0	35				
11	S	NGC 4151	12	08	+39	41	+7.0	30				
12	R	3C 273	12	27.7	+02	14	+7.0	55 (bin)				
13	RX	Virgo A, M87	12	29.3	+12	34	+7.5	60				
14	R	Centaurus A	13	23.6	-42	52	+7.0	35				
15	R	3C 295	14	10.4	+52	19	+6.5	<5				
16	X	Sco XR-1	16	15	-15	12	+7.5	5 (bin)	+6.0	20		
17	X	Sco XR-2	17	08	-36	24	+6.0	60				
18	R	3C353	17	19	-00	57	+6.0	55				
19	R	Kepler S'nova	17	29	-21	16	+6.0	45				
20	X	Ophi XR-1	17	32	-20	42	+6.5	90				
21	R	Galactic Nucleus	17	44.1	-28	50	+7.5	40				
22	X	Sgr XR-2	18	10	-17	00	+7.5	40				
23	R	Omega Neb., M17	18	18.6	-16	18	+7.5	<5				
24	X	Ser XR-1	18	45	+05	18	+6.0	25				
25	R	3C 392	18	54.6	+01	17	+7.5	<10				
26	X	Cygnus XR-1	19	57	+34	00	+4.0	60 (bgd)				
27	RX	Cygnus A, XR-3	19	58.4	+40	39	+7.0	10				
28	R	Cygnus X	20	21.5	+40	17	+2.5	10				
29	R	HB 21	20	45.6	+50	34	+7.0	25	+7.5	20		
30	RX	Cygnus Loop	20	50.8	+29	34	+7.5	25	+6.5	60		
31	R	N. America Neb.	20	54	+43	57	+6.5	10	+4.0	35		
32	X	Cygnus XR-2	21	45	+39	00	+7.5	10	+7.0	20	+4.4	45
33	R	Cassiopea A	23	22.1	+58	38	+4.5	50 (var.mult.)				

R - radio sources
X - x-ray sources
S - Seyfert Nebula

bin - binary
bgd - also background
var. mult. - variable multiple

ing it a ± 45 -degree freedom of rotation in two orthogonal axes. Each gimbal is positioned by means of a DC torquer motor to the commanded angle. A resolver is used for the angle readout, which is the feedback in the closed-loop gimbal operation.

The tracker telescope optics are shown schematically in figure 2. The photon flux collected from the guide star is divided by means of the roof reflector into two equal converging beams, each focused in the plane of an aperture. The two apertures move in two orthogonal directions. This motion, governed by respective vibrating reeds, encodes upon the two flux components a modulation pattern that is a function of the image position with respect to the center of aperture vibration. A photomultiplier tube converts the recombined photon fluxes into

two electron current components. Separated by means of synchronous detection, these currents provide the tracker error signals referenced to the axes of modulation (ref. 1).

The scanner amplitudes provide a telescope field-of-view of 1 degree by 1 degree. For this field-of-view, a second magnitude star can be resolved to an rms position stability of ± 5 arc seconds in a bandwidth of 3 hertz. The actual predicted tracker accuracy, including gimbal angle readout errors and servo stability, was 20 arc seconds, for which the predicted OAO spacecraft pointing was 1 arc minute circular error for a duration of 50 minutes during each orbit.

Based on spacecraft data in the first month of operation in orbit (ref. 2), the average sensing and pointing results obtained were 25 percent better than the predicted

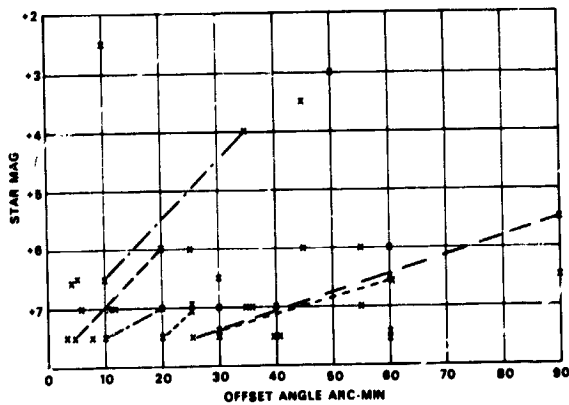


Figure 1. Guide stars, +7 magnitude and brighter, as a function of offset angle from targets. (See table 1.)

values. Moreover, this performance was obtained with 0.3 magnitude dimmer stars.

After approximately five months of space operation, the star tracker sensitivity decreased to the level predicted by ground calibration; however, the spacecraft pointing

is better than 30 arc seconds (60 arc seconds predicted).

The detailed star tracker characteristics are listed in the Orbiting Astronomical Observatory Handbook (ref. 3). Table 2 compares the performance of the Kollsman OAO star tracker performance with other star trackers. This tabulation, prepared by The Franklin Institute (ref. 4), was reprinted to include the latest corrections.

Another gimballed star sensor, also with a ± 45 -degree angular coverage but using solid-state digital detectors, was developed by Kollsman for space application. With a telescope field-of-view of 10 by 10 arc minutes, scanner accuracies in the order of 1 arc second were measured while including the gimbal readout errors; tracker accuracies of 5 arc seconds were obtained in a laboratory test. Figure 3 is an exploded phantom view of this digi-optic star sensor; figure 4 shows the prototype configuration. This digital solid-state star tracker is suitable as the coarse

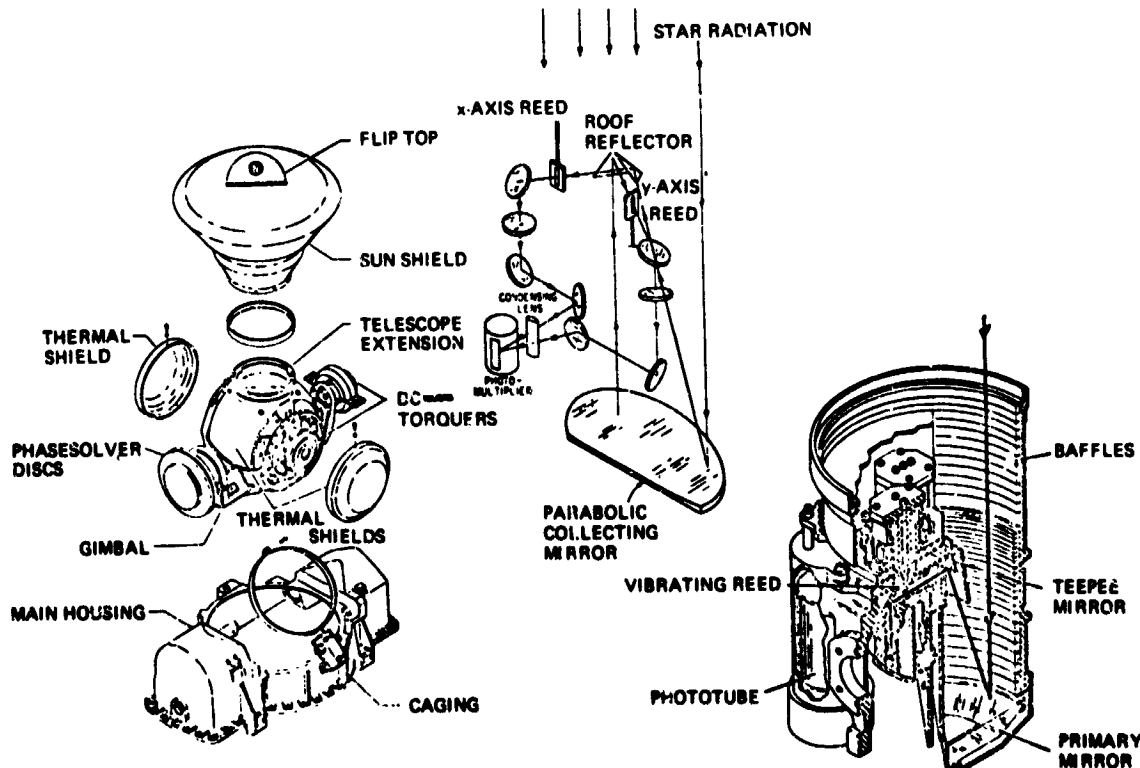


Figure 2. OAO star tracker.

Table 2. Summary of Star-Tracker Characteristics (ref. 3); Revised 2/20/69

Identity	Manufacturer	Scanned Field-of-View	Accuracy	Axes	Sensitivity (Star Magnitude)	Detector	Size (in.)	Weight (lbs.)	Power (watts)	Life	Status (12/31/65)
OAO Star Tracker	Kollman	1° x 1°	5 sec	2	+2	PM	9 x 5 x 4 1/2	4.8	4.1	1-year mission	Flown
Canopus Tracker	Barnes Eng. Co.; JPL	5° x 11°	0.1° null	1	+2.3	ID	4 x 5 x 11	5	1.5	2.0 x 10 ⁶ hours	Flown
Dual Mode Star Tracker	ITT	8° x 8° or 32 min. x 32 min.	5 sec. rms	2	+3	ID	5 x 10 1/2 x 5	9.5	8.0	—	Prototype
Sun/Star Sensor	Nortronics	30 min.	10 sec.	2	+3	PM	(105 cubic inches)	9	8.0	—	Prototype
Canopus Tracker	Santa Barbara Research Center	±2° x 5°	0.1°	1	Can. ±0.5	PM	—	4.9	—	2-week mission	Flown
NON 121 Star Tracker	Nortronics	10 min. x 10 min.	2.8 sec. x 1.0 sec.	2	+3.5	VID	(265 cubic inches)	9.5	12	1.8 x 10 ⁶ hours	Prototype
OAO Backup Star Tracker	Bendix Corp.; ITT	1° x 1°	9 sec	2	+2.5	ID	5-5/8 x 5 1/4 x 5 1/4	6	4.5	1-year mission	Prototype

JPL - Jet Propulsion Laboratories
 ITT - International Telephone and Telegraph Corporation, Federal Laboratories

PM - Photomultiplier tube
 ID - Image disector tube
 VID - Vidicon tube

sensor on the large space telescope. The advantages of a direct digital input to the computer, its high reliability enhanced by lack of a scale voltage, are obvious. A strap-down detector of similar basic design may be considered for the intermediate and fine-pointing sensors for the 3-meter telescope.

Other star sensors, of the analog solid-state type are being built at the present time by Kollman for space application. These work on the track-to-null method, possess the same high reliability as the digital sensors, and, in addition, have simplified signal-processing electronics. Figure 5 shows one of the scanners that uses analog solid-state detection.

Kollman has also built the Goddard Experiment Package (GEP) ultraviolet spectrophotometer, which will be flown in 1970 as the OAO-B. This environmentally tested and NASA-accepted system (both prototype and flyable units have been delivered) provides a fine-pointing sensor with a noise-limited resolution of 0.1 arc second for a +2 magnitude star in a field-of-view of 4.5 arc minutes and 3-hertz bandwidth. It

provides error readouts in pitch and yaw, offers high reliability through 100 percent redundancy, and was designed for a star magnitude range from +1 to +10 or an input flux range of 10⁴:1 with resulting error changes below 3 decibels, achieved by a closed-loop operation of the photomultiplier tube. This sensor uses "ruggedized," low-noise, photomultiplier tubes with an S-17 cathode spectral response. The mechanical light modulators are of a balanced, temperature-compensated type, maintaining its amplitude through a feedback operation. Synchronous detection provides noise limitation. This sensor is generating accurate star magnitude signals, which will be transmitted via the telemetry. Based on the results of these transmissions, some of OAO-II magnitude discrepancies will be resolved.

Extrapolation of this GEP fine error sensor into a 3-meter system offers the required error sensing of 0.003 to 0.005 arc second for stars of +9 magnitude.

For the large telescope, it is envisioned that the spacecraft may be pointed to an accuracy of approximately 0.1 second of arc

- FLEXIBILITY ALL ORBIT CAPABILITY SMALL STAR CATALOG
- GIMBALS PROVIDE LARGE F.O.V. ASSURE STAR AVAILABILITY
- DIGI-OPTICS PROVIDES FINE VERNIER OF STAR POSITION
- NON-NULLING RATE SERVO APPROACH ALLEVIATES CRITICAL SERVO DESIGN

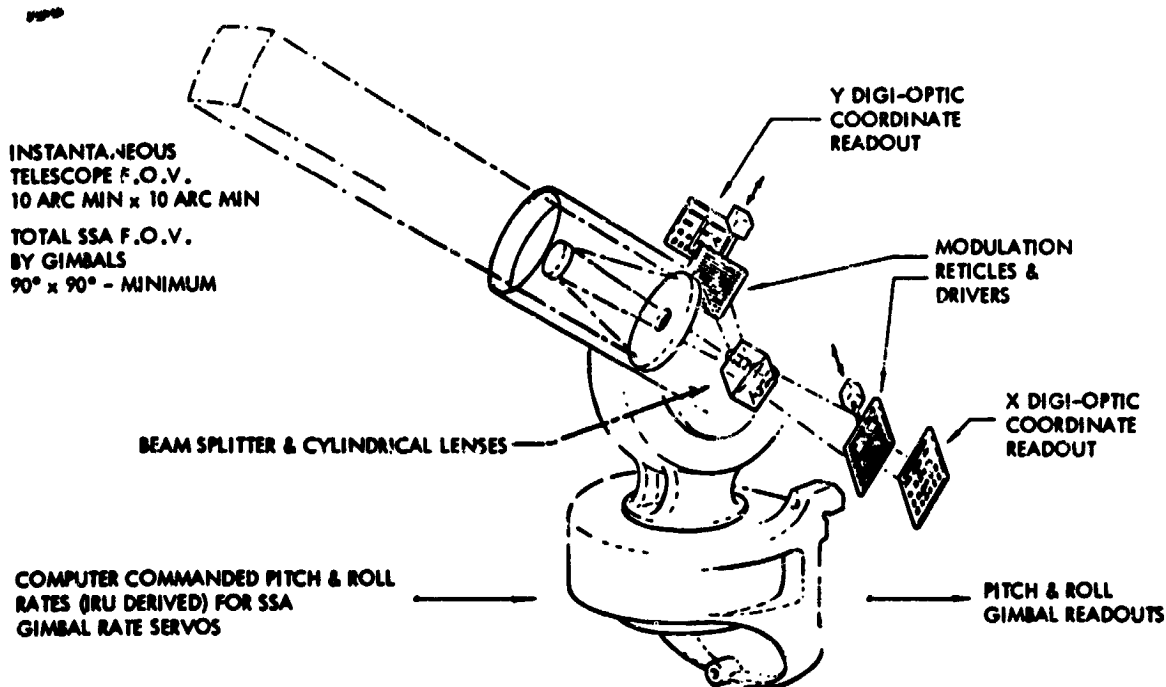


Figure 3. Star sensor assembly (SSA), digi-optics star sensor.

using two intermediate solid-state or photomultiplier-tube star sensors for controlling all three spacecraft axes (roll, pitch, and yaw) and viewing at least two stars. One spacecraft control axis (pitch or yaw) shall be aligned in the plane given by the line-of-sight to the experimenter's target and the line-of-sight to the brighter guide star. One intermediate sensor, located along this control axis, shall be offset by the angle denoting the guide star location in respect to the experimenter's target. A second intermediate sensor shall have a wide freedom of rotation about the roll axis as well as an offset range in order to accommodate a second guide star, preferably offset in the opposite direction from the optical axis (180 degrees \pm 30 degrees from the first guide star).

To provide the experiment pointing to the required 0.01 second of arc, an optical beam-steering device is proposed. Kollman

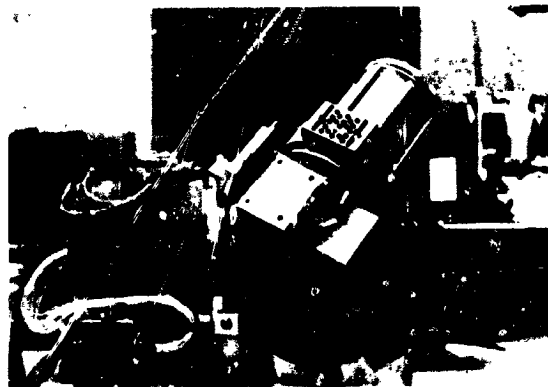


Figure 4. Precision digi-optic star sensor, prototype.

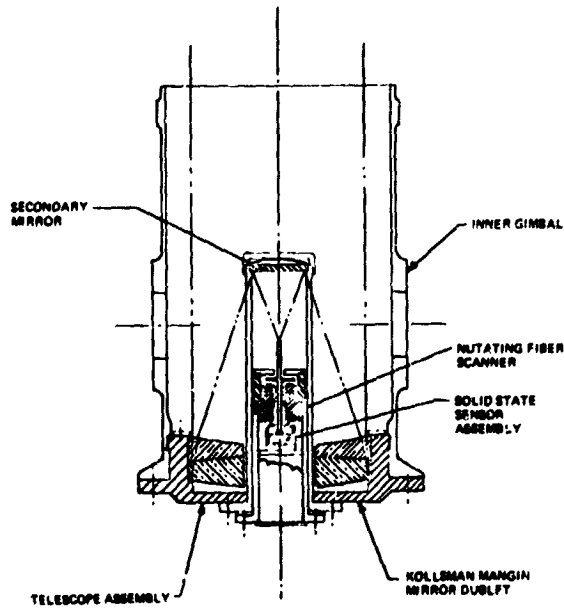


Figure 5. Solid-state telescope.

has evaluated electromagnetic and piezoelectric beam-steering mechanisms; these concepts are illustrated in figures 6 and 7, respectively. The beam-steering solution will permit a higher frequency response due to highly reduced inertia as compared to the overall telescope. Previous piezoelectric beam-steering studies were also performed by General Telephone and Electronics (Sylvania)

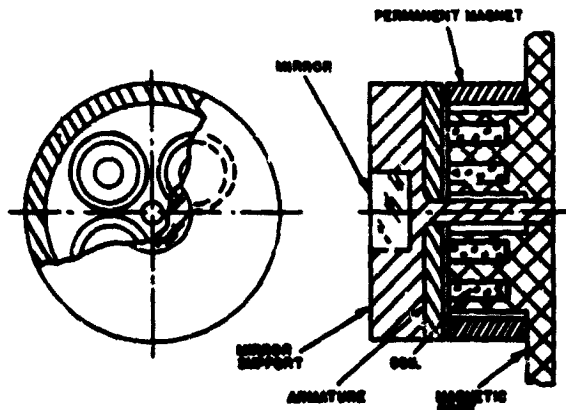


Figure 6. Beam steering, electromagnetic actuator.

in Bayside, New York. The decision between piezoelectric (high voltage) and electromagnetic (low voltage) or a third type of beam steering shall be made after a detailed study of the problem and the available solutions, including the longevity, space environment influence, low power dissipation, and the reliability aspects.

Testing

Two major error sources in testing are commonly known to optical designers who evaluate precision optical systems. One is the error caused by vibration of the optical bench; the other is the error caused by air turbulence between the transmitter and the receiver.

As a general rule, decoupling from the ground-transmitted wave is obtained down to frequencies between 1 and 5 hertz. For a large optical system, using a 30-meter-long optical bench, the Kollsman study under the OATES* revealed that the seismic block attenuation of an actual facility (ref. 5) ceases at

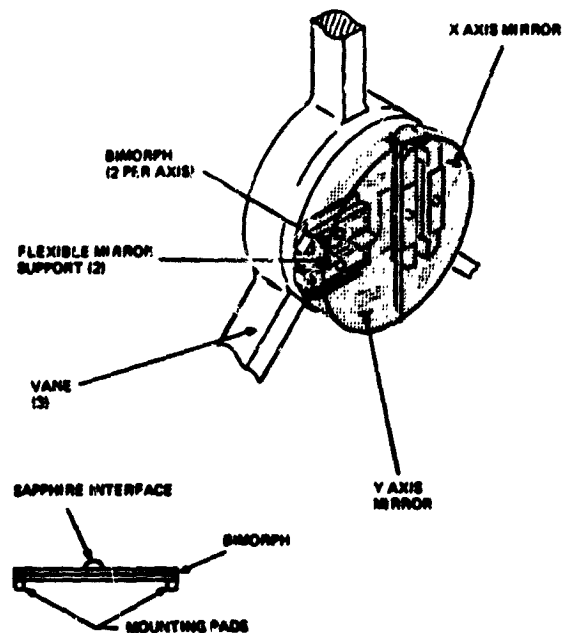


Figure 7. Beam steering, piezoelectric actuator.

* Orbiting Astronomical Telescope Earth Satellite

approximately 1 hertz. An amplification of the inputs is obtained at frequencies below 0.1 hertz.

A brief review of seismic activities as a function of geographic location (ref. 6) revealed that a high microseismic activity is detected near the coasts, probably due to tidal wave couplings. In areas remote from the coast, as a general assumption, the microseismic wave period varies from 0.03 to 9.0 seconds, and the amplitude range is between 0.5×10^{-6} and 5.0×10^{-6} meter. A seismic survey indicated that the level was much higher near the coast. Therefore, the test facility had to be moved to another location.

For a representative condition, the wave velocity is $V \cong 3000$ meters per second, and, for a 20-hertz wave frequency, the wavelength is $\lambda = 150$ meters. At a certain time, the 30-meter block will rest on the crest of the seismic wave, and, assuming that it is supported in the middle, it will incur a sag of approximately 0.2×10^{-6} meter. Accordingly, a collimator mirror mounted at the end of the block will be tilted by an angle of $\theta = 0.005$ arc second, and the change in the transmitted light beam direction is $2\theta = 0.01$ arc second. Because of the receiver tilt at the other end of the bench, a total error of $8\theta = 0.04$ arc second will result. These are only hypothetical numbers; in reality, much higher errors may be encountered.

The second difficulty is the air turbulence and attenuation when the ultraviolet is

involved. Some statements were made to the effect that evacuation will be necessary. As far as it is known, the present vacuum techniques are inadvertently connected with a high degree of vibration.

Since a solution of the vibration is not in sight, a drift-free environment with an extreme-temperature, long-term stability may be sought. In the Kollman OATES study, an investigation of old mining shafts or caves away from the coastline was proposed for this application. A further study may be necessary, including the progress in vacuum facilities.

References

1. Zuckerbraun, J. S.: High Reliability Scanners for Stellar Navigation. *Electronics*, May 11, 1962.
2. OAO Star Tracker - 30 Day Report. General Electric MSD, Philadelphia, February 28, 1969.
3. Orbiting Astronomical Observatory Handbook. Grumman Aircraft Engineering Company, Bethpage, New York.
4. Man-Computer Roles in Space Navigation and Guidance. The Franklin Institute Research Laboratories Systems Science Department, N68-34882, February 19, 1968.
5. Isolation of an Optical Test Bed. Barry Corporation, Patrick AFB, Florida.
6. Murphy, L. M.: A Survey of Microseismic Activity. *Earthquake Notes*, vol. XX, no. 3, 1949.

4 N70-36732

PRECEDING PAGE BLANK NOT FILMED.

Precision Pointing of Large Aperture, Diffraction-Limited, Space Telescopes

Herbert F. Wischnia

The Perkin-Elmer Corporation

In the Large Telescope Experiment Program (LTEP) at NASA's George C. Marshall Space Flight Center, there are a group of interrelated experiments and demonstrations that are associated with the development of optical space technology, particularly in the area of ultrafine pointing. The justification for conducting this group of experiments on the LTEP is based upon the principle that the performance of a precision space telescope is equally dependent on both the stability of its guidance system and the quality of its optics. A diffraction-limited optical instrument in space requires a correspondingly precise pointing system.

There are very few pointing techniques that can provide the foundations for a space experiment in pointing to 1/100 arc second or less. Specifically, the two most promising techniques are:

1. Transfer lens techniques, such as used on Stratoscope II flights
2. Body point techniques with free float, such as those developed for the Princeton Advanced Satellite.

The transfer lens technique by itself does not provide the image rotational stability that is required for space astronomy. Rotational pointing operations about the line of sight (RLOS) require expanding this list of two techniques to include RLOS approaches applicable to space telescope systems:

- Risley prism beam orientation techniques, which are most useful for laser communication experiments
- * Body point techniques with vehicle orientation, such as the Orbiting Astronomical Observatory (OAO)

- Body point techniques using flexure gimbals, such as Stratoscope II and the Apollo Telescope Mount (ATM)

- Image motion-compensation techniques.

The Perkin-Elmer approach to the pointing experiments and feasibility demonstrations for the LTEP is based upon conducting space flight experiments in 1/100 arc-second pointing and using astronomical types of instrumentation to evaluate pointing performance.

The minimum pointing error of a servo-controlled, optical line-of-sight, tracking a star via image-splitting techniques, has been derived to be a direct function of the diffraction-limited resolution of the telescope and an inverse function of the signal-to-noise ratio of the sensor. As the telescope diameter increases, the minimum pointing error reduces in square-law fashion while the required pointing error reduces linearly. Hence, the ultimate pointing figure of merit for a system tends to increase with telescope diameter if visual magnitude and bandwidth remain constant.

In the Perkin-Elmer study on the Optical Technology Experiment System (OTES) for the Marshall Space Flight Center, a 2-meter, diffraction-limited-telescope pointing system was analyzed. The OTES is illustrated in figure 1. Figure 2 presents the basic data of minimum pointing error as a function of telescope diameter, servo bandwidth, and star brightness. The curves show (for an example, see sample point) that the 2-meter OTES telescope, utilizing a 1-hertz servo-equivalent noise bandwidth and having 33 percent

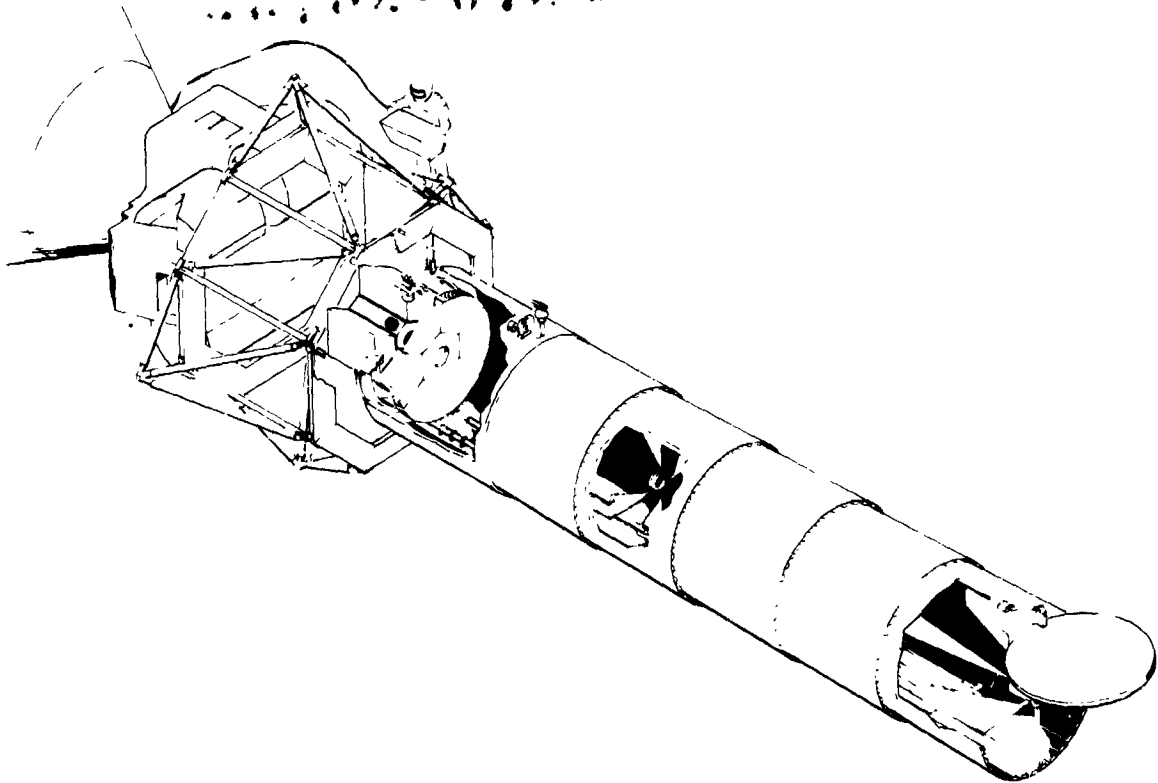


Figure 1. The 2-meter, optical technology experiment system (OTES) telescope.

optical and 6 percent quantum efficiencies, can theoretically achieve a 0.0005 arc-second rms performance tracking twelfth magnitude stars. Additional pointing errors caused by background light, phototube dark current, and noise from electronic control circuitry can generally be reduced by straightforward design measures and, like quantum noise, by a servo bandwidth reduction. Unfortunately, the attainment of arbitrarily high performance by resorting to extremely low bandwidth is prevented by the presence of telescope torque disturbances that cause increasing errors as the bandwidth is reduced in a given control system. The torque disturbances produce pointing errors. Although a smaller error due to noise results as servo bandwidth is reduced, torque-induced errors increase.

The gravity-gradient, magnetic, and solar pressure-induced disturbance torques are at a constant frequency and within the servo

bandwidth. All three disturbance sources could potentially limit the pointing-system performance. If, however, the system bandwidth is not structural-resonance-limited but is maintained constant, only gravity-gradient disturbances would be of any concern. Whether or not such disturbances are a problem depends upon the many system parameters, including those that determine torque magnitude (and frequency), such as orbital altitude and asymmetry of mass distribution. It is noteworthy that an orbital change from a 20,000-mile orbit to a 260-mile orbit will increase the gravity-gradient magnitude by the cube of the radius ratio; i.e., 600,000 times.

The corresponding disturbance frequency, moreover, would increase by a factor of 16 and, hence, would appear at a frequency where the lead-lag stabilized OTES telescope could have its gain increased by proportional plus integral characteristics. The gravity-gradient-induced error for a telescope

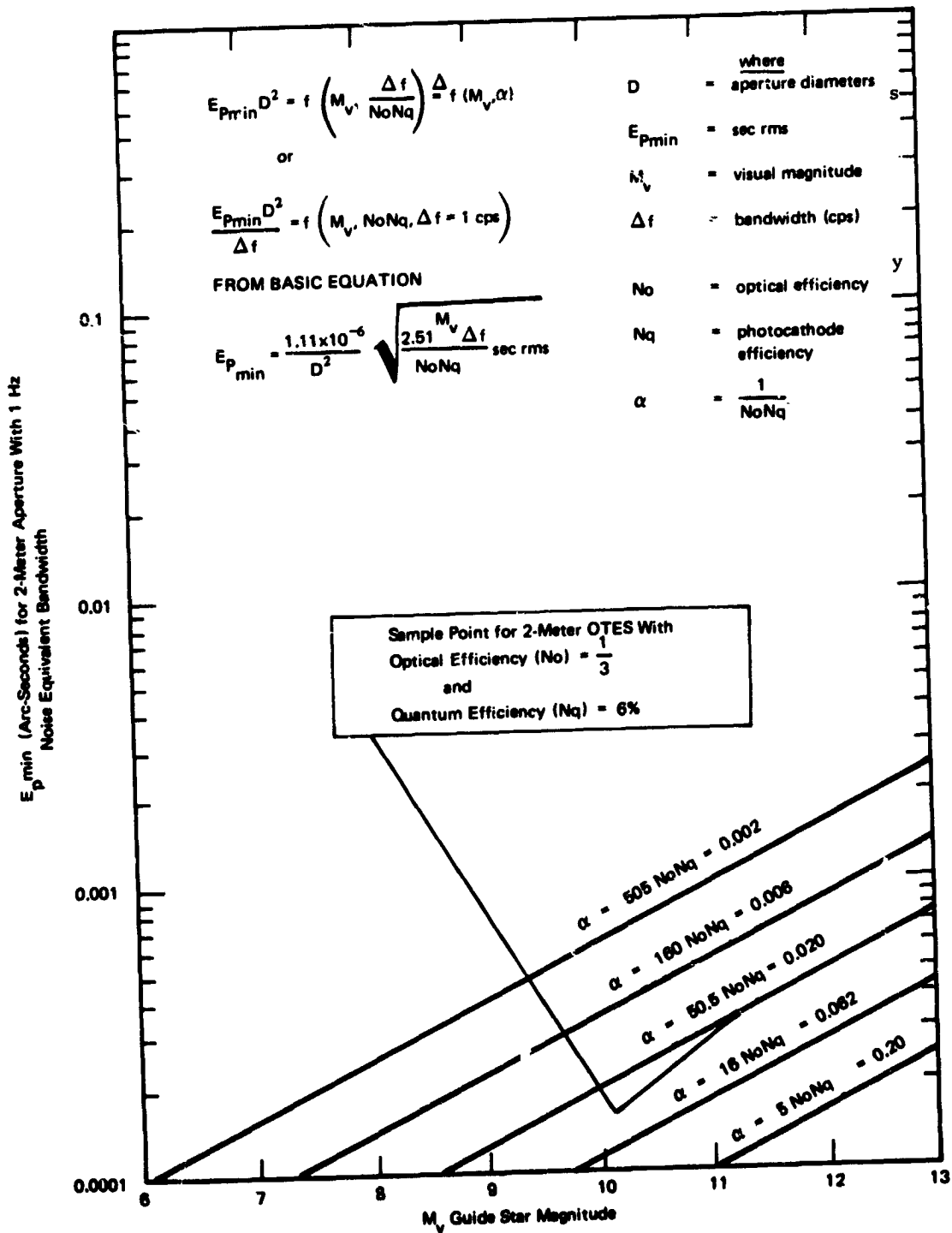


Figure 2. Limit of stellar tracking capability.

in synchronous orbit is negligible in comparison to that for near-earth orbits. Similar considerations for magnetic torques also indicate the desirability of a synchronous orbit. Solar pressure, on the other hand, primarily induces static or bias torque, which is very effectively combatted by incorporating this proportional plus integral servo control.

It seems clear that a large, low-orbit, space telescope will have torque disturbances that will limit the overall pointing accuracy.

Up to this point, only gross line-of-sight pointing errors due to torque disturbances and noise have been considered. The roll (about the line-of-sight) telescope error is equally important, and magnitude constraints can be computed based upon the assumption that recorded image smear due to roll should be no larger than that due to gross line-of-sight errors.

For the 2-meter OTES, the roll precision requirement was computed to be 1.5 arc seconds maximum to 0.14 arc second minimum.

The total field-of-view of the 2-meter OTES must be somewhat larger than the recorded field-of-view to ensure a reasonably high probability of containing at least two guide stars. The guidance field must be large enough so that the guidance photosensors can see the guide stars with the maximum initial mispointing angle of the telescope. The diameter of the guidance field during tracking may be smaller than the guidance field required for acquisition in order to avoid excessive degradations due to stellar background light.

For the 2-meter OTES, the structural pointing error is estimated at 7.5 arc seconds while the frequency is one cycle per 90 minutes. This structural-pointing-error frequency can be used to determine the open-loop gain required at this frequency to reduce optical pointing error to one-tenth the diffraction-limited resolution of the telescope. A minimum wavelength of 1000 angstroms was used to establish the pointing requirement for the 2-meter OTES telescope. There will be a deterioration of the guidance precision due to photon noise. The disturbance

caused by photon noise is to be held to one-tenth the diffraction-limited performance of the 2-meter telescope at 1000 angstroms. The guidance error contribution allocated to photon noise was computed (ref. 1) to be 0.00084 arc second. Note that the pointing precision needed to take advantage of the 2-meter diffraction-limited aperture is 0.005 arc second (ref. 2).

If the allowed photon-noise-induced error is one-tenth the optical resolution at the minimum wavelength of $\lambda = 0.1$ micron, then the offset guide star magnitude for pointing will be 15 for the 2-meter OTES.

The total optical field can be established with the aid of figures 3 through 6. Figure 3 shows the average number of guide stars per square degree as a function of galactic latitude and star magnitude; i.e., approximately 240 per square degree for $M_V = 15.4$ at 90-degree latitude. Figures 4 and 5 indicate the probability statistics of star occurrence in the field, assuming a Poisson occurrence spatially; i.e., from figure 5, the area of field required for 90-percent probability is $(\pi/4)(8.6)^2$ square arc-minute field area. Figure 6 shows the results based upon 90-percent coverage.

Note that figures 4 and 5 have the field-of-view for the 2-meter OTES sketched in at 30 arc minutes. The optical design of the system was then based upon achieving a flat diffraction-limited guidance field of this value.

Acknowledgment

Mr. E. R. Schlesinger performed the photometric analysis for this paper.

References

1. Wischnia, H.F.: Optical Technology Apollo Extension System (OTES) Phases I and IA. Perkin-Elmer Report No. 8500, November 1966.
2. Danielson, R.E.: Large Telescopes in Orbit. International Science and Technology, July 1967, p. 54.

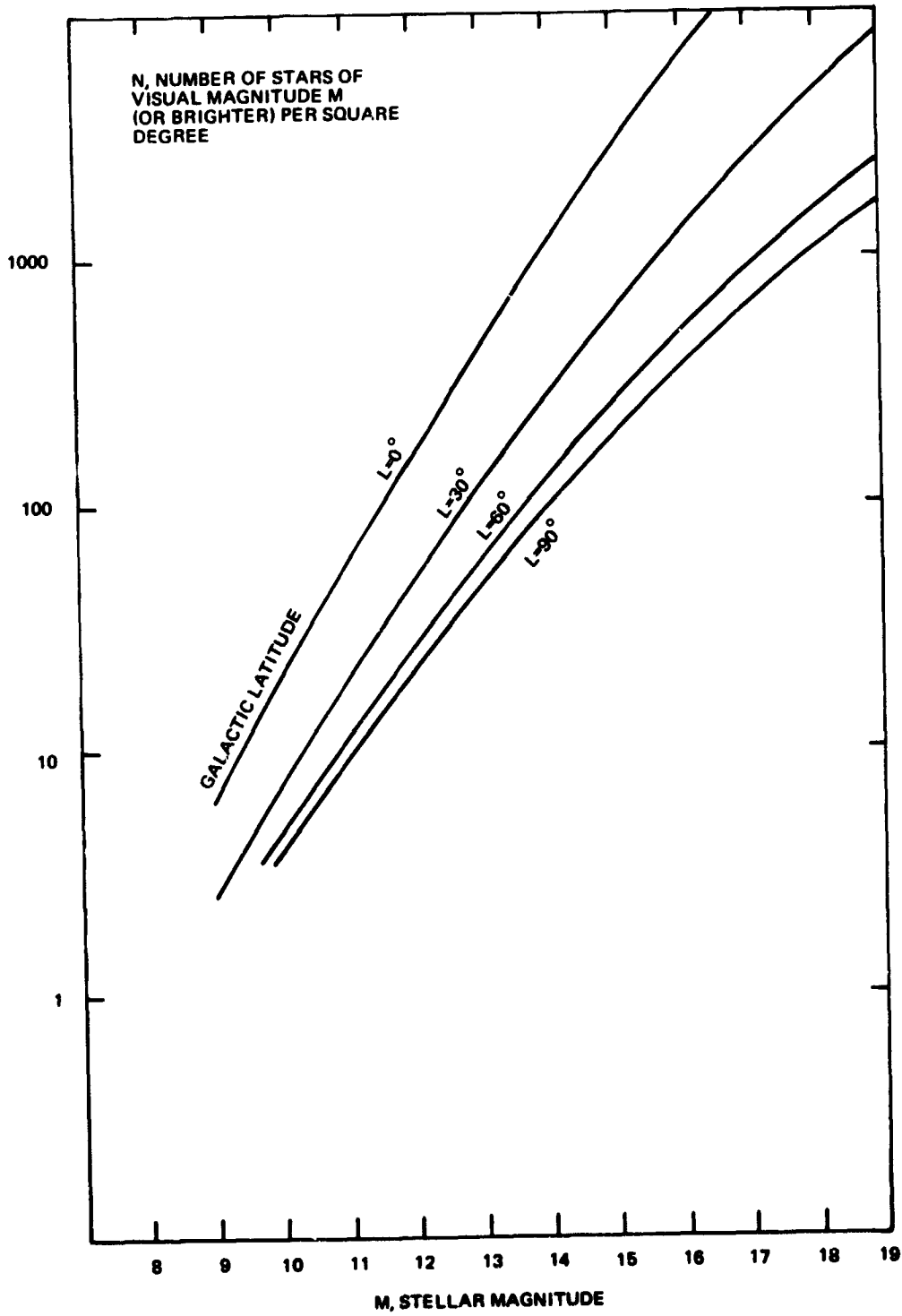


Figure 3. Availability of guide stars.

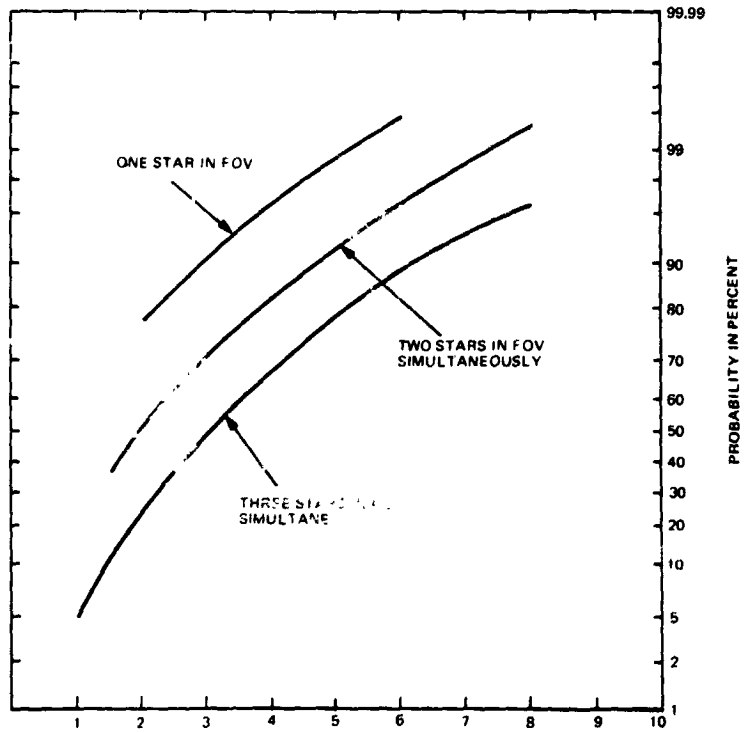


Figure 4. Guide star probability.

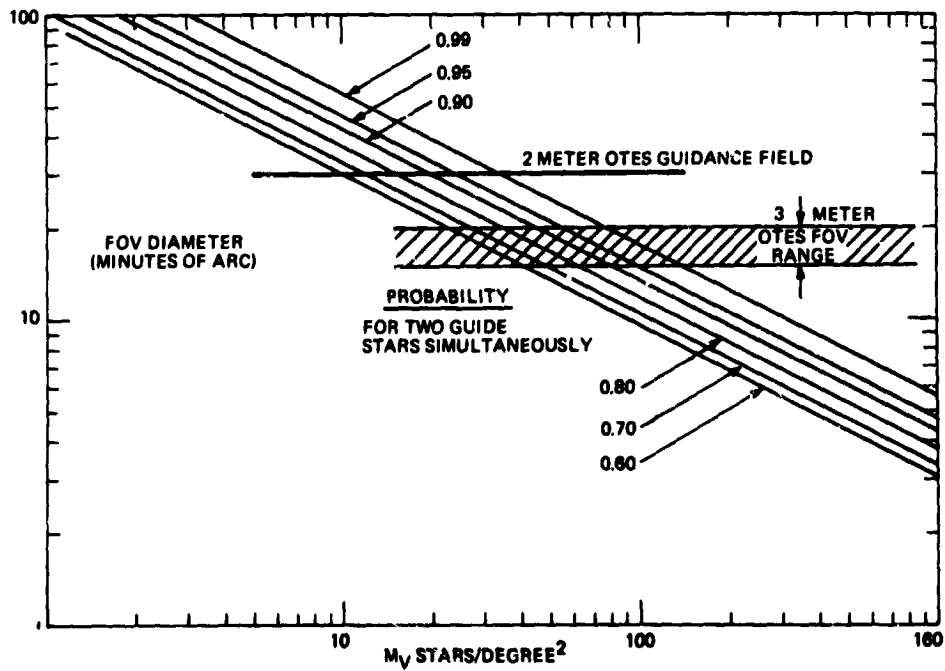


Figure 5. The 2-meter and 3-meter telescope-guidance field-of-view.

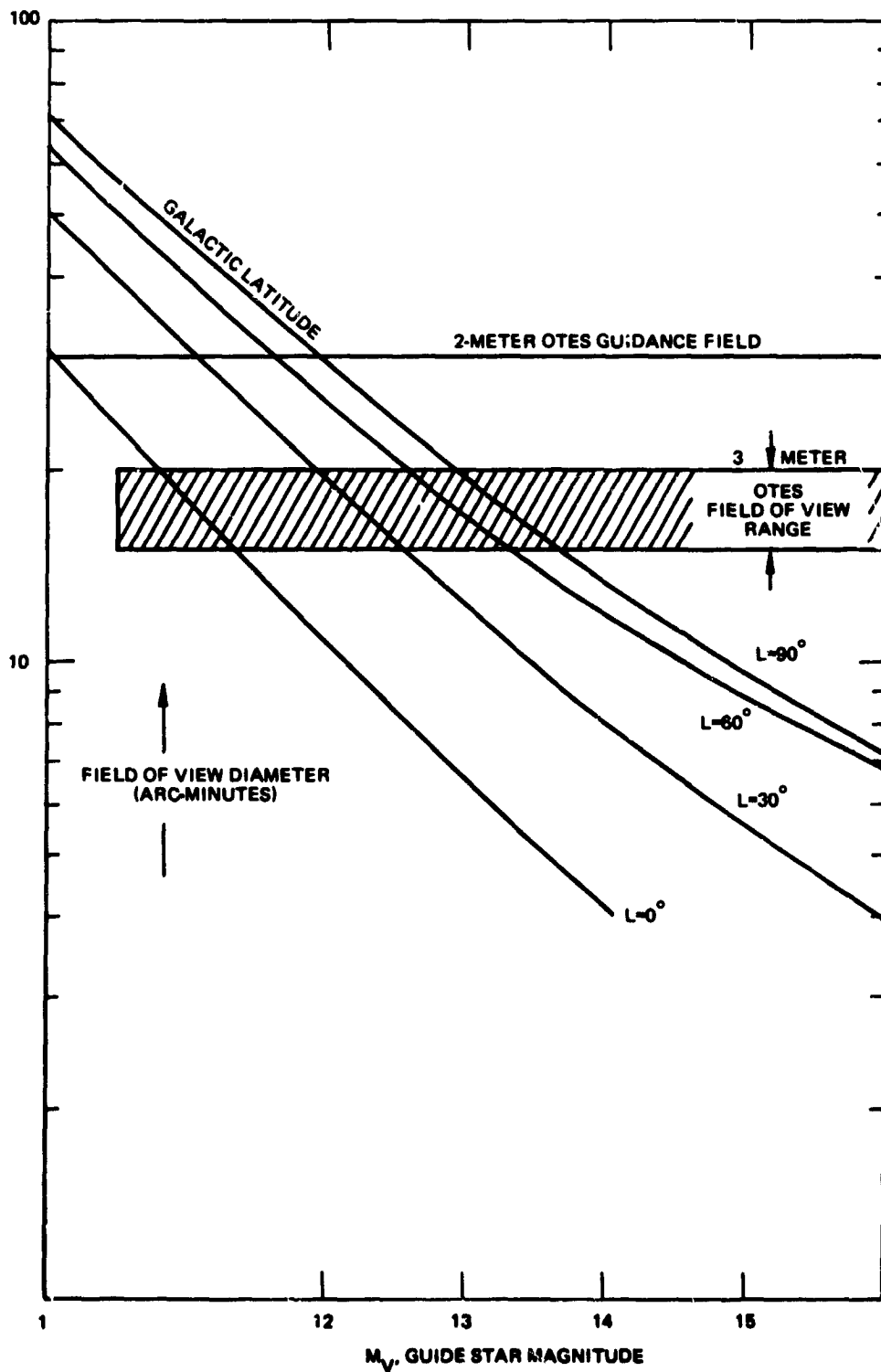


Figure 6. Ninety-percent probability of at least two guide stars.

PRECEDING PAGE BLANK NOT FILMED.

N70-36733

Control Technology for Large Orbiting Telescopes

Gordon F. Bullock, Frederick R. Morrell,
and Aaron J. Ostroff

NASA Langley Research Center

Introduction

This paper describes the work accomplished at Langley Research Center and concerned with the stabilization and fine pointing of a 120-inch-diameter orbiting telescope. Four subjects are discussed.

1. *Telescope Isolation Analysis.* The results of an analysis of an attitude-stabilized telescope passively coupled to a crew module are presented. The purpose of this analysis was to determine the feasibility of stabilizing the entire telescope to better than 0.01 arc second.

2. *Fine-Pointing Guidance Sensor.* The principle of operation and the experimental results of a fine-pointing sensor applicable to large orbiting telescopes are explained.

3. *Optical Image Stabilization.* A technique for star-image motion compensation by the use of optics internal to the telescope is described. This approach may be used to minimize the stringent requirement of pointing the entire telescope structure. Experimental results are discussed.

4. *Scaling Technique.* An error scaling technique that allows the attitude control system to be simulated (using representative hardware) is discussed.

Telescope Isolation Analysis

The configuration shown in figure 1 has been suggested as a likely mode of operation (ref. 1). The vehicle consists of three bodies: a 120-inch-diameter telescope, a soft spring-suspension system, and a service module.

The attitude control problem that we are investigating for this mode of operation is this:

Since the resolution of a 120-inch diffraction-limited telescope is 0.04 arc second, can it be stabilized to 0.01 arc second or better when subjected to a disturbance environment?

The vehicle is shown schematically in figure 2. The telescope is attached to the suspension system, which consists of a two-axis gimbal assembly and a spring suspension



Figure 1. Artist's conception of soft gimbaled vehicle.

OPTICAL TELESCOPE TECHNOLOGY

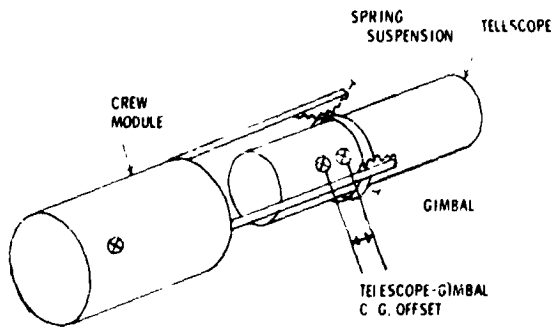


Figure 2. Schematic diagram of soft gimbaled vehicle.

made up of three sets of springs located symmetrically around the gimbal. The suspension system is connected to the crew module by the truss assembly. The purpose of the suspension system is to isolate the telescope from disturbances in the crew module. This isolation is optimized when the center of mass of the telescope and center of rotation of the suspension system are aligned. Damping must be provided to limit gimbal motion; however, this damping torque will directly couple into the telescope.

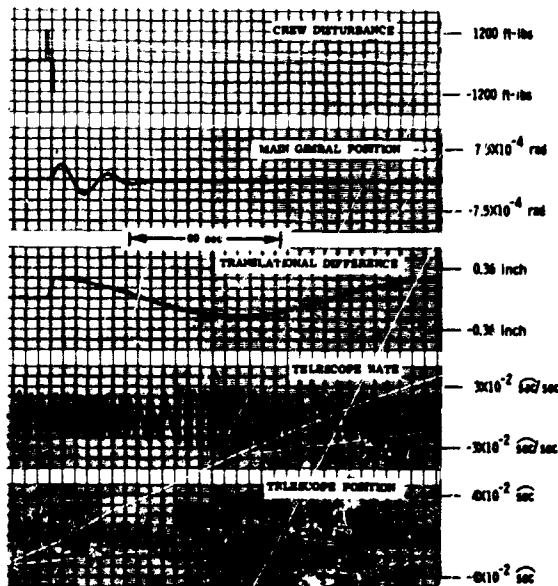
To stabilize the telescope against crew motion disturbances as well as disturbances caused by the orbital environment, the control system design has been based on a single-axis, twin-rotor, control moment gyro (CMG). This configuration was chosen because of the operational simplicity and high torque-gain capabilities.

The analysis of this vehicle (ref. 2) consisted of an analog computer simulation of the planar rigid-body equations of motion of the vehicle. These equations consist of four translational modes—two for the crew module and two for the telescope—and three rotational degrees-of-freedom, which include the crew module, main gimbal assembly, and the telescope. Control systems were added to the telescope and the crew module. The equations of motion take into account the center of mass offset between the telescope and the main gimbal. Damping and breakout friction on the main gimbal-to-telescope bearing connection has been considered as well as CMG

breakout friction. Noise was included in the simulation to take into account typical signal-to-noise ratios for the pointing sensor, which was assumed to be operating from the main optics of the telescope. Environmental torques acting on the vehicle are caused primarily by gravity gradient. Crew motion disturbances of 1200 foot-pounds on the crew module were included.

The vehicle response to a crew motion disturbance and small environmental torques is shown in figure 3. The disturbance is shown in the top trace and consists of two 1200-foot-pound impulses, acting in opposite directions, 2.5 seconds apart. The main gimbal attitude reaches an amplitude of approximately 1/40 of a degree. It stops when the disturbance torque acting on the gimbal is less than the breakout friction in the telescope-to-gimbal bearing connection. The difference in the vertical translation between the crew module and the telescope is indicated on the next trace. The peak amplitude is 1/4 inch, and the motion is undamped. The horizontal motion between the crew module and telescope was uncoupled from the other degrees of freedom and, therefore, is not shown; this motion is also undamped.

Some form of damping must be provided to limit the motion of these translational modes. The next two traces indicate the telescope angular rate and position. The limit cycle is caused by the gyro gimbal friction nonlinearity, which was assumed to be 0.05 inch-ounce per gimbal. The variations in limit cycle amplitude are caused by variations in the magnitude of disturbance torque acting on the telescope. The amplitude of this limit cycle reaches approximately 0.03 arc second, which does not meet the desired pointing accuracy of the telescope. The limit cycle in telescope attitude decreases when noise is taken into account for the pointing sensor as shown in figure 3(b). All other conditions were exactly the same. The noise causes a dithering effect on the gyro gimbal and tends to reduce the amplitude of the limit cycle in the control system. In this case, the telescope remains within the pointing specification requirement of 0.01 arc seconds, but the



(a) Nonlinear system response.



(b) Vehicle attitude response to a crew motion disturbance with sensor noise included.



(c) Vehicle attitude response to a crew motion disturbance with sensor noise included and dither torque added.

Figure 3. Vehicle response to a crew motion disturbance.

operation is marginal. Because noise in the signal tends to reduce the limit cycle in telescope attitude, external dither torque was added to the gyro gimbals; the effect is shown in figure 3(c). Comparing this trace with the others that were run for the same conditions shows improvement in pointing accuracy to well within the desired goal of 0.01 arc second.

In summary, the analog simulation of the planar rigid-body equations of motion of the vehicle and its control systems has been completed. The results have demonstrated the initial feasibility, from the control and stabilization viewpoint, of coupling the telescope to a manned service module through a passive suspension system. It has also been indicated that the desired pointing accuracy of 0.01 arc second can be met when the vehicle is subjected to a disturbance environment and when the effect of nonlinearities in the telescope control system and the suspension system are considered. The studies have also indicated that some form of damping will be needed to limit the translational motion of the vehicle since unrestricted crew motion could increase these oscillations to intolerable levels. The flexible modes of the vehicle will be added to this investigation in the near future.

Fine-Pointing Guidance Sensor

To stabilize a telescope to 0.01 second of arc, a fine-pointing guidance sensor is required for attitude information. A technique to detect star image motion on the focal plane of a telescope and to generate position information has been developed and evaluated using an image dissector tube as the transducer. A NASA technical note (ref. 3) containing this information will be available in the near future. The discussion and results to be presented are for a single-axis case; however, this technique is also applicable to a two-axis system.

The schematic representation of the laboratory configuration used to evaluate the system is shown in figure 4. The configuration consists of a source that simulates the star, a collecting lens, an image dissector, and digital electronics. The optical system was designed to produce a star image having the same size and motion on the focal plane of the simulated telescope as it has in the 120-inch-diameter telescope. The diameter of the image is equal to the diameter of the first dark ring of the Airy disk.

An image dissector tube is shown schematically at the top of figure 5. A star

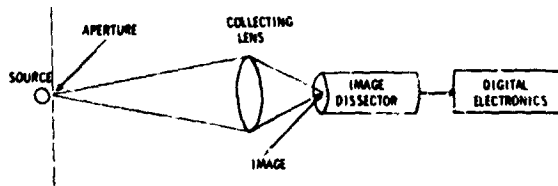


Figure 4. Schematic of laboratory configuration.

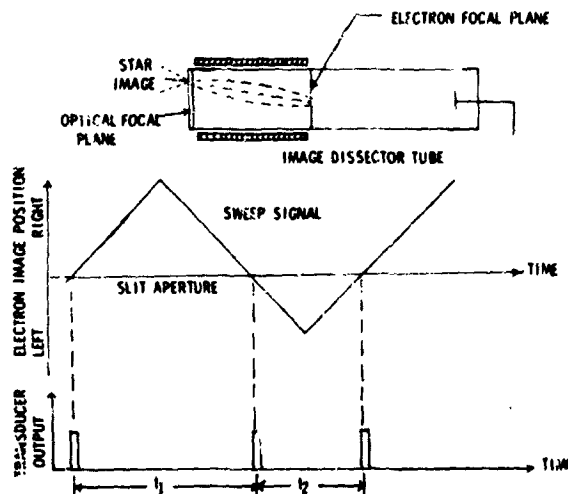


Figure 5. Schematic representation of image dissector tube, sweep signal, and output pulses.

image is focused on the front face of the tube, located on the optical focal plane; this produces photoelectrons, which are refocused onto the electron focal plane. The defining aperture, which is a slit for the single-axis case, is centered in the electron focal plane. The electron image is scanned vertically across the slit by passing a sweep signal through the magnetic deflection coils. A triangular sweep signal was used for the experiments made on the system.

The sweep signal is plotted on the upper trace with the vertical axis representing the electron image position and the horizontal axis representing time. In this illustration, the star image is off-axis; therefore, the path of the electron image is not centered about the

slit aperture. When the electron image crosses the slit, an electrical pulse is generated. The pulses are shown idealized in the lower half of figure 5. The time interval between successive pulses is measured and the difference in the two times (t_1 and t_2) is proportional to the angular error between the guide star and telescope. The sign of the resulting number indicates direction. It should be noted that other symmetrical curves could have been used for the sweep signal; however, the triangular sweep was selected because of its linearity.

The pulse train is processed as shown in figure 6. The signal pulses containing noise are first amplified and then filtered. The principal effect of this filter is to lower the noise bandwidth of the system. The leading and trailing edges of the resulting pulses are then detected by a Schmitt trigger, producing a squared pulse. Both edges of the signal pulse are detected because this minimizes errors due to noise. There is a sufficiently high correlation between the leading and trailing edge-detection times so that the time variations tend to subtract out because the high frequency noise is filtered. Therefore, the assumption has been made that the center of the squared logic pulse is the center of the star image.

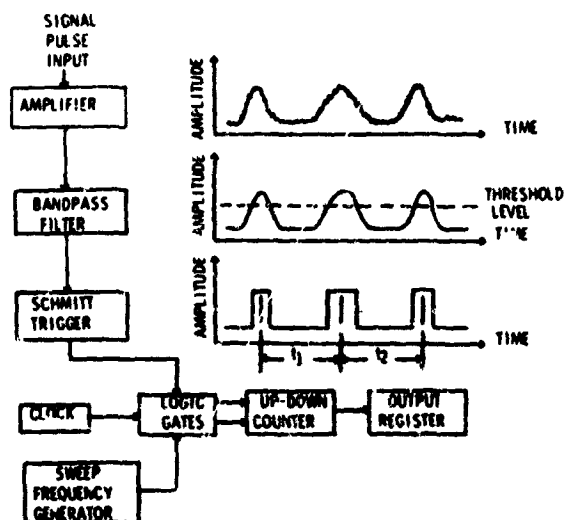


Figure 6. Schematic representation and typical waveforms of the signal processing system.

The output of the Schmitt trigger, in conjunction with the sweep frequency signal, controls logic gates that determine the direction of an up-down counter. These gates also provide passage for the clock pulses going to the counter. The up-down counter operates in the up mode during time t_1 and in the down mode during time t_2 . At the end of a complete counting period, the resulting digital number ($t_1 - t_2$) is shifted to the output register.

Several tests were made to determine the stability of the system and its ability to detect small motions of the star image.

Figure 7 shows the experimental results of varying the sweep frequency and star magnitude. The star magnitude is based on the 120-inch-diameter telescope and the S-20 response-image dissector tube used in the experiments. The vertical axis represents the system stability error and is plotted in terms of image diameters that relate directly to angular errors. The system stability error is defined as the two-sigma deviation in measuring the star image when the star image is stationary on the optical focal plane. The amplitude of the sweep signal was maintained constant for all cases at 28 image diameters, which is equivalent to a field-of-view of 2 arc seconds. This is based on a 120-inch diameter telescope operating at $f/100$.

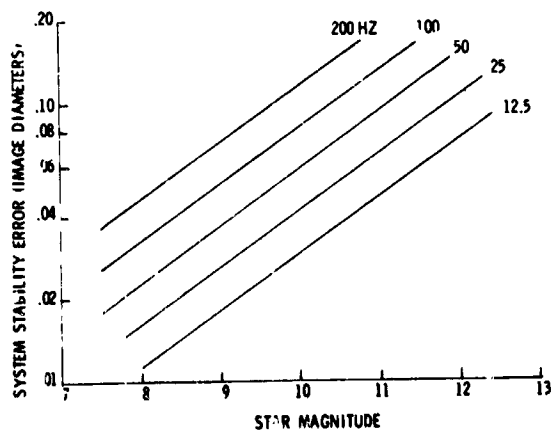


Figure 7. System stability error versus star magnitude for several sweep frequencies.

Five different sweep frequencies, varying from 125 hertz to 200 hertz, were used for this set of experiments. The bandpass filter was varied directly with the sweep frequency. The results show that a 12.4 magnitude star is the dimmest star that can be seen by the transducer when the sweep frequency is 12.5 hertz. For a 100-hertz sweep, an 11.1 magnitude star can be seen; at 200 hertz, it is possible to guide on a 10.7 magnitude star. The system is stable to within 0.08 image diameter when guiding on a 10th magnitude star and using a sweep frequency of 100 hertz.

A few relationships can be seen from these curves, which have also been proved analytically. There is a linear relationship between the log of the system stability error and star magnitude; a change of five star magnitudes will change the system stability error by a factor of 10. In addition, the system stability error increases with the sweep frequency in a square-root relationship.

Tests were made to observe the effect of detecting the signal pulse on both leading and trailing edges. A plot of system stability error versus threshold level for several star magnitudes and for double-edge detection is shown on the left-hand side of figure 8. Threshold level is defined as the amplitude at which the signal pulse is detected. In this test, the

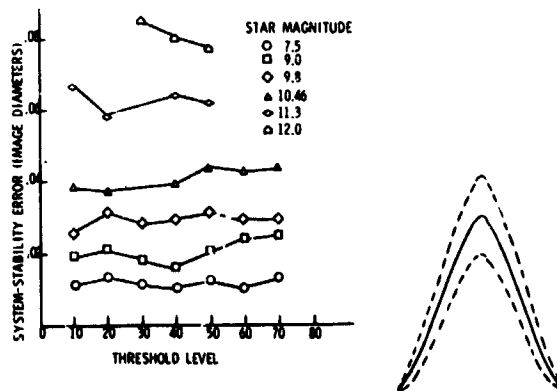


Figure 8. System stability error versus threshold level and schematic representation of typical signal pulse with noise envelope.

threshold level was varied from 10 to 70 percent of the nominal pulse amplitude. The bottom curve in figure 8 is for a 7.5 magnitude star, and the top curve is for a 12.0 magnitude star. Each of these curves is relatively flat, which indicates that threshold level has little effect on system stability.

Earlier tests showed that the threshold level does have an effect if single-edge detection is used. This can be seen from the diagram on the right-hand side of figure 8. A signal pulse has been drawn, and the dotted lines represent envelope of the pulse due to noise. The time variation is smallest at the lower threshold levels; the variation increases as the threshold level increases. When the pulse is detected on both the leading and trailing edges, the time variation tends to subtract out because high-frequency noise has been filtered.

Figure 9 contains experimental data showing the linearity of the system. The image dissector was mounted on a calibrated micrometer base that was moved to simulate the effect of image displacement. The digital output number was recorded for each position of the transducer. In this figure, the vertical axis represents the deviation from best straight line, in percent of full scale, and the horizontal axis represents image displacement in image diameters. The system is linear within 0.1 percent over the entire field-of-view of approximately 60 image diameters except at the end points where some distortion existed. The standard deviation is 0.06 percent of full scale.

One other test made was to observe the effect of averaging the data over a number of sweep periods. As expected, the system stability varied with the square root of the number of periods averaged. Based upon the experimental results, several conclusions can be made; these are described as follows.

The purpose of this research was to design and evaluate a technique by which star image motion on the focal plane of the telescope is detected and position information is generated by using an image dissector tube as the transducer. This was successfully accomplished. The measuring technique employed

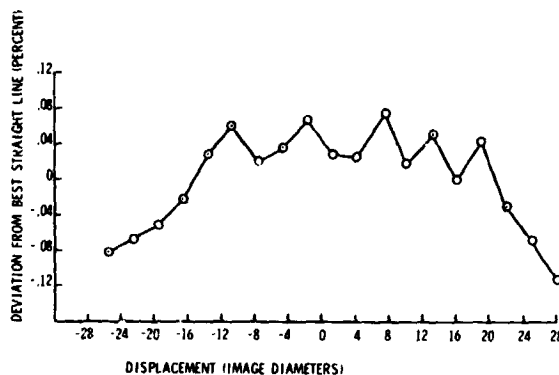


Figure 9. Linearity of system.

has proved to be practical because pulses from the image dissector are inherently digital and can be digital-processed with little signal conditioning. The versatility of the image dissector provides great flexibility to the user. The sweep frequency, amplitude, and wave-shape can be easily changed. When the signal pulses are detected on both the leading and trailing edges, the effect of threshold level becomes negligible because the time variation for both edges tends to subtract out. The system has been shown to be linear within 0.1 percent of best straight line over the complete field-of-view of 60 image diameters, which is a very large dynamic range. The linearity, accuracy, and flexibility of this sensor make it a prime candidate for fine-pointing control systems in large orbiting telescopes.

Optical Image Stabilization

The results of the first study discussed in this paper indicated the feasibility of stabilizing an entire telescope to 0.01 arc second when connected to a crew module through a soft spring-suspension system. A different approach is possible with the star image motion on the focal plane being controlled by internal optics. When this approach is used, the requirement for controlling the entire telescope structure can be reduced; and the control system can have a high bandwidth without large control torques because of the small inertia of the system. An all-reflecting

experimental model, designed and fabricated at the Langley Research Center, has been used to demonstrate the principles involved.

The purpose of an image-motion-compensation system is to maintain the star image fixed on the focal plane despite small motions between the guide star and telescope. In the illustration at the top of figure 10, rays from a star are shown imaged on the focal plane after reflecting from two plane-parallel mirrors. In an actual case, the telescope will move, thereby causing all star images to be moved on the focal plane. The two mirrors will then be rotated in order to bring the star images back to the original position.

For ease of experimental evaluation, we have chosen to assume the telescope stationary and to analyze the motion of a star image on the focal plane when the mirror system is moved. First, the two mirrors must be maintained parallel to each other as they are rotated. By doing this, all stars within the field-of-view will be imaged on a plane that is parallel to the focal plane, but the star images will be changed in focus. Second, the change in focus can be eliminated if the path length from the top mirror to the focal plane is maintained constant. This can be accomplished by translating the bottom mirror as it is rotated. An illustration of this is shown in

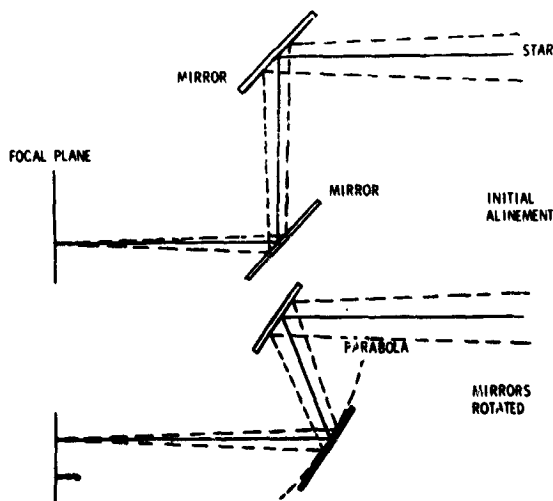


Figure 10. Schematic representation of image motion compensator.

the bottom section of figure 10. Both mirrors have been rotated through the same angle, and the image has been translated along the focal plane. The distance between the two mirrors has been changed, but the total path length remains constant. It can be shown that the motion of the bottom mirror describes a parabola.

The hardware, shown in figure 11, contains the complete assembly, the top plate containing the two mirrors, and the base assembly. The guide bearing, shown mounted on the base, functions as the directrix of the parabola; the shaft, which is the center of rotation, serves as the focus.

In order to evaluate the laboratory model, a Twyman-Green interferometer has been used to measure the change in path length as the mirrors are rotated. Basically, the interferometer system is comprised of a laser, a beam splitter, and two flat mirrors, as shown in figure 12. The image motion compensator is included in one leg and is indicated by the dotted lines in figure 12. Any change in path length as the mirrors are rotated will cause the fringe pattern on the screen to change. Each fringe is equivalent to 12.5 microinches.

The Twyman-Green interferometer was used only for measuring the change in path length caused by misalignments in the model. Figure 13 illustrates the various misalignment errors associated with this model. The following errors have been measured and calculated:

1. Both mirrors need to be parallel to each other and at an angle of 45 degrees to the optical axis when initially aligned.
2. The front surface of the top mirror should be directly over the point of rotation, which is the focus of the parabola.
3. The bottom mirror is physically connected to a guide that determines the amount of translation. The front surface of the bottom mirror should be directly over the point of attachment to the guide; otherwise, the mirror will not be tangent to a parabola.

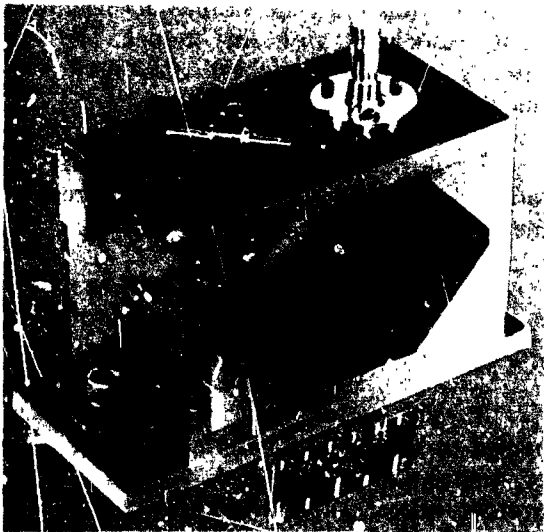
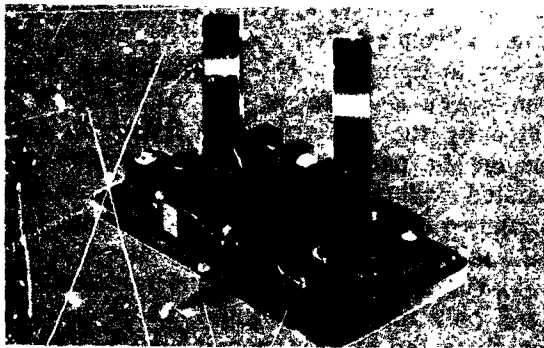
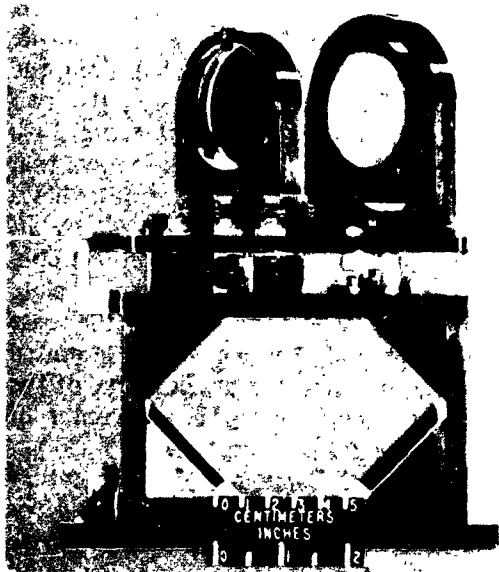


Figure 11. Image motion compensator hardware.

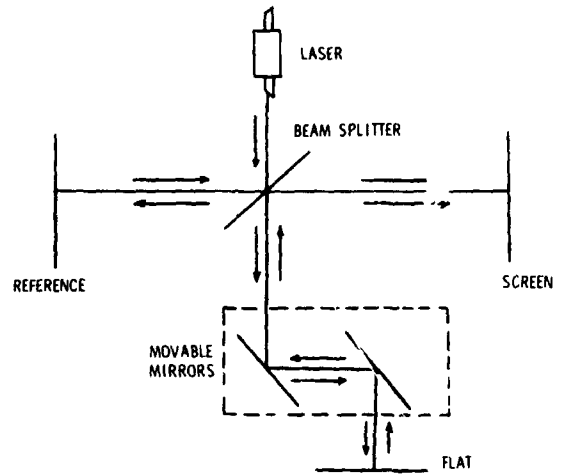


Figure 12. Schematic diagram of instrumentation used to evaluate system.

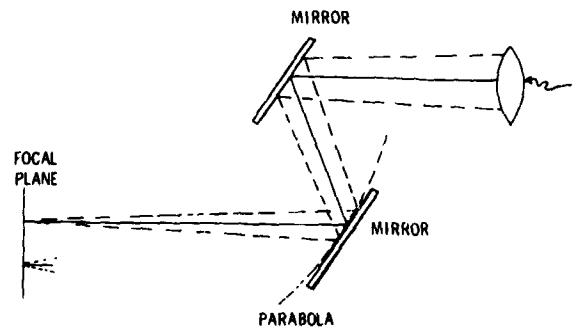


Figure 13. Schematic representation for evaluating errors in system.

4. The guide is a linear bearing that is at an angle of 45 degrees to the optical axis and thus parallel to the two mirrors when initially aligned.

5. The translation motion of the bottom mirror should be toward or away from the center of rotation.

The change in path length was measured for each misalignment error described. In figure 14, some typical experimental results illustrate the error in path length caused by the bottom mirror when it is not directly over the point of attachment to the guide. The vertical axis represents the error in path length

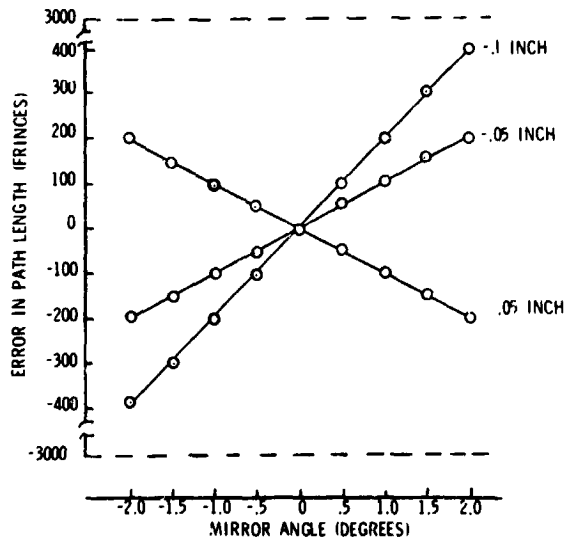


Figure 14. Error in path length versus mirror rotation angle for several misalignment errors.

plotted in terms of fringes. (Based on the Rayleigh criterion for a $1/4$ wavelength path difference, an $f/20$ system has a focal range tolerance of over 3000 fringes.) The horizontal axis represents mirror rotation angle and has been plotted over a range of ± 2 degrees, which is the rotation angle necessary to correct for a disturbance of ± 2 arc seconds in a 120-inch-diameter telescope operating at $f/100$. The numbers shown on the error curves represent the distance and direction that the mirror is misaligned from the perfect case. The values shown on these curves are very conservative because a physical model can be fabricated with misalignment errors that are two orders of magnitude smaller. It can be seen that the error in path length is proportional to the misalignment both in magnitude and direction; this is typical of the error curves in this system. When a system has all linear errors, only one adjustment is needed for alignment.

As a final check, several parameters were misaligned, and the complete assembly was rotated to compensate for all the other errors. The results are shown in figure 15. In this figure, the error in path length is plotted as a function of mirror rotation angle. There is a very small fluctuation and hysteresis value

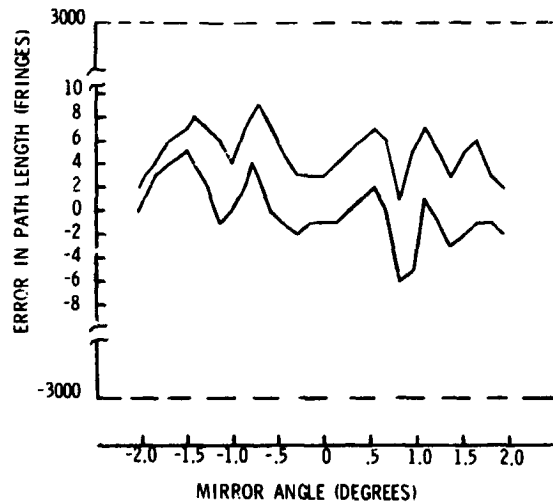


Figure 15. Error in path length as a function of mirror rotation angle for best alignment.

associated with this model. The peak-to-peak deflection was only 10 fringes, and the hysteresis was 5 fringes. This error is very small when compared with the focal range tolerance of 3000 fringes. Notice that the path-length error for the two runs have almost the identical shape. This is typical of the repeatability observed in this system.

The previous discussion has been for a single-axis image motion compensator. In reality, a two-axis system is needed. The main change is that one of the mirrors should be tangent to a surface that is a paraboloid of revolution. As can be seen in figure 16, motions in the vertical plane remain parabolic while those in the horizontal plane will be circular.

In conclusion, the experimental results have shown that optical image stabilization appears feasible. If small optics are used internal to the telescope, a control system for star image stabilization can be designed that reduces the stringent pointing requirements on the large telescope structure. The image-motion-compensation system uses only two mirrors for two-axis control. All the appreciable errors for the model described are linear; therefore, only one adjustment is needed to align the system.

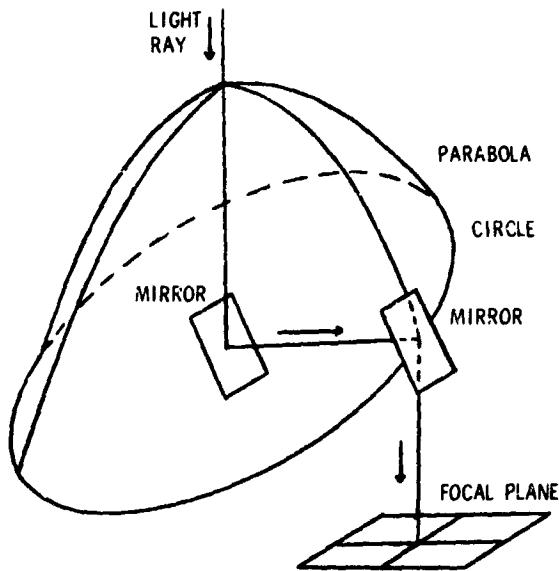


Figure 16. Schematic diagram illustrating two-axis technique.

Scaling Technique

An error scaling technique that allows the attitude control system to be simulated by using representative hardware is reviewed in this paper. The technique will be used to evaluate the performance of control systems suitable for a 120-inch-diameter telescope. Because of the large moments of inertia about the axes of the telescope and because of the stringent pointing requirements and the small disturbance torques exerted upon the telescope, scaling techniques are required for the simulation where the torque-to-inertia ratio is not maintained.

Figure 17 is a simplified block diagram of the telescope control system that incorporates a single-axis, twin-rotor, control moment gyro as the momentum exchange device. A disturbance torque is acting on the vehicle and is causing changes in both body rate and body attitude. A star sensor will detect changes of the star image caused by the disturbance torque. The output from the CMG is a control torque that is equal and opposite to the disturbance torque.

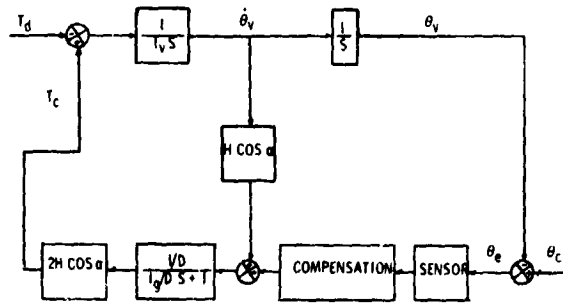


Figure 17. Block diagram of vehicle control system.

The block diagram in figure 18 is the control system that incorporates the scaling technique developed at Langley. In this method, the torque-to-inertia ratio has been changed because the disturbance torque is decreased by \sqrt{K} and the body inertia is scaled by K . Thus, both the rate and position have been increased by \sqrt{K} . The value of \sqrt{K} is chosen so that the disturbance torque remains above the noise sources in the airbearing, and the telescope position-pointing accuracy is above the noise level caused by the air currents in the room.

It is important that the star sensor see unscaled star image motions so that actual hardware may be used. This can be accomplished by optical scaling techniques, where the focal length of the optical system is decreased by \sqrt{K} . The gain change is represented by the box in front of the star sensor. The angular momentum of the gyro rotor has been decreased by \sqrt{K} to compensate for the increase in body rates. The inputs to the CMG

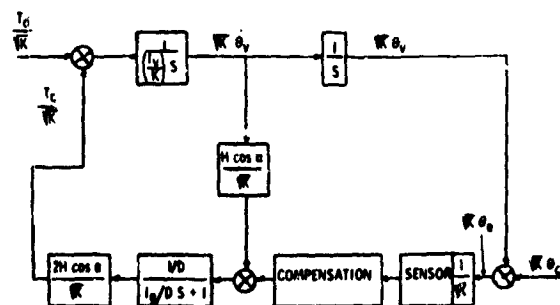


Figure 18. Block diagram of scaled vehicle control system.

have not been scaled; thus, both the gimbal angle and gimbal rates are realistic. The control torque from the CMG is decreased by \sqrt{K} , which is the same scale factor used for the disturbance torque. In this scaling method, the dynamic response is exactly the same as in the unscaled case because system time constants and both open- and closed-loop frequency response remain unchanged. Since the gimbal angle, gimbal rates, and inputs to the CMG gimbal remain unscaled, it is possible to use flight hardware in this simulation.

In a vehicle-control simulation of a proposed telescope control system now in

progress at Langley, a value of K was chosen so that the vehicle moment of inertia was scaled from approximately 10^5 slug-ft² to a value of 30 slug-ft². This was easily achieved on the simulator used in the test. The vehicle position was scaled from 0.01 arc second to a more easily detected 10 arc seconds of pointing accuracy.

Some typical results of the scaled model are shown in figure 19. A step disturbance torque of 0.05 foot-pound was applied to the telescope. The steady-state vehicle-position error is shown to be less than 10 arc seconds, which is equivalent to 0.01 arc second in the

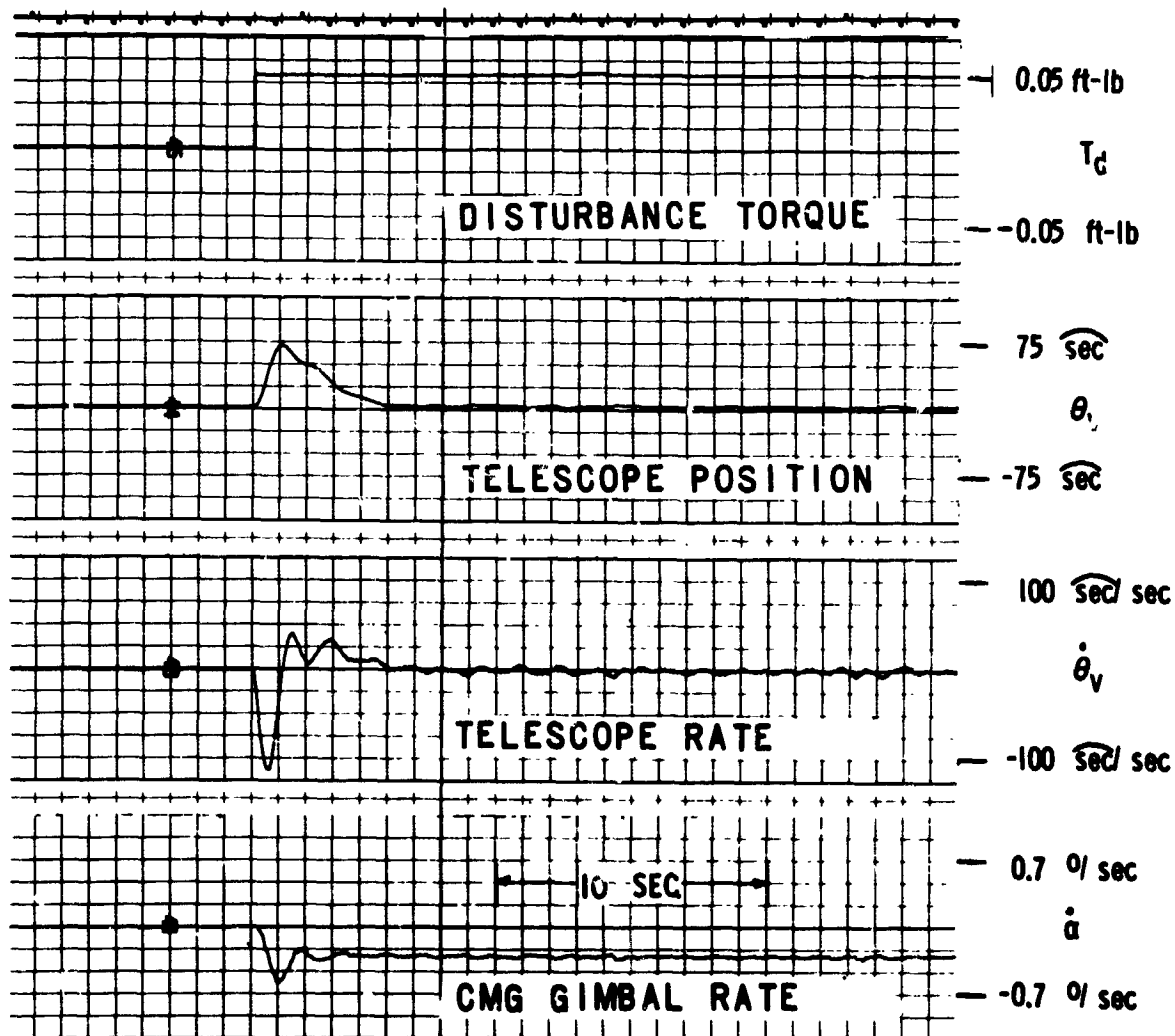


Figure 19. Experimental results of scaled model.

unscaled case. The telescope rate is approximately 5 arc seconds per second. The gimbal rate is constant at approximately 0.4 degree per second. For this gimbal rate, the control moment gyro generates a control torque of magnitude equal to the disturbance torque.

Concluding Remarks

Four subjects concerned with the stabilization and fine pointing of large orbiting telescopes have been presented in this paper. Future plans can be summarized with the aid of figure 20.

A simulation will be made incorporating the components and scaling techniques discussed. There will be two control modes: a coarse-pointing mode and a fine-pointing mode. The coarse-pointing sensor will provide attitude information to the control moment gyro through a digital computer. The control

moment gyro has been selected to prove the concepts developed and to provide the necessary control torque to maintain the position of the telescope structure within 2 arc seconds. The telescope structure is the air-bearing in the simulation. The fine-pointing control system will maintain all star images within the field-of-view stabilized on the focal plane within 0.01 arc second. The fine-pointing system includes the image motion compensator and the digital pointing sensor.

By virtue of the development of the fine-pointing sensor and optical image-stabilization techniques, it has been shown that it is possible to obtain the resolution necessary to provide attitude information to control a large orbiting telescope to better than its diffraction limit. Hopefully, the airbearing simulation will demonstrate this concept of pointing the telescope to the required accuracy.

References

1. Anon: A System Study of a Manned Orbiting Telescope. D2-84042-1, Contract NAS1-3968, Boeing Company, October 1965.
2. Morrell, Frederick R.: An Investigation of the Fine-Pointing Control System of a Soft-Gimballed Orbiting Telescope. Ph.D. Thesis, School of Engineering and Applied Science, University of Virginia, March 1968.
3. Ostroff, Aaron J.; Romanczyk, K. C.: Design of an Electronically Scanned Star Sensor with Digital Output. NASA TN D-5281, 1969.

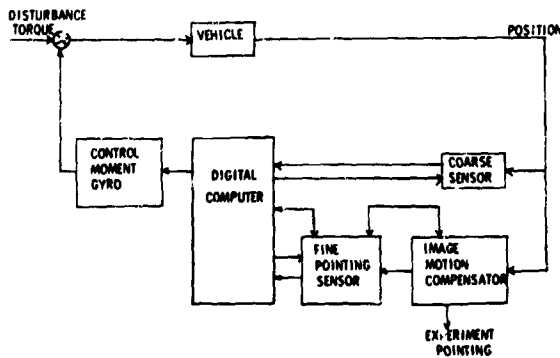


Figure 20. Block diagram for future control system.

The Requirements, Design, and Manufacture of Optical Gratings for Space Telescopes

John Strong

University of Massachusetts

Abstract

Various approaches for the fabrication of large gratings suitable for astronomical instrumentation were discussed.

The suitability of replica gratings for the vacuum ultraviolet is still inadequately known for long-term satellite use.

Two transmission objective gratings as large as 18 inches on a side have been made by evaporative techniques with 300 lines per inch for spectra centered at 4800 angstroms.

Ruled or etched grids are useful in a number of ways. By adjusting the grid line spacing over the grid area, diffraction can be controlled in such a way as to either focus incident radiation or correct for off-axis aberrations. Grids made by use of specially ruled gratings are used in the manufacture of special purpose photocathodes. Specially ruled grids also are used as spatial discriminators in the focal plane of instruments, such as multi-slits in a spectrometer, or as pattern comparators for optical alignment and performance.

Methods of manufacture of gratings and grids are diverse, ranging from mechanical ruling engines to holographic techniques. Mechanical ruling of optical gratings uses a shaped diamond, which is drawn across a softer surface material such as evaporated aluminum. Diamond wear limits the total coherent ruling length achievable. Newer techniques that have been tested include ion-beam etching, chemical etching, and evaporative deposition.

Suitably stable optical surfaces for grating substrates is a particular technology problem deserving more attention. Large, single, strain-relieved plates for reflective gratings are extremely difficult to achieve. Optical surface preparation by figuring and polishing needs to be better understood. Present theories of polishing are inadequate. For the far ultraviolet spectral region, large, strong, transparent films are needed for the substrate.

PRECEDING PAGE BLANK NOT FILMED.

N70-36734

The Requirements, Design, and Manufacture of Optical Filters for Astronomical Space Telescopes

Daniel J. Schroeder
Beloit College

The current technology of optical filters suitable for space telescope applications and suggested directions for future development are the subjects of this report. The emphasis is on the ultraviolet down to 1000 angstroms although the far infrared is considered briefly. A brief discussion of the various types of filters and their characteristics, and the availability of suitable materials, is given. The discussion is limited to the interference type of filters capable of providing a spectral resolution of one to ten percent of the peak wavelength of the passband. Except for special situations, greater resolution can be attained more easily with gratings.

Types of Ultraviolet Filters

There are a number of possibilities to consider for filters in the ultraviolet. There are the Fabry-Perot interference type of transmission filters using semitransparent metal films, as described by Schroeder (ref. 1), by Bates and Bradley (refs. 2 and 3), and Harrison (ref. 4), to provide passbands for wavelengths as short as 1300 angstroms. For wavelengths shorter than 4000 angstroms, aluminum is the best metal for this filter variety. All-dielectric interference filters have been made for wavelengths as short as 2400 angstroms. In this type of filter, the metal films are replaced by dielectric stacks consisting of alternate layers of high- and low-index transparent materials. In the visible and infrared, there are a variety of materials suitable for use in these stacks, but in the ultraviolet there are few suitable materials, particularly of high-index (ref. 5). A summary of some of the properties of suitable ultra-

violet materials is shown in table 1. The properties of bandpass filters with a single metal layer, called induced transmission filters, have been studied by various investigators (refs. 6 and 7) for wavelengths as short as 2600 angstroms. The films on either side of the metal film can be either all-dielectric stacks or combinations of metal and dielectric layers. In either case, the bandpass characteristics are somewhat superior to those of the conventional Fabry-Perot interference filter. In the ultraviolet, aluminum is the most suitable metal for these types of filters. For wavelengths shorter than 1000 angstroms, interference transmission filters of the type outlined above are not feasible at present because of the lack of materials. For this spectral range, unsupported metal films have been used as broadband filters, primarily to discriminate against long-wavelength radiation (ref. 8).

In addition to these various types of transmission filters, there are also examples of broadband reflectance filters that can help in shaping overall bandpasses. A recent example of such a filter with high reflectance in the 2000-angstrom region was reported by Osantowski and Toft (ref. 9).

Properties of Filters

Let us consider in more detail the properties of each of the filter types mentioned and discuss what has been attained in the ultraviolet.

A schematic of a Fabry-Perot type of filter with two highly reflecting, semitransparent films separated by a dielectric film is shown in figure 1. The first-order transmission

Table 1. Dielectric Materials for Thin Films

Substance	Index (Na D)	Absorption Onset (Å)	Comments
Sb ₂ O ₃	1.85	3200	Quite suitable as high-index material in near ultraviolet
CaF ₂	1.3-1.4	1200	
CsI	2.0(0.25μ)	2500	Hygroscopic, requires protection
CsBr	1.8(0.23μ)	2300	Hygroscopic, requires protection
LaF ₃	1.6	2200	Stable and usable well into ultraviolet
LiF	1.35-1.4	1000	Suitable into far ultraviolet
MgF ₂	1.35-1.4	1200	Very suitable into far ultraviolet
NdF ₃	1.6	2200	
ZnS	2.3-2.4	4000	Used in reflectance coatings in far ultraviolet
PbF ₂	2.1(0.25μ)	2400	

band is centered at that wavelength, λ_0 , for which the dielectric spacer has an optical thickness of $\lambda_0/2$. Higher order transmission bands are centered at wavelengths λ_0/m , where m is the order number. An analysis of the transmission properties of such a filter leads to the well-known Airy formula (ref. 10) plotted in figure 2 for various values of reflectance, R , as a function of wavelength. In figure 2, it is assumed that the absorption, A , of the films, B_1 and B_2 , is zero. Analysis of these results shows that, as R increases, (1) the bandwidth (spectral width at the half-intensity value) decreases, and (2) the contrast (maximum transmittance/minimum transmittance) increases. If there is absorption in the films, the peak transmission of the

filter is decreased although the general shape of the transmission curve is unaffected (ref. 10). In practice there is generally a trade-off between bandwidth and peak transmittance.

As previously noted, each of the reflecting films is generally one of the following types: (1) a semitransparent metal film, silver in the visible and aluminum in the ultraviolet or (2) a stack of dielectric layers, alternately high- and low-index of refraction, each of which has an optical thickness of $\lambda_0/4$, as shown in figure 3. The main problem in fabricating a dielectric stack for the ultraviolet is in the choice of materials. From the near ultraviolet to well into the infrared (about 20 microns) there are dielectrics with negligible

An ADI filter has the advantages of narrow bandwidth and high peak transmission but the disadvantage of high-transmission sidebands on either side of the peak. This is a consequence of an ADI stack having a high reflectance over a relatively small spectral range (normally a few hundred angstroms) centered on the peak wavelength. Elimination of the long-wave sideband in an ADI filter is difficult although the short-wave sideband is easily eliminated by proper choice of substrate material.

The MDM filter, by comparison, has a larger bandwidth with a lower peak transmission, a consequence of the metallic absorption. It has the advantage, however, that the aluminum has high reflectance at longer wavelengths and hence the filter is self-blocking (no long-wave sidebands). A typical ADI filter of the type shown has a first-order bandwidth of one to two percent of the peak wavelength, depending on the number of layers, with a peak transmission of greater than 0.60. A typical 3MDM filter with aluminum films has a first-order bandwidth of about 8 to 10 percent of the peak wavelength for a peak transmission of 0.25-0.30 (ref. 1). The bandwidth of an MDM filter can be decreased by using a thicker spacer layer and a higher order of interference; this, however, is at the expense of long-wave blocking because transmission peaks would be present at longer wavelengths.

Hence, for wavelengths longer than 2400 angstroms, either MDM or ADI filters can be made with a transmission peak at a specified wavelength, provided that auxiliary blocking is used with the ADI type. For shorter wavelengths, MDM filters must be used because there are no suitable high-index dielectrics, needed to make the ADI stacks.

Examination of the optical properties of aluminum suggests that MDM filters are feasible to 1500 angstroms and possibly to 1200 angstroms. Because, however, of the decreasing reflectance of aluminum toward shorter wavelengths and because of the increasing absorption, it is found that the first-order bandwidths are larger for shorter wavelengths. At a peak transmission of 0.25

at 1300 angstroms, the computed bandwidth is about 300 angstroms (20 to 25 percent of the peak wavelength), a value in reasonable agreement with experiment (ref. 4).

Multiple Stack Filters

Although the results to date indicate that 3MDM filters are feasible in the far ultraviolet, their usefulness is limited because of the long transmission "wing" on the main transmission peak. Attempts to obtain filters with greatly suppressed wings, and more nearly rectangular bandpasses, have resulted in improved transmission characteristics. Berning and Turner (ref. 6) showed that filters of the form metal-spacer-metal-spacer-metal (5MDM) have these superior characteristics, with silver used as the metal. The center metal film in such a filter has twice the thickness as either of the outer films for best results.

Schroeder (ref. 1) investigated the properties of these multiple stack filters of the 5MDM variety with aluminum as the metal. Calculation and experiment give the following results: (1) Given the same peak transmission as a 3MDM filter, the bandwidth of a 5MDM filter is essentially the same as that of the 3MDM filter; (2) The transmission wings are considerably suppressed. A 5MDM filter with its transmission peak at 2500 angstroms has about 20 times less transmission at 4000 angstroms than a 3MDM filter (ref. 1). Figure 5 shows computed transmission curves on a semilog plot for these two types. Independent of the peak wavelength, the relative shapes of these two curves are generally as shown (ref. 1). Figure 6 shows measured transmission curves of two 5MDM filters and the long-wave wing of a 3MDM filter whose transmission peak is near 2200 angstroms. The increased wing suppression is evident. Shown in figure 7 are the same curves on a linear plot (ref. 1).

In addition to wing suppression, it is possible to decrease the bandwidth of a 5MDM filter if one of the spacers is of first-order thickness and the other spacer is of

second-order thickness for the same wavelength. Computed characteristics of such a filter are shown in figure 8 for a peak wavelength of 2200 angstroms. Although there is now a long-wavelength peak at twice this wavelength, its peak transmission is down about a factor of 100 as compared to the main peak. Since the bandwidth is inversely proportional to the order number, bandwidths of about five percent of the peak wavelength are possible with a combined first- and second-order filter of this type.

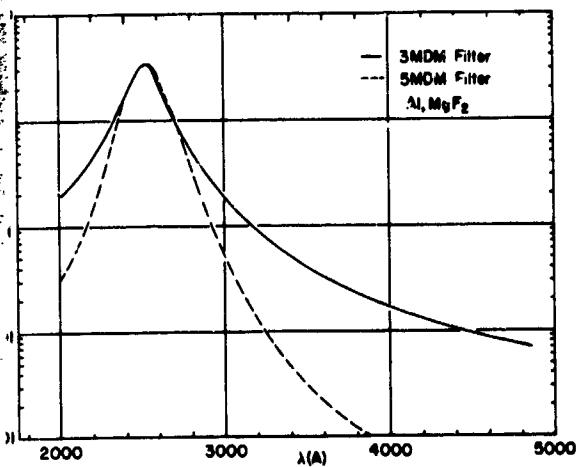


Figure 5. Transmission curves for 3MDM and 5MDM filters.

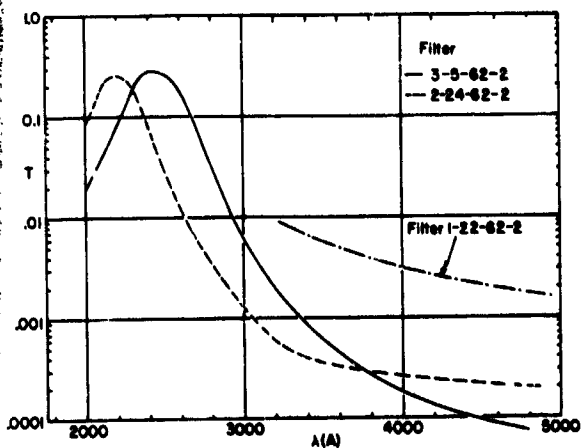


Figure 6. Transmission curves of two 5MDM filters and long-wave wing of 3MDM filter.

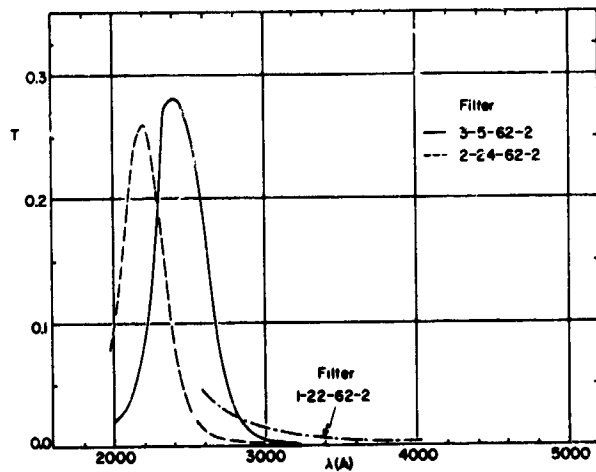


Figure 7. Linear plot of transmission curves (shown in figure 6) of two 5MDM filters and long-wave wing of 3MDM filter.

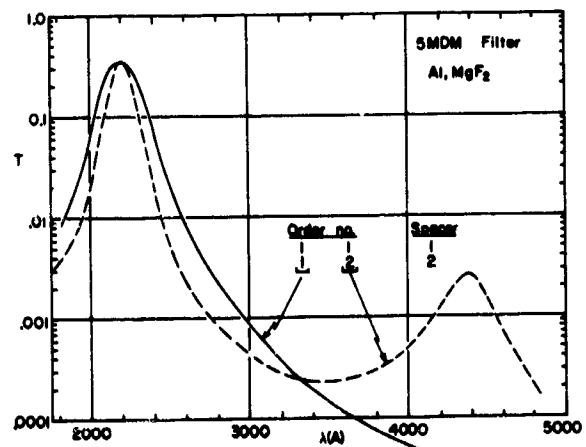


Figure 8. Computed characteristics of 5MDM having one spacer of first-order thickness and the other spacer of second-order thickness for a peak wavelength of 2200 angstroms.

Spacerless Filter

The 5MDM filter is an example of a "spacerless" filter in the sense that the center layer is not a half-wave dielectric but an absorbing metal film. Properties of such filters were investigated in detail by Berning and Turner (ref. 6), who considered the following design: dielectric stack, metal, dielectric

stack. In such a design, the dielectric stack essentially replaces the outer metal films of the SMDM type. This type of single metal layer (IM) filter is essentially a metal film anti-reflected on both sides by dielectric stacks. Such a IM filter can have a narrower first-order bandwidth than an MDM filter and a higher peak transmission. At the same time, the filter is self-blocking at longer wavelengths because of the metal film although not as effective as with a SMDM filter.

An example of an ultraviolet IM filter is one designed by Baumeister, Costich, and Pieper (ref. 7) with a transmission peak at 2600 angstroms. Using thorium fluoride and cryolite as high- and low-index materials, respectively, they made a filter with a peak transmission of 0.55 and a bandwidth of 65 angstroms (2.5 percent of the peak wavelength). With lead fluoride in place of thorium fluoride and with a thicker aluminum film, they obtained a IM filter with a peak transmission of 0.20 and a bandwidth of 55 angstroms at the same peak wavelength (ref. 7). Both filters had a ratio of peak transmission to transmission at longer wavelengths of better than 10 to 1. The designers concluded that with two such filters in series it is possible to obtain a peak transmission of 0.25 and a rejection at all other wavelengths away from the peak of better than 100 to 1 (ref. 7). Filters of this type require transparent high- and low-index materials and at the present time can be made only for wavelengths longer than 2400 angstroms. The SMDM filters, on the other hand, require only a single low-index dielectric and are suitable for shorter wavelengths.

Double Half-Wave System

Another type of filter with better bandpass characteristics than the conventional ADI filter is the double half-wave (DHW) system first investigated by Smith (ref. 11). Such a filter has the following design: dielectric stack, spacer, dielectric stack, spacer, dielectric stack. A filter of this type has a more rectangular bandpass than an ADI filter and, depending on the particular arrangement of

the layers, either a single or double transmission peak. As with an ADI filter, there is, however, the problem of transmission sidebands. To my knowledge, there have been no reports of filters of this type in the near ultraviolet although they should be feasible to the transmission limit of lead fluoride.

Broadband Reflectance Filters

Recent work on broadband reflectance filters for the ultraviolet has been reported (ref. 9). In place of the usual dielectric-protected aluminum-coated mirror (ref. 12), a film combination having a selective spectral reflectivity is used. The design is substrate, opaque metal, dielectric, semitransparent metal with aluminum and magnesium fluoride as the materials. Reflectance filters with high peak reflectance in the 2000-angstrom range have been made (ref. 9). These filters could be used to discriminate against unwanted transmission filter sidebands. It is also possible that two different reflectance filters in series could provide an adequate passband without any additional transmission filters. For example, a filter with a first-order reflection peak at some ultraviolet wavelength in series with a filter having a second-order reflection peak at the same wavelength could be considered.

Filters for Infrared Region

The infrared spectral region from 1 to 20 microns has barely been mentioned in the preceding discussion. In this range, most of the filter types considered can be and have been made. Transmission filters of the ADI or DHW variety with bandwidths of one to ten percent of the peak wavelength and good peak transmission are commercially available. This is a result of the availability of transparent high-index materials that can be deposited by vacuum deposition. At still longer wavelengths, there are problems because of mechanical stresses in the thick, evaporated layers.

Neugebauer (ref. 13) has suggested that the infrared beyond 50 microns is of particular interest to astronomers. Although the

basic principles of interference-filter design remain the same, the techniques by which filters are made are quite different. For wavelengths from 50 microns to 0.3 millimeters, Ulrich (ref. 14) has made bandpass, low-pass, and high-pass filters by spacing metal grids by mechanical means. Because of the construction method, the shorter wavelength filters within this range are more difficult to make. It is worth noting that multiple stacks of metal grids give better bandpass characteristics than a simple Fabry-Perot type of arrangement in the same way that a 5MDM filter in the ultraviolet is better than a 3MDM filter. For these filters, both the fabrication techniques and the best forms for the metal grids are under investigation (ref. 14).

Future Development

There are several directions for future development in the design and manufacture of ultraviolet filters. It is well-known that the highest reflectance film in the 1000-to-2000-angstrom range is rapidly deposited aluminum that is overcoated with magnesium fluoride (ref. 12). The rapid deposition in a system at 10^{-5} torr and the overcoat are necessary to prevent the formation of a thin oxide film, which reduces the reflectance in this range. In the manufacture of MDM filters, rapid deposition of aluminum films of controlled thickness requires automatic monitoring control (ref. 3). It is likely that oxide-free aluminum films can be produced at slower deposition rates if the evaporation chamber pressure is 10^{-7} torr or lower. If experimentation shows that this is the case, the thickness control of the aluminum films becomes less difficult. Further development is needed along these lines.

Continued investigation of the properties of multiple stack filters in the 1200-to-1800-angstrom range is needed, such as on 5MDM filters having different combinations of transmission orders. With the evaporation and

control conditions as noted above, the properties of 7MDM filters should be investigated. Calculations suggest that such a filter has the same general bandpass shape as a 5MDM filter but with still greater suppression of the wings near the transmission peak.

ADI or DHW filters are possibilities at wavelengths shorter than 2400 angstroms only if some one high-index, dielectric material transparent to shorter wavelengths is found. Systematic investigations (ref. 5) have thus far uncovered no such suitable material.

References

1. Schroeder, D. J.: *Journal of the Optical Society of America*, vol. 52, no. 1380, 1962.
2. Bates, B.; Bradley, D. J.: *Nature*, vol. 202, no. 579, 1964.
3. Bates, B.; Bradley, D. J.: *Applied Optics*, vol. 5, no. 971, 1966.
4. Harrison, D. H.: *Applied Optics*, vol. 7, no. 210, 1968.
5. Honcia, G.: *Dissertation*, Technical University of Berlin, 1960.
6. Berning, P. H.; Turner, A. F.: *Journal of the Optical Society of America*, vol. 47, no. 230, 1957.
7. Baumeister, P. W.; Costich, V. R.; Pieper, S. C.: *Applied Optics*, vol. 4, no. 911, 1965.
8. Hunter, W. R.; Angel, D. W.; Tousey, R.: *Applied Optics*, vol. 4, no. 891, 1965.
9. Osantowski, J. F.; Toft, A. R.: *OSA Spring Meeting*, March 1969.
10. Longhurst, R. S.: *Geometrical and Physical Optics*. Second ed., John Wiley, New York, 1967, Chapter 9.
11. Smith, S. D.: *Journal of the Optical Society of America*, vol. 48, no. 43, 1958.
12. Hass, G.; Tousey, R.: *Journal of the Optical Society of America*, vol. 49, no. 593, 1959.
13. Neugebauer, G.: *Optical Telescope Technology*. NASA Workshop.
14. Ulrich, R.: *Applied Optics*, vol. 7, no. 1987, 1968.

PRECEDING PAGE BLANK NOT FILMED.

N70-36735

The Space Radiation Environment in Low Altitude and Low Inclination Orbits

M. O. Burrell and J. W. Watts, Jr.

NASA George C. Marshall Space Flight Center

Introduction

Most of the satellites orbited from the Kennedy Space Center (KSC) at Cape Kennedy, Florida, go into 30-degree-inclination orbits because the location of KSC at approximately 30 degrees north latitude makes this the most energetically acceptable orbit. With the planning of long-duration manned flights, such as the Orbital Workshop mission, there has been some interest in the charged-particle dose rate expected in these low orbits for men and for radiation-sensitive materials such as photographic film.

Charged Particle Sources

There are three sources of charged particles in these low altitude orbits: cosmic rays, solar-flare proton events, and trapped Van Allen radiation-belt particles. The cosmic-ray dose rate is at most perhaps one or two rads per year at low latitudes and altitudes. (A rad corresponds to the deposition of 100 ergs of energy per gram of material.) Solar-flare proton events are fairly infrequent occurrences, and the earth's magnetic field provides fairly good shielding for low-altitude, low-inclination orbits against even the large ones. Most of the charged particle dose received in these orbits, therefore, will be due to trapped Van-Allen-belt electrons and protons. The proton component of the lower part of the belt is fairly stable in time, but the electron component has been decreasing in intensity ever since the artificial increase induced by the Starfish explosion in 1962. Calculations, using a projected 1968 environ-

ment determined by Vette*, show that protons will be the predominant dose-inducing particles at that time. Figure 1 shows a comparison of dose rates expected in 1968 for protons and proton-produced secondary neutrons and protons, from electrons, and from electron-produced *bremstrahlung*. The proton and electron integral energy spectra used in calculating these dose rates are shown in figures 2 and 3. (It should be pointed out that the proton environment is uncertain by a factor of two and the electron environment by a factor of four.)

Spatial Distribution of Protons

The spatial distribution of the Van Allen protons is determined by the earth's magnetic field. A distortion of the field over the South Atlantic, known as the South Atlantic Anomaly, results in a dip in the radiation belts to fairly low altitudes. It can be seen from the isoflux plot for protons over the South Atlantic (fig. 4) that the 30-degree-inclination orbits pass very near the peak of the anomaly. Both higher and lower inclination orbits are exposed to lower proton fluxes. Figure 5 shows dose rates as a function of shield thickness for several orbital inclinations in circular orbits at an altitude of 240 nautical miles. Large reductions in dose rate can be achieved if low inclination orbits are used.

*Vette, J.I., et al.: Models of the Trapped Radiation Environment, Vols. 1-3, NASA SP-3024 (1966, 1967).

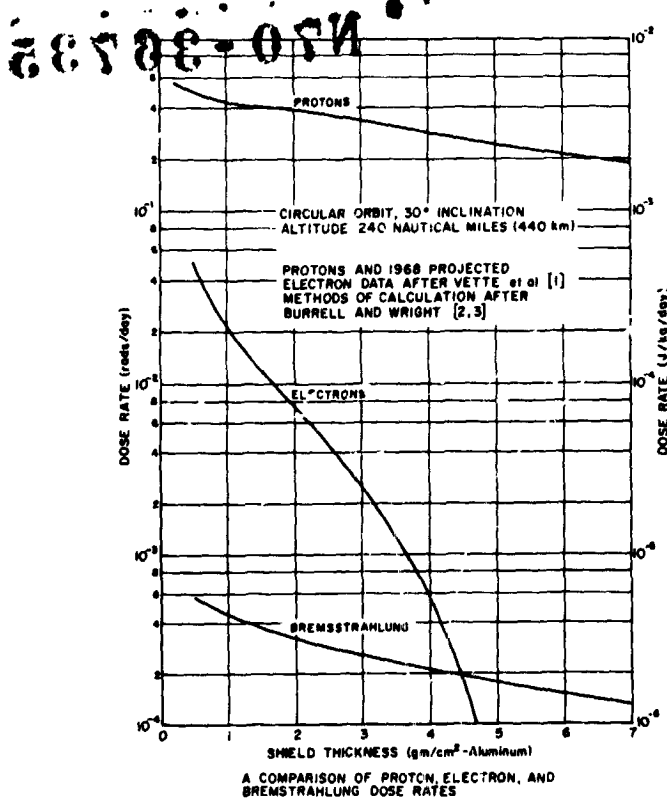


Figure 1. Comparison of proton, electron, and bremsstrahlung dose rates.

Another way of avoiding the high fluxes in the anomaly is to go to lower altitudes. Protons that mirror in the upper atmosphere are soon removed from the radiation belts so that, around an altitude of 150 nautical miles, the radiation belts have practically disappeared. The dose rate in 30-degree-inclination orbits as a function of altitude for several shield thicknesses is graphed in figure 6. Figure 7 shows the variation of proton flux as a function of time in a typical orbit. Each one of the spikes on the curve corresponds to a passage through the anomaly. It is obvious that the greater part of the radiation dose will be received during these passes. Note that there are fairly long periods of time with no anomaly passages. It would be preferable to

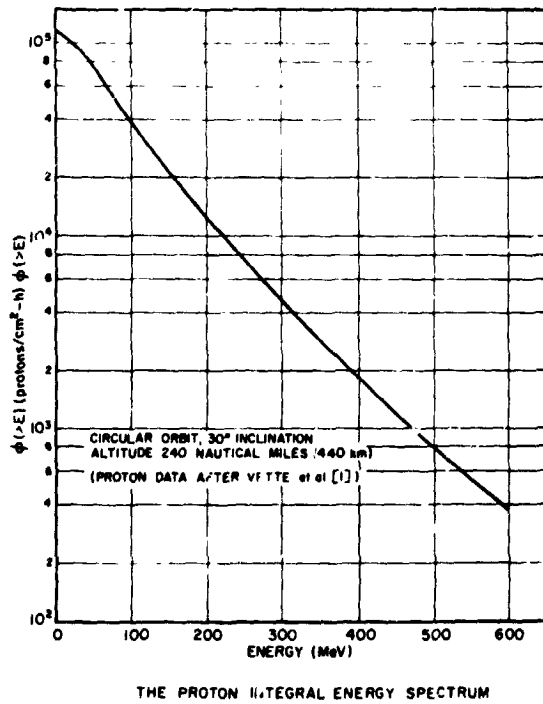


Figure 2. The proton integral energy spectrum.

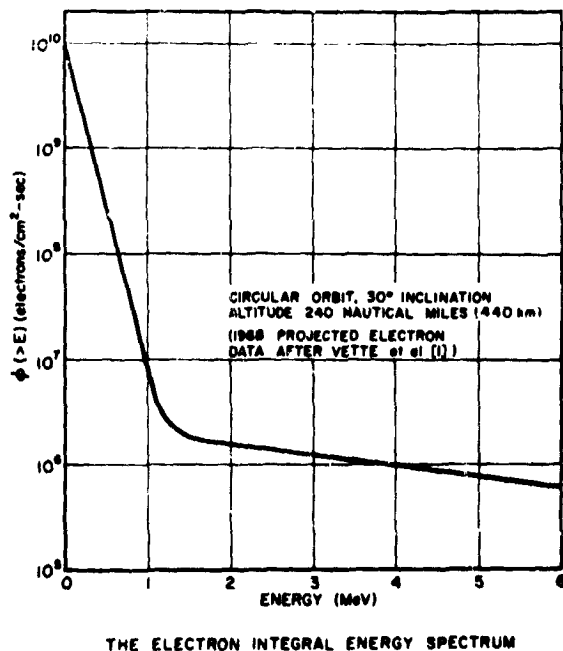


Figure 3. The electron integral energy spectrum.

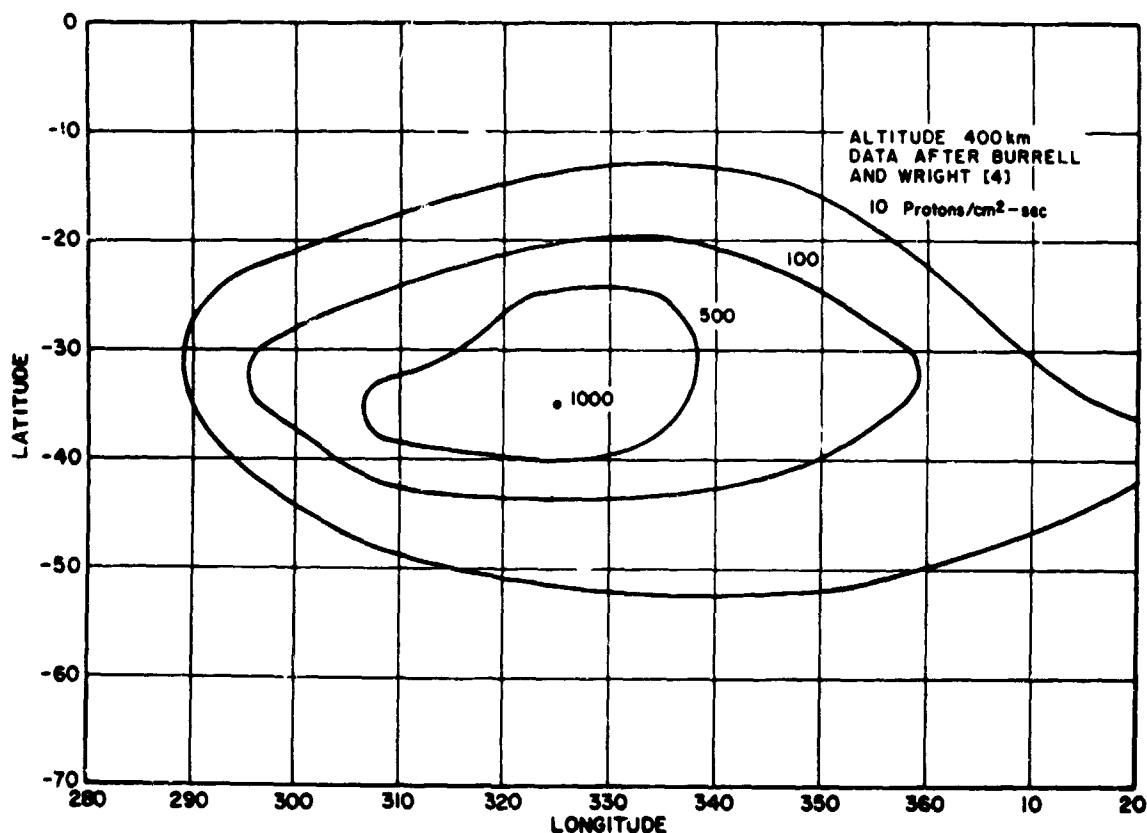


Figure 4. An isoflux plot for protons in the South Atlantic Anomaly at an altitude of 400 kilometers.

plan extravehicular activities so that they occur during these periods. The dose rate at the peak of the anomaly is compared in figure 8 with the dose rate averaged over several orbits.

Conclusions

All dose rates shown are point doses calculated for the center of a spherical aluminum shell whose thickness is given in g/cm^2 units. (The thickness in centimeters can be obtained by dividing the thickness in g/cm^2 by the material density.) This geometry was chosen because the calculation is

fairly simple and because the results obtained give some idea of dose rates to be expected in more complex geometries.

One important geometrical factor that should be considered in predicting the dose rate expected for men is the self-shielding provided by the body. A point on the chest has good shielding from radiation of about 180 degrees in space. The dose rates expected in 30-degree-inclination low-altitude orbits behind the usual shielding provided by the spacecraft (thickness $\geq 1 \text{ g/cm}^2$) will not be dangerous for men if the mission is not too extended (beyond several months). Table 1 gives the dose limits set for astronauts by the

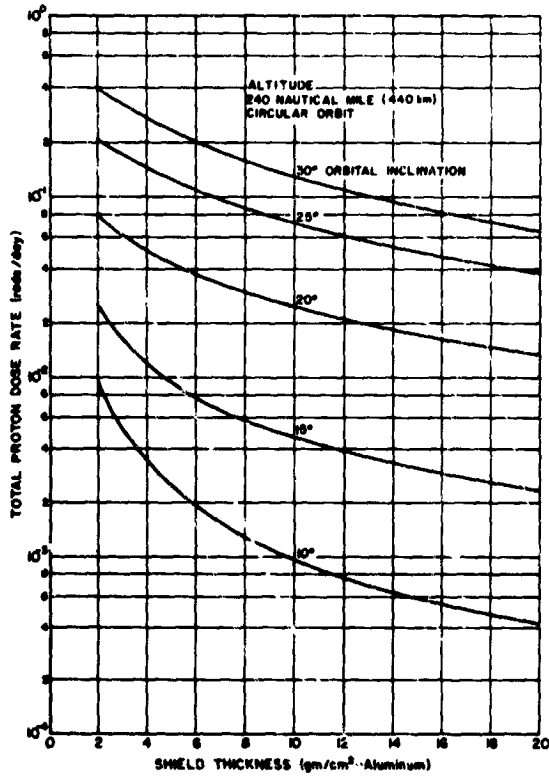


Figure 5. Proton dose rate as a function of shield thickness for several orbital inclinations.

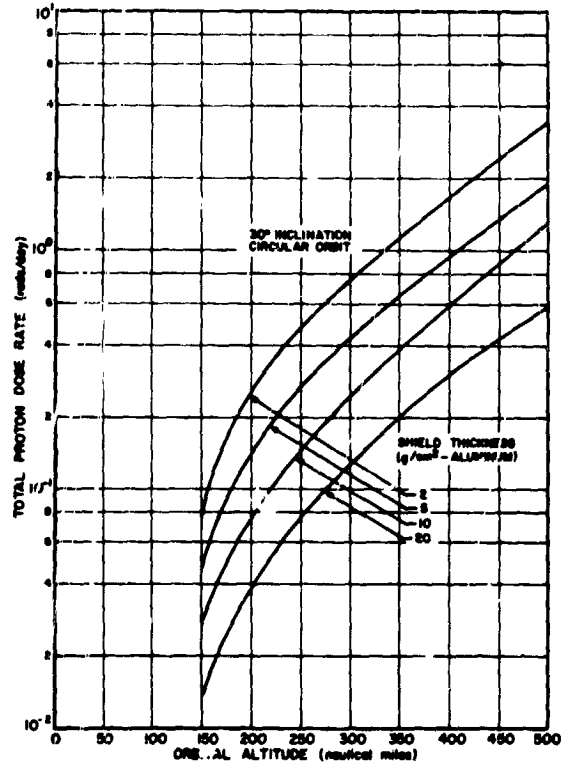


Figure 6. Proton dose rate as a function of altitude for several shield thicknesses.

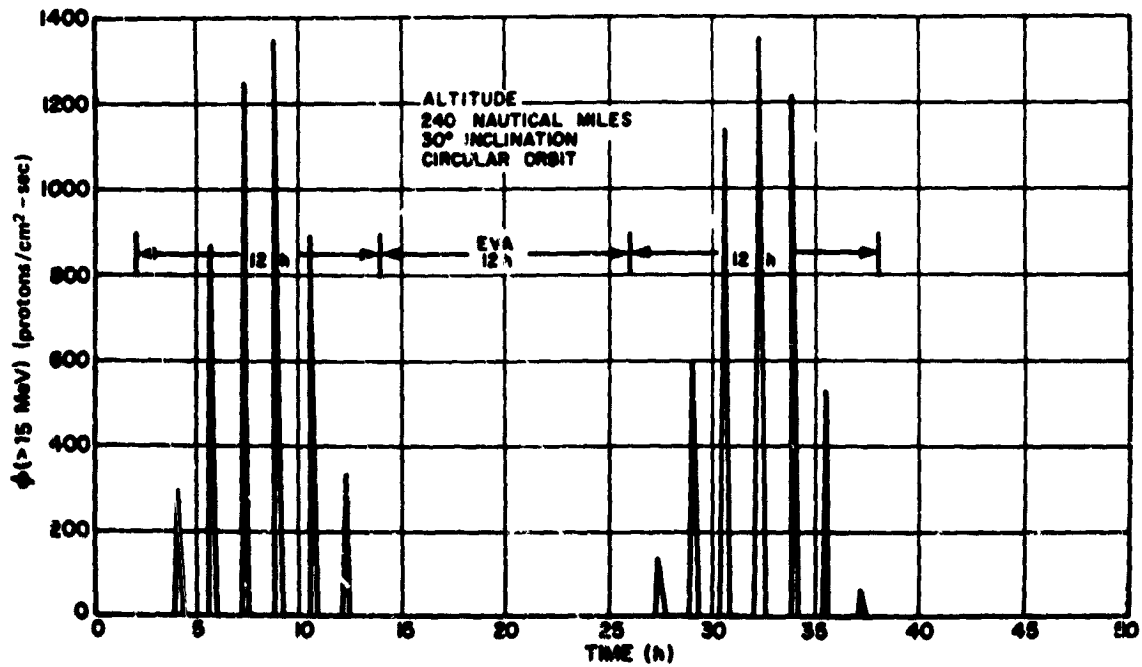


Figure 7. Proton flux integrated above 15 MeV as a function of time.

Table 1. Dose Limits for Astronauts*

Type of Response	Planned Operational Dose (rads)	Maximum Operational Dose (rads)
Gastrointestinal	13	25
Skin	100	200
Hematological	25	50
Cataracts	40	80

*From Manned Space Center Medical Office

Manned Space Center Medical Office for mission AS-503.* If it is assumed that the spacecraft has 1.0 g/cm^2 of aluminum shielding and if a correction is made for self-shielding by dividing doses by a factor of two, the expected skin dose for an astronaut on a 2-month mission is approximately 12 rads, which is well within the prescribed limits.

Possibly the most easily damaged material to be carried into space is the photographic film; some is completely fogged by doses of a few rads. Because there are many parameters associated with the exposure and development of photographic film, no common standard can be established for

*Apollo Saturn 503; Apollo 8 mission.

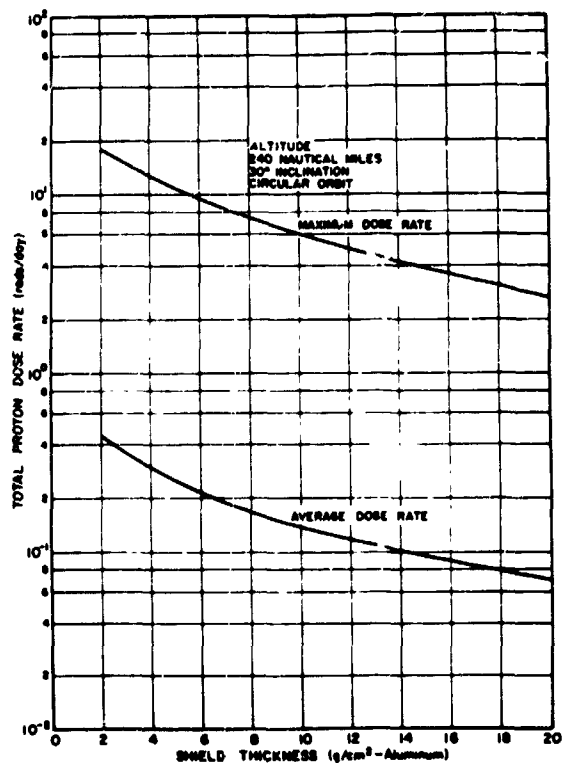


Figure 8. A comparison of the peak proton dose rate at the center of the anomaly with the dose rate averaged over several orbits.

radiation damage. The limits for acceptable radiation will have to be determined according to the specific application of the film. In general, however, some radiation shielding must be provided on long missions for most photographic film, at least while it is in storage.

PRECEDING PAGE BLANK NOT FILMED.

N70-36736

Image Converters and Image Intensifiers

Martin Rome
Weston Instruments, Inc.

Introduction

The subject of this paper is limited to tubes with radiant image outputs (that is, with phosphors) and therefore does not include electronographic devices. By definition, an image converter is an image tube in which the input and output are in different spectral bands; for example, an ultraviolet input and a visible output. It is implicit that the photon flux at the output is greater than that at the input. Thus, an image intensifier is an image tube in which the wavelengths of both input and output radiation are substantially the same. Its primary function is to provide intensification or gain. The discussion in this paper will be focused on the properties of single-stage and multistage tubes, such as gain and resolution, and some of the tube elements, with particular emphasis on photocathodes.

There are three basic types of single-stage image tubes, shown in figure 1.

1. The *proximity focus* is the simplest of the three and, as the name implies, depends on plane-parallel, phosphor photocathodes in close proximity. Because both gain and resolution in proximity tubes are limited, this type of image tube is not in general use in the simple form shown in figure 1. It does have application in more advanced development devices.

2. The *electrostatic inverter* can tolerate a much higher voltage than the proximity design and thus is capable of higher gain. Its center resolution is generally quite good; it does not require a highly regulated power supply and can be used in lightweight assemblies. On the other hand, it is subject to

off-axis distortion and loss in resolution. Furthermore, the photocathode and often the anode surfaces are curved; this complicates cascading although coupling can be accomplished with fiber optic plates.

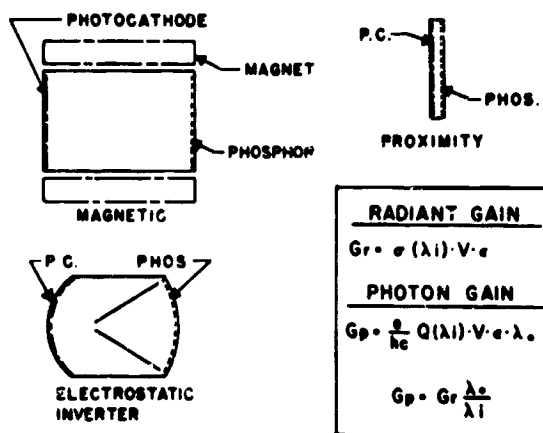


Figure 1. Single-stage image tubes.

3. *Magnetic image-tube* assemblies are heavy because of the magnet associated with the tube, and the power supply must be very well stabilized in order to maintain focus. Its resolution capability, however, is very good, and the uniformity of resolution across the output image can be maintained. The focal surfaces are all planar, which assists in cascading.

Photocathodes

Photocathodes can be discussed in terms of spectral response and dark current.

Spectral Response

The photocathode, which almost invariably is a semitransparent type (the exceptions being in the specialized reflective type of tubes not shown here), determines such basic parameters as spectral response, detection efficiency, and contrast at low light levels. Many window-photocathode combinations are possible. The spectral response curves of some representative combinations are shown in figure 2, to which the following refer.

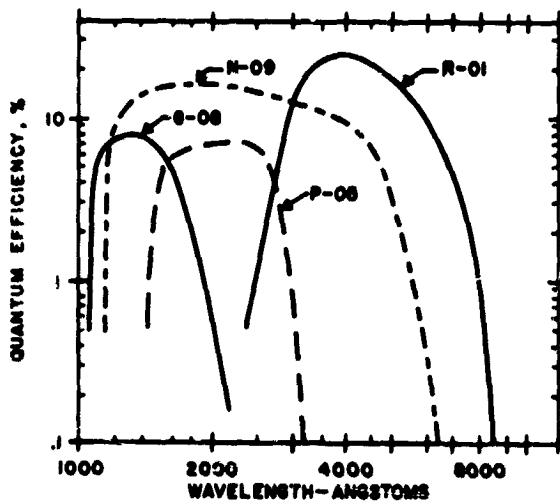


Figure 2. Spectral response for several photocathode-faceplate combinations.

1. The curve labeled G-08 is for image converters with selective response in the far ultraviolet. The photocathode is cesium iodide on a lithium-fluoride window substrate. As is the general case, the spectral response range is determined at the short wavelength end by the cutoff of the window material, which for lithium fluoride is at 1050 angstroms. Because of the large bandgap energy of cesium iodide, its long wavelength response is limited to about 2000 angstroms. Selective far ultraviolet photocathodes are the most efficient bandpass devices in this spectral region.

2. The solar blind surface, shown as P-05, is rubidium telluride on sapphire; it covers the range of 1425 angstroms, the

cutoff of sapphire, to 3000 angstroms. As in the case of the far ultraviolet cathode, the peak quantum efficiency is in the order of eight percent.

3. The N-09 curve of a bialkali photocathode on magnesium fluoride has a broad-band spectral response extending from the magnesium fluoride cutoff at 1130 angstroms to about 6000 angstroms. The peak quantum efficiency is of the order of 15 percent.

4. The R-01 curve represents the response of a multialkali photocathode on a glass faceplate, covering the entire visible spectrum into the near infrared. The peak quantum efficiency is about 25 percent.

Dark Current

Each photocathode type has a characteristic dark current. For the principal far ultraviolet surfaces, which, in addition to cesium iodide, include potassium bromide, copper iodide, and rubidium iodide, the dark current is generally less than 1 count/sec/cm².

For the cesium-telluride and rubidium-telluride solar blind photocathodes, the dark-current count rate at room temperature is 1 to 2 counts/sec/cm². In visible-sensitive photocathodes, the dark current is thermionic in nature. For the bialkali photocathode, the room temperature rate is less than 20 counts/sec/cm². In the case of trialkali photocathodes, a single figure for thermionic dark current is inadequate because it varies so widely between cathodes of the same nominal composition. Dark current is a function of the long wavelength response, which, in trialkali photocathodes, is dependent upon the method of fabrication. The variation in long wavelength sensitivity of trialkali photocathodes is shown in figure 3 for a group of photosurfaces, all having essentially the same blue sensitivity. The general shape of the spectral response at the cutoff is the same; that is, the slope of quantum efficiency with photon energy in electron volts is constant.

The long wavelength response of each photosurface may be characterized by its photoelectric threshold, which is taken as the wavelength where the quantum efficiency is

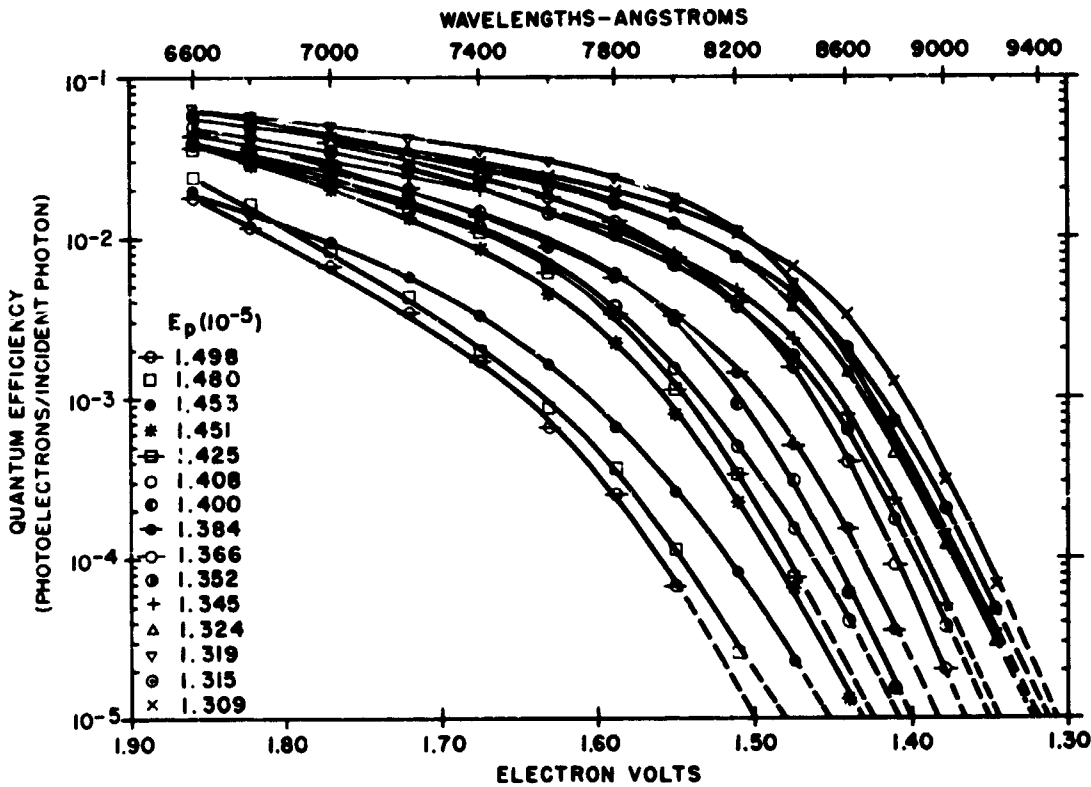


Figure 3. Long wavelength response for a variety of trialkali photocathodes.

equal to 10^{-5} . These data are shown in electron volts for the individual photosurfaces in figure 3. The photoelectric threshold covers the range of 1.309 to 1.498 volts, which is approximately equivalent to 8200 to 9400 angstroms. The room temperature dark current (in counts/sec/cm²) for each of the photosurfaces is plotted in figure 4 as a function of the photoelectric threshold of the surface. The strong dependence of dark current on long wavelength cutoff is evident; the dark current increased by more than a factor of ten for a decrease of less than 0.1 electron volt in photoelectric threshold. Therefore, trialkali photocathodes can be said to have thermionic-dark-current count rates up to several thousand per second per centimeter squared at 20°C for surfaces with high red response.

Trialkali photocathode dark current is dependent on red response but not on its blue sensitivity; this can be seen from the curves of

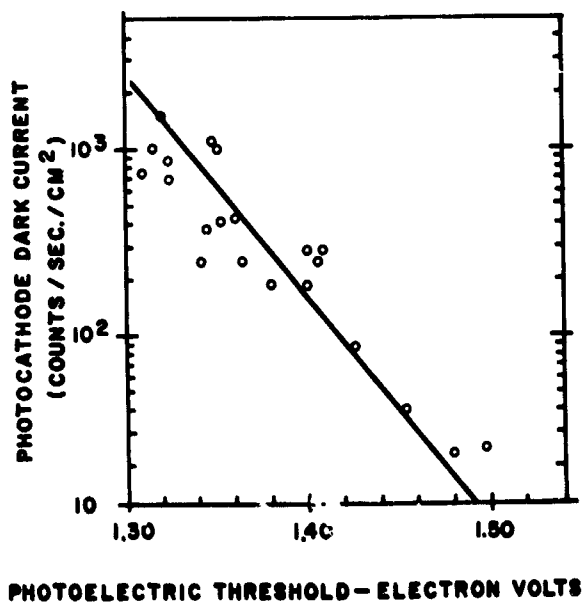


Figure 4. Dark current of trialkali photocathodes as a function of photoelectric threshold at 20°C.

noise equivalent input (figure 5). The curves are presented as a function of wavelength for six surfaces (cathode area = 5 cm²) with different photoelectric thresholds. For incident radiation of 4100 angstroms, the noise equivalent input for the photocathode with the least red response ($E_p = 1.480$ electron volts) is 3×10^{-17} watt, a factor of five less than that of the highest red response ($E_p = 1.309$ electron volts) surface. Quite interestingly for incident radiation around 7000 angstroms, the noise equivalent input for all six surfaces is nearly the same, about 5×10^{-16} watt. Farther out toward longer wavelengths, the high red response surfaces become the much better choice; the noise equivalent inputs beyond 8000 angstroms are orders of magnitude

lower than the surfaces with less dark current but reduced red sensitivity. The conclusion to be drawn for optimum performance at very low light levels is that a photocathode with no more red response than is required should be used. When working beyond 7400 angstroms, however, the greater the red response the better, for the increased sensitivity more than makes up for the noise of the increased dark current.

Thermionic dark current can be reduced by cooling. Figure 6 shows dark current in counts/sec/cm² for a trialkali cathode as a function of temperature. The slope is constant above 0°C with the dark current doubling for approximately every 5-degree increase. The significant region is at low

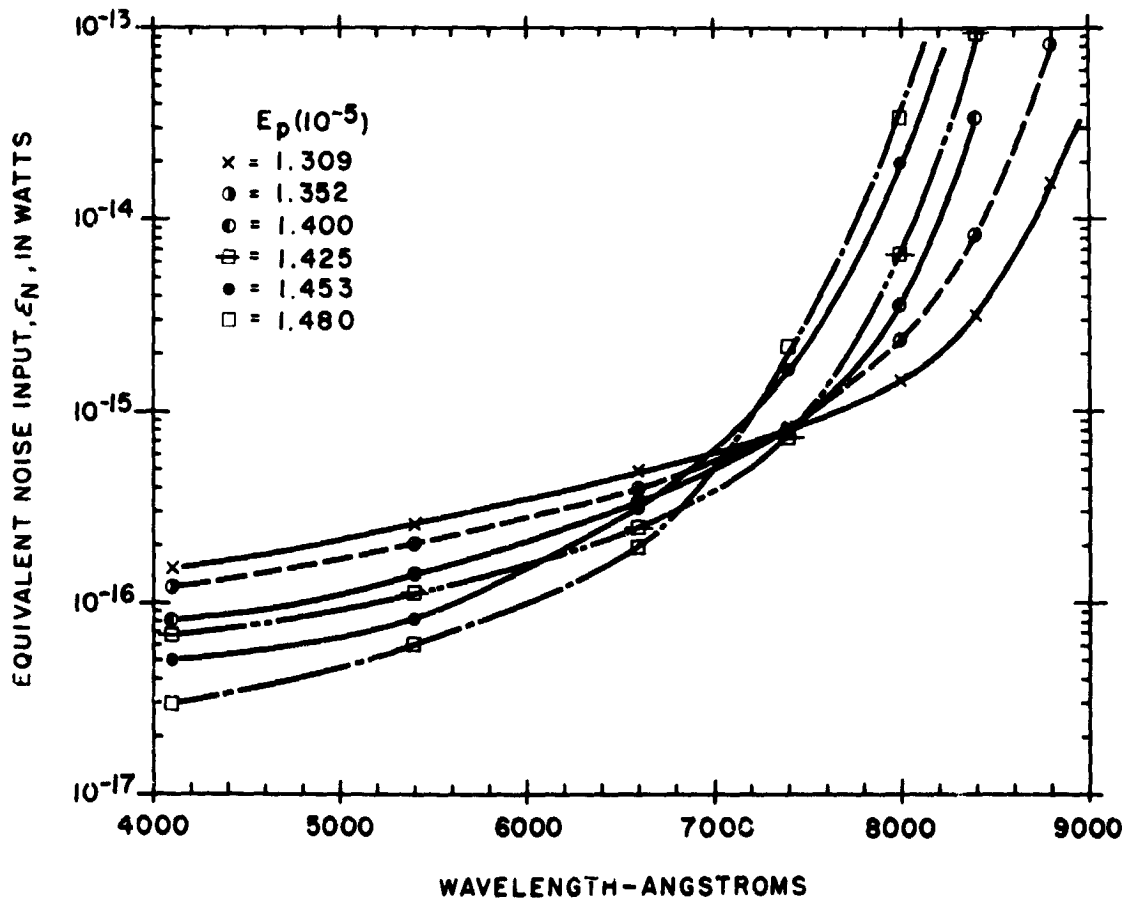


Figure 5. Noise equivalent input at 20°C as a function of wavelength for trialkali photocathodes with different photoelectric thresholds.

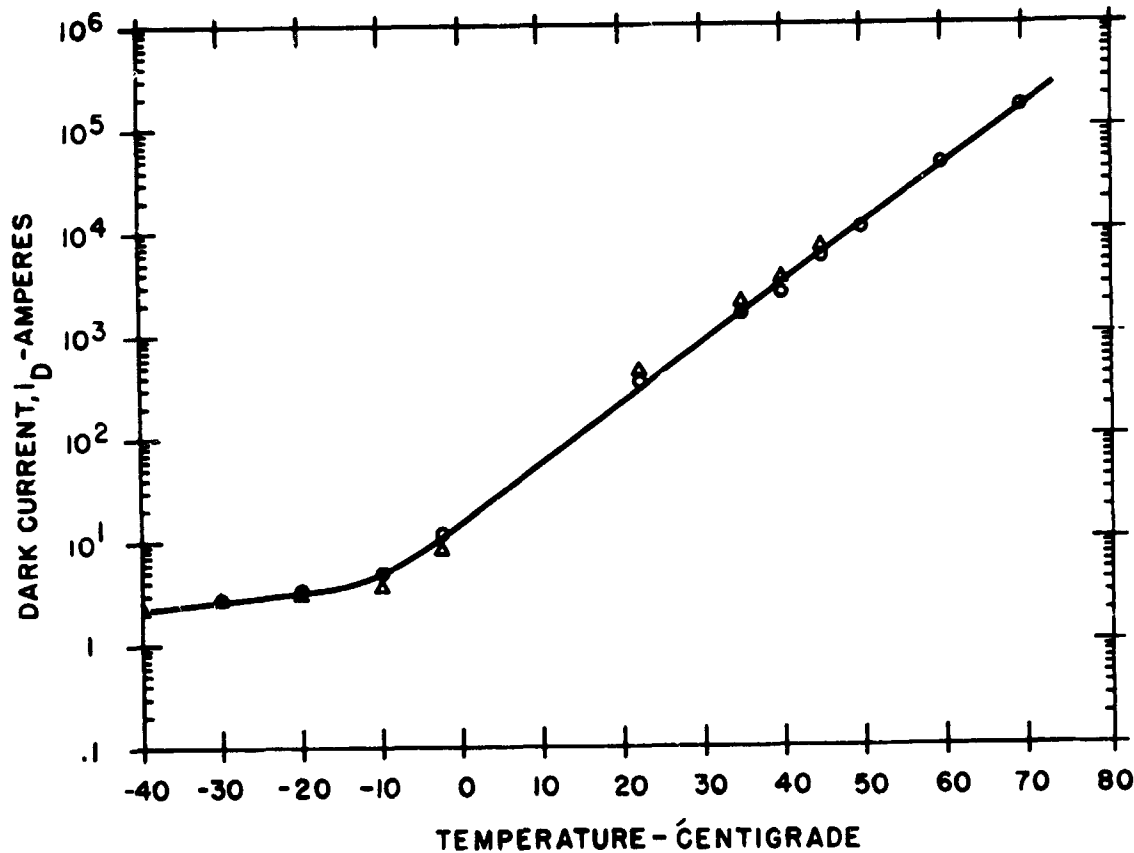


Figure 6. Anode dark current as a function of temperature for a typical trialkali photocathode. (Δ = counts/sec/cm²; O = anode current/cm²/G)

temperatures where the dark current bottoms out; very little improvement is found by cooling much below -10°C. The leveled-off dark current, which is not thermionic, is of the order of 2 counts/sec/cm².

Phosphors

The relative spectral energy emission curves for some of the more widely used phosphors in imaging tubes is given in figure 7, to which the following refer.

1. P-16 is used only where very rapid response is required. Its efficiency is low, of the order of five percent, but its decay time is less than 0.1 microsecond.

2. P-11, which is very widely used because of its good spectral match to film and most photosurfaces, has a decay time of less

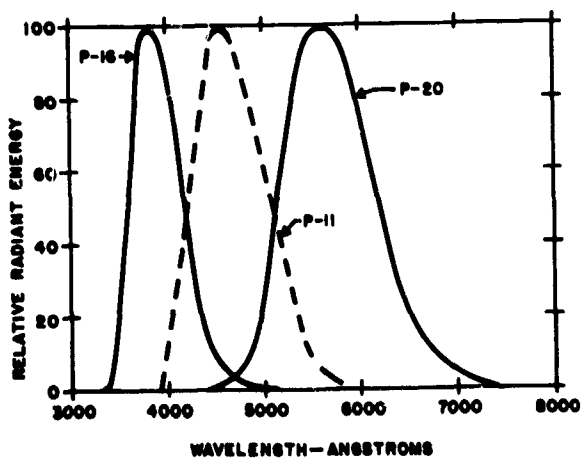


Figure 7. Spectral-energy emission characteristic of phosphors P-11, P-16, and P-20 (JEDEC).

than 100 microseconds. Its efficiency is high; intrinsic efficiencies of the order of 20 percent have been reported; however, in fine-grain high-resolution layers, the efficiency is of the order of 10 percent or less.

3. P-20 is used primarily for direct viewing because of its high luminous efficiency; its distribution closely matches the human eye response. Its absolute efficiency is fairly high, about 15 percent. A rather slow phosphor, its decay time is of the order of 1 millisecond. In all cases, phosphor efficiency is very much a function of grain size, and quite often efficiency is sacrificed for resolution.

Gain

Gain relationships can be examined in terms of single-stage image tubes and cascading tubes.

Single-Stage Image Tubes

The gain relations useful in astronomical applications of a single-stage image tube are radiant gain, G_r , and photon gain, G_p .

$$G_r = \sigma(\lambda_i) \cdot V \cdot \epsilon$$

where $\sigma(\lambda_i)$ is the photocathode sensitivity in amperes per watt at wavelength λ_i . V is the effective voltage and ϵ is the phosphor efficiency in watts per watt. The photon gain is usually expressed in terms of photocathode quantum efficiency, $Q(\lambda_i)$.

$$G_p = \frac{e}{hc} Q(\lambda_i) \cdot V \cdot \epsilon \cdot \lambda_0$$

where λ_0 is the mean wavelength of the phosphor output.

Still another gain relationship is in terms of flux density, which is the ratio of radiant emittance to irradiance. It depends upon image magnification. Flux density gain is simply

$$\frac{G_r}{m^2}$$

where m is the linear magnification of the tube.

The radiant and photon gains for single-stage image tubes with different cathodes at different wavelengths are given in table 1. The typical values of photon gain range from 45 to 50 in the ultraviolet to 100 or more in the visible. Other parameters being equal, if the quantum efficiency were constant, the photon gain would be the same throughout the spectrum.

Table 1. Radiant and Photon Gain of Single-Stage Image Tubes

Photocathode	λ_i	G_r	G_p (Typical)
Cesium Iodide	1200 Å	8 - 15	45
Rubidium Telluride	2000 Å	20 - 30	50
Multialkali	3000 Å	30 - 45	90
Multialkali	4000 Å	70-100	100

Cascaded Tubes

The gain of image tubes can be increased by cascading; that is, by coupling the output of one stage to the input of the following stage. In so doing, the match between the spectral response of the phosphor and the photocathode of the succeeding stage enters into the determination of the resultant gain (fig. 8). The spectral matching factor, M , is the integral of the product of phosphor distribution and the photocathode distribution $P(\lambda)$ and $S(\lambda)$, respectively. The factors are given for the three phosphors with two types of multialkali photocathodes, designated E and R, which differ somewhat in spectral response. P-11 and P-16, as can be seen, match well with the photocathodes; P-20 is a somewhat poorer match. λ_0 , the mean wavelength of emission, is given for the three phosphor types.

The gain relationship for cascaded tubes is the product of the gain for the individual stage, G_r , the spectral matching factor between stages, M , and the transmission of

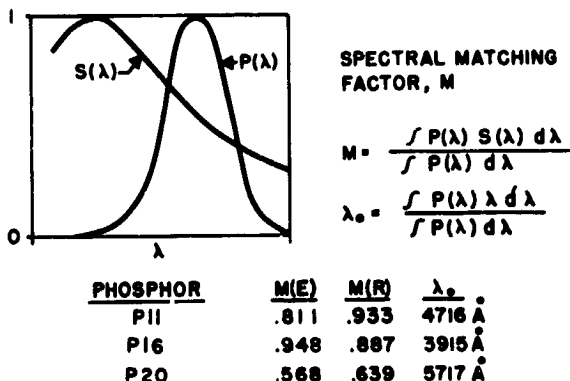
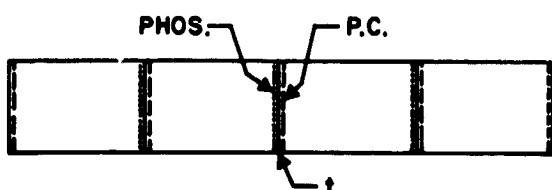


Figure 8. Spectral matching factors for P-11, P-16, and P-20 phosphors.

the coupling material, t. (See fig. 9.) For image intensifiers in which the stages are identical, the overall gain

$$G_{IT} = G_r^n (tM)^{n-1}$$

where G_r is the stage gain; however, because phosphor efficiency varies with current density, these relationships are not universally valid. At low current densities, ϵ drops. For the two-stage cascaded device, the range of photon gain is between 500 and 5000. For three stages, the gain is from 10^4 to roughly 3



$$G_{IT} = G_{r1} (t_2 M_2 G_{r2}) (t_3 M_3 G_{r3})$$

$$G_{IT} = G_r^n (tM)^{n-1} \quad G_p = G_r \frac{\lambda_0}{\lambda_1}$$

No. OF STAGES	PHOTON GAIN G_p
2	500 - 5000
3	$10^4 - 3 \times 10^5$
4	$\sim 10^6$

Figure 9. Photon gain of multi-stage image tubes.

$\times 10^5$. For four-stage tubes, gains of several million are feasible.

Coupling between stages of electrostatic inverter tubes is by means of shaped fiber-optic plates. For magnetic tubes, because the focal surfaces are planar, either thin membranes of glass or mica (usually mica) or fiber optics may be used. The resolution of a fiber-optic coupling plate is shown in figure 10 in terms of its modulation transfer function (MTF). For the fiber-optic plate containing 6-micron diameter fibers, the lambertian or diffuse resolution has a limiting value of about 115 line pairs per millimeter. If the exit angle is coned down, such as occurs when viewing with a lower numerical aperture, the resolution is improved. The curve is for a plate with EMA (interstitial absorber), which improves contrast by cutting down crosstalk between fibers. The numerical aperture is a nominal figure computed from the indices of refraction of the core and glass cladding. In practice, NA 1.0 fiber optics have lambertian transmission of the order of 0.6 to 0.7. For a mica sheet to have an equivalent MTF, it would have to be of the order of 7 microns thick. In practice, mica couplers of this thickness and less have been used. The transmission factor for mica sheet is close to unity; however, the fragility of mica couplers precludes their application in flight hardware.

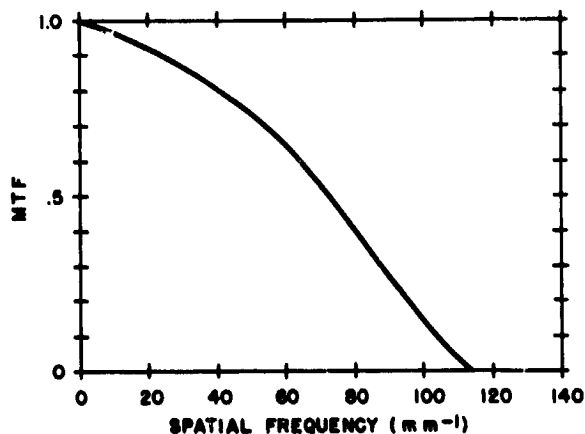


Figure 10. Modulation transfer function of fiber optic plate, N.A. 0.98 with EMA fiber diameter=6μ (Kapany).

Resolution

The resolution of a single-stage and a three-stage cascaded tube is shown as the MTF (fig. 11). The single-stage tube is an ultraviolet image converter with photon gain of the order of 50. The three-stage tube is an electrostatic tube with a fiber-optic coupling. The single-stage magnetic tube has a limiting resolution of better than 80 line pairs per millimeter. The electrostatic three-stage tube, measured on axis, has a limiting resolution of better than 30 line pairs per millimeter. In general, the resolution of a single-stage magnetic tube is better than that of a single-stage electrostatic tube because higher field gradients at the cathode are possible. The lower curve is very much in keeping with that anticipated from the MTF's of the individual components.

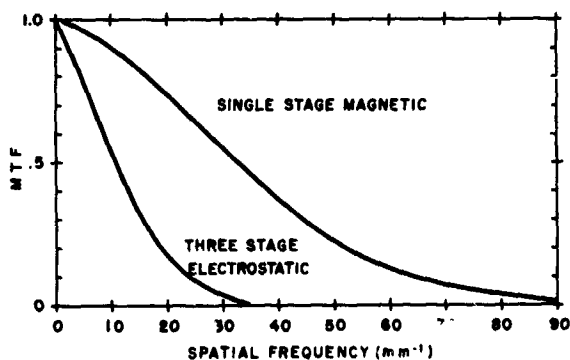


Figure 11. Modulation transfer functions for single-stage magnetic and three-stage electrostatic image tubes.

In terms of limiting resolution, some general relationship can be established among gain, the number of stages, and resolution. In figure 12, the crosshatch regions show the gain and resolution ranges for one-, two-, three-, and four-stage tubes. The solid line is not intended as a continuous function but indicates the approximate trend. The trade-offs between resolution and gain are clear; the former is sacrificed for the latter.

Secondary-Emission Intensifiers

The only means of obtaining high gain discussed thus far has been cascading. There

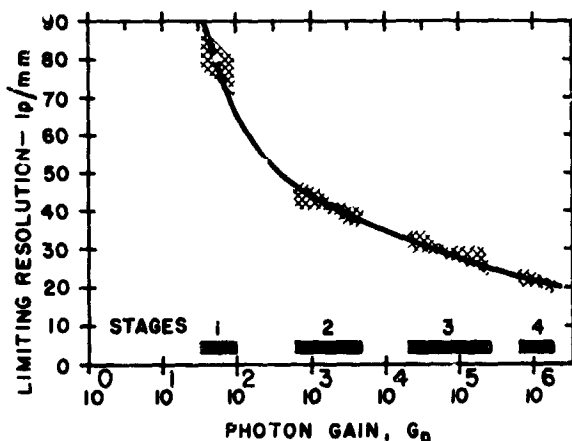


Figure 12. Limiting resolution and photon gain for one-, two-, three-, and four-stage image tubes.

are also two types of secondary-emission intensification that should be mentioned, if only briefly. The first, called transmission secondary-emission multiplication (TSEM), is embodied in a magnetic focus tube consisting of several stages of thin secondary-emitting films interspersed between photocathode and phosphor. In general, the gain-resolution performance falls on the curve shown in figure 12, but, whereas cascaded tubes have a Poisson pulse-height distribution, in TSEM's the distribution is exponential, with a resultant two-fold degradation in signal-to-noise ratio. In addition, TSEM's have a high probability of terminated events; that is, photoelectrons that do not result in output pulses. This factor is 25 percent or greater as compared to a negligible fraction for a cascaded system. An image tube development of greater significance is the channel image intensifier, which consists of a thin plate with many fine axial holes. Electrons striking the interior surfaces of the channels undergo secondary-electron-emission multiplication. The channel plate may be incorporated between cathode and phosphor in any of the three basic types described. The gain and resolution of a channel tube are such that they may fall well above the line shown in figure 12. The experience to date on channel plates also shows an exponential pulse height distribution with its attendant increase in noise factor. Intrinsically, however, the

secondary emission of reflective surfaces, as used in channels, is not exponential. At very low light levels, the saturated mode operation, possible with channels, should yield the lowest noise figure.

Summary

In summary, a variety of image intensifiers and image converters have been dis-

cussed. There is a fairly substantial array of devices currently available and under development; the best choice of device is very much dependent upon the specific application. With the advent of continuing research and development, there is promise for improvement in the important resolution-gain characteristics.

PRECEDING PAGE BLANK NOT FILMED.

Electronography

N70-36737

James A. Hall

Westinghouse Aerospace Division

Introduction

Extreme requirements occasionally justify the difficulty and inconvenience of recording with electrons on a medium like photographic film within a vacuum enclosure. Among these are simultaneous requirements for high total resolution, signal-to-noise ratio, and sensitivity. Unfortunately, television techniques do not satisfy these requirements because the contrast or modulation transfer function of a television camera tube falls rapidly at higher line numbers and much of the degradation occurs at the storage target or in the scanning process. The electron-optics of the image section, however, can present a high quality image to the target or to an electron recording plate or to film.

Furthermore, if one attempts to form a very high resolution television image, one usually has to sacrifice the ability to follow rapid motion, to make some compromise between the data rate (bandwidth) of the transmission link and the speed with which one can present complete pictures. For example, it can be shown that if one wishes to double the resolution of normal television pictures in both directions, thereby doubling the number of scanning lines in the raster as well as the fineness of detail, one will need four times the datalink bandwidth, about 18 megahertz instead of the present 4.5 megahertz; and this bandwidth begins to be inconveniently large to handle although the resolution is still not really high. Therefore, when designing a system for very high resolution, one almost inevitably allows a longer time to reproduce a single picture. Unfortunately, today there is no fully satis-

factory all-electronic device that can present to the observer a high resolution picture repeated only once every few seconds. The eye is definitely not a satisfactory storage device, and displays such as long persistence cathode-ray tubes or storage display tubes fail on the grounds of poor resolution for various reasons.

Recording images directly on film with photoelectrons is attractive for extremely high resolution partly because the display of high resolution television pictures will probably require recording the image on film at the receiving location before viewing. Another reason for making a "hard copy" has to do with the limited-information-rate capability of the human observer. When viewing a scene or a picture with a large total amount of information, that is, a high resolution picture of a complex scene, the observer may require many seconds or tens of seconds to examine the picture, area by area, in order to locate and to identify small objects in the field-of-view. This time can at present be provided to the observer only by making hard copies even though this imposes a delay between picture taking and analysis. In most cases, the hard copy will have higher quality if made initially by electron exposure.

The Work of Lallémand

The astronomers, however, began to use electronography simply for its gain in sensitivity. The legitimate father of photoelectron image recording is Dr. André Lallémand, whose first papers were published in 1936 (ref. 1). Lallémand adopted this means of image recording primarily because work on

high-energy particle recording had shown that, if photoelectrons are accelerated sufficiently, each will form a developable grain or group of grains in the emulsion.

From data available in 1936, an integrated flux of approximately 10^9 photons per square centimeter were necessary to obtain a photographic density of 0.1 using traditional photography, whereas that same density could be obtained with as few as 10^5 blackened grains in the emulsion. Available photocathodes had quantum efficiencies of about 10^{-2} . Therefore, one would need 10^2 photons to get one electron and 10^5 electrons to get 10^5 blackened grains, thus requiring a total integrated flux of only 10^7 photons as compared to 10^9 for the best photographic emulsions—a sensitivity gain of 100 times. To realize this sensitivity gain, Lallémand conducted many years of careful research. The first papers reporting the results of astronomical observations, which was his objective, were published 16 years later in 1952 (ref. 2).

Lallémand found experimentally that the predicted sensitivity gain could be realized (refs. 3 and 4). First, by using a cesium-antimonide photocathode with about 6×10^{-4} -ampere-per-watt (30-microampere-per-lumen) sensitivity to I.C.I.* illuminant A, he recorded sensitivity gain in the order of 100 times as compared to the best photographic plates then used by astronomers. He was also able to use this technique with S-1 infrared-sensitive photocathodes.

Second, he could use finer grain emulsions. In general, in trying to obtain better sensitivity with classical photography, one must use emulsions with larger grain. The grain limits the detail that can be recorded without objectionable texture. Lallémand found that certain types of emulsion originally designed for nuclear track recording were very sensitive to electrons yet had a grain size competitive with all except the microfilm types of emulsions. Thus, for those emulsions, he realized not only a 100 times gain in sensitivity but also a substantial gain in resolution capability. In a sense, his gain bandwidth product was significantly larger.

* International Commission on Illumination.

Third, and very important from the astronomer's point of view, the density-versus-exposure characteristic for Ilford G5 emulsions was linear over a significant range and had no threshold. Normal photographic film has a transfer characteristic, like that shown in figure 1, so that as exposure (the product of film irradiance and exposure time) is increased at very low values, there is a toe on the transfer characteristic, a threshold region where density increases only very slowly or not at all. This means that the astronomer exposes a very faint image for a disproportionately long time to get the image above fog. He also found the fog level in these nuclear track plates was significantly lower than that found in classical photography, thereby making it easier to detect faint images.

In trying to apply his concept, Lallémand had to solve some difficult problems. The first was to get the plate into and out of the enclosure without spoiling the photocathode, and the second was how to keep the photocathode sensitive after it and the plate were in place in the electron-optical structure.

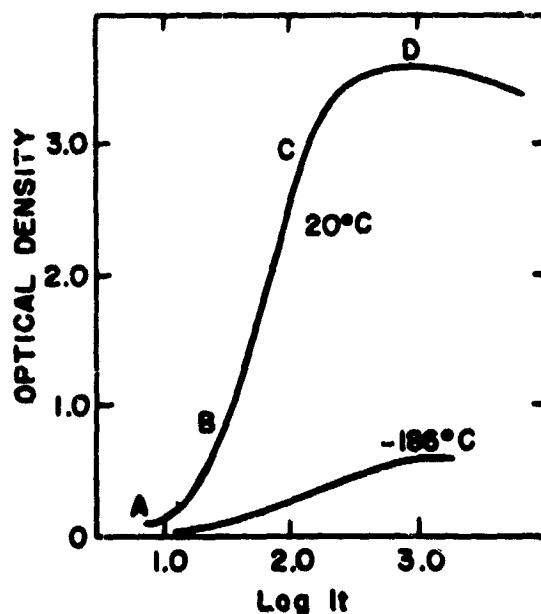


Figure 1. Density versus exposure curves for a pure AgBr emulsion exposed to room temperature and at liquid air temperature.

Figure 2 shows a cross-section of camera equipment that Lallémand was using three years ago. The electronic camera itself is in the center of the figure. The procedure was to make the photocathode (7) separately in a small, thin-walled, glass vessel (8), to introduce the assembly into the side arm (upper right) of the vacuum enclosure of the camera, which had been preevacuated and prebaked, to produce a good vacuum, and to bake again. The pumping path runs perpendicular to the diagram toward the rear, with a valve to permit disconnecting from the pumps, and is not shown to avoid complicating the diagram. At top center is a window (1), which, in this camera, was sealed in place with Apiezon wax "W." In some more recent experiments, Lallémand placed indium in a groove around the faceplate in order to make a better seal.

The electron optics is in the upper center. To lower residual vapor pressure, there is a Dewar flask (10) at the bottom for liquid-nitrogen cooling of the plate magazine (5), and a Dewar flask (not shown) at one side for liquid-nitrogen cooling of the photocathode support (2) and therefore of the photocathode, and, finally, an ingenious construction in which activated charcoal contained in

an electrode (20) is also cooled by the liquid nitrogen. After exhaust, bakeout, and refrigeration, the photocathode (7) is liberated from its ampoule (8), with the aid of a magnetic hammer (11), and is pulled into place on the support (2). The chilled, activated charcoal maintains the vacuum as the tube is valved off and detached from the pumps and mounted on the telescope for exposures.

In early experiments 15 years ago, photocathode response decayed 50 percent in an hour, but, with the arrangement shown, sensitivity is stable over a period of many hours as long as the liquid-nitrogen supply is maintained. In fact, photocathodes are now so stable that Lallémand's coworkers (refs. 5 and 6) have expanded the technique to the study of photoemission. Electronography is a worthwhile tool for this purpose because one can record individual photoelectrons and dark-current emission.

Lallemand's arrangement permitted taking eight pictures spaced on small plates mounted around the periphery of a drum. The drum was advanced by a prewound spring, using a magnetically activated escapement for each advance and a magnetically activated shutter. Electronic focus was maintained by resetting voltages with a potentiometer after an initial focusing experiment. With continuous cooling, the photocathode could be kept sensitive for more than one night of observations. When the eight exposures were completed, however, the atmosphere was readmitted for removal of the exposed plates, thus destroying the photocathode. To prepare for another run, one had to prepare another cathode in its ampoule, install it in the side arm, install new plates in the magazine, seal the enclosure, and begin again the exhaust and outgassing cycle.

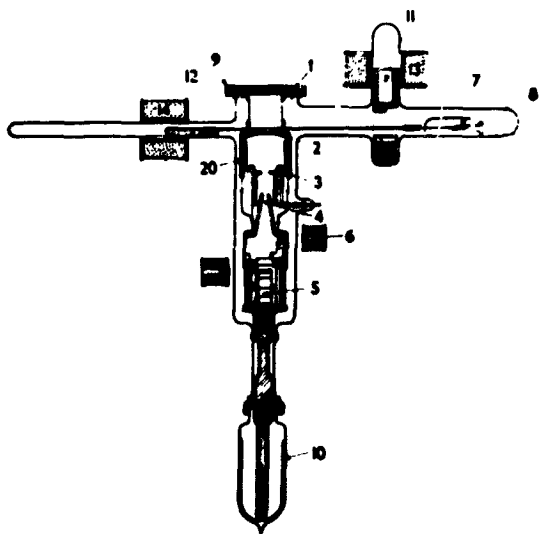


Figure 2. Cross-section of Lallémand's electronic camera.

The Work of Kron and Associates

The most significant advances in electronography in this country have been made by Dr. Gerald Kron and his associates of the Flagstaff Station of the Naval Observatory (refs. 7, 8, and 9). Their most important single contribution is the provision of a vacuum

valve in the electron-optical structure to separate the photocathode and the image-forming electrodes from the plate, the magazine, and the shutter assembly. As shown in the simplified schematic diagram of figure 3, in the electrostatic image-converter optics, there is a field-free region beyond the anode of the electron-optical system where the electrons all pass through a rather small area in space. The valve placed at this point consists simply of a copper disc that can be clamped between a pair of valve seats. The seats are parts of vacuum envelope members, which have a flexible annulus between them, with jack screws to spread them apart when the disk is moved to one side and to clamp them together when the valve is closed. A small annular volume around the valve disc is pumped continuously and provides a guard vacuum whenever the plate chamber is at higher pressure.

In operation, the valve disc is simply rolled on edge by turning the tube to open or to close it. The plate, 2-3/4 inches in

diameter, and its support may be rotated by a simple magnetic driver to make six exposures in a single loading. The magnet may be removed during each exposure to avoid interference with electron-optical fidelity. As in Lallémand's work, Kron refrigerates his magazine with a liquid-nitrogen Dewar flask; however, through use of glass-to-metal seals, a modern high-vacuum valve in the pumping line, two small ion pumps, one on the valve annulus and one on the plate chamber, plus the valve itself, he does not need to refrigerate the photocathode nor to use activated charcoal. With this scheme, Kron has been able to replace the plate many times and to use the same photocathode for as long as 15 months.

To make the cathode initially, Kron removes the magazine assembly and attaches the image section and valve assembly with its attached ion pumps to a vacuum station. After normal exhaust and baking, the coin valve being open, the photocathode is formed in place by evaporators that are easily introduced through the valve opening and the anode to the center of curvature of the cathode support. The evaporator assembly is then withdrawn; the ion pump for the guard vacuum is activated; the valve is closed; and the tube is removed from the pumping station. Then, and indeed for every replacement, the magazine assembly with a new electron-sensitive plate is mounted in place with a soft wire seal, and this chamber is evacuated through a side pumping path, not shown in the diagram. The small ion pump for the plate chamber is then activated; the valve to the processing system is closed and the system detached. To ready the tube for use, the Dewar flask is filled to chill the plate support and the plate, and the coin valve is opened.

As shown in figure 3, the resulting package is compact and relatively easy to mount on a telescope. For the last 2 or 3 years, Kron and his associates have used it to obtain astronomical data with the 61-inch telescope at the Flagstaff Station of the Naval Observatory. Some of their findings, which have instrumental importance, are given in

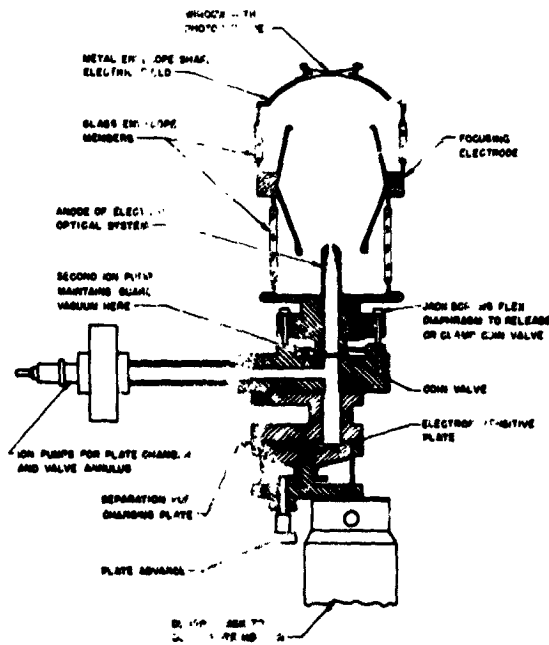


Figure 3. Schematic cross-section of U. S. Navy electronic camera.

this paper. For a discussion of their astronomical significance, one should refer to their publications (refs. 10, 11, 12, and 13). A significant qualification is that their selection of plates and techniques was directed toward the recording and photometric measurement of faint astronomical images with high signal-to-noise ratio and a wide range in a single exposure. Another set of choices might be more suitable for other applications.

Most exposures at Flagstaff have been made using Ilford L4 and K5 emulsions. As shown in figure 4, when L4 is developed for five minutes in full strength D-19 developer at 68°F, density is proportional to exposure, at least up to density 6, and is limited only by the ability to measure. The reason is probably the very fine-grain structure of this emulsion. As shown in figure 5, the grain count for a given density is far higher than for a classical photographic plate. Kron estimates a saturation density of more than 30. Theory indicates that density should be an exponential function of exposure, much like the voltage time curve for a capacitor charged through a resistor from a constant voltage source, and, for $D/D_{sat} \ll 1$, this function is approximately linear. Like Lallémand, Kron and his associates found the Ilford plates essentially free of fog.

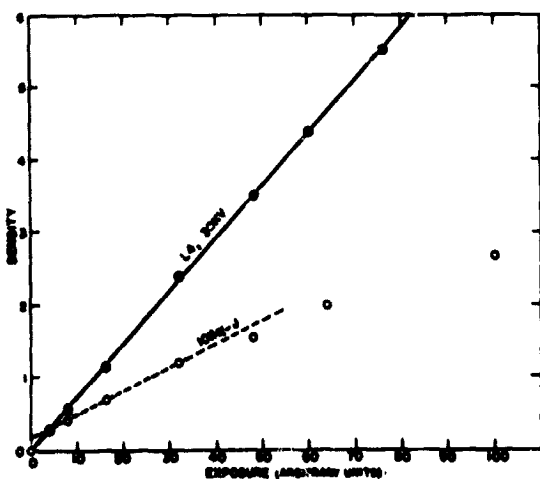


Figure 4. Density proportional to exposure for electronography with L4 emulsion.

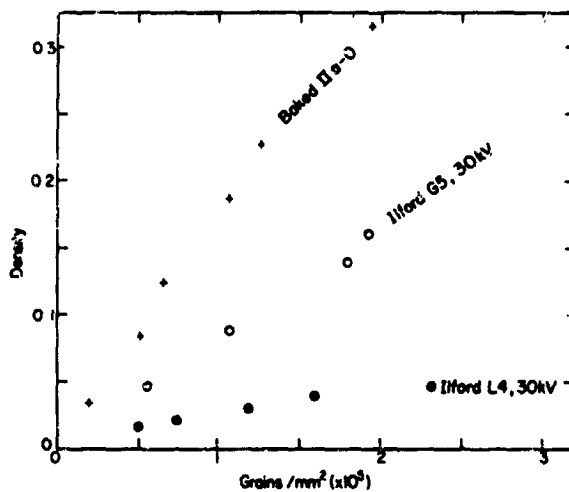


Figure 5. Grain counts for photography and electronography.

To determine an information gain with respect to classical photography (ref. 12), shown in figure 6, one must recall the application. Electronography is a perfect electro-optical imaging device in the sense that every photoelectron results in a developable grain or small group of grains in the emulsion and the information is therefore represented by counting grains in each area; the interfering fluctuations or noise is due primarily to the randomness of photoemission. From Poisson

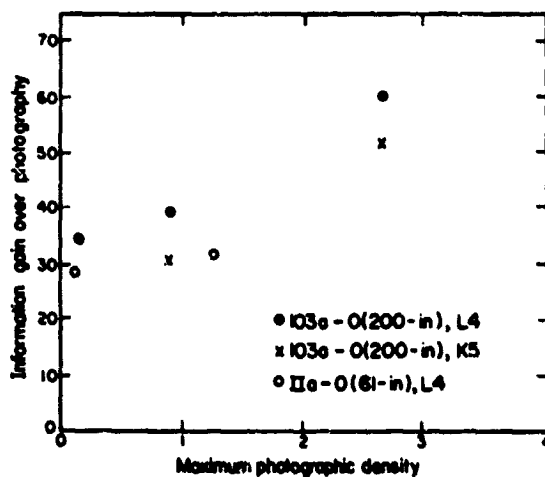
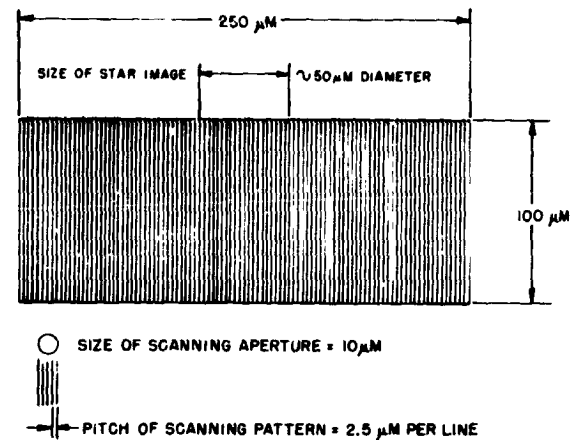


Figure 6. Information gain of electronography with respect to classical photography.

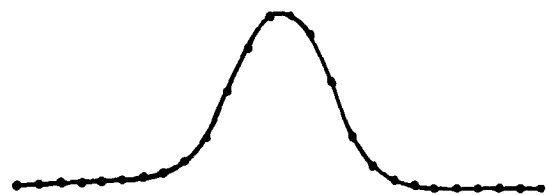
statistics, the rms value of the fluctuation for any small sampling area should be proportional to the square root of the average number of grains which would be darkened in that area during the exposure time.

Instead of counting grains directly, Kron and his associates measured density with a modified Joyce-Loebl microdensitometer. Their present practice is to scan a star image in a raster pattern, as shown in figure 7. For the optical and electron-optical system used, a typical star image has a diameter of about 50 micrometers on the plate. By scanning the region near it as well as the image itself, they obtain a good estimate of the local background. To use all the information in the star image as signal, they integrate electrically the densitometer output along each scanning line and use the output of the integrator for each line to drive a strip-chart recorder. The resulting center curve, in figure 7, is a type of intensity profile, and the area under this curve but above background is proportional to the total flux from the star. This method appears relatively independent of seeing conditions. A comparison with a single densitometer trace through the center of the star image shows a convincing gain in signal-to-noise ratio.

This method of measurement can, of course, be applied both to electronography and to classic photography. The relative merits for the two exposure methods is related to the signal-to-fluctuation ratio actually found for a given method of analysis compared to that due to the photoemission statistics. Measurements were made using a small sampling aperture in the Joyce-Loebl microdensitometer, with no integrator, to enhance the fluctuations. The fluctuation level was arbitrarily set to be the peak-to-peak fluctuation envelope amplitude, ignoring the occasional large spike. This figure is thought to be about four times the rms fluctuation value. The total area above noise under a trace was then divided by the square of the noise envelope amplitude to yield a figure of merit. The reasoning is that the rms fluctuation should have been proportional to the square root of the signal; hence, the signal equivalent to the observed noise is proportional to the



(a) Microdensitometer scanning pattern.



(b) Mean profile from integrator output for each scan, including all data in image.



(c) Profile from single scan through star image.

Figure 7. Kron-Ables method for extracting photometric information.

square of that noise. Constant factors are ignored because they are constant through the experiment. In electrical terms, the method is analogous to quoting an equivalent DC current for an emission-limited diode to characterize a noise source.

Using their method, as shown in figure 6, Kron and Ables calculate their information gain as at least 30 but comment that the eye does not notice this difference. This, in turn, is related to their use of a very fine-grain emulsion for maximum information density. The fluctuations that limit the accuracy of their measurements are very small in scale, corresponding to the high frequency noise that the eye can ignore in a television system. Their use of an integrator to improve signal-to-fluctuation ratio in the final record corresponds to the use of a low-pass filter for more accurate measurement of signal amplitude. For terrestrial uses, a greater sensitivity gain might be produced by use of a larger grained emulsion, but, for astronomy, the fine-grained L4 has permitted photometry in a single exposure over eight stellar magnitudes, a tremendous intensity range of 1500:1 with very high resolution, and an extremely large information density.

Based upon this type of analysis, Kron and Ables calculate a minimum gain in speed of information-recording of about 30. Translated into telescope terms, this means that their 61-inch telescope with an electronographic camera has the capability of a 300-inch telescope using classical photography, or that use of electronography with the Hale 200-inch telescope would give the same result as a 1000-inch instrument. Because of these results, workers in Europe and at Westinghouse in the United States are now attempting to make larger sized electronographic cameras to use more of the field-of-view available from existing telescopes.

The Work at Westinghouse

In view of the successes of Lallémand, Kron, and their astronomer colleagues, it is logical to ask whether electronography could be applied usefully to terrestrial photography where sensitivity is at a premium. Several years ago, the Photoreconnaissance Branch of the U.S. Air Force Avionics Laboratory at Wright Field initiated a program at Westinghouse to determine the feasibility of making an electronographic camera into which many

feet of 4½-inch-wide, electron-sensitive film could be introduced, exposed, and removed (ref. 14). For maximum sensitivity to natural ambient illumination, we considered use of a trialkali S-20 photocathode necessary (ref. 15), and, since the astronomical cameras used principally the less fragile S-9 photocathode and far smaller recording plates, we decided on a rather basic approach. After first developing a paper design for a complete camera to guide our investigation, we considered the possible ways of introducing and handling the recording medium and the problems we would have to solve with each.

Actual experiments fell into two main groups. First, we used a high-vacuum mass spectrometer system to measure the amounts and types of gases that would be liberated by each of the materials and components we wished to use in the camera, and we determined how pretreatment could be used to minimize or to control gas or vapor evolution. Included, of course, were vacuum lubricants, typical film-base materials, and Kodak's SO-159 electron-beam-recording film as well as metal, glass, and plastic parts. Second, we made good S-20 photocathodes and determined their sensitivity to low pressures of the pure gases found as components in the gases evolved from the materials. During the investigation, we revised the initial paper design for the camera and its method of operation whenever the experimental data indicated a serious problem.

The equipment used both for gas evolution studies and for photocathode contamination studies is shown in figure 8 and schematically in figure 9. As shown, the entire system is made of stainless steel, kovar, ceramic, and glass with O.F.H.C. copper gasket seals at all flange joints. It can be baked at temperatures to 500°C for outgassing and is evacuated by cryogenic sorption pumps or by titanium ion pumps to rule out oil-vapor contamination completely. The system is divided into individually pumped subsections by high vacuum valves so that only the immediate sample chamber need be exposed to the laboratory atmosphere when a

new sample is inserted. The mass spectrometer is a General Electric magnetic-deflection residual-gas analyzer. The ultimate background pressure in the system approached 10^{-10} torr.

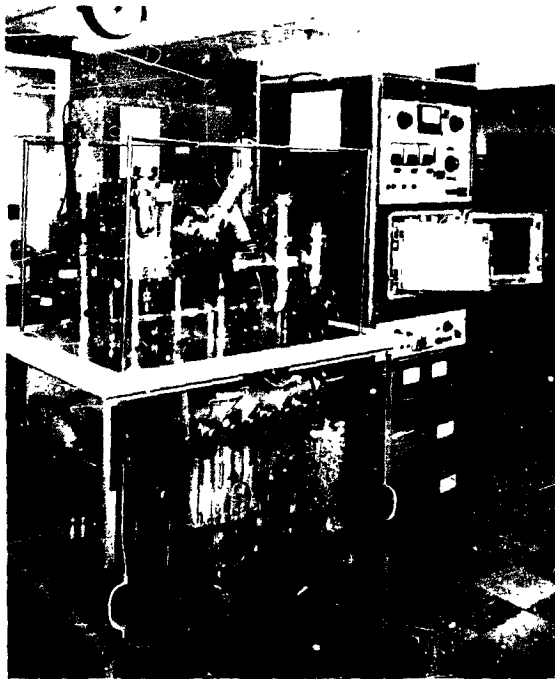


Figure 8. Vacuum system for analysis of evolved gases and their effects on photocathodes.

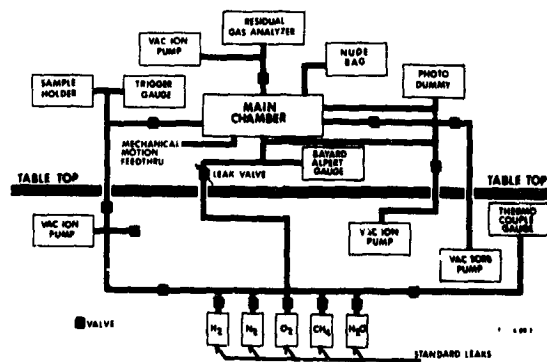


Figure 9. Simplified diagram of vacuum system used for photocathode contamination study.

For outgassing studies, samples were introduced into the sample chamber, in the upper left foreground of figure 8. Photocathodes were made in a standardized experimental tube structure mounted from the side of the sample chamber, and contaminating gases were available from the manifold, which appears beneath the table in figure 8. All gases evolved by the camera parts could be duplicated except for fluorine, which was considered too difficult to handle.

Some results of the investigation are summarized in figures 10 and 11. Most proposed camera materials could be thoroughly outgassed prior to photocathode formation and presented no problems. Experience on one of our earlier programs with Westinghouse dry-film lubricants confirmed that these materials could be treated to be compatible with a photocathode, but the film and its substrate emitted large quantities of water vapor. As shown in figures 10 and 11, a multialkali photocathode is relatively unaffected by hydrogen or nitrogen and reacts to methane and carbon monoxide between 10^{-5} and 10^{-4} torr, to oxygen between 10^{-6} and 10^{-5} torr, and to water vapor for pressures between 10^{-8} and 10^{-7} torr. Therefore, the design program was concentrated on ways to reduce the water-vapor evolution within the camera.

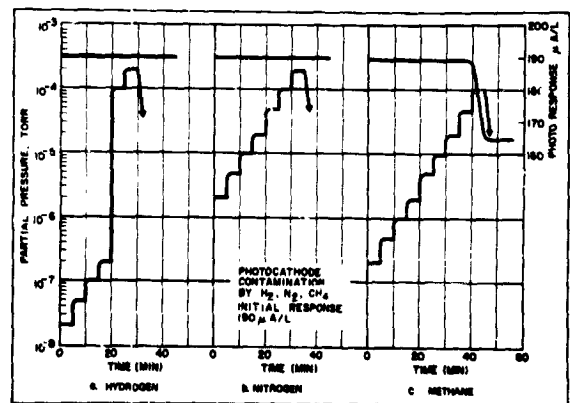


Figure 10. Reaction of hydrogen, nitrogen, and methane on a multialkali photocathode.

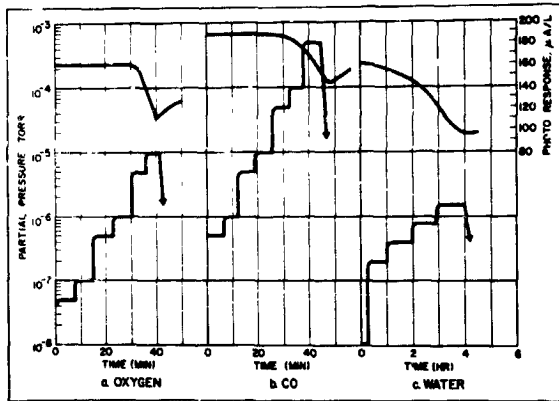


Figure 11. Reaction of oxygen, carbon monoxide, and water vapor on a multi-alkali photocathode.

The initial camera-design concept, based upon a desire to develop and to view the film soon after exposure as well as a natural tendency to parallel classical camera designs, was to store film in a magazine at atmospheric pressure, to introduce it through vacuum locks, to expose it, to retrieve it through a second set of vacuum locks, and to store it on a takeup reel in a second magazine at atmospheric pressure. For aerial photography, however, we sought to avoid the liquid-nitrogen cooling used by the astronomers. The investigation outlined above, however, appears to rule out this approach. Water-vapor partial pressure must be held below 10^{-8} torr to avoid a decay in photocathode sensitivity. In a vacuum, however, vapor is evolved from the surface of any material or component that has not been baked and from the volume of materials like a Mylar or Estar film base or a gelatin-emulsion film. In our magnetically focused structure, the film must face the photocathode with a broad direct path for vapor transfer.

We found experimentally (1) that the film and film base could be dried out considerably by storing them under vacuum for 48 hours, assisted by warming the film to 40°C to speed vapor release, but (2) that even a brief exposure to the atmosphere of an air-conditioned laboratory substantially restored its water content. Thus, batch film prepara-

tion and storage in vacuum cassettes seems required.

Based upon these and other considerations, the final camera design is like that shown in the simplified schematic of figure 12. The vacuum film cassette is in the upper part of the figure with the exposure plane in the center. Just below this is a high-vacuum gate valve with a positive mechanical actuator. The photocathode is formed on the inner surface of a window at the bottom of the camera. For optimum uniformity of focus and geometric fidelity, we chose magnetic focusing, provided by the indicated focusing coils, which were split to accommodate the valve actuator. To accommodate 100 feet of $4\frac{1}{2}$ -inch film, with a 7-inch-diameter photocathode, the unit is approximately 24 inches tall, and the body of the camera is 11 inches in diameter. At the present time, the actuator assembly extends 24 inches beyond the camera body in order to withdraw the 7-inch-diameter valve fully. The film is advanced with magnetic clutch units and is held flat on the cooled platen at the exposure position by electrostatic attraction. Continuous titanium ion and getter pumping is provided in both the film magazine and the exposure chambers with sufficient pumping impedance between them to permit maintaining a high vacuum at the photocathode. Cooling of the film before

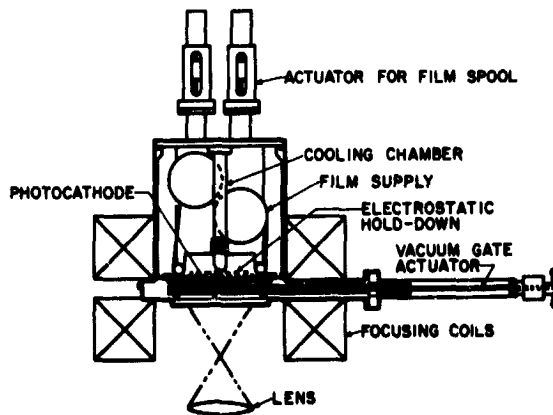


Figure 12. Simplified scale drawing of electronographic camera.

it enters the exposure chamber is also provided, but we now believe a Freon cooling unit with a small compressor for airborne use should be sufficient to provide an adequate safety factor.

The electron-optical section uses a 20- to 30-kilovolt accelerating potential, a 330-Gauss focusing field, and short length for a high field to minimize the effects of electronic "chromatic aberration"; i.e., the effects of the spread in emission velocities; it is computer-designed for a resolution of over 500 line pairs per millimeter. Since the film, the objective lens, and the image stabilization will set substantially lower limits, this design assures that the electronographic camera will not measurably degrade the system modular transfer function.

To use the camera, it is necessary to load a spare film cassette and to place it in or to seal it to a vacuum system for 48 hours (or longer pretreatment) to outgas the film. The camera proper would be sealed to a photocathode processing station, with the valve opened and exhausted, and would be baked; the photocathode would be formed; and the valve closed. Small ion pumps, built into the camera to evacuate both the exposure section and the chamber between the dual valve seats, are activated.

To avoid exposure to atmospheric moisture, both units are removed from their vacuum systems and joined together in a dry glove box, using either dry nitrogen or dried air. In such enclosures, we routinely produce a -70°C dewpoint, at which atmospheric moisture is reduced to a few parts per million and the interiors of the units may be exposed long enough to seal them together without objectionable contamination. The pumping stem on the film cassette is sealed to a local vacuum system; the cassette is evacuated; the pumping valve is closed; the holding pumps in the cassette are activated; and the camera is ready for use.

Conclusions

We conclude that such a large roll-film electronographic camera is feasible and that photocathode life should be sufficient for

many missions with the recommended operating cycle.

It should be possible, by storing spare, loaded, pretreated cassettes under vacuum or perhaps by storing batches of film under vacuum and loading cassettes in the dry box, to reload a camera in less than an hour, with much of that time taken for final exhaust of the cassette after installation.

Resolution of the complete system should be greater than that for classical photography because shorter exposure times may be combined with electronic image-motion stabilization for small-amplitude, high-frequency motions. Sensitivity gains for terrestrial use have not yet been established although Lallémand's figure of 100 times may be bettered with the availability of more sensitive photocathodes.

The same camera should also be useful for astronomical observations. The $4\frac{1}{2}$ -inch by $4\frac{1}{2}$ -inch picture size should make far more efficient use of the existing telescope fields-of-view, thus expanding significantly the usefulness of electronography.

References

1. Lallémand, A.: Application de l'Optique Électronique à la Photographie. C. R. Acad. Sci., vol. 203, no. 243, Paris, 1936.
2. Lallémand, A.; Duchesne, M.: Application à l'Astronomie d'un Récepteur Idéal de Photons. C. R. Acad. Sci., vol. 235, no. 503, Paris, 1952.
3. Lallémand, A.; Duchesne, M.; Wlerick, G.: La Photographie Électronique. Advances in Electronics and Electron Physics, Vol. XII, 1960.
4. Lallémand, A.: Quelques Réflexions sur la Caméra Électronique. Advances in Electronics and Electron Physics, Vol. XVI, 1962, p. 1.
5. Charrier, S.; Wlerick, G.: Propriétés des Photocathodes Libérées Dans un Vide Élevé. Advances in Electronics and Electron Physics, Vol. XVI, 1962, p. 5.
6. Duchesne, M.: Sur une Nouvelle Technique d'Utilisation de la Caméra Électronique. Advances in Electronics and Electron Physics, Vol. XVI, 1962, p. 19.

7. Kron, G. E.: A Modified Lallémand Image Tube. *Advances in Electronics and Electron Physics*, Vol. XVI, 1962, p. 25.
8. Kron, G. E.; Papiashvili, I. I.: Progress in the Development of the Lick-Stromlo Electronic Camera. *Advances in Electronics and Electron Physics*, Vol. XXII-A, 1966, p. 59.
9. Kron, G. E.; Ables, H. D.; Hewitt, A. V.: A Technical Description of the Construction, Function and Application of the U.S. Navy Electronic Camera. *Advances in Electronics and Electron Physics*, Vol. 28A, 1969, p. 1.
10. Breckenridge, J. B.; Kron, G. E.; Papiashvili, I. I.: Transfer Efficiency and Storage Capacity of Electronographic Image Tubes. *Astronomical Journal*, Vol. 691, 1964, p. 534.
11. Kron, G. E.; Walker, M. F.: Application of Electronography to Stellar Photometry. *Astronomical Journal*, Vol. 72, 1967, p. 1348.
12. Ables, H. D.; Kron, G. E.: The Linearity and Information Gain of an Electronic Camera. *Publications of the Astronomical Society of the Pacific*, Vol. 79, 1967, p. 423.
13. Walker, M. F.; Kron, G. E.: The Determination of Stellar Magnitudes by Electronography. *Publications of the Astronomical Society of the Pacific*, Vol. 79, 1967, p. 551.
14. Decker, R. W.; Mestwerdt, H. R.: Large Image Electronographic Camera. *Advances in Electronics and Electron Physics*, Vol. 28A, 1969, p. 19.
15. Decker, R. W.: Decay of S-20 Photocathode Sensitivity Due to Ambient Gases. *Advances in Electronics and Electron Physics*, Vol. 28A, 1969, p. 357.

PRECEDING PAGE BLANK NOT FILMED.

1A N70-36738

Camera Tubes Employing Electron-Imaging Charge-Storage Targets

G. W. Goetze

Westinghouse Electric Co. poration

Introduction

Charge-storage camera tubes were developed with the inception of the vidicon well over 15 years ago and have formed the class of tubes most extensively employed in television for commercial and military purposes. Basically, tubes in this class utilize the integrating and storage capability of suitable thin films for the purpose of enhancing sensitivity.

Two basic types of charge-storage camera tubes can be defined as: (1) those in which a single element acts as both the primary radiation sensor and charge-storage element and (2) those in which the role of radiation sensor and charge-storage element are separated. Of the highly developed camera tubes, the first type is exemplified by the vidicon, which is a direct-beam readout tube. The second type is exemplified by the image orthicon and secondary-electron-conduction (SEC) camera tubes. The image orthicon is a return-beam type of device; the SEC tube is basically a direct-beam readout type but may be used in the return-beam mode of operation.

Tubes of the second type employing high-gain charge-storage targets, such as the SEC target, are extremely attractive for television cameras. The separation of the role of radiation detector and charge storage offers versatility in the choice of both the radiation-detector and charge-storage elements. These tubes employ a photocathode to convert radiation into an electron stream and the charge-storage target to insure suitable characteristics such as low lag and high gain.

The direct readout mode of operation of this second type of tube offers, among other

features, a desirable simplicity and stability. The SEC tube is the only device that has been highly developed and which offers this type of operation. Such operation could, however, be extended to charge-storage targets other than the SEC target, and, indeed, tubes employing silicon-diode array targets are in the early stages of development.

This paper is concerned with camera tubes employing electron-imaging charge-storage targets. Although the image orthicon falls in this class, it is omitted in this discussion because of its long history and wide use in commercial broadcasting. Only tubes being highly developed and employing the secondary-electron-conduction principle are included. Properly, silicon-diode array-target camera tubes should also be included, but, because of their early development status and very close similarity to the SEC type of tubes, the discussion of this development has been deferred to Appendix A.

The discovery of the SEC phenomenon was the ultimate outgrowth of researches initiated in this country and abroad on the process of secondary-electron emission. The Westinghouse Electric Corporation, intimately involved in this research, extended efforts toward the study of transmission secondary-electron emission from thin films and its application in photoelectronic imaging devices. In order to increase significantly the secondary-electron yield from transmission secondary-emission dynodes, the use of smoke deposits and low-density layers of materials known to possess inherently high secondary-emission ratios was employed. These efforts resulted in high-gain dynodes; however, extensive employment of these

dynodes was limited due to the charging of the exit surface. It is this charging that made the SEC process possible and, in turn, offered a unique opportunity for development of a charge-storage-signal target. The development of the SEC target was accomplished simply by altering the mode of operation of the low-density dynodes so that the emitted secondary electrons were conducted back through the vacuum interstices of the layers rather than away from the exit surface.

The research that led ultimately to the discovery of the SEC process spanned a period of roughly 10 years. The excellent charge multiplication and storage properties of the SEC layers made them natural candidates for charge-storage targets in camera tubes, and, during the following five years, a variety of SEC camera tubes was developed.

At the present time, SEC camera tubes are a regular production item. They have found a variety of uses as camera tubes for very-low-light-level television for military and space applications, astronomical observations, and various scientific and industrial purposes. Their use in commercial broadcast television is also becoming evident.

The portion of this discussion concerned with the SEC tube consists of a condensation of published articles on the SEC process and its application to devices. Included is information on recent applications, but the paper is based primarily upon papers presented at the Third and Fourth Symposia on Photoelectronic Imaging Devices at Imperial College, London, during September 1965 and September 1968. (The papers from the 1965 Symposium have been published in Academic Press in *Advances in Electronics and Electron Physics*, Volume 22. The papers from the 1968 Symposium are being published in a future volume of the same series.)

In particular, credit is due the following individuals whose original papers formed the basis of this condensation (see Appendix B): G. W. Goetze (refs. 3, 8, 27, 28, and 42), A. H. Boerio (refs. 3 and 42), R. R. Beyer (refs. 3, 26, 27 and 28), M. Green (ref. 28), and H. Anderton (ref. 26).

The discussion relating to the silicon-dynode array target tube covered in Appendix A is based in part upon information obtained from the general literature pertaining to targets of this type. There being no published information on camera tubes using these targets in the electron-imaging charge-storage mode, the performance data presented is based entirely on early-stage evaluation tubes fabricated and tested at the Westinghouse Electronic Tube Division. The targets for these tubes were made available through the efforts of R. Schneeberger, H. Nathanson, D. Green, W. Harper, and R. Wickstrom of the Westinghouse Research and Development Center. Their efforts particularly are acknowledged.

Physics of the SEC Layer

Transmission Secondary-Electron Emission from Low-Density Targets

The basic structure of the low-density film is indicated in figure 1. It consists of an aluminum-oxide supporting layer, an aluminum signal plate, and a low-density layer of a

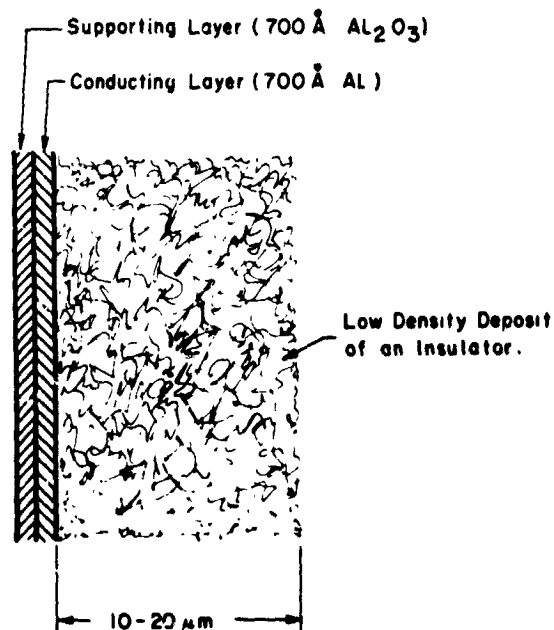


Figure 1. Structure of the SEC target.

suitable insulator. Normally, the aluminum oxide and the aluminum layers are each about 700 angstroms thick. The insulating layer is about 20 micrometers thick with a density of only 1 to 2 percent of the normal density, corresponding to a mass per unit area of roughly $50 \mu\text{g}/\text{cm}^2$. The low-density layer is formed by evaporating the material in an inert gas atmosphere at a pressure of approximately 2 torr. For most of these applications, potassium chloride has been used as the insulator; however, similar results have been obtained with sodium bromide, lithium fluoride, and barium fluoride.

In order to understand the electrical properties of a low-density layer of an insulator in terms of secondary-electron emission and electron conduction, it must be emphasized that, as a result of the fibrous structure of the insulator, 98 to 99 percent of the volume occupied by the active layer is vacuum. The average thickness of the fibers is estimated to be approximately 100 angstroms. This is small compared with the mean free path of low-energy electrons in the solid, and, consequently, there is a large escape probability for secondaries into the vacuum interstices of the layer. The energy absorption for high-energy primary electrons does not appear to be altered when compared with a solid layer of equal mass thickness and should therefore result in the same number of secondary electrons produced within the layer.

In operation, the low-density film is bombarded with primary electrons of approximately 10-kiloelectron-volt energy incident on the aluminum-oxide support film. Approximately 2 kiloelectron volts are lost in penetrating the aluminum oxide supporting layer and the aluminum signal plate. For the purpose of discussion, we assume a uniform rate of ionization across the thickness of the potassium chloride (KCl) layer, which is probably a good approximation since the peak gains are normally obtained with 50-percent transmission. Figure 2 shows the two principal modes in which the low-density film can be operated.

The top half of figure 2 schematically indicates operation as a transmission dynode

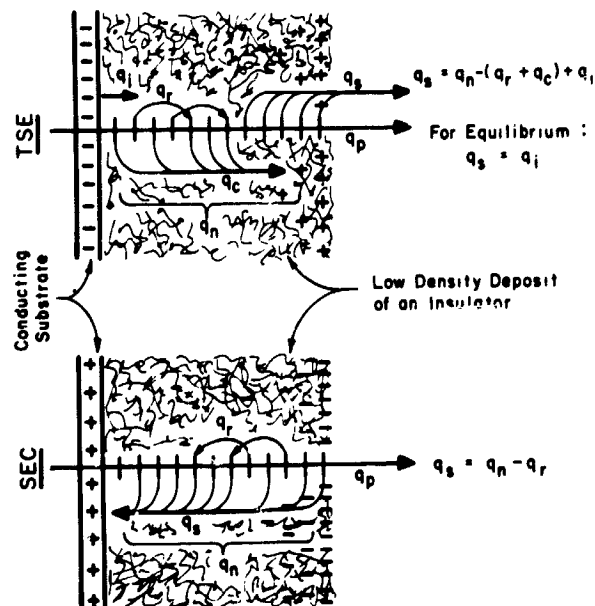


Figure 2. Operation of the low-density layer in the TSE and the SEC modes.

for secondary-electron multiplication. A primary electron beam, with charge q_p , in passing through the low-density layer, creates a certain number of free secondary electrons, with charge q_n , which have a high probability of escaping from the KCl fibers into the vacuum interstices. A fraction of these electrons, with charge q_s , escape through the surface and are collected by a positive collector electrode. Some of the secondary electrons, represented by charge q_r , will recombine on their way to the surface with positive charge centers left behind by the emission of secondary electrons from KCl particles closer to the surface. Since the escape probability will be higher for secondary electrons generated close to the surface than for those created deeper inside the layer, a positive charge will be established near the exit surface.

Under continued operation, this positive space charge will intercept an additional portion of the secondary electrons of charge q_c , coming from deeper inside the layer, on their passage through the surface. Under conditions of equilibrium, the charge, q_s , leaving the layer has to be replenished by an

equal charge, q_i , supplied from the signal plate. The balance between the charge generated, q_n , and the charge that recombines with positive charge centers along the ionization path of the primary electrons, q_r , and with the positive surface charge, q_c , can be regarded as the mechanism that supplies and regulates charge transport across the layer. The equation $q_s = q_n - (q_r + q_c) + q_i$ describes this simplified model. While the quantity $q_n - q_r$ describes the secondary-electron charge approaching the surface, and is therefore representative of the initial secondary emission, the term q_c will increase with time and will cause the secondary emission current to drop to its equilibrium value. Therefore, the positive charge established in equilibrium at, or close to, the surface has two effects.

1. By establishing a field across the layer, the forward velocity of secondary electrons is increased; hence, the probability is decreased of secondary electrons created deep inside the layer recombining with charge centers left by secondary electrons emitted from close to the surface. This effect seems to increase the secondary emission ratio.

2. An increase in the positive surface charge will decrease the escape probability for a secondary electron on its way through the surface. This will have a detrimental effect on high secondary emission ratios. The net result of these two effects is, however, an increase in the steady-state gain.

Briefly, this indicates that a positive surface charge tends to decrease the exit escape probability for secondary electrons but, at the same time, through the influence of the resulting electric field, increases the mean free path of secondary electrons within the low-density layer.

Secondary-Electron Conduction Process

The lower half of figure 2 shows the operation of the low-density films under reverse bias. It is this mode of operation that is of interest in camera-tube applications. The vacuum side of the low-density layer is polarized negatively with respect to the conductive signal plate by scanning it with a low

energy electron beam and applying a positive potential to the signal plate. We assume that the same amount of energy is expended by the primary electrons in creating secondary electrons as in the mode of operation shown in the upper half of figure 2. The internal electric field, however, is now directed so as to conduct free secondary electrons towards the conductive signal plate. The significant difference is the absence of any residual, steady-state, positive space charge within the low-density layer. Therefore, none of the secondary electrons with charge q_s will be intercepted by such a space charge. Again, a certain fraction of the secondary electrons with charge q_r will recombine with positive charge centers left behind by the emission of secondary electrons along the path of the initial primary electrons. A total charge of $q_s = q_n - q_r$ will reach the signal plate, thereby causing a local discharge of the target, which can be recharged by a periodic scanning of the vacuum side with the low-energy electron beam.

Because conduction across the target is due to the internally emitted low-energy secondary electrons, the effect has been termed *secondary electron conduction* (SEC). In this case, the electric field is utilized to increase the mean free path of secondary electrons within the layer. The whole process is similar to field enhanced emission except that the collected charge, q_s , does not have to penetrate a positive charge cloud. In the SEC mode, we obtain the benefit of an electric field acting on the mean free path of secondary electrons without having to pay the price of secondary electrons recombining with a positive surface charge. A higher gain, $G = q_s/q_p$, is expected for the SEC mode than for the TSE* mode, and this is indeed the case.

Application of the SEC Target to Television Camera Tubes

The SEC target has been successfully applied to television camera tubes.

*Transmission Secondary Emission

Principle of Operation

It has already been indicated that, in actual employment, the SEC layer serves only the purpose of supplying a charge storage surface with a high charge-multiplication capability. The detection or conversion of radiation into electric charge is accomplished by the use of a variable photocathode. The SEC target may be used with various photocathodes, thus permitting the devices to be tailored to the spectral energy available. Figure 3 shows the response characteristics of photocathodes that have been used with SEC targets.

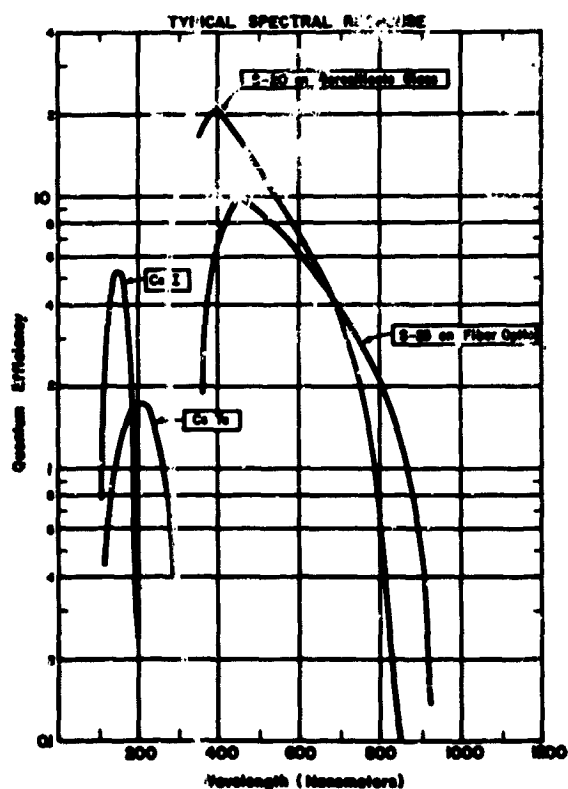


Figure 3. Photocathodes used in SEC tubes.

Because the operation of the SEC target is independent of the particular detecting surface employed, it is only necessary to consider the influence of an incident electron stream and a reading beam in order to describe the mode of operation of the target.

Figure 4 is a schematic of the SEC target and shows the currents involved in its operation. The photocurrent is incident from the left and the scanning readout beam from the right. Under normal operation, with the target signal plate at a small positive potential, V_T , the scanning beam charges the target surface to ground potential and thus establishes an electric field within the low-density KCl layer. The layer is then bombarded by photoelectrons having an energy of from 6 to 10 kilo-electron volts. If, on the average, 30 electron volts are sufficient for each excitation, the energy dissipated in the low-density layer is sufficient to generate as many as 200 to 300 secondary electrons per incident photoelectron. Because of the internal electric field, the secondary electrons are conducted through the voids of the layer to the signal plate, thereby discharging the target layer.

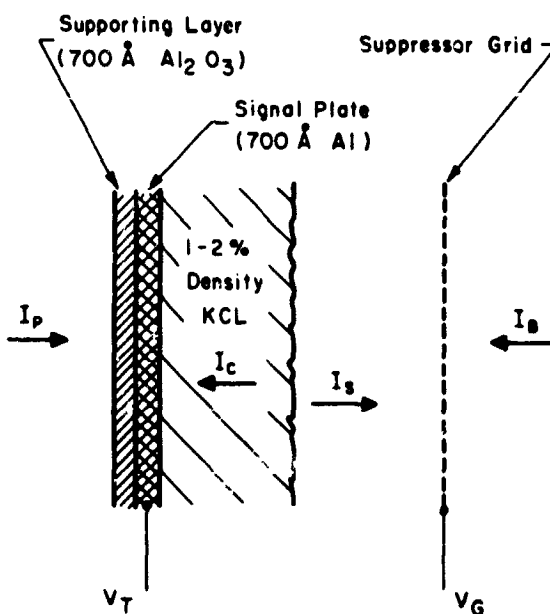


Figure 4. Schematic diagram of the SEC target.

Recharging of the target layer by the scanning beam provides the video signal. This combined reading and priming process is similar to that of the vidicon. Unlike the vidicon, however, the charge transport involved in writing is accomplished by secondary electrons rather

than by electrons in the conduction band. Another significant difference is that the SEC layer can charge positive with respect to the signal plate. If an exposure is continued until the electric field across the target is sufficiently small, charging by transmission secondary emission becomes significant. This electron flow, shown in figure 4 as I_s , can drive the surface of the target beyond the signal-plate potential toward the suppressor grid potential, V_g .

Performance Characteristics

The manner in which the signal is developed can be explained with the aid of figure 5. Here, the target gain, defined as the signal charge divided by the input charge, is plotted as a function of the signal plate or target potential V_t . This curve applies to small signals; that is, signals producing only a small voltage excursion of the target surface.

As shown in figure 5, the gain is 200 at a target potential of about 35 volts. At higher potentials, the target shows higher gain due to the onset of electron-bombardment-induced conductivity, but under these conditions the response time is poor; and there are nonuniformities in the output signal. At these higher electric fields, the target shows a significant dark current. Thus, the maximum target potential is limited to about 30 to 50 volts, depending on the target thickness.

The SEC gain decreases sharply as the target potential, and therefore the electric

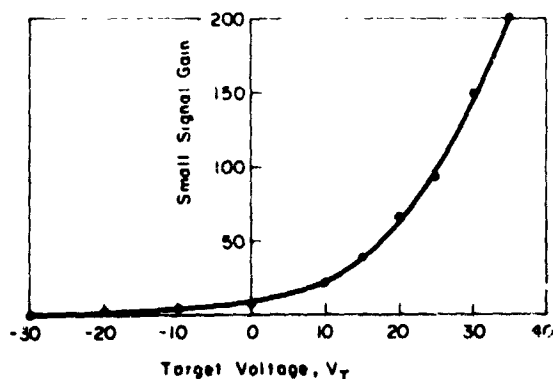


Figure 5. Small signal target gain as a function of target voltage.

field within the SEC layer, is reduced. The gain, however, remains finite at zero and also negative target potentials. This is the result of charging by electrons that escape from the exit surface and are collected by the suppressor mesh. At negative target potentials, the gain depends on the electric field at the exit surface. This, in turn, is dependent on the potential difference between the suppressor grid and the signal plate. The gain ultimately goes to zero when the target exit surface reaches its equilibrium value.

The small-signal gain curve can be used to determine the average gain for large signals. For example, at a target potential of 30 volts for a small signal, figure 5 gives a gain of 150. If the input signal is increased so that a 10-volt potential change is developed on the target surface, the potential across the SEC layer at the end of the integration time will be 30 minus 10, or 20 volts. At this point, the small-signal gain corresponds to that shown on the curve for a 20-volt target potential or about 70. The average gain for the 10-volt excursion is about 110.

In addition to the influence of the target potential on the SEC target gain, it is clear that the kinetic energy of the incoming photoelectrons plays a significant role. As increasing amounts of kinetic energy are dissipated within the SEC layer, the production of secondary electrons increases and so does the gain. In fact, if the average excitation energy for a secondary electron is considered to be independent of primary electron energy, the SEC target gain would increase linearly with the incoming electron energy at a fixed target potential. This actually occurs; it is shown in figure 6 where the gain has been normalized to unity at the energy corresponding to the maximum gain, which occurs at about 8 kiloelectron volts. At higher energies, a significant fraction of the incident electrons penetrates the entire target, and the energy dissipated in the SEC target begins to fall off. At quite low incident electron energies the dissipation of energy in the aluminum oxide and aluminum layers is responsible for the threshold at several kiloelectron volts.

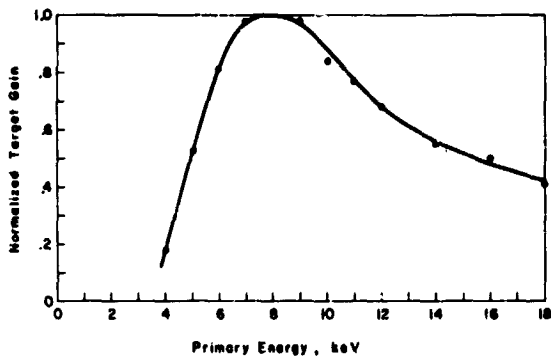


Figure 6. Relative gain as a function of primary voltage at a constant target voltage.

Transfer Characteristic. Perhaps the most important characterization of a charge-storage target or of a camera tube is the transfer characteristic. This relates the input information, whether in terms of illumination on

the input sensor or target input current, to the corresponding signal current derivable from the target. Important to the nature of this relationship are the target gain, target storage capacitance, and mode of signal read-out. A typical transfer curve for the SEC target is shown in figure 7. This curve shows the video signal current versus photocurrent density for a target with a storage capacity of about 200 picofarads/cm² and was measured at a 525-line, 30-frame-per-second, scanning rate. The slope of the curve is very nearly unity over a range of two orders of magnitude in input current. In this linear region of the curve, the average target gain is nearly constant and equal to about 100. At input currents greater than about 3×10^{-10} amperes/cm², the target approaches saturation, and the slope of the curve tends to zero.

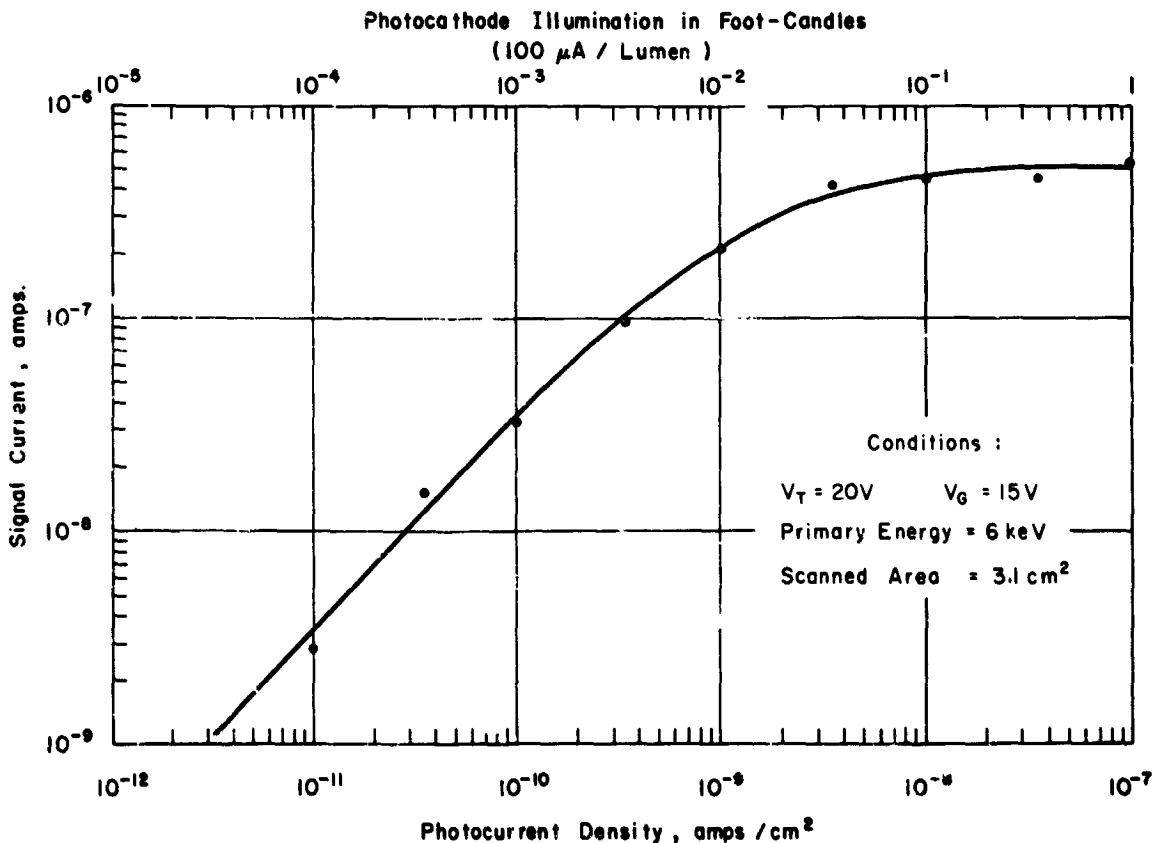


Figure 7. SEC target transfer curve.

For most applications, the maximum voltage excursion is limited by the first crossover for secondary-electron emission in reflection. With the KCl target, first crossover occurs at a scan-beam landing energy of about 15 electron volts. At greater energies, the scanning beam will not charge the target to ground but instead will drive its surface more positive. In order to avoid this possibility, the suppressor grid is normally operated at 15 volts. If a higher voltage is applied to the signal plate, the target surface may, by secondary-electron conduction, exceed first crossover potential. The scanning beam will still return the target to ground because the reflected secondaries it generates will be repelled by the 15-volt suppressor grid; however, because beam bending becomes significant for large voltage excursions, the maximum useful excursion is about 10 volts, corresponding to a signal current of about 10^{-7} amperes. Depending on the preamplifier noise current, this gives a dynamic range of approximately 100 for large area signals.

Response Time. In order to maintain high sensitivity, a camera-tube target must exhibit a fast response. The signal current is at maximum when all the charge stored in the target during the integration period is read out in a single frame. In addition, a fast response eliminates the after-image effect of a moving object. With the SEC target, very fast response is achievable, and, generally, the charge remaining in the target is reduced to only several percent of the original value in the third field readout. The response time, however, is influenced by the magnitude of the charge density originally stored in the target and the target storage capacity. For very low charge densities, which result in quite small excursions of the target surface potential, the response time increases due to the small but finite energy distribution of the electrons in the scanning readout beam.

Storage Capacity. As long as discharge lag is avoided, it is otherwise desirable to have a large storage capacity. There are two reasons for this. First, for a given permissible voltage excursion, higher target capacity provides a larger signal current and, therefore, better

signal-to-noise ratios and larger dynamic range. Second, a more fundamental reason is that, in order to obtain high resolution with low contrast scenes, it is necessary to store a charge representing a large number of photons. This means that either a low target gain or a large storage capacity is required.

The capacity of the SEC target has been measured by determining the signal charge and the voltage excursion for a given area. The voltage excursion was measured by integrating a signal and by reducing the target voltage before readout. The reduction required in order to reach the threshold of beam landing, as observed on a monitor, gives directly the voltage excursion. Capacity measurements for two targets are shown in figure 8, where the capacity per unit area is plotted as a function of target voltage. The upper curve was measured on a target that was about 15 micrometers thick, corresponding to a mass thickness of $35 \mu\text{g}/\text{cm}^2$. The increase in capacity with increasing target voltage can be explained by the fact that, in charging the target, the scanning beam electrons come under the influence of the internal electric field and can therefore

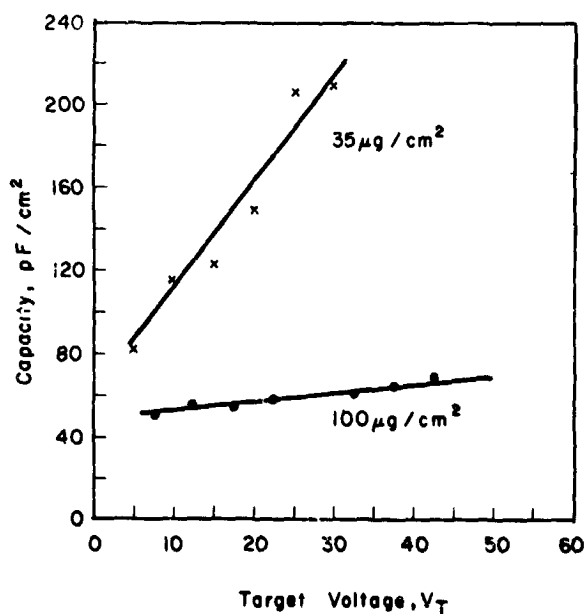


Figure 8. Target capacity as a function of signal plate voltage for two targets of different thickness.

penetrate a significant fraction of the potassium chloride. Since higher target voltages result in higher internal fields, the penetration increases with increasing target voltage, thereby resulting in a higher effective capacity. At low target voltages, we would expect the charge to be deposited very near the surface and the capacity to be given by the target thickness. For a 15-micrometer-thick target, the calculated capacity is about 60 picofarads/cm², showing good agreement with the curve.

The lower curve was measured on a thicker target. Its relatively slight dependence on voltage can be explained by: (1) at a given target voltage, the electric field within the layer is smaller for this thicker target; and (2) the absolute distance the scanning beam can penetrate for a given field represents a smaller fraction of the total thickness.

Typical targets have a mass thickness of about 50 micrograms/cm² and are normally operated at a target voltage of from 15 to 25 volts. The capacity for such targets ranges from 100 to 150 picofarads/cm². For a voltage excursion of 10 volts, this corresponds to a stored charge of about 8×10^9 photoelectrons/cm². Depending on the gain required, this means that the SEC target can store from several times 10^7 to 10^9 photoelectrons/cm².

Integration. In applications involving the detection of static, low-light-level scenes, the ability to integrate for long periods is extremely useful. The long integration times possible with the SEC target are, perhaps, its most outstanding feature. The video signal obtained from integrating a constant-light-level input signal for various times is shown in figure 9. With the integrating times of 2, 4, and 8 minutes, the signal increases almost linearly with exposure time; this results in a transfer curve identical to that obtained when the integration time is held constant and the light level is increased. Such reciprocity is possible because of the high resistivity of the layer. A lower limit for the resistivity was established by integrating any possible background signal due to target leakage. The inte-

gration was continued for 1.5 hours at a target potential of 30 volts. Whatever leakage did occur during the integration time was not sufficient to generate a detectable video signal. Since a 2-volt signal could easily have been detected, this means that the resistivity of the SEC layer is greater than 10^{17} ohm-centimeters.

Integration time

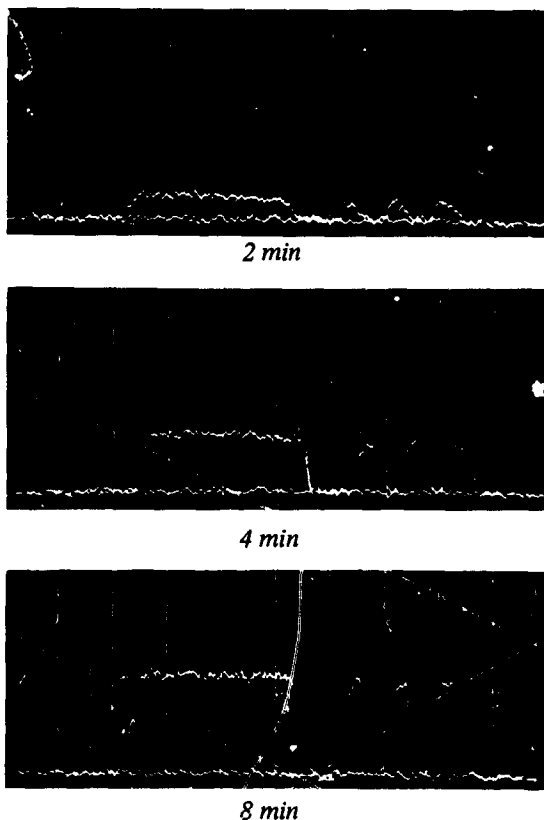


Figure 9. Integrated video signal for various exposure times.

The ability to integrate for long periods implies that long storage times are possible. In one experiment, a signal was stored for 48 hours and showed no deterioration. It is very likely that much longer storage times are possible.

Resolution. The highest resolution that has been measured in an SEC camera tube so far is about 1500 TV lines per inch. This was limited primarily by the scanning section of

the tube. Higher resolution has actually been obtained in an optically scanned tube and is described further on in this paper. Because of the very high resistivity of the target, it seems likely that its intrinsic resolution capability will be limited by electron scattering rather than by leakage. Thus, ultimate resolutions of 3000 to 4000 TV lines per inch should be obtainable.

Halation. Any image tube that employs energetic electrons from a photocathode for charging the storage target will exhibit halation to some extent. Halation is most apparent when a tube is driven into saturation by an intense signal. This is a consequence of the ejection of secondary electrons from the target. In the operation of the SEC target, there are always some emitted secondary electrons directed away from the exit surface, and, in principle, due to the influence of the suppressor mesh, these should be redistributed on the exit surface. Because of the voltage excursion of about 15 volts required to saturate the SEC target, the emitted secondaries are not sufficiently energetic to be distributed on the uncharged regions and thus return, essentially, to their point of origin; therefore, halation is not discernable in SEC tubes.

SEC Tube Types

Since the inception of the SEC principle, a wide variety of camera tubes have been developed and produced. Many were developed for specific purposes, such as the Uvicon for project Telescope and the SEC tube specifically designed for the hand-held lunar camera. Other tube types developed for general low-light-level television applications make up the bulk of SEC tube production.

Figure 10 illustrates the general configurations and types of SEC tubes presently being produced on a regular basis. The tube to the extreme right has an electrostatic image section and an electronic zoom capability of 2 to 1. The second tube from the right uses a

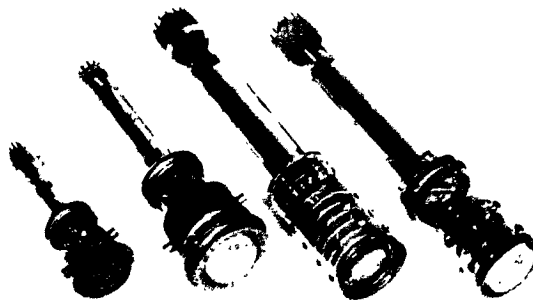


Figure 10. SEC camera tube types.

magnetic image section and is characterized by superior performance in resolution and geometric fidelity. Both of the two tubes to the left use a diode type of electrostatic image section and differ only in size; namely, 25-millimeter and 40-millimeter photocathode diameters.

Aside from their performance capabilities, certain general features of the tubes should be mentioned.

Suppressor Mesh. All standard SEC tubes employ a suppressor mesh in close proximity to the exit surface of the SEC target. The suppressor mesh is not basic to the operation of the SEC target but is used primarily to limit the potential excursion of the target under high signal conditions and to prevent crossover. Crossover is the result of the SEC target surface attaining a potential such that its secondary-electron emission ratio is greater than unity when scanned by the reading beam. Under this condition, the scanning beam does not deposit electrons, and the target surface cannot be returned to its normal operating condition at gun cathode potential. In addition, the suppressor mesh eliminates the possibility of electrical breakdown due to excessively high electric fields and thus protects the target. For some applications in which the tubes are operated under well-defined conditions, the suppressor mesh has been eliminated.

Generally, the suppressor mesh degrades the aperture response of the tube from what would otherwise be achievable. It also increases the target shunt capacity.

Image Section Focus. Both electro-magnetic- and electrostatic-focus image sections are employed in SEC tubes. The highest quality imaging is generally obtainable with magnetic focusing; however, this method leads to a cumbersome and heavy system.

Electrostatically focused image sections that permit compact and lightweight equipment appear to be the most desired. For most types of tubes, the electrostatic image section is of the diode type with electro-optical minification between the photocathode and the charge-storage target. With a diode type of image section, electro-optical focusing is independent of the photocathode potential. Thus, automatic gain control is possible by electronically adjusting the image section potential with reference to the average video signal over a television frame.

Departing from the simple diode type of image section, we find that electrostatic focusing offers the opportunity of incorporating electronic zoom into the camera tube.

Gun Focus and Deflection. Four combinations of focus and deflection methods are generally available.

1. *Magnetic focus and magnetic deflection.* This method generally provides the highest center and corner resolution but requires the most electrical power.

2. *Magnetic focus and electrostatic deflection.* This method provides quality comparable to combination #1 and requires slightly less power. Its chief advantage is the potentially short gun length.

3. *Electrostatic focus and magnetic deflection.* With this combination, intermediate resolution is achievable while power requirements are moderate.

4. *Electrostatic focus and electrostatic deflection.* This combination requires the least consumption of electrical power but provides poorer resolution capability than the other methods.

SEC Tube Performance Characteristics. The general performance of SEC tubes can be assessed from that of the smallest tube shown in figure 10. This tube, designated WL-30691, uses a 1-inch vidicon type of gun, employing magnetic deflection and magnetic focus and a 16-n millimeter-diameter SEC target. The larger tubes offer higher performance, which can be estimated by simple scaling.

The transfer curve for the WL-30691 based upon production-run tubes is shown in figure 11. The tube is intended for operation from approximately 10^{-5} to 10^{-2} foot-candle photocathode illumination. The linear portion of the transfer curve indicates a gamma of close to unity. It can also be seen that saturation takes place around 10^{-2} foot-candle with a knee type of characteristic similar to that of the image orthicon. A signal current of 150 nanoamperes is delivered at a photocathode illumination of about 5×10^{-3} foot-candle.

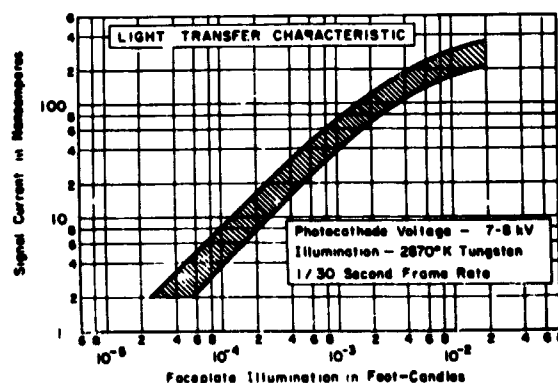


Figure 11. Transfer characteristic (WL-30691).

Since SEC tubes were, until recently, almost exclusively used for extreme low-light-level television, particular care was taken to

reduce lag as much as possible by proper adjustment of target parameters. Figure 12 shows the temporal response as a function of signal current. The residual signal was measured in the third field, corresponding to 50 milliseconds after the illumination was removed. Under normal operating conditions the lag in the third field is only about 5 percent and due only to discharge lag. There is no build-up lag. A further improvement could be obtained at the sacrifice of storage capacity, if necessary. The performance indicated in figure 12, however, makes it possible to use an SEC tube for such demanding applications as field sequential color transmission at a scan rate of 180 frames per second.

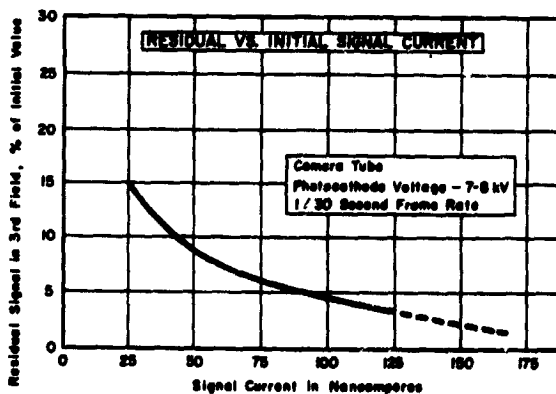


Figure 12. Lag characteristic (WL-30691).

Combining the information contained in figures 11 and 12 with a resolution measurement gives an indication of the practical sensitivity, shown in figure 13. Discernable resolution for a black-and-white bar pattern is plotted as a function of photocathode illumination. The three curves are for a static condition and for the cases where an image point traverses the picture width in a period of 20 and 10 seconds. An increase in illumination of about $2\frac{1}{2}$ times and $3\frac{1}{2}$ times, respectively, is needed for the 20 second- and the 10-second-per-picture-width movement. When the image

moves much faster than 10 seconds per picture width, the results are dominated by signal mixing on the target due to exposure smear and are therefore not very meaningful in evaluating the basic dynamic performance of a camera tube.

The loss in sensitivity due to either camera or object movement must be considered for low-light-level television. In addition, very few practical scenes contain 100-percent-contrast objects; hence, even greater sensitivity is required to view real scenes under starlight conditions, for example.

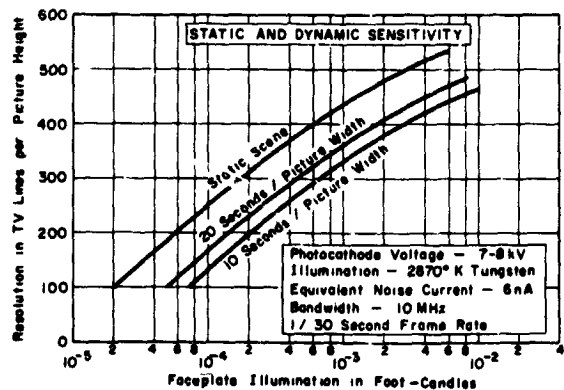


Figure 13. Static and dynamic sensitivity (WL-30691).

Intensifier-SEC Tube Combination. The SEC tube alone is not sensitive enough for televising night scenes. This problem, however, can be overcome with the addition of one stage of image intensification coupled fiber-optically to the camera tube.

Figure 14 shows such an assembly intended for nighttime television. The image intensifier is of the 40/25 millimeter variety with an S-25 photocathode on fiber optics. Figure 15 shows the performance of this combination in television lines per picture height plotted against faceplate illumination in foot-candles for 100-percent scene contrast (solid lines) and 30-percent scene contrast (dotted lines). Both contrast measurements were



Figure 14. Image intensifier/SEC camera tube combination (WL-32000).

made for static scene conditions (upper curves) as well as for a 20-second-per-picture-width movement (lower curves). In most cases, one must contend with low contrast, dynamic conditions. These curves indicate that the intensifier/SEC combination described is a practical device for nighttime viewing. A combination of larger tubes could be used to improve this performance even further.

Special Experiments with the SEC Target

In the preceding sections, the operation of the SEC target and performance characteristics of SEC tubes were described. For the most part, the characteristics of the target and tubes were derived from standard test procedures in which test patterns or scenes that simulated the usual operating conditions for the tubes were imaged. It is not always possible in such tests, however, to ascertain the ultimate performance of the SEC devices nor to predict how the tubes will operate under unusual conditions. To achieve a more thorough understanding of the SEC target capabilities and limitations and to extend the SEC target to use in very high performance devices, it was necessary to perform special experiments, described in the following paragraphs.

The Optically-Scanned SEC Camera Tube

The optically-scanned SEC camera tube is a photoelectronic device developed to offer an alternative to the use of photographic emulsion. This device requires the following three features:

1. A photocathode with high-quantum yield
2. An electrical storage element with high integration capability and storage capacity
3. Resolution approaching that of a coarse photographic emulsion.

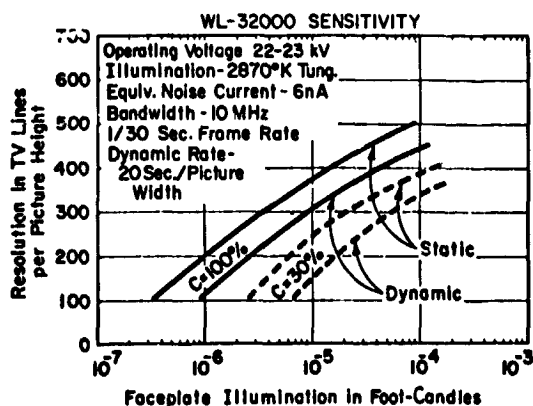


Figure 15. Intensifier/camera tube sensitivity.

The optically-scanned tube was designed, for simplicity, to record one-dimensional images such as the line images present at the output of a spectrometer. Figure 16 shows a schematic of the tube and scanning system. High resolution is obtained by use of magnetic focusing. Because of the intense magnetic field, electromagnetic deflection of the read beam is not desirable; therefore, the read-beam source was chosen to be a photocathode; and the read beam scanning was accomplished by an external optical scan of the read photocathode.

In operation, light from the scene is focused onto the write photocathode. The electrons released from this are accelerated toward the target by a primary potential difference of between 5 and 10 kilovolts. The primary electrons passing through the signal plate produce an amplified charge image on

the surface of the SEC target. The charge is then read out by scanning the low-velocity electron beam across the insulating layer.

The low-velocity scanning beam is generated by projecting the image of a narrow slit onto the read photocathode. Deflection of the slit across the read photocathode generates the scanning read beam.

A complete cycle of operation proceeds in the following manner. During integration, the reading section is turned off by applying a positive voltage to the read photocathode. After integration has been completed, the read photocathode is returned to a potential of -20 volts, and the reading beam discharges the target. This operation is followed by the flooding of the whole target with the flood lamp shown in figure 16. Since only a portion of the target is scanned by the slit image, a

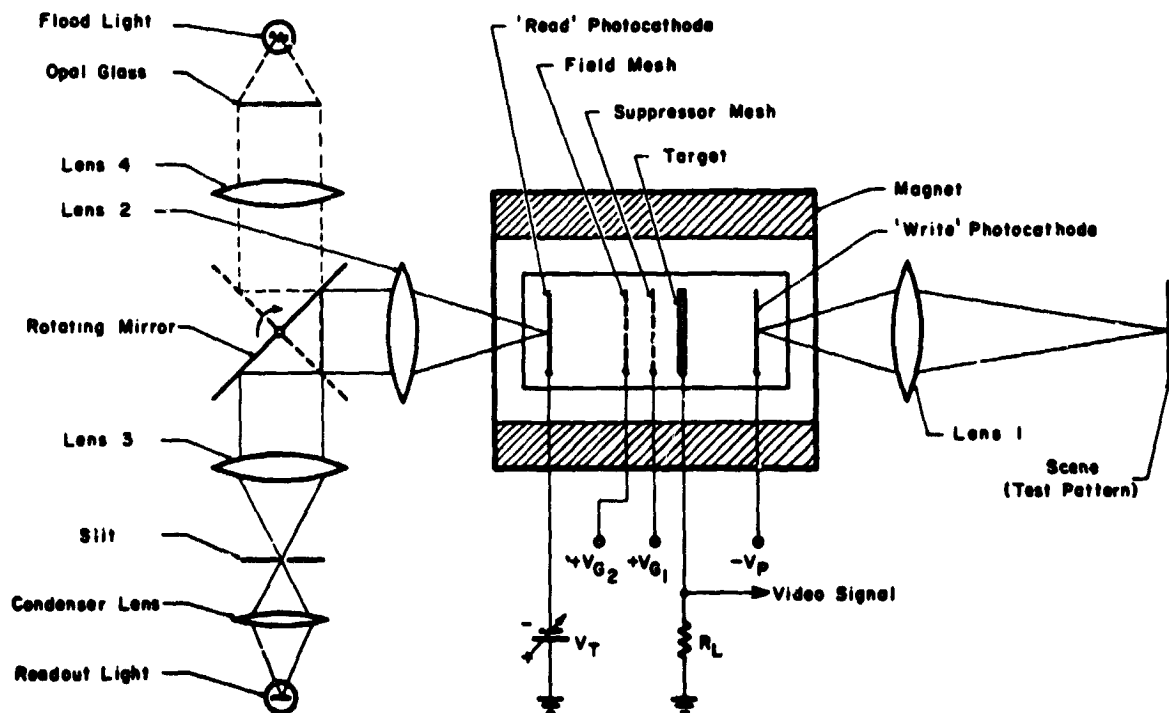


Figure 16. Schematic of optical scanning system.

flooding operation has to be introduced between the read and write cycles in order to discharge those portions of the target which have not been discharged during readout.

Because resolutions approaching those of photographic emulsions were desired, experiments with the optically-scanned SEC tube were carried out to determine resolution limitations and to measure the signal-to-noise ratio of the tube. No attempt was made to operate at low illumination levels nor to determine the absolute sensitivity of the tube.

Experimentally, a bar pattern with increasing line numbers was projected onto the write photocathode in such a manner as to give 10 steps in resolution in increments of 4 line pairs per millimeter, starting with 4 line pairs per millimeter and progressing to 40 line pairs per millimeter. The signal was read out and displayed on a storage oscilloscope from which it was photographed. Figure 17 is a typical photograph. The upper trace shows the full test pattern; the lower trace shows an expanded view of the higher line numbers. From these traces, the modulation as a func-



Figure 17. Output signal (optically-scanned SEC camera tube).

tion of line number as well as the signal-to-noise ratio can be obtained.

Figure 18 is a plot of the response as a function of spatial frequency. The upper curve is the square-wave response as it was obtained from figure 17. The lower curve is the sine-wave response computed from the upper curve. Both the square-wave and sine-wave responses are close to 3 percent at 40 line pairs per millimeter.

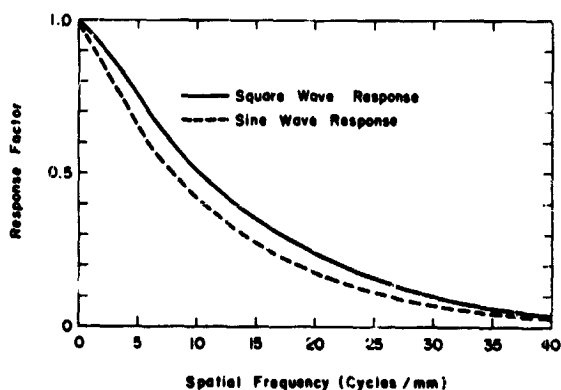


Figure 18. Response factors (optically-scanned SEC camera tube).

From figure 17, a signal-to-noise ratio of only about 50 was obtained. This was for 1.5-millimeter-long bars projected onto the write photocathode. For an appraisal of the instrument as a practical device for use with a spectrometer, bars 8 millimeters long were employed. For this experiment, the signal-to-noise ratio as a function of line number is shown in figure 19. It may be noted that a signal-to-noise ratio of 25 can be obtained at 30 line pairs per millimeter and a ratio of 10 at 40 line pairs per millimeter.

To assess the resolution performance of the SEC target, it was necessary to determine the sine-wave responses of the various parts of the system. These are shown in figure 20. From these and from the response of the

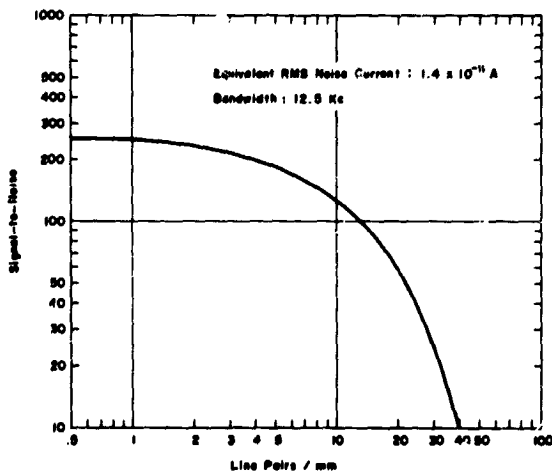


Figure 19. Signal-to-noise ratio as a function of line number.

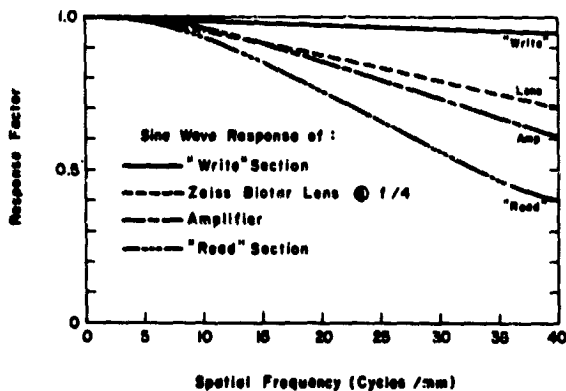


Figure 20. Response factors of the various tube and system components (optically-scanned SEC camera tube).

entire system, the lower limit of SEC target response (fig. 21) was calculated.

Experiments with the optically-scanned SEC camera tube demonstrated the high resolution potential of the SEC target and, in addition, the potential of the system for achieving the high resolution and the high signal-to-noise ratio required for efficient recording of optical information.

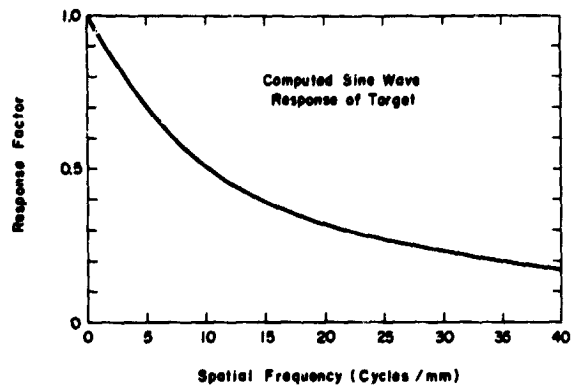


Figure 21. Computed lower limit of the SEC target response.

Point Source Imaging with the SEC Target

In astronomical applications where stellar objects appear as weak point sources, a camera tube should be capable not only of detecting point sources but also of measuring their intensity with reproducible accuracy. To determine the capability of camera tubes employing SEC targets to fulfill this function, it was necessary to measure sensitivity, reciprocity at low electron fluxes, photometric range, and reproducibility.

Measurements were made using the Westinghouse Uvicon camera tube. This is an ultraviolet-sensitive SEC tube employing electrostatic focus and electrostatic deflection. The tube was designed for the Telescope experiment on the Smithsonian Astrophysical Observatory and does not employ a suppressor mesh. The photocathode was of the cesium-iodide type on a lithium-fluoride window and thus exhibited very low thermionic emission.

To form a point-source image on the photocathode, an opaque screen with a 45-micrometer-diameter aperture is placed over the lithium-fluoride faceplate of the camera tube. The aperture is illuminated by a small ultraviolet source fitted with a mechanical shutter. Electron optical demagnification

in the image section of the tube gives a geometrical image size of 25 micrometers at the target, but aberrations in the tube increase this value to a minimum diameter of 50 micrometers at the half intensity point. Thus, the conditions for true point-source imaging are met, since the image size is determined in all cases by the performance of the camera tube and not by the diameter of the faceplate aperture nor by the size and distance of the ultraviolet source. The intensity of the point-source image is found by measuring the photoelectron current with the image section of the tube operated as a photodiode. A range of known photoelectron flux is obtained by calibrating the source-to-faceplate distance.

The camera chain employed a 525-line, 30-frame-per-second, noninterlaced scan. The video system had a bandwidth of 2 megahertz and an equivalent rms noise current at the amplifier input of 2×10^{-9} amperes. The experiments are carried out by exposing the image section for predetermined time intervals with the reading beam shut off. Following each exposure, a single frame is read out, and the signal current is displayed on an oscilloscope and photographed.

To obtain high sensitivity, it is necessary to increase the target voltage between integration and readout. Scanning of the SEC target before integration commences drives the target surface below gun cathode potential. This effect is caused by the small fraction of beam electrons that have large thermionic-emission energies. If the positive charge that develops on the target during integration is small, it may not be sufficient to drive the target surface potential to a positive value that will permit readout by the majority of the electrons in the reading beam.

Loss of small signals in this way is avoided by increasing the target potential by about 2 volts before readout. The result of this operation is clearly seen in figure 22, where the minimum detectable signal (in photoelectrons), N_0 , is plotted as a function

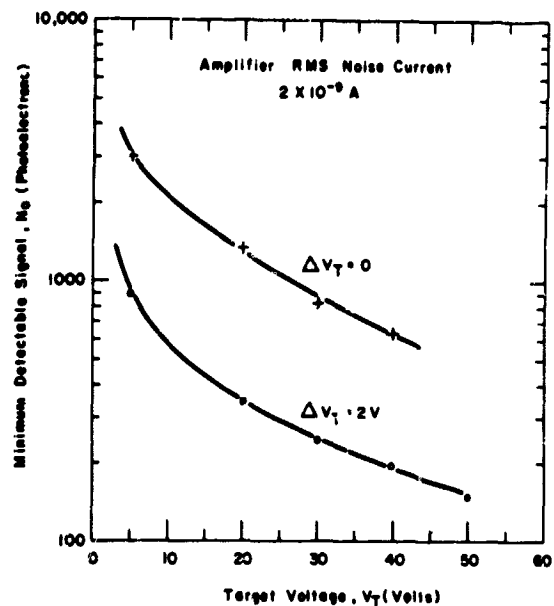


Figure 22. Minimum detectable signal as a function of target voltage.

of target voltage, V_T . A minimum detectable signal is that which gives a peak signal-to-rms-noise ratio of 5. The curves in figure 22 were measured on a relatively thick target. The upper curve, which shows the poorer sensitivity, was measured with no change in target potential before readout. The lower curve, showing a minimum detectable signal of 150 electrons at $V_T = 50$ volts, was measured with a 2-volt increase in target voltage between integration and readout.

The SEC target shows no significant deviation from reciprocity over a wide range of integration periods. Thus, a point source producing one photoelectron per second produces a signal, after 1,000 seconds of integration, within ± 10 percent of the signal produced from a photoelectron flux of 30,000 electrons per second in 1/30 second.

The SEC-target photometric range was studied by obtaining measurements from a series of progressively more intense point sources. The pertinent quantities measured were peak signal current and the total output charge for each point-source image. Figure 23

is a plot of the output-signal charge as a function of the total number of photoelectrons emitted from the photocathode during the period of integration. The curve was obtained at a target voltage of $V_T = 13$ volts. The curve covers a photometric range of 10^4 .

The change in slope of the charge curve between 10^{14} and 10^{13} coulombs shows that there are two distinct stages in the accumulation of signal charge on the target. During the initial part of the integration period, increasing charge storage causes the peak voltage excursion on the target to increase in the same manner as it does for an extended area image. Unlike the case of an extended area, however, the attainment of the maximum voltage excursion does not produce a corresponding saturation in the amount of

stored charge. Instead, further charge is stored on the target by a steady growth in the size of the image. Over the intensity variation of the source shown in figure 23, the image radius was found to increase linearly on the log-log plot from 50 micrometers to 350 micrometers. The signal current variation over this range was from about 10^8 angstroms to 3×10^7 angstroms.

Dynamic Imaging

For many years, evaluation of television camera tubes was carried out by imaging static scenes. Recent interest in low-light-level television has, however, indicated that such tube evaluation is not adequate. It is generally

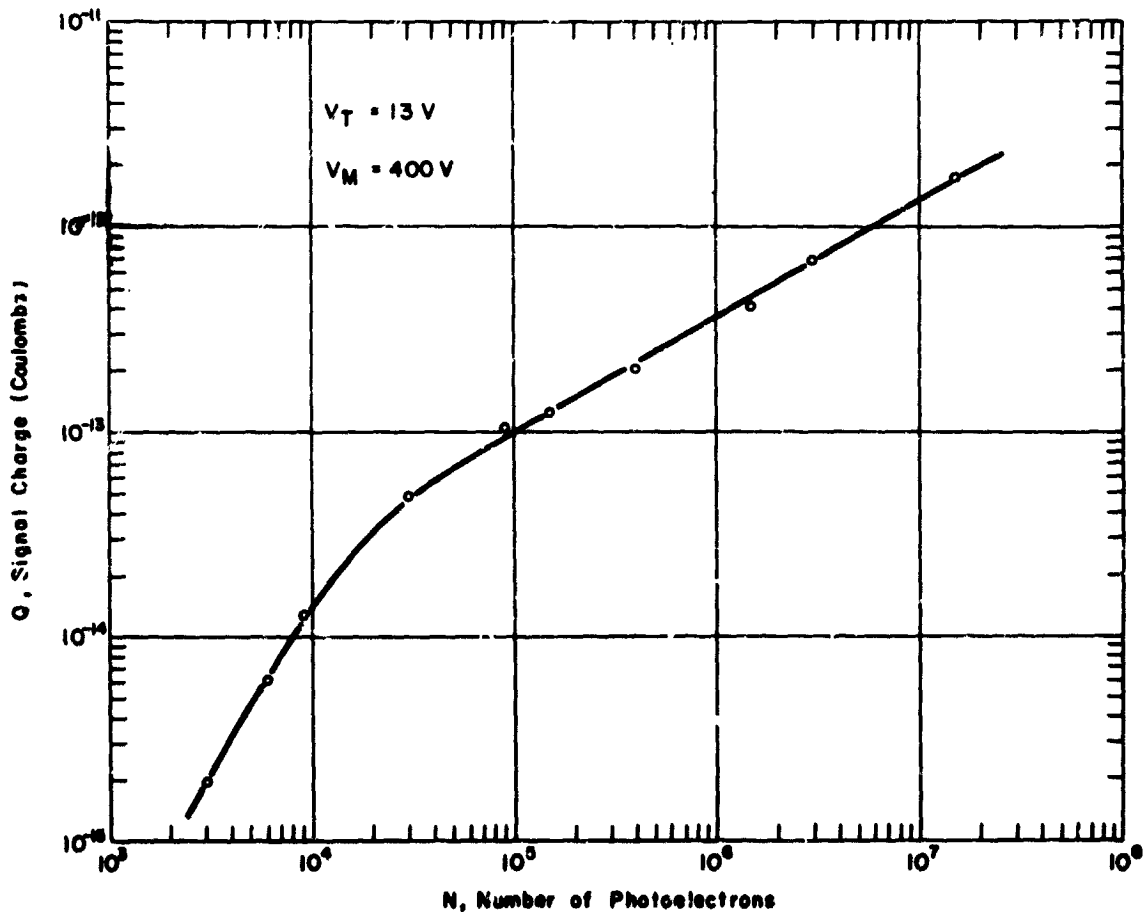


Figure 23. Output signal charge as a function of the integrated flux.

found that a performance loss occurs when a scene is in motion, thus complete specification of tube performance should include information on the dynamic performance. The primary causes of performance loss are signal mixing and discharge lag.

Signal Mixing. Signal mixing is a type of interference process that occurs in all tubes employing charge-storage targets under all illumination conditions. It can be best described by considering what happens when a periodic bar chart with fixed period is imaged onto the camera-tube photocathode. Due to the emission of photoelectrons, a corresponding charge-pattern bar chart will appear on the storage target.

Let us consider the effect of image motion. As the speed of translation of the bar chart (normal to the bars) is increased, the leading edge of a white bar will increasingly overlap the trailing edge of a black bar; and the original sharp discontinuity in the charge distribution pattern on the storage target will disappear. This results in degradation of the resulting image sharpness and, consequently, a loss in resolution. As the speed increases, the white bar will move to cover the entire position of the black bar; and a black bar will shift to coincide with what was, originally, a white bar. As a result of this, during the frame period, it is possible that the charge distribution on the storage target will become uniform and zero contrast will result. Further increase in translation of the bar chart can result in images having negative contrast. These effects can be observed with a bar chart of fixed period by varying the speed of translation of the chart. Similarly, for a given speed, the effect can be observed by employing bar charts having different periodicities. From the latter, one can determine the contrast as a function of resolution with chart speed as a parameter. Figure 24 illustrates this effect calculated for a system operating at 60 fields per second with traverse times of the bar chart of 5 seconds and 10 seconds per raster width. Figure 25 shows the limiting resolution as a function of pattern traverse rate. It should be realized that the degrading

effect of image mixing is always present although the negative contrast is generally not apparent in the imaging of real scenes that do not contain regular periodic structures.

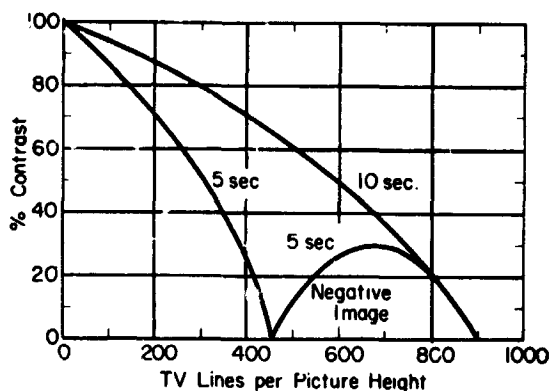


Figure 24. The contrast reduction of a bar chart.

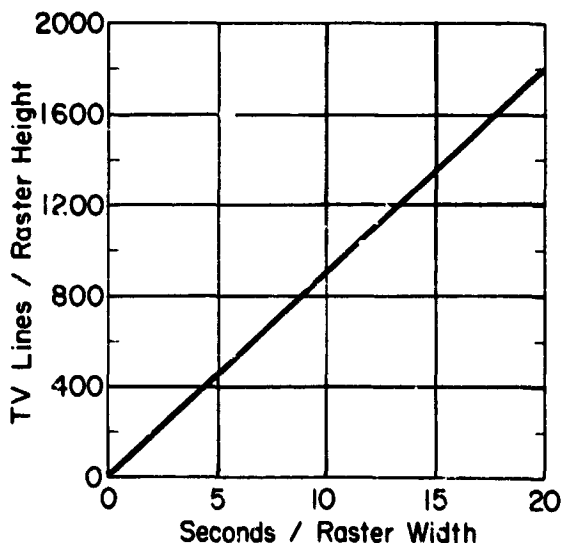


Figure 25. Resolution limit due to signal mixing as a function of pattern traverse rate.

Discharge Lag. Lag may be of two types: semiconductor lag and discharge lag. For devices used in low-light-level television, semiconductor lag may be disregarded because tubes susceptible to this type of lag are generally not sufficiently sensitive for this application. Discharge lag, on the other hand,

increases markedly as the radiant flux into the camera is decreased.

Discharge lag is a consequence of the inability of the scanning readout beam to neutralize all of the charge on the storage target in the period of a frame. Under conditions of low-light-level imaging in which the voltage excursion on the target surface is small, the readout beam may charge the scanned region of the storage-target negative by an amount depending upon the target storage capacity, energy distribution of the read-beam electrons, and read-beam current density. If, after integrating a signal onto the target for one frame period, the voltage excursion is too small to raise the surface potential to zero, only a fraction of the read-beam electrons will be energetic enough to land on the target to achieve discharge. Both the signal current and lag are deleteriously affected. Because this type of lag occurs only at low voltage excursions, it is most prominent at low-light levels.

Measurement of Dynamic Imaging Performance. Figure 26 shows schematically an arrangement for evaluating tube performance under dynamic conditions. The figure is self-explanatory and involves simply a method of imaging a moving bar pattern onto the photocathode of a camera tube. Image speeds of 10 seconds and 20 seconds per raster width, which give signal-mixing resolution limits of 900 and 1800 TV lines per raster height, were used.

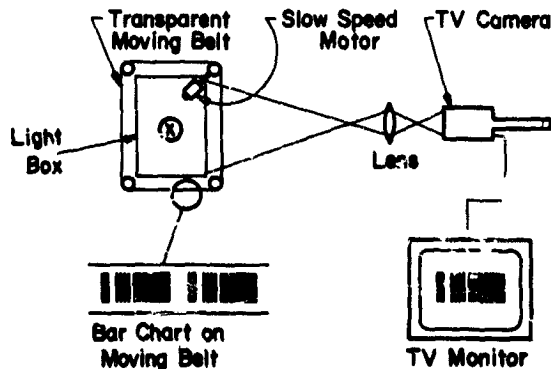


Figure 26. System used to obtain moving scene data.

The tube performance characteristic evaluated was the perceptible resolution for various light levels as determined by an observer from a television monitor display. This method possesses an advantage of simplicity although it is somewhat limited because of its subjective nature.

Moving scene data was obtained for the SEC camera tube (WX-30654) and the intensifier-SEC camera tube (WL-32000). The input format of both tubes is identical. The WX-30654 employs a storage target of 1.0-inch diameter while the WL-32000 uses a 0.6-inch-diameter storage target. Figures 27 and 28 show the static and dynamic sensitivities for these two types of tubes. It should be

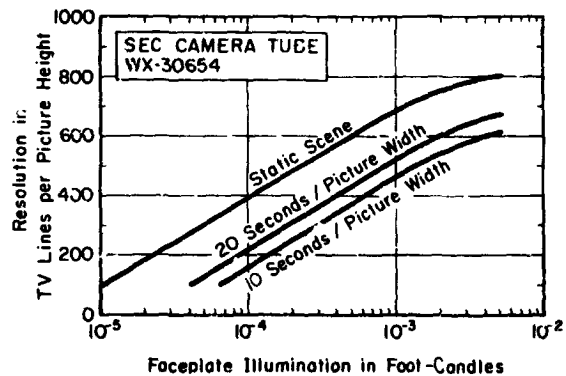


Figure 27. Static and dynamic sensitivity for an SEC camera tube.

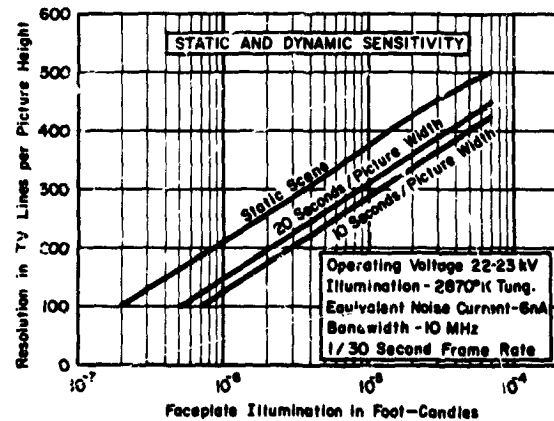


Figure 28. Static and dynamic sensitivity for an intensifier SEC camera tube.

noted that for both types the dynamic sensitivity is within one order of magnitude of the static scene sensitivity. This compares with a deviation of about two orders of magnitude for the image orthicon.

The significant but relatively small deviation in sensitivity between the static and moving scenes in the SEC tubes is due to the high target-gain-to-capacitance ratio and thus high voltage excursion.

Applications of the SEC Camera Tubes

The most extensive employment of the SEC camera tubes is in nighttime observation and surveillance. These tubes exemplify present state-of-the-art achievement in low-light television and have found broad application in remote-viewing systems for the military. Figure 29 is a reproduction of a television-monitor presentation of a scene imaged by one of the SEC camera tubes that employs electronic zoom in the image section. The four zoom ratios indicated on the figure are 1 to 1, 1 to 1.5, 1 to 2, and 1 to 3.

Aside from military applications, the SEC camera tubes and intensifier/camera tube combinations have achieved a significant place as a tool in scientific research. The intensifier/SEC package coupled fiber-optically to an electron microscope has proved useful in dealing with extremely low current densities in the microscope. Figure 30 illustrates this arrangement; its desirable features are the large input format and excellent integrating properties of the SEC tube. The high sensitivity and integrating capability of this arrangement (fig. 30) made possible the Fresnel diffraction patterns shown in figure 31. The patterns shown cover exposure times of 0.2, 10, and 20 seconds at electron-microscope current densities of 4.0×10^{-14} , 5.75×10^{-15} , and 1.16×10^{-15} amperes/cm².

Use of SEC and intensifier/SEC tubes have been employed in ground-based astronomy at the McDonald, Allegheny, and Lick

Observatories. Figure 32 illustrates images of two galaxies obtained with the SEC tube WL-30691 and the intensifier/SEC tube WL-32000. The upper picture illustrates a 0.5-second exposure of the spiral galaxy M51 with the WL-32000 tube; the lower picture shows a 210-second exposure of galaxy ARP82 with the WL-30691 tube.

At the Lick Observatory of the University of California, Santa Cruz, Drs. E. J. Wampler and J. S. Miller utilized an SEC camera tube with the 120-inch telescope to study the light flashes of the pulsar embedded in the Crab Nebula. Time resolutions of 0.004 second were obtained. Pictures were obtained at various phases of the pulsar cycle by using a suitable shutter. Figure 33 shows a television-monitor photograph of the pulsar, which is the lower right star of the pair of stars located to the right of center.

In addition to applications in ground-based astronomy, SEC tubes have been selected for and are being employed in a number of space programs. The Apollo camera employed on the lunar excursion module and to be carried ultimately to the surface of the moon employs an SEC tube. Figure 34 is a picture of the hand-held lunar SEC camera. Figure 35 is a television-monitor photograph from the interior of the lunar excursion module taken with this model camera.

The unmanned Orbiting Astronomical Observatory (OAO), which NASA launched on December 7, 1968, contained four SEC tubes, denoted Uvicons. The Uvicons employed ultraviolet-transmissive faceplates and ultraviolet-sensitive photocathodes. The SEC targets were operated without suppressor meshes, and the tubes were employed in a digital readout mode of operation. Each tube was used in conjunction with a 12½-inch Schwarzschild telescope. From launch date to the middle of January 1969, the OAO had collected twenty times more ultraviolet information concerning stars than had been accumulated in 15 years of rocket launchings.



1:1



1:1.5



1:2



1:3

Figure 29. Monitor presentation generated by an SEC tube with electronic zoom.

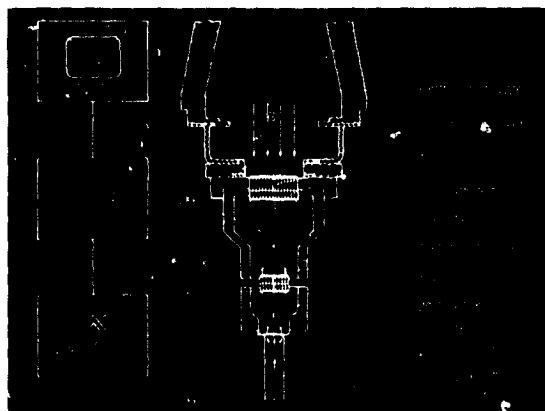


Figure 30. Camera tube/electron microscope arrangement. (Courtesy of Dr. K. Herrmann, Siemens.)

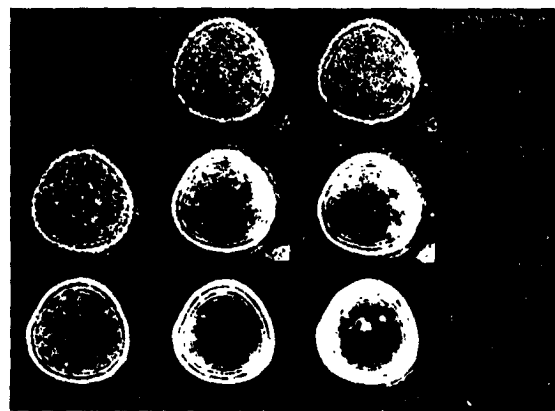
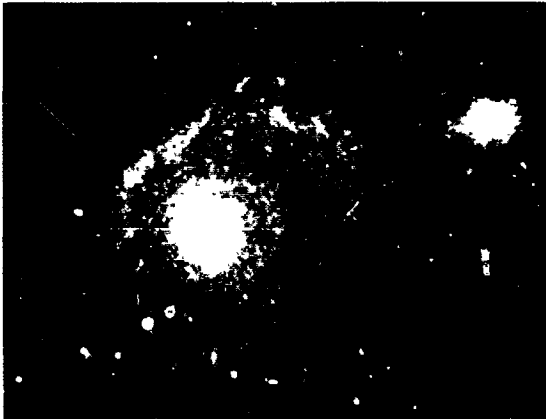


Figure 31. Fresnel diffraction patterns generated by fig. 30 arrangement. (Courtesy Dr. K. Herrmann.)



Top: A 0.5-second exposure of MSI with the WL-32000 Intensifier/SEC Camera Tube. Field-of-view: 380 inches by 510 inches.

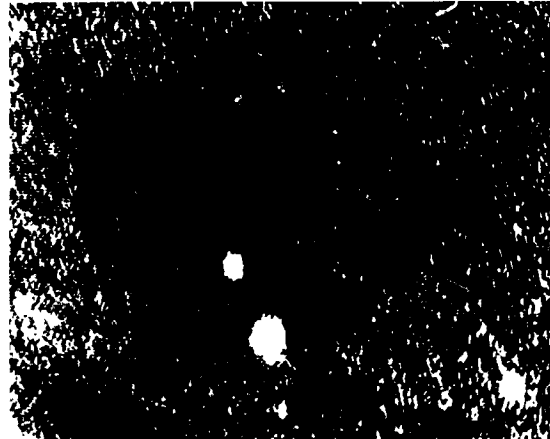
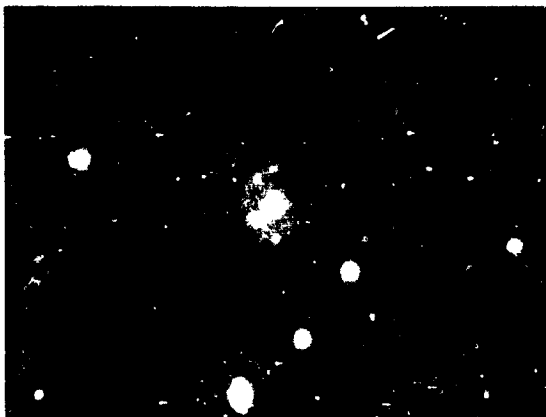


Figure 33. Photograph of TV monitor presentation of pulsar embedded in the Crab Nebula. (Courtesy of Dr. E. J. Wampler and J. S. Miller, Lick Observatory.)



Bottom. A 210-second exposure of ARP 82 (NGC 2535/6) with the WL-30691 SEC Camera Tube. Field-of-view: 240 inches by 320 inches. (Courtesy M. Green, J. R. Hansen.)

Figure 32. Photographs of galaxies obtained with SEC devices.

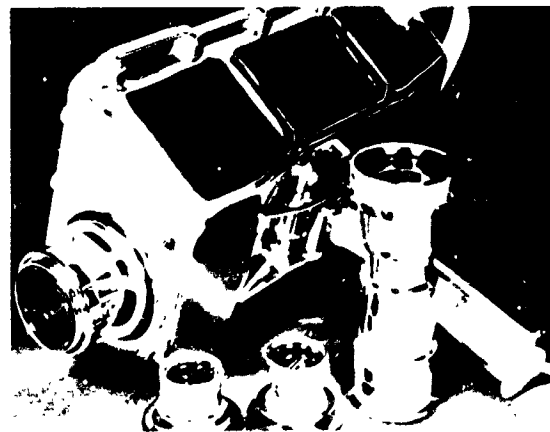


Figure 34. Hand-held lunar SEC camera. (Courtesy of Westinghouse Aerospace Division.)

The most widespread use of television camera tubes is in the broadcast and closed-circuit television applications. The growth of color television has posed increasingly severe requirements on camera tube performance. In this area, acceptance of the SEC tubes is increasing rapidly due to the achievable high sensitivity and extremely low lag. SEC tubes have been employed in three-tube NTSC color cameras and have demonstrated the improvements achievable with very low lag.

Utilizing both the high sensitivity and low lag characteristics of the SEC tube, the CBS Laboratories was successful in developing a field sequential camera for closed-circuit color transmission. The camera uses a single SEC tube and operates at 180 frames per second. This camera made possible the viewing, in color, of the interior of the human body at very low light levels.



Figure 35. Photograph of TV monitor picture taken aboard the lunar excursion module. (Courtesy of National Aeronautics and Space Administration.)

Summary

In this paper, the evolution of the SEC target, its operating characteristics, and SEC camera tubes have been described in some detail. The unusual attributes of the SEC camera, such as high gain, very low lag, long storage, excellent integration capability, and point-source imaging characteristics, have been described and related to the variety of uses to which these tubes have been applied.

The discussions have not been exhaustive. Considerable detail is available in the numerous reports and publications relating to SEC tube development, manufacture, and use.

To complement this discussion, three appendices are included. Appendix A discusses the employment of the silicon-diode array charge-storage target in the electron-imaging mode of operation. Appendix B is a bibliography of significant reports and articles pertaining to secondary electron conduction (SEC) and transmission secondary emission (TSE) phenomena from low-density films, devices employing these phenomena, and systems employing the SEC and TSE devices. Appendix C characterizes various SEC tube types with regard to significant parameters.

Appendix A

Camera Tubes Employing the Silicon-Diode Array as an Electron-Imaging Charge-Storage Target

(G. W. Goetze and A. B. Lapovsky)

Introduction

Following the initial introduction of the silicon-diode array charge-storage-target vidicon by the Bell Telephone Laboratories, a

general interest in silicon-diode array targets developed. This type of target has been extensively described in published literature (refs. 1-6). In this appendix, the employment of the silicon-diode array charge-storage target

in the electron-imaging mode of operation is discussed. In this mode, high-target gain is achievable, thereby yielding the potential for development of camera tubes of very high sensitivity for low-light-level television viewing. Such operation has been suggested by Gordon and Crowell (ref. 5), and investigations of electron-imaging on a silicon-diode array target for a scan converter tube have been described.

The use of the silicon-diode array target as the charge-storage element in a camera tube leads to a device virtually identical in construction to the SEC camera tubes already described. The primary difference between these two tube types is that the SEC target and suppressor-mesh assembly is replaced with a silicon-diode array target. Thus, in operation, the two tube types are essentially interchangeable, each type offering the advantages and disadvantages determined by the nature of the charge-storage target.

In the following paragraphs, the silicon-diode array target is described briefly. (Detailed information is available in the literature.) This is followed by a presentation of some experimentally determined characteristics of early prototype camera tubes employing silicon-diode array targets and using electron-imaging. Finally, an assessment of the performance of silicon-diode array camera tubes (electron-imaging mode), particularly for low-light-level applications, is made with regard to present status and problems yet to be solved.

Silicon-Diode Array Target

This brief description of the silicon-diode array target includes target fabrication, operation, resolution, lag, and leakage or dark current.

Target Fabrication

The silicon-diode array target is fabricated by using standard techniques employed in the manufacture of integrated circuits. Fabrication is based upon a highly developed technology. In some respects, the requirements of the silicon-diode array targets are

relaxed from those of integrated circuits in that only simple diodes are required and interconnections are eliminated. On the other hand, high-density arrays of elements are required, and reduction of leakage current by several orders of magnitude over that permissible in integrated circuitry is necessary. In addition, the silicon-diode array target necessitates the employment of very thin silicon slices, and a high degree of perfection of the slice is necessary at the outset.

The procedures for target fabrication are available in the literature; only the general method of fabrication is briefly described in this appendix. The targets are made from thin slices of the N-type of silicon. The process begins with a slice of approximately 0.010-inch thickness; the silicon is oxidized. Standard photolithographic methods are used to open windows in the oxide on one side of the slice, and P-N junctions are formed through the open windows in the oxide by the diffusion of boron into the N-type of silicon. The target is then thinned to the desired thickness by etching away the N-type of material on the side opposite the P-N junction diodes. After several processing procedures have been followed to remove impurities and surface states and to establish an N^+ layer on the front surface, the basic fabrication is complete. This results in a N-type of silicon wafer with an N^+ layer on one face and an array of P-type islands on the opposite face.

The last step in fabrication is either (1) the application of a thin highly resistive layer (resistive sea) to the surface containing the P-type of elements (refs. 3 and 5) or (2) the application of isolated metallic pads over the diodes (ref. 3). Both methods serve to control the influence of excessive charging of the silicon-dioxide insulating layer. Method #2 serves, in addition, to shield the silicon from infrared and visible radiation from the reading-beam cathode.

Target Operation

This description of target operation can be best understood by referring to figure A-1. Consider the N-type of silicon slice to be

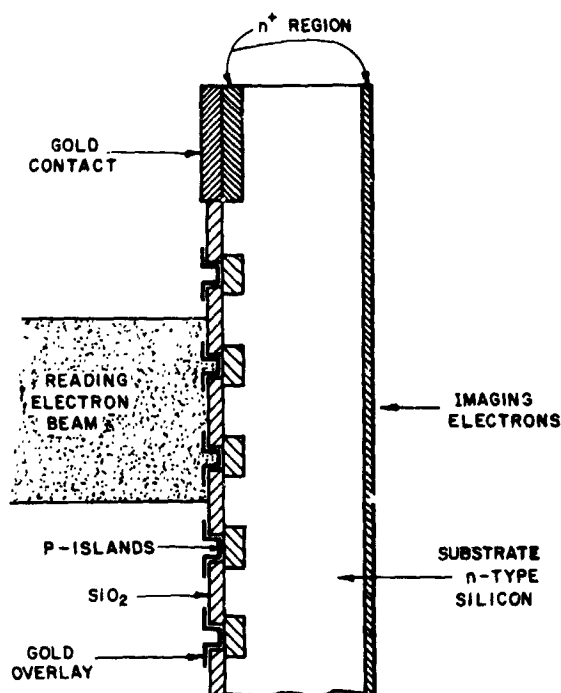


Figure A-1. Schematic of silicon-diode array target.

biased to a potential of about 5 volts positive with respect to the read-gun cathode. Upon scanning the back surface of the target with the reading electron beam, the P-type of islands and the silicon-dioxide surface are charged to the cathode potential of the read gun, and the P-N junctions are thus reverse-biased. Because of the low leakage current, this bias is retained until the generation of holes in the N-type of silicon and their diffusion to the P-type of islands alters the charge on the diodes. The extent to which the diodes are discharged by the holes produced by imaging electrons is measured by the read-beam charge deposited in recharging the diodes to the full 5-volt, reverse-bias condition. Thus, the acceptance of read-beam current by the target at any instant is a measure of the stored information, and the resulting current is the video signal. At any element, the readout of the diodes occurs at the television frame rate of 30 per second while, during the intervening period, information is integrated and stored as charge across the target depletion-layer capacitance.

During the charging period of the read beam, the exposed silicon-dioxide regions are charged to the read-gun-cathode potential at which they remain and isolate the N-type of silicon from the reading beam.

The excitation of charge carriers in the N-type of silicon occurs at the rate of about one electron hole pair for each 3.4 electron volts of imaging-electron kinetic energy. Imaging electrons of 10-kiloelectron-volt energy would then produce approximately 2900 holes. The potentially high gain of the target is apparent. The actual gain is somewhat less and is controlled by the loss of holes due to recombination at the front surface and in the bulk of the target material. If the target is sufficiently thin, the holes readily diffuse to the P-type of islands; and collection efficiencies of about 50 percent are obtainable, thereby giving a target gain of about 1500 for 10-kiloelectron-volt imaging electrons.

Resolution. Because of the discrete nature of the silicon-diode array target, the resolution capability of the device will be limited by the diode density. In addition, due to the lateral diffusion of holes, the resolution is also influenced by the target thickness (ref. 5). For any sufficiently thin target (thickness approximately the same as the diode spacing), the absolute limiting resolution to be expected is given in TV lines per unit length by the linear density of diodes.

Lag. All the lag exhibited by the diode-array targets is essentially due to capacitive discharge. Influencing this are the target bias, diode voltage excursion, and beam acceptance characteristics of the surface. Increasing the target reverse bias decreases the dynamic capacitance. This permits a greater voltage excursion for a given input signal and improved electron-beam acceptance. All of these factors tend to improve the target lag characteristic. The target should be designed to present the maximum effective beam landing area.

The silicon-diode array target exhibits a relatively high dynamic capacitance; hence, the lag exhibited by this target is greater than that of lower capacity targets, such as the SEC target, for a given signal current. For a

target voltage of about 5 volts, lag of about 25 percent at a signal current of 100 nanoamperes can be deduced from reported experiments (ref. 3).

Leakage Current. The leakage or dark current of the diode-array targets is influenced by temperature, irradiation of the depletion region by visible and infrared radiation, and the volume of the depletion region. Increasing temperature and irradiation of the depletion region increases the dark current; decreasing the capacitance to minimize lag also results in dark current increase.

The dark current manifests itself by introducing noise, reducing effective target gain, and reducing contrast. Sufficiently low dark current is generally achievable to preclude difficulties for operation at room temperature (refs. 2 and 3); however, because of the sensitivity of dark current to temperature variations, the minimizing of the dark current is of particular importance for devices to be used under the rugged conditions involved in military applications.

Characteristics of Silicon-Diode Array Target Tube

The characteristics described are based on the use of the WL-30691 type of camera tube. This type of tube, highly developed and qualified for military use, was modified for early evaluation purposes by simply replacing the SEC-target-suppressor-mesh assembly with silicon-diode array targets. Standard processing procedures were followed in the tube fabrication including formation of S-20 photocathodes.

The targets employed were made from 10-ohm-centimeter N-type of silicon. The spacing between the diodes was 25 micrometers, and target thicknesses of approximately 25 micrometers were employed. Typically, the target capacitance at a 5-volt bias was about 3500 picofarads/cm². Basic target leakage currents of about 1.6×10^{-9} amperes/cm² were achieved at a 5-volt bias; however, in actual tube operation under the influence of infrared radiation from the read-gun

cathode, the leakage currents increased by at least one order of magnitude.

Transfer Characteristic

Figure A-2 illustrates a transfer characteristic for a silicon-diode array target camera tube of the type described in the preceding paragraph. The transfer characteristic was obtained by measuring the signal current for various photocathode illuminations under standard television-scan conditions. The solid curves represent measured data obtained at the three different, image-section accelerating potentials indicated. The broken curve corresponding to a 10-kilovolt accelerating potential was calculated from the measured target gain characteristic. Significant is the wide dynamic range and the linear characteristic representing a unity slope. No real tendency for saturation to occur is observed although an apparent beginning of saturation was due to insufficient reading-beam current density to discharge the target at the highest signal currents. The large achievable signal currents are a consequence of the high storage capacity of the silicon-diode array target. The transfer characteristic was found to be independent of the target bias over a range of voltages from 0.5 volt to at least 5.0 volts.

Target Gain

The charge gain attributable to the target is shown in figure A-3. This was calculated from measurements of the signal current for various image-section accelerating potentials at a constant photocathode illumination (4.24×10^{-4} foot-candle) and constant target bias (1.0 volt). As previously described, the gain is approximately a linear function of accelerating voltage, yielding a value of 1500 at 10 kilovolts.

Tube Resolution

When a 100-percent-contrast, static, bar pattern was used, preliminary measurements

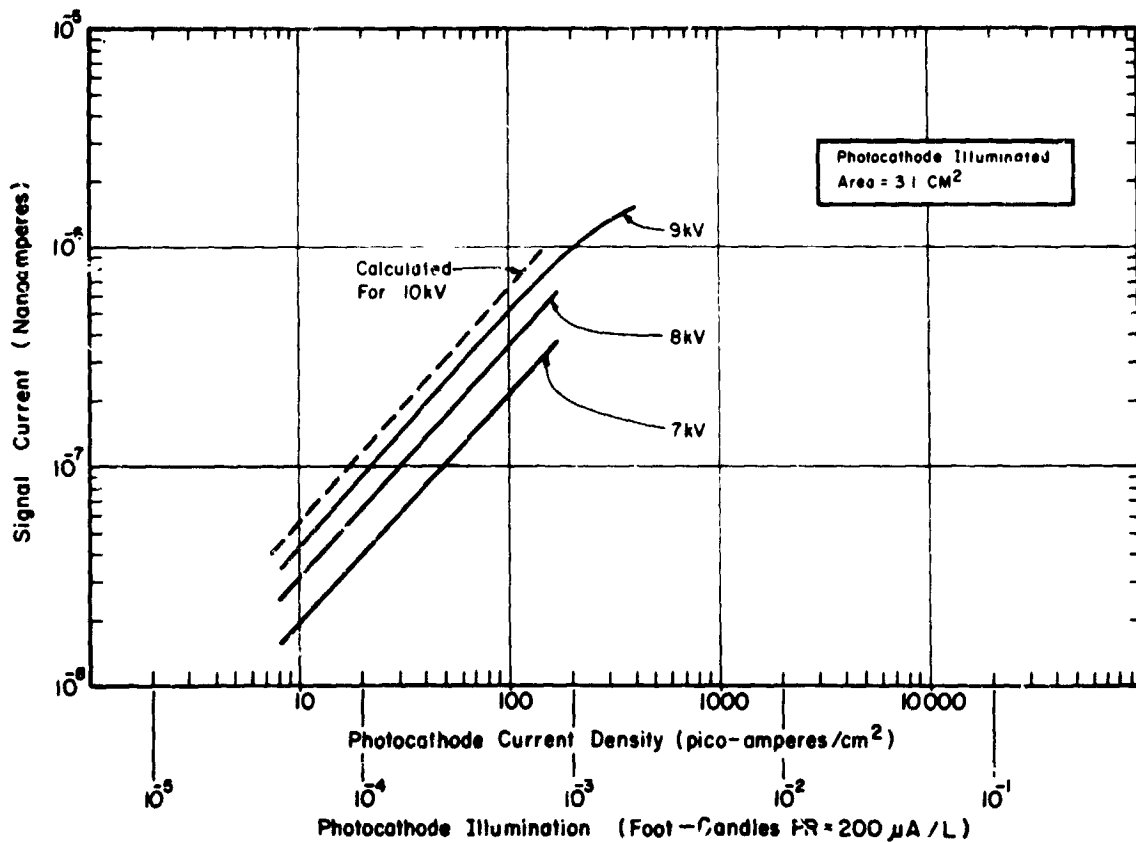


Figure A-2. Light transfer characteristic for a silicon-diode array target camera tube (based on the WL-30691).

of limiting resolution as a function of photocathode illumination at low-light levels yielded the curve shown in figure A-4. Under high illumination conditions, the best limiting resolution obtained was about 350 TV lines per raster height. This closely approaches the theoretical limit of about 375 imposed by the 25-micrometer diode spacings.

Lag and Dark Current

Extensive measurements of these two quantities were not carried out in early evaluation tubes; however, both of these quantities were found to exhibit the expected variations with target voltage. With increasing target voltage, the dark current was found to increase, and values ranging from 12 to 40 nanoamperes/cm² were obtained at a target voltage of 5 volts. Lag was found to decrease

with increasing target voltage. The lowest lag observed at a signal current of 100 nanoamperes was approximately 25 percent.

Picture Quality

Television-monitor presentations of pictures of reasonable quality have been achieved by using the silicon-diode array modified WL-30691. A typical monitor picture is shown in figure A-5. Apparent in the figure are numerous blemishes, essentially all of which are due to target imperfections. The existence of a regular array of black squares should be noted in this figure. These squares are not due to fabrication blemishes but represent small test arrays distributed over the target for electrical evaluation purposes during the early stages of target development.

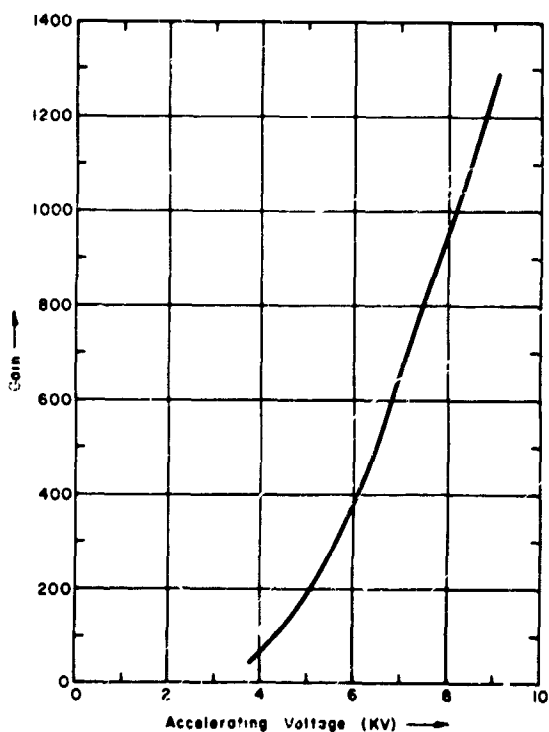


Figure A-3. Gain versus electron accelerating voltage for a silicon-diode array target.



Figure A-5. Photograph of a TV monitor presentation of a static scene imaged with a silicon-diode array target camera tube (based on the WL-30691).

Conclusions

Early evaluation studies of silicon-diode array targets employed in camera tubes in the electron-imaging mode have established the feasibility of these charge-storage targets for devices of very high sensitivity. Generally, a factor of 10 to 20 increase in sensitivity over the SEC tube is available. This, in principle, permits attainment of photon-noise-limited performance with only one additional stage of intensification. To a certain extent, however, some of this impressive gain is lost in actual, low-light-level, viewing applications where dynamic scenes must be imaged. Under these conditions, the high static sensitivity of the silicon-diode array tubes is degraded due to the image build-up and discharge lag inherent in the target.

The gain-to-storage-capacitance ratio of the silicon-diode array target is comparable to that of the SEC target. Therefore, the degradation in tube sensitivity for dynamic imaging can be anticipated to be about the same as the degradation for the SEC. For a scene traversing the tube photocathode at the rate of 10 seconds per picture width, the dynamic sensitivity can be expected to be reduced by roughly a factor of 6 for those light levels for which the SEC tube is operative. At lower

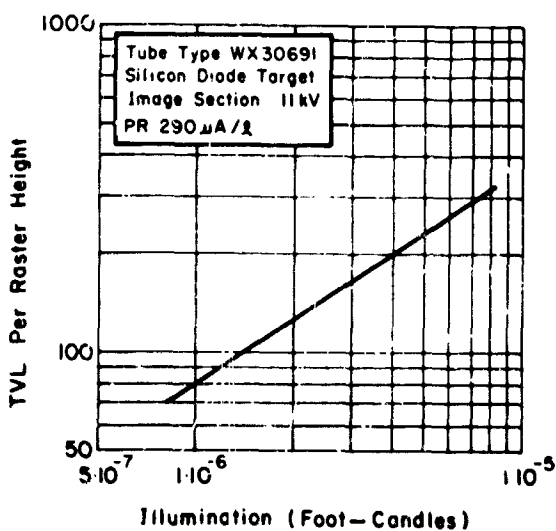


Figure A-4. Static sensitivity for a silicon-diode array target camera tube (based on the WL-30691).

light levels, the silicon-diode array camera tube continues its operation due to the high target gain. The resolution under dynamic (as compared to static) conditions can be expected to deteriorate rapidly with decreasing illumination level. This is a consequence to be expected from the low target voltage excursion that would occur and the high target capacitance. Thus, at very low light levels, the advantage of the high gain of the silicon-diode array target may be seriously diminished due to discharge lag, which results in image smear. Although the silicon-diode array target will certainly offer additional picture information at low illumination levels, it remains to be determined how effectively this information can be utilized by an individual observing a television monitor screen. It is possible that discharge lag may preclude the attainment of the ultimate sensitivity anticipated for the silicon-diode array target tubes under dynamic conditions.

In addition to possessing high gain, the silicon-diode array target is electrically rugged, there being no degradation or burn due to high input illumination. This leads to anticipation of long life.

Under electron-beam scanning of the reading surface of the target, a "whiting out" (MOS effect) has been frequently observed and reported by Crowell and Labuda (ref. 3). This deleterious effect is attributed to the formation of an inversion layer at the interface of the N-type of silicon and the silicon dioxide; this effect appears to be a function of scanning time and target bias. Although targets have operated for many hours and have not exhibited this "whiting out," it remains to be seen if this deleterious effect places a significant limit on target life.

The largest single use of low-light-level television is in military applications. Such applications require highly "ruggedized" tubes capable of operation over a broad range of environmental conditions. The existing family of SEC tubes has been found to satisfy these requirements; hence, the simple retrofitting of these types of tubes with silicon-diode array targets is a natural anticipation. Success in achieving this will depend upon the ultimate reduction of target dark current, lag, and the adjustment of target mechanical resonances to permit satisfactory tube operation.

References

1. Buck, T. M.; Casey, H. C., Jr.; Dalton, J. V.; Yamin, M.: Influence of Bulk and Surface Properties on Image Sensing Silicon-Diode Arrays. *B.S.T.J.*, vol. 47 no. 9, 1968.
2. Crowell, M. H.; Buck, T. M.; Labuda, E. F.; Dalton, J. V.; Walsh, E. J.: A Camera Tube with a Silicon-Diode Array Target. *B.S.T.J.*, vol. 46, no. 4, 1967.
3. Crowell, M. H.; Labuda, E. F.: The Silicon-Diode Array Camera Tube. *B.S.T.J.*, vol. 48, no. 7, 1969.
4. Gordon, E. L.: A Solid-State Electron Tube for the PICTURE-PHONE Set. Bell Laboratories Record, vol. 45, no. 6, 1967.
5. Gordon, E. L.; Crowell, M. H.: A Charge Storage Target for Electron Image Sensing. *B.S.T.J.*, vol. 47, no. 9, 1962.
6. Wendland, P. H.: A Charge-Storage Diode Vidicon Camera Tube. *IEEE Trans. Elect. Devices*, vol. ED-14, no. 6, 1967.

Appendix B

(Compiled by A. B. Laponsky)

This is a bibliography on Secondary Electron Conduction and Transmission Secondary Emission from Low Density Lasers, divided into the following categories:

- I. Secondary Electron Conduction and Transmission Secondary Emission Phenomena
- II. Secondary Electron Conduction and Transmission Secondary Emission Devices
- III. Systems Using Secondary Electron Conduction and Transmission Secondary Emission Devices.

I. Secondary Electron Conduction and Transmission Secondary Emission Phenomena

1. Akagi, M. and S. Yoshida: "Energy Distribution of Transmitted Secondary Electrons from Thin Porous KCl Films," *Japanese Journal of Applied Physics*, Vol. 6, p. 1028, 1967.

This is a short note describing a method of measuring the secondary electron energy distribution. A short discussion of film charging is given, and a resistance value for the films under electron bombardment is given.

2. Boerio, A. H.: "The Effect of Intense Exposures on SEC Targets," Westinghouse Electronic Tube Division, Elmira, report April 13, 1965. (Westinghouse Confidential)

Two WX-5419A SEC camera tubes were used in this investigation to determine to what levels an SEC camera tube can be exposed before a temporary or permanent reduction in gain results.

3. Boerio, A. H., R. R. Beyer, and G. W. Goetze: "The SEC Target," *Advances in Electronics and Electron Physics*, (Academic Press, L. Marton, Editor), Vol. 22A, p. 229, 1966.

An excellent and thorough description of the operation and characteristics of SEC targets.

4. deVries, H. R. and K. F. Boll: "An SEC Target With High Storage Capacity," Technical Report, Westinghouse Electric Corporation, ETD.

Report presents a theoretical and experimental evaluation of the significance of increasing the SEC target capacity per unit area.

5. Edgecumbe, J. and E. L. Garwin: "CsI As a High Gain Secondary Emission Material," *Journal of Applied Physics*, Vol. 37, pp. 3321-3322, 1966.

Good brief communication on low density CsI as a TSE element.
Gives a comparison with KCl.

6. Garwin, E. L. and J. Edgecumbe: "Response of Low-Density KCl Foils to Multi-Mev Electrons," *Advances in Electronics and Electron Physics*, (Academic Press, L. Marton, Editor), Vol. 22A, p. 635, 1966.

A good article on high energy electron detection including the preparation of low density targets and their detection capabilities.

7. Goetze, G. W.: "On The Use of Transmission Secondary Emission for Electrical Storage Devices," Research Report, Westinghouse Research Laboratories, Pittsburgh, Pa., Report No. 12-1505-1-R3-X (Westinghouse Confidential), October 3, 1960.

This paper deals theoretically with the problem of charge storage in transmission type dynodes employing a low density insulator on a conductive backing.

8. Goetze, G. W.: "Secondary Electron Conduction (SEC) and its Application to Photo-Electronic Image Devices," *Advances in Electronics and Electron Physics*, (Academic Press, L. Marton, Editor), Vol. 22A, pp. 219-227, 1966.

Excellent and thorough discussion of the SEC and TSE modes of operation of low density layers including basic considerations regarding the mechanisms involved.

9. Goetze, G. W.: "Transmission Secondary Emission from Low Density Deposits of Insulators," *Advances in Electronics and Electron Physics*, (Academic Press, L. Marton, Editor), Vol. 16, p. 145, 1962.

Discusses dynode fabrication and characteristics in some detail with regard to TSE.

10. Goetze, G. W., A. H. Boerio, and M. Green: "Field Enhanced Secondary Electron Emission from Films of Low Density," *Journal of Applied Physics*, Vol. 35, No. 3, p. 482, 1964.

Excellent and thorough discussion of the preparation of low density TSE layers and their TSE characteristics.

11. Green, M. and A. H. Boerio: "Primary Penetration Measurements on the SEC Target," Technical Report, Westinghouse Electric Corporation, ETD, Report No. ET-7 (Westinghouse Confidential), July 1, 1965.

This is an excellent short report describing a method of monitoring SEC targets in sealed-off tubes by making measurements of

transmission secondary emission of the targets. A means for determining the mass per unit area of the KCl layer from the primary penetration data is given along with experimental results.

12. Green, M., A. H. Boerio, and G. W. Goetze: "Research on High Gain Transmission Secondary Emission Films," Research Report, Westinghouse R & D Center, Pittsburgh, Pennsylvania, Research Report No. 64-9Z27-252-R1, August 3, 1964, Final Report, Contract No. DA-44-009-ENG-4858, USAERDL, Fort Belvoir, Virginia.

A thorough and broad description of the nature of TSE from low density KCl films.

13. McMullan, D. and G. O. Towler: "Stable SEC Target for Television Camera Tubes," *Electronics Letters*, Vol. 4, pp. 360-362, August 23, 1968.

Various aspects of the overload signal stability of SEC targets formed from good and poor secondary emitting materials are considered. It is shown that a target consisting of two layers can be made to be inherently stable to signal overload while still having a high gain.

14. Raykhel, T. and V. Yaresh: "An Investigation of Transmission Secondary Electron Emitters," *Radio Engineering and Electronic Physics*, Vol. 11, pp. 1606-1609, 1966. Russian and English.

The mechanism of transmission secondary electron emission is considered utilizing emitters that consist of a metal grid or aluminum-oxide foil serving as substrate, intermediate conducting aluminum layer, and compact or porous MgO or KCl secondary emission layers.

15. Reynolds, G. T.: "Secondary Electron Multiplication in Image Intensifier Dynode Structures," *IEEE Transactions on Nuclear Science*, Vol. NS-13, No. 3, pp. 81-87, June 1966.

Statistics on transmissive secondary electron emission (not low density).

16. Schackert, P. H.: "The Influence of Water Vapor on the SEC Targets Made From Standard KCl and Ultra-High Purity KCl," Westinghouse Electronic Tube Division, Elmira.

Presentation of some of the results from experiments that indicate the severe effects of water vapor on targets. It may be noted that both the ultrahigh purity and standard KCl materials used are equally affected.

17. Seiler, H. and M. Stark: "Hohe Sekundärelektronen-Emission aus BaF₂ - Schichten geringer Dichte," *Zeitschrift für angewandte Physik*, Vol. 19, p. 90, 1965.

A thorough discussion of reflection secondary electron emission from low density BaF_2 layers, including properties of the layers, experimental apparatus and methods, results of measurements, and the secondary electron energy distribution.

18. Serebrov, L. A. and S. A. Fridrikhov: "Results of Investigation of Field Enhanced Secondary Electron Emission From Thin Films of Sodium Chloride," *Soviet Physics - Solid State*, Vol. 6, No. 6, p. 1336, December 1964.

Gives experimental results of studies of secondary emission from porous NaCl films of 0.5 to 5.0 micron thickness.

19. Serebrov, L. A. and V. I. Salin: "Field Enhanced Secondary Electron Emission During Transmission Through Magnesium Fluoride Films," *Soviet Physics - Solid State*, Vol. 7, No. 5, p. 1261, November 1965.

A short technical article dealing with transmission secondary electron emission through low density layers of MgF_2 .

20. Serebrov, L. A. and V. I. Salin: "Field Enhanced Secondary Electron Emission on Transmission Through Thin Zinc Sulfide Films," *Soviet Physics - Solid State*, Vol. 7, No. 4, p. 988, October 1965.

This is a short technical article dealing with transmission secondary emission through porous films of ZnS.

21. Zernov, D. V. and N. L. Yasnopolsky: "Electron Emission From Dielectric Films in Which a High Electric Field is Present," *Radio Engineering and Electronic Physics*, Vol. 9, No. 11, p. 1583, 1964.

This article reviews possible mechanisms for electron emission from dielectric films including porous layers. Gives status as of 1964.

II. Secondary Electron Conduction and Transmission Secondary Emission Devices

22. "A Proposal For a Study of the Design Problems on an Integrating Television Tube for Astronomical Research," Proposal, CBS Laboratories, Stamford, Conn., No. CLD-572, January 16, 1964.

The proposal discusses the use of the vidicon, image orthicon, ebicon, and SEC vidicon as integrating television tubes for astronomical research. It is indicated that any CBS integrating camera tube would use a low-density, alkali halide target.

23. Altling-Mees, H. R.: "Uvicon Contract SD-22-13," Final Report, Westinghouse Electric Corporation, ETD, Electro-Mechanical Research No. DS-22-13, Smithsonian Astrophysical Observatory, No. S1-522, NASA No. NAS5-1535.

Report describes manufacture and testing of Uvicon tubes during the period October 1964 to September 1966. Included are tables giving detailed test information and an addendum discussing the digital-scan-crossover problem.

24. Alting-Mees, H. R.: "Test of Charging Effect on a Uvicon Target," Technical Report, Westinghouse Electric Corporation, ETD, October 18, 1966.

A brief report of experimental data on the charging of the exit surface of a Uvicon tube during the presence of the readout beam.

25. Anderton, H. and H. Alting-Mees: "The Development of a Long Integration SEC Camera Tube," Westinghouse Electric Corporation, ETD, Elmira, New York, ET-30, Final Technical Report on Contract No. 86PE-87-43387-0S, November 1967.

This report describes the modification of the Westinghouse SEC tube WX-5419B to achieve long-time integration for astronomical observations.

26. Anderton, H. and R. R. Beyer: "Dynamic Imaging With Television Cameras." Paper presented at Fourth Symposium on Photoelectronic Image Devices (London, 1968) in *Advances in Electronics and Electron Physics*, (Academic Press, L. Marton, Editor), volume in press.

This is a general paper on dynamic imaging; however, performance curves are given for SEC tubes, intensifier SEC tubes, and image orthicons.

27. Beyer, R. R. and G. W. Goetze: "An Optically Scanned SEC Camera Tube," *Advances in Electronics and Electron Physics*, (Academic Press, L. Marton, Editor), Vol. 22A, pp. 241-250, 1966.

A good article indicating the resolution and noise capabilities of SEC tubes with optical scanning replacing the readout gun.

28. Beyer, R. R., M. Green, and G. W. Goetze: "Point Source Imaging With The SEC Target," *Advances in Electronics and Electron Physics*, (Academic Press, L. Marton, Editor), Vol. 22A, pp. 251-260, 1966.

A comprehensive article discussing sensitivity, reciprocity, photometric range, and photometric reproducibility of image tubes using SEC targets with point source images.

29. Boerio, A. H.: "ATM Program NAS8-20860," Final Report Phase I, March 1969.

The primary objective for Phase I of the ATM Project was to redesign the WX-31189 SEC camera tube to satisfy the vibration requirement. This resulted in the WX-31189N.

30. Boerio, A. H. and G. W. Goetze: "The Application of the Low Density KC1 Target to Signal Amplification and Storage in Camera Tubes," Scientific Paper, Westinghouse Research Laboratories, Pittsburgh, Pennsylvania, No. 62-112-252-P3, August 1, 1962.

An excellent report describing parameters effecting contrast and the characteristics of direct readout tubes using low-density KC1 targets.

31. Boerio, A. H. and J. Mueller: "Exploratory Development of Ultraviolet Imaging Devices," Final Technical Report, Westinghouse Electric Corporation, ETD, No. AFAL-TR-66-4, Final Report Contract No. AF33(615)-1991, Wright-Patterson Air Force Base, Ohio, February 1966.

A comprehensive study of enhancing the capability of ultraviolet camera tubes in the radiation region of 2800 to 3200 angstroms.

32. Burns, J.: "Modern Image Tube and Their Applications," *IEEE International Convention Record*, Part 7, p. 49, March 1967.

Discusses image tubes in general. Indicates advantages in use of low density layers for TSE and the important advantages of the SEC tube over the vidicon and image orthicon.

33. "Camera Tube For Ultra-Violet Radiation," *Radio and Electronic Engineer*, Vol. 37, p. 46, January 1969.

Brief discussion of the Uvicon, used in NASA's unmanned satellite, the Orbiting Astronomical Observatory, OAO-A2.

34. Doughty, D. D.: "Ultraviolet Sensitive Camera Tubes Incorporating the SEC Principle," *Advances in Electronics and Electron Physics*, (Academic Press, L. Marton, Editor), Vol. 22A, p. 261, 1966.

Describes the general properties of the Uvicon, including the types of photosurfaces and input windows and the overall tube performance characteristics.

35. Doughty, D. D., W. Divens, and E. G. Vaerewyck: "Fabrication of Uvicon Tubes," Final Report, Westinghouse Research Laboratories, Pittsburgh, Pennsylvania, Subcontract No. SD-22-12, Electro-Mechanical Research, Inc., January 10, 1965.

An extensive report on design, manufacture, and testing of Uvicon tubes.

36. Doughty, D. D., W. A. Feibelman, and G. W. Goetze: "Task Force Report on Uvicon Tubes," Westinghouse Research Laboratories, Pittsburgh, Pennsylvania, Research Report No. 63-112-252-R1, July 16, 1963.

Describes efforts to improve the characteristics of Uvicon tubes to meet performance specifications for flight models.

37. Filby, R. S., S. B. Mende, and N. D. Twiddy: "A Television Camera Tube Using a Low Density Potassium Chloride Target," *Advances in Electronics and Electron Physics*, (Academic Press, L. Marton, Editor), Vol. 22A, p. 273.

A good article describing the characteristics of the SEC type of camera tube and including some detail on target fabrication and structure.

38. Filby, R. S., S. B. Mende, and N. D. Twiddy: "The Detection of Faint Optical Images by Charge Integration," *International Journal of Electronics*, Vol. 19, p. 387, 1965.

A new television camera, intended for scientific application, having a very high sensitivity and good storage properties. Excellent and complete discussion of SEC and TSE of low density targets in direct readout camera tubes and tube characteristics.

39. Filby, R. B., S. B. Mende, M. E. Rosenbloom, and N. D. Twiddy: "A New Television Camera, Intended for Scientific Applications, Having a Very High Sensitivity and Good Storage Properties," *Nature*, Vol. 201, p. 801, February 22, 1964.

A brief article describing the operation, characteristics, and use of camera tubes using low density targets (i.e., SEC tubes).

40. Goetze, G. W.: "On The Use of Transmission Secondary Emission for Electrical Storage Devices," Research Report, Westinghouse R & D Center, No. 12-1505-1-R3X, October 1960.

The influence of charging of thin film layers on secondary electron emission is discussed and the beneficial effects of such charging on low density layers for use in TSE-type devices is indicated. This report is primarily analytical in nature.

41. Goetze, G. W. and A. H. Boerio: "SEC Camera Tube Performance Characteristics and Applications." Paper presented at Fourth Symposium on Photoelectronic Image Devices (London, 1968) in *Advances in Electronics and Electron Physics*, (Academic Press, L. Marton, Editor), volume in press.

This paper describes in some detail the types of SEC camera tubes in regular production and their employment in low-light-level television, color television cameras, and scientific applications.

42. Goetze, G. W. and A. H. Boerio: "Secondary Electron Conduction (SEC) For Signal Amplification and Storage in Camera Tubes," *Proceedings of the IEEE*, Vol. 52, pp. 1007-1012, 1964.

Good brief discussion of the SEC operation and parameters of tubes of the direct readout type employing SEC targets.

43. Goetze, G. W., A. H. Boerio, and H. Shabanowitz: "Applied Research on SEC Amplification Camera Tube," Westinghouse Research Laboratories, Pittsburgh, Pennsylvania, Research Report No. 63-912-255-R8, August 23, 1963.

Report describes the design, construction, and evaluation of several camera tubes using the SEC target and S-20 photocathode. The use of low-velocity, direct-beam target scanning and target suppressor mesh is discussed.

44. Green, M., R. R. Beyer, and H. R. deVries: "Exploratory Development of High Resolution Television Camera Tubes," Final Technical Report, Westinghouse Electric Corporation, ETD, No. AFAL-TR-65-271, Final Report Phase I, Contract AF33(514)-1271, Wright-Patterson Air Force Base, Ohio, November 29, 1965.

This is an extensive report on the development of high-performance television camera tubes by exploiting the capabilities of the SEC target. Covers work performed from May 1964 through June 1965.

45. Green, M.: "The Influence of the Reading Beam Diameter on the Transfer Function of an SEC Camera Tube," Westinghouse ETD, Elmira, ET-13, December 15, 1965.

A detailed report on the transfer function of an SEC tube from both theoretical and experimental analyses.

46. Green, M.: "Image Subtraction With The SEC Vidicon," Research Memorandum, Westinghouse Research Laboratories, Pittsburgh, Pennsylvania, August 31, 1964.

Report discussed differential operation of an SEC vidicon in which images can be formed on the target as either positive or negative potential distributions. Through proper operation, subtraction of one image from another can be achieved.

47. Heimann, W., M. Hermann, and C. Kunze: "SEC Television Pick-Up Tube." Paper presented at Fifth Symposium International de Télévision, Montreaux.

A general review of the SEC tube and how it operates.

48. Hertel, Richard James: "The Porous KCl Layer Vidicon as an Electron Microscope Image Detector," (MS Thesis), Cornell University (Ithaca, New York), Materials Science Center, Report 1053, February 1969.

A discussion and comparison of the use of photographic materials and a special electron image tube as high-resolution, electron-microscope image detectors. Particular attention is given to determining what is necessary to achieve the minimum detector noise. The limits of performance of the photographic plate and the image tube are analyzed, and the optimization of the noise performance vs. bandwidth, resolution, and storage capacity are discussed.

49. Klotzbaugh, G. A.: "Research and Development of a Camera Tube For Night Viewing," Westinghouse R & D Center, Research Report No. 64-912-255-R7, December 3, 1964. Final Report Contract No. DA 36-039-AMC-03205(E).

This is a good report describing the complete results on a low-light-level camera tube which employs an SEC target with two TSE dynodes for pre-beam multiplication.

50. Marshall, F. B. and G. D. Roane: "Performance Comparison of the SEC Camera Tube and the Image Orthicon," *Advances in Electronics and Electron Physics*, (Academic Press, L. Marton, Editor), Vol. 22A, p. 291, 1966.

Gives quantitative comparison data.

51. Mengers, Paul: "Noise Limited Resolution of Low Light Level Camera Tubes," Dalmo-Victor Company, Report No. R-00-3258, September 16, 1963.

Presents theoretical analysis of the image orthicon and the Westinghouse SEC vidicon.

52. Parrish, W. F. and P. D. Lee: "Comparison of Underwater Camera Tubes," Westinghouse OR+EC, Annapolis, Maryland, Report.

A vidicon and SEC camera were compared on the basis of noise, MTF at high and low contrasts, sensitivity, response to scene motion, and response to bright sources within the field of view; 90-percent and 40-percent contrast underwater resolution charts were used. For underwater use, SEC shows promise because of its ability to operate at low light levels and because of its better response to low contrasts and moving scenes.

53. Pietrzyk, J., R. Harder, and M. Green: "Exploratory Development of High Resolution Camera Tubes," Westinghouse Electric Corporation, ETD, Elmira, Technical Report No. ET-22, October 1966. Contract No. AF33(615)-1271, Wright-Patterson Air Force Base, Ohio. Report No. AFAL-TR-66-255.

This report covers Phase II of the high-resolution camera-tube development program. Included are discussions of the WX-5419B SEC camera tube design, tests, photocathode development (S-20 and S-1), and performance characteristics.

54. Randels, R. B.: "Behavior of SEC Camera Tube Under Gamma Irradiation," Westinghouse, Elmira, Electronic Tube Division, Image Tube Engineering Memorandum No. 27, February 28, 1969.

Four SEC camera tubes were subjected to gamma irradiation from a cobalt 60 source to determine whether or not any change took place in performance of the irradiation. No permanent irreversible effects were observed.

55. Randels, R. B.: "Development of Manufacturing Methods for Production of Wide Dynamic Range Television Pickup Tubes," Westinghouse Electric Corporation, ETD, Elmira, Technical Report, AFML-TR-67-58, Part I, March 1967 (Classified).

This is an extensive report on the design and process engineering studies affecting tube performance and production yield of three SEC camera tube types.

56. Randels, R. B.: "Manufacturing Methods for Production of a Wide Dynamic Range Television Pickup Tube," Air Force Materials Laboratory Technical Report AFML-TR-67-58, Part II, "Three-Inch Magnetic and Electrostatic Tube Environmental Tests," November 1967 (Classified).

57. Santilli, V. J.: "The Design, Development, and Production of the WX-30690 SEC Camera Tube," Final Report, January 16, 1969.

The development and manufacture of WX-30690 SEC camera tube and the study of the techniques associated with its fabrication are discussed. The WX-30690 is an SEC camera tube designed specifically to provide a higher resolution television image under the environmental conditions of military use.

58. Schneeberger, R. J. and J. W. Coltman: "Optical Sensor Systems for Underwater Search," Westinghouse Research Laboratory, Pittsburgh, Pennsylvania, Research Memorandum 67-1C2-TAADS-M2, May 3, 1967.

This is a good report on the imaging of low contrast scenes by use of camera tubes. Comparisons are presented of the use of two television sensors: one with a WX-31189 SEC vidicon and the other with an 8057 vidicon. Comparison with respect to the human eye is also given.

59. Schneeberger, R. J. and R. J. Hansen: "Ultra-Violet Camera Tube Development," Westinghouse Electric Corporation, Pittsburgh, Pennsylvania, Technical Report No. RTD-TDR-63-4188, December 1963, Final Report, Contract No. AF33(657)-9198, Wright-Patterson Air Force Base, Ohio.

A good report describing design considerations, construction, operation, and performance of a solar-blind sensor using an SEC pickup tube for detection in the 2000 to 3000 angstroms spectral region.

60. Smith, H. M., J. E. Ruedy, and G. A. Moiston: "Performance of a Photomultiplier With a Porous Transmissive Dynode," *IEEE Transactions on Nuclear Science*, Vol. NS-13, No. 3, pp. 77-80, June 1966.

Discusses statistics of transmissive secondary electron emission from low density dynodes of KCl.

61. Soule, H. V.: "Electro-Optical Photography at Low Illumination Levels," New York, Wiley, 1968.

The first book devoted exclusively to the subject of low-light-level, electro-optical photographic systems. See especially:

- 6.3 Low Light Level Vidicons (p. 136 f.)
- 12.4 Low Light Level Television (p. 305 f.)
- 12.5 System Comparisons (p. 308 f.)

62. Sternglass, E. J. and G. W. Goetze: "Field Enhanced Secondary Emission for High Speed Counting," *IRE Transactions on Nuclear Science*, Vol. NS-9, No. 3, pp. 97-102, 1962.

Good comprehensive discussion on the use of low density KCl as particle detectors for high speed counting.

63. "Study of the Design Problems on a Integrating Television Tube for Astronomical Research," Final Report, Westinghouse Electric Corporation, ETD, Subcontract No. 1, NASA Grant NSG-414, December 1964.

Contains a detailed analysis of integrating television tubes and compares the SEC and Optechon.

64. Szepesi, Z. and M. A. Novice: "Solid State Radiographic Amplifiers and Infrared Converters," Paper presented at the Fourth Symposium on Photoelectronic Image Devices (London, 1968), *Advances in Electronics and Electron Physics*, (Academic Press, L. Marton, Editor), volume in press.

While dealing primarily with photoconductive electroluminescent radiation conversion panels, this paper discusses their use in extending the spectral response of SEC tubes.

65. Turk, W. E.: "A Survey of Camera Tubes for Television Broadcasting," *Journal of the SMPTE*, Vol. 75, pp. 1082-1085, 1966.

Discusses various camera tubes and indicates the expected characteristics of the SEC tube in terms of those of the vidicon and image orthicon.

66. Vine, J.: "Design of a 40/32mm Zoom Image Section for an SEC Camera Tube," Westinghouse Research Laboratory Report No. 68-8C4-COMPA-R1, May 21, 1968, Contract F33(615)-68-C-1597.

This report describes the electron optical design of a 40/32mm zoom image section for an SEC camera tube. The design incorporates a distortion-correcting element. Estimated performance data given include zoom characteristics, resolution, and distortion.

67. Vine, J.: "Design of a Small Image Section for an SEC Camera Tube," Westinghouse Research Laboratories, Pittsburgh, Pennsylvania, Technical Report No. 67-8C4-COMPA-R1, August 2, 1967, Contract No. N00014-67-C-009 (DO-C9).

Design for a small image section for an SEC camera tube is presented. Both spherical and aspherical photocathode surfaces are considered.

68. Vine, J.: "Final Report on the Resolution Study Program for the Lunar Camera Tube," Westinghouse Electric Corporation, Electronic Tube Division Report No. ET-21, August 21, 1966, Contract No. NAS9-3548, NASA Manned Spacecraft Center, Houston, Texas.

An extensive report on the electron optical properties of the Lunar Camera Tube. Separate studies of the reading and image sections were carried out by construction and testing of experimental hybrid vidicons and image intensifiers.

69. White, R. A., H. S. Wilcox, and G. W. Goetze: "Development of a Secondary Electron Conduction (SEC) Camera Tube for Space Applications," *Journal of the SMPTE*, Vol. 76, p. 254, 1967.

Abstract of paper presented at 101st Technical Conference of SMPTE, New York, April 19, 1967. Discusses the use of the SEC effect, making possible the hand-held camera tube for the Apollo lunar mission.

70. Wilcox, H. S.: "Production of WX-31034 Lunar Camera Tube," Final Technical Engineering Report, Prime Contract No. NAS9-3548, Subcontract No. 86PK-87-96641-OS, January 1967 (Classified).

III. *Systems Using Secondary Electron Conduction and Transmission Secondary Emission Devices*

71. Davis, R. J.: "The Telescope Experiment," in Smithsonian Astrophysical Observatory, Special Report No. 282.
72. Davis, R. J.: "The Use of the Uvicon-Telescope Television System for Ultraviolet Astronomical Photometry," *Advances in Electronics and Electron Physics*, (Academic Press, L. Marton, Editor), Vol. 22B, p. 875, 1966.

A fine article discussing the characteristics of the system comprised of the Uvicon SEC camera tube and telescope.

73. Green, M.: "Observation With an Ultrasensitive TV Camera," *Sky and Telescope*, Vol. 35, pp. 140-143, March 1968.

Discusses use of SEC camera tube and image intensifier operating together to view faint astronomical objects.

74. Green, M. and R. Hansen: "The Application of SEC Tubes and Electrostatic Image Intensifiers to Astronomy." Paper presented at Fourth Symposium Photoelectronic Image Devices (London, 1968), *Advances in Electronics and Electron Physics*, (Academic Press, L. Marton, Editor), volume in press.

Describes experiments carried out at the Allegheny and McDonald Observatories. This is an excellent detailed paper.

75. Grodski, J. J. and B. W. Schumacker: "Local Density Determinations in Rarefied Gas Glows by Measuring the Large-Angle Single Scattering From an Electron Beam," *I.S.A. Transactions*, Vol. 6, p. 103, 1967.

Includes in the discussion the advantage of using an SEC tube to obtain a two-dimensional cross-section of the local density distribution in the gas flow.

76. Hansen, J. R.: "High Resolution X-Ray Non-Destructive Testing," Westinghouse Research Laboratories, Pittsburgh, Pennsylvania, Research Memorandum 67-102-TAACP-M2, December 15, 1967.

This report describes a system for nondestructive testing using a WX-30691 SEC camera tube with X-ray sensitive fluorescent screens. Use of commercially available X-ray screens and two thicknesses of CsI (T1) as wavelength converters is discussed and evaluated. Preliminary results on the use of a fiber optic magnifier are presented.

77. Hansen, J. R.: "Use of an SEC Camera Tube for Recording Faint Celestial Objects," Westinghouse Research Laboratories, Pittsburgh, Pennsylvania, Research Memorandum 67-1C2-TAACP-M1, December 5, 1967.

This is an excellent report describing results of experiments using a WX-30691 SEC camera tube in a Westinghouse STV 606 camera chain for viewing and recording celestial objects through the Allegheny Observatory 30-inch Thaw refractor. Photographs of television presentations of nebulae, double stars, star clusters, etc., are given.

78. Hansen, J. R. and M. Green: "Versatility of the SEC Camera Tube for Astronomical Applications," Westinghouse Research Laboratories Memorandum No. 68-1C2-TAACP-M1, May 27, 1968, (Westinghouse Confidential).

An experiment at McDonald Observatory, University of Texas, demonstrated some of the advantages of using an SEC television camera to observe and to record a variety of celestial objects. The equipment used consisted of the Westinghouse WL-30691 SEC camera tube installed in an improved Westinghouse STV 606 camera chain.

79. Laponsky, A. B.: "Test of Beta Particle Source Imaging Using the WL-32000 Intensifier SEC Camera Tube," Westinghouse Electronic Tube Division, Elmira, Engineering Report ET-35, January 21, 1969.

Autoradiography is a method of nondestructive testing that has found extensive use in medical and industrial applications. In this method, specimens to be studied may be rendered radioactive by the use of tracer elements and the sources of the radioactivity imaged on photographic film. In this report, the imaging of beta particle sources from tracers of low activity is considered by electronic camera tube techniques.

80. Lowrance, J. L. and P. M. Zucchini: "Integrating Television Sensors for Space Astronomy," Princeton (N.J.) University Report, October 18, 1968.

Reviews the requirements with particular emphasis on the optimum interface with a large diffraction-limited telescope and with an echelle spectrograph. Data presented include results both from theoretical analysis and from laboratory evaluation of the Westinghouse WX-5419B SEC vidicon and of the 1-mil mesh spacing image isocon.

81. Mende, S. B. and B. J. O'Brien: "A High Sensitivity Satellite-Borne Television Camera for the Detection of Auroras," *Applied Optics*, Vol. 7, pp. 1625-1634, 1968.

A high sensitivity satellite-borne television camera, using an SEC television camera tube as the light sensor, has been developed to measure such faint light sources as auroras.

82. Mende, S. B.: "A Low-Light-Level Slow-Scan TV Camera for Satellite Applications," Rice University (Houston, Texas), Dept. of Space Science Report, January 1968.

A short description of the Owl Satellite television camera system and of several unique design features used with the SEC vidicon tube is presented.

83. Miller, J. S. and E. J. Wampler: "Television Detection of the Crab Nebula Pulsar," *Nature*, Vol. 221, pp. 1037-1038, 1969.

This article discusses the use of a Westinghouse television camera using an image intensifier coupled to an SEC camera tube to photograph a pulsar in the Crab Nebula at Lick Observatory, California, February 3, 1969.

84. Nozawa, Y.: "A Digital Television System for a Satellite-Borne Ultraviolet Photometer," *Advances in Electronics and Electron Physics*, (Academic Press, L. Marton, Editor), Vol. 22B, p. 865, 1966.

A good article discussing the vidicon characteristics and problems in relation to its use in the ultraviolet photometer system.

85. "Visible Pulsar," *Scientific American*, Vol. 220, p. 46, March 1969. (Photographs on p. 49.)

A WL-32000 SEC camera tube coupled with an image intensifier was used, and Pulsar NP 0532 was associated with an optically visible object. The observations and photographs were made at Lick Observatory, California.

Appendix C

(G.W. Goetze)

This appendix is comprised of fourteen illustrations of condensed data on five SEC camera tubes.

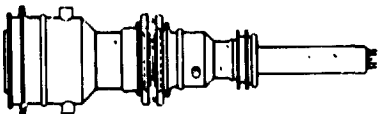
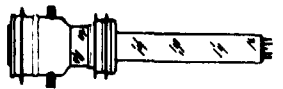
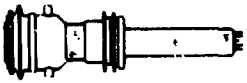
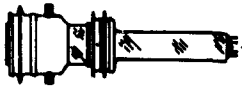
Westinghouse SEC Camera Tubes	Physical Data									
	Tube Type	Photocathode Diameter	Target Diameter	Image Section Focus	Reading Section Focus	Magnetic Deflection	Length	Diameter	Shunt Capacity (pf)	Photo-Cathode Type
	WX54198	1.6"	1.6"	Magnetic	Magnetic	M	17.5"	3.3"	50	S-20 GLASS
	WL32000	1.6"	.625"	Electrostatic	Magnetic	M	13.9"	4.0"	25	S-25 FIBER OPTIC
	WX30854	1.6"	1.0"	Electrostatic	Magnetic	M	13.5"	4.0"	35	S-20 FIBER OPTIC
	WX30893	1.0"	1.0"	Electrostatic	Magnetic	M	9.0"	2.9"	35	S-20 FIBER OPTIC
	WX30891	1.0"	.625"	Electrostatic	Magnetic	M	8.5"	2.9"	25	S-20 FIBER OPTIC

Figure C-1. Physical data on SEC camera tubes.

Operating Tube Data								
Tube Type	Photocathode Voltage Image Section	Anode Cone Voltage	Target Voltage	Suppressor Mesh Voltage	Thermionic Cathode Voltage	Magnetic Focus Field	Peak Deflection Current	
							Horizontal	Vertical
WX5419B	-7.5 KV	Ground	10-30 Volts	15 Volts	Ground	80 Gauss	1.2 Amps	280 ma
WL 32000	-22 KV -7.5KV	Ground	10-30 Volts	15 Volts	Ground	40 Gauss	170 ma	35 ma
WX30654	-7.5KV	Ground	10-30 Volts	15 Volts	Ground	40 Gauss	300 ma	32 ma
WX30893	-7.5KV	Ground	10-30 Volts	15 Volts	Ground	40 Gauss	200 ma	50 ma
WX30691	-7.5KV	Ground	10-30 Volts	15 Volts	Ground	40 Gauss	170 ma	35 ma

Figure C-2. Operating data on SEC camera tubes.

Life	500 Hour Warranty (Expected Life Time Several Thousand Hrs.)
Thermal Extremes	-82°C, +55°C
Mechanical Stress (Hard Mounting)	
Shock	15g, 11ms
Sinusoidal Vibration	
5 to 50 Hz	0.1" DAD
50 to 500 Hz	10g

Figure C-3. General life and environmental characteristics of SEC camera tubes.

	Typical Value	Units
Sensitivity	15,000	$\mu\text{A}/\text{m}$
Resolution	20	lp/mm
Distortion	2	%
Residual Signal after 80ms (3rd field)	5	%
Gamma	1.0	
Dark Current:		
Filament on	(10^{-11})	A/cm^2
Filament off	(10^{-12})	A/cm^2
Maximum Integration Time:		
Filament on	2	minutes
Filament off	30	minutes

Figure C-4. Electrical characteristics of SEC camera tubes.

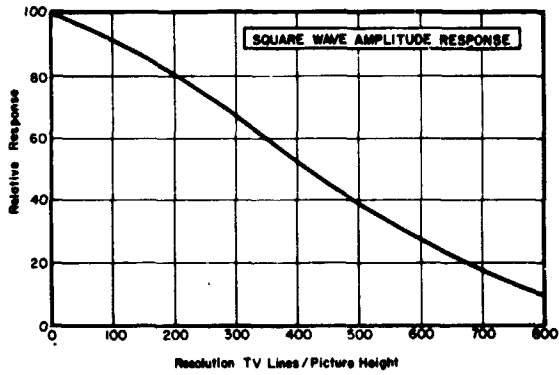


Figure C-5. WX-5419B: square wave amplitude response.

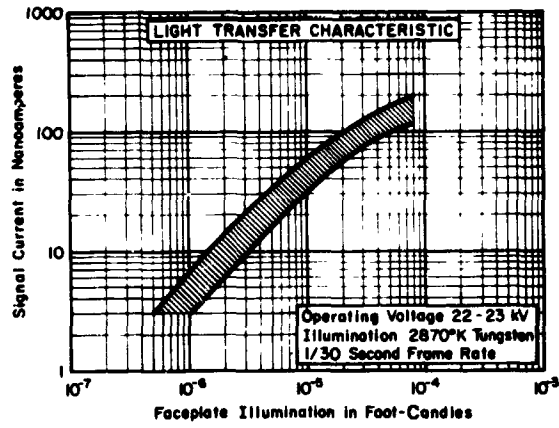


Figure C-8. WL-32000: light transfer characteristic.

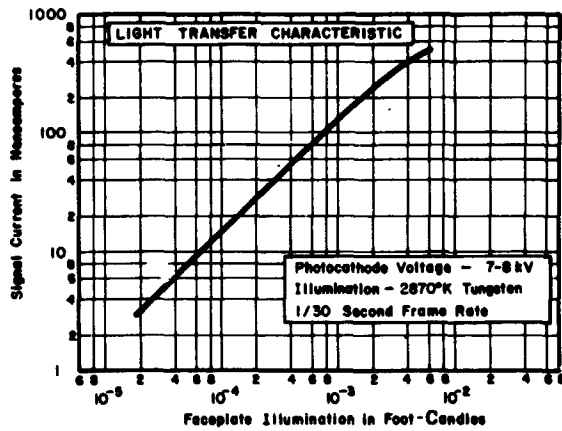


Figure C-6. WX-5419B: light transfer characteristic.

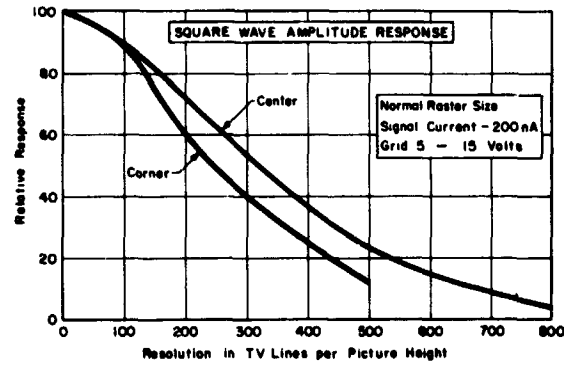


Figure C-9. WX-30654: square wave amplitude response.

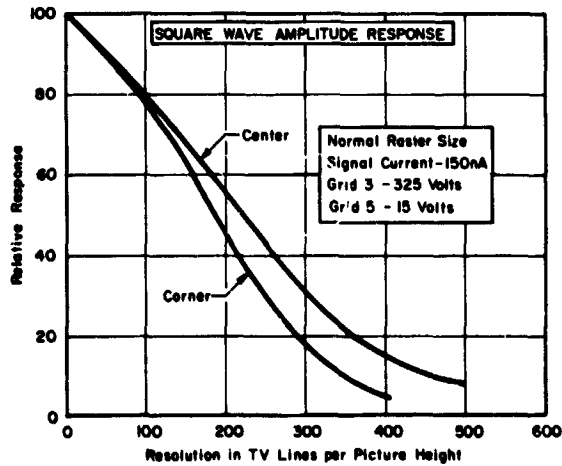


Figure C-7. WL-32000: square wave amplitude response.

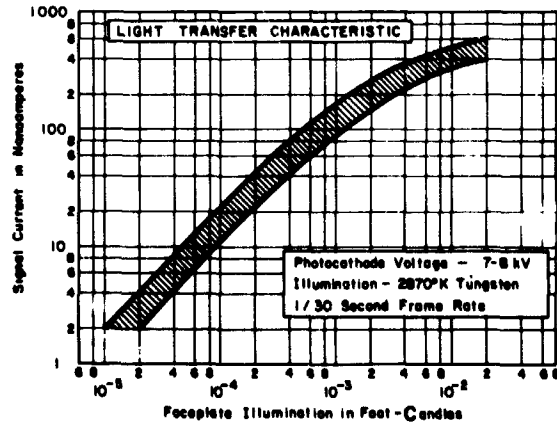


Figure C-10. WX-30654: light transfer characteristic.

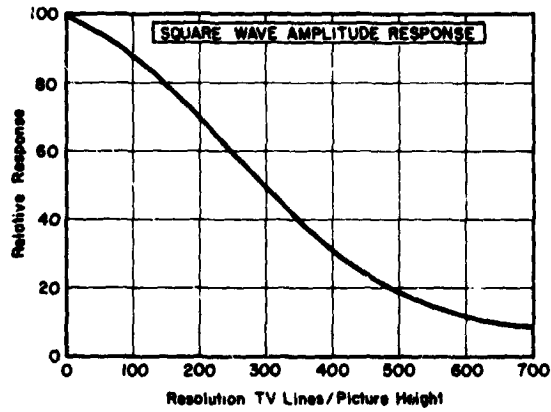


Figure C-11. WX-30893: square wave amplitude response.

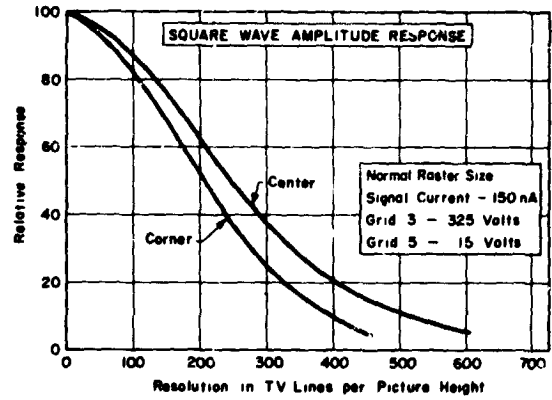


Figure C-13. WX-30691: square wave amplitude response.

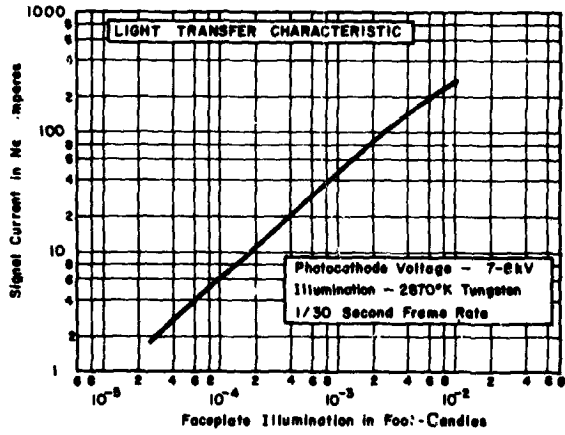


Figure C-12. WX-30893: light transfer characteristic.

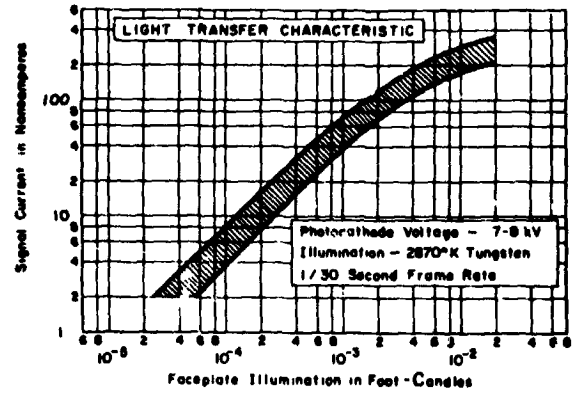


Figure C-14. WX-30691: light transfer characteristic.

N70-36739

The Performance and Capabilities of Recently Developed Plumbicon TV Camera Pickup Tubes

R. S. Levitt

Amperex Electronics Corporation

Introduction

The Amperex Plumbicon[®], developed (refs. 1, 2, 3) by the Philips Research Laboratories of Eindhoven, The Netherlands, some 10 years ago, and introduced into the United States only 3 years ago, has now become the standard and most widely-used color television camera tube in the world (ref. 4).

The Plumbicon is a vidicon type of television-camera pickup tube, which uses for its photosensitive element a layer of semi-conducting oxide of lead (ref. 1). (Lead is *plumbum* in Latin; hence, the name "Plumbicon.") Recent developments in the Plumbicon have resulted in improved versions that have improved wavelength sensitivity (ref. 5), lag (ref. 6), resolution, smaller size, and various electron guns (ref. 7) while retaining all the other quality features of the original Plumbicon. In the course of this paper, we will review the properties of the currently used Plumbicon (ref. 8), update its performance specifications, describe the results of our most recent developments, and discuss a new electron gun (ref. 9) currently under investigation by J.H.T. van Roosmalen of the Philips Research Laboratories. This new electron gun can greatly extend the dynamic range of the Plumbicon upwards by several orders of magnitude and, hence, can correct "comet-tailing" (ref. 10).

We should like to note that the Plumbicon, although originally invented (ref. 1) and developed (ref. 2) in Holland, is currently being manufactured and further developed by the Electro-Optical Devices Division of the Amperex Electronic Corpora-

tion of North American Philips Co., Inc., Slatersville, Rhode Island. The work and data to be described is, however, primarily the work of the staffs of the Research and the Professional Tube Development Laboratories of Philips. They are responsible for the present excellent state-of-the-art of the Plumbicon.

Plumbicon Characteristics

By the use of lead oxide as the photosensitive element (ref. 11), it has been possible to realize some rather unique features for the Plumbicon (ref. 2). These are outlined in figure 1. The first seven of these features (high sensitivity, very low dark current, non-dependence on target voltage, near-unity gamma, very fast lag or signal decay, very adequate resolution, and little or no temperature dependence) occur because the thin, evaporated, polycrystalline lead-oxide layer (ref. 12) behaves as if it were a layer of closely packed, reverse-biased, wide-gap, nearly intrinsic photodiodes with blocking contacts (refs. 13, 2, and 3).¹ In the more common vidicons, the photosensitive layer is a p-type photoconductor with injecting contacts and, hence, is very dependent on bias voltage and temperature, and has a very high, variable dark current and a very long lag. We do not intend to explain in detail how these Plumbicon features occur; rather, we will only present and describe them briefly, referring

¹ duChatenier, F. J.: Private communication. Research Labs, N. V. Philips' Gloeilampenfabrieken, Eindhoven, The Netherlands. This description is now preferred to the earlier ones (refs. 2 and 3), which likened the PbO layer to a layer of p-i-n photodiodes.

[®]Registered Trademark, North American Philips Co., Inc.

1. SENSITIVITY	HIGH
2. DARK CURRENT	NEGLECTIBLY LOW & STABLE
3. DEPENDENCE ON TARGET VOLTAGE	RELATIVELY NONE
4. GAIN (TRANSFER CHARACTERISTICS)	UNITY (LINEAR)
5. LAG	VERY FAST
6. RESOLUTION	GOOD
7. TEMPERATURE DEPENDENCE	RELATIVELY NONE
8. HIGHLIGHT HANDLING	ADEQUATE (POTENTIALLY EXCELLENT)
9. BURN-IN (IMAGE RETENTION)	VERY LOW
10. SIGNAL TO NOISE RATIO	HIGH (AMPLIFIER LIMITED)
11. RUGGEDNESS	GOOD (POTENTIALLY EXCELLENT)
12. OPERATION	SIMPLE & STABLE
13. LIFE	EXCELLENT

Figure 1. Features of the Plumbicon.

the more interested reader to the pertinent published works for the physics (ref. 14). We also intend to cover only features 1 through 7 in figure 1. We will, however, discuss the claimed "potentially excellent" highlight-handling capabilities of the new van Roosmalen "flyback highlight-discharge" electron gun. As far as features 9 to 13 (fig. 1) are concerned, we claim the following: (1) the burn-in or retention of brightly lit images is very low and is mostly absent, even up to several 10's of foot-candles on the faceplate; (2) the signal-to-noise ratio is very high and is, as is generally the case with vidicons, usually limited by the noise of the first video pre-amplifier stages (ref. 15); (3) the Plumbicon is relatively rugged and can be made more so; (4) the operation of the Plumbicon is simple and straightforward and remains stable during operation (ref. 16); and, (5) it has an excellent life, in excess of 1000 hours for most types.

Sensitivity and Dark Current

The first of the distinguishing features of the Plumbicon are illustrated in figure 2 for the XQ1020, a 30-millimeter-diameter, separate-mesh Plumbicon. This camera tube has a typical luminous sensitivity of 400 microamperes per lumen in 2870°K tungsten light.² This is a good deal better than has

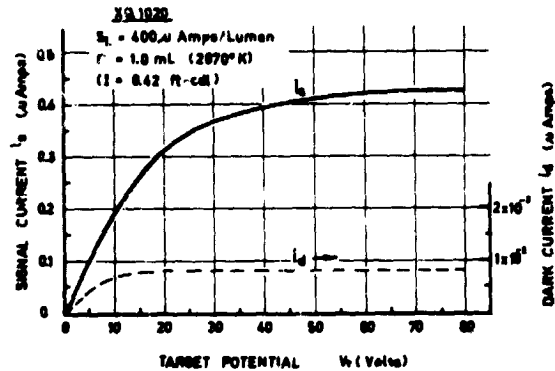


Figure 2. Signal current and observed dark current versus target potential of a typical XQ1020 type Plumbicon with a fixed 1-millilumen (2870°K) target illumination. In practice, a value of 45 volts is generally used, at which point both i_s and i_d have reached or nearly reached saturation.

been previously quoted (refs. 17 and 2). Likewise, the observed dark current is typically about 0.8 nanoamperes, considerably lower than the usually quoted (refs. 17 and 2) maximum allowable value of 3 nanoamperes. Moreover, most of the observable dark current is thought to originate from, and to be controlled by, the light of the filament striking the layer. The true "intrinsic" dark current is thought to be considerably lower.

We see in figure 2 that the signal current saturates as the target voltage is increased. This is just what is expected for a reverse-biased, nearly intrinsic photodiode with blocking contacts (ref. 13).³ In practice, a target bias of 45 volts is used. With the signal current of 400 nanoamperes resulting from a 1-millilumen 2870°K illumination on the faceplate (about one-half of a foot-candle), the observed dark current is some five hundred times smaller than the signal current and, hence, completely negligible over the entire area of the faceplate. It is not the dark current, therefore, which limits the low-level response of the Plumbicon but rather the

² Alternately, 8.2 mA/watt (2870°). To convert from luminous to radiant units, see Appendix.

³ duChatsnier, *op. cit.*

equivalent input noise (about 3 nanoamperes rms) of the video preamplifier stages.

Transfer Characteristics

In figure 3 are given the transfer characteristics for the tube in figure 2. The slope of this curve is defined as the gamma; for the Plumbicon, the curve is between 0.9 and 1.0, typically 0.95. This is the result we would expect if all the photogenerated charge carriers were swept across the bulk of a nearly-intrinsic photodiode in a short time ("short" as compared to their lifetime). In the lead-oxide layer of the Plumbicon, almost all of the layer constitutes the nearly-intrinsic region. A p-region faces the electron gun, and an n-region faces the lens. These regions are very thin layers that serve mainly as blocking contacts to the nearly-intrinsic region to prevent injection of charge carriers (ref. 18). Therefore, a very low dark current should result. The high sensitivity comes about due to a high photon-to electron conversion efficiency

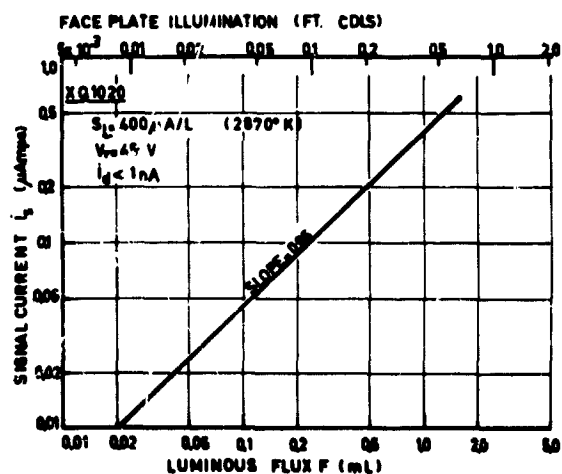


Figure 3. Transfer characteristics for a typical XQ1020 type of Plumbicon at a target potential of 45 volts in 2870°K illumination. As the slope or "gamma" of this curve is nearly unity, then the sensitivity in $\mu\text{Amp/lumen}$ is nearly constant over the entire range of target illuminations; i.e., $<2 \times 10^3$ to $>5 \times 10^1$ foot-candles ($<5 \times 10^6$ to $>1 \times 10^3$ lumens). The target area is 2.2 cm^2 .

(quantum efficiency)—close to 100 percent—over a wide portion of the visible spectral region (ref. 19). The upper limit to the transfer characteristic is set by the available beam current, and the lower limit is set to detectability; i.e., equivalent amplifier-input noise.

Lag

In figure 4 is shown heretofore undisclosed data on Plumbicon lag. Lag is the decay of signal after the source has been turned off, measured in this figure after 60 milliseconds (in the third field of the 625-line, 50-fields-per-second, European system in which the measurements were made) and expressed as the percentage of initial value of the signal (i.e., with the source on). For normal scene illumination, the signal current can be typically 100 to 200 nanoamperes so that lag, as shown here, is typically less than 4 percent. The rise in lag as the signal current

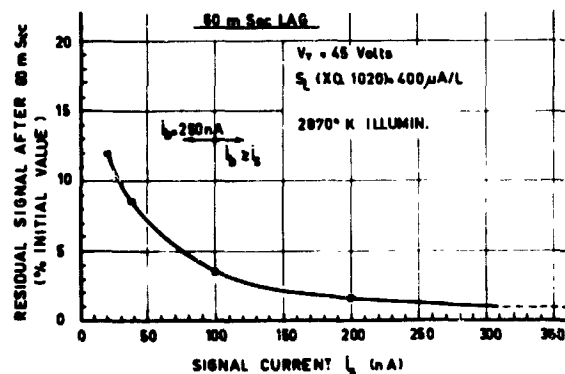


Figure 4. A 60-millisecond (third field) decay lag of the XQ1020 type of Plumbicon as a function of signal current i_s . Lag is measured as the percent of initial value; i.e., the signal level in the "zeroth" field. The current i_b is the maximum possible "beam current" incident at the target and, as such, represents the maximum value of signal current that can just be stabilized. The rise in lag as i_s (and hence target illumination) decreases is due mostly to the reduction in the number of electrons in the beam which during any one scan can land on the target discharging the potential distribution created there by the incident low-level photon flux.

decreases is mostly due to the inability of the electron beam to discharge the layer adequately during one or more fields. This type of lag is called "beam-discharge" lag and is characterized by a dependence on the capacitance of the layer and on the beam acceptance characteristics of the gun (ref. 6). Although the rise in lag seen here at low signal levels (resulting from low light levels) looks rather poor, we claim this performance to be quite comparable to and even to exceed that of the published curves for the very highly rated, low-capacitance-target, SEC vidicon (ref. 20).

Resolution

In figure 5, we have illustrated the resolution performance of the XQ1020 by plotting modulation depth in the center of the picture against the number of TV lines in a square-wave test pattern. Although a value of signal current of 300 nanoamperes is given, there is virtually no dependence on signal current (i.e., light level) except that the resolution is deteriorated in a quite predictable way at very low levels by video noise (ref. 21). As we will see, the absorption of red light is much weaker than that of green or blue;

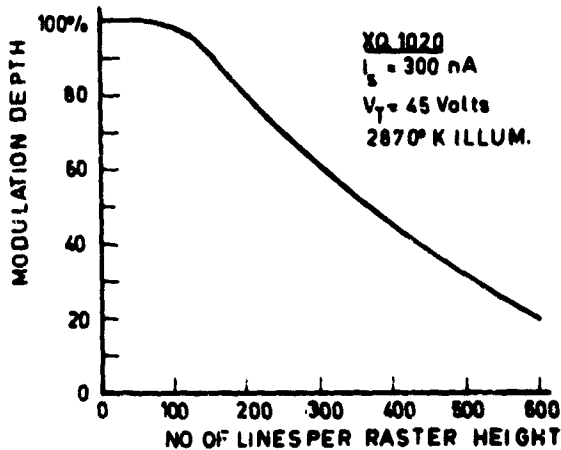


Figure 5. Resolution for a typical XQ1020 type of Plumbicon in terms of modulation depth (square-wave test pattern) at the center of the faceplate, illuminated with 2870°K illumination.

hence, red light is more scattered by the layer; and, consequently, resolution of reds can be expected to be somewhat poorer than that for blues.

Temperature Dependence

The temperature dependence of sensitivity, lag, and resolution is indicated in figure 6. It should be noted that these curves are only representative and not necessarily typical. We show the relative or percentage change in the room temperature (+20°C) value over the temperature range from -30° to +60°C.⁴ We see that the sensitivity is relatively constant with temperature. Because the dark current is thought to be controlled mostly by filament light, we expect it to have no temperature dependence up to 60°C; and, indeed, none is observed. The modulation depth at 400 TV lines fluctuates about the

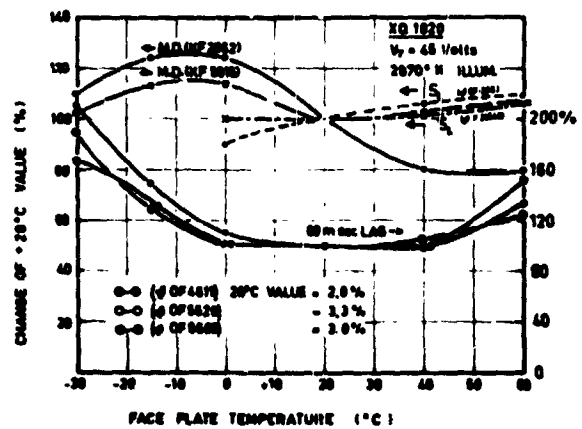


Figure 6. Temperature dependences of specific XQ1020 type of Plumbicon; modulation depth (M.D.), luminous sensitivity (S_L), and 60-millisecond lag (left-hand scale). The ordinates are in terms of the percent of change in the respective 20°C value, the magnitudes of which are given in the insert for lag. The figures in brackets are tube serial numbers. The performance indicated may differ considerably for different tubes and are not necessarily representative of all Plumbicons.

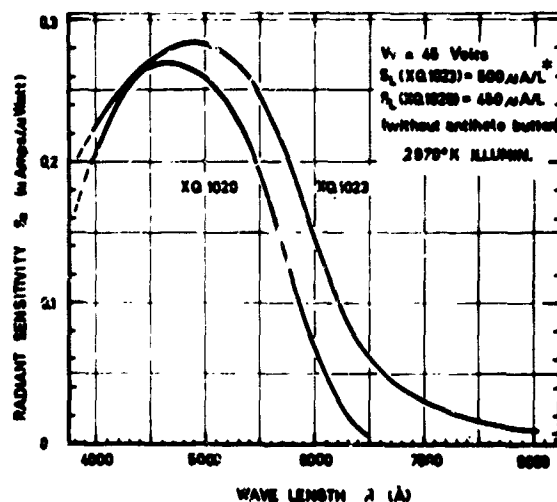
⁴The absolutely maximum safe operating temperature (to meet the guaranteed life, for example) is given in data sheets for the XQ1020 as 50°C.

mean 20°C value, but other samples may show the exact opposite fluctuation. Lag does exhibit a consistent temperature dependence, increasing to about 200 percent (a factor of 2) at low temperatures and 150 percent at high temperatures. But even so, the resulting value for lag of 5 to 9 percent is still quite acceptable, especially when compared to vidicon operated at these temperature extremes (ref. 22).

Spectral Response

If we were asked to point out any major disadvantage of the XQ1020 Plumbicon, it would be its sensitivity at the red end of the spectrum. The sensitivity is poor here because the absorption of lead oxide (PbO) cuts off at about 6200 angstroms. This is not very serious, but it can be objectionable when looking at deep reds, purples, or magentas. It is possible now to correct this condition (ref. 5). For this purpose, the XQ1023, the extended red-sensitive Plumbicon (ref. 23) has been recently introduced. In figure 7, we show the typical spectral response or radiant sensitivity in microamperes per microwatts for this tube along with that for the XQ1020. It should be noted that the XQ1023 has an overall improved sensitivity in green as well as in red. This has been accomplished by incorporating a small amount of sulphur into the layer to form a lead-oxide lead-sulfide complex. The extended red sensitivity can then be attributed in part to the small energy gap of lead sulfide (approximately 0.4 electron volts). Almost all the other unique features of the standard XQ1020 Plumbicon are retained in the new, extended-red-sensitivity XQ1023.

It is necessary to comment that, in order to make a correct measurement of the luminous sensitivity, S_L , we must use an infrared cutoff filter (for example, a Balzer type B1/K1, which has a wavelength cutoff of 6500 to 7000 angstroms) to exclude the considerable number of nonluminous infrared photons from the 2870°K tungsten source, to which the XQ1023 is quite sensitive. The infrared sensitivity of Plumbicons is illus-



*Because of the considerable sensitivity of the XQ1023 to nonluminous (infrared) photons, an I.R. attenuating filter is used and incorporated in the determination of S_L .

Figure 7. Absolute spectral sensitivity for typical Plumbicons. The extended red response and overall improvement in sensitivity of the XQ1023 Plumbicon is due to the incorporation of sulphur as an impurity in the lead-oxide layer. For comparison, the luminous sensitivities (S_L) in $\mu\text{Amp}/\mu\text{W}$ of 2870°K illumination (without antihalate "button") is given in the insert for the respective tubes. (With the "button," S_L is decreased by 12 percent.)

trated in figure 8. In specially constructed tubes, sensitivity out to 1.8 microns has been observed. One interesting feature seen in this curve is the very high quantum efficiency of lead oxide towards shorter wavelengths. The measurements of Mulder and deJonge (ref. 19) of Philips Research Laboratories indicate a quantum efficiency of 100 percent for $\lambda < 4000$ angstroms for single crystals of PbO measured as photoconducting detectors. It is just this high quantum or conversion efficiency, together with a very high collection efficiency that is also close to 100 percent, which has given the Plumbicon its highly rated place in the television industry (ref. 10).

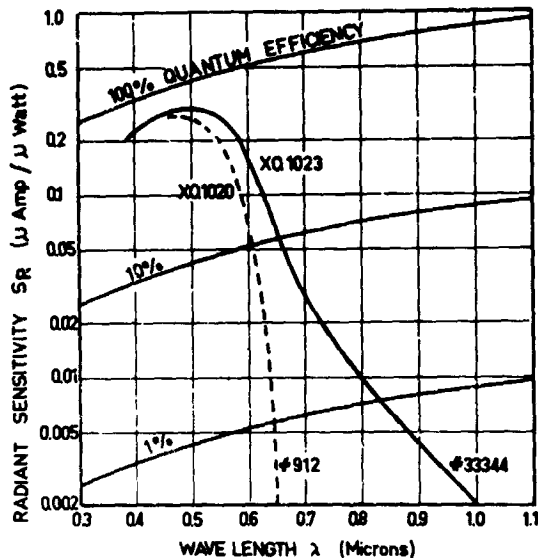


Figure 8. Absolute spectral sensitivity of typical Plumbicons plotted on a log scale compared with lines of constant quantum efficiency. The differences in sensitivity beyond 0.6 microns are more readily apparent in such a plot, which otherwise is the same as figure 7. The high quantum efficiency of the PbO layers is to be noted.

The Plumbicon Family

Let us discuss the most recent developments in Plumbicons. In table 1, we show our most recent portrait of the Plumbicon family (with not all the members present, however). We can separate the types by size: (1) the standard 30-millimeter size (21-millimeter target), which includes those now available, (2) the "developmental" vidicon size or 1-inch versions (16-millimeter target), and (3) the "mini" or 12X size, 16-millimeter-diameter version (10-millimeter target). Sketches of the relative sizes of these types are shown in the table. For electron guns, all combinations of focus and deflection can be achieved. The so-called FPS gun (magnetic focus and deflectron electrostatic deflection), although being investigated initially in a vidicon version, could easily be adapted to a lead-oxide target.

For layers, both the standard and extended red versions are possible for any size and gun combination. Although this list is not inclusive, but rather indicates only some of our current investigations, the other possibilities could certainly be achieved, given the time, personnel, money, and especially the demand.

Plumbicon Specifications

The following is a summary of some of the specifications of several types of Plumbicons and a comparison of these specifications with those for a modern, high quality, separate mesh, all-magnetic vidicon, the Amperex XQ1040 (ref. 24). This summary is shown in table 2. Because several parameters of the tube—namely, output capacitance, layer capacitance, and resolution—depend upon the dimensions of the target, it is necessary to compare these properties for the three sizes of Plumbicons: the mini-size 12XQ/12XQLR, the 1-inch-size 16XQ, and the 30-millimeter-size standard XQ1020/XQ1023. The 16XQ has been developed to be an exact replacement for the XQ1040 or the 8507 1-inch vidicon; therefore, it is valid to make a one-to-one comparison between the 16XQ and XQ1040, especially for those parameters directly effected by target diameter.

Several explanatory remarks are necessary in order to make the rather large amount of data contained in table 2 more useful:

1. The luminous sensitivities, S_L , of the extended red-sensitivity tubes (12XQER and XQ1023) are measured by incorporating a suitable infrared absorbing filter placed on the faceplate or between the faceplate and the 2870°K color-temperature illumination source. A single figure for Plumbicon sensitivity suffices to specify the performance of the Plumbicon over its entire operating range, as already discussed. For the vidicon, however, it is necessary to specify both light level (or signal level) and dark current (or target voltage) as is done in this table; i.e., target voltage set to give 20 microamperes of dark

Table 1. Members of the Plumbicon Family *

TARGET DIAG		10 mm		16 mm		21 mm			
TYPE		12 XQ	12 XQER	16 XQ	VIDICONS	XQ1020	XQ1023	3 XQ	15 XQ
GUN	ALL MAG			⊗	⊗	⊗	⊗		
	HYBRID	X	X		X			X	
	FPS			•	X				
	ALL E.S.				⊗				X
LAYER	STD.	X		⊗		⊗		X	X
	EXT. RED		X	•			⊗	•	•
RELATIVE SIZE									
<p>⊗ STUDIO OR INDUSTRIAL GRADES PRESENTLY OR SOON AVAILABLE</p> <p>• POSSIBLE COMBINATIONS</p> <p>X UNDER INVESTIGATION</p>									

*This list is not inclusive; it indicates only some of the current possibilities. A version of the XQ1020 with a fiber-optic faceplate, called the 7XQ, is also under development.

current and 0.75-foot-candle faceplate illumination (refs. 22 and 24).

2. The maximum radiant sensitivity, S_R , is the maximum signal in microamperes per microwatts which occurs at the wavelength λ_p , the wavelength of the peak in the pertinent spectral-response curve. It is actually a measure of the quantum efficiency of the photosensitive layer. (We should actually compare photosensitivities in electrons per photon, but this is not commonly done.)

3. The low value of dark current of the Plumbicon should be especially noted (ref. 10). This low value persists over the -30°

to $+50^\circ\text{C}$ operating range of the Plumbicon (as does its sensitivity and resolution). This is not so for the vidicon; its dark current and sensitivity are very temperature-dependent (ref. 22). The value of 20 microamperes used for the XQ1040 vidicon is the room temperature value for a target potential of 30 volts. A lower value, comparable to that of the Plumbicon, can be achieved by severely reducing the target potential but at the cost of a drastic loss in sensitivity.

4. The figures given for resolution are in terms of the percent modulation depth at 400 TV lines at the center of the target. By "limiting resolution," we mean the number of

Table 2. Typical Properties of Plumbicons Compared With Those of a Typical XQ1040 Type of High Performance Vidicon, Both Under Normal Operating Conditions.

TYPICAL PROPERTIES OF PLUMBICONS -----VIDICONS (NORMAL OPERATION) UNDER 2870°K ILLUMINATION							
TYPE	PLUMBICONS					VIDICON	
	12 XQ †	12 XQER *†	16 XQ	XQ 1020	XQ1023 *	XQ1040	
SIZE: DIAM. / LENGTH (IN.)	65 / 5.1	65 / 5.1	1.0 / 6.25	1.2 / 8.7	1.2 / 8.7	1.0 / 6.25	
TARGET DIAG. (mm)	10	10	16	21.4	21.4	16	
OUTPUT CAP. (pF)	1.5	1.5	4.5	5.0	5.0	4.5	
LUMINOUS SENSITIVITY, S_L (mA/Lm)	350	440 **	400	400	440 **	200 †† ($i_d = 20 \text{ nA}$)	
RADIANT SENSITIVITY AT λ_p, S_R (mA/MW)	~.25	~.29	.27	.27	.29	.15 ($i_d = i_s = 20 \text{ nA}$)	
DARK CURRENT (nA)	1.0	~1.5	0.5	0.8	1.6	20 ($V_T = 30 \text{ V}$)	
GAMMA	.95	.95	.95	.95	.95	.65	
RESOLUTION: CENTRAL MOD. DEPTH. 400 TVL (%)	15	~30	30	43	55	60	
LIMITING RESOLUTION (M. D. = 10 %) (TVL)	450	~600	650	700	900	800	
(i_{sig} / i_{beam}) FOR RESOL VALUES (nA)	(150/300)	(150/300)	(200/400)	(300/600)	(300/600)	(100/100)	
LAYER CAP. (pF)	~350	~400	550	900	~1100	1500	
LAG:	3rd field (%)	3.0	5.0	3.5	3.5	6.5	30 ††
	12th. field (%)	1.2	1.8	1.2	1.1	2.0	9 ††
	(i_{sig} / i_{beam}) FOR LAG VALUES (nA)	(50/100)	(50/100)	(100/100)	(100/100)	(100/100)	(100/100)

* EXTENDED RED LAYER TYPES.

** WITH I.R. ABSORBING FILTER, BALZER TYPE B1/K1

† TYPES 12 XQ UNDER INVESTIGATION.

†† 0.75 FT. CDL. (2870°K) ON FACEPLATE

TV lines at which the modulation depth is 10 percent of the modulation depth at 100 TV lines. The pertinent values of signal current, i_{sig} , and beam current, i_{beam} , at which the resolution is measured should always be stated, as is done in this table. By "beam current" we mean the maximum signal current that can be just stabilized; i.e., the maximum current that the beam can deliver to the target.

5. The values quoted for lag are the percentages of the signal current remaining in the

third field and twelfth field, respectively, after a bright target illumination has been turned off in the zeroth field. Because of the dependence on signal current (in general, lag increases as signal current, that is, light level, decreases; ref. 6), and the dependence to a lesser degree on "beam current," the pertinent values are so given in the table.

Vidicons of other manufacturers may perform differently (better or worse) than the one illustrated in table 2. In general, however, the Plumbicon will almost always be

superior in dark current, gamma, sensitivity, and lag. The size difference between the standard Plumbicon and the vidicon has now disappeared with the introduction of the 1-inch-diameter 16XQ Plumbicon. The specifications for the 12XQ "mini" Plumbicon have not yet been fully determined; hence, the values listed, except for those of geometry, are projections based upon the performance of experimental models. For example, as the size of the target decreases, we would expect the resolution to decrease; but it is not target size alone that controls resolution. Through good design of the half-sized target, the resolution loss is only about one-half at 400 TV lines. This is because a thinner layer is used; a thinner layer will result in a small loss of sensitivity. We might then expect an increase in lag due to the increase in layer capacitance attendant with a thinner layer, but the capacitance of the layer is proportional also to area. Since the area is reduced almost fourfold, the net effect is a sizable reduction in layer capacitance; and, hence, a tube with even less lag.

Highlight-Handling Capabilities

There has been a most recent and exciting development from the Philips Research Laboratories (ref. 9). As shown in figure 3, the slope of the transfer characteristics for the Plumbicon is near-unity up to a maximum set by the available current in the beam. This, of course, restricts the dynamic range of the Plumbicon to values of the faceplate illumination below about one-half of a foot-candle (1 to 2 millilumens). At higher light levels on the faceplate, the signal is unstabilized, and a type of "blooming" occurs. In the Plumbicon, of course, "blooming" causes no permanent effects; i.e., there is no permanent "burn-in" nor long-term change in sensitivity, and the tube recovers very quickly from this "blooming." Recently, J. H. T. van Roosmalen has been successful in developing a gun that imparts an adjustable knee or light-level-saturation characteristic to the transfer curve. This is well-illustrated in figure 9. By pulsing the cathode

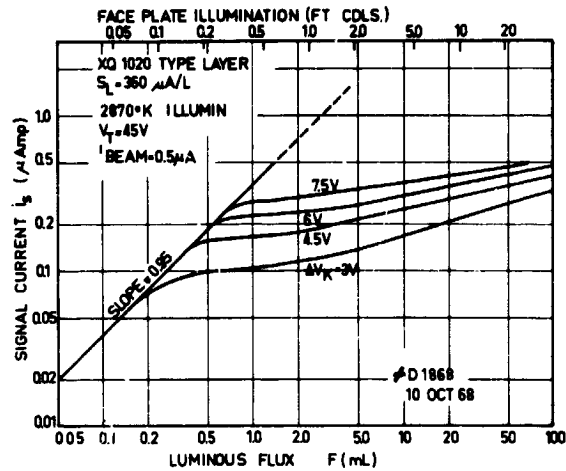


Figure 9. Transfer characteristics of a Plumbicon (XQ1020 type of layer) equipped with a "Flyback Highlight-Discharge" gun. ΔV_k is the cathode potential during horizontal flyback; it is also, then, the maximum voltage fluctuation allowed to remain on the PbO target after the discharge of the highlights, which takes place during the horizontal flyback interval. This gun is, therefore, able to establish a transfer characteristic with an adjustable "knee" or saturation for the Plumbicon, which otherwise has a near-unity transfer characteristic (dashed curve). It is to be noted that beyond the "knee" the slope is not zero; hence, there does exist a highlight "grey scale" although greatly compressed. Furthermore, for the example illustrated, the dynamic range is increased more than two orders of magnitude, thereby completely eliminating "blooming" or "comet-tailing," which otherwise could occur.

to the various voltages, ΔV_k , during horizontal flyback and, at the same time, by greatly increasing the beam current, the beam during horizontal flyback erases, several lines at a time, all voltage excursion on the layer greater than ΔV_k . The potential excursion of the layer caused by excessive highlights are then reduced to values more comparable with the less bright but still stabilized part of the image. Therefore, for this illustration, all signal currents up to $I_{\text{beam}} = 500$ nanoamperes can be stabilized, and, because of the action of the beam during flyback, highlights

even as high as 20 to 30 foot-candles (approximately 100 millilumens) on the target can be stabilized.

In essence, the dynamic range of a Plumbicon with the van Roosmalen gun can be extended by at least two orders of magnitude at the upper end and, as the curves in figure 9 show, even exhibits a grey scale, greatly compressed no doubt, but nevertheless still usable. Furthermore, there is no deterioration of the image from the low-light-level parts of the scene. In one performance of this gun, we were able to satisfactorily illuminate a scene with only a single match and, with flyback highlight discharge operating, could easily resolve the various light-emitting zones of the flame. In another example, we took a standard frosted light bulb, wrote the word "Philips" on it in opaque black letters and used the bulb to illuminate a scene.⁵ With the Plumbicon gun operating normally, only the outline of the bulb with a severe halo was seen on the monitor. The letters were not at all visible. With flyback highlight-discharge operating, however, both the edge of the bulb and the lettering were clearly visible. Interestingly enough, an intensity gradient across the bulb was also apparent. We see this effect nicely demonstrated in figure 10, which includes copies of polaroid pictures taken of the monitor screen during the test.

The applications of a Plumbicon with such a gun can be very wide indeed, especially in the field of low-light-level TV surveillance or any other case in which low contrast details and very bright, high contrast objects may appear together in the same scene. Such objects could be flares, muzzle flashes, searchlights, jet engine exhausts, bright sky, etc., even the sun. The application can be of more value if any of the bright objects are moving or, as is the more usual case, if the pickup tube is moving with respect to these objects. Much additional work must be done on this gun to perfect it before it will be generally available in Plumbicon camera tubes.

⁵ We are grateful to Louis A. Arpino for suggesting the idea for this demonstration.

Appendix

To convert luminous units (foot-candles, lumen, milliamperes per lumen) into their radiant equivalent (watts/m², watts, milliamperes per watt) for a 2870°K color-temperature tungsten source, multiply the number of foot-candles of 2870°K tungsten light by 0.525, the number of lumens of 2870°K tungsten light by 0.049, and the number of milliamperes per lumen of 2870°K tungsten light by 20.4. This is possible because a tungsten lamp at 2800°K (color temperature of 2870°K) emits 20.4 lumens per watt of total radiant flux. For example, a sensitivity of 400 milliamperes per lumen corresponds to 8.2 milliamperes per watt, etc. (Ref: Hardy & Perrin, *Principles of Optics*, McGraw Hill, 1932.)

Acknowledgments

We would like to acknowledge the gracious assistance and criticism received from Dr. P.G. van Zanten and Dr. W. P. Weyland, of the N.V. Philips' Professional Tube Development Department (Elcoma), and their staffs, and Kenneth V. Spitzer, Vice President and General Manager of the Electro-Optical Devices Division of Amperex Electronic Corporation.

References

1. Heijne, L.: The Lead Oxide Vidicon. *Acta Electronica*, Vol. 2, 1957-1958, p. 124.
2. deHaan, E. F.; van den Drift, A.; Schampers, P. P. M.: The Plumbicon: A New Television Camera Tube. *Philips Technical Review*, Vol. 25, 1963-1964, p. 133.
3. deHaan, E. F.; van Doorn, A. G.: The Plumbicon: A Camera Tube with a Photoconductive Lead Oxide Layer. *Journal of SMPTE*, Vol. 73, 1964, p. 473.
4. van Doorn, A. G.: The "Plumbicon" Compared with Other Television Camera Tubes. *Philips Technical Review*, Vol. 27, 1966, p. 1.



Figure 10. Illustration of the effectiveness of the "Flyback Highlight-Discharge" gun, which allows super-highlights in a scene to be imaged without "blooming." The transfer characteristics of this unique camera tube are given in the previous figure. The pictures shown are $2\frac{1}{4}$ " x $3\frac{3}{4}$ " Polaroid prints taken of a closed circuit 19-inch television monitor screen. In the upper pictures, the "F.H.D." gun is not operating; and the scenes are as normally viewed: stationary on the left and with movement on the right. The scene is a 60-watt, frosted glass, light bulb (on which is written in opaque letters the word "Philips"), which illuminates a full-tonal, full-color object (half-tone print). Only the highlights in the image of the print have been stabilized so that "blooming" and "comet-tailing" in the image of the light bulb occurs. In the lower pictures, the "F.H.D." gun is operating but with no change in beam current or other parameters. Not only is the opaque lettering on the bulb clearly imaged but also the normal intensity distribution of light across the bulb. The previously stabilized parts of the image are unaffected. (The loss of sharpness of the light bulb in the lower right-hand picture is due to its motion during the Polaroid exposure.)

5. deHaan, E. F.; Klaasen, F. M.; Schampers, P. P. M.: An Experimental "Plumbicon" Camera Tube with Increased Sensitivity to Red Light. *Philips Technical Review*, Vol. 26, 1965, p. 49.
6. van de Polder, L. J.: Target-Stabilization Effects in Television Pick-Up Tubes. *Philips Research Reports*, Vol. 22, 1967, p. 178.
7. van Roosmalen, J. H. T.: Experimental Electrostatically Focused "Plumbicon" Tubes. *Philips Technical Review*, Vol. 27, 1967, p. 27.
8. Levitt, R. S.: Operating Characteristics of the Plumbicon. *Photoelectronic Imaging Devices Summer Course*, University of Rhode Island, Kingston, R. I., July 1968, to be published.
9. van Roosmalen, J. H. T.: Adjustable Saturation in a Pick-Up Tube with Linear Light Transfer Characteristics. *4th Symposium on Photoelectronic Image Devices*, Imperial College, London, September 1968.
10. Turk, Walter E.: Some Problems of Pick-Up Tubes for Television Cameras. *Journal of SMPTE*, Vol. 77, 1968, p. 1189.
11. Heijne, L.: Photoconductive Properties of Lead Oxide Layers. *Philips Research Reports*, Supplement No. 4, 1961.
12. van den Drift, A.: Texture of a Vapor-Deposited Lead Monoxide Layer. *Philips Research Reports*, Vol. 21, 1966, p. 289.
13. van den Broek, J.: The Electrical Behaviour of Vapour-Deposited Lead-Monoxide Layers. *Philips Research Reports*, Vol. 22, 1967, p. 367.
14. Stupp, E. H.: Physical Properties of the Plumbicon. *Photo Electronic Imaging Devices Summer Course*, University of Rhode Island, Kingston, R. I., July 1968, to be published.
15. Breimer, H.; Holm, W.; Tan, S. L.: A Colour Television Camera with "Plumbicon" Camera Tubes. *Philips Technical Review*, Vol. 28, 1967, p. 336.
16. Streeter, Richard G.; Cobler, Robert L.: CBS Experience with Plumbicon Color Cameras. *Journal of SMPTE*, Vol. 75, 1966, p. 749.
17. XQ1020 Plumbicon. Data sheet, Philips Electronic Components and Materials Div., Eindhoven, The Netherlands, June 1968.
18. van den Broek, J.: Contact Barriers in Red Lead Monoxide. *Philips Research Reports*, Vol. 20, 1965, p. 674.
19. Mulder, B. J.; deJonge, J.: Quantum Efficiency of Photoconduction in Lead Oxide. *Solid State Commun.*, Vol. 4, 1966, p. 293.
20. WL-30691 SEC Camera Tube. Data sheet, Westinghouse, Electronic Tube Div., Elmira, N. Y., March 1968.
21. Schade, O. H., Sr.: The Resolving Power Functions Quantum Process of Television Cameras. *RCA Review*, Vol. 28, 1967, p. 460.
22. 8507 Vidicon RCA Electronic Components and Devices. Data sheet, Lancaster, Pa., October 1963.
23. XQ1023 Plumbicon, Development Sample Data. Data sheet, Philips Electronic Components and Materials Div., Eindhoven, The Netherlands, March 1968.
24. XQ1040 Vidicon. Data sheet, Philips Electronic Components and Materials Div., Eindhoven, The Netherlands, October 1968.

14N70-36740

New Camera Tube Developments

R. E. Simon

RCA Electronic Components

The application of semiconductor technology to camera tubes promises to bring forth a new family of devices with exceptional characteristics that should be of great interest to astronomers as well as to other users of camera tubes. The vidicon type of tubes, based upon semiconductor materials and technology and having higher sensitivity, wider spectral response, and much greater stability than any other tubes, are already available. New low-light-level tubes are under development and will be available in the near future. The ultimate camera device, the all-solid-state scanned array, which utilizes the switching and circuitry concepts of the semiconductor technology, has also shown great promise.

The application of semiconductor technology to camera devices is not new. As early as 1951, it was recognized that arrays of p-n junctions could be used effectively in vidicons (ref. 1). It is only recently, however, that the technology resulting from the planar silicon concept and from large scale integration have made useful silicon camera tubes possible. This was first demonstrated at Bell Laboratories (ref. 2).

It would be a disservice to those who have brought camera tubes to their present state of development to imply that earlier efforts in this field have not depended upon sophisticated semiconductor and materials technology; however, in the case of silicon devices, which are the principal but not exclusive subject of this paper, we are dealing with devices made from a material that has been subjected to greater study and development than perhaps any other. Thus, in developing silicon camera devices, we take

advantage of the many thousands of man-hours of effort that have gone into this material to produce pickup devices with outstanding characteristics.

The silicon-target vidicon is the first of the new camera tubes.¹ It is shown schematically in figure 1. The target, figure 2, consists of an array of more than 5×10^5 individual p-n junctions produced in a single crystal of n-type silicon.

The operation of this device is similar to that of a standard vidicon. A positive potential, relative to the thermionic cathode, is applied to the n-type region of the target. A low-energy electron beam scans the surface of the silicon-depositing charge so that the p-regions exposed to the beam are brought to cathode potential; thus, p-n junctions are reverse-biased by the beam. During the time that the electron beam is not on an element, the reverse bias voltage across the p-n junction decreases as the result of transfer of charge across the junction. This charge arises from either internal generation of free carriers in the material or by photoexcited carriers in the material. These result in dark current and signal current, respectively. The output current is equal to the current that the electron beam must deliver to a p-region to restore it to cathode potential. This, in turn, is equal to the dark current plus the signal current that flowed in the associated p-n junction during

¹The work reported on the silicon-target vidicon has been performed by G. Briggs, E. Cave, A. D. Cope, F. D. Heiman, W. Henry, J. Leaman, E. Luedicke, C. Mueller, R. L. Rodgers, E. C. Savoye, and R. E. Simon.

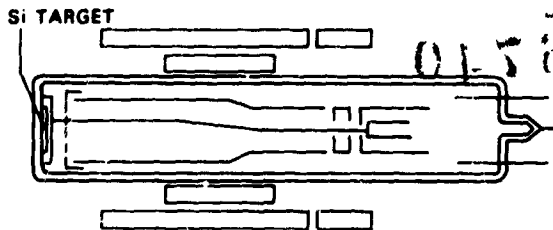


Figure 1. Schematic diagram of a silicon-target vidicon pickup tube.

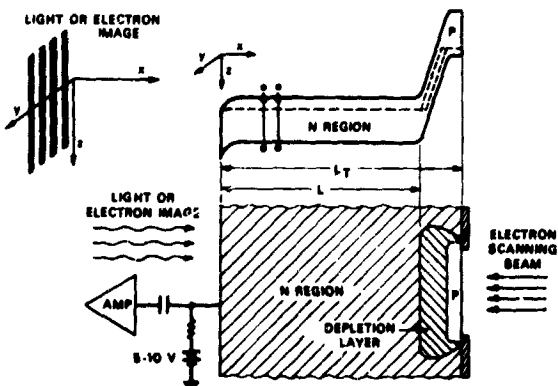


Figure 2. Diagram of silicon target.

the time the beam was not scanning this element.

The sensitivity of the silicon vidicon is shown in figure 3 in terms of quantum efficiency; i.e., the number of electrons that flow in the external circuit for each incident photon. It can be seen that sensitivities as high as 70 percent can be achieved. Furthermore, the response extends in the infrared to 1.1 microns; thus, the silicon-target vidicon has considerably greater response in the near infrared region of the spectrum than any other vidicon now available. Figure 4 shows the response of a silicon-target vidicon especially treated for ultraviolet response and in an envelope with a quartz window. It can be seen that the high sensitivity extends to at least 0.2 micron.

The resolution of the silicon-target vidicon is determined by several factors, including the diode density, the sideways diffusion of carriers, and the electron-beam size. An amplitude response curve for a silicon-target vidicon is shown in figure 5. With present silicon-target vidicons, an amplitude response

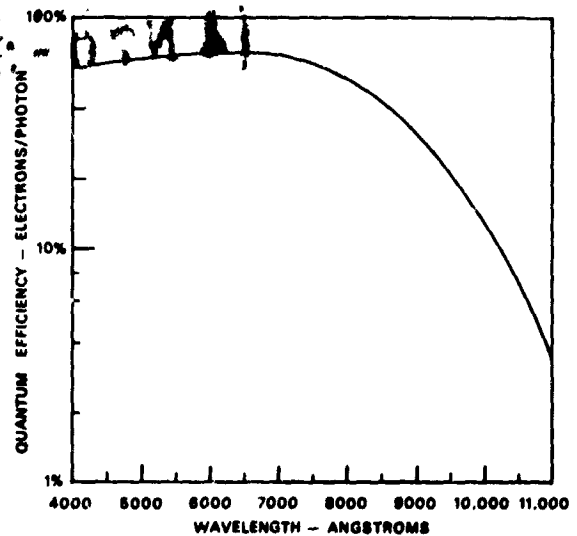


Figure 3. Spectral response of a silicon-target vidicon.

of 30 percent at 400 TV lines and a limiting resolution in excess of 700 TV lines have been achieved.

The lag or image retention of a silicon-target vidicon is determined by the capacity of the target and the electron-beam resistance. No photoconductive trapping effects are observed with silicon. As expected for vidicons limited by capacitive lag, the lag varies with light level (ref. 3), as shown in figure 6. With 200-nanoampere signals, the lag is 8 percent after 50 milliseconds (three frame times).

The dark current of silicon-target vidicons varies with target voltage as shown in figure 7. Since the targets are operated at

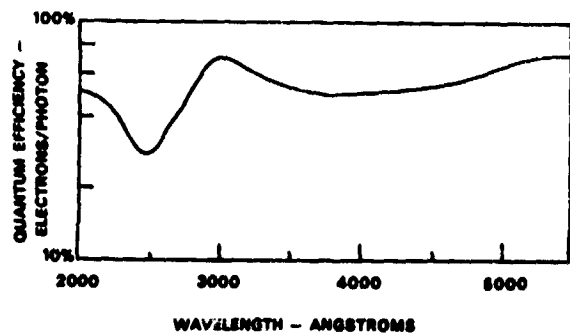


Figure 4. Ultraviolet response of a silicon-target vidicon.

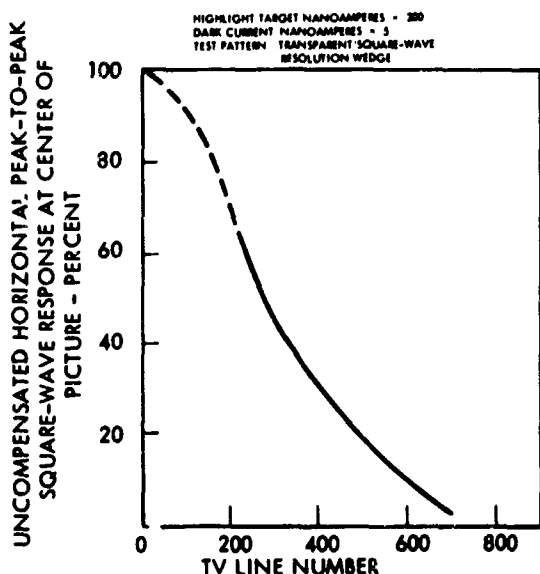


Figure 5. Amplitude response curve for a silicon-target vidicon.

approximately 6 volts, the normal dark current is in the range of 5 to 10 nanoamperes at 30°C. The dark current varies with temperature; it increases by approximately a factor of two for each 10°C increase in temperature.

The silicon-target vidicon is unique in its stability against high intensity radiation. It shows no spreading of overloaded regions, no burn, and no after-image even after exposure to signals orders of magnitude greater than that which the vidicon electron beam can handle.

Of particular interest to astronomers are the slow scan capabilities of the silicon-target vidicon. It has the interesting property of not losing resolution as a function of storage time. The silicon-target vidicon is different in this respect from other vidicons where charge-spreading and therefore loss of resolution occurs with time. This performance is expected with silicon because, once photo-excited carriers are collected by a p-n junction, they can no longer spread sideways. A vidicon can, of course, be used in slow scan applications only for times shorter than the time it takes the dark current to discharge the target. We have operated targets with delayed readouts for times on the order of several

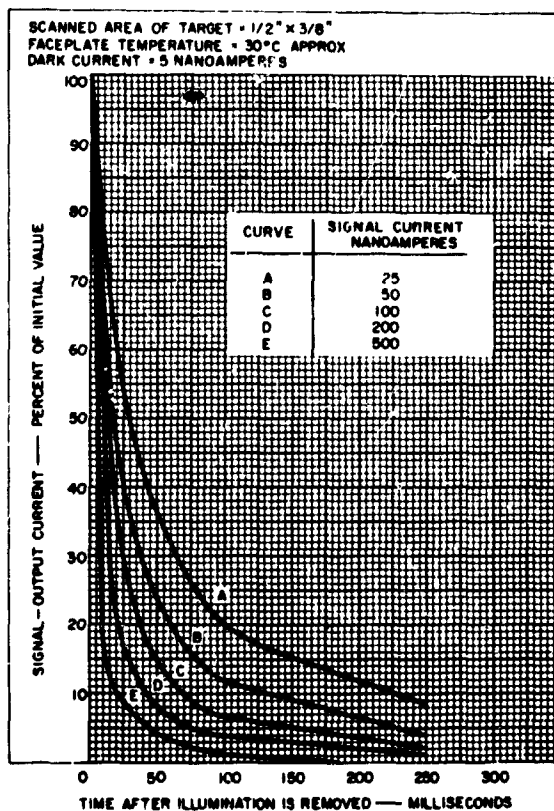


Figure 6. Signal output as a function of time after illumination is removed for several values of illumination.

seconds. By use of a properly designed tube and cooling, it should be possible to produce silicon-target vidicons with delayed readouts of minutes.

Figure 8 is a photograph of a picture tube display of a picture produced by a silicon-target vidicon.

The second device to be considered is a low-light-level intensifier camera tube, which also uses a silicon target.² It will not be possible to discuss the performance of this

² The silicon intensifier camera tube program has been supported in part by the U.S. Naval Electronics Systems Command, Washington, D. C., and the Night Vision Laboratory, US Army Electronics Command, Ft. Belvoir, Va. Work on the silicon intensifier camera tube has been performed by P. W. Kaseman and R. L. VanAsselt as well as those listed in footnote 1.

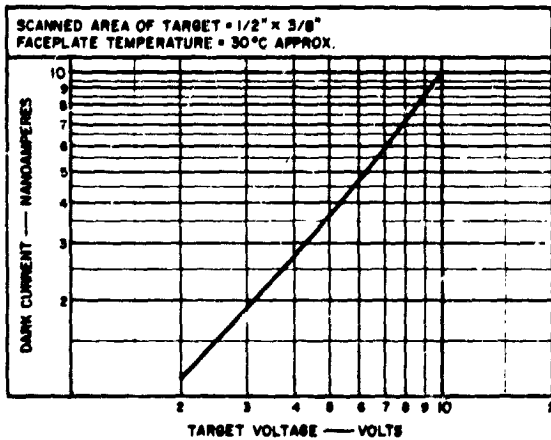


Figure 7. Dark current as a function of target voltage.

device in detail because of the limitations imposed by security classification.

The silicon-intensifier camera tube, shown schematically in figure 9, operates in the following way. Radiation incident upon the photocathode produces photoelectrons that are accelerated to high energy and imaged on a silicon target. The incident electrons produce secondary electrons and holes

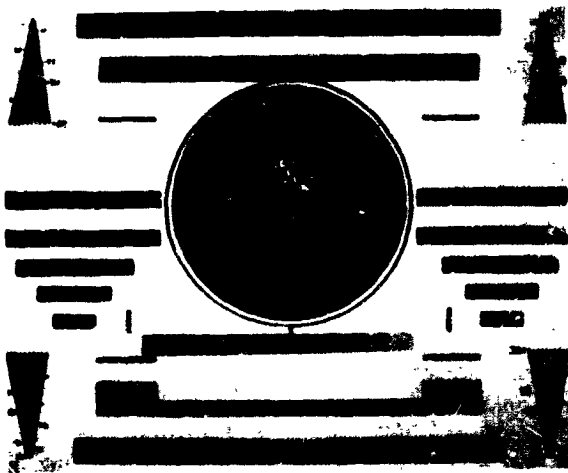


Figure 8. Photograph of picture tube display of a test pattern produced by a silicon-target vidicon.

in the silicon by the process of impact ionization; i.e., in which one electron is excited from the valence band of silicon into the conduction band for each 3.5 electron volts of energy carried by each primary electron. The holes thus produced are collected by the p-n junctions in the target. The silicon target, which is similar in performance to the silicon target of the vidicon previously described, is scanned by an electron beam to produce an output signal. By putting 10 kilovolts on the image section target, gains of more than 2500 have been achieved. The gain of the silicon-intensifier camera tube is therefore greater than that of other single camera tubes now available. The implications of this gain for low-light-level performance are obvious.

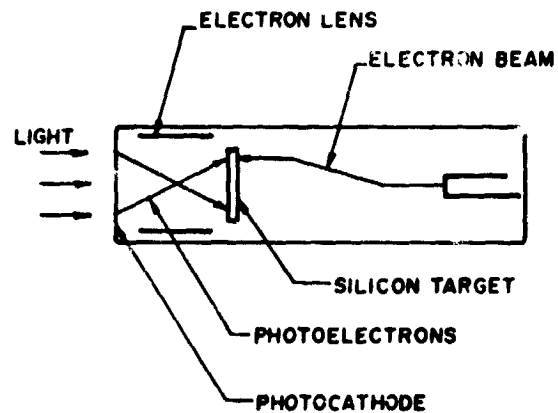


Figure 9. Schematic diagram of a silicon-intensifier camera tube.

An outstanding feature of the silicon-intensifier camera tube is its ability to withstand high light levels. This type of tube has been operated with light overloads, as has the silicon-target vidicon, of more than 10^5 times the maximum useable signal. This extreme ruggedness greatly simplifies the use of this tube because no protective filters or shutters are required. Since no mesh is required other than the normal vidicon field mesh, this tube is less microphonic and has a lower capacity to ground than other low-light-level tubes. Thus, it is possible to design an amplifier for this tube resulting in an improved signal-to-noise ratio.

Other characteristics of this device such as dark current, lag, and resolution, which are determined by the silicon target, are similar to that of the silicon-target vidicon. The spectral response and sensitivity of the silicon-intensifier camera tube are determined by the photocathode.

Somewhat further in the future than the silicon-target vidicon and the silicon-intensifier camera tube is the multielement, self-scanned, mosaic sensor.³ This is an all-solid-state device consisting of an array of photosensitive elements, each located at the intersection of mutually perpendicular address strips, which are connected to scan generators and video coupling circuits. The application of sequential scan pulses to address strips permits an image to be scanned and a video signal to be produced which is similar to that produced by a camera tube. As in the devices described previously, a large array of discrete elements is required. In addition to the photosensitive elements, switching elements and address strips must be produced in the array.

Solid-state camera devices, though still far behind camera tubes in cost and performance, offer significant potential advantages. Among these are geometric accuracy and versatility of scan as well as greater compactness and reduced power consumption.

Two approaches have been followed in attempting to produce solid-state scanned arrays. These include the silicon approach, in which all elements are produced on a single crystal of silicon as in the silicon-target vidicon and the Sketicon, and the thin film approach, in which all elements of the array are deposited on a glass substrate by evaporation techniques. At the RCA Laboratories, both approaches have been pursued; however, only the thin film approach will be described in this presentation.

³The work on the solid-state self-scanned arrays reported here has been performed by P. K. Weimer, W. S. Pike, G. Sadasiv, F. V. Shallcross, and L. Merayt Horvuth. For a more complete summary of this work, see *IEEE Spectrum* 6, 52 (1969).

The thin-film solid-state array differs from the silicon-target vidicon approach in that it utilizes "excitation storage" to integrate the light energy that is generated in an element during the time in which the element is not being addressed. In excitation storage, the light energy is stored in excited carriers whose lifetime, ideally, should approximate the scanning period. This differs from the silicon-target vidicon in which photoexcited carriers are collected and stored across a p-n junction.

The advantage of the use of excitation storage is that it allows a simplification of the structure, thus permitting a high density of elements. A single photosensitive element of the sensor is shown in figure 10. It can be seen that the sensor element consists simply of a photoconductor in series with a diode.

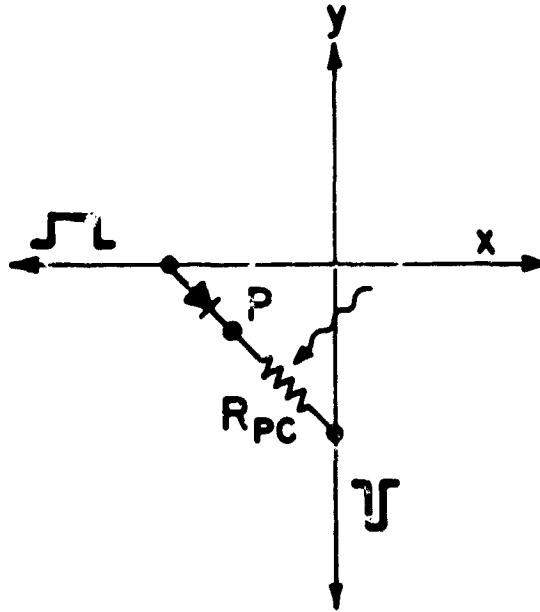


Figure 10. Schematic diagram of a photosensitive element of a thin-film self-scanned array.

The thin film arrays are produced by evaporation of the following elements: cadmium sulfide, cadmium selenide, gold, indium, and tellurium. The proper geometry is obtained by use of evaporation masks made of fine wire grills. A portion of a 256 x 256 array is shown in figure 11.

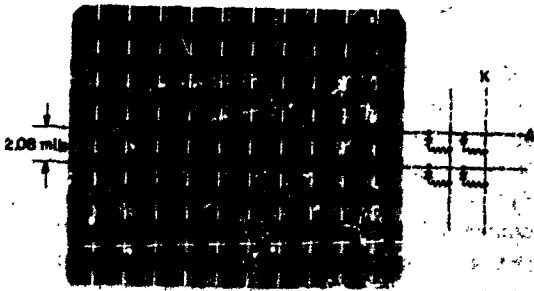


Figure 11. Photograph of a portion of a 256 x 256 thin-film self-scanned array.

The scanning circuitry and video coupling circuits are essential parts of the self-scanned sensor. The design and fabrication of this part of the sensor are comparable in difficulty to the design of the photosensitive array. The scan generator must provide parallel outputs equal to the number of elements in a line (256 in the array to be described below) and must operate at pulse rates comparable to those used in conventional TV systems if television standards are to be met. The scanning circuitry used in the thin film sensors has been built by the same evaporation techniques that are used to produce the photosensitive arrays.

An experimental 256 x 256 array has been recently built and tested. A schematic circuit diagram for this system, including elements for signal enhancement by line storage, is shown in figure 12. A photograph of the complete thin-film image sensor is shown in figure 13. The sensor and scanning circuitry are deposited upon two glass substrates, shown mounted on a printed circuit board.

Figure 14 shows two pictures transmitted by the 256 x 256 thin-film array operating at 4.8 megahertz. The resolution as indicated by a test pattern was 200 TV lines. The sensor had sufficient sensitivity to operate under normal laboratory illumination.

The vertical streaks in the pictures arise from nonuniformities in the sensor, in the horizontal scan circuitry, or in connections between the two. Horizontal resolution loss can be caused by unwanted broadening of

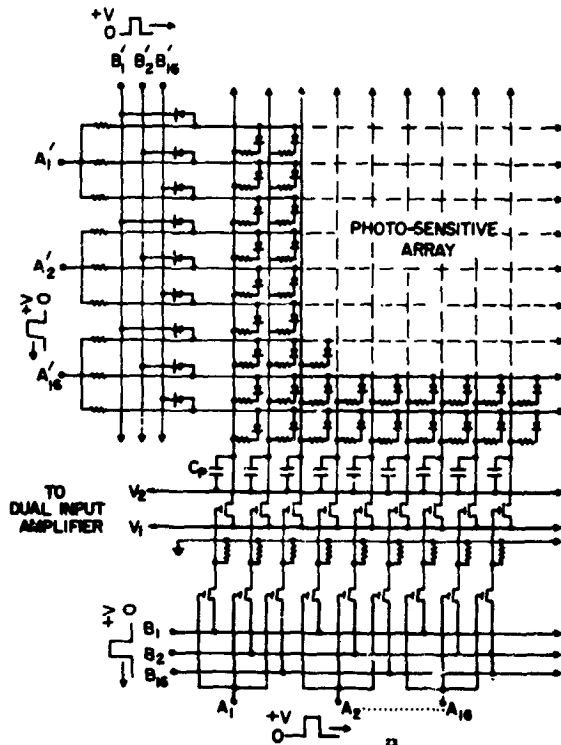


Figure 12. Schematic diagram of a 256 x 256 thin-film self-scanned array with line storage.



Figure 13. Photograph of a 256 x 256 photosensitive array and scan circuits mounted on a printed circuit board.



Figure 14. Photographs of pictures transmitted by a 256 x 256 self-scanned array.

horizontal scanning pulses. Recent work indicates that these nonuniformities can be greatly reduced.

Although picture quality of the 256 x 256 array can be improved by improved measuring techniques, it is evident that a higher number of elements will be required to obtain performance comparable to camera tubes. The thin-film approach appears capable of extension to at least 500 x 500 elements spaced on 25-millimicron centers.

It is recognized that considerably more effort will be required to produce a solid-state scanned array that can compete in performance with electron-beam-scanned devices. Furthermore, it is not clear that the thin-film approach described will be superior to a silicon approach. It seems evident, however, that, with the expected advancements in tech-

nology and the start that has been made, practical solid-state scanned camera devices will become a reality in the future.

In summary, the application of semiconductor technology has led to a series of new camera devices consisting of arrays of discrete elements. The silicon-target vidicon, with high sensitivity over a broad range of the spectrum, low lag, low dark current, and great stability, is available today. The use of silicon as the target in the silicon-intensifier camera tube has resulted in a low-light-level tube with higher gain than heretofore available in a single tube, with high resolution, and unique stability such that the tube is not affected by light overloads of 10^5 . Progress on solid-state scanned arrays indicate that, with further developments in the technology, small, compact, low-power sensor arrays should be available in the future.

References

1. Reynolds, R.W.: Unpublished Work, 1951. U.S. Patent No. 3011,089, November 28, 1961.
2. Crowell, W. H.; Buck, R. M.; Labuda, E. F.; Dalton, J.V.; Walsh, E. J.: B.S.T.J., vol. 46, no. 491, 1967.
3. Redington, R. W.: IRE Transactions on Electronic Devices. Fourth ed., No. 220, 1957.

PRECEDING PAGE BLANK NOT FILMED.

1 N70-36741

The Image Isocon and Related Developments for Astronomical Space Telescopes

A. D. Cope

RCA Electronic Components

Introduction

The discussion in this paper is focused on the image isocon, its astronomical applications, and the main features of an ideal camera tube.

Relating the Camera Tube to Astronomical Imaging Problems

Although the invention and development of modern television-camera tubes extends over the past 40 years, their operation had been fully studied only for the operating conditions dictated by broadcast standards. All varieties had been optimized for operation under continuous illumination and continuous scan at 30 frames per second. When image sensors whose output signal is generated by a scanning beam were first applied to instrumentation in space vehicles, the opportunity came to broaden the understanding of just how these devices function with other cycles of operation. Camera systems operating with shutter-controlled exposures and with the readout at a much slower rate than is normally used require that the camera tubes be modified for optimum performance under the new operating conditions. Several new problems were uncovered for which solutions were evolved.

The first RCA work on a television camera system capable of integrating an exposure lasting one or more hours before being read out was sponsored by Project Stratoscope under the direction of Martin Schwartzschild of Princeton University. The techniques associated with an extended, integrating mode of operation were incompletely

understood at that time. During the first phase, the details of the internal operation of the image orthicon tube when recording low level inputs of both extended and point images were thoroughly investigated. From this study, the major parameters controlling the image quality and sensitivity were identified. It then was possible to define completely a camera operating cycle capable of giving reproducible results. A new camera that can be programmed to cycle automatically through various sequences was assembled and was used initially to test image orthicons and, later, image isocon tubes. Tests in both the laboratory and on the telescope of the Princeton University Observatory were fairly extensive.

The Image Isocon

The image isocon tube shown in figure 1 differs from the image orthicon only in the means by which the charge image stored at the target is converted to a video signal as it is read by the scanning beam.

Exposure to light imaged on the photocathode excites photoelectrons that are imaged upon the storage target. This electrode consists of a thin membrane of insulator suspended between two mesh electrodes. A positive charge image three to five times greater than the incident photoelectron charge is generated by secondary emission. This charge pattern modulates the previously established equipotential at the scanned surface of the target. A low capacitance target assembly yields a greater potential modulation per incident photoelectron than a high capacitance target. The maximum integration

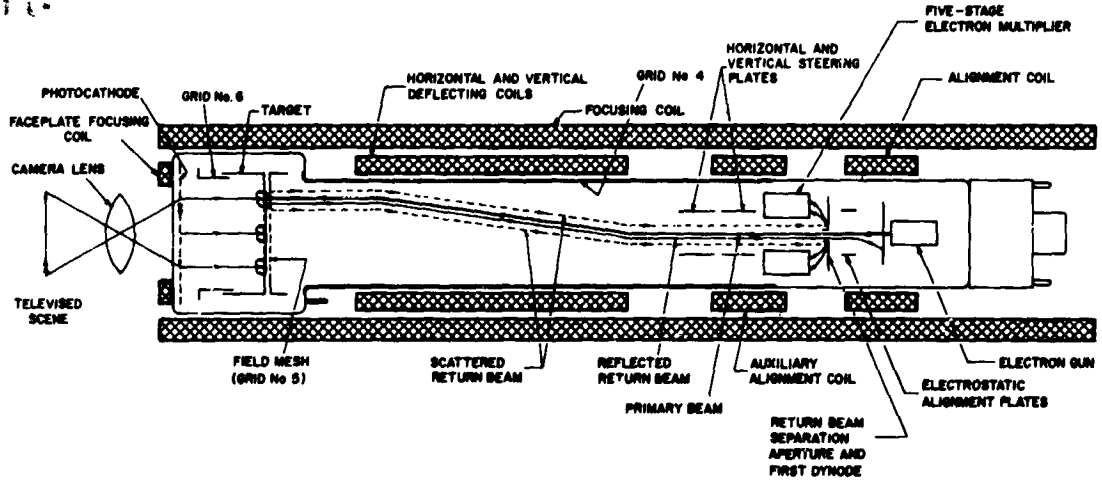


Figure 1. Image isocon tube; schematic arrangement of C21093.

time will depend upon the resistivity of the membrane that can be selected between 10^{11} and 10^{17} ohm-centimeters.

The well-focused electron beam that approaches the target with only a few volts of energy responds to the potential modulation at the scanned surface by depositing sufficient electrons to restore the original equipotential. In detail, only the most energetic portion of the beam is induced to contact the positively modulated areas, and only a portion of these contacting electrons remain at the target to erase the stored charge pattern. Typically, for modulations between 0 and 5 volts, two out of every three electrons striking the target are elastically scattered and are returned along with the unused portion of the beam to the entrance of the electron multiplier at the gun end of the tube.

If the cross-section of the return beam is examined at this plane where there is maximum dispersion of the electrons according to their component of energy normal to the tube axis, the spatial distribution of scattered and reflected electrons is that shown in figure 2. The reflected electrons are confined to the small circular area. The scattered electrons occupy the larger area, which increases in diameter as the potential of the point of scan becomes more positive. When the return beam is directed over an appropriate aperture, the

reflected electrons are removed; and the scattered electrons are allowed to enter the electron multiplier. The function of the multiplier is to amplify the video current (the scattered electron current) sufficiently so that amplifier noise does not degrade the signal. The scattered electrons entering the multiplier are two to three times the amplification of the stored target charge or six to ten times the amplification of the photoelectron current.

The experimental astrometric work was done using laboratory-design isocons. The new RCA image isocon tube, along with its associated focus and deflecting coils, is a more highly perfected electron optical design with superior performance. Nonuniformities in scanning-beam landing energies at various points in the scanning raster have been reduced to less than 0.1 volt, and improved

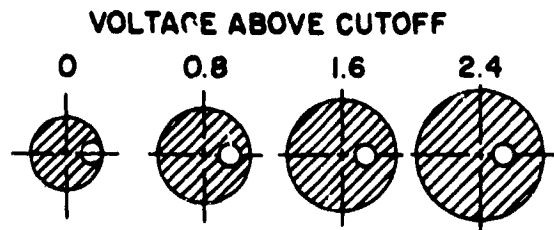


Figure 2. Return beam (cross-section) distribution at plane of separation.

control of the signal separation has been achieved. The tube setup has been simplified. The image isocon tube features:

1. High signal-to-noise ratio, particularly in the dark area of a scene
2. A linear light-to-signal transfer characteristic over a brightness range of at least 100
3. An intra-scene dynamic range of 100 that retains photometric accuracy
4. High geometric fidelity in the image with excellent resolution
5. No tube adjustments needed to cover these ranges.

Two versions of the tube are available: Type 21093 contains a bi-alkali photocathode and a high capacitance target; Type 21095 has a fiber optics faceplate, an S-20 photocathode, and a low capacitance target.

Variations for slow-scan, long-integration tubes include smaller gun and separation apertures, finer meshes in the target assembly, and Elcon glass targets of 10^{15} ohm-centimeter resistivity.

Astronomical Applications of the Image Isocon

Figure 3 lists a number of requirements for an image-sensing system that would have wide application in astronomy. How capably the image isocon fulfills these needs is examined in the following discussion.

REQUIRED CAPABILITIES OF AN ASTRONOMICAL IMAGE SENSOR SYSTEM	
1.	IMAGE INTEGRATION FOR VARIABLE BUT CONTROLLED EXPOSURE LASTING FROM < 1 SEC TO SEVERAL HOURS
2.	TRANSMISSION OF THE IMAGE DATA FROM ONE EXPOSURE IN A SMALL NUMBER OF SCANS
3.	AN ABILITY TO DETECT POINT IMAGES IN A DARK FIELD
4.	PHOTOMETRIC AND GEOMETRIC FIDELITY IN THE TRANSMITTED IMAGE CAPABLE OF QUANTITATIVE EVALUATION
5.	A CAPABILITY TO RECORD SPECTROMETER DATA WITH MAXIMUM FIDELITY

Figure 3. Requirements for an integrating camera tube system for use in astronomy.

Camera-Tube Operating Cycle of the Stratoscope Television System

The experimental work has confirmed that the operating cycle established for the Stratoscope Television System does yield reproducible data when an intermittent cycle of expose-store-and-read is employed.

The first step calls for *preparation of the target*. This is necessary to erase any residual modulation from the storage target that remains from previous operation. It also establishes a known reference potential at the target surface. With target resistivities as high as 10^{17} ohm-centimeters, this erasure becomes an increasingly important factor in obtaining reproducibility since the relaxation time of the insulator is measured in days.

The tube is now ready for the *optical exposure*. During the extended time of light exposure, the photocathode and the electrodes of the image section that focus the charge image on the storage surface are the only parts of the isocon that must be active. Exposures as long as three hours have been made with the reciprocity between light intensity and exposure time being rigidly maintained.

For the *readout of the stored charge*, the image section of the tube is made inactive, and, after time has been allowed for the gun temperature to stabilize, a single readout scan of the target is made. The scattered electron current, which is proportional to the target potential modulation, is the output signal that is recorded.

This camera system uses a 1-second vertical sweep time for the 500-line raster. Recording of the video output can be on magnetic tape, by direct visual display, or on photographic film.

The single slow-speed readout scan removes 97 to 98 percent of the stored charge at the target as compared with 70 percent for the normal scan velocity. A reduction of the beam current to one-thirtieth its normal value provides a finer beam-spot diameter and an improved modulation transfer function (MTF).

Camera systems intended for quantitative photometric use, particularly at slow readout rates, must have very well stabilized voltage and current sources if the performance capabilities of the sensor tube are to be fully realized.

To provide an image signal with the most favorable signal-to-noise ratio from the object of interest, it is necessary to know something of the signal intensity. This foreknowledge permits the exposure to be adjusted so that the charge stored at the target from this part of the scene is at the maximum established by the target capacitance. Overexposure leads to distortion of the photometry. Overloads in various amplifiers, the transmitter, the receiver, or the display system must also be avoided by careful calibration of permissible ranges for the signals.

Sensitivity and Photometric Fidelity for Point Images

Point sources such as diffraction-limited stellar images present a special problem for scanning sensors. This results from having a limited area of positive charge surrounded by a large region at cathode potential. This negative coplanar grid repels the beam, making it necessary to have between five and ten times as much stored charge density in an isolated 50-micrometer spot than in an extended area in order to obtain an equivalent output signal near the threshold illumination level.

The means adopted to overcome this problem in the operation of the image orthicon and image isocon was to bias the target 1 or 2 volts positive before initiating the readout scan. The beam now lands at all points of the raster, and the point image produces the normal signal amplitude relative to the background.

In the Stratoscope, the philosophy adopted for determining the appropriate size of the stellar image at the photocathode of the camera tube is that indicated in figure 4. The 50-percent response point of the isocon modulation transfer, which is at 10 cycles per millimeter for the high target-capacitance

type, determines the image size. The net MTF of the optics and the image sensor is 85 percent that of the optics alone. An even greater target capacitance would be desirable from the point of view that the highest attainable signal-to-noise ratio and resolution are desired.

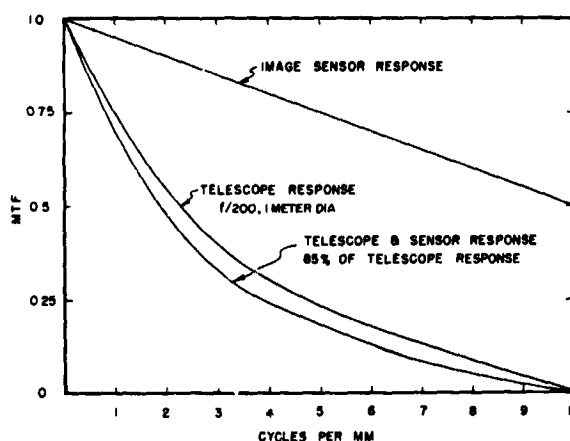


Figure 4. Modulation transfer function (MTF) of isocon and telescope optics.

Table 1 lists a number of performance capabilities of a high target-capacitance isocon in the Stratoscope camera. The maximum exposure to charge the target to 80 percent of its full capacity is indicated. This ensures that the transfer characteristic remains linear. When the 50-percent MTF of a 50x50 micrometer point image is used, the maximum signal-to-noise ratio is 138. For a minimum signal-to-noise ratio of 10, the elemental target charge is 400.

In the telescope tests carried out at Princeton, a 16-millimeter-diameter aperture and a focal ratio of $f/250$ showed that a 9 ± 1 magnitude, diffraction-limited, stellar image could be recorded with a 100-second exposure. Figure 5 shows the monitor display and 16 successive line traces of an oscilloscope display recorded during one scan of the isocon. The star image covers 7 or 8 lines in this instance.

The equivalent condition for a 900-millimeter-diameter aperture at $f/250$ is that a

Table 1. Isocon Performance in Stratoscope Camera, with 50x50 Micrometer Point Image, 1-Second Vertical Scan, 500 Scan Lines

Exposure for maximum target charge	9.6×10^9 photons/cm ²
Exposure for minimum useful target charge	7.7×10^8 photons/cm ²
Photon flux	F quanta/cm ² /sec
Quantum efficiency of photocathode	0.15
Target gain	3
Charges/mm ² /sec at target	0.45 F
Scatter gain	2.5
Input to multiplier	1.1 F
Maximum target charge in 50x50 μ spot	2×10^4 electron charges
Maximum p-p signal/rms noise	62
Minimum useful target charge in 50x50 μ spot	1.6×10^3 electron charges
Minimum p-p signal/rms noise	10

13 ± 1 magnitude star image would be recorded with a 1-second exposure. The corresponding situation for 103 a G photographic film used in Stratoscope II with a 900-millimeter-diameter aperture and f/100 focal ratio is that a 10 ± 1 magnitude star would be recorded with an exposure of 1 second. The new isocon design, optimized for the slow scan, is expected to give improved capabilities.

Spectrometer Data Recording with the Integrating Television Camera

An astrometric problem for which an integrating television-camera system should be helpful is that of measuring the spectra of faint sources. Preliminary results were obtained by using a spectrometer having a dispersion of 1 angstrom per millimeter attached to the 23-inch refractor in the Princeton Observatory.

By orienting the spectrum so that the dispersion axis is at right angles to the scan lines, it is possible to integrate the output of each scan line and to use this signal as one point in the recording of signal intensity versus wavelength. In this test, it was not convenient to use cylindrical optics to spread the spectral image to cover the full horizontal width of the raster. Instead, only one-fiftieth of the horizontal dimension was illuminated, and a gating circuit was used to select and to integrate the signal from only that portion of the line which contained image information (about three times the spectrum width).

Figure 6 shows the oscilloscope display from the 500 active scan lines covering a 70-angstrom portion of the spectrum of Arcturus (magnitude 0.2). The single isocon readout scan was made following an 8-second exposure. The line integrator was not employed in this instance.

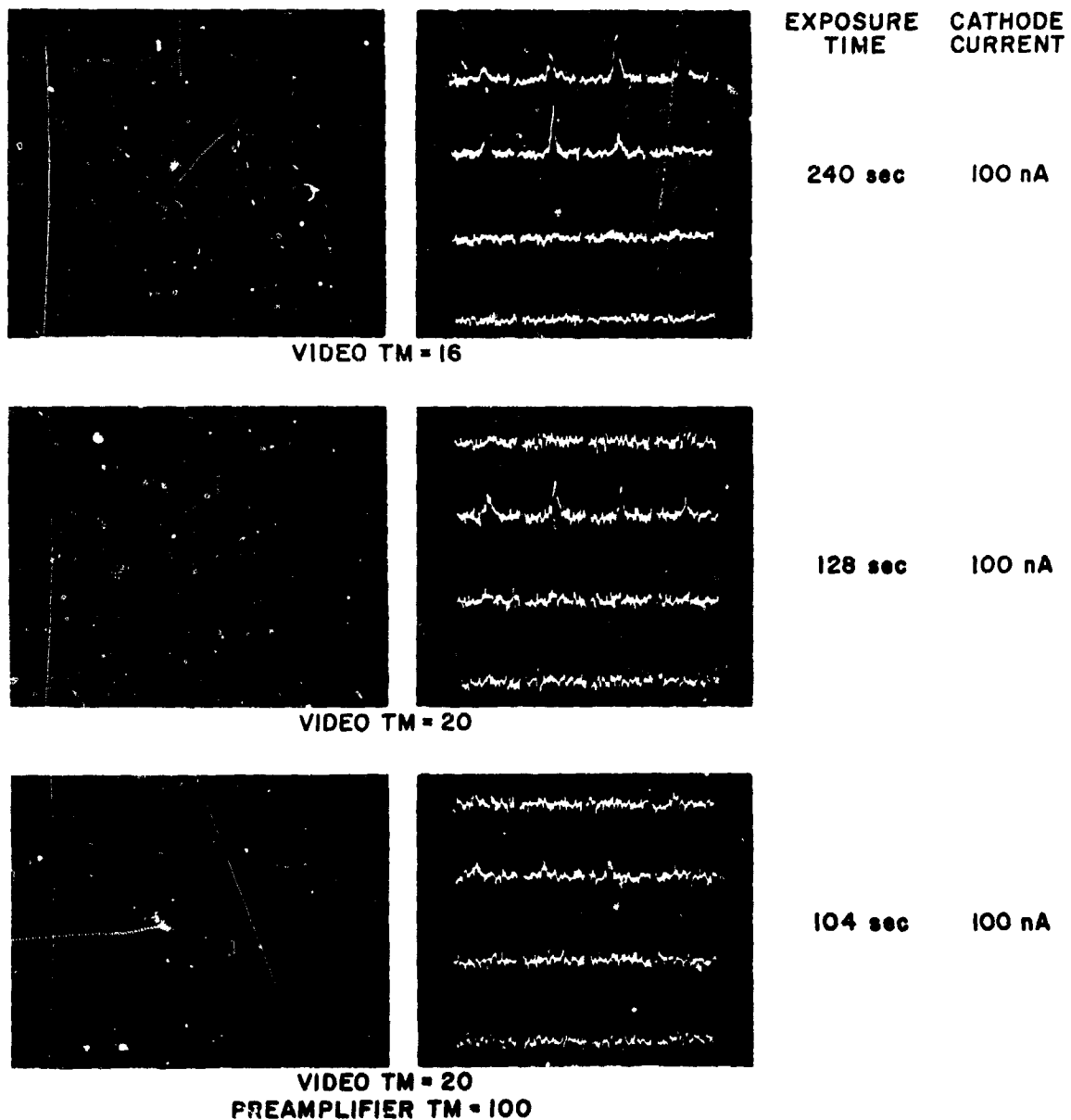


Figure 5. Star images; isocon readout of Star No. 4 in $29b^3$ Cygni; using different exposure times.

Figure 7 shows the display from a single isocon readout following a 176-second exposure of a third magnitude star with the line integrator accumulating all of the signal that passed through the gate.

The conventional intensity-recording technique for this spectrometer employs

pulse-height discrimination of the output from a photomultiplier. Counts are taken for intervals of 10 to 15 seconds at successive points 1 angstrom apart. The total time is equivalent to the camera tube exposure. The signal-to-noise ratio of this camera tube display is within a factor of three of that

obtained by counting 10^3 pulses per point with the photomultiplier.

The newer generation of isocon tubes should permit a further reduction of noise and improved sensitivity from that shown here.

Summary

The characteristics of the image-isocon camera tube in performing various astrometric tasks have been given. Further optimization of isocon tubes for one particular slow-scan camera system is continuing. From the present experimental results and projected performance, it is possible to define the characteristics of a more ideal camera tube. Its main features can be summarized in relation to photosurface, storage targets, and readout.

Photosurface

The maximum signal-to-noise ratio from a small stellar image is fundamentally determined by the integrated electric charge resulting from the exposure of the photosurface. Increased efficiency in the conversion of photons to electric charges will result in an increase of signal-to-noise ratio. The attainable quantum efficiency will depend upon which portion of the electromagnetic spec-

trum interest is centered—ultraviolet, visible, or infrared. Typically, to ensure good focus in the optics, the astronomer restricts the visible wavelengths to 1000-angstrom intervals.

Storage Targets

The finite capacity of an elemental area of the storage target to amass a charge image determines the maximum-permissible photo-excited input from one exposure. Increasing the capacitance of the target will permit a larger signal to be stored with higher signal-to-noise ratio. Gain introduced between the photosurface and the storage target does not enhance the signal-to-noise ratio of the stored charge image.

Readout

The best capability for readout of the target image is obtained with isocon scan. The low noise from dark portions of the scene and the wide dynamic range of the isocon output signal provides the capability for readout of the lowest-level stored image while retaining the capability to handle the largest amplitudes.

Increasing the target capacity would make available a range of more than 100 in the photometric brightness variations within one scene.

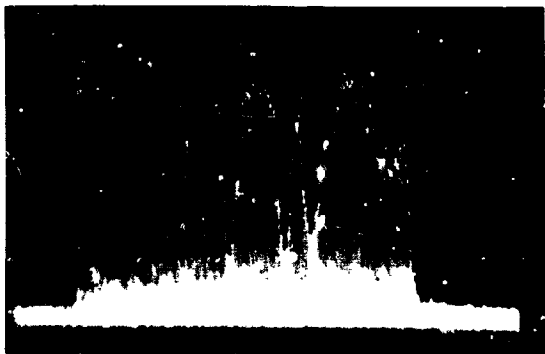


Figure 6. Spectrometer signal display without line integrator.

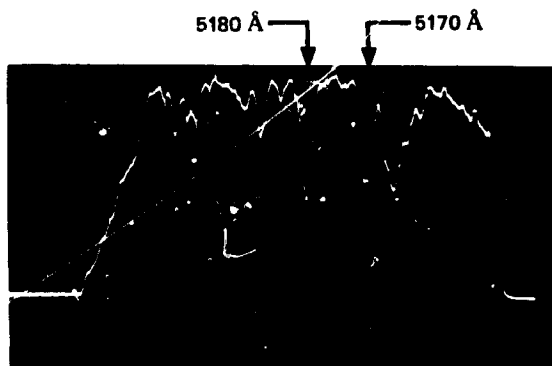


Figure 7. Spectrometer signal display with line integrator.

N70-36742

PRECEDING PAGE BLANK NOT FILMED.

Recent Developments in Image Devices

Kurt Schlesinger
General Electric Company

In recent years, the Imaging Devices Operation of General Electric Company has been engaged in several advanced development projects in the field of image converters, image intensifiers, and camera tubes. Some of these developments were performed under sponsorship of government agencies for national defense, notably the U. S. Army Signal Corps, the U. S. Air Force, and the U. S. Navy Night Vision Laboratory. Others were supported by company funding.

This short review is limited to developments representing unconventional approaches to or advances beyond the state-of-the-art as it was known until 1968.

Image Inverters

The classic problem of the electrostatic image inverter is curvature of field. Although a planar window suffices for the viewing screen in most cases, the cathode substrate of modern, electrostatic, image tubes is invariably spherical. Field flattening by optical means becomes increasingly difficult in modern image tubes. This is so because cathode curvature increases with the third power of the anode-subtended angle of view. The latter has much increased following current trends to reduce the aspect ratio of image tubes.

An attempt has been made at General Electric to achieve field flattening internally by electron-optical means. The result is the electrostatic image inverter shown in figure 1. It features planar windows at both ends, hence the name *Planotron*. The planar photocathode is practical because of a curved internal mesh. This field mesh is shown in

figure 1 at M. It may be seen again in more detail in figure 2.

Figure 3 shows an image obtained with a 3-inch laboratory sample of the Planotron

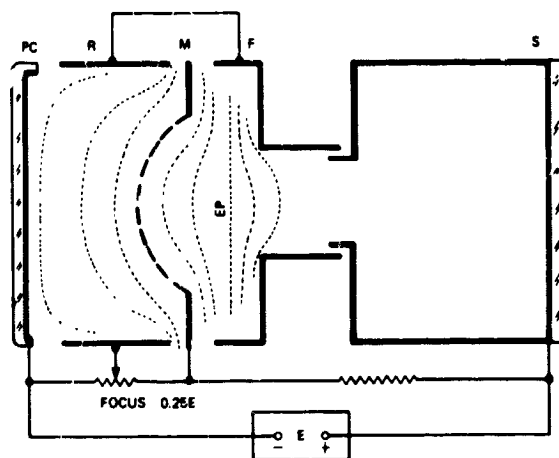


Figure 1. Plane-to-plane electrostatic image tube.



Figure 2. Field flattening by curved-mesh electrode.

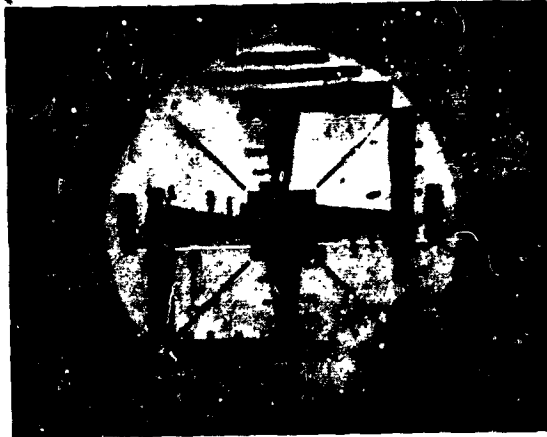


Figure 3. Image obtained with Planotron inverter.

having unity magnification. In practice, a curved mesh of this type actually performs a dual function: it flattens the cathode curvature, and it also takes care of pincushion distortion. Resolution in the Planotron is limited only by microlens action in the mesh. With the materials presently available, the ultimate lies between 20 and 25 line-pairs per millimeter. In a 3-inch tube, this implies a capability of 1200 lines.

Further Improvements in Image Converters

With increasing sophistication, modern applications of image tubes often demand controlled image geometry as well as image positioning by electronic means. Figure 4 shows an electrostatic image tube having both of these capabilities. The tube features a separate ring electrode, between anode cone and viewing screen, which is used for format control. The effect of this corrector lens on image geometry is shown in figure 5.

Furthermore, this tube features a "deflectronized" anode cone, shown in figure 6. This permits image displacement by a balanced, uniform, electric field acting transverse to the beam. Tubes of this type are useful for image motion compensation. An action photo is presented as part of figure 4.

Zoom Lenses

Electronic "zooming" in an image inverter was first announced by Dr. Schagen at an

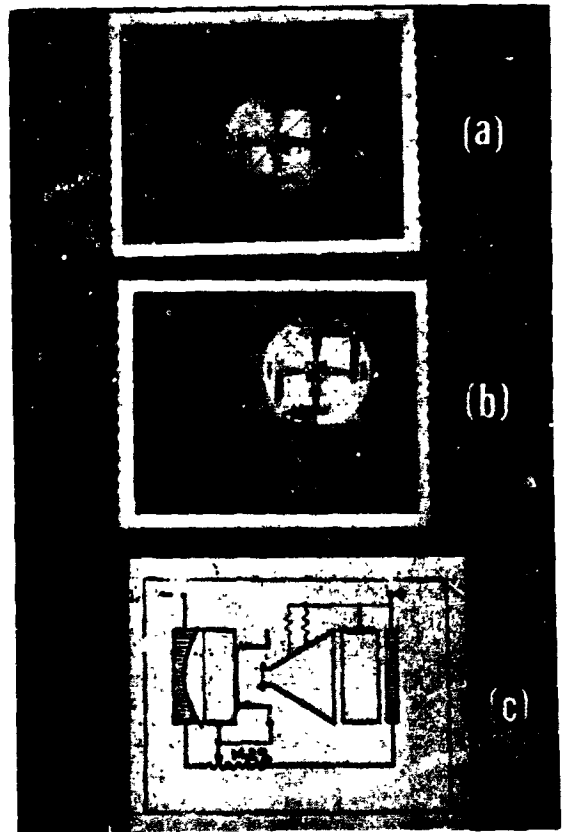


Figure 4. Image positioning (a) and (b); geometry control (c).

I.R.E. Convention in Washington in 1962. This device demonstrated a zoom range of about 4:1.

In the meantime, zoom lenses with "extended range" have been developed. One of these was pioneered at General Electric; the laboratory model is shown in figure 7. It has a zoom range of 10:1, as evidenced in figure 8. The same tube also includes an image intensifier with a maximum current gain in the order of $10^3:1$.

Magnetic Image Tubes

The magnetic image converter is inherently capable of image formation from plane to plane. Its chief disadvantages are size, weight, and power of the focus coil as well as the absence of inherent voltage regulation, which is a most welcome feature in electrostatic inverters.

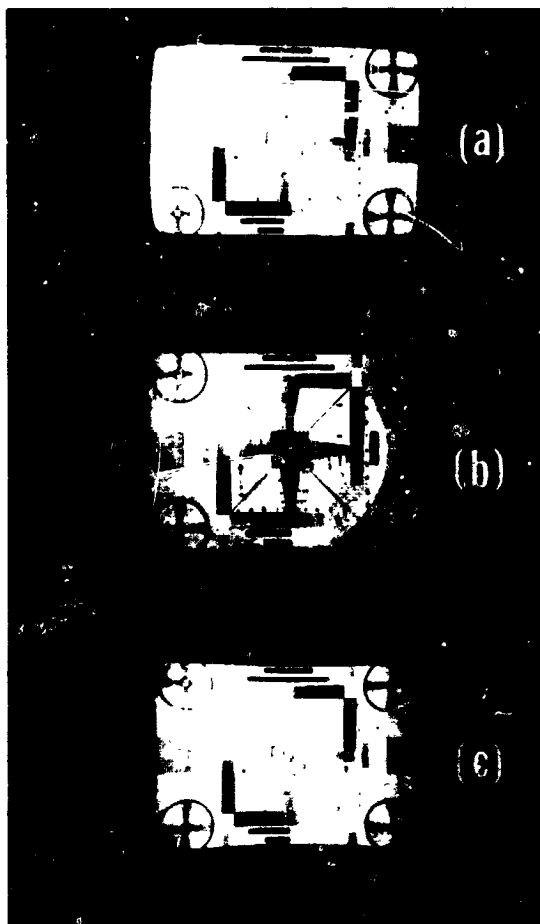


Figure 5. Control of image geometry.

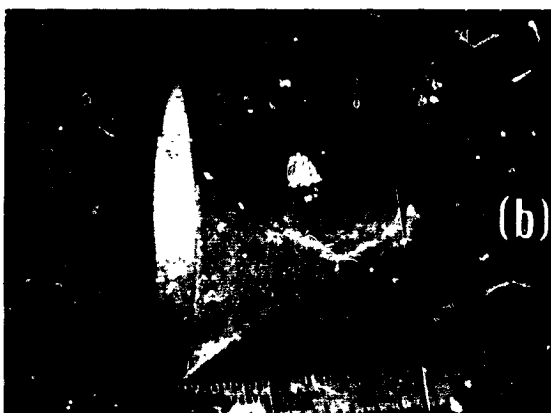
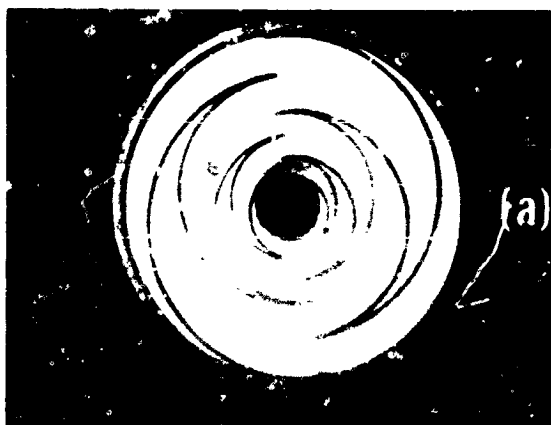


Figure 6. Image-positioning by deflectronized anode.

General Electric has taken a fresh approach to the field-coil problem for image tubes. It can readily be shown that image size and focus become independent of anode voltage if the magnetic field is contributed by two components. One of these should vary in direct proportion to line voltage; the other is held constant. If the latter field component is generated by a set of permanent magnets, rather than by a separate solenoid, we achieve not only the desired conservation of image focus and position but also a power saving of 4:1 because the remaining solenoid contributes only one-half of the total field requirement.

Figure 9 shows the basic circuit arrangement of General Electric's *Permafoc* system. The image tube (1) is exposed to the combined fields from an electromagnet (2) and from a set of magnetized bars (3). Both the solenoid (2) and the anode voltage for the tube (1) are derived from a common source (7) through rectifiers (4) and (5), respectively. The latter do not have to be stabilized.

In operation, the image becomes inherently immune to fluctuations of the power supply. This can be seen in figure 10, which shows two sets of images, each taken with anode voltages of 2000, 4000, and 6000 volts



Figure 7. Image intensifier with extended zoom range (3:1:1/3).

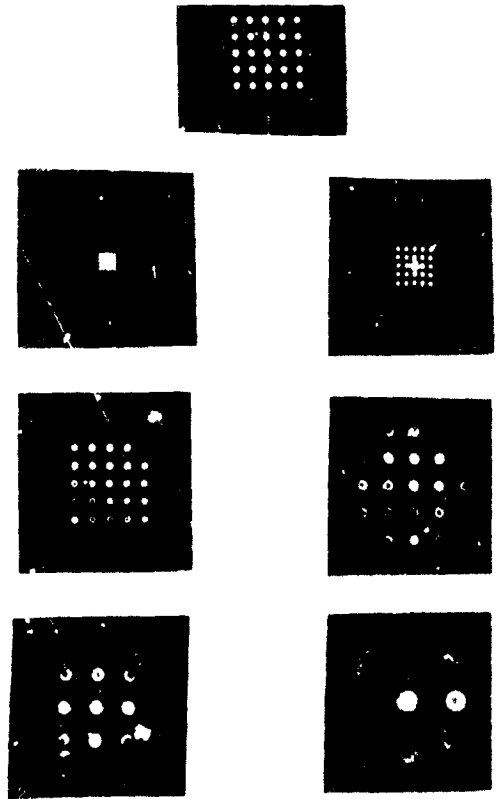


Figure 8. Action photo of zoom intensifier shown in figure 7.

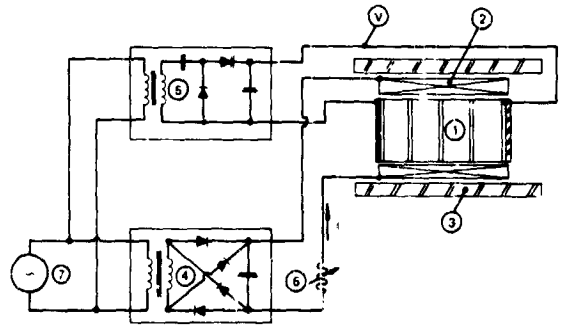


Figure 9. Permafoc circuitry for magnetic image converters.

shown at the left in figure 11. The test pattern on the right in figure 11 shows a 600-line RETMA test chart, which is fully resolved. This, considering the small size of the target image (3/8-inch diagonal), implies an effective resolution of 44 line-pairs per millimeter.

while the Permafoc circuit is ON (fig. 10a) or OFF (fig. 10b).

Camera Tubes

Unconventional pickup tubes were illustrated in the lecture by slides showing an all-electrostatic Image Orthicon, and also two samples of a mixed-field vidicon, the latter using magnetic focus and electrostatic deflection. This system has since become known by the acronym FPS (Focus-Projection and Scan). FPS combines the high resolution performance of magnetic focus with the small size, power, and weight associated with electrostatic deflection. Both features are best illustrated by the smallest member of the FPS family, shown in figure 11. This tube was developed by R. A. Wagner and J. Blackham of the Imaging Devices Operation.

The tube itself measures only 3-1/2 inches by 5/8 inches outer diameter. It is enclosed by a coil with a 3/4-inch outer diameter,

A successful readout of the 1600-line RETMA chart, optically demagnified down to a height of 11 millimeters on target, is shown in figure 12. This feat requires a spot size of 7 microns; i.e., a resolution capability of 3600 lines per inch.

Such tasks are routinely accomplished by the largest and the most recent arrival in the FPS family: the 3-inch vidicon shown in figure 13. The ultra-high resolution of this tube is due to an unconventional

beam-forming system, which includes a demagnifying magnetic lens as well as a high intensity source. The latter threads a very narrow beam of 20 microamperes through a $\frac{1}{2}$ -mil aperture. This beam has an electron-optical brightness of 10,000 amp/cm² steradian, or 53 percent of the Langmuir ultimate. Tubes of this kind may find many future applications in such fields as satellite communication and aerospace technology.

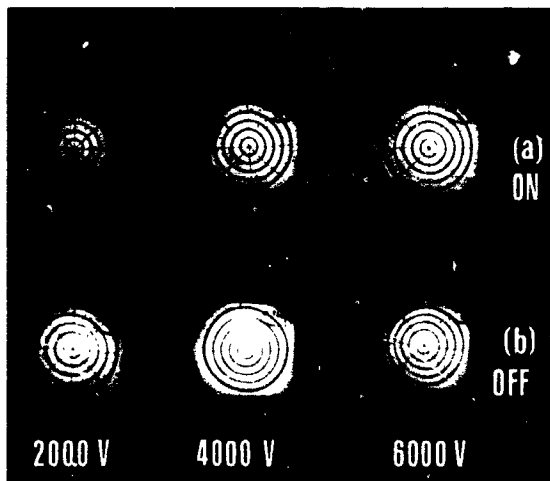


Figure 10. Magnetic image converter at 2000, 4000, and 6000 volts with Permafocuss ON and OFF.

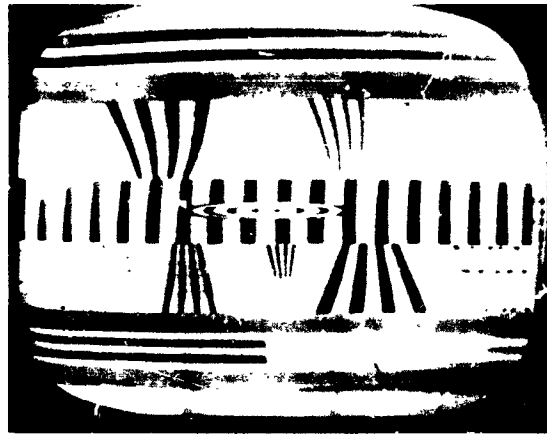


Figure 12. The 3-inch FPS vidicon, reading 7-micron detail.

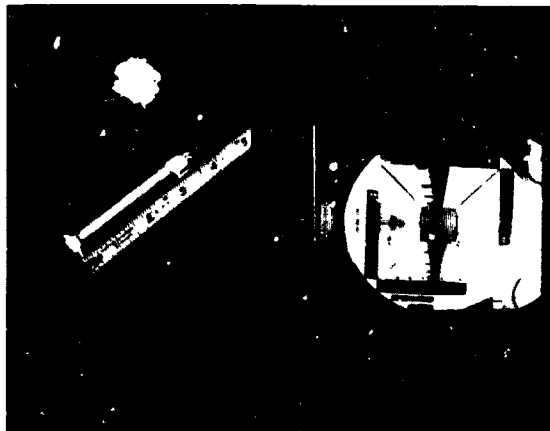


Figure 11. Miniature vidicon in FPS family.

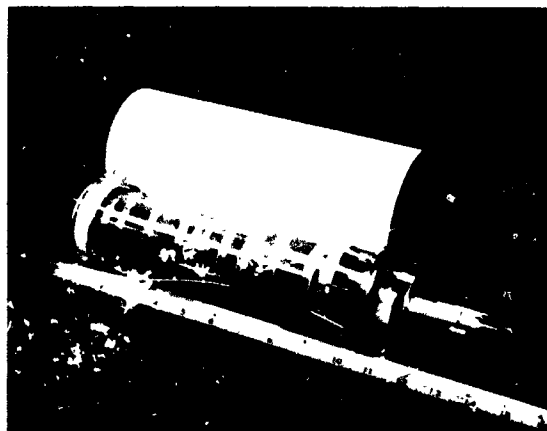


Figure 13. The 3-inch FPS vidicon, reading at 3600 lines per inch.

PRECEDING PAGE BLANK NOT FILMED.

N70-36743

Infrared image Recording Systems

George I. Zissis
University of Michigan

The availability of many sensitive detectors responding to radiation in the 1.0- to 25-micron spectral region has led to the recent increase in infrared astronomical research. Infrared sky surveys, planetary studies, and thermal maps of the earth's moon are among the works reported in recent years. Such observations can be classified broadly as studies either to measure distributions of the radiance of extended sources or to obtain the values of radiant intensity for point sources (sources whose angular subtense is less than the angular spatial resolution of the observing system). Astronomers are interested in quantitative and, where possible, absolute radiometric measurements of these quantities as well as their variation with wavelength, their spatial and angular distribution, their temporal variations, and the nature of polarization and coherence.

This surge in activity has been most recently described by Frank J. Low (ref. 1), by G. Neugebauer and R. B. Leighton (ref. 2), and, for "rocket astronomy," by D. P. McNutt (ref. 3). A review of the extremely exciting high-resolution spectroscopic research by the Connes is included in a brief review of planetary spectroscopy in the near-infrared by D. M. Hunten (ref. 4); the overall field is covered in the recent publication of papers presented at the 1966 NASA-Goddard conference on infrared astronomy (ref. 5).

The use of infrared image-recording systems has furnished considerable valuable information in the form of lunar and planetary thermal maps in the eight years that have elapsed since my last cursory review of infrared astrophysics (ref. 6). Well-known examples of infrared imaging of extended

sources are presented in the works by Hunt, Salisbury, and Vincent (ref. 7), by Shorthill and Saari (ref. 8), and by Murray (ref. 9). Some work has been done with infrared image tubes (e.g., by Kuprevich at the Pulkovo Observatory, ref. 10), but the studies on thermal features (refs. 11, 12, 13, 14, and 15) have required the use of systems operating at wavelengths longer than 3 microns (ref. 16).

Although infrared image tubes have been under development for several years, imaging in the spectral regions beyond 3 to 4 microns has been most successfully done by systems using detectors or detector arrays in optical-mechanical scanners. One of the earlier treatments of the applicable technology was prepared in 1959, but it is still a very useful reference (ref. 17). Infrared imaging systems were covered in the September 1968 issue of *Applied Optics* (ref. 18), which includes papers by R. W. Astheimer and F. Schwarz ("Barnes Engineering Co. Thermograph T-6"), Sven-Bertil Borg ("AGA Thermovision"), E. W. Kutzscher and K. H. Zimmermann ("A Scanning IR Inspection System"), L. W. Nichols and J. Lamar ("Three-Color Line-Scanning Image Converter"), E. Sundstrom ("Bofors IR Camera"), R. Blythe and E. Kurath ("Bendix Thermal Mapper"), and J. Yoder ("Scanning IR Microscope").

Most of these systems are ground-to-ground, object-plane scanning, using a single element detector. An interesting laboratory system of this type has been designed by G. Suits (ref. 19). His goal was to create an inexpensive (less than \$2,000) scanner, and, with photovoltaic detectors, the cost of reproducing the system is well within his goal.

Figure 1 shows the Suits scanner that is programmed in figure 2. As used by LaRocca and Lindquist at the University of Michigan Infrared and Optical Laboratory, it has a 2-milliradian field-of-view, can be scanned vertically over an angle as large as 60 degrees, and can cover any desired azimuthal angle. It uses a 9-inch-focal-length spherical mirror in a Newtonian configuration. Scan rates can vary from 5 vertical scan lines per second to 1 scan

every 4 seconds or slower. At the speed of about 1.8 degrees per minute, the scanner picture of the completely dark laboratory room shown in figure 3 took about 1-½ hours.

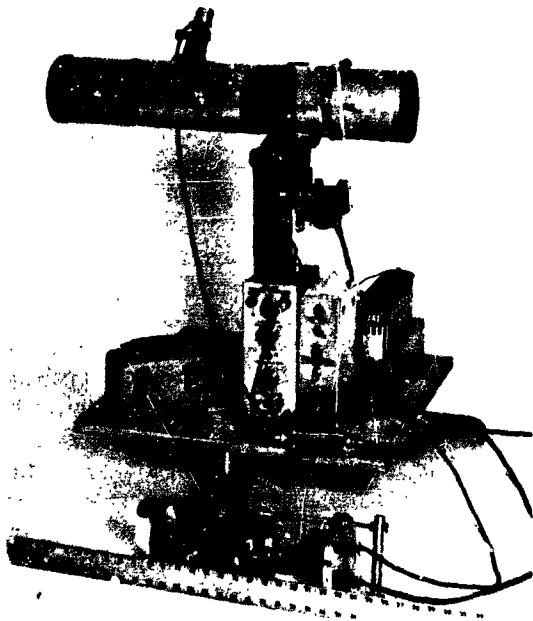


Figure 1. Suits scanner.

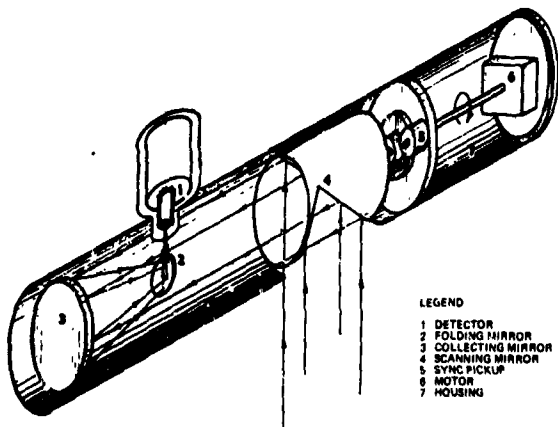


Figure 2. Diagram of Suits scanner.

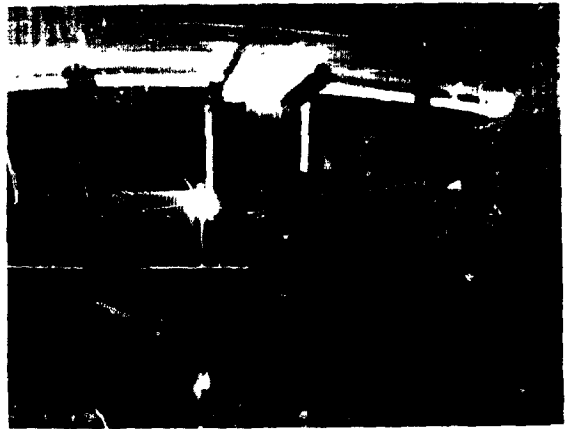


Figure 3. Infrared image of a totally dark laboratory room.

Because the electronics are DC-coupled, true radiance values may be obtained from A-scope or chart recorder traces of the detector output. In figure 4, an outside scene is imaged in a 0.1-micron region at 4.7 microns during daytime. The image obtained with the unfiltered, cooled, photovoltaic, indium-antimony (InSb) detector is obviously overloaded. This particular detector was selected to hold down costs. LaRocca and Lindquist (ref. 20) have stated that:

1. Photovoltaic detectors are available for from \$750 to \$1000 as compared to \$2000 to \$3000 for photoconductive InSb.

2. As used, with operational amplifiers and output feedback, no detector bias is needed.

3. Theoretically, the D^* is $\sqrt{2}$ times that of a photoconductive detector while, experimentally, the factor is still larger. (This gain in D^* is not often realized because of impedance matching problems).

4. The response time is about one-tenth that of the photoconductive detector.

5. The response was found to be more uniform across the face of the photovoltaic detector.

6. The detector was linear over a wide range.



Figure 4. Two infrared images obtained by the Suits scanner; top image: at $4.7 \mu\text{m}$ with a $\Delta\lambda = 0.1 \mu\text{m}$; bottom image: unfiltered InSb.

On the other hand, they point out that photoconductive InSb has a lower impedance and a higher responsivity, which may be important if high-gain, low-noise preamplifiers are a problem. For these reasons, they used a photovoltaic InSb detector, cooled directly to liquid nitrogen temperatures, with a sapphire window.

Returning to the capabilities of existing unclassified infrared scanners, several are now available for use in aircraft in the mode illustrated in figure 5. Note the boresighted radiometer shown in this figure. The need for quantitative radiometric data can be met in this way or by internal calibration sources

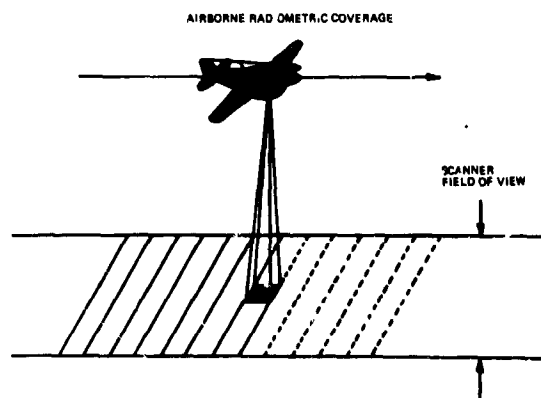


Figure 5. Airborne infrared scanner operations.

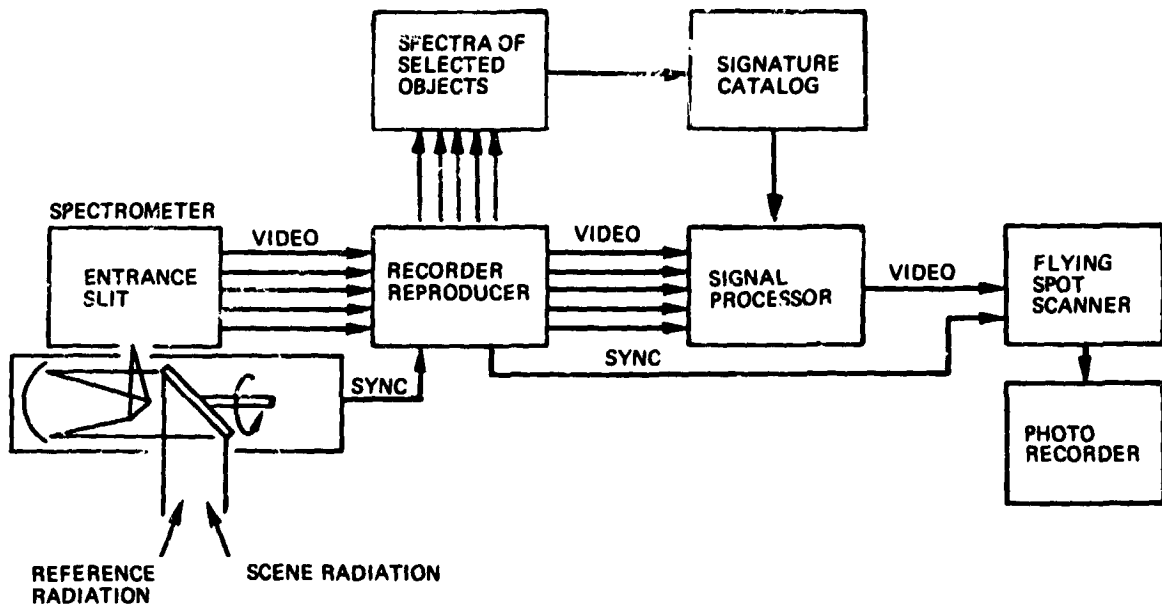


Figure 6. Schematic of University of Michigan multispectral scanner and data processor.

(fig. 8) for a scanner with DC-coupled electronics. Unclassified air-to-ground scanners are now available from the Bendix Aerospace Systems Division, HRB-Singer, Texas Instruments, Daedalus Enterprises, and probably others.

Recently, multispectral scanners have also become available. The system built by the University of Michigan is shown in block diagram form in figure 6. The spectrometer is shown in figure 7. The scanner carries internal calibration sources (fig. 8).

Obviously, the heart of any of these infrared imaging systems is the detector. Figure 9 is a summary of the characteristics of available infrared detectors, published in the January 1969 issue of *Electronics* (ref. 21). These data have not changed greatly from older summaries such as those appearing in figures 10 and 11.

Particular interest has been generated in the low-temperature germanium bolometer developed and used in the early 1960's by F. J. Low (refs. 22 and 23), and in mercury-cadmium-tellurium (HgCdTe) detectors made by Minneapolis-Honeywell and Société Anonyme de Télécommunications, among

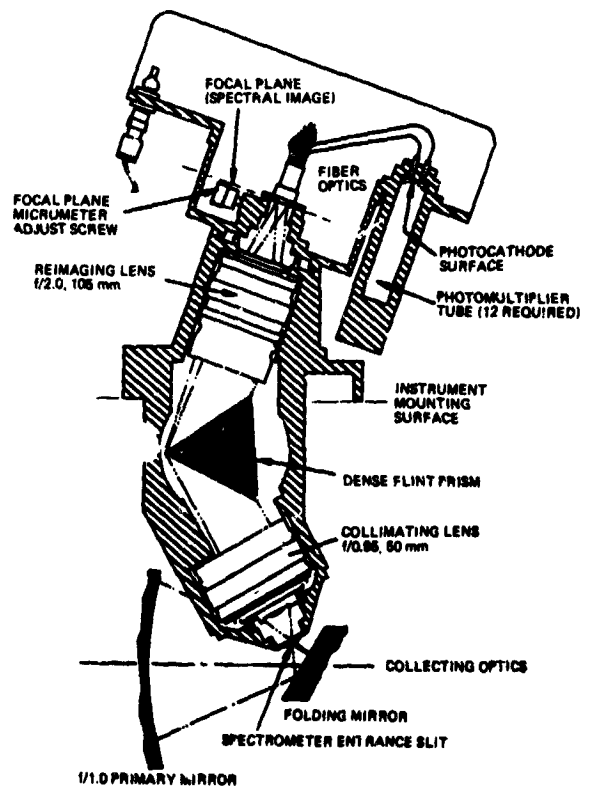


Figure 7. Spectrometer for multispectral scanner.

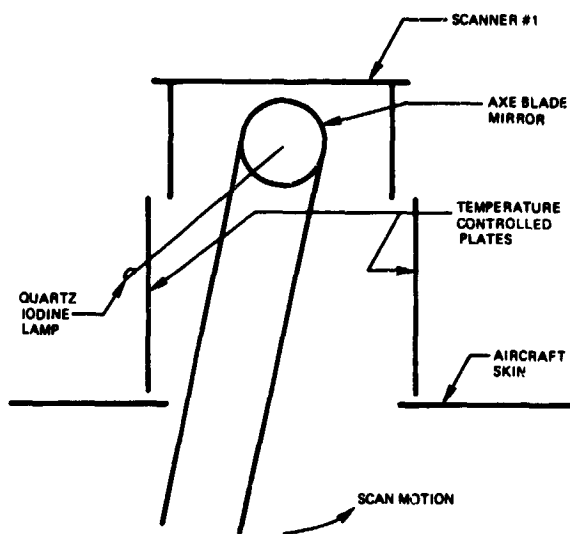
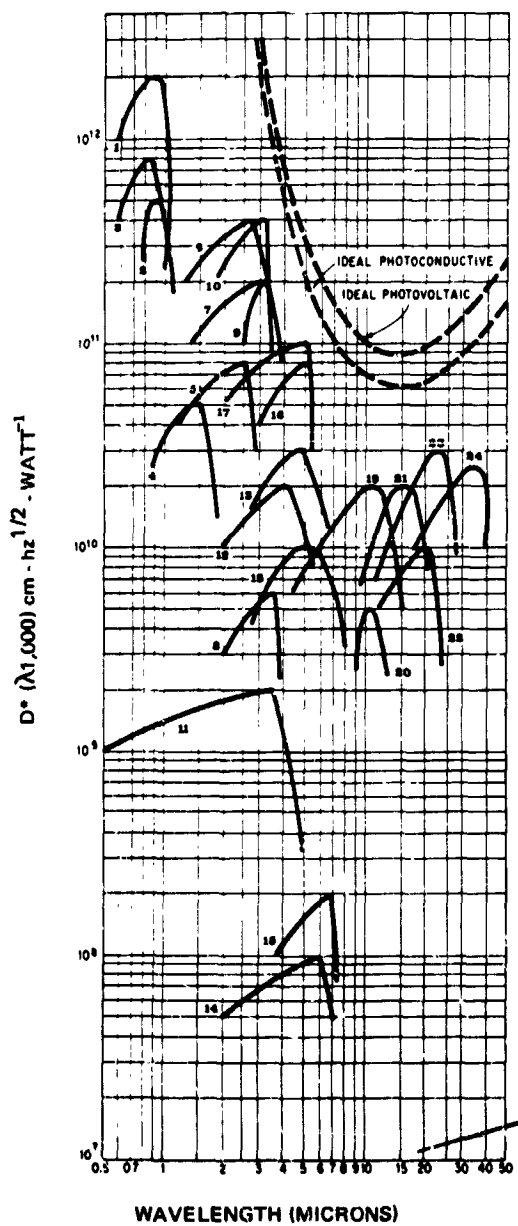


Figure 8. Internal calibration sources for multispectral scanner.

others. At wavelengths less than 9 microns, these detectors are said to be within one-half of the ideal (BLIP) value of D^* . The lessened cooling requirements for response in the 8- to 13-micron region makes these detectors particularly attractive for space use.

For image plane scanning at fairly fast rates but with good signal-to-noise ratios, reasonable integration times, etc., arrays seem particularly attractive. These have been made with elements from a few to many tens and with materials such as lead sulfide, mercury-doped germanium, and indium antimonide. A mercury-germanium (HgGe) array (fig. 12) made by the Santa Barbara Research Center is at the Mt. Haleakala Observatory, Maui, Hawaii, a facility constructed by the University of Michigan under sponsorship of the Advanced Research Projects Agency. This facility, having one 60-inch and two 48-inch telescopes, has a particular capability for infrared research.

Finally, there remains the question of cryogenics. Space systems using radiation cooling, as prepared by the Goddard Space Flight Center, have achieved temperatures lower than 90° absolute. Studies have indicated that about 60 pounds of a solid



Spectral detectivities of manufactured detectors tested under 80° field-of-view and 295° K background temperature. Theoretical values of peak D^* lie on the dashed curves. Numbers on graph refer to column numbers in figure 9, parts 2 and 3, on following two pages.

Figure 9. Characteristics of available infrared-region detectors (Part 1 of 3). [Copyright by McGraw-Hill, Inc., 1969. Reprint from Electronics Magazine, 20 January 1969.]

1 2 3 4 5 6 7 8 9

Detector Material Operating Mode	Si Silicon (pv)	Si Silicon (pc)	GaAs Gallium Arsenide (pv)	Ge Germanium (pv)	PbS Lead Sulfide (pc)	PbS Lead Sulfide (pc)	PbS Lead Sulfide (pc)	InAs Indium Arsenide (pv)	InAs Indium Arsenide (pv)	Indi	
Typical Peak D* (cm ² ·hz ^{1/2} ·watt ⁻¹) at 1,000 hz modulation frequency (wavelength, in microns) (field of view, degrees) (background temperature, °K)	2 x 10 ¹² 0.9	5 x 10 ¹¹ 0.9	8 x 10 ¹¹ 0.85	5 x 10 ¹⁰ 1.5	8 x 10 ¹⁰ 2.5	4 x 10 ¹¹ 2.7 60 295	2 x 10 ¹¹ 3.1 60 295	6 x 10 ⁹ 3.5	2 x 10 ¹¹ 3.2 60 295	4	
Best Measured Peak D* (cm ² ·hz ^{1/2} ·watt ⁻¹) (conditions as above)	1 x 10 ¹²	1 x 10 ¹²			1.5 x 10 ¹¹	7 x 10 ¹¹	4 x 10 ¹¹	1 x 10 ¹⁰	3.5 x 10 ¹¹	7	
Spectral Range Exhibiting Greater Than 50% Relative Response (microns)	0.6 to 1.0	0.8 to 1.06	0.6 to 0.95	0.9 to 1.7	1.2 to 2.8	1.3 to 3.2	1.4 to 3.8	2.0 to 3.8	2.5 to 3.4	1.	
Normal Operating Temperature (°K)	295	295	295	295	295	195	77	295	195		
Operating Temperature Limits (°K); 50% peak D* degradation points	-320	-350			-310	160,250	-160	-320	-210	-	
Typical Time Constant (seconds)	5 x 10 ⁻⁷	5 x 10 ⁻⁶	1 x 10 ⁻⁶	1 x 10 ⁻⁷	3 x 10 ⁻⁶	5 x 10 ⁻⁷	3 x 10 ⁻⁷	<1 x 10 ⁻⁶	<1 x 10 ⁻⁶	5 x	
Nominal Resistance (ohms)	1 x 10 ⁴	1 x 10 ⁴	1 x 10 ⁴	2 x 10 ⁵	1 x 10 ⁴	1 x 10 ⁴	2 x 10 ⁴	3 x 10 ¹	5 x 10 ⁴	5 x	
Area Configuration	Single Detectors Size Range - Min. to Max. (inches)	.004 to .5	.004 to .7	.004 to .060	.004 to .5	.001 to 1.0	.001 to 1.0	.001 to 1.0	.004 to 0.1	.004 to 0.1	.004
	Shape (round, square or rectangular)	any	□ □	□ □	any	□ □	□ □	□ □	○	○	Glass
	Typical Package	TO-5/18	Flat Mount	TO 18	TO 5/18, BNC	Flat Mount	Glass Dewar	Glass Dewar	TO 5/16	Glass Dewar	Glass
	Detector Arrays Minimum Size per Detector (inches) Minimum Size per Spoce (inches)	.004 .002	.004 .001			.001 .001	.001 .001	.001 .001	.003 .002	.003 .002	.0 .0
Dimensions - see code	±.002	±.020			±.001	±.001	±.001	±.002	±.002		
Typical Detector Unit Price	\$ 40	\$ 40	\$ 50	\$ 100	\$ 40	\$ 600	\$ 600	\$ 175	\$ 600	\$ 1	
Manufacturer(s) - see reference	f,h,m,r,s	k	m	h,m,r	e,g,j,o,q	g,j,o,q	g,j,o,q	c,h,m,r	c,m,r	c,i	

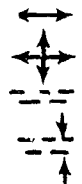
Detector Manufacturers

- a. Aerojet-General Corp.
- b. Avco Corporation, Electronics Div.
- c. Barnes Engineering Co.
- d. Block Engineering, Inc.
- e. Catron Electronic Corp.
- f. E. G. and G.
- g. Electronic Corp. of America
- h. Electro-Nuclear Laboratories, Inc.
- i. Honeywell Radiation Center
- j. Infrared Industries, Inc.
- k. Mithras, Inc.
- l. Networks Electronic Corp.
- m. Philco-Ford Corp.
- n. Raytheon Co.
- o. Santa Barbara Research Center
- p. SAT - Paris, France; (U.S. Representative; Elteck Corp.)
- q. Sensor Precision Ind.
- r. Texas Instruments Inc.
- s. United Detector Technology

- Azusa, California
- Cincinnati, Ohio
- Stamford, Conn.
- Cambridge, Mass.
- Geneva, Ill.
- Boston, Mass.
- Cambridge, Mass.
- Menlo Park, Calif.
- Boston, Mass.
- Waltham, Mass.
- Cambridge, Mass.
- Chatsworth, Calif.
- Spring City, Penn.
- Waltham, Mass.
- Goleta, Calif.
- Larchmont, N.Y.
- Medfield, Mass.
- Dallas, Texas
- Santa Monica, Calif.

Array Dimension Code:

- Linear
- Two-dimensional
- Linear staggered
- Space between rows



Legend:

- pv - photovoltaic mode
- pc - photoconductive mode
- pem - photoelectromagnetic mode

Figure 9. Characteristics of available infrared-region detectors (Part 2 of 3). [Copyright by McGraw-Hill, Inc., 1969. Reprint from Electronics Magazine, 20 January 1969.]

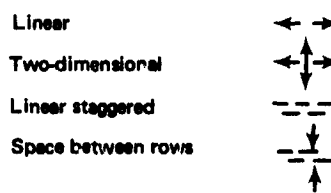
11 12 13 14 15 16 17 18 19 20 21 22 23 24

PbSe Selenide (pc)	PbSe Lead Selenide (pc)	PbSe Lead Selenide (pc)	InSb Indium Antimonide (sem)	InSb Indium Antimonide (pc)	InSb Indium Antimonide (pc)	InSb Indium Antimonide (pc)	Ge:As Gold-Doped Germanium (pc)	Ge:Hg Mercury-Doped Germanium (pc)	Bi-CdTe Mercury Cadmium Telluride (pv)	Ge:Cd Cadmium-Doped Germanium (pc)	Si:Sn Antimony-Doped Silicon (pc)	Ge:Cu Copper-Doped Germanium (pc)	Ge:Zn Zinc-Doped Germanium (pc)
1×10^9	2×10^{10}	3×10^{10}	1×10^8	2×10^8	8×10^{10}	1×10^{11}	1×10^{10}	2×10^{10}	5×10^8	2×10^{10}	1×10^{10}	3×10^{10}	2.5×10^{10}
3.4	4.1 60 295	4.8 60 295	6.0	6.8	5.3 60 295	5.1 60 295	5.0 60 295	10.5 60 295	10.6 80 295	16 60 295	20 60 295	23 60 295	36 60 295
1×10^{10}	5×10^{10}	5×10^{10}	3×10^8		1×10^{11}	2×10^{11}	2×10^{10}	5×10^{10}	2×10^{10}	4×10^{10}	2×10^{10}	5×10^{10}	5×10^{10}
5 to 4.2	2.0 to 5.3	2.7 to 6.3	2.0 to 7.0	3.6 to 7.3	3.0 to 5.4	2.0 to 5.4	3.0 to 7.5	6 to 14	9 to 13	11 to 20	12 to 23	15 to 27	20 to 40
295	195	77	295	295	77	77	60	27	77	4.2	4.2	4.2	4.2
-310	-230	-160			-95	-105	-80	-40	-100	-26	-10	-20	-6
1×10^{-6}	3×10^{-5}	4×10^{-5}	2×10^{-7}	1×10^{-6}	6×10^{-6}	$< 1 \times 10^{-6}$	1×10^{-7}	2×10^{-7}	$< 1 \times 10^{-8}$	1×10^{-7}	1×10^{-7}	5×10^{-7}	2×10^{-8}
1×10^4	5×10^4	5×10^4	1×10^1	2×10^1	1×10^4	1×10^5	1×10^5	1×10^5	2.5×10^1	1×10^5	7×10^4	1×10^5	2.5×10^5
.03 to .3	.003 to .5	.003 to .5	.015 to .040	.040 to .1	.003 to .1	.003 to .1	.003 to .1	.003 to .1	.020 to .080	.003 to .1	.004 to .1	.003 to .1	.003 to .1
□□	□□	□□	□	□□	□□	□□	□□	□□	□□	□□	□□	□□	□□
at Mount	Glass Dewar	Glass Dewar	Metal Cont.	Flat Mount	Glass Dewar	Glass Dewar	Glass Dewar	Metal Dewar	Glass or Metal Dewar	Metal Dewar	Metal Dewar	Metal Dewar	Metal Dewar
.003 .002	.003 .002	.003 .002			.003 .002	.003 .002	.003 .002	.003 .002	.003 .002 Developmental	.003 .002 .002	.004 .004	.003 .002	.003 .002
$\frac{\Delta}{\nabla} .001''$	$\frac{\Delta}{\nabla} .001''$	$\frac{\Delta}{\nabla} .001''$			$\frac{\Delta}{\nabla} .001''$	$\frac{\Delta}{\nabla} .002''$	$\frac{\Delta}{\nabla} .002''$	$\frac{\Delta}{\nabla} .002''$		$\frac{\Delta}{\nabla} .002''$	$\frac{\Delta}{\nabla} .004''$	$\frac{\Delta}{\nabla} .002''$	$\frac{\Delta}{\nabla} .002''$
\$100	\$900	\$900	\$400	\$90	\$750	\$600	\$800	\$2,500	\$4,900	\$3,000	\$2,500	\$2,500	\$3,300
l,o	j,o	j,o	h,i,j	d,i	h,i,l,m,n,o	b,c,l,m,o,r	c,m,n,o	a,m,n,o,r	p	n,o,r	a	a,m,n,o,r	o

Detector Manufacturers

- a. Aerojet-General Corp.
 - b. Avco Corporation, Electronics Div.
 - c. Barnes Engineering Co.
 - d. Block Engineering, Inc.
 - e. Catron Electronic Corp.
 - f. E. G. and G.
 - g. Electronic Corp. of America
 - h. Electro-Nuclear Laboratories, Inc.
 - i. Honeywell Radiation Center
 - j. Infrared Industries, Inc.
 - k. Mithras, Inc.
 - l. Networks Electronic Corp.
 - m. Philco-Ford Corp.
 - n. Raytheon Co.
 - o. Santa Barbara Research Center
 - p. SAT - Paris, France; (U.S. Representative; Elteck Corp.)
 - q. Sensor Precision Ind.
 - r. Texas Instruments Inc.
 - s. United Detector Technology
- Azusa, California
 - Cincinnati, Ohio
 - Stamford, Conn.
 - Cambridge, Mass.
 - Geneva, Ill.
 - Boston, Mass.
 - Cambridge, Mass.
 - Menlo Park, Calif.
 - Boston, Mass.
 - Waltham, Mass.
 - Cambridge, Mass.
 - Chatsworth, Calif.
 - Spring City, Penn.
 - Waltham, Mass.
 - Goleta, Calif.
 - Larchmont, N.Y.
 - Madfield, Mass.
 - Dallas, Texas
 - Santa Monica, Calif.

Array Dimension Code:



Legend:

- pv - photovoltaic mode
- pc - photoconductive mode
- pam - photoelectromagnetic mode

Figure 9. Characteristics of available infrared-region detectors (Part 3 of 3). [Copyright by McGraw-Hill, Inc., 1969. Reprint from Electronics Magazine, 20 January 1969.]

cryogenic could supply useful cooling for approximately a year in orbit. Obviously, one could imagine systems using Peltier coolers or other cryogenic engines if satisfactory power, weight, and reliability specifications could be achieved.

Most of the advances in infrared technology have come as a result of Department of Defense interest and funding. As the National Aeronautics and Space Administration faces its special needs for spaceborne infrared systems, the requirement for research and development directed toward these particular needs must be met by NASA programs and funds.

References

1. Low, Frank J.: Infrared Astrophysics. Science, vol. 164, no. 164, 2 May 1969, p. 501.
2. Neugebauer, G.; Leighton, R. B.: The Infrared Sky. Scientific American, vol. 219, no. 2, August 1968, pp. 51-60.
3. McNutt, D. P.: Rocket Infrared Astronomy. Astronautics and Aeronautics, vol. 7, no. 3, March 1969, p. 44.
4. Hunt, D. M.: Fourier Spectroscopy of Planets. Science, Vol. 162, 18 October 1969, p. 313.
5. Brancazio, P. J.; Cameron, A. G. W.: Infrared Astronomy. Gordon and Breach, 1968.
6. Zissis, G. J.: Infrared Techniques in Astrophysics. Presentation, Georgetown University Summer Conference for College Professors on Physics and Astronomy, 1961.
7. Hunt, G. R.; Salisbury, J. W.; Vincent, R. K.: Infrared Images of the Eclipsed Moon. Sky and Telescope, vol. 36, no. 4, October 1968.

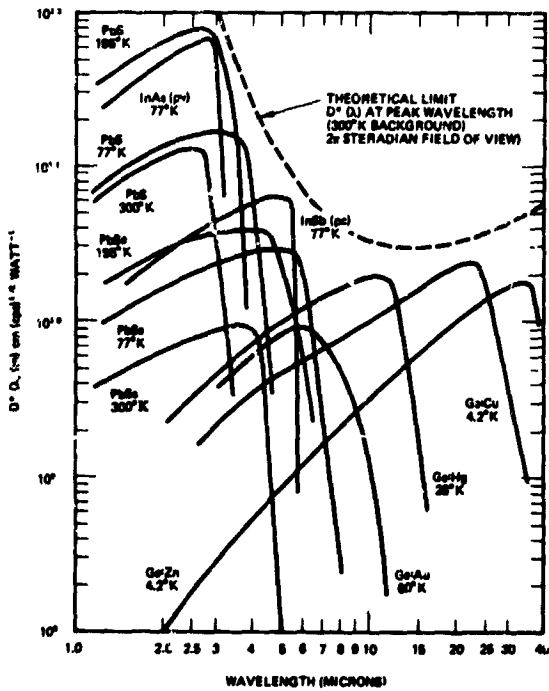


Figure 10. Early tabulation of detector characteristics.

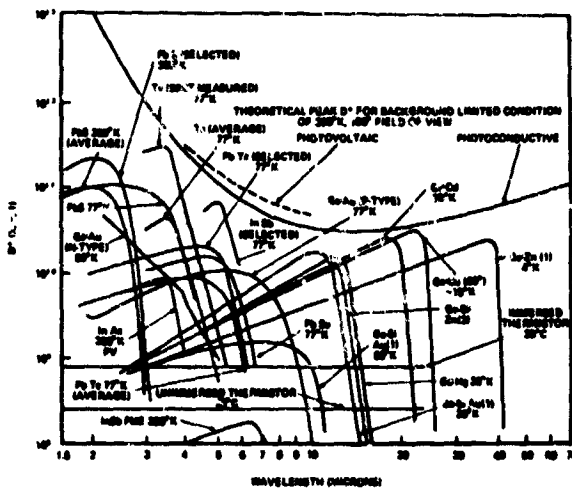


Figure 11. D* tabulation of 1968 by T. Limpert.

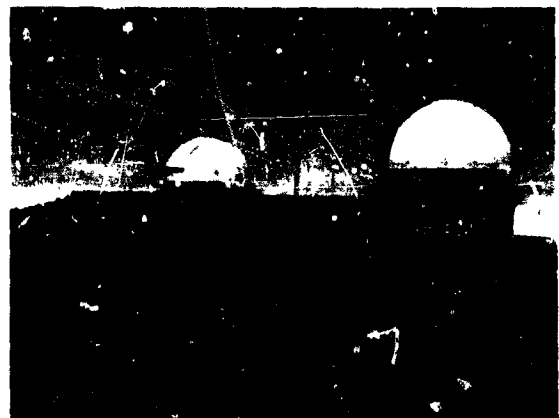


Figure 12. Mt. Haleakala Observatory.

8. Shorthill, R. W.; Saari, J. M.: Nonuniform Cooling of the Eclipsed Moon: A Listing of Thirty Prominent Anomalies. Reprint, *Science*, vol. 150, no. 3693, October 8, 1965, pp. 210-212.
9. Murray, B. C.: Infrared Evidence of Differential Surface Processes on the Moon. Summary of Remarks, Royal Society Symposium on the Physics of the Moon, London, June 1-4, 1965, reprint, 19 January 1966.
10. Kuprevich, N. F.: Experimental Television Photographs of the Moon in the Spectral Region 0.8-2.3 μ . Translation, *Astronomicheskii Zhurnal*, vol. 39, no. 6, November-December 1962, original article submitted June 6, 1962.
11. Allen, D. A.; Ney, E. P.: Lunar Thermal Anomalies: Infrared Observations. *Science*, Vol. 164, 25 April 1969.
12. Saari, J. M.; Winter, D. F.: A Differential Method for Comparing Lunar Eclipse Cooling Curves with Theoretical Models. *Transactions*, vol. 49, no. 1, March 1968, p. 225.
13. Roelof, E. C.: Thermal Behavior of Lunar Surface Rocks, 2, Rocks of Submeter Size. *Transactions*, vol. 49, no. 1, March 1968, p. 226.
14. Ulrichs, J.; Campbell, M. J.: Heat Transfer by Radiation in the Lunar Soil. *Transactions*, vol. 49, no. 1, March 1968, p. 226.
15. Ronca, L. B.; Green, R. R.; Saari, J. M.; Shorthill, R. W.: The Distribution of Thermal Anomalies and Craters on the Lunar Surface. *Transactions*, vol. 49, no. 1, March 1968, p. 273.
16. Hunt, G. R.; Salisbury, J. W.: Lunar Surface Features: Mid-Infrared Spectral Observations. *Science*, Vol. 146, 30 October 1964.
17. Special Issue on Infrared Physics and Technology. *Proceedings, IRE*, Vol. 47, September 1959, pp. 1413-1700.
18. Non-Destructive Testing. *Applied Optics*, vol. 7, no. 9, September 1968.
19. Suits, G. H.: Private Communication. University of Michigan.
20. LaRocca, A. J.; Lindquist, G.: Private Communication. University of Michigan.
21. Characteristics of Available Infrared-Region Detectors. Reprint from *Electronics*, 20 January 1969, copyrighted, McGraw-Hill Inc., 1969.
22. Low, Frank J.: Low-Temperature Germanium Bolometer. *Journal of the Optical Society of America*, vol. 51, no. 11, November 1961.
23. Low, Frank J.; Hoffman, A. R.: The Detectivity of Cryogenic Bolometers. *Applied Optics*, vol. 2, no. 6, June 1963.

PRECEDING PAGE BLANK NOT FILMED.

70-36744

Surveyor Spacecraft Real-Time Payload Operations

Jack N. Lindsay
California Institute of Technology

Introduction

The Surveyor Project of the National Aeronautics and Space Administration was designed to explore the moon with an automated soft-landing spacecraft equipped to respond to earth commands and to transmit scientific and engineering data from the lunar surface. The objectives of the project were:

1. Accomplish successful soft landings on the moon.
2. Obtain data on the lunar surface in support of the Apollo Program.
3. Add to scientific knowledge of the moon.

The program provided for a total of seven flights. Five of the seven spacecraft launched successfully landed on the moon, and each fulfilled all objectives. The Jet Propulsion Laboratory (JPL) of the California Institute of Technology was responsible for project management and spaceflight operations; the Hughes Aircraft Company (HAC) was responsible for design and fabrication of the Surveyor. The alpha-scattering instrument was designed and developed by the Laboratory of Astrophysics and Space Research of the Enrico Fermi Institute for Nuclear Studies at the University of Chicago.

A complete discussion of each mission may be found in references 1 through 5.

Description of the Surveyor

The Surveyor spacecraft was a fully attitude-stabilized vehicle designed to receive and to execute a wide variety of earth commands as well as to perform certain automatic functions, including the critical terminal-

descent and soft-landing sequences. In the Surveyor, complexity was reduced to a minimum by placing the responsibility for mission control and decision-making on earth-based people and equipment wherever possible. In addition, the Surveyor had the capability of transmitting data from the spacecraft over a large number of different data channels. All of the subsystems in the spacecraft were made as autonomous as practicable.

The Surveyor command system represented a major change in the concept of unmanned spacecraft control. Virtually all in-flight and lunar operations were initiated from the earth, as opposed to prior practices of using automatic, preprogrammed instructions initiated by a timer or a single, direct command from the earth. Only 11 commands were sent to the earlier Ranger lunar-impact spacecraft throughout its entire 67-hour mission; Surveyor VII received some 335 commands during transit and some 150,000 commands following touchdown.

The basic elements of the spacecraft provided transportation, power, and communication services to the designated variety of payloads. The various elements of the spacecraft (figs. 1 and 2) were mounted on a tubular structure whose configuration was dictated by a tripod landing gear with three foldable legs for use in soft-landing. The remaining significant features were the center-mast-mounted solar panel and planar array high-gain antenna, two thermally-controlled equipment compartments, two boom-mounted omnidirectional antennas, and the scientific payload. This payload consisted of a television camera (on all missions), a surface sampler (on missions III and VII), and an

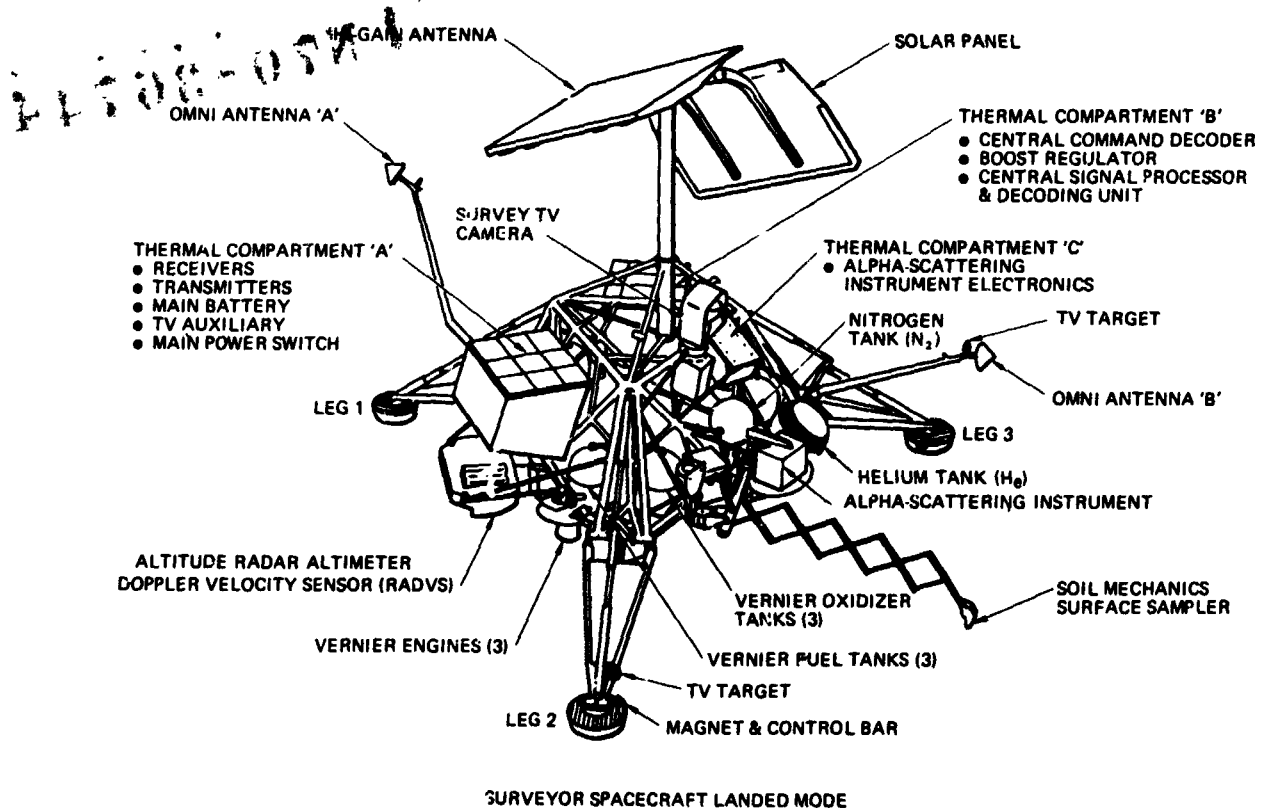


Figure 1. Principal units of Surveyor spacecraft.

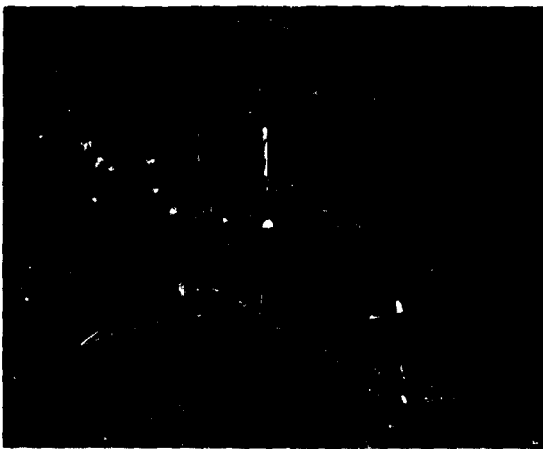


Figure 2. Surveyor spacecraft.

alpha-scattering instrument (on missions V, VI, and VII).

A continuous watch was maintained over each spacecraft, which remained within the field-of-view of at least one of the tracking stations at all times during the mission. The command link between the earth and the spacecraft was in continuous use, transmitting either real or fill-in commands every one-half second to maintain word synchronization. Approximately 200 commands were available to set the configuration or to control the function of the several subsystems in the Surveyor. From the payload operating viewpoint, the available commands provided the capability of controlling power, temperatures, telemetry configuration for data transmission, and payload operations in support of data acquisition.

At each Deep-Space Instrumentation Facility (DSIF) the spacecraft telemetry and video data transmitted from the spacecraft was recorded, displayed for internal requirements, and processed for transmission to the JPL Space Flight Operations Facility (SFOF). Approximately 260 items were available on the spacecraft as commutated data to provide information on the condition of the spacecraft subsystems. This data was available from any of seven commutator word-frame configurations (15 to 117 words per frame) at selectable bit rates of from 17.2 to 4400 bits per second. In the event telemetry data or video was not present at the SFOF because of earth transmission or processing difficulties, an analysis was available at the DSIF from the crew of the command and data-handling console (CDC) upon request.

Video data was displayed on monitors at each command and data-handling console, but only the video data received at Goldstone was transmitted by microwave to the SFOF in real-time. In addition to magnetic tape recordings of telemetry and video at each of the receiving sites and at the SFOF, high-quality 70-millimeter film recordings of each frame of video were made at Goldstone and at the SFOF as video was received.

Spacecraft command was accomplished by voice instructions to the Surveyor operations chief of the command and data-handling console, where either prepared punched tape or manual inputs could be made for the transmitter. Punched command tapes were used in a tape reader at the command and data-handling console whenever long command sequences were required that were repeated many times. Commands could be transmitted as desired at one-half-second intervals. Outgoing commands were relayed back to the SFOF for confirmation of the requested transmission.

Mission Operations System

The mission operations system was organized to carry out the project operational functions of:

1. Continuous assessment and evaluation of mission status and performance
2. Determination and implementation of appropriate command sequences required to maintain spacecraft control and to carry out desired spacecraft operations during transit and while on the lunar surface.

In addition to support for the areas of data acquisition, data processing, and communications, three groups of space flight specialists provided technical support under the space-flight operations director (SFOD) in the areas of flight-path analysis, spacecraft performance, and spacecraft science.

Flight-Path Analysis and Command Group

The flight-path analysis and command (FPAC) group handled those space flight functions that related to the location of the spacecraft. The FPAC group made specific recommendations for maneuvers and generated the specific command requirements to effect their accomplishment. Five subgroups of specialists covered trajectory, tracking data, orbit determination, maneuver analysis, and computer-support functions.

Spacecraft-Performance Analysis and Command Group

The spacecraft-performance analysis and command (SPAC) group was responsible for the operation of the spacecraft itself. The SPAC group implemented commands for all functions other than science payload. They determined response to commands, spacecraft status, and performance of the basic spacecraft. Four subgroups of specialists covered performance analysis, command preparation and control, computer support, and failure analysis.

Space-Science Analysis and Command Group

The space-science analysis and command (SSAC) group performed those functions that related to the operation of the scientific payload, television camera, surface sampler, and alpha-scattering instrument. Each instrument

was supported by a team composed of two subgroups: a performance-analysis group, who were concerned with the performance and analysis of the instrument from an engineering aspect, and a science-analysis group, who were concerned with data requirements and results from a scientific viewpoint. In addition to these instrument teams, there were specialists covering computer support, DSIF command communications, video-recording coordination, and log-keeping.

The SSAC director operated from a control station at the center rear of the science operations area and had his support specialists and instrument teams to either side and in front of him. The television team was immediately in front of the SSAC director with special video and computer data displays for performance-data analysis. Directly at the front of the science operations area were located slow-scan television monitors with cameras for rapid, hard-copy photo acquisi-

tion, the mosaicing teams for panorama mosaic construction, and a large wallboard displaying television-camera parameters. The surface sampler team were located to the SSAC director's right; to his left were the command controller and video-recording coordinator/log-keeper. The alpha-scattering team took over the television team's stations when the alpha-scattering instrument was operated because the two instruments could not send back data simultaneously.

The head of each instrument group reported analysis results and recommendations directly to the SSAC director (on a personal, verbal basis). Command requirements for utilization of each instrument were submitted on a command form (figs. 3, 4, and 5), which, after implementation, became a record of action taken.

Authority to send commands to the spacecraft rested with the space-flight operations director and was delegated to the

Time (GMT) _____ Day _____ Hour _____ Min _____ Sec
 Command Type No. _____
 Operation Sequence No. _____
 Number of Frames _____
 Estimate Time to Complete _____ Min

Transmitted to DSB _____ 11. _____ 42. _____ 51. _____ Other
 Message No. _____
 Remarks: _____

PARAMETER	PRESENT STATUS	DESIRED STATUS	COMMAND TO BE EXECUTED	COMMAND	NO. OF TIMES	COMMAND INTERVAL	SEQUENCE OF COMMANDS
Camera Power			Survey Camera Power - ON Survey Camera Power - OFF	1103 1104		40 sec to Start FM 70 sec to Start FM	* 40 sec to PWA-ON
TV Mode	200 400	200 400	EMERG Mode - ON	1107			
TV-2 Mirror Azimuth	_____	_____	Stop Mirror Right (3") 2 Stops Mirror Right (6") Stop Mirror Left (3") 2 Stops Mirror Left (6")	1115 1117 1116 1120			
TV-3 Mirror Elevation	_____	_____	Stop Mirror Down (3") Stop Mirror Up (3")	1121 1122			
TV-4 Focal Length	_____ mm	_____ mm	Set 25 mm Focal Length Set 100 mm Focal Length	1110 1111		5 sec 5 sec	
TV-5 Lens Focus Setting	Stop _____	Stop _____	Stop Focus - IN Stop Focus - OUT Multi-Stop Focus - IN Multi-Stop Focus - OUT	1123 1124 1125 1126		____ sec ____ sec	
TV-6 Lens Iris Setting	f/_____ 4 5.6 8 11 16 22	f/_____ 4 5.6 8 11 16 22	Stop Iris Open Stop Iris Closed	1113 1114		1 sec 1 sec	
TV-7 Lens Iris Servo ON/OFF	ON OFF	ON OFF	Iris Servo ON Stop Iris Open Stop Iris Closed	1112 1113 1114		5 sec 1 sec 1 sec	
TV-8 Filter Wheel	C G B R C 0" 5"	C G B R C 0" 5"	Stop Filter Position Right Stop Filter Position Left	1127 1128		2 sec 2 sec	
TV-11 Shutter Mode	Norm Open Integrate	Norm Open Integrate	Shutter - Norm Shutter - Open	1105 1106			
Start Frame			Start Frame	1100			

Figure 3. Television-camera command selection form.

SURFACE SAMPLER COMMAND SELECTION FORM	S/C RECONFIGURATION		S/C CMD	NO OF TIMES	CMD INT.(sec)	SEQ OF CMDS
	A MODE CHANGE TV 4/7 TO SS 4					
	XFER SWITCH A LOW POWER		0126			
	NBVCXO ON		0112			
	PM SUM AMP A ON		0210			
	SM/SS POWER ON (IF REQ'D)		(0131)			
	ESP COMM 4 ON (IF REQ)		(0231)			
	B MODE CHANGE SS 4 TO TV 4/7					
	ESP COMM 4 OFF (IF REQ)		(0232)			
	SM/SS OFF (IF TVID REQ'D)		(0134)			
	SUM AMPS OFF		0214			
	NBVCXO OFF		0113			
	XFER SWITCH A HI POWER		0125			
	SURVEY CAMERA START FRAME		1100			
	SM/SS KEYBOARD COMMANDS		SC CMD			
	POWER ON/EXECUTE		0131			
	SM/SS DIGITAL "1"		0132			
	SM/SS DIGITAL "0"		0133			
	POWER OFF		0134			
	AUX. HEATER CONTROL OFF		0614			
	AUX. HEATER CONTROL ON		0616			
	MAJOR SEQ'S	MINOR SEQ'S	COMMAND TAPE			
			901 STANDARD SEQ.			
			903 STOP MOTION W/O TLM			
			904 STOP MOTION W/TLM			
		907 SPECIAL BEARING TEST				
		COMMAND TAPE #902				
1047		COMMAND GLOSSARY				
	2450	OPEN SCOOP (FINE)				
	2452	CLOSE SCOOP (FINE)				
	2453	CLUTCH RELEASE (COARSE)				
	2454	ALL MOTORS OFF				
	3650	FINE TIMING MODE				
	3651	EXTEND 0.1 SEC.				
	3652	RETRACT 0.1 SEC.				
	3653	LEFT AZIMUTH 0.1 SEC.				
	3654	RIGHT AZIMUTH 0.1 SEC.				
	3655	LOWER 0.1 SEC.				
	3656	ELEVATE 0.1 SEC.				
	3750	COARSE TIMING MODE				
	3751	EXTEND 2.0 SEC.			3 SEC	
	3752	RETRACT 2.0 SEC.			3 SEC	
	3753	LEFT AZIMUTH 2.0 SEC.			3 SEC	
	3754	RIGHT AZIMUTH 2.0 SEC.			3 SEC	
	3755	LOWER 2.0 SEC.			3 SEC	
	3756				3 SEC	
REMARKS:						

Figure 4. Surface-sampler command selection form.

S/C RECONFIGURATION							
ASE 4 TO ENRG 4		COM'D	ENRG 4 TO ASE 4		COM'D		
SUMMING AMPS OFF		0214	PM PRE-SUMMING AMP ON		0207		
PM SUMMING AMP A ON		0210					
ASE 4 TO ASE SCO'S			ASE SCO'S TO ASE 4				
33Kc, 7.3Kc, 3.9Kc SCO'S OFF		0220	7.35 A/D SCO ON (1100 BPS)		0216		
ASE SCO'S TO ENRG 4			ENRG 4 TO ASE SCO'S				
SUMMING AMPS OFF		0214	33Kc, 7.35Kc, 3.9Kc SCO'S OFF		0220		
7.35 A/D SCO ON (1100 BPS)		0216	PM PRE-SUMMING AMP ON		0207		
PM SUMMING AMP A ON		0210					
MODE CHANGE *							
ASE 4 TO ASE 5		COM'D	ASE 5 TO ASE 4		COM'D		
ESP COMMUTATORS OFF		0232	AESP COMM OFF		0510		
COAST PHASE COMM ON		0506	ENGR COMM 4 ON		0231		
ASE 4 TO ASE 2			ASE 2 TO ASE 4				
ENGR COMM 2 ON		0227	ENGR COMM 4 ON		0231		
ASE 5 TO ASE 2			ASE 2 TO ASE 5				
AESP COMM OFF		0510	ESP COMMUTATORS OFF		0232		
ENGR COMM 2 ON		0227	COAST PHASE COMM ON		0506		
FUNCTION	STATUS				COMMAND TO BE EXECUTED	COM'D	SEQ OF COM'D
	PRESENT		DESIRED				
	ON	OFF	ON	OFF			
POWER					AS POWER ON	3501	
					AS POWER OFF	3502	
CALIBRATION					CALIBRATION ON	3510	
					CALIBRATION OFF	3520	
ALPHA DETECTORS	1				A1 ON	3507	
	2				A2 ON	3523	
					A1 A2 OFF	3515	
PROTON DETECTORS	1				P1 ON	3517	
	2				P2 ON	3513	
	3				P3 ON	3522	
	4				P4 ON	3511	
					P1 P2 OFF	3516	
					P3 P4 OFF	3512	
HEATERS					AS HEATER ON	3503	
					AS HEATER OFF	3504	
					COMP C ON	0136	
					COMP C OFF	0135	
DEPLOY INTERLOCKED COMMANDS					TO BACKGROUND	3505	
					TO LUNAR SURFACE	3506	
* VERIFY DECOMM LOCK AFTER EACH COMMAND.							

Figure 5. Alpha-scattering-instrument command selection form.

SSAC director as long as the scope of endeavor was within the planned sequence of events. Deviation from standard procedures or sequences required approval by the space-flight operations director. The task of briefing and directing the Surveyor operations chief was performed by the command director via voice communications under the direction of the SSAC director. Within the SSAC area, intergroup activities were primarily on a face-to-face relationship, but local intercom facilities were also used. Contact with groups outside the SSAC area was by intercom voice network.

Spacecraft Operations

The daily operations cycle started with the Goldstone view period and continued through the two DSIF view periods that followed (Australia and Spain) until Goldstone again resumed control. During the lunar operations phase, an operational plan was developed daily on the requirements for that day's efforts as an update of the prelaunch lunar operations plan. Two hours before each Goldstone rise, an operations planning meeting was held at which the operating requirements for the following period were developed. The project scientist submitted the day's requirements at this time, based upon detailed analysis (by investigator teams) of data acquired from preceding operating periods. Instrument requirements were considered in their proper perspective along with basic spacecraft housekeeping needs and data requirements from the various spacecraft subsystems. Following this meeting, the space-flight operations director and the SPAC and SSAC directors developed specific technical area plans for the three DSIF view periods that followed.

The SSAC group's detailed planning required fitting the various instrument requirements into the most efficient sequences with as much as possible of the command strings worked out ahead of time. The alpha-scattering instrument and surface sampler were relatively easy to plan for once the gen-

eral objectives were decided upon since, in most cases, operations had to be determined in real-time based upon preceding results. Although this was also true to a large extent in the case of television, many of the commands required for a series of specific pictures could be worked out ahead of time.

Television operations requiring real-time analysis support could only be conducted during Goldstone reception because video was not available to JPL from overseas stations, although it was available at any receiving station for its own viewing. Some TV was managed during overseas visibility when the efforts were routine, the requirements could be defined in detail, and the data could be acquired with limited analysis by station personnel or with support from SSAC based upon a verbal description of the overseas video reception. Since TV support was necessary to monitor the surface sampler, it could only be operated during Goldstone reception. On the other hand, since alpha-scattering data was available in the SFOF from any of the three DSIF stations, that instrument could be operated at any time instrument temperatures permitted.

Prior to each DSIF moonrise, all applicable support areas of the mission operations system confirmed their readiness to support operations by completing a standard count-down that exercised or calibrated all data-acquisition, processing, recording, and display equipment. In addition to normal preparations to receive and to process telemetry data, special precautions were taken to support TV data acquisition. Video test patterns, conforming to the last-measured spacecraft parameters, were fed through the complete video system from receiver to recording-and-display equipments. In the case of Goldstone reception, this involved the video microwave transmission system and the Surveyor television ground data-handling system (TVGDHS) with support from the SSAC video analyst to measure system performance and to assure that the system would be adequate for reception of spacecraft video.

Real-time data arrived at the SFOF via microwave (Goldstone video only), high-speed

data line, and teleprinter circuits. Video was recorded on magnetic tape and film and processed for TV monitor display by the TV ground data-handling system. Telemetry data was processed by the computer complex for display as calibrated engineering data or for performance analysis. The computer complex consisted of three strings of IBM-7040 and 7094 computers. The 7040 computer, acting as an input-output processor for telemetry data, collected data and performed preliminary processing such as data calibration, alarm monitoring, parity checking, and averaging data channels when more than one word of a channel occurred in a frame. The 7094 computer provided analysis capability. For TV-frame identification data (TVID), certain position signals were calibrated by a telemetered TV calibration reference voltage. All temperatures and TV-frame identification data were calibrated by polynomial approximations and were scaled to engineering units.

Although operation of the instrument payload was of primary importance, there were always conflicting requirements that prevented the payload from being operated much over a maximum of 80 percent of the available time under the best of conditions. Due to telemetry limitations, payload operation had to cease during times of spacecraft house-keeping functions, such as solar panel/planar array antenna repositioning (for maintaining antenna pattern alignment or battery charge rate or for providing shade), and engineering interrogation of spacecraft subsystems. This normally required 20 minutes every hour or two during which time the spacecraft telemetry system was reconfigured to sample various engineering data points at appropriate bit rates from any one of seven different commutators. Because of the high subsystem temperatures that were encountered around lunar noon, there were periods during which either no instrument operations were possible or they were, at best, severely restricted. There were times under these conditions when a few high-sun TV pictures were important enough to spend up to 5 minutes for two or three pictures and then to shut the camera down for 60 minutes while it dissipated the internal heat build-up.

Since instrument capabilities and requirements varied daily, as a function of sun position, spacecraft shadows, and thermal constraints, ability to predict changing conditions was important in developing requirements. Once the attitude and orientation of the spacecraft was established after landing, computer plots of spacecraft shadows became available and were valuable aids in predicting instrument temperatures and viewable areas under or near the spacecraft. The project scientist and the principal investigators were supported by investigator teams whose function, during the mission, was to analyze data in near-real-time and to submit requirements for the subsequent operating period. Working groups of these investigator teams had a full-scale spacecraft mockup with an operable TV camera from which situation estimates could be made on shadows and view factors as a function of sun position. This visual aid became a valuable supplement to the shadow plots and lunar TV pictures in supporting the analysis of results and the generation of requirements for subsequent operating periods.

Television-Camera Operations

Television-camera operations included command and data acquisition and both data display and analysis.

Command and Data Acquisition

The television camera was mounted at a height of approximately 65 inches so that it gave the best view of the surrounding lunar surface. It was also mounted at a tilt of 16 degrees in order to improve the viewability of the nearest footpads and the area to be worked on by the surface sampler and alpha-scattering instruments. It used a vidicon imaging system with a rotating, tilting mirror that permitted viewing the surrounding surface through a full 360 degrees of azimuth and up to 50 degrees in elevation above the plane normal to the vertical axis of the camera (figures 6 and 7).

The camera was equipped with a variable-focal-length lens (imaging either a 6-degree or 25-degree field-of-view), a variable

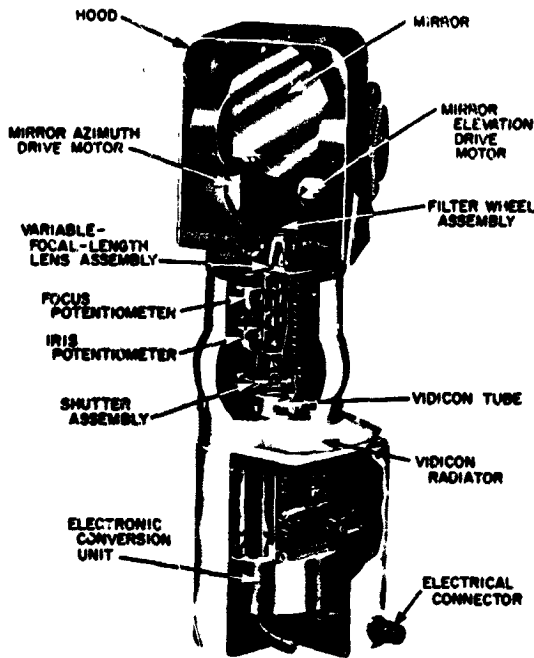


Figure 6. Television camera, cutaway view.

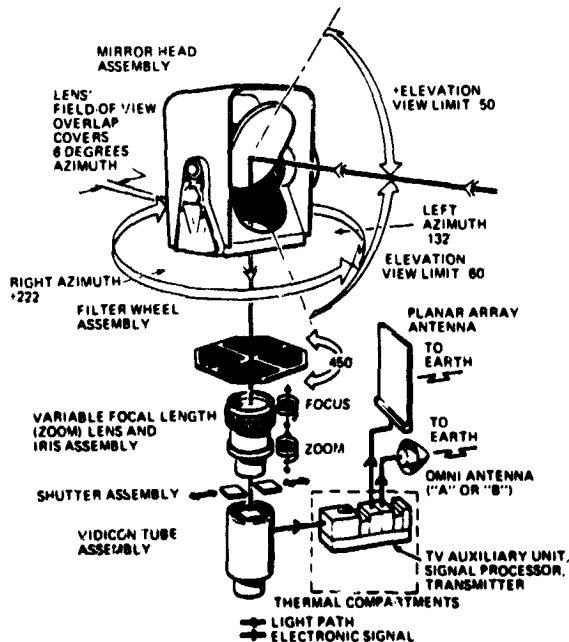


Figure 7. Television camera, functional exploded view.

lens aperture that could be used in an automatic mode or could be set from $f/4$ to $f/22$ in ten steps, a four-position filter wheel that had three colored filters and one polarizing filter, focus control from 4 feet to infinity in 50 steps, and a focal-plane shutter that could be set for a normal 0.15-second exposure or could be left open for any desired period of time for timed exposures. The camera was able to accommodate luminance levels from approximately 0.008 to 2600 foot-lamberts. The resolution capability was approximately 1-millimeter at 4 meters. The light-sensing system used to provide automatic aperture control was also used to inhibit shutter operation when excess light intensity was present. Each picture, or frame, was imaged through the optical system onto the vidicon sensor, which could be read out in either a 200-line or 600-line mode. The 200-line mode was a low-power backup option; the 600-line mode was a 220-kilohertz-bandwidth normal mode requiring high power and the planar array high-gain antenna.

There were 25 camera commands available to control the various camera functions of power, mirror stepping, focal length, focus, iris, filter, shutter mode, and shutter actuation. In the 600-line mode, the vidicon was scanned every 1.2 seconds. When a frame of video was commanded, video readout of the vidicon occurred during the scanning cycle following shuttered vidicon exposure. Each frame required one second for readout with the following 0.2 second being used to transmit pulse code modulated (PCM) data of the TV-frame identification data. The TVID contained 15 camera parameters defining the status of the camera and the optical system. The two vidicon scans that followed were used to complete the erasure of the vidicon image so that the minimum picture cycle was 3.6 seconds. The maximum picture rate used in practice was a frame about every 5 seconds, which was a more comfortable and practical rate for data consumption and provided enough free time so that synchronization of shutter actuation commands with the free-running vidicon-erasure cycles was no problem.

In addition to the constraint on frame rate, there were also constraints on other functional commands to various camera response requirements. For instance, no commands could be sent for a period of 5 seconds after a focal-length change was commanded; an iris change required a period of 1 second; a filter change required 1.5 seconds; etc. Command requirements were implemented at the DSIF stations in accordance with voice instructions from the SFOF, either by manual keyboard entry or by means of prepared punched tape.

A full panoramic survey of narrow-angle pictures required approximately 1000 pictures; a complete wide-angle survey required 120 pictures; and a particular collection of ten special-interest groups of pictures of the spacecraft and its areas of contact with the surface required about 130 pictures. Tapes of this type were developed before a mission; others that were dependent upon the surrounding surface features were assembled after landing. Running such a tape required that operation of the camera be initiated ahead of tape start by manual commands so that camera configuration agreed with the starting requirements of the tape for azimuth, elevation, focus, focal length, and an iris setting suitable for the brightness. If the sun was near the horizon, suitable avoidance action had to be taken to skip both the tape and the camera past that area in order to eliminate any possibility of burning the vidicon in the event of failure of the shutter inhibit.

The assembly of strings of commands and generation of the tapes was done by computer. Tape length was limited to approximately 2000 commands, which was the number required to obtain 200 frames at 5-second intervals with a 1/2-second command rate. The 1000-picture, 360-degree, narrow-angle survey required five tapes, each suitable only for its segment of azimuth. Since the camera was tilted by mounting design as well as by the nature of the surface upon which the spacecraft rested, every different azimuth presented a different profile of slope relative to the vertical axis of the camera. Distance to the surface and the location of the horizon, as

a function of elevation, changed with camera azimuth (as did picture rotation within a frame). Although command tapes prepared before launch were designed to provide for a vertical spacecraft and a flat lunar surface, the small deviations encountered were accommodated by biasing focus settings from nominal.

Each of the five narrow-angle, 2000-command, survey tapes contained approximately 200 shutter commands, 450 mirror-stepping commands, and 120 focus commands, with the remaining commands being fill-ins to provide proper camera-response timing. The five tapes, run in succession, provided the 1000 panoramic survey pictures in about 1 1/2 hours of camera running time. The survey to provide the same coverage in wide-angle consisted of 120 pictures and took about 10 minutes. Reference charts that were used in controlling tape operation for two of the sequences are shown in figures 8 and 9.

Data Display and Analysis

The TV camera data that was available to the television team in the SSAC area was displayed in the following manner.

1. One slow-scan video TV monitor for viewing of the image as it was received
2. Three oscilloscope displays of video waveform for analysis of video circuit-performance and camera focus and exposure
3. Computer printout of all camera parameters received after each frame of video
4. Analog strip-chart recordings of various camera parameters
5. A volatile wallboard display of all camera parameters for the last picture received (fig. 10)
6. TV monitor display of camera parameters using computer graphic techniques
7. A polaroid camera providing pictures from a slow-scan monitor on an "as required" basis
8. Two automatic "paper cameras," which exposed sensitized paper directly from

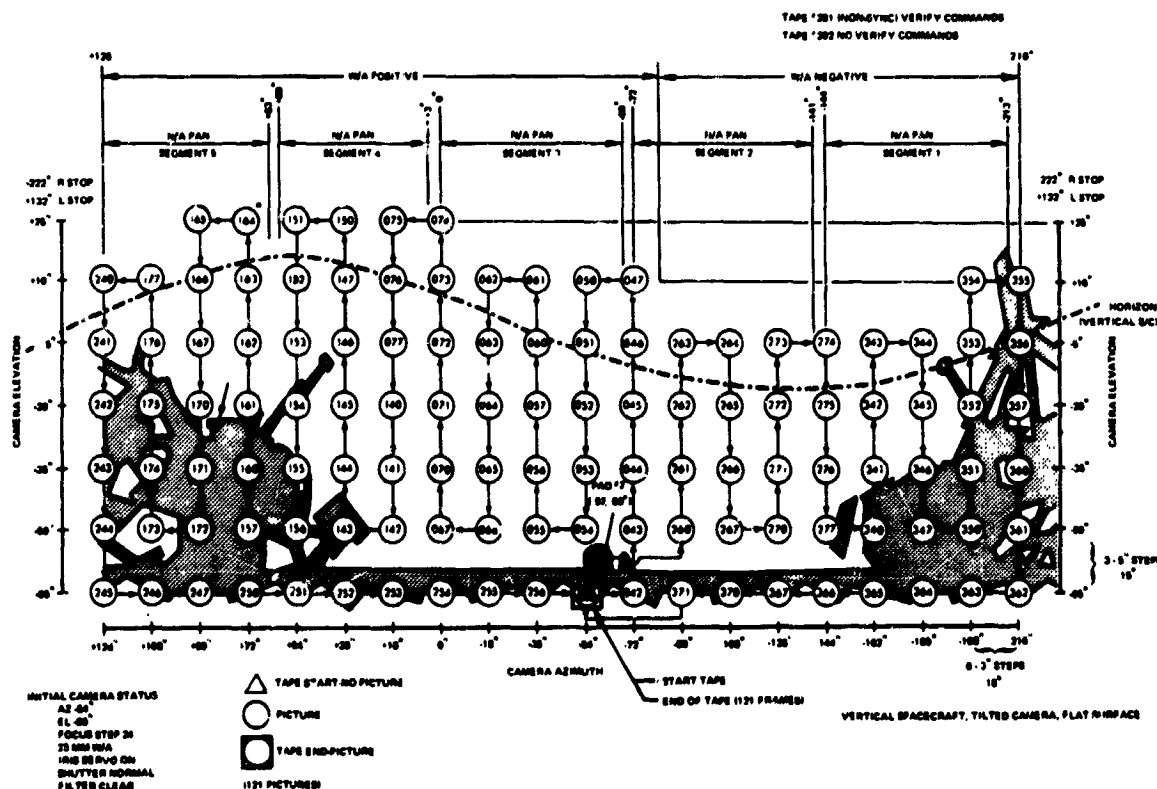


Figure 8. Wide-angle (360-degree) command tape chart.

negative images on slow-scan monitors and provided quick pictures (within 15 seconds) for real-time mosaic generation (fig. 11)

9. Scan-converted, closed-circuit, RETMA TV display for general viewing of last received image (continuously refreshed image from storage tube)

10. Closed-circuit TV display of teletype listings of transmitted commands.

The television-performance analysis group was responsible for camera control and performance analysis of the video and electromechanical systems of the camera. The camera video sync and sweep circuitry performance as well as the video communications system performance from Goldstone were monitored by the video analyst with his display of oscilloscope video waveforms and imagery from a slow-scan monitor. The electromechanical analyst was able to monitor the camera response to commands from the display of the TV-frame identification data,

which was printed or plotted after each frame of video. His knowing the sequence of commands permitted the analyst to spot-check critical parameters and to confirm that the camera was responding as commanded.

Analysis of the picture content in order to ascertain that quality was satisfactory and that objectives were being met was the responsibility of the television-science analysis group. The photo analyst monitored each picture and an oscilloscope display of the waveform from which he could determine that exposure and focus were satisfactory. In the event a change was indicated, the survey would be stopped; changes would be made in focus or iris settings; and the survey would then continue. In order to obtain an early evaluation of the overall results of multi-picture surveys, panoramic mosaics were constructed in near-real-time; i.e., as soon as pictures were available from the paper camera. Without trying to match image

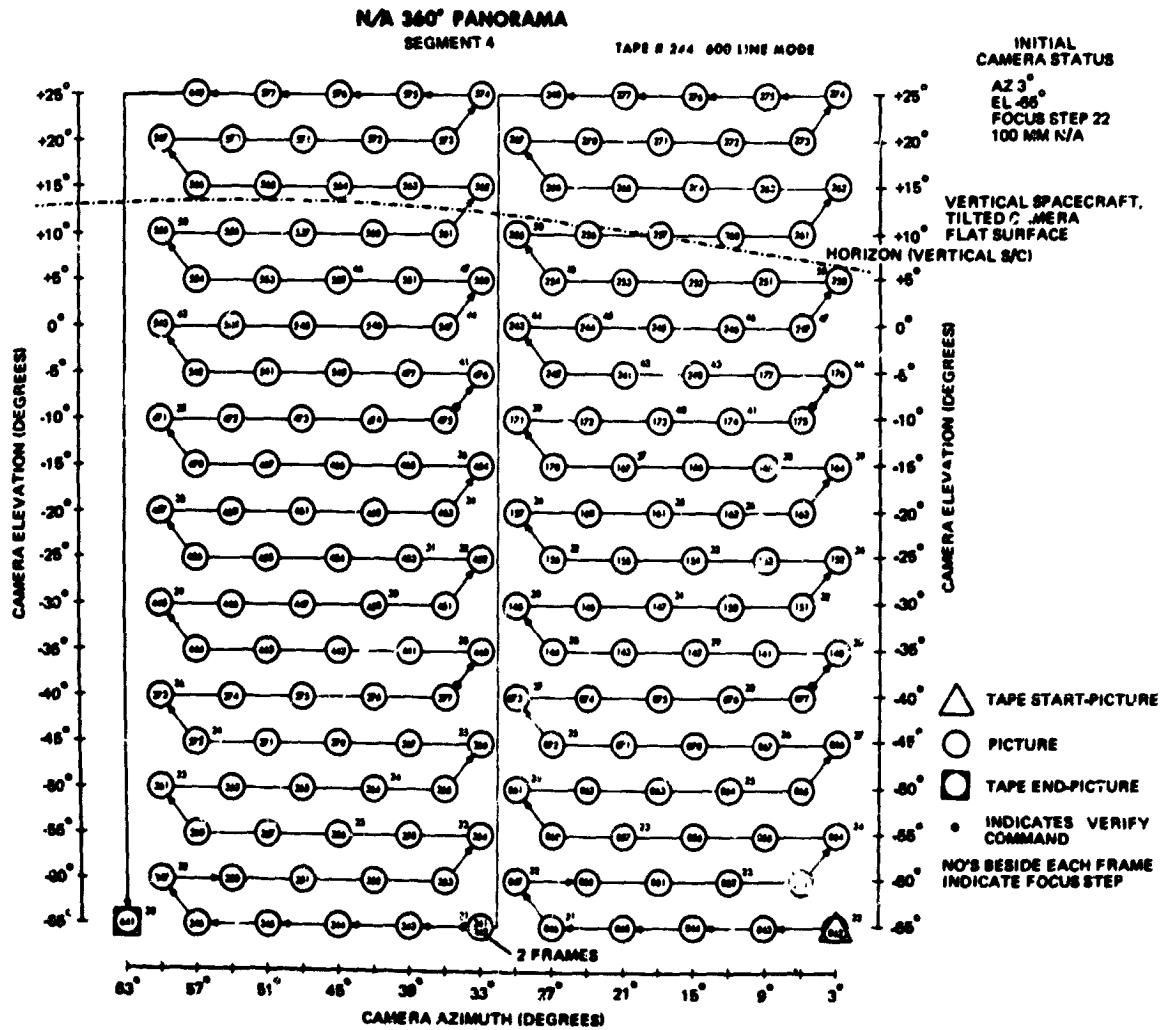


Figure 9. Narrow-angle-segment command tape chart.

content, rough trimmed pictures were stapled to prepare grids by mosaic teams in the order received. The mosaic team, knowing the planned sequence of picture taking and with the help of an azimuth/elevation tab on each picture, made a complete mosaic available in a very few minutes after the last picture of a sequence had been taken (fig. 12). Improved mosaics were made later in non-real-time, as shown in figure 13, which illustrates the effect of camera tilt.

During the five missions, the TV camera sent back approximately 88,000 frames of video in response to approximately 600,000 camera commands. The majority of the

pictures were obtained from lunar surface panoramas at various solar angles to satisfy topography requirements, viewing of the spacecraft and its effect on the lunar surface, and color (fig. 14) or polarimetric surveys. In addition, special pictures were also obtained of the following:

- Earth through colored and polarized filters
- Sun eclipsed by earth
- Solar corona after sunset
- Surface pictures after sunset, by earthshine

- Viewing of planets, stars, and laser beams from earth.

Command and Data Acquisition

Surface-Sampler Operations

The surface-sampler operations included command and data acquisition and both data display and analysis.

The surface-sampler instrument was a soil-manipulative device that consisted of a scoop on the end of a pivoted, lazy-tongs arm. It had four motors to control extension, azimuth, and elevation of the scoop as well as position of a scoop door. This provided the

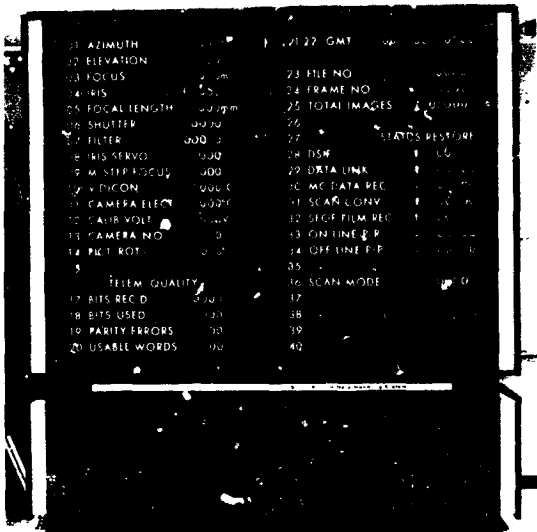


Figure 10. TV-frame identification data (TVID) wallboard display.

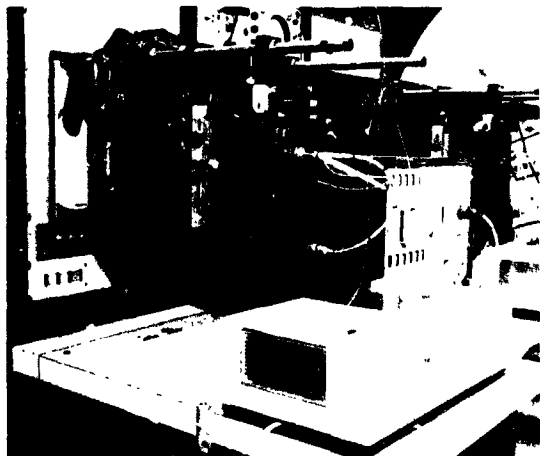


Figure 11. "Paper cameras" for real-time mosaics.

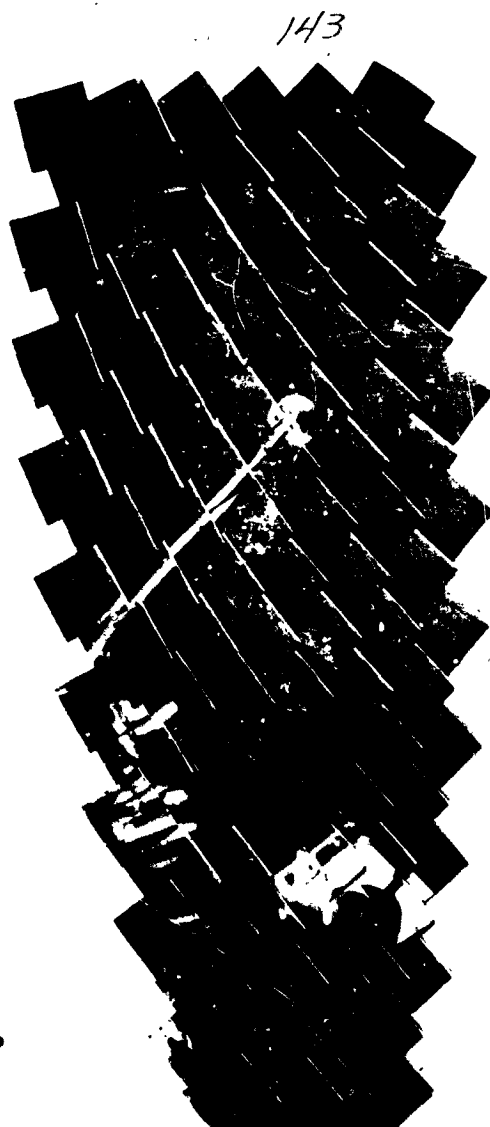


Figure 12. Narrow-angle (36-degree) real-time rough mosaic.



Figure 13. Wide-angle (360-degree) improved mosaic.



Figure 14. Surveyor III, pad 2.

capability of reaching the surface through an arc of 112 degrees at a radius of from 23 to 58 inches. A mosaic of the working area is shown in figure 15. The instrument was able to dig, scratch, push, pull, grasp at, and trench the lunar surface. There was no position, force, or acceleration instrumentation

provided for the mechanism. There were only telemetry readings of motor current, temperatures, and voltages; hence, all operations had to be carried out by visually monitoring the results with the television camera and by interpreting the telemetry measurements.

Because installation of the instrument on the spacecraft was a late adaptation to an interface previously provided for an approach television camera, only four usable commands existed to provide for 19 deployment and control functions. A unique approach was employed to enable the generation of the necessary commands although it did complicate commanding procedures; i.e., several spacecraft commands were required for each function. An instrument auxiliary was used that provided a four-element shift register and a 16-command decoding matrix. Each function thus required four commands, representing either a digital "1" or a digital "0," to generate a unique combination for the command decoder, a fifth command to initiate execution, and a sixth command to clear the shift register for subsequent use. The four spacecraft commands provided power on/execute, digital one, digital zero/reset, and power off. To facilitate transmission of all the spacecraft commands required to accomplish the operating functions, punched command tapes were used; they consisted of a series of prepared sequences selected in accordance with real-time requirements. The motors were operated by timed pulses of either 0.1 or 2.0 seconds duration; thus, the scoop was positioned in a series of short steps, with a fine or coarse step for each execute of whichever command logic was present in the register. Pictures of the surface sampler could not be taken while the sampler was operating; therefore, the mechanism was moved and then photographed to determine the results. With the television camera on during all sampler operations, the TV-frame identification data had to be inhibited whenever the surface sampler was on in order to prevent the television commutated telemetry from interfering with the surface-sampler telemetry. Whenever the camera parameters had to be identified, the surface sampler was turned off.

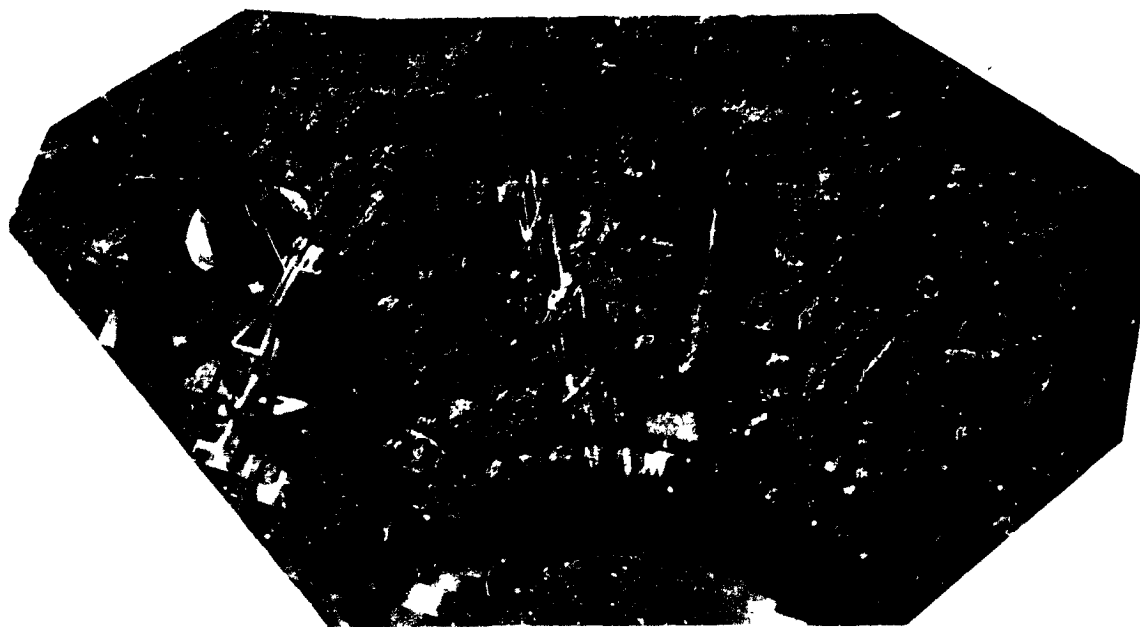


Figure 15. Working area mosaic of surface sampler on Surveyor VII.

Data Display and Analysis

Telemetry data on motor current, temperatures, supply voltages, and the command register status (seven channels) were displayed on a strip-chart recorder and a printer. This data was monitored by the surface-sampler performance analyst and provided sufficient information to indicate the ability of the instrument to support its operation. Although the various motor torques had been calibrated as a function of current, temperature, and voltage for purposes of determining applied forces for post-mission data reduction, this information had little value in support of operations although motor current telemetry did provide information about a stalled motor condition, beyond which no further motion could be expected.

Evaluation of performance and results was based upon an analysis of TV pictures. Since pictures were taken at relatively long intervals of time, polaroid photographs were provided to the surface-sampler science analyst after each series of commands.

Subsequent command requirements were then determined, and operations were carried out on a step-by-step basis.

During the two missions carrying the surface-sampler, the instrument was operated for 55 hours. There were some 19,000 spacecraft commands sent to perform 6000 sampler functions.

The more obvious results of these efforts led to the observation that the lunar soil appears to be fine-grained, irregular in depth, and relatively shallow, ranging in the areas tested from depths of less than 2.5 centimeters to a depth of at least more than 15 centimeters, where substantial rock fragments were encountered. Evaluation of the data also provided estimates of the soil cohesion, angle of friction, bearing capacity, strength, and density.

Alpha-Scattering Operations

The alpha-scattering operations included command and data acquisition and both data display and analysis.

Command and Data Acquisition

The sensor head for the alpha-scattering instrument was a cube, 6 inches on each side, that was deployed to the lunar surface on a nylon cord, under its own weight, when it was released (fig. 16). It contained six source capsules of alpha-emitting curium-242, two detectors measuring scattered alpha particles from the surface and four detectors measuring protons from alpha-proton nuclear reactions in some of the lighter surface elements. The outputs from each set of detectors were fed to separate 128-channel pulse-height analyzers to generate two data streams of the total alpha and proton events. Digital outputs representing the energy level of detected events were multiplexed in a combined telemetry channel with the engineering measurements of the instrument. This was a relatively simple device to operate, requiring only that its various capabilities be turned on



L 305. ID # 0344. GMT. 255-00-39-53.
 DIGITIZED #1.
 FILTERED 15X15. MM=3. TAPE # 5021.
 24 SEPT 1967.

Figure 16. Alpha-scattering instrument.

or off, in accordance with a preliminary analysis of data, to confirm that the detectors were working satisfactorily.

The instrument had 19 commands to control power, heaters, deployment, and calibration and to turn the detectors on or off. Because the number of commands required at any one time were very few, all commands were transmitted by manual keyboard from the DSIF as directed from the SSAC area.

The science and engineering data were multiplexed for simultaneous transmission to earth. The science data consisted of the combined output of the two alpha detectors plus the combined output of the four proton detectors. The engineering data consisted of seven measurements to monitor instrument voltages, temperatures, and detector configuration.

For purposes of monitoring the experiment in real-time, the signal was separated at the DSIF station into the two science data streams of alpha and proton data plus the engineering parameters. The science data streams were input to a computer at the DSIF station. The computer established synchronization of the data words and assembled within its memory four spectra of 128 channels each. Two of these four were alpha spectra, one parity-correct and one parity-incorrect, and two were proton spectra, one parity-correct and one parity-incorrect. Spectra of the data were accumulated at the tracking site in any length duration (nominally 40 minutes) within the computer storage capability during spacecraft data transmission. Following a period of accumulation, during which the only analysis possible was the verification that data was being received, the data was dumped in the format of a teletype message for transmission to the SFOF, and a new accumulation was started. Control of the DSIF computer accumulations and spectra transmission was by voice direction from SSAC to the DSIF station.

Prior to deployment, with the instrument still in its stowed position, the alpha-scattering instrument was turned on to obtain a spectrum of a standard sample of known

composition, which was part of the supporting platform. The data satisfactorily confirmed that the instrument was capable of providing analyses in the lunar environment. The instrument was then deployed to the surface in two stages. The first command released the support platform and permitted the instrument to swing free on its nylon cord about 22 inches above the surface from whence reference spectra were obtained of the background radiation. The second deployment command freed the alpha-scattering instrument to descend to the surface under its own weight. There was no telemetry data to indicate satisfactory deployment; therefore, this was determined by TV pictures. A minimum of 25 operating hours of data collection with all detectors operating properly on the surface was the objective for each sample spectrum. Periodically during data accumulation, the instrument performance was calibrated by turning on an electronic pulser and accumulating its data for 2 minutes.

Operation was rather straightforward and was complicated only by the competition for time from the other operational requirements and by the difficulty of maintaining temperatures below the critical operating and survival limits. Surveyors V and VI landed in equatorial regions, and the solar panel and planar array were very effective in providing shade. Surveyor VII landed in a southerly latitude, and this shading was not possible; hence, the data collection was severely limited around lunar noon.

Surveyor VII was the only spacecraft that had all three of the payload instruments aboard at the same time. Both the surface sampler and the TV camera were used very effectively in assisting the alpha-scattering instrument to attain its objectives. Because of a jamming in the nylon-cord release system, the alpha-scattering instrument had to be forced to the surface by a downward force from the surface-sampler scoop. During periods of high temperature, the shadow of the surface-sampler scoop was positioned over the sensor head to provide some shade. After sufficient data collection had been obtained

from the first surface sample, the surface-sampler scoop was able to pick up the sensor head and to redeploy it to a second and then to a third position.

Data Display and Analysis

In addition to the compressed-spectra teletype display of the data as it was received from the DSIF stations, there were seven channels of engineering telemetry related to the instrument performance that were continuously being updated and displayed during reception of data from the spacecraft. These monitored supply voltages, temperatures, and detector ON status.

Since there was no need to determine the chemical analysis of the surface samples in real-time, the only requirement in addition to recording sufficient data was to ascertain that the recorded data represented reliable detector output. If a detector were to become faulty, any accumulation from that group of detectors would be useless because the outputs from two alpha detectors and the four proton detectors were summed into their respective data streams. Gross anomalies could be observed in the teleprinter listing, but subtle discrepancies could be detected only by a more thorough analysis of accumulations and calibration data. This was accomplished at the SFOF by a computer program that made a preliminary spectrum analysis for the purpose of confirming instrument performance. As the raw spectra were received at the SFOF, they were fed to a computer for analysis. If unreliable data were noted, it was necessary to isolate the faulty detector. This was done by cycling through the detectors, determining which isolated data were faulty, and turning off the appropriate detector.

The alpha-scattering instrument operated on three missions for a total of 248 hours of data collection in analyzing the material of six different samples. Results from these measurements permitted an estimate of the atomic percent of these elements: carbon, oxygen, sodium, magnesium, aluminum, silicon, a calcium group, and an iron group.

The analysis indicates that the material resembles basaltic rocks of the earth. The results of Surveyors V and VI show that the chemical composition of the two Mare landing sites was essentially the same although, in the Surveyor VII highland region, a lesser amount of the iron group of elements (on the order of a factor of two) was indicated.

Training

Training in preparation for participation in television payload operations took place over a period of approximately 15 months prior to the first mission. Training on surface-sampler and alpha-scattering instruments was conducted between subsequent missions after plans to include these instruments were made firm. Development of the capability within SSAC to operate the payload consisted of three broad categories of effort:

1. Development of techniques and procedures using a laboratory type of simulation of the instrument and data-processing
2. Application of operating procedures to command and data acquisition system for mission operations by using a fully simulated data source but excluding the operational group interface not directly involved in data acquisition or data analysis
3. Participation in complete dress rehearsals involving all operational interfaces of the mission control system.

During this period, detailed operating procedures and sequences of events were developed and documented. Training was conducted by commanding the simulated instruments and by analyzing the displayed data in an environment simulating that expected during the mission. Development of the simulation system and training progressed simultaneously although earlier development of simulation would have permitted a greatly reduced training effort. Training of the various supporting-element personnel and the development of their systems (such as the TV ground data-handling system, the command and data-handling console, data-processing, and communications) evolved, in part, as a result of their support for SSAC training.

The final simulation capability consisted of an operable camera mounted on a space-frame mockup at the JPL with a system capable of commanding the camera through the Goldstone command and data-handling console. The video and computer-simulated, commutated, TV-frame identification data were transmitted to Goldstone, and the data was processed through the mission support system all the way from the antenna to the final display.

For Surveyor III, an operating surface sampler was added to the mockup. The addition of the alpha-scattering capability for Surveyor V required bringing the remote laboratory data from its vacuum-chamber environment to the system via a dataphone link and simulating its engineering data by computer. Training of overseas CDC crews for participation in payload data acquisition was done through the use of simulated data recording.

Although the final system provided a reasonable simulation of real-time data response, it was a complex and difficult system and produced, on its own, most of the problems one might expect to encounter in a mission. Operating the Surveyor on the moon turned out to be quite easy in comparison to operating the simulated system.

Conclusions

The data returned by Surveyor has provided significant information about the surface of the moon, not only from the instruments described but also from an analysis of the behavior of various operational subsystems of the spacecraft. The operational control procedures described have proved very effective in acquiring a large amount of data from the surface of the moon over relatively short periods of available time. Optimum results with rapid response were obtained from a complex set of data sensors on a vehicle some 230,000 miles away. The availability of a highly flexible spacecraft system teamed with man in the real-time data-analysis and decision loop provided an exploratory ability that was capable of

achieving mission objectives. The success of this program demonstrates the achievements possible in scientific exploration of space by using unmanned, instrumented spacecraft.

References

1. Technical Report 32-1023. Surveyor I Mission Report - Part I: Mission Description and Performance; Part II: Scientific Data and Results; Part III: Television Data, Jet Propulsion Laboratory, Pasadena, California, 1966.
2. Technical Report 32-1177. Surveyor III Mission Report - Parts I, II, and III, as above, Jet Propulsion Laboratory, 1967.
3. Technical Report 32-1246. Surveyor V Mission Report - Parts I, II, and III, as above, Jet Propulsion Laboratory, 1967.
4. Technical Report 32-1262. Surveyor VI Mission Report - Parts I, II, and III, as above, Jet Propulsion Laboratory, in publication.
5. Technical Report 32-1264. Surveyor VII Mission Report - Parts I, II, and III, as above, Jet Propulsion Laboratory, in publication.

PRECEDING PAGE BLANK NOT FILMED.

1 N70-36745

Orbiting Astronomical Observatory Mission Operations

H. Robert Lynn

NASA Goddard Space Flight Center

Introduction

Mission operations involves all aspects of in-orbit operation and is particularly directed to meeting mission objectives efficiently. Much preparation is required to accomplish these objectives. A ground system must be developed, mission plans completed, and testing and training conducted to integrate all aspects of mission operations into a unified system.

Mission planning and ground system design are iterative processes. Mission plans generate ground system requirements for which a design is engineered; likewise, the ground system design discloses capabilities and difficulties that require new mission plans. The mission planner would continue this iterative process indefinitely if the various system designs were not finally frozen. Throughout development of the system, requirements change as system capabilities, operational timing, and priorities become clear. There are always worthwhile improvements to be made, and there are always risks in flying the "present system." Management of the mission operations system involves many difficult decisions based upon calculation of the risk, assessment of the capability of the system to cope with the risk, and the resources available to eliminate the risk.

Within the Goddard Space Flight Center, the talents of people from varied disciplines have been pooled together under the mission operations manager to accelerate the iterative procedures of mission planning and ground-system design. To complete the mission preparation, the ground system must be extensively tested with actual spacecraft data;

in addition, exercises and simulations must be conducted in order to train personnel and to verify operations procedures in a realistic environment.

Spacecraft Description

The Orbiting Astronomical Observatory (OAO), figure 1, weighs 4400 pounds; it is 10 feet high and 21 feet wide with the solar paddles deployed. The solar array can produce 1200 watts of peak power and can sustain an average orbital load of 550 watts. The normal operating load is approximately 420 watts. The spacecraft is three-axis stabilized and is in a 480-statute-mile, circular orbit, having an inclination of 35 degrees.

The stabilization and control system includes:

1. Six gimballed star trackers that provide a coarse pointing accuracy of ± 30 arc seconds
2. One boresight star tracker with a pointing accuracy of ± 5 arc seconds
3. Rate and position gyros for backup control with a drift rate of 0.1 to 0.2 degree per hour
4. Inertia wheels for slewing and attitude control
5. A magnetic unloading system for the inertia wheels
6. Gas jets for attitude control and for unloading the wheels.

The spacecraft communication system is fully redundant (fig. 2) and consists of two wideband telemetry transmitters, two narrowband transmitters, two radio tracking beacons, and quad-redundant command receivers. The wideband link is used primarily

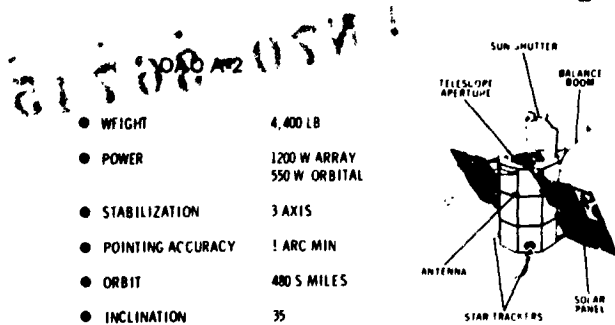


Figure 1. OAO A-2 configuration and performance characteristics.

to transmit scientific data from data storage at a rate of 50,000 bits per second, spacecraft data from the tape recorder at 67,000 bits per second, and command-memory dumps at 50,000 bits per second. The narrowband link is used to transmit spacecraft status data at 1042 bits per second.

The PCM command system operates at 1042 bits per second and uses two 32-bit words and their complements for each command. The complement command words are used by the spacecraft for error detection. Command verification is provided to the ground via the narrowband telemetry link.

A total of 256 commands with their designated execution time can be stored in randomly addressable locations in the command memory. These commands are automatically executed in sequence from the memory at the designated time. There are actually 229 different commands that can be sent to the spacecraft. These are categorized as: *control commands* either to turn equipment on and off or to select modes of operation; *data-handling commands* to establish the way status data is sampled, stored, and transmitted; *gimbal angle commands* to point the star trackers; *attitude commands* to slew the spacecraft by using the inertia wheels; *address transfer commands* to change the sequence of command memory execution; and *experiment commands* to select the mode and sequence of experiment operations.

The onboard data-handling system provides 264 8-bit analog words and 288 bilevel bits of spacecraft status data. It also provides

S/C COMMUNICATION

- WIDEBAND LINK - TWO REDUNDANT TX.
 - MODULATION - FM
 - FREQUENCY 400 MHZ BAND
 - NOMINAL PWR - 8 WATTS
 - TYPE DATA - VIDEO - (FM)
 - DIGITAL (PCM/FSK)
 - a. 1042 bps
 - d. 50 kbps
 - c. 67 kbps
- NARROWBAND LINK - TWO REDUNDANT TX.
 - MODULATION - PCM/S or PM
 - NOMINAL PWR - 1 WATT
 - FREQUENCY 136 MHZ BAND
 - TYPE DATA - DIGITAL @ 1042 bps
- BEACONS - TWO REDUNDANT TX.
 - MODULATION - NONE
 - NOMINAL PWR. - 100 MW
 - FREQUENCY 136 MHZ BAND
- COMMAND LINK
 - MODULATION - PCM/FSK/AM
 - FREQUENCY - 148 MHZ BAND
 - COMMAND BIT RATE - 1042 bps

Figure 2. Fully redundant, spacecraft communication system.

30 analog and 200 bilevel bits in the experiment data-handling equipment. Spacecraft data and experiment data are simultaneously generated on board the observatory at 1042 bits per second. Both types of data can be selectively loaded in a core storage device that can store 8192 25-bit words with nondestructive readout rates of either 1042 bits per second or 50,000 bits per second. The spacecraft data are continuously recorded on a tape recorder having a 12-hour capacity. This recorder plays back at a 64:1 speedup ratio, or 67,000 bits per second.

The Wisconsin Experiment Package consists of seven telescopes operating in the ultraviolet region. Four stellar photometers, each spanning 1000 angstroms in 250-angstrom steps with selectable 2-minute and 10-minute apertures, cover the region from 1000 to 4000 angstroms with considerable overlap. One scanning spectrometer covers the spectrum from 1000 to 2000 angstroms in 10-angstrom steps. Another scanning spectrometer covers from 2000 to 4000 angstroms in 20-angstrom steps. A nebular photometer covers from 1500 to 3800 angstroms in 600-angstrom steps. Gain, filter, and exposure

of each instrument may be individually controlled along with data sampling rates and selection of digital or analog readouts.

The Smithsonian Experiment Package (Telescope) consists of four ultraviolet cameras (Uvicons), each with a 2-degree field-of-view and operating at 1200 to 1600 angstroms, 1300 to 1600 angstroms, 1600 to 2900 angstroms, and 2300 to 2900 angstroms, respectively. Control is provided for exposure time and selection of digital or analog readouts.

Observatory Operations

The OAO is operated by pointing the optical axis at a designated point in the sky, conducting a planned series of observations, and recovering the data. Throughout this process, the power system of the spacecraft must maintain an acceptable state of charge, and the thermal system must maintain proper balance. Both of these considerations are greatly aided by maintaining optimum roll, which means that the spacecraft is rolled about the optical axis into a position where maximum power is received by the fixed solar arrays. At this attitude, the sun's rays strike the solar paddles at the most direct angle possible for the designated pointing. There is an optimum roll that provides maximum power for every pointing.

The actual angle of incidence of sunlight on the solar arrays is measured in terms of the angle β between the minus optical axis and the sunline. As shown in figure 3, the optical axis makes a 33-degree angle with the solar paddles. As β increases from zero to 57 degrees, the power increases to a maximum. From 57 to 90 degrees, the power decreases and would continue to decrease above 90 degrees on the side of the paddles called the "A side." Since solar cells are located equally on both the A and B sides of the paddles, the spacecraft can be rotated 180 degrees about the optical axis and operated with the B side exposed. As β is increased from 90 degrees to 123 degrees, power again increases to a maximum. Above 123 degrees, the power once again begins to decrease. It should be

noted that the sun shade protects the experiment from direct solar-light impingement for β greater than 90 degrees on the B side. Figure 4 shows that any given β angle represents a locus of possible pointings in the sky and that β -angle restrictions exist in accordance with corresponding power considerations and solar impingement on the experiment.

Gimballed star-tracker control is the primary method for slewing the spacecraft

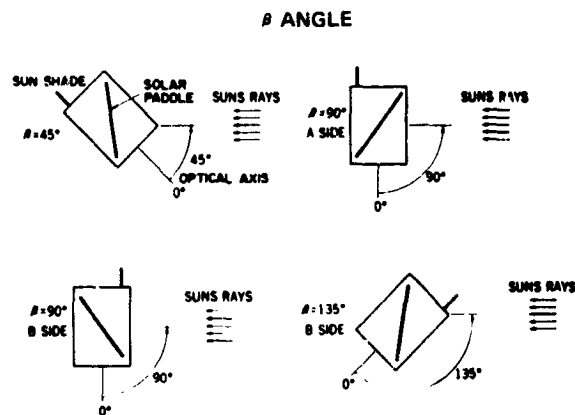


Figure 3. Actual angle of incidence of sunlight on solar arrays; measured in terms of β angle between minus optical axis and sunline.

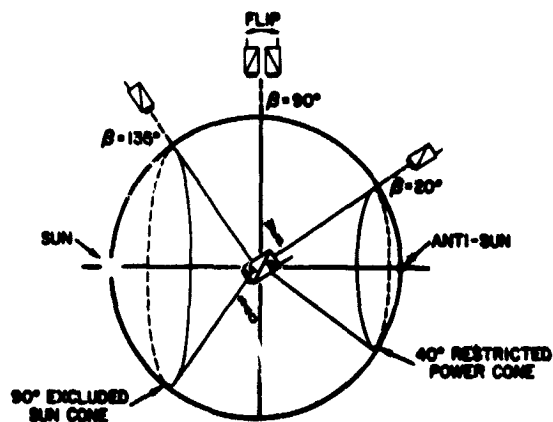


Figure 4. Celestial viewing boundaries.

and maintaining pointing. The six star trackers each have two gimbals (an inner one and an outer one) allowing two degrees-of-freedom with ± 43 degrees of movement in both axes. The trackers can be operated in either the command mode or track mode. When in the command mode, a tracker points at its commanded angles; when in the track mode, it tracks a star and produces an error signal for both gimbals by comparing the actual angles to the commanded angles, which are always present in the tracker logic. The six trackers produce 12 gimbal-angle errors, two from each tracker, which are resolved into six error signals for each of the three spacecraft axes: roll, pitch, and yaw. These errors are averaged and applied to the inertia wheels. The spacecraft can maintain its attitude as long as it has unobstructed stars assigned; however, as the spacecraft revolves about the earth, the guide stars are occulted by the earth (fig. 5). When this happens, other trackers must be assigned. These assignments are made from the command memory of the spacecraft.

The command memory is the heart of the spacecraft. While all operations can be done in real-time from the ground, almost all pointing and slewing are done from memory. (The Wisconsin Experiment is normally operated from memory.) The 256-command capacity of the memory is divided into two halves, and a "ping-pong" technique is used for loading and operating the memory; that is, while one-half of the memory is operating, the opportunity is taken to load the other half. Each half of the memory that is loaded has a "coast-hold" series at the end that will maintain the spacecraft in a safe attitude as long as possible in case the other half of the memory is not loaded in time to take over operating from the first.

Also located in the memory are two series of emergency commands that the spacecraft automatically switches to if the stellar reference is lost or if the batteries go into an undervoltage condition. The command memory is loaded at a rate of 1042 bits per second and can be dumped at 50,000 bits per second for verification on the ground.

There are certain constraints under which the spacecraft must be operated. For example, the trackers cannot be reliably used to track stars within certain specified angles of the sun, moon, and earth. Some trackers have special restricted angles because of possible reflections or obstructions from the spacecraft itself. In addition, there are restrictions with respect to the availability of stars during slews. The spacecraft may be required to point to parts of the sky where it is impossible to maintain stellar reference through the entire orbit; when this happens, the spacecraft can be held by gyro control. There are also constraints with respect to whether or not the experimenter's target is occulted.

Operational constraints must be monitored to ensure: that the command memory does not overflow, that the time allotted for specific operation is consistent with spacecraft location in orbit, that the flip circle (either the A side or the B side of the solar array) is observed, and that real-time passes are of adequate duration to support the operation.

Basic Ground-System Requirements

The OAO operational philosophy is to maintain centralized control of the mission.

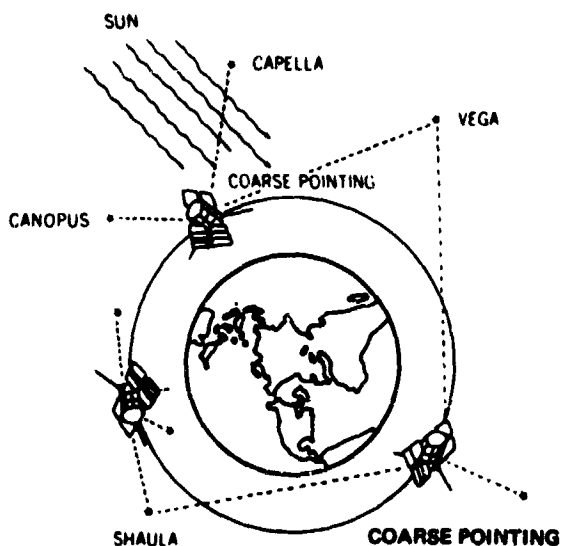


Figure 5. Gimballed star-tracker assignments.

Remote stations are used to relay telemetry data to Central Control and to relay commands to the spacecraft. The Central Control Station is the focal point of mission planning and the master facility for monitoring and control of the spacecraft.

The remote station can command the spacecraft on the basis of previously received command messages from Central Control, or it can command under the direction of Central Control during real-time operations when deviation from plans is required. The remote station records all wideband data.

Ground-System Description

The OAO ground system consists of five remote STADAN* stations and a central control facility at the Goddard Space Flight

*Space Tracking And Data Acquisition Network.

Center. Three of the stations—Rosman, North Carolina (USA), Quito, Ecuador, and Santiago, Chile—were selected to form a fence through which the OAO must pass each orbit (fig. 6). The stations at Tananarive, Madagascar and Carnarvon, Australia were added to provide additional real-time coverage for spacecraft control and monitoring, especially for the Smithsonian Experiment, which requires real-time operation. The five stations provide approximately 24 12-minute real-time contacts per day.

Figure 7 shows a simplified block diagram of the ground system. The remote stations provide three communications links to the spacecraft: (1) a narrowband telemetry link, (2) a wideband telemetry link, and (3) a command link. They also perform the necessary data-handling and recording functions. Each station is equipped with a

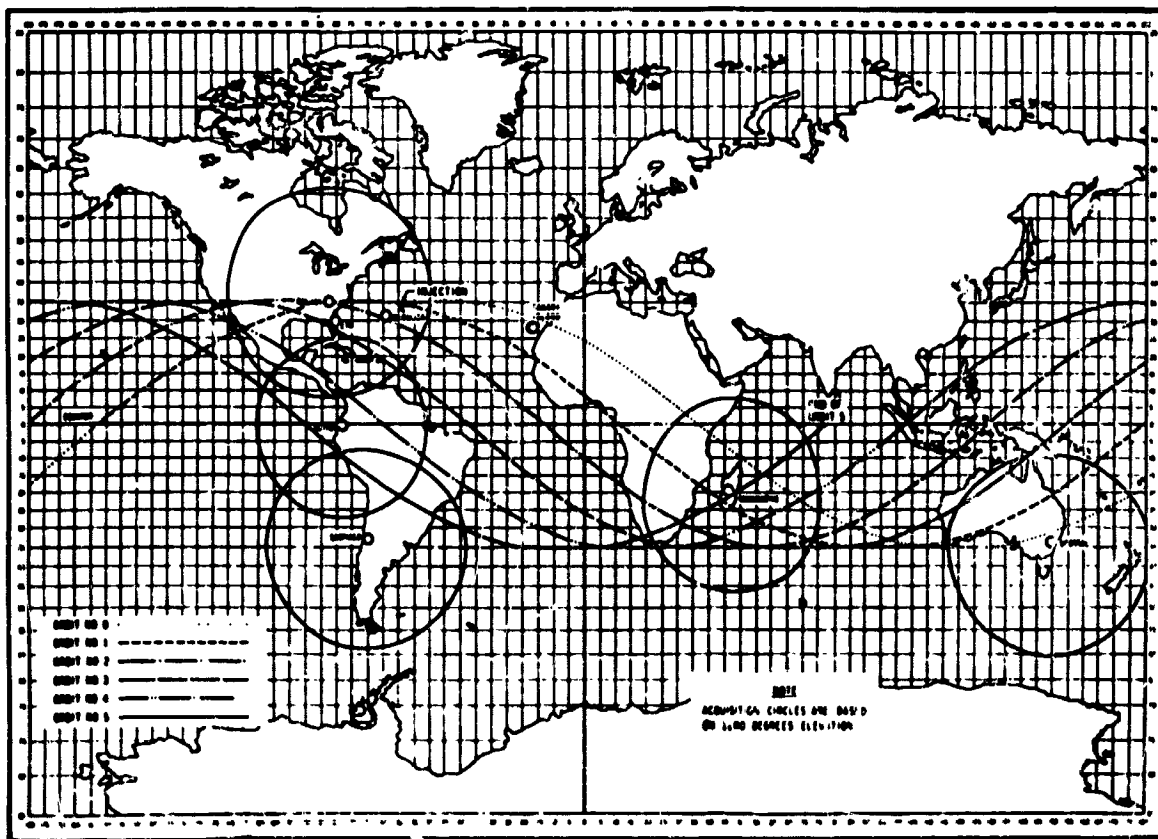


Figure 6. Map of orbital coverage.

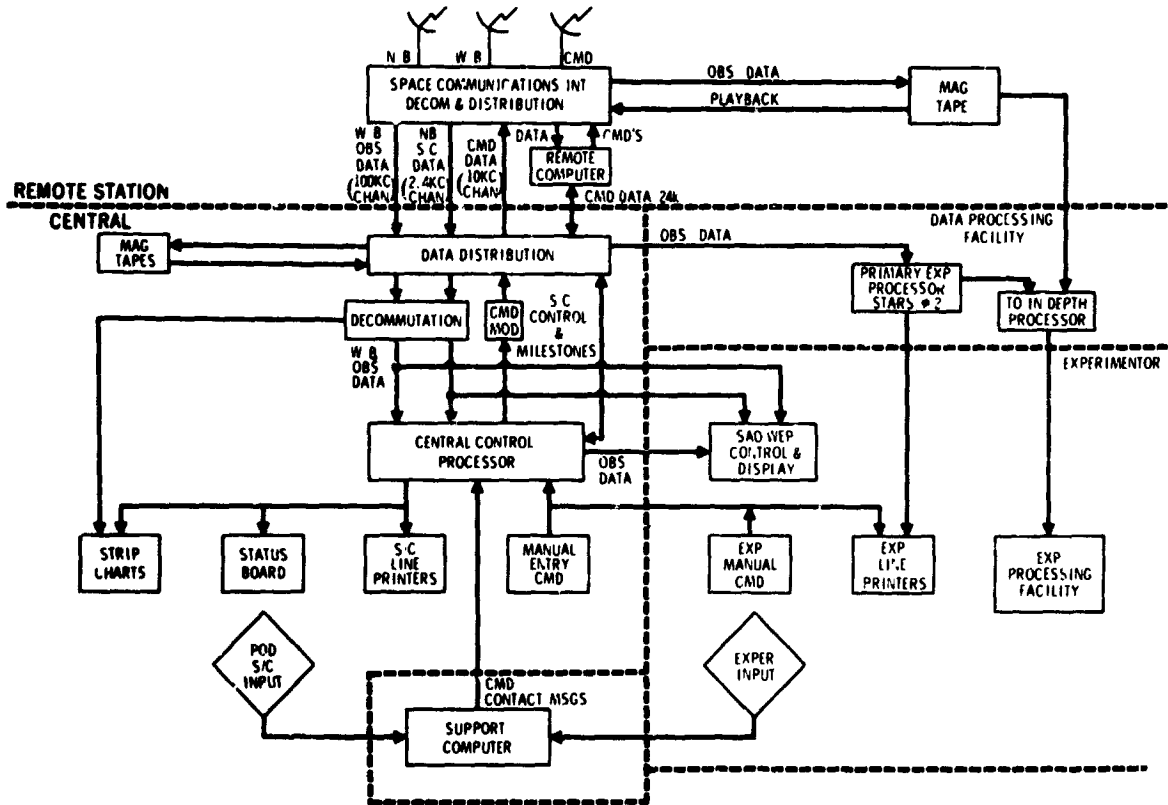


Figure 7. Simplified system block diagram for OAO.

computer to perform the functions of commanding the spacecraft, controlling the station data-handling equipment, and relaying data to the Central Control Station. The 100-kilohertz and 10-kilohertz communications links shown in figure 10 are available only to the station at Rosman, North Carolina. The 2.4-kilohertz communications link is used to transmit narrowband telemetry data and remote-computer "milestone" messages (describing the results of each operation performed) to the Operations Control Center. This link is also used to transmit instructions and commands from the Operations Control Center for execution by the remote computer. Special communication modems are provided to interlace the 1042-bit-per-second narrowband telemetry data with the computer milestones between the remote station and Central Control. By using this computer-to-computer interface and real-time telemetry transfer, the OAO

monitoring and control is performed at the Operations Control Center.

At the Rosman station, full advantage is taken of the 100-kilohertz and the 10-kilohertz microwave communications links available. All forms of wideband and narrowband data are transmitted to Central Control. Spacecraft commands are generated at Central Control and are transmitted directly to the spacecraft via the microwave link.

There are three OAO computer centers at the Goddard Space Flight Center. The *Operations Control Center* (figs. 8, 9, and 10), which performs the real-time control and monitoring function and houses the mission operations staff and experimenters, contains three computers, pulse-code-modulated (PCM) decommutation equipment, 14 strip-chart recorders, a large spacecraft-status board displaying 375 bilevel and 90 analog parameters, 15 display consoles for control and monitoring of the spacecraft, and Wisconsin



Figure 8. Central control mission-operations room.

and Smithsonian Experiments control and display equipment. The *Support Computer Center* (fig. 11) is a large digital computer with cathode-ray-tube (CRT) terminals for access by the mission operations staff and support computer personnel. The *Data Processing Center* (fig. 12) consists of two large digital computers, one to provide in-depth quick-look and the other to reduce scientific data.

Operating the Ground System

The OAO requires constant attention from the ground-based mission operations staff. Figure 13 shows the major components



Figure 9. Experimenter operations room.



Figure 11. Support computer center.



Figure 10. Central-control equipment room.



Figure 12. Data-processing center.

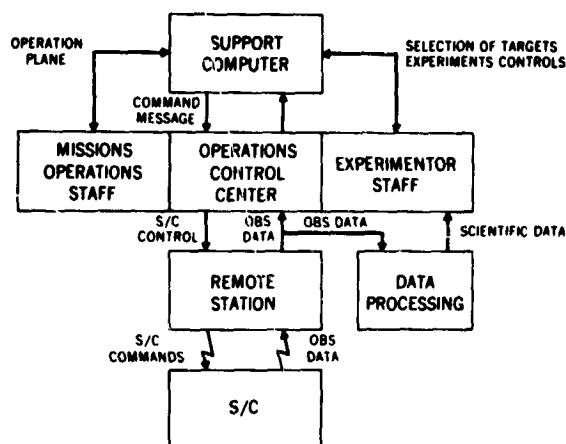


Figure 13. Major mission-operation components.

of the ground system with their normal interfaces. In this figure, as in the real operations, the mission operations staff and experimenter staff are integral parts of the Operations Control Center. The ground-system operation starts with the experimenter's plan of observation. The plan is then traced through the support computer, the Operations Control Center, the remote station, the OAO, and back through data-processing to the experimenter.

In order to develop an experiment target list, the experimenter uses spacecraft ephemeris data, a list of available remote stations, and the support computer in an iterative process. This process catalogs available stars, selects experiment operating parameters, and alerts the experimenter to possible conflicts with OAO operation restrictions. When the experiment target list has been completed, inputs are provided to the support computer by the mission operations staff, which defines spacecraft operations and directs remote station activities. This completes the mission plan for one segment of orbital operation, usually seven orbits. The support computer is then run to compute a contact-message tape that contains a detailed schedule of activities for every real-time contact in the segment, including all commands to be sent. It also contains the types of data to be taken from the OAO and the commands to be loaded into command

memory to carry the spacecraft through its next series of operations.

In the process of computing the contact messages, the support computer formats every command necessary to assign the trackers for slewing to the designated pointings, to re-assign the tracker for occultations, to maintain optimum roll, and to check for all the spacecraft restrictions previously mentioned. Printouts describing the contact messages are provided by the support computer in varying levels of detail for review and use by different mission-operations elements. One of these printouts, used by the mission operations staff to monitor the performance of the spacecraft, is an integrated printout that lists chronologically every event to occur in the spacecraft, including ephemeris events, real-time operations, and command memory operations. After the contact message has been approved by the support-computer operations personnel, the experimenter, and the mission operations staff, it is cleared for transmission to the remote stations.

Contact messages are transmitted to the remote stations via the Operations Control Center; normally, this is done a day in advance of use. These messages are validated by both the Operations Control Center and the remote station.

Activity for each spacecraft contact starts 40 minutes prior to the estimated time of arrival (ETA) of the spacecraft at each remote station. Diagnostic programs are run at the station; the proper contact message is called in by the remote station computer; and the operational configuration of the station is established for the satellite. At ETA minus 20 minutes, communication is established between Central Control and the remote station. Central Control is configured for remote operations, and the prepass confidence checks are run. These are single-thread data-flow tests, which originate at the remote station as radiofrequency signals modulated by OAO tape-recorded data and which are passed through the complete data path from the remote station antenna to display devices at Central Control. When the test is accomplished, the radiofrequency source at the

remote station is turned off, and no patches or configuration changes are made anywhere in the system until the contact is completed.

At the ETA, the remote station computer automatically begins the contact by establishing communications with the spacecraft. By commanding the spacecraft and controlling the station data-handling equipment, the computer establishes a narrowband telemetry link with the spacecraft and uses this link to verify all commands sent to the spacecraft. The remote station computer then proceeds with the schedule of activities as directed by the contact message. For example, the schedule may be to load the command memory with the commands specified in the contact message, to dump data storage, or to change the mode of various spacecraft systems. Throughout the contact, narrowband data from the spacecraft are passed directly to the Central Control Station at the Goddard Space Flight Center (GSFC), thus allowing the Operations Control Center to display the complete spacecraft configuration and status for the mission operations staff. The Data-Processing Center may also receive and process these narrowband data to provide near real-time, quick-look, spacecraft-performance information. The Data-Processing Center has a remote printer located in the Operations Control Center, thus allowing access to this information by the mission operations staff.

Throughout the contact, the remote station computer and the Operations Control Center computer communicate via the 2400-bit-per-second, high-speed datalink. Via this link, the remote station sends milestone messages describing the results of each operation it performs. From a control panel in the Operations Control Center at GSFC, the mission operations staff can control the remote station computer; i.e., they can change the sequence of events, stop and start the operation, add new events, and send command groups to the spacecraft. This capability is used in emergencies or whenever changes are made to the mission plan after the

contact message has been sent to the remote station.

After the contact is over, wideband data taken during the contact are played back to the Operations Control Center at a slowed-down rate for processing. The data tapes are mailed to the Data-Processing Center, where they are reduced and supplied to the experimenter.

Testing and Training

The system was extensively tested before being committed to operational status. Central Control proof tests were run to verify the system performance in handling contact messages, contact operations, and post-contact operations. Remote-station integration tests were conducted with spacecraft equipment aboard aircraft flown over the stations. Tests were also made on the high-speed communications links to the remote stations.

Using the actual flight spacecraft before launch, tests were carried out to ensure compatibility with the ground system. Extensive records were kept during all systems tests to provide statistical performance evaluation as a function of time as well as to record every anomaly so that possible problems could be investigated, eliminated, and monitored for recurrence.

Mission training was conducted in the form of network exercises, mission simulations, command-message generation exercises, and prelaunch spacecraft operations. The network exercises included the remote station and the Operations Control Center. These exercises were run with tape-recorded data and used operational configurations and procedures; their purpose was to train ground system personnel in the setup, checkout, and use of the ground system. Mission simulations were conducted to give the mission operations staff realistic experience in operating the Orbiting Astronomical Observatory, in diagnosing system faults, and in instituting proper corrective actions.

PRECEDING PAGE BLANK NOT FILMED.

N70-36746

Apollo Telescope Mount Operations and Data-Handling

James M. Rives

NASA George C. Marshall Space Flight Center

Introduction

The objectives of the Apollo Telescope Mount (ATM) mission are to obtain precise scientific data and information on the characteristics of the sun through observations of various portions of its electromagnetic spectrum (fig. 1). The ATM is a module of an orbital assembly (OA), which also includes a lunar module (LM), a command service module (CSM), a multiple docking adapter (MDA), an airlock module (AM), and the orbital workshop (OWS). Figure 2 shows the ATM in its cluster configuration.

The ATM is physically integrated with a lunar module that provides the habitation area for the crew and the necessary controls and displays to enable the crew to control and to operate the ATM systems and experiments. The LM/ATM has been designated the AAP-4 of the AAP-3/4 missions.* This manned mission (fig. 3), planned for 56 days duration, begins with a manned command service module (AAP-3) liftoff and rendezvous with the orbital assembly, which is in an approximately 200-nautical-mile orbit altitude with a 35-degree orbital inclination. Following CSM rendezvous and docking with the OA and checkout, AAP-4 with the LM/ATM will be launched 3 to 5 days after AAP-3. After insertion into orbit and separation from the launch vehicle, the LM/ATM will perform an unmanned automatic rendezvous with the orbital assembly and will dock with the multiple docking adapter under remote control by a crew member in the MDA. The crew will then activate the LM/ATM and proceed

*AAP = Apollo Application Program.

with solar observations on an open-ended, 56-day mission. Of the total 56 mission days, 37 days have been set aside for ATM experiment operations and 19 days for other mission activities.

Because of the complexity of the LM/ATM, it will require not only many of the resources currently being used in manned spaceflight but also additional resources and advanced techniques that are being developed. The crew will assume the role of the principal investigator in the operation of all experiments and will control the operations of all ATM experiments, but they will be complemented by some automation. The ground network will monitor experiment operations and will serve only in advisory capacity to the crew when required. In general, the crew will:

- Precisely point the solar instruments at selected targets of interest, such as sunspots, filaments, and flares, and will increase the resolution as necessary
- Make on-the-spot decisions that will enhance the quality and integrity of data
- Retrieve the film cameras, which contain high-resolution photographs, by extra vehicular activities (EVA).

These activities will also be used to evaluate man's ability to operate complex scientific instruments in the space environment. The results of this evaluation will help to determine man's role in future space flights.

The crew also has the prime responsibility for the operation of all ATM systems; however, unlike its role in the experiments, ground operations has a large role by assuming control to relieve the crew of repetitious tasks and the bookkeeping type of functions

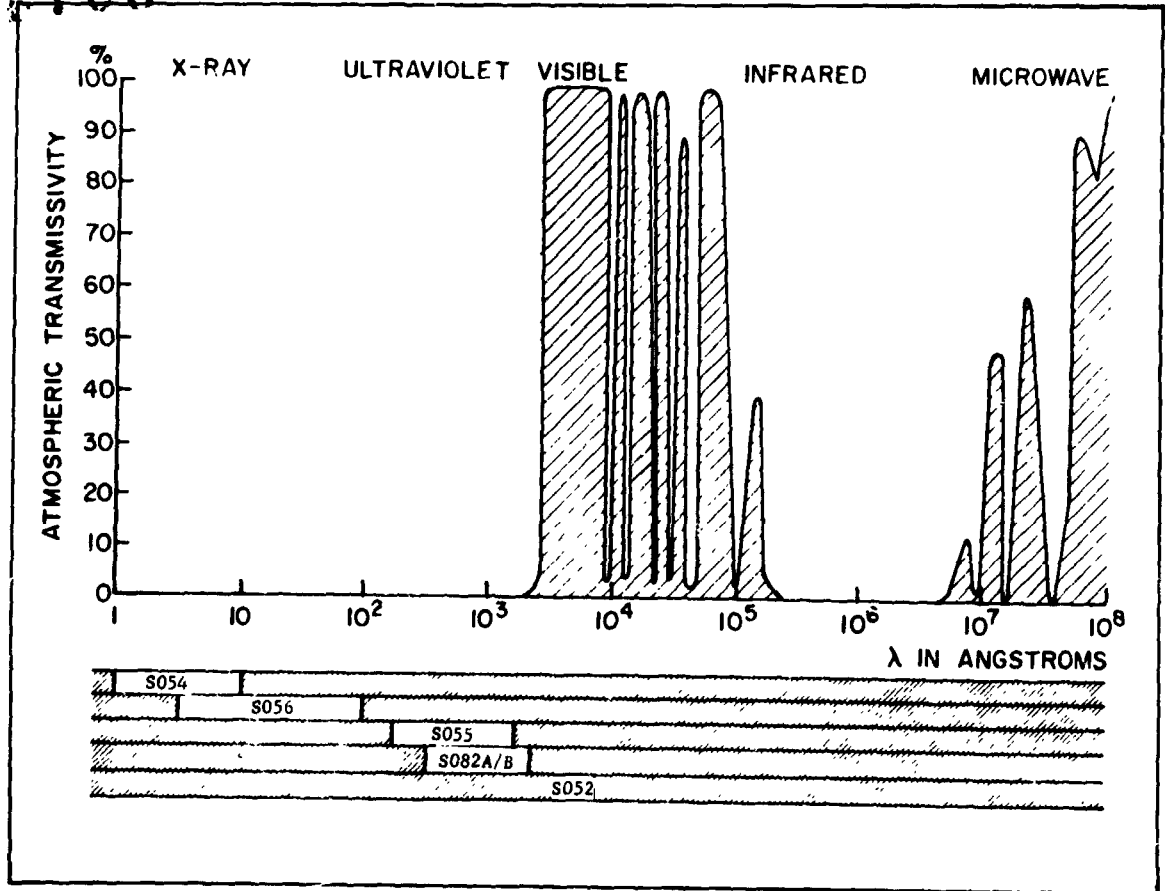


Figure 1. Regions of spectrum of interest to ATM, including atmospheric transmissivity as a function of wavelength.



Figure 2. Apollo Telescope Mount (ATM) in its cluster configuration.

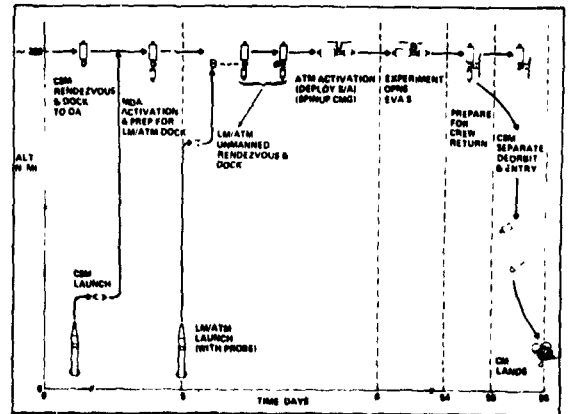


Figure 3. AAP-4 baseline mission profile.

as well as assuming control when ground-based computing facilities can be more efficiently utilized, when the crew has insufficient or hard-to-access data, and when the crew is absent. The ATM consists of five major experiments (fig. 4):

1. S052: White light coronagraph
 2. S054: X-ray spectrographic telescope
 3. S055: Ultraviolet spectrometer
 4. S056: Dual x-ray telescopes
 5. S082A: Coronal extreme ultraviolet spectroheliograph
- S082B: Chromospheric extreme ultraviolet spectrograph.

These experiments are supported by four major systems on the ATM:

1. Thermal control system
2. Pointing control system
3. Electrical power system
4. Instrumentation and communication system.

All these experiments and systems are housed in the ATM rack assembly (fig. 5). Physical access to the experiment film canisters by the crew will be accomplished by EVA at appropriate times during the mission. Crew control and monitor will be accomplished in the lunar module by means of a control and display (C&D) panel.

ATM Experiments

The ATM experiments are designed to observe and to record solar features or regions of interest by using a variety of scientific instruments and recording devices. Observations are to be made and data obtained over a wide range of energy wavelengths in the form of both solar images and solar spectra. The experiment operations will be conducted so that one experiment (e.g., S055), relative to the others, is primary for crew activity while another experiment (e.g., S082A) may

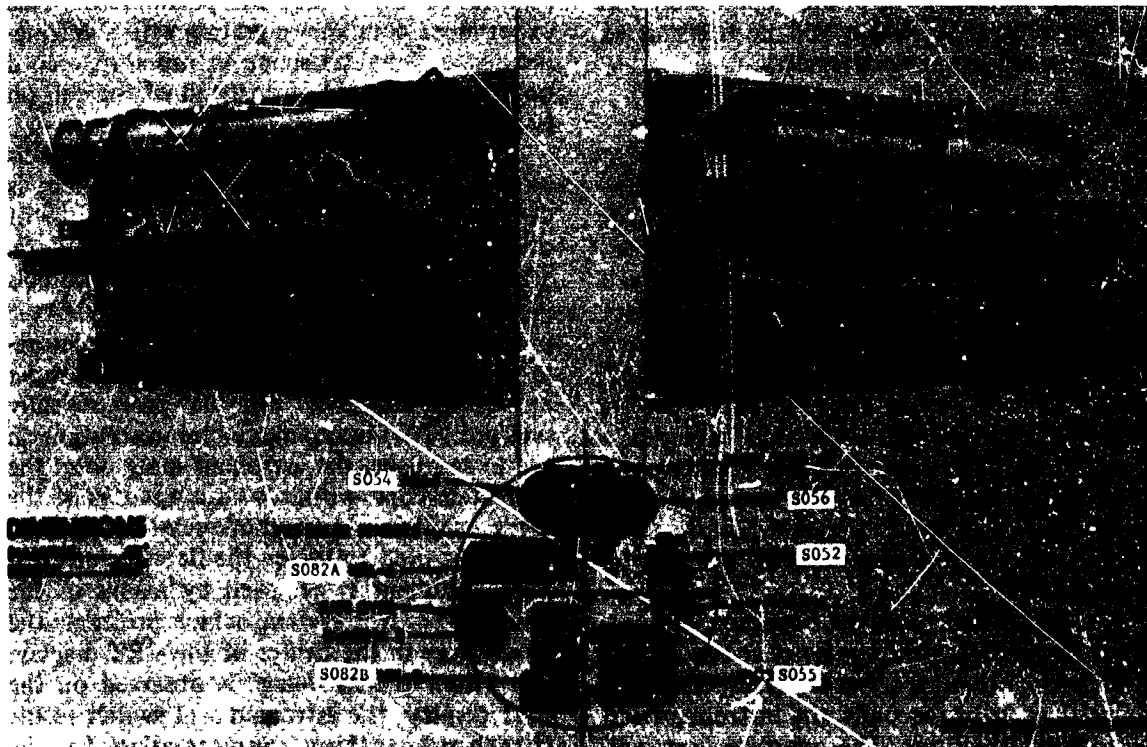


Figure 4. ATM experiments and experiment package.

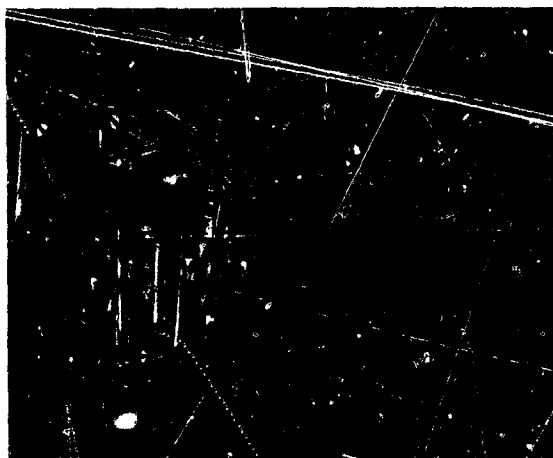


Figure 5. ATM cannister cut, showing electrical, pointing-control, instrumentation, and communication systems.

be active in a secondary mode, etc. The experiment observations and data will be recorded primarily on photographic film and on magnetic tape, which will be transmitted to a ground station via telemetry.

S052 White Light Coronagraph

The primary purpose of the S052 experiment is to make observations on the solar corona to determine its form, polarization, and brightness from 1.5 to 6 solar radii as well as correlations with sunspot and solar flare activity. The instrument used is a standard Lyot coronagraph with the three external occulting disks modified to allow precise pointing of the experiment. It includes a polarization wheel inserted behind the internal occulting disk and a system of mirrors to bend or "fold" the light path to allow a more compact arrangement of the camera and electronics.

The normal mode of operation requires that the instrument be pointed at sun center. If pointing becomes offset from sun center by more than 20 arc seconds, the instrument will stop taking pictures. The aperture door will automatically close if the pointing error exceeds 5 arc minutes. Exposures will be

made through both polaroid filters and unpolarized lens. When camera film must be replaced, the astronaut will replace the entire camera during an EVA, thus eliminating any requirement for direct film handling. Each camera contains 750 feet of 35-millimeter film, or enough for 7600 frames of data; four cameras are required to provide sufficient film for the duration of the ATM mission.

S054 X-Ray Spectrograph Telescope

The primary purpose of experiment S054 is to study solar-flare emission in the soft x-ray wavelengths between 2 to 8 angstroms with a high spectral resolution of a fraction of an angstrom and a spatial resolution of 2 arc seconds. The secondary objective is to obtain soft x-ray images of the sun during non-flare conditions. These measurements will be correlated with ground-based observations and associated records for the purpose of constructing a comprehensive picture of the solar-flare phenomena. This experiment combines a grating with a grazing-incidence x-ray telescope in order to record both an image and a spectrum of the sun on film.

The primary mode of operation of this experiment is the flare mode, which is designed to maximize the probability of obtaining data on the initial rise of a flare. The astronaut will set the experiment controls so that an increase in x-ray intensity above a predetermined level will initiate the picture-taking sequence. At the same time, the proper exposure sequence will be automatically selected. To obtain maximum resolution in the experiment, the astronaut must point the x-ray telescope within ± 2 arc minutes of the flare region. A cathode-ray-tube (CRT) display is used to locate the flare; pointing of the instrument is achieved by means of the pointing control system, which positions the flare image in the center of the CRT display.

When a flare image is observed on the CRT display, the astronaut will switch to the threshold setting corresponding to the exposure-count reading. With optimum intensity of the image on the CRT display,

the astronaut will then maneuver the spacecraft to center the image on the scope and will lock the spacecraft in this position until the solar activity ceases. All functions started by this solar flare will continue to operate until the intensity count produced by solar-flare activity diminishes below the preset discrimination level. The camera records both the dispersed and undispersed x-ray images of the sun. The film magazine in each of the four cameras to be used during the ATM mission contains 1000 feet of 70-millimeter film. The telescope assembly also has a proportional counter, which will provide a solar-flare warning and a TV image to the astronaut, as well as telemetry for the x-ray data.

S055 Ultraviolet Spectrometer

The purpose of experiment S055 is to observe the solar atmosphere spatially and spectrally and to obtain data in the 300- to 1334-angstrom ultraviolet region. Atomic lines having ionization energies in the range of 13.6 to 367 electron volts will be observed. Spectroheliograms constructed in these lines will be used to examine the temperature change across the boundaries between regions of solar supergranulation. The experiment obtains spectral data in seven distinct bands in the 300- to 1334-angstrom region and spectroheliograms of the solar disc with a resolution of better than 2 arc seconds.

A grating mount in the spectrometer provides the capability of scanning the entire wavelength range over the entrance slit of a single detector and also the capability of selecting any other wavelengths for the raster operation. In addition, the telescope is provided with a small raster pattern (5 arc minutes by 5 arc minutes) to permit the reconstruction of solar images. In support of the experiment, a narrow bandpass hydrogen-alpha filter telescope is used to provide spectroheliograms of the solar disc. Filtergrams in hydrogen-alpha will be obtained at regular intervals in each orbit or more frequently when ultraviolet experiments are in progress. This hydrogen-alpha data will be recorded on 35-millimeter film. Unlike the other experi-

ments, S055 experiment data will be recorded and provided to the ground only by telemetry.

S056 Dual X-Ray Telescope

The purpose of experiment S056 is to measure the intensity of solar flares with spatial and temporal resolution and to obtain data on the solar chromosphere in the soft x-ray region from 2 to 60 angstroms. Data obtained as spectrograms and spectroheliograms can be used to verify models of energy and mass transport mechanisms through the solar chromosphere and models of solar-flare initiation and development. This experiment utilizes two separate and independent instruments to obtain complementary data. One instrument is the x-ray event analyzer (X-REA), which provides spectral data (intensity versus wavelength) in two adjacent channels, divided further into 10 wavelength bands from 2 to 20 angstroms, using proportional counters and pulse-height analyzers. The other instrument is an x-ray telescope (X-RT) employing grazing-incidence optics to provide spatial data in the form of x-ray filtergrams (solar images of narrow wavelength intervals) in six bandwidths from 4 to 60 angstroms. The solar images formed by the camera system are recorded on ultraviolet sensitive film while the data from the proportional counters are displayed in the lunar module or to the ground via telemetry. The film canister for the camera contains 1000 feet of film; there are four canisters for the ATM mission.

S082A Coronal XUV Spectroheliograph

The purpose of this experiment is to obtain high-resolution, extreme ultraviolet (XUV) images of short time variations in the solar atmosphere and to collect spectra data on solar centers of activity with emphasis on solar flares. The instrument has a diffraction grating of 3600 lines per millimeter that receives light directly from the sun and forms a spectrum of solar images on film in wavelengths between 150 and 650 angstroms.

The astronaut will detect the initiation of a flare by monitoring images of the sun in different wavelengths on a scope. The "active prominences" are observed by hydrogen-alpha telescopes on the ground and observation information relayed to the astronaut by voice communications from the ground. The normal operation for the instrument is in the sun-centered mode. It may also be operated when pointing if offset to record data on a specific feature. The resolution is approximately 5 arc seconds, depending on wavelength, and the field-of-view is 45 arc minutes. Each of the four cameras for the ATM mission contains 200 filmstrips with one exposure per strip (each 25 millimeters by 258 millimeters).

S082B Chromospheric Extreme Ultraviolet Spectrograph

The S082B extreme ultraviolet spectrograph instrument will be used to record photographically ultraviolet spectra of the sun in the spectral range of 970 to 3940 angstroms and to provide video pictures of the solar image in a band of approximately 170 to 550 angstroms. The solar radiation will be obtained from various small areas on the solar disk and at different levels across the limb. The instrument employs a normal incidence spectrograph using a 2-meter-radius, 600-line-per-millimeter grating. This grating will focus the dispersed light on the filmstrip in the camera. An extreme ultraviolet monitor will assist the astronaut in deciding which extreme ultraviolet emitting regions of the sun should be photographed. The observations of both the spectrograph and the extreme ultraviolet monitor will cover periods of greater or lesser activity during two rotations of the sun and will record temporal changes of centers of activity and flares.

The instrument is normally offset-pointed to a precise feature of interest and can be manually operated in either of its two operating modes. The field-of-view with this instrument is 3 arc seconds by 60 arc seconds with a resolution of approximately 2 arc seconds. Each of the four cameras for the ATM mission has 200 filmstrips (35 milli-

meters by 258 millimeters) for 1600 exposures. There will be approximately 1600 feet of 35-millimeter filmstrips from the S082A and S082B experiments.

ATM Systems

The ATM solar experiments mounted in an experiment canister are supported by five primary ATM systems: thermal control, electrical power, pointing control, instrumentation and communications, and the LM/ATM control and display panel.

Thermal Control

The thermal control system (TCS) provides a controlled thermal environment for the ATM experiment canister. The fluid, 80-percent methanol and 20-percent water by weight, circulates through cold plates on the canister wall. A heater and radiator provide thermal conditioning of the fluid and maintain a constant fluid temperature at the cold-plate inlets. The thermal control systems are designed to maintain an acceptable thermal environment for the experiment optics and electronics as well as for support-systems equipment. Systems components are mounted on racks that surround and structurally support the canister. The experiments are mounted on a cruciform spar that is attached to and enclosed by the canister.

The canister walls are maintained at essentially constant temperature to prevent misalignment of the optics by deflections of the spar resulting from thermal stresses and to ensure that the electronics components do not overheat. A semipassive thermal system is used to control radiation heat transfer between the rack-mounted components and their surroundings. Thermostatically controlled heaters are provided to prevent critical components from becoming excessively cold during inoperative periods on night portions of the mission.

Electrical Power

The ATM electrical power system (EPS) conditions, stores, controls, and distributes

26.0- to 30.0-volt DC power to the ATM system and experiment loads as well as power to the lunar module. In normal orbital operation, power is provided by a solar array and rechargeable nickel-cadmium (Ni-Cd) batteries. The power system for the airlock module provides a source of power during contingency operation. The solar array is configured to supply an average power output at the beginning of operational life of 10,480 watts. The solar cells will convert solar energy to electrical power, which is used to satisfy the load requirement and to recharge the batteries. There are 18 solar panels mounted in a four-wing array and 18 charger-battery-regulator modules (CBRM). The output of each solar panel is connected directly to a single CBRM to form one of 18 separate power-generation units. Between launch and solar panel deployment, the nickel-cadmium battery will supply power to the loads.

Initially, the solar array is stowed in a folded position and is mechanically cinched to a backup structure on the ATM. After deployment, the cluster will be oriented by the pointing-control system so that the array is held normal to the sun during the orbital day. Deployment will be performed, after lunar module docking is completed, by utilizing a system of redundant electro-explosive devices controlled from the ATM control and display panel. Actuation of the solar-array unlock switches will fire pyrotechnic initiators to release the four wings from their restrainers. Actuation of the solar-array deploy switches will cause electro-mechanical actuators to extend hinged scissor arms to deploy the folded panels. Telemetry signals are provided to indicate that each wing has been deployed and locked.

Pointing Control

The ATM pointing control system (PCS) provides three-axis stabilization and attitude control of the cluster and permits fine-pointing and stabilization of the experiment canister. The PCS operations assure stable orbital-assembly orientations for experimental tasks. The flight crew has systems manage-

ment responsibility while ground personnel conduct status and performance evaluations based upon telemetered data. These ground operations require capabilities for detecting failure effects or degradation in system performance that could compromise mission objectives and for advising the crew on their utilization of given equipment redundancies and/or backup modes.

In the context of these requirements, the PCS telemetry becomes highly important whenever off-nominal status changes occur. Very few ground-commanded PCS functions are planned at the present time. Maximum reliance is on highly automatic, crew-supervised, programmed, digital-computer control. Computer and timer updates are mission-critical transmissions from ground to orbit. There are two major PCS subsystems: control moment gyros (CMG) and experiment pointing control (EPC).

Instrumentation and Communications

The instrumentation and communications (I&C) system provides four functions (fig. 6):

1. Collection and processing of ATM systems and experiment data
2. Transmission of these data to ground station
3. Execution of ATM ground commands
4. Experiment support for the astronauts via closed-circuit television.

The I&C system in the ATM includes the telemetry subsystem, the radiofrequency command subsystem, and the television subsystem. The purpose of the ATM telemetry system is to transmit to the ground the data generated aboard the ATM and some parts of the lunar module and orbital assembly. These data include results and measurements made to monitor the status and performance of ATM systems and experiments.

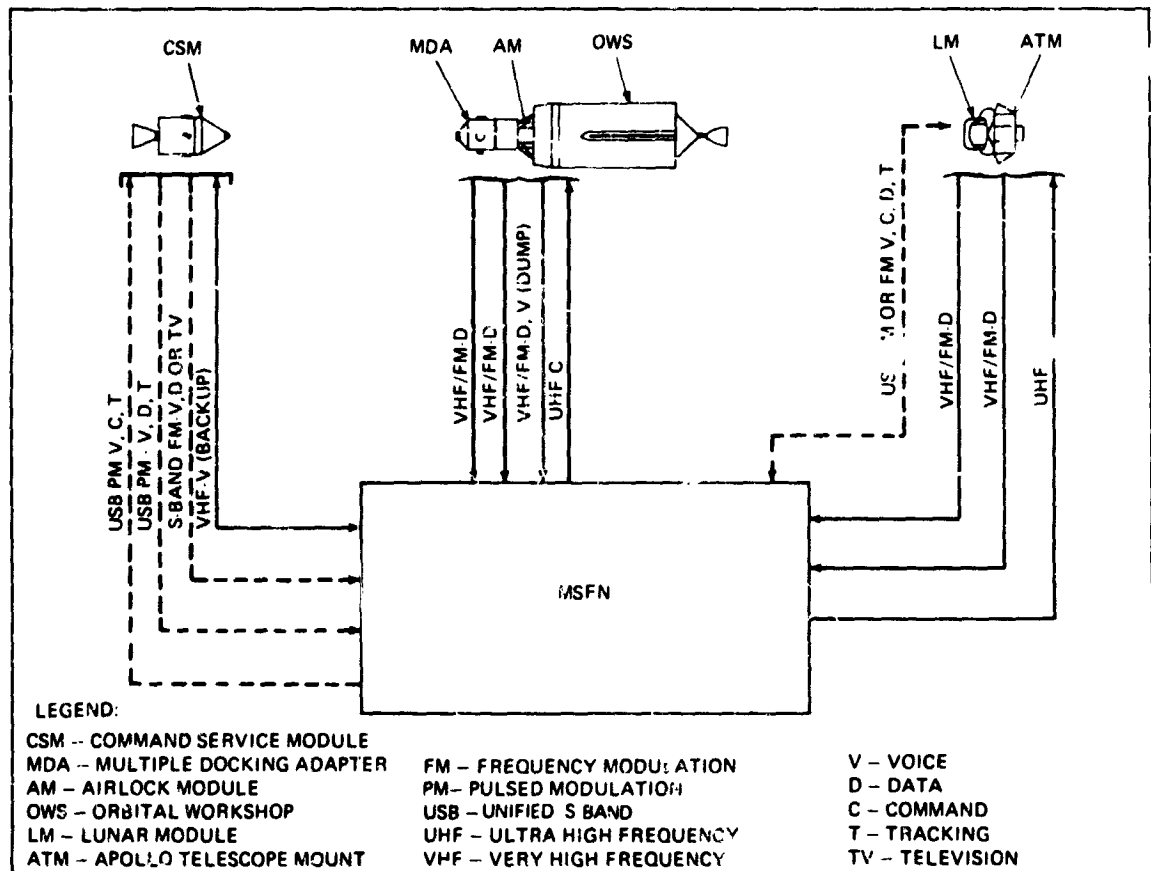


Figure 6. Module/MSFN communications interface.

The purpose of the radiofrequency command system is to provide the ground with control over various spacecraft systems. During any manned mission, the crew provide the primary source of control; however, some of their control functions are made available to the ground when the ground can usefully assist the flight crew in one of four general areas: crew safety, data downlink management, routine or repetitive and time-consuming tasks, and commands required when the crew are dispersed throughout the orbital assembly and are not available to execute such commands. The majority of ground commands are used for switching-on or switching-off functions and for updating the ATM computers.

The principal function of the television system is to act as a viewfinder for the astro-

nauts. Using the television system in conjunction with the two hydrogen-alpha experiments and the S082 experiment, the crew can select the areas of the sun at which they want to aim the ATM experiment canister, and they can monitor the pointing of the canister.

The ATM telemetry system consists of two PCM/FM-FM* links, each having capability of 72,000 bits per second of data. The real-time output (from the PCS/DDAS*) is 72,000 bits per second. This is a non-return-to-zero output that can modulate either of the two very high frequency (VHF) transmitters and that can be transmitted to the

*PCM/FM-FM=Pulse Code Modulation/Frequency Modulation-Frequency Modulation., PCS/DDAS= Pulse Code Shift/Digital Data Acquisition System.

ground station. The delayed time output is generated by the auxiliary storage and playback (ASAP) assembly and is a 72,000-bit-per-second biphase signal that can also modulate either of the VHF transmitters. (See fig. 7.) The ASAP assembly records 100 words out of each PCM/DDAS* master frame. It is preprogrammed with the addresses for 400 words, which it selects out of four consecutive PCM/DDAS master frames. An ASAP master frame consists of 6000 words during which every measurement (including those from experimental submultiplexers) is sampled at least once. The data is recorded at 4000 bits per second. In the playback mode, the tape recorder plays the data back at 18 times the record speed (72,000 bits per second). Since the maximum recording time is 90 minutes and the tape moves in the same direction for both the record and playback modes, the playback time is 5 minutes and is independent of the amount of data recorded.

LM/ATM Control and Display Panel

In conjunction with the above experiments and systems, the control and display (C&D) panel located in the lunar module (fig. 9) provides the crew with controlling and monitoring devices (control, switches, meters, TV monitors, etc.) as a means of commanding and monitoring the ATM experiments and systems. The layout of some of the main controls on this panel includes:

1. Experiment grouping is on the left side.
2. Pointing-control-system grouping is on the right side.
3. Caution and warning are at upper center.
4. Power control is at lower right.
5. ATM systems are in the center.
6. The bottom panel provides the x-ray activity-history plotter, digital data address system, TV monitors, and displays for the x-ray spectroheliograph experiment.

A. Operational Characteristics of Recording System

1. It will record onboard 4000 bits per second of scientific and housekeeping data for 90 minutes.
2. It will play data back to ground site at 18:1 ratio for 5 minutes.
3. Onboard recording is interrupted during playback.
4. Two telemetry downlinks provide real-time data transmission simultaneous with tape playback.

B. Ground is prime in operation of tape recorder, including time-lining and control. Crew provides backup in contingencies.

C. Ground retrieval of all pertinent scientific data will be insured by:

1. Selected deletion of recording during some nighttime passes with all daylight passes recorded
2. Use of backup recorder to complement prime when possible loss of valuable mission and/or scientific data is evidenced.

D. Ground site selection for data dump will be influenced by:

1. Real-time activities
2. Radiofrequency predictions
3. Ground station operations (i.e., station manning)
4. Data continuity
5. Data flow, processing, and handling.

*PCM/DDAS=Pulse Code Modulation/Digital Data Acquisition System.

Figure 7. Considerations for tape recorder operation.

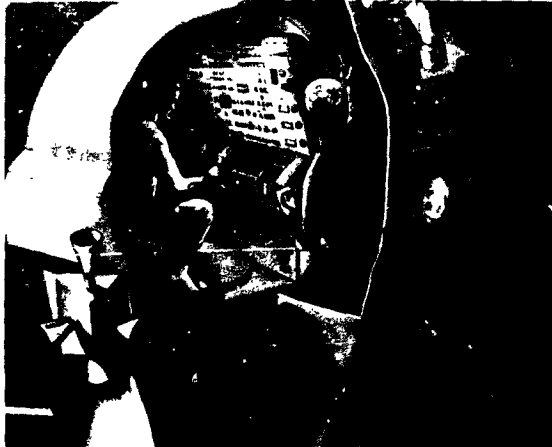


Figure 8. Control and display panel located in lunar module.

Ground Operations and Data-Handling

In support of the ATM experiments, it is planned to have ground operations accomplish the following functions:

- Verify the status of experiment operation by analyzing telemetry parameters.
- Perform real-time flight planning as a function of mission solar activity being observed.
- Predict solar-activity periods, and advise astronaut on observations.
- Assist astronaut in film management by monitoring film utilization and by correlating this with predicted solar activity and experiment planning.
- Perform experiment trend analysis based upon available telemetry data.

These functions will be performed primarily by operations personnel located at the mission control center (MCC) in Houston, Texas. The principal investigator, or his representative, will also be located at the mission control center, and, during the times when his experiment is being exercised, he will be located in the mission-operations con-

trol center in the MCC and will be actively participating in the real-time operations. At all other times, an experiment room will be provided for the principal investigator so that he can make detailed analysis of his scientific data and can provide recommendations pertinent to the experiment operations. In addition to the primary manned space-flight network (MSFN) and the mission control center, the Environmental Science Services Administration (ESSA) solar observatories will be linked to the mission control center and will provide the principal investigator with solar-flare prediction data.

To perform these functions, crew-voice, telemetry, and ground-based solar-observatory data will be utilized. Telemetry data can be either real-time (transmitted as occurring) or continuously recorded and played back over an MSFN station. The total bit stream of data is recorded at the remote site, and the hard copy is later shipped back to the processing center (fig. 9). That portion of the total bit stream needed to perform operations function is called "flight control data." Flight control data are those data which undergo some form of processing, other than direct recording at a remote-site ground station, and which are sent to the mission control center during the conduct of the mission to influence the progress of the mission. There are three forms of flight control data:

1. *Real-Time Data*: selected data received, processed, relayed, and displayed during ground station contact
2. *Delayed Real-Time Data*: selected data received during ground-station contact, and processed, relayed, and displayed between station contacts
3. *Hard Copy Data*: data recorded at the sites on tape, and the tape expedited back to the mission control center.

Real-time data are always transmitted to the control center during the appropriate mission phase for a gross assessment of the experiments. Delayed real-time data are transmitted only as required for trend or contingency analysis. The various types of mission

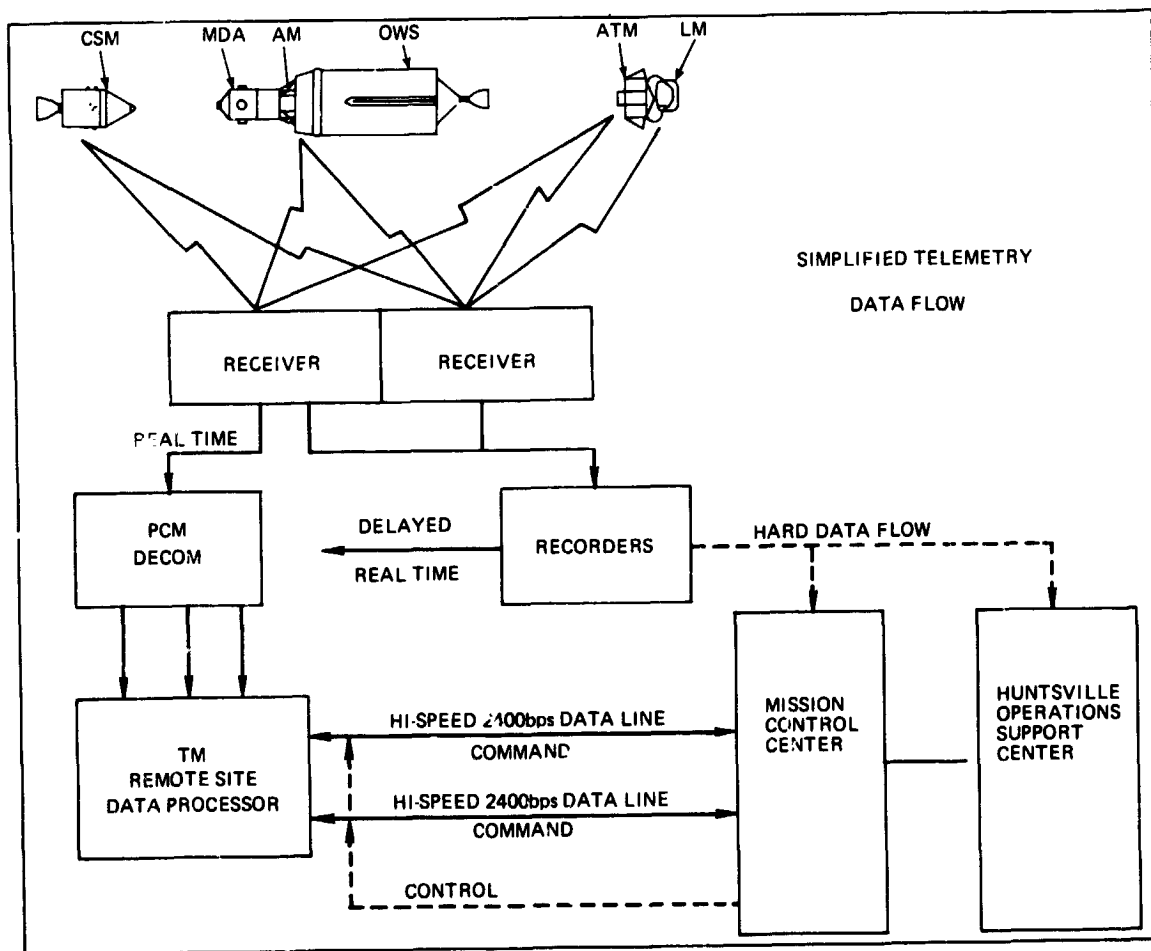


Figure 9. Simplified telemetry data flow.

data for scientific evaluation consist principally of recoverable experiment data (film and voice recordings) returned with the spacecraft and the telemetry data recorded at each ground site.

ATM data returned with the spacecraft consist primarily of special film canisters containing exposed experiment film taken during the mission. It is anticipated that approximately 16,600 feet of experiment film will be exposed during the 56-day mission. The film to be returned with the spacecraft requires special storage compartments within the spacecraft and also, upon recovery at sea, special handling and storage on the recovery vessel. The film will be expedited to each principal investigator (as soon as practical) for

his use in detailed scientific analyses. Normally, film processing will remain the responsibility of each principal investigator.

The real-time data received at each ground site in support of operations, along with the auxiliary-storage-and-playback tape recorder data, are recorded simultaneously on magnetic tape and used for post-pass playback in support of operations. They are also shipped (in a timely manner) to the processing center to be used in post-event and post-mission system and experiment scientific evaluations. If estimated on the basis of a fixed inclination and orbit, a substantial amount of recorded data would result from ground-site acquisition utilizing the entire MSFN. The volume of magnetic tape will be

greatly reduced, however, through the application of such current state-of-the-art recording techniques as reduced recording speeds, recording of multipasses on a tape, and the like.

The amount of data reduction and processing anticipated for this volume of ground-recorded data will be directly influenced by the information and data actually obtained by MSFN station coverage and the problems actually experienced during the real-time and near real-time operations activities. Such activities as astronaut time-lines, day and night cycles, "on" and "off" modes for experiments, and ground-site acquisition and loss times will greatly enhance the post-mission data-handling and management of data received from all ground sites (fig. 10). Minimum utilization of mobile support is planned.

The extent of data-processing back at the "home plant" consists primarily of utilizing ground stations (analog-to-digital

converters, computers, etc.) for converting analog telemetry information into basically digital or computer-compatible data (fig. 11). The processing center will digitize and strip all the data measurements and will output the data in various forms; e.g., binary computer-compatible tapes, oscillograms, and strip charts. These data may be furnished to data users in this "raw" form; however, the bulk of the data will require further data reduction and processing. Through computer utilization, calibration information will be applied to the "raw" telemetry information, and the data may be output in engineering values. Various processing techniques may be applied to the data at this point, such as limit-sensing, data analysis, data correlation, and the like. The basic data outputs as a result of data reduction and processing will be primarily in the form of binary tapes, microfilm, and printouts. Various data reduction techniques will be applied to reduce the total quantity of these data.

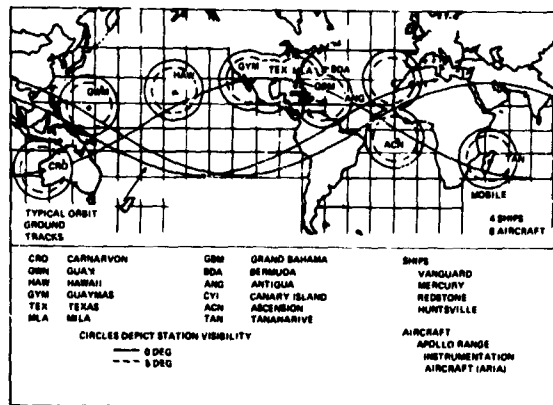


Figure 10. Manned space-flight network (MSFN).

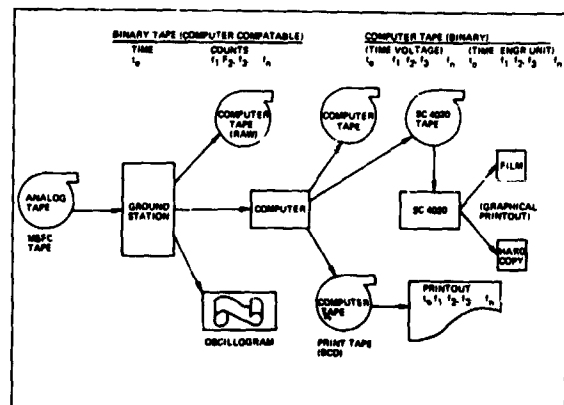


Figure 11. Standard telemetry-processed data outputs.

N70-36747

Ground-Based Astronomical Optical Data-Handling

Edwin W. Dennison

California Institute of Technology

Perhaps the most helpful contribution that those working with ground-based astronomical instrumentation can make is to indicate what has been done, what is now planned, and what is the nature of the basic concepts that are behind the instrumentation designs. Hopefully, this will lead to two further steps. First, with the help of those involved in space instrumentation, the ground-based techniques can be modified to make space astronomy and ground-based astronomy so similar that most astronomers will be able to use either with equal dexterity. Second, some of the astronomical observing concepts that have been found practical for ground-based stations may give some clue as to the general character of instruments for a space station.

Existing Instruments

At the present time, approximately one-half of all astronomical observations made at the Mt. Wilson and Palomar Observatories are made photographically. Of these, approximately 90 percent are spectra, and 10 percent are direct photographs of the astronomical objects. Some of the photographic observations are made with the help of image intensifier tubes, which reduce the exposure time substantially. The principal reasons for using the photographic materials are: (1) they are readily available and easy to handle, and (2) most of the optical instrumentation has been designed to accommodate photographic materials easily. Perhaps the most important advantage is that a photographic plate is able to integrate over an enormous number of independent picture elements, and, if care-

fully handled, the total number of discernable photometric levels is also very high. It is unlikely that astronomers would continue to use photographic materials if other techniques were equally effective.

The remaining half of the astronomical observations are made by using photoelectric detectors of one kind or another. By far the vast majority of these are photomultipliers. At the Mt. Wilson and Palomar Observatories, all of the photomultiplier photometers used for nighttime astronomy are used in a pulse-counting mode. For the solar magnetograph observations, photomultipliers are used in an analog mode because they are not strictly involved in photometry but are used as comparison devices. Pulse-counting photometers have proved to be simpler to operate, able to handle a much larger dynamic range than DC measurements, and appear to be far more stable than DC photometric methods. These pulse-counting systems have a time resolution of approximately 27 nanoseconds. Digital data systems are used in conjunction with these photometers. In these data systems, a certain amount of "housekeeping" information is recorded; i.e., telescope coordinates, time of day, the name of the object, etc. Also recorded are the observational data, which consist of the total number of pulse counts accumulated in electronic counters, the time of counting, and, in the case of scanning photometers, the position of the grating. These data are both recorded and presented to the observer in the form of Nixie tube displays.

The recording is generally done in two modes: the first is a printed paper tape, and the second is either summary punch cards or

51500-050
magnetic tape. The printed paper tape serves two purposes: first, to operate as a redundant recording medium, and second, to enable the observer to refer back to data that he has gathered earlier the same night. These numbers are also useful in checking the stability of the equipment because the observer can estimate the square root of the total number of counts he has accumulated and therefore can calculate the standard deviation. In general, if the observational values fall within one or two standard deviations, the system is working well; if the successive values fall outside of this range, there is an indication of instability, variable sky conditions, etc.

In some parts of the data systems, mechanical action is controlled from the data system itself. An example of this is the Coude spectrophotometric scanner. In this case, there are two photomultipliers, one monitoring the continuum and the other behind a movable slit that scans through a particular spectral line in the object being observed. In the normal mode of operation, the scanning slit is set at one edge of the spectral line, and a preset number of counts from the continuum monitor is accumulated in the counting channel. At this time, the scanning slit advances one step, and the continuum monitor again collects data until the preset number has been reached. In this way, the numbers in the scanning channel are normalized by the continuum, and variations in sky transparency seeing and the like are removed. It is also possible to operate the system in the reciprocal mode, in which the counts in the scanning channel always reach a preset number, and the monitor records a number that is proportional to the reciprocal of the intensity in the scanning channel. In this case, all observational points have equal accuracy. This is a mode of operation that uses the observing time most efficiently.

Other more sophisticated instruments have also been constructed, such as a compact spectrum scanner that rides on the telescope and a 32-channel photomultiplier spectro-photometer. These, however, are simply

extensions of the general techniques previously described.

Future Instruments

Many new instruments are either being constructed or are being planned for future construction. For photographic observations, it would appear that the use of the new image-analysis techniques, which have been so successfully employed by the Jet Propulsion Laboratory (JPL) and others, could result in a great improvement in the amount of data recoverable from photographic materials. In order to accomplish this goal, however, improved microphotometers must be constructed; and the resources for the software programming must be available. This type of project is certain to be successful because there are few, if any, state-of-the-art technological advances that must be made.

In the area of digital data systems, the plans for current and future projects include the use of small computers as central processing units for the entire data system and telescope control. The most compelling reason for going to these computers is that, by introducing new software techniques and programs, it is possible to reconfigure a data system for any new observational problem. It is also possible to add new pieces of peripheral equipment that can be used for new observing functions. These new peripheral devices may have a very complex relation to the other peripheral devices, but this relationship can be handled by software programming without requiring a complete, new, hardware configuration. It is also possible to keep the operator controls extremely simple by using computers. Cathode-ray-tube displays will be used for both alpha-numeric data gathered by the data system and graphical displays of either the raw or the interpreted data. These new systems will use a computer character generator, which has a composite video output and, therefore, can be used to feed many simple television monitors at a number of locations around the telescope. Magnetic tape recording

will be used almost exclusively except for those cases where the data rate is so slow that punched cards are more desirable.

In the immediate future, some on-line calculations will be done. For example, calculations will be made of the standard deviation for photometric measurements as the measurements are being made, thereby enabling the observer to immediately determine the accuracy of his data. In the future, more sophisticated on-line calculations will be possible. Perhaps someday the point will be reached at which the final reduced data can be presented to the observer essentially at the time of observation. Finally, the central processing units will be used for telescope control in the following ways: (1) they will calculate the coordinates and control the telescope for accurate settings; (2) they will generate control signals for raster scans, which will enable the entire telescope to scan across an extended object; and (3) they will be used to control scanning spectrophotometers.

An additional device that is on the future horizon for astronomy is, essentially, the equivalent of a two-dimensional array of photomultipliers, all acting in a pulse-counting mode, with the output data stored in a computer memory. From the point of view of practical memory sizes and computer access time, the entire project appears feasible; however, photometric two-dimensional detectors are not yet able to record single photon events nor even to have an accumulated signal-to-noise ratio that would be characteristic of a system in which no noise was introduced after the photocathode. Such a device would be very important to astronomy because of its potential speed gain, because of improved linearity in both the linear coordinates and the photometric coordinate, and also because the output would be directly in a computer-compatible medium. This would facilitate computer image analysis and processing. The entire future of both ground-based and space astron-

omy may depend upon the development of such a device.

The need for a two-dimensional, pulse-counting photometer is obvious, but it is also true that for measurement of spectra it would be desirable to develop a one-dimensional, pulse-counting photometer having an array of detectors in a single line. In order to be practical, such an array should have at least 1,000 to 10,000 independent elements.

Over the last several years, experiments have been performed at the Mt. Wilson and Palomar Observatories to determine the effectiveness of good human engineering. The results have fully demonstrated that, when an instrument and its controls are observer-oriented, the effectiveness of the instrument is greatly increased. The loss of effectiveness comes from equipment malfunction resulting from operator errors or the introduction of systematic errors. This does not mean that it is always necessary to have a skilled operator in addition to the observer but rather that, if some care is given to the control design, it is possible to have a fully effective, observer-operated instrument.

When designing instruments, it is often productive to consider the factors that will make the best use of the observer's talents. For example, if the observer needs to know the ratio of two numbers, he can more quickly interpret his data if he is given the ratio rather than the two observed numbers. When the observer is able to interpret his data, he is able to intelligently change his observing equipment to test a new idea or "hunch." There are, of course, times when a series of observations must be made under identical conditions, but even then the observer can be assisted by having his data presented to him in a meaningful way so that he can perform self-consistency checks on the data. These concepts are not new, but they have not yet been fully utilized in ground-based astronomy.

PRECEDING PAGE BLANK NOT FILMED.

N70-36748

System Aspects of the Kitt Peak Automatic Telescope

Peter R. Vokac and Frank E. Stuart

Kitt Peak National Observatory

Preliminary Description

The remotely controlled automated telescope at Kitt Peak National Observatory was conceived in 1961 as a general-purpose, computer-controlled system capable of automatically executing a predetermined program of astronomical observations, carrying out some on-line data reduction, and tabulating the results in suitable format. The 50-inch aluminum telescope is located on Kitt Peak, and the Raytheon 250 computer with all its input and output equipment is in Tucson, Arizona, 50 miles away. These two parts of the system are joined by commercial telephone lines (four wires in a Bell System "Telpak A") attached to digital-signal-conditioning hardware at both ends (built by Astrodata, Inc., of Anaheim, California).

In automatic mode, the operation of the telescope and all associated equipment is under the control of the computer, which receives its instructions either from a previously prepared paper tape or from an operator who may enter control information at the control center in Tucson. In addition to automatic control from Tucson, the telescope and instrumentation can be operated manually from the telescope dome in the conventional manner whenever desired.

The automated telescope system presents different aspects to the user, the designer, and the builder. This paper will concentrate primarily on the point of view of the designer, who might describe the system in the following way. The automated telescope is an active interface between an observer and the night sky. It is an automatic information generator made up of three inti-

mately related components: (1) optical-mechanical hardware, (2) electronic hardware, and (3) logical software. It is a complex system that contains in the computer memory all the information needed to accomplish a wide variety of tasks with the simplest possible operator input.

In addition to internal information stored in the computer memory and generated in commands and monitors, there is external information that flows into the system from both ends. From the sky comes data and weather information; from the operator comes control information.

System Design Philosophy

The system was designed to enable the automated telescope to perform most of the tasks of an ordinary astronomical telescope. It acquires point sources of light to a given precision; it operates data-acquisition instrumentation; and it takes protective action in the event of potentially harmful contingencies. Automatic control of this system is faster than manual control by an approximate overall factor of 10 because the manual observer does not have access to much of the precise, real-time, monitored information available to the computer.

Communications System Description

The digital communication system is based upon a one-second "frame" time. It enables the telescope to fill six 32-bit shift registers, to transmit their contents twice each frame, and to strobe and to transmit the contents of 30 11-bit analog-to-digital channels to

RI 708-07A

the computer once each frame. There are 15 32-bit storage registers at the telescope that are filled sequentially once each frame by a 32-bit shift register accepting serial command bits from the computer.

The input to the computer arrives serially from the data link and is fed into a 22-bit shift register, which, when full, is dumped into a 22-bit storage register that can be parallel-accessed by the high-speed (24-microsecond) input/output buffer of the computer. Output from the computer is parallel through the high-speed input/output buffer to a 22-bit output storage register, parallel to a 22-bit output shift register, and serial into the data link. Because the computer has no "interrupt" capability, protection against loss of data-servicing sync is accomplished through "overflow" flip-flops, on both input and output, available as flags to the computer.

The serial output-data rate from the computer to the mountain is 512 bits per second. The serial input-data rate to the computer from the mountain is 1024 bits per second. Each input and output frame requires one parity bit, 20 "phase select" bits, and an 11-bit "Barker Word" for frame sync. The input frame contains 714 data bits and 278 unused bits; the output frame contains 480 data bits (fig. 1).

System Timing

The system software must be compatible with hardware timing restrictions. The communications system is serial; therefore, the data can be distinguished only by its position in a frame. Because any given information bit can be received only once each frame, all real-time control must allow for one-second increments in both commands and monitors.

During the frame, there are two shorter cycles that restrict the software. One of these short cycles is in the computer itself. The Raytheon 250 computer is a serial machine with magnetostrictive delay-line memory and registers. Its memory-line cycle time is 3 milliseconds; hence, interrupts are not feasible. The other short cycle is determined by

the 22-bit input and output registers in the communication system at the computer terminal. They require servicing by the computer so that their serial stream of outgoing and incoming data remains unbroken. The 22-bit storage register plus the 22-bit shift register at 1024 bits per second allow time blocks, between servicing, of approximately 44 milliseconds.

This time must be reduced by four computer machine cycles: two cycles to allow for lack of sync between the data cycle and the computer cycle and two cycles to allow the computer the time necessary to carry out all the housekeeping functions servicing the on-line input/output devices. Under these timing restrictions, the frame was broken up into 23 blocks of computer time, each block being 32 milliseconds long. Since the optimized "word time" of the computer is 24 microseconds, there were up to 1,500 operations possible during each block; and there were up to 34,500 operations possible for the on-line software during a one-second frame. (Only 6,000 on-line operations were needed to operate the system. Another 2,000 might have been added for on-line data reduction.) The two computer machine cycles involved in data sync were salvaged for on-line output to an asynchronous high-speed punch (fig. 2).

Computer Interrupts

The Raytheon 250 computer is a serial machine without interrupts; however, even if a computer with interrupt capability were used, there would be little advantage in servicing a serial data link. Experience in the system indicates that interrupts would be advantageous only with parallel data links and only when a well-defined hierarchy of priorities can be assigned.

Computer Limitations

Computer speed was not a limitation in this system. The primary computer limitation was memory capacity. The total of 9,000 22-bit words imposed a restriction against any major on-line data reduction. There are about

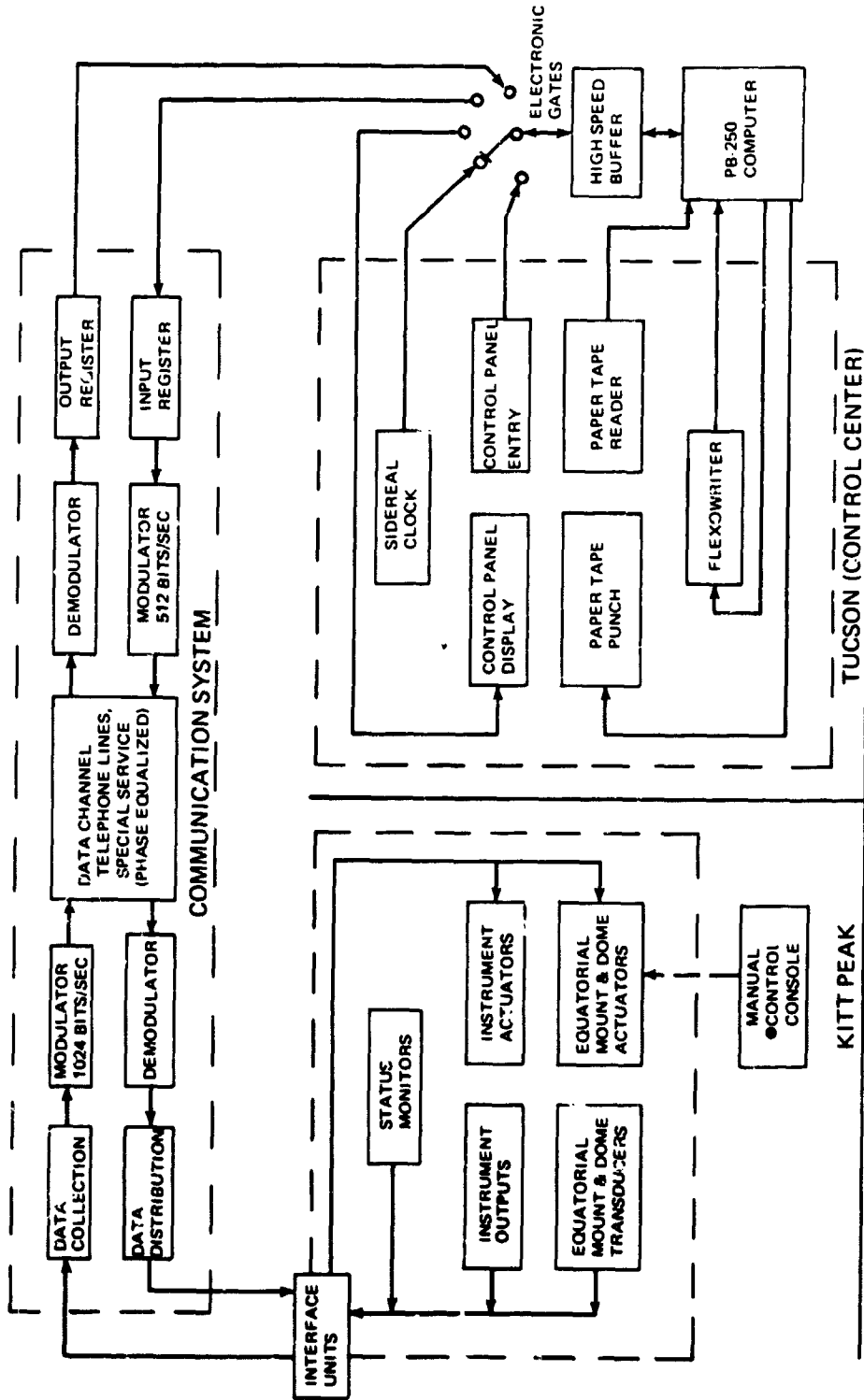


Figure 1. System block diagram of 50-inch automatic telescope.

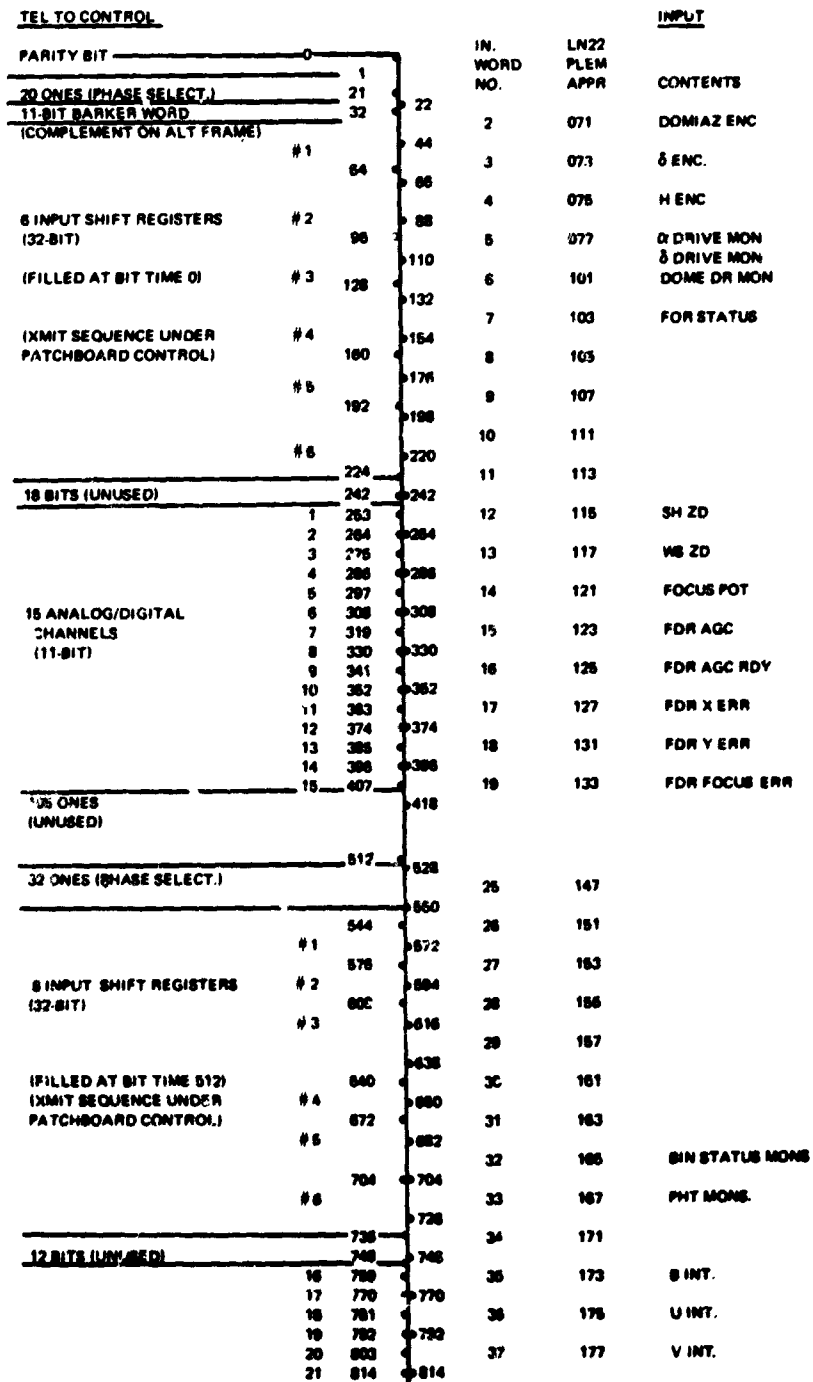


Figure 2. Remotely-controlled-telescope (RCT) system frame (one second real-time).
(Sheet 1 of 2)

KITT PEAK AUTOMATIC TELESCOPE

665

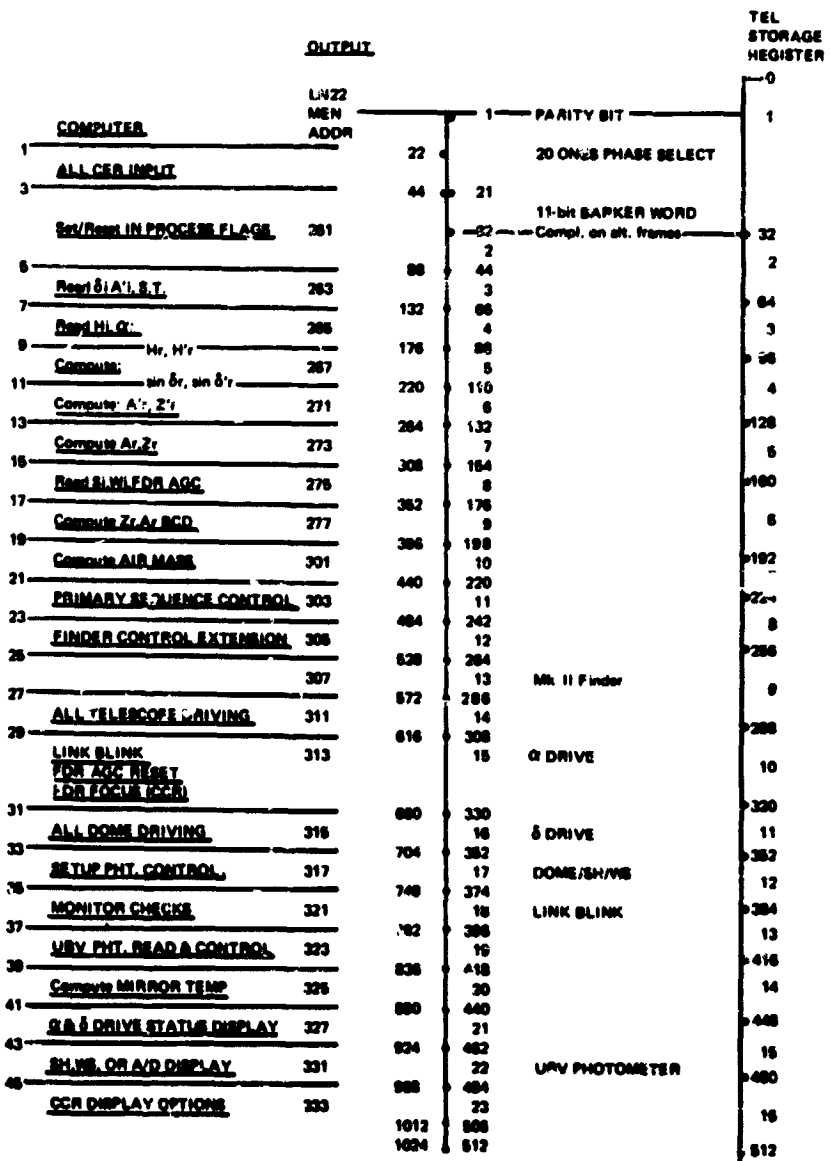
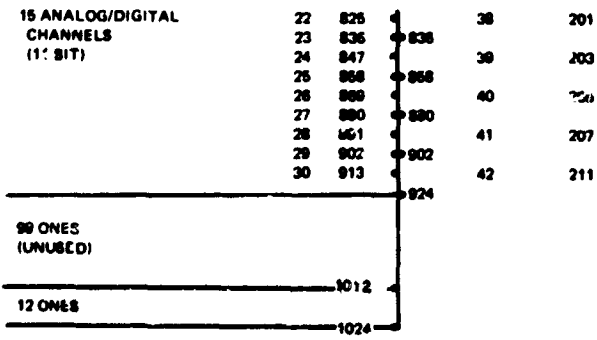


Figure 2. Remotely-controlled-telescope (RCT) system frame (one second real-time).
(Sheet 2 of 2)

1,500 words occupied by essentially off-line debugging and hardware testing programs that could be put on tape outside the computer during on-line operation. If this were done, however, any on-line program filling those positions could not be software debugged; and any marginal system-hardware failure could not be checked without writing over part of the control program. This experience indicates that any modern computer used to control a system of this complexity should have a fast, multiheaded, peripheral disk memory to relieve its core of all programs and data not on immediate on-line call.

One other important limitation of the Raytheon 250 computer was the requirement that all the software be written in machine language. This was necessary (1) because the system is primarily logical instead of arithmetic, (2) because the programs must be optimized for speed (a time factor of 128 is involved), and (3) because the memory capacity is small. This language limitation meant that the final, complete, software system required two years for an experienced programmer to design and write. A system of equivalent complexity might be written for a modern core machine with a good assembly language in only about 8 man-months of time.

Data Link Limitations

Although the one-second serial data frame requires some delay, received data or transmitted commands need not be delayed a full second. All information in this system can be more current if the data and the commands are scheduled properly in the frame so that receipt, computer response, and transmission follow sequentially. The layout of useful bits in this frame imposes the following minimum delays: 64-millisecond data generation/receipt, 44-millisecond computer response, 32-millisecond command transmission/actuation—resulting in minimum delay time of 140 milliseconds.

Because the mechanical subsystems of the automated telescope are relatively slow, the communication delay is not a significant

problem. A major problem, however, is posed by the fact that a full second must elapse between any given "data-response-command" sequence. The motor drives and the data acquisition are continuous mode devices, but they must be controlled through an incremental data link. In most cases, it is possible to stop a device short of the target or short of saturation. The solution for these cases is to read "on the fly," to extrapolate differences, and to make the "stop" decision that comes closest to the goal. The cases requiring precision target acquisition are solved by either deliberate sacrifice of time (as in the photoelectric finder) or by buffering through digital counter-registers that store a binary number of "steps" and cause a drive motor to turn until the number is counted down to zero by pulses from an incremental shaft encoder.

Target Acquisition

The computer can point the telescope to a desired star by commanding it to a position where the telescope coordinates, as measured by the 16-bit right ascension and declination shaft encoders, are equal to the tabulated coordinates of the star. However, the residual uncertainty in the position of the stellar image, due to telescope flexure, encoder-telescope misalignment, least-significant-bit quantization error of the encoders, and sidereal clock error, is too large for most purposes. It is therefore necessary to provide a photoelectric star finder to enable the system to position the image more accurately. This instrument is called a "finder," rather than a "guider," because it does not control the position of the image during observation. Instead, the entire telescope beam is diverted first to the finder, which supplies the computer with image-position information for aiming the telescope. When this has been accomplished, the full telescope beam is allowed to enter the observing instrument. During the observation, the sidereal drive of the telescope maintains the image in its proper position. The observations made with

the automatic telescope are of relatively short duration, there is no present need to provide a beam-splitting device to permit closed-loop guiding of the telescope during an observation.

Finder Outputs

The finder has two analog outputs, which vary linearly with the rectilinear components of the displacement of the target star from the center of the finder field. These error voltages vary between zero and 5 volts, with on-target (or null) values of 2.5 volts; this range is dictated by the 0-to-5-volt input range of the analog-to-digital converter in the system. For a moving image, the output voltages do not vary smoothly; instead, they are updated every two seconds and held until updated again, resulting in stepwise changes in these error voltages.

In addition to position information, the finder can indicate the approximate target brightness (magnitude), the image size (focus or seeing quality), and whether or not there is a strong enough star in the field to make the position signals valid.

The finder has two field sizes, 5 arc minutes and 30 arc seconds. The field size to be used in any given situation is determined by the requirements that the target star be in the field and that all background stars in the field be somewhat fainter than 0.3 magnitude beneath the target star.

Open-Loop Offset

A further option is target acquisition in the "open-loop offset" mode. Since the incremental shaft encoders are located on the main-drive worm gear, it is possible to find a bright star by using the absolute 15-bit encoders and the finder and then to offset to a target whose brightness is beneath the threshold of the finder (12th magnitude). The reach of this open-loop mode is limited to about a 3-degree range from the bright star; the data acquisition time is limited by the accuracy of the sidereal drive to about one minute. To date, there has been very little operational experience with this mode.

Philosophy of System Software

The design philosophy for the software developed into the simple principle that no operational limitation in the system should be due to software. This requires that the system must be strictly hardware-limited, both within any given mode and among any new modes.

Two ideas, primarily, make this possible: modular software and macrocommands. Vertically, the software is a multilayered structure of subroutines. Horizontally, each major-subsystem control program is separate, removable, or modifiable, independent of the others. Each of these major programs is designed to be small in size by making maximum use of common subroutines. The macrocommand is a simple, practical input technique with a very high information content.

General Description of System Software

There are five basic types of operator commands:

1. Transfer program control.
2. Set up parameters.
3. Set up labels.
4. Set up control sequence (macrocommand).
5. Initial on-line operation.

All of these operator commands have an identical three-part format: first, an alphabetical character to define the class of the command; second, a set of numerical characters to define elements within the class (this set is empty in some classes); third, a carriage return code (c/r), which is the "GO" signal enabling the command. This format is simple, versatile, and tolerant of operator error.

Examples of System Software

The most versatile operator command is the Primary Control Sequence. It is a macrocommand that provides the operator with customized input for his specific control problem. The macrocommand is a sequence of from zero to ten elements. Each element

calls a command routine controlling a single, major, hardware subsystem. The elements are sequential in time; that is, they do not usually operate concurrently in the system. Since there may be as many as ten different elements each in as many as ten different positions in the macrocommand sequence, the operator has the option of 10^{10} different control modes.

From the operator's point of view, the Primary Control Sequence macrocommand requires three to twelve characters chosen from a brief table of element descriptions.

One subsystem complex enough to require control by its own macrocommand is the photoelectric finder.

Any data acquisition instrumentation involving a complex time sequence would also require a macrocommand. The UBV photometer, however, is adequately controlled by a nine-digit parameter setup wherein each element, distinguished by its position in the command, sets a specific parameter level. The photometer has two dichroic filters dividing the light into three phototubes, each feeding an operational amplifier connected as an integrator. The gain setting of each integrator depends upon which one of its four capacitors is enabled. Output voltage from each integrator is accessible to the computer through an analog-to-digital converter channel. An integrator is said to be filled when its output voltage is just under the saturation level of its 11-bit analog-to-digital channel.

On-line computer control of this instrument creates two particularly useful features. The computer is able to determine the proper gain setting for each of the three colors, independently, in only four seconds time. The computer is also able to monitor each of the three integration rates and to keep a running absolute sum of the second differences, which indicates a measure of the quality of the observation.

Each of the three colors has a selection of four gain settings that span an intensity range of 10^4 . The operator commands a maximum integration time; then, if he does not want to select each gain setting himself, he can command the computer to determine the proper gain for each of the three colors ac-

ording to one of these two criteria: (1) to guarantee that the integrators will be filled within the specified maximum time or (2) to guarantee that the integrations will continue throughout the specified maximum time. The first criterion is usually chosen for bright stars; the second is chosen for faint stars. The computer, watching the integration, stops any integrator just before saturation is reached.

The absolute sum of the second differences read during a truly linear integration should be zero except for least-significant bit errors. Any deviation from this low level can indicate spotty thin clouds, marginal integrators, or a number of other phenomena that result in poor quality observations. (See figs. 3 and 4.)

System Reliability

At first, the Raytheon 250 computer was the least reliable part of the system. Later experience, however, demonstrated that an adequate solution to this reliability problem is to have an imaginative, competent, on-site technician and a set of good test routines. After the first year, preventive maintenance techniques reduced computer downtime to a level equivalent to that of the other hardware.

From the very beginning, the Astrodata communications system has proved to be the most reliable part of the system. It was conservatively designed, and it has contributed an insignificant percentage to the downtime over a span of nearly 7 years. On the other hand, the telephone lines have proved to be sensitive to bad weather, which causes mostly spike noise.

Most "bugs" appeared in the electro-mechanical subsystems, especially those exposed to environmental extremes in the dome. These bugs are generally caused by initial design, corrosion, or wear and fatigue.

The large number of monitors accessible by the computer has contributed much to reduction of system downtime. These monitors are checked on-line by the computer for marginal or incipient failure; nearly a hundred detailed typewriter messages are available to the computer for alerting the operator. (See figs. 5, 6, and 7.)

RCTS 23

MAIN CONTROL SEQUENCE INPUT COMMAND

Prefix character: "s"

Elements: from zero to ten decimal digits, each representing a control mode in a sequence.

Final character: "c/r"

CONTROL MODE CODES

- 0: System goes to STANDBY and remains there until manually returned.
- 1: TELESCOPE and DOME are directed toward target coordinates using shaft encoders only.
- 2: Mark II FINDER sequence is begun.
- 3: UBV PHOTOMETER is operated as previously setup.
- 4: An OPEN LOOP OFFSET is effected, in magnitude equal to an amount previously commanded.
- 5: A DELAY COUNTER counts down to zero from some previously set value, holding the system in stasis until the countdown is completed.
- 6: TELESCOPE is directed toward target coordinates; DOME is held in stasis.
- 7: DOME/SHUTTER/WINDSCREEN is directed toward target coordinates; TELESCOPE is held in stasis.
- 8: PASSIVE WATCH monitors and D/S/W inhibited NO STBY & NO TEL DRIVE.
- 9: Unused code

Figure 3. Main-control-sequence input command and control mode codes for remotely controlled telescope system (RCTS).

RCT 25C

PHOTOMETER INPUT COMMAND

PRELIMINARY CHARACTER i: FIXED GAINS or l: AUTO GAINS
(requires 2 or 4 extra seconds)

FIRST DIGIT: **OUTPUT FORMAT**

- 0 = LONG FORMAT ALL
- 1 = SHORT FORMAT ALL
- 2 = LONG FORMAT PUNCH & SHORT FORMAT TYPEWRITER

SECOND DIGIT:	OUTPUT DEVICE	
	0 = NO OUTPUT (TEST)	5 = FLEX TYPEWRITER & HSP
	1 = FLEX TYPEWRITER	3 = FLEX TYPEWRITER & FLEX PUNCH
	2 = FLEX PUNCH W/CH 8 PARITY	6 = FLEX PUNCH & HSP
	4 = HSP OFFLINE W/CH 8 PARITY	7 = FLEX TYPEWRITER & PUNCH & HSP
THIRD DIGIT:	APERTURE SIZE	
	0 = SMALL	
	1 = LARGE	
FOURTH DIGIT:	MOST SIGNIFICANT DECIMAL DIGIT	MAX TIME IN SECONDS OF INTEGRATION (LIMIT 511 secs or 8½ mins)
FIFTH DIGIT:	DECIMAL DIGIT	
SIXTH DIGIT:	LEAST SIGNIFICANT DECIMAL DIGIT	
SEVENTH DIGIT:	(FIXED GAIN) U GAIN	
	1 = SET TO #1 LARGEST CAPACITOR (brightest stars)	
	2 = SET TO #2	
	3 = SET TO #3	
	4 = SET TO #4 SMALLEST CAPACITOR (faintest stars)	
	(AUTO GAIN)	
	1 = Tmax priority (T = Tmax) (1/10 Vmax < V < Vmax)	
	0 = Vmax priority (V = Vmax) (1/10 Tmax < T < Tmax)	
EIGHT DIGIT:	B GAIN (do not use after I)	
NINTH DIGIT:	V GAIN (do not use after I)	
FINAL CHARACTER:	c/r signifies that the previous consecutive 7 or 9 digits are correct.	
NOTE:	Vmax is set off-line through the OUP by inserting 2VU @ Q ₂₁ into [160/17] (5V = 3777 BVU).	

Figure 4. Photometer input command for remotely controlled telescope (RCT).

<i>Dome Command Field</i>		<i>Telescope Command Field</i>	
± Dome Az	SLEW INCH	± RA:	FAST SLEW 3°/sec SLOW SLEW 30'/sec COARSE DDR 100"/sec FINE DDR 5"/sec
SHUTTER	UP DOWN	± DEC:	FAST SLOW COARSE FINE
WINDSCREEN	UP DOW.	FOCUS:	IN OUT
STOW		TRACK STOW SECONDARY MIRROR COVER:	OPEN CLOSE
<i>Dome Monitor Field</i>		<i>Telescope Monitor Field</i>	
Dome Azimuth Encoder, 10 bit Gray		R. A. Shaft Angle Encoder, (16-bit Gray Code ±20 arc sec)	
Shutter Altitude, 0-5 volt pot, 11 bit A/D		DEC Shaft Angle Encoder, (16-bit Gray Code ±20 arc sec)	
Windscreen Altitude, 0-5 volt pot, 11 bit A/D		Photoelectric Finder Large Field, ±4 arc sec	
Observing Platform, Parked or Not Parked		Photoelectric Finder Small Field, ±1 arc sec	
System Manual or Auto		Focus error, minimum → good focus	
Emergency Stop		RA Drive Status & Limit Switches	
Weather: Rain Dew Snow Wind Daylight		DEC Drive Status & Limit Switches	
Mirror Temperature, 0-5 volt, 11 bit A/D		DEC Drive Status & Limit Switches	
All Power Supplies, ok or not ok		Photoelectric Finder Status	
		Secondary Mirror Cover, open or not open	
		Digital Drive Registers, empty or not empty	
		System, stowed or not stowed	

Figure 5. RCT dome command and monitor fields; telescope command and monitor fields.

<i>UBV Photometer Command Field</i>						
Start Integration:	START UBV					
Stop Integration:	STOP U STOP B STOP V					
U Gain Setting:	<table border="0"> <tr><td>#1 - 10^1</td><td rowspan="4">} Gain Factors</td></tr> <tr><td>#2 - 10^2</td></tr> <tr><td>#3 - 10^3</td></tr> <tr><td>#4 - 10^4</td></tr> </table>	#1 - 10^1	} Gain Factors	#2 - 10^2	#3 - 10^3	#4 - 10^4
#1 - 10^1	} Gain Factors					
#2 - 10^2						
#3 - 10^3						
#4 - 10^4						
B Gain Setting:	<table border="0"> <tr><td>#1 - 10^1</td><td rowspan="4">} Gain Factors</td></tr> <tr><td>#2 - 10^2</td></tr> <tr><td>#3 - 10^3</td></tr> <tr><td>#4 - 10^4</td></tr> </table>	#1 - 10^1	} Gain Factors	#2 - 10^2	#3 - 10^3	#4 - 10^4
#1 - 10^1	} Gain Factors					
#2 - 10^2						
#3 - 10^3						
#4 - 10^4						
V Gain Setting:	<table border="0"> <tr><td>#1 - 10^1</td><td rowspan="4">} Gain Factors</td></tr> <tr><td>#2 - 10^2</td></tr> <tr><td>#3 - 10^3</td></tr> <tr><td>#4 - 10^4</td></tr> </table>	#1 - 10^1	} Gain Factors	#2 - 10^2	#3 - 10^3	#4 - 10^4
#1 - 10^1	} Gain Factors					
#2 - 10^2						
#3 - 10^3						
#4 - 10^4						
Photometer	LARGE					
Diaphragm:	SMALL					
Enable Start Integration:	READY—must precede START command by 30 ms NOT READY					
<i>UBV Photometer Monitor Field</i> is one-to-one with the UBV Command Field, delayed by one data frame time (1 second).						

Figure 6. *UBV photometer command and monitor fields for RCTS.*

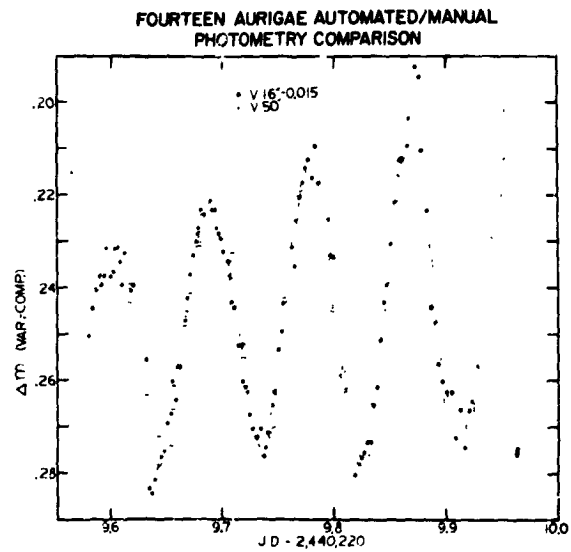


Figure 7. *Automated/manual photometry comparison of 14 aurigae. (Courtesy of Kitt Peak National Observatory.)*

N70-36749

Considerations for Digital Image-Processing

F. C. Billingsley

California Institute of Technology

Introduction

In recent years the ability to process images to emphasize details, to sharpen the picture, to modify the tonal range, to aid picture interpretation, to remove anomalies, and to detect differences between pictures has evoked interest. This paper is a discussion of the kinds of processing that can be accomplished, a discussion of some of the parameter boundaries and limitations, and a discussion of some of the system techniques that have proven helpful at the Jet Propulsion Laboratory (JPL).

The two prime contenders for image-processing are digital processing and coherent light processing (ref. 1). In general, it can be stated that the main advantages of a coherent optical system are its efficient storage of the large amount of data in a picture and the high processing speed due to the implicit parallel processing of all elements simultaneously. Coherent processing is rather touchy to operate properly. It is subject to anomalies and cannot handle nonlinear problems. In addition, the large aperture systems required have relatively high cost.

Digital processing has the advantages of being extremely flexible and of being rather trouble-free and easy to use once the programming system has been worked out. It has the ability to handle problems that are nonlinear in both intensity and geometry and can do these with an accuracy limited only by the user's knowledge of the incoming data. To gain the advantages of digital processing requires high-quality signals with low noise and accurate, associated analog-to-digital conversion equipment. This equipment for

either scanning film or digitizing analog magnetic-tape signals is fairly expensive and requires appreciable time to operate. Although the possible high cost of a digital computer system is a potential disadvantage, this cost can be traded for processing speed by using a smaller computer that will require longer to do the processing.

The remainder of this paper will assume that the data will be reduced to digital form for computer processing. The discussion applies to image-processing in general, regardless of the specific field of application. For example, the concept and understanding of the requirements of image-processing have been developed for the processing of pictures as returned from the NASA space vehicles to the Jet Propulsion Laboratory. In general, these same concepts and, to a very large extent, even these same specific programs have been utilized to process pictures from the electron microscope, light microscope, medical and industrial x-ray photographs, various telescope pictures, and others.

Examples of Digital Processing

Table 1 breaks down the broad area of image-processing into six applications areas with some examples of the kinds of processing that may be applied in each.

Generation

Figure 1 is a computer-generated test target used in the testing of the MM'69 TV camera systems. It contains a number of sinusoids of transmittance (in the positive transparency actually used in test) of various

Table 1. Some Uses for Image-Processing

Area	Technique	Uses
Generation	Computer-Originated	Test Targets Graphical Displays
	Computer Substitutions	To Insert Windows in Pictures To Insert Good Data for Bad
Intensity Manipulation	Intensity Calibration of Systems	Photometry
	Nonlinear Lookups	Film Curve Corrections Grey Scale Alterations
	Chromaticity Calculations	Color Shift, Balance, Alteration
Geometric Manipulation	Geometric Calibration of Systems	Good Geometry Needed for Stereo
	Reprojection	To Convert Slant Pix to Gnd Projection
	Overlay Match of Two Pix	Rubber Sheet Stretching
	Independent X and Y Adjustments	Aspect Ratio Corrections
Spatial Frequency Operations	Spatial High-Frequency Boost	To Correct for Detail Losses in System
	Spatial Low-Frequency Reduction	To Minimize Broad-Brush Shading To Remove Effects of Glare
	Single Frequency Filtering	To Remove Coherent Noise
Analysis	Fourier Transform	Analysis in Spatial Frequency Plane
	Image Light Distribution	Star Cluster Analysis
	Pattern Extraction	Counting Blood Cells, Autos, Stars, Etc. Analyzing Shapes of Objects
	Convolution	Filtering, Correlation
Multipicture	Subtraction	Change Detection Stereo Information Extraction
	Addition	Averaging, Noise Removal
	Multiplication	Spatial Domain Filtering
	Division	Normalizing

modulation amplitudes superimposed on various steady-state light intensities, plus several step-changes of intensity for transient response calibration of the camera.

Figure 2 shows a segment of computer-calculated data inserted as a window in a picture. The picture is an electron micrograph of a catalase crystal showing a number of artifacts due to the heavy metal staining. The repeating structure was located by computer analysis of the original and was substituted for one repeating image cell.

Intensity Manipulation

Typical TV camera tubes have a spatially nonuniform response to light. Accurate photometry requires that the response-versus-light-level calibration curve be known for each picture element, called a *pixel*. Application of the corresponding curve at each pixel point will recover the true light value at that point. Figure 3 illustrates this technique as applied to a Surveyor picture. The shading of the ground brightness from left to right at the top

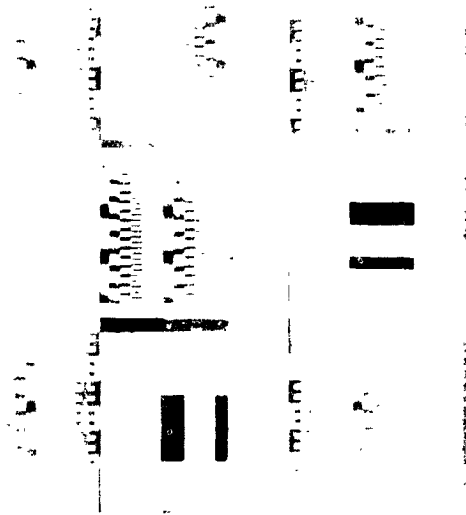


Figure 1. Computer-generated test target.



Figure 2. Computer-calculated data inserted in a picture.



2 305 ID * 0344 GMT. 255-00-39-53.
 DIGITIZED *1.
 D.P.R. T.H.P. * 5013 23 SEPT 1967.

(a) Uncorrected.



2 305 ID * 0344 GMT. 255-00-39-53.
 DIGITIZED *1.
 FILTERED 15:15. INI*3. T.H.P. * 5011.
 24 SEPT 1967.

(b) Corrected.

Figure 3. Correction of nonuniform camera response (Surveyor).

of the uncorrected picture has been removed in the corrected picture to produce a uniform ground light level.

The test target of figure 1 has been calculated to produce accurate sinusoids of transmittance in the projected positive transparency. This calculation compensates for the nonlinear density-log exposure curve of both the original recording film and the film on which the transparency is produced. This was done by first producing, by calibration, a nonlinear output/input lookup table, which characterized the entire system, and then applying this table as a prefacto distortion.

Color balance in a picture, or the visual color appearance of a picture, may be shifted by computer manipulation. The Mare Imbrium area of the moon was photographed to show several different ways of illustrating the red-blue color differences (ref. 2). The original pictures were photographed through #29 and #47B filters to produce a red-blue color separation pair. These photographs were digitized, and the digital values were transferred to the log-exposure domain by nonlinear table lookup, using the complete system calibration data. Subtraction of one from the other produced a picture whose values were a measure of hue. This difference picture can be stretched and clipped in various ways to produce varied results. The photographs in figures 4, 5, and 6 illustrate the possibility of separating the color domain into blue, gray, and red areas. In figure 4, the blue areas are rendered white; in figure 5, the gray areas are rendered white; and in figure 6, the red areas are rendered white.

Geometric Manipulation

Typical camera systems will have some degree of geometric nonlinearity. This may be determined by measurement of the distortion in a photograph of a known rectangular grid or a known array of stars. A known grid photographed by the Surveyor camera system before and after correction is shown in figure 7. In the JPL GEOM* program, up to

*Geometric Manipulation



Figure 4. Mare Imbrium area on the moon; showing blue areas in white.



Figure 5. Mare Imbrium area on the moon; showing gray areas in white.



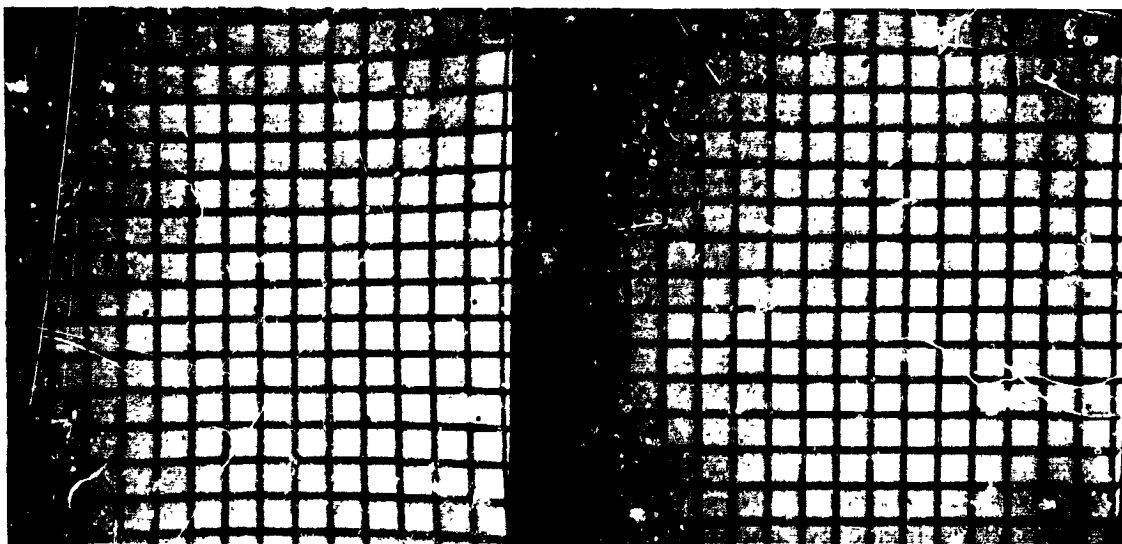
Figure 6. Mare Imbrium area on the moon; showing red areas in white.

100 individual pass-points may be simultaneously shifted, with automatic computer interpolation of all in-between points.

The GEOM type of program may be used to reproject a photograph for rectification or other purposes. Figure 8 illustrates the rectification of a Ranger IX photograph to produce true ground coverage. Figure 9 illustrates the application to an earth-based photograph of a building.

Comparison of two pictures requires accurate overlay matching. Figure 10 is the difference picture of the Mare Imbrium area as produced with incorrect and correct registration. In this specific case, registration was obtained by horizontal and vertical translation plus rotation. In the general case, a change in magnification might also be present.

Due to various factors, it may well occur that the horizontal and vertical spacing of the picture elements should be independently varied for aspect ratio corrections. The Surveyor pictures of figures 3 and 7 contain 684 samples per line and 600 lines. The vertical and horizontal spacing have been adjusted to produce the correct aspect ratio of the reticle marks and are quite unequal.



(a) Before correction.

(b) After correction.

Figure 7. Correction of geometric camera distortion (Surveyor).

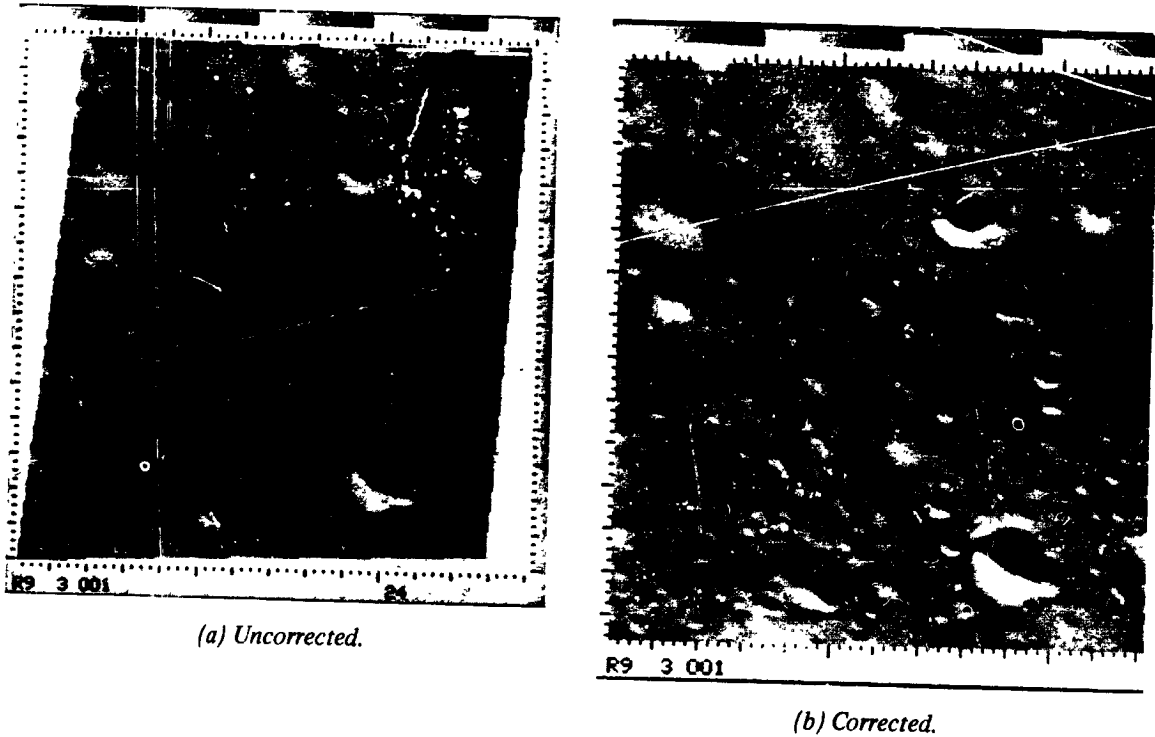


Figure 8. Use of geometric correction for rectification (Ranger IX).

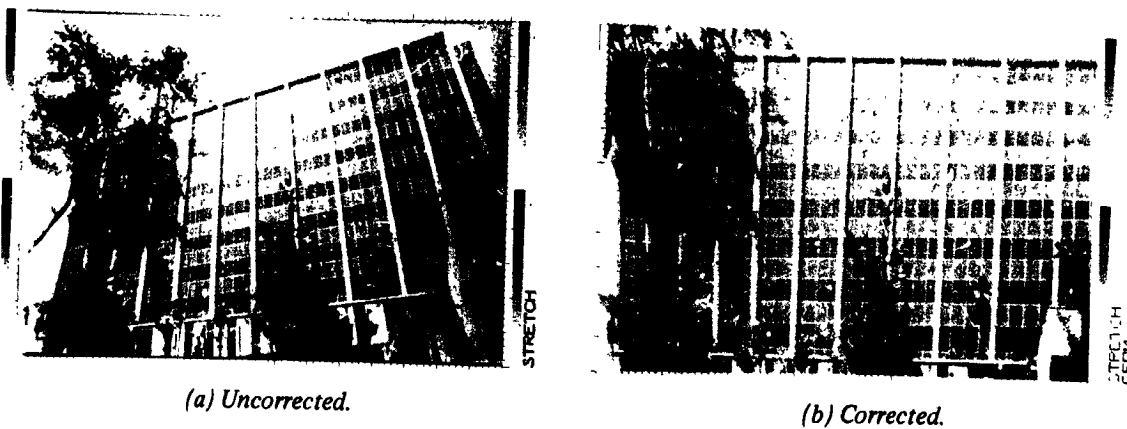


Figure 9. Use of geometric correction for correction of perspective.

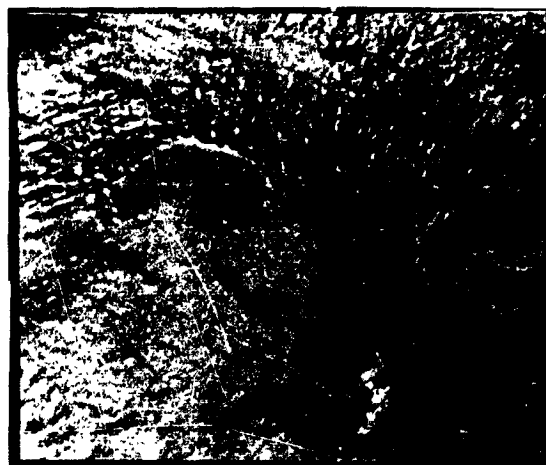
Spatial Frequency Operations

High spatial-frequency response of a system is commonly limited within the pass-band defined by the Nyquist sample spacing, thus resulting in a loss of high-frequency detail. The amount of this loss may be

measured in the X and Y directions by photographing sinusoidal test charts, such as shown in figure 1. The two-dimensional inverse of this roll-off curve is produced and then Fourier-transformed. Next, it is applied by convolution to the picture, resulting in a

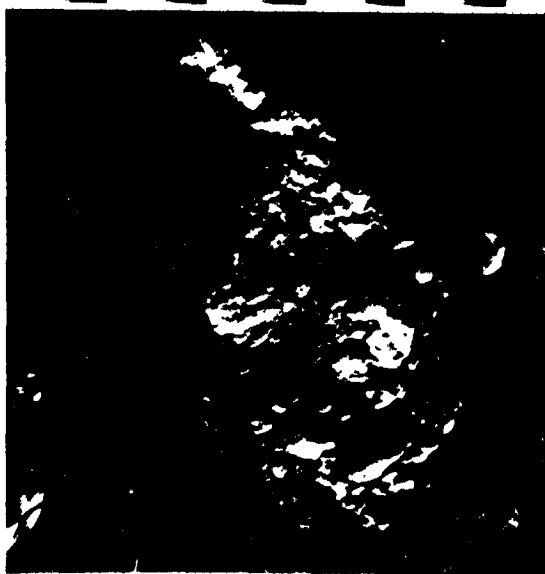


(a) Registered.



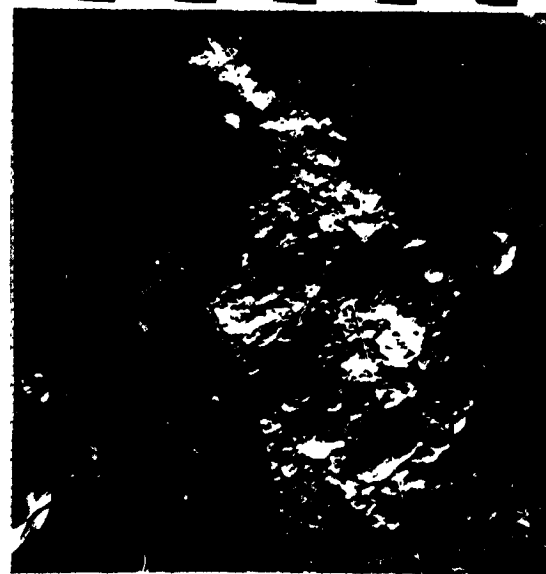
(b) Nonregistered.

Figure 10. Illustration of effects of nonregistration.



11 40442 194-15-24-34 P44 3843

(a) Before enhancing high frequencies.



11 40442 194-15-24-34 1HPF 3843

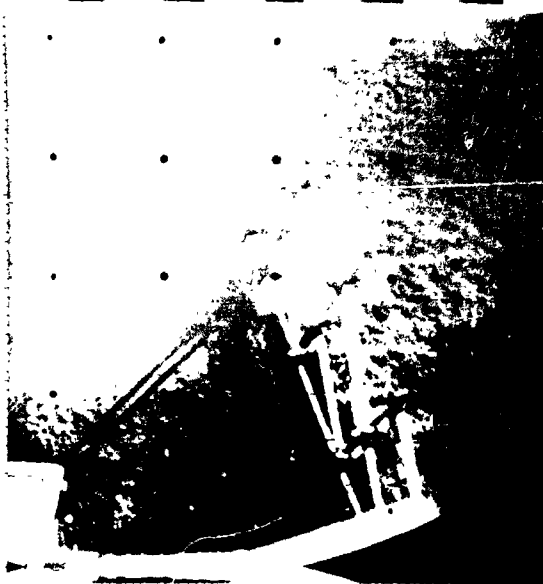
(b) After enhancing high frequencies.

Figure 11. Picture sharpening by enhancement of high frequencies.

restoration of the high-frequency details. The effect of such a process is shown in figure 11.

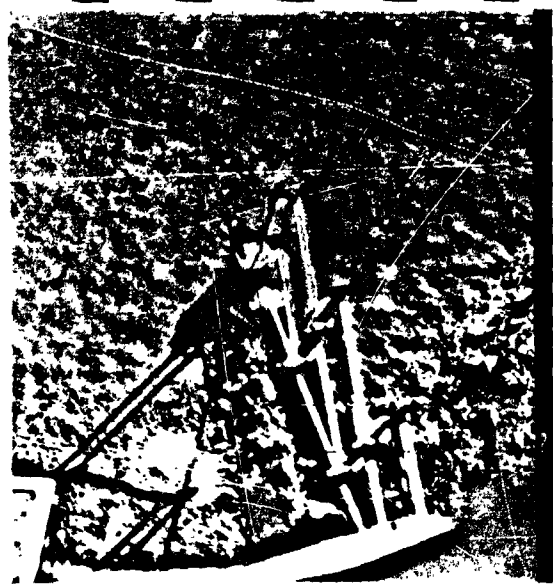
Other manipulation in the spatial frequency domain may be accomplished. Figure 12 illustrates the removal of glare from

a Surveyor III picture by a partial elimination of the low-frequency components. The low-frequency components may be completely eliminated, as shown in figure 13, resulting in the loss of all shading and the reproduction of



53

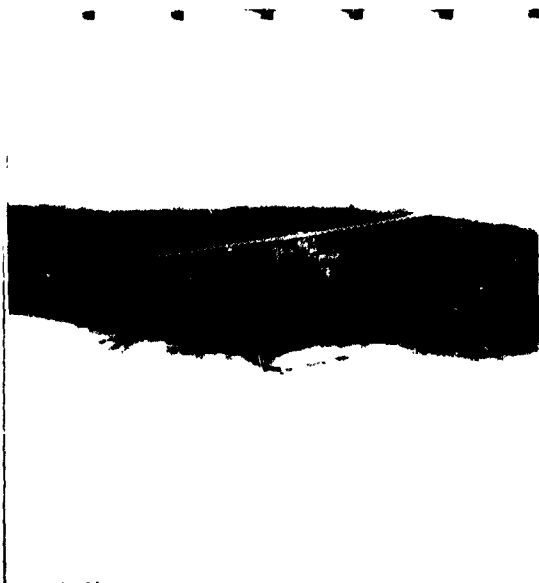
(a) Before partial removal of low frequencies.



54 AFTER GLARE FILTER

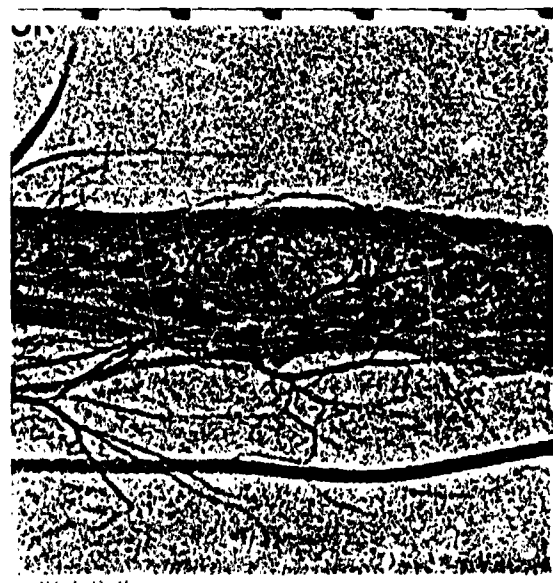
(b) After partial removal of low frequencies.

Figure 12. Removal of glare by partial removal of low frequencies.



55

(a) Before removal of all low frequencies.



56

(b) After removal of all low frequencies.

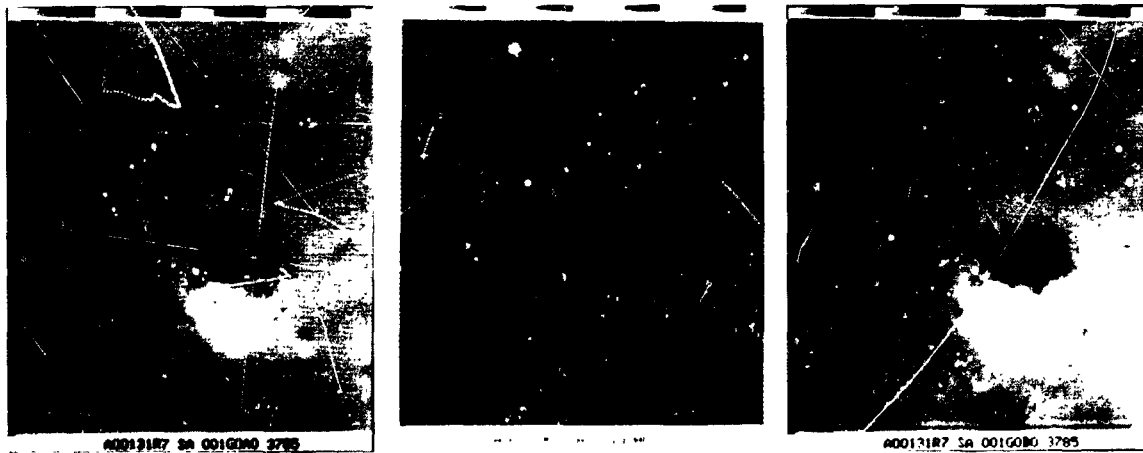
Figure 13. Edge enhancement by removal of all low frequencies.

only fine details and edges. Figure 13 shows the enhancement of this fine detail in the x-ray photograph of a tumor of the arm.

The spatial frequencies to be removed may be isolated sinusoids. Figure 14(a) is a portion of a Ranger VII picture in which a sinusoidal interference is present in the transmitted picture. A convolution filter was used to isolate this noise, which is shown alone in figure 14(b). After isolation, it may be subtracted from the original to produce the picture shown in figure 14(c).

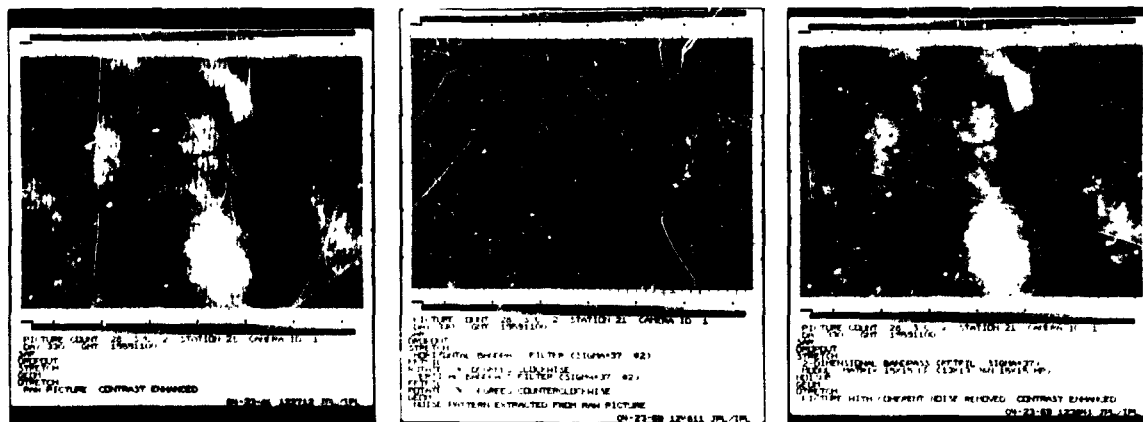
Analysis

The MM'69 camera system produces a picture with considerable noise, as illustrated in figure 15(a). A one-dimensional Fourier transform is taken of each line, and the results are averaged and plotted in figure 16. The strong noise frequencies are apparent; they are isolated in figure 15(b). In this particular exercise, a Fourier-domain filter was designed to eliminate the noise spikes with the results shown in figure 15(c).



(a) Original picture. (b) Interference only. (c) After removal of interference.

Figure 14. Location and removal of discrete two-dimensional sinusoids.



(a) Original picture. (b) Noise only. (c) After noise removal.

Figure 15. Multicomponent noise removal.

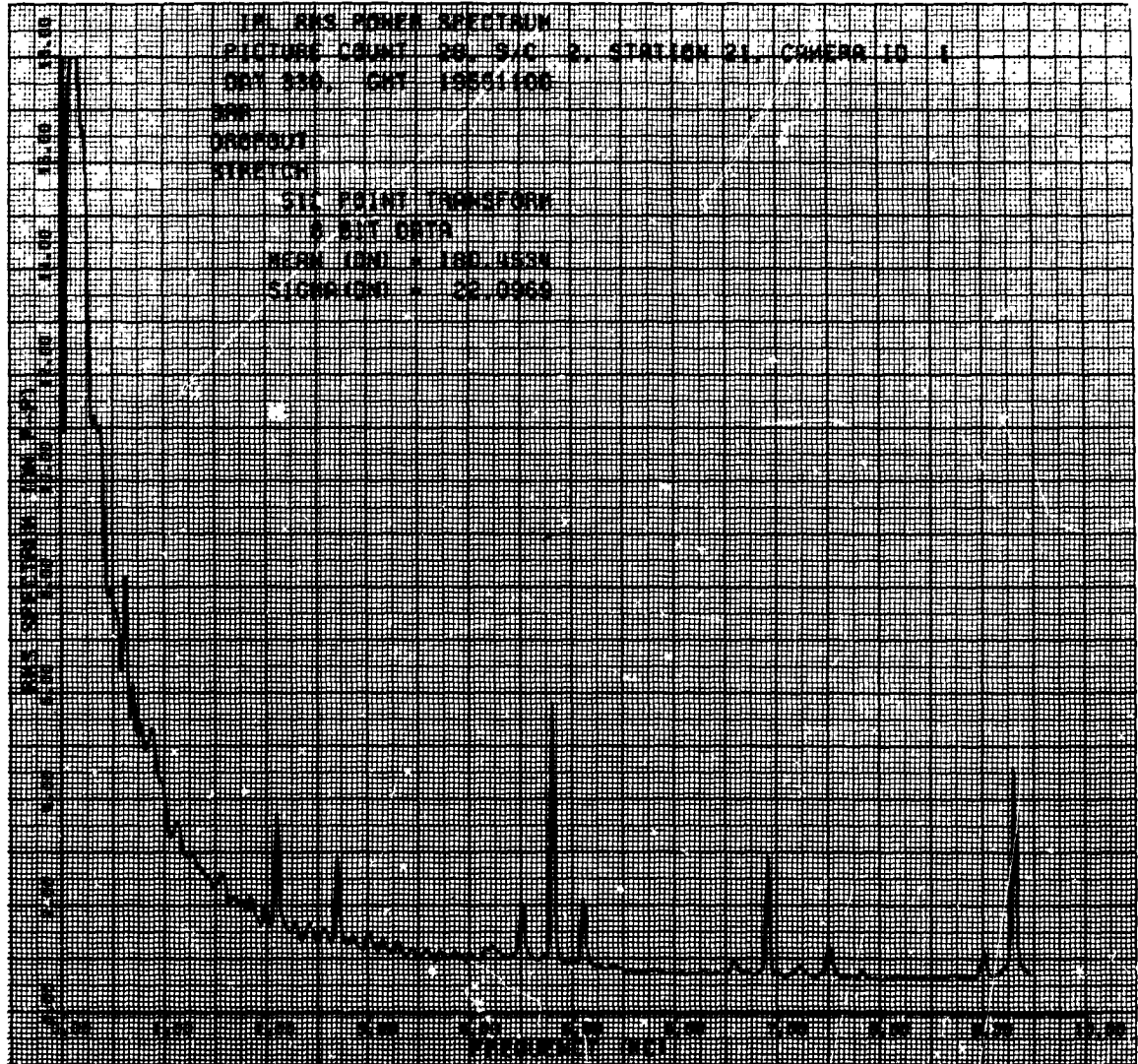
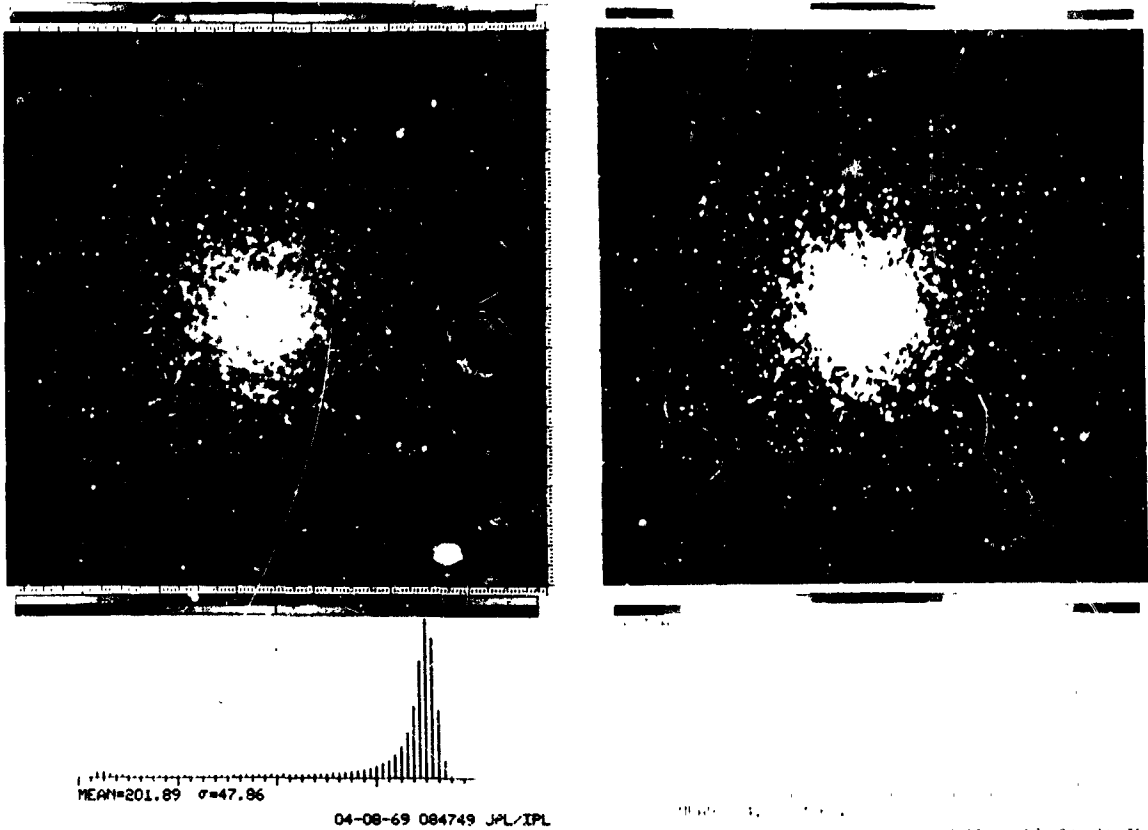


Figure 16. Noise spectrum (horizontal) of the picture in figure 15.

Although the spatial frequency manipulations shown in figures 11 through 14 were produced by convolution, the same effects could have been produced by taking a two-dimensional Fourier transform of the picture, followed by multiplication in the Fourier domain of the desired frequency-response map. This would then, in turn, be followed by a retransform back to the real image domain. This is the procedure used for figure 15. Even

with the Cooley-Tukey algorithm, this is a lengthy procedure, and most practical applications still seem best performed by the convolution method.

The distribution of stars in a number of different star clusters have been analyzed by computer. The digitized pictures are scanned by using a number of different criteria to determine the presence or absence of stars, after which the center of the cluster is located



(a) Original picture.

(b) Result of threshold at 50 percent.

Figure 17. Globular star cluster.

and the spherical distribution of the stars is determined. Figure 17 shows one of the clusters and the application of one of the separation criteria (slicing at 50-percent amplitude). Figure 18 is the data output resulting from the process.

Multipicture Operation

The use of picture subtraction for color-difference determination was illustrated with the Mare Imbrium pictures. Subtraction is also useful for detecting changes, as illustrated in figure 19. Here, motion of cars on a freeway is clearly shown in the difference picture as half-black, half-white objects with all

constant detail cancelling. Translation of one picture causes the subtraction to eliminate vehicles going at the appropriate velocity.

The use of picture addition for averaging was shown in figure 2, the catalase crystal, in which the repeating detail was produced by averaging all of the unit cells of the original picture.

Some Parameter Boundaries

In designing an imaging system, a number of things must be considered more or less simultaneously. Some of these will be found to have rather practical hardware limitations due to the current state-of-the-art,

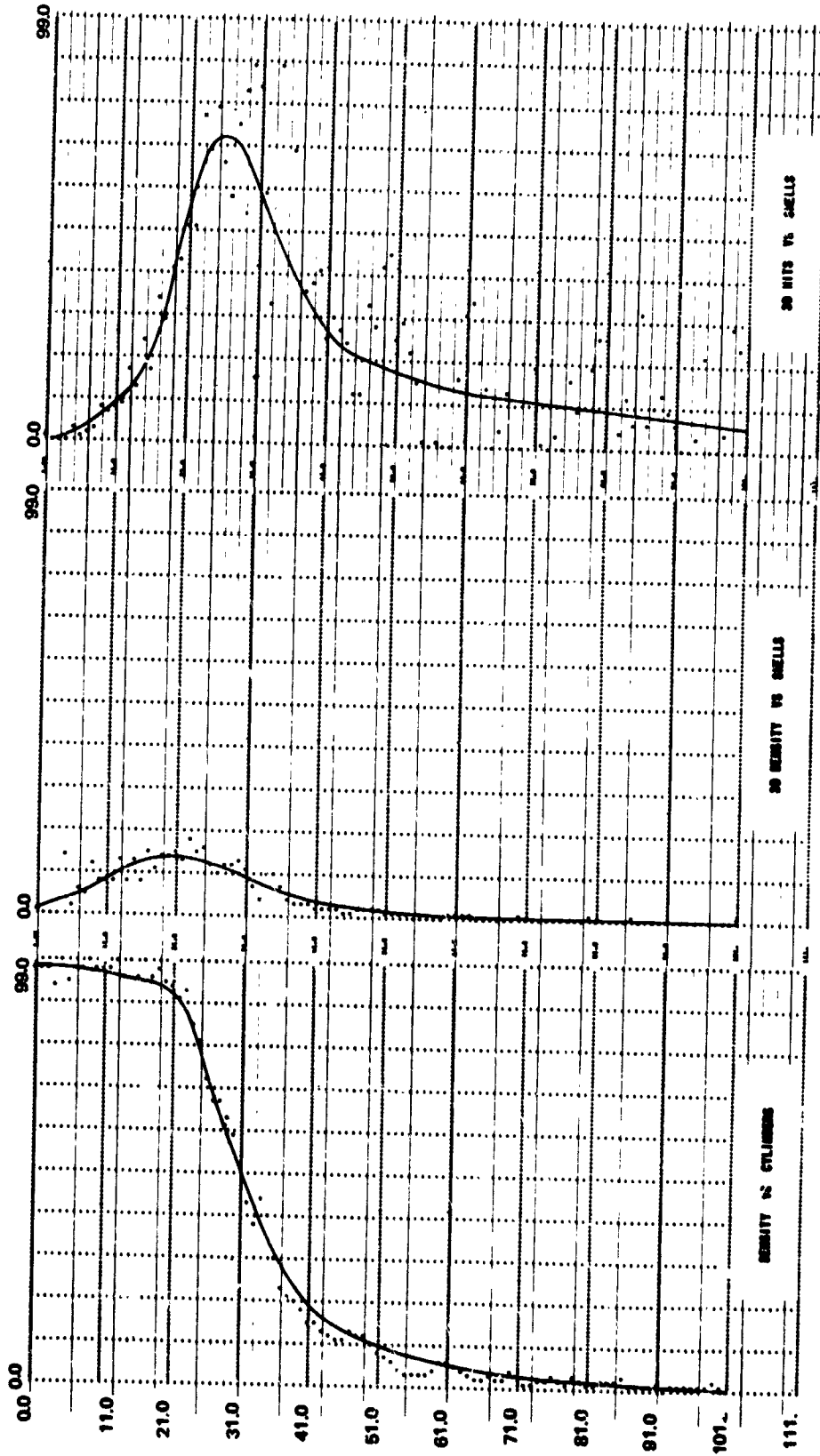


Figure 18. Data output from star-cluster analysis.

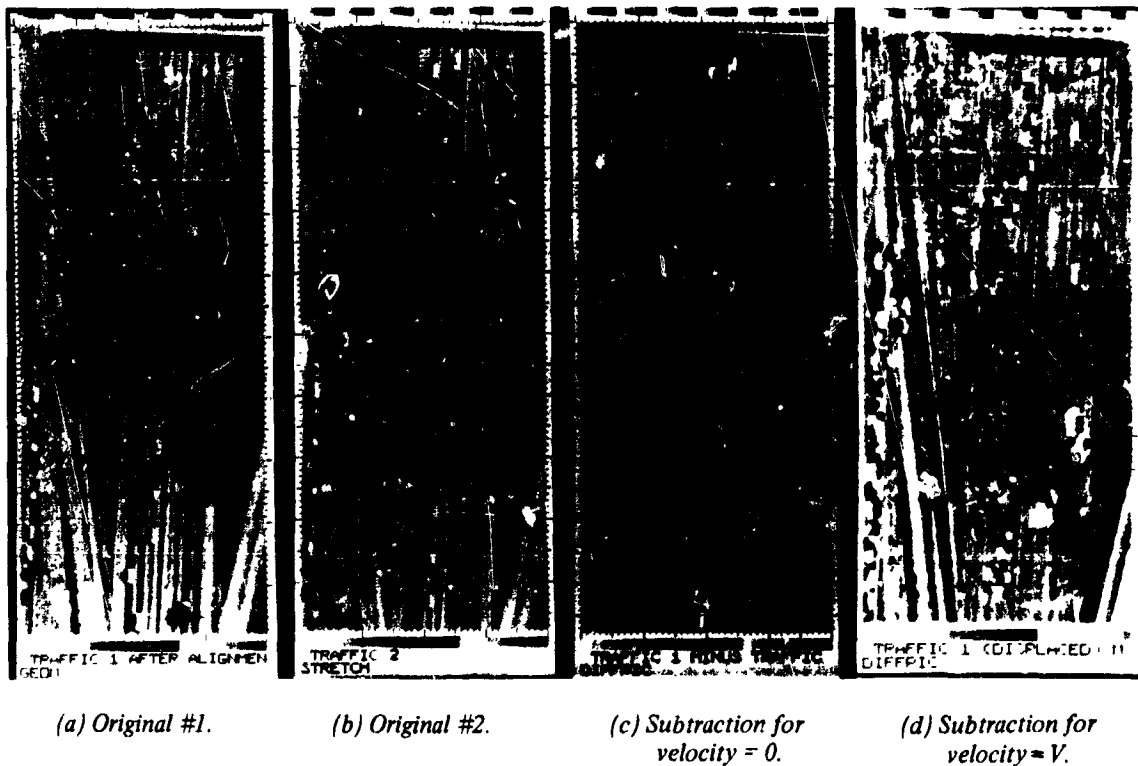


Figure 19. Picture subtraction for motion detection in traffic-motion study.

while others may be open-ended in this respect but limited by cost of implementation.

Briefly, the considerations to be covered in detail are:

Resolution: The sharpness of the image as recorded on film or as presented spatially to the imaging device will determine the required spatial density of sampling points.

Quantizing accuracy: The finer the digital steps used to characterize the points the better. This will ultimately be limited by noise.

Recording considerations: Any film used for recording will contribute noise and therefore is to be avoided, if possible. Some forms of image tube sensors, however, cause even more problems; therefore, a tradeoff between methods is needed.

Data-processing: Minimizations of computer time suggest that a small picture is

desirable, but this limits either resolution or area coverage; hence, another tradeoff must be made. Design of a data-handling system geared to picture-processing will greatly facilitate this procedure.

Conversion to output film: Specifications for film-recording equipment must be quite stringent because very small deviations will cause noticeable artifacts.

Resolution

The quoted or desired resolution in the object domain must be converted to the image domain because this is the quantity of importance to the image-recording system. In general, the resolution will be limited by the imaging optics and by the scanning and reproduction devices. The modulation transfer function (MTF) of the complete system may be found by combining the

MTF's for each of the components (ref. 6). The spacing of the samples in a scanned system (including the line-spacing in a line-scanned system) must satisfy the Nyquist criteria of having at least two samples per cycle of the highest frequency at which there is picture information.

The finite size of the image-scanning spot will further limit the high-frequency response of the overall system. In particular, practical flying-spot scanner systems and camera tubes may have apertures (i.e., spot size) of 10 to 25 micrometers. While, in principle, these apertures may be imaged into the scanning plane at reduced size, in practice, a projection lens of $f/4$ or larger must be used to minimize resolution loss due to lens diffraction limit. This is discussed in detail in reference 7.

Data Quantity

Although, from the viewpoint of minimizing picture information loss and minimizing the possibility of moiré, it is desirable to use as many pixels as possible, minimization of computer operating time dictates that the number of pixels be reduced to a minimum. The practical number of pixels per line is bounded by several parameters:

1. One standard, 2400-foot, digital magnetic tape recorded at 800 samples per inch will hold a picture of about 4000 elements square; this therefore becomes a convenient breakpoint. If the picture is formatted to contain one picture line per digital record, this results in about 4000 records containing approximately 4000 pixels each.

2. Since the processing time increases as the square of the number of pixels per line, it behooves the user to minimize this quantity to minimize computer time.

3. High-resolution cathode-ray tubes for film scanning are generally, but not necessarily, limited to a 7-inch diameter. With a tube of this type, a raster containing as many as 8000 by 8000 pixels can be obtained although a more practical value may be 4000 by 4000. Scanning of the image with a normal camera tube limits the data to approximately

1000 by 1000 pixels although the newer return-beam vidicons promise to raise this limit to 6000 by 6000.

Quantification

A given pixel will be converted to digital form by quantifying it into some number of steps for ultimate digital processing. The quantification is normally in terms of equal increments of light or, in the case of film-scanning, of equal increments of film transmittance. On a high-quality print or a film transparency, the eye can readily discern a difference in quality as produced by four-bit (16-level) and five-bit (32-level) quantifying, but it cannot readily see any extra quality at 6 bits. In order to maintain five-bit quantification of the output of the digital processing, the input quantifying must be at least 6 bits or 64 levels.

It is found that the limiting factor in image-processing is noise. This is particularly true for the high-frequency enhancement that is used to sharpen fine details. For this reason, considerable attention must be devoted to noise considerations.

The quantifier transforms the magnitude of a signal into a discrete number of steps. In a noiseless system, there is no ambiguity in the designation of a particular signal level as a certain digital number. In the presence of noise (assumed to be random), however, it is the signal-plus-noise that is quantified, and the level of the signal alone is somewhat uncertain from inspection of the digital number. As a rule of thumb, the rms noise should be kept between one-half and one-third of the size of one digital step to ensure that the number produced by the quantifying is not perturbed by the noise. This choice of noise limitation is quite arbitrary and produces a probability of correct classification of 0.73.

The signal-to-noise ratio in decibels (SN_{db}) required in the system may be shown to be (ref. 7):

$$S/N_{db} = 20 (\log m + \log 3)$$

where m = number of steps

S = total signal range, black to white

N = rms noise

In a scanned film system, the film grain also contributes to the noise. The maximum allowable rms film noise may be derived (ref. 7) to be:

$$\sigma_D = 0.0005 \times SA$$

where σ_D = maximum allowable rms density fluctuations at $D = 1$ and aperture = 24 micrometers
 SA = scanning aperture diameter in micrometers

Perusal of film specifications will show that normal film has a fluctuation considerably higher than this value for small apertures; hence, the system will be film-limited. For this reason, it is desirable, where possible, to go to direct camera pickup of the light image rather than to use film as an intermediary step. The signal-to-noise of the system may be increased by reducing the system bandwidth. This reduction in bandwidth requires an increase in the optimum sampling pulse width. A good value of the sampling pulse width is given by:

$$T = \frac{1}{2B}$$

where T = sampling pulse width in microseconds and B = bandwidth in megahertz.

Electronic Cameras

It has been indicated that the introduction of a film into the system will result in appreciable extra noise and is therefore to be avoided, if possible. In those instances for which the direct image digitizing time is not satisfactory and where sufficient light for film exposure is available, initial photographing of the image onto film with subsequent film-scanning may be the only alternative. Scanning the photographic film for digitizing purposes to achieve high quality results should be done at slow-scan rates. Scanning at video rate with a TV camera tube can derive only low quality data.

Commercial TV cameras such as closed circuit TV systems generally use a vidicon camera tube. The operating illumination range (known as dynamic range) is low for such

camera tubes and is limited by the signal-to-noise ratio (S/σ) obtainable. The reproduced image from such tubes will possess much noise, especially in the low-light-level areas of the image. Image quality is further degraded by spatial shading and blemishes that are added to the reproduced image by vidicon camera tubes. Slow-scan vidicons have, however, been successfully used by JPL in its lunar and planetary missions (ref. 8).

Typical performance parameters for some candidate cameras are shown in table 2. The high-level illumination listed in the table corresponds to the saturation point of the tube. The threshold level of illumination is set by a S/σ of unity. These two levels define the dynamic range capability of the tube. Resolution values listed in the table are those corresponding to an MTF response of 10 percent.

Because of the inherently poor S/σ of electronic systems at the high bandwidth required for high rate scanning (for example, commercial rate video), the temptation to use a video camera system must be avoided where ultimate digitization and processing is the goal.

Data-Recording

Scanning of either the original image or a film with a scanning system is ultimately required, and the electronic image must be disposed of. Once the image has been converted to electrical form by some type of camera, the signal should be FM-recorded on magnetic tape (if it cannot be quantified in real-time) to minimize degradations in the S/σ ratio. Irretrievable data loss in both noise and resolution occurs in the recording of a signal onto film; hence, film-recording of an electronic camera signal with the intent of future film-scanning should be avoided.

In the best of all possible worlds, the data will be digitized directly during the image-scanning process, thus avoiding all intermediate forms of recording. At moderate digitizing rates (for example, between 10 and 100 kilosamples per second, with the exact

Table 2. Performance Parameters for Some Camera Systems

Camera Tube	Sensitivity* (high light illumination on faceplate)		Dynamic Range	Gamma	S/ σ at High Light (pk-pk/rms)	Center Resolution at High Light (~)/mm)
	Flux at 30 fr./sec. (lm/ft ²)	Density (lm sec/ft ²)				
Vidicon, Video Mode	10^{-1}	3×10^{-3}	10	0.7	80	37
Vidicon, Slow-Scan Mode	10^{-2}	3×10^{-4}	9	0.4	430 (ultimate)	34
Vidicon, Surveyor V Spacecraft	60	2	32	0.7	100	42
SEC Vidicon	10^{-2}	3×10^{-6}	30	0.7	50	26
Image Orthicon, 3 inches	2.5×10^{-2}	8×10^{-6}	20	0.75	30 to 60	25
Image Orthicon, 4½ inches	6×10^{-2}	2×10^{-3}	25	0.75	90	25
Image Orthicon, High Sensitivity	10^{-5}	3×10^{-7}	10	0.75	3	25
Image-Intensifier Vidicon	10^{-6} to 10^{-2}	3×10^{-6} to 3×10^{-4}	30	0.7	80	20
Image-Intensifier Image Orthicon	10^{-7} to 10^{-2}	3×10^{-9} to 3×10^{-4}	25	0.75	75	14

*Based on white light. The photocathodes spectral sensitivity must be applied to estimate the response of the tube to other light.

number depending upon the computer system used, the input data can be handled directly by the computer by recording it, on either magnetic tape or disk, simultaneously with its receipt.

In the present state-of-the-art, there is no device for recording large quantities of samples at high sample rates. It is therefore desirable to replay the analog magnetic tapes at a fraction of the original speed to get the digitizing rate down to the rate that can be handled by the system.

An immediate problem is encountered if, for some reason, the input data has been analog-recorded on a helical-scan or rotary-head magnetic tape recorder because these machines cannot be slowed down for replay. If this type of machine has been used and if the required data rate is above that which the computer system can handle, the input signal may be dubbed onto a longitudinal tape recorder for subsequent replay at slow speeds. This dubbing process will add more noise to the signal and will result in further degradation.

The output film-recording device generally will take the form of a cathode-ray-tube flying-spot device. Precisely the same set of limitations apply as were previously outlined for a cathode-ray-tube flying-spot film scanner. In addition to the requirements previously outlined for the scanning of film, the geometrical accuracy in the placement of the recording spot is of added importance because slight displacement of the spot during film-recording will cause visible line streaks and other degradations. Therefore, additional effort must be made to ensure that both the actual displacements and the rate of change of displacement with position are minimized.

Cathode-ray tubes are normally quite nonlinear in output light with respect to input drive and, therefore, will produce a distorted grey scale unless corrective efforts are made. In addition, specular variations and phosphor aging must be compensated for. One method that has been used at JPL is to monitor part of the light being produced by the cathode-ray tube by using a beam-splitter that diverts part of the light into a photomultiplier tube.

This is a feedback input that closes a servo-loop around the cathode-ray tube and includes the light path, thus ensuring the light is a reasonably linear function of the input voltage.

The development of processing techniques and the determination of the parameters to be applied during the processing are very subjective and require the continued attention of the analyst to the result of his processing. This is a time-consuming, iterative procedure in which the analyst examines his latest results and submits new processing accordingly. The time required to obtain a picture from the computer system will be minimized if a data display is available. This display must be of high enough quality to present the details required by the analyst. It may take the form of either hard-copy print-out or cathode-ray-tube display.

The cathode-ray-tube display requires repeated presentation to avoid flickering. The picture-refreshing provided by storage tubes or image converter tubes is not of adequate quality for display of small processing effects; therefore, a refreshing system such as rotating disc or computer memory must be used with a high quality cathode-ray tube.

System Techniques

The development of the processing algorithms and the accomplishment of some moderate amount of actual processing can be done on almost any general-purpose computer. It will be found, however, that the smaller computers will be quite inefficient for picture-processing because the smaller machines do not have adequate capability for the large amount of pixel manipulation that must be done to handle the large arrays present in pictures. Therefore, if the analyst is concerned with either fast turn-around from the computer or with processing either large pictures or a large number of small pictures, he must eventually consider going to a medium or large size computer.

Since even the normal large-size-computer installations do not have adequate core memory for storing an entire picture,

some form of picture rotation is required. In this mode, a few lines of picture at a time are read into core, processed, and then read out to allow room for more lines for further processing. In addition to the core space required for the program storage, capacity must be provided for pixel storage. Some of the processing algorithms operate on one pixel at a time and could conceivably work with a picture memory as small as a few pixels. Other programs, such as the two-dimensional convolution program for filtering, require simultaneously a number of picture lines at least as high as the convolution matrix size and, for efficient operation, should have room for several times this amount. For a picture of 1024 pixels per line, the total memory size for picture storage rapidly gets out of hand. The state-of-the-art in computer memories is now such that memories of 65,000 to 130,000 bytes are now quite practical.

Whether or not magnetic disks are useful will depend upon the type and mix of the processing to be done. We have found it convenient to group the pixels in one record per line, with a complete picture occupying one file or data set. The lines are normally recorded sequentially along the recording medium. For those processes in which sequential line access is adequate, obtaining a picture from tape is entirely satisfactory. For those processes in which a number of lines simultaneously must be accessed or for which nonsequential pixels from several lines must be used, magnetic tape is very inconvenient; and it will be better to read serially a complete picture from tape onto disk and then to access randomly the required pixels or lines from the disk. If the disks are organized in a cylindrical mode, access time will be further reduced. At least one disk drive is recommended.

It can thus be seen that image-processing can be done on almost any size computer from the table-top model up to the largest installations. Processing time on a large machine will be much less than that on a small one, and a larger memory and more rapid processing speeds will allow much more

ambitious algorithms to be performed than would be attempted on a small machine.

Software

As with the hardware, a large amount of picture-processing can be done with normal general-purpose computers and the standard Fortran batch-processing software. This is not particularly efficient, however, as the Fortran compilers with their associated input/output routines are often much slower than the response that could be obtained by specific programming. For this reason, with large numbers of pictures to be processed, special attention must be given to reducing or bypassing the inefficient parts of the Fortran language and/or doing programming in machine language. In addition, an image-processing laboratory should make available to the analyst an efficient data-handling system for the development of algorithms and for the recording, processing, and display of pictures.

To facilitate the use of the system by the analyst and to enable him to call for new processes rapidly, an image-processing software system must be designed that is based upon English language commands. This system should require a minimum of programming knowledge and data inputs from the analyst and should perform automatically as much of the input/output processing and routine bookkeeping as possible. Such a supervisory language has been developed for the Image-Processing Laboratory of JPL. This language has been designed to allow the analyst to process easily and quickly one picture or a string of pictures through one or more processes automatically. This is done with a fairly simple set of commands, which, together with the required numerical parameters, are submitted as a card deck.

Only a supervisory program is permanently resident in core. The various processing programs, as required, are read from the disk libraries by these commands to the core, thus minimizing the amount of core that must be reserved for programs. The system contains

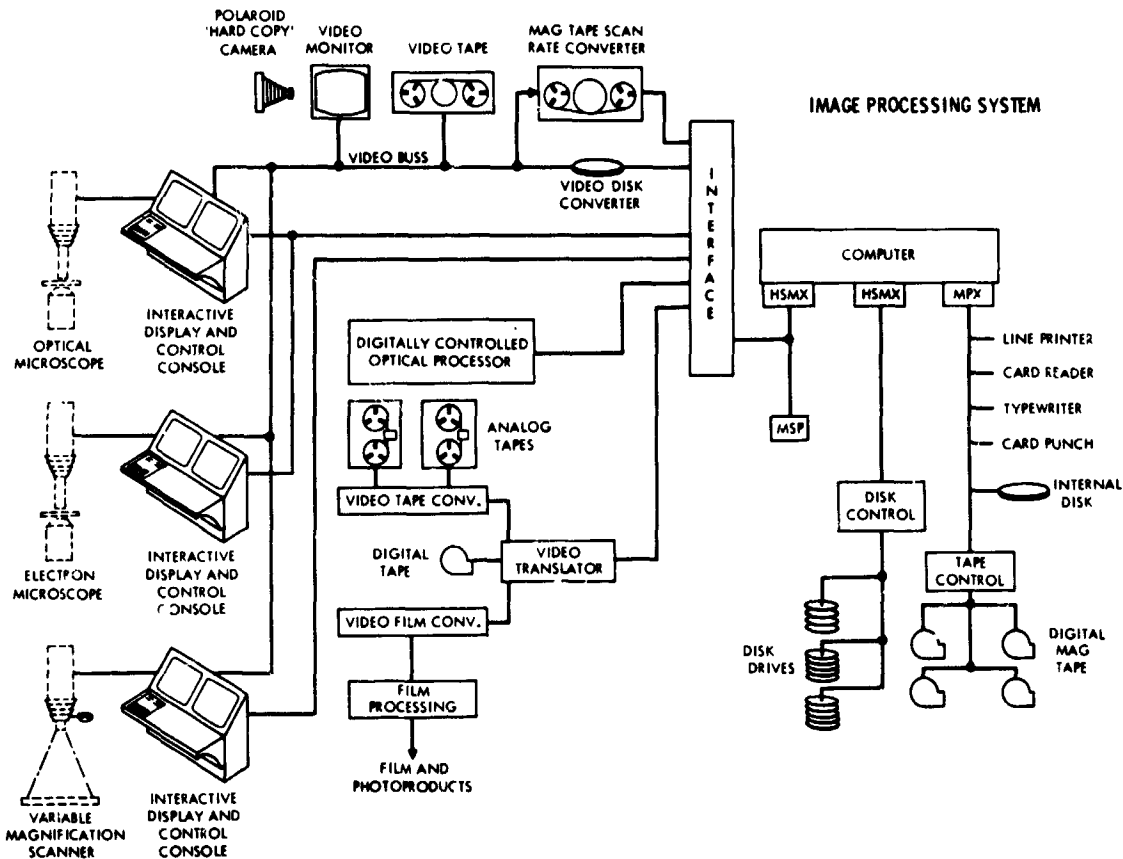


Figure 20. Block diagram of an image-processing system.

special-purpose input/output routines optimized for picture-handling; these are used instead of the normal Fortran input/output routines. This saves considerable space in the program libraries and obviates the necessity of writing these routines for each processing program. As a result, the writing of processing programs (which may be in either assembly language or Fortran) is considerably simplified.

A Complete System

A complete, digital, image-processing laboratory embodying the above considerations (either at the present time or in plans to be included in the future) is being established at the Jet Propulsion Laboratory. A

block diagram of this image-processing system is shown in figure 20.

The system has been designed to allow rapid computer-processing of the images, direct entry of the image data from films, hard copy, or optical devices such as a microscope. It will provide the analyst with a computer-driven video display and the capability of rapid selection of processing by keyboard entry. The computer also serves as a control for the peripheral devices when they are operated in a system mode.

Picture Acknowledgments

The picture processing algorithms and their applications have been developed by the JPL staff,

including Dr. Robert Nathan (ref. 3), Tom Rindfleisch (ref. 4), Howard Frieden, Robert Selzer (ref. 5), Elbert Johnson, and Jack Lindsley.

References

1. Huang, T. S.: Combined Use of Digital Computers and Coherent Optics in Image Processing. SPIE Computerized Imaging Techniques Symposium, Washington, D. C., June 1967.
2. Billingsley, F.C.; Goetz, A.F.H.; and Lindsley, J.N.: Color Differentiation by Computer Image Processing. Approved for publication in *Photographic Science and Engineering*, January-February issue, 1970.
3. Nathan, R.: Digital Video Data Handling. Technical Report 32-877, Jet Propulsion Laboratory.
4. Rindfleisch, T. C.: Photographic Method for Lunar Topography. *Photogrammetric Engineering*, Vol. XXXII, March 1966, p. 262.
5. Selzer, R.: Digital Computer Processing of X-Ray Photographs. Technical Report 32-1028, Jet Propulsion Laboratory.
6. Perrin, F. H.: Methods of Appraising Photographic Systems. *J. Soc. Mot. Pict. and TV Engrs.*, vol. 69, no. 3, March 1960, p. 151 and April 1960, p. 239.
7. Billingsley, F. C.: A Digital Image Processing Rationale, SPSE Symposium on Photo-Electronic Imaging, Washington, D. C., November 1968.
8. Smokler, M. I.: Calibration of the Surveyor Television System. *J. Soc. Mot. Pict. and TV Engrs.*, vol. 77, no. 4, April 1968, p. 317.

N70-36750

Onboard Computer for Orbiting Astronomical Observatory Mission

Ronald M. Muller

NASA Goddard Space Flight Center

Introduction

About three years ago, a developmental effort was started to produce a spacecraft computer that was general purpose and yet had "reasonable" weight, size, and power requirements. At the time, we had no specific mission in mind except that a relatively large payload was needed to keep the machine busy. An astronomy type of mission, such as the Orbiting Astronomical Observatory (OAO), is ideally suited to carry this computer. It can be used by all subsystems and experiments and can actually save weight and power while improving performance. We are now fabricating the flight computer for the OAO-C (fourth flight) mission where the machine will have "experiment" status. Later missions will use the machine as prime spacecraft hardware, and much of the experiment processing, the spacecraft control functions, and the operations will be built into it.

Design Philosophy

Major design requirements, in decreasing order of importance, were:

1. High reliability
2. Ease of programming and reprogramming
3. Low power consumption
4. Low weight
5. Small size.

These requirements were satisfied even though certain compromises were necessary because of conflicting requirements.

Onboard Processor Characteristics

The onboard processor (OBP) occupies less than 1000 cubic inches for one central

processing unit (CPU), input/output (I/O), and 16,384 words of memory. The processor weighs less than 40 pounds and consumes a peak power of 36 watts. Average power consumption is proportional to memory usage; i.e., if the OBP is busy only half the time, average power is 22 watts. Standby power consumption is 8 watts. Other characteristics are an 18-bit word, two's complement number representation, a 2.5-microsecond memory-cycle time, 50 instructions, and up to 16 priority interrupts. Typical execution times for instructions are:

Add	6.25 microseconds
Multiply (av.)	45 microseconds
Divide	90 microseconds
Shift	6.25 + 1.25 (number of bits shifted) microseconds
Conditional transfer	5 microseconds
AND/OR	6.25 microseconds

Background and Philosophy

The questions we always have to answer are: "Why use a computer? Why not build spacecraft in a conventional way?" My answer is that spacecraft can be built without a computer, but this relatively new tool has so many advantages that I have to ask: "How can you afford not to build a computer into your spacecraft?" The total hardware approach incorporates all the logic and memory of a computer, but it is organized in a way that makes it a "non-computer." For instance, OAO-A-2 contained approximately 300 flip-flops, approximately 3000 gates, 2.1

0-7282-05011
 x 10⁵ bits of memory in core, and 192 bits in delay lines. OAO-B will contain about the same amount of logic but will have an additional core for a total of 3 x 10⁵ bits. These are the parts that could be replaced by the computer. In contrast, the replacement CPU and I/O unit of the computer contain a total of 375 flip-flops and 2600 gates, and the memory may contain up to 11.5 x 10⁵ bits of core storage. In this comparison, I have not considered potential savings in hardware in the experimental package itself, but this will also be quite substantial.

Spacecraft Hardware Versus Computer Software

The comparison above does *not* imply that everything should be done in the computer. In fact, there are some functions that must not be put into software. Examples of these functions are the command subsystem and the emergency modes of operation that would be used if trouble should develop in the computer. Time must be allowed for ground personnel to diagnose the trouble and then to command in redundant hardware or new programs to "work around" the trouble.

Other functions are not put into the computer because they are simple functions that require wide bandwidth capabilities. An example of these would be the "fine-pointing" analog error signals generated by the experiment, which are used directly to control the reaction wheels. There is a continuum of this class of functions, and there is no sharp line between "all hardware" and "all computer." In fact, we have to make many choices as to how much hardware to fly and whether to put it into the spacecraft or into the computer. There are also some functions that are used so infrequently that it is obvious not to put them into the computer.

Multiple Small Computers Versus Central Computers

Our evaluation of the tradeoff between multiple small computers and a central computer is definitely in favor of the central

machine. If the multiple machines are not allowed to talk to each other and to share memories and other parts, in the event of failures we end up with something not much better than the present all-hardware spacecraft. The central machine easily allows all subsystems to talk to each other and to the spacecraft. It can be built to contain enough "spare parts" to accommodate multiple failures. Its time-sharing naturally fits the spacecraft operations. For instance, when the control function that is used to slew the spacecraft from one star to the next is occupying the computer, the experiment is relatively dormant. Once the spacecraft is on the new star, the experiment becomes active; and use of the computer by the control system declines. The present design includes a powerful priority-interrupt capability, which insures that each job gets its share of the computer and each job is done fast enough so that the individual subsystem is serviced as if it had its own computer.

Software for a Central Time-Shared Computer

Because of the expensive nature of software, we have designed the computer with features that permit programmers to program with relative ease. Each user writes his program as if the computer were his alone; the priority and other time-sharing problems are handled for him by a program called the Executive Program. The machine assembly language uses standard English words for the program code, resulting in programs that read much like normal English. The following is an example of this type of program:

$$\text{NORM} = \sqrt{X^2 + Y^2}$$

Let X times X yield X squared. Let Y times Y plus X squared, transformed by square root, yield norm.

The fact that the OBP language resembles English provides the assembly-language program with the desirable feature of self-documentation; in other words, the program is an English-language explanation of itself. This makes program maintenance and

modification efficient. Because a given program may require modification at any time, from the time it is written until long after launch, complete and up-to-date documentation is essential. The English-like language also facilitates understanding of the program by persons other than professional programmers; thus, the scientist engaged in a spacecraft experiment can determine if the programmer has faithfully carried out his duties.

Another design feature that simplifies programming is a movable binary point. This allows easy scaling and is a compromise between floating point and fixed point. Floating point was not implemented primarily because of the additional memory required to hold the accuracy. Memory is by far the most expensive, heaviest, and highest power-consuming part of the computer.

Reliability

The successful application of a central general-purpose computer to a spacecraft, such as OAO, requires the highest reliability possible within the constraints of size, weight,

and power consumption. Obviously, we are using high quality parts. In addition, we have chosen to implement this computer in a manner similar to the way ground computers are implemented; i.e., when it fails, we go off the air for a short time, replace the offending item or reprogram if the program is at fault, and then go back on the air. At first glance, not having the computer for 100 percent of the time appears to be a risky thing to plan into the system, but there are sufficient hardware safeguards so that the spacecraft will not sustain damage between computer failure and computer restoration. All that will be lost is the experiment observing time during this period. "Failure" is broadly defined to include software failures (bugs) as well as hardware malfunctions. This computer repair is accomplished by ground command.

Figure 1, a simplified block diagram of the OBP, shows the basic dual-bus interconnection used to achieve both flexibility and high reliability. The two sets of buses are electrically independent so that no single failure can cause the loss of more than half the memory. Only a few kinds of failures can

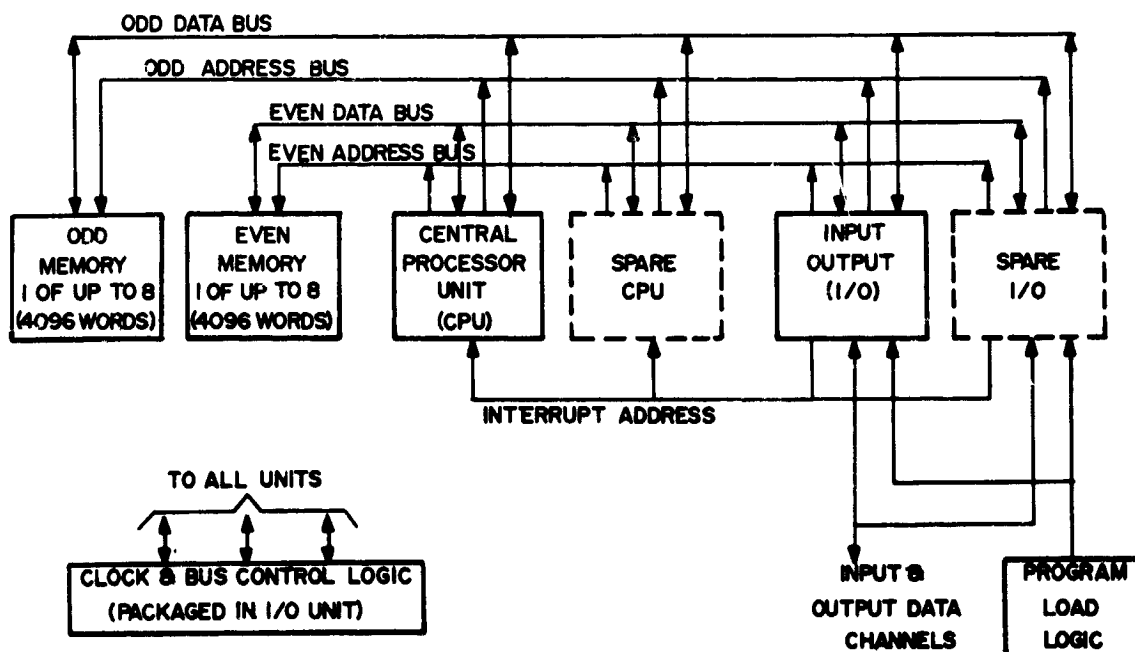


Figure 1. Onboard processor, functional block diagram.

cause the permanent loss of even this much memory; for example, a bus wire shorted to the structure. If the failure is internal to any of the boxes, the ground can command that box OFF and turn a spare ON. The OFF command disconnects both power and ground so that all nonoperating boxes are electrically "floating." This approach permits operation in spite of failures and allows a "graceful" rather than a catastrophic loss of capability. The dual bus, the standby redundancy, and the ability to reprogram by command — all three features enhance the reliability of the system.

It should be noted that high reliability schemes, such as triple redundancy with voters, do not allow tradeoff of weight for reliability; three of everything must be flown. The standby redundancy schemes take only the power of one computer; the triple redundancy implementations take triple the power. Another advantage to standby redundancy lies in the fact that the "off" units are not under electrical stress and will have a higher reliability than the units that are continuously operating. The improvement factor is variously estimated at between 2 and 10. Another advantage of the bus scheme is that it allows the memory, CPU's, and I/O's to be treated as separate items for reliability purposes. The memory has much redundancy built into each unit, and most missions will normally fly many units. The memory will not limit computer system reliability. The CPU and I/O are each of the same complexity; hence, I will discuss only the CPU. The calculated time to reach a reliability of 90 percent for one CPU is 3000 hours. Using two CPU's gives 11,000 hours; using three gives 16,000 hours. This assumes no improvement in failure rate for the standby units. If a factor of 5 is assumed in improvement in the standby units, one spare unit improves from 11,000 to 13,000 hours; and two spare units improve from 16,000 to 25,000 hours. It should be noted that a breadboard unit has operated without failure for 4,500 hours.

Another aspect of reliability is the overall mission reliability. For instance, the com-

puter can be programmed to back up many of the hardware black boxes should certain of their functions fail. This would generally be implemented after a failure is diagnosed and a suitable work-around program devised. For example, the loss of the gimballed star tracker system would place reliance on the fixed head tracker, the digital sun sensor, and the experiment for an inertial fix. The primary function of the OBP would be to provide the command and logic capability to operate the spacecraft efficiently under such circumstances.

Operations

There is no question that the change to a programmable onboard system for OAO will impact the ground operations in several ways. For instance, the ground computers and their software must be able to determine the health of the computer and must be versatile enough to implement the various work-around features previously discussed. They must also be able to process the OBP outputs into meaningful information. In exchange for this added burden, the OBP adds a new dimension to the flexibility with which the OAO may be operated. Evidence of this is the ability to operate from only two ground stations rather than the present five.

Any function that is monitored by the ground stations may be monitored all the time by the OBP. Furthermore, if the ground would normally take command action if a given function went out of limits, this, too, could be put into the OBP. Unfortunately, it is very hard to predict all the combinations and to determine the appropriate responses; however, the reprogrammability allows us "to grow into" this kind of operation. In effect, we can treat the computer as if it were a full-time control station and can allow it to monitor and to correct things if necessary. (At the present time, that same problem might continue for a few orbits before it could be corrected.) In addition, highly complex decision algorithms can be implemented, much more complex than would be attempted in hardware.

Conclusion

The spaceworthy general-purpose computer is a natural tool for use in an astronomical observatory. The technology is

adequate for such a machine and its costs in terms of dollars, size, weight, and power consumption are competitive with an all-hardware spacecraft

REPRODUCIBILITY OF THE ORIGINAL PAGE IS POOR.

N70-36751

Vacuum Systems for Space Simulation

David H. Holkeboer
AeroVac Corp.

Simulation of Space Vacuum

Simulation of the space environments is used as a means of testing spacecraft and spacecraft components to assure satisfactory performance and to calibrate instruments. *Simulation is not the same as duplication.* The environmental parameters believed to be significant in a particular investigation are reproduced in the simulator while other parameters that may be difficult to handle are not reproduced.

Some of the parameters of space that may be simulated are:

1. **Pressure Forces.** Low atmospheric pressure or rapid change in atmospheric pressure, as in ascent, produce mechanical forces on structures.
2. **Mechanical Damping Forces.**
3. **Thermal Conductivity.** Thermal conductivity of residual gases in high vacuum is normally negligible compared to radiation.
4. **Outgassing.** Volatile materials escape from surfaces.
5. **Surface Contamination.** Background vapors and gases impact on surfaces.
6. **Electrical Discharge Effects.** Arc or glow discharges can occur readily in some vacuum ranges.
7. **Optical Effects.** Absorption or scattering of photons by the residual gas in high vacuum is very small.

Types of Vacuum Systems

There are three types of vacuum systems: the basic system, cold wall vacuum, and ultra-high vacuum.

Basic Vacuum System

If high vacuum testing is contemplated, the vacuum system is comprised basically of a test chamber and a pump. The test chamber will normally be fitted with a variety of devices for observing the effects of the test on the test item and for measuring the test parameters. A variety of other equipment may be used, including motion devices, solar simulators, thermal heat loads and heat sinks, surface bombardment devices, ingress-exit equipment, and the like.

In this basic vacuum system, the vacuum level may be described in terms of the absolute pressure in the vacuum chamber. The pressure is given as

$$P = \frac{Q}{S} + P_0 \quad (1)$$

where

- P = the pressure in torr
- Q = the total gas load from leaks and outgassing
- S = the pumping speed
- P₀ = the ultimate pressure of the pumping system

This equation may also be applied to the partial pressures of the components. Typical gas loads vary from 10⁻⁶ or 10⁻⁷ torr liters/sec-cm² for clean, dry metals after several hours in vacuum to 10⁻⁴ or 10⁻⁵ torr liters/sec-cm² for common polymers. Typical pumping speeds range from 0.01 liter/sec-cm² of chamber surface area to 1 liter/sec-cm². The ultimate pressure of the pumping system,

P_o is usually not significant with a trapped diffusion pump or an ion pump. The typical range of pressures is 10^{-4} to 10^{-5} torr.

Cold Wall Systems

Space simulators frequently incorporate a liquid-nitrogen-cooled liner or shroud in the vacuum chamber for thermal simulation. These cold panels provide a remarkably effective pump for "condensable" vapors (principally water vapor), which are the major components of outgassing. Hidden panels operated at about 20°K are often incorporated in large facilities to pump gases like nitrogen, oxygen, and argon. (There are some facilities where the cold panels are maintained at 4°K with liquid helium. These facilities pump all gases except hydrogen and helium.) The cold surfaces are supplemented with conventional ion or diffusion pumps to handle the noncondensable gases.

In these vacuum facilities, the high-speed, widely distributed pumping produces a residual gas environment with strongly directional properties for the gases and vapors pumped. The pressure and temperature of the gases are difficult to define. Instead, it is useful to think of the rate of arrival of gas molecules on the surface of the item tested (molecular flux density) and the average energy of these molecules. Typically, the gas molecules impinging on the test item will consist mostly of test-item outgassing products imperfectly pumped by the cold panels lining the test chamber. There may also be some vacuum-chamber outgassing products and pump-oil backstreaming. Because the space environment has a low density of naturally occurring gas, the incidence rate of environmental gas on the spacecraft is low; and the return of spacecraft outgassing products to spacecraft surfaces is also low. The cold-wall vacuum chamber tends to simulate this kind of environment.

Ultra-High Vacuum Systems

Two approaches are used when seeking ultra-high vacuum. First, the pumping speed

may be increased; second, the gas load may be reduced. Usually both are employed. A third factor to be considered is the ultimate pressure capability of the pumping system used.

Increasing the pumping speed has practical limitations closely approached by the systems with 4°K or 20°K cold liners. Sometimes they are provided with fins or wedges like an anechoic chamber. While these pumping methods can reduce the molecular flux incident on the test item to a very low level, little can be done about the density of the outgassing stream emitted by the test item.

The more conventional approach to ultra-high vacuum relies upon reducing the gas load by a careful choice of materials and by bakeout of the high vacuum zone while pumping. With small gas loads, it is possible to reach 10^{-8} to 10^{-9} torr without bakeout and to reach 10^{-12} to 10^{-14} torr with bakeout and special pumping systems. Baked systems offer a relatively high degree of cleanliness but are often not applicable to space simulation.

Types of Pumping Systems

Pumping systems can be divided into two general types: those used for initial exhaust starting from atmospheric pressure, the "roughing process," and those used for high vacuum pumping. The crossover from one pumping type to another occurs at a pressure between a few tenths of a torr and a few thousandths of a torr in a typical system. This pressure level also marks the transition from continuum behavior of gases (viscous flow) to molecular behavior.

Roughing Pumps

Mechanical, positive-displacement, roughing pumps are usually oil-sealed, rotary vane or rotary piston pumps, but they are often supplemented in large facilities with positive displacement blowers. The latter offer relatively high pumping speeds and somewhat greater vacuum capability but must be limited to pressure ratios of not more than

2 or 3. Consequently, they are frequently used as boosters ahead of oil-sealed pumps. The principal advantages of mechanical roughing pumps are that they remove all the constituents of air equally well, that they can pump continuously for long periods of time, and that they can be used to "back" diffusion pumps. The principal disadvantage is that they backstream relatively large quantities of a relatively high vapor-pressure oil whenever inlet pressures become less than 0.01 torr.

Cryosorption on liquid-nitrogen-cooled zeolite or molecular sieve material is often used as a roughing method. The principal advantage of this method is the avoidance of possible oil backstreaming. The principal disadvantage of this method is the difficulty of pumping air constituents such as helium, hydrogen, neon, and argon. These residues are difficult to pump with an ion pump if this is the mode of high vacuum pumping chosen. Therefore, for best performance, the air should be purged from the high vacuum chamber with nitrogen before cryosorption pumping is started. Cryosorption pumps are seldom used except on small, ion-pumped systems but are quite common on this type of equipment.

Several other types of roughing pumps exist, such as air or water aspirators and steam ejectors, but they are in limited use.

High Vacuum Pumps

High vacuum pumping is commonly accomplished with one or more of four types of pumps: diffusion pumps, ion pumps, sublimation pumps, and cryogenic pumps. Variations on these and additional types of pumps are too numerous to mention.

Oil-vapor diffusion pumps have been a workhorse of the vacuum industry for several decades. These pumps can pump most gases and vapors with high efficiency; about 40 to 50 percent of the molecules entering the mouth of the pump will be pumped. The principal difficulties of the diffusion pump result from the presence of the pump oil and its vapor. The oil has limited life and, in some cases, is severely degraded if exposed to air

when hot. The oil vapor and possibly oil droplets are backstreamed into the high vacuum zone unless carefully trapped. This oil often represents an unacceptable degree of contamination. The most important features of traps are (1) as a barrier to prevent oil vapor bypassing the baffles, (2) as an efficient baffle structure that prevents oil molecules from passing through the trap without contacting the baffle surface at least once or preferably twice, and (3) as an operating technique that minimizes the operating time in the viscous-to-molecular-flow transition regime where the scattering of oil molecules by air molecules makes the trap ineffective. Notwithstanding the oil problems, the efficient pumping and easy starting of the diffusion pump make it a very useful and widely used device.

Ion pumping is done principally with the several varieties of cold-cathode, sputter-ion pumps and to a lesser extent with hot-cathode "orbitron" pumps. These pumps have the advantages of being quiet, oil-free, not requiring traps, and providing a pressure readout. An ion-pump system forms a sealed-off vacuum system that does not have to be vented in case of power failure. On the other hand, the pumps are sometimes difficult to start, have limited life because the gases pumped remain inside the pump, have relatively poor pumping speeds for noble gases and hydrocarbons, tend to re-emit gases previously pumped and have strong magnetic fields. Chemical reactions occur in the high voltage discharge and on the clean metal surfaces inside the pump. Water vapor reacts with carbon in the pump metals to produce a variety of light hydrocarbons in appreciable quantities.

Between these two major pump types, ion pumps are most useful where gas loads are relatively small, and liquid nitrogen for traps is inconvenient to provide. Diffusion pumps are most useful where gas loads may be large or of a type not pumped well by ion pumps. Diffusion pumps usually require vapor traps. Surprisingly, upon comparing well-trap, diffusion-pumped systems with good ion-pumped systems, there is very little difference

in the ultimate vacuum attainable, the cleanliness, the residual gas atmosphere, or the cost. In our experience, the diffusion pump comes out slightly ahead on all counts.

The other two pumping techniques are generally used to supplement the two just described. Cryopumping was described in connection with cold-wall vacuum systems. It is commonly used in large facilities where it is the only practical means of obtaining the desired pumping speeds. The principal disadvantage is the release of condensed materials when the cold panels are warmed prior to shutting down the vacuum system.

Sublimation pumps capture gases by absorbing them on clean, metallic surfaces formed by subliming metals under vacuum. The effect is greatly enhanced if the surfaces are cooled to liquid nitrogen temperatures. Chemically active gases are pumped quite well by sublimators, but noble gases are pumped to a very limited extent. Sublimators are a relatively cheap way to provide a very high pumping speed. Two interesting results occur when a cryosublimator is used as a trap. First, extremely high levels of cleanliness can be

realized. Second, if the outgassing load in the vacuum chamber is low, the cryosublimation trap reduces the gas load contributed by the pumping components appreciably, thus giving a substantial improvement in vacuum level. In fact, in baked systems, this technique permits reaching pressures of 10^{-13} and 10^{-14} torr quite easily.

Summary

Three major types of vacuum systems have been described: the basic system, the cold-wall system, and the ultra-high vacuum system. The vacuum level achieved is dependent on the gas load, pumping speed, and ultimate pressure of the pump subsystem. Pumping subsystems consist of roughing systems and high vacuum systems. The latter are principally ion pumps, diffusion pumps, cryopumps, and sublimation pumps. The major advantages and disadvantages of these have been discussed. The proper operating techniques are important in obtaining good performance from these systems.

N70-36752

Space Thermal-Simulation System

Henry Maurer

NASA Goddard Space Flight Center

Introduction

This paper gives (1) an overview of space thermal-simulation used in testing full spacecraft systems and suggestions of research areas thought to be significant in advancing technology in order to provide a capability to test large ultraviolet telescopes of the future and (2) an abbreviated state-of-the-art review of the system test, space thermal-simulator field, and some of the factors influencing the results obtained in thermal-balance testing of spacecraft.

Overview of Space Thermal-Simulation

Simulation of the space thermal environment in spacecraft system testing is done to help to determine whether the craft is capable of performing the functions specified for orbit. This determination often requires phasing of the thermal tests so that functional limits of various design features can be properly investigated. Space thermal-simulation approaches used in system testing are numerous. They are related to the confidence in the thermal design of a given spacecraft and the data needed to determine the adequacy of the design.

Nearly all spacecraft design criteria specify the temperature range in which the equipment and structure are to be maintained throughout the mission. When there is adequate confidence in the thermal design, the primary concern in thermal simulation is to create temperature-vacuum boundary levels so that operational aspects of the craft can be properly demonstrated. It is clear that the conditioning can be conservative and that the operational performance of the spacecraft

may be demonstrated at temperatures (in vacuum) more severe than those expected for the mission; however, care is required in thermal-vacuum functional testing so that the less obvious interactions are not omitted. Programs such as the Interplanetary Monitoring Platform (IMP), Tiros Operational Satellite (TOS), Nimbus, and the Orbiting Solar Observatory (OSO) are examples where similarity between spacecraft models coupled with orbital experience has permitted a number of spacecraft to be flown after thermal-vacuum tests but without thermal-balance tests. A further step in this direction is the experience of the Lockheed Missiles and Space Company, where a one-of-a-kind design was flown without thermal-balance testing (ref. 1).

For the complex one- or two-of-a-kind spacecraft designs, the technical uncertainty and economic risk of overlooking a critical thermal/functional interaction has created demands for obtaining spacecraft-system-test thermal simulators in which the uncertainties can be resolved. Today's space thermal simulation and test practices actually result in a convergence and minimizing of the unknowns in the risk situation. The thermal-control treatment of the spacecraft system is usually evaluated under a closely controlled heat-balance experiment. Depending upon the spacecraft design and simulator fidelity, critical spacecraft functional interactions may be demonstrated during the thermal-balance test. Where simulator limitations or stimulus requirements do not permit this, separate functional tests under forced temperature conditions are called for.

Thermal-control or thermal-balance testing of most complex spacecraft systems

(in today's best solar simulator) requires an intimate coupling with thermal analytical models that are used to predict the temperature performance of the craft in orbit. This is particularly necessary since the best simulator does not duplicate the space thermal environment—thus, the need for the experimental approach. The simulator inputs and sinks are defined, and a thermal result is predicted for the craft by using the orbital analytic model. Refinements are usually required to perfect the algorithm to describe the physical model more adequately. Where analytic modeling is not possible due to intractability or lack of capability, the demands for realism in the environmental simulation are severe.

In the past, such problems have been primarily where there is lack of art in predicting multiple reflections between surfaces of the spacecraft; e.g., the thermally sensitive open-frame type of structures. It does appear that mathematical corrections can be made for solar simulator imperfections in spectral distribution, total intensity, and heat sink properties. The effect of deviations in field angle (subtense angle) of the simulated source as compared to the space source, however, is difficult to analyze and could prove intractable for some designs, such as an expanded mesh structure. This point is also indicative of the problems and uncertainty in simulating space thermal flux using heater elements, heater blankets, etc. In such approaches, the reflection (and flux trapping) characteristics of the spacecraft configuration are not tested.

Two simulation approaches are used in thermal-balance testing of spacecraft systems. Either technique also may be used to validate the functional performance of the spacecraft:

1. Simulation of the incident solar irradiation by using light sources and optical systems to produce total flux and spectral irradiance at subtense angles approaching the sun for wavelengths 0.25 micron to 2.6 microns.

2. Simulation of the effects of space thermal sources by inducing an equivalent absorbed flux by the craft—heater blankets, plates, or infrared lamps used.

For solar simulation, an energy uncertainty band on the order of 5 to 7 percent due to radiometry and spectroradiometry capability and a $\pm 2^\circ\text{C}$ thermocouple accuracy are estimated for the well-run spacecraft system test. For a spacecraft with a mean temperature of 25°C , the uncertainty in boundary flux and temperature leads to an uncertainty in average temperature on the order of 6°C . Experience with the enclosed-shell, passive-thermal-control type of spacecraft structures indicates that thermal analytic models of the spacecraft can be adjusted to agree with test results within 5°C . Correlations better than this should not be expected because uncertainties in the boundary do not warrant it. The degree of temperature correlation between predictions from the perfected analytic model (by test) and orbit seem biased; the predictions are generally colder. Orbital experience on passive thermal designs seems to indicate that correlation on some occasions has been within 5°C , often is within 10°C , and occasionally is as poor as 30°C . These results are attributed to (1) inaccuracies in measuring the test boundary and/or in the analytic processing, (2) unexpected degradation or change in thermophysical properties, (3) test/analytic omissions, and (4) uncertainties in the natural environment. While accuracy in predicting temperature level is on the order of 10°C for passive systems, active systems indicate control on the order of 4°C and less. Prediction of gradient across a thermally isolated, solid member such as a mirror is estimated to be better. Almgren and Coyle estimate that prediction of gradients on the order of 1°C is possible for members one meter or so in length (ref. 2).

R. E. Danielson pointed out the nature of the thermal control problem with telescope primary mirrors of 40 inches in size (ref. 3). Active focus adjustment of the secondary mirror could compensate for uniform distortion of the primary mirror; i.e., where the primary curls in or out uniformly. Small non-uniform temperature gradients through the primary, side-to-side or front-to-back, would be detrimental to the optical performance. In reference 3, it was indicated for the assumed

materials that calculated temperature gradients across the 40-inch diameter of 4°C and through the thickness (one side of the mirror to the other) of 0.1°C would cause the mirror to distort beyond acceptable tolerances. Extrapolation of these tolerances places the acceptable gradient tolerance for a 120-inch mirror in the range of 1°C and less. It seems that the accuracy in thermal-simulation testing and analytical treatment would have to be improved considerably in order to design and to verify the temperature control of large diffraction-limited telescopes of the future. The question, however, is what to improve?

In considering this aspect, it is assumed that the telescope/spacecraft thermal design could generally proceed along the lines already being used in the OAO program. Thus, the problem is scale and improved accuracy. The following list includes those areas of research thought (by the author) to be fruitful toward thermally testing and evaluating future spacecraft with large ultraviolet telescopes:

1. Advance analytical programs to predict the design performance by integrating the thermal, structural, and optical disciplines. (Reasonable computing time and mechanization of the input and output is essential.) Advance subelement analysis and testing of joints, insulation, coatings, etc. to provide a boundary on the uncertainties in those properties which influence the accuracy of the analytical prediction.

2. Advance thermal/structural/optical scale modeling in concert with item #1 above. Develop fidelity in the modeling to magnify an effect or parameter so as to better resolve the accuracy in the design; e.g., model to increase thermal gradients by a factor of two or more.

3. Advance simulation of earth albedo and infrared irradiance for inclusion in medium-sized solar test chambers for scale model testing. Develop analysis that would permit better prediction of the effect of these flux on a given spacecraft configuration.

4. Advance methods to simulate earth albedo and infrared irradiance across full-sized

telescope apertures. (This may not be required, but it seems wise to prepare for it.)

5. Advance temperature sensing accuracy for both attached and detached (e. g., radiometric) sensing of temperature across the surface of a mirror.

6. Advance infrared spectroradiometry for accurate chamber calibration.

7. Perfect infrared simulation techniques, particularly the heater skin concept. Improve flux uniformity, density, and control accuracy.

8. Continue advancement of solar simulation (sources, instrumentation, etc.) to perfect small area simulators for maximum utility in scale model testing. Develop design approaches adaptable to large area system in case the need arises.

State-of-the-Art Survey

Consideration of the state-of-the-art in the simulation of the space thermal environment has as a starting point the natural environment and the assumptions that pertain to it. If only near-earth orbits are considered and lunar effects are neglected, the natural thermal environment affecting the heat balance of a spacecraft includes the space heat sink, vacuum, and thermal flux from the sun and earth.

Except for the sun and earth, space viewed by the spacecraft has the property of an infinite heat sink with a temperature near absolute zero. If reflection and radiation between spacecraft members are omitted, heat emitted by the spacecraft is not returned to it.

The molecular flux density varies with distance from the earth, and, at altitudes on the order of 300 nautical miles, vacuum of 10^{-8} and 10^{-10} torr prevails. Heat transfer in nonsealed systems is by radiation and by conduction through contacting members of the spacecraft.

The following sun and earth thermal flux influence the heat balance of the spacecraft and are of major importance to thermal design and to simulation: (1) solar insolation, (2) earth reflection (albedo), and (3) earth

emitted (infrared). Two factors to be considered about these flux on the surface of a spacecraft are the total irradiance and the spectral distribution.

Solar Irradiance

The total irradiance due to the sun at the average sun-earth distance (1 angstrom unit) in the absence of the earth's atmosphere is defined as the solar constant. Most authorities consider the irradiance to be highly constant, at least within the limits of experimental error. Variability due to sunspot cycles, solar flares, and other visible surface phenomena of the sun is not over ± 1 percent (ref. 4).

Seasonal variations are approximately ± 3.4 percent with minimum irradiance at aphelion in July and the maximum at perihelion in January. For most purposes, the sun can be considered a point source at planetary distances, and the solar irradiance follows the inverse square law. At 1 angstrom unit, the sun subtends an angle of 32 minutes.

The value of the solar constant has undergone numerous revisions. Table 1 shows the proposed revisions of the solar constant since 1940.

Prior to 1968, the value of the solar constant most commonly accepted in the United States was 139.6 mW cm^{-2} . This value was derived by F. S. Johnson from ground data obtained by the Smithsonian Institution and supplemented by the measurements of the Naval Research Laboratory in the ultraviolet by rocket-borne instruments. Johnson also proposed a spectral irradiance curve for the wavelength range 0.22 to 7.0 microns which has been widely accepted (ref. 5). Recently, direct measurements obtained from above most of the atmosphere seem to show that the Johnson value of the solar constant is too high. The Goddard measurements are most extensive and were obtained by using four different total energy detectors over a 15-hour sampling period (ref. 6). The value by Laue and Drummond was obtained during a 23-second interval at 82 kilometers from an X-15 aircraft (ref. 7). The Murcra group obtained data from nine observations on three

Table 1. Revisions of the Solar Constant

Author	Year	Solar Constant (mW cm^{-2})
P. Moon	1940	132.3
L. B. Aldrich & G. C. Abbot	1948	132.6
W. Schupp	1949	136.7 to 141.6
C. W. Allen	1950	137.4
L. B. Aldrich & W. H. Hoover	1952	134.9
F. S. Johnson	1954	139.6
R. Stair & R. G. Johnston	1956	143.0
C. W. Allen	1958	138.0
E. G. Laue & A. J. Drummond	1968	136.1
D. G. Murcra <i>et al.</i>	1968	133.4
M. P. Thekaekara <i>et al.</i>	1969	135.1

different days from a 31-kilometer altitude (ref. 8). Additional data has recently been obtained from a cone radiometer on board the Mars-Mariner 69 flight; however, the data have not yet been published.

On the basis of the new flight data, it has been proposed by the Goddard group that 135.1 mW cm^{-2} be accepted as the revised value of the solar constant (ref. 6). An important fact is that a difference of 3.3 percent exists between the Johnson value and the proposed revision. Further, the accuracy of the new value is placed at $\pm 2.8 \text{ mW cm}^{-2}$, approximately ± 2 percent.

Solar Spectral Irradiance

The Goddard experimenters have also proposed a table of values of spectral irradiance of the sun for zero air mass and for the average sun-earth distance, shown in table 2

Table 2. Solar Spectral Irradiance (Based on Measurements on Board NASA-711 "Galileo" at 38,000 feet.)

λ	P_λ	D_λ	λ	P_λ	D_λ	λ	P_λ	D_λ	λ	P_λ	D_λ
0.140	0.0000048	0.00050	0.395	0.1191	8.189	0.630	0.1542	39.26	3.8	0.00111	98.902
0.150	0.0000176	0.00059	0.400	0.1433	8.675	0.640	0.1517	40.39	3.9	0.00103	98.982
0.160	0.000059	0.00087	0.405	0.1651	9.245	0.650	0.1487	41.50	4.0	0.00095	99.055
0.170	0.00015	0.00164	0.410	0.1759	9.876	0.660	0.1468	42.00	4.1	0.00087	99.122
0.180	0.00035	0.00349	0.415	0.1783	10.53	0.670	0.1443	43.67	4.2	0.00078	99.182
0.190	0.00076	0.00760	0.420	0.1758	11.19	0.680	0.1418	44.73	4.3	0.00071	99.238
0.200	0.00130	0.0152	0.425	0.1705	11.83	0.690	0.1398	45.78	4.4	0.00065	99.283
0.205	0.00167	0.0207	0.430	0.1651	12.45	0.700	0.1369	46.80	4.5	0.00059	99.335
0.210	0.00269	0.0288	0.435	0.1675	13.06	0.710	0.1344	47.80	4.6	0.00053	99.376
0.215	0.00445	0.0420	0.440	0.1823	13.71	0.720	0.1314	48.79	4.7	0.00048	99.414
0.220	0.00575	0.0609	0.445	0.1936	14.41	0.730	0.1290	49.75	4.8	0.00045	99.448
0.225	0.00649	0.0835	0.450	0.2020	15.14	0.740	0.1260	50.69	4.9	0.00041	99.480
0.230	0.00667	0.1079	0.455	0.2070	15.90	0.750	0.1235	51.62	5.0	0.000383	99.509
0.235	0.00593	0.1312	0.460	0.2080	16.66	0.800	0.1107	55.95	6.0	0.000175	99.716
0.240	0.00630	0.1534	0.465	0.2060	17.43	0.850	0.0988	59.83	7.0	0.000099	99.817
0.245	0.00723	0.1788	0.470	0.2045	18.19	0.900	0.0889	63.30	8.0	0.000060	99.876
0.250	0.00704	0.2053	0.475	0.2055	18.95	0.950	0.0835	66.49	9.0	0.000038	99.912
0.255	0.0104	0.2375	0.480	0.2085	19.72	1.000	0.0746	69.42	10.0	0.000025	99.935
0.260	0.0130	0.2808	0.485	0.1986	20.47	1.1	0.0592	74.37	11.0	0.0000170	99.951
0.265	0.0185	0.3391	0.490	0.1959	21.20	1.2	0.0484	78.35	12.0	0.0000120	99.962
0.270	0.0232	0.4163	0.495	0.1966	21.92	1.3	0.0396	81.61	13.0	0.0000087	99.969
0.275	0.0204	0.4960	0.500	0.1946	22.65	1.4	0.0336	84.32	14.0	0.0000055	99.975
0.280	0.0222	0.5758	0.505	0.1922	23.36	1.5	0.0287	86.62	15.0	0.0000049	99.9785
0.285	0.0315	0.6752	0.510	0.1882	24.07	1.6	0.0244	88.59	16.0	0.0000038	99.9817
0.290	0.0482	0.8225	0.515	0.1833	24.76	1.7	0.0202	90.24	17.0	0.0000031	99.9843
0.295	0.0584	1.020	0.520	0.1833	25.43	1.8	0.0159	91.58	18.0	0.0000024	99.9863
0.300	0.0614	1.223	0.525	0.1852	26.12	1.9	0.0126	92.63	19.0	0.0000020	99.9879
0.305	0.0602	1.430	0.530	0.1842	26.80	2.0	0.0103	93.48	20.0	0.0000016	99.9893
0.310	0.0686	1.668	0.535	0.1818	27.48	2.1	0.0090	94.19	λ_∞		100.0
0.315	0.0757	1.935	0.540	0.1783	28.14	2.2	0.0079	94.82			
0.320	0.0819	2.227	0.545	0.1754	28.80	2.3	0.0068	95.36			
0.325	0.0958	2.555	0.550	0.1725	29.44	2.4	0.0064	95.85			
0.330	0.1037	2.925	0.555	0.1720	30.08	2.5	0.0054	96.287			
0.335	0.1057	3.312	0.560	0.1695	30.71	2.6	0.0049	96.664			
0.340	0.1050	3.702	0.565	0.1700	31.34	2.7	0.0043	97.001			
0.345	0.1047	4.090	0.570	0.1705	31.97	2.8	0.0039	97.305			
0.350	0.1074	4.483	0.575	0.1710	32.60	2.9	0.0035	97.579			
0.355	0.1067	4.879	0.580	0.1705	33.23	3.0	0.0031	97.823			
0.360	0.1055	5.271	0.585	0.1700	33.86	3.1	0.0028	98.034			
0.365	0.1122	5.674	0.590	0.1685	34.49	3.2	0.0026	98.214			
0.370	0.1173	6.099	0.595	0.1665	35.11	3.3	0.0022	98.368			
0.375	0.1152	6.529	0.600	0.1648	35.72	3.4	0.0018	98.501			
0.380	0.1117	6.949	0.605	0.1626	36.33	3.5	0.0016	98.616			
0.385	0.1097	7.359	0.610	0.1611	36.93	3.6	0.0015	98.720			
0.390	0.1099	7.765	0.620	0.1576	38.11	3.7	0.0013	98.816			

 λ —wavelength in microns; P_λ —Solar Spectral Irradiance averaged over small bandwidth centered at λ , in watts $\text{cm}^{-2}\text{micron}^{-1}$; D_λ —percentage of the Solar Constant associated with wavelengths shorter than wavelength λ .Solar Constant 0.13510 watt cm^{-2} .

(ref. 6). The solar spectral irradiance curve, shown in figures 1 and 2, was derived from table 2. These graphs display the difference between the Johnson curve and the new curve. The wavelength range covered by the

Goddard measurements is 0.3 to 15.0 microns; however, for completeness and for obtaining an integrated value, the table of values has been extended to 0.14 micron in the ultraviolet and to 20 microns in the

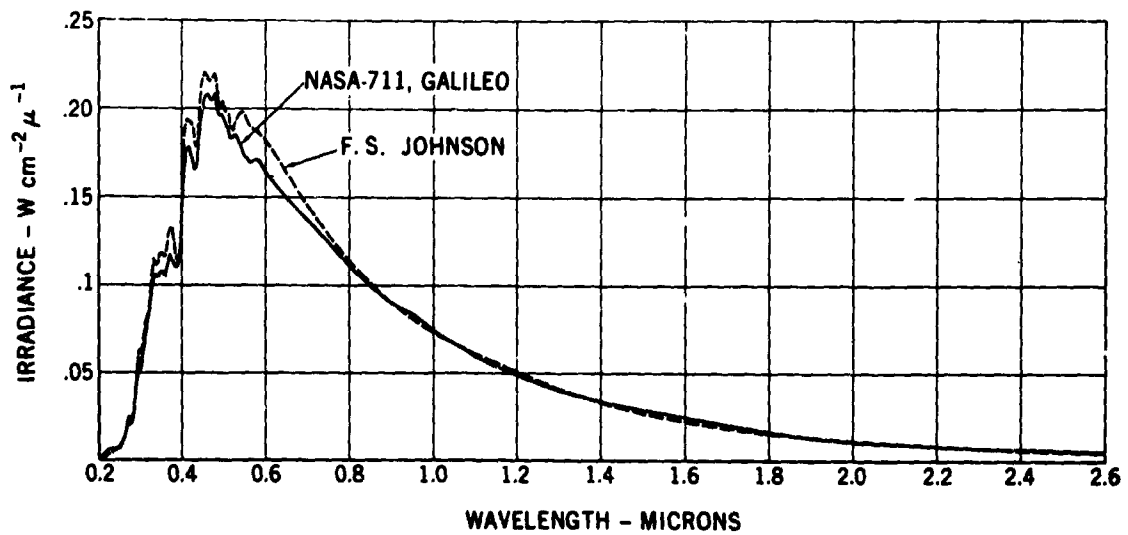


Figure 1. Solar spectrum for zero air mass from NASA 711 Galileo; 0.2 to 2.6 microns, compared with F. S. Johnson curve.

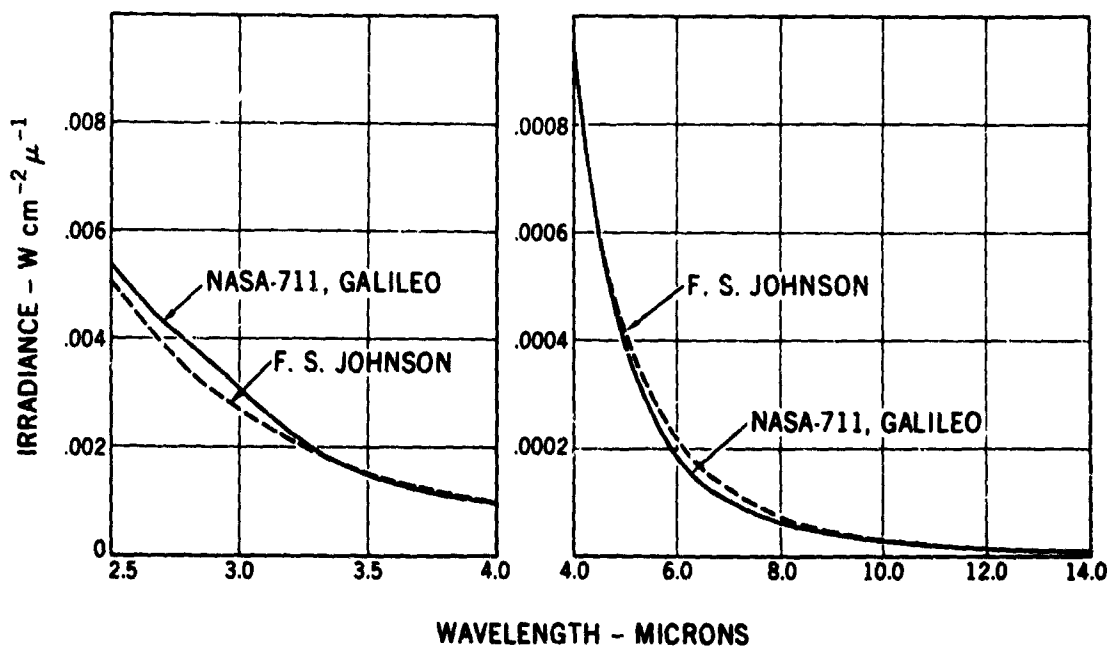


Figure 2. Solar spectrum for zero air mass from NASA 711 Galileo; 2.5 to 14 microns, compared with F. S. Johnson curve.

infrared. The final curve was obtained by scaling down the total irradiance, 135.1 mW cm^{-2} , by 0.1 percent and by using the weighted average of five spectroradiometric instruments (Perkin-Elmer 0.3-to-4.0-micron instrument, Leiss monochromator, filter radiometer, and polarization interferometer for 0.3 to 2.6 microns, and Michelson interferometer for 2.6 to 15 microns).

Table 2 and figures 1 and 2 appear to represent the first direct and detailed measurements of the solar spectrum from above practically all the atmosphere water vapor. The Goddard experimenters estimate that the overall accuracy of the spectral irradiance values is ± 5 percent. Table 3 compares the absorption percentage of solar cells and 18 coatings for proposed solar curves versus the Johnson solar curve (ref. 9). It is interesting that variation between the most recent Goddard data and the Johnson curve for the coatings selected is on the order of 2 percent maximum.

Solar irradiance at different distances using the proposed revision to the solar constant value are given in table 4.

Earth Reflection (Albedo)

Solar radiation reflected by the earth presents a second source of thermal flux to the near-earth orbiting spacecraft. A number of meteorological studies of the albedo since 1948 estimate the average value between 0.33 and 0.38 of the incident solar radiation. The widely accepted average value for spacecraft design is 35 percent or approximately 49 mW cm^{-2} . The amount of albedo flux incident on a spacecraft is dependent upon the subtense angle of the sunlit side of the earth as viewed by the spacecraft.

The albedo results from reflection by cloud layers and various surface features. The instantaneous total irradiance and spectral irradiance is variable due to nonuniform surface reflections and is further complicated by (1) variable molecular and particle scattering and (2) absorption by atmospheric constituents. Figures 3 and 4 are selected examples

of data that show graphically the variability in spectral distribution versus sky condition and the albedo and infrared irradiance as a function of latitude for a mean sky condition. It is generally thought that approximately 75 percent of the total albedo arises from cloud reflection with terrestrial/atmospheric reflection accounting for the remainder.

A precise model of the earth albedo for precise thermal design and simulation is not available. The albedo models being used at the present time vary, depending upon the orbit, spacecraft design, and designers' preference. For greater orbital distances, the albedo is often assumed to have an average value of 35 percent of the incident solar and a spectral distribution similar to the sun. For near-earth orbits, the generalized models are less adequate, and, in some instances, a range of albedo is used rather than the average. Table 5 presents a suggested energy distribution as given by Mann and Benning for thermal simulation (ref. 10). It is important to note that, since 1962, large amounts of data have been gathered by spacecraft-borne radiometers. These new data are currently being reviewed, and a NASA design-criteria monograph is being prepared.

Earth Emitted (Infrared)

A significant third source of irradiation is due to the earth and is made up of two components: (1) direct radiation, from the earth's surface, which is transmitted through the atmosphere and (2) radiation that is emitted by the atmosphere. Of the 65 percent of the solar irradiation which is absorbed, approximately 2.5 percent is re-radiated through the atmosphere; and 62.5 percent is re-radiated by the atmosphere (ref. 11). Based on earth heat-balance relationships, the average radiant emission from the earth is 23 mW cm^{-2} . This is equivalent to the emission of a blackbody at a temperature of 251°K . Except for a variation on the order of several mW cm^{-2} associated with the 8.3-to-12.5-micron window and the emissivity of the atmosphere, the 251°K equivalent blackbody model has favorable acceptance.

REPRODUCIBILITY OF THE ORIGINAL PAGE IS POOR.

Table 3. Absorptance Percentage of Solar Cells and 18 Coatings for Proposed Solar Curve versus F. S. Johnson Curve

SOURCE OF SOLAR SPECTRAL IRRADIANCE DATA	RANGE OF INTEGRAL		WIDTH OF INTERVAL	ABSORPTANCE PERCENTAGE									
	From μ	To μ		1 Solar Cell	2 Ev. Au.	3 Coat. White	4 Evap. Ag	5 Pure Au	6 Al ₂ O ₃ Coated	7 Al ₂ O ₃ Mirror	8 TiO ₂ Coat.	9 Buffed Silver	
1 P. Moon Johnson	0.30	4.8	0.02	41.4 40.9	8.4 J.D.	19.3 19.1	2.1 4.2	11.1 11.7	18.3 19.0	14.5 14.6	8.0 8.0	17.9 18.3	27.6 28.4
2 Nicplet Johnson	0.24	2.0	0.02	43.0 42.8	18.9 20.5	15.5 16.8	4.4 5.7	11.7 13.0	17.5 16.6	14.8 15.1	8.3 8.3	14.9 16.0	25.2 25.8
3 Star Johnson Johnson	0.22	2.4	0.02	42.5 41.8	20.0 20.1	17.3 17.8	4.1 5.1	12.6 12.8	18.5 18.8	14.9 14.9	8.3 8.2	16.4 16.8	26.9 27.3
4 Allen Johnson	0.20	4.0	0.02	41.0 40.7	19.2 19.6	19.2 19.5	4.4 4.9	12.0 12.7	19.1 19.5	14.6 14.7	8.0 8.1	18.1 18.4	26.4 28.8
5 Star Mirrors, Ellis Johnson	0.24	4.8	0.02	41.5 40.5	18.3 19.5	19.4 19.9	4.6 5.0	11.7 12.5	19.3 19.8	14.6 14.6	8.1 8.0	18.4 18.8	28.1 29.1
6 P. Moon Johnson	0.30	2.5	0.01	42.7 42.1	19.0 19.6	16.0 17.0	3.8 4.3	11.2 11.9	17.2 17.9	14.7 14.8	8.2 8.2	15.2 16.0	25.7 26.6
7 Nicplet Johnson	0.23	2.19	0.01	42.4 42.3	18.7 20.4	15.9 17.2	4.3 5.2	11.5 12.9	17.6 18.7	14.7 15.0	8.2 8.3	15.3 16.4	25.4 27.0
8 Star Johnson Johnson	0.23	2.44	0.01	42.6 41.8	19.9 20.1	17.3 17.3	4.6 5.1	12.6 12.7	18.5 18.8	14.9 14.9	8.3 8.2	16.4 16.9	26.8 27.3
9 Allen Johnson	0.23	2.5	0.01	42.2 41.7	19.6 20.1	17.2 17.9	4.6 5.1	12.1 12.7	18.2 18.8	14.8 14.9	8.2 8.2	16.3 16.9	26.3 27.4
10 Star Mirrors, Ellis Johnson	0.23	2.5	0.01	42.7 41.7	18.8 20.1	17.3 17.9	4.7 5.1	12.0 12.7	18.2 18.8	14.8 14.9	8.2 8.2	16.4 16.9	26.3 27.4
11 NASA 711 Johnson	0.25	2.75	0.01	41.1 41.4	19.3 19.9	18.3 18.3	4.8 5.0	12.2 12.6	18.7 18.9	14.6 14.8	8.1 8.1	17.3 17.3	27.3 27.7
				10 Ev. Au on Cu	11 Ev. Ag on Cu	12 Ev. Al SiO ₂	13 Ev. Ag SiO ₂	14 Ev. Al Al ₂ O ₃	15 Glossy Coat Black	16 Au Paste	17 Buffed Al	18 Ev. Au SiO ₂	
12 P. Moon Johnson	0.3	2.6	0.01	34.9 36.4	20.3 20.9	49.6 49.5	30.5 31.1	20.8 21.0	85.0 85.0	24.0 24.7	16.6 16.8	41.9 42.6	
13 Nicplet Johnson	0.24	2.19	0.01	34.8 35.3	20.6 21.9	49.5 49.4	30.9 31.8	21.0 21.2	85.0 85.0	24.0 25.6	16.7 17.2	41.7 43.5	
14 Star Johnson Johnson	0.24	2.44	0.01	35.9 36.0	21.4 21.7	49.4 49.4	31.5 31.8	21.1 21.2	85.0 85.0	25.1 25.3	17.1 17.0	42.9 43.3	
15 Allen Johnson	0.24	2.6	0.01	35.5 35.1	21.1 21.7	49.5 49.4	31.3 31.7	21.0 21.1	85.0 85.0	24.7 25.2	16.8 17.0	42.6 43.1	
16 Nicplet Johnson	0.24	2.6	0.01	36.6 34.3	17.3 19.1	49.1 49.7	29.0 29.9	20.0 20.5	85.2 85.0	19.5 23.4	14.7 16.5	37.6 41.3	
17 Star Mirrors, Ellis Johnson	0.24	2.6	0.01	34.8 35.3	21.0 21.7	49.5 49.4	31.3 31.7	21.1 21.1	85.0 85.0	24.1 25.2	16.8 17.0	41.8 43.1	
18 NASA 711 Johnson	0.25	2.75	0.01	40.2 40.9	21.2 21.6	49.6 49.4	31.6 31.7	21.2 21.1	85.0 85.0	24.3 25.0	16.7 16.9	42.4 43.0	

Table 4. Solar Irradiance at Moon and Planetary Distances

Location	Distance From Sun (cm)	Solar Irradiance in Units of		
		Solar Constant	mW/cm ²	Cal/cm ² /min
Earth at 1 Astronomical Unit	1.4960×10^{13}	1	135.1	1.936
Earth at Perihelion	1.4710×10^{13}	1.034	139.7	2.002
Earth at Aphelion	1.5210×10^{13}	0.967	130.7	1.873
Moon at Minimum Distance	1.4669×10^{13}	1.040	140.5	2.013
Moon at Maximum Distance	1.5251×10^{13}	0.962	130.0	1.863
Venus at Average Distance	1.0821×10^{13}	1.911	258.2	3.700
Mars at Average Distance	2.2794×10^{13}	0.431	58.2	0.834

It has been noted, however, that for near-earth (300-nautical-mile) orbits some designers prefer to use a warmer equivalent blackbody temperature on the order of 265°K. The amount of earth-emitted flux incident on the surface of a spacecraft is dependent on the subtense angle of the earth as viewed by the spacecraft. A suggested energy distribution for simulation of earth-emitted radiation for thermal testing, as given

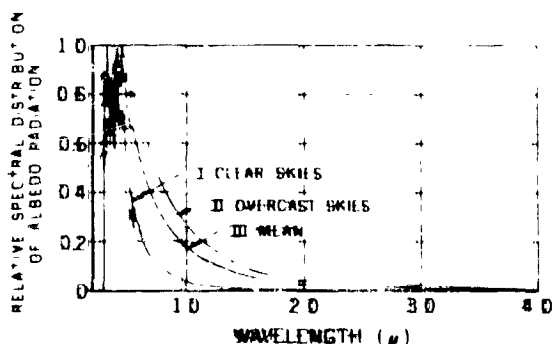


Figure 3. Spectral distributions of Albedo radiation versus sky condition.

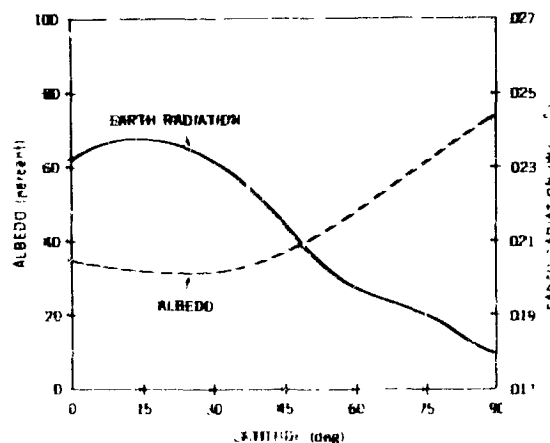


Figure 4. Albedo and earth radiation in under moon sky conditions as a function of latitude (tentative).

by Mann and Banning, is shown in table 6 (ref. 10).

It is obvious from the preceding description that knowledge of the natural environment is not precise and that an engineering

Table 5. Earth-Albedo Spectral Distribution

Wavelength Band (μ)	% of Total Energy	Energy in Band (W/cm^2)	Tolerance (%)
0.3 to 0.4	6.1	0.003	± 30
0.4 to 0.7	42.8	0.021	± 20
0.7 to 1.3	36.8	0.018	± 20
1.3 to 2.7	14.3	0.007	± 20

Table 6. Earth-Emitted Spectral Distribution

Wavelength Band (μ)	% of Total Energy	Energy in Band (W/cm^2)	Tolerance (%)
5.0 to 8.3	8	0.0018	± 30
8.3 to 12.5	27.5	0.0062	± 30
12.5 to 20.0	31	0.0071	± 30
20.0 to 40.0	28	0.0064	± 30

tolerance pertains to thermal design and simulation. Thus, designers and environmentalists devise boundary values that hopefully are conservative to use in design and testing. The root sum square of the tolerance values for the irradiance terms in the heat-balance equation, in the method described by Kline and McClintock, is felt to yield a mathematically conservative 2-sigma value for incident flux (ref. 12). The engineering judgment in selecting the value of the Δ tolerance is, of course, a very important consideration. Absorbed flux is derived by including, in a similar manner, the tolerance for uncertainty in the absorption coefficient and emissivity of the spacecraft surfaces (plus any flux absorbed due to re-reflection and re-radiation by other parts of the spacecraft). Expected spacecraft nodal (or equipment) temperatures are predicted, or found by testing, using these parameters and the internal heat dissipated by the electronics of the spacecraft. (It is normal

test policy at Goddard to have temperature conditions $10^\circ C$ hotter and $10^\circ C$ colder than the predicted temperatures applied for functional tests of prototype hardware; whereas, the $10^\circ C$ margin is not used for testing of the flight hardware.)

Solar Simulation

Simulation of the space thermal environment for testing full spacecraft systems has grown rapidly over the past 10 years and has given rise to at least three generations of solar simulator equipment. Despite the progress, it is certain that no solar simulator capable of illuminating a full spacecraft system duplicates space solar insolation. Table 7 compares pertinent solar parameters to the author's estimate of today's precise, operational, solar simulator.

Figure 5 shows the results of a recent survey of solar simulators in use for spacecraft system testing (refs. 13, 14, 15, 16, 17, and 18). An arbitrary limit of 27 square feet of irradiance area was used as the lower cutoff point to define a spacecraft system-test capability. The survey shows 14 simulators of varying capability. Four simulators provide a horizontal beam; the remaining ten are vertical. Only one simulator provides both a 416-foot-squared horizontal beam and a 125-foot-squared vertical beam. Three simulators, one in each size range, are presently capable of vertical irradiation much greater than one solar constant; their maximum is in the range of 1.9 to 2.2 solar constants.

The grouping shown by the three columnar fields in figure 5 conveys the author's opinion of the relative capability of these simulators. The criteria are twofold: (1) provision for energy boundary conditions such that the absorbed energy by a fixed spacecraft having equal areas of multiple coatings (ultraviolet absorber, flat absorbers, and visible and infrared absorbers) would attain temperature levels and a distribution similar to direct solar insolation and (2) complexity in measurement and mathematical adjustments to obtain a known energy

Table 7. Comparison of Solar Parameters Versus Today's Precise Solar Simulator (5-Foot-Diameter Beam)

Parameter	Sun at 1 A. U.	Precise Solar Simulator
Total Irradiance	139 mW cm ⁻²	139 mW cm ⁻² , <i>average</i> Stability: 2% of irradiance setting
Spectral Irradiance	F.S. Johnson or GSFC Curve	(a) Energy match basis: ±10% except ultraviolet (-45) and infrared (+30) (b) Effective absorptance basis for one solar constant total energy: ±10% of solar value
Uniformity of Irradiance	Uniform	±4%
Uniformity of Spectral Irradiance 0.25 to 2.6μ Bandwidth	Uniform	Energy basis: ±9% (estimated) Effective absorptance basis: ±5% (estimated)
Subtense Angle	32 Minutes	3°



Figure 5. Operational solar simulators with beam area 27 to 400 ft.²; one solar constant and greater intensity - 1969.

boundary condition for the fixed multiple-coated spacecraft such that the thermal balance of the spacecraft can be predicted.

The "column one" simulator has performance properties similar to that described as "today's precise solar simulator." All simula-

tors in this group are of an off-axis design, use xenon, high-pressure, short-arc lamps, and are closely filtered.

The "column two" simulators are excellent large-area solar systems and are the offspring of the third-generation simulator design. These systems are also the off-axis type and use 5- and 20-kilowatt, xenon, high-pressure, compact-arc lamps. They have nearly all the properties of the most precise simulator except that they are not closely filtered. The spectral distribution is that of the xenon source as modified by the optics (fig. 6). This group contains those simulators capable of irradiance levels as high as 2.2 solar constants. The most collimated system (2-degree total subtense angle and 1-degree incidence angle) is also in this group. Planar uniformity on the order of 3 percent has been measured on one of these systems (ref. 19).

In the "column three" category are the first-generation simulators, which are the on-axis system and the earliest version of the off-axis system. This group is characterized by

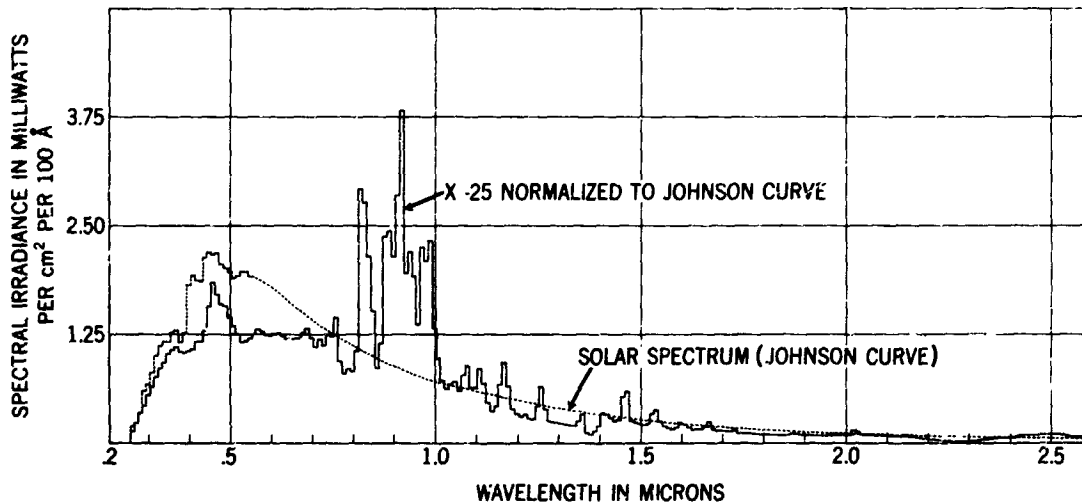


Figure 6. Spectral distribution of X-25, xenon simulator; center of beam at 95 amperes, no filter.

having carbon arc, mercury-xenon or xenon sources and also the largest 416-foot-squared horizontal beam and 220-foot-squared vertical beam. One simulator has both a 416-foot-squared horizontal beam and a 125-foot-squared vertical beam. Uniformity varies from a maximum of 10 percent in depth of field to ± 25 percent across a plane. Spectral filtering is not done, and spectral nonuniformity of ± 8 percent, reckoned on the basis of effective absorptance, has been reported (ref. 20).

The spectral match to the solar irradiance curve over the bandwidth 0.25 to 2.6 microns is worthy of more discussion. The degree of spectral match can be reckoned on an energy basis or on an effective absorptance basis. The modern, closely filtered, high-pressure, compact-arc xenon simulator has an energy distribution matching that of the solar spectrum on the order of ± 10 percent for most bands 0.05 to 0.20 micron wide across the total band of 0.26 to 2.6 microns (refs. 17, 21, 22, and 23). The 0.26- to 0.33-micron (ultraviolet) and the 1.4- to 1.6-micron (infrared) bands are exceptions, and the match is on the order of -45 percent and $+30$ percent, respectively. This distribution appears to be rather poor, but, on an effective absorptance basis, most coatings typical of those listed in table 3 would fall within 10 percent of the solar absorptance value. Spec-

tral distribution surveys across the larger filtered systems are not generally reported in the literature; however, it is estimated on the basis of smaller systems (table 8) that nonuniformity would raise the 10 percent figure to approximately 15 percent (ref. 21).

The nonfiltered xenon simulator system, for example, would yield effective absorptances within as much as 25 percent* of the solar value (ref. 19). Including a tolerance for spectral nonuniformity in the test zone could increase the variance to 30 to 35 percent. Similarly, for carbon arc and mercury-xenon, the variance range is 35 to 160 percent*, respectively (ref. 19). It is noteworthy that this comparison is of particular value when test considerations are for a spacecraft with multiple coatings of near equal area and the objective of the test is to obtain temperature level and distribution throughout the craft similar to orbit.

It is an important point to note that certain spacecraft designs could be tested in any of the three groups of simulators with equally adequate results. It is also true that a spacecraft consisting of an open structure covered with a fine mesh, such as might be used on a deployable antenna, could only be

*For a particular group of materials.

Table 8. Calculated Total Absorptance of Surfaces at Center, Edge, and Intermediate Positions of X-25 Filtered Xe Simulator

Surfaces	CB 70 a (1)	CB 70 a (2)	EB 70 a	EB 95 a	IB 95 a	CB 95 a	CB 95 (No Filter)	Solar
Solar Cell	0.418	0.409	0.394	0.405	0.422	0.408	0.494	0.416
Evap. Gold	0.192	0.187	0.206	0.213	0.195	0.193	0.151	0.199
Cat-a-Lac White	0.187	0.193	0.216	0.200	0.185	0.188	0.165	0.180
Evap. Silver	0.041	0.040	0.043	0.045	0.041	0.043	0.042	0.050
Rae Silver	0.119	0.116	0.125	0.130	0.120	0.121	0.101	0.126
Seidenberg White	0.187	0.189	0.197	0.195	0.187	0.190	0.167	0.188
Alzak	0.148	0.146	0.147	0.149	0.148	0.147	0.148	0.148
Evap. Aluminum	0.081	0.080	0.080	0.081	0.082	0.081	0.086	0.082
Ti O White	0.171	0.177	0.190	0.180	0.170	0.174	0.162	0.170
Menthyl White	0.274	0.276	0.303	0.296	0.276	0.275	0.236	0.274

tested with accuracy in the most uniform and collimated simulator.

The system-test solar simulators shown in figure 5 may be typed by their optical systems and are either collimated or direct projection. The collimated type are further typed as modular on-axis or massive off-axis.

Modular On-Axis Collimator

Beam sizes of 17½-foot-diameter vertical to 32-by-13-foot horizontal have been in operation for 3 to 5 years. (A fourth-generation advanced simulator of 25-foot-diameter beam is currently under development.)

Both reflective and refractive optical elements are used in each module to collect and to shape the energy from the source. A Cassegrainian optical system internal to the vacuum vessel is utilized to collimate the input energy and to direct it to the test zone. Figure 7 shows the module concept and the

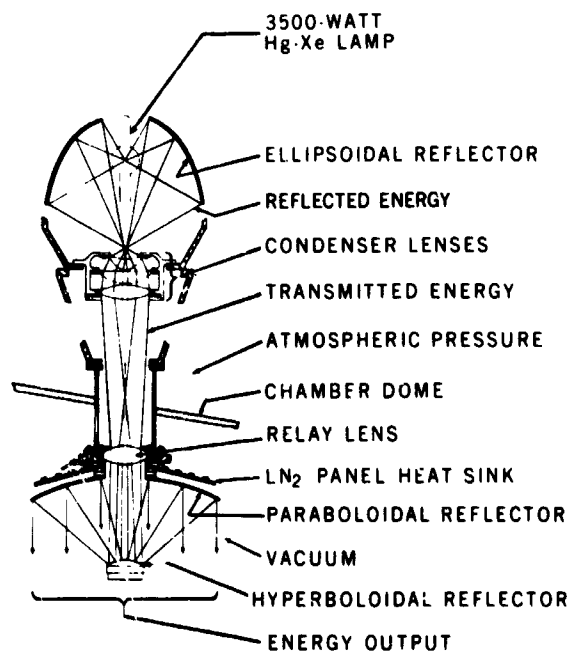


Figure 7. On-axis module, Goddard Space Flight Center.

configuration typical of the GSFC solar simulator design. An array of modules are used to obtain the desired beam size; figure 8 shows a typical arrangement. Although module size and optics differ amongst the simulators, the concept is basic. Sources such as 3.5-kilowatt mercury-xenon, 30-kilowatt carbon arc, and 20-kilowatt xenon are currently being used. Ray parallelism of 3 degrees to 4.4 degrees prevails. The better parallelism of the rays results in fewer modules contributing energy to an elemental area in the test zone. In the closely collimated system, the loss of a module due to source failure and the like results in a dark area in the beam. In the 2.2-degree, half-angle, collimated system, loss of a module would reduce the intensity by about 15 percent for test planes 25 feet from the Cassegrain optics.

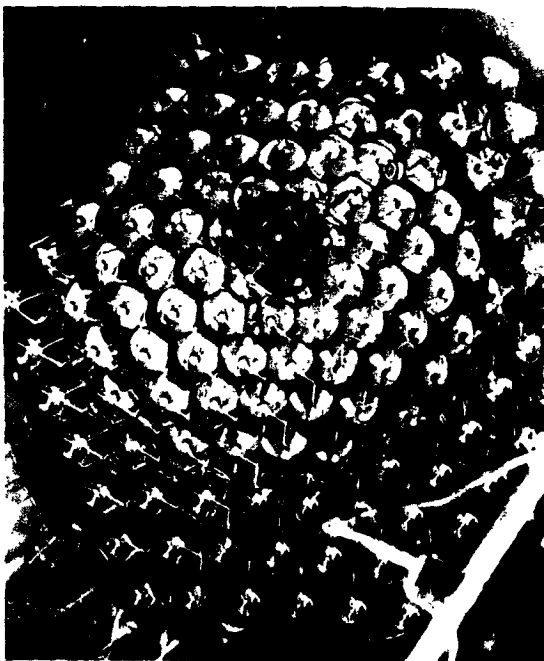


Figure 8. On-axis array, Cassegrainian configuration from inside the GSFC solar simulator.

Fill-in optics typical of figure 9 for the lower Cassegrain element does provide improved intensity uniformity at closer approach distances to the Cassegrain. Uniformity of total intensity on the order of

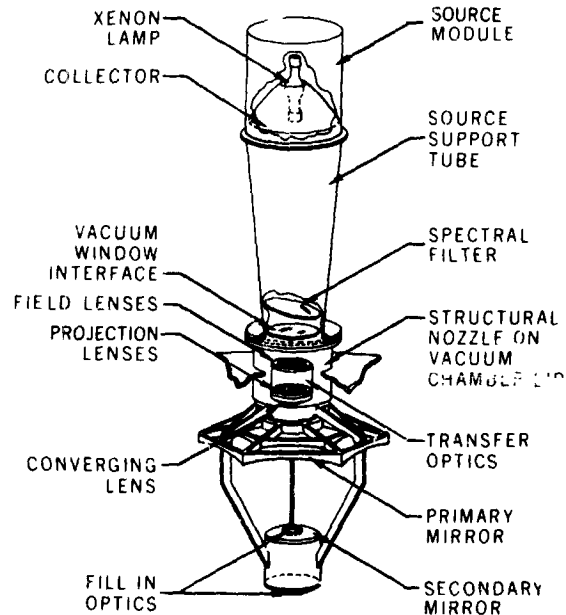


Figure 9. On-axis xenon module, vertical configuration, Spectrolab.

± 4 percent is theoretically possible for this type of design; however, because of the real world of optic surface and figure imperfections, plus difficulty in stacking and aligning large arrays of modules, uniformity on the order of ± 10 percent per square foot and ± 25 percent per 2 cm^2 * is routine. Spectral distribution for the carbon arc and mercury-xenon modular system is that of the bare source modified by the optics. Data on spectral distribution for the sources are available in the literature (ref. 17).

For many spacecraft thermal coatings, the effective absorptance at one-solar-constant total intensity is within ± 20 percent of the solar value for the carbon arc (ref. 17). The mercury-xenon spectral distribution is not as good a match (figure 10). For one-solar-constant total intensity and coatings typical of table 9, the effective absorptance varies from 3 percent to 125 percent of the solar value. Spectral nonuniformity across the test volume is another parameter. In the closely

* 2 cm^2 is a typical size for solar cells that are used to measure uniformity of intensity.

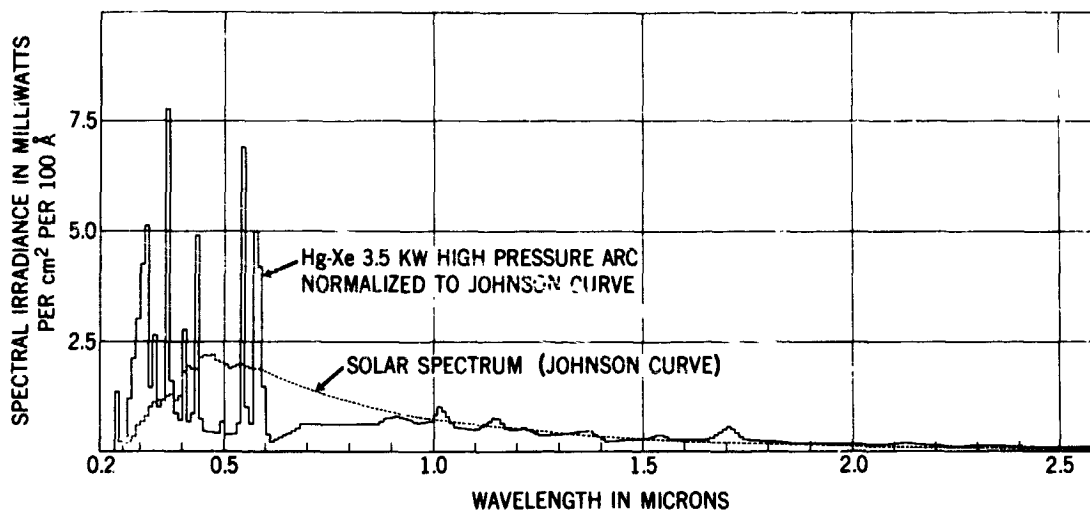


Figure 10. Spectral distribution of 3.5-kilowatt mercury-xenon lamp versus Johnson curve.

Table 9. Computed Total Absorptance of 10 Materials for New (T367) and Old 3.5 KW Hg-Xe Lamps After 800 Hours Operation, Compared to Solar Radiation

Surfaces	T367	T97	T58	646356	Solar
Solar Cell	0.270	0.312	0.301	0.312	0.415
Evap. Gold	0.257	0.244	0.249	0.247	0.200
Cat-a-Lac White	0.339	0.286	0.297	0.300	0.181
Evap. Silver	0.149	0.115	0.119	0.133	0.051
Rae Silver	0.222	0.194	0.198	0.207	0.127
Seidenberg White	0.306	0.261	0.269	0.278	0.188
Alzak	0.144	0.144	0.144	0.145	0.148
Evap. Aluminum	0.074	0.076	0.075	0.076	0.082
Ti O White	0.318	0.266	0.276	0.284	0.171
Methyl White	0.396	0.361	0.370	0.372	0.275

collimated system, the variability is on the order of ± 10 percent across the area of illumination of each module (with the differences between the center and the edge of each module beam, ref. 24). In the less-collimated mercury-xenon system, spectrum varies on the order of 5 to 10 percent across the test plane and less in depth of field. The improvement is from more mixing of the irradiance from the modules. Reckoned on an effective absorptance basis, the spectral nonuniformity of the mercury-xenon system is approximately ± 8 percent for a white coating (ref. 20).

Figure 9 illustrates the most advanced module design under development for a 25-foot-diameter simulator. Each module utilizes a 20-kilowatt xenon source and illuminates an area 48 inches across the tips of the hexagonal output beam. The inclusion of lenticular mixing optics, fill-in optics, and spectral filtering provides performance improvements over past modular systems. Uniformity of total intensity on the order of ± 15 percent per 4 cm^2 area has been demonstrated across a 7-foot-diameter beam, and ± 10 percent appears probable after adjustments are made. Spectral distribution typical of the smaller filtered xenon systems is

expected (fig. 11), and, on an energy basis, a match to the solar spectrum on the order of ± 10 percent (except ultraviolet and infrared -40 and +30, respectively) is probable (ref. 23).

The basic advantages of the modular solar systems is the capability to tailor the illuminated area to the size needed by the craft. No limit is placed on beam growth potentials. The problem of nonuniformity in total intensity and, to a lesser degree, nonuniformity of spectrum places great demands on automated data-handling and computer reduction capability to resolve accurately the energy incident on a spacecraft under test. Aside from obvious differences in spectrum between the carbon-arc and compact-arc sources, the stability and reliability of the irradiance for the compact arc is much better. With the use of automatic intensity servo-controlled systems, stability of the compact-arc system is on the order of 2 percent of an average setting for 100 hours or more; the stability of the carbon arc is on the order of ± 7 percent for a 24-hour period (ref. 24). A decided disadvantage of the on-axis system is the inability to obtain wide ranges of irradiance for a given module design. Another disadvantage is that re-reflection of energy from the illuminated spacecraft can return to the

test volume. Although this is not a large factor, 2 to 3 percent of returned energy adds to the uncertainty in boundary values unless careful calibration is done prior to testing.

Off-Axis Collimator

Beam sizes up to a 17-foot diameter are currently operational. In all simulators of this type of optical design, the collimating element is a reflector located inside the vacuum vessel. Illumination is by a source projection system (or systems) located external to the vessel. The projection of the illumination from the source to the collimator is at an acute angle with respect to the longitudinal axis of the test zone. Energy reflected by the spacecraft back to the collimator does not return to the usable test zone. Figures 12 and 13 show the Jet Propulsion Laboratory (JPL) configuration and optical schematic. Simulators of this type utilize 5-kilowatt xenon and 20-kilowatt xenon sources, and most of them employ an integrating lens to gain maximum mixing of the individual sources contributing to the total beam.

Spectral filtering is used on the smaller systems; however, for beam sizes greater than an 8-foot diameter, the spectrum of the unfiltered xenon source of figure 6 prevails. The

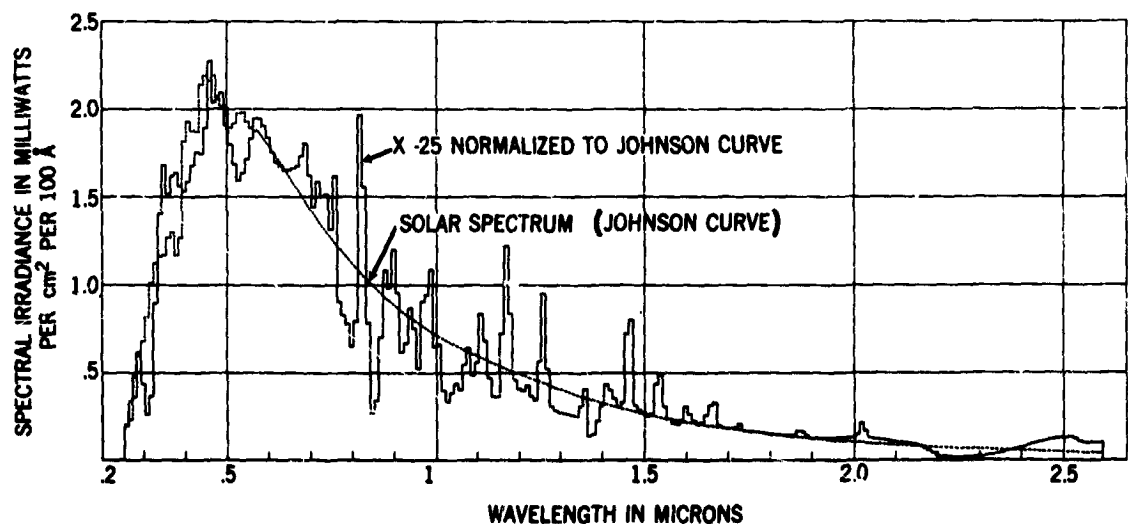


Figure 11. Spectral distribution of X-25, xenon simulator; center of beam at 95 amperes, with filter inserted.

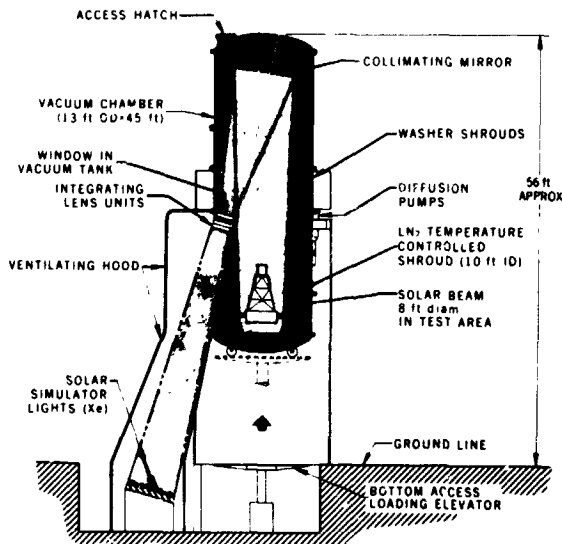


Figure 12. Off-axis solar simulator, cross-section of JPL 10-foot space simulator.

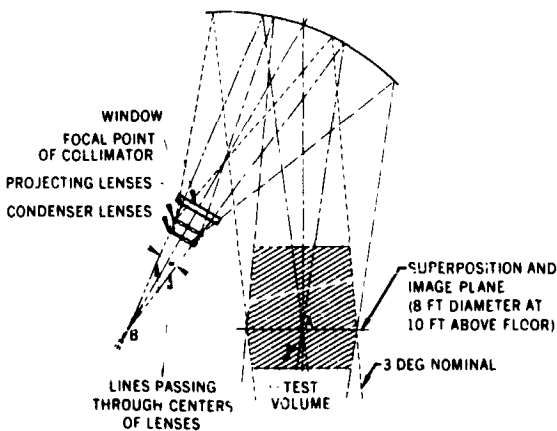


Figure 13. Off-axis optical schematic, JPL 10-foot space simulator.

intensity uniformity for most of these systems is excellent. The most uniform is on the order of ± 3 percent. Spectral uniformity on the nonfiltered system has not been thoroughly reported; however, available information does indicate the nonuniformity for the single-element collimator system to be less than a few percent. Ray parallelism is also excellent; the best has a subtense angle of

2 degrees and an incident angle of 1 degree. Stability is within 2 percent over a 24-hour period. All off-axis systems except two use a single-element collimator. The largest collimator in operation has a 23-foot diameter (ref. 14).

The two multiple-sector, off-axis simulators utilize mirror segments arranged to yield a collimated beam. An operational 17-foot-diameter system utilizes over 1900 segments for the collimating function. The most recent multiple-element collimator system placed in operation is a combination of the off-axis and on-axis designs. Figure 14 illustrates the optical schematic. Two sources (20-kilowatt xenon) entering a single optical integrator illuminates one-fourth of one sector of the four-piece collimator. One lamp is capable of producing energy sufficient for a one-solar-constant output (ref. 18). In general, the multiple-element collimator systems are not as uniform as the single-element systems. Uniformity of intensity is approximately ± 10 percent, and nonuniformity of

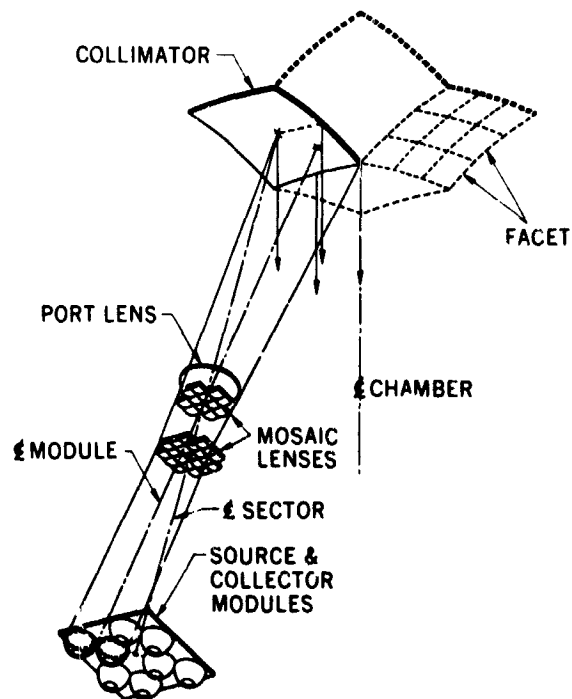


Figure 14. Off-axis/modular optical schematic, TRW.

spectral distribution is also estimated to be greater than that of the single-element collimated system.

The advantage of the off-axis system is excellent performance regarding intensity uniformity, spectral uniformity, and collimation. Great flexibility is available in irradiation level without compromise in optical performance.

A disadvantage of the off-axis system is lack of efficiency; electrical power "in" versus illumination "out" is approximately 5 percent. (The on-axis system efficiency is approximately 14 percent.)

A limiting factor toward larger beam diameters is the ability to construct collimators greater than a 23-foot diameter with equivalent optical performance.

Direct Projection System

The direct projection system produces a beam of irradiation with fair uniformity across a plane. The solar subtense angle changes with depth of field, and the solar normal incident angle changes across the plane of uniformity. Intensity in depth of field varies according to the square of the difference in distance between the plane closest to the source and the plane of interest. One of two simulators shown in the 6-foot- to 8-foot-diameter size interval in figure 5 is a unique direct projection system. A number of small sources (2.5-kilowatt xenon) with unique, segmented collectors are used in an overlapping mode to produce a beam 8 feet in diameter by 9 feet deep. Each lamp illuminates the entire test plane from a distance of 50 feet. The resulting solar test volume, 8 feet in diameter by 5 feet deep, has a uniformity of ± 10 percent throughout. Spectral distribution is that of unfiltered xenon.

The disadvantage of this system design is the lack of collimation. Irradiance along surfaces parallel to the longitudinal axis of the test volume are unrealistically high. Eclipse shields or mathematical correction factors would be required for most spacecraft tests in this simulator.

Albedo Simulators For Spacecraft System Irradiation

Simulation of earth albedo by using light sources and appropriate optical systems is extremely limited. To the best of the author's knowledge, the only operational system capable of producing irradiation with a field angle on the order of 160 degrees (necessary for near-earth orbits) is in use at the Manned Space Center (MSC). The simulator utilizes quartz iodine and tungsten sources, properly masked to produce an irradiance field 4 feet by 7 feet. The uniformity is on the order of ± 10 percent. The spectrum is that of tungsten iodine, a poor energy match to albedo spectral irradiance. (The system has been used for space-suit testing.) Lamp power is adjusted to obtain an energy level to force a precalculated absorbed flux condition by the test surface.

Many infrared heating systems are used to produce an equivalent temperature or an absorbed flux level that could result from earth albedo and/or earth-emitted radiation (ref. 16). These methods, however, do not provide a spatial distribution of the input energy typical of the field angle for near earth orbits.

Earth-Emitted Simulators for Spacecraft System Irradiation

As is the case with albedo simulators, simulators for earth-emitted irradiance in conjunction with simulation of solar irradiance are not generally available. The MSC chamber "A" facility does include a lunar plane in addition to simulated solar irradiance, but the author does not know whether or not it is suitable for simulating earth infrared. (In many cases of spacecraft testing where this flux is thermally significant to the thermal balance, plate radiators, infrared lamps, or heater blankets are used. The resulting simulation lacks fidelity, particularly with regard to field angle; i.e., incident angle and reflections are most often not typical of orbit.)

Other Simulation of Solar Albedo and Earth-Emitted Flux

A complete departure from simulating the irradiance of the sun and earth is to sim-

ulate its effects by inducing an equivalent absorbed flux or simply a known flux into the spacecraft by using infrared radiators.

Two forms of this type of simulation for thermal-balance testing are (1) to use heated plates and to attach them directly to the spacecraft as replacement shell elements or (2) to use heated plates and to place them near the spacecraft. For the latter case, a predetermined radiative coupling is utilized, and the radiator temperature is adjusted to a calculated value. Dr. G. Gordon described this method several years ago when it was used in testing the Relay spacecraft.

The more popular case is to use resistive heating and to attach the radiators directly to the spacecraft. The typical radiator would consist of a substrate and a bonded heater element. Nichrome-ribbon wire mesh embedded in a high-temperature, high-conductivity plastic or a conductive carbon-sprayed coating are typical of the heater configurations in use.

Regardless of the type of heater, there is a temperature gradient, across the composite, that is not identical to the actual flight shell or element. The ΔT across the composite must be accounted for in the thermal-balance analysis when precision is required. For the simple spacecraft configurations (one type of surface coating—no reentrant corners, cavities, projections, holes, or skin-mounted subsystems), this method should be carefully considered. Heater power control can be accurate within 1 percent or better, and absorbed flux can be obtained accurately. The uniformity of flux density is dependent on heater element placement and the circuitry used.

Care is needed in applying the heater elements to avoid undesired cold spots near the edges of the radiator and the hot spots caused by overlapping of the conductor. The emissivity of both the internal and external surfaces of the composite is usually matched to the flight-skin properties. This simulation was used for testing the OAO-A1 and OAO-A2 and is presently being implemented for use on OAO-B.

Solar Simulation Measurement Uncertainties

As mentioned earlier, the concept underlying thermal-balance tests on spacecraft systems is the creation of a known set of boundary conditions in which the performance of a given thermal-control treatment can be predicted. This concept accepts that the simulation is not a duplication of the natural environment but does force reflections and modes of heat transfer similar to orbit. Mathematical extrapolation is required to predict the orbital thermal performance of the craft.

In solar irradiance simulation, measurement of total intensity, spectral irradiance, and ray parallelism is necessary to define the incident boundary flux. It is also important to the thermal-balance test to define the effective heat-sink temperature and its low temperature emissivity and to resolve the direction and level of energy that is contributed by reflections plus any direct infrared due to fixturing, etc. The measurement requirements are complex because a number of these parameters are variable with time. The thermal interaction of the chamber/solar simulator and spacecraft configuration can also vary. Thus, careful calibration of the chamber/solar simulator is necessary and should be scaled to the precision required of the test.

Simulator measurements and calibration techniques vary throughout the industry and are reported widely in the literature (ref. 11). A detailed discussion on the subject is not attempted in this paper, but some estimate of the uncertainties in total and spectral irradiance measurements is discussed because these two parameters are very important.

Total irradiance measurements across large solar beam areas is often done by using fast response radiometers, thermopiles, or solar cells. Calibration of these detectors is done by comparison to secondary standard sources. With available standards and careful techniques, a calibration accuracy of ± 2 percent absolute is possible. Recent advances in cavity detectors based on the absolute standards of the ampere and volt offer an improvement in calibration to within 1 percent

of absolute (ref. 2). In the application of detectors to simulator measurements, the transfer of the standard to a suitable chamber detector results in some degradation in accuracy. Spectral differences between the standard source and the simulator source leads to additional uncertainty. In addition, data transmission and processing carry a further degradation. In all, the expected accuracy in sensing total irradiance under test conditions is estimated to be on the order of ± 3 to ± 5 percent absolute for the most precise tests.

Spectral irradiance measurements are more difficult and less precise than total irradiance measurements in the solar simulator. Standards of spectral irradiance for the 0.25- to 2.6-micron wavelength band have an uncertainty of 3 to 8 percent, depending upon the band of interest. Below 0.25 micron, no acceptable standard of irradiance is available.

The spectral irradiance in a solar simulator has been measured using monochromators, filter radiometer and, most recently, interferometers. Occasionally, spectral distribution has been inferred from the stabilization temperature of samples coated similar to the spacecraft. The problem in spectral mapping of a large area simulator is that a very small area of the beam is measured by these instruments, and time to make a single measurement (0.25 to 2.6 microns) is on the order of 10 to 30 minutes. Thus, occasional beam sampling is done rather than continuous point-by-point beam mapping. For the 0.25- to 2.6-micron wavelength range, the accuracy in spectral measurements inside a simulator is estimated to be ± 5 percent overall for narrow bands in the 0.2- to 0.3-micron range and for infrared in the 1.5- to 2.6-micron range, the measured values could be inaccurate to ± 10 percent.

Recently, it has become obvious and necessary to extend simulator spectral measurements into the infrared beyond 2.6 microns. In thermal-balance testing of a coating such as Alzak, 6 mW/cm^2 in the 2.6- to 25-micron bandwidth caused an unexpected error in energy absorbed by the test item on the order of 25 percent (ref. 25).

Thermal Analytical Models

Prediction of the spacecraft temperature distribution requires the solution of the transient heat-transfer equation by using specified boundary and initial conditions. Graphical methods, electrical analogy, or the lumped parameter method, utilizing thermal analyzer programs, are all in use (ref. 26). The thermal analyzer program and digital computer provides an ability to perform sophisticated simulations on large networks.

The thermal analyzer program is a transform of the spacecraft physical model. The algorithm consists of networks of thermal conductors and capacitors. The distributed heat capacitance of the craft is concentrated at isothermal nodes, and the distributed conductance is represented by conductors joining the nodes. The size of the thermal-balance network varies with the problem; e.g., 20 nodes for the simple 140-pound spacecraft, 300 nodes for a 4400-pound spacecraft, etc. The network capacity of today's large analyzer program (e.g., CINDA, GTA-1, etc.) is on the order of 2000 to 3000 nodes and over 500 conductors. Steady-state and transient temperature or heat fluxes can be computed for three-dimensional configurations.

A. Bartilucci, E. Lee, and M. N. Tawil describe the nodal equation and logic diagram showing the typical subroutines inputting to the thermal analyzer program (ref. 26). Figure 15 and the following is adapted from reference 26.

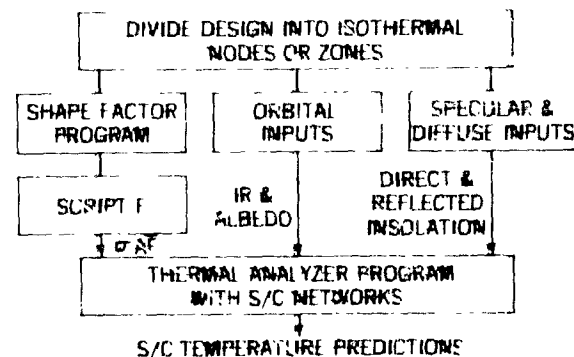


Figure 15 Typical thermal-computer flow diagram for spacecraft design.

The heat balance equation at node *i* is

$$(MC_p)_i \frac{dT_i}{dt} = \sum_{j=1}^n [K_{ij} (T_j - T_i)] + Q_i \quad (1)$$

Rewriting equation 1 in different form and solving for *T* gives.

$$T_{i,t+\Delta t} = \frac{\Delta t}{(MC_p)_i} \left[\sum_{j=1}^n K_{ij} T_j + Q_i - T_{i,t} \sum_{j=1}^n K_{ij} \right] + T_{i,t} \quad (2)$$

where:

$T_{i,t+\Delta t}$ temperature of node *i* at new time, °R

Δt time step which is always less than $\frac{(MC_p)_i}{\sum_{j=1}^n K_{ij}}$

to ensure stable solution, seconds

MC_p thermal capacitance, mass times specific heat, BTU/°R

K_{ij} conductance between node *i* and node *j*, BTU/sec-°R = $\frac{kA}{L}$ for conduction

= $2AF\epsilon (T_1^2 + T_2^2)(T_1 + T_2)$ for gray body radiation

= $\sigma A \epsilon_{eff} (T_1^2 + T_2^2)(T_1 + T_2)$ for radiation through thermal blankets

k thermal conductivity of material, BTU/sec-in-°R

A cross-sectional area of the conductive path, in²

L length of the conductive path, in

σ Stefan-Boltzmann constant, BTU/sec-in²-°R⁴

\bar{F} radiant exchange factor (Script F) including multiple reflection

ϵ_{eff} effective emittance of the thermal blanket, a measure of blanket performance (experimentally determined)

Q_i heat source at node *i*, BTU/sec (e.g., electrical equipment thermal dissipation, direct and reflected solar fluxes)

$T_{i,t}$ temperature of node *i* at old time, °R

T_j temperature at node *j*, °R

Subroutines to calculate insolation, planetary radiation, configuration factors and Script F mechanize the analysis process:

Config: Determines geometric configuration factors between surfaces. The output is used to generate radiant exchange factors by using the Script F program.

Script F: Solves matrix equation to determine radiant exchange factor (Script F) between surfaces, σAF . *F* is used by the analyzer program to generate radiation conductors $\sigma AF (T_1^2 + T_2^2)(T_1 + T_2)$.

Specular Solar: Determines net amount of energy absorbed by a craft with specularly reflecting surfaces. Shadowing by surfaces is also included.

Diffuse Solar: Same as for specular solar except for diffuse reflecting surface.

Planetary Flux: Determines albedo and infrared heat flux from planet.

The Grumman Corporation authors point out that the detailed networks of the analyzer program are large and the computing time is approximately 1 percent of the mission duration. Therefore, simplified networks of smaller size are used for short-time analyses.

Verification of the analytic model (thus evolved) is done through controlled thermal-balance tests. In one form, the input terms for solar and planetary radiation are adjusted for the simulator boundary, and test temperatures are predicted. In another form, the predicted orbital absorbed flux is simulated and test temperatures are predicted. Despite this difference, the succeeding process is to compare test temperature data to predicted temperatures and to adjust the conductor values until the analytic model more accurately predicts the physical model performance. This can be a long and tedious process if done by inspection. Matrix methods show promise in mechanizing the process. As stated earlier, for passively controlled thermal designs, the uncertainties in total energy for the solar simulator test are estimated to be on the order of 7 percent. For these designs and simulator capability, correlation of analytic models much better than 5°C does not appear to be warranted; however, for active thermal control systems using louvers, heaters, and the like, model correlation for the internal nodes can be much better, if needed.

Correlation: Validated Analytic Model Versus Orbit Performance

One result of thermal-control testing is a validated thermal analytic model. A comparison of predicted temperatures versus orbital actuals is one measure of the fidelity in simulation and analysis. A cursory review of this area shows that experience varies depending on the thermal treatment and configuration of the craft. For passive designs having a variety of surface coatings, the correlation appears to be on the order of $\pm 10^\circ\text{C}$, excluding coating degradation (ref. 27). For active thermal-control designs, the idea of

correlation is not as good a measure of fidelity in simulation and analysis because the ability of the design to compensate for error is greater. This is, of course, the exact purpose of this treatment. Despite this problem, correlation between predicts and actuals for the active thermal-control systems seems to be in the 5°C range and better (refs. 28 and 29). For large spacecraft using both active and passive thermal treatments, experience data reflects close correlation in some areas and wider correlation in others, depending on the local treatment. For example, according to reference 30, the Surveyor spacecraft experience could be summarized as shown in table 10.

A second example is the Mariner V spacecraft, which also included both passive and active thermal-control treatments. This spacecraft included provisions for "simple boundary conditions" and was purposely tailored to be insensitive to solar spectrum and intensity. According to reference 29, the correlation between predict and actual for nodal temperatures inside the structure during cruise was 4°F, with typical components running 1 to 2°F warmer than predicted. External node predictions were based upon analysis and "heavily corrected space simulator data", the deviations ranged up to 30°F.

A final extreme comparison is to examine recent results on the correlation of analytical prediction where thermal-balance testing was not performed on a first-of-a-kind design. There is scant data in this area because the idea of flight without thermal-control validation is unusual; however, some data do exist. M. C. Morris and R. K. Widel of Lockheed Company (ref. 1) discuss the correlation for a passive, temperature-controlled, secondary battery of a satellite power-generation system. The comparison of analytical predictions versus flight shows that, for internal and external battery temperatures, the deviations ranged from 5 to 15°F and from 0 to 7°F, respectively. Degradation of the thermal-control coatings was experienced and caused additional deviation of 3 to 13°F during the flight. The analysis suggests the degraded value for a white Thermatrol coating.

Table 10. Temperature Prediction Accuracy (Transit Flight)

Surveyor	Number of Preflight Temperature Predictions at Steady-State, Falling Within Given Range of Actual Temperatures °F (~°C)				
	±5 (±3)	±10 (±7)	±20 (±11)	±30 (±17)	> ±30 (> ±17)
I	27	21	18	5	3
II	41	28	6	—	—
III	43	16	15	1	—
IV	57	14	3	1	—
V	39	25	8	2	—
VI	48	20	6	—	—
VII	53	16	3	—	3

From the preceding discussion, it is obvious that a capability for thermal-control testing of a full spacecraft under simultaneous simulation of solar and earth irradiance does not exist. The thermal balance of a spacecraft such as the OAO (fig. 16), however, is significantly affected by the three inputs: (1) solar

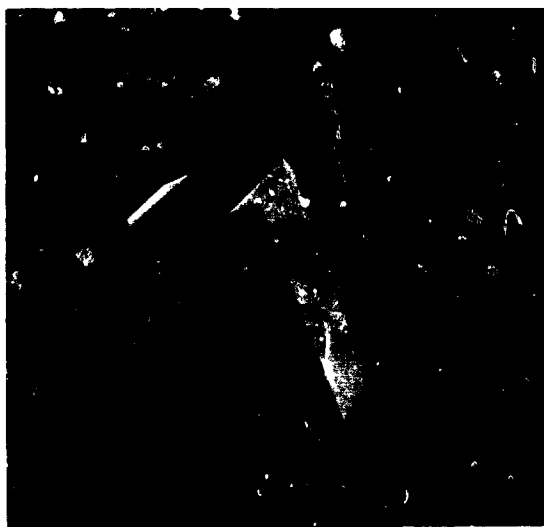


Figure 16. Artist's concept of OAO spacecraft.

insolation, (2) earth-emitted irradiance, and (3) earth-reflected irradiance. Table 11 illustrates the OAO-A2 flux situation for the cold and hot cases. Although it is beyond the scope of this paper to discuss detailed aspects of the thermal design and test results, the following illustrates the approach used and the results of the thermal system tests of the OAO-A2.

The simulation concept proposed for the OAO by the Grumman Aircraft Engineering Corporation, and accepted by the Goddard Space Flight Center (GSFC), for the system thermal test was orbital flux using heater skins attached to the spacecraft structure. Flux across the experiment aperture was simulated by a cooled panel.

The exterior configuration of the spacecraft was ideal for application of the heater-skin technique. By design, the flight skins were of a single coating (Alzak) and were mounted on isolators. The predominant heat transfer was by radiation between the skin and internal sinks on which most of the equipment was mounted. The heater skins were replicates of the flight skins except for a Nichrome-ribbon element that was bonded to

Table 11. Example of Computed Flux on Surface of OAO-A2 Showing Relative Contribution of Three Sources and the Spacecraft Solar Array Paddles

Source	Cold Case: $\beta=0$, 65% Sun		Hot Case: $\beta=90$, 83% Sun	
	% of Total Incident	% of Total Absorbed	% of Total Incident	% of Total Absorbed
Solar	56	24	76	49
Albedo	12	5	4	3
Earth-Ir	23	51	13	32
Paddle	9	20	7	16
	Cold Case: $\alpha=0.14$; $\epsilon=0.75$		Hot Case: $\alpha=0.24$; $\epsilon=0.75$	

Orbit: 435 N. Miles, 34° Incl., Circular

the inner surface. The coatings on the heater skin were similar to the flight skin; i.e., Alzak on the exterior surface and black on the internal surface. Precision power supplies were used to obtain a predetermined, equivalent, absorbed flux input. Figure 17 is a picture of the black internal surface of the heater skin. Figure 18 shows the spacecraft configuration in the GSFC test chamber. Figure 19 shows the star-tracker housing and minaret.

The star trackers and other sensors requiring stimulation during test were sources of error to the thermal-balance phase of the test. The uncertainty in the analytical correction factors for these devices was not resolved by test; however, the effect of the uncertainty was believed to be insignificant to acceptable thermal performance of the craft. The cryopanel configuration used to simulate orbital flux as well as flux from the experiment cover into the experiment aperture is shown in figures 20 and 21. The double panel arrangement offered an added capability to measure the heat leak of the experiment to space. This was particularly important to the thermal balance of both the experiment and the spacecraft. Predicted and measured heat leaks for both experiments to space were on

the order of 47 and 65 watts, respectively, for the most severe conditions.

The system test program was comprehensive; the more important phases of testing

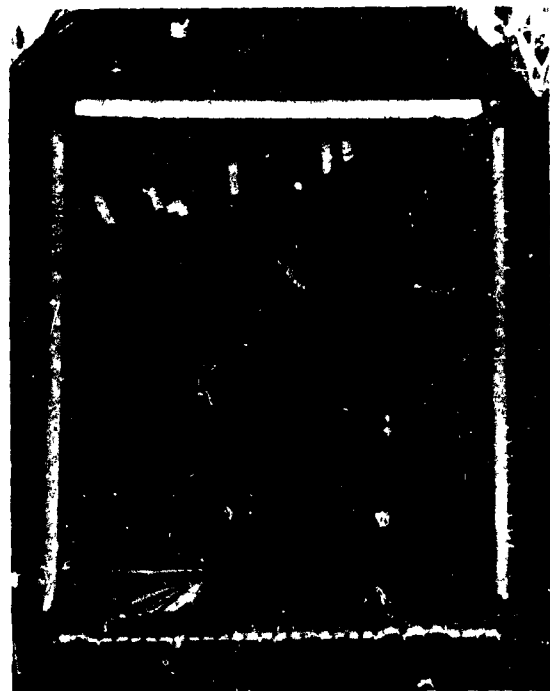


Figure 17. OAO heater-skin configuration used in testing OAO spacecraft.



Figure 18. OAO-A2 thermal-model test configuration in the GSFC simulator.



Figure 20. OAO-A2 experiment aperture cryopanel configuration used in system tests.



Figure 19. OAO-A2 spacecraft with star-tracker configuration intact.

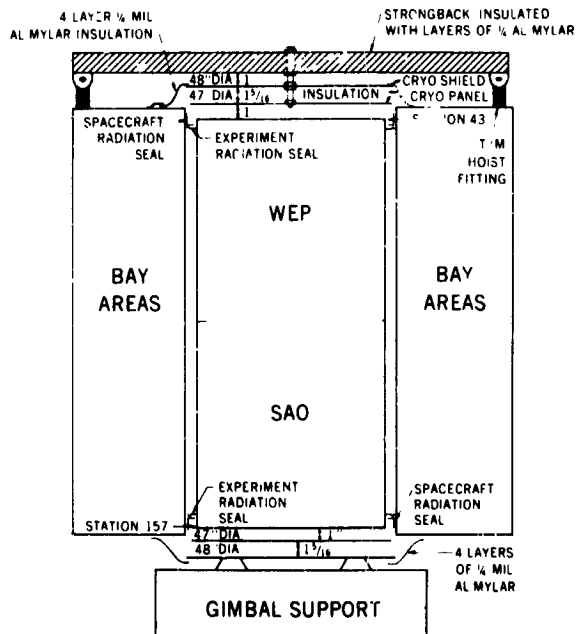


Figure 21. OAO-A2, WEP-SAO experiment, aperture cryopanel, schematic diagram; configuration used for heat leak measurement and conditioning during system tests.

that affected the verification of the thermal-control treatment at the system level of testing are listed in table 12. (This list omits many important thermal tests at a lower level of assembly; e.g., optical properties of flight

Table 12. Important Phases of Testing that Affected Verification of System Thermal-Control Treatment

Configuration	Objective	Test Environment
Heater Skin	Determine α and ϵ , and compare Q solar versus Q infrared.	Solar and Infrared
Inertial Model	Determine paddle reflected and infrared inputs to skins and determine experiment cover inputs to aperture of experiment.	Solar and Infrared
Thermal Model	Determine adequacy of thermal design and validate analytic model.	Infrared—except brief solar test to check thermal balance of star-tracker housing
A-2 Early TV	A secondary objective of this test was obtaining steady-state conditions to further the adequacy of the analytic model.	Infrared
A-2 Final TV	A secondary objective of this test was obtaining steady-state conditions to further the adequacy of the analytic model.	Infrared

skins, tests of louvers, thermostat/heaters, star tracker, solar arrays, experiments, etc.)

The thermal analytic model of the spacecraft was originated by the Grumman Aircraft Engineering Corporation (GAEC), contained 305 nodes, and was a lumped parameter type. The average temperature of a group of equipment in a bay was represented at a single node. Separate analytic programs were available for the most critical of the 48 bays making up the spacecraft, and separate detailed analytic programs were available via Arthur D. Little (ADL) Company for each experiment. Considerable effort was expended by GAEC, ADL, and GSFC in validating the analytic models. During the thermal-model test phase, an arbitrary limit of 10°C was established as a goal for correlation of the 305-node model. Predicted tempera-

tures from the analytic model and temperatures resulting from the tests were compared, and some 12 revisions were made to the coupling parameters in the model before the results shown in table 13 were obtained.

It was obvious that although the analytic model was not perfected in many respects, the design (with few adjustments) was sound with regard to maintaining equipment temperatures within acceptance limits. The early TV tests on the A-2 flight were to obtain proof of functional capability; data for further perfection of the analytic model was secondary to the test. During the functional test phase, the boundary flux was raised to the maximum expected for orbit and was doubled for a short time by inputting an equivalent maximum absorbed solar flux into both sides of the observatory, simultaneously. This was a

Table 13. OAO-A2 Telemetry Steady-State Temperature: Predict Versus Test Summary

Orientation	Node Area	No. of Nodes	Nodes Monitored	Predict to Test $\Delta T, ^\circ C$		
				0-5°	5-10°	> 10°
$\beta=123^\circ$	Structure	48	8	8		
	Skins	56	50	12	24	14
	WEP	45	6	5		1
	SAO	51	6	3	1	2
	Components	51	43	31	10	2
$\beta=45^\circ$	Structure	48	8	8		
	Skins	56	50	20	13	17
	WEP	45	6	5		1
	SAO	51	6	4	1	1
	Components	51	43	28	13	2
$\beta=90^\circ$ "A"	Structure	48	8	8		
	Skins	56	50	10	20	20
	WEP	45	6	5		1
	SAO	51	6	1	1	4
	Components	51	43	29	9	5

WEP = Wisconsin Experiment Package

SAO - Smithsonian Astrophysical Observatory

maximum temperature stress and did provide confidence in the design and function of the craft. Several steady-state thermal conditions typical of the thermal model test were obtained. Analytic model refinements were continued by GAEC and ADL.

The final TV test on the observatory was run at expected orbital boundary conditions, and additional data were used by GAEC for further refinement of the analytic model. The ΔT between predict and test was brought within $10^\circ F$.

Throughout the thermal testing, the nodes with poorest correlation between analytical prediction and test were the skins. The problem was caused in part by the position of the thermocouple used to monitor the average skin temperature. The 54 stimuli used to exercise the sensors and the test cabling that blocked the structure from emitting between skins contributed to the uncertainty in the configuration effects.

Despite the uncertainty, the testing was believed to be thermally conservative. It is essential to point out that optical functional testing of the experiments was not done during the system thermal-control or functional testing; means were not available to do so. The optical testing of the experiments was done at a subsystem level under room-temperature vacuum conditions. Alignment checks were performed in air at uniform low temperature at the experiment subsystem level and in air at the spacecraft system level of assembly.

The OAO-A2 was launched on December 7, 1968. Flight data on the thermal performance of the A-2 are being evaluated; however, preliminary information indicates:

1. Approximately 94 percent of the predicted spacecraft equipment temperatures are within $10^\circ F$ of the flight data. All bays except one are within $15^\circ F$ of the predictions.

2. The average structure temperature is higher but within 10°F of prediction except on the sunlit side of the craft where the truss temperatures near the ends of the craft are 12 to 19°F warmer than predicted. Circumferential gradients are, in general, larger than predicted or observed in testing.

3. Both the WEP* and SAO* are influenced by the higher average structure temperature. WEP, being more closely coupled to the structure, has Nebular, Stellar 1, Stellar 2, Stellar 4, and structure running approximately 10°F warmer than predicted at $\beta=123^\circ$ and 101° and 1 to 7°F warmer at $\beta=78^\circ$. SAO Uvicons, telescopes, and calibration lamps are running 6 to 28°F warmer than predicted at $\beta=78^\circ$.

The candidate causes for the lack of correlation between predicted and orbital temperatures appear to be related to unexpected flux trapping between skins along the truss line and at the hinge line of the experiment cover. The skin-temperature-predict problem appears to be due to instrumentation and configuration effects in the ground tests only.

References

1. Morris, M. L.; Wedel, R. K.: Passive Temperature Control of the Secondary Batteries of a Satellite Power Generation System. AIAA Paper 68-795, June 1968.
2. Almgren, D.; Covle, M.: Thermal Control Design Engineer, SPO Program. Arthur D. Little Company and GSFC, private communication.
3. Danielson, R. E.: Large Telescopes in Orbit. *International Science and Technology*, July 1967.
4. Johnson, H. L.; Iriarte, B.: The Sun as a Variable Star. *Lowell Observations*, Bull. 96, vol. IV, no. 8, March 1962.
5. Johnson, F. S.: *Satellite Environment Handbook*. Stanford University Press, Stanford, California, 1965.
6. Thekaekara, M. P., et al.: The Solar Constant and the Solar Spectrum Measured From a Research Aircraft at 38,000 Feet. Report X-322-66-304, GSFC, Greenbelt, Maryland, August 1968.
7. Laue, E. G.; Drummond, A. J.: *Science*, Vol. 161, 1968.
8. Murcray, D. G., et al.: The Measurements of the Solar Constant From High Altitude Balloons. University of Denver, Denver, Colorado, August 1968.
9. Thekaekara, M. P.: Private communication.
10. Man, A. E.; Benning, F. N.: Reaching for the Sun. *Environmental Quarterly*, March 1964.
11. Nelson, L. A.: Tutorial Lecture Series, Section 3. Institute of Environmental Sciences, April 1968, pp. 3-9.
12. Kline, S. J.; McKlintock, F. A.: Describing Uncertainties in Single Sample Experiments. *Mechanical Engineering*, January 1953.
13. Lund, D. E.: The 10-Foot Space Simulator. Jet Propulsion Laboratory, Pasadena, California, 1967.
14. Argoud, M. J.: Preliminary Description of the Modified JPL 25-Foot Space Simulator. Technical Report 33-319, Jet Propulsion Laboratory, Pasadena, California, 1967.
15. Harmon, H. N.: Four-Foot Solar Simulator System. The Boeing Company, Kent, Washington.
16. *Test Facilities Handbook*. Sixth ed., Arnold Engineering Development Center, Arnold Air Force Station, Tennessee, Vol. 6, pp. 1.1-8.1.
17. Radiometer Progress Report. First Trimester, NASA TM X-55827 X-Report no. X-713-67-126, Radiometry Section, Thermophysics Branch, GSFC, Greenbelt, Maryland, pp. IV-15-IV-30, and Table 3 p. A-1-9.
18. Levantine, A. D.: Operational Report on TRWs Conceptually New Solar Simulator. TRW Systems Group, Redondo Beach, Los Angeles, California.
19. Benning, F. N.: 1968 Tutorial Lecture Series, Section 5. Institute of Environmental Sciences. April 1968, pp. 5-20.
20. Thekaekara, M. P.: Spectral Irradiance Measurements in the SES. Internal Office Memorandum Report 69-2-2, DIRS: 01609-I-2-MR-148-161-222, Thermodynamics Branch, GSFC, Greenbelt, Maryland, January 1969.

*Wisconsin Experiment Package and Smithsonian Astrophysical Observatory.

21. Thekaekara, M. P.: Solar Spectral Irradiance Curves and Absorptance of Satellite Coatings. R&D Quarterly Report, Systems Reliability Directorate, GSFC, Greenbelt, Maryland.
22. Thekaekara, M. P.: Recent Advances in Solar Simulation Radiometry. Proceedings of the Fourth Conference on Solar Simulation Radiometry, Jet Propulsion Laboratory, Pasadena, California, Space Vehicles Division, NASA, Headquarters, Washington, D. C.
23. Castle, J. A.: Modular Xenon Solar Simulator for Large Area Application. Spectrolab, Division of Textron Electronics, Inc.
24. Maurer, H.; Williams, F. U.: Private Communication. MSC, Houston, Texas, April 1969.
25. Rogers, J. F.: Infrared Spectral Measurements in a Space Environment Simulator. TN-G896, NASA, GSFC, Greenbelt, Maryland.
26. Bartilucci, A.; Lee, E.; Tawil, M. N.: LM Passive Thermal Design on Test. AIAA Paper Number 68-748, June 1968.
27. Medlin, J. W.: Thermal Design Verification Testing of the Anchored Interplanetary Monitoring Platform "D". NASA TN D-4112.
28. London, A.: Shutter System Design for the Nimbus Spacecraft. AIAA Paper Number 67-309, April 1967.
29. Dumas, L. N.: Temperature Control of the Mariner-V Spacecraft. Jet Propulsion Laboratory, California Institute of Technology, Pasadena, California.
30. Vickers, J. M.; Garipay, R. R.: Thermal Design Evolution and Performance of the Surveyor Spacecraft. AIAA Paper Number 68-1029, October, 1968.

PRECEDING PAGE BLANK NOT FILMED.

N70-36753

Vibration Isolation of Large Masses and Vacuum Chambers

Robert W. Crawford
Barry Wright Corporation

Introduction

The theory of vibration isolation is well developed and has been successfully applied for many years. When the isolation requirements are modest and the equipment to be isolated is very simple, simple equations can be used to describe the motion of the system; and simple, inexpensive isolators can be used to solve the problem. On the other hand, when the equipment is complex or very precise isolation requirements must be met, an analytical solution often becomes impractical. It is then that engineering judgment and experience become useful tools to augment and refine the solutions indicated by analysis of an idealized system.

The purpose of an isolation system can be either to protect the isolated equipment from its dynamic environment or, as is commonly the case for machinery, to protect the surrounding structures from the equipment.

Until relatively recent times, "large loads" were limited to such things as freight cars, diesel generators, passenger vehicles, and the like, where equipment breakage or human comfort were the principal design criteria.

Conversely, delicate equipment that required a high degree of vibration isolation were limited in size to table-top experiments or relatively small assemblies of electronic or electromechanical equipment.

Technological advances beginning in the second quarter of this century have made new demands on vibration isolation systems. Several notable areas are:

1. *Microwave Communication Systems.* Physical distances between critical elements in

the system and the tolerances on these dimensions vary inversely with the signal frequency. Dynamic relative displacements within the equipment must be limited to very small values.

2. *Nuclear Warfare: Protection of Structures.* Ground shocks from nuclear weapons can disable strategic military installations if precautions are not taken. In some cases, entire buildings have been spring-mounted, and in many other cases isolation has been required for relatively large portions of the building (e.g., rooms or floors).

3. *Airborne Electronics.* High-speed aircraft and missiles are subject to severe buffeting and acoustically induced vibration. Consequently, the relatively fragile electronics and navigation systems require increasingly effective isolation.

4. *Optical Technology.* Optical systems are becoming simultaneously larger and more precise. In order both to inspect (during manufacture) and to use these systems, vibration must be reduced to the lowest possible level.

To meet the demands of the advancing technology in these areas, the technology of vibration isolation has been forced to keep pace. In many cases, conventional rubber or steel springs are hopelessly inadequate. Pneumatic isolators have overcome many of the problems and are now fairly common in the scientific laboratory.

There are many variations of pneumatic isolation systems. Some of these together with their control systems will be discussed in this paper. In addition, some applications will be discussed using the case-study method.

Basic Vibration Theory

Several good textbooks (refs. 1 through 6) on the subject of mechanical vibration are listed in the references at the end of this paper.

Single Degree-of-Freedom Systems

Figure 1(a) shows the simplest model of a single-degree-of-freedom, undamped, isolated mass. The natural frequency, f_n , of this system is calculated with the equation

$$f_n = \frac{1}{2\pi} \sqrt{\frac{k}{m}} \quad (1)$$

where k is the spring stiffness and m is the mass of the isolated equipment.

Other forms of this equation are obtained by using the relationships:

$$\delta_{st} \text{ (static deflection)} = W/k \quad (2)$$

and

$$W = mg \quad (3)$$

where W is the weight of the isolated mass and g is the acceleration of gravity. Then, equation (1) can be expressed as:

$$f_n = \frac{1}{2\pi} \sqrt{\frac{kg}{W}} = 3.13 \sqrt{\frac{k}{W}} \\ = 3.13 \sqrt{\frac{1}{\delta_{st}}} \quad (4)$$

A single-degree-of-freedom model incorporating viscous damping is shown in figure 1(b). The damper is shown as a dashpot (with damping coefficient C) in parallel with the spring. The natural frequency of this system, f_{nd} , is

$$f_{nd} = f_n \sqrt{1 - \left(\frac{C}{C_c}\right)^2} \\ = \left(\frac{1}{2\pi} \sqrt{\frac{k}{m}}\right) \sqrt{1 - \left(\frac{C}{C_c}\right)^2} \quad (5)$$

where C_c is the value of critical damping for the system. For most systems with practical application, the damping ratio (C/C_c) is small and

$$f_{nd} \approx f_n \quad (6)$$

If $C=0$, then the two systems are identical.

Figure 2 shows the transmissibility characteristics for these two systems and lists a number of values of C/C_c . It can be seen that increasing damping has two effects:

1. Reduction of the amplification at resonance and
2. Degradation of the isolation efficiency at high frequencies.

Improved characteristics can be obtained by a slight modification of the system. Figure 3 shows two systems incorporating relaxation (or "spring") damping. The two models are mathematically equivalent, but the model illustrated in figure 3(a) will be more useful in understanding its properties.

An analysis of this system is given in the *Shock and Vibration Handbook* (Chapter 7.3) and in other vibration textbooks. For the purpose of this paper, adequate understanding can be reached by taking an "intuitive" approach.

If you imagine that the damper can have any coefficient between zero and infinity, two limiting conditions will be obtained. The first, corresponding to $C=0$, yields an undamped transmissibility curve (fig. 4) with

$$f_0 = 3.13 \sqrt{\frac{k}{W}} \quad (7)$$

where

$$k = \frac{1}{\frac{1}{k_1} + \frac{1}{k_2}} \quad (8)$$

The second limiting condition is obtained by letting $C \rightarrow \infty$. Then the spring, k_2 , is "locked out," and a different undamped transmissibility curve is obtained for which

$$f_{\infty} = 3.13 \sqrt{\frac{k_1}{W}} \quad (9)$$

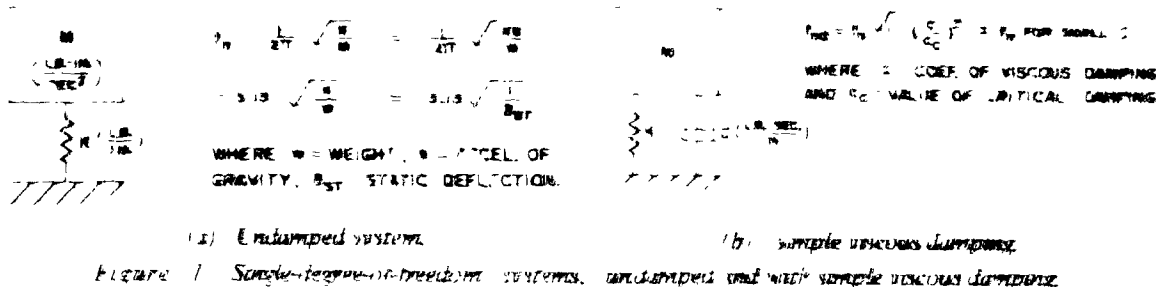


Figure 1. Single-degree-of-freedom systems, undamped and with simple viscous damping.

For all values of C between zero and afinity, transmissibility curves bounded by these two curves will be obtained. We may define "optimum damping" as that value for C that will give us the least amplification at resonance. If we draw the corresponding transmissibility curve, we find that the natural frequency and maximum amplification occurs where the two limiting curves intersect.

The curve indicated by a broken line in figure 4 is the transmissibility of a single-degree-of-freedom system with rigidly connected viscous damping (ref. fig. 2). At high frequencies, the isolation of the system with relaxation damping is seen to be superior.

Multidegree-of-Freedom Systems

The analysis of multidegree-of-freedom systems can be very complex, and a detailed discussion of this field is beyond the scope of this paper. A brief discussion of simple systems, however, may serve as a helpful introduction to the terminology and to the problem of coupled rocking modes of response.

Assuming that an isolated body is rigid and not restrained except by the isolators, it will have six degrees-of-freedom and, consequently, six natural frequencies. The six degrees-of-freedom are translation in three directions as well as rotation about three axes. The three axes defining these degrees-of-freedom are arbitrarily assigned and are usually mutually perpendicular, as shown in figure 5.

A center-of-gravity isolation system is defined as one in which the elastic center of the system of isolators coincides with the center of gravity of the isolated mass. Such a

system is also said to be "decoupled." When this condition exists, it is theoretically possible to excite a natural mode of response in each of the coordinate directions (x, y, z, α , β , γ) separately.

In most cases, however, there is coupling between two or more of the coordinates and then it is impossible to excite the isolated equipment into pure translation or rotation.

Consider, for example, the simple base-mounted cube shown in figure 6(a). Because of symmetry, there exists an uncoupled mode in the vertical direction; that is, if the system is deflected vertically and released, it will oscillate vertically at some frequency given by

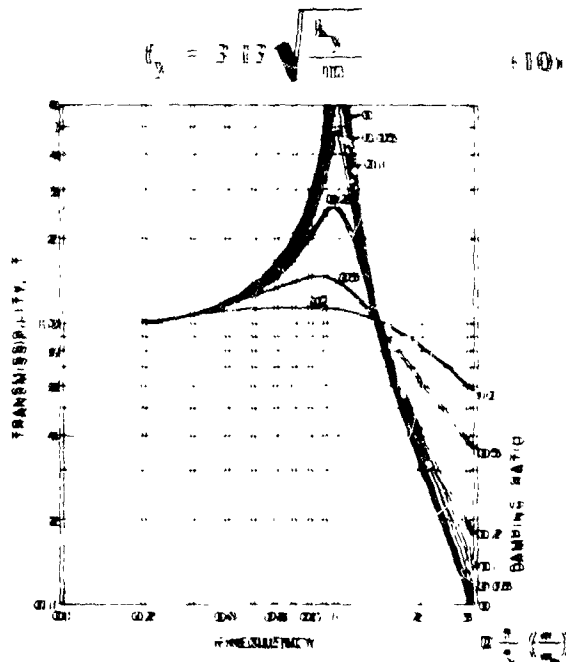


Figure 2. Transmissibility curves for single-degree-of-freedom systems, variously damped.

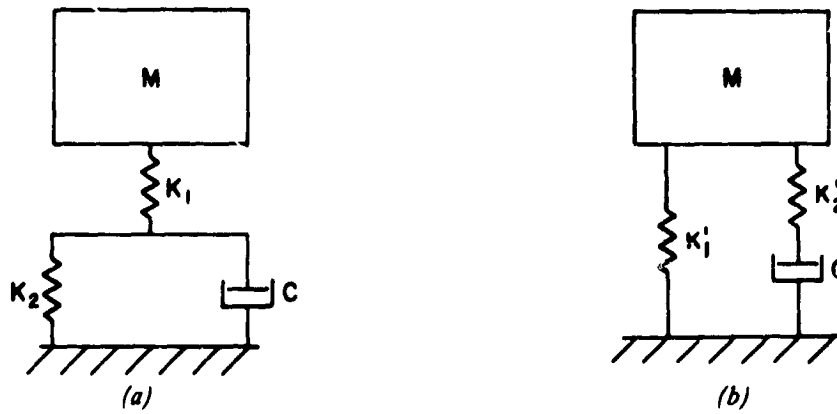


Figure 3. Single-degree-of-freedom systems with relaxation damping.

However, any attempt to excite the system into a purely horizontal natural mode of response will be futile; the system will rock instead. The coordinates x and α are coupled.

This is a significant point from the standpoint of writing (or trying to satisfy) a system specification. Suppliers of isolation systems

are often faced with the dilemma of showing acceptance test results that "prove" they have met a horizontal stiffness requirement by measuring the horizontal natural frequency of the system.

Figure 7 is a useful nomograph for relating the rotational properties of a system to the translational stiffnesses of the springs and the inertial properties of the mass. In this figure, ρ is the radius of gyration; k_x and k_y are the horizontal and vertical stiffnesses; ω_y is the vertical natural frequency, which has two values. Dimensions and coordinates are as

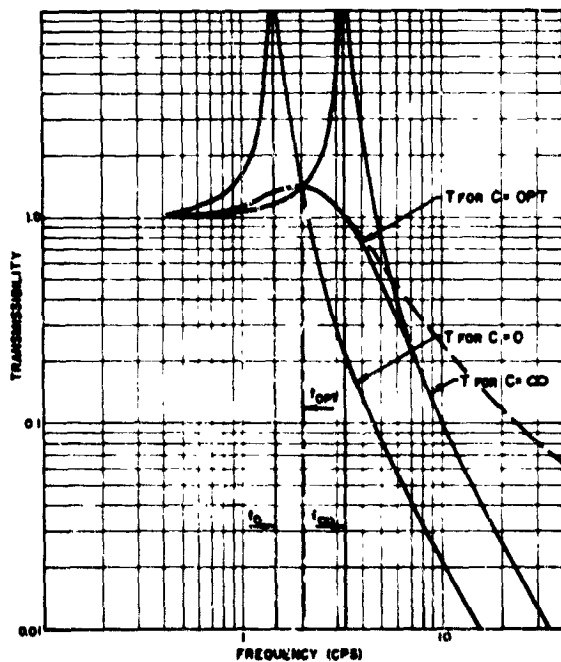


Figure 4. Transmissibility curve for system with relaxation damping.

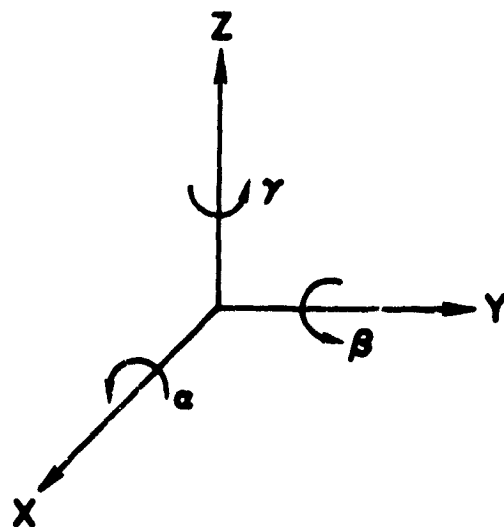


Figure 5. Definition of coordinates.

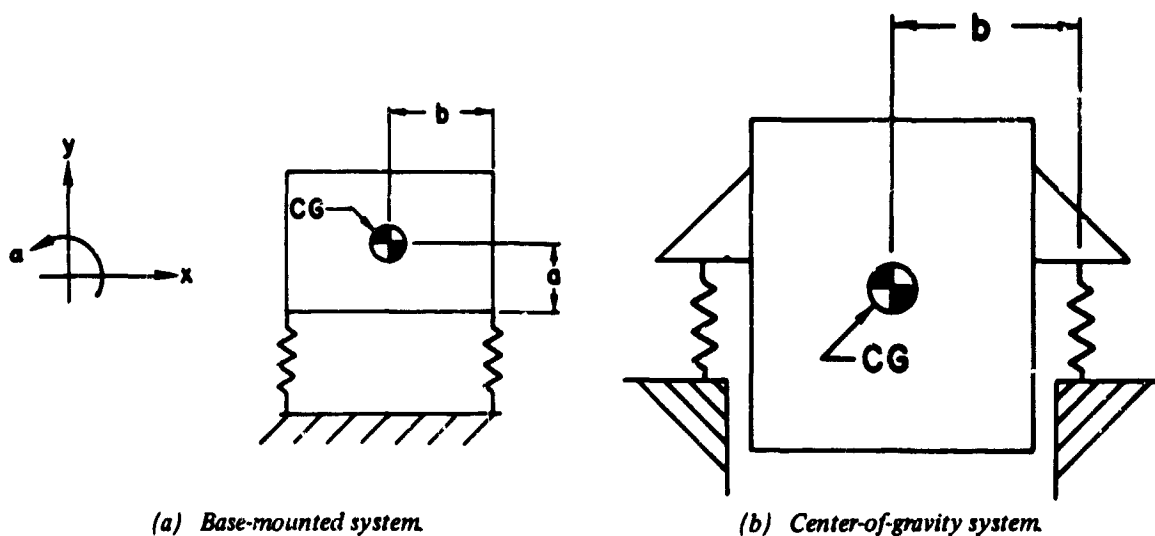


Figure 6. Multidegree-of-freedom systems.

defined in figure 6. The following numerical example has been worked out to illustrate its use. Suitable symmetry conditions have been assumed.

Example: Assume the load is a homogeneous 3-inch cube with a density of 50 lb/ft³. The system is to have a vertical natural frequency of 3 hertz, and the springs have a horizontal to vertical stiffness ratio of 2:1. Springs are located as shown in figure 6(a). What are the coupled, rotational, natural frequencies?

Reference to figure 7 reveals that, aside from the dimensions a and b (each being 18 inches), the radius of gyration ρ is the only other parameter required before the values for ω_c can be determined. This can be evaluated by using the relationships

$$J = \frac{m}{3} (a^2 + b^2) \quad (11)$$

$$\rho = \sqrt{J/m} \quad (12)$$

where J is the polar moment of inertia about an axis parallel to the z -axis and passing through the center of gravity and where m is the total mass of the body.

After performing the arithmetic, it is found that the two values of ω_c are 2.2 and 7.1 hertz. Note that one of these frequencies

is above the vertical natural frequency and the other is below it; this is normally the case.

Dynamic Environments

For most optical applications, it is desired that the mounting surface be fixed in space and "vibration-free." Neither of these two criteria can be absolutely achieved. Tilt and vibration to some degree are unavoidable. The problem in the design of each experiment or facility is to determine the tradeoffs between cost and performance and to negotiate a compromise between the two.

The tilt of a foundation can be caused by earthquake waves, earth tides, thermal distortion of buildings or surrounding ground, and instability of construction materials. Daily variations normally fall within the range of ± 3 arc seconds, and yearly variations up to 90 arc seconds have been recorded. Transient tilts are most commonly the result of changing thermal conditions, and permanent tilts are usually the result of earthquake waves or the settling of a structure on a soil foundation.

If tilt is a critical factor and the building tilt exceeds the allowable amount, a compensation system must be provided under the experiment. Such systems normally are referenced to the local gravity vector and may or

may not be incorporated into an isolation system. Usually, they are.

Figure 8 illustrates schematically one type of sensor used in gravity reference systems. A pendulum is suspended from the platform to be stabilized. The nozzles on each side of the pendulum are also attached to the platform. When the platform tilts, the gaps between the pendulum and the two nozzles change; this causes the back pressure to go up in one nozzle and down in the other. The difference between the two pressures is converted to an error signal, which is used to control a leveling mechanism.

Long-term tilts can be compensated for very accurately with this type of system. Figure 9 is a plot of actual data from a gravity reference system (installed by the Barry Controls Division of the Barry Wright Corporation) at a military facility for the testing and

calibration of inertial guidance equipment. Tilts of the foundation measured over a 62-hour period reached a value of 2.1 arc seconds while the tilt of the platform never exceeded 0.2 arc second.

In most cases, however, tilt is not a problem but vibration definitely is. The vibration environment may be due to many factors and will usually contain components with significant amplitudes in the frequency range from less than 1 hertz to several thousand hertz. The frequency range of interest is usually limited from approximately 1.0 to 500 hertz. In response to disturbing frequencies lower than 1.0 hertz, the structure of concern will normally respond as a rigid body, and, in most cases, this will allow the experiment to be conducted successfully. For disturbing frequencies higher than 500 hertz, a number of factors usually exist that contribute to the success of the experiment:

1. Support structure tends to isolate high frequencies.
2. Amplitudes of high-frequency disturbances are small.
3. Hysteresis damping in the materials of the structure or equipment tend to reduce the effect of high-frequency disturbances.
4. Important structural resonances in the equipment are usually well below 500 hertz.

One common method of classifying vibration is shown in figure 10. In this scheme, earth motion due to the forces of nature are divided into two ranges: (1) strong motion (in the seismic range) associated with earthquakes and (2) microseismic vibration that exists to some degree all the time and everywhere. The "industrial" range represents man-made vibration, which is generally higher in both intensity and frequency.

In the field of laboratory vibration isolation, we are not usually concerned with strong motion earthquakes, and, for the sake of simplicity, we abbreviate "microseismic" to "seismic" and limit our attention to the two regions defined approximately by figure 11.

Figures 12, 13, and 14 show some typical vibration-survey data. Figures 12 and 13

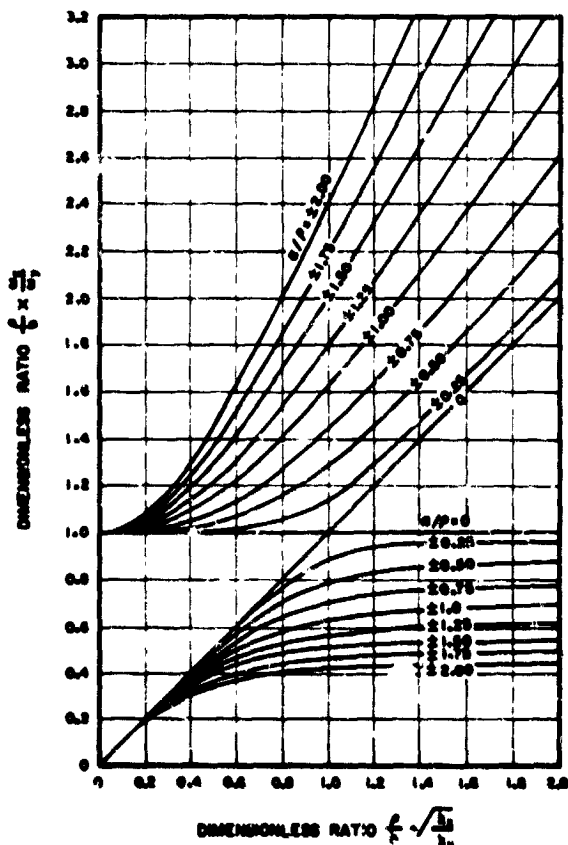
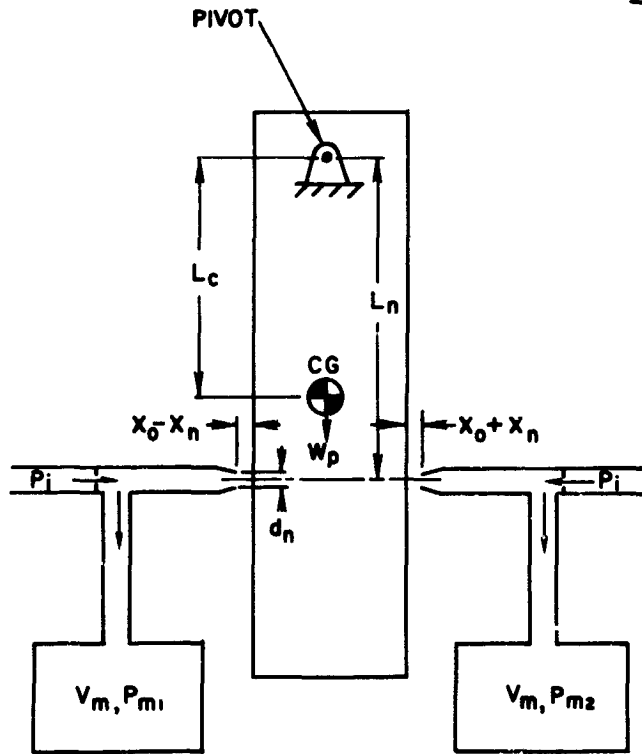


Figure 7. Nomograph for resolving frequencies.



The notations are defined as follows:

- A - orifice area, in²
- d - diameter, in
- k - C_p/C_v
- P - absolute pressure, psia
- R - gas constant, $2.5 \times 10^5 \text{ in}^2/\text{sec}^2 \cdot \text{R}$
- T - temperature, °R
- V - volume, in³
- W_p - weight of pendulum
- X₀ - steadystate position of pendulum relative to nozzle, in
- X_n - relative displacement of pendulum from mean position, in

Subscripts denote the following:

- i - air supply
- m - sensing circuit
- n - nozzle

Figure 8. Schematic diagram of flapper-nozzle amplifiers.

show the nature of the vibration environment at a relatively quiet research facility, indoors and outdoors, during normal working hours. Figure 14 shows similar data for a manufacturing facility. In this figure, the method of analysis yielded the rms magnitude of vibration over a time interval; therefore, these data do not show the maximum magnitude of transient vibrations such as might be caused by punch presses and other short-duration events.

Specifications

Perhaps the best way to obtain a good specification for an isolation system is by collaboration between the user and the supplier. All too often when the user writes the specification by himself, he inadvertently incurs unnecessary expense by specifying properties he does not really need. On the

other hand, he can also incur additional expense by overlooking a critical point that will eventually require a "field fix."

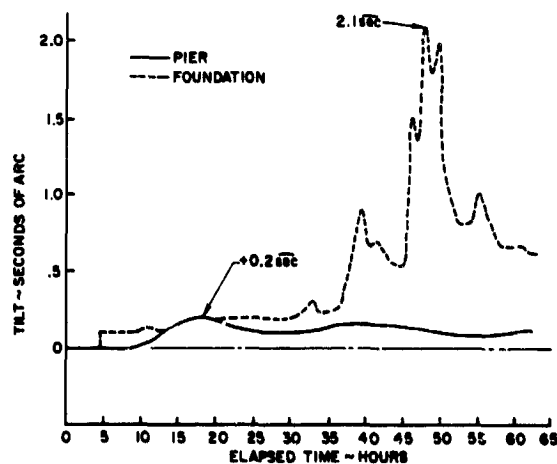


Figure 9. Platform tilt versus foundation tilt.

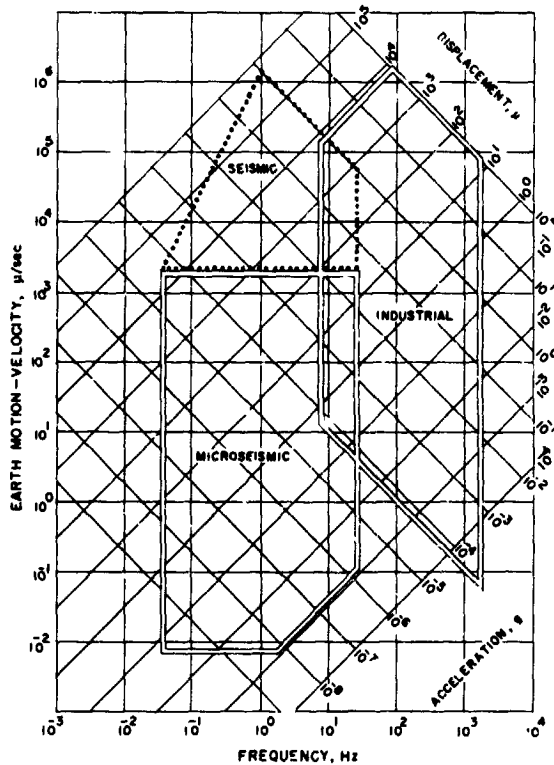


Figure 10. Arbitrary classification of vibrations.

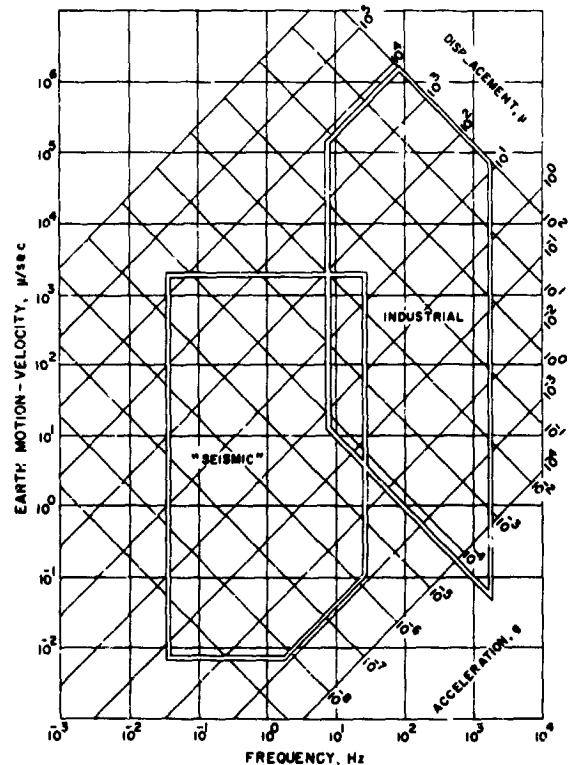


Figure 11. Modified classification of vibrations.

It is sometimes desirable, however, especially in the early stages of a program, to write a preliminary specification without the help or influence of a potential supplier. The following is a brief discussion of the critical points of a specification to indicate to the experimenter what can and should be expected of a typical isolation system.

Although the outline of a specification will vary somewhat with the application, a typical outline would cover the following topics:

1. *General*

a. Description of the equipment to be isolated, including dimensions and inertial properties

b. Description of the site, including allowable floor-loading, space available for the isolation system, and the preferred installation configuration, if there is one

2. *Performance*

a. *General objectives.* (for reference and understanding only)

b. *Natural frequency or frequencies.* Usually, the best way is to specify the most important direction and then to lump the remaining five. For example: The vertical natural frequency shall be 2 hertz or less. All others shall be 4 hertz or less.

c. *Transmissibility.* Transmissibility may have different characteristics in the different modes of response. It is best to be specific only in regard to the most important direction(s). A maximum transmissibility envelope is the clearest and simplest way to attain the objective.

3. *Materials and Workmanship* (Self-explanatory.)

4. *Work Schedule* (Self-explanatory.)

5. *Accessories Required*

a. *Air supply.* Pneumatic systems normally use available "shop air" supply, but the user may desire the supplier to provide a compressor with the system.

b. *Interface.* Interfacing requirements should be stated regarding attachment

VIBRATION SURVEY AT AN AEROSPACE RESEARCH LABORATORY
(WESTERN U.S.A. DESERT LOCATION)

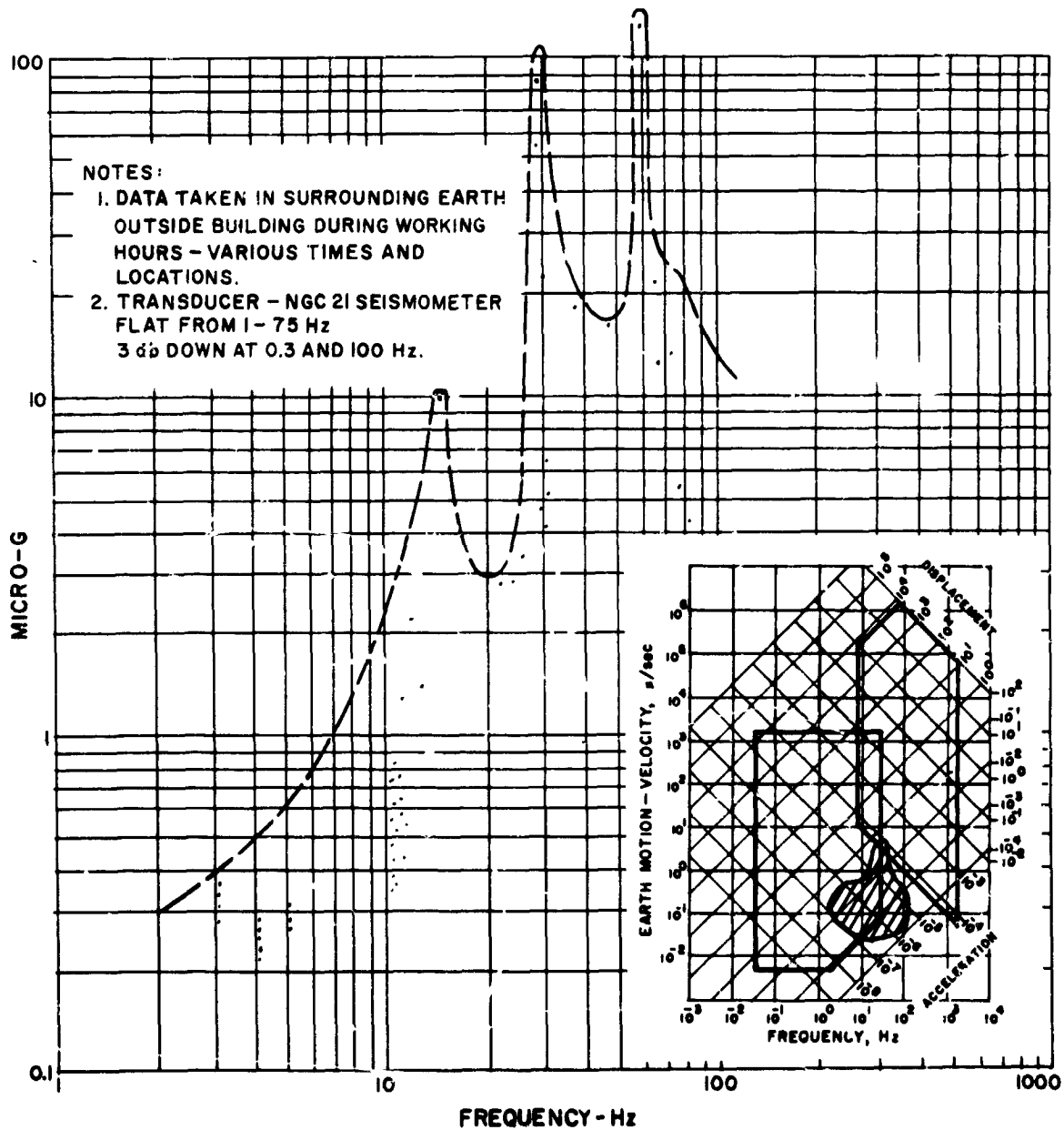


Figure 12. Vibration survey data for normal outside environment.

hardware, reaction mass (if one is necessary), flexible couplings, etc.

c. *Controls.* Dual controls may be desirable, especially if the system occupies two levels in a building.

d. *Indicators.* Remote indicators of the system status are sometimes desired.

e. *Spare parts.*

f. *Operating and maintenance manuals.*

VIBRATION SURVEY AT AN AEROSPACE RESEARCH LABORATORY
(WESTERN U.S.A. DESERT LOCATION)

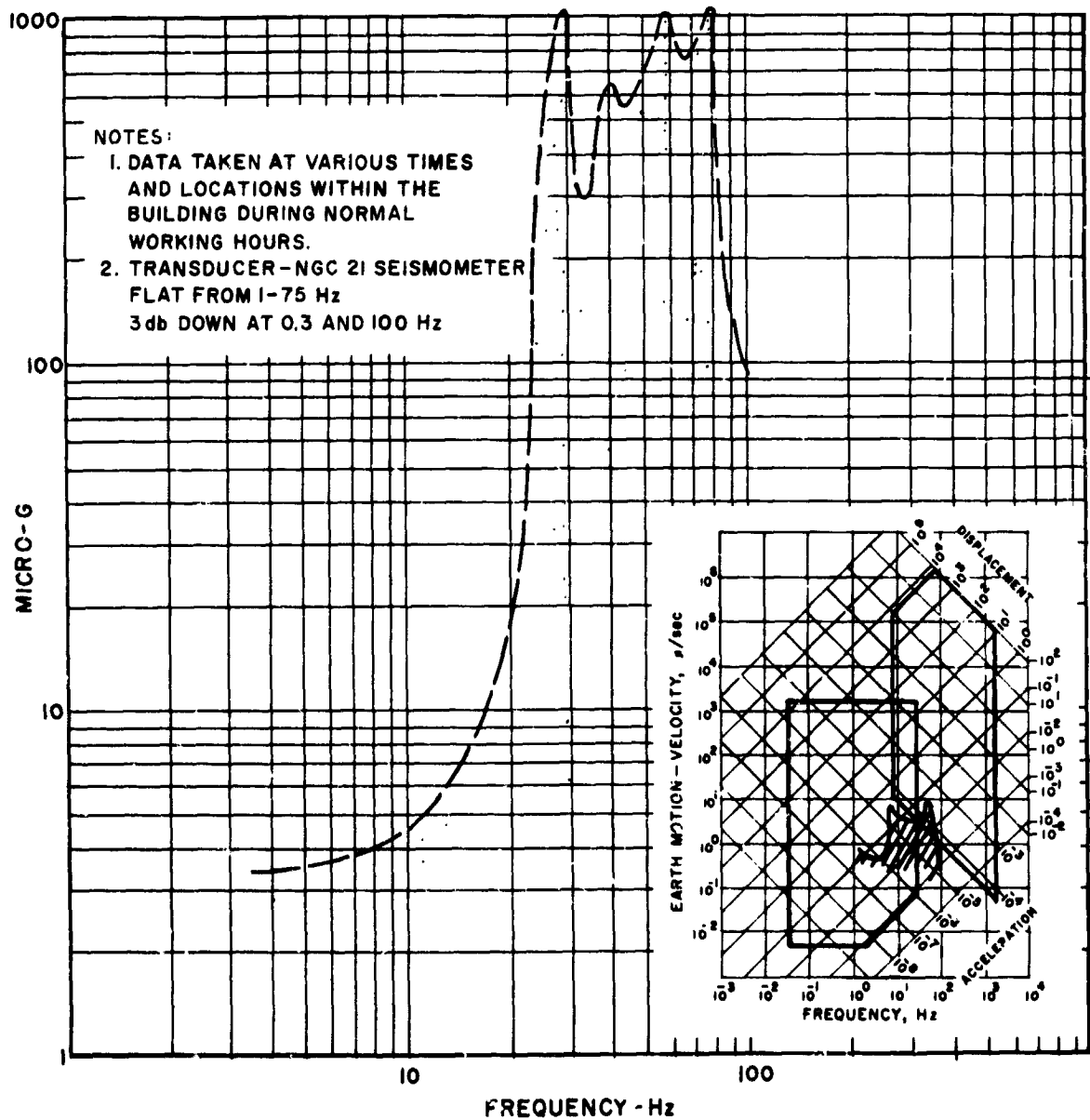


Figure 13. Vibration survey data for normal laboratory environment.

6. *Warranty*

Typically, 30 to 90 days is offered. The user must state what he expects; otherwise, he will get what the manufacturer normally offers.

7. *Acceptance Criteria*

The extent of acceptance testing required can greatly influence the cost of a system. Therefore, the user should keep it to the absolute minimum, but he should not buy

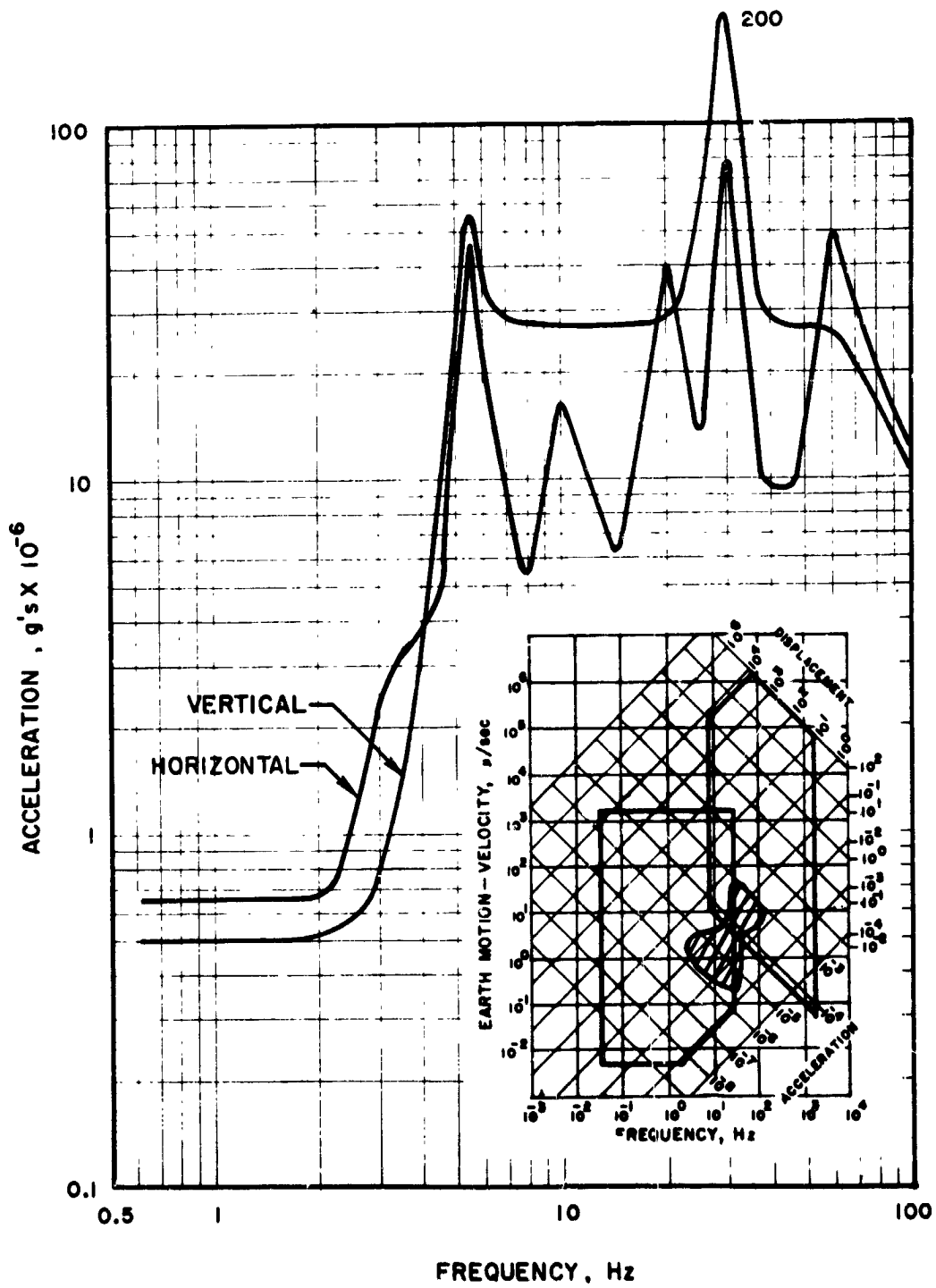


Figure 14. RMS ground vibration level in an industrial facility.

a "pig in a poke." Often, a combination of test and calculation is the most practical and least expensive way to evaluate performance.

Perhaps the most important aspect of a specification is the acceptance-test procedure prescribed. The supplier of the isolation system cannot be held responsible for the internal dynamic properties (resonances) of the isolated equipment, but these characteristics will often confuse the test data to the point of making them useless. (An example of this is given in the case studies discussed further on in this paper.) Even if the isolated equipment is a rigid body (this is never really true, but sometimes approximately so), coupling between the modes of response often makes it difficult to identify the component of response being tested. The experimenter usually wants experimental proof that the isolation system does everything it is supposed to do, but, in practice, this proof is usually very difficult and very expensive to obtain. The experimenter would be well advised to discuss this thoroughly with his supplier and independent consultants before specifying the acceptance procedure.

Advantages of Pneumatic Isolators

Steel springs have four disadvantages as isolators:

1. They are undamped.
2. They ring (transverse vibration of the wire in the spring).
3. They surge.
4. They transmit high frequencies through the wire.

All of these cause vibration to be introduced to the isolated equipment. In non-critical applications, these disadvantages may be outweighed by the relatively low cost of steel springs, but, in most critical applications, they are not satisfactory.

Rubber pads (shear or compression) overcome the first three disadvantages of steel springs fairly well, but they have their own disadvantages: (1) high-frequency isolation better than steel springs but still not good enough and (2) impractical for achieving low natural frequencies.

Pneumatic springs, on the other hand, have a number of properties that make them especially well suited to low-frequency, high-quality isolation:

1. The low mass density (essentially that of air) reduces surge energy to practically zero.
2. High-frequency isolation is extremely good (transmission only through the shell or bag material).
3. Very low natural frequencies are attainable with low volume requirement.
4. Constant operating height and levelness can be maintained because pneumatic springs are controllable.
5. Free height of spring is approximately equal to the operating height (zero static deflection).
6. "Sprung-damping" can be achieved, which further improves high-frequency attenuation.

Within the general class of pneumatic springs a number of types exist. The many control systems possible further multiply the variations in design and performance that can be encountered. There are two basic types of pneumatic springs in common usage: (1) *air "bags,"* which are usually rubber-coated fabrics with appropriate stiffeners and fittings, and (2) *air cylinders,* which are rigid containers with a piston and some sort of flexible seal between the two.

The air cylinders offer two distinct advantages:

1. The diaphragms used in the better types are relatively narrow. As a result, the stresses induced are low, and the diaphragm can be made very thin and flexible. The lack of mass and cross-sectional area enable very effective isolation at very high frequencies.
2. Column stiffness is provided by the rigid cylinder, enabling relatively tall (and therefore low-frequency) isolators to be used without sacrificing static stability.

The control systems used vary in details, but all perform the same function; namely, they sense the height of the isolated equipment and adjust the air pressure as required to maintain the system at some predetermined height. The accuracy with which this is done

varies greatly, but very precise height controls (± 0.0001 inch) are available.

Case Studies

Case Study I: Isolation of a Large Vacuum Chamber

This story is based upon an actual case; however, some details have been simplified for the sake of clarity.

The vacuum chamber was approximately 6 feet in diameter and 10 feet long. Rigidly attached to each end was an antechamber about 3 feet in diameter and 5 feet long. The total weight of this assembly was about 50,000 pounds. The assembly was supported by a pneumatic isolation system on the second floor of a modern research facility. Suspended from the main chamber were two large diffusion pumps, which penetrated the floor and came to within approximately 2 feet of the base slab of the building. The mechanical pumps associated with the chamber were on two concrete blocks that were also pneumatically isolated on the lower level. Figures 15 and 16 show schematically the installation configuration with most interconnecting details omitted.

Other than the mechanical equipment in the vacuum system, there was no machinery in the vicinity to generate disturbing vibrations; "background" vibration caused by equipment elsewhere in the building was at a low enough level to be easily isolated.

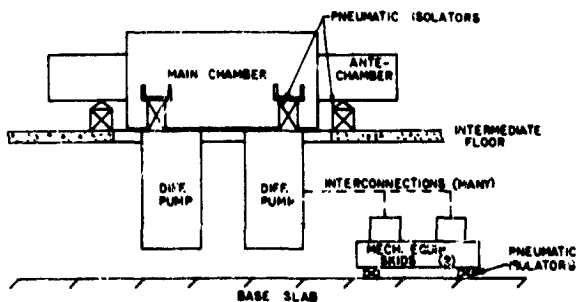


Figure 15. Isolated vacuum chamber system, side view.

The principal direction of concern for the chamber was vertical. It was decided that the natural frequency in this direction should be 0.75 hertz or less. The horizontal natural frequency selected was 2.5 hertz or less.

The pump pallet was isolated with isolators providing a vertical natural frequency of 2.2 hertz, and a pallet with a large, rather violent compressor was provided with a 1.5-hertz isolation system.

The flexible couplings connecting the mechanical pumps to the chamber were important to the performance of the system. Because there was concern about the high-frequency transmissibility of the conventional bellows type of couplings, couplings of a superior type were recommended and provided. Other interconnections to the vacuum chamber that had to be considered were:

1. Electrical cables for instrumentation and control
2. Flexible couplings in the liquid nitrogen lines
3. Coolant water lines
4. Pneumatic control lines for the valves in the vacuum system
5. Bracketry for supporting all of the first four items listed.

The designers of the vacuum system kept rigidity in mind and attempted to support all piping in the manner that would yield the highest structural-resonant frequencies and to provide adequate flexible connections in all interconnections to the chamber.

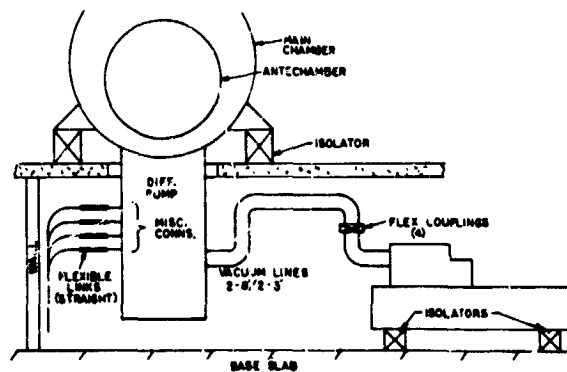


Figure 16. Isolated vacuum chamber system, end view.

The system design and installation proceeded at the usual "gotta-meet-the-schedule" pace, was finished only slightly behind schedule, was turned on, and "didn't work"; that is, vibration of the vacuum chamber was too great for the intended use of the system.

A lengthy test-and-analysis phase ensued in which every possible vibration source and transmission path was evaluated. At the conclusion of this study, it was determined that the main problem was the existence of high "Q" structural resonances in the plumbing attached to the chamber, which were being excited by relatively low-level vibrations being transmitted through all of the various flexible connections. (There was an estimated total of about 30 such connections.)

Everyone involved did not agree with this diagnosis. In fact, there was strong support for the conclusion that the isolation system was inadequate, and particular blame for this was directed toward the special flexible couplings in the vacuum lines. Fortunately, this viewpoint did not prevail, and a "fix" was instituted that consisted of:

1. Detaching the 8-inch and 3-inch vacuum lines from the chamber as close to the chamber as possible and inserting additional couplings
2. Rigidly mounting the piping between the two sets of coupling to the building floor
3. Rechecking all other interconnections and improving the flexible couplings in them wherever possible.

These modifications are illustrated schematically in figure 17. It should be noted that the isolation system itself (the isolators supporting all of the equipment) was not altered in any way.

At the conclusion of this rework, the system was tested once again and found to surpass the specification requirements.

There are two points to be made by this case study. First, flexible couplings from isolated equipment to the foundation or other equipment can and often do transmit more vibration to the equipment than do the vibration isolators. Second, even with good

isolation and flexible couplings, internal resonances can be excited to very high levels by small amounts of energy.

Case Study II: The Design and Isolation of a 50-Foot Optical Bench

The purpose of this example is to illustrate typical design approaches to optical bench problems and some further advantages of low-frequency pneumatic systems.

The basic requirements for an optical bench are that it provide a work surface that is rigid and well isolated. The specific requirement in this case was for a reinforced concrete bench 50 feet long and 4 feet wide. The depth of the beam in this case was 4.5 feet. (A length-to-height ratio of about 10 is typical.)

If the effect of the reinforcing steel is neglected (which can be done with small error), the natural frequency of a solid beam of these dimensions, simply supported, would be about 7.8 hertz.

Supporting the beam on a soft isolation system ($f_r \ll f_b$, where f_r and f_b are the natural frequencies of the isolator and of the beam, respectively) has the effect of causing the beam to vibrate in a free-free mode. When this condition exists, the frequency of the first bending mode of vibration is increased by a factor of about 2.3. In this specific case, the frequency of this mode increases from 7.8

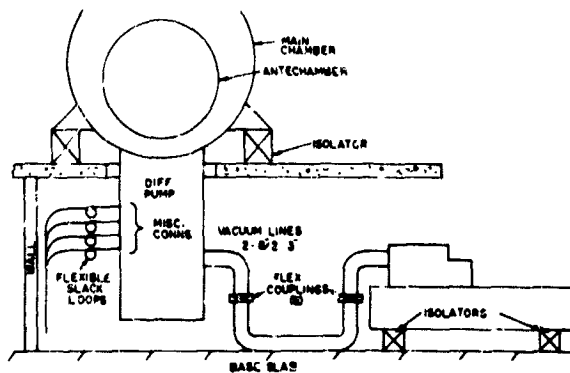


Figure 17. Improved isolated vacuum chamber system, end view.

hertz to 17.8 hertz. This is equivalent to increasing the stiffness of the beam by a factor of about 5.

A further improvement can be obtained by increasing the stiffness-to-weight ratio of the beam. In the case being reviewed, this was done by casting a 30-inch-diameter cylindrical void through the length of the beam (fig. 18). This increased the fundamental frequency of the beam another 14 percent to about 20.3 cycles per second while decreasing the weight to be isolated by 36,800 pounds, a 27-percent decrease in weight.

To illustrate the improvement in performance of the isolated hollow block over the solid, simply supported block, let us assume that the floor has a predominant disturbing frequency of 10 hertz (which is not uncommon). A block of this construction would be moderately well damped, having a transmissibility at resonance of about 5. Using transmissibility curves for viscously damped systems (fig. 2), it is found that the 10-hertz disturbance would be amplified by the simply supported, 7.8-hertz beam by about 50 percent.

The isolated hollow beam has to be considered in two steps: (1) the response of the beam to inputs at its support points and (2) the attenuation of the disturbing frequency by the isolators. With regard to Step 1, the beam now has a fundamental frequency of about 20 hertz, and, instead of amplifying 10-hertz inputs, it will attenuate them by about 60 percent. This difference alone accounts for an improvement of approximately 4 to 1 over the simply supported solid beam.

If the isolation system is assumed to have a 1.6-hertz natural frequency (which is typical), the transmissibility of the 10-hertz disturbing frequency will be about 0.1 (attenuation of about 90 percent before it gets to the block). The combined effects will result in approximately a 40:1 improvement with regard to the relative transmissibility of the 10-hertz disturbance.

Secondary benefits of the hollow block are that the floor loadings will be lower and that an isolation system with lower load capacity can be used. Both of these will result in a lower installation cost.

Development and Trends in the Vibration Isolation of Optical Systems

The isolation systems that have been discussed in the two case studies represent state-of-the-art techniques now available to solve the more critical vibration isolation problems. The solutions are not always perfect, however, and one wonders what is being done or can be done to make better solutions available to science and industry.

Actually, there is a continuous effort being exerted in this field. The now famous Rolamite, developed at Sandia, has been cited as the only significant mechanical invention of the twentieth century. It is a spring that has infinitely variable force-deflection characteristics. Research and development by other companies is being carried on with other objectives; for example, to obtain systems with very low natural frequencies

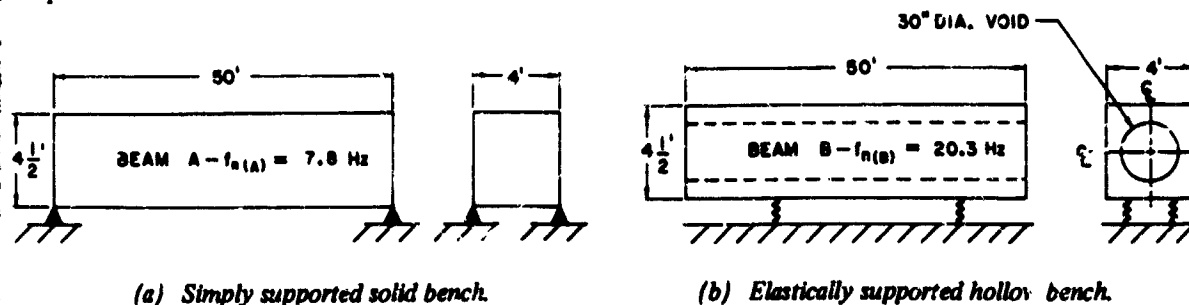


Figure 18. Optical-bench bending frequencies.

without paying the price of large static deflections. The pneumatic systems now available were the first step in this direction; the adverse effects of static deflection have been eliminated by using servo-valves to vary pressure with load. These systems have literally zero static deflection. The properties of these systems, however, are still space-limited in a sense. The natural frequency depends on the volume of air in the isolators.

A large portion of the research and development in this field is being directed at active servocontrolled isolation systems. With the use of electronic control systems in conjunction with hydraulics, pneumatics, and mechanisms, the relationship between the static deflection of a spring and its isolation properties has been eliminated. Electrohydraulic systems that have been made and have been successfully demonstrated occupy a space of about one cubic foot and have a natural frequency of 0.1 hertz (refs. 7, 8, 9, and 10). If a passive, conventional spring were used, such a system would have a static displacement of over 80 feet, which would require a spring at least as long as that and probably 200 feet or more in length. Furthermore, these systems can be made with unilateral properties so that forces applied to one end "see" a very soft spring, but, when viewed from the other end, the system appears to be very, very stiff. In certain applications, this is a tremendous advantage over passive systems.

Another development, recently revealed, is an electromechanical feedback control system, which, when used with a pneumatic isolation system, will lower its natural frequency by an order of magnitude. These, too, can be designed with unilateral properties; however, most of the advantages obtained by the active feedback systems occur in the frequency range from very low frequencies (a fraction of 1 hertz) to about 30 hertz. Although this is frequently a very important frequency range, the optical researcher is affected as much or more by structural resonances within or around his equipment; and these resonances are usually in the approximate range of 20 to 200 hertz.

In this range, isolation efficiencies of 95 percent or better are now attainable by using well designed and well applied systems.

It has been the experience of the author that the isolation goals are often thwarted by so-called "peripheral effects." Probably the most common and most disturbing of these peripheral effects is acoustic coupling between the isolated equipment and the surroundings. This is especially true with vacuum chambers. Most vacuum chambers are excellent gongs; they have a multitude of resonant frequencies (most of them in the audible range) and extremely little damping.

Another problem often encountered results from the tendency of experimenters to build their equipment "à la Erector set." Lens and mirror makers have long recognized the necessity of designing good supports for their optics, but they often overlook the same requirement when designing auxiliary structures, brackets, and instrumentation. Consequently, structural resonances in this equipment often cause trouble.

If the adage "an ounce of prevention is worth a pound of cure" is applied, then new research facilities should be planned with the vibration problem in mind. This includes selection of the site as well as the architecture of the building. Vibration and noise transmissibility should be included in the criteria for selection of building materials and techniques. The mechanical equipment in a building (air compressors, pumps, etc.) should be remotely located, if possible, as should be any auxiliary support functions, such as machine shops, printing facilities, and any others that generate acoustical noise or mechanical vibration. Effort in these areas will greatly reduce the isolation requirements and also the problems to be solved for the sensitive experiments to be conducted in the building.

Another area that definitely requires more study and development is the design of vacuum chambers. Materials and designs to date have been selected primarily on the basis of strength and outgassing properties. Stainless steel cylinders and spheres satisfy these requirements but are frustrating to deal with from the standpoint of vibration control.

Solid (homogeneous) and laminated materials have been developed that have excellent damping properties, but these materials have been developed for quite different applications (primarily for chassis and mounting bases for airborne electronics); hence, the materials and techniques are not suitable for vacuum chamber applications. On the other hand, the principles used would apply to vacuum chambers. This is a field that forward-looking manufacturers of vacuum systems might be well advised to investigate.

Externally applied materials to absorb vibration energy would seem to be a practical alternate approach, but, to the best of the author's knowledge, little or no effort has been spent on developing this idea. Studies of the effect of externally applied materials need not involve drastic redesign of the chambers; thus, the studies would be easier and less expensive.

Summary

Although the theory of vibration isolation is well developed and has been successfully applied for many years, the ever-increasing demand for better isolation forces a much closer scrutiny of the environment, of the equipment to be isolated, and of the isolation systems and their controls.

Electronic feedback control systems are being developed which make many heretofore unattainable isolation characteristics feasible. These are concerned primarily with attitude and position control and with improvements in low-frequency (up to approximately 30 hertz) isolation. Although these are often matters of concern to optics experimenters, isolation of higher frequencies is just as important, or more so.

No great breakthroughs are currently envisioned that will make a dramatic improvement in the isolation of vibration in the middle to high frequency ranges; however, significant improvement can be achieved by taking the "systems approach." The vibration sources (including the natural environment) must be considered, and steps must be taken, where possible, to control the source. In

many cases, vibration transmission paths, which include the building structure and the air within it, can be improved at moderate cost. Finally, the laboratory equipment, including the instrumentation and its supports, can usually be designed with high resonant frequencies and good damping properties. Such design will greatly reduce the vibration problem.

Vibration exists and, in all likelihood, will continue to cause problems as long as man continues to make things that go. The most effective and economical approach to solving these problems is to search them out at the earliest possible stage, preferably in the conceptual phase of a program, and to consider the isolation as part of the system and not merely an accessory to it.

References

1. Jacobsen, L. S.; Ayre, R. S.: *Engineering Vibrations*. McGraw-Hill Book Co., 1958.
2. Crede, C. E.: *Vibration and Shock Isolation*. John Wiley & Sons, Inc., 1951.
3. Den Hartog, J. P.: *Mechanical Vibrations*. McGraw-Hill Book Co., 1956.
4. Timoshenko, S.: *Vibration Problems in Engineering*. D. Van Nostrand Co., Inc., 1928.
5. Crede, C. E.; Harris, C. M.: *Shock and Vibration Handbook*, vol. 2, chap. 33. McGraw-Hill Book Co., 1961.
6. Krach, F. G.: Reinforced Concrete Beam Resonances. *Shock and Vibration Bulletin*, No. 38, pt. 2, August 1968.
7. Ruzicka, J. E.: Active Vibration and Shock Isolation. SAE Paper No. 680747. October 1968.
8. Calcaterra, P. C.: Performance Characteristics of Active Systems for Low Frequency Vibration Isolation. SM Thesis, MIT, June 1967.
9. Calcaterra, P. C.; Schubert, D. W.: Research on Active Vibration Isolation Techniques for Aircraft Pilot Protection. Air Force Report AMRL-TR-67-138, (DDC Report AD 664090), October 1967.
10. Pepi, J. S.: Vibration Isolation of Optical Reconnaissance Sensors. Air Force Report AFAL-TR-67-277, (DDC Report AD 822872), October 1967.

PRECEDING PAGE BLANK NOT FILMED.

Degradation Due to Contaminants Throughout the Test Cycle

Fred W. Paul
NASA Goddard Space Flight Center

N70-36754

Contamination rather than degradation is the principal concern of the discussion within this paper. If we devote our attention to the optical system, the type of degradation to be expected is a weakening or loss of the optical signal. In many cases, this will be wavelength-dependent; hence, some distortion of the spectrum will occur. Other types of degradation also occur. For example, a stray bit of lint or a dust particle, when illuminated by sunlight, may look enough like a star to confuse a tracking system. Solid contaminants may degrade the performance of a mechanical system. Bits of electrically conductive material may short out an electrical circuit element, thereby causing loss of power, or failure of a logic circuit, or some other failure.

In the long process from the start of fabrication to the launch into space, there are, however, a great many opportunities for contamination. Let us assume for this discussion that the fabricator takes all the precautions necessary to avoid contamination in fabrication and assembly. (Sometimes he does not take these precautions, and his failure often becomes apparent during test and evaluation.) In addition to the measures used to avoid contamination in fabrication, telescope systems are customarily protected in transportation and storage by shock mountings to prevent mechanical damage and by bagging in an above-atmosphere pressure of dry nitrogen and at a controlled temperature. These precautions are generally effective, but an occasional failure does occur.

When an item is ready to be shipped to the Goddard Space Flight Center (GSFC) for testing, we perform the first inspection at the supplier's plant and a similar inspection after

receipt at GSFC. These inspections help us to determine whether the item is in a flight-readiness state as supplied and whether contamination has occurred in shipment. They also provide a baseline for determining whether contamination has occurred during the test cycle. The detailed procedure that has been developed for the Goddard Experiment Package of the Orbiting Astronomical Observatory (OAO) is attached to this paper as Appendix A. Briefly, the procedure is to subject the equipment to careful visual scrutiny with enhanced light and with ultraviolet to bring out any fluorescence. In addition, a vacuum-sampling procedure is used; all particulate matter thus collected is examined with a microscope and identified. This vacuum sampling is done by passing the end of a tube through which air is being drawn over critical or representative parts of the apparatus. The most frequently found particles are epithelial cells, hair, eyelashes, cosmetics, food, smoke particles, dust, plastics, carborundum, glass, paint, and metal. Wipe tests are also made when appropriate. The material collected in the wipe test is ordinarily analyzed by spectroscopy or chromatography. The things we find most frequently are fingerprints, grease, oil, hydrocarbons, monomers or plasticizers, and paint residues.

We have been concerned about the possibility of contamination in the test-and-evaluation building by particulate matter and by gaseous components of the air such as water, hydrocarbons, and corrosive vapors. We attack the particulate problem by maintaining a class-10,000 clean room and meticulous clean-room procedure and by

controlling the temperature and humidity of the air. When the equipment is not undergoing a test or inspection, it is bagged in dry nitrogen. In addition to these steps, we have made extensive examinations of the air that is in our laboratories or is drawn in from the outside in order to learn what undesirable constituents there may be which would not be removed by mechanical filtering and humidity control. Samples of air were collected in various ways and were submitted to a local analytical laboratory for analysis. Table 1 summarizes the resultant findings. In addition to the items listed in the table, we made a special effort to find sulfur compounds. A 72-hour pumping of outside air through a liquid-nitrogen-cooled trap, after which the collection in the trap was analyzed, uncovered no trace of hydrogen disulfide or sulfur dioxide. The estimated sensitivity of detection is 0.7 parts per million (ppm) of the ambient air.

One of the most difficult aspects of contamination and, at the same time, one of the most interesting is contamination by condensation while the equipment being tested is in the test chamber. If we consider an instrument designed for use in the vacuum ultraviolet, 200 to 2000 angstroms, where nearly every substance we can think of is a poor reflector and a good absorber, we can see immediately what the problem is. If this instrument uses one or more reflecting surfaces and perhaps a diffraction grating, the

loss of performance is likely to be sudden and substantial if a layer of material is condensed on one or more surfaces. Since many of our test chambers are evacuated by oil diffusion pumps, the designer or user of the equipment to be tested is concerned about the possibility of contamination with a layer of pump fluid. He justifiably demands that no loss of performance shall occur in his equipment. Because we do not know very much about the effects of such layers, his demand is usually stated: "No contamination shall be permitted." Furthermore, because we do not know how to define "no contamination," the test conductor is in a quandary to know how to meet this demand.

Although pump fluids have been mentioned specifically, the problem is much broader. There is a great variety of possible sources of condensable contaminants; for example, materials associated with welds and soldered joints, electrical insulating materials, potting compounds, solutions used to clean the test chamber or the experiment, paints and paint thinners, plastics, and many others. The problem is not confined to vacuum ultraviolet wavelengths; it exists through the whole optical spectrum. A system for a 10.6-micron laser is less sensitive to contamination but is by no means immune. A very great amount of effort has gone into studies of this problem. I shall review some of the work that has been done at GSFC, some related studies elsewhere, the methods that have been developed, and the results that are being obtained.

Let us examine our ability to predict the effects of a contaminant layer. Most of this information is drawn from the publications of Dr. Georg Hass and his colleagues at Fort Belvoir, GSFC, and the Naval Research Laboratory (NRL). Figure 1 shows a contamination effect. This was an aluminum mirror overcoated with aluminum oxide to give a reflectance curve, shown by the solid line. After irradiation with 200 KeV protons to a dose of 4×10^{15} protons cm^{-2} in an oil-pumped system at 10^{-5} torr, it showed the dashed line of reflectance. There are two interesting points to make about this illustration. First, this was not an effect on the

Table 1. Summary of Contaminants

Sample No.	Conc. ppm for Samples		
	4	5	6
Acetone	~0.06	12	15.2
Benzene	~0.02	2	0.10
Butane	---	10	1.0
Ethanol	---	5	0.2
Ethyl acetate	---	3	0.04
Freon TF	~0.1	13	0.2
n-Hexane	~0.4	16.0	0.03
2-Hexene	~0.5	1.0	0.02
Methanol	~1.	---	0.02
2-Pentanone	---	1.0	---
1-Propanol	---	3.0	0.1
2-Propanol	~0.5	5.5	0.2

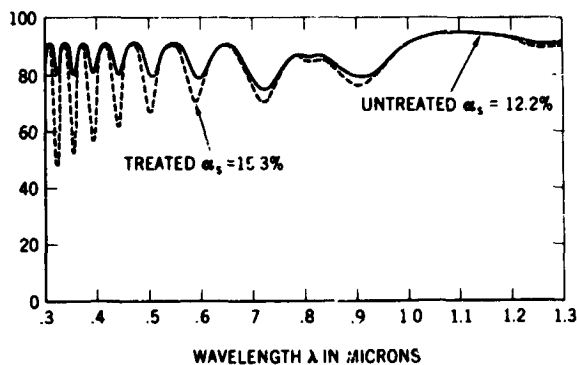


Figure 1. Effect of absorption on reflectance.

reflectance due to protons but was due to a layer of contaminant, most likely carbon, separated from the pump oil by proton bombardment of the residual vapor in the test chamber. Second, the effect depends very strongly on the location of the maxima and minima of the reflectance curve. Imperceptible losses at the maxima are followed by very substantial losses at the minima.

Figure 2 shows the computed influence on a pure aluminum surface of a layer that has little absorbance at Lyman alpha but absorbs quite strongly at Lyman beta. If the optical constants of a contaminant layer are known, the effect on a particular mirror can be computed. Figure 3 shows the computed effect of an absorbing layer of refractive index $n = 1$ and extinction coefficient $\mu = 1$. This is for an aluminum mirror overcoated with magnesium fluoride for peak performance at Lyman alpha for the

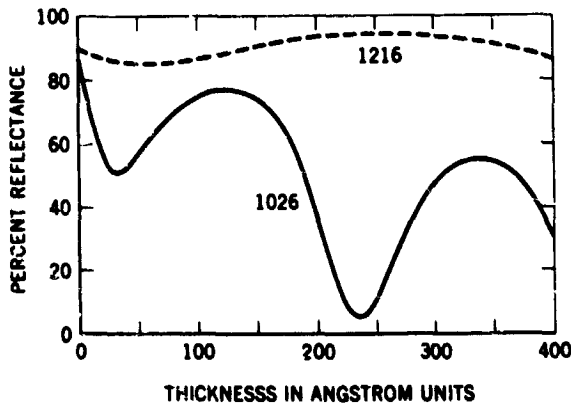


Figure 2. Effect of an absorbing layer.

curve marked " $\lambda/2$ effective" and for magnesium fluoride layers one-half as thick and 1-1/2 times as thick, respectively marked $\lambda/4$ and $3\lambda/4$. This figure illustrates again the difference in performance at maxima and minima. It also shows that a reflector at peak reflectance does not make a very sensitive monitor mirror for contamination. Hass has recommended using one of the lower curves.

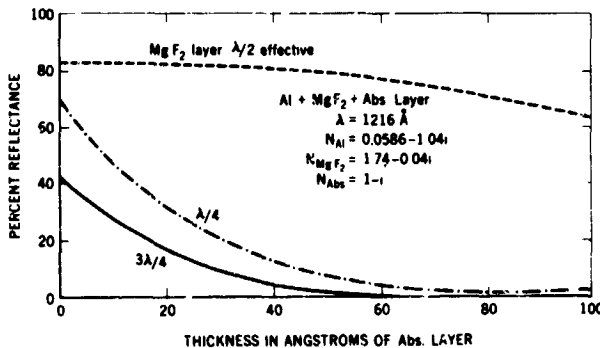


Figure 3. Dependence of absorption on effective coating thickness.

Figure 4 also graphs some computed results and illustrates another point Hass likes to make; i.e., that an absorbing layer does not always reduce reflectance. Notice the way the reflectance of gold rises with the increasing thickness of the absorbing layer. These illustrations suffice to show that, knowing the optical constants of the pertinent materials, we can predict the effects on a reflecting surface of the addition of layers of contaminants. They also show that the effects are sometimes different from our naive expectations.

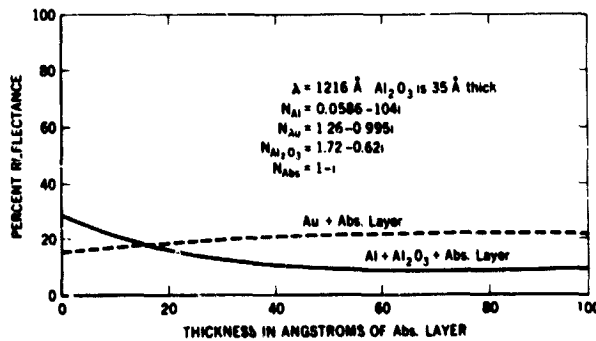


Figure 4. Computed reflectance.

There are several ways of determining whether or not condensable contaminants are present and, if so, what they are. The arsenal of instruments used in this work at GSFC has grown steadily since 1964. As new methods become known, they are pressed into service and seldom, if ever, are any old methods eliminated. At the present time, we are using the following: (1) a quartz crystal microbalance, (2) a residual gas analyzer, (3) mass spectrometer, (4) monitor mirrors, (5) collection on a cold finger, (6) wipes of the interior surfaces of chambers and the interior and exterior surfaces of both spacecraft and experiments. The material collected by wiping is analyzed by infrared spectroscopy and by gas chromatography. With these instruments, we keep a constant vigil for contamination problems.

Recently, when we baked out a large environmental chamber at 60° to 85°C for 36 hours at 10^{-6} torr, we found a contaminant that was identified as butyl cellosolve. The material was identified by infrared spectroscopy and gas chromatography. It was also detected by the residual gas analyzer (RGA). (Both models GE 300 and CEC 614 have been used.) The quartz crystal microbalance (QCMB) did not show anything. DC 704 oil showed up in wipes from the pump elbow but in no other place. The pumps in this chamber are 30 inches in diameter, hang on the sides of the chamber, and pump out through a stainless steel elbow that contains a liquid-nitrogen-cooled opaque baffle. The source of the butyl cellosolve has not yet been determined.

In a series of tests in a 7-foot by 8-foot chamber over a period of 2½ months, before and after several Orbiting Geophysical Observatory (OGO) and Radio Astronomy Explorer (RAE) tests, a chlorinated biphenyl called "Arachlor" was consistently found in the washings from a condenser plate (sometimes used instead of a cold finger). Several other condensable vapors were found in trace amounts, but the Arachlor was the principal contaminant. Efforts to locate its source in the pump oil or hardware were unsuccessful.

In another chamber, 3 feet by 4 feet, when a valve was installed between the diffusion pump and the chamber, bakeout and valve cycling tests were run. Instrumentation included RGA, infrared, and QCMB. On the QCMB, a frequency change of 31 hertz occurred in the first 8 hours. This corresponds to 1/2 monolayer of DC 704 oil. In the next 32 hours, further frequency change corresponding to 1/8 monolayer of DC 704 oil was observed; however, spectroscopy and RGA showed no trace of DC 704 oil. The contaminants that were identified were freon TF, aliphatic esters, cyclic amines, and methyl siloxane. During the bakeout, the chamber pressure decreased from 1.8×10^{-6} to 1.3×10^{-7} torr.

In the tests performed on the OAO-A2 in the large environmental chamber, we used all of the instrumentation already mentioned including wipes of the Wisconsin and Smithsonian Experiment Packages. In preliminary thermal vacuum tests, several parts of the spacecraft and the experiments showed visible evidence of contamination like a stain or a coating of oil. From a study of the circumstances, we concluded that the observatory was contaminating itself; i.e., that residues of condensable vapors were left in the spacecraft and experiments and were being relocated during television tests to places where they were apparent. Infrared analysis of cold-finger deposits showed phthalate, esters, hydrocarbons, and dimethyl silicones. Monitor mirrors did not show any loss of reflectance at Lyman alpha.

After these tests, the observatory was carefully cleaned and inspected. Approximately 5 months later, it was returned to the large chamber for flight acceptance tests. The QCMB and the RGA showed no signs of contamination. Visual inspection showed no contamination. Infrared analysis of the chamber cold-finger deposits showed the customary traces of hydrocarbons, esters, and silicones. (The silicones that were seen could not have been derived in any reasonable way from the DC 704 oil.) Monitor mirrors showed no loss of reflectance. The conclusions drawn from the contamination studies were:

1. There was no contamination of the experiment packages either from the spacecraft or from the test chamber.

2. Contamination of the chamber by the spacecraft or by self-contamination was negligible.

Although we looked for contamination by diffusion pump oil throughout all of these tests, in none of the experiments described has any such contamination been identified. It has been our experience that contamination due to pump oil does not represent a great hazard. We run about 300 tests a year in a variety of chambers, nearly all of which are evacuated with oil diffusion pumps using silicone oils. We look constantly for pump oil contamination. During the 5 years that we have been doing this, we have identified only six cases of pump oil contamination; *every one* of these cases was identifiable with some malfunction of the pumping system, such as an explosion or a cooling water failure or a power failure. In Goddard's Test and Evaluation Division, it is our belief that the probability of contamination by pump oil during a thermal vacuum test in a well-designed, properly operating chamber is very small.

The subject of contamination in a test chamber is an extensive one with a great many interesting ramifications. Some fascinating studies are being done by Shapiro at GSFC, by Gillette at Boeing, and by Hass at Fort Belvoir. There is also an excellent report on Apollo Telescope Mount (ATM) contamination by McPherson at Ball Brothers Research Corporation and the very fine work being carried on at Huntsville.

Another item that must be mentioned is the technique for cleaning. In the case of

contamination of reflecting surfaces by pumping fluids, we have had good success with the technique suggested by Hass; namely, to wash the surface with free-flowing, virgin-pure, freon TF and to follow this at once with dry nitrogen. We have found that the reflectance at Lyman alpha is completely restored by this technique even though the surfaces thus cleaned still look dirty sometimes.

In conclusion, this is what I see as the urgent supporting research-and-technology needs in this particular area. What we need more than anything else are contamination tests that can be directly related to expected performance in space. We go to great lengths to provide clean rooms free of particulate matter, but we do not have any test that tells us of the presence of dust particles in a strategic location that can float away in space and become a synthetic star to confuse the guidance system or the experiment. We have splendid instrumentation for sensing and identifying contaminants in various parts of the test chamber and in or on the observatory, but we have no direct way to learn if the reflectance of a mirror or the transmittance of a window has deteriorated or will deteriorate in the space environment due to a layer of contaminant. Another need I see in this area of contamination is the establishment of realistic tolerance levels. With the very sensitive instrumentation that is now at hand, and which is constantly being improved, test facilities are not able to meet a "no contamination" specification. We need a specification that will insure proper functioning of the spaceborne equipment and yet is different from zero.

Appendix A

Incoming Inspection Procedure For OAO Experiment

1. In order to determine the condition of the prototype and flight Goddard Experiment Package (GEP) and to continue the chronological historical records of same, inspections of these packages are to take place. These inspections will be conducted by a Quality Engineering Branch staff member assigned to the OAO Project with a GEP representative in attendance. Two inspections for each package, prototype and flight, will be conducted: one at the vendor's plant immediately prior to shipping and another at the Goddard Space Flight Center (GSFC) immediately after receiving.

2. Prior to shipment from the vendor's plant, the experiment package, installed in a turnover fixture and located in a clean room, will be checked for proper identification, such as model or type, part number, serial number, nomenclature, etc., and for proper documentation, such as shipping papers, test reports, data package, etc.

3. The dust covers will be examined for apparent damage, such as dents, holes, tears, discolorations, etc., and to assure that the end cover is properly secured in place. This examination will be conducted by using greater-than-ambient light unless the ambient light level is considered by the inspector to be satisfactory. An additional examination of the exterior of the package will be made with an ultraviolet lamp, and wipe tests or vacuum sampling of contaminants will be employed at the discretion of the inspector.

4. The experiment package/spacecraft support points will be inspected for cleanliness and damage (scratches, discolorations, dents, grease or oil, dirt, corrosion, etc.).

5. The optical-reference tool mount will be examined for contamination and/or damage.

6. The exterior of the experiment package will be examined for general good workmanship: all nuts, bolts, clips, clamps, washers,

etc. present and properly installed; painted surfaces clean, of good finish, free from flaking, etc.; all finish surfaces clean, free from scratches or discolorations, etc.

7. The end cover will then be removed; a cap will be installed on the light shield; and an examination will be made of the telescope tube interior, primary mirror, light shield, secondary mirror, and spectrometer mirror. These areas will be inspected for cleanliness, good workmanship, freedom from damage and contamination, etc. Ultraviolet and greater-than-ambient light will be used at the discretion of the inspector (safety glasses to be used for ultraviolet inspection). Vacuum sampling of contamination will be performed on the inner telescope-tube wall, portions of the light shield, the shield support ring, and other surfaces (except optical surfaces) as necessary.

8. A similar inspection will be made of the Analog and Digital Electronic Assemblies for general workmanship, cleanliness, and contamination.

9. A review of the packing and shipping arrangements, per Grumman Aircraft Engineering Corporation (GAEC) shipping procedure, will be conducted. This will be done in order to verify that adequate protection and cleanliness for the experiment package will be provided during its transportation to GSFC from the vendor's plant and that the data package accompanying the shipment is complete.

10. Subsequent to the experiment package inspection and prior to the final enclosure of the package for shipment to GSFC, the quality documentation of the package will be examined with Knollman Instrument Company (KIC) quality assurance or quality control representatives. Particular attention will be given to open malfunction reports and other quality problem documents, such as

"crab" sheets, DMT's, etc. Each open item will be discussed with a view toward determining what action is necessary to effect closing out the item, on the part of either GSFC or KIC. If possible, copies will be made of each documented open item for examination by the OAO Project Quality Manager at GSFC.

11. Upon its arrival at GSFC, the experiment package will be inspected again to insure that no damage has resulted from its being transported. This inspection will be conducted in accordance with the pre-shipment procedures except that, in addition, the environmental systems (air cooling/heating and gaseous nitrogen purge) are checked to determine if they were functioning properly throughout the shipment. Trip records will be examined and copied. If accelerometers or other types of instrumentation have been installed, their systems will be checked, the records ex-

amined, and copies of the records will be made, if possible.

12. Prior to removal of the outer shipping container, this enclosure will be examined for visible damage: dents, holes, cracks, loose mountings, moisture leaks, etc.

13. Upon removal of the outer shipping container, the experiment package will be examined to assure that the bag is properly inflated, that there is no damage to either the bag or the shipping dolly, and, as far as is practicable, that the experiment is properly secured in the dolly.

14. Upon removal of the experiment from the dolly and the installation of the experiment in a suitable clean enclosure, steps 2 thru 9 of this procedure will be repeated.

15. The Quality Assurance Division will submit a report of these inspections 30 days after completion of the incoming inspection at GSFC.

PRECEDING PAGE BLANK NOT FILMED.

N70-36755

Hard Radiation Environment Simulation

Fred W. Paul

NASA Goddard Space Flight Center

Introduction

In this paper, I shall discuss the local earth-circling orbits out to a few thousand kilometers because this is the region in which most of the optical telescope studies will be performed. We must, however, also keep in mind the possibility of a moon-based observatory. The components of the "hard radiation environment" that I will consider are: galactic and solar cosmic radiation, solar x-rays and ultraviolet, solar wind, trapped charged particles, and ionized layers of the upper atmosphere. Although some of these components are far from being hard or penetrating radiation in the usual sense, it seems desirable to consider them together because of certain common characteristics; for example, to treat all the charged particles in one discussion.

Effects of Hard Radiation

The effects that we might expect to be caused by the hard radiation include:

1. Fluorescence
2. False counts in counter circuits
3. Triggering and perhaps enhancement of electrical breakdown discharges
4. Degradation of reflecting surfaces, both by loss of reflectance and by change of figure
5. Loss of transmittance of materials used in windows and filters
6. Changes in thermal control coatings
7. Deterioration of solid-state components.

This list suggests limitation of the discussion by restricting the range of hardware items to which we refer. For example, we might include the entire spacecraft with its

structure, propulsion, attitude control, guidance, communications, data acquisition, and data-processing. On the other hand, we might consider only the telescope mirrors. For most of this discussion, I shall talk about the telescope and any wavelength-separating apparatus, such as filters or dispersing systems; I shall stop short of the radiation detectors, whether they be photographic or photoelectric.

Galactic and Solar Cosmic Radiation

Let us examine the amount of energy of various constituents of the hard radiation environment by starting with the most penetrating. Figure 1, from the second edition of

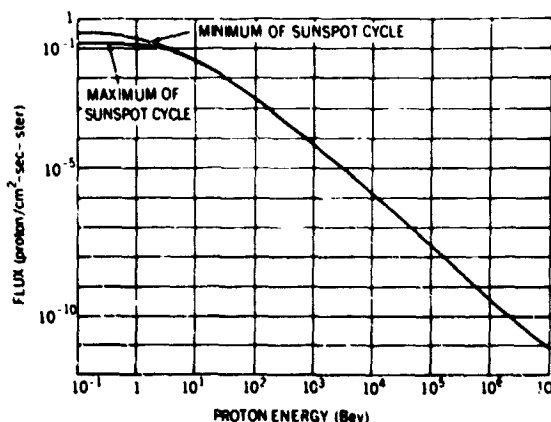


Figure 1. Integral-cosmic-ray energy spectrum at extremes of the sunspot cycle. Space-probe measurements give a flux value of approximately $0.2 \text{ particle/cm}^2\text{-sec-sterad}$ above about 40 MeV near sunspot maximum; this value should increase by a factor of about 2.5 near sunspot minimum. (From Second Edition of Satellite Environment Handbook, edited by F. S. Johnson.)

the *Satellite Environment Handbook* edited by F. S. Johnson, shows combined solar and galactic energetic proton flux. The low energy side shows the influence of sunspot activity on the flux of protons. Changes of the order of 2 or 3 are observed to occur. In addition to the protons, the cosmic radiation contains 10 to 15 percent by number of alpha particles and much smaller amounts of heavier ions.

Solar X-Rays and Ultraviolet

Table 1 shows the x-rays received outside the atmosphere at different stages of solar activity. The wavelength bands given would usually be called soft x-rays, and they are absorbed by very thin layers of most solids. Nevertheless, they can produce deterioration of optical materials and are consequently of importance to us. The units used in the table are 10^{-8} watts cm^{-2} . The amount of radiation varies by 5 orders of magnitude in the shortest wavelength band and by about 2 orders in the longest as we progress from sunspot minimum to the brightest flare recorded in Johnson's data. Usually very little radiation of wavelengths less than 2 angstroms is observed; however, in the first few minutes

Table 1. Intensities of Solar X-Rays, 10^{-8} w/cm² (from Second Edition of *Satellite Environment Handbook*, edited by F. S. Johnson)

	2-8 Å	8-20 Å	20-200 Å
Sunspot Min (Quiet Sun)	0.00003	0.004	1.3
Sunspot Max (Quiet Sun)	0.02	0.23	10.
Class 3 Bright Surge Prominence 7-24-59	0.13	0.89	8.
Class 2+ Flare 8-24-59	0.26	1.6	21.
Class 2+ Flare 8-31-59	>2.20	>4.5	92.

of a vigorous flare, wavelengths as small as 0.1 angstrom (125KeV) have been recorded. The flux at wavelengths less than 0.6 angstrom was about 4×10^{13} watts cm^{-2} .

Figure 2 shows the solar spectral radiance outside the earth's atmosphere. This graph does not attempt to show the fine structure at short wavelengths but only the overall features. From approximately 200 angstroms to Lyman alpha, the irradiance ranges between 10^{-10} and 2×10^{-9} watts per square centimeter per angstrom. At Lyman alpha, the value rises to nearly 10^{-7} , then falls again, and begins to rise (similar to a black-body distribution) from approximately 1400 angstroms up to the edge of the visible spectrum. The radiation at wavelengths less

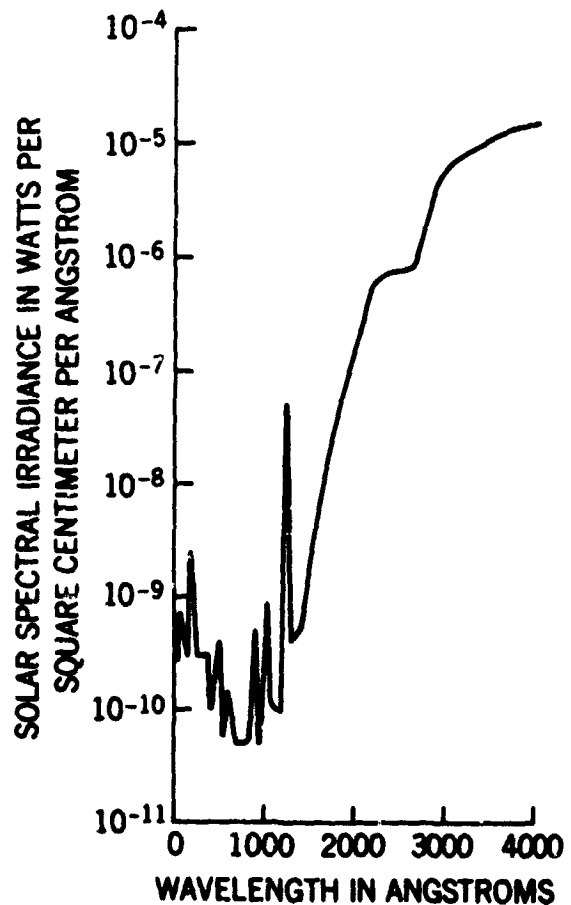


Figure 2. Solar spectral irradiance outside atmosphere. (From Second Edition of *Satellite Environment Handbook*, edited by F. S. Johnson.)

than 1400 angstroms has a substantial fraction of atomic line radiation; some of these lines vary greatly with solar activity.

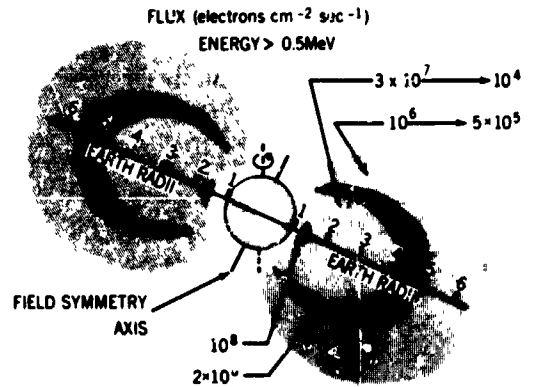
Solar Wind

The solar wind is a flow of protons and electrons in equal numbers outward from the sun. Reported values for the concentration of protons range from 0.1 to 1000 per cubic centimeter with energies in the range from 300 to 5000 electron volts. The simulators with which I am familiar are designed to give fluxes and energies adjustable to values within this range.

Trapped Charged Particles

The spatial distribution of electrons and protons trapped in the earth's magnetic field is very complex. Consequently, in order to assess the exposure that a telescope will experience, it is necessary to do a detailed computation for the specific mission involved. The input to the program must contain the altitude and orientation of the trajectory relative to the earth as well as the relative positions of the sun, earth, and satellite for the actual date of flight. The latest information about the trapped particle environment is available from the National Space Sciences Data Center at the Goddard Space Flight Center (GSFC). Computation programs for specific missions are available at many places; for example, the Laboratory for Theoretical Studies and the Spacecraft Technology Division at GSFC; the Flight Instrumentation Division at Langley; the Radiation Effects Information Center, Battelle Memorial Institute; the Boeing Aircraft Corporation, Seattle, Washington. Some of these places have shielding code calculations as a part of their program.

A few examples will illustrate the results for typical missions. Figure 3 shows schematically the distribution of the trapped particle belts. Figure 4 shows an enlarged view of the inner belt of protons as of September 1963 with contours of constant flux values. Figure 5 is a similar chart for electrons at about the same date. (These illustrations are



Electron fluxes in the outer zone are extremely variable in time, whereas proton fluxes are quite stable with a flux concentration of 2×10^8 protons $\text{cm}^{-2} \text{ sec}^{-1}$ (energy > 0.4 MeV) occurring at ~ 3 earth radii.

Figure 3. Trapped radiation.

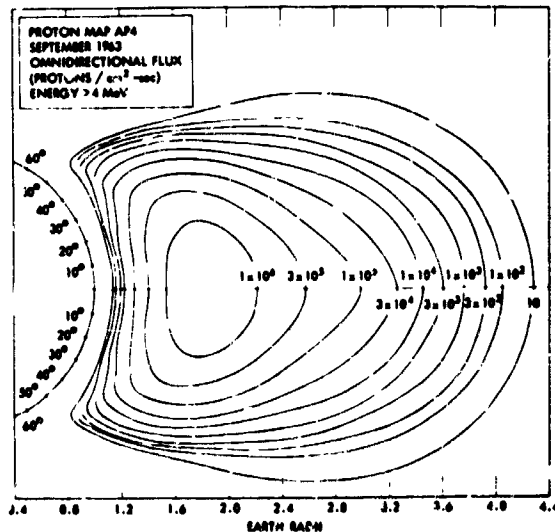


Figure 4. Proton map AP4.

from NASA SP 3024, Vol. I-IV, which contain much additional information.) Figure 6 shows the annual accumulation of proton dose per square centimeter for circular orbit at a 35-degree inclination. The curves show the number per square centimeter of energy greater than E_0 . E_0 is given values from 5 to 50 MeV. Figure 7 shows a similar set of curves for the same orbits for electrons. The range of E_0 used is from 0 to 3 MeV. Figure 8 shows the time-integrated flux of protons for three typical orbits, two circular and one elliptical. Figure 9 shows the time-integrated electron

flux for one of the same orbits as shown in figure 8 and for two new orbits. These illustrations of orbital calculation were made for Spring 1968. The environment has changed substantially since then; hence, these results

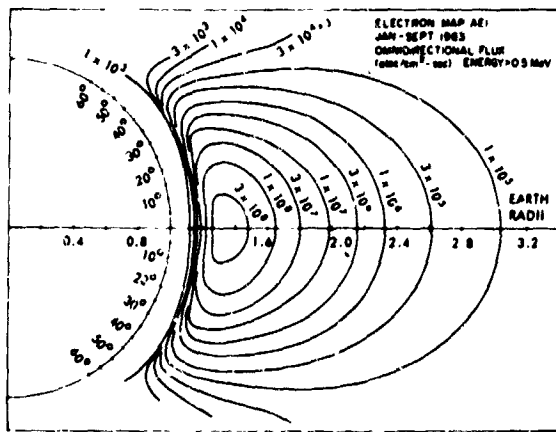


Figure 5. Flux map AEI ($E > 0.5 \text{ MeV}$).

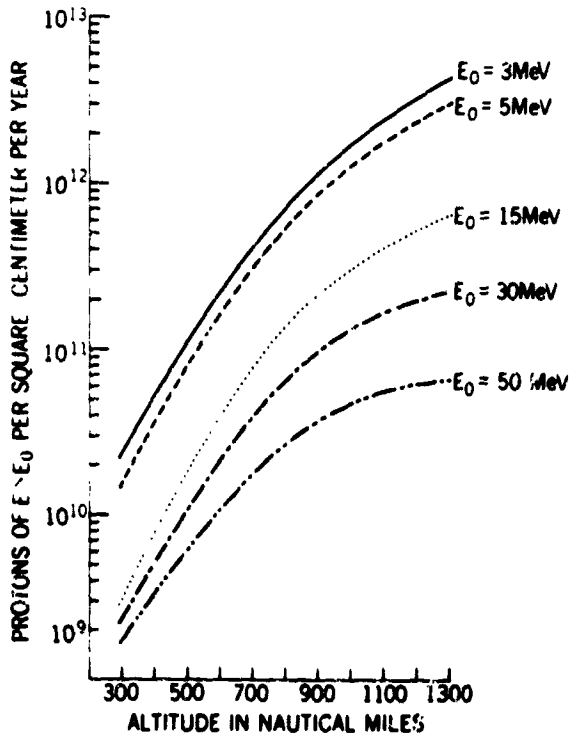


Figure 6. Number of protons of energy greater than E_0 incident per square centimeter per year as a function of altitude in nautical miles for circular orbits at 35-degree inclination.

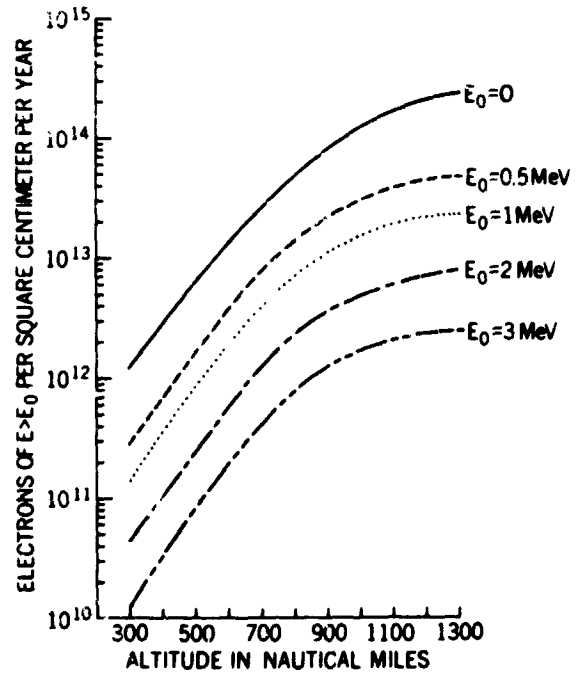


Figure 7. Number of electrons with energy greater than E_0 versus altitude in nautical miles for circular orbits at 35-degree inclination.

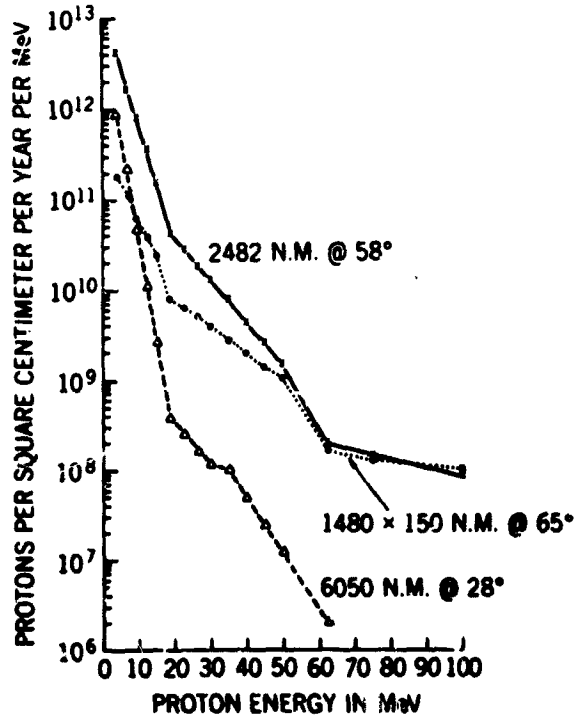


Figure 8. Differential fluence of protons for three typical orbits.

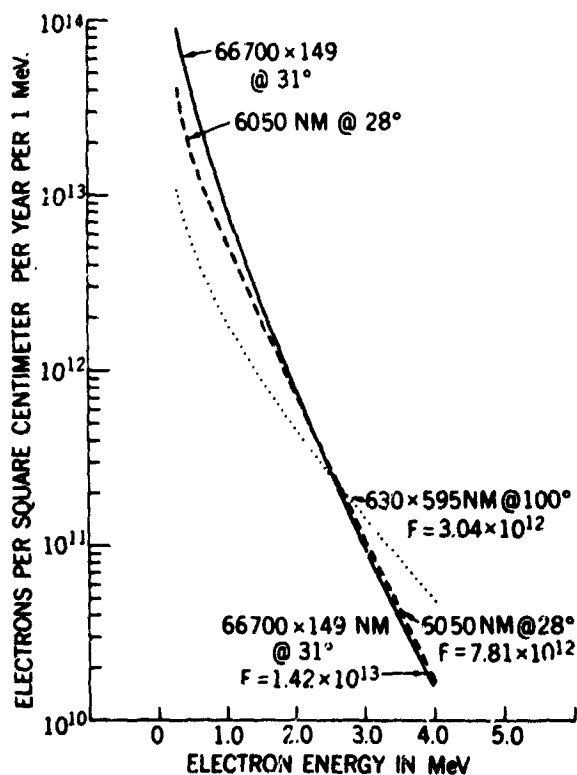


Figure 9. Calculated differential fluence of electrons per year for one circular and two elliptical orbits.

are now obsolete. Calculations specific to planned missions should be used for practical testing procedures.

The Ionosphere

The last environmental factor to be discussed is the charged particles in the ionized layers of the atmosphere, namely, the ionosphere. The variation of the number of charged particles per cubic centimeter with altitude is shown in figure 10. In essence, this chart shows the number of electrons per unit volume. In most of the ionosphere, there are an equal number of positively charged particles. At lower altitudes, they are molecular ions such as NO^+ and O_2^+ . At higher altitudes, O^+ and H^+ and He^+ predominate. These charged particles, of both signs, have thermal energies and are not at all penetrating. They can, however, cause surface

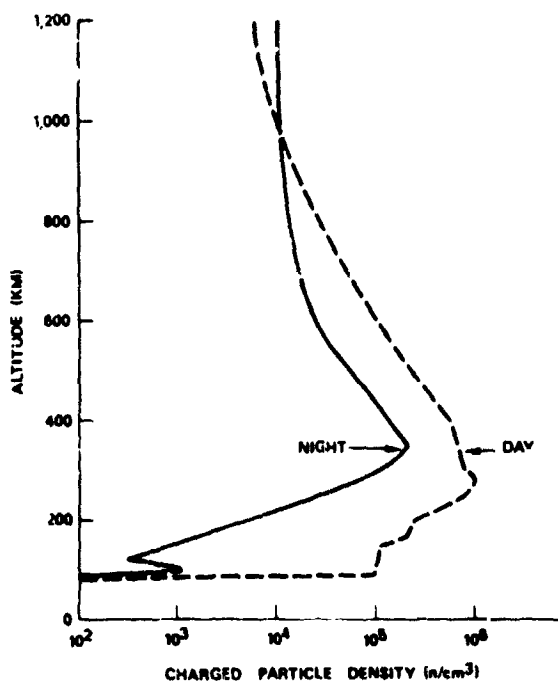


Figure 10. Ionospheric density variation.

effects. They provide ions for the initiation of electrical breakdown of high voltage systems. They can produce false signals in open-window photon detectors.

Simulation

How shall we simulate such an environment? Obviously, true reproduction of the radiation environment is an enormous task. Because of its complexity, we are forced to consider not how to produce a copy of the environment but rather how to devise tests that will determine the behavior of our test object when it finds itself in the real environment. When we think about this task, we realize there will not be only one answer. We shall expect to get different answers for different classes of things. For example, the reflecting surface of a large mirror will require different testing than a solar cell; a solar cell will be different from an open-end channel multiplier; and a passive-thermal-control coating will need still another test to determine its in-space performance.

What is usually done is to study the characteristics of a particular class of devices and decide what part of the hard radiation environment is most likely to modify their performance. Then typical devices are subjected to irradiation with the particles or waves, selected at rates that correspond to the natural environment, or some enhancement of it, for accelerated testing, and to levels where damage occurs or lifetimes in excess of mission life are indicated. Often the decision about the effect a single environmental component has is not clear-cut; therefore, we have to try exposure to more than one component. Sometimes, it seems likely that synergistic effects or spontaneous healing of damage may occur; then we would like to be able to expose the device to more than one environmental component at a time.

Case Histories

Because I am unable to offer any overall guiding principle for making decisions on how to test and under what radiation conditions, I would like to present three brief case histories to show what some investigators have done.

Case I: Studies of High Reflection Surfaces Such as Aluminum With Overcoats

Canfield, Hass, and Waylonis (ref. 1) studied aluminized mirrors overcoated with magnesium fluoride to peak performance in the vacuum ultraviolet. They irradiated their samples with Lyman Alpha at a certain level for 20 hours. This was adequate to reduce the reflectance of unprotected aluminum to one-half its initial value but had no effect on the protected surface. They irradiated many samples with 1-MeV electrons at total doses ranging from 10^{14} to 10^{16} electrons per square centimeter. They also irradiated with 5-MeV protons to a dose of 10^{12} protons per square centimeter. No loss of reflectance resulted from any of these exposures. A loss as small as $\frac{1}{2}$ percent would have been detectable.

Case II: Ultraviolet Transparent Optical Materials

Heath (ref. 2) and Sacher (ref. 3) have measured the transmittance in the wavelength range 1050 to 3000 angstroms of several materials before and after charged-particle irradiation. The materials studied included lithium fluoride, magnesium fluoride, calcium fluoride, barium fluoride, aluminum oxide, and fused silica. They measured transmittance before and after irradiation with 1-MeV and 2-MeV electrons at 10^{14} electrons per square centimeters at each energy. A similar study was done with 10^{11} protons per square centimeter at energies ranging from 3.0 to 4.6 MeV. Some of these materials lost considerable transparency; others were not much affected. They concluded that magnesium fluoride, barium fluoride, and sapphire have the greatest potential for use in the hard radiation environment.

We note that in these two cases the investigators have used components of the environment singly. Those who are studying spacecraft coatings for passive thermal control also started with single environmental factors. Much of the early work involved exposure to radiation from a strong mercury lamp. At the present time, the thermal control coatings are being studied in facilities that combine two or more environmental components for simultaneous exposure.

Case III: Round Robin Program for Combined Environment Testing

Under the auspices of Committee E21, ASTM, several industrial and governmental laboratories have joined together in a program to learn what is the state-of-the-art of combined environment testing. Materials are to be exposed simultaneously to simulated solar electromagnetic radiation and proton flux simulating the solar wind. Results from different laboratories will be compared both with each other and with flight experiments. To the best of my knowledge, this case represents the first concerted effort to combine components of the hard radiation environment.

Although the ultraviolet and solar wind are the main items of interest in the Round Robin study, many of the participating organizations are capable of including higher energy protons, electrons of a wide range of energy, x-rays, gamma rays, and neutrons in their irradiation program.

Irradiation Facilities

Table 2 lists a number of organizations and the characteristics of their irradiation facilities. Some of these organizations are participating in the Round Robin study. In

the first column is the name of the organization and the name of an individual who is familiar with the details of the facility and to whom inquiries may be directed. In subsequent columns, the amount and energy of the radiations are listed for protons, electrons, gamma rays, x-rays, and ultraviolet.

References

1. Applied Optics, Vol. 5, Jan. 1966, p. 45.
2. Applied Optics, Vol. 5, June 1966, p. 937.
3. Sacher, P. A.: GSFC Document X-622-67-416, Greenbelt, Maryland, August 1967.

Table 2. Combined Radiation Environment Facilities

Organization (Individual)	Protons	Electrons	γ -rays	X-rays	Ultraviolet	Additional Information
Martin Denver (J. Cooley)	100 to 4000 e.v. 10^8 - 10^{14} cm ⁻² sec ⁻¹	100 to 4000 e.v. 10^8 - 10^{18} cm ⁻² sec ⁻¹			Xenon lamp; 0.5 to 5 suns	
Lockheed. Pa'o Alto, Calif. (R. Breuch)	0 - 120 KeV 10^{10} - 10^{13} cm ⁻² sec ⁻¹	0 - 120 KeV 10^{10} - 10^{13} cm ⁻² sec ⁻¹	Yes Co ⁶⁰	Flash X-ray	Xenon or Mercury lamps	Also neutrons Temperatures of specimen LN ₂ to 500°F (See footnote 1.)
G. E. Valley Forge, Pa. (J. Scannapieco)	1 to 130 KeV 5×10^8 - 10^{12} cm ⁻² sec ⁻¹	100 to 20000 e.v. 5×10^8 - 10^{12} cm ⁻² sec ⁻¹		90 Kilovolt	Xenon, Mer- cury, or Hy- drogen lamps; 1 to 4 suns	12" diam holding 30 specimens simultaneous e, p, and UV -50° to 150°C (ref 1) 30" Bell Jar (See footnote 2.)
Boeing, Seattle, Wash. (R. Brown)	0 to 20 MeV 10^8 - 10^{12} cm ⁻² sec ⁻¹	500 e.v. to 25 MeV 10^8 - 10^{12} cm ⁻² sec ⁻¹	Yes	Yes	Xenon or Mercury lamps; 1 sun	Also neutrons simultaneous e, p, and UV -100°C → +100°C chamber 6" x 12"
Aerospace Corp. (E. Borson)	2 MeV	2 MeV			Xenon or Mercury lamps	

Footnotes:

1. There are two entries for Lockheed in this table.
2. The GE facility has a turntable permitting sequential exposure of specimens. Long λ UV or Lyman alpha may be applied at the same time as particles of either sign.

Table 2. Combined Radiation Environment Facilities (Concluded)

Organization (Individual)	Protons	Electrons	γ -rays	X-rays	Ultraviolet	Additional Information
IITRI (J. Gilligan)	20 KeV and 2 MeV and 500 to 5000 e.v. at $10^8 \text{ cm}^{-2} \text{ sec}^{-1}$	2 MeV			Xenon or Mercury lamps	
TRW Systems (E. Luedke)	600 to 3000 e.v. $10^7 - 10^{10} \text{ cm}^{-2} \text{ sec}^{-1}$				Xenon lamp	
Comsat (C. Naag) Not Operational	100 to 500 e.v. $10^6 - 10^{11} \text{ cm}^{-2} \text{ sec}^{-1}$	May be added			Lyman α may be added; Xenon lamps 0.5 to 5.0 suns	10 cm square irradiated area
EMR (M. J. Brown)	10 to 35,000 e.v. 10^9 to $10^{15} \text{ cm}^{-2} \text{ sec}^{-1}$	10 to 35,000 e.v. $10^9 - 10^{15} \text{ cm}^{-2} \text{ sec}^{-1}$			Xenon lamp; 0 to 10 suns	
McDonald Douglas, St. Louis, Mo. (E. R. Rusert)					Solar simulator 2 foot circle at 4 suns	Argon Plasma (ref. 2) are to supplement solar down to 1800Å on P.O. Vac to 10^{-11} with LN ₂ LHe
Ames R.C. (Donald Anderson)	C-W 2 - 240 KeV VdG 200 KeV-3 MeV VdG 3 MeV Modified for microparticles				Xenon, Mercury, and hydrogen lamps	(See footnote 2.)
General Dynamics, Ft. Worth, Tex. (J. Romanko)	Up to 145 KeV $10^{12} - 10^{13} \text{ cm}^{-2} \text{ sec}^{-1}$	Up to 145 KeV $10^{12} - 10^{13} \text{ cm}^{-2} \text{ sec}^{-1}$			BH-6' up to 10 suns	Drum carries 60 1-inch samples
Lockheed, Palo Alto, Calif. (R. Breuch)	200 - 5000 e.v. $10^{10} - 10^{12}$ Can also be mated to 130 KeV to 1.3 MeV Van de Graaff				Xenon or Mercury	Solar wind and UV (See footnote 1.)

Footnotes:

1. There are two entries for Lockheed in this table.
2. Ames has a 2-foot-square test area. Microparticle, up to 20 km/sec in addition to charged particles and UV. They have tested flight hardware for JPL (solar cells for Mariner), for GSFC (a particle counter), and a Pioneer type of vehicle in the research stage for a Jupiter flight.

N70-36756

Light Sources for Stellar Telescope Calibration From 700 to 7000 Angstroms

William R. Hunter
Naval Research Laboratory

This paper describes light sources that may be useful in calibrating stellar telescopes between 700 and 7000 angstroms that are intended to operate in space. Such telescopes will be useful only for wavelengths longer than approximately 912 angstroms, the ionization limit of hydrogen, because the interstellar hydrogen absorbs all the shorter wavelengths down to about 100 angstroms. A calibration to 200 angstroms shorter than the interstellar cutoff is perhaps unnecessary; however, it will permit some extrapolation of observations past the cutoff that could be of value.

Ideally, a calibration source should have good stability during periods of operation, have essentially the same spectral distribution from one period of operation to the next, and have an intensity high enough to allow meaningful calibrations at those wavelengths where the telescope is least efficient. In practice such sources are rare, if they exist at all, and it is usually necessary to use a number of different types of sources to cover the wavelength range from 700 to 7000 angstroms. Many different types of sources have been reported in the literature that, in combination, can cover this region. The greatest diversity of design occurs for sources of extreme ultraviolet radiation; for wavelengths longer than approximately 2600 angstroms, fewer types of sources are available. Standardization of sources is an extremely difficult task, as evidenced by the results obtained by the various investigators who have tried to do so. In the visible and near ultraviolet, somewhat better agreement is obtained than in the vacuum ultraviolet; however, the truth is that there is no such thing as a standard source.

Most sources for the visible and near ultraviolet are continuous in time. This is not always the case for vacuum ultraviolet sources, some of which are excited by condensed discharges; i.e., a capacitor discharged periodically and producing very short, intense flashes of radiation. If the detector of the instrument to be calibrated counts photons, such a pulsed source may be useless if, during the radiation flash, the number of photons to be counted drives the counting system beyond its capacity. Difficulties also arise in using photographic detection with pulsed light sources; the intermittency effect may make it difficult to obtain H and D curves and to calibrate the film. Thus, the mode of excitation of the vacuum ultraviolet source is important to consider when deciding which source to use for calibration.

Vacuum Ultraviolet Sources

The only single source capable, in principle, of covering this entire spectral range is the synchrotron, which provides a highly polarized continuum that peaks in the vacuum ultraviolet at a wavelength dependent on the instrument parameters. This continuum extends into the visible with ever-decreasing intensity. The most attractive feature of this type of source is that the spectral energy distribution can be calculated; hence, no measurement of intensity need be made. The peak intensity of the National Bureau of Standards (NBS) machine (ref. 1) is approximately 5×10^8 photons/sec/Å for a wavelength of 340 angstroms and an electron energy of 180 MeV when measured 2 meters

from the current ring through a slit 1 millimeter wide by 10 millimeters high. The intensity fluctuates 20 to 30 percent each time electrons are injected into the magnetic field, which is 60 times a second, because of fluctuations in the number of electrons captured in stable orbits.

Special instrumentation problems arise because of the unique radiation pattern of the synchrotron. Because of relativistic effects, the instantaneous radiation from an electron with several MeV of energy is confined to a narrow cone in the direction of motion; hence, the emerging radiation lies in a very thin disc that is in the plane of the electron orbit. Horizontal and vertical perturbations of the electrons in their orbits determine the disc thickness. Observations must be made tangentially to the orbit. Madden, Ederer, and Codling (ref. 2) have published a discussion of the instrumental problems associated with the use of synchrotron radiation.

There are certain disadvantages to this type of source. First, it is immobile; any instrument to be calibrated must be transported to the synchrotron and must be housed in a vacuum system connected to the synchrotron for extreme ultraviolet calibration. Second, because of the high energy electrons periodically colliding with the walls, there is a radiation hazard to experimenters so that the experiment must be done by remote control and the calibration instrumentation must operate in a radiation background that is not negligible.

More conventional and convenient sources for the vacuum ultraviolet use are electrical discharges in gases, which can produce both line and continuum spectra. Of the many types of sources available, only those that, in the author's opinion, are most useful for telescope calibration will be discussed.

Figure 1 shows the Hopfield helium continuum, as observed by Huffman et al (ref. 3), which extends from 584 angstroms to approximately 1100 angstroms, with the most intense region lying between 700 and 900 angstroms. Although the helium was purified by passing it through charcoal traps cooled to liquid nitrogen temperature, some impurity

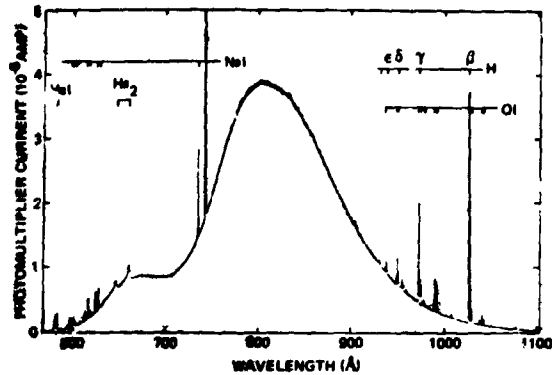


Figure 1. Helium continuum using thyatron modulator. Conditions: sodium salicylate photomultiplier detector (EMI 9514S) at 1630 V; 0.5 Å bandwidth using 100- μ slits; power supply at 116 mA and 10 kV; 5-kc sec pulse repetition frequency; 44-mm Hg helium pressure; 1.0-sec time constant. (Courtesy R. E. Huffman et al).

lines were present; the most conspicuous were those of neon at 736 angstroms and 744 angstroms and hydrogen. The excitation conditions for this trace were: 44-millimeter mercury pressure of helium, condensed discharge with a 5-kilocycle repetition rate controlled by a thyatron switch, and an average discharge current of 116 milliamperes at 10 kilovolts. A slit width of 100 microns was used, thus giving a bandpass of 0.5 angstrom. Because of the high gas pressure, a differential pumping system was used to keep the gas out of the monochromator.

The observations have not been corrected for the spectral response of the grating and detector; hence, the shape of the continuum will probably be different when different instruments are used. According to Huffman et al, the shape did change when different gratings were used; however, when thyatron control of the condensed discharge was used, there were always two maxima: one at 810 angstroms and a second smaller maximum at approximately 670 angstroms. At 810 angstroms, the average number of photons emerging from the slit was about 2.5×10^7 /sec or a flux of 5×10^9 photons/cm²/sec.

The radiation pulse begins about 0.14 microsecond after the current pulse terminates, reaches a peak at about 1.4 microseconds, and then slowly decays with a total duration of 16 microseconds. Thus, during the 200 microseconds between flashes, the radiation exists only for 8 percent of that time so that at peak intensity the photon flux is calculated to be about 6×10^{10} . The noise was about 3 to 4 percent of the mean intensity at all usable intensity levels; the long-term drift over 90 minutes was even less.

Figure 2 shows the discharge tube in which the continuum was excited. Except for the graded seals, the construction is of quartz. After about 125 hours of use, it is necessary to clean deposits from the electrodes with a sodium hydroxide solution.

A condensed discharge in argon is also useful in this region and produces many intense lines from below 700 angstroms to approximately 1100 angstroms (ref. 4).

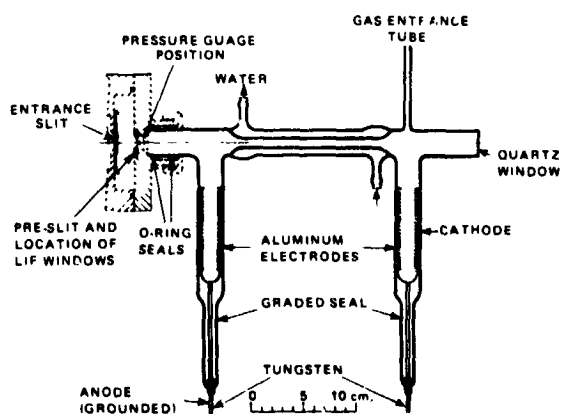


Figure 2. Light source used to obtain the helium continuum.

Other rare gas continua, reported by Tanaka (refs. 5, 6, 7), are available and cover the wavelength region up to 1800 angstroms. The best results have been obtained using argon, krypton, and xenon; the continua are shown in figure 3 (ref. 8). These curves are the measured values and have not been corrected for the spectral response of the grating

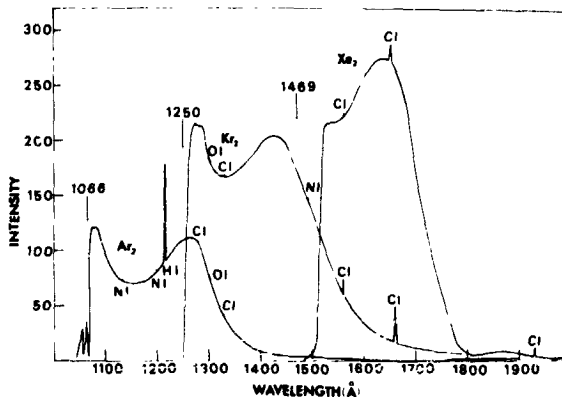


Figure 3. Rare gas continua of argon, krypton and xenon obtained with radio-frequency excitation.

and detector. About 100 watts of radio-frequency (RF) excitation from a Raytheon microtherm unit was used; gas pressures were about 40 to 50 millimeters mercury; the lamps were sealed and had lithium fluoride windows. It is possible to obtain these continua with a free-flow lamp if the gas is purified; however, economic considerations make it undesirable to do so except with argon.

Figure 4 shows a picture of some lamps and the microwave cavity used for coupling. The large bell-shaped end is a ground glass joint by means of which the lamp is mounted at the entrance slit. The lamps are prepared by evacuating, baking, and backfilling with



Figure 4. Light sources used to obtain the rare gas continua in figure 3.

purified gas and are supplied with a barium getter in the side arm to aid in cleanup.

Perhaps the best known source for the vacuum ultraviolet region is a DC glow discharge in hydrogen. Figure 5 (ref. 9) shows the spectrum obtained from such a source. From approximately 850 to 1600 angstroms, the spectrum is a series of bands due to molecular hydrogen. Because of the sharpness of these bands, the name "many-lined spectrum" is often used. The most conspicuous feature is the Lyman-alpha line, at 1216 angstroms, of atomic hydrogen. Occasionally the Lyman-beta line at 1026 angstroms can be seen, but often its intensity is about the same as that of the neighboring bands; and identification is difficult. A molecular continuum extends from 1500 angstroms well up into the violet end of the visible spectrum region.

From 900 to 1600 angstroms, the intensity is usually enough for most practical

purposes although there are small regions, just above 1300 angstroms and at 900 angstroms, where it is low. Even less energy is available in the continuum although commercial spectrophotometers make use of it to wavelengths as long as 4000 angstroms. The intensity is pressure-sensitive and increases as the pressure increases but not equally in all parts of the spectrum. Therefore, the repeatability from day to day in free-flow sources depends on the ability to reset the pressure ± 10 percent in the Naval Research Laboratory (NRL) instruments while the stability depends on the constancy of the pressure and discharge current. Generally, with a well-regulated power supply, the fluctuations over the period of a few hours to a day are usually less than 5 percent.

Figure 6 (ref. 4) shows a drawing of the discharge tube used to produce the spectrum of figure 5. The capillary consists of a tube, 10 centimeters long with a 4-millimeter bore,

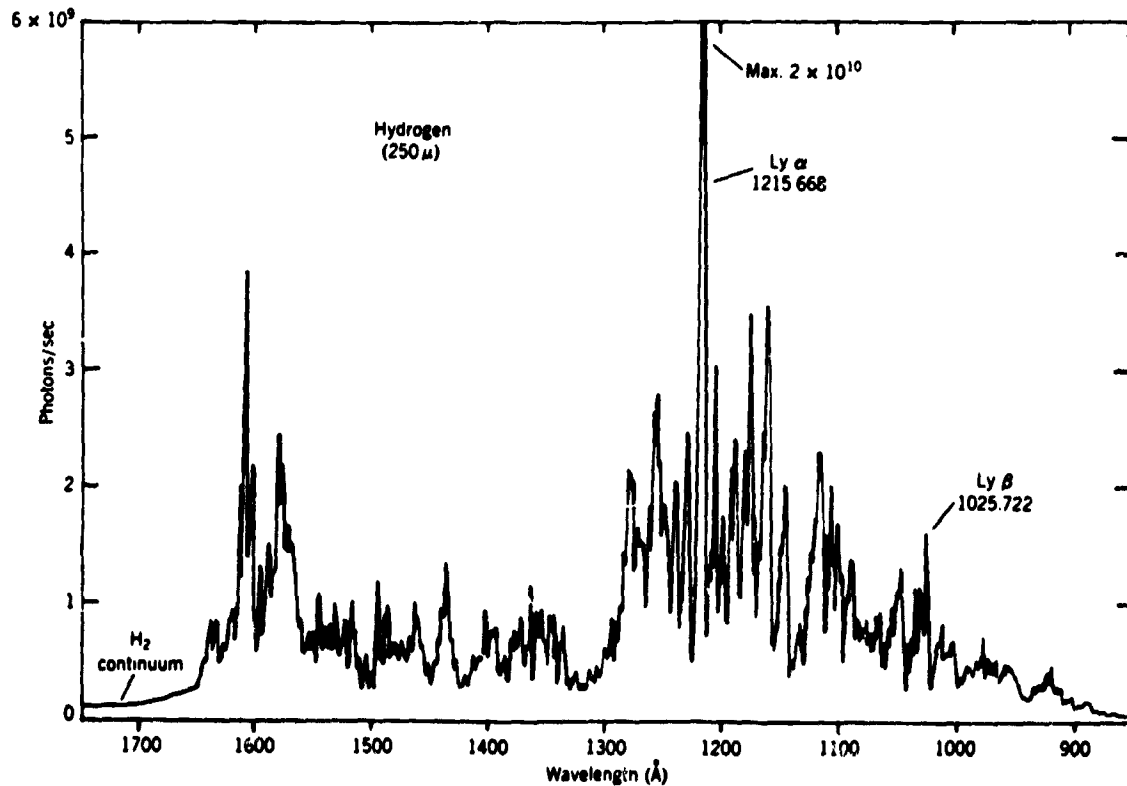


Figure 5. Spectrum of hydrogen obtained with DC glow discharge.

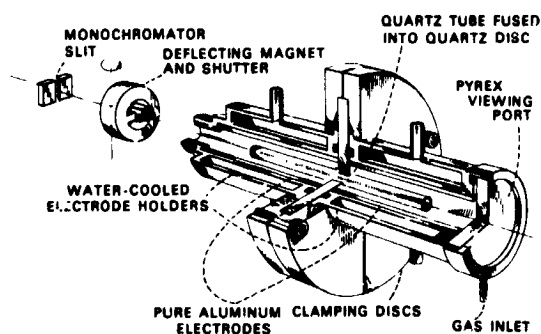


Figure 6. Light source used to obtain the hydrogen spectrum in figure 5.

and a disc made from the same piece of material. Quartz, alumina, lava, and boron nitride have been used. In the case of quartz, the tube was fused into a quartz disc. The purpose in this particular design was to avoid water-cooling of the capillary because it was intended to be used with a condensed discharge as well as with a glow discharge. Under condensed discharge conditions, the capillaries gradually wear away; thus, water-cooled capillaries are subject to breakage that would flood the monochromator with water. Consequently, the capillary is uncooled except by the gas. Quartz and boron nitride, however, withstand either the condensed or glow discharge conditions, and the other two materials are quite suitable for glow discharges.

In summary thus far, electrical discharges in gases can be used to cover the wavelength range from 700 to 4000 angstroms; i.e., from 700 to 900 angstroms, the Hopfield helium continuum or a condensed discharge in argon are used; from 900 to 1600 angstroms, the band spectrum of hydrogen or the rare gas continua of argon, krypton, and xenon; and from 1500 to 4000 angstroms, the hydrogen continuum.

Near Ultraviolet and Visible Sources

For wavelengths longer than approximately 1850 angstroms, which is the air cutoff, vacuum systems are no longer needed to house the test instrument and measuring

equipment; this simplifies matters somewhat. Sources more intense and stable than gas discharges are available. Two such sources will be discussed: the tungsten-ribbon lamp and the carbon arc.

Tungsten-ribbon lamps have been used for years as secondary radiance standards when calibrated against a blackbody. DeVos (ref.10) has reviewed the measurements obtained up to 1954. More recently Larrabee (ref.11) has measured the emissivity of tungsten at different temperatures with the results shown in figure 7. The slightly wavy lines are the measurements; the other lines are analytical approximations. Larrabee estimates the rms error of the experiment at 0.002 "dimensionless emissivity units."

Generally, tungsten-ribbon lamps are stable with respect to long-period drift and have very small short-period fluctuations. There is, however, a gradual deterioration. As the tungsten evaporates, the temperature rises for a constant heating current; the evaporated tungsten coats the lamp window, thereby causing its transmittance to decrease. As a result, the lamps must be recalibrated periodically. Recently, tungsten lamps have been made with quartz envelopes and containing a small amount of iodine, which inhibits the tungsten evaporation.

The ability to standardize this type of lamp is best judged from figure 8, taken from

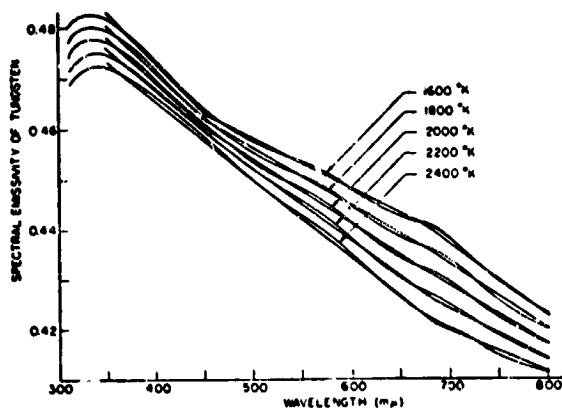


Figure 7. Spectral emissivity of tungsten (experimental results and analytic approximation).

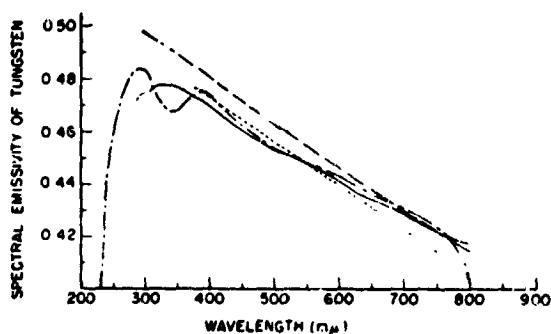


Figure 8. Emissivity of tungsten at 2000°K, values obtained by several observers; W. B. Nottingham and W. E. Mutter [Phys. Rev. 74, 1261 (1948)]; J. C. De Vos [Physica 20, 690 (1954)]; H. C. Hamaker [Physica 3, 561 (1936)]; W. E. Forsythe and E. Q. Adams [J. Opt. Soc. Am. 35, 108 (1945)].

Larrabee's paper, which shows the measured emissivity values obtained by a number of workers. From just under 4000 to 7500 angstroms, the agreement is fair, but outside of this region the results diverge.

Better agreement occurs on measurements of the spectral radiance of the anode crater of the carbon arc. Figure 9 shows some unpublished measurements of Packer and Lock made at NRL. The values are shown by the triangles and the solid line. For comparison, the measurements of McPherson (ref. 12) are indicated by circles, and those of Krygsman (ref. 13) by plus signs. The dashed

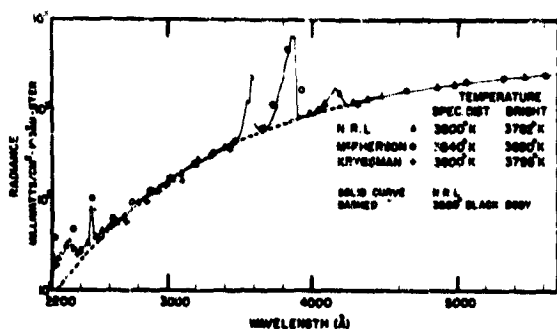


Figure 9. Spectral radiance of the carbon arc in air from 2200 to 5700 angstroms, as measured by D. M. Packer and C. Lock.

line is the calculated spectral radiance of a 3800°K blackbody and shows excellent agreement with the measured values from approximately 2700 angstroms to the longest wavelength measured, 7500 angstroms, which is not shown in figure 5. Grouped around 4000 angstroms are cyanogen bands. As shown, they are rather gross features, but under higher resolution the spacing is sufficient to see the blackbody background. Below 2700 angstroms, the arc-stream contribution becomes important as the blackbody radiation becomes weaker. Packer and Lock estimate that at wavelengths longer than 2700 angstroms, the arc-stream contribution is approximately 1 percent. Some of their measured values are listed in table 1.

Since these measurements were made, Null and Lozier (ref. 14) and Hattenburg (ref. 15) have made similar measurements with results fairly close to those of Packer and Lock.

Johnson (ref. 16) has measured the spectral radiance from 2500 to 1900 angstroms with the results shown in figure 10. By measuring the arc stream from the side rather than looking through it at the anode crater, he found that below 2100 angstroms the radiation was only that of the arc stream. This is reasonable because, at this wavelength, the

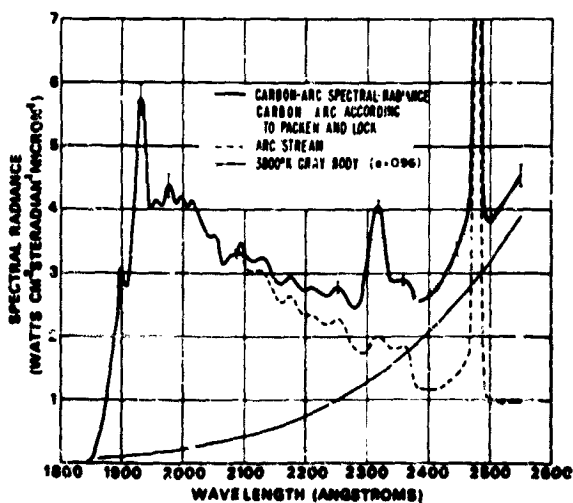


Figure 10. Spectral radiance of the carbon arc in air from 1850 to 2550 angstroms.

Table 1. Measured Spectral Radiance of the Carbon Arc*

Wavelength	Radiance (milliwatts/cm ² -100 Å U-steradian)
2200	15
250	23
300	31
350	29
400	27
450	33
500	39
550	45
600	50
650	55
700	64
800	90
900	121
3000	153
100	199
200	248
300	308
400	380
672	607
990	907
4091	1170
190	1510
290	1190
387	1300
487	1420
867	1760
983	1870
5469	2320
959	2690
6445	2930
925	3070
7402	3200

*Conditions of operation:

11.0 to 11.5 amperes

70 to 75 volts

5/16" positive lampblack electrode

1/8" negative graphite electrode

blackbody radiation must have a very low intensity.

Conclusions

A number of sources are available that can furnish radiation for calibrating instruments in the wavelength region 700 to 7000 angstroms. The synchrotron is useful over this entire spectral range and requires no standardization. Electrical discharges in gases can be used for the vacuum ultraviolet and both tungsten-ribbon lamps and the carbon arc for the near ultraviolet, visible, and near infrared. Because of the difficulty in standardizing these sources (especially vacuum ultraviolet sources), frequent calibration against a known source will be required.

References

1. Codling, K.; Madden, R. P.: *Journal of Applied Physics*, vol. 36, no. 380, 1965.
2. Madden, R. P.; Ederer, D. L.; Codling, K.: *Applied Optics*, vol. 6, no. 31, 1967.
3. Huffman, R. E.; Tanaka, Y.; Larrabee, J. C.: *Applied Optics*, vol. 2, no. 617, 1963.
4. Hunter, W. R.: *A Pulsed Light Source for the Extreme Ultraviolet*. Proceedings of the Xth Colloquium Spectroscopicum Internationale, E. R. Lippincott, M. Margoshes, eds., Spartan Books, Washington, D. C., 1963, p. 247.
5. Tanaka, Y.: *Journal of the Optical Society of America*, vol. 45, no. 710, 1955.
6. Tanaka, Y.; Jursa, A. S.; LeBlanc, F. J.: *Journal of the Optical Society of America*, vol. 48, no. 304, 1958.
7. Huffman, R. E.; Larrabee, J. C.; Tanaka, Y.: *Applied Optics*, vol. 4, no. 1581, 1965.
8. Wilkinson, P. G.; Byram, E. T.: *Applied Optics*, vol. 4, no. 581, 1965.
9. Samson, J. A. R.: *Techniques of Vacuum Ultraviolet Spectroscopy*. J. Wiley & Sons, New York, 1967, p. 139.
10. DeVos, J. C.: *Physica*, vol. 29, no. 690, 1954.
11. Larrabee, R. D.: *Journal of the Optical Society of America*, vol. 49, no. 619, 1959.

12. McPherson, H. G.: *Journal of the Optical Society of America*, vol. 30, no. 189, 1940.
13. Krygsman, C.: *Physica*, vol. 5, no. 918, 1938.
14. Null, M.R.; Lozier, W. W.: *Journal of the Optical Society of America*, vol. 52, no. 1156, 1962.
15. Hattenburg, A. T.: *Applied Optics*, vol. 6, no. 95, 1967.
16. Johnson, F. S.: *Journal of the Optical Society of America*, vol. 46, no. 101, 1956.

N70-36757

Absolute Radiometry in Space Astronomy

William G. Fastie
The Johns Hopkins University

Introduction

Although it is perhaps one of the less glamorous facets of space astronomy, there are many important astrophysical problems that require absolute radiometric and spectrometric intensity measurements in the spectral range 0.1 micron to 30 microns. Even in the visible and near-visible range available to ground-based observations, uncertainties in atmospheric losses and variations in telescope transmission limit the magnitude of secular variations that can be observed. Precise absolute-intensity measurements of astronomical objects over wide spectral ranges are necessary for studying stellar atmospheres. Precision radiometric measurements over long time intervals will provide information about the distribution of planetary systems among the near stars; this information will expedite the planning of experimentation for interstellar spacecraft.

It therefore appears imperative that the post-OAO space astrophysics experiments on both manned and unmanned spacecraft be more precisely calibrated, including in-flight calibration. The purpose of this paper is to review the present state-of-the-art and to point out the areas where improved standards and techniques are needed.

Absolute Radiometric Standards

Most of this discussion is based upon the basic radiation equation, the Planck Blackbody Law

$$E_{\lambda}^{BB} d\lambda = C_1 \lambda^{-5} \left(e^{\frac{C_2}{\lambda T}} - 1 \right)^{-1} d\lambda \quad (1)$$

and its corollaries, the Stefan Boltzmann Law

$$E_T^{BB} = C_3 T^4 \text{ (}^\circ\text{K)} = \int_0^{\infty} E_{\lambda}^{BB} d\lambda \quad (2)$$

and the Wien Displacement Law

$$\lambda_{\max}(\mu) = \frac{0.2898}{T \text{ (}^\circ\text{K)}} \quad (3)$$

Equation 1 describes the spectral distribution from a perfect blackbody. An imperfect radiator, a nonblackbody, emits less at each wavelength by a factor e_{λ} , which is called the spectral emissivity

$$E_{\lambda}^{NB} d\lambda = C_1 \lambda^{-5} e_{\lambda} \left(e^{\frac{C_2}{\lambda T}} - 1 \right)^{-1} d\lambda \quad (4)$$

and which must be experimentally evaluated at each wavelength.

Equation 2 describes the total energy emitted by a perfect blackbody. For a nonblackbody, the total energy emitted is

$$E_T^{NB} = \int_0^{\infty} e_{\lambda} E_{\lambda}^{BB} d\lambda \quad (5)$$

Equation 3 shows how the wavelength at which maximum emission occurs varies with temperature. It demonstrates that all practical radiometric standards have the major portion of their emission in the infrared region.

From the above relationships, it is clear that, in order to establish a spectral radiation

standard, it is only necessary to measure the temperature and the spectral emissivity at that temperature of a stable radiation source or to compare the spectral radiance of the source to a blackbody throughout the spectral range of interest.

The spectral emissivity, ϵ_λ , of an opaque radiator is related to the spectral reflectivity, r_λ , of the radiator by the equation

$$\epsilon_\lambda + r_\lambda = 1 \quad (6)$$

This important relationship makes it possible to construct a physical blackbody or a blackbody cavity in which the observed target area is surrounded over a large fraction of the total solid angle by surfaces which are at the same temperature as the target area and which add by reflection the radiation deficiency from the target itself, according to equation 6.

For calibrating far infrared optical systems that can use a target at a low temperature (1000°K or less), the simple radiation source shown in figure 1 will provide a perfect blackbody cavity.

When higher temperatures are required, refractory materials must be used in place of highly conductive copper; and the design of a blackbody cavity becomes much more difficult. In fact, the design is so difficult that secondary standards; i.e., stable nonblack-

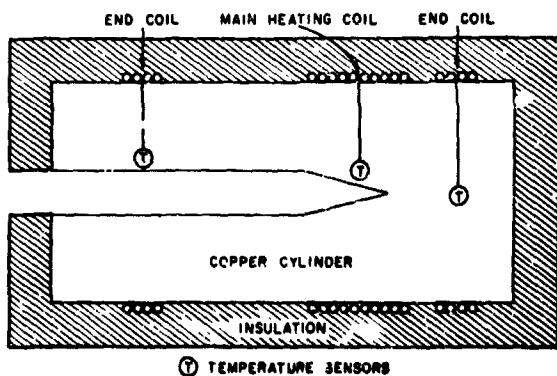


Figure 1. Low temperature blackbody cavity.

body sources that have been calibrated against a blackbody standard, are almost universally used. More specifically, in this country we depend upon the National Bureau of Standards to maintain a primary, high-temperature, radiation standard and to measure the spectral radiance of the various secondary standards; an example is the tungsten-strip-filament lamp, which we use to calibrate absolutely our optical instruments. This first step away from the primary standard introduces a minimum uncertainty of approximately 2 percent in the calibration procedure in the ultraviolet and approximately 1/2 percent in the infrared.

Calibrations in the Visible and Near Visible Range

The next step involves the use of auxiliary lenses or mirrors to form an image of the filament at a focal plane of the flight instrument or to form a collimated beam at the entrance aperture of a flight telescope. Aberrations and transmission variations can introduce very large errors unless extreme precautions are taken.

A calibration system that appears to be free of systematic and aberration errors is shown in figure 2. We have used this system for calibrating our rocket packages and also for the two Mariner ultraviolet telescope spectrometer experiments that are in flight to Mars. The technique involves projecting a

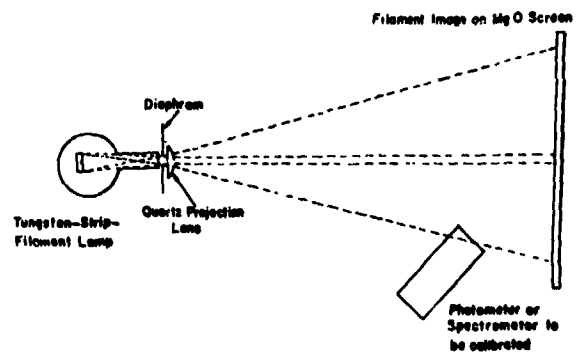


Figure 2. Standard lamp, projector, and diffusion screen.

large image of a strip-filament lamp onto a diffusing screen of freshly made magnesium oxide (MgO), which is a true Lambert surface, with a diffuse reflectivity (R_D) in excess of 0.98 throughout the near infrared, the visible, and the near ultraviolet. The radiance of the screen is given by the relationship

$$B_{\text{Scr}}^{\text{S}} = \frac{B_{\text{F}}^{\text{S}} A_{\text{L}}}{\pi D_{\text{LS}}^2} T_{\text{L}} R_{\text{D}} \quad (7)$$

where $B_{\text{Scr}}^{\text{S}}$ is the radiance of the screen in photon per $\text{cm}^2/\text{sec}/\text{ster}$

B_{F}^{S} is the radiance of the filament (same units)

A_{L} is the area of the lens

D_{LS} is the screen to lens distance

T_{L} is the lens transmission

R_{D} is the diffuse reflectivity of the screen

Note that the physical dimensions are easily measurable to high precision and that the optical factors ($T_{\text{L}} = 0.93$ for a quartz lens and $R_{\text{D}} = 0.98$) are close to unity and are highly reliable optical quantities.

Even this system is subject to subtle errors. When the lens diaphragm has a diameter of the order of a millimeter, dust and dirt can materially decrease the value of A_{L} . Long-term operation of the standard lamp can produce an evaporated tungsten film on the lamp window. It is necessary to maintain a reference standard lamp that is used only periodically to cross-check the working standard. It is also necessary to employ a well-calibrated optical pyrometer to check periodically that the prescribed lamp current is providing the proper filament temperature.

We determine that the diffuse reflectivity of the screen is maximized by recoating with fresh MgO smoke after a calibration run and then repeating the calibration. We also

check the spectral quality of the screen with the test setup shown in figure 3. By measuring the relative spectral brightness of the strip filament directly and then reversing the lamp and lamp mirror and putting an MgO screen at the lamp filament image (as shown in figure 3 by the dotted lines), we can prove that the MgO screen has invariant spectral reflectivity. Figure 4 shows the result of tests made in this way on the screens used for calibrating the Mariner instruments. The ratio of the two readings was constant from 2700 to 3600 angstroms, in which range MgO screens may fall off in reflectivity because of impurities, laboratory dirt, or radiation damage to the material.

By employing the above precautions with the diffusion screen technique, we believe we are obtaining absolute calibrations that are accurate in absolute terms over the calibrated range of the strip-filament lamp to within 3 or 4 percent.

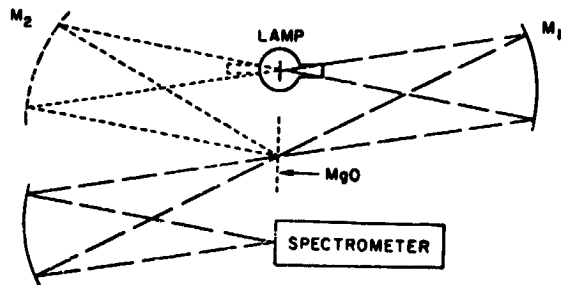


Figure 3. Experimental check of MgO screen.

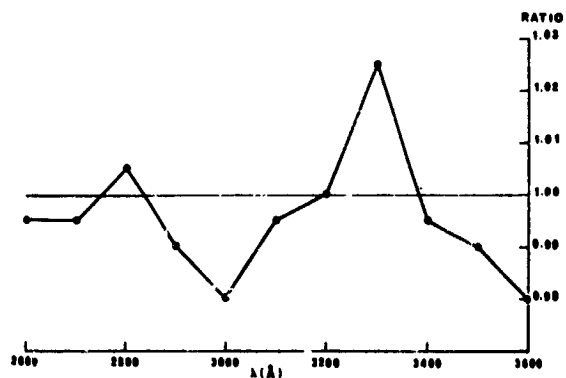


Figure 4. Relative diffuse reflectivity of MgO screen.

Far Ultraviolet Calibrations

Below 2000 angstroms, the shortest wavelength at which tungsten-strip-filament lamps are currently calibrated, no radiation standard exists. It becomes necessary to calibrate detectors against a standard detector for which the quantum efficiency is close to unity. The percentage of calibration errors that can be expected with this procedure increase by at least an order of magnitude.

The standard procedure upon which most calibrations are based is to calibrate a photocell, a photomultiplier tube, or a photoionization cell against a blackened radiation thermopile that has been absolutely calibrated by measuring its response to the total radiation signal (eq. 2) from a low-temperature blackbody, such as that shown in figure 1. In addition to the infrared calibration, it is necessary to measure the specular and diffuse reflectivity of the receiving area in the ultraviolet region, to measure the variation of ultraviolet sensitivity across the surface of the receiver, and to measure the loss of energy from the receiving area by emission of photoelectrons.

Fortunately, as a result of proper design and choice of blackening materials for the receiving area, none of the above sources of error exceed a few percent. The necessary measurements require, however, an expertise that is not broadly available; hence, in practice, experimenters usually assume the value of 82-percent quantum efficiency at 1216 angstroms for a flowing-gas, nitric-oxide photoionization chamber. This value was determined with radiation thermopile techniques by a number of investigators. A sealed nitric-oxide chamber is usually compared periodically with a flowing gas cell, and a photomultiplier tube is calibrated at 1216 angstroms against the sealed nitric-oxide cell. Calibration of the photomultiplier tube at other wavelengths is accomplished by calibrating a sodium-salicylate-coated photo tube against the nitric-oxide cell. This is based upon the assumption that the fluorescent quantum efficiency of sodium salicylate is constant in the wavelength range from 300 to

2500 angstroms (an assumption that many investigators have shown to be valid to within 20 percent). This standard is calibrated against the working photomultiplier tube at all wavelengths of interest. By now, we are about five stages removed from a radiation standard; hence, some of the experimental steps are fraught with experimental difficulties. For example, the minimum detectable signal with a radiation thermopile is about the maximum signal for which the final detector is to be calibrated; likewise, the current from a photomultiplier tube is 10^3 to 10^7 times the current from a nitric-oxide cell for the same input flux.

Thus far we have only a calibrated detector. Next we must measure the optical transmission of a flight instrument in two polarizations and over the spectral range required for the experiment, or we must use the calibrated detector to measure the flux incident on the first optical element of the flight instrument. In our experiments we have used both techniques.

Measuring Optical Transmission

For the transmission measurement, we employ two identical sets of flight optics in a double-monochromator vacuum optical system, which has identical geometry to the mechanical optical system of the flight package. The first plane grating is slightly under-filled. The intensity of several bright lines of a stable-flowing-gas discharge tube is measured at the intermediate slit with a reference detector. The detector is placed at the exit plane of the second monochromator, for which no exit slit is used. The ratio of the line brightnesses provides transmission measurements that typically have values of 10 to 20 percent in the range of 1150 to 1800 angstroms. The polarization is determined by rotating the second monochromator through 90 degrees. Typically, the 3600 g/mm gratings we use in this spectral region show less than 3-percent polarization. The optical elements are then mounted in the flight package; the calibrated detector is installed; and the instrument is declared flight ready.

Measuring the Flux Incident

The technique of using an absolutely calibrated detector to measure the flux incident on the first element of an assembled flight instrument is employed in the Vacuum Optical Bench (VOB) facility at Goddard Space Flight Center. This facility was constructed specifically for the OAO program.

We have used this facility to calibrate the Mars Mariner VI and Mariner VII ultraviolet telescope-spectrometer systems and for our rocketborne astronomical telescope. In the VOB facility, the exit hole of a far ultraviolet monochromator acts as a star source. A collimating system provides a parallel beam incident on the primary telescope mirror of the flight instrument. The image on the entrance slit of the flight spectrometer is smaller than the entrance slit and can be scanned over the entire slit area at a scan period that is long when compared to the spectrometer scan period. Before and after this scanning operation, the calibrated detector is moved over the entire area of the beam, which is intercepted by the primary mirror to determine the average incident flux. Errors that can degrade this measurement are scattered light in the pre-spectrometer and polarization in the optical elements. These possible errors must be evaluated by separate tests.

In view of all of the experimental hazards associated with far ultraviolet calibrations of the type already described, it is amazing that a valid calibration of an instrument can be accomplished at all. It would appear, however, that an absolute accuracy of ± 50 percent can be realized. In our Mariner calibrations, we extended the VOB calibrations based on nitric-oxide-cell standards to 3900 angstroms, a 1200-angstrom-range crossover of the MgO screen calibration that was much more reliable. We found less than 30-percent disagreement between the two methods.

The use of synchrotron radiation as a standard of spectral radiance in the far ultraviolet rather than the Planck radiation laws appears to offer the possibility of improved accuracy. The work of R. P. Madden at the National Bureau of Standards has shown

experimentally that the synchrotron-source spectral radiance follows the basic theory.

Conclusion

The future requires much better absolute accuracy in far ultraviolet measurements. One necessary step will be improvements in the present techniques so that the cumulative error in the many-stepped process can be minimized.

The use of barium sulfate (BaSO_4) as a diffusion screen for the 2000-to-4000-angstrom region would provide a diffuse reflectivity much closer to unity (above 0.99). BaSO_4 is less sensitive to radiation damage than MgO.

One important area which would improve absolute accuracy would be to extend the calibrated range of a strip-filament lamp to lower wavelengths. In our laboratory, we have been able to measure the signal from a sapphire-windowed, tungsten-strip-filament lamp to about 1700 angstroms. Below this wavelength, the filling gas appears to absorb. We are presently experimenting with a carbon-strip-filament lamp, which we believe can be made stable at high temperatures (perhaps 3000°K) and which should have an emissivity near unity. With such a lamp and with photomultiplier tubes employing high work-function photocathodes, which are insensitive to the near ultraviolet and visible region and which have dark currents of less than one false event per second, there appears to be a reasonable chance that the calibrated lamp range can be extended as far as 1200 angstroms.

Another desirable improvement would be the development of sealed-gas discharge tubes with long term stability in the spectral radiance of their continuum and line emission features. More stable window materials for such tubes, for example magnesium fluoride (MgF_2) in place of lithium fluoride (LiF), are also desirable. Such sources would be invaluable for in-flight calibration.

We believe that two steps should be initiated: (1) the National Bureau of Standards should increase their effort in this area,

particularly with respect to extending the lower wavelength limit of the strip filament lamp and developing the technique of using synchrotron radiation as a standard and providing absolutely calibrated photodiodes; (2) one of the NASA centers should establish a standards laboratory for the purpose of improving the techniques and providing a facility for detector calibration.

Solar-blind photodiodes with stable quantum efficiency might prove superior to

photoionization cells as secondary detector standards.

Acknowledgement

I wish to thank Dr. Henry Kostkowski and Dr. Robert Madden of the National Bureau of Standards for helpful discussions in the preparation of this presentation.

N70-36758

Optical Research Facilities

William R. Pershing
USAF Avionics Laboratory

The Optical Science Facility of the U.S. Air Force Avionics Laboratory (Wright-Patterson Air Force Base) is an optical laboratory of 18,000 square feet, equipped for precision optical measurements. This laboratory provides a capability for research and for the development of techniques applicable to the design, fabrication, and evaluation of optical components and optical systems ranging in size up to 100 inches in diameter.

The facility is centered around a large, 100-inch-diameter, optical collimator, including the necessary instrumentation and equipment for conducting extensive research investigation and analyses of large diameter optics and optical systems. The collimator diameter must be equal to or greater than the optics being evaluated in order to provide full illumination of the aperture and formation of the corresponding target image. The 100-inch collimator is the largest of its kind in the United States and provides a capability hithertofore nonexistent.

Qualified personnel (including advanced degree students), from all branches of the Defense Department, NASA, industry, and educational institutions, may utilize the facility when needed in connection with programs deemed to be in the best interest of the government.

The 100-inch-diameter collimator is housed in a steel vacuum chamber as shown in figure 1. The chamber has an exterior diameter of 14 feet, is 150 feet measured vertically from top to bottom, and is bisected by a horizontal section 20 feet in diameter by 50 feet long. The entire chamber, weighing 360 tons, is supported by a three-axis, air-

filled, rubber, isolation mounting system, designed to reduce the effects of mechanical vibration and seismic shock, which can effectively degrade the collimator capability.

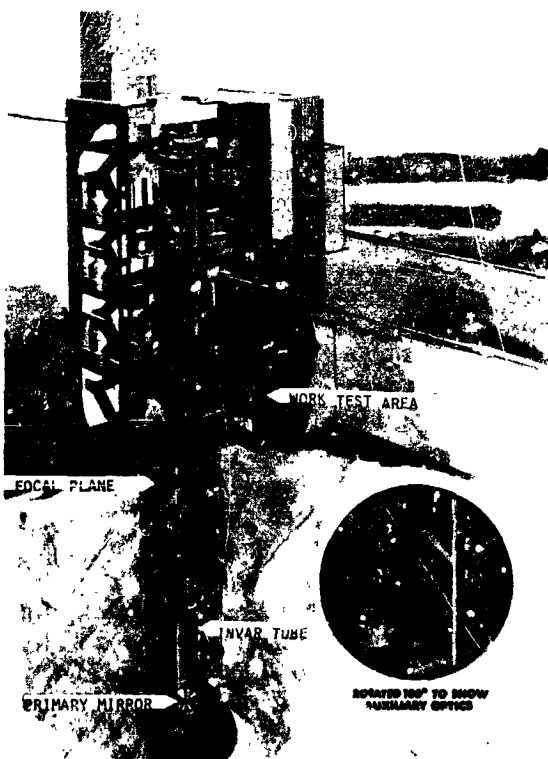


Figure 1. The 100-inch collimator vacuum chamber.

Temperature around the collimator is controlled to $\pm 1/2^\circ\text{F}$. To avoid the degrading optical effects caused by air currents, it is possible to evacuate the 33,000-cubic-foot chamber to an equivalent atmospheric altitude of 270,000 feet (5×10^{-3} torr) in

hours. A mechanical vacuum pump system is used. A circular door 20 feet in diameter provides access to the horizontal chamber. A personnel door and additional ports are located at various operating positions on the vacuum chamber. An Invar tube, 10 feet in diameter and 55 feet long, is mounted in the lower section of the vacuum chamber. The primary mirror, in its mounting cell, is supported at the bottom of the Invar tube.

The primary mirror is 103 inches in diameter by 12 inches thick and has a focal length of 601 inches. Its weight is approximately 7500 pounds. Fabrication of the mirror blank required 10 months. Twelve pieces of fused silica were fused together to form the mirror blank, which was, at the time of fabrication, the largest piece of fused silica ever made. The grinding, polishing, and final finishing of the primary mirror required 22 months. The mirror is supported in its mounting cell by an arrangement of 50 thermal isolation pads, each connected to a counterbalance system having a 10 to 1 ratio. Near the top of the Invar tube, an auxiliary structure bolted to the tube supports the accessory optics, targets, and light source. Two locations for the auxiliary structure provide in an optional alternate arrangement either a nominal 600-inch, 1200-inch, or 2000-inch focal length collimator.

Ring elevators are located in both the upper and lower vertical sections of the vacuum chamber, thus providing the capability to transfer the collimator assembly from the lower to the upper section of the vacuum chamber. In the upper position, the mirror in its mount would be inverted at the top of the Invar tube and supported by the counterbalance system. Relocation of the accessory optics-target-light-source auxiliary package would provide a capability to evaluate an upward-looking optical system.

It is not anticipated that the collimator will be utilized in the upper chamber unless an urgent requirement exists to determine the effects of gravity upon an optical system. Some measure of such effects could be evaluated from successive upward and downward positioning of the optical system.

The ring elevators can be positioned at selected levels within the vacuum chamber to serve as working platforms to hold instrumentation and the personnel making various measurements.

The design of the facility will allow expansion of the collimator to a maximum diameter of 120 inches by replacing the present mirror and accessory optics.

A large test cart, mounted on rails, provides support for the optical device to be evaluated. Precision rails allow accurate successive relocation of the optics over the collimator. Instrumentation for a remote read-out capability will be utilized when operation in the vacuum condition is required.

Additional facilities supporting the large optics area include:

1. A 60-inch-diameter precision rotary table for centering optical elements and assembling elements into an optical system.
2. A vacuum coating chamber that can deposit various types of coatings on optical surfaces up to 100 inches in diameter.
3. A future planned capability will be a precision aspheric generating and polishing machine that will handle up to 100-inch diameter optics. Provisions are included for evaluation of the surface being generated or polished by supporting a mirror and suitable instrumentation over the machine on a superstructure integral with the vibration-isolated seismic block supporting the machine.

For programs concerning medium size optics, a large David Mann optical bench and a collimator with a 30-inch aperture and a focal length of 20 feet are mounted on a vibration-isolated seismic block. A vertical test camera is also mounted in a position to utilize the 30-inch-diameter collimator on a share basis with the optical bench.

Programs for smaller optics having a maximum 16-inch diameter and focal length up to 6 feet (dependent on lens quality) can utilize two 14-foot-focal-length collimators with 16-inch apertures. One is a diffraction-limited collimator with a test camera; the second collimator is mounted with both an

optical bench and a test camera for small optics (up to 8 inches in diameter).

Measurement of distortion on mapping lenses may be accomplished with a lens bench-mounted on a seismic block with 19 small collimators presenting a 120-degree field of targets, which can be recorded through the mapping lens on a glass plate. The imaged position of the targets may then be measured on a comparator to determine the distortion in the lens.

A precision nodal slide bench coupled with a 168-inch-focal-length collimator is instrumented for performing image analysis of lenses by employing the transfer function concept.

The illumination characteristics of lenses can be measured with an illumination analyzer, which utilizes an 8-inch, collimated, light source with integrating sphere photomultiplier.

Optical glass blanks to 24 inches in diameter may be measured for index variation to 1×10^{-6} . A white-light interferometer is used for measuring physical thickness, which is then compared to optical thickness measured by a laser interferometer.

A well-equipped darkroom is available for processing films and plates. Other major instruments available include: Gaertner spectrometer, Bausch and Lomb recording spectrophotometer, Mann comparator, and Zeiss gauge block interferometer.

Instrumentation for optical surface evaluation, laser light sources, and assorted equipment common to optics laboratories is also located in the facility. A small shop is available for minor repairs, making parts for lens mounts, and quick-fix items needed in the facility. Larger mechanical jobs are done in shops nearby. Personnel using the optics facility have access to the computer facility located on the base.